

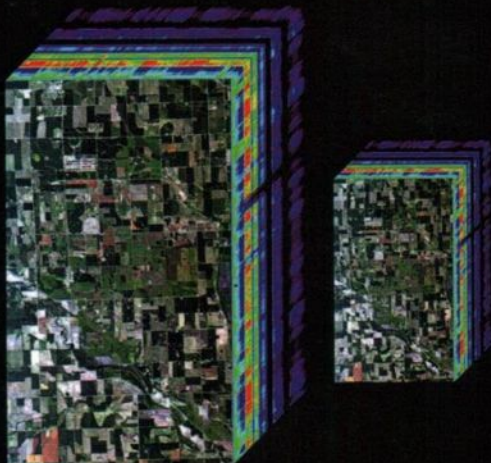
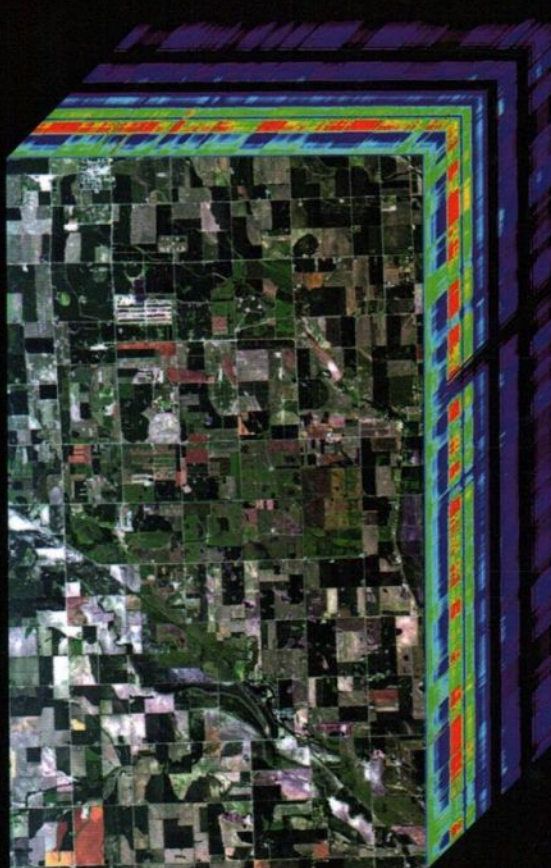
Hyperspectral Imaging Remote Sensing

Physics, Sensors, and Algorithms

Dimitris Manolakis

Ronald Lockwood

Thomas Cooley



Hyperspectral Imaging Remote Sensing

A practical and self-contained guide to the principles, techniques, models, and tools of imaging spectroscopy. Bringing together material from essential physics and digital signal processing, the book covers key topics such as sensor design and calibration, atmospheric inversion and model techniques, and processing and exploitation algorithms. Readers will learn how to apply the main algorithms to practical problems, how to choose the best algorithm for a particular application, and how to process and interpret hyperspectral imaging data. A wealth of additional materials accompany the book online, including example projects and data for students, and problem solutions and viewgraphs for instructors.

This is an essential text for senior undergraduate and graduate students looking to learn the fundamentals of imaging spectroscopy, and an invaluable reference for scientists and engineers working in the field.

Dimitris G. Manolakis is a Senior Member of Technical Staff at MIT Lincoln Laboratory in Lexington, Massachusetts. He is the co-author of *Applied Digital Signal Processing* (Cambridge University Press, 2011), and has taught at various institutions including Northeastern University, Boston College, and Worcester Polytechnic Institute. He is an IEEE Fellow, and in 2013 he received the IEEE Signal Processing Society Education Award.

Ronald B. Lockwood is a Member of Technical Staff at MIT Lincoln Laboratory. He previously worked at the Air Force Research Laboratory, where he developed imaging spectrometers for both space-based and airborne applications. He has also developed vicarious calibration techniques in collaboration with colleagues at the University of Arizona and the NASA Goddard Space Flight Center.

Thomas W. Cooley is the Air Force Research Laboratory Senior Scientist for Space Situational Awareness, and has made significant contributions to the fields of atmospheric compensation and spectral data analysis. He developed the ARTEMIS sensor program, which was successfully launched in 2009, and he has published over 70 research papers.

“The authors have done a masterful job of integrating and presenting the diverse subjects that form the foundation of the field of hyperspectral imaging and applications. This comprehensive textbook will clearly become one of the standard references for all who wish to learn about both fundamentals and advanced applications in this important field.”

Charles Bachmann, Rochester Institute of Technology

“An extraordinarily comprehensive treatment of hyperspectral remote sensing by three of the field’s noted authorities. An indispensable reference for those new to the field and for the seasoned professional.”

Ronald G. Resmini, George Mason University

Hyperspectral Imaging Remote Sensing

Physics, Sensors, and Algorithms

DIMITRIS G. MANOLAKIS

Massachusetts Institute of Technology
Lincoln Laboratory

RONALD B. LOCKWOOD

Massachusetts Institute of Technology
Lincoln Laboratory

THOMAS W. COOLEY

CAMBRIDGE

UNIVERSITY PRESS

University Printing House, Cambridge CB2 8BS, United Kingdom

Cambridge University Press is part of the University of Cambridge.

It furthers the University's mission by disseminating knowledge in the pursuit of education, learning and research at the highest international levels of excellence.

www.cambridge.org

Information on this title: www.cambridge.org/9781107083660

© Cambridge University Press 2016

This publication is in copyright. Subject to statutory exception and to the provisions of relevant collective licensing agreements, no reproduction of any part may take place without the written permission of Cambridge University Press.

First published 2016

Printed in the United Kingdom by TJ International Ltd. Padstow Cornwall

A catalogue record for this publication is available from the British Library

Library of Congress Cataloging-in-Publication Data

Names: Manolakis, Dimitris G., author. | Lockwood, Ronald B., author. | Cooley, Thomas W., author.

Title: Hyperspectral imaging remote sensing : physics, sensors, and algorithms / Dimitris G. Manolakis (Massachusetts Institute of Technology, Lincoln Laboratory), Ronald B. Lockwood (Massachusetts Institute of Technology, Lincoln Laboratory), Thomas W. Cooley

Description: Cambridge, United Kingdom : Cambridge University Press, 2016.

Identifiers: LCCN 2016025909 | ISBN 9781107083660 (hardback) | ISBN 1107083664 (hardback)

Subjects: LCSH: Multispectral imaging. | Remote-sensing images. | Imaging systems. | Image processing—Digital techniques.

Classification: LCC TR267.733.M85 M36 2016 | DDC 771—dc23

LC record available at <https://lccn.loc.gov/2016025909>

ISBN 978-1-107-08366-0 Hardback

Additional resources for this publication at www.cambridge.org/9781107083660

Cambridge University Press has no responsibility for the persistence or accuracy of URLs for external or third-party internet websites referred to in this publication, and does not guarantee that any content on such websites is, or will remain, accurate or appropriate.

To Anna
DGM

To Susan
RBL

To Claire, Kate, and Mary
TWC

Contents

<i>Preface</i>	<i>page xi</i>	
1	Introduction	1
1.1	Introduction	1
1.2	Infrared Sensing Phenomenology	3
1.3	Hyperspectral Imaging Sensors	8
1.4	Data Preprocessing	15
1.5	Data Exploitation Algorithms	19
1.6	Applications of Imaging Spectroscopy	25
1.7	History of Spectral Remote Sensing	28
1.8	Summary and Further Reading	33
1.9	Book Organization	33
2	The Remote Sensing Environment	36
2.1	Electromagnetic Radiation	36
2.2	Diffraction and Interference	41
2.3	Basic Radiometry	50
2.4	Radiation Sources	55
2.5	Quantum Mechanical Results	61
2.6	Spectral Line Shapes	76
2.7	Atmospheric Scattering Essentials	84
2.8	Optical Thickness	95
2.9	Properties of the Atmosphere	102
2.10	Summary and Further Reading	114
3	Spectral Properties of Materials	117
3.1	Introduction	117
3.2	Geometrical Description	118
3.3	Directional Emissivity	126
3.4	Volume Scattering of Materials	128
3.5	Elements of Mineral Spectroscopy	131
3.6	Organic Spectroscopy	144
3.7	Man-Made Materials	148

3.8	Long Wave Infrared Spectra	150
3.9	Summary and Further Reading	151
4	Imaging Spectrometers	154
4.1	Telescopes	155
4.2	Imaging Spectrometer Common Concepts	161
4.3	Dispersive Imaging Spectrometer Fundamentals	171
4.4	Dispersive Imaging Spectrometer Designs	195
4.5	Interference Imaging Spectrometer Fundamentals	209
4.6	Data Acquisition with Imaging Spectrometers	222
4.7	Summary and Further Reading	224
5	Imaging Spectrometer Characterization and Data Calibration	228
5.1	Introduction	228
5.2	Application of the Measurement Equation	229
5.3	Spectral Characterization	231
5.4	Radiometric Characterization	238
5.5	Spatial Characterization	261
5.6	Advanced Calibration Techniques	262
5.7	Error Analysis	263
5.8	Radiometric Performance Modeling	269
5.9	Vicarious Calibration	280
5.10	Summary and Further Reading	292
6	Radiative Transfer and Atmospheric Compensation	295
6.1	Radiative Transfer	295
6.2	General Solution to the Radiative Transfer Equation	303
6.3	Modeling Tools of Radiative Transfer	312
6.4	Reflective Atmospheric Compensation	322
6.5	Estimating Model Parameters from Scene Data	330
6.6	Reflective Compensation Implementation	344
6.7	Atmospheric Compensation in the Thermal Infrared	351
6.8	Summary and Further Reading	358
7	Statistical Models for Spectral Data	360
7.1	Univariate Distributions – Variance	360
7.2	Bivariate Distributions – Covariance	363
7.3	Random Vectors – Covariance Matrix	367
7.4	Multivariate Distributions	371
7.5	Maximum Likelihood Parameter Estimation	383
7.6	Statistical Analysis of Hyperspectral Imaging Data	387
7.7	Gaussian Mixture Models	394
7.8	Summary and Further Reading	403

8	Linear Spectral Transformations	406
8.1	Introduction	406
8.2	Implications of High-Dimensionality	408
8.3	Principal Components Analysis: Theory	411
8.4	Principal Components Analysis: Application	421
8.5	Diagonalizing Two Different Covariance Matrices	424
8.6	Maximum Noise Fraction (MNF) Transform	428
8.7	Canonical Correlation Analysis (CCA)	429
8.8	Linear Discriminant Analysis	432
8.9	Linear Spectral-Band Estimation	437
8.10	Summary and Further Reading	441
9	Spectral Mixture Analysis	443
9.1	Spectral Mixing	443
9.2	The Linear Mixing Model	446
9.3	Endmember Determination Techniques	451
9.4	Fill-Fraction Estimation Techniques	453
9.5	The Method of Least Squares Estimation	454
9.6	Least Squares Computations	463
9.7	Statistical Properties of Least Squares Estimators	466
9.8	Generalized Least Squares Estimation	468
9.9	Maximum Likelihood Estimation	470
9.10	Regularized Least Squares Problems	471
9.11	Consequences of Model Misspecification	475
9.12	Hypotheses Tests for Model Parameters	477
9.13	Model Selection Criteria	480
9.14	Variable Selection in Linear Signal Models	482
9.15	Linear Spectral Mixture Analysis in Practice	487
9.16	Summary and Further Reading	492
10	Signal Detection Theory	494
10.1	A Simple Decision-Making Problem	494
10.2	Elements of Statistical Hypotheses Testing	496
10.3	The General Gaussian Detection Problem	503
10.4	Gaussian Detectors in the Presence of Unknowns	511
10.5	Matched Filter and Maximization of Deflection	517
10.6	Performance Analysis of Matched Filter Detectors	522
10.7	Detectors for Signals in Subspace Clutter and Isotropic Noise	533
10.8	Eigenvector Matched Filters	539
10.9	Robust Matched Filters	541
10.10	Adaptive Matched Filter Detectors	547
10.11	Summary and Further Reading	548

11	Hyperspectral Data Exploitation	551
11.1	Target Detection in the Reflective Infrared	551
11.2	Target Detection Performance Assessment	570
11.3	False Alarm Mitigation and Target Identification	577
11.4	Spectral Landscape Classification	581
11.5	Change Detection	586
11.6	Unique Aspects of Spectral Exploitation in the Thermal Infrared	591
11.7	Remote Sensing of Chemical Clouds: Physics	595
11.8	Remote Sensing of Chemical Clouds: Algorithms	605
11.9	Summary and Further Reading	620
Appendix	Introduction to Gaussian Optics	621
A.1	The Optical Path	621
A.2	Ideal Image Formation	624
A.3	The Paraxial Approximation	628
A.4	The Limiting Aperture	633
A.5	Example: The Cooke Triplet	640
A.6	Afocal Systems	642
A.7	Aberration Theory	644
A.8	Summary and Further Reading	652
	<i>Bibliography</i>	654
	<i>Index</i>	678

Color plate section between pages 338 and 339.

Preface

Τῆς παιδείας τὴν μὲν ρῖζαν εἶναι πικράν, τὸν δὲ καρπὸν γλυκύν.

The roots of education are bitter but the fruit is sweet.

Isocrates, 436-338 BC
Greek orator and rhetorician

Sir Isaac Newton invented the first monochromator with two slits and a prism in 1666, and is largely credited with founding the field of spectroscopy based on his publication of *Opticks* in 1704. Over a century after Newton's optics experiments, Joseph von Fraunhofer made the significant advance in the field with the use of a diffraction grating to replace the prism as the dispersion element. His ground-breaking studies of emissions from the sun, in which he cataloged the series of absorption features in the solar spectrum that bear his name, established the discipline of spectral remote sensing. An early demonstration of the power of spectroscopy for identification was when Joseph Foucault showed that two of the Fraunhofer lines corresponded to sodium emission. The precision afforded by the diffraction grating facilitated the field of spectroscopy becoming a mainstay for the fields of chemistry, astronomy and, in recent decades, remote sensing. Imaging spectroscopy is a relatively recent discipline which has been made possible by progress in several technology areas including detectors, optical design, optical components, atmospheric radiative transfer, and computer processing, to name just a few. While spectroscopy and imaging techniques have advanced independently, imaging spectroscopy is the merger of both, using spectroscopic techniques to form a multi-band-imaged scene or "hyper-spectral" image.

The hallmark of imaging spectroscopy is the utilization of spectroscopic techniques in which measurements can be used for unambiguous direct and indirect identification of surface materials and atmospheric trace gases. The measurement of the relative concentrations of materials and the ability to distinguish between subtle absorption features of differing materials for a two-dimensional scene are examples of imaging spectroscopy.

The main objective of this book is to present the fundamentals of remote sensing imaging spectroscopy from the perspective of the user. There is a strong interconnection between foundational phenomenology, sensing technology, atmospheric propagation effects, and exploitation algorithms. Successful application of remote sensing imaging spectroscopy requires a working knowledge and fundamental understanding of all

these aspects. Providing the reader this foundation is the objective of this book. Imaging spectroscopy is also used by meteorologists and atmospheric scientists to directly characterize the properties of the atmosphere. Our focus is on the use of imaging spectrometer data to identify attributes of the surface.

The book covers material from different disciplines ranging from physics, optics, spectroscopy, linear algebra, statistics, and signal processing. Integrating material from such disparate areas is not easy, but we have tried to provide smooth and coherent coverage. The reader is expected to have a basic background in physics, chemistry, electrical engineering, or a related field. We attempt to proceed by introducing concepts from first principles to provide both foundational ideas and consistent nomenclature throughout the text.

We have tried to provide balanced coverage of topics of general interest. However, the selection and emphasis has been, we hope only slightly, biased by our own experience and backgrounds. We have selected material and references to reflect fundamental work and provide useful and practical techniques, insights, and applications. We apologize for any omissions or oversights of areas which may be sought by the reader, but the foundations found throughout the book can be applied to a variety of applications. We provide seminal bibliographic citations to provide historical context for the evolution of the technology both from our direct experience in the field and through judicious examination of the literature.

Special thanks go to Eric Truslow and Mike Piper for their cautious and thorough review, helping with figures, and preparing the solutions manual. Michael Chriss, Steve Miller, and Kurt Thome lent their considerable expertise in reviewing several chapters. Their contributions are gratefully acknowledged.

Also, RLB was privileged to study atomic physics under the guidance of Chun C. Lin and in close collaboration with L. Wilmer Anderson and James Lawler at the University of Wisconsin at Madison. The presentation in Chapter 4 is extensively based on the course in applied optics that was part of the curriculum there in the late 1980s, co-developed by Edward Miller and Frederick Roesler. In particular, the instrumental spectroscopy formalism here parallels Roesler's notes and has been adapted for the modest performance of an imaging spectrometer in comparison to the instruments used in, for example, atomic and molecular physics or astrophysics. Fred Roesler collaborated with Pierre Jacquinot early in his career, and his thinking, and therefore this presentation, was heavily influenced by the French spectroscopy school.

RBL would also like to thank his parents, Robert and Sharon Lockwood. Both are educators and farmers who instilled a keen interest in the natural world in each of their children, leading to careers in science and mathematics. Having raised us on a family farm in West Texas, they also ensured that we all have healthy work ethics! This book is a result of their support and encouragement.

Most importantly, we must thank our families for their patience and enduring support for this project. No undertaking of this magnitude and duration is accomplished without a foundation of support to see it through. Anna, Susan, and Mary know the effort and time invested in this undertaking, and each is a pillar of forbearance for the time we have taken to complete this text. We are grateful for their wisdom, support, and endurance.

This undertaking required significant encouragement from our families, friends, and colleagues who recognized the opportunity to provide this compilation for the broader community of scientists, researchers, and students entering the field. We are grateful for the many voices of encouragement throughout this project. We wish also to thank the team at CUP, including Phil Meyler and Heather Brolly, who have patiently awaited the completed manuscript and provided valuable comments and guidance throughout. We hope you find benefit from our enterprise.

Acknowledgments

We have been fortunate to build upon the work of many other researchers, and to have access and help from many colleagues leading up to and through this project. We would like to thank the many scientists and researchers who have contributed directly and indirectly to this undertaking, and specifically want to thank: Gail Anderson, Peter Armstrong, Gregory Berthiaume, Stuart F. Biggar, William Blumberg, Rebecca N. Breiding, Michael Brueggeman, Thomas G. Chrien, James Dodd, David Driscoll, Richard Dunn, Janet Fender, James Gardner, Mary Ann Glennon, Steven Golowich, Peggy Grigsby, Lynn Hatfield, David Hardy, John Jacobson, Angela Kim, Steven Lipson, Joaquin Mason, Karis W. Miles, Dan Mooney, Richard Nadile, Sidi Niu, Martin Pilati, Ryan M. Pospisal, C. Richard Quade, Frederick L. Roesler, Stephanie Schieffer, John Schummers, Vittala Shettigara, Krista Steenbergen, Stanley Straight, Johnny L. Touchstone, Klaes Wandland, Christopher J. Ward, Andrew Weisner, Benjamin Worker, and Randall Zywicki.

1 Introduction

This chapter provides an introduction to the basic principles of hyperspectral remote sensing. The main objective is to explain how information about the earth's surface is conveyed to a remote hyperspectral imaging sensor, which are the key factors determining the nature and quality of the acquired data, and how the data should be processed to extract meaningful information for practical applications. By definition, hyperspectral imaging systems collect co-aligned images in many relatively narrow bands throughout the ultraviolet, visible, and infrared regions of the electromagnetic spectrum.

1.1 Introduction

The term “remote sensing” has several valid definitions. In the broadest sense, according to Webster’s dictionary, remote sensing is “the acquisition of information about a distant object without coming into physical contact with it.” For our purposes, remote sensing deals with the acquisition, processing, and interpretation of images, and related data, obtained from aircraft and satellites that record the interaction between matter and electromagnetic radiation.

The detection of electromagnetic radiation via remote sensing has four broad components: a source of radiation, interaction with the atmosphere, interaction with the earth’s surface, and a sensor (see Figure 1.1). The link between the components of the system is electromagnetic energy transferred by means of radiation.

Source The source of electromagnetic radiation may be natural, like the sun’s reflected light or the earth’s emitted heat, or man-made, like microwave radar. This leads to a classification of remote sensing systems into active and passive types. *Active systems* emit radiation and analyze the returned signal. *Passive systems* detect naturally occurring radiation either emitted by the sun or thermal radiation emitted by all objects with temperatures above absolute zero. With active systems, like microwave radar, it is possible to determine the distance of a target from the sensor (range); passive systems cannot provide range information.

Atmospheric interaction The characteristics of the electromagnetic radiation propagating through the atmosphere are modified by various processes, including absorption and scattering. This distortion is undesirable and requires correction if we wish to study the earth’s surface, or desirable if we wish to study the atmosphere itself.

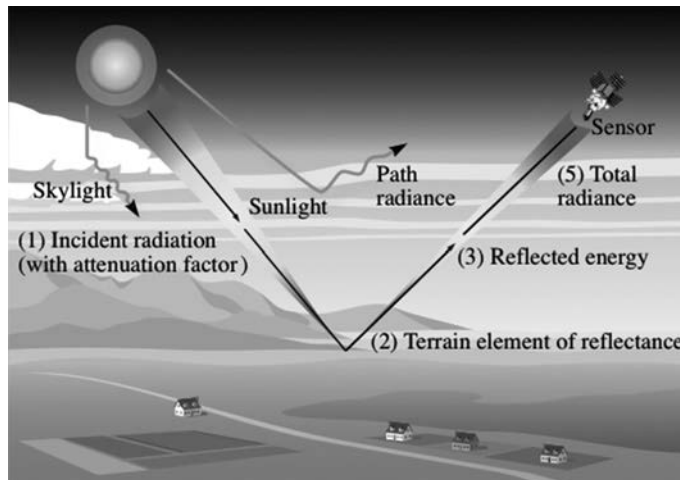


Figure 1.1 Pictorial illustration of how the atmosphere, the solar illumination, and the spectral response of the sensor affect the relationship between the observed radiance spectrum and the wanted reflectance spectrum of the ground resolution cell. (A black and white version of this figure will appear in some formats. For the color version, please refer to the plate section.)

Earth's surface interaction The amount and spectral distribution of radiation emitted or reflected by the earth's surface depend upon the characteristics of the involved "target" materials. The interaction between matter and electromagnetic energy is determined by (a) the physical properties of the matter, and (b) the wavelength of electromagnetic energy that is remotely sensed.

Sensor The electromagnetic radiation, which has interacted with the surface of the earth and the atmosphere and has undergone some form of spectral discrimination as it is transmitted through a spectral detector, is recorded by an electro-optical detector which converts electromagnetic radiation into an electrical signal directly related to the radiation in a particular spectral band from the scanned scene. The electrical signal is amplified, converted to digital data, and organized into a data structure for further processing.

Once the data have been collected by the sensor, they must be analyzed in real time or offline. However, before we start talking about analysis techniques, we should understand what information about the target material is conveyed by the reflected or emitted electromagnetic radiation and how this information has been modified by the sensor.

The radiation received by the sensor can be measured at different locations of a scene, over a range of wavelengths, and sometimes at different times (see Figure 1.2). This leads to rich data sets which can be organized and explored in many different ways. We consider electro-optical systems that include the visible, near infrared, and thermal infrared regions of the electromagnetic spectrum. We are interested in remote sensing imaging systems designed to form a two-dimensional representation of the two-dimensional distribution of radiant energy across the target at one or multiple spectral bands. Traditionally, data from a single wavelength band are used to form a digital image, where each pixel represents the radiant energy of a corresponding

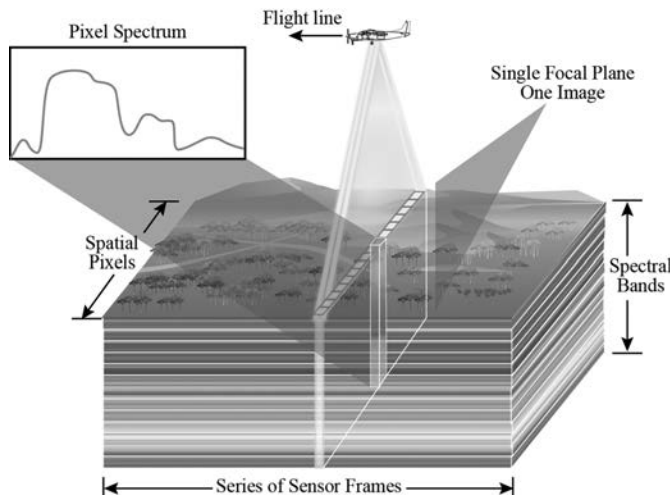


Figure 1.2 Principle of hyperspectral imaging sensing. The resulting “data cube” can be viewed as a set of co-registered images at multiple wavelength regions or as a set of spectra corresponding to each pixel of the image. (A black and white version of this figure will appear in some formats. For the color version, please refer to the plate section.)

ground element area. Each individual image can then be processed and analyzed using established image processing techniques that exploit geometrical or shape information. However, if we collect radiation measurements at different wavelength bands for the same spatial sample, and arrange them in a vector, we can analyze the resulting “spectral” data using multivariate statistical techniques.

In the remainder of this chapter, we discuss the basic principles underlying each part of the remote sensing system, we outline the key ideas of data preprocessing and exploitation techniques, and we summarize some common applications.

1.2 Infrared Sensing Phenomenology

The main sources of radiation in passive remote sensing is the electromagnetic radiation emitted by the sun and the self-emission of objects in the scene due to their temperature. Electromagnetic radiation is the means by which electromagnetic energy is propagated in the form of waves.

Electromagnetic waves are characterized by their location within the electromagnetic spectrum. The division of the electromagnetic spectrum into different regions, such as visible, infrared, or microwave, has more to do with the different methods used for sensing it rather than the nature of the radiation itself. Figure 1.3 shows the regions used in electro-optical remote sensing and the typical applications for each region.

1.2.1 Sources of Infrared Radiation

All objects with temperatures greater than absolute zero emit radiation whose amount changes as a function of wavelength. An object that absorbs all incident energy, converts

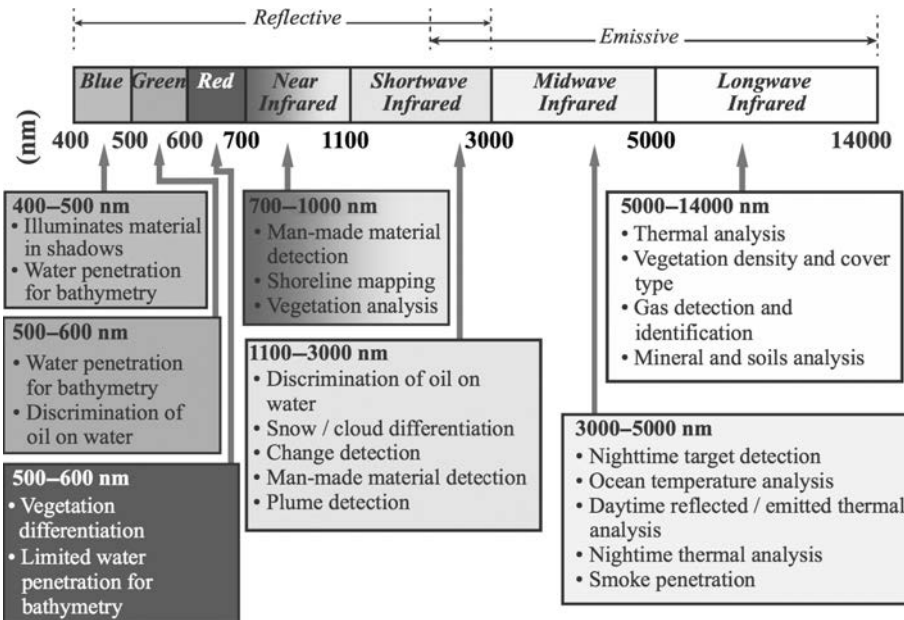


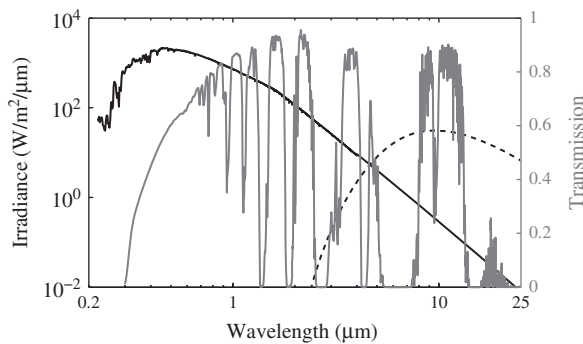
Figure 1.3 Typical examples of spectral information present at different spectral regions of the electromagnetic spectrum for different applications.

it to heat energy, and transforms the heat back into radiant energy at the maximum possible rate allowed by thermodynamic laws, is a perfect thermal emitter known as a *blackbody*. The spectral radiant emittance of a blackbody is given by Planck's law.

For our present purpose, the spectral radiant exitance, the power per unit area emitted by the sun, as seen from above the earth's atmosphere, can be approximated by a blackbody curve at a temperature of 5800 K. Thus the sun, with a temperature of 5800 K, will have a maximum emittance at a wavelength of $0.50 \mu\text{m}$. In contrast, the earth's ambient temperature on a warm day, due largely to heating by the sun, is about 300 K or 27°C and the maximum spectral radiant emittance from earth's features occurs at a wavelength of about $9.7 \mu\text{m}$. This radiation is known as "thermal infrared" energy because it is related to terrestrial heat.

In the visible and near infrared regions of the electromagnetic spectrum we study the radiation from the sun as it is modified by the earth's atmosphere and surface. In the thermal infrared region we study the radiation emitted by the earth's atmosphere and surface. The dividing line between reflective and emissive wavelengths is approximately $4 \mu\text{m}$. Reflective energy predominates below this wavelength and emissive energy predominates above it. This difference in the nature of radiation also has profound effects on the sensors used in the reflective and emissive regions of the electromagnetic spectrum.

Figure 1.4 shows the contrast between the solar spectral irradiance and the spectral irradiance from a blackbody at 300 K. Irradiance will be discussed in more detail in Chapter 2, but it describes the spectral energy per second that flows through a real or

**Figure 1.4**

Irradiance and atmospheric absorption for the wavelength range 0 to 25 μm . The black curve is the exoatmospheric spectral irradiance and the dashed curve is the spectral irradiance from a blackbody at a temperature of 300 K with both referenced to the left vertical scale. The gray curve is the atmospheric transmission referenced to the right vertical scale. Note the presence of atmospheric windows in the thermal wavelength regions 3 to 5 μm and 8 to 14 μm .

imaginary aperture of unit area. The two curves cross at slightly longer than the 4 μm dividing line defined above.

1.2.2 Atmospheric Propagation

All radiation observed by remote sensing systems passes through some distance or path length of atmosphere, which has a profound effect on its radiant energy and spectral composition. The main mechanisms causing these effects are atmospheric scattering and absorption. Atmospheric *scattering* is the unpredictable diffusion of radiation by particles in the atmosphere. Unlike scattering, atmospheric absorption results in the effective loss of energy from the radiation field as it is converted to other forms.

The transmission curve, illustrated in Figure 1.4, also defines the spectral regions where remote sensing can occur. Aerosol scattering and molecular absorption limit the transmission range at the shortest wavelengths. The spectral region from about 0.35 to 2.5 μm defines the reflective range that is dominated by solar illumination and where the atmosphere is broadly transmissive. The large absorption features throughout the 0.2 to 25 μm range, where light transmission is severely attenuated or completely absorbed, are largely due to absorption by water although minor constituents such as carbon dioxide play an import role as well.

The regions of the electromagnetic spectrum in which atmospheric absorption is low are called *atmospheric windows* and it is through these “windows” that remote sensing of the earth’s surface takes place. We note that the peak of the solar spectrum coincides with the visible atmospheric window at 0.4–0.9 μm , whereas the peak of emitted “heat” from the earth extends through the atmospheric windows at 3–5 μm and 8–14 μm . The important point to note from Figure 1.4 is that *remote sensing of radiation is not possible if there is not sufficient energy from the radiation source within the atmospheric windows.*

1.2.3 Reflectance and Emissivity Spectra

When electromagnetic radiation interacts with earth's surface, various fractions of the energy are reflected, absorbed, and/or transmitted. In general, these fractions vary as a function of wavelength depending on the type and condition of the surface material. Therefore, it is important to describe those variations and investigate whether they can be used to characterize different materials.

In the reflective part of the spectrum, where solar illumination predominates, the reflectance properties of the earth's features are used to describe the surface characteristics. Depending on the surface roughness, there are two general classes of reflectors. *Specular* reflectors are flat surfaces that act like mirrors; that is, the angle of reflection equals the angle of incidence. In contrast, *diffuse* or *Lambertian* reflectors are rough surfaces that reflect uniformly in all directions. The behavior of real surfaces, which is between these two cases, is dictated by the surface's roughness in relation to the wavelength of the incident electromagnetic radiation.

In remote sensing, we are primarily interested in diffuse reflectance because this is the dominant type of reflectance for most materials, although there are exceptions such as water. The reflectance characteristics of an earth surface material may be quantified by its *reflectance spectrum*, which measures the percentage of incident radiation, typically sunlight, that is reflected by a material as a function of the wavelength of the radiation. Reflectance spectra are measured by special instruments called reflectometers in the laboratory or the field. Figure 1.5 shows typical reflectance spectra of green vegetation, dry vegetation, and soil. Dips of the spectral curve represent absorption of the incident radiation and are known as *absorption features*. In contrast, upward excursions

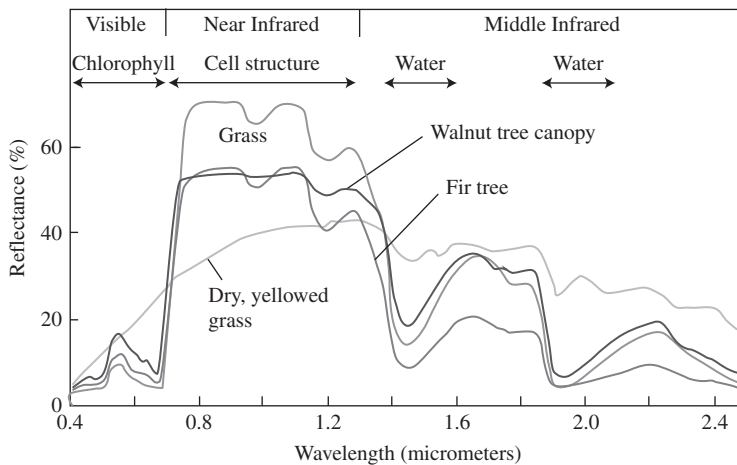


Figure 1.5

Typical spectral reflectance curves for different types of green and yellowed (dry) vegetation. The spectral curves for green vegetation at different regions are shaped by the components shown at the top.

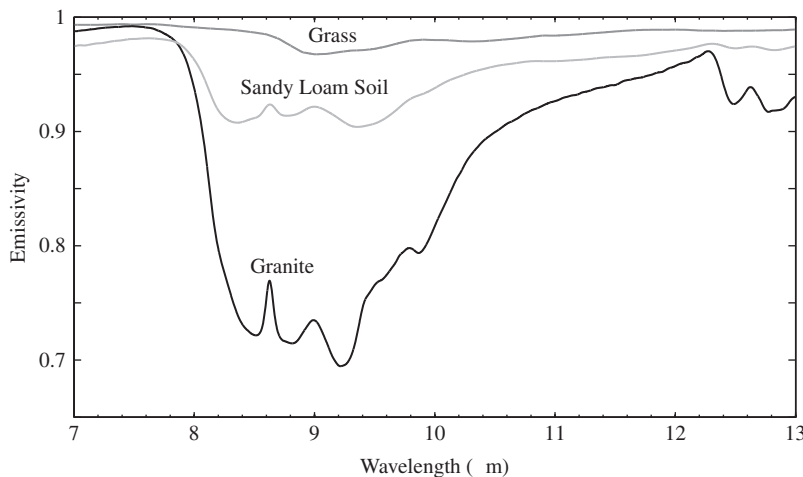


Figure 1.6 Typical emissivity spectra of grass, granite, and sandy loam soil materials in the thermal infrared window from 7 to $13\ \mu\text{m}$.

are called *reflectance peaks*. These spectral features provide valuable information for the identification of different materials.

Real materials are not perfect blackbodies, but instead emit radiation in accordance with their own characteristics. The ability of a material to emit radiation can be expressed as the ratio of its radiant emittance at a given temperature to the radiant emittance of a blackbody at the same temperature. This ratio is known as the *spectral emissivity* of the material. The plot of emissivity as a function of wavelength is called the *emissivity spectrum* of a material. Figure 1.6 shows examples of emissivity spectra with unique spectral features; the data were obtained from the ASTER spectral library described by Baldridge et al. (2009a).

Radiance in the thermal infrared, the mid-wave infrared and the long-wave infrared (MWIR and LWIR) is determined by both the emittance and temperature of the materials. Variations in temperature can cause both large radiance variations and large spectral variations at the input of a remote sensor. Furthermore, it is not possible to measure separately the spectral emissivity and temperature using hyperspectral sensing alone. Emissivities of most materials vary between 0.8 and 0.95 in the 8 to $14\ \mu\text{m}$ thermal IR window. Thermal emission is generally the dominant term; the variations caused by variations in spectral emittance are small by comparison. This causes additional variability in the statistics of target and background clutter, which makes detection and discrimination in the thermal infrared more challenging.

In conclusion, the signal of interest in spectral remote sensing applications, that is, the information-bearing signal, is the reflectance or emissivity spectrum of the imaged material. The details and relationships between spectral reflectance, emittance, and temperature will be fully developed in subsequent chapters.

1.3

Hyperspectral Imaging Sensors

Hyperspectral sensors, more properly known as imaging spectrometers, collect simultaneously digital images in many relatively narrow, contiguous and/or noncontiguous spectral bands of the ultraviolet, visible, and infrared regions of the electromagnetic spectrum. The collection of spectral reflectance and emittance information in hundreds of spectral bands for each spatial location requires the design of special sensors. Hyperspectral imaging sensors consist of a scanning mechanism, an imaging system, and a spectrometer. Figure 1.7 illustrates the basic elements of a hyperspectral data collection sensor. All imaging spectrometers require some sort of scanning and pointing system in order to accumulate data and assign position coordinates. The imaging system, or fore optic, collects and images radiant energy from a location on the earth's surface (spatial sampling) with a certain spatial resolution. The image plane of the fore optic becomes the optical input, or the object, for the spectrometer. Finally, the spectrometer measures the radiant energy at a number of spectral bands (spectral resolution) for each spatial sample with a certain accuracy (radiometric resolution).

From a signal processing perspective, to acquire hyperspectral imaging data requires three sampling operations: spatial, spectral, and radiometric. Temporal sampling, which refers to how often data are obtained for the same area, is related to operational rather than signal processing considerations. Therefore, we concentrate on the physical implementation and the key parameters required for the characterization of spatial, spectral, and radiometric sampling operations.

1.3.1

Spectral–Spatial Data Collection and Organization

It is helpful at this point to discuss how the data from an imaging spectrometer are organized. Consider the data in the raw format of digital numbers as it is read from the

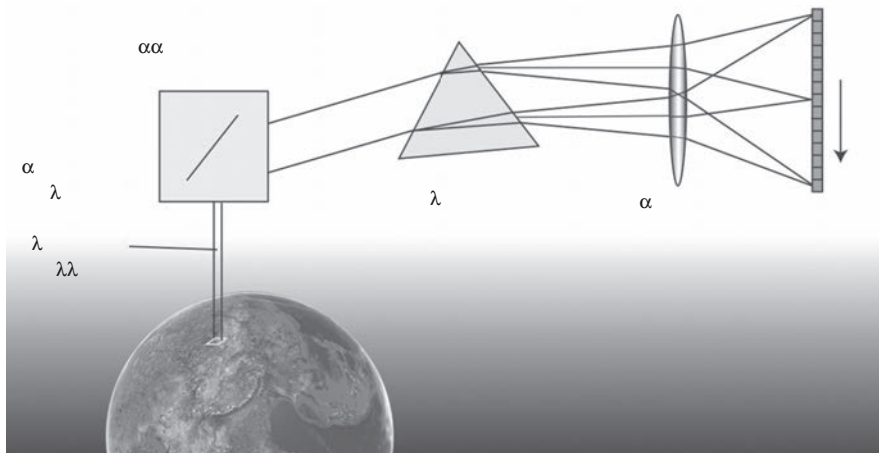


Figure 1.7 Basic principle of a hyperspectral remote sensor

individual detector elements. The data are stored in a data structure, known as a data cube, consisting of two spatial dimensions and one spectral dimension. Each datum in the cube is associated with a particular spatial location of a certain size and its value is proportional to the spectral radiant energy contained within that particular spectral sample and area.

The order and procedure by which each datum in the cube is populated are determined by the details of the imaging spectrometer. The challenge faced by the optical designer is to record a three-dimensional data set using the signal generated by either a two-dimensional array of detectors, a line array of detectors, or a single detector. Additionally, there is a limited number of ways that light can be separated into its spectral components.

As described above, the fore optic presents an image of a scene location at the input of a spectrometer. The spectrometer input is often a spatial mask of some sort. For example, a slit spectrometer employs a two-dimensional opening that is long and narrow. One can think of this imaging process in the reverse sense with the spectrometer input mask being imaged onto the scene. The spatial dimensions of the cube are then assembled as this projected mask is scanned across the scene of interest.

Figure 1.8 illustrates some of the different methods by which the data cube is populated depending upon the type of imaging spectrometer. The data subset marked with an “A” is from a slit spectrometer, which relies on a dispersing element to spatially separate the light into the different wavelength samples which are recorded by a two-dimensional detector array. A scanning mechanism is utilized to move the projected slit image across

**Figure 1.8**

Three-dimensional illustration of a data cube showing the spatial dimension (x, y) and the spectral dimension λ . The numbers of spatial and spectral samples will depend upon the details of the sensor design. The regions, labeled A, B, and C, illustrate the portion of the data cube that is acquired during one acquisition cycle as described in the text.

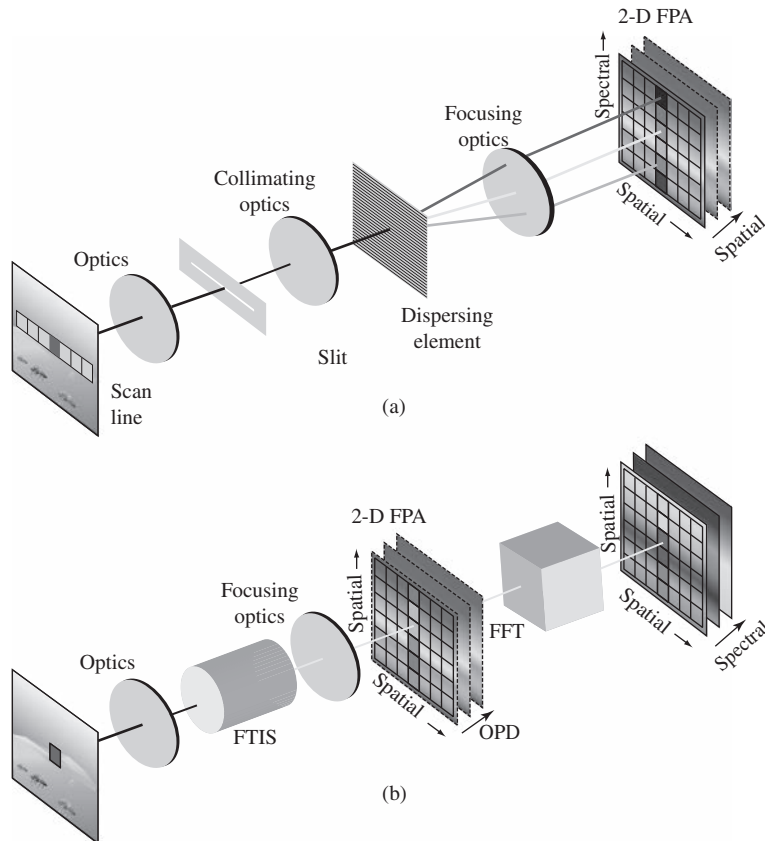


Figure 1.9 Illustration of two types of imaging spectrometers. Illustration (a) is a slit spectrometer with each data frame composed of spatial and spectral dimensions and the second spatial dimension generated through scanning the projection of the slit onto the scene. Illustration (b) is of a FTIS, with each data frame corresponding to both spatial dimensions at a particular OPD. The spectral information is recovered by taking the fast Fourier transform (FFT) of the interference data for each spatial location. (A black and white version of this figure will appear in some formats. For the color version, please refer to the plate section.)

the scene. The spatial image recorded by a single data frame has $m - 1$ samples with m being the number of spatial samples along the long axis of the slit. The spectral information is recorded in the perpendicular direction by n detector elements. The entire data cube is assembled by scanning the slit along the scene and reading out the array of detector elements at an appropriate rate. This is often referred to as *pushbroom scanning*, with the forward motion of the airborne or space-based platform providing the slit scanning motion. The diagram in Figure 1.9(a) sketches this common and highly successful design.

A second example illustrated in Figure 1.8 and labeled as “B” is a *staring system* that utilizes a series of spectral filters mounted in a filter wheel. A system of this type “stares” at an area of the scene and cycles through a series of filters. A two-dimensional array records an area of the scene at the various filter wavelengths and the cube is populated

as the filter wheel cycles. Once the spectral data corresponding to the spectral bandpass from each filter in the wheel has been recorded, the scanning mechanism transitions to the next portion of the scene and the process is repeated until the full scene has been imaged. This is not a commonly employed imaging spectrometer, but it does introduce the concept of a staring sensor.

A staring imaging spectrometer that is employed, particularly for remote sensing of the atmosphere, is a Michelson interferometer, or Fourier Transform Imaging Spectrometer (FTIS), which is illustrated in the sketch of Figure 1.9(b). This spectrometer utilizes interference of light to record the spectral information. The interference pattern is introduced by splitting the light into two unequal paths and recombining it. The light will constructively and destructively interfere after recombining depending upon the *optical path difference (OPD)* and the wavelength. A moving mirror produces the necessary OPD and the interference pattern is recorded by repeatedly reading out the data from each detector element in a two-dimensional array at a particular mirror position. Each element of the two-dimensional array records the spectral information for a particular spatial sample. In this case, the spectrum is recovered by taking the Fourier transform of the interference signal for each spatial location. Once the full mirror travel has been completed the spatial scanning mechanism transitions to the next portion of the scene and another area corresponding to the projection of the two-dimensional detector array is recorded, as was done for the filter wheel system. The details of this type of imaging spectrometer will be addressed in Chapter 4; it is mentioned here as a practical staring system for some applications.

The final example, labeled as “C”, is an imaging spectrometer that measures a complete spectrum for a single spatial sample. A system of this type employs either a line array, as in the case of a slit spectrometer, or a single detector element, if the imaging spectrometer is a Michelson interferometer. The full data cube is assembled by raster-scanning the single spatial element until the full scene area has been collected. This is often referred to as *whiskbroom scanning*, since the forward motion of the platform generates one axis of the scanning motion and a rotating mirror “whisks” the projected spatial sample in the perpendicular direction. An example slit imaging spectrometer that utilizes this scanning method is the widely used Airborne Visible/Infrared Imaging Spectrometer (AVIRIS) system built at the Jet Propulsion Laboratory (Vane et al., 1993).

Armed with this background in the collection of a full hyperspectral data cube, we will now introduce the concepts critical to our discussion of the details of the sensor systems. The spatial, spectral, and radiometric figures of merit are defined. These ideas are critical in order to fully understand the details of each spatial-spectral datum in the image cube.

1.3.2 Spatial Sampling

Hyperspectral imaging data are acquired by sensors that can systematically scan parts of the earth’s surface, recording radiation reflected or emitted from a scene location, known as a *ground resolution element*, at multiple regions of the electromagnetic spectrum. A key component of the sensor is an optical system which collects the radiation originating

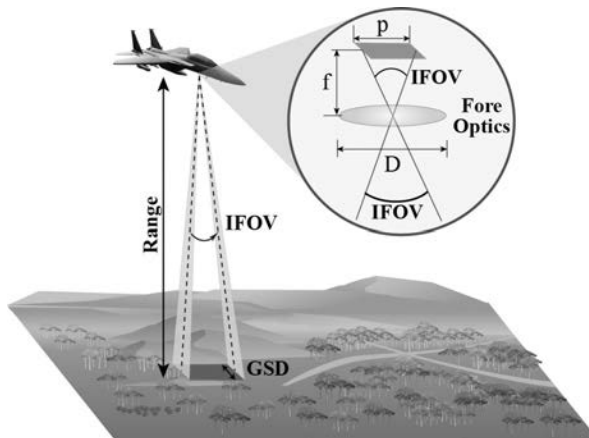


Figure 1.10 Illustration of the ground resolution element and the geometrical figures of merit for an imaging spectrometer. The IFOV is alternatively defined as the ratio of the pixel width p to the focal length f .

from the ground surface area and focuses the intercepted rays onto the surface of a detector element, as in the filter wheel case, or onto a spatial mask such as a slit. For those systems with a spatial mask, the area is further segmented depending upon the number of spatial samples as was described above for a slit spectrometer. Figure 1.10 illustrates this concept for a single spatial element from either case. The area of the detector or segment of the spatial mask projected through the system's optics onto the earth's surface coincides with the ground resolution element. Each ground resolution element is mapped onto one *picture element* or *pixel* of the image collected by the sensor as the surface is properly scanned.

The minimum solid angle through which radiant energy originating from the scene is accepted by the optical system and reaches a single detector element or mask segment is called the sensor's *instantaneous field of view* (IFOV). The IFOV is a strictly geometric factor used as a rule of thumb to describe the smallest spatial resolution element that is sampled by the imaging spectrometer. The true spatial resolution is determined by an analysis of the optical aberrations and the effects of diffraction. The *angular field of view* is the full angular extent of all the IFOVs. This is often restricted to the *cross track* dimension, as in the case of a slit spectrometer that is pushbroom scanned. The cross track direction corresponds to the projection of the long axis of the slit onto the scene. In this case, the *along track* dimension is accumulated by scanning as described above and is arbitrary in its extent.

The *ground sample distance* or GSD is the simple geometrical representation of a detector element or mask segment projected onto the scene. It is calculated by multiplying the IFOV by the *range*, the distance from the sensor to the scene location. However, the true spatial sampling is somewhat different from this idealization. As mentioned above, the light from a given scene point is modified due to optical aberrations and diffraction as it is sampled by the imaging optics. This smearing effect is described by a weighting function, known as the *point spread function* of the sensor.

The spatial resolution is further smeared by transmission through the atmosphere and the scanning process. The resulting spatial resolution is known as the *ground resolution distance* or GRD. The GSD defines the smallest area viewed by the sensor and establishes a lower limit for the level of spatial detail that can be represented in a digital image.

Although scanning mechanisms vary according to sensor type, after geolocation processing, each measurement corresponds to a location in the scene and is presented as a pixel in an image. A sensible geometrical correspondence exists between scene locations and image pixels, such that the image can be considered as a projection of the earth's surface onto an image plane.

1.3.3 Spectral Sampling

An imaging spectrometer is designed to recover the spectral information inherent in the electromagnetic radiation from a given ground sample. This recovery is by its nature imperfect due to finite spectral sampling with the data binned into particular spectral bands. The *spectral response function* (SRF) is the weighting function that describes the range of wavelengths that are transmitted to a particular spectral sample. The width of the SRF, measured at half of the peak transmittance, is a measure of the spectral resolution of the spectrometer. The narrower the width, the more spectral details that can be resolved, such as the narrow absorption features inherent in the transmission of light through the atmosphere. Naturally, the signal-to-noise ratio is also proportional to the SRF, with less light transmitted for a narrow SRF. Figure 1.11 shows a comparison of the spectrum recovered by spectrometers with high and low resolutions.

There are various ways that this spectral sampling can be achieved, but they fall into two broad categories. The first relies upon the interaction of an electromagnetic wave with matter and the second utilizes the wave nature of the light itself. The familiar prism, where light of different colors is refracted at different angles due to the wavelength dependent index of refraction of the prism material, is an example of the first category. The second category uses the physics of diffraction and interference to recover the spectral information and is represented by instruments that employ diffraction gratings or interferometry as examples. The number of bands recorded can range from a few to a few hundred depending upon the application with the spectral distance between samples on the order of 5 to 25 nm. For a well designed and manufactured imaging spectrometer, the shape of the function that describes the spectral sampling will be uniform for all spectral channels for every ground sample. This will minimize the spectral artifacts introduced by the spectral imager that could compromise the exploitation of the data.

1.3.4 Radiometric Sampling

The function of the detector is to transform radiant power into an electrical signal. The electrical signal is converted into a number by an analog-to-digital converter.

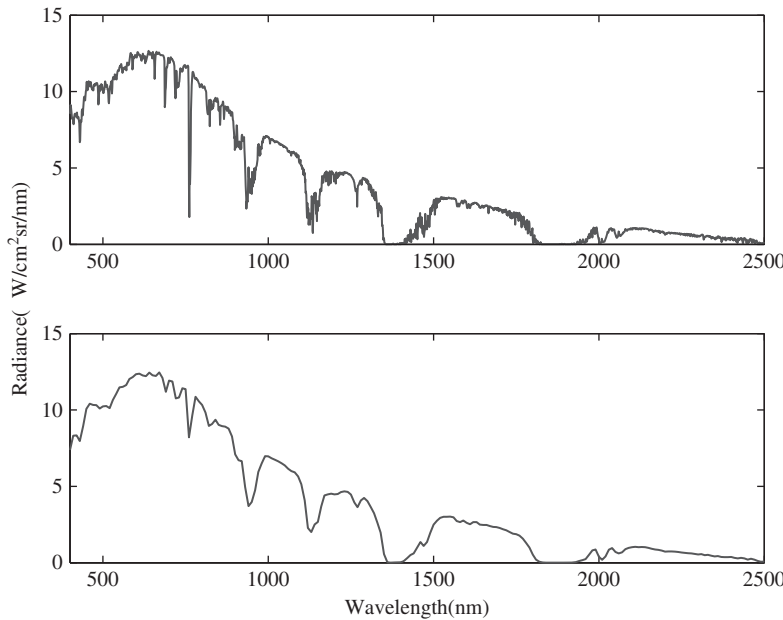


Figure 1.11 The two graphs depict MODTRAN® 5 spectral radiance simulations from 400 to 2500 nm for the same scene radiance. The broad absorption features at 940 and 1115 nm are due to water absorption. The opaque absorption features at about 1400 and 1900 nm are also due to water with the scene radiance completely absorbed by the atmosphere. The deep and narrow absorption feature at 760 nm is due to oxygen absorption. The upper graph is a high-resolution model that shows the details of the molecular absorption features at a resolution of 1 nm. The lower graph shows a similar result but at a resolution of 10 nm.

Detectors are classified on the basis of the physical mechanisms that cause the conversion from radiant to electrical energy. The two main classes are thermal detectors and quantum (or photon) detectors with imaging spectrometers employing the latter type.

The line or area arrays employed in an imaging spectrometer are composed of individual photoconductors. These semiconductor devices work quantum-mechanically with photons being absorbed to produce free charge carriers. Photoconductors function over a broad spectral range and are employed throughout our spectral region of 0.350 to 14 μm . The wavelength range is determined by the details of the semiconductor quantum structure with the quantum efficiency, the ratio of a quantum of light input to the device to a charge carrier generated within the device, varying as a function of wavelength.

The resulting current generated by applying a voltage across the detector element is collected and stored in a capacitor for measurement. This voltage is converted to a *digital number* (DN) using an analog-to-digital converter with a set number of bits B , typically 12 or 14. A B -bit converter records 2^B levels. The number of bits determines the radiometric resolution. For example, if the maximum range of the electrical signal is R , then the radiometric resolution is $R / 2^{-B}$.

1.3.5 Signal Considerations

The strength of the signal generated by a detector is a function of the following factors (Sabins, 2007):

Terrain composition: The amount of radiant energy reflected or emitted from the ground resolution element depends on its material composition.

Range: For a given ground resolution element, the amount of energy reaching a detector element is inversely proportional to the square of the distance between sensor and ground location.

Spectral bandwidth: The output signal of a detector element is proportional to the spectral bandwidth of the detector.

Instantaneous field of view: Decreasing the IFOV increases the spatial resolution but results in a weaker signal, assuming other aspects of the optical design, particularly the size of the limiting aperture, remain unchanged.

Dwell time: This is the time required for the IFOV to sweep across a ground resolution element (“time-on-pixel”). A longer dwell time allows the accumulation of more photons by the detector, which results in a stronger output signal.

The design of an imaging spectrometer will be guided by these basic signal characteristics. Typically, a sensor model will be constructed that includes each of these factors, appropriately characterized optically, in order to evaluate the potential performance. A metric such as the signal-to-noise ratio or the noise equivalent spectral radiance is used to quantify the performance of the first-order design.

1.4 Data Preprocessing

Hyperspectral imaging sensors have a sufficient number of spectral bands to allow extraction of spectra that closely resemble those acquired by laboratory spectrometers. This makes possible, at least in principle, the use of such spectra to identify materials based upon their reflectance or emissivity properties. This is the key to most HSI applications. In order to use these library spectra, the raw data must go through a series of processing steps to convert it to a usable format.

The first step in the conversion process is to calibrate the data to the physical units of radiance. Radiance will be addressed in detail in Chapter 2 but, to briefly introduce the term, it quantifies the energy at a given time passing through the input aperture of the sensor within a certain angular extent (solid angle) as a function of sensor viewing direction. The second step is the application of physical radiative transfer models to convert the radiance data to either reflectance, in the case of the reflective spectral range, or temperature and emissivity, in the case of the thermal spectral range. This is known as *atmospheric compensation*. These models account for atmospheric transmission and the atmosphere’s thermal emission. The difficulty with radiative transfer models lies with having a rather detailed understanding of the atmospheric

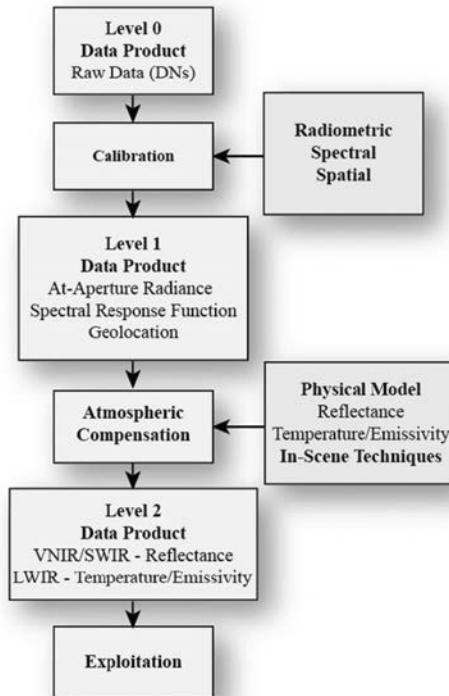


Figure 1.12 Flow diagram of the processing steps that are necessary for data exploitation. Refer to Table 1.2 for a taxonomy of the possible exploitation processing.

constituents. For example, the number and distribution of the small suspended particles, called aerosols, is typically unknown and often difficult to estimate. There are also in-scene methods that assume the presence of materials with known spectral signatures. These techniques enable the retrieval of the desired reflectance or emissivity signature.

A retrieved reflectance spectrum is the ratio of the reflected radiance to the incident radiance as a function of spectral bands. It is therefore a dimensionless quantity that varies from 0 to 1, *assuming the reflectance is well characterized as a diffuse Lambertian*. The emissivity spectrum is more complicated. For an object at a known temperature, it is defined as the ratio between the measured emitted radiance to the theoretical maximum radiance that is possible for the object. Like the reflectance, the emissivity varies from 0 to 1 as a function of the spectral bands. The requirement that both the temperature and the emissivity be known greatly complicates the atmospheric compensation of data in the emissive spectral range. These two concepts, reflectance and emissivity, will be addressed in detail in Chapters 2 and 3. It is these two quantities that enable the data to be quantitatively analyzed.

1.4.1 Data Calibration

Data calibration is the process by which the raw data recorded by the detector of an imaging spectrometer is converted to physical units. This is accomplished through the use of optical radiometry, the science of measuring electromagnetic radiation. Through the application of radiometric principles it is possible to design a source that has an accurately known, spatially uniform, and spectrally understood radiation field for presentation to the input aperture of a spectral sensor. The calibration of the data, for an imaging spectrometer with a linear response, is the simple ratio of the value from a known radiometric source in the appropriate units, averaged over each spectral band, divided by the dark-subtracted raw signal in digital numbers. The dark subtraction removes the thermal signal that is present in detectors even when they are not illuminated. The efficacy of this simple procedure rests upon a large body of technological development.

Any spectral sensor will modify the radiant energy at the input, often quite significantly. This modification affects the spatial, spectral, and radiometric properties of the scene radiation field. A sensor is characterized in order to understand how it modifies these quantities and to enable the calibration of the raw data recorded to physical units that can in turn be used in quantitative data processing and exploitation. Some quantities, such as the ground resolution and the spectral response functions, are characteristics of the system that cannot be fundamentally changed but whose characterization is highly desirable or absolutely required for data utilization. Other quantities, such as the scattered light performance, can be quantified and used to correct for some of the deleterious artifacts that can be introduced by even the most well-designed sensor. Additionally, the pointing characteristics must be understood for the generation of georectified data products.

Fundamentally, sensor characterization and data calibration are required so that the data user knows the projected scene location of each spatial sample, the spectral content of the data recorded by each spatial-spectral detector element, and the amplitude of the signal in physical units for each detector element. Armed with this information, it is possible to produce accurate and quantitative data products that include a detailed treatment of the effects of the atmosphere and utilize the wealth of signature-based processing tools that rely upon laboratory- or field-measured spectral signatures.

1.4.2 Atmospheric Compensation

In this section we discuss the approach used to obtain reflectance spectra from the sensor measurements by removing the interfering effects introduced by atmospheric absorption and scattering, solar illumination, and instrumental biases. The deleterious effects of the transmission through the atmosphere on the measured radiance, as illustrated in Figure 1.1, are twofold: modification of the downwelling radiance on the target and of the upwelling radiance transmitted from the target to the sensor. It should be clear that the fundamental property characterizing ground surface materials is their reflectance or emissivity spectra.

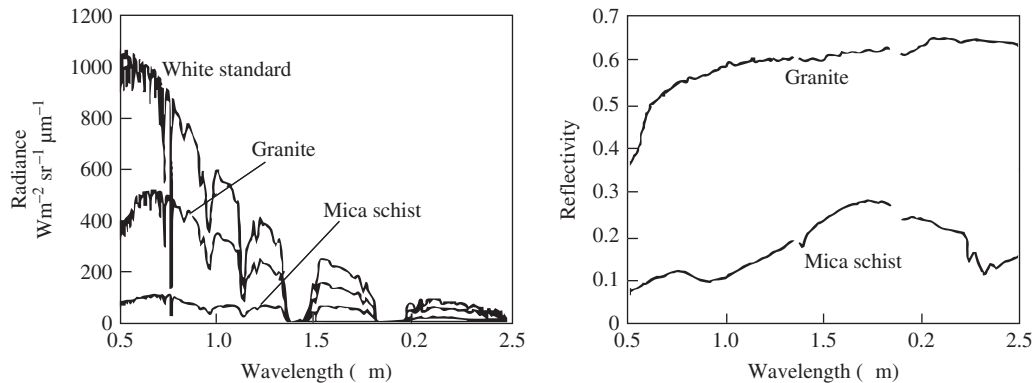


Figure 1.13 Comparison of radiance and reflectance spectra measured by a field spectrometer (Adams and Gillespie, 2006).

Thus, in the reflective part of the spectrum from $0.4 \mu\text{m}$ to $2.5 \mu\text{m}$, the property that we desire to obtain from the measured data for the surface characteristics is the apparent reflectance spectrum of each ground resolution cell. Similarly, in the emissive part the spectral features that are characteristic of a particular material and provide the basis of comparison to a spectral library in the thermal IR are the spectral emissivity. The region between the reflective and thermal IR can be characterized by either the spectral reflectance or emissivity. The MWIR bands are particularly difficult because both reflectance and emissive radiation can be at appreciable measurement levels.

The challenge of atmospheric compensation in the reflective domain can be understood by considering Figure 1.13. The left image gives the spectral radiance signature as measured by a calibrated sensor for three materials: a spectrally white reference pixel, a granite pixel, and a mica pixel. The right image shows the reflectance spectral albedo for granite and mica samples as measured in a laboratory in the absence of an intervening atmosphere and referenced to a white lambertian reflectance standard (reflectance of 1 for all spectral channels). It is obvious that the two graphs for each material appear significantly different and that the rich spectral content introduced by the atmosphere dominates the spectral radiance signature for all three samples. In the forward calculation converting from a surface reflectance to expected spectral radiance, the radiance spectrum measured by the sensor can be calculated from the product of the reflectance spectrum, the solar spectrum, the downward and upward transmission functions of the atmosphere, and the spectral response of the sensor plus the addition of scattered light from the atmosphere or sensor.

Meaningful analysis of spectral imaging data requires visual or mathematical comparison with field or laboratory reflectance spectra of known materials. Several freely available libraries of reflectance spectra of natural and man-made materials can be used to provide *reference* or *training* spectra to aid the analysis and interpretation of spectral imaging data. This requires the conversion of the sensor-measured radiance spectra to reflectance spectra, a process known as *atmospheric compensation*.

There are two basic families of atmospheric compensation techniques: scene-based and physics-based. Scene-based statistical or empirical methods use in-scene reference

objects (calibration panels) with known reflectance characteristics to estimate the relation between the at-sensor radiance and the known surface reflectance. Empirical line method (ELM) is the most widely used statistical method for atmospheric compensation. ELM uses a linear (“line”) model to relate reflectance to radiance. Physics-based methods estimate the parameters of the relationship required to convert from radiance to reflectance, using physical models and knowledge of the atmosphere either obtained from the spectral data itself or obtained (or assumed) from some other source. A detailed discussion of atmospheric compensation techniques is provided in Chapter 6.

Both ELM and physics-based atmospheric compensation have been successfully employed by various research groups. If a pixel in the image can be identified as being uniformly one material, and the spectral reflectance properties are known, the ELM approach to atmospheric compensation will likely provide satisfying results but will do so at a small computational cost. The analyst is forced to the physics based model for atmospheric compensation when a uniform pixel of adequately known spectral reflectance cannot be identified. Even if a physics-based model compensation is used, the presence of known materials provides a check for the analyst.

1.4.3 Unique Aspects of Preprocessing in the Thermal Infrared

The thermal Infrared spectral region deserves additional discussion because the spectral emission of the surface and atmosphere are intrinsically part of the measured signal and more typically the dominant signature. Although a complete treatment of the thermal IR spectral bands would include the solar illumination and reflectance, in fact the solar contribution to the measured thermal IR or long-wave (typically $5 \mu\text{m}$ to $15 \mu\text{m}$) radiance is small compared to the thermal emission from the surface and atmosphere. Additionally, the spectral measurement obtained by the sensor is not fundamentally different from a measurement of a well-characterized and stable source, such as the sun as in the case of the reflective portion of the spectrum, but the source radiance is now strongly dependent on its temperature.

The Mid-Wave Infrared Region (typically $3 \mu\text{m}$ to $5 \mu\text{m}$) is further complicated by the crossover of the thermal sources as in the LWIR and the solar reflective source. The unscrambling of the source data, which requires a model for the thermal and solar radiance mixing during daytime measurements, makes the MWIR data particularly difficult to extract useful results.

The unique aspects of thermal IR sensors, systems and data exploitation are treated throughout the subsequent chapters of this book but the purpose of this discussion is to ensure the reader is sensitive to the unique aspects of the thermal infrared dependencies.

1.5

Data Exploitation Algorithms

Historically, interpretation of passive imagery has generally depended upon either human analysis of visual information in a live video or a still image, or else upon machine measurement and analysis of parameters that distinguish a man-made object (target) from the natural surroundings. However, the large number of spectral bands in

Table 1.1

μ	μ
Spatial Processing	Spectral Processing
Information is embedded in the spatial arrangement of pixels in every spectral band (two-dimensional image)	Each pixel has an associated spectrum that can be used to identify the materials in the corresponding ground-resolution cell
Image processing exploits geometrical shape information	Processing can be done one pixel at a time
Very high spatial resolution required to identify objects by shape (many pixels on the target)	No need for high spatial resolution (one pixel on the target)
High spatial resolution requires large apertures and leads to low signal-to-noise ratio	Spectral resolution more important than spatial resolution
Data volume grows with the square of the spatial resolution	Data volume increases linearly with the number of spectral bands
Limited success in developing fully automated spatial-feature exploitation algorithms	Fully automated algorithms for spectral-feature exploitation have been successfully developed for select applications

hyperspectral imagery precludes the full exploitation of the information through simple visual analysis of the data. In fact, the visual representation of such “high-dimensional” data is itself a challenge, and the essence of hyperspectral exploitation algorithms is the extraction of information of interest from high-dimensional data.

In practice, hyperspectral sensors represent a deliberate trade-off in which spatial resolution is degraded in favor of improved spectral resolution. By implication, hyperspectral imaging is therefore best matched to applications in which spectral information is more reliable or measurable than morphology or shape information. For example, traditional analysis of passive imagery of military vehicles depends strongly upon being able to determine the length, width, and distinguishing features of a vehicle. If the vehicles are partially hidden under foliage or camouflaged nets, the morphological information is unreliable and alternate means of detection and identification are needed. Since hyperspectral imaging does not rely on shape information, it is less impacted by attempts at concealment and deception. The analysis of different materials in a scene exclusively through the use of spectral information is sometimes termed *nonliteral exploitation*, in reference to the fact that this analysis does not rely on literal interpretation of an image by means of morphological analysis and inference. A concise comparison between spatial versus spectral exploitation, see Manolakis et al. (2003), is provided in Table 1.1.

The main objective of *spectral remote sensing* is the identification of materials or phenomena from their reflectance or emissivity spectra. Although this desirable objective is often achieved in practice, this is *not* always the case. Therefore, it is important to find out how spectra from different materials differ, how unique are the spectra of the same material, and to what extent spectra can be used to differentiate and identify different

materials. In addition, to analyze hyperspectral imaging data and interpret the results requires an understanding of what properties of the ground materials we are measuring, and how they are related to the actual measurements produced by the sensor.

Since the fundamental property characterizing ground surface materials is their reflectance or emissivity spectra, a key operation in many applications is the conversion of hyperspectral data from the radiance into reflectance or emissivity using the techniques discussed in Section 1.4. In this section we overview some key challenges and processing algorithms for the exploitation of hyperspectral imaging data after conversion to the reflectance or emissivity domains. However, there are some applications where it is possible to perform data exploitation in the radiance domain.

1.5.1 Spectral Exploitation Challenges

To understand the key challenges concerning the exploitation of hyperspectral imaging data, we start with Figure 1.14, which shows radiance and reflectance from a homogeneous ground area of grass. The variability of radiance and reflectance spectra corresponding to the same ground cover, which is an inherent characteristic of real-world materials, is known as *spectral variability* and has important implications in spectral remote sensing. We emphasize that reflectance spectra are unique only to the sample and the environment in which they are measured. For example, mineral spectra vary from sample to sample and vegetation spectra are even more variable, being dependent on growth stage, plant health, moisture content, and season of the year.

The amount of variability is even more profound in remote sensing applications because of variations in atmospheric conditions, sensor noise, material composition, location, surrounding materials, illumination and measurement geometry, and other factors. As a result, measured spectra corresponding to pixels with the same surface

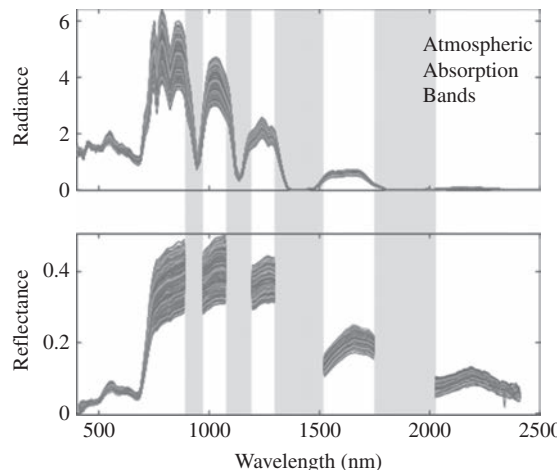


Figure 1.14 Radiance and reflectance spectra from a homogeneous area of grass.

type exhibit an inherent spectral variability that prevents the characterization of homogeneous surface materials by unique spectral signatures. The pixel-to-pixel spectral variability of natural and cultural scenes is known as *background clutter*.

The term *spectral signature*, which is often used to refer to reflectance or emissivity spectra, is *misleading* because it implies that each material reflects or emits radiation in a unique and identifiable manner. This is not “exactly” true, because it would be more accurate to represent the spectral signature as a “ribbon,” which shows the envelope of all measured spectra, and not as a single line. The situation is further complicated by the fact that there are different materials with almost identical reflectance spectra and materials whose spectra look like the mixture of spectra from two other materials (Rice 1994).

Several libraries of high-resolution reflectance and emissivity spectra of natural materials, man-made materials, and gases have been compiled by various organizations and are available for public use. Spectral libraries provide a source of reference of spectra that can be used to facilitate the analysis and interpretation of remotely obtained spectral measurements. We note that quite often the spectral signatures provided for various materials represent “averages” or “typical” examples. However, we must stress that if specific materials are not separable within a spectral library, they are unlikely to be spectrally distinct in a remote sensing data set.

Another significant complication arises from the interplay between the spatial resolution of the sensor and the spatial variability present in the ground scene. The sensor integrates the radiance from all materials within the ground surface, which is “seen” by the sensor as a single image pixel. In this case, the spectrum observed by the detector is a mixture of the individual spectra of the spatially mixed materials, and the corresponding pixel is called a *mixed pixel*. Therefore, depending on the spatial resolution of the sensor and the distribution of surface materials within each ground resolution cell, the result is a hyperspectral data cube comprising “pure” and “mixed” pixels, where a pure pixel contains a single surface material and a mixed pixel contains multiple materials. Figure 1.15 illustrates spectral mixing for a pixel with two materials. We clearly see that the observed spectrum looks different from the spectra of the constituent materials.

In conclusion, all natural materials exhibit some variability in composition and structure that results in variability in their reflectance spectra; temperature variations introduce additional variability in emissivity spectra. Additional variability is introduced by the surrounding materials, the viewing geometry, and the illumination conditions. Spectral variability is the prominent limitation for the exploitation of data with pure pixel spectra. Mixing introduces additional obstacles in the spectral identification of materials because, for each material of interest, all other materials act as interference sources. Material spectra and mixtures of constituents with examples will be addressed in Chapter 3 in more detail.

1.5.2

Taxonomy of Spectral Exploitation Algorithms

The best way to extract the maximum amount of information from hyperspectral imaging data is to use physics-based models to connect the spectroscopic and optical

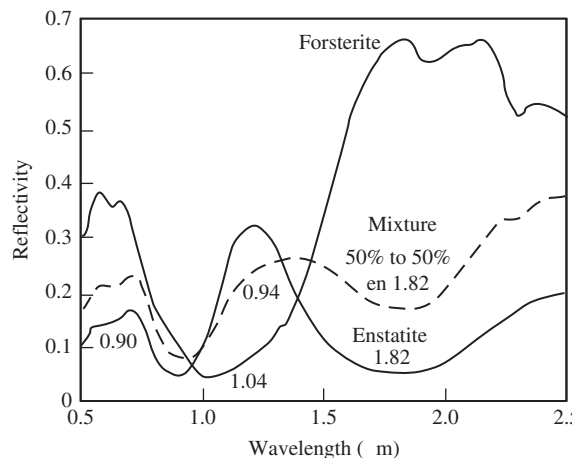


Figure 1.15 Illustration of spectral mixing for a pixel including two materials (Adams and Gillespie, 2006).

properties of known materials, which are the laboratory and field spectra in spectral libraries, with the radiance spectra measured by the sensor. However, to obtain laboratory-like reflectance and emissivity spectra remotely requires suitable standards on the ground in each field of view. This is simply not practical for most remote sensing applications. To work around the problem we convert radiance spectra into reflectance or emissivity spectra using the techniques discussed in Section 1.4; we note that these methods are sufficiently accurate for many applications. Alternatively, if we have sufficient information, we can replace library spectra with “image-derived” spectra. However, in many practical applications, library spectra perform well as proxies of field spectra.

In principle, each pixel in a hyperspectral data set has a high-resolution spectrum that can be used to identify the surface materials. Since most data sets include both pure and mixed pixels, the analysis of spectral mixtures is very important. When we analyze a mixed spectrum there are two questions to answer. What are the spectra of the individual materials? And, what are the proportions of the individual materials? This is a very difficult inverse problem known as spectral unmixing. In general, determining proportions is more difficult, and follows identification. As we move from the laboratory scale to the scale of remote sensing, spectral mixing can be adequately characterized by a linear mixing model. Therefore, we can address the problem of linear unmixing using techniques from the areas of variable selection and parameter estimation in linear regression models and linear estimation. Since the library or in-scene spectra used in the model may significantly differ from the actual components of the mixed pixel in number and shape, the estimated proportions may be inaccurate for practical applications. In practice, linear spectral unmixing is used to estimate the proportions of materials in a pixel only in special cases or applications.

The linear mixing model is an example of a physics-based model that helps to establish a physical connection between the remotely measured spectra and the materials

on the ground. Physics-based models require the conversion of data into reflectance or emissivity domains. A simple way to bypass this obstacle is to compare the radiance spectrum of a well-understood training area with the spectra of other areas in the same image. In fact, this is the basic idea behind all classification techniques developed during the early days of multispectral remote sensing.

Classification algorithms compare spectra with one another and define groups having similar properties. Typically, the analyst selects a pixel or group of pixels that have meaning for the application, and the algorithm finds all other pixels that are similar. The first step in the development of classification algorithms is to define what we mean by “similarity” and what we mean by “class.” Then, we have to choose between unsupervised and supervised classification approaches.

As the name implies, unsupervised classification is done without guidance from an analyst; the algorithm automatically organizes spectrally similar pixels into groups that become the basis for different classes. However, in the end, the analyst must label and identify the classes produced by an unsupervised classifier. In contrast, supervised classification requires human guidance. The analyst selects groups of pixels from part of an image known as “training area” to determine “training” data sets for each material class present in the image. The classification algorithm uses the training data to form the rule by which each pixel in the image, outside the training area, is assigned to a class. The result is a classification or thematic map, like the one illustrated in Figure 1.16. Classifiers are evaluated based on how often they assign a pixel to the wrong class. The probability of error is the criterion used in classification applications because interpretation of a scene is based on correctly classifying the majority of pixels in each class and each class includes a sizable number of pixels.

In an important class of practical applications, known collectively as target detection, we seek to determine whether a rare object with a known spectral signature is present or not in the imaged scene. The term “rare” is used here to signify a relatively small number compared to the total number of pixels; for example, a few pixels in a million-pixel image. The processing methods developed for landscape classification are not applicable to target detection for two reasons. First, even if there are targets in the scene, their

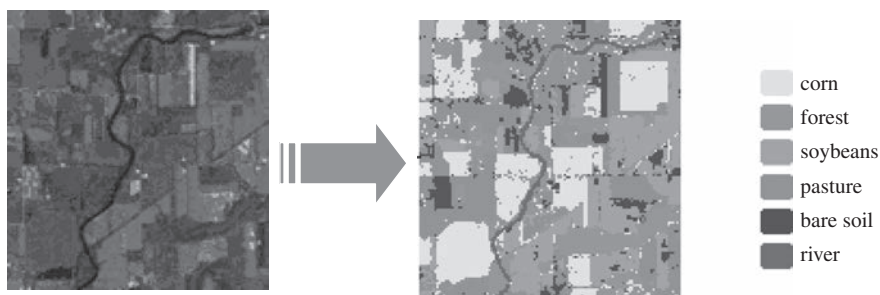


Figure 1.16 A classification map of an agricultural area created from Thematic Mapper multispectral data (Landgrebe, 2003). (A black and white version of this figure will appear in some formats. For the color version, please refer to the plate section.)

number is typically too small to support estimation of statistical properties of the target class from training data. Second, depending upon the spatial resolution of the sensor, targets of interest may not be clearly resolved, and hence they appear in only a few pixels or even as part of a single pixel (subpixel target). The isolated character of the targets makes confirmation by means of clustering of like samples problematic. Target detection is still possible, however, in these situations by developing algorithms using statistical decision theory. Since targets are rare, we can minimize the probability of error by classifying every pixel as “non-target.” We also note that the consequences of failing to detect a target differ from the consequences of falsely detecting one. Therefore, in target detection applications we use the Neyman–Pearson criterion, which seeks to maximize the probability of detection while keeping the probability of false alarm below some acceptable value.

To understand the fundamental ideas underlying most hyperspectral exploitation algorithms, it helps to view the spectra in a data cube as a scattering of points in a p -dimensional Euclidean space, where p is the number of spectral bands. Each spectral band is assigned to one axis of the space, all axes being mutually orthogonal. Therefore, the spectrum of each pixel can be viewed as a vector. The tip of this vector corresponds to an p -dimensional point whose Cartesian coordinates are the radiance, reflectance, or emissivity values at each spectral band. The basic idea is illustrated in Figure 1.17, which shows the scatterplot for two spectral bands of a hyperspectral data cube. We note that different materials tend to occupy different, and often overlapping, regions of the spectral space; this behavior is a consequence of spectral variability and spectral mixing. Establishing a correspondence between regions of the spectral space and classes of materials is the major cornerstone of hyperspectral landscape classification and target detection algorithms.

Since high-dimensional spaces have a huge volume, data tend to occupy a very small subspace; in essence, high-dimensional spaces are mostly empty. As a consequence high-dimensional data can be projected to a lower-dimensional subspace without losing significant information, at least, for classification applications. For target detection applications, dimensionality reduction must be avoided or has to be used with extreme care. Therefore, dimensionality reduction algorithms are used to reduce the computational complexity in some applications or to help understand the structure of the data with visualization in two- or three-dimensional projections.

A general taxonomy of hyperspectral exploitation algorithms is shown in Table 1.2. In closing, we emphasize that the development of algorithms for hyperspectral data exploitation is a challenging undertaking, involving resources from the areas of spectroscopy, remote sensing, high-dimensional Euclidean geometry, statistics, and signal processing.

1.6

Applications of Imaging Spectroscopy

The full range and treatment of the applications of imaging spectrometer data is beyond the scope of this book, but is summarized here to provide the reader with a point of

Table 1.2

Category	Objective	User input
Unmixing	Determine the material composition of each pixel in the scene	Material library
Classification	Provide classification map	Class training data
Target Detection	Provide target detection map	Target library
Dimensionality Reduction	Compress data, reduce computational complexity, visualization	Number of dimensions

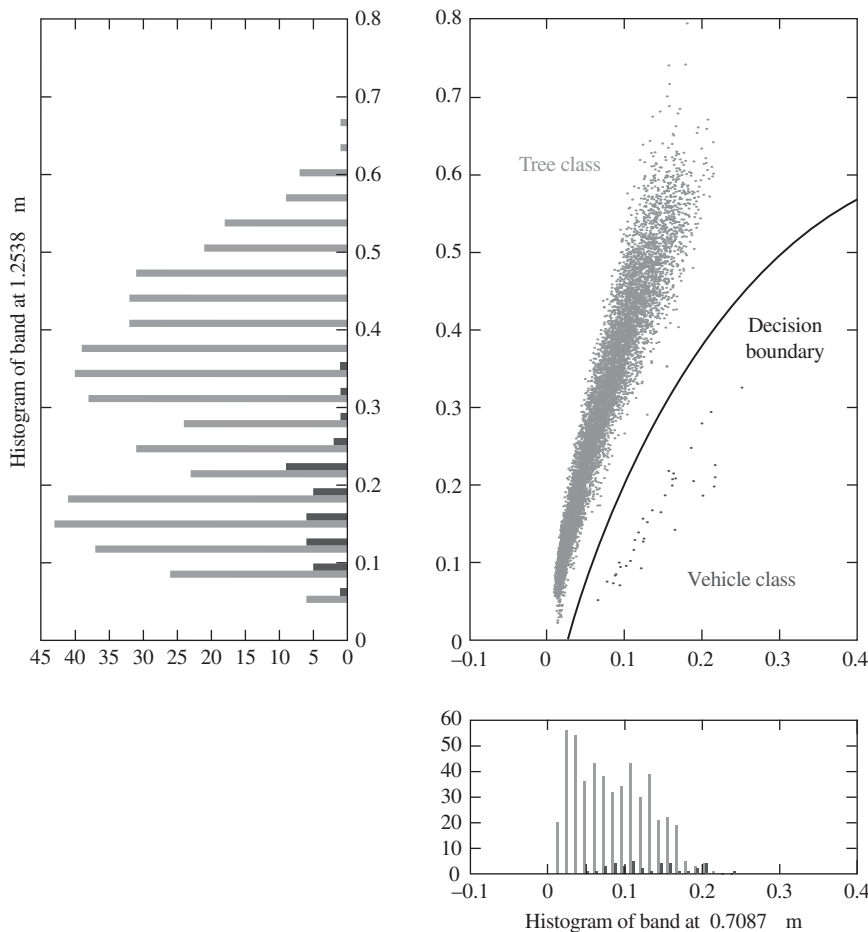


Figure 1.17 Illustration of spectral space concept using a two-dimensional scatter diagram. As shown by the band histograms, joint exploitation of the two bands provides more information than each individual band (Manolakis et al., 2003).

departure so that further investigation and study can commence. However, many of the applications which have been developed can also be addressed with the fewer spectral channels provided by a multispectral sensor (typically, two to tens of spectral bands) rather than the hundreds of spectral channels provided by an imaging spectrometer. If the sensor is tailored to a specific application, a set of optimal spectral bands can be identified for that application. An imaging spectrometer (or hyperspectral sensor) is often preferred by the research community, and sometimes even the operational community, because it has the advantage of providing data at a high spectral resolution over a large number of bands, and may hence be used for a variety of applications. Once the optimal bands are determined for a specific application, a multispectral sensor is able to provide a better solution because it is generally less expensive, and produces smaller, tailored datasets. The generic term of spectral imaging will be used for the remainder of this section to provide sample applications for these data.

Spectral remote sensing applications grew rapidly with the availability of Landsat data beginning in 1972. Although Landsat spectral bands were selected based on the overall mission objective to categorize land use and land resources, the ability to tease additional information out of the data by processing co-registered scenes taken of the same site at different times invited deeper analysis into the ability to exploit subtle spectral changes for information. In addition to using Landsat for dominant spectral feature extraction to perform relatively simple functions like distinguishing deciduous trees from conifers, the data were investigated to establish if specific vegetative species could be identified or to characterize chemical properties such as nitrogen deficiency. The data were found lacking. The dominant spectral observables used to sort full pixel materials or classes into simple, easily separated categories became the core use of Landsat. This mission may seem technologically simple but the dynamic nature of the earth's surface provides ample utility from the multispectral system with a global land-cover revisit rate of 16 days.

This initial Landsat system pointed researchers toward imaging spectrometers with the recognition that small changes in the spectral characteristics could be related to the physical properties of the scene. Scientists and engineers delved into application development and the possibility of adding additional bands which could yield information on important features that may have subtle observables which are smeared out with the broad spectral bands of sensors like Landsat. Beginning in the 1980s, JPL began the development of an Airborne Imaging Spectrometer (AIS) which was the forerunner of the AVIRIS program. This new data source opened many more applications which did not rely on the dominant spectral observables but enabled applications development using minority species or features to be pulled out of the data because of the added spectral channels and resolution.

Spectral imaging applications are many and span the civil, environmental and military needs. When there is a spectral observable to solve a problem, a spectral imager can be considered as a possible solution. Additional factors, such as the ground sample distance and the signal-to-noise ratio, must be considered before concluding that a spectral imager is best for any particular application. Some applications that are well suited to imaging spectrometers include the detection of specific terrain features, vegetation,

mineral or soil types for resource management; detecting and characterizing materials, surfaces or paints; the detection of man-made materials in natural backgrounds for the purpose of search and rescue; the detection of specific plant species for the purposes of counter narcotics; and the detection of military-related materials. The unique power of a spectral imaging is to exploit those characteristics of solids, liquids or gases that are invariant over a range of observing conditions while variable traits and characteristics are ignored.

Provided that there are spectral observables, applications in biological sciences characterizing vegetation health and chemistry can be accomplished with an imaging spectrometer; geological mapping of a wide range of minerals can be produced for mining and exploration industries; the monitoring of atmospheric trace gasses or emission sources can be accomplished; it is possible to uncover small spectral anomalies in a complex background; and myriad other applications yet to be discovered will be exploited based on the spectral characteristics of the materials observed.

1.7

History of Spectral Remote Sensing

According to Lord John Fisher, British Admiral of the Fleet, “History is a record of exploded ideas.” This section provides the brief history of spectral remote sensing and the ideas that have shaped the present. We include it to provide the reader with stories and insights that help us better understand our own path of discovery.

Commercial aerial photography companies began collecting imagery for mapping and city planning prior to World War II, while early developments envisioned a time when color images could be collected to provide more detailed information (Gen, 1938). With the advent of the Space Age, the idea of collecting imagery from a satellite gave birth to the Corona spy satellite program in the United States, which would later give rise to the National Reconnaissance Office. Weather satellites had begun monitoring earth’s atmosphere in 1960 but no application to terrain information extraction was done until the mid-1960s. Color imagery from a satellite was first discussed seriously in 1965, when the director of the US Geological Survey (USGS), William Pecora, proposed the idea of a remote sensing satellite program to gather facts about the natural resources of our planet. Pecora stated that the program was conceived in 1966 largely as a direct result of the demonstrated utility of the Mercury and Gemini orbital photography to earth resource studies. The Department of Defense feared that a civilian program such as Landsat would compromise the secrecy of their reconnaissance missions. Following years of internal government debate, including a clever move by the USGS which convinced the Secretary of the Interior, Stewart L. Udall, to announce in 1966 that the Department of the Interior (DOI) was going to proceed with its own earth-observing satellite program, NASA eventually was told to proceed in 1970 and LandSat-1 (initially known as *Earth Resources Technology Satellite-1*) was launched in July 1972. With four spectral bands on the first Multi-Spectral Scanner (MSS) instrument (green, red, and two near-IR), the era of space-based spectral remote sensing began.

Table 1.3 $\mu\mu$ μ μ

Sensor (Org) <u>Air/Space</u>	Spectra (μm)	No. Bands	Year*
AIS (JPL) A	1.2–2.4	128	1980
AVIRIS (JPL) A	0.4–2.5	224	1987–Present
GERIS-63 (US) A	0.47–2.44	63	1986
CASI (Can) A	0.48–0.805	288	1986
ROSIS (Ger) A	0.45–0.85	128	1992
HYDICE (NRL) A	0.4–2.5	210	1995
LEWIS (NASA) S	0.4–2.5	220	1997**
SEBASS (US) A	8.0–13.0	128	1996–Present
HYPERION (NASA) S	0.42–2.4	224	2000–Present
PROBA/CHRIS (ESA) S	0.41–1.06	63	2001
HYMAP (Aus) A	0.45–2.5	126	1998–Present
ARTEMIS (AFRL) S	0.4–2.5	420	2009–2012
HICO (NRL)	0.38–0.96	128	2009
EnMAP (DLR) S	0.4–2.5	200	2017*
HYSUI (JAXA) S	0.4–2.5	200	2017*
HYSPRI (NASA) S	0.4–2.5 & 8–10	240	2020
Shalom (Israel–Italy) S	0.4–2.5	220	2018*

* Estimated Launch date or first flight

** Failed three days after launch, before collecting any data

In parallel to the space sensor program, ground truth and field instruments were developed so that validation of the new data types could be accomplished. The MSS image interpretation effort precipitated the development of the first truly portable field reflectance spectrometer (PFRS) in the mid-1970s which supported continuous spectral sample measurements. The sharp pyrophyllite absorption feature was used to define the spectral resolution of 10 nm required for imaging spectrometers to identify, conservatively, 95 percent of the materials likely to be encountered (Goetz, 2009).

The Shuttle Multispectral Infrared Radiometer mission was launched in 1981 to acquire radiance values in 10 spectral bands covering the VNIR and SWIR regions along a 100 m-wide track beneath the spacecraft. The experiment was successful and resulted in the first direct identification of soil minerals from orbit through the use of the five closely spaced spectral channels in the 2.2–2.5 μm region (Goetz, 2009).

In 1979 the first hybrid focal plane array became commercially available. The two-dimensional detector array consisted of a matrix of HgCdTe detectors bonded to a matched silicon charge-coupled device (CCD) readout array. Although the first detectors contained only 32 by 32 elements, they enabled the construction of an imaging spectrometer that covered the spectral region beyond the 1.1 μm cutoff of silicon. Under internal JPL funding, Gregg Vane and Alex Goetz used one of these new infrared arrays to develop the first Airborne Imaging Spectrometer (AIS) (Vane et al., 1984). Many challenges had to be overcome to realize the potential of the new data, including geo-registration, robust spectral libraries, and atmospheric compensation. AIS is the first and earliest imaging spectrometer in the brief history of sensor systems summarized in Table 1.3.

Following AIS, the hyperspectral sensor AVIRIS development was begun in 1984 at JPL and the sensor first flew aboard a NASA ER-2 aircraft at 20 km altitude in 1987. Since then it has gone through major upgrades as technology changed in detectors, electronics, and computing. AVIRIS is arguably the finest, best calibrated airborne imaging sensor ever flown, which is the result of the dedication of the instrument leaders and their teams at JPL (Goetz, 2009). Regular campaigns to collect AVIRIS imaging spectrometer data over various sites supported the development of different applications including invasive species tracking, vegetation health characterization, biomass and combustible fuel quantification, and other ecological monitoring measurements.

With results published on the abilities demonstrated by the NASA/JPL hyperspectral sensors, new sensors began to be developed for commercial and other applications. Because of the low cost and wide availability of silicon detector FPAs, several commercial companies began building Visible-Near-IR (0.4–1.1 μm) hyperspectral sensors. The demonstrated utility of the SWIR from AVIRIS also helped to motivate other sensors which included the full reflective spectral band from (0.4–2.5 μm). Geophysical and Environmental Research (GER) Corporation in the USA developed the first commercial imaging spectrometer sensor, beginning in 1981, with a reported 576 channels across the reflective spectral bands (0.4–2.5 μm). This early development may have been premature for the fledgling field, as not many scientists were at that time familiar with the technology; nor were they educated on the applications which could be pursued with the data (Wendisch and Brenguier, 2013). Because of the expense associated with flying AVIRIS on the ER-2, the GER imaging spectrometers played an important role in making imaging spectrometer data available to the global research community, including one which was brought to Europe to support the European Imaging Spectroscopy Campaign-1989. A near-parallel effort began in Canada to develop a commercial imaging spectrometer sensor which later became known as CASI and included high spectral resolution (2.5 μm) over the Vis/NIR spectral range. Other airborne sensors began to be developed by both government laboratories and commercial sensor companies to provide new sources for the emerging demand of hyperspectral data (see Table 1.3 for additional sensor details or Wendisch and Brenguier (2013) for a detailed discussion of the historical developments of airborne sensors).

The spaceborne multispectral Landsat MSS instrument evolved into Thematic Mapper (TM) that included 7 spectral bands into the mid-wave IR was first flown on Landsat-4, launched in 1982. This sensor provided almost 19 years of data for the remote sensing world, which allowed for temporal changes to be well recorded and quantified because of the synoptic view from the TM instrument. Variables such as sun illumination angle and viewing angle were intentionally minimized so that subtle changes could be detected from the temporal history. The Landsat program was recognized for the unique data record so that in 1992, the US Congress passed the Land Remote Sensing Act which requires the continuous record of Landsat-like data to be maintained and requiring continuous data to be acquired which can be rendered as the TM sensor data.

Following the early failure of the Lewis Spacecraft, with its imaging spectrometer primary payload in August of 1997, three days after it was launched, the NASA technology program office responded with the Earth Observing-1 (EO-1) satellite which included

the primary payload of Advanced Land Imager (ALI), a multi-spectral Focal Plane Array (FPA) as a demonstration for future Landsat sensors, and Hyperion, a secondary HSI payload which was assembled with the spare parts from the Lewis imaging spectrometer (Pearlman et al., 2000). Hyperion has provided a wealth of data for the global research community to investigate applications of imaging spectroscopy (Middleton et al., 2013).

Concepts to both continue the ongoing record of Landsat while enabling the advanced technology of capable imaging spectrometers have been proposed (Chrien and Cook, 2003), but to date neither NASA nor NOAA has pursued this spectral imaging transition. The primary penalty of an imaging spectrometer is the added burden of the large volume of data. However, advances in processing and communication technologies are providing options to support the additional data generated by an HSI sensor.

With the basis of applications and the availability of processing tools and techniques to process the data, commercial airborne HSI sensors in the solar reflective domain blossomed and are now widely available. Following the success of Hyperion, space HSI sensors in the reflective bands has been led by the Air Force Research Laboratory with the ARTEMIS program and the Naval Research Laboratory with the HICO instruments. The ARTEMIS program provided data for some civil applications (Cipar et al., 2011; Felde et al., 2010) but the majority of the data has not yet been made available to the public. The coastal ocean sensor aboard the International Space Station, HICO, continues to provide a spectral/temporal record for detailed analysis (Lucke et al., 2011). China has also reported to have flown imaging spectrometers in space but to the knowledge of these authors, no calibrated data has ever been provided to the broader scientific community to support the attestations of these accomplishments by the Chinese.

Historically, spectrometers in the thermal IR are largely based on a Michelson Fourier transform interferometer design. The advantages of a Fourier transform design include very large spectral resolving power and accuracy which led to the development of many laboratory sensor systems. The first significant effort to develop a Fourier transform spectrometer was by a group at Johns Hopkins University in the early 1950s. For some space applications, a Michelson design has been used, including the Nimbus III satellite launched in 1969. A more detailed history of Fourier transform spectrometry can be found in Bell (2012).

It was not until advances in infrared focal planes in the 1980s and 1990s that an imaging spectrometer system based on a Fourier transform design could be realized. Several laboratories embarked on the task, but the commercially available Bomem MB-series of Fourier transform interferometer, with a small 8 by 8 pixel IR FPA replacing the single IR detector, proved to be an early successful approach by Villemaire et al. (1995). Other interferometer imaging spectrometers have been built and multiple companies build and sell a wide variety of sensors. In nearly all cases, the scanning mechanism limits the utility of moving interferometer designs to stable stationary or slow-moving platforms. Airborne or low-Earth spaceborne systems change in viewing geometry during the course of a collection, scrambling the spectral information in the Fourier domain.

Fourier transform techniques are not limited to the IR spectral domain, as other optical designs to produce an interferogram were also developed and, because of the availability of silicon-based detectors, implemented in the visible wavelengths as well. One example of this approach resulted in the Sangac interferometer, which was built and flown on a small experimental satellite by the US Air Force (Otten III et al., 1995).

An alternative to the Fourier transform design is the simple and elegant Fabry-Pérot etalon based on the work of Charles Fabry and Alfred Pérot of the University of Marseille (Fabry and Pérot, 1897). An excellent discussion of the development and use of the Fabry-Pérot etalon is found in Vaughan (1989). Like the closely related Fourier transform imaging spectrometer, the use of the Fabry-Pérot optical form had to await the arrival of an infrared focal plane array to be made into an imaging spectrometer.

The more challenging effort to build a dispersive thermal IR imaging spectrometer was first undertaken by the Aerospace Corporation in the USA with the construction of the SEBASS sensor in 1996 (Hackwell et al., 1996). Multiple data collection campaigns have been conducted with the SEBASS instrument; see Vaughan et al. (2003) as one significant example. However, the challenges of building and operating a high-quality sensor in the thermal IR are significant, and are therefore the likely culprit for the slower availability (and therefore adoption) of thermal spectral technology. The University of Hawaii was also an early developer of thermal hyperspectral sensors which have provided data to support a range of applications development (Lucey et al., 2000). Several instruments from both the commercial and government laboratories have included bands in the thermal IR, including the DAIS instrument from GER which provides seven spectral channels in the 3–12.6 μm region. Many multispectral sensors have thermal bands including MODIS, ASTER, Landsat-TM, just to name a few. The reader interested in a more complete list of multispectral thermal systems is referred to Schott (2007).

The future of space-based imaging spectrometers is developing rapidly with efforts by the German research laboratory, DLR, the Japanese ministry of commercial enterprise and other efforts. The most probable next major space-borne imaging spectrometer to be launched is the German EnMAP sensor, with an expected launch date of 2017 (Stuffler et al., 2007). Not far behind in its development is the Japanese Minister of Economy, Trade, and Industry (METI), which has funded effort to build and launch the HISUI satellite, as the Japan Aerospace Exploration Agency (JAXA) Advanced Land Observation Satellite 3 (ALOS-3) (Iwasaki et al., 2011). Both efforts plan to collect data at 30m ground sample distance resolution but they fundamentally differ in their data policy. The EnMAP program plans to provide free and unlimited access to the imaging spectrometer data to the global research community while the HISUI program, although not yet firm in their policy, is considering a commercial data mode, charging data users for new “ordered collections” as well as data held in archive. The best source of information on the emerging hyperspectral space is the International Space Imaging Spectrometer (ISIS) working group, which is chartered under the IEEE Geoscience and Remote Sensing Society (GRSS) and maintains information from the ISIS working group on their web page (grss-ieee.org). Presentations from the annual meeting can be downloaded

and include details from China, Israel, Italy, Canada, Australia, and the United States in addition to the aforementioned German and Japanese programs.

1.8

Summary and Further Reading

In this chapter we provided an introduction to the basic principles of hyperspectral imaging remote sensing and its applications. The main objective was to provide an overview of the major topics covered more thoroughly in subsequent chapters. Since the basic phenomenology underlying all electro-optical remote sensing systems is the same, part of our discussion is similar to the coverage found in various remote sensing books (Sabins, 2007; Lillesand et al., 2007; Schowengerdt, 2007; Elachi and van Zyl, 2006; Schott, 2007; Eismann, 2012). However, we have made a special effort to include and emphasize topics that are pertinent to the hyperspectral imaging aspects of remote sensing. In this respect, we have chosen to emphasize the four sampling operations in the time, space, wavelength, and radiometric variables underlying the operation of hyperspectral sensors and processing algorithms. Furthermore, we introduce a taxonomy of exploitation algorithms for hyperspectral imaging which is inspired by the capabilities enabled by the unique spectral–spatial information provided by hyperspectral imaging sensors. Information about a wide range of hyperspectral imaging applications is provided by Ustin (2004); Lu and Fei (2014); Manolakis et al. (2003, 2014a,b). The chapter concluded with a brief history of spectral remote sensing and plans for future hyperspectral sensors.

1.9

Book Organization

1

Chapter 1 (this chapter) provides an introduction to the basic concepts of remote imaging spectroscopy and serves as a guide for the topics covered in the remaining chapters.

2 μ μ

The mathematical description of electromagnetic radiation is introduced, as well as the sources of radiation that are remotely sensed by an imaging spectrometer. The transmission of this radiation through the atmosphere is addressed in some detail, including absorption, emission, and scattering with some background provided for the relevant quantum mechanical concepts and outcomes. Finally, the basic radiative transfer equation is presented.

The spectral variation in reflectance and emissivity is addressed in some detail. Additionally, the distribution function that governs the spatial variation of quantities is introduced with a discussion of the practical limitations inherent in its measurement. Examples from different materials illuminate the discussion and demonstrate their variability.

$\mu \quad \mu$
 This chapter describes the operation of imaging spectrometers with an emphasis on unifying principles. The measurement equation and figures of merit are introduced to provide a universal description of the radiometric performance of any imaging spectrometer. A taxonomy of the different imaging spectrometers is introduced with a discussion of their strengths and weaknesses. Finally, an approach to sensor performance modeling is presented.

$\mu \quad \mu$
 Advanced radiometry is introduced to augment the discussion presented in Chapter 2. These principles are then applied in both laboratory and field calibration measurements with the errors elucidated. The entire discussion rests upon traceability to the appropriate standards maintained by the national physical laboratories, such as the National Institute of Standards and Technology. Practical examples are used to illustrate the steps in this critical process that enables quantitative data analysis.

$\mu \quad \mu$
 A more detailed description of atmospheric transmission is presented, building upon the introductory material from Chapter 2. Radiative transfer models are described in some detail and the inversion processes used to convert from at-aperture radiance to apparent reflectance are presented. Finally, the more challenging process of performing temperature–emissivity separation in preparation for LWIR data exploitation is introduced.

In this chapter we introduce statistical distribution models useful for the characterization and analysis of spectral data. We focus on multivariate normal distributions, mixtures of normal distributions, and elliptically contoured distributions.

μ
 The main objective of this chapter is to discuss linear spectral transformations for dimensionality reduction and feature extraction applications. The major algorithm for practical applications is the principal components transformation. However, we discuss whitening transformations, orthogonal transforms that increase class separability, and transformations that maximize signal-to-noise ratios.

This chapter is dedicated to a detailed discussion of the spectral linear mixing model and its applications in hyperspectral imaging applications. We focus on fundamental and practically useful algorithms; however, we provide a concise overview of other algorithms that have theoretical interest or are useful in special applications.

1

This chapter provides the theoretical framework for the development and evaluation of classification and detection algorithms. We develop algorithms using the theory of statistical hypothesis testing by optimizing criteria providing meaningful performance metrics for classification and detection applications. The material in this chapter is used to develop and evaluate target detection and landscape classification algorithms.

11

In this chapter we apply the analysis techniques and algorithms developed in previous chapters to real-world hyperspectral imaging applications with emphasis on hard-target detection and chemical plume detection. Then we develop performance prediction models and show how to improve performance with false alarm mitigation algorithms. We conclude with a brief discussion of change detection and classification algorithms for hyperspectral imaging applications.

2 The Remote Sensing Environment

Remote sensing as presented here relies upon the detection and quantification of electromagnetic radiation from a scene utilizing a spectral imager such as an imaging spectrometer. In all cases, this scene radiation is due to reflected solar energy, emitted thermal energy, or a combination of the two. The details of the scene radiation depend upon the wavelength range of interest and the physical properties that govern the way in which the scene materials reflect, absorb, and emit radiation. The intervening medium of transmission, the earth's atmosphere, impacts the radiation from the scene through the processes of absorption, emission, and scattering that play a central role in modifying, and sometimes obscuring, the spectral signatures of interest to the remote sensing scientist. This chapter will introduce the broad physical concepts that underpin the propagation, interference, and measurement of electromagnetic radiation; the sources of this radiation; the processes of absorption and reflection from a surface; present an overview the underlying quantum physics of atoms and molecules involved in determining atmospheric transmission; and introduce scattering from atoms, molecules, and particulates. An overview of the atmosphere itself will also be presented.

2.1

Electromagnetic Radiation

As described by classical electromagnetic theory, light propagating in a vacuum or medium is an electromagnetic wave composed of sinusoidally oscillating electric and magnetic fields that are perpendicular to each other and to the direction of propagation of the wave itself at any instant in time. Figure 2.1 illustrates an electromagnetic wave with the electric and magnetic fields confined to perpendicular planes. The distance between identical points in successive cycles, the wavelength, is also delimited and is related to the frequency ν through

$$\lambda = \frac{v}{\nu} \quad (2.1)$$

where v is the speed of light as it propagates through an arbitrary medium. The speed of light is denoted as c for a wave propagating in a vacuum.

A mathematical derivation of the wave equation from Maxwell's equations can be found in many texts (see, for example, Lorrain and Corson, 1979) with only the solution for a plane wave presented here. The general solution for both the electric and magnetic fields is most succinctly written in a complex form and, for the electric field, is given by

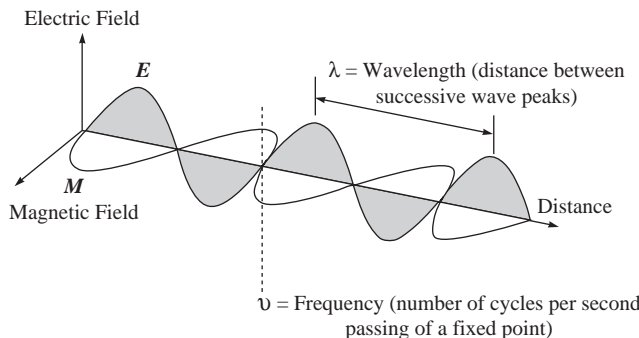


Figure 2.1 A plane electromagnetic wave with the time and space dependent oscillation of the electric and magnetic fields, the wavelength, and the frequency illustrated.

$$\mathbf{E}(\mathbf{r}, t) = \mathbf{E}_o \exp(-\mathbf{k}_i \cdot \mathbf{r}) \exp[i(\mathbf{k} \cdot \mathbf{r} - \omega t)] \quad (2.2)$$

where $\mathbf{E}(\mathbf{r}, t)$ is the spatially and time varying electric field vector, \mathbf{E}_o is the amplitude of the electric field vector at a convenient origin, \mathbf{k} and \mathbf{k}_i are the real and imaginary components respectively of the complex wave vector $\mathbf{k}_c = \mathbf{k} + i\mathbf{k}_i$, \mathbf{r} is the spatial location of an arbitrary point in space at time t , and ω is the angular frequency. An analogous solution can be written for the magnetic field. The solution is presented in the complex form for mathematical convenience with the real portion of the solution being of physical interest. The $\mathbf{E}_o \exp(-\mathbf{k}_i \cdot \mathbf{r})$ term represents an exponential decay in the amplitude of the wave as it propagates through the medium and is absorbed. A medium for which \mathbf{k}_i is zero is therefore non-absorbing. The directions of \mathbf{k}_i and \mathbf{k} are not necessarily the same, but will be for all the cases considered here.

Complex numbers are particularly powerful in the solution of problems that would be almost impossible with real numbers alone, even though the real part of the complex solution corresponds to the physical quantity in question. Recall from the mathematics of complex variables that a complex number is an ordered pair written as $z = x + iy$, where i is $\sqrt{-1}$. The complex conjugate, written as z^* , is defined as $z^* = x - iy$. An ordered pair in the complex plane can alternatively be written as $z = a \cos \theta + ia \sin \theta$ to describe the point (x, y) , similar to the description of an ordered pair in the real plane. The length of the vector in the complex plane is a and θ is the angle between the vector and the real or x -axis. From these definitions it can be shown that the product of z and z^* is

$$zz^* = |z|^2 = x^2 + y^2 = a^2. \quad (2.3)$$

Yet another, but extremely useful notation, is to define

$$\exp(i\theta) = \cos \theta + i \sin \theta, \quad (2.4)$$

so that $z = a \exp(i\theta)$, which is the notation that was used to describe a plane wave with the real part being proportional to $\cos(\mathbf{k} \cdot \mathbf{r} - \omega t)$. The properties of complex numbers will be further explored in the problems at the end of the chapter.

Returning to (2.2), we will first examine the properties of the second exponential function. The phase ϕ is equal to $\mathbf{k} \cdot \mathbf{r} - \omega t$ and the *wavefront* is defined as the surface across which ϕ is constant. For a plane wave this definition implies that, at a given instant, $\mathbf{k} \cdot \mathbf{r}$ is a constant and defines a plane whose position vectors have the same projection onto the real component of the wave vector, \mathbf{k} . Explicitly, for two locations \mathbf{r} and \mathbf{r}_o on the plane of constant phase, \mathbf{k} is perpendicular to the wavefront since $\mathbf{k} \cdot \mathbf{r} = \mathbf{k} \cdot \mathbf{r}_o$ equals a constant. This implies that $\mathbf{k} \cdot (\mathbf{r} - \mathbf{r}_o) = 0$ with the vector $\mathbf{r} - \mathbf{r}_o$ in the wavefront plane. Although this result was derived for a plane wave, it is generally true that \mathbf{k} is perpendicular to the wavefront. In geometrical or Gaussian optics, the ray is defined as the normal to the geometrical wavefront and is therefore parallel to \mathbf{k} .

It remains to provide a physical explanation for \mathbf{k} . This can be accomplished by freezing the plane wave in time and examining the sinusoidal variation of the electric and magnetic fields in space along a line s that is parallel to \mathbf{k} and in the same direction so that $\mathbf{k} \cdot \mathbf{r}$ reduces to ks . In this case the real part of $\exp[i(ks - \omega t)]$ is given by $\cos(ks - \omega t)$, which varies sinusoidally with s while keeping t fixed. The magnitude of \mathbf{k} , denoted by k , is related to the wavelength λ . If a maximum in the amplitude is located at s then the next successive maximum will be at $s + \lambda$ and so on. This implies that the phase must have advanced through one cycle of 2π or $k(s + \lambda) = ks + 2\pi$. Solving yields

$$k = \frac{2\pi}{\lambda} \quad (2.5)$$

for the magnitude of the wave vector. A similar argument can be applied to the time dimension by fixing the spatial position and allowing t to vary over a cycle which yields

$$\omega = \frac{2\pi}{T} = 2\pi\nu, \quad (2.6)$$

where T is the period of one cycle and ν is the frequency.

An individual wavefront moves in the direction of \mathbf{k} at a certain rate called the phase velocity. This is demonstrated by imagining the progression of a point fixed to a maximum of $\cos(ks - \omega t)$. The wavefront is the surface of constant phase that satisfies the condition $ks - \omega t = 2\pi m$, where m is an integer. The phase speed is defined as $v = ds/dt$ or

$$v = \frac{\omega}{k} \quad (2.7)$$

and is equivalent to the speed of light c for an electromagnetic wave propagating through a vacuum.

Returning to the complex wave vector \mathbf{k}_c , it can be shown that it is related to the complex index of refraction through the following

$$n_c = \frac{c}{\omega}(\mathbf{k} + ik_i) = n + in_i = \frac{c}{c'}, \quad (2.8)$$

where again k is the magnitude of the wave vector, k_i is the magnitude of the imaginary wave vector, n is the real index of refraction, n_i is the imaginary index of refraction, and c' is a constant related to electrical permittivity and magnetic permeability of the

medium. For a wave propagating through a vacuum or through a non-absorbing medium, k_i is equal to zero and the complex index of refraction reduces to the familiar equation

$$n_c = n = \frac{c}{v} \quad (2.9)$$

with c' equal to v . The relationship between c' and v is only approximately true for an absorbing medium. In all the cases considered here, n is greater than one, which means that the phase speed is slower than the speed of light in a vacuum. It should be noted that n_c is a property of the medium with a strong dependence upon frequency.

An additional property of electromagnetic radiation is polarization. A plane wave as described above is linearly polarized with the direction of the perpendicular electric and magnetic field vectors maintaining their orientation in space and time. For a plane wave in a lossless medium this implies that \mathbf{k} and \mathbf{E} are in a stationary plane. If two plane waves are co-propagating then their electric field vectors will add according to the principle of superposition. If they are in phase, i.e. $\mathbf{k} \cdot \mathbf{r} - \omega t$ is the same for both waves, the resulting wave will also be linearly polarized. If there is a phase difference between the two waves then a more complicated polarization state results. Light typically is the result of an ensemble of emitters with each separately emitting a brief burst of polarized radiation, with the phase of the individual waves being uncorrelated. The resulting radiation field is randomly polarized with no coherent polarization state discernible. We will be concerned with light in the random polarization state, although light scattered in the atmosphere has important polarization properties.

2.1.1 The Energy of an Electromagnetic Wave

It is a familiar experience that sunlight incident upon a surface will transfer energy that is detected in the form of heat. How is that energy transfer related to the electromagnetic properties of light? Consider light passing through an area that is perpendicular to the direction of propagation. This could be a real aperture or just an area in free space. The rate at which energy flows through the area is the flux Φ in units of energy per unit time. The energy density or *irradiance* is the flux per unit area.

The governing relationship between the irradiance and the electromagnetic wave is given by

$$\mathbf{S} = \mathbf{E} \times \mathbf{H}, \quad (2.10)$$

where \mathbf{S} is called the Poynting vector whose magnitude is the instantaneous irradiance of the wave, \mathbf{E} is the electric field, and \mathbf{H} is the magnetic field. The direction of \mathbf{S} is in the direction of propagation of the wave. However, the quantity of interest is not the instantaneous irradiance but is the average over a period of time. A convenient period is one cycle of the harmonic wave or

$$\langle \mathbf{S} \rangle = \langle \mathbf{E} \times \mathbf{H} \rangle = \frac{1}{2} c \epsilon_0 |\mathbf{E}|^2, \quad (2.11)$$

with $|\mathbf{E}|$ being the magnitude of the electric field vector and the factor of $1/2$ due to the average of a harmonic wave over the single cycle. The critical fact is that the irradiance

is proportional to the square of the amplitude of the electromagnetic field. The letter E is used to signify irradiance in the radiometry literature, which is the notation that will be followed here. Atmospheric scientists tend to use the letter F to signify irradiance and refer to it as the flux density, or sometimes as just the flux.

2.1.2 Absorption

The first term of (2.2) is the amplitude given by $E_o \exp(-\mathbf{k}_i \cdot \mathbf{r})$ at \mathbf{r} and describes the absorption of the electromagnetic wave in a medium. Substituting this result into (2.11) yields

$$E = E_o \exp(-2\mathbf{k}_i \cdot \mathbf{r}) \quad (2.12)$$

for the irradiance E at \mathbf{r} with E_o being the initial irradiance at $\mathbf{r} = 0$. For a plane wave propagating in the direction of \mathbf{r} , the dot product reduces to $k_i r$ and (2.12) becomes

$$E = E_o \exp(-2k_i r) \quad (2.13)$$

with magnitude of \mathbf{k}_i given by (2.8) as

$$k_i = \frac{\omega}{c} n_i = \frac{2\pi\nu}{c} n_i = \frac{2\pi}{\lambda} n_i. \quad (2.14)$$

Upon substitution into (2.13) this yields

$$E = E_o \exp\left(-\frac{4\pi n_i}{\lambda} r\right) = E_o e^{-k_a r} \quad (2.15)$$

for the irradiance with the *absorption coefficient* k_a defined as

$$k_a \equiv \frac{4\pi n_i}{\lambda} \quad (2.16)$$

with dimensions of inverse length. Note that k_a generally has a strong dependence upon wavelength. The a subscript is added to avoid confusion with the magnitude of the wave vector k .

The transmission through the medium from $r = 0$ to an arbitrary point r is calculated by rearranging (2.15) to give

$$T(r, \lambda) = \frac{E}{E_o} = e^{-k_a(\lambda)r}, \quad (2.17)$$

which is known by various names for the scientists that developed it, including, but not exclusively, Beer's law, the Beer–Lambert law, and the Beer–Lambert–Bouguer law. It will be referred to as Beer's law for convenience here, although the first to develop it was Pierre Bouguer (Thomas and Stammes, 1999). The λ is explicitly called out as a reminder of the spectral dependence.

Figure 2.2 shows graphs of the components of the index of refraction of water. The real index n is important for the reflection and refraction of light as it passes from one medium to another, and we have shown that the complex index n_i is responsible for absorption in the medium. Water is essentially transparent at the visible wavelengths from about 0.4 to 0.7 μm but is strongly absorbing in the infrared.

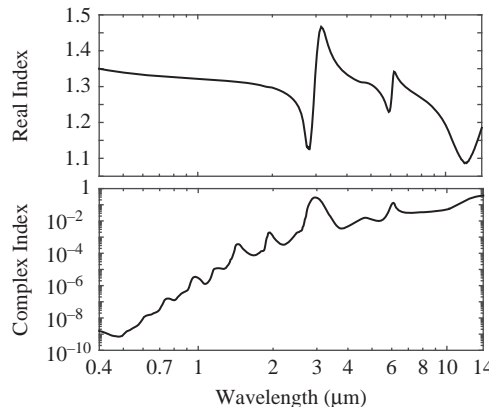


Figure 2.2 The real and imaginary components of the index of refraction for water. The y-axis of the imaginary index plot is logarithmic.

2.2 Diffraction and Interference

Even though this chapter is primarily a description of the generation and propagation of electromagnetic radiation, we will also introduce the phenomena of diffraction and interference since they are critical to the understanding of all spectroscopic instruments and also for scattering. These terms describe the same physical process in different contexts and are fundamentally wave phenomena. The qualitative discussion of diffraction that follows is based on the presentation in Chapter 6 of Stone (1963), which is well worth reading for a more comprehensive understanding. A quantitative introduction to diffraction from a slit and from a circular aperture will also be introduced. Finally, the results of Young's experiment will be presented to demonstrate the combined results of both diffraction and interference. This last discussion will be particularly useful when the action of a diffraction grating is addressed in Chapter 4. Later in this chapter the concepts will be applied in a qualitative description of scattering by a particle. Without an understanding of interference the directionality of scattering is unintelligible.

2.2.1 Qualitative Description of Diffraction

A relatively simple experiment that is fairly easy to perform, thanks to the availability of laser pointers, is to illuminate a pinhole with a laser beam. Take an opaque sheet (a good choice is to fold a sheet of tin foil into several layers) and punch a small hole in it with a needle. In a darkened room, illuminate the hole with the beam perpendicular to the foil surface and observe the projected light on a wall some distance away. The resulting image will display approximately concentric rings of light and dark areas, known as interference fringes, rather than just an image of the hole with a hard edge. The image probably won't be of perfect rings, because it is difficult to make a perfectly circular hole, but with a little effort you will quite clearly produce a ringed pattern due to diffraction.

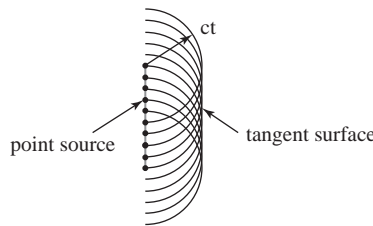


Figure 2.3 Huygens' construction. Note that the wavelets only propagate into the forward hemisphere at the speed of light in the medium.

The diffraction pattern is due to a combination of the incident, or primary, wave and the secondary waves produced by the interaction of the light with the screen. When an electromagnetic wave interacts with any matter the electrons in the material are set into oscillatory motion by the time-varying electric field vector of the wave and, since an accelerated charge radiates, a secondary wave is produced. The force from the magnetic field is much smaller and is neglected. The charges oscillate at the same frequency as the exciting wave and therefore the secondary waves are also at the same frequency. The principle of superposition, whereby the total electric and magnetic field vectors at a point is the vector sum of the individual contributing fields, can be applied to calculate the resulting fields. At the opaque screen and far from the hole, the incident and secondary waves will completely cancel, typically within a depth of a few wavelengths inside an absorbing material.

The primary wave and the secondary waves produced by the electron oscillations proximate to the hole are what produces the interference fringes; however, the method used to calculate the diffraction pattern relies upon the concept that the primary wavefront is the source of spherical secondary wavelets such that the primary wavefront at some later time is the tangent surface of the wavelets, as illustrated in Figure 2.3. One can visualize this by replacing the hole in the screen with the same material, thereby eliminating the diffraction pattern due to the superposition principle where the primary and secondary waves perfectly cancel each other. Next, imagine removing the rest of the screen but leaving the portion that filled the hole behind with the electrons distributed through it continuing to oscillate. The diffraction pattern reappears on the screen due to these imaginary oscillators. The original case with the hole can now be viewed as an equivalent case of an ensemble of oscillators within the hole with the rest of the opaque screen ignored. This is known as Huygens' construction after Christian Huygens; it was expanded by Fresnel and Kirchhoff and is the usual method to calculate diffraction (Born and Wolf, 1999). It should not be interpreted that the empty aperture is a source of electromagnetic radiation; only oscillating charges can do that! Stone (1963) provides a description of the assumptions and approximations used in the approach for the interested reader.

2.2.2 Quantitative Description of Diffraction

Fully rigorous solutions of diffraction problems are quite challenging and, as a result, powerful approximation techniques have been developed. Huygens' construction, and

particularly Kirchhoff's application of it, is typically used and provides results that are sufficient for most purposes and certainly for the systems that we will encounter. Diffraction is further divided into two cases: Fresnel and Fraunhofer diffraction. The Fresnel case is more general and describes diffraction in which the light source, aperture, and image screen or some combination are close enough together so that the wavefronts are spherical. Fraunhofer diffraction is the limiting case of Fresnel diffraction when the source and the screen are so distant that the wavefronts at the aperture and the screen are essentially planar. Fortunately diffraction in many optical systems can be adequately described by the Fraunhofer case and that is the only case that we will address. For the full development of both cases and for a discussion of their application to optical systems see Born and Wolf (1999).

First, a little background to conceptualize interference will be provided. An important property of waves of any kind that interfere in an observable way is known as *coherence*, where the waves have the same frequency and have a stationary phase relationship in both time and space. Like many physical concepts, coherence is an idealization since no source is perfectly monochromatic, which implies perfect temporal coherence, and all sources, even lasers, have a finite coherence length. From (2.2), a plane electromagnetic wave propagating along the x -axis in a non-absorbing medium can be written as

$$\mathbf{E}_1(x, t) = \mathbf{E}_{1o} \exp[i(kx - \omega t + \phi_1)], \quad (2.18)$$

where ϕ_1 is an arbitrary phase shift that can be determined from the initial conditions. A second wave, which is also a solution to the wave equation, propagates in the same direction and is written as

$$\mathbf{E}_2(x, t) = \mathbf{E}_{2o} \exp[i(kx - \omega t + \phi_2)], \quad (2.19)$$

where ϕ_2 is its phase shift. It is convenient to pick the initial conditions where either ϕ_1 or ϕ_2 is zero. Figure 2.4 shows how the two waves add, through the principle of superposition, for three different phase relationships. Setting ϕ_1 equal to zero, if ϕ_2 is equal to 0 or 2π then the two forms are identical and they add constructively. If ϕ_2 is π

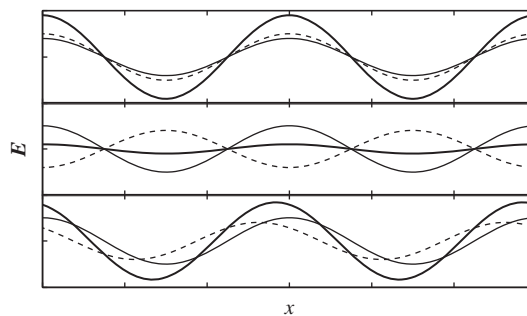


Figure 2.4

The superposition of two waves with $\mathbf{E}_{2o} = 0.8\mathbf{E}_{1o}$. The thin solid and dotted lines are the individual waves and the heavy solid line is the superposition. The top graph illustrates constructive interference where the phase difference is 0, the middle graph is destructive interference where the phase difference is π , and the bottom graph is the superposition of the two waves with a phase difference of $\pi/4$.

then they are 180° out of phase and they add destructively. The final case illustrated is an intermediate one with an arbitrary phase relationship. Such waves are generated by sources made up of radiators that have a fixed spatial relationship to each other, called coherent sources, and interference is not possible for a source that lacks this property.

The irradiance from the two waves is given by (2.11) and, in the complex representation, $|\mathbf{E}|^2$ is equal to $\mathbf{E} \cdot \mathbf{E}^*$. For simplicity we will assume that \mathbf{E}_{1o} and \mathbf{E}_{2o} are parallel so that the vector sum reduces to simple addition. From the principle of superposition the resulting wave at a particular location x is

$$\mathbf{E}(x, t) = \mathbf{E}_1(x, t) + \mathbf{E}_2(x, t) = (\mathbf{E}_{1o}e^{i\phi_1} + \mathbf{E}_{2o}e^{i\phi_2}) \exp[i(kx - \omega t)]. \quad (2.20)$$

The irradiance is therefore

$$E = \frac{1}{2}c\epsilon_o|\mathbf{E}|^2 = \frac{1}{2}c\epsilon_o(E_{1o}^2 + E_{2o}^2 + 2E_{1o}E_{2o} \cos \Delta\phi), \quad (2.21)$$

where $\Delta\phi = \phi_2 - \phi_1$ is the relative phase that could be due to the two waves being generated at different times or locations. The final term in (2.21) is due to interference between the two waves, which vanishes for incoherent sources.

Consider the case where the two monochromatic waves with the same wavelength were generated coherently at two different locations at the same time. The phase difference is proportional to the path difference δ between the two sources or

$$\frac{\Delta\phi}{2\pi} = \frac{\delta}{\lambda}, \quad (2.22)$$

since the wavelength represents one spatial cycle of the wave. This relationship will be used repeatedly to develop the interference phenomena required to understand optical systems and in the scattering discussion below.

Diffraction from a Slit

A slit will be utilized to develop the quantitative description of diffraction through the irradiance at a distant screen. The slit is addressed as a two-dimensional problem and it is left as an exercise to generalize it to three dimensions for the description of diffraction from a rectangular aperture. The diffraction pattern is produced on a screen a large distance away from the slit so that the width a of the slit is much less than the screen distance. The approach utilizes Huygens' construction and the slit is divided into a series of spherical sources as illustrated in Figure 2.5. Spherical wavelets are not described by a plane wave and the solution to the wave equation in a non-absorbing medium for a spherical wave is of the form

$$\mathbf{E}(r, t) = \frac{\mathbf{E}_o}{r} \exp[i(kr - \omega t)], \quad (2.23)$$

which reduces to a plane wave at large distances for Fraunhofer diffraction. For an individual source element (2.23) becomes

$$d\mathbf{E} = \frac{\mathbf{E}_o}{r} \exp[i(kr - \omega t)] dx \quad (2.24)$$

for sources of width dx .

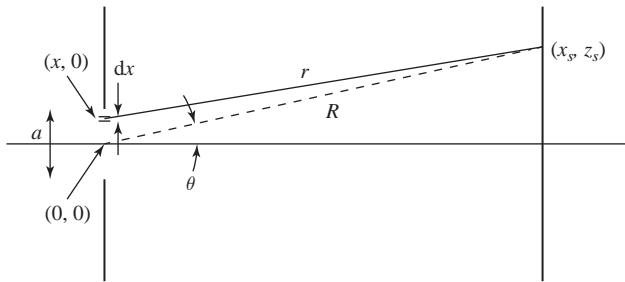


Figure 2.5 Slit diffraction geometry

The distance from an arbitrary source element to a point on a screen is given by r and the distance to the same point from the center of the slit by R . These two distances are written as

$$r^2 = (x_s - x)^2 + z_s^2 \quad (2.25)$$

and

$$R^2 = x_s^2 + z_s^2, \quad (2.26)$$

allowing r to be rewritten as

$$r = R \left[1 + \frac{x^2}{R^2} - \frac{2x x_s}{R^2} \right]^{1/2} \approx R \left[1 - \frac{2x x_s}{R^2} \right]^{1/2} \quad (2.27)$$

since x^2/R^2 is vanishingly small. Equation (2.27) is expanded using a binomial expansion yielding

$$r = R \left[1 - \frac{x x_s}{R^2} - \frac{1}{8} \frac{(x x_s)^2}{R^4} - \dots \right] \approx R - x \sin \theta, \quad (2.28)$$

where all of the higher-order terms are neglected and x_s/R has been replaced by $\sin \theta$.

The distance r is used in the phase of (2.24) because it is sensitive to small variations, while \mathbf{E}_o/r is replaced by \mathbf{E}_o/R since the wave is planar after having traveled the lengthy distance to the screen. The electric field at a point on the screen is the sum of the contributions from the coherent sources at the slit or

$$\begin{aligned} \mathbf{E} &= \frac{\mathbf{E}_o}{R} \int_{-\frac{a}{2}}^{\frac{a}{2}} \exp\{i[k(R - x \sin \theta) - \omega t]\} dx \\ &= \frac{\mathbf{E}_o a}{R} e^{i(kR - \omega t)} \frac{\sin(\frac{ka}{2} \sin \theta)}{\frac{ka}{2} \sin \theta}, \end{aligned} \quad (2.29)$$

and the irradiance E as a function of θ is

$$E(\theta) = \frac{1}{2} c \epsilon_o \left(\frac{\mathbf{E}_o a}{R} \right)^2 \left(\frac{\sin \alpha}{\alpha} \right)^2 = E(0) \left(\frac{\sin \alpha}{\alpha} \right)^2, \quad (2.30)$$

where (2.11) has been applied, $E(0)$ is the on-axis irradiance, and α is defined as $(ka/2) \sin \theta$. The ratio $\sin \alpha / \alpha$ is known as a sinc function and (2.30) is often written as

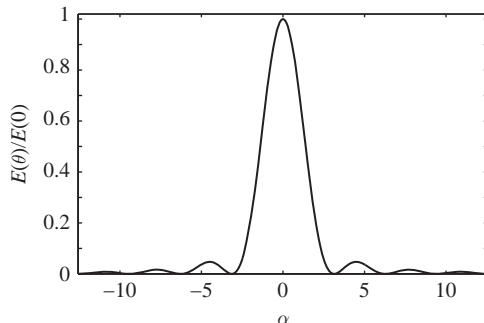


Figure 2.6 Irradiance pattern for Fraunhofer diffraction from a slit.

$E(\theta) = E(0)\text{sinc}^2\alpha$. It can be shown by applying L'Hospital's rule that the sinc function is equal to unity when θ is zero.

Figure 2.6 illustrates the irradiance as a function of α . The irradiance is concentrated within the central maximum bounded by $\alpha = \pm\pi$ that integrates to 0.903 when $E(0)$ is unity, which is about 19 times the amount in the first two adjacent side lobes ($\alpha = \pm\pi$ to $\pm 2\pi$). The minima are located at $\pm m\pi$ where m is a positive integer, which combined with α yields

$$a \sin \theta = m\lambda \quad m = 1, 2, 3, \dots \quad (2.31)$$

for positive values of θ . Notice that the distance across the central maximum becomes larger as a approaches λ . Equation (2.31) is understood physically by dividing the slit in half and considering wavelets that originate from the top and middle and travel at an angle θ to a point P on the screen corresponding to the first minima. The two waves will have a path difference δ that is equal to $(a/2) \sin \theta$. The path difference is also equal to $\lambda/2$ for destructive interference. There is nothing special about the choice of the two radiators and we could have picked any two that were a distance $a/2$ apart. The resulting condition for destructive interference is $a \sin \theta = \lambda$. The successive minima correspond to even divisions of the slit with $m = 2$ corresponding to $\delta = \lambda/2 = (a/4) \sin \theta$ and so on.

Diffraction from a Circular Aperture

Diffraction from a circular aperture is critical to understanding optical systems since it establishes the lower bound for spatial resolution. For example, every imaging spectrometer has a telescope that focuses the light from a distant source onto an image plane. For now, we will assume that the focusing occurs perfectly with no aberrations from the optics marring the image. Considering light from a point source alone, such as a star, the wavefronts that are incident on the telescope's circular aperture will be planar due to the large distance that they have traveled. The pattern that is produced at the image plane will not be a point but rather a circular diffraction pattern. This pattern is the minimum spot size that the system can produce.

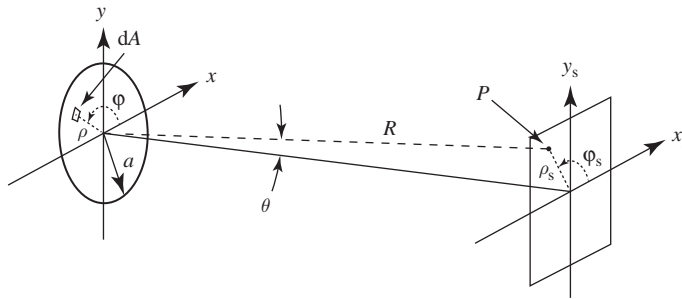


Figure 2.7 Geometry used in the calculation of the irradiance pattern at a screen with point P identified by θ for a circular aperture of radius a .

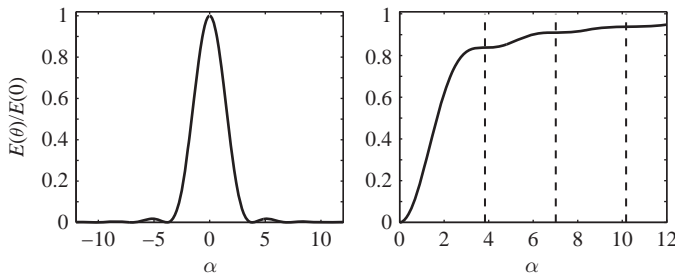


Figure 2.8 The left graph is a one-dimensional cross section of the Airy disk and the right graph illustrates the irradiance contained within the pattern as a function of α adapted from Born and Wolf (1999). The vertical dashed lines are the locations of the first three minima.

The calculation of the Fraunhofer diffraction pattern from a circular aperture is conceptually identical to that of a rectangular aperture except with spherical polar symmetry, and only the results will be presented. As illustrated in Figure 2.7, a plane wave is normally incident from the left on the circular aperture of radius a . The diffraction pattern is the sum of the contributions from each element of area dA requiring a double integration, which can most easily be accomplished using the polar coordinates ρ and ϕ at both the aperture and screen. The irradiance is given by

$$E(\theta) = E(0) \left[\frac{2J_1(\alpha)}{\alpha} \right]^2 \quad (2.32)$$

where

$$\alpha = ka \sin \theta \quad (2.33)$$

and $J_1(\alpha)$ is a Bessel function. The two-dimensional pattern illustrated on the left in Figure 2.8 is known as the Airy disk after G. B. Airy, who first demonstrated it (Airy, 1838). The right side shows the fraction of the total irradiance contained within successive minima with over 80 percent of it inside the central maximum. The first minimum of the diffraction pattern is located at

$$\sin \theta = 1.22 \frac{\lambda}{d}, \quad (2.34)$$

where d is the aperture diameter and θ is the angular diameter of the Airy disk.

2.2.3 Interference

Diffraction is the result of interference from the primary wave incident on the aperture and the secondary waves originating proximate to the aperture. What is typically meant by the distinction between diffraction and interference is that interference is the interaction of light from two or more coherent sources rather than just one. All interference patterns from apertures are manifestations of diffraction (interference from a single aperture) and interference between coherent sources. The simplest case is that of two coherent sources and is known as Young's experiment.

Two slits, each of width a and a distance d apart, are illuminated by a monochromatic plane wave with the geometry illustrated in Figure 2.9. Paralleling the derivation in Section 2.2.2, the distance from the upper slit to an arbitrary point on the screen is

$$r_1 = [(x_s - x_1)^2 + z_s^2]^{\frac{1}{2}} = [R^2 - 2x_1 x_s + x_1^2]^{\frac{1}{2}} \quad (2.35)$$

and similarly for the lower one

$$r_2 = [(x_s - x_2)^2 + z_s^2]^{\frac{1}{2}} = [R^2 - 2x_2 x_s + x_2^2]^{\frac{1}{2}}, \quad (2.36)$$

where $R^2 = x_s^2 + z_s^2$, which is much larger than the distance from the origin to either x_1 or x_2 . It is left as an exercise to show that, in the limit of $R^2 \gg x_1^2$ and x_2^2 , the two distances reduce to

$$r_1 = R - x_1 \sin \theta \quad (2.37)$$

$$r_2 = R - x_2 \sin \theta, \quad (2.38)$$

where $\sin \theta = x_s/R$ has been used. The path difference δ between the slits is

$$\delta = r_2 - r_1 = (x_1 - x_2) \sin \theta = d \sin \theta \quad (2.39)$$

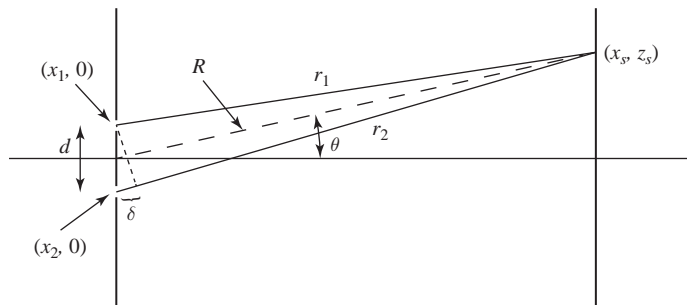


Figure 2.9 Young's experiment geometry.

and the geometrical interpretation of (2.39) is illustrated in Figure 2.9. The light from the two slits will interfere at (x_s, z_s) and the interference will be constructive if the path difference is an integer multiple of λ or

$$d \sin \theta = m\lambda \quad m = 0, 1, 2, \dots \quad (2.40)$$

with the derivation of the similar equation for destructive interference left as an exercise. Overlaid on the interference pattern will be a diffraction pattern from each slit.

The irradiance at the screen is calculated by applying the principle of superposition and (2.11). Again, the spherical waves that originate at the two slits as described by (2.23) have become planar at the screen for the Fraunhofer case. The $1/R$ factor will be absorbed into the amplitude as a convenience and the superposition of the two waves at (x_s, z_s) is written as

$$\mathbf{E} = \mathbf{E}_1 \exp[i(k_1 r_1 - \omega t)] + \mathbf{E}_2 \exp[i(k_2 r_2 - \omega t)] \quad (2.41)$$

and the relative phase between the two waves is due to the different path lengths. The irradiance is proportional to $\mathbf{E} \cdot \mathbf{E}^*$ or

$$|\mathbf{E}|^2 = E_1^2 + E_2^2 + 2\mathbf{E}_1 \cdot \mathbf{E}_2 \cos(k_1 r_1 - k_2 r_2), \quad (2.42)$$

which is further reduced to

$$\begin{aligned} |\mathbf{E}|^2 &= E_1^2 + E_2^2 + 2\mathbf{E}_1 \cdot \mathbf{E}_2 \cos[k_1 r_1 - k_2(r_1 + \delta)] \\ &= E_o^2 + E_o^2 + 2\mathbf{E}_1 \cdot \mathbf{E}_2 \cos(kd \sin \theta), \end{aligned} \quad (2.43)$$

where (2.39) has been applied and the magnitudes of the two wave vectors are identical for monochromatic light. It will also be assumed that the amplitudes of the interfering waves are the same, given by E_o and $\mathbf{E}_1 \cdot \mathbf{E}_2$ reduces to E_o^2 . The final form of (2.43) is

$$|\mathbf{E}|^2 = 2E_o^2[1 + \cos(kd \sin \theta)] = 4E_o^2 \cos^2\left(\frac{1}{2}kd \sin \theta\right), \quad (2.44)$$

where the trigonometric identity $\cos^2(\frac{1}{2}A) = \frac{1}{2}(1 + \cos A)$ has been applied. The total irradiance due to both diffraction and interference is proportional to the product of (2.30) and (2.44).

2.2.4 Diffraction and Interference Summary

This completes our brief discussion of interference and diffraction. The critical concept that should be taken away is that waves that have a stable phase relationship will interfere and, depending upon the context, the different terminologies are applied. This fundamental wave phenomena enables the production of many of the spectroscopic imagers that will be described in Chapter 4. In a spectroscopic instrument the phase difference is due to an optical path difference such as the one introduced to describe Young's experiment. Interference also governs scattering in the atmosphere as we will develop below.

2.3

Basic Radiometry

Radiometry is the science that governs the quantification of electromagnetic radiant energy. It is through radiometry that physical units are assigned to measurements of light enabling the application of physical models to data and vastly increasing its usefulness. In our context the light to be measured is broadband within some wavelength limits and is incoherent, i.e. the amplitude and phase are not fixed for some relatively large period of time and distance but fluctuate randomly. This incoherence means that the measured power from, for example, the waves incident upon a surface, is just the sum of the powers of the individual waves. Radiometry will be approached from the standpoint of geometrical optics where the transfer of radiant energy is characterized by rays that are perpendicular to the wavefronts and the effects of physical optics, such as diffraction, can be neglected. This works very well for most cases, but there are exceptions that will be recognized as we proceed.

2.3.1

Radiometric Quantities

In our discussion of the Poynting vector, we have already introduced the concept of flux flowing through or being received by a real or imaginary area, which we defined as the irradiance E . Formally, the irradiance at time t is given by

$$E(x, y, t) \equiv \frac{d\Phi(x, y, t)}{dA}, \quad (2.45)$$

where Φ is the flux in energy per unit time at position (x, y) and A is the receiving area. We are typically interested in radiometric quantities that do not vary with time and the t is dropped. The irradiance is due to the totality of flux from the entire hemisphere that is received by the area. A complementary term describes the flux leaving a surface, such as a light source, and is similarly defined as

$$M(x, y) \equiv \frac{d\Phi(x, y)}{dA}, \quad (2.46)$$

where M is the *radiant exitance*. Both the irradiance and exitance describe the distribution of flux with respect to position only, regardless of the direction of ray propagation. In the literature the irradiance is sometimes expressed as a function of the illumination direction of the incident flux from, for example, a collimated beam. An example of this is presented in Chapter 3 when the formalism for reflectance is developed. This does not imply that irradiance is a directional quantity; only that the illumination is from a particular direction.

The remaining radiometric quantities are dependent upon the direction of propagation of the radiant flux. We will first develop the concept of solid angle that is necessary to describe complex radiation fields. Consider an area S in space that is outside of, but viewed from, the center of a sphere as illustrated in Figure 2.10. Lines are drawn from the center of the sphere to each point on the outside perimeter of the area. These lines in turn pierce the surface of the sphere and map out an area A there. The solid angle is defined as

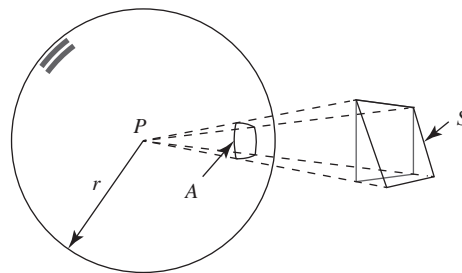


Figure 2.10 Illustration of the definition of the solid angle for an arbitrary shape with respect to a point P .

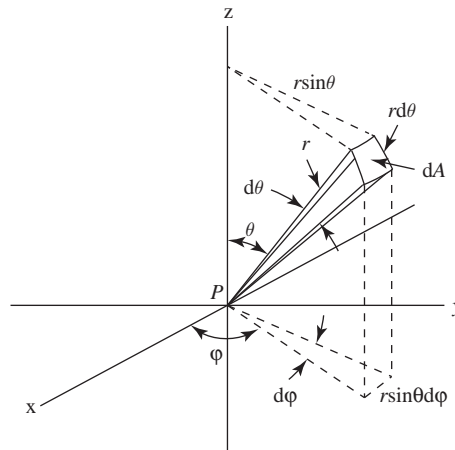


Figure 2.11 Illustration of the definition of the differential solid angle in spherical polar coordinates with respect to a point P .

$$\omega \equiv \frac{A}{r^2}, \quad (2.47)$$

where r is the radius of the sphere. It is unfortunate that the symbol for solid angle and angular frequency is the same, but it should be clear from the context which is the appropriate quantity. The unit for solid angle is the steradian, abbreviated as sr. This is directly analogous to the concept of an angle being defined as an arc length divided by the distance from the vertex of the arc. For a sphere with a surface area given by $4\pi r^2$ the solid angle is 4π sr.

Referring to Figure 2.11, the differential solid angle is obtained by taking the differential area dA , given by the product of $r d\theta$ and $r \sin \theta d\phi$, divided by the square of the distance from the vertex. The differential solid angle is therefore given by

$$d\omega = \frac{dA}{r^2} = \sin \theta d\theta d\phi \quad (2.48)$$

in spherical polar coordinates. It can be shown that for a right circular cone of half angle α , (2.48) yields

$$\omega = 2\pi(1 - \cos \alpha) = 4\pi \sin^2 \frac{\alpha}{2}, \quad (2.49)$$

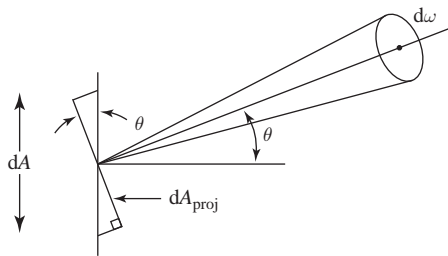


Figure 2.12 The projected area used in the definition of the radiance L .

which reduces to

$$\omega = \pi \alpha^2 \quad (2.50)$$

if the small angle approximation can be applied to $\sin(\alpha/2)$.

The fundamental and most important radiometric quantity is the *radiance* L , which is defined as the flux per unit projected area per unit solid angle leaving or falling upon any reference surface. The projected area is the effective area of the emitted or received flux in the direction of propagation as illustrated in Figure 2.12. This is physically visualized by considering a collimated beam composed of N_o photons per unit time that is incident upon an aperture of area A . If the aperture is perpendicular to the beam then the number of photons per unit time per area flowing through it is N_o/A . If, however, the aperture is tilted with respect to the beam, with its normal vector \hat{n} tilted by the angle θ to the direction of the collimated beam, the number of photons per second N flowing through the area A will be $N_o \cos \theta$. Therefore, the original case N_o/A is related to the present case through

$$\frac{N_o}{A} = \frac{N}{A \cos \theta}, \quad (2.51)$$

where $A \cos \theta$ is the aperture area projected perpendicular to the beam of photons.

Formally the radiance is defined as

$$L(x, y, \theta, \phi) \equiv \frac{d^2\Phi(x, y, \theta, \phi)}{dA_{\text{proj}} d\omega} \quad (2.52)$$

with the projected area given by

$$dA_{\text{proj}} = dA \cos \theta, \quad (2.53)$$

where θ is the angle between the surface normal of the differential area dA and the observation direction. Equation (2.52) can be formulated slightly differently by grouping the angular quantities separately from the area, giving

$$L(x, y, \theta, \phi) = \frac{d^2\Phi(x, y, \theta, \phi)}{dA d\Omega} = \frac{d^2\Phi(x, y, \theta, \phi)}{dA d\omega \cos \theta}, \quad (2.54)$$

where the projected solid angle $d\Omega$ is just the original solid angle multiplied by $\cos \theta$. Radiance from incoherent sources is always additive. It will be shown in Chapter 5 that the radiance is a conserved quantity in any lossless optical system.

The irradiance or exitance is calculated from (2.54) by expressing the flux at a real or imaginary surface as

$$d^2\Phi(x, y, \theta, \phi) = L(x, y, \theta, \phi) \cos \theta d\omega dA$$

and integrating over the full hemisphere appropriate to the direction of propagation. Taking the exitance from a source as an example, the flux from an infinitesimal area dA into the full hemisphere is given by

$$\begin{aligned} d\Phi(x, y) &= dA \int_{\omega} L(x, y, \theta, \phi) \cos \theta d\omega \\ &= dA \int_0^{2\pi} \int_0^{\pi/2} L(x, y, \theta, \phi) \cos \theta \sin \theta d\theta d\phi \end{aligned}$$

and the exitance is therefore

$$M(x, y) = \int_0^{2\pi} \int_0^{\pi/2} L(x, y, \theta, \phi) \cos \theta \sin \theta d\theta d\phi, \quad (2.55)$$

where (2.46) has been applied. If the propagation had been toward the area dA rather than away from it, the derived quantity would have been the irradiance.

The last radiometric quantity is the radiant intensity I which is the flux per unit solid angle emitted by a source in a given direction or

$$I(x, y, \theta, \phi) = \frac{d\Phi(x, y, \theta, \phi)}{d\omega}, \quad (2.56)$$

where the flux originates from the x, y location and propagates into the solid angle associated with θ and ϕ . Intensity is most useful in the description of the flux emitted by a point source, i.e. a source whose diameter is much less than the distance from the point of observation. The intensity describes the distribution of the total flux emitted by the entire source that reaches an infinitesimal area some distance away but with respect to direction only. A way to think about the intensity from an extended source is to apply (2.52) and to integrate over the projected area of the source to yield

$$I(\theta, \phi) = \int_{A_s} L(x, y, \theta, \phi) \cos \theta_s dA_s,$$

where the radiance is a function of position on the source and of the direction given by θ and ϕ . Note that in general the projected area, and therefore θ_s , varies as a function of source surface coordinate while the intensity is described for a particular direction.

In the context of imaging spectroscopy the radiometric quantities are generalized to include a spectral interval such as wavelength, wavenumber, or frequency. An example is the spectral radiance as a function of wavelength defined by

$$L_{\lambda}(x, y, \theta, \phi, \lambda) \equiv \frac{d^3\Phi(x, y, \theta, \phi, \lambda)}{dA_{\text{proj}} d\omega d\lambda}, \quad (2.57)$$

where $L_{\lambda} d\lambda$ is the radiance in a wavelength interval from λ to $\lambda + d\lambda$. This last comment employed some imprecise language. What is really meant is that $L_{\lambda} \Delta\lambda$ is approximately

the radiance within the λ to $\lambda + \Delta\lambda$ interval with the approximation approaching an exact value as $\Delta\lambda$ is shrunk. We will use this kind of description in the future with the understanding that we are referring to finite quantities. The other radiometric quantities can be similarly generalized spectrally. It is the spectral radiance that is measured by an imaging spectrometer.

It is a simple process to convert between different spectral intervals. For example, if the spectral radiance is known as a function of wavenumber \tilde{v} it can be converted to spectral radiance as a function of wavelength λ by noting that the amount of radiance within a spectral interval is the same regardless of the unit of the interval as long as the intervals are equivalent. For this example it must be true that

$$L_{\tilde{v}} d\tilde{v} = L_{\lambda} d\lambda \quad (2.58)$$

for equivalent spectral intervals. The wavenumber is defined as

$$\tilde{v} = \frac{1}{\lambda}, \quad (2.59)$$

which by convention is always recorded in units of inverse centimeters (cm^{-1}). The relationship between the two spectral intervals is obtained by differentiating (2.59), which yields

$$d\tilde{v} = -\frac{1}{\lambda^2} d\lambda, \quad (2.60)$$

from which the spectral radiance in the two different spectral intervals is related by

$$\int_{\tilde{v}_1}^{\tilde{v}_2} L_{\tilde{v}}(\tilde{v}) d\tilde{v} = \int_{\lambda_1}^{\lambda_2} L_{\tilde{v}}[\tilde{v}(\lambda)] \frac{d\tilde{v}}{d\lambda} d\lambda, \quad (2.61)$$

where $d\tilde{v}/d\lambda$ is the Jacobian for the transformation from \tilde{v} to λ . The spectral radiance in terms of wavelength, L_{λ} , is the integrand on the right of (2.61). Notice that the upper integration limit on the right-hand side is smaller than the lower limit but the integral is positive since the Jacobian is negative from (2.60). A shorthand notation for the mathematical change of variable is

$$L_{\lambda} = L_{\tilde{v}} \left| \frac{d\tilde{v}}{d\lambda} \right| = \frac{L_{\tilde{v}}}{\lambda^2} = \tilde{v}^2 L_{\tilde{v}}. \quad (2.62)$$

Wavenumbers are the natural unit from some imaging spectrometers, as will be shown in Chapter 4.

Even though the radiometric quantities have been defined in terms of infinitesimal variables, real measurements always involve finite spectral intervals and physical dimensions, where geometric optics applies, and yield only average values for the quantities involved. Table 2.1 lists the various radiometric quantities, their definitions, and units. It also includes an alternative list of symbols and terminology that is used in other scientific disciplines such as the atmospheric and astrophysical sciences. Each quantity can be generalized spectrally.

Table 2.1 Basic radiometric quantities.

Quantity	Symbol	Definition	Unit	Alternative
Energy	Q	$\int \Phi dt$	joule(J)	Energy E
Flux	Φ	$\frac{dQ}{dt}$	watt(W)	Flux f
Exitance	M	$\frac{d\Phi}{dA}$	W/m ²	Flux density F
Irradiance	E	$\frac{d\Phi}{dA}$	W/m ²	Flux density F
Radiance	L	$\frac{d^2\Phi}{dA_{\text{proj}} d\omega}$	W/m ² sr	Intensity I
Intensity	I	$\frac{d\Phi}{d\omega}$	W/sr	—

2.4

Radiation Sources

The electromagnetic spectrum that is used in the various remote sensing applications spans an enormous range from ultraviolet to microwave regions but, as discussed in Chapter 1, the wavelength range of interest here is from the ultraviolet to the long-wave infrared, or roughly from $0.350\text{ }\mu\text{m}$ to $14\text{ }\mu\text{m}$. This broad range is divided into regions, with two of those referred to as the reflective and the emissive based upon the source of the radiation measured by a spectral sensor. The reflective corresponds to the range of wavelengths for surface illumination by solar radiation where the atmosphere is also transmitting while thermal emission from the surface at typical terrestrial temperatures is so small that it can be neglected, roughly from about $0.350\text{ }\mu\text{m}$ to $2.5\text{ }\mu\text{m}$. The emissive radiation corresponds to the range where solar illumination is negligible and the radiance is due to emission from the thermal properties of the earth and atmosphere, and it is in the atmospheric window ranging from about $7.5\text{ }\mu\text{m}$ to $14\text{ }\mu\text{m}$. There is an additional portion of the spectrum where the atmosphere is highly transmissive, that ranges from about $2.8\text{ }\mu\text{m}$ to $5.5\text{ }\mu\text{m}$ and has both reflected solar and emissive radiation.

2.4.1

Solar Radiation

The sun is the source of the overwhelming majority of the energy that the earth receives, with most of the electromagnetic radiation originating near the sun's surface in the photosphere. The orbit of the earth about the sun is slightly elliptical and is perturbed by gravitational forces from the other planets within the solar system. For our purposes the orbit will be treated as strictly elliptical with the sun located at one of the two foci. The earth's orbit is almost circular, with a mean value for the eccentricity of about 0.02. The axis of rotation of the earth is also tilted by about 23.5° relative to the sun–earth orbital plane, which accounts for the seasons.

These factors are taken into account when calculating the top of the atmosphere solar spectral irradiance for a given time and location. This can be understood through a conservation of energy argument. At a given instant and distance r_o from the sun, a spectral irradiance $E(r_o, \lambda)$ will cross a unit area perpendicular to the direction of propagation of

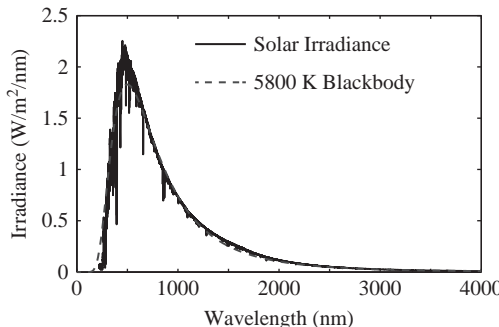


Figure 2.13 The solar irradiance at the mean earth–sun distance and the similar blackbody irradiance for the same distance.

the light. Considering the entire sphere centered on the sun at the distance r_o , the total amount of flux the sun emits is given by $E(r_o, \lambda)4\pi r_o^2$. The total flux will be the same at any other distance r from the sun. This equivalence yields the following relationship for the spectral irradiance at a distance r

$$E(r, \lambda) = E(r_o, \lambda) \left(\frac{r_o}{r}\right)^2 \quad (2.63)$$

with r_o typically being the average earth–sun distance for which the spectral irradiance is known. Equation (2.63) is an example of the inverse square law that applies in general to any point or spherical source.

Figure 2.13 shows the solar spectral irradiance at the mean earth–sun distance along with the irradiance at the same distance for a blackbody in place of the sun at a temperature of 5800 K. A blackbody is described in Section 2.4.2. The top of the atmosphere solar irradiance is not a constant but changes, not only due to the changing distance from the sun, but also due to the solar cycle and the sun’s day-to-day volatility. The solar cycle is a well-established phenomenon, associated with magnetic features on the photosphere called sunspots, relatively dark regions of varying size and abundance, and faculae, areas of bright emission that surround a sunspot. The sunspot abundance peaks about every 11 years and these peaks are correlated with variation in the solar irradiance. The day-to-day variation in solar irradiance is also correlated with the sunspot distribution.

The solar constant is the quantity that describes the total solar irradiance reaching the top of the atmosphere. Measurements of the solar constant were initially performed from the earth’s surface, but state-of-the-art measurements are now done from satellites using active cavity radiometers, thereby removing the influence of the earth’s atmosphere. An understanding of the variation in the total solar irradiance is critical to establishing the energy balance that determines the earth’s climate. Active cavity radiometer measurements are simple in principle and use an absorbing cavity with a precision aperture whose normal is pointed toward the sun. The cavity is designed to be perfectly absorbing so that the irradiance that falls on the precision aperture cannot escape. The cavity is periodically shuttered and the temperature difference between the cavity in its absorbing

mode and its shuttered mode is measured by actively heating it while precisely measuring the power required to maintain a set temperature difference. The ratio of this power measurement to the aperture area gives the value of the total solar irradiance.

There has been significant controversy surrounding the measurements of the solar constant in the past since the disagreement between measurements using different active cavity radiometers has been greater than the reported uncertainties in the measurements. Recent work appears to have resolved this discrepancy through laboratory measurements of the different designs employed, and scattered light contamination has been identified as the cause. The proposed value for the solar constant is now $1360.8 \pm 0.5 \text{ W/m}^2$ as compared to the previous value of $1365.4 \pm 1.3 \text{ W/m}^2$ (Kopp and Lean, 2011). This small difference has very little effect on the solar spectral irradiance in a narrow spectral channel since the solar constant is the sum of the irradiance for all of the emitted wavelengths.

2.4.2 Thermal Radiation

All objects emit electromagnetic radiation through the conversion of some of the object's internal energy to emission. At the typical temperatures of the earth and the atmosphere this radiation is primarily in the long-wave infrared. The functional form of the spectral radiance from thermal emission was not fully understood until Max Planck's work was published in 1900, building upon the theoretical concept of a blackbody that had been published by Gustav Kirchhoff in 1860 (Planck, 1901). A full understanding of thermal emission was not possible until the development of the quantum theory.

The detection of objects or gases is more complicated in the thermal emissive due to thermodynamics. In this case, the detection problem that utilizes data from an imaging spectrometer that viewed a scene without active radiation sources requires that there be a temperature difference between the object or gases of interest and the surrounding background. When the object or gas is cooler than the background it absorbs more energy than it emits and is observed as a net absorber, and when the object or gas is hotter than the background it is a net emitter. If thermodynamic equilibrium has been achieved and there is no temperature difference then the object or gas is spectrally undifferentiated from the background. This is quite different from the reflective case when the sun serves as an active source. The basic physical concepts governing these processes will be developed in this section.

Blackbody Radiation

An early triumph of quantum theory was the development of Planck's law by Max Planck, which described the relationship between the temperature and emitted radiance of a perfectly absorbing body in thermodynamic equilibrium. A blackbody is an idealized object that absorbs all incident radiation and is therefore "black." It is intuitive that such a body must also emit the same amount of radiation or its temperature would continually increase. Perfect blackbodies do not exist, but a cavity with nonzero emissivity at all wavelengths, held at a constant temperature with an entrance aperture whose dimensions are small compared to the overall dimensions of the cavity, is a very

good approximation. Such a cavity will absorb virtually all the radiation incident on the aperture and will emit radiation with a distribution given by Planck's law.

The derivation of Planck's law can be found in many texts with only the results presented here (see Reif, 1965, for example). The spectral radiance emitted by a blackbody as a function of wavelength and temperature T is given by

$$B_\lambda(T) = \frac{2hc^2}{\lambda^5(e^{hc/k_B\lambda T} - 1)}, \quad (2.64)$$

where Planck's constant h is 6.626×10^{-34} Js, Boltzmann's constant k_B is 1.381×10^{-23} J/K, and the units of $B_\lambda(T)$ are typically expressed as $\text{W/m}^2\text{sr}/\mu\text{m}$ or $\text{W/m}^2\text{sr}/\text{nm}$. Planck's law can also be expressed as a function of frequency

$$B_\nu(T) = \frac{2h\nu^3}{c^2(e^{h\nu/k_B T} - 1)} \quad (2.65)$$

in units of $\text{W/m}^2\text{sr}/\text{Hz}$. The conversion from one spectral unit to another follows the same procedure as was used in (2.61) and is written as

$$B_\lambda = B_\nu \left| \frac{d\nu}{d\lambda} \right| = \frac{\nu^2}{c} B_\nu \quad (2.66)$$

for conversion from frequency to wavelength. Implicit in Planck's law is the quantization of the energy of an electromagnetic wave into photons with the energy of a photon given as

$$\epsilon = h\nu. \quad (2.67)$$

The blackbody distribution is plotted in Figure 2.14 for a range of terrestrial surface temperatures, including the warmest recorded temperature of 56.7°C (329.8 K) and the coldest of -89.4°C (184 K). Also plotted is Wien's displacement law that describes the wavelength dependence of the radiance maximum as a function of temperature given by

$$\lambda_{max} = \frac{k_W}{T} \quad (2.68)$$

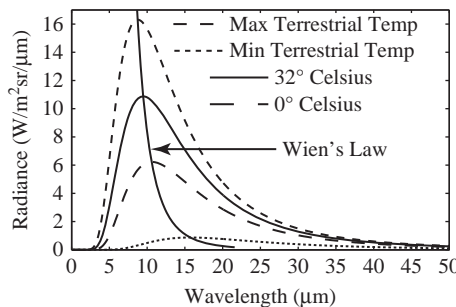


Figure 2.14 The Planck function for a range of terrestrial temperatures. The extremes correspond to the highest and lowest recorded temperatures.

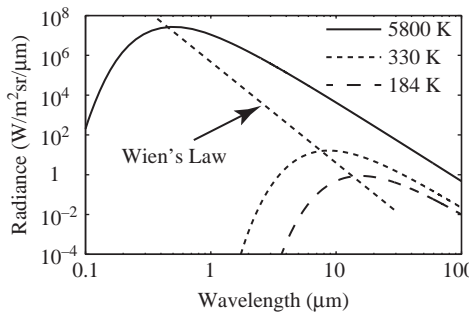


Figure 2.15 The Planck function for a 5800 K blackbody and the high and low terrestrial temperatures.

with Wien's constant, k_W , equal to $2897 \mu\text{mK}$. A 5800 K blackbody has about 0.52 percent of its radiance above $5 \mu\text{m}$ while 329.8 K and 184 K blackbodies have 2.5 percent and 0.01 percent of their radiance below $5 \mu\text{m}$ respectively. The corresponding blackbody radiance curves are illustrated in Figure 2.15 plotted on a log–log scale.

Emissivity and Absorptance

Planck's law corresponds to the theoretical maximum for thermal radiation from a perfectly absorbing body whose dimensions are much larger than the wavelength. The emissivity ϵ is used to account for the difference between a real object at a certain temperature and the idealized blackbody. It is defined as the ratio between the flux per unit area or exitance $M_{\lambda,e}$ emitted by the real object at a temperature T to the exitance that would be emitted by a blackbody at the same temperature, and is given in terms of the radiance by

$$\epsilon(\lambda, \theta, \phi, T) \equiv \frac{L_{\lambda,e}(\lambda, \theta, \phi, T) \cos \theta \, d\theta \, d\phi \, d\lambda}{B_\lambda(\lambda, \theta, \phi, T) \cos \theta \, d\theta \, d\phi \, d\lambda} = \frac{L_{\lambda,e}(\lambda, \theta, \phi, T)}{B_\lambda(\lambda, \theta, \phi, T)} \quad (2.69)$$

for the emissivity at a particular wavelength λ with a particular emission geometry since it will generally also depend upon the direction of propagation of the emitted radiance. If the dimensions of the object are much larger than the wavelength, the emissivity ranges between 0 and 1 because the radiance from a blackbody is the theoretical maximum emitted into any solid angle and at any wavelength.

The absorptivity α is defined as the ratio between the absorbed flux divided by the incident flux. This is written in terms of radiance analogous to (2.69), specifically

$$\alpha(\lambda, \theta, \phi, T) \equiv \frac{\Phi_{\lambda,a}}{\Phi_{\lambda,i}} = \frac{L_{\lambda,a}(\lambda, \theta, \phi, T)}{L_{\lambda,i}(\lambda, \theta, \phi, T)}, \quad (2.70)$$

again for a particular wavelength, illumination geometry, and shared temperature since thermodynamic equilibrium is assumed. It should be noted that in the most general case both the emissivity and the absorptivity can also depend upon the light polarization.

Often, in a measurement, the emissivity is unknown and the concept of a brightness temperature is introduced to characterize the source. This is the temperature that would correspond to the measured emission of a blackbody over the range of wavelengths of

interest, such as over the spectral response function of the imaging spectrometer. The brightness temperature is a useful concept since the integral of (2.64) over a spectral range is unique.

Kirchhoff's Law

We noted above that a perfect absorber of radiation was also a perfect emitter. This concept will be more fully developed by applying the principle of detailed balance (Reif, 1965). Consider a closed cavity whose walls are held at a constant temperature and that may contain a number of opaque bodies within it. It can be shown that the photon density in the resulting radiation field is independent of position, of propagation direction (i.e. it is isotropic), of polarization direction, and of the shape of the cavity. An opaque body within the cavity will have radiation incident upon it that, in general, will be partly absorbed and partly reflected, and the body will emit radiation due to its temperature. If the body and the cavity are in thermodynamic equilibrium, then no thermal changes can occur. Thus the processes of emission and absorption must be in balance.

This argument can be extended by considering the placement of a narrow-band spectral filter between the body and the cavity walls that excludes radiation of wavelengths different from a wavelength range between λ and $\lambda + \delta\lambda$. This cannot affect the nature of the radiation field within the cavity so the energy must remain in balance and this precludes a case where more radiation is absorbed than radiated at one wavelength while less is absorbed than radiated at another, thereby maintaining an overall equilibrium. A similar argument holds for a polarization filter or a blocking filter with a small hole in it so that only a certain location on the body is illuminated. It also holds for radiation incident from a certain direction and solid angle range. Thus the equilibrium holds in detail with the amount of emitted and absorbed radiation balanced for each increment of wavelength, each polarization state, at each location, and for each increment of solid angle.

The above result is known as Kirchhoff's law which can be expressed mathematically in terms of the emissivity and absorptivity. We have shown that the absorbed radiance $L_{\lambda,a}$ and the emitted radiation $L_{\lambda,e}$ are in balance since the body is inside an isothermal cavity and is in thermal equilibrium. Also $L_{\lambda,i}$ is equal to B_λ for the cavity. These two facts imply that

$$\epsilon(\lambda, \theta, \phi, T) = \alpha(\lambda, \theta, \phi, T) \quad (2.71)$$

where (2.69) and (2.70) have been used. This can be further extended by noting that conservation of energy requires that the sum of the fractions of absorbed, reflected, and transmitted energy must equal unity. For an opaque body there is no transmitted energy, so

$$\alpha(\lambda, \theta, \phi, T) + \rho(\lambda, \theta, \phi, T) = 1 \quad (2.72)$$

with the reflectivity ρ defined as the fraction of incident radiation that is reflected from a surface again for the particular wavelength and illumination geometry.

The Validity of Kirchhoff's Law

Kirchhoff's law has been presented in the context of an environment in thermodynamic equilibrium with a body that is isothermal in an isothermal cavity at the same temperature. The conditions that are encountered in remote sensing are quite different from this idealized state. Thermal processes are dominated by solar heating of surfaces and the exchange of energy with the atmosphere through conduction, convection and radiation. How valid is Kirchhoff's law when the absorbing material and the surrounding radiation field are characterized by different temperatures? To what extent does (2.72) hold?

There are persuasive theoretical arguments that justify (2.72) based upon the concept of a freely radiating object. Such an object radiates independently of the surrounding radiation field. Kirchhoff's law will be followed if the energy states characteristic of the body obey the Boltzmann distribution and are therefore in thermal equilibrium at the object's temperature. It is imperative that the object has a uniform temperature to the depth to which the incident radiation penetrates. If the surface is isothermal within this penetration depth then (2.72) holds despite the difference in temperature between the object and its surroundings. This has been shown to hold in both laboratory and field experiments. This isothermal condition is met for almost all materials that make up the Earth's surface (see Salisbury et al., 1994, and Korb et al., 1999). There is also an implicit assumption in the detailed balance argument that Helmholtz reciprocity, the invariance of the light path under time reversal, holds. This is typically, but not always, true and we will defer the full discussion until Chapter 3 when the framework for reflectance has been developed.

2.5

Quantum Mechanical Results

Transmission of radiation through the atmosphere is governed, in part, by atomic and molecular absorption and emission processes. Atmospheric radiative transfer models, which are critical to the processing of imaging spectrometer data, utilize detailed spectroscopic information to retrieve the reflectance signature, in the reflective spectral range, or the temperature and emissivity in the emissive range. A full understanding of the emission and absorption spectra from atmospheric species requires the theory of quantum mechanics. A brief introduction to this vast topic will be provided here in order to familiarize the reader with the concepts that govern the phenomena that are critical to atmospheric transmission. These concepts enable an understanding of the energy distribution of the emitted and absorbed radiation due to the quantization of molecular energy states, the transitions between energy states due to the absorption or emission of a photon, and the broadening mechanisms that govern the wavelength or energy distribution of those photons for a particular transition.

2.5.1

The Historic Development

It was pointed out in Section 2.4.2 that the energy of an electromagnetic wave is quantized into photons. This quantization broadly underlies all physics at the microscopic

scale and includes the quantization of mass, electric charge, and energy in addition to light. One of the impetuses for the development of quantum mechanics was due to the emission of light observed for atoms and molecules. Spectroscopic measurements of excited gases showed that the emitted light was only at discrete wavelengths. Scattering experiments had shown that the atom was composed of a positively charged nucleus surrounded by electrons. A classical model that is mechanically stable would contain electrons orbiting about a nucleus analogous to a planetary system, but this stability fails since an accelerated charge radiates light, causing the electrons to spiral into the nucleus as they lose energy. Additionally, the predicted spectrum from this classical model would be a continuum since the wavelengths emitted are proportional to the frequency of revolution that is continually changing as the electron's orbit decreases.

In 1913 Neils Bohr proposed a model of the atom that postulated the existence of stationary states with the electrons fixed in stable orbits at precise energies (Bohr, 1913). In his model the electrons did not radiate a continuous spectrum due to their accelerated motion, but rather emitted discrete wavelengths as the electrons made a transition from one stationary state to another. He further postulated that the angular momentum of the electrons was also quantized. His model, with some modifications, was remarkably successful in predicting the wavelengths emitted by simple atoms with few electrons but was unable to predict the intensity of the observed spectral lines and it proved to be impossible to generalize to describe the line spectra of the heavier atoms with many electrons.

The deficiencies of the Bohr model of the atom were ultimately addressed in the modern theory of quantum mechanics introduced separately by Werner Heisenberg in 1925 and Erwin Schrödinger in 1926 (van der Waerden, 1967; Schrödinger, 1926). The theory was motivated in part by the discovery that particles such as electrons, protons, and neutrons exhibit wave behavior just as photons exhibited particle properties. Schrödinger proposed a wave equation, analogous to a classical wave equation, that is satisfied by a wave function that describes the propagation of a particle such as an electron. A crucial difference is the interpretation of the wave function. Recall from our discussion of the Poynting vector that the average energy density in an electromagnetic wave is proportional to the square of the amplitude of electric field vector. How is this reconciled with the energy of a single photon contained in a given volume? The interpretation is that the classical electromagnetic wave theory gives the correct average answer for a large number of photons but, when the number of photons is few, $|E|^2$ is proportional to the probability of detecting a photon in a volume. Similarly, in quantum mechanics the wave function ψ describes the motion of a single particle such as an electron and the quantity ψ^2 is proportional to the probability of detecting the particle in a volume.

The resulting wave theory explained the quantization of energy and angular momentum for a confined particle, such as an electron confined by the electric field of a nucleus, in terms analogous to the classical description of standing waves. The requirement that the wave function be single-valued, continuous, and normalized introduces this quantization. Quantum mechanics forms the basis of our understanding of the physical processes at the microscopic level for all matter.

2.5.2 Atomic Emission and Absorption

Although the atmosphere is overwhelmingly dominated by molecular species with only trace amounts of atomic gases such as argon, which makes up about 0.9 percent of the atmosphere, it is instructive to develop some of the quantum mechanical concepts using an atomic model. An atom has the advantage of having a single nucleus with a number of orbiting electrons. This results in energy states that are governed by the electromagnetic interactions between the electrons and between the electrons and the nucleus. Quantum mechanics does not provide an exact solution for any atom that has more than one electron, but powerful approximation and computational techniques have been developed that enable any atom to be modeled to the desired level of accuracy. The results for hydrogen illustrate the pertinent electronic properties that are applicable to all atoms and can be extended to molecules.

The quantum mechanical solution for the electronic energy of a hydrogen atom leads to discrete values for the energy. The energy levels are characterized by the principal quantum number n and the energy of a particular energy level is given by

$$E_n = -\left[\frac{\mu}{2\hbar^2}\left(\frac{e^2}{4\pi\epsilon_0}\right)^2\right]\frac{1}{n^2} \quad n = 0, 1, 2, \dots, \quad (2.73)$$

where μ is the reduced mass of the electron given by

$$\mu = \frac{mM}{m + M}, \quad (2.74)$$

where m is the electron's mass and M is the mass of the nucleus, \hbar is Plank's constant divided by 2π , e is the charge of an electron, and ϵ_0 is the permittivity of space. The reduced mass is often approximated as just the mass of the electron, since a proton is three orders of magnitude more massive than an electron. The energy is negative since it is referenced to the binding or ionization energy of the atom. The ground state energy is

$$E_1 = -\left[\frac{\mu}{2\hbar^2}\left(\frac{e^2}{4\pi\epsilon_0}\right)^2\right] = -13.6 \text{ eV}, \quad (2.75)$$

which implies that a hydrogen atom in its lowest energy state would have to absorb 13.6 eV of energy to remove the electron. An eV is the common unit of energy used at the atomic scale and is the amount of energy an electron gains when it is accelerated through a potential difference of 1 V.

Absorption or emission can only occur for a photon whose energy corresponds to the difference between the upper and lower states. Conservation of energy requires that

$$E_u = E_l + h\nu, \quad (2.76)$$

where E_u and E_l are the energies of the upper and lower stationary states. The photon's wavelength is calculated using (2.73) and (2.76) combined with the energy of a photon expressed as $\epsilon_\lambda = hc/\lambda$, which gives

$$\frac{1}{\lambda} = R\left(\frac{1}{n_l^2} - \frac{1}{n_u^2}\right), \quad (2.77)$$

where n_u and n_l are the upper and lower principal quantum numbers respectively for the stationary states and R is the Rydberg constant, defined as

$$R \equiv \frac{\mu}{4\pi c\hbar^3} \left(\frac{e^2}{4\pi\epsilon_0} \right)^2 = 1.097 \times 10^7 \text{ m}^{-1}. \quad (2.78)$$

As an example, if the photon is absorbed then the final state of the atom is the upper state, the photon vanishes, and the total energy is conserved.

The quantization of energy is one necessary condition for the generation of line spectra, but it is not the only condition. The emission or absorption of a photon is caused by the interaction of the photon's electromagnetic field with the bound electron. Selection rules are derived that govern whether or not a transition can occur at all. These selection rules depend upon the type of electromagnetic interaction, such as an electric dipole or an electric quadrupole interaction. The absorption and emission processes of atoms and molecules are typically dominated by the electric dipole interaction, which is usually several orders of magnitude stronger than any of the other multipole interactions. The strength of these transitions depends upon the wave functions of the upper and lower energy states and the magnitude of the dipole moment. If there is no dipole moment, or if the wave functions are incompatible, then that transition is excluded.

The selection rules for the absorption or emission of a photon are governed by conservation of angular momentum and parity, the resulting sign-change of the portion of the wave function that describes the angular momentum when the spatial coordinates are inverted. Both photons and electrons have quantized angular momentum vector states and only certain changes in angular momentum are allowed. Angular momentum conservation implies that the vector sum of the angular momenta before the transition between stationary states is equal to the vector sum of the final angular momenta. The general solution yields a selection rule of $\Delta l = \pm 1$ for the allowed change in the electron's azimuthal quantum number l which is the quantum number that describes the electron's angular momentum. There are additional rules that apply to the other quantum numbers that are developed in the full quantum mechanical description. These selection rules greatly limit the allowed transitions in the atom. Figure 2.16 is the energy level diagram for hydrogen showing a subset of the allowed transitions.

2.5.3

Emission and Absorption Rates

We have introduced the selection rules that govern the absorption or emission of a photon but have not established the rate at which a possible transition will occur in a radiation field. This was addressed by Albert Einstein in 1917 well before the development of modern quantum mechanics (Einstein, 1917). Einstein's theory relies upon the concepts of quantum mechanics that are inherent in Planck's law and were central to Bohr's atomic theory.

Einstein considered a population of atoms (or molecules) in thermal equilibrium composed of two stationary states. The population of the lower state, level 1, is N_1 atoms while the population of the upper state, level 2, is N_2 atoms with the relative abundance derived from a Maxwell–Boltzmann distribution and described by

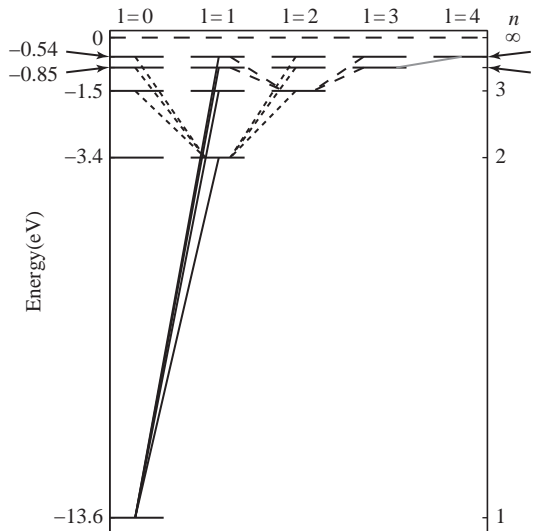


Figure 2.16 The energy level diagram for hydrogen with lines connecting particular energy states to signify some of the allowed transitions. The series of vertical numbers on the right-hand side correspond to the principal quantum number n . The solid black lines correspond to the Lyman series ($n_l = 1$), the fine dashed lines to the Balmer series ($n_l = 2$), the coarse lines to the Paschen series ($n_l = 3$), and the gray line for a single transition in the Brackett series ($n_l = 4$). Each series is named for the spectroscopist that performed the original observations.

$$\frac{N_1}{N_2} = \exp\left(\frac{E_2 - E_1}{k_B T}\right), \quad (2.79)$$

where E_1 and E_2 are the energies of level 1 and level 2 respectively, k_B is Boltzmann's constant, and T is the temperature. This equilibrium distribution is maintained by balancing the upward and downward transitions through absorption and emission of photons that satisfy (2.76). No collisional processes are considered that might change the distribution of states.

He further assumed that emission resulting from a transition from level 2 to level 1 could occur spontaneously or through stimulation from the radiation field. A transition from the lower state to the upper state, on the other hand, could only be induced by absorption from the radiation field. The downward rate W_{21} from level 2 to level 1 is given by

$$W_{21} = A_{21}N_2 + B_{21}\rho_\nu N_2, \quad (2.80)$$

where A_{21} is the Einstein coefficient for spontaneous emission, B_{21} is the Einstein coefficient for stimulated emission, and ρ_ν is the spectral energy density per unit frequency interval of the radiation field with the frequency ν corresponding to the energy difference between the two states. The stimulated emission is in the same direction and has the same phase as the inducing radiation. Spontaneous emission will occur in the absence of a radiation field and is inversely proportional to the natural lifetime. Similarly, the upward rate W_{12} from level 1 to level 2 is given by

$$W_{12} = B_{12}\rho_v N_1, \quad (2.81)$$

where B_{12} is the Einstein absorption coefficient. The B -coefficients have dimensions of volume \times frequency divided by energy \times time. The B -coefficients were considered by Einstein to be the same phenomenon of energy transfer to and from the radiation field with only a sign change.

For a system in thermal equilibrium the transition rates between the two states must be equal which yields

$$(A_{21} + B_{21}\rho_v)N_2 = B_{12}\rho_v N_1 \quad (2.82)$$

or

$$\frac{N_1}{N_2} = \frac{A_{21} + B_{21}\rho_v}{B_{12}\rho_v} \quad (2.83)$$

for the relative abundance of the two states. Equation (2.83) is equivalent to (2.79) which, upon substitution and solving for ρ_v , yields

$$\rho_v = \frac{A_{21}}{B_{12}e^{h\nu/k_B T} - B_{21}}, \quad (2.84)$$

where (2.76) has been used. For a system in thermal equilibrium, (2.84) is equivalent to Planck's law given by (2.65) modified from spectral radiance to energy density per unit frequency.

Consider the flux $d^2\Phi$ in an isotropic radiation field passing through an imaginary surface of area dA at an angle θ to the normal and within a solid angle $d\omega$ as illustrated in Figures 2.12 and 2.17. Equations (2.52) and (2.53) yield

$$d^2\Phi = L dA \cos \theta d\omega \quad (2.85)$$

for the flux. Since the flux is the energy per unit time passing through dA , the energy density is just the flux times the time interval dt divided by the appropriate volume. Referring to Figure 2.17, the volume occupied by the flux during the time dt is just the projected area times the distance the light travels. Therefore, the energy density for a radiation field at frequency ν within the volume is

$$d\rho_v = \frac{d^2\Phi dt}{d^2V} = \frac{L_v dA \cos \theta d\omega dt}{dA \cos \theta c dt} = \frac{L_v d\omega}{c}, \quad (2.86)$$

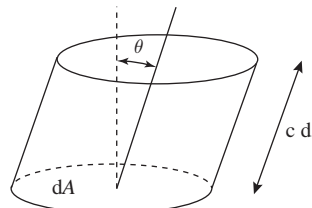


Figure 2.17 The volume used to determine the energy density associated with a blackbody radiation field.

which is integrated over all angles yielding

$$\rho_\nu = \frac{L_\nu}{c} \int_0^{2\pi} \int_0^\pi \sin \theta \, d\theta \, d\phi = \frac{4\pi L_\nu}{c} \quad (2.87)$$

for the total energy density for the isotropic radiation field. Here L_ν is equal to Planck's law $B_\nu(T)$, given by (2.65), which implies that

$$\rho_\nu = \frac{8\pi h\nu^3}{c^3} \frac{1}{e^{h\nu/k_B T} - 1} \quad (2.88)$$

is the final form of the energy density. Comparing (2.84) and (2.88), which must be valid at all temperatures, yields

$$B_{12} = B_{21} \quad (2.89)$$

and

$$A_{21} = \frac{8\pi h\nu^3}{c^3} B_{12} \quad (2.90)$$

for the relationships between the Einstein coefficients. Equations (2.89) and (2.90) must be modified if the upper or lower levels are composed of multiple quantum states having the same energy, known as degenerate states. If there are degeneracies, which is typically the case, then (2.79) is modified to include the weighting due to the degeneracy, yielding

$$\frac{N_1}{N_2} = \frac{g_1}{g_2} \exp\left(\frac{E_2 - E_1}{k_B T}\right), \quad (2.91)$$

where g_1 and g_2 are degeneracy factors, which account for the additional states that are populated. It is left as an exercise to show that the resulting relationship between the Einstein coefficients, (2.89) and (2.90), becomes

$$B_{12} = \frac{g_2}{g_1} B_{21} \quad (2.92)$$

and

$$g_2 A_{21} = \frac{8\pi h\nu^3}{c^3} g_1 B_{12}. \quad (2.93)$$

The degeneracy factors are simply the number of different configurations, as described by the various quantum numbers, where an atom or molecule can have the same energy.

There are other ways to define the B -coefficients, such as using the radiance rather than the energy density in the derivation, so care must be taken to interpret the literature. Einstein's formulation has subsequently been fully developed using quantum mechanics and, since the coefficients only depend upon the the internal structure of the atom or molecule, it is also generally true for non-equilibrium conditions. The Einstein coefficients are constant for a particular transition and are determined through experiments or theoretical calculations. Knowledge of them is required in order to perform radiative transfer calculations for the atmosphere.

It is left as an exercise for the student to show that the Einstein coefficients can be equivalently expressed in terms of the spectral radiance rather than the energy density

of the radiation field. In this case, the relationship between the A -coefficient and the B -coefficients in terms of the transition frequency ν is given by

$$A_{21} = \frac{2h\nu^3}{c^2} B_{12}^L \quad (2.94)$$

with the notation B_{12}^L to signify spectral radiance. Additionally, the coefficients can be expressed as functions of wavelength, wavenumber, or angular frequency.

2.5.4 Summary of Atomic Overview

The above description provides a brief and simplified account of the energy level structure and the processes that govern transitions and transition rates between stationary states. The description did not include the quantization rules for other quantities, such as the angular momentum of the electron itself (referred to as *spin*), does not discuss the consequences of parity conservation, and does not include any of the higher-order effects that will split a particular energy level into a manifold of closely spaced energy levels that are only resolved in emission spectra using spectroscopic instruments of high resolution. It does introduce the concepts of the quantization of energy and angular momentum, of the selection rules that govern the transitions between states, and of transition rates. These concepts are also applicable to the molecules that are the dominant species in the atmosphere.

2.5.5 Molecular Emission and Absorption

The atmosphere is primarily composed of nitrogen and oxygen molecules, but minor constituents such as water and carbon dioxide play a critical role in determining atmospheric transmission. Molecules have an electronic structure that is analogous to that of atoms, but also have energy associated with rotation and vibration. The effect of these two additional sources of energy on the structure of the stationary states will be developed using simple models that illustrate the concepts and are the starting points for a more detailed and accurate analysis. The treatment here draws heavily from the text by Herzberg (1950).

Molecular Rotation

The rotation of the molecule as a whole is about its center of mass and is characterized by its rotational kinetic energy given by

$$K = \frac{1}{2}I_x\omega_x^2 + \frac{1}{2}I_y\omega_y^2 + \frac{1}{2}I_z\omega_z^2, \quad (2.95)$$

where I_x is the moment of inertia and ω_x is the angular velocity with both quantities about the x -axis and, similarly, for the y - and z -axes. In this case there is no potential energy term and the kinetic energy is the total energy associated with rotation. The simplest case is a linear molecule, such as any diatomic molecule, treated as a rigid rotator or dumbbell where the constituent atoms are in a row.

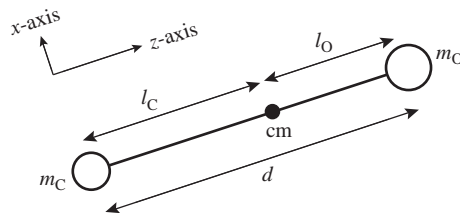


Figure 2.18 Carbon monoxide as an example of a diatomic molecule. The oxygen nucleus is to the right and the filled circle along the internuclear axis is the location of the center of mass (cm) and the origin of the coordinate system. The y-axis is out of the plane of the figure. Drawing not to scale.

Classically, the rigid rotator is composed of two or more masses connected by massless rigid rods, as illustrated for carbon monoxide in Figure 2.18. The moment of inertia for the x -axis is given by

$$I_x = \sum_{k=1}^n I_{cm_x, k} + \sum_{k=1}^n m_k(y_k^2 + z_k^2) \quad (2.96)$$

where n is the number of masses in the system, two for a diatomic molecule, $I_{cm_x, k}$ is the moment of inertia about the center of mass of the k^{th} particle, and y_k and z_k are the distances from the axis of rotation, which is the center of mass of the system for a freely rotating rigid rotator. Students familiar with classical mechanics will recognize the application of the parallel-axis theorem. Similar equations apply to both I_y and I_z . The masses are the nuclei of the molecule and the electron masses are neglected since they are three orders of magnitude smaller than the protons and neutrons that make up a nucleus.

Considering each nucleus as a sphere, the moment of inertia for each is given by

$$I_{cm} = \frac{2}{5}mR^2 \quad (2.97)$$

where m is the nuclear mass, R is the nuclear radius, and I_{cm} is the moment of inertia about the center of mass of a nucleus and is the same for all three dimensions. As an example, (2.96) is applied to the diatomic molecule carbon monoxide yielding

$$I_x = I_y = \frac{2}{5}(m_C R_C^2 + m_O R_O^2) + m_C l_C^2 + m_O l_O^2 \quad (2.98)$$

for I_x and I_y and

$$I_z = \frac{2}{5}(m_C R_C^2 + m_O R_O^2) \quad (2.99)$$

for I_z where m_C and m_O are the masses of the carbon and oxygen atoms respectively, R_C and R_O are their respective radii, and l_C and l_O are the respective distances from the center of mass of the molecule. The radius of a nucleus is modeled using

$$R = r_o A^{1/3}, \quad (2.100)$$

where r_o is equal to 1.3×10^{-15} m and A is the nuclear number. For carbon monoxide this yields a radius of 3.0×10^{-15} m for the carbon atom and 3.3×10^{-15} m for the

Table 2.2 The values used to calculate the moments of inertia for carbon monoxide. A picometer (pm) is equal to 10^{-12} m.

atom	$m(\times 10^{-23}$ g)	A	$l(\text{pm})$	$R(\text{pm})$	I	value(g·pm 2)
C	1.994	12	64.4	0.0030	$I_x = I_y$	1.45×10^{-19}
O	2.657	16	48.4	0.0033	I_z	1.85×10^{-28}

oxygen atom. With the origin of the coordinate system located at the center of mass, the location of the oxygen nucleus is calculated using

$$l_O = \left(\frac{m_C}{m_C + m_O} \right) d, \quad (2.101)$$

where d is the internuclear distance, which is 112.8 pm for carbon monoxide (Chakraborty and Ghosh, 2010). The location of the carbon nucleus is simply the difference between d and l_O . Table 2.2 details the moment of inertia calculation for carbon monoxide. The moment of inertia about the z -axis, which is along the molecular axis, is nine orders of magnitude smaller than the equivalent moments of inertia about the x - and y -axes. The rotational energy about the x - and y -axes represents degenerate modes of rotation.

The results for carbon monoxide are generally true for all linear molecules and (2.95) is simplified by neglecting the energy of rotation about the z -axis and defining the coordinate system to eliminate one of the degenerate terms. The energy is therefore expressed as

$$E = \frac{L^2}{2I}, \quad (2.102)$$

where the angular momentum expressed as $L = I\omega$ has been used. The quantum mechanical solution for the energy yields

$$E = \frac{\hbar^2}{2I} J(J + 1) \quad (2.103)$$

with the rotational quantum number J taking on integer values 0, 1, 2, \dots . Comparing (2.103) to (2.102) yields

$$L = \hbar \sqrt{J(J + 1)} \quad (2.104)$$

for the magnitude of the quantized angular momentum vector.

The possible frequencies are again calculated by applying (2.76) and (2.103), giving

$$\nu = B[J_u(J_u + 1) - J_l(J_l + 1)], \quad (2.105)$$

where B is the rotational constant defined as

$$B \equiv \frac{\hbar}{4\pi I} \quad (2.106)$$

and J_u and J_l are the upper and lower values for the rotational quantum number with B in units of Hz. The corresponding dipole selection rule is $\Delta J = \pm 1$ so the change in rotational energy in the absorption or emission of a dipole photon is in single steps. Applying the selection rule to (2.105) with $J_u = J_l + 1$ yields

$$\nu = 2B(J_l + 1) \quad (2.107)$$

and the absorption line spectrum for a linear rigid-rotator molecule is composed of lines with $\Delta\nu = 2B$ spacing. The moment of inertia of carbon monoxide is 1.456×10^{-19} g·pm² calculated from the value of the rotational constant derived from spectroscopic measurements, in agreement with the classical calculation of I_x given in Table 2.2 (Nolt et al., 1987).

As noted in Section 2.5.2, a necessary condition for a transition between stationary states is the existence of a dipole moment. Homonuclear molecules such as N₂ do not have permanent dipole moments because of the symmetry of the charge distribution within the molecule and generally do not exhibit rotational absorption or emission spectra, unlike molecules such as CO, which do have permanent dipole moments. Carbon dioxide is another linear molecule that does not have a permanent dipole moment and does not have a pure rotational spectrum. In general, a molecule must have some asymmetry in its structure in order for it to have a permanent dipole moment.

Linear molecules are a subset of the molecules present in the atmosphere. Methane is an example of a spherical top where, just as in a linear molecule, two of the moments of inertia are equal, but the third moment is not zero. Despite this difference the analysis for a spherical top is similar to that of a linear molecule. Methane does not have a permanent dipole moment and does not have a pure rotational spectrum. Water and ozone are important atmospheric absorbers and both are asymmetric tops. An asymmetric top is one for which the three moments of inertia, I_x , I_y , and I_z , are all unequal. They also have permanent dipole moments resulting in rotational absorption spectra. Equation (2.103) must be modified in this case with the addition of higher-order terms.

Molecular Vibration

The molecules of interest for the atmosphere are bound together by the attractive and repulsive electrostatic forces between the nuclei and electrons that form covalent or ionic bonds. These forces can be modeled to first order as springs, with the molecule behaving like a simple harmonic oscillator. The quantum mechanical solution yields

$$E = \hbar\nu_{osc}(\nu + \frac{1}{2}), \quad (2.108)$$

where ν_{osc} is the resonance frequency of a simple harmonic oscillator and ν is the vibrational quantum number which can only take on values of 0, 1, 2, The $\nu = 0$ case corresponds to the zero point energy with the molecule still undergoing vibration. Once again (2.76) is combined with the possible energy states, which in this case yields

$$\nu = \nu_{osc}(\nu_u - \nu_l), \quad (2.109)$$

where ν_u and ν_l are the vibrational quantum numbers for the upper and lower stationary states respectively. The dipole selection rule for the vibrational quantum number is $\Delta\nu = \pm 1$, which corresponds to $\nu = \nu_{osc}$ for the frequency of the emitted or absorbed photon.

The above model is easily visualized for a diatomic molecule with one vibrational mode. In that case, the two nuclei simply oscillate about the equilibrium separation

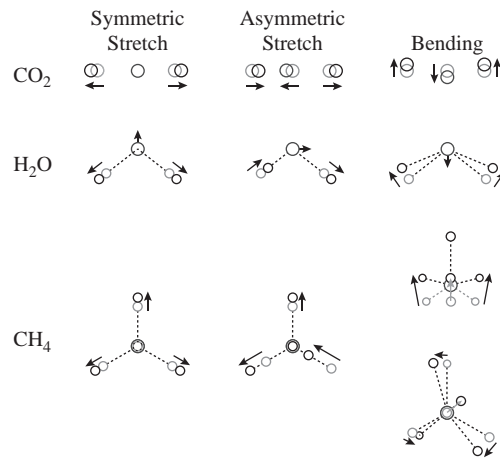


Figure 2.19 The vibrational modes of CO_2 , H_2O , and CH_4 . The left two diagrams for CH_4 view the molecule from the top with one of the H atoms out of the page while the right two views of the bending modes are side views showing all four H atoms.

distance along the axis that connects them. Molecules with more than two nuclei exhibit several vibrational modes. For example, a linear molecule with three nuclei such as carbon dioxide has three vibrational modes that are termed symmetric stretch, asymmetric stretch, and bending modes. These modes are treated separately and have their own energy level structure and quantum numbers.

As the number of atoms in the molecule increases, so does the number of vibrational modes and the richness in the resulting line spectra. A nonlinear molecule will have $3N-6$ normal modes of vibration while a linear molecule with three or more atoms will have $3N-5$ normal modes, where N is the number of atoms. Some of the modes will be indistinguishable or degenerate and have the same energy. For example, methane, a spherical top with five atoms, has nine normal modes but three are degenerate, leaving only four unique solutions for the energy. Figure 2.19 is an illustration of the possible vibrational modes for carbon dioxide, water, and methane.

Deviations from the Rigid Rotator and Simple Harmonic Oscillator Models

Both the rigid rotator and harmonic oscillator models are idealizations of the behavior of a molecule with the results accurate to first order. The added complexity is due to several factors. First, the molecule does not behave as a harmonic oscillator but rather as an anharmonic oscillator, with the potential energy having higher-order terms. This added anharmonicity is illustrated in Figure 2.20, which shows the succession of vibrational energy levels that are no longer equally spaced within the potential energy curve for a diatomic molecule. Recall from classical mechanics that

$$F(R) = -\frac{dV(R)}{dR}, \quad (2.110)$$

where F is the force and V is the potential energy, both as a function of the internuclear distance R . There is no net force at the equilibrium distance R_o while the force becomes

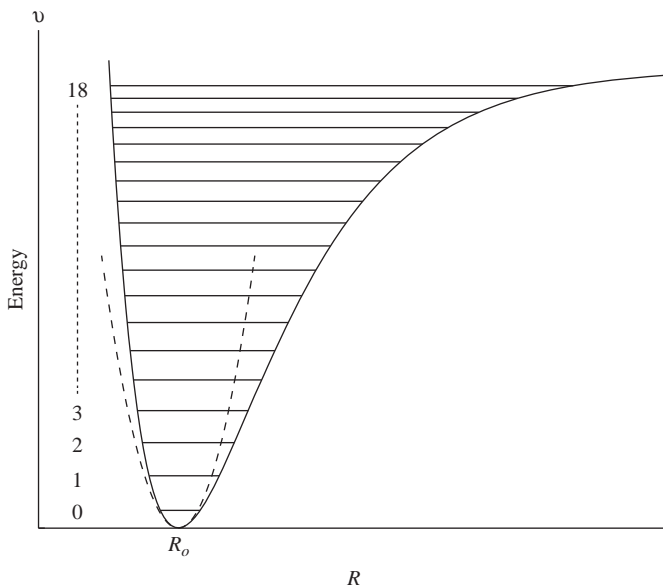


Figure 2.20 The anharmonic oscillator potential energy curve (solid black), the quantized vibrational energy states (horizontal black lines), and the harmonic oscillator potential energy curve (dashed) are shown as a function of the internuclear distance R . The equilibrium distance, R_0 , is the point of minimum potential energy in both cases. The vibrational quantum number v ranges from 0 for the ground state to 18.

repulsive at internuclear distances less than R_0 due to electrostatic repulsion between the two nuclei, and attractive at internuclear distances greater than R_0 due to the covalent bonds. At large internuclear distances the molecule dissociates into its constituent atoms. Additionally, molecules bend as they rotate and their vibration changes the moments of inertia slightly. These effects cumulatively alter the molecular energy level structure by reducing the separation between adjacent vibrational levels in a nonlinear fashion.

Rotational–Vibrational Structure

Up to this point the effects of rotation and vibration have been treated separately, but molecules often undergo transitions that involve a change in both the rotational and vibrational quantum numbers at once, leading to rotational–vibrational, or just ro–vibrational, spectra. In this case the energy states are characterized by the sum of the vibrational and rotational contributions. The energy difference between adjacent vibrational levels is typically considerably greater than the energy splitting between adjacent rotational levels. This leads to a series of closely spaced emission or absorption lines, as illustrated for the carbon monoxide absorption feature at $4.7 \mu\text{m}$ in Figure 2.21. The absorption spectrum calculation was performed using a spectroscopic database, in this case the High Resolution Transmission (HITRAN) database (Rothman et al., 2013), with a concentration of 200 parts per million by volume (ppmv) in a dry atmosphere over a 100 cm path length with a pressure of 1 atm and at a temperature of 276 K. It will

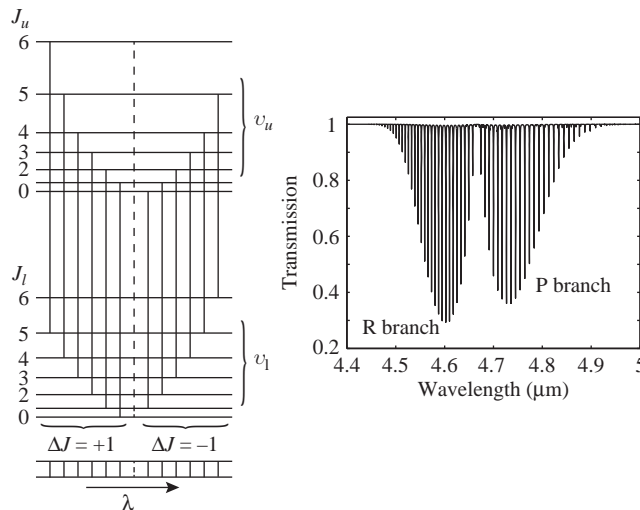


Figure 2.21 The left figure is the energy level diagram for a diatomic molecule that follows the $\Delta J = \pm 1$ selection rule and the right figure is the CO absorption spectrum at $4.7 \mu\text{m}$. The energy level diagram is based on the presentation in Herzberg (1950).

become clear why the temperature and pressure are required for the calculation as we address the collisional processes in the atmosphere. This example is only for illustration purposes as the actual concentration of carbon monoxide in the atmosphere is highly spatially variable and is on the order of 0.1 ppmv.

The energy level diagram on the left in Figure 2.21 is for a generic diatomic molecule with a dipole moment that follows the $\Delta J = \pm 1$ selection rule. Spectroscopists refer to the $\Delta J = +1$ series as the R branch and the $\Delta J = -1$ series as the P branch. The separation between the upper and lower vibrational states is much larger than the separation between individual rotational states and obeys the $\Delta v = \pm 1$ selection rule. The horizontal ladder at the bottom represents the progression of spectral lines with shorter wavelengths to the left. The separation between vibrational states is typically about 1000 cm^{-1} while the separation between rotational levels is in the 10 to 100 cm^{-1} range.

Previously we stated that since carbon dioxide lacks a permanent dipole moment it doesn't have a pure rotational spectrum; however, when CO_2 vibrates in the bending or asymmetric stretch modes a rotational–vibrational spectrum results. This is due to the rotation of the molecule when an asymmetry exists, which does provide a dipole moment. In the case of the asymmetric stretch mode, the rigid rotator selection rule $\Delta J = \pm 1$ continues to hold since the moment of inertia about the axis connecting the nuclei is still essentially zero. For the bending mode this is no longer true as the two oxygen nuclei move relative to the carbon nucleus to break the linear symmetry. In this case the $\Delta J = \pm 1$ selection rule is modified to include $\Delta J = 0$. Figure 2.22 illustrates the energy level diagram on the left and the carbon dioxide absorption spectrum at $15 \mu\text{m}$ on the right. The ensemble of absorption features that correspond to $\Delta J = 0$

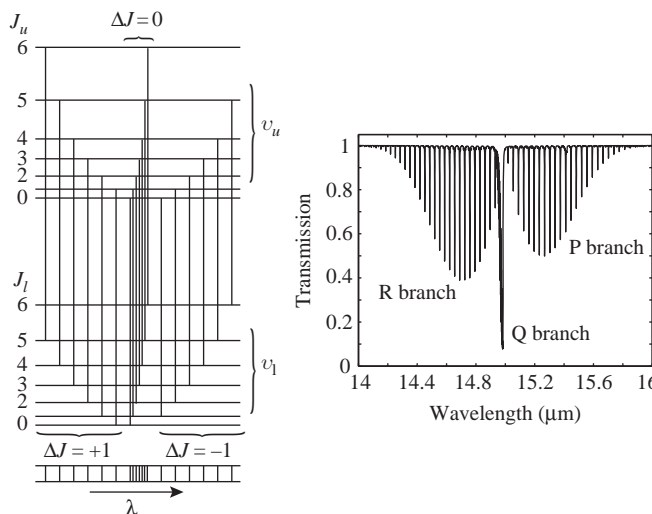


Figure 2.22 Energy level diagram for the CO_2 bending mode and the corresponding absorption spectrum at $15 \mu\text{m}$. The energy level diagram is based on the presentation in Herzberg (1950).

is known as the Q branch. In this case the calculation utilizes a CO_2 density of 395 ppmv over a 100 cm path length at an atmospheric pressure of $2.65 \times 10^4 \text{ Pa}$ and a temperature of 223 K. This corresponds to an altitude of 10 km in the US Standard Atmosphere (see Section 2.9) and to CO_2 measurements performed in 2014. Carbon dioxide is approximately uniformly mixed up to an altitude of about 80 km.

Ro-vibrational spectra are of particular importance to atmospheric transmission for remote sensing in the 0.4 to $14 \mu\text{m}$ spectral range because they are typically manifest at infrared wavelengths. Pure rotational spectra occur in the microwave region and are used extensively in meteorological remote sensing for the retrieval of atmospheric temperature and water vapor content but are not important for our purposes.

Electronic Structure

The molecular electronic structure is responsible for the covalent bonds that form the molecule and also produce the spring-like forces that are the basis for the vibrational structure. The resulting spectra are extraordinarily complex with a multitude of lines due to the combination of changes in the electronic, vibrational, and rotational structure at once. The energy of a given stationary state is

$$E = E_e + E_v + E_r, \quad (2.111)$$

where the subscript refers to electronic, vibrational, or rotational energy. Figure 2.23 shows an example of a transition between electronic states for a diatomic molecule.

We will limit the discussion to the case of a simple, diatomic molecule but the concepts are general to all molecules. Each different electronic state will have its own potential energy curve that depends upon the internuclear distance with the equilibrium internuclear distance typically increasing in the excited states when compared to

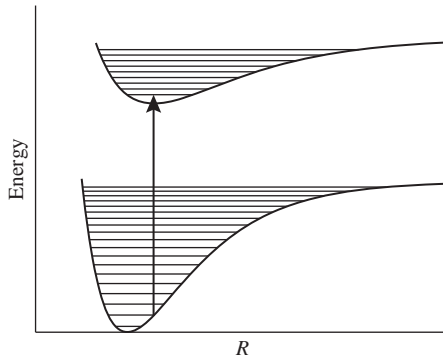


Figure 2.23 Energy level diagram as a function of internuclear distance for a diatomic molecule, showing the absorption of a photon from the ground electronic state to an excited electronic state. The lower vibrational level is $v_l = 2$ and the upper is $v_u = 1$. The rotational structure is not illustrated.

the ground state due to the reduction in bond strength. The shape of the curve will also be different, which leads to a different vibrational energy structure. The typical change in energy between electronic states is on the order of $10,000 \text{ cm}^{-1}$.

In general there is no strict selection rule for the change in vibrational quantum number, but the strength of the transition depends upon the overlap between the wave functions that describe the upper and lower states at the same internuclear distance. The probability that a particular vibrational transition will occur is governed by the Franck–Condon principle, where the wave functions for the upper and lower states of the transition are near their maximum values. These tend to be close to the edges of the upper and lower electronic potential energy curves, which, classically, correspond to turning points. At these locations the electrons are moving slowly and their positions and velocities are virtually unchanged during the transition between the two electronic states. The exception to this observation is the ground vibrational state within an electronic state, where the wave function peaks in the center of the potential well. The selection rule for the rotational quantum number is $\Delta J = \pm 1$ and 0. Thus, the quantum number Λ , for the projection of the electronic angular momentum onto the internuclear axis can change by ± 1 . Λ is the appropriate quantum number due to the strong electric field along this axis of molecular symmetry.

Absorption between different electronic states is particularly important in the ultraviolet, where oxygen and ozone make the atmosphere opaque. This defines the lower wavelength bound for remote sensing using imaging spectroscopy with the cutoff at about 325 nm for a non-scattering atmosphere. Ozone has an additional electronic absorption feature between 400 and 800 nm.

2.6

Spectral Line Shapes

In our description thus far, the emission and absorption of radiation has been treated as if it were monochromatic with the energy of the photon corresponding to the difference

in the quantized stationary states. In reality, spectral lines always have a finite width. The narrowest line shape possible is the natural line width that is due to the spontaneous decay of an undisturbed atom or molecule in an excited state. Most excited states are short lived and, due to the Heisenberg uncertainty principle, it is not possible to specify the energy levels exactly. As a result there is a spread of possible wavelengths for the emitted photon. The typical natural line width is extremely narrow. Atmospheric line widths are invariably much larger due to broadening by collisional and thermal processes, so natural line widths are unimportant for our purposes.

The mathematical framework used to describe a generic line shape will be addressed before treating the two broadening mechanisms. The line shape or shape factor, $f(\nu - \nu_o)$, is used to describe a line profile as a function of frequency and is defined by

$$k_a \equiv Sf(\nu - \nu_o), \quad (2.112)$$

where k_a is the absorption coefficient, S is the line strength, and ν_o is the frequency of an unbroadened transition. The shape factor is normalized to unit area and it follows that

$$S = \int_{-\infty}^{\infty} k_a \, d\nu, \quad (2.113)$$

which represents the integral line absorption for a single rotational–vibrational transition. Symmetric shape factors are characterized by the line width α , which is half the full width at half maximum, referred to as the half width.

The line shape function $f(\nu - \nu_o)$ is an example of a probability distribution function that is defined by

$$\int_{\nu_1}^{\nu_2} f(\nu - \nu_o) \, d\nu \quad (2.114)$$

specifying the fraction of emitted photons corresponding to the ν_o transition with frequencies between ν_1 and ν_2 . If the limits of integration are set to frequencies that are much higher and lower than ν_o , signified mathematically by setting $\nu_1 = -\infty$ and $\nu_2 = \infty$, then the integral equals one since all the possible fractions are added.

Line shapes evolve as a function of temperature and pressure. At a low atmospheric pressure, where the mean free path between collisions is long, the line shape is determined by shifts due to the Doppler effect. As the pressure increases and molecular collisions become frequent, the shape factor changes form and the broadening becomes linear as a function of pressure. At intermediate pressures the line shape is determined by a combination of thermal and collisional processes.

2.6.1

Doppler Broadening

Molecules that compose a rarefied gas, where the time between collisions is long compared to the lifetime of an excited state, emit light that is shifted due to the Doppler effect. Similarly, a molecule that is in motion will also absorb a photon at a slightly different frequency than that predicted by quantum theory. The Doppler effect for electromagnetic waves is a relativistic phenomena that describes the shift in frequency due to the relative motion of a source and a receiver. In the atmosphere the molecular speeds

are much less than the speed of light and the frequency shift to ν , from the stationary frequency ν_o , is given, to good approximation, by

$$\nu = \left(1 + \frac{\nu}{c}\right)\nu_o, \quad (2.115)$$

where it is understood that the molecular speed ν is the component of the velocity along the direction of interest. The speed is positive if the relative velocity is of approach and negative if it is of recession.

The probability distribution function for molecular velocity is given by the Maxwell–Boltzmann distribution

$$p(\nu) d\nu = \left(\frac{m}{2\pi k_B T}\right)^{\frac{1}{2}} e^{-m\nu^2/2k_B T} d\nu, \quad (2.116)$$

where m is the molecular mass, k_B is Boltzmann's constant, and T is the temperature. Equation (2.116) is the fraction of the total number of molecules which have a velocity between ν and $\nu + d\nu$. Rewriting (2.115) as

$$\nu = \left(\frac{c}{\nu_o}\right)(\nu - \nu_o) \quad (2.117)$$

and substituting it and its derivative into (2.116) yields

$$p(\nu) d\nu = \left(\frac{mc^2}{2\pi k_B T \nu_o^2}\right)^{\frac{1}{2}} \exp\left[-\frac{mc^2}{2k_B T} \frac{(\nu - \nu_o)^2}{\nu_o^2}\right] d\nu \quad (2.118)$$

for the Maxwell–Boltzmann distribution as a function of frequency. This will be simplified by defining

$$\sigma \equiv \frac{\nu_o}{c} \sqrt{\frac{k_B T}{m}}, \quad (2.119)$$

which yields

$$p(\nu) d\nu = \frac{1}{\sigma \sqrt{2\pi}} \exp\left[-\frac{(\nu - \nu_o)^2}{2\sigma^2}\right] d\nu, \quad (2.120)$$

where $p(\nu)$ is the familiar form for a Gaussian or normal distribution function and σ is the standard deviation.

Since the Gaussian distribution function is normalized, it is identified as the shape factor $f_D(\nu - \nu_o)$, yielding

$$f_D(\nu - \nu_o) = \frac{1}{\sigma \sqrt{2\pi}} \exp\left[-\frac{(\nu - \nu_o)^2}{2\sigma^2}\right] \quad (2.121)$$

for the Doppler profile. The frequency half width, α_D , is determined by setting ν equal to ν_h , $f_D(\nu - \nu_o)$ equal to $1/2$ its maximum value, and solving for $\alpha_D = \nu_h - \nu_o$. This yields

$$\alpha_D = \sigma \sqrt{2\ln 2} = \frac{\nu_o}{c} \sqrt{\frac{2k_B T \ln 2}{m}} \quad (2.122)$$

for the half width in Hz. Equation (2.122) is equivalently expressed as

$$\alpha_{D,\lambda} = \alpha_D \frac{\lambda_o^2}{c} = \frac{\lambda_o}{c} \sqrt{\frac{2k_B T}{m} \ln 2} \quad (2.123)$$

in terms of wavelength. As an example, the Doppler half width for the carbon dioxide absorption feature at $2 \mu\text{m}$ is about 2.6×10^{-3} nm for a temperature of 300 K.

2.6.2 Collisional Broadening

The treatment of collisional broadening in detail requires the application of quantum mechanics to describe the time-dependent perturbation, which can be quite large, that molecules experience during a collision. The full range of collisional phenomena includes everything from brief impacts of the type that dominate in the atmosphere, where the time between collisions is long compared to the interaction during a collision, to the creation of composite molecules during the collision and the subsequent formation of a new set of stationary states and the possible collision-induced transitions between states. We will settle for a brief discussion of a semi-classical model and present the results.

A first-order treatment of collisional broadening assumes that the collision duration is brief compared to the time between collisions, the collisions are elastic, and they perturb the absorption or emission of radiation during the transition between stationary states. An isolated molecule will emit or absorb radiation that is almost monochromatic with a frequency that is proportional to the difference between the initial and final stationary states. If, however, a molecule undergoing a transition collides with another, the result is the destruction of the phase relationship between the emitted radiation before and after the collision. This reduces the coherence lifetime of the emitted wave train and broadens the spectral line. Since the collisions occur randomly, the new phases are randomly distributed and will follow a Poisson distribution. An analysis that decomposes the frequency distribution of the emitted wave train, i.e. a Fourier analysis, yields the shape factor as

$$f_C(v - v_o) = \frac{1}{\pi} \frac{\alpha_C}{(v - v_o)^2 + \alpha_C^2}, \quad (2.124)$$

which is a Lorentz profile of half width α_C . Equation (2.124) is commonly used to describe pressure broadening, although it is not a perfect description, particularly in its disagreement with measurements of the wings of the line shape (Goody and Yung, 1989).

The behavior of the half width as a function of temperature and pressure can be derived from kinetic theory yielding

$$\alpha_C = \alpha_o \left(\frac{T_o}{T} \right)^n, \quad (2.125)$$

where α_o is the experimentally determined value of the half width at a laboratory reference value such as standard temperature and pressure. The value of the exponent n is $1/2$ from kinetic theory, but in practice is experimentally determined and ranges from

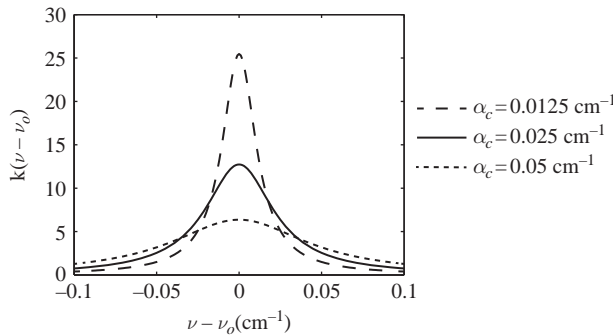


Figure 2.24 Examples of three shape factors for a collisionally broadened line. The pressure variation ranges from an atmospheric pressure of 1000 mbar at sea level to 250 mbar at a 10 km altitude.

0.5 to 1. Often (2.124) is expressed spectrally, in wave numbers, rather than frequency with typical measured values for α_o between 0.01 cm^{-1} and 0.1 cm^{-1} . The value of α_o is the weighted sum of the broadening due to collisions with the ensemble of atmospheric gases and with the same molecule for each transition. The values for α_o are tabulated in a spectroscopic database such as HITRAN where they are in units of $\text{cm}^{-1}/\text{atm}$, in which case the weighting is given by

$$\alpha_o = \alpha_s p_i + \alpha_a (p_a - p_i), \quad (2.126)$$

where α_s and α_a are the half widths for self- and air-broadening respectively, p_i is the partial pressure of the i th molecular species, and p_a is the atmospheric pressure. This also enables α_o to be adjusted to the appropriate pressure. Figures 2.21 and 2.22 included both α_s and α_a in the calculation of the transmission spectra.

Equations (2.125) and (2.126) are required to calculate the effect of pressure broadening for light transmission through the lower atmosphere. Atmospheric pressure at sea level is about a thousand millibars (a millibar is equal to 100 Pa) and falls to about 1 millibar at a 50 km altitude, a change of three orders of magnitude. The variation in temperature is less extreme with a smaller impact on α_C . At sea level a line width of about 0.05 cm^{-1} is a typical value for a rotational-vibrational transition. At a 10 km altitude, α_C has fallen to about 0.0125 cm^{-1} . Figure 2.24 illustrates this variation in shape factor due to collisional broadening.

2.6.3 Intermediate Broadening

At altitudes between about 20 km and 50 km both collisional and Doppler broadening contribute to the shape factor. It is assumed that both processes are independent and, in the time domain, the two effects can be simply multiplied together. In the frequency domain this becomes a *convolution* of the two shape factors. A convolution is defined as

$$f(x) * g(x) = \int_{-\infty}^{\infty} f(y)g(x - y) dy, \quad (2.127)$$

where y is a dummy integration variable. The convolution is used to calculate the amount of overlap between the function g as it is shifted over the function f (Bracewell, 2000).

In this case the two functions to be convolved are $f_C(v - v_o)$ and $f_D(v - v_o)$. Physically, the convolution of the two shape factors captures the shift in frequency due to the Doppler effect at a particular frequency within the collisionally broadened line. For example, a portion of an ensemble of molecules will emit or absorb at a frequency v' . These molecules will be moving relative to the observer and the frequency v' will be shifted by the Doppler effect with the shape function given by (2.121).

The convolution over v' is given by

$$\begin{aligned} f_V(v - v_o) &= \int_{-\infty}^{\infty} f_C(v' - v_o) f_D(v - v') dv' \\ &= \frac{\alpha_C}{\sqrt{2}\sigma} \frac{1}{\pi^{3/2}} \int_{-\infty}^{\infty} \frac{1}{(v' - v_o)^2 + \alpha_C^2} \exp\left[\frac{-(v - v')^2}{2\sigma^2}\right] dv', \end{aligned} \quad (2.128)$$

which can be evaluated by setting y equal to $(v - v')/\sqrt{2}\sigma$ and x equal to $(v - v_o)/\sqrt{2}\sigma$ yielding upon substitution

$$f_V(v - v_o) = \frac{\alpha_C}{2\sigma^2} \frac{1}{\pi^{3/2}} \int_{-\infty}^{\infty} \frac{e^{-y^2} dy}{(x - y)^2 + (\alpha_C/\sqrt{2}\sigma)^2} \quad (2.129)$$

for the Voigt line profile or just the Voigt profile.

There are various methods that are used to calculate the Voigt profile, but a discussion of its shape and properties will suffice for our purposes. The Voigt profile is normalized as required by (2.113). Figure 2.25 illustrates the difference between the three shape factors when the half widths for the collisionally-broadened and Doppler-broadened shape factors are equal to one. The Voigt profile has the smallest amplitude of the three shape factors but is larger than the collisional profile at values greater than about 87 percent of the half width α_C although the difference is slight for the far wings. It also has a half width of 1.64 as compared to 1. Figure 2.26 illustrates the cases when Doppler broadening and collisional broadening dominate. It can be shown that the Voigt profile

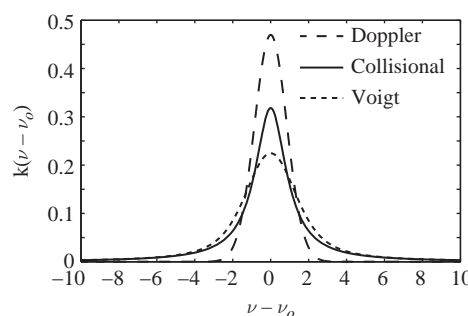


Figure 2.25 Illustration of the Voigt profile resulting from the convolution of Doppler and collisional shape factors with α_D and α_C unity.

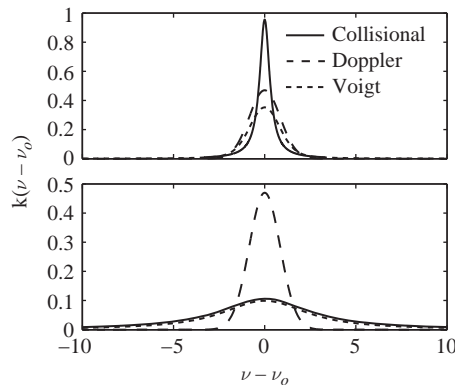


Figure 2.26 Illustration of the Voigt profile when Doppler broadening (upper graph) or collisional broadening (lower graph) dominate. The Doppler half width equals one in both cases while the collisional half width equals $1/3$ in the upper graph and 3 in the lower one.

reduces to the Doppler profile as α_C approaches zero and similarly it reduces to the Lorentz profile as α_D approaches zero.

2.6.4 Thermodynamic Equilibrium

Planck's and Kirchoff's laws were presented in Section 2.4.2 and derived using an idealized cavity held at a constant temperature. The atmosphere is quite different from this theoretical construct. What are the circumstances when atmospheric radiation is characterized by Planck's law? In Section 2.5.2 the emission and absorption rates between single upper and lower stationary states were examined for a population of atoms or molecules in thermal equilibrium. The Maxwell–Boltzmann distribution (2.79) was introduced into that derivation and was used in conjunction with Planck's law to derive the Einstein coefficients. Einstein showed in his original paper that Planck's law results if (2.79) is true for the two states. The equivalence between Planck's law and the Maxwell–Boltzmann distribution is generally true so that if a molecular population is described by one, then it is equally described by the other.

A Maxwell velocity distribution is a special case of the general Maxwell–Boltzmann distribution when it is applied to the translation of molecules in thermal equilibrium. The molecules in the atmosphere obey this distribution at densities that are high enough that collisions frequently adjust their velocities. The local temperature and pressure of the atmosphere changes as a function of altitude with the velocity distribution and the distribution of stationary states, or a subset of stationary states, obeying (2.79) at the particular local temperature. When this is true, velocities and the levels in question are said to be in local thermodynamic equilibrium. Molecules will diffuse into the altitude of interest and have molecular velocities and state distributions that differ, affecting this local balance, but, at sufficient densities, will be rapidly thermalized. The Maxwell–Boltzmann distribution does not describe the energy states of the atmospheric gases above an altitude of about 50 km and local thermodynamic equilibrium fails as the atmosphere becomes

more rarefied. At these higher altitudes the period between collisions becomes longer than the natural lifetimes of the molecular rotational and vibrational states and the microscopic radiative transfer processes, as described in Section 2.5.3 for a two-state system, must be developed based on the incident radiances.

Full thermodynamic equilibrium, with the translational energy and the distribution of all of the stationary states obeying a Maxwell–Boltzmann distribution, is not generally achieved. Radiative effects, described by the Einstein coefficients, will disrupt the distribution that would be established by collisions alone. The two processes are determined by their respective lifetimes. The collisional lifetime or relaxation time is proportional to the atmospheric pressure at a given altitude while the radiative rates are determined by the natural lifetimes of the particular stationary states. When the relaxation time is much shorter than the natural lifetime for a given stationary state or set of stationary states, Planck's law will describe the radiation field and the states will be in local thermodynamic equilibrium. If the relaxation rate is long compared to the natural lifetime of the state or states in question then the radiation field is described by some other function. Rotational levels tend to have longer lifetimes than vibrational levels and remain in local thermodynamic equilibrium at lower pressures.

It is possible to provide an estimate of the relative populations of stationary states for an altitude where local thermodynamic equilibrium holds by an application of (2.79). For room temperature, 20 °C, $k_B T$ corresponds to 205 cm⁻¹ so the relative populations of the upper and lower states will be on the order of $\exp[-(E_u - E_l)/205]$ with $E_u - E_l$ expressed in wavenumbers. We stated earlier that the separation between molecular electronic states was on the order of 10,000 cm⁻¹ so the relative population between the ground and first excited state is about $\exp(-49)$ or 10^{-21} so all of the molecules are in their ground electronic state. The vibrational state separation is on the order of 1000 cm⁻¹ so the relative populations are about 10^{-2} , again most molecules will be in their ground vibrational states. The closely spaced rotational levels will have appreciable populations relative to the ground state since their separation is about 10 to 100 cm⁻¹ corresponding to about 0.6 to 1, so a large fraction are in excited rotational states.

A question emerges concerning the impact of the Einstein's theory upon Kirchhoff's law, particularly when the body is not in thermal equilibrium with the radiation field, since the processes governing absorption, stimulated emission, and spontaneous emission apply to all states of matter. The concept of a freely radiating body was introduced in Section 2.4.2, where a sample is at a much different temperature than its surroundings. How does the process of stimulated emission impact Kirchhoff's law? The distinction to be addressed is whether the emissivity, and therefore the absorptivity, is due to the spontaneous and stimulated emission combined, or only to spontaneous emission. This question is thoroughly addressed in Baltes (1976), where it is shown that the emissivity is only due to spontaneous emission and is independent of the radiation field. It is required that the stationary states populated in the material be described by a Maxwell–Boltzmann distribution. This is also consistent with absorption measurements where the signal is proportional to the difference between the absorption of photons from the lower state and the stimulated emission of photons from the upper state, both of which share the same directionality. For example, in a high temperature gas confined to a region such

as an experimental cell, where the spontaneous emission is negligible compared to the product of the B -coefficients and the energy density ρ_ν , the measured absorption of any externally incident radiance along a particular path will be due to the difference between the processes of absorption and stimulated emission. This is consistent with Einstein's definition that stimulated emission is negative absorption.

2.7

Atmospheric Scattering Essentials

As an electromagnetic wave propagates through the atmosphere it encounters a variety of particles ranging from atoms and molecules to suspended aggregates such as dust and pollen. When the wave interacts with the particle the charges present are set into oscillatory motion due to the driving forces from the harmonic electromagnetic field. The accelerated charges will in turn radiate in all directions and this radiation is the scattered light. Scattering is always a combination of absorption and reradiation even though the absorption part is not explicitly stated. In this section the concepts required for an understanding of scattering will be introduced. These include the cross section, which describes the probability that a physical process such as scattering will occur, and the phase function that describes the probability of scattering into a particular direction if scattering has occurred. Rayleigh scattering will be discussed in some detail and aerosol scattering will be qualitatively described.

Particle size is a critical parameter that determines the category and degree of scattering. If the dimensions of the particle are small relative to the wavelength of the incident light, the scattering will be relatively weak. This is the case for scattering from molecular species such as nitrogen and is known as Rayleigh scattering. If the size of a homogeneous particle, such as a water droplet, is on the order of the wavelength of incident light, and the particle is spherical, the scattering is known as Lorenz–Mie scattering or just Mie scattering. For even larger particles, ones for which the dimensions are large compared to the wavelength, the behavior is governed to good approximation by the properties of light transmission and reflection as captured by the laws of reflection and refraction. This is the domain of geometrical optics. A dimensionless parameter, the size parameter, is used as a succinct shorthand notation to capture this relationship. It is defined as

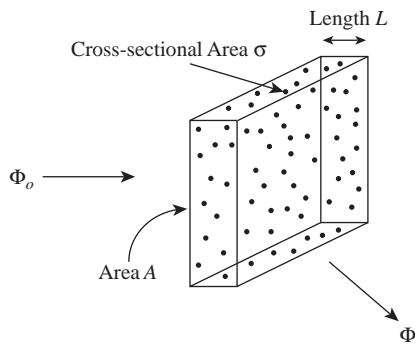
$$x \equiv \frac{2\pi a}{\lambda}, \quad (2.130)$$

where a is the particle radius. Table 2.3 lists the size parameter for wavelengths ranging from 350 nm to 1 μm , the most important range for our purposes.

There are some general statements that can be made about atmospheric scattering. Scattering in the atmosphere is elastic with the scattered component having the same wavelength as the incident wave. Phenomena, such as Raman scattering, are not observed under natural conditions. Scattering can occur just once, as in single scattering, or more than once, as in multiple scattering. Multiple scattering occurs when light previously scattered by a particle is rescattered by one or more other particles. At high

Table 2.3 Size parameter variation

Particle	Size	Size Parameter	Scattering Category
O ₂ , N ₂ , H ₂ O	~ 0.3 nm	0.0054 – 0.0019	Rayleigh
Aerosols	~ 1 μm	18 – 6.3	Mie
Water Droplet	~ 10 μm	180 – 63	Mie
Ice Crystal	~ 100 μm	1.8×10^3 – 630	Geometrical Optics
Raindrop	~ 1 mm	1.8×10^4 – 6.3×10^3	Geometrical Optics

**Figure 2.27** Scattering due to an ensemble of atoms or molecules within the volume $A \times L$. The molecules of cross-sectional area σ are represented by the black dots.

altitudes, where the density is low, light can be scattered back into space after a single scattering event. Multiple scattering becomes more prevalent as light propagates downward through the atmosphere and the particle density becomes high. Scattering is directional and becomes anisotropic with the scattered energy becoming increasingly dominated by forward and backward components as the particle size increases. This directionality will be illustrated for Rayleigh and aerosol scattering.

2.7.1 Cross Sections and Transmission Coefficients

We will now define a new concept, and broaden one introduced earlier, that is generally applicable in atmospheric transmission before we delve into the details of scattering phenomena. The new concept, the *cross section*, is introduced here because it is quite easily and intuitively illustrated using scattering as an example. Cross sections are widely used in radiative transfer to describe the probability that a particular interaction will occur.

Consider a volume filled at low density with a molecular species that is being uniformly irradiated with a flux Φ_o as illustrated in Figure 2.27. The incident flux is normal to the area A and along the path L . The length L is much less than either of the dimensions of A . Each molecule has a cross-sectional area denoted by σ , and the total “target” area illuminated by the flux is $N_\sigma \sigma$, where N_σ is the number of molecules within the volume. There is no geometrical overlap between the different scatterers. The scattered flux is Φ_s .

The molecules will be treated as hard spheres. In this approximation, the ratio of the target area to the area A is equal to the fraction of flux that is scattered as described by

$$\frac{\Phi_s}{\Phi_o} = \frac{N_\sigma \sigma}{A} \quad (2.131)$$

for the single scattering case considered here. Equation (2.131) could also be expressed in terms of the total flux per unit area scattered in all directions divided by the incident flux per unit area (irradiance), in which case A is equal to 1. The hard sphere approximation has little meaning in our situation where the wavelength of the incident light is much larger than the dimensions of a molecule. The cross section is therefore interpreted as the effective area of the scatterer and is proportional to the likelihood that light will be scattered by a molecule, in which case (2.131) is the probability that scattering will occur.

Equation (2.131) can be rewritten as

$$\frac{\Phi_s}{\Phi_o} = n_\sigma A L \left(\frac{\sigma}{A} \right) = n_\sigma \sigma L \quad (2.132)$$

where N_σ has been replaced by the number of molecules per unit volume, n_σ , times the scattering volume AL . The *scattering coefficient* k_s is defined as

$$k_s \equiv n_\sigma \sigma = \frac{1}{L} \frac{\Phi_s}{\Phi_o} \quad (2.133)$$

in units of inverse length, and is the probability that scattering will occur per unit length of propagation.

We are interested in the loss of flux along the original path. Allow the length L in (2.133) to shrink to the infinitesimal distance dr with the associated scattered flux Φ_s becoming $d\Phi$. The flux lost is equal to $d\Phi$ but has the opposite sign, and the loss over the distance dr is

$$\frac{1}{\Phi} \frac{d\Phi}{dr} = -k_s, \quad (2.134)$$

where Φ_s has been replaced by $-d\Phi$ and L has been replaced by dr . Equation (2.134) is integrated to yield

$$\Phi = \Phi_o e^{-k_s r} \quad (2.135)$$

for the amount of light remaining in the beam after scattering. The transmission solely attributed to the scattering of light from the beam is

$$T(r, \lambda) = \frac{\Phi}{\Phi_o} = e^{-k_s(\lambda)r}, \quad (2.136)$$

where the wavelength dependence for scattering has been made explicit.

Equation (2.136) has the same form as (2.17) with the only difference being the coefficient. Beer's law can be generalized to account for both loss mechanisms by combining (2.17) and (2.136) to yield

$$T(r, \lambda) = e^{-k_a(\lambda)r} e^{-k_s(\lambda)r} = e^{-[k_a(\lambda) + k_s(\lambda)]r} \quad (2.137)$$

for the total transmission. The *extinction coefficient* k_e is defined as

$$k_e(\lambda) \equiv k_a(\lambda) + k_s(\lambda) \quad (2.138)$$

and characterizes the contributions from absorption and scattering as a function of the spectral unit. Similarly, the absorption and extinction cross sections, denoted by σ_a and σ_e , respectively, are related to the absorption and extinction coefficients in the same manner that the scattering cross section, σ_s , is related to the scattering coefficient as defined in (2.133), and they are derived in a similar fashion.

The derivation of the cross section assumed a single type of scatterer or absorber, which is unrealistic for radiative transfer through the atmosphere. However, it can be generalized since each particle type within a volume will have its own probabilities of absorption and scattering that will be described by their respective cross sections. Again, using scattering as an example and returning to (2.131), consider the case where there are several different scatterers present in the volume AL . Equation (2.131) becomes

$$\frac{\Phi_s}{\Phi_o} = \sum_i \frac{N_{\sigma,i} \sigma_i}{A}, \quad (2.139)$$

where the sum is over the different scatterers present (molecules, aerosols, etc.), with each different scatterer having a unique cross section σ_i and number $N_{\sigma,i}$ present in the volume. Equation (2.133) is also generalized, yielding

$$\frac{1}{L} \frac{\Phi_s}{\Phi_o} = \sum_i n_{\sigma,i} \sigma_i = \sum_i k_{s,i} = k_s, \quad (2.140)$$

where k_s is identified as the total scattering coefficient. Similar expressions are obtained for total absorption and extinction coefficients. The results are summarized as

$$k_a = \sum_i k_{a,i} = \sum_i n_i \sigma_{a,i} \quad (2.141)$$

$$k_s = \sum_i k_{s,i} = \sum_i n_i \sigma_{s,i} \quad (2.142)$$

$$k_e = \sum_i k_{e,i} = \sum_i n_i \sigma_{e,i} \quad (2.143)$$

for the three total coefficients. In this more realistic case, (2.138) will refer to the total extinction, absorption, and scattering coefficients.

The above derivation of a cross section used scattering as an example; however, the concept of a cross section is generic and broadly applicable. For example, an aurora is produced by the interaction of charged particles, electrons and protons, with nitrogen and oxygen atoms in the upper atmosphere. The collision between a charged particle and an atom will often be inelastic with the atom in an excited state following the interaction. The light observed in an aurora is the subsequent decay of the atom from the excited state to a lower state, typically the ground state, through the emission of a photon. Again the probability that this process will occur is described by a cross section, an electron or proton excitation cross section in this case.

2.7.2 Scattering Geometry

The above discussion of the scattering cross section ignores any directional dependence and describes the total probability of scattering into a sphere. The directionality of scattering is mathematically described by the scattering phase function $p(\Theta)$. The phase function quantifies the angular distribution of the scattered radiance at a particular wavelength as a function of the scattering angle Θ , the angle between the incident and scattered rays as illustrated in Figure 2.28. Unit vectors, $\hat{\omega}_o$ and $\hat{\omega}_s$, describe the directions of the incoming and scattered rays and the scattering angle is obtained from $\cos \Theta = \hat{\omega}_o \cdot \hat{\omega}_s$. Forward scattering occurs when $\cos \Theta$ is between 1 and 0 and backward scattering occurs when it is between 0 and -1 .

The framework that we constructed to describe total scattering will be modified to take the directionality into account and to define the scattering phase function. This function describes the probability that flux will be scattered into a particular direction. This is a rather unfortunate name for a function that has nothing to do with the phases of waves, but rather it is associated with the phases of an astronomical body. Returning to (2.131), the scattering cross section is replaced by the differential cross section $\sigma_{s,\omega}(\theta_o, \phi_o; \theta_s, \phi_s)$, in units of area per solid angle, to describe the scattered flux into the solid angle $d\omega$ centered on $\hat{\omega}_s$ yielding

$$\frac{\Phi_s(\theta_o, \phi_o; \theta_s, \phi_s) d\omega}{\Phi_o} = \frac{N_\sigma \sigma_{s,\omega}(\theta_o, \phi_o; \theta_s, \phi_s) d\omega}{A}, \quad (2.144)$$

where $\Phi_s(\theta_o, \phi_o; \theta_s, \phi_s)$ is the scattered flux per solid angle as a function of the incident and scattered flux directions. Equation (2.144) is the probability that incident flux in the $\hat{\omega}_o$ direction will be scattered into the differential solid angle $d\omega$ centered on $\hat{\omega}_s$. The differential scattering cross section is related to the total scattering cross section through

$$\sigma_s = \int_{\omega} \sigma_{s,\omega}(\theta_o, \phi_o; \theta_s, \phi_s) d\omega = \int_0^{2\pi} \int_0^{\pi} \sigma_{s,\omega}(\theta_o, \phi_o; \theta_s, \phi_s) \sin \theta d\theta d\phi \quad (2.145)$$

and the differential scattering coefficient is given by $k_{s,\omega}(\theta_o, \phi_o; \theta_s, \phi_s) = n \sigma_{s,\omega}(\theta_o, \phi_o; \theta_s, \phi_s)$, analogous to (2.133). Often the differential scattering cross section is written as

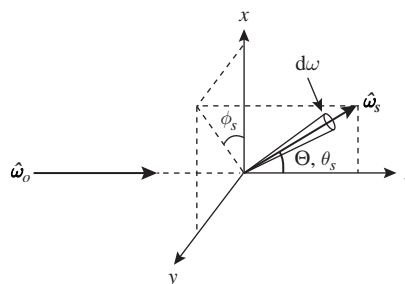


Figure 2.28 Illustration of the scattering geometry. Θ is the angle between the unit vectors describing the direction of the incoming ray, $\hat{\omega}_o$, and the scattered ray, $\hat{\omega}_s$. In the most general case for an arbitrary coordinate system, Θ and θ_s will not be aligned and $\cos \Theta$ will be a function of $\theta_o, \phi_o, \theta_s$, and ϕ_s , the angles that determine $\hat{\omega}_o$ and $\hat{\omega}_s$.

$$\sigma_{s,\omega} \equiv \frac{d\sigma_s}{d\omega},$$

particularly in physics. This should not be interpreted as taking the derivative of a function of solid angle ω ; rather, it is strictly a notational convention.

The phase function is defined as the differential scattering cross section divided by the average of the differential scattering cross section over a unit sphere, or

$$p(\Theta) \equiv \frac{\sigma_{s,\omega}(\theta_o, \phi_o; \theta_s, \phi_s)}{\int_{4\pi} \sigma_{s,\omega}(\theta_o, \phi_o; \theta_s, \phi_s) d\omega / 4\pi} = 4\pi \frac{\sigma_{s,\omega}(\theta_o, \phi_o; \theta_s, \phi_s)}{\sigma_s} \quad (2.146)$$

which is dimensionless. The normalization is over a unit sphere and is

$$\int_{4\pi} \frac{p(\Theta)}{4\pi} d\omega = \int_0^{2\pi} \int_0^\pi \frac{p(\theta_o, \phi_o; \theta_s, \phi_s)}{4\pi} \sin \theta d\theta d\phi = 1 \quad (2.147)$$

and $p(\Theta)d\omega/4\pi$ is interpreted as the probability of scattering into the solid angle $d\omega$ centered on the direction $\hat{\omega}_s$ if scattering has occurred. The phase function can also be defined as the differential scattering cross section divided by the total scattering cross section, as in Bohren and Huffman (1983). If that definition is employed then the normalization lacks the 4π in the denominator of (2.147).

The critical concept is that the angular dependence of the scattered light must be quantified in order for the transfer of radiation through the atmosphere to be calculated. The scattering phase function serves that purpose. In practice, it can be quite challenging to determine except in a few cases, one of which is Rayleigh scattering, the topic of our next section.

2.7.3 Rayleigh Scattering

The theory of molecular scattering as first developed by Lord Rayleigh is presented to introduce and illustrate the concepts that are common to all scattering phenomena (Strutt, 1871a,b). As a plane-polarized electromagnetic wave perturbs a spherical molecule, or any spherical particle whose dimensions are small compared to the wavelength, its electrons and nuclei experience a force due to the oscillating electric and magnetic fields of the incident light. The force is dominated by the electric force and the magnetic force is neglected. Additionally, since the size of the molecule is much less than the wavelength, all the charged particles experience the same oscillating force at any instant. This results in the polarization of the molecule forming an oscillating electric dipole. This charge oscillation generates its own electromagnetic wave that propagates away from the molecule and is the scattered light.

As stated above, the acceleration of a charged particle will produce radiation of light. This acceleration induces an oscillating dipole moment \mathbf{p} that is proportional to the electric field amplitude \mathbf{E}_0 of the incident plane wave. In general, the proportionality constant α has components in all three dimensions, but for simplicity we will assume that the induced dipole moment is only in the direction of the applied electric field. The scattered or induced electric field \mathbf{E} is described by Larmor's formula with the electric field given by

$$\mathbf{E} = \frac{1}{4\pi\epsilon_0} \frac{1}{c^2 r} \frac{\partial^2 \mathbf{p}}{\partial t^2} \sin(\gamma), \quad (2.148)$$

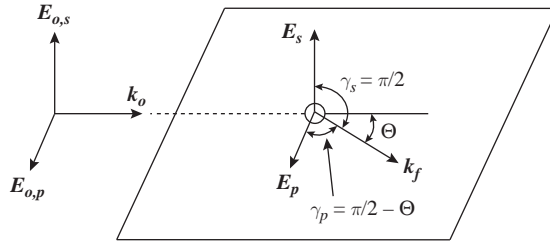


Figure 2.29 The Rayleigh scattering geometry with the scattering angle Θ defined as well as γ_s and γ_p .

where ϵ_o is the permittivity of free space, c is the speed of light, r is the distance from the accelerated charge to the observer, and γ is the angle between the dipole moment and the line from the dipole to the observer.

The oscillation of the induced dipole moment will have the same functional form as the second exponential term in (2.2) and is therefore

$$\mathbf{p} = \alpha \mathbf{E}_0 e^{i(kr - \omega t)}, \quad (2.149)$$

which, upon substitution into (2.148), yields

$$\mathbf{E} = -\frac{1}{4\pi\epsilon_o} \mathbf{E}_0 \frac{e^{i(kr - \omega t)}}{r} k^2 \alpha \sin(\gamma), \quad (2.150)$$

where $\omega = kc$ has been used. The r^{-1} dependence is indicative of a spherical wave and (2.150) is a spherical wave weighted by $\alpha \sin(\gamma)$. The electric field is decomposed into two orthogonal components relative to the scattering plane which is defined as the plane containing the incident and scattered rays as depicted in Figure 2.29. The component perpendicular, *senkrecht* in German, to the scattering plane is given by

$$\mathbf{E}_s = -\frac{1}{4\pi\epsilon_o} \mathbf{E}_{0s} \frac{e^{i(kr - \omega t)}}{r} k^2 \alpha, \quad (2.151)$$

where $\gamma_s = \pi/2$ has been used. Similarly, the component parallel to the scattering plane is

$$\mathbf{E}_p = -\frac{1}{4\pi\epsilon_o} \mathbf{E}_{0p} \frac{e^{i(kr - \omega t)}}{r} k^2 \alpha \cos(\Theta) \quad (2.152)$$

with $\gamma_p = \pi/2 - \Theta$. Equations (2.151) and (2.152) have a simple interpretation. If the oscillating dipole is perpendicular to the scattering plane then the electric field of the scattered wave is also perpendicular to the plane and has no dependence upon Θ . If, however, the dipole is parallel to the scattering plane and if it is viewed along the dipole axis then there is no scattered light since there is no component of oscillation in that direction; hence the $\cos \Theta$ dependence.

Equation (2.11) gives the irradiance averaged over a cycle of a harmonic wave; however, the quantity of interest is the radiance. Recall that radiance can be expressed as the irradiance per unit solid angle. Applying (2.11) divided by the solid angle $\Delta\omega$ to (2.151) and (2.152) yields

$$L_s = \frac{1}{32\pi^2\epsilon_o} \frac{E_{0s}^2}{\Delta\omega} \frac{ck^4}{r^2} \alpha^2 = L_{0s} \frac{k^4\alpha^2}{r^2} \quad (2.153)$$

and

$$L_p = \frac{1}{32\pi^2\epsilon_o} \frac{E_{0p}^2}{\Delta\omega} \frac{ck^4}{r^2} \alpha^2 \cos^2(\Theta) = L_{0p} \frac{k^4\alpha^2}{r^2} \cos^2(\Theta) \quad (2.154)$$

for the respective polarization radiance values.

Sunlight is unpolarized and is modeled as a mixture of two independent linearly polarized beams of the same radiance, with each component equal to half of the total radiance L_0 . The total radiance is therefore

$$L = L_s + L_p = L_0 \left(\frac{\alpha}{r} \right)^2 \left(\frac{2\pi}{\lambda} \right)^4 \left[\frac{1 + \cos^2(\Theta)}{2} \right], \quad (2.155)$$

where L_{0s} and L_{0p} have been replaced with $L_0/2$ and k has been replaced by $2\pi/\lambda$. Figure 2.30 is a polar plot of the individual polarization components and the total radiance. For unpolarized light one can imagine rotating the outer curve about the horizontal axis to achieve a dumbbell-shaped surface that will describe the scattering in all directions. Note the λ^{-4} dependence of (2.155) with the scattered light heavily biased to the shorter wavelengths.

The phase function for Rayleigh scattering is derived using (2.147) but referenced to the geometry depicted in Figure 2.29. Equation (2.147) becomes

$$\int_0^{2\pi} \int_0^\pi \frac{p(\cos \Theta)}{4\pi} \sin \Theta d\Theta d\phi = 1, \quad (2.156)$$

where the z -axis is along the original direction of propagation. The angular portion of the scattered radiance is given by the quantity in brackets in (2.155) and the phase function is identified as

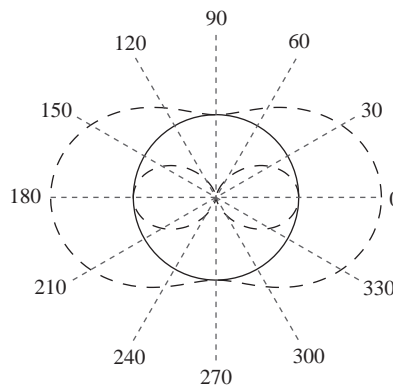


Figure 2.30 Polar plot of the angular dependence of Rayleigh scattering. The black line corresponds to the perpendicular radiance component, the dumbbell-shaped dashed line corresponds to the parallel radiance component, and the outer dashed line corresponds to the scattered radiance from unpolarized light.

$$p(\cos \Theta) = \frac{A}{2}[1 + \cos^2(\Theta)], \quad (2.157)$$

where A is the constant of proportionality that remains to be determined. Substituting (2.157) into (2.156) and solving for A yields

$$p(\cos \Theta) = \frac{3}{4}[1 + \cos^2(\Theta)] \quad (2.158)$$

for the final form of the Rayleigh phase function.

Rayleigh scattering illustrates the general concept that scattering is highly directional. This directionality is characteristic of all scattering phenomena, with the functional form varying with the type of scatterer. The above derivation outlines how one goes about calculating the scattered radiance and the phase function. For larger particles, whose size is not small compared to the wavelength, the problem of solving for the scattered electric and magnetic fields becomes much more complicated.

2.7.4 Aerosol Scattering

Aerosols include water droplets, dust, volcanic ash, smoke, anthropogenic particles, and any other type of particle injected and temporarily suspended in the atmosphere. These particles will, in the absence of wind or other atmospheric mixing, settle out due to the action of gravity. That said, their presence is nearly ubiquitous and requires significant attention for the art and practice of atmospheric compensation in the processing of data from an imaging spectrometer. Aerosol scattering is highly directional and a detailed analysis is beyond our scope. In order to provide some physical insight into the process, we will introduce a qualitative description to motivate this directionality based on the presentation in Bohren and Clothiaux (2006).

An aerosol particle is composed of a large number of atoms, each of which can be considered as a dipole. Consider two identical dipoles separated by a distance d , as illustrated in Figure 2.31, that are being excited by a monochromatic plane wave described by

$$\mathbf{E}_i(\mathbf{r}, t) = \mathbf{E}_o \exp[i(\mathbf{k}_i \cdot \mathbf{r} - \omega t)], \quad (2.159)$$

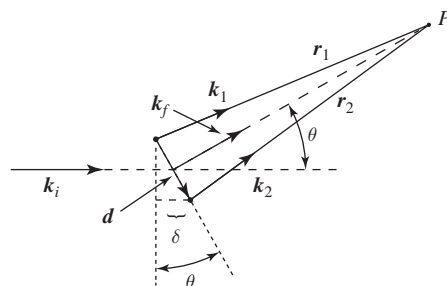


Figure 2.31 A monochromatic plane wave is incident from the left in the \mathbf{k}_i direction and two dipoles are excited to emit secondary waves. The interference pattern is observed at point P . Adapted from Bohren and Clothiaux (2006).

which is just the non-absorbing portion of (2.2). The two scattered waves are described by (2.150) if the wavelength is much longer than the dipole dimensions. At a great distance from the two scatters this results in plane waves to good approximation that will have a definite phase relationship since they are generated by dipoles that are a fixed distance apart and excited by the same plane wave. There is a phase shift in the exciting plane wave at the second dipole relative to the first due to the distance between the two that is given by

$$\Delta\phi = \frac{2\pi}{\lambda} d \sin \theta = kd \sin \theta \quad (2.160)$$

from (2.22) with θ illustrated in Figure 2.31. This phase shift is also present in the wave generated by the second dipole since it is proportional to the induced dipole through (2.149) and (2.150).

Our interest is in the phase relationship at point P between the two scattered plane waves. The principle of superposition is applied to calculate the resulting electric field at P yielding

$$\mathbf{E} = (\mathbf{E}_1 \exp[i(\mathbf{k}_1 \cdot \mathbf{r}_1)] + \mathbf{E}_2 \exp[i(\mathbf{k}_2 \cdot \mathbf{r}_2 + \Delta\phi)]) e^{i\omega t}, \quad (2.161)$$

where \mathbf{r}_1 and \mathbf{r}_2 are the distances from the two dipoles to the observation point and \mathbf{E}_1 and \mathbf{E}_2 are the scattered electric field vector amplitudes. Let's simplify the problem by stipulating that the exciting plane wave is polarized perpendicular to the scattering plane and α from (2.149) is one-dimensional so that the scattered waves have parallel electric field vectors. In this case (2.161) reduces to

$$\mathbf{E} = \mathbf{E}_s (\exp[i(\mathbf{k}_1 \cdot \mathbf{r}_1)] + \exp[i(\mathbf{k}_2 \cdot \mathbf{r}_2 + \Delta\phi)]) e^{i\omega t}, \quad (2.162)$$

where \mathbf{E}_s is the scattered electric field vector perpendicular to the scattering plane whose magnitude is assumed to be the same for both dipoles. The irradiance at P is proportional to $|\mathbf{E}|^2$ from (2.11) or

$$\begin{aligned} |\mathbf{E}|^2 &= \mathbf{E} \cdot \mathbf{E}^* \\ &= 2E_s^2 + E_s^2 [2 + e^{i(\mathbf{k}_1 \cdot \mathbf{r}_1 - \mathbf{k}_2 \cdot \mathbf{r}_2 - \Delta\phi)} + e^{-i(\mathbf{k}_1 \cdot \mathbf{r}_1 - \mathbf{k}_2 \cdot \mathbf{r}_2 - \Delta\phi)}] \\ &= 2E_s^2 [1 + \cos(\mathbf{k}_1 \cdot \mathbf{r}_1 - \mathbf{k}_2 \cdot \mathbf{r}_2 - \Delta\phi)], \end{aligned} \quad (2.163)$$

where \mathbf{E}^* is the complex conjugate of \mathbf{E} and $2 \cos z = e^{iz} + e^{-iz}$ has been used. The argument of the cosine function in (2.163) is the desired phase difference $\Delta\Phi$.

The phase difference is rewritten by noting that for elastic scattering the magnitude of the wave vector is the same for both scattered waves. The geometry is depicted in Figure 2.31, where \mathbf{r}_1 equals $\mathbf{r}_2 + \mathbf{d}$, \mathbf{k}_i is the incident wave vector for the exciting wave, and \mathbf{k}_1 and \mathbf{k}_2 are the wave vectors in the direction of the scattered waves. Since P is a great distance from the two dipoles, \mathbf{k}_1 equals \mathbf{k}_2 to good approximation and is signified by \mathbf{k}_f . The phase difference is therefore given by

$$\begin{aligned} \Delta\Phi &= \mathbf{k}_1 \cdot \mathbf{r}_1 - \mathbf{k}_2 \cdot \mathbf{r}_2 - \mathbf{k}_i \cdot \mathbf{d} \\ &= \mathbf{k}_1 \cdot \mathbf{r}_1 - (\mathbf{k}_2 \cdot \mathbf{r}_1 - \mathbf{k}_2 \cdot \mathbf{d} + \mathbf{k}_i \cdot \mathbf{d}) \\ &= (\mathbf{k}_f - \mathbf{k}_i) \cdot \mathbf{d}, \end{aligned} \quad (2.164)$$

where (2.160) and $\mathbf{r}_2 = \mathbf{r}_1 - \mathbf{d}$ have been substituted.

The phase shift, which governs the directionality of scattered light from an aerosol, can now be understood based on this simple model. The derivation of (2.164) was for two dipole radiators while an aerosol is composed of a large number of them, but, for coherent excitation by an incident wave, they behave as a coherent source array. Also, mutual excitation between the dipoles has been ignored so that the secondary wavelets from each dipole do not interact with any of the other dipoles. The description is limited but remains useful for the physical insight it provides. For example, in the forward direction where \mathbf{k}_f and \mathbf{k}_i are parallel, $\Delta\Phi$ is zero and there is always a peak in the scattering phase function there regardless of the angle between $\mathbf{k}_f - \mathbf{k}_i$ and \mathbf{d} .

If the aerosol size is much smaller than the wavelength of the exciting radiation then d/λ is small, the phase shift is essentially zero, and the scatter light interferes constructively regardless of the direction. As the particle size increases, phase shifts on the order of π become possible and destructive interference occurs for some angles. This is illustrated through two dipoles that are situated so that \mathbf{k}_i and \mathbf{d} are parallel with (2.164) reducing to

$$\Delta\Phi = \mathbf{k}_f \cdot \mathbf{d} - k_i d = kd(\cos\theta - 1), \quad (2.165)$$

where θ is the scattering angle between \mathbf{k}_i and \mathbf{k}_f . For forward scattering, $\Delta\Phi$ is zero as expected, while for backward scattering it is $-2kd$, which, at the extremes, can be either constructive or destructive depending upon whether it is equal to an odd (destructive) or even (constructive) integer multiple of π . Note that the sign of $\Delta\Phi$ is not relevant since the interference term in (2.163) is determined by a cosine.

Mie Theory

The starting point for the modeling of scattering by aerosols is to approximate them as spheres composed of a single material and having uniform physical properties in all directions. This is largely a matter of computational convenience rather than an accurate reflection of the composition and geometry of actual aerosols. The general solution to the scattering of spherical particles which have a diameter on the order of the wavelength of the incident electromagnetic wave was developed by Gustav Mie in 1908 by solving the electromagnetic wave equations. The full solution includes diffraction of the light around the particle, refraction as light passes through the particle, and reflection from the surface of the particle. Because the full derivation of the Mie theory is lengthy and can be found in multiple sources in the literature, we will discuss the general characteristics of aerosol scattering based on the Mie formulation (Bohren and Huffman, 1983; Liou, 2002). More recently, non-spherical solutions to the scattering problem have also been developed, and the interested reader is directed to Mishchenko et al. (1999).

Mie scattering theory is characterized by the large increase in forward scattering and enhanced backward scattering of the incident wave energy. As is found in dielectric scattering for geometric optics, light incident on a dielectric material will either be transmitted or reflected specularly from the surface. As the size parameter x increases above the Rayleigh assumption, the scattering in the forward and, to a lesser extent, the backward direction increases. Figure 2.32 illustrates two calculations that utilize Mie theory, with the first being scattering from a water droplet and the second scattering from a

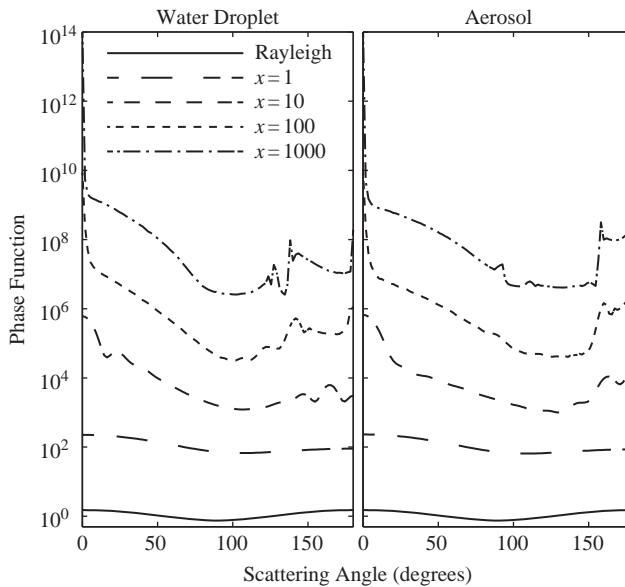


Figure 2.32 Modeled Mie scattering for an ensemble of particles of various size parameters ranging from $x = 1$ to 1000. The phase function is modeled based on a particle size parameter distribution using a Gaussian model with a standard deviation of 0.3 times the size parameter. The water droplet has a complex index of refraction given by $n = 1.3328 + i1.132 \times 10^{-8}$ for a wavelength of 605 nm and the aerosol particle is non-absorbing with a wavelength independent index of refraction of 1.5. Each curve is offset by a multiplicative factor of 100 from the one below it with the exception of the bottom curve.

non-absorbing aerosol particle. The calculation is based on the presentation in Bohren and Huffman (1983).

2.8 Optical Thickness

As has been demonstrated, as light propagates through the atmosphere it is absorbed and scattered according to Beer's law (2.137), which is completely general. There are two limiting cases that will be examined. The first is known as *optically thin*, where the amount of light that emerges from an atmospheric path after having traveled an arbitrary distance is linearly proportional to the radiance at the entry point. The second case is known as *optically thick*, where (2.137) must be applied. First, the application of Beer's law will be expanded from the homogeneous case, where the rays travel through a uniform medium and the extinction coefficient is constant, to the inhomogeneous case, where the atmospheric density, temperature, and constituents vary. Subsequently, optically thin and thick cases will be examined in detail.

2.8.1 Beer's Law Revisited

Beer's law was introduced in Section 2.1.2 to describe absorption in a homogeneous medium and was extended to include scattering through (2.137). Implicit in the

derivation of Beer's law was the assumption that the extinction coefficient did not vary along the path of the ray. This is obviously not true for the atmosphere. Equation (2.136) can be expressed in terms of the radiance along a ray as it propagates through a short distance r , giving

$$T_\lambda = \frac{L_\lambda}{L_{\lambda,o}} = e^{-k_e(\lambda)r}, \quad (2.166)$$

where the geometrical dependence of the radiance is understood. The extinction coefficient has a constant value for an infinitesimal distance dr and, in this infinitesimal case, (2.166) reduces to

$$d \ln L_\lambda = \frac{dL_\lambda}{L_\lambda} = -k_e(\lambda) dr \quad (2.167)$$

as the radiance is attenuated by both absorption and scattering.

The problem now becomes specifying the attenuation over the finite path that the ray traverses through the atmosphere. Considering the ray propagating between r_1 and r_2 , (2.167) is integrated along the path to yield

$$L_\lambda(r_2) = L_\lambda(r_1) \exp \left[- \int_{r_1}^{r_2} k_e(r, \lambda) dr \right] \quad (2.168)$$

for the radiance at r_2 . This is the form of Beer's law that can be applied to this finite propagation. The optical path is defined as

$$\tau_r(r_1, r_2) \equiv \int_{r_1}^{r_2} k_e(r, \lambda) dr \quad (2.169)$$

and, in the case of vertical propagation between z_1 and z_2 , is referred to as the *optical depth* and is given by

$$\tau(z_1, z_2) \equiv \int_{z_1}^{z_2} k_e(z, \lambda) dz, \quad (2.170)$$

with the caveat that z_2 is greater than z_1 to ensure that the optical depth is positive.

2.8.2 Equivalent Width

As we have shown, light is absorbed at particular wavelengths or frequencies as it passes through a medium due to the quantum mechanical properties of the gases present. The spectral radiance that is transmitted through a path of length r is given by

$$L_\nu(r) = L_\nu(0) e^{-\tau_r(r_1, r_2)}, \quad (2.171)$$

where the spectral dependence of τ_r is understood and ν represents a generic spectral unit. As an example where scattering is neglected, if the absorption from an isolated line is not too strong, the radiance observed will have a depression as illustrated in Figure 2.33. We'll get back to what we mean by "too strong" shortly; for now it is sufficient to note that the incident radiance is not completely absorbed over the distance r .

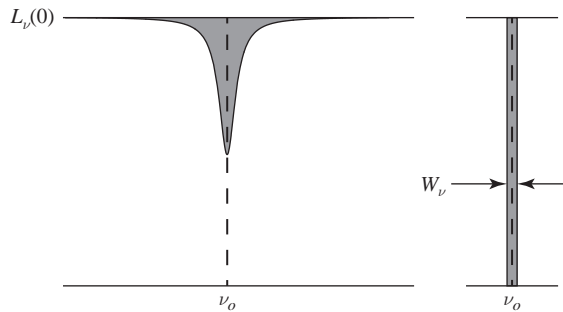


Figure 2.33 Definition of the equivalent width W_ν . The illustration on the left shows the absorption from a single feature centered at ν_o while the figure on the right shows the equivalent amount of absorption depicted as a rectangle. The areas of the two shaded regions are equal.

Absorption at a particular frequency is related to transmission through $A_\nu = 1 - T_\nu$, and is expressed as

$$A_\nu = \int \left[1 - \frac{L_\nu(r)}{L_\nu(0)} \right] d\nu \quad (2.172)$$

for absorption over a frequency range. A_ν is the area within the absorption feature and is known as the equivalent width W_ν , which is visualized as the width of a rectangular area that has the same amount of absorption. The equivalent width is expressed in terms of the absorption coefficient by substitution of (2.171) into (2.172) and is a succinct way to record the strength of the absorption feature. It has great utility since it is a relative measurement referenced to the background level, which can be fully transmissive or a continuum, as is often the case in atmospheric absorption. Additionally, the measurement of the full absorption feature does not have to resolve the details of the rotational-vibrational structure, although there are limitations when a background or spectrally adjacent absorber is present that can contaminate the equivalent width.

2.8.3 Optically Thin Extinction

The optical path for an optically thin atmosphere is much less than unity, allowing Beer's law to be reduced to

$$L_\nu(r_2) = L_\nu(r_1)e^{-\tau_r(r_1, r_2)} \approx L_\nu(r_1)[1 - \tau_r(r_1, r_2)], \quad (2.173)$$

where the exponential has been expanded using a Maclaurin series with the quadratic and higher terms discarded. If the medium is optically thin, then the probability that a photon will be absorbed or scattered is small, and the probability that it will be absorbed or scattered twice is vanishingly small. In order to develop the concept of an equivalent width, which applies to absorption, (2.173) will be evaluated for a single absorption line with scattering neglected. This approximation is valid for wavelengths longer than about 1 μm in an atmosphere with low aerosol loading.

The development of the Einstein coefficients assumed thermal equilibrium between the upper and lower states and strictly monochromatic emission. For typical atmospheric

temperatures and in the wavelength range of interest (0.4 to 14.5 μm), the population in the upper state is negligibly small due to (2.79) implying that both spontaneous and stimulated emission from the upper state can be neglected. The absorption coefficient is therefore proportional to B_{12} alone, but modified to account for the width of the spectral line. In Section 2.6 the absorption coefficient was defined as the product of the line strength and the shape factor as given by (2.112). The connection between the two concepts will now be established.

Consider a volume in space containing a two-level atom that is within an isotropic radiation field of spectral energy density ρ_v . Recall that the rate of absorption from the lower level to the higher one is given by (2.81). This will be expressed as the absorption rate per unit volume or

$$W_{12} = B_{12}\rho_v n_1, \quad (2.174)$$

where n_1 is the number density of absorbers in level 1. The goal is to make the connection between this rate and the absorption coefficient. Rearranging (2.167) and applying (2.87) yields

$$\frac{dL_v}{dr} = -k_a L_v = -k_a \frac{c}{4\pi} \rho_v \quad (2.175)$$

for the absorption of radiance over an infinitesimal length. The rate of energy absorbed per unit volume within the solid angle $d\omega$ over the frequency interval v and $v + dv$ is

$$\frac{dL_v}{dr} dv d\omega = -k_a \frac{c}{4\pi} \rho_v dv d\omega$$

which, for the assumed isotropic radiation field, integrates to

$$4\pi \frac{dL_v}{dr} dv = -ck_a \rho_v dv \quad (2.176)$$

for the flux absorbed per unit volume within the frequency interval. The rate of photon absorption is obtained by dividing (2.176) by the energy of the absorbed photon or

$$W_{12} = c \int k_a \frac{\rho_v}{hv} dv \approx \frac{c}{hv_o} \rho_v \int k_a dv = \frac{c}{hv_o} \rho_v S, \quad (2.177)$$

where the integration is over the frequency interval that encompasses the line shape centered at v_o with the radiation field assumed to be constant over the width. Equating (2.174) and (2.177) yields

$$S = \frac{hv_o}{c} B_{12} n_1 \quad (2.178)$$

for the line strength from which the absorption coefficient

$$k_a = \frac{hv_o}{c} B_{12} n_1 f(v - v_o) \quad (2.179)$$

is obtained for a single line. Note that even though (2.179) was obtained for an isotropic radiation field, it is generally valid since the Einstein coefficients are properties of the

absorber and the absorption line shape depends upon both the molecular properties and the local temperature and pressure. The absorption cross section is

$$\sigma_a = \frac{h\nu_o}{c} B_{12} f(\nu - \nu_o), \quad (2.180)$$

developed analogously to (2.133), although it is typically expressed in terms of the Einstein A -coefficient. The above derivation was accomplished in terms of the frequency ν , but could have been done using any spectral unit.

The line strength S is now grounded in the quantum mechanical description of the absorbing atom or molecule through the Einstein coefficients. We have assumed a non-degenerate atom or molecule; however, in reality the statistical weights that enumerate the number of degenerate quantum states that compose either or both of the upper and lower levels are included, with (2.89) appropriately modified (Penner, 1959). It is sufficient to know the A -coefficients, which are compiled in a spectroscopic database, for the line strength calculation. For example, in the HITRAN database, both the line strengths and the Einstein A -coefficients are included for each atmospheric species. From (2.113), the units for line strength are the particular spectral units per unit distance. In the HITRAN database, the line strengths are divided by a unit number density of the particular molecular species at a temperature of 296 K. This results in the line strengths being in units of wave numbers per molecule per unit area ($\text{cm}^{-1}/(\text{molecule} \times \text{cm}^{-2})$), which facilitates their use in a radiative transfer code where the number density at every altitude is known. The evolution of the line strength with temperature and pressure as the radiance propagates through the inhomogeneous atmosphere is also included within a radiative transfer model (Šimečková et al., 2006).

The weak oxygen absorption feature at 630 nm, known as the γ band and illustrated in Figure 2.34, will be used as an example for the optically thin case with the absorption distance varying from 10 m to 1 km. The left graph is a high-resolution model using a pressure-broadened Lorentzian line shape, and the right graph shows the modeled transmission for an imaging spectrometer that samples every 10 nm starting from 600 nm and has a uniform 12 nm FWHM spectral response function.

Returning to (2.173), the requirement that $\tau(r_1, r_2) \ll 1$ is driven by the number of absorbers, the line strength, which is proportional to B_{12} , and the length of travel as

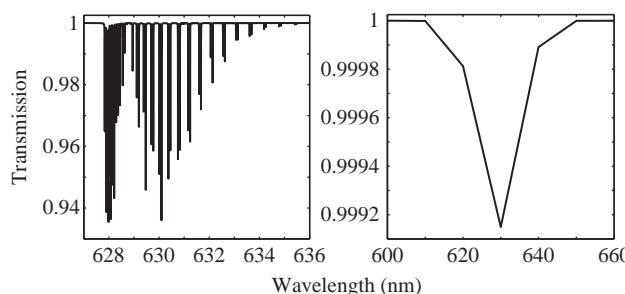


Figure 2.34 Transmission of the oxygen γ band over 1 km with a partial pressure of 20.94 percent at a pressure of 1 atm and a temperature of 296 K.

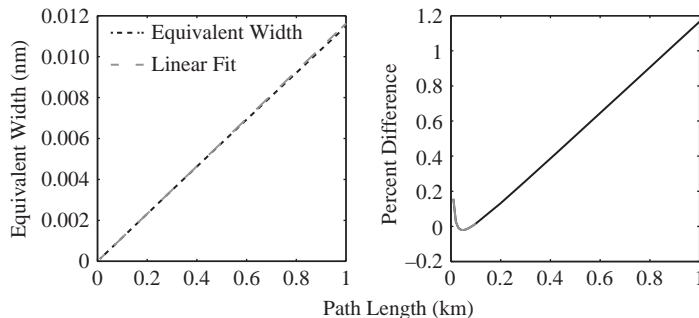


Figure 2.35 Equivalent width for the 630 nm oxygen band compared to a linear fit.

captured in (2.170). The equivalent width in the optically thin case for a single line is determined through (2.172) and (2.173) or

$$W_v = \int k_a \cdot (r_2 - r_1) dv = \frac{h\nu_o}{c} B_{12} n_1 \cdot (r_2 - r_1) \quad (2.181)$$

over the path length $r_2 - r_1$ because the line profile is normalized. In the case of an unresolved spectrum composed of many lines, as illustrated in Figure 2.34, the equivalent width for the 630 nm oxygen feature was calculated directly from (2.172) for a range of optical path lengths. First, W_λ , rather than W_v , was computed for a path length ranging from 10 to 100 m. Next, the calculation was extended to a path length varying from 100 m to 1 km. The relationship between W_λ and the path length satisfies (2.173) over the shorter range, as illustrated in Figure 2.35. The left graph shows the equivalent width from (2.172), the black dashed line, compared to a line from a fit to the shorter range but extended to the full path length. Notice that the linear fit departs from the equivalent width as the atmospheric path approaches 1 km. The right graph presents the same information as a percent difference with the gray section of the curve corresponding to the 10 to 100 m range that was linearly fit. Due to the abundance of oxygen in the atmosphere, the relatively weak absorption of the γ band is no longer optically thin when the optical path is long.

2.8.4

Optically Thick Extinction

The medium is called *optically thick* at a particular frequency or wavelength if the probability that a photon will be scattered or absorbed multiple times is high. For example, a visible wavelength photon traveling through a dense cloud will be scattered many times before it exits from either the cloud top or bottom, and the final direction of travel will have no relationship with its initial direction. Considering absorption alone, in the typical case where the lower state is the ground state of the atom or molecule, the assumption that $\tau(r_1, r_2) \ll 1$ fails and the probability that an emitted photon from level 2 is reabsorbed becomes high.

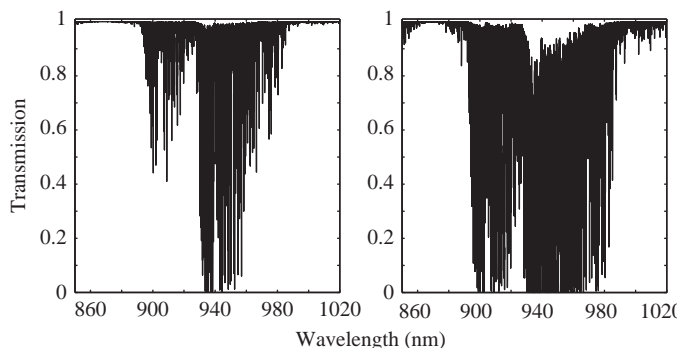


Figure 2.36 Transmission of the 940 nm molecular water band over 0.5 km path, a pressure of 1 atm, and a temperature of 296 K with a relative humidity of 10 percent in the left graph and 100 percent in the right one.

Molecular water will be taken as a concrete example because of its impact on remote sensing as the principal absorber in the atmosphere. The amount of water varies from trace amounts in very dry environments to up to about 4 percent by volume. This maximum amount is due to the saturation pressure when the processes of evaporation and condensation are in balance at a particular temperature. The maximum amount that can be present increases as the temperature increases, so that tropical environments have more water vapor on average than colder climates. The amount of water is typically quantified in terms of the relative humidity, which is the ratio of the actual vapor density to the saturation vapor density at a given temperature expressed as a percentage, or, alternatively, the ratio between the actual vapor pressure to the saturation vapor pressure.

The 940 nm water band will be treated in some detail since, at the spectral resolution of a typical imaging spectrometer, it is not opaque in contrast to the bands at longer wavelengths, such as the ones at 1400 nm and 1900 nm, which are under most viewing conditions. Figure 2.36 illustrates the rich rotational-vibrational absorption structure of the water molecule for two different relative humidities and over a 500 m path at a pressure of 101,325 Pa. The variation in absorption for the different molecular transitions is from a small amount, for the transitions in the wings of the band, to fully opaque near the band center. The higher humidity graph on the right demonstrates the increase in the number of opaque bands as the amount of water is increased to the maximum value of 100 percent humidity. Both graphs utilize a Lorentzian line shape.

The effective transmission of the 940 nm water band within the spectral response functions with 10 nm spacing and a uniform 12 nm FWHM is illustrated by the left graph in Figure 2.37. The right graph shows the corresponding equivalent width with the calculation extended down to 1 percent relative humidity. The nonlinearity, which is more typical of absorption from atmospheric species over long path lengths, is present for water even at a very low relative humidity and over the rather short 500 m atmospheric

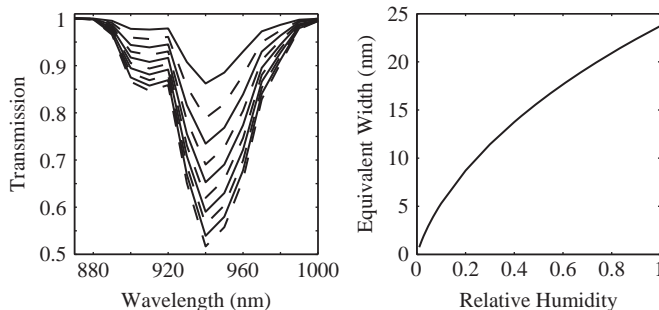


Figure 2.37 940 nm water band-averaged transmission on the left for different relative humidity values ranging from 10 percent to 100 percent in 10 percent steps, illustrated with alternating solid and dashed lines, and the equivalent width as a function of relative humidity on the right.

path. This presents challenges for the conversion of imaging spectrometer radiance data to reflectance as will be shown in Chapter 6.

2.9 Properties of the Atmosphere

The fundamental phenomena of absorption, emission, and scattering that govern the transfer of radiation through the atmosphere have been introduced. The final topic for this chapter is a brief description of the composition and structure of the atmosphere, including the atomic and molecular species present and their transmission properties, as well as an introduction to the vertical and size distributions of aerosols. A smoothly varying atmosphere will be assumed without abrupt inhomogeneities, such as those from weather patterns and local aerosol loading. Additionally, the structure of the atmosphere will only be addressed in the vertical direction. Much of the data presented are from the 1976 US Standard Atmosphere, which is an average representation based on long-term measurements for a 45°N latitude (NOAA, NASA, and USAF, 1976).

2.9.1 Atmospheric Structure

From the remote sensing point of view we are interested in the transmission of light through the atmosphere that is governed by the molecular and aerosol constituents. The composition, expressed in a relative sense or in terms of number density, varies as a function of altitude, as does the temperature. The atmosphere is classified into regions according to the temperature behavior and the pressure. The lowest layer of the atmosphere, the troposphere, ranges from the surface to an altitude of 10–15 km depending on the latitude and time of year and is characterized by decreasing temperature and relatively uniform mixing of constituents with the exception of water. This layer contains 75 percent of atmospheric gases and most of the aerosols. The next layer is the stratosphere up to about 50 km where the temperature increases with altitude due to heating from absorption of ultraviolet radiation by ozone. The mesosphere extends from about

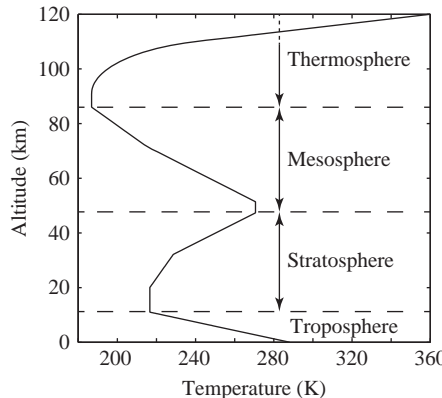


Figure 2.38 Temperature profile of the atmosphere up to 120 km.

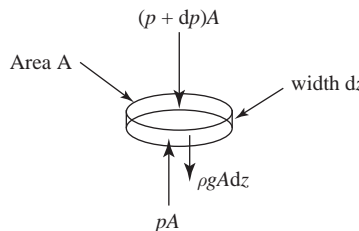


Figure 2.39 Forces on a gas volume in equilibrium.

50 km to 85 km with the temperature again falling, in this case due to radiative cooling as carbon dioxide radiates energy to space. The final layer of interest for our purposes is the thermosphere which ranges up to about 500 km and is also characterized by increasing temperature due to absorption of high energy solar radiation at wavelengths less than 170 nm. Figure 2.38 is a plot of the temperature behavior with the different layers identified up to 120 km.

The variation of pressure with altitude for a static atmosphere is developed through fluid statics and the ideal gas law. Figure 2.39 illustrates a parcel of gas of area A and thickness dz . The downward force at the top of the parcel due to pressure is $(p + dp)A$ with the similar upward force from the bottom being pA . The parcel also weighs $\rho g A dz$, where ρ is the gas density in the parcel and g is the local acceleration due to gravity. There is no acceleration of the parcel horizontally and therefore the resultant forces must be zero. Since the system is in static equilibrium, the upward force is equal to the sum of the downward forces, which yields

$$\frac{dp(z)}{dz} = -\rho g(z), \quad (2.182)$$

where the altitude dependence of the acceleration due to gravity has been made explicit.

The atmosphere is well approximated by the ideal gas law, which is written as

$$pV = nRT, \quad (2.183)$$

where n is the number of moles of gas present in the volume V at a temperature T and $R = 8.314 \text{ J/mol}\cdot\text{K}$ is the universal gas constant. Recall that one mole is equal to Avogadro's number of atoms or molecules which is $N_A = 6.022 \times 10^{23} \text{ mol}^{-1}$. The ideal gas law is modified by applying the average molecular weight of air, $M_{\text{air}} = 28.97 \text{ g mol}^{-1}$, and expressing (2.183) in terms of the gas density ρ through

$$\rho = \frac{m}{V} = \frac{nM_{\text{air}}}{V}, \quad (2.184)$$

where m is the gas mass in the volume. When applied to (2.183) this yields

$$\rho(z) = \frac{M_{\text{air}}p(z)}{RT(z)}, \quad (2.185)$$

where the altitude dependence of the density, pressure, and temperature is noted. Applying (2.185) to (2.182) produces

$$\frac{dp}{p} = -\frac{dz}{H} \quad \text{where} \quad H \equiv \frac{RT}{M_{\text{air}}g}, \quad (2.186)$$

with H known as the scale height. Equation (2.186) integrates to

$$p(z) = p(z_o) \exp \left[- \int_{z_o}^z \frac{dz'}{H(z')} \right], \quad (2.187)$$

which can alternatively be expressed in terms of density through (2.185). Figure 2.40 is the pressure profile for the 1976 US Standard Atmosphere.

So far the pressure or density has been expressed as a function of the average molecular weight but the atmosphere is a mixture of many species. The HITRAN database contains spectroscopic information for 47 atoms and molecules, although many are trace species. The most radiatively active species in our spectral range of interest are water, carbon dioxide, ozone, and nitrous oxide. Oxygen and nitrogen make up the bulk of the atmosphere; however, since they are homonuclear molecules and lack a dipole moment, they are relatively inactive. Oxygen does have an important feature at 760 nm that can be used to estimate surface altitude through a measurement of the pressure (Barton and Scott, 1986). These species have vertical mixing profiles that partially govern their impact on remotely sensed data. For example, water is present in the lowest portion of the atmosphere with typically opaque bands at 1.4 and 1.9 μm . If data are

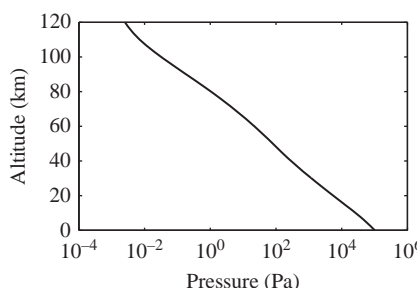


Figure 2.40 Pressure variation as a function of altitude.

taken over a high-altitude mountain range with a cold atmosphere that doesn't contain a great deal of water, these bands become transmissive. Another example is ozone, whose concentration peaks in the stratosphere at around 25 to 30 km and is highly absorbing at $9.6 \mu\text{m}$ in the middle of the LWIR window. If an airborne LWIR imaging spectrometer is being flown well below the ozone layer then the impact of ozone absorption will be significantly less, and must be taken into account in the atmospheric compensation.

The volume mixing ratio for the i th species is defined as

$$r_i(z) \equiv \frac{c_i(z)}{c_{\text{total}}(z)}, \quad (2.188)$$

where c_i is the molar concentration (n_i/V) of the particular species and c_{total} is the total molar concentration of air. Often, mixing ratios are defined with respect to dry air since the amount of water vapor is dependent on temperature and humidity. The mixing ratio can also be expressed through the ideal gas law as the ratio of the partial pressure of the particular species p_i to the total pressure p , or in terms of the mass, in which case r_i^m is the mass mixing ratio and is equal to ρ_i/ρ , where ρ is the density. Water is a special case, since it changes state at typical terrestrial temperatures and pressures. As was introduced in Section 2.8.4, its concentration is often given in terms of the relative humidity or

$$RH \equiv 100 \frac{p_w}{p_w^s} \quad (2.189)$$

where p_w is the partial pressure of water and p_w^s is its saturation pressure where the processes of condensation and evaporation are in equilibrium. Relative humidity has a strong dependence upon temperature. Figure 2.41 illustrates the volume mixing ratios for several molecules under average mid-latitude conditions.

2.9.2 Atmospheric Absorption

The mechanisms that govern absorption have been described above with some examples from particular molecular features presented. Nadir transmission for the primary

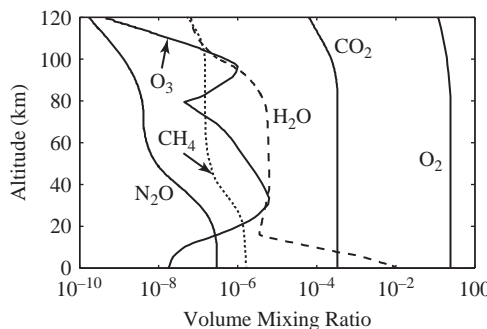


Figure 2.41 Vertical mixing ratio profiles for the primary absorbing atmospheric species. Nitrogen is not included, but its curve would be to the right of the oxygen curve and parallel to it with a sea-level value of 0.78. Adapted from Goody and Yung (1989).

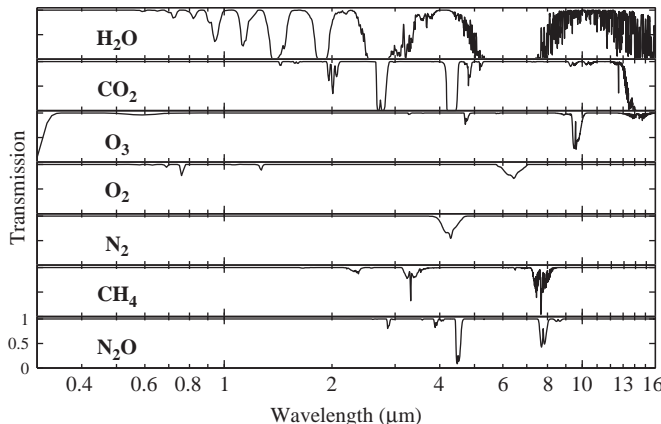


Figure 2.42 Nadir transmission through the full atmosphere for the most absorbing species. The transmission scale is between 0 and 1.05 for each panel.

molecular species over the 0.3 to 16 μm range is presented in Figure 2.42. The atmospheric windows, where radiance from the surface reaches the top of the atmosphere, are largely bracketed by water absorption, although the long wavelength sides of both the MWIR and LWIR windows are demarcated by a set of carbon dioxide absorption features. Additionally, the short wavelength cutoff corresponds to absorption due to ozone at around 0.3 μm . There is considerable overlap between the absorption from the different absorbers and the total transmission is the product of the transmission from the individual species.

It is somewhat counterintuitive that the primary absorbers in the atmosphere in our spectral range are trace species. For example, nitrogen and oxygen make up 78.1 percent and 20.9 percent respectively of the volume of the atmosphere, but are transparent for almost all of the spectral range of interest. As was developed in Section 2.8, the absorption coefficient depends upon the number density of absorbers and the Einstein coefficients. The molecules that are not homonuclear and that contain three or more atoms have much richer rotational–vibrational structures and much larger absorption coefficients.

Ozone is an example of a trace species that extensively varies both with latitude and season over a range of 200 to 500 Dobson units (DU). A Dobson unit is a measure of columnar density and corresponds to the thickness of a particular gas within a column of unit cross-sectional area from the surface to the top of the atmosphere if it were brought to standard temperature and pressure ($p_s = 101,325 \text{ Pa}$, $T_s = 273.15 \text{ K}$). Combining (2.183) with the number density n_g of an ideal gas,

$$n_g = \frac{nN_A}{V}, \quad (2.190)$$

yields

$$n_g = \frac{pN_A}{RT} \quad (2.191)$$

in units of molecules per unit volume. A Dobson unit is a $10 \mu\text{m}$ thick layer of gas of unit cross-sectional area under standard conditions and is obtained by multiplying (2.191) by $10 \mu\text{m}$, with the units being molecules per unit area.

By comparison, the column density n_a for the total atmosphere is calculated using

$$n_a = \frac{N_A}{R} \int_0^{z_{top}} \frac{p(z)}{T(z)} dz, \quad (2.192)$$

with the integration depending upon the pressure and temperature profiles. Performing this integration using data for pressure and temperature as a function of altitude from the US Standard Atmosphere yields a column density of 2.16×10^{26} molecules per square meter. The column depth z at standard conditions is obtained through

$$z = n_a \frac{R}{N_A} \frac{T_s}{p_s}, \quad (2.193)$$

which yields 8.02 km or $8.02 \times 10^8 \text{ DU}$. The total fraction of ozone in the atmosphere is therefore about 3.7×10^{-7} if the value for the ozone concentration in the column is 300 DU. As is shown in Figure 2.42, the atmosphere absorption due to ozone becomes high as the wavelength is reduced to 300 nm even with this small concentration. Transmission of ozone becomes zero at wavelengths shorter than this.

Water is the primary absorber in the atmosphere and is also highly variable, as noted in Section 2.8.4. It also departs from the Lorentzian line shape in the wings in what is termed the water vapor continuum. One explanation for the continuum is that water forms dimers where two molecules are held together through hydrogen bonds. These are predicted to represent less than one percent of the water vapor in the atmosphere, and until recently there were no direct measurements of dimers under conditions that are similar to those of the atmosphere; but see Tretyakov et al. (2013) for evidence from the laboratory. Other mechanisms that have been suggested to explain the continuum are collision induced absorption and the superposition of the far wings of collisionally broadened lines since water has such a rich ro-vibrational structure. Figure 2.43 illustrates the continuum which is taken into account in radiative transfer calculations.

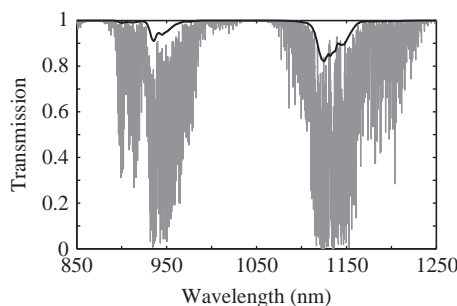


Figure 2.43 MODTRAN® calculation demonstrating the continuum water vapor absorption for the 940 and 1140 nm bands. The gray curve is the transmission excluding the continuum contribution and the black curve is the continuum alone.

2.9.3 Aerosol Properties

The distribution of aerosols as a function of both altitude and size is highly variable in the atmosphere and the models included in a radiative transfer code are averages based upon the best available measurements. In the 1960s and 1970s, as part of the development of the predecessor codes to the MODerate spectral atmospheric TRANsmission (MODTRAN®) code, at what was then the Air Force Cambridge Research Laboratory that later became the Air Force Geophysics Laboratory, extensive work was performed to quantify aerosol distributions in the atmosphere. This research culminated in the seminal publication by Shettle and Fenn (1979) that incorporated the work from the aerosol research community at that time. The models presented there were later updated in d'Almeida et al. (1991). Subsequently an extensive literature for aerosol measurements has emerged, much of it utilizing NASA systems such as the MODerate resolution Imaging Spectrometer (MODIS). A full review of that literature is beyond our scope, and we will settle for a description primarily based on d'Almeida et al. (1991), but also from a valuable review article with representative data for tropospheric aerosols (Jaenicke, 1993).

Size Distribution Functions

The aerosols in a given volume are typically composed of a mixture of types from different sources and several distribution functions have been developed to describe size distributions. First we will define what is meant by an aerosol size distribution and develop the mathematical description. The number of aerosols in a given volume with radii in the range of r to $r + dr$ is defined as $n(r) dr$ where $n(r)$ is the size distribution function. This implies that the cumulative size distribution function $N(r_a)$ that describes the number of aerosols per unit volume having radii smaller than r_a is

$$N(r_a) = \int_0^{r_a} n(r) dr, \quad (2.194)$$

which integrates to the total number of particles in the volume if the upper limit of integration is set to infinity. If (2.194) is differentiated the size distribution function is written as

$$n(r) = \frac{dN}{dr}, \quad (2.195)$$

typically expressed as the number per cm^3 per μm with the last unit referring to the particle radius.

Aerosol sizes vary over several orders of magnitude in the atmosphere, with the range of radii going from a thousandth of a micron to about $100 \mu\text{m}$. Expressing this variation on a linear scale can obscure the structure and therefore logarithmic distributions are typically employed. The drawback to displaying the data this way is that the area under the curve is no longer equal to the cumulative number of particles. Nevertheless, the size distribution function is often expressed in terms of logarithmic functions. For example, the number of particles in a unit volume in a size range $\log r$ to $\log r + d \log r$ is $n_{10}(\log r) d \log r$. In this formulation the size distribution function becomes

$$n_{10}(\log r) = \frac{dN}{d \log r}, \quad (2.196)$$

analogous to (2.195) with n_{10} signifying that the size distribution function is given in terms of a base 10 or common logarithm. Note, however, that $n_{10}(\log r)$ is per unit volume, typically cm^{-3} , since $\log r$ is dimensionless. This should be thought of as $\log(r/r_o)$ with the radius expressed in terms of microns and r_o is 1 μm . The preceding discussion is equally applicable to the natural logarithm.

An early example of a size distribution function is the Junge, or power law, distribution, where the idea of using logarithmic scales was introduced (Junge, 1955). The Junge distribution is defined using a common logarithm given by

$$n_{10}(\log r) = \frac{C}{r^\beta}, \quad (2.197)$$

where C and β are positive constants. Taking the logarithm of both sides of (2.197) yields

$$\log n_{10} = \log C - \beta \log r, \quad (2.198)$$

which is a monotonically decreasing function when plotted on a log–log scale. In that case, $-\beta$ is the slope and C equals n_{10} when the radius is 1 μm obtained by setting r equal to 1. The Junge distribution has limited utility given that aerosol distributions tend to have multiple modes. When it is appropriate, the value of β typically ranges from 2 to 5.

The empirical model that often fits the aerosol size distribution is the log-normal distribution. Its usefulness is due to the skewed nature of aerosol distributions where the variance is large compared to the mean, there are no negative values, and the range of particle sizes can be spread over several orders of magnitude. The Gaussian or normal distribution was introduced in Section 2.6.1 to describe the Doppler profile through (2.121). This mathematical form will now be modified for the log-normal distribution. The normal distribution is given by

$$f(r) = \frac{1}{\sigma \sqrt{2\pi}} \exp \left[-\frac{(r - \bar{r})^2}{2\sigma^2} \right], \quad (2.199)$$

where \bar{r} is the mean radius and σ is the standard deviation. In order for (2.199) to be used as a size distribution function it must be integrable to the total number of particles present through (2.194). In this case, $n(r)$ becomes

$$n(r) = N_t f(r) = \frac{N_t}{\sigma \sqrt{2\pi}} \exp \left[-\frac{(r - \bar{r})^2}{2\sigma^2} \right], \quad (2.200)$$

where N_t is the total number of particles present in the unit volume. Equation (2.200) integrates to N_t since (2.199) is normalized.

The log-normal distribution is developed by replacing r , \bar{r} , and σ by $\log r$, $\log r_m$, and $\log \sigma_m$ respectively, or

$$n_{10}(\log r) = \frac{N_t}{\log \sigma_m \sqrt{2\pi}} \exp \left[-\frac{(\log r - \log r_m)^2}{2(\log \sigma_m)^2} \right], \quad (2.201)$$

where r_m is the median radius, $\log r_m$ is the mean value of $\log r$, and $\log \sigma_m$ is the standard deviation of $\log r$. It can be shown that (2.201) also integrates to N_t as required. In many cases the particle size distribution will have more than one mode due to multiple sources and it is modeled using a sum of log-normal distributions or

$$n_{10}(\log r) = \sum_{i=1}^n \frac{N_i}{\log \sigma_i \sqrt{2\pi}} \exp \left[-\frac{(\log r - \log r_i)^2}{2(\log \sigma_i)^2} \right], \quad (2.202)$$

with N_t , σ_m , and r_m replaced by N_i , σ_i , and r_i respectively, where i is the index for an individual source. The log-normal distribution has been presented in term of the common logarithm but it could have been developed using the natural logarithm. The statistical properties of log-normal distributions are comprehensively described in Aitchison and Brown (1957).

2.9.4

Aerosol Models

The modeling of aerosols is difficult given the variability in space and time of the different types and their optical properties. The models that have been developed, and are employed in radiative transfer calculations, are based on extensive measurements of size, distribution, and variability. Individual models are typically composites of different aerosol components. For example, the average continental model is made up of water-soluble, soot, dust-like, and mineral components for which there are known optical properties and size distributions. Additionally, aerosol properties vary with humidity as water vapor condenses onto the particles, altering their size and index of refraction. The models in d'Almeida et al. (1991) and Jaenicke (1993) are labeled according to the applicable environment such as rural, maritime, continental, desert, and polar. They also have different subcategories depending upon the amount of pollution or other components present.

Tropospheric aerosol models are the primary drivers in radiative transfer modeling for imaging spectroscopy although there are cases where stratospheric aerosols could become important, such as following volcanic eruptions. Table 2.4 provides the data used to develop the size distribution function for the polar, rural, and urban models applying (2.202). The models are all composed of the sum of three log-normal distributions and demonstrate the multimode nature of many aerosols. These models are illustrated in Figure 2.44 utilizing both a log-log plot on the left and a semi-log plot on the right.

The vertical mass distribution of tropospheric aerosols in many cases shows an exponential decrease with increasing altitude to a scale height H_m similar to that developed for pressure variation given by (2.187). The form is

$$m = m_o \exp \left(\frac{-z}{H_m} \right), \quad (2.203)$$

where m_o is the surface concentration. The vertical variation is illustrated for several models in Figure 2.45, all of which are based on empirical data. Note the rapid fall in concentration as a function of altitude with most of the aerosol load in the lower

Table 2.4 Log-normal aerosol model parameters. Data from Jaenicke (1993).

Aerosol	i	$n_i(\text{cm}^{-3})$	$r_i(\mu\text{m})$	$\log \sigma_i$
Polar	1	21.7	0.0689	0.245
	2	0.186	0.375	0.300
	3	0.000304	4.29	0.291
Rural	1	6650	0.00739	0.225
	2	147	0.0269	0.557
	3	1990	0.0419	0.266
Urban	1	99300	0.00651	0.245
	2	1110	0.00714	0.666
	3	36400	0.0248	0.337

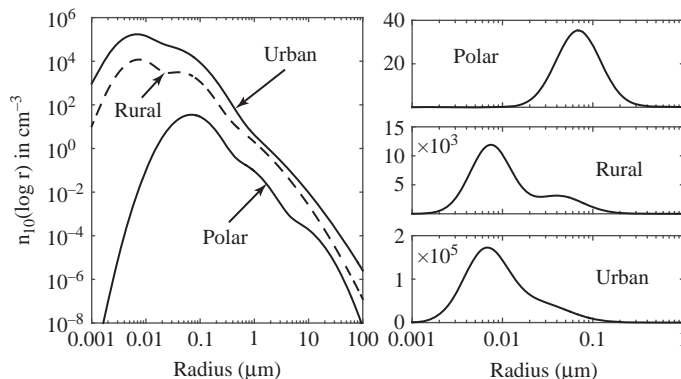


Figure 2.44 Log-normal size distributions for the polar, rural, and urban models. Note the scale change on the semi-log plot to the right with the multiplicative factor inside the individual panels. Based on Jaenicke (1993).

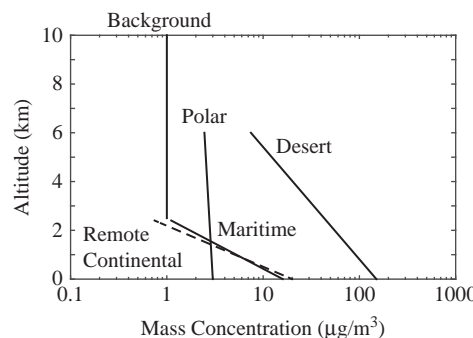


Figure 2.45 Vertical distribution of aerosol mass concentrations for several model types. The remote continental model is illustrated by the dashed line to distinguish it from the maritime model with a similar slope. Data from Jaenicke (1993).

Table 2.5 The six reference atmospheres used in MODTRAN®.

Model Atmosphere	Latitude	Time of Year
Tropical	15 N	Annual Average
Mid-latitude Summer	45 N	July
Mid-latitude Winter	45 N	January
Sub-arctic Summer	60 N	July
Sub-arctic Winter	60 N	January
Standard	US	1976

troposphere. This has important consequences for atmospheric compensation for high-altitude scenes where aerosol scattering will be minimal.

2.9.5

Model Atmospheres for Radiative Transfer Calculations

Modeling transmission through the atmosphere is accomplished through computer programs that capture the extinction of the radiation as it propagates through the atmosphere as well as thermal emission. Chapter 6 has an introduction to the theoretical basis of these programs, but it does not contain a description of the atmospheric models that provide the underlying data required for the calculation to be performed. The modest introduction to the atmospheric structure and aerosol models utilized in radiative transfer calculations presented here is based on the documentation for MODTRAN®, and all radiative transfer codes must contain similar information (Kneizys et al., 1996).

In addition to the US Standard Atmosphere, there are five other model atmospheres that attempt to span the broad variability of the earth's atmosphere. Each model atmosphere contains vertical profiles of temperature, pressure, number density, and mixing ratios that are primarily based on measurements. Table 2.5 lists the six reference atmospheres, their applicable latitudes, and the time of year when they are appropriate and Figure 2.46 illustrates the variation as a function of temperature for both pressure and altitude for all of them. There are 41 molecular species whose absorption can be modeled using MODTRAN® with the constituent profiles ranging from sea level to 120 km. All are from the HITRAN database. The mixing ratios of the various species vary to a relatively small degree as a function of reference atmosphere with the exception of water. Figure 2.47 illustrates the default water mass concentration as a function of altitude for each reference atmosphere, which can be varied through an input parameter in a typical radiative transfer program.

The aerosol models in MODTRAN® are based on Shettle and Fenn (1979), with the atmosphere divided into four regions. The first is the boundary layer model from 0 to 2 km with most of the aerosol loading, the second is the upper troposphere model from 2 to 10 km, the third is the lower stratosphere model from 10 to 30 km, and the final is the upper atmosphere model from 30 to 100 km. The boundary layer model is composed of rural, urban, maritime, tropospheric, and desert sources that vary with humidity and whose vertical distribution is assumed to be constant with altitude. The local conditions,

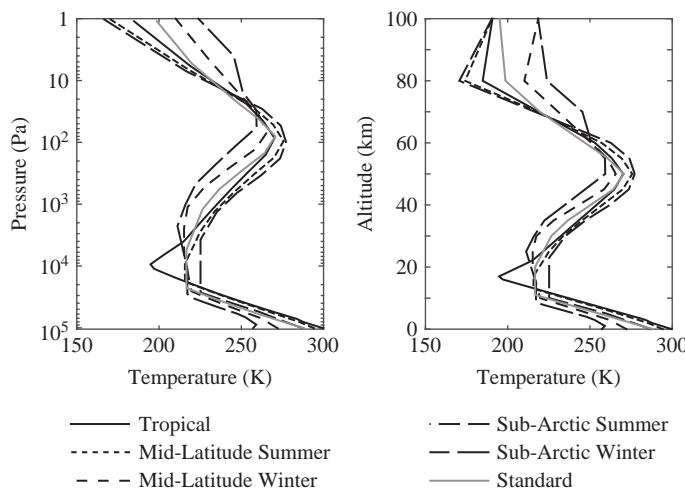


Figure 2.46 Temperature variation as a function of pressure and altitude for the six reference atmospheres included in MODTRAN®.

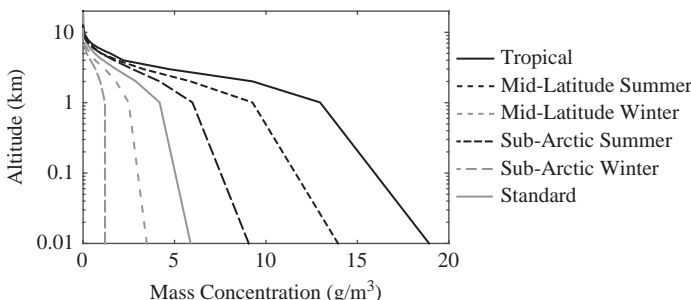


Figure 2.47 Default water mass concentrations for the six reference atmospheres included in MODTRAN®.

such as weather patterns and geographic variation, dominate the aerosol loading in the boundary layer, which transitions to a distribution dominated by seasonal variations in the upper troposphere, where the rural model is applied without the largest particles. Above 10 km the default models are a background stratospheric distribution up to 30 km followed by an upper atmosphere model.

The transmission of the atmosphere due to aerosols alone is illustrated in Figure 2.48. The left graph shows the variation in extinction for the various models, except for the desert model, as a function of wavelength. Rayleigh scattering is included as a reference and is the lower bound for atmospheric scattering. The right graph is an example of the increase in transmission as aerosol scattering declines with increased altitude for the rural model with the visibility parameter set to 5 km. The visibility parameter is described in Chapter 6 and it is sufficient to note here that this corresponds to an aerosol rich atmosphere. Both graphs are generated using the mid-latitude summer reference atmosphere with the default molecular mixing ratio altitude profiles.

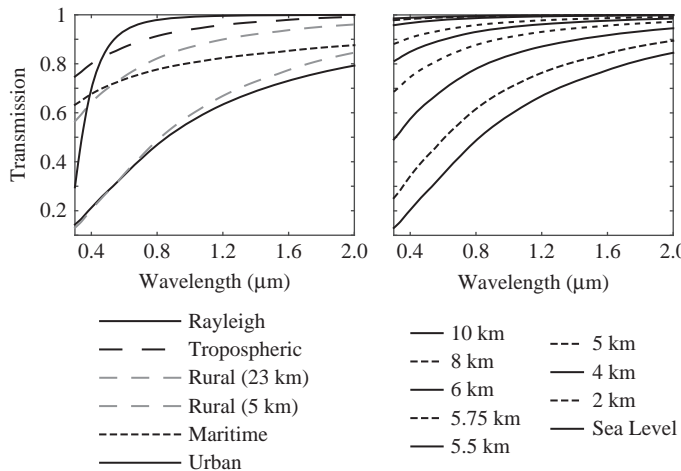


Figure 2.48 The left graph illustrates the variability for the different aerosol models for transmission from sea level to the top of the atmosphere with the bottom solid curve corresponding to Rayleigh scattering. The right graph shows the reduction in aerosol extinction as a function of altitude with the lowest curve corresponding to transmission from sea level. Calculations were performed using MODTRAN®.

2.10 Summary and Further Reading

The goal of this chapter was to provide the reader with an overview of the physical processes that govern the propagation of radiation through the atmosphere without getting so detailed as to be overwhelming. As has been illustrated, the science of remote sensing using imaging spectroscopy requires knowledge from many scientific disciplines. Quantum mechanics is required to understand the line spectra and the transition rates between states. Electromagnetism is used for the propagation of an electromagnetic wave through different media. Finally, atmospheric science provides the fundamental description of the medium of propagation that includes absorption and scattering. Other disciplines, such as statistical mechanics and collisional physics, have been given little or no attention here but are important nonetheless in the solution to the full radiative transfer problem. The scientific background that applies to the topics of this chapter can be found in a multitude of books, and the list that follows is the barest introduction. The theory of atomic and molecular spectra and structure can be found in Herzberg (1944), Herzberg (1950), and Woodgate (1983). Electromagnetic theory is developed in Purcell (1965) and Lorrain and Corson (1979). Atmospheric radiative transfer is presented in Bohren and Clothiaux (2006), Goody and Yung (1989), Thomas and Stamnes (1999), and Liou (2002), while aerosol scattering is well developed in Bohren and Huffman (1983). Finally, the wave phenomena of diffraction and interference are introduced in Jenkins and White (1976) and rigorously treated in Born and Wolf (1999).

Problems

1. Show that

$$\frac{d}{d\theta}(\cos \theta + i \sin \theta) = \frac{d}{d\theta} \exp(i\theta). \quad (2.204)$$

Additionally, take the derivative of $z = \cos \theta + i \sin \theta$ with respect to θ and show that the integral of this quantity is $z = \exp(i\theta)$.

2. Show that the magnitude of a complex number $z = x + iy$ is $|z| = (z^*z)^{1/2}$.
3. Develop (2.21) from (2.20).
4. Show that the irradiance from the diffraction pattern from a rectangular aperture with the geometry defined in Figure 2.49 is given by

$$E(\theta, \phi) = E(0) \left(\frac{\sin \alpha}{\alpha} \right)^2 \left(\frac{\sin \beta}{\beta} \right)^2, \quad (2.205)$$

where $\alpha = \frac{1}{2}kW \sin \phi$ and $\beta = \frac{1}{2}kH \sin \theta$.

5. Derive (2.49).
6. A source that emits or reflects radiance that is independent of the angle of observation is known as a *Lambertian* source. Show that the irradiance from the spatially uniform and Lambertian emitting disk illustrated in Figure 2.50 is given by

$$E_d = \pi L_s \sin^2 \alpha, \quad (2.206)$$

where L_s is the constant source radiance. What does this reduce to in the limits of $d \ll R$ and $d \gg R$?

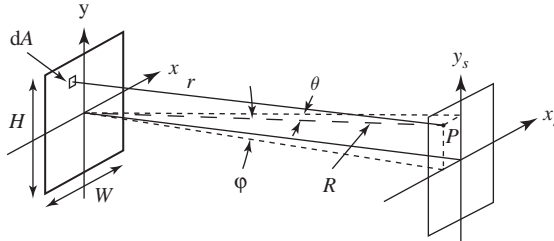


Figure 2.49 Geometry for the irradiance pattern due to diffraction from a rectangular aperture.

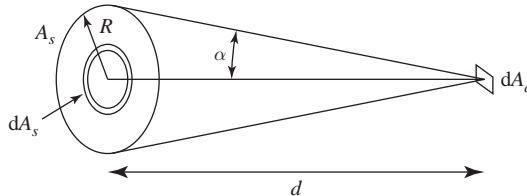


Figure 2.50 Geometry to calculate the irradiance from a Lambertian source of area A_s received by a small detector of area dA_d .

7. Show that if the radiance in Problem 6 is no longer Lambertian but has the functional form $L_s = L_o \cos \theta$, the irradiance at the detector is

$$E_d = \frac{2\pi L_o}{3} (1 - \cos^3 \alpha). \quad (2.207)$$

8. Assuming the sun is both uniform and Lambertian, what is the radiance at the top of the earth's atmosphere at the average earth–sun distance?
9. Calculate the wavelengths associated with each transition illustrated in Figure 2.16.
10. Derive (2.92) and (2.93).
11. Show that the relationship between the Einstein coefficients, when expressed in terms of wavelength and energy density, is given by

$$A_{21} = \frac{8\pi hc}{\lambda^5} B_{12}^\lambda. \quad (2.208)$$

What is the similar equation when expressed in wave numbers?

12. The Einstein coefficients can be expressed in terms of radiance rather than energy density. Derive (2.94). What are the units of B_{12}^L ? What is the equivalent expression when B_{12}^L is expressed in terms of wavelength rather than frequency?
13. What is the energy for the first five levels for pure rotational motion of a diatomic molecule? Draw the corresponding energy level diagram.
14. The vibrational potential energy of a diatomic molecule can be modeled using the Morse potential given by

$$V = V_o (1 - e^{-\beta x})^2, \quad (2.209)$$

where V_o is the minimum in the potential energy curve relative to the dissociation energy, β is a constant that determines the width, and x is the displacement of the nuclei from their equilibrium positions equaling $R - R_o$. Show through an expansion argument that, for small values of x , this reduces to simple harmonic motion with the potential energy proportional to x^2 .

15. Show that for the optically thin case W_v is proportional to S to good approximation.
16. A measurement of ozone in the atmosphere yields a value of 300 DU; what is the number density of ozone molecules at standard conditions?

3 Spectral Properties of Materials

Having laid the foundation of the physical mechanisms involved in scattering and absorption of light in the previous chapter, we now turn to the spectral reflectance and emittance properties of materials encountered in remote sensing using imaging spectroscopy. Here, we will qualitatively describe how those fundamental processes are observed in the spectra of common materials. Although we are not seeking to provide a comprehensive review of either the spectra or materials encountered in the practice and application of imaging spectroscopy, our goal is to provide a sufficient familiarity with both the principals and observations typically encountered and provide a basis for further analysis.

3.1 Introduction

The discipline of spectroscopy was created by Isaac Newton and has become an integral part of how the identity, physical structure, and environment of atoms, molecules, and solids are described. Its development goes back to the early seventeenth century when William Wollaston improved upon Newton's original spectrometer to show that the solar spectrum had gaps, which were further investigated by Joseph Fraunhofer, who created a catalog of what we now know as Fraunhofer lines. Joseph Foucault later identified two of the Fraunhofer lines as being from sodium emission. It is the description of this process of identification, using the unique spectral features characteristic of a particular material and captured in an imaging spectrometer measurement, that is the overarching goal of this book. In this chapter we will address the features themselves, while Chapter 4 is devoted to a description of how spectral measurements are performed using an imaging spectrometer, which is an evolution of the classical systems. The spectra are divided into those from reflectance, where the sun is an active source, or emittance, where the temperature and emissivity determine the spectral signature. The measured spectra will further be divided into those signatures that are due to organic materials, minerals, or are from man-made surfaces.

The interaction of photons with the solid state structure of the surface materials introduces the features that are indicative of a particular substance. This interaction can be described at the macroscopic level through the classical theory based on Maxwell's equations; however, the interaction at the microscopic scale is between photons and the atoms that compose the solid and requires a quantum mechanical description. The

characteristic reflectance and emission spectra of a solid are a combination of scattering and absorption. Many of the physical processes developed in the previous chapter provide the mechanisms for various reflectance and emittance spectra observed from materials. For solids, absorption is due to electronic and vibrational transitions since rotational transitions don't occur. The electronic transitions produce broad absorption features at the short wavelengths, roughly 380 nm to 1000 nm, while the vibrational transitions are narrower and at longer wavelengths since much less energy is involved in the transition. The resulting spectra are quite different than those from atomic and molecular transitions because the energy levels for solids become comparatively broad bands, leading to wider absorption and emission features.

Scattering occurs in the material as photons penetrate the surface and interact with the atoms and molecules. Again, scattering is the absorption and then re-emission of radiation with elastic scattering occurring when the incident and exitent photon energies are the same. Scattering is the process from which the reflectance spectrum originates, since it changes the directionality of the incident beam while absorption occurs along the beam. As a photon enters the material it can undergo absorption as it interacts with the solid state structure, sometimes being converted into different forms of energy such as vibrational, and sometimes being re-radiated in a different direction through scattering. Some calibration laboratory materials utilize the process of multiple scattering within the material to completely randomize the direction of the emerging light so that the reflected light is diffuse to good approximation. Many surfaces in nature have this same diffuse reflection characteristic due to internal scattering.

In this chapter we will introduce the basic definitions, terminology, and principles that are used to geometrically characterize the reflectance of materials with the understanding that the emission can be similarly developed since, through conservation of energy, the sum of the reflected and absorbed light is given by (2.72). The directional emissivity is also connected to the distribution function that describes reflectance. The presentation proceeds to an overview of the types of reflectance and emission spectra observed with some motivation for the structure. A detailed description would again involve a foray into the quantum mechanical details of solid state physics and we will settle for a strictly qualitative introduction with examples of the spectra observed.

3.2

Geometrical Description

The possible distributions of reflected light from surfaces vary between the two extremes of purely specular and purely diffuse reflectance. In all cases the reality is that any surface will depart from these ideals, although either extreme can be achieved to a good approximation in laboratory or field measurements. This diversity is addressed by defining a proportionality function that describes the geometry of the incident and reflected light. The function, known as the bidirectional reflectance distribution function or BRDF, is flexible and broadly adaptable to address the particulars of any given situation. The definitions and description presented here are derived from that developed at the National Institute of Standards and Technology (NIST) (Nicodemus et al., 1977).

3.2.1 Bidirectional Reflectance Distribution Function

In the BRDF discussion that follows it is understood that the radiometric quantities are also a function of the spectral unit such as wavelength. Figure 3.1 illustrates a surface illuminated by a beam of light from the (θ_i, ϕ_i) direction falling on an element of surface area dA located at (x_i, y_i) . The beam is reflected by the surface in a variety of directions depending upon its physical properties. The reflectance of the illumination from the collimated beam into a particular solid angle is defined as

$$\rho(\theta_i, \phi_i; \theta_r, \phi_r; L_i) \equiv \frac{d\Phi_r}{d\Phi_i}, \quad (3.1)$$

where $d\Phi_r$ and $d\Phi_i$ are the reflected and incident fluxes respectively. However, we would like to describe this reflectance process in terms of radiance rather than flux. In the most general case the reflected radiance is proportional to the incident flux $d\Phi_i$ with the proportionality constant S . The constant S , which will depend upon the locations and directions of incident flux and the exitent radiance, is given by

$$S(\theta_i, \phi_i, x_i, y_i; \theta_r, \phi_r, x_r, y_r) = \frac{dL_r(\theta_i, \phi_i, x_i, y_i; \theta_r, \phi_r, x_r, y_r)}{d\Phi_i(\theta_i, \phi_i, x_i, y_i)}, \quad (3.2)$$

where the flux is incident at (x_i, y_i) from the (θ_i, ϕ_i) direction and the reflected radiance in the (θ_r, ϕ_r) direction originates at (x_r, y_r) , the observation point. No assumptions have been made about the details of the physical interaction of the light and the material. For example, some of the light could be internally scattered and emerge from the surface some distance away from the illumination point. Also, the atoms that compose the solid state structure of the material could absorb the incident radiance, converting it to internal energy depending upon the details of their quantum mechanical structure. An important example of the later process is the absorption of light by chlorophyll within the leaves of living plants.

There are several simplifying but reasonable assumptions that will be applied to (3.2) in order to make the problem more tractable. First, it is assumed that the surface is uniformly illuminated over a reasonably sized area so that the dependence on the incident coordinates vanishes. The incident flux is therefore

$$d^2\Phi_i(\theta_i, \phi_i) = L_i(\theta_i, \phi_i) \cos \theta_i d\omega_i dA_i = dE_i(\theta_i, \phi_i) dA_i, \quad (3.3)$$

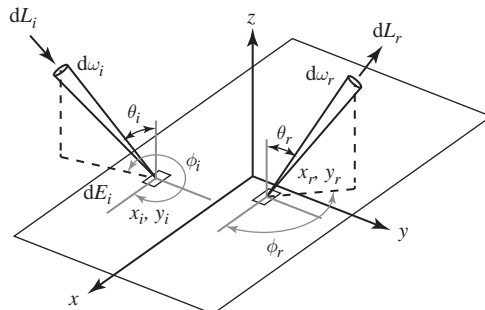


Figure 3.1 The geometry used to develop the formalism to describe the geometric properties of reflectance.

where the dE_i is the incident irradiance. Note that irradiance is not a directional quantity and, in this instance, the angular dependence is specified to emphasize the illumination geometry (θ_i, ϕ_i) . Additionally, the scattering properties within the material are assumed to be uniform and isotropic so that only the distance r between (x_i, y_i) and (x_r, y_r) is relevant enabling (3.2) to be rewritten as

$$\begin{aligned} dL_r(\theta_i, \phi_i; \theta_r, \phi_r; E_i) &= \int_{A_i} S(\theta_i, \phi_i; \theta_r, \phi_r; r) d\Phi_i(\theta_i, \phi_i) \\ &= dE_i(\theta_i, \phi_i) \int_{A_i} S(\theta_i, \phi_i; \theta_r, \phi_r; r) dA_i. \end{aligned} \quad (3.4)$$

The function defined by

$$f_r(\theta_i, \phi_i; \theta_r, \phi_r) \equiv \int_{A_i} S(\theta_i, \phi_i; \theta_r, \phi_r; r) dA_i \quad (3.5)$$

is called the BRDF because it only depends upon the incident and reflected directions due to the illumination and material property assumptions. The BRDF is equivalently written as

$$f_r(\theta_i, \phi_i; \theta_r, \phi_r) = \frac{dL_r(\theta_i, \phi_i; \theta_r, \phi_r; E_i)}{dE_i(\theta_i, \phi_i)} \quad (3.6)$$

in terms of the radiometric quantities of interest. The BRDF can take on any value from zero to infinity and is in units of inverse steradians.

The BRDF is related to the reflectance through (3.1) and (3.6). Recall from Chapter 2 that the flux associated with a particular area dA is expressed in terms of the radiance by

$$d\Phi = dA \int_{\omega} L(\theta, \phi) \cos \theta d\omega, \quad (3.7)$$

where the flux is either incident or exitent. Combining (3.6) and (3.7) to describe the exitent flux in terms of f_r yields

$$d\Phi_r = dA \int_{\omega_r} \int_{\omega_i} f_r(\theta_i, \phi_i; \theta_r, \phi_r) L_i(\theta_i, \phi_i) \cos \theta_i d\omega_i \cos \theta_r d\omega_r \quad (3.8)$$

since

$$L_r(\theta_r, \phi_r) = \int_{\omega_i} f_r(\theta_i, \phi_i; \theta_r, \phi_r) L_i(\theta_i, \phi_i) \cos \theta_i d\omega_i. \quad (3.9)$$

The reflectance is therefore

$$\rho(\theta_i, \phi_i; \theta_r, \phi_r; L_i) = \frac{\int_{\omega_r} \int_{\omega_i} f_r(\theta_i, \phi_i; \theta_r, \phi_r) L_i(\theta_i, \phi_i) \cos \theta_i d\omega_i \cos \theta_r d\omega_r}{\int_{\omega_i} L_i(\theta_i, \phi_i) \cos \theta_i d\omega_i} \quad (3.10)$$

from (3.1), (3.7), and (3.8). If the incident radiance is uniform and isotropic within the beam, removing the dependence upon θ_i and ϕ_i , from (3.10) we obtain

$$\rho(\theta_i, \phi_i; \theta_r, \phi_r) = \frac{\int_{\omega_r} \int_{\omega_i} f_r(\theta_i, \phi_i; \theta_r, \phi_r) \cos \theta_i d\omega_i \cos \theta_r d\omega_r}{\int_{\omega_i} \cos \theta_i d\omega_i}, \quad (3.11)$$

which is known as the *biconical reflectance*.

3.2.2 Bidirectional Reflectance Factors

If the assumptions of uniform illumination and uniform and isotropic material scattering properties are met, the BRDF describes the reflectance properties of a material, but it is difficult to measure, requiring specialized equipment (see Barnes et al., 1998, for example). The *bidirectional reflectance factor* (BRF) is a practical alternative that is based upon the concept of a perfectly diffuse and completely reflective surface used as a reference. The reference reflector is well characterized with a reflectance calibration that is traceable to a standard maintained at a national metrology laboratory such as NIST. For an ideal reference surface, the BRDF is directly proportional to the BRF.

The bidirectional reflectance factor R is defined as the ratio of the reflected flux from a surface to the flux that would be reflected from an ideal reflector in an identical illumination geometry, or

$$R(\omega_i, \omega_r) \equiv \frac{d\Phi_r}{d\Phi_{r,id}}, \quad (3.12)$$

where $d\Phi_{r,id}$ is the reflected flux from the ideal diffuse reflector. A diffuse reflector is one that reflects light uniformly in all directions independent of the illumination geometry; in other words, $L_r(\theta_r, \phi_r)$ is a constant. Such a reflector obeys Lambert's cosine law, named after Johann Lambert, who first presented it in 1760 (Darrigol, 2012). Lambert's cosine law, derived using (3.3), is generically expressed as

$$\frac{d^2\Phi}{dA d\omega} = L(\theta_r, \phi_r) \cos \theta = L_d \cos \theta, \quad (3.13)$$

where L_d is the constant diffuse reflected radiance. Lambert's cosine law states that, as a consequence of the projected area, the flux from a unit surface area into a unit solid angle received from a Lambertian radiator or reflector is proportional only to $\cos \theta$, where θ is measured with respect to the surface normal. This law describes the emission properties of some sources, such as an ideal blackbody, as well as Lambertian surfaces. Surprisingly, nature is replete with sources and reflective surfaces that exhibit Lambertian behavior, particularly for angles less than about 45°.

The diffuse radiance for such a reflector, which is derived from (3.6), is

$$L_r(\theta_r, \phi_r) = L_d = \int_{\omega_i} L_i(\theta_i, \phi_i) f_r(\theta_i, \phi_i; \theta_r, \phi_r) \cos \theta_i d\omega_i, \quad (3.14)$$

which is a constant. This implies the $f_r(\theta_i, \phi_i; \theta_r, \phi_r)$ must also be a constant since L_i does not depend upon θ_i and ϕ_i and L_r by definition has the same value for all directions (θ_r, ϕ_r) regardless of how the surface is irradiated. Therefore the diffuse BRDF is

$$f_r(\theta_i, \phi_i; \theta_r, \phi_r) = f_{r,d} \quad (3.15)$$

and describes a surface that uniformly reflects the incident flux from any direction into the upper hemisphere. Equation (3.14) reduces to

$$L_d = f_{r,d} \int_{\omega_i} L_i(\theta_i, \phi_i) \cos \theta_i d\omega_i = f_{r,d} E_i \quad (3.16)$$

and the perfectly diffuse BRDF, in terms of the radiometric quantities, is

$$f_{r,d} = \frac{L_d}{E_i}. \quad (3.17)$$

The diffuse reflectance into the full upper hemisphere, expressed in terms of the diffuse BRDF, is developed from (3.1). The result is

$$\rho_d(\omega_i; 2\pi) = \frac{d\Phi_r}{d\Phi_i} = \frac{L_d dA \int_{2\pi} \cos \theta_r d\omega_r}{E_i dA} = \frac{\pi L_d}{E_i} = \pi f_{r,d} \quad (3.18)$$

since, for reflection into the full upper hemisphere, we have

$$\int_{2\pi} \cos \theta_r d\omega_r = \int_0^{2\pi} \int_0^{\pi/2} \cos \theta_r \sin \theta_r d\theta_r d\phi_r = \pi. \quad (3.19)$$

Note that (3.18) implies that the diffuse reflectance is a constant regardless of the illumination geometry, or $\rho_d(d\omega_i; 2\pi) = \rho_d(\omega_i; 2\pi) = \rho_d(2\pi; 2\pi)$. The ideal diffuse standard reflector is one for which all of the incident flux is reflected, that is

$$\rho_d = \rho_{d,id} = 1 \Rightarrow f_{r,id} = \frac{1}{\pi}. \quad (3.20)$$

The BRF is therefore

$$R(\omega_i, \omega_r) = \frac{\int_{\omega_r} \int_{\omega_i} f_r(\theta_i, \phi_i; \theta_r, \phi_r) L_i(\theta_i, \phi_i) \cos \theta_i d\omega_i \cos \theta_r d\omega_r}{\frac{1}{\pi} \int_{\omega_r} \int_{\omega_i} L_i(\theta_i, \phi_i) \cos \theta_i d\omega_i \cos \theta_r d\omega_r}, \quad (3.21)$$

which follows from (3.7), (3.9), and (3.12). If the further assumption is made that within the beam the radiance is uniform and isotropic, then (3.21) reduces to

$$R(\omega_i, \omega_r) = \frac{\pi}{\Omega_i \Omega_r} \int_{\omega_r} \int_{\omega_i} f_r(\theta_i, \phi_i; \theta_r, \phi_r) \cos \theta_i d\omega_i \cos \theta_r d\omega_r, \quad (3.22)$$

where Ω_i and Ω_r are defined from

$$\Omega = \int \cos \theta d\omega \quad (3.23)$$

with the integration over the appropriate illumination and exitent geometries.

The relationship between the BRF and the BRDF can also be expressed in an alternative way. Using (3.12) the BRF is written in terms of the radiances that correspond to the fluxes as

$$R(\theta_i, \phi_i; \theta_r, \phi_r) = \frac{L_r(\theta_i, \phi_i; \theta_r, \phi_r) \cos \theta_r d\omega_r dA}{L_{id} \cos \theta_r d\omega_r dA} = \frac{dL_r}{dL_{id}}.$$

Returning to (3.6), the ratio of the sample reflected radiance to the reflected radiance from an ideal diffuse standard reflector in the same geometry is

$$R(\theta_i, \phi_i; \theta_r, \phi_r) = \frac{dL_r}{dL_{id}} = \frac{f_r(\theta_i, \phi_i; \theta_r, \phi_r) dE_i}{f_{r,id} dE_i} = \frac{f_r(\theta_i, \phi_i; \theta_r, \phi_r)}{1/\pi}.$$

The BRF is therefore proportional to the BRDF through

$$R(\theta_i, \phi_i; \theta_r, \phi_r) = \pi f_r(\theta_i, \phi_i; \theta_r, \phi_r), \quad (3.24)$$

which may also be deduced from (3.22) by converting it to the infinitesimal case where Ω_i and Ω_r are replaced with $\cos \theta_i d\omega_i$ and $\cos \theta_r d\omega_r$ and the integrals are removed.

A Lambertian reflector is often described by combining (3.17) and (3.20) by

$$L_d = \frac{E_i}{\pi}, \quad (3.25)$$

and is used to describe a perfectly diffuse and spatially uniform reflector. In actuality, a location, however small, on a reflective surface can closely approximate a Lambertian reflector while the surface is not broadly uniform as a function of position. The correct description for an extended area of a single material that diffusely reflects radiance is that it is both Lambertian and spatially uniform.

3.2.3 Reflectance Property Measurement

The measurements of either the BRDF or the BRF of a sample is accomplished through the use of a reflectometer that is composed of a collimated light source, a goniometer, and a spectral radiometer. A goniometer is a device designed to either precisely and accurately measure an angle or to rotate an object to a particular angular position with respect to a reference direction. The sample under test is mounted in the goniometer and illuminated by a collimated light source, such as a laser or monochromator in the laboratory or the sun for a field measurement, and the spectral radiometer is used to measure the reflected spectral radiance at a particular angle. In the context of remote sensing, the term goniometer is often used as a shorthand reference for the entire system.

A reflectance standard is one that has been characterized either directly by a national metrology laboratory, such as NIST, or by a commercial supplier and is accompanied by the calibration data for the type of characterization that was performed. The calibration data for the standard obtained from a commercial supplier is typically referenced to an absolute standard characterized by a national metrology laboratory and will include both the reflectance information and the measurement uncertainty. The standard commercial BRF product most applicable to remote sensing is the *directional-hemispherical reflectance factor*. These standards are designed to be as Lambertian as possible and are well matched to the reflectances that dominate scenes in nature, which are often approximately Lambertian. A good rule of thumb is that the reflectance properties of the standard should be as similar as possible to that of the sample.

The directional-hemispherical reflectance factor is measured by illuminating a sample mounted in an integrating sphere at a small off-normal angle and then measuring a portion of the flux using a detector mounted on the sphere. The collimated light for the characterization of the spectral reflectance factor is monochromatic. The sphere collects almost the entire reflected flux, except for the small fraction that exits through the entrance hole where the light is input. An identical measurement is performed using a reflectance standard enabling the unknown sample BRF to be referenced to the known BRF of the standard. These measurements are often performed with the collimated beam at 6° or 8° from the normal to the sample with the notation written as, for example,

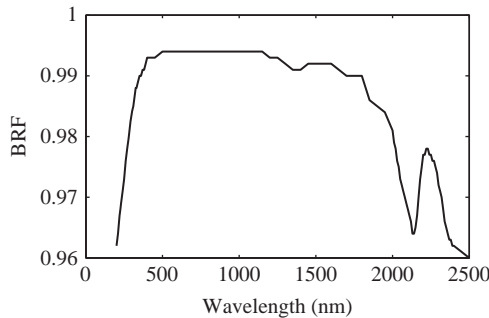


Figure 3.2 The spectral reflectance of pressed PTFE for the VNIR/SWIR.

6° /hemispherical reflectance factor. In this case the reflectance factor is related to the BRDF through (3.22) rewritten as

$$R(\theta_i, \phi_i; 2\pi) = \int_{2\pi} f_r(\theta_i, \phi_i; \theta_r, \phi_r) \cos \theta_r d\omega_r, \quad (3.26)$$

where Ω_i has been converted to the infinitesimal case and (3.19) has been used. Note that this is equivalent to the reflectance $\rho(\theta_i, \phi_i; 2\pi)$ from (3.11), again with Ω_i converted to the infinitesimal case. The NIST directional-hemispheric characterization includes two pairs of measurements in order to account for the integrating sphere reflectance, with each pair including the standard or sample and the integrating sphere wall (Barnes et al., 1998).

Reflectance standards can be constructed from paints that contain barium sulfate (BaSO_4) or from a form of polytetrafluoroethylene (PTFE). In the laboratory, pressed PTFE powder (Weidner and Hsia, 1981) has been used in the past, while in the field sintered PTFE such as Spectralon®, a fluoropolymer containing PTFE manufactured by Labsphere, is often employed. Reflectance standards have some variation with respect to wavelength, as illustrated in Figure 3.2. The inclusion of wavelength in the BRF requires that the measurement be performed at a range of wavelengths for both the standard and the sample.

Field Reflectance Measurement

Measurement of the reflectance in the field has unique problems and requires rather specialized equipment. Field goniometers are distinct from laboratory reflectometers, where the sample is mounted in the goniometer and rotated. In contrast, a field goniometer relies on the sun as a source and the spectral radiometer is moved to record the reflected light at different angles as illustrated in Figure 3.3. The illumination in this situation has both a collimated component due to direct illumination from the sun, and a diffuse component due to the scattering processes in the atmosphere, which are addressed in Chapters 2 and 6. Accurate measurements require that the atmosphere be stable with low aerosol loading and little surface wind. Ideally the atmospheric aerosol optical thickness and the water content is monitored through the use of a solar radiometer or similar

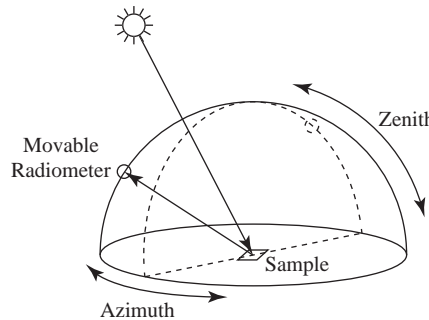


Figure 3.3 Sketch of a field goniometer. The radiometer is repositioned to measure a signal proportional to the radiance for a variety of different zenith and azimuthal angles. The sample is replaced by a reference standard for absolute calibration.

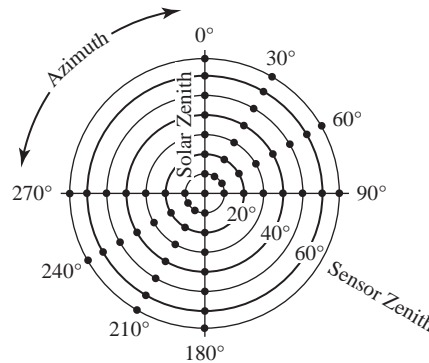


Figure 3.4 Example sampling pattern for a field goniometer.

device (see Chapter 5 for a discussion of these instruments in the context of vicarious calibration).

Four series of measurements are required in order to correct for the contribution from diffuse atmospheric radiance. First the field sample is measured at a variety of different angles under full solar illumination. This measurement series is followed by, or interleaved with, a similar series with the direct illumination occulted so that only the diffuse component illuminates the sample. Identical measurements are performed using a reflectance standard. The reflectance factor is recovered using

$$R^{\text{dir}}(\theta_i, \phi_i; \theta_r, \phi_r) = \frac{L_r^{\text{tot}}(\theta_r, \phi_r) - L_r^{\text{dif}}(\theta_r, \phi_r)}{L_{r,s}^{\text{tot}}(\theta_r, \phi_r) - L_{r,s}^{\text{dif}}(\theta_r, \phi_r)} R_s^{\text{dir}}(\theta_i, \phi_i; \theta_r, \phi_r), \quad (3.27)$$

where the total and diffuse radiance values are measured at a particular θ_r and ϕ_r . The measured radiances are the result of the irradiance incident on the sample or panel that is from the collimated direct solar illumination and from scattered light distributed over a variety of directions. The direct solar illumination component, $E^{\text{dir}}(\theta_i, \phi_i)$, is analogous to the equivalent laboratory irradiance but cannot be isolated, while the diffuse irradiance is due to radiance from the entire upper hemisphere. The contribution from

the diffuse irradiance will be quite small, on the order of a few percent, under clear and stable viewing conditions (Jackson et al., 1987). Figure 3.4 is a polar diagram of the sampling that is employed during the field measurements. A more detailed review for the interested reader is found in Sandmeier (2000) and the references therein.

3.3 Directional Emissivity

LWIR spectral signatures are governed by the temperature and emissivity of the material through (2.69). The spectral emissivity as a function of direction is typically determined by either comparing the spectral radiance in a particular geometry from the material of interest to that from a well-understood blackbody source, or as a derived quantity based upon the measurement of the reflectance properties, specifically the BRDF. The first method is not conceptually difficult but can be very challenging in practice with a spectroradiometer, such as a Michelson interferometer, viewing both the material at a well-quantified temperature and a blackbody in turn. The apparatus is in a vacuum and the optics are designed so that only the targets of interest are viewed. Additionally, care is taken so that no unaccounted-for external sources of radiance contribute to the measurement. This method is presented in detail in Germer et al. (2014).

In the second method the emissivity can be related to a BRDF measurement with some theoretical development. Consider the notional arrangement in Figure 3.5, where a sample of size dA_s is imbedded in a flat surface and at the center of a hemisphere of radius r . The flat surface, other than the sample, and the hemisphere are perfect blackbodies that emit radiance given by $B_\lambda(T)$ from (2.64). The entire system is held at a uniform temperature T . Two arbitrary areas, dA_i and dA_j , are identified on the surface of sphere and, since the entire system is in thermodynamic equilibrium, the net flux from a surface element must be zero. In the discussion that follows all of the quantities are at a particular wavelength and the blackbody spectral radiance will be given by $B(T)$.

The flux $d\Phi_{sn}$ traveling from dA_s to an arbitrary element dA_n of the hemisphere is given by

$$d^2\Phi_{sn} = L_s(dA_s \cos \theta_n) \frac{dA_n}{r^2} = L_s dA_s d\Omega_n, \quad (3.28)$$

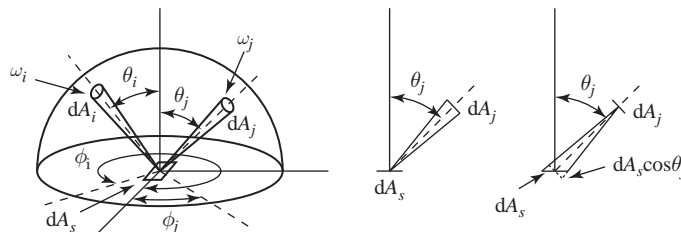


Figure 3.5 Geometry employed for the directional emissivity derivation. The hemispherical and planar surfaces are blackbody emitters with the exception of dA_s and the hemisphere has a radius r .

where the definition of radiance given by (2.52) has been applied with the projected area given by $dA_s \cos \theta_n$, the solid angle is dA_n/r^2 , and the projected solid $d\Omega_n$ is $dA_n \cos \theta_n/r^2$ from (2.54). This flux is due to a combination of reflected and emitted light. Similarly, the flux from an infinitesimal element on the hemisphere to dA_s is given by

$$d^2\Phi_{ns} = L_n dA_n \frac{dA_s \cos \theta_n}{r^2} = B(T) dA_s \frac{dA_n \cos \theta_n}{r^2} = B(T) dA_s d\Omega_n, \quad (3.29)$$

since the projected area is equivalent to dA_n and the solid angle subtended by dA_s is $dA_s \cos \theta_n/r^2$, as illustrated in Figure 3.5. The infinitesimal area could be either dA_i or dA_j . The reflected flux from dA_s to dA_j due to emission from dA_i is obtained from (3.6) and (3.28) yielding

$$d^3\Phi_{sj}^r = f_r(\theta_i, \phi_i; \theta_j, \phi_j) B(T) dA_s d\Omega_i d\Omega_j, \quad (3.30)$$

where $dE_s(\theta_i, \phi_i)$ is obtained from $d\Phi_{is}/dA_s$ and the r superscript on Φ_{sj} signifies reflectance. The total reflected flux from dA_s to dA_j from the entire hemisphere is therefore

$$d^2\Phi_{sj}^r = B(T) dA_s d\Omega_j \int_{2\pi} f_r(\theta_i, \phi_i; \theta_j, \phi_j) d\Omega_i. \quad (3.31)$$

The flux due to thermal emission from dA_s to dA_j involves replacing L_s in (3.28) with $\epsilon(\theta_j, \phi_j)B(T)$ to produce

$$d^2\Phi_{sj}^e = \epsilon(\theta_j, \phi_j) B(T) dA_s d\Omega_j, \quad (3.32)$$

where the superscript corresponds to emissivity in this case. The flux from dA_j to dA_s is given by (3.29) with n replaced by j . The sum of the flux due to reflection and emission, (3.31) and (3.32) respectively, is equal to (3.29) and, combining the three, yields

$$\epsilon(\theta_j, \phi_j) = 1 - \int_{2\pi} f_r(\theta_i, \phi_i; \theta_j, \phi_j) d\Omega_i \quad (3.33)$$

for the relationship between the directional emissivity and the BRDF.

A similar analysis is applied to relate the absorptivity $\alpha(\theta_j, \phi_j)$ and the BRDF with the flux from dA_j to dA_s , either absorbed by dA_s or reflected by it into the full hemisphere. In this case the reflected flux into the full hemisphere is

$$d^2\Phi_{s,\text{hem}}^r = B(T) dA_s d\Omega_j \int_{2\pi} f_r(\theta_j, \phi_j; \theta_i, \phi_i) d\Omega_i \quad (3.34)$$

and the absorbed flux $d^2\Phi_{js}^a$ is

$$d^2\Phi_{js}^a = \alpha(\theta_j, \phi_j) B(T) dA_s d\Omega_j. \quad (3.35)$$

The sum of (3.34) and (3.35) is equal to the emitted flux from dA_j and therefore the absorptivity is

$$\alpha(\theta_j, \phi_j) = 1 - \int_{2\pi} f_r(\theta_j, \phi_j; \theta_i, \phi_i) d\Omega_i. \quad (3.36)$$

Note the difference in order of the angular coordinates for the BRDF in (3.33) and (3.36). In a typical laboratory measurement employing an integrating sphere, it is

the directional-hemispheric reflectance that is measured, with the reflectance given by $\rho(\theta_i, \phi_i; 2\pi)$, which is equal to (3.26). The absorptivity is therefore

$$\alpha(\theta_j, \phi_j) = 1 - \rho(\theta_i, \phi_i; 2\pi) \quad (3.37)$$

and the emissivity is only known if $\alpha(\theta_i, \phi_i)$ equals $\epsilon(\theta_j, \phi_j)$, which was defined as Kirchhoff's law in Section 2.4.2. If the absorptivity and emissivity are equal then the incident and exitent geometries in the BRDF are interchangeable, with this property known as the Helmholtz reciprocity law. This law is usually valid, but there are some instances where it does not hold (Snyder et al., 1998).

The spectral emissivity spectrum of a material is often calculated from a reflectance measurement, either in the laboratory or as a derived quantity from field measurements. The ASTER spectral library is an example where the LWIR spectra are collected using an integrating sphere to measure the directional-hemispheric reflectance and the emissivity spectrum is calculated by applying (3.33) and assuming reciprocity (Baldridge et al., 2009b). A Fourier transform interferometer is employed for the measurement and care is taken to remove the background spectrum by employing a reference standard. A full review of the various measurement techniques is provided in Germer et al. (2014).

3.4

Volume Scattering of Materials

We now consider the effect of scattering from solid objects as it contributes to the observed reflectance. Most object surfaces are comprised of a complex melange of particles of different materials and not simple surfaces, as a beach is comprised of many particles of silicates and other “grains of sand.” Building on the theoretical basis of Chapter 2, we introduce the variety of ways in which surface types can be characterized in reflectance models. Photons incident on or through a surface are absorbed or scattered and, if scattered, they may be reflected away from the material and potentially observed, or they may have a second interaction (absorption or scatter) within the material, and a third and so on until absorbed or scattered out of the material.

The internal scattering in a material is sometimes characterized by a random walk of photons which provides a useful parameter of the mean depth of photon penetration (Clark and Roush, 1984). Particles which have a large scattering cross section will support a long random-walk process deep into the material and have hundreds of scattering encounters before being absorbed or transmitted out of the material. However, a small number of particles with small scattering or large absorption cross sections, such as magnetite or carbon, can quickly arrest the random walk process. This ability of a small number of absorbing particles to alter the observed scattering character also enhances the diagnostics for the minority absorbing particle in the material.

Consider two bands of differing absorption strengths, one strong and one weak. A photon in the stronger absorption band will penetrate less deeply into the surface, encountering fewer molecules because the photons are absorbed. A photon in the weaker absorption band will go further into the material in a random walk, increasing the average photon path length. The greater path length of the photon in the weak absorption

band will result in more absorption opportunities, thus strengthening the signature of the weak absorption in a reflectance spectrum.

Materials consisting of two or more particle types are characterized as a mixture of particles. Clark et al. (1999) defines the four distinct mixture types as:

1. *Linear mixture*: The materials in the field of view are optically separated, so there is no multiple scattering between components. The combined signal is simply the sum of the fractional area times the spectrum of each component. This is also called areal mixture.
2. *Intimate mixture*: An intimate mixture occurs when different materials are in intimate contact in a scattering surface, such as the mineral grains in soil or rock. Depending on the optical properties of each component, the resulting signal is a highly nonlinear combination of the material component spectra.
3. *Coatings*: Coatings occur when one material coats another. Each coating is a scattering-transmitting layer whose optical thickness varies with material properties and wavelength.
4. *Molecular mixtures*: Molecular mixtures occur on a molecular level, such as two liquids or a liquid and a solid mixed together. Examples include water adsorbed onto a mineral, or gasoline spilled onto a soil. The close contact of the mixture components can cause band shifts in the adsorbate, such as the interlayer water in montmorillonite or the water in plants.

An example mixture comparison from Clark et al. (1999) is shown in Figure 3.6. In this mixture of low and high reflectance particles of charcoal grains mixed with

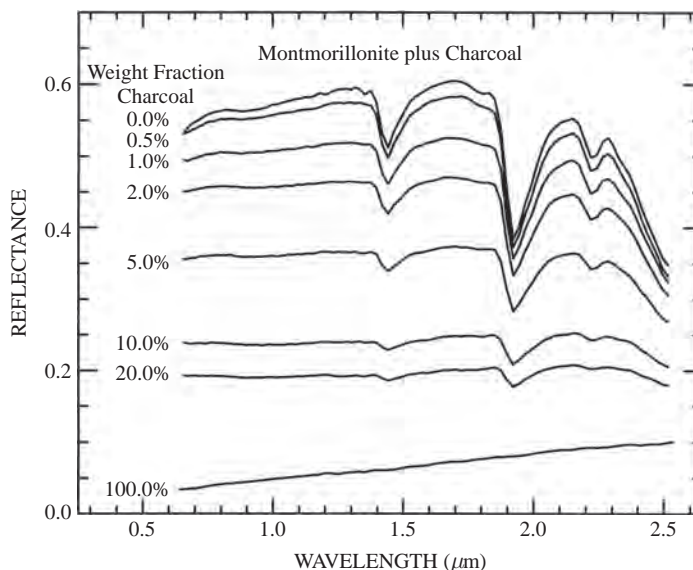


Figure 3.6 Intimate mixture of various proportions of charcoal grains mixed with montmorillonite (Clark et al., 1999).

montmorillonite respectively, the photons have such a high probability of encountering a dark grain that a few percent of absorbing grains can drastically reduce the reflectance, much more than their fraction by weight of the material. This demonstrates the important difference from a linear mixture model, which would result in a negligible difference for small amount of added charcoal.

3.4.1 Grain Size Effect

The fraction of light scattered and absorbed by an individual encounter with a scattering grain is dependent on grain size (Hapke, 2012). A larger grain size affords a photon a greater internal path where photons can be absorbed according to Beer's law. In a material with smaller grains, the ratio of surface reflections to path length is higher as is the surface to volume ratio. Accordingly, when multiple scattering dominates for two otherwise identical materials which only vary in the mean grain size, the smaller grain sample will exhibit a higher reflectance than the larger grain sample. This is usually the case in the visible and near-infrared, where the reflectance decreases as the grain size increases, as demonstrated in the pyroxene visible to near-infrared spectra in Figure 3.7. With an increase in the absorption probability for a photon encountering a particle, the grain size effects are much more complex and this trend may even reverse. This is commonly the case for observations at midwave wavelengths and longer, because the reflectance of most materials decreases at these longer wavelengths.

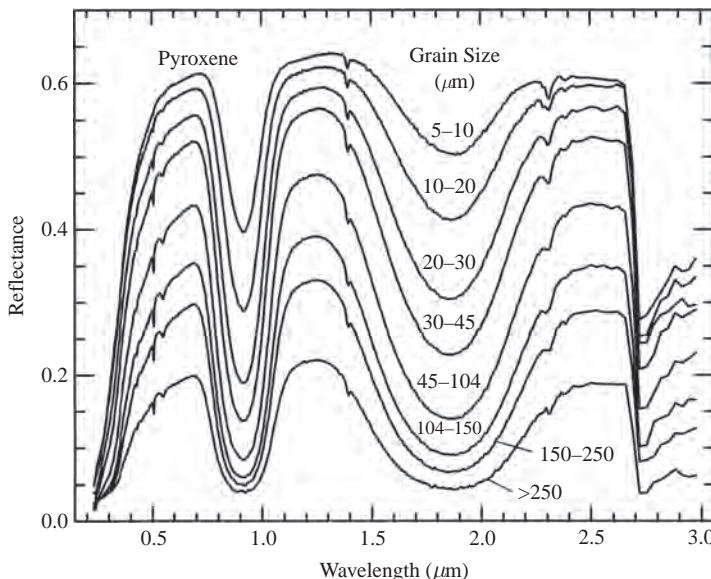


Figure 3.7 Effect of grain size on spectral reflectance: pyroxene for range of grain sizes (Clark et al., 1999).

3.4.2 Continuum and Band Depth

One important concept in mineral spectroscopy is the depth of an absorption band in the presence of an absorption continuum. Absorptions in a spectrum can be characterized as resulting from the superposition of two distinct components: the continuum and the individual absorption feature. The continuum is the background absorption onto which other absorption features are superimposed. This concept is used in many diagnostic applications in spectroscopy and is known as the continuum interpolated band ratio (CIBR) technique. First applied by Fowle (1912) for the estimation of the amount of atmospheric water vapor, the concept applies equally to characterizing an absorption feature in the presence of an absorbing continuum. A thorough discussion of this concept can be found in 6.5.1 as applied to atmospheric compensation techniques.

3.5 Elements of Mineral Spectroscopy

We consider any inert, non-biologic, and naturally occurring solid as a mineral for the purposes of this discussion. Surface materials which are comprised of crystalline solids provide a lattice structure of atoms which can be characterized by quantum levels of energy states as described in the previous chapter. Even solid materials which are best described as non-crystalline or amorphous may exhibit some characteristics of an ordered solid or crystal. At an atomic level, a material will have some absorption or emission features which are defined by the energy state of the atoms in the material itself. In the case of ordered crystal materials, the spectra will be modified by the interaction of the atoms through bonding. Spectral features which result from the transition of an electron from one allowed state to another are known as electric spectral features. The features may or may not be altered by the surrounding crystal and the electric field influence. The other energy transition type, which does not involve electrons, is known as vibrational features based on photon or vibrational process energy modes.

As discussed in Chapter 2, the electronic absorptions arise from electron transitions from one energy state to another. In a crystal, the field effects of the transition metals and conduction bands define the allowed energy states. The spectral region $0.4\text{--}1.35\text{ }\mu\text{m}$ is often referred to as the electronic absorption region. Vibrational absorptions arise from the materials' vibrational modes of the molecular bonds. In the reflected light region, overtone and combination band absorptions are normally observed because the fundamental vibrational modes are of smaller energies and are therefore observed at longer wavelengths in the infrared. Although the overtone absorptions occur at shorter wavelengths corresponding to higher energy transitions than the fundamental absorptions, they are considerably weaker in strength, but in many cases they are sufficient to be detected from remote sensing sensors. The observable overtones are most common below energies corresponding to $1.3\text{ }\mu\text{m}$ and longer, leading to the observation that electronic and vibrational processes are active at different wavelength regions. Therefore, spectral identifications can be made of the classes of surface materials using information

from these two spectral regions above and below 1.35 μm (Hunt, 1977; Clark et al., 1999).

The following discussion may be best appreciated when readers recall their introductory chemistry course. For a review of the basic principles which are referenced in the next sections, the authors recommend Cotton et al., 1999. All figures of reflectance spectra are BRF unitless data taken from laboratory measurements for a nadir viewing of the material and slightly off-nadir illumination source. For nearly all materials discussed, a Lambertian model is typically assumed, even when the material deviates significantly from this assumption.

3.5.1

Electronic Processes

Recall that the energy values of the electronic states may be calculated based on quantum mechanics, which enables a thorough description of each energy level based upon the wave function and the appropriate quantum numbers. The resulting energy level diagram completely characterizes the available energy states of the atom or ion in the solid and the transition rules determine which are accessible from a given state. Atoms are not isolated in minerals where they constitute either a constituent of the pure form or an impurity, and one or more of their electrons may be shared by the solid through covalent bonds. The electronic energy levels for electrons that form the bonds become broadened over a range of values to form the energy bands of the solid. However, the remaining bound electrons of the resultant ion still have discrete energy states that uniquely identify a pure material.

Crystalline solids are an important class of minerals that are governed by an underlying symmetry. The atoms that compose the crystal have a well-defined structure that can often be simply described. For example, a nickel crystal is face-centered cubic, with an atom at every corner of a cube and one centered on each face. In a pure crystal the basic structure, known as the unit cell, is replicated in the three dimensions. These symmetries lead to the observed energy levels responsible for the absorption and emission features. When the crystal has atoms that have loosely bound outer electrons, known as the valence electrons, the energy levels essentially form a continuum or band, with the valence electrons shared by the crystal as a whole. The energy structure that results in this case has a lower band, known as the valence band, and an upper band, known as the conduction band, with a band gap in between of forbidden energy. Impurities and defects modify the energy structure by, for example, reducing the width of the band gap. The energy structure is determined by the crystal structure as well as the number and binding energies of the valence electrons. The shared electrons will be more closely coupled to one of the crystal constituents to produce an electric field known as the *crystal field* or ligand field which often leads to a complicated reflectance spectrum. In chemistry, a *ligand* is an ion or molecule that is attached to a central atom, often a metallic element, through a covalent bond. Ligands usually act as electron donors to the metal atom at the center.

The absorption in a crystal can be through charge transfer where an electron moves from one atom to another within the valence band or through a transition to the

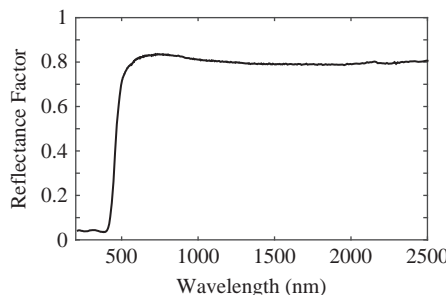


Figure 3.8 Reflectance spectra of sulfur demonstrating the distinct band-gap. Spectra from Clark et al. (2007).

conduction band. An important example of the former is the strong absorption present in iron oxides at ultraviolet wavelengths that transitions to high reflectance in the visible. For transitions across the band gap, absorption will be large for photons with sufficient energy to promote an electron from the valence to the conduction band with the reflectance rapidly increasing as the photon energy is reduced to the band gap energy. As an example, sulfur has very low reflectance below 400 nm and transitions to high reflectance by 500 nm as the photon energy falls below the band gap, as illustrated in Figure 3.8.

We'll first examine minerals that contain one of the rare earth elements that include scandium, yttrium, and the lanthanides, which all have a similar structure for their outer electrons. Rare earth elements have electrons which are deeply shielded from outside interaction of neighboring atoms and crystal structure, so the energy levels available are not significantly influenced by the arrangement of the neighbors. Thus, the absorption spectra of rare earth elements do not change, or change very little, in different crystals or mineral compositions. The top spectrum in Figure 3.9 is that of europium oxide (Eu_2O_3). It is widely used as a red or blue phosphor in old-style CRT televisions and fluorescent lamps. The second spectrum, offset by a reflectance unit, is samarium oxide and the final spectrum is of neodymium oxide (Nd_2O_3). The indicated spectral ranges identify the electronic region from the vibrational region of the absorption features. Neodymium is of particular interest for spectral calibration because of its numerous spectral features in the visible to near-IR spectral region. Figure 3.10 provides a detail look at the many electronic transitions found in Nd_2O_3 .

Transition Element Minerals

Minerals that have atoms of the transition elements, which include iron, chromium, cobalt, and nickel, as part of their composition have loosely bound outermost electrons which determine the location of the energy levels due to the crystal fields. The different electric fields of the crystal lattice cause dissimilar arrangements of the energy levels in different crystals, which leads to the appearance of quite different spectra for the same element. However, we recall from the discussion of Section 2.5.3 that the probability of a transition between levels is dependent on multiple factors, including the energy of

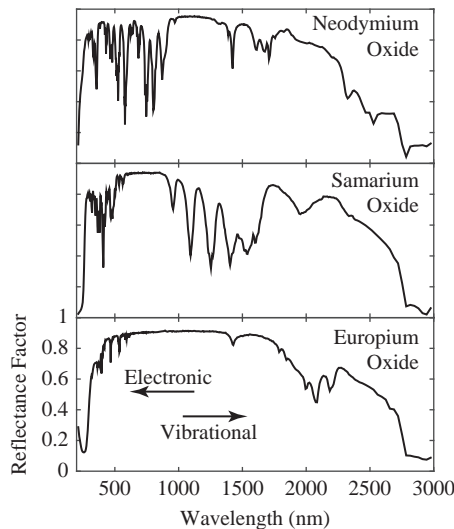


Figure 3.9 Reflectance spectra of three rare earth oxides. These absorptions are due to crystal-field transitions involving deep-lying electrons of the rare earth element and do not shift when the rare earth ion is in another mineral. The reflectance factor scales are the same in the three graphs. Spectra from (Clark et al., 2007).

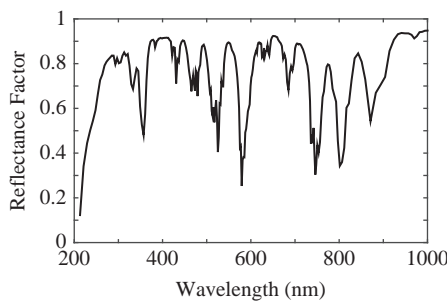


Figure 3.10 Visible to Near-IR (200–1000 nm) reflectance spectra of Neodymium oxide. Spectra from Clark et al. (2007).

the transitions; therefore, the probability of transition is also dependent on the altered energy states and thus, the depth of the absorption features can vary substantially for the same atomic transition due to the influence of the surrounding electric field (Hunt, 1977, and internal references).

The most frequently encountered electronic features in the visible to near infrared spectra of transition elements in minerals, and consequently of rocks and soils, result from the presence of iron (Fe). The locations of the energy levels are primarily determined by the valence state of the ion, which is ferrous, Fe^{2+} , or ferric, Fe^{3+} , and the symmetry of the site it occupies. The iron atom is referred to as an ion since it has donated its outer electrons. The energy levels are secondarily determined by the specifics

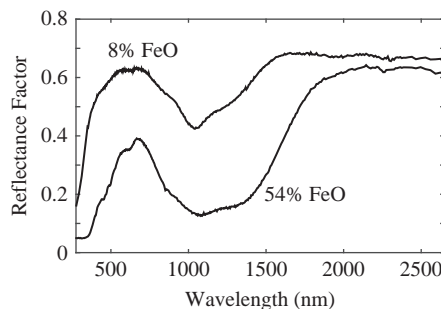


Figure 3.11 Reflectance spectra of two olivines showing the change in band position and shape with composition. The $1 \mu\text{m}$ absorption band is due to a crystal field absorption of Fe^{+2} . Forsterite (Mg_2SiO_4), which is the mineral depicted, is in the forsterite-fayalite ($\text{Fe}^{+2}\text{SiO}_4$) olivine solid solution series (King and Ridley, 1987).

of the ligand, the extent of distortion of the atomic site, and the value of the metal–ligand interatomic distance (Hunt, 1977).

When the basic geometry of an atomic site in a lattice is distorted, the field experienced by the ion may cause some levels to be split further, so that additional allowed transitions may occur. In the common mineral, olivine $[(\text{Mg}, \text{Fe}) \text{SiO}_4]$, the ferrous ions may reside in two non-equivalent sites, and transitions in each of these ions contributed differently to the spectrum. Consequently, the olivine spectrum generally displays a very broad absorption region centered near $1.0 \mu\text{m}$ composed of at least three separate transition features. Figure 3.11 provides spectra from two different olivine samples with similar grain size but substantially different iron content. The abundant iron sample where it composes 54 percent of the material present in the lower olivine spectra results in two distinct differences from the magnesium-rich but iron-poor sample (Fe = 8 percent):

1. Broad absorption feature near $1 \mu\text{m}$ from the abundance of iron in lattice locations provides additional opportunities for Fe to reside in distorted field sites.
2. Reduced overall reflectance resulting from the additional absorption associated with Fe.

The olivine structure contains two sixfold coordinated Fe sites, which give rise to the inflection points, or wavelengths where there is a distinct change in reflectance trend, which, for the two distinct samples, remains consistent as it does for all olivine. The spectral location of the visible peak and valley, as well as other features which can be extracted from the two curves, provide the distinct spectral features which identify the samples. These robust and consistent features in the spectra are the principal tools for the geologist using spectroscopy for identification (King and Ridley, 1987).

The spectra of iron absorption features change when placed in different lattice environments which exhibit different electric fields. Figure 3.12 shows the reflection spectra of several minerals that contain ferrous iron. Because spectral features due to ferrous iron occur at different wavelengths for different minerals, the differences in the

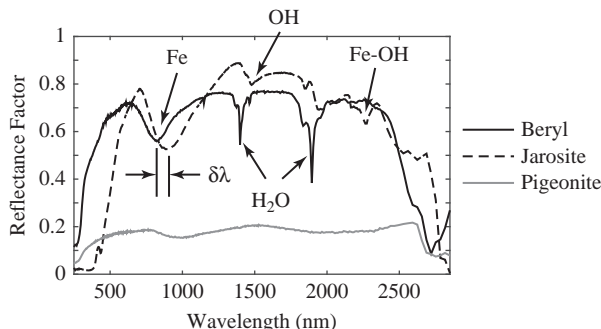


Figure 3.12 Iron-based mineral spectra examples of beryl, jarosite, and pigeonite. Note that the Fe absorption feature shifts to longer wavelengths (Clark et al., 2007; Hunt, 1977).

absorption features relate mostly to the nature of the site in which the ion resides. Consequently, important information concerning the bulk structure of the mineral is provided in this somewhat indirect manner. This type of information is extremely valuable from a remote sensing viewpoint.

In beryl ($\text{Be}_3^{+2}\text{Al}_2\text{Si}_6\text{O}_{18}$), the first absorption feature, and the only feature in the electronic region, is due to the ferrous ion in sixfold coordination located in an almost perfect octahedral Al^{+3} site, where it replaces the aluminum atom, and is due to a single transition. Coordination geometries describe the arrangement of nearest neighbor atoms about a central atom and sixfold coordination describes an octahedral geometry. Jarosite $[\text{KFe}_3^{+3}(\text{SO}_4)_2(\text{OH})_6]$ only forms in the presence of water and was discovered based on the interpretation of the data from the Mars Exploration Rovers (Klingelhöfer et al., 2004). The crystal structure of jarosite is similar to beryl, with a ferrous ion surrounded by oxygen and hydrogen, but the different elements in the lattice impose differing electric fields on the ferrous ion resulting in different (lower) energy features than beryl characterized by $\delta\lambda$ in the figure. Pigeonite $[(\text{Mg},\text{Fe}^{+2},\text{Ca})(\text{Mg},\text{Fe}^{+2})\text{Si}_2\text{O}_6]$ displays a band near $1\ \mu\text{m}$ and another at wavelengths longer than $1.8\ \mu\text{m}$. Both these features arise from transitions in the sixfold coordinated ferrous ion located in one of two possible sites. Here the octahedron is so highly distorted that the degeneracies of the levels in the pure octahedron are removed, providing levels for two distinct spin-allowed transitions (Crowley et al., 2003; Hunt, 1977).

Charge Transfer Absorption

Absorption bands can also be caused by inter-element transitions or charge transfers where the absorption of a photon causes an electron to move between ions or between ions and ligands. The transition can also occur between the same metal in different valence states, such as between ferric (Fe^{+2}) and ferrous (Fe^{+3}) ions. The band centers usually occur in the ultraviolet, with the wings of the absorption extending into the visible wavelengths. Charge transfer absorptions are the main cause of the red color of iron oxides and hydroxides, as demonstrated in Figure 3.13. The intense charge-transfer band in the UV ($<0.4\ \mu\text{m}$) absorbs nearly all of the photons except those which are

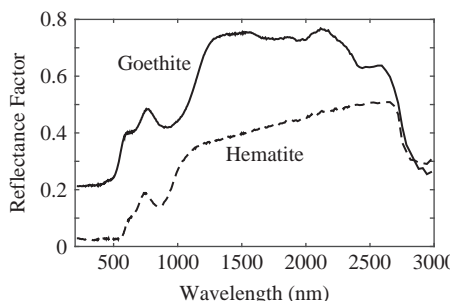


Figure 3.13 Reflectance spectra of the iron oxide hematite (Fe_2O_3) and iron hydroxide goethite (FeOOH , from Clark et al., 1993). The goethite reflectance spectrum is offset upward 0.2 for clarity.

specularly reflected from the surface. The absorption at $2.7\text{--}3\ \mu\text{m}$ is due to trace water or OH absorption features in the samples (Clark et al., 1999).

3.5.2 Vibrational Process

As discussed in Section 2.5.5, molecular vibration, whether in a gas, liquid or solid, provides spectral absorption features which can be exploited for identification. The bonds in a molecule or crystal lattice can be thought of as springs with attached weights for which there are specific frequencies of vibration which depend on the strength of each spring (the bond in a molecule) and their masses (the mass of each element in a molecule). Each vibration can also occur at higher-order harmonics or in combinations of multiples of the original fundamental frequency, as we will shortly demonstrate.

The fundamental band for vibrational absorption will be seen in the infrared spectrum only, and it is necessary for the molecule responsible to have a dipole moment. This is known as being infrared active. A symmetric molecule, such as N_2 , is not normally infrared active unless it is distorted as, for example, when it is under high pressure. The influence of the surrounding atoms will affect the vibrational energy in a similar fashion as the electronic states were modified. A molecule that would have degenerate vibrational modes in isolation may have modes at slightly different frequencies in a crystal, breaking the degeneracy due to the non-symmetric influences of the crystal field. A free molecule can rotate and translate, while in a solid the modes are restricted to vibration, where partial rotation and slight translation can occur. These motions are called lattice modes and typically occur at very low energies, with the spectral features beyond $20\ \mu\text{m}$ (Clark et al., 1990).

If a molecule has vibrational fundamental modes ν_1 , ν_2 and ν_3 then it can have overtones at approximately $2\nu_1$, $3\nu_1$, $2\nu_2$ and higher multiples and combinations at approximately $(\nu_1 + \nu_2)$, $(\nu_2 + \nu_3)$, $(\nu_1 + \nu_2 + \nu_3)$ and so on. These examples used summations of modes, but subtractions are also possible (e.g. $\nu_1 + \nu_2 - \nu_3$). Each higher overtone or combination is typically 30 to 100 times weaker than the last. Consequently, the spectrum of a mineral can be quite complex. In reflectance spectroscopy, these weak absorptions can be measured easily and diagnostic information routinely gained

Table 3.1 Water and Carbonate Vibration Modes

Molecule	Vibration Mode	Wavelength (μm)	Description
H_2O gas	ν_1	2.738	symmetric OH stretch
	ν_2	6.270	H–O–H bend
	ν_3	2.663	asymmetric OH stretch
H_2O liq	ν_1	3.106	symmetric OH stretch
	ν_2	6.079	H–O–H bend
	ν_3	2.903	asymmetric OH stretch
CO_3^{2-}	ν_1	9.407	symmetric stretch
	ν_2	11.4	out-of-plane bend
	ν_3	7.067	asymmetric stretch
	ν_4	14.7	in-plane bend

Vibrational modes and their wavelengths for water in both gas and liquid form and CO_3^{2-} including a description of the vibration mode. Two of the six modes in CO_3^{2-} are degenerate modes (Hunt and Salisbury, 1971).

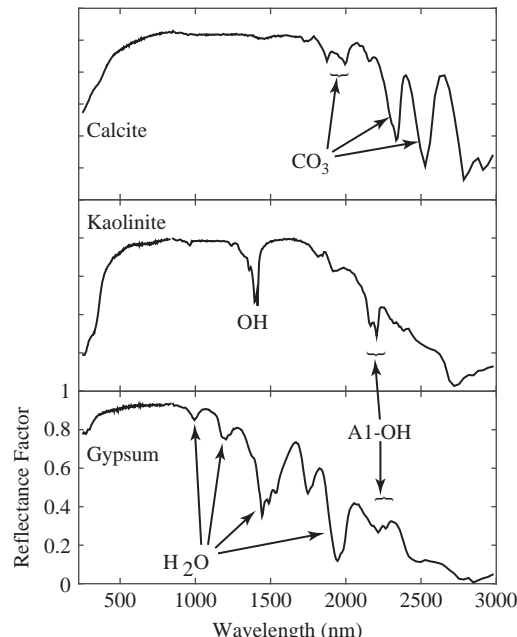


Figure 3.14 Reflectance spectra of H_2O in gypsum, OH bonds in kaolinite and CO_3 in calcite demonstrating the distinct overtone features (Clark et al., 2007). The reflectance factor scales are the same in the three graphs.

from second and third overtones and combinations (Clark et al., 1999, and internal references).

Water and hydroxyl (OH) produce particularly diagnostic absorptions in minerals. The water molecule has $N = 3$, so there are $3N - 6 = 3$ fundamental vibrations. In the isolated molecule (vapor phase) the absorption spectra are given in Table 3.1. The overtones of water are seen in reflectance spectra of H_2O -bearing minerals. Figure 3.14

provides the reflectance spectrum of gypsum, which contains water with the absorption features attributable to it identified in the graph. The first overtones of the OH stretch vibrational mode occur at about $1.4 \mu\text{m}$ and the combinations of the H–O–H bending mode with the OH stretch are found near $1.9 \mu\text{m}$. Thus, a mineral whose spectrum has a $1.9 \mu\text{m}$ absorption band contains water as can be seen from the gypsum spectra, but a spectrum that has a $1.4 \mu\text{m}$ band but no $1.9 \mu\text{m}$ band indicates that only hydroxyl is present, as in kaolinite. It is important to note that the kaolinite sample in Figure 3.14 has only a small amount of water because of the weak $1.9 \mu\text{m}$ absorption but a large amount of OH. The hydroxyl ion has only one stretching mode and its wavelength position is dependent on the ion to which it is attached. In spectra of OH-bearing minerals, the absorption is typically near 2.7 to $2.8 \mu\text{m}$, but can occur anywhere in the range from about $2.67 \mu\text{m}$ to $3.45 \mu\text{m}$ (Clark et al., 1990). Hydroxyl commonly occurs in multiple crystallographic sites of a specific mineral and is typically attached to metal ions. Thus, there may be more than one OH feature. The metal–OH bending mode occurs near $10 \mu\text{m}$ and the combination metal–OH bend plus OH stretch occurs near 2.2 to $2.3 \mu\text{m}$. This last feature is diagnostic of mineralogy (Clark et al., 1990, 1999).

There are additional vibrational features evident in Figure 3.14. The observed carbonate absorptions are due to the planar CO_3^{2-} ion. There are four vibrational modes in the free CO_3^{2-} ion, which are also included in Table 3.1. The ν_1 band is not infrared active in minerals. There are actually six modes in the CO_3^{2-} ion, but two are degenerate with the ν_3 and ν_4 modes. In carbonate minerals, the ν_3 and ν_4 bands often appear as a doublet. The doubling has been explained in terms of the lifting of the degeneracy due to the mineral structure and negative ion site (White, 1974). Combination and overtone bands of the CO_3^{2-} fundamentals occur in the near infrared. The two strongest shown in Figure 3.14 are $\nu_1 + 2\nu_3$ at 2.50 to $2.55 \mu\text{m}$ (4000 – 3900 cm^{-1}), and the $3\nu_3$ band at 2.30 to $2.35 \mu\text{m}$ (4350 – 4250 cm^{-1}). Three weaker bands occur in the 1.85 to $2.16 \mu\text{m}$ spectral region (Hunt and Salisbury, 1971; Hunt et al., 1972).

The band positions in carbonates also vary with composition. An example of a band shift is seen in Figure 3.15 where the carbonate feature position moves from calcite, CaCO_3 , to dolomite, $(\text{CaMg})(\text{CO}_3)_2$. Three distinct absorption features from combinations of CO_3^{2-} are manifested at slightly longer wavelengths (lower energies) in the

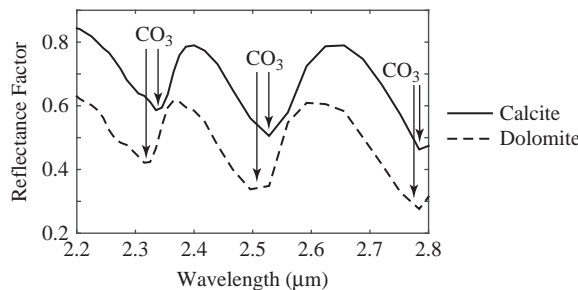


Figure 3.15 Reflectance spectra of calcite and dolomite indicating the effects of the absorption feature shifts resulting from the small differences in the crystal vibrational modes (Clark et al., 2007).

calcite as compared to the dolomite (Hunt and Salisbury, 1971; Gaffey et al., 1993). This important and clearly observable shift in the absorption feature provides the geologist with a clear difference in the spectral signature, allowing the two similar minerals to be identified.

Thermal Infrared Spectra of Minerals

As noted, vibrational features with lower energies populate not only the SWIR spectral region, but are also the source of absorption features in the mid- and long-wave infrared reflectance and emissivity spectra. As in the shorter wavelengths, water and hydroxyl features contribute to the signatures observed in the reflectance spectrum as water is so ubiquitous. However, new lower energy vibration modes from various elemental bonds are also found in the thermal infrared spectral region which are not present in the shorter wavelengths.

We have previously examined hematite (in Figure 3.13), which does not have many distinct features in the shorter wavelengths and the $3\ \mu\text{m}$ absorption feature is attributed to water in the sample. Examining the reflectance spectrum in full infrared spectrum, provided in Figure 3.16, we can also identify other foreign bonds, including a moderate amount of organics from the C–H bond at $3.4\ \mu\text{m}$. The ferrous ion bond with oxygen (Fe^{+3}O) has very little vibrational energy due largely to the mass of the Fe ion, thus providing the long wavelength absorption features identified in the figure. Hematite has three strong stretching modes between 14 and $30\ \mu\text{m}$. Because iron oxides and hydroxides tend to be fine grained, typically less than the wavelength of mid-infrared photons,

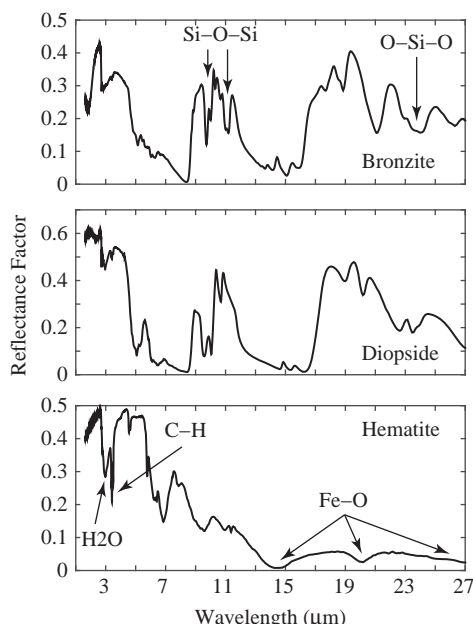


Figure 3.16 Infrared reflectance spectra of bronzite, diopside, and hematite (Clark et al., 2007).

and because of the strong absorption in the mid-infrared, iron oxides tend to be dark in reflectance or highly emissive, showing few features beyond about $12\ \mu\text{m}$ (Clark et al., 1999).

We compare the ferrous dominated mineral in Figure 3.16 to two silicate dominated minerals. The thermal infrared spectrum of both diopside ($\text{MgCaSi}_2\text{O}_6$) and bronzite (a ferriferous variety of enstatite, a magnesium silicate MgSiO_3 with the magnesium partly replaced by ferric ions $(\text{Mg},\text{Fe})\text{SiO}_3$) are also given in Figure 3.16. The strong $9\ \mu\text{m}$ asymmetric stretch fundamental band is an obvious indicator to a spectroscopist of the Si–O–Si molecular constituent. The Si–O–Si asymmetric stretch fundamental band occurs near $11\ \mu\text{m}$, and a weaker symmetric absorption occurs near $12\ \mu\text{m}$. The absorption between 12 and $13\ \mu\text{m}$ is the Si–O–Si symmetric stretch fundamental. The O–Si–O bending mode occurs near $25\ \mu\text{m}$ and is the second strongest absorption feature common to the two silicates (Clark et al., 1999). Because iron is more massive than silicon, Fe–O fundamentals will be at longer wavelengths than Si–O stretching modes.

3.5.3 Water

Water is a challenging material to quantitatively measure in the solar reflective range due to its very low reflectance. It is highly emissive in the LWIR, making it a good choice for a vicarious calibration target, as discussed in Chapter 5. Additionally, there is a tremendous amount of variability associated with water bodies that depends upon the organic content, suspended particulates, the depth, and the bottom material reflectance. The spectral features of water have been studied extensively by the ocean color and bathymetry communities. Figure 3.17 shows the absorption coefficient for pure liquid water from 0.1 to $14\ \mu\text{m}$. Water appears blue in the visible wavelengths due to the vibrational overtones that are responsible for the rising absorption in the red (Braun and Smirnov, 1993). Scattering also plays a role in the color of water similar to Rayleigh scattering in the atmosphere. At both shorter and longer wavelengths the absorption coefficient increases and almost no light is transmitted over an appreciable path.

The fundamental vibrational modes for water are listed in Table 3.1. There are mode combinations and overtones that are evident in the absorption spectrum of water

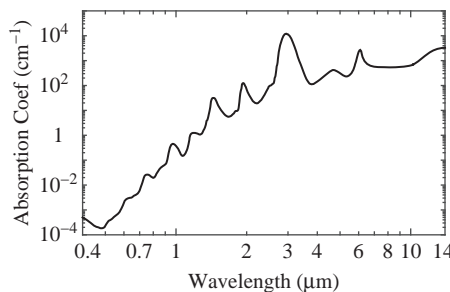


Figure 3.17 Spectral variation in the absorption coefficient of water over the solar reflective and emissive spectral ranges (Hale and Querry, 1973).

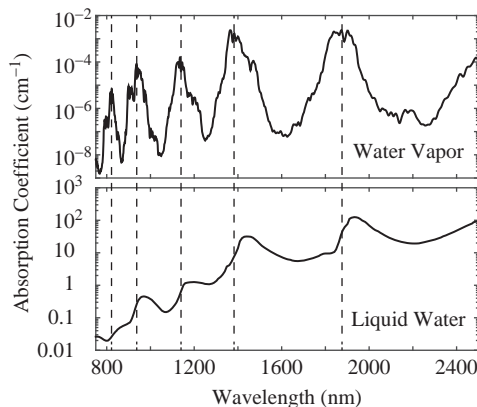


Figure 3.18 The upper graph illustrates the absorption features for water vapor calculated using the HITRAN database, which have been smoothed to eliminate the high frequency rotational lines. The lower graph is the equivalent for liquid water. The vertical dashed lines are to aid in showing the shift in the peaks of the main features.

vapor and in the reflectance spectra of ice and water. For example, the absorption that composes the atmospheric water band at about $1.88 \mu\text{m}$ is due to a combination of vibrational transitions from the ground state, given by (ν_1, ν_2, ν_3) equal to $(0, 0, 0)$, to both the $(1, 1, 0)$ and $(0, 1, 1)$ excited states. The absorption spectrum of both liquid and solid water is governed by these vibrational modes with Figure 3.18 illustrating how the absorption features in liquid water vapor correlate with those in water vapor but are shifted to longer wavelengths. The absorption features for ice shift a little farther to the longer wavelengths.

Seawater

The reflectance properties of bodies of water are highly dependent on wave height and sediments or organic material suspended in the water. The seminal work on the effects of wave statistics on ocean BRDF properties, which captures the specular feature of reflectance of the sun from still or turbid water, was done by Cox and Munk (1954). Many researchers have used this basic model with small variations or enhancements for specific situations. The specular component of any body of water dominates the signature if the measurement is made close to a specular geometry. Various airborne and space-borne sensors of the ocean are designed with this fact in mind. In the absence of a strong specular feature, the reflectance properties of seawater for the open ocean and coastal zones have been measured and provided in Figure 3.19 (Clark et al., 2007). The very low reflectance of clear water and the transmission in the visible and near-infrared spectral ranges provides the opportunity to exploit these wavelengths to measure materials below the surface of the water. Murky water which contains a plume of material, sediment or other well-mixed material which is transported with the water current, can be detected and characterized by spectral remote sensing.

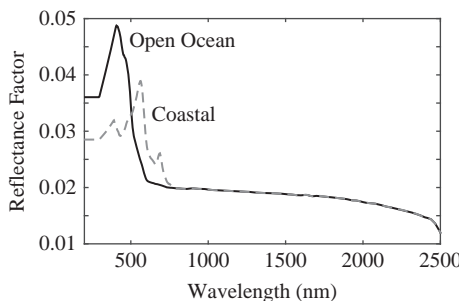


Figure 3.19 Example spectra of clear water diffuse reflectance (not in the specular geometry) for open ocean and coastal examples (Clark et al., 2007).

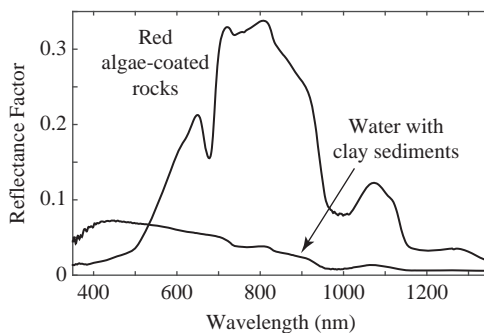


Figure 3.20 Example spectra of shallow clear water diffuse reflectance (not in the specular geometry) for red algae-coated rocks as a subsurface beneath 10 cm of fresh water. Clay sediment is mixed into clear fresh water to produce example reflectance spectra for turbid water with clay sediments (Clark et al., 2007).

A series of experiments was conducted to characterize this effect for clay soil (montmorillonite) mixed with water at varying concentrations. Even for small concentrations of clay powder, the spectral changes are obvious. The convolution of the sediment clay reflectance with the spectral absorption yields a distinctly visible and NIR spectral output. Figure 3.20 has the spectral reflectance for the smallest montmorillonite quantity (0.5 g/l H₂O), which was mixed with water and actively stirred with the spectra measured while the mix was still moving to minimize settling effects (Clark et al., 2007).

In another field campaign experiment conducted by Clark et al. (2007), the spectral reflectance was measured for red algae in a clear fresh water stream. The reflectance spectrum for red algae-coated rocks under about 10 cm in the Arkansas River is also given in Figure 3.20. Clearly, the signature of the red algae can be seen well past the visible spectrum. In this shallow water example, the formidable absorption of H₂O in the IR suggests that shallow water applications can exploit wavelengths $>1\ \mu\text{m}$. In a littoral zone example, with a known or assumed sea bottom material (sand or seagrass), spectral remote sensing data has been used to derive shallow water bathymetry in coastal zones.

Because the spectral data allows the analysts to associate a finite number of spectral features with a finite number of physical phenomena, bimodal bottom surface models can be effectively exploited to arrive at useful bathymetry products (Bachmann et al., 2009). The importance of the costal ocean color and the ability to correlate it with important bio-physical and physical phenomena have inspired the construction of a Visible–NIR Hyperspectral Imager for the Coastal Ocean (Lucke et al., 2011). A well-characterized sensor is required for these challenging applications.

3.6

Organic Spectroscopy

Chlorophyll in a maple leaf is the same as chlorophyll found in blue grass or a cabernet grapevine leaf. Similarly, the hydroxyl molecular vibration mode and wavelength is the same whether in leather, wood or blood. Organics are comprised of a small number of basic “building block” molecules and compounds, and yet, due to the diversity of structure and complex environment in which the building blocks are arranged, an enormous diversity of spectra can be discriminated. At larger spatial scales, as is generally the case for remote sensing applications, the influence of complex scattering structures and arrangement of observable elements becomes increasingly important. The illumination and measurement geometries are also important in terms of the reflective properties of the organic material.

Consider how differently a tree appears as viewed from overhead as opposed to viewing from the side. From the top of a dense forest canopy it is possible to see only leafy material, although the biomass may be mostly wood. Further, the effective reflectance can vary substantially with the solar illumination angle, which is an important factor in determining the earth energy balance for global models. A large body of literature exists which describes and models many of these effects from the single plant to the field or regional scale, so as to relate biophysical parameters, such as biomass or leaf area index, to spectral observations. In this section, we will introduce the reader to the spectroscopic features likely to be encountered in the study of spectral remote sensing of organic material and point to appropriate references for a more in-depth treatment.

3.6.1

Vegetation Characteristics

All vegetation contains the basic constituents of chlorophyll as well as other light-absorbing pigments, of structural biochemical molecules such as lignin and cellulose, proteins, starches, waxes and water (Elvidge, 1990). Because of pigment absorptions including chlorophyll, the visible region of green plants shows a maximum reflectance at approximately $0.55\text{ }\mu\text{m}$ and lower reflectance in the blue ($0.45\text{ }\mu\text{m}$) and red ($0.68\text{ }\mu\text{m}$). At the infrared wavelengths, the spectra of fresh plants show a strong rise in reflectance in the near-infrared followed by the spectral features of water and other constituents. The rise is referred to as the vegetation red-edge, which is strongly correlated to the health and condition of green vegetation. The region of high plant reflectance

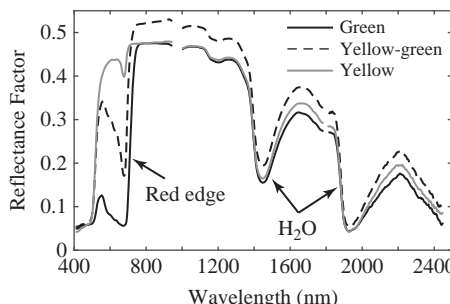


Figure 3.21 Spectra of aspen leaf: “Green”, “Green-Yellow” and “Yellow” leaves as measured by Clark et al. (2007).

in the near-infrared (0.75–1.30 μm) is often referred to as the near-infrared plateau (NIR-plateau).

The high reflectance results from an absence of pigment absorption, an increased amount of light scattering at cell–wall interfaces due to a change in the index of refraction, and the smaller absorption of water in leaves at those wavelengths. Figure 3.21 provides leaf spectra from an aspen tree. The “Green” spectra is a sample from a healthy full-summer green leaf while the “Yellow-Green” and “Yellow” leaf spectra represent the progressive change in the leaf spectrum for the autumnal/dormant season. In particular, note the loss of the red-edge as the leaf ages. Two absorption features centered near 0.98 μm and 1.20 μm are evident on the NIR-plateau and are due to starch. At 1.40 μm and 1.90 μm are two strong water-absorption features which reduce the reflectance and obscure subtle features nearby. Although there are changes in reflectance between these samples, the shapes of the reflectance spectrum at wavelengths longer than 0.8 μm are nearly identical indicating that the principal change is in the chlorophyll and other light-absorbing pigments. The depth of the water absorption feature in all three samples confirms that the change is not due to the change in water content but simply the result of seasonal changes in the photosynthetic pigments.

Small reflectance “offsets” from measured data, especially when less than 5 or 10 percent, are often attributable to changes in the sample or measurement configuration rather than intrinsic material spectra. Great care was taken by Clark et al. (2007) in measuring these samples in the laboratory, but the reader should appreciate the challenge of obtaining absolute reflectance spectra. Relative spectral shapes are more robust since it is quite difficult to exactly duplicate the measurement conditions for a range of samples, especially for organic materials with irregular surface properties.

Plant Pigments

There are striking changes in the visual appearance of a plant, which seem striking to the eye but are perhaps less remarkable to the spectroscopist. There are many examples of these changes and we will focus on the differences manifest in closely related plant varieties. Again, relying on reflectance measurements carefully collected and compiled by Clark et al. (2007), a comparison of different petunia varieties illustrates these spectral differences. Figure 3.22 provides three spectra for domestically grown petunias

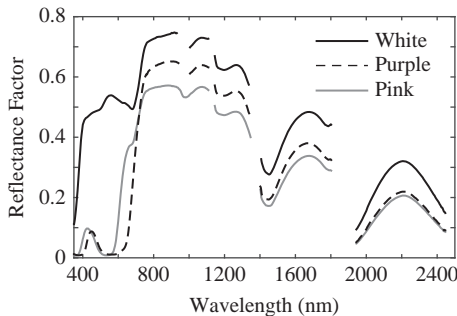


Figure 3.22 Three petunia samples from Hale and Querry (1973).

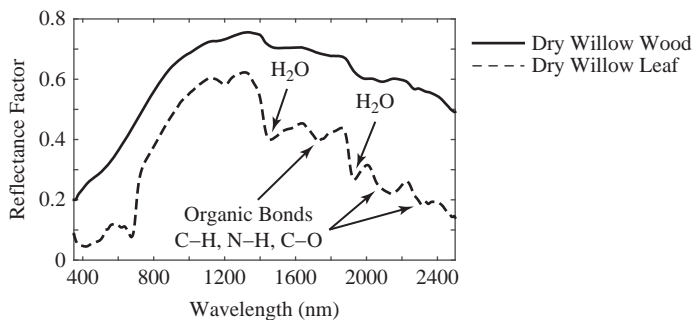


Figure 3.23 Spectra of dry willow tree leaf and willow tree wood with the organic bond features identified in leaf spectra. Wood spectra offset by 0.2 for clarity. Spectra from Clark et al. (2007), Peterson and Hubbard (1992), and Kokaly (2001).

with pink, purple, and white varieties. As with the aspen leaf of Figure 3.21, there is no significant difference in the spectral shape above a wavelength of about $0.75 \mu\text{m}$. It is instructive that the measured spectral reflectance in the visible bands for the pink petunia has a stronger violet reflectance than that from the purple sample, but the small knee in the red ledge adapted for the pink flower dominates the human perception. The white petunia has a similar mid-green reflectance peak as a healthy green leaf but the overall reflectance across the visible spectrum is elevated. As noted previously, the absolute reflectance differences in the infrared may be the product of sample structure differences rather than repeatable absolute differences (see description of collection technique in Clark et al., 2007).

Senescence and Dormancy Vegetation Spectra

In dried vegetation, the water absorptions no longer conceal the absorption features at $1.73 \mu\text{m}$, $2.10 \mu\text{m}$, and $2.30 \mu\text{m}$ that are caused by organic bonds in plant biochemicals. Proteins, lignin, and cellulose all contribute to these features. C–H, N–H, and C–O bonds in the organic molecules have overtones and combinations that absorb in the near-infrared region of the spectrum (Peterson and Hubbard, 1992; Kokaly, 2001; Kokaly et al., 2003). Figure 3.23 is taken from the dry leaf of a willow tree which has

a reduced water absorption feature in comparison to the similar one of the healthy and wet aspen leaf of Figure 3.21. Clark et al. (2007) provides a detailed description of samples.

One of the important uses of vegetation spectra is the mapping of senescent or dormant vegetation in order to identify the available fuel for a fire. Due to the individual and characteristic spectra for various plant species, which result from a combination of structural surface types such as leaves, canopy density, bark, and leaf litter, spectral data has been used for pre-fire assessment and post-fire regrowth assessment (Riano et al., 2002). Spectral features have also proved effective in mapping the burn severity or the magnitude of fire effects on vegetation and soil and related ecological processes (Kokaly et al., 2007).

Fluorescence

Another interesting and diagnostic spectral characteristic of vegetation is the solar-induced chlorophyll fluorescence emission, which provides an additional signal in the apparent reflectance. The emission of light as fluorescence in the 650 to 800 nm spectral range is produced after absorption of light by a mechanism in direct competition with the photochemical conversion. Photons are absorbed at higher energies and shorter wavelengths and, through various processes, lower energy photons are emitted with the energy difference stored in the plant. The induced fluorescence peaks at $0.685 \mu\text{m}$ for many plants but is observed over a broader range dependent upon species and health of the vegetation (Papageorgiou, 1975). This fluorescence signal is a small signature but provides the opportunity for researchers to explore how this signature is correlated with plant health and physiology, and so remains an active topic of research (Meroni et al., 2010).

Summary

Since the advent of Landsat in 1972, scientists have been using spectral measurements of vegetation to characterize the spatial, spectral, and temporal changes of the environment. Because of the limited spectral bands that were available to characterize the dominant vegetative features, simple ratioing techniques were developed that captured the dominant spectral characteristics and broad categories. For example, the normalized difference vegetation index (NDVI), defined as

$$\text{NDVI} = \frac{\text{NIR} - \text{VIS}}{\text{NIR} + \text{VIS}}, \quad (3.38)$$

where NIR is the reflectance in a near-infrared band and similarly VIS is the reflectance for a visible band, was developed as a quick classification technique that utilized the limited number of multispectral bands. With an imaging spectrometer, subtle features can be extracted and exploited to identify specific vegetation characteristics. Chlorophyll and water-absorption features in plant spectra have been used in combination to successfully identify vegetation land cover (Kokaly, 2001). Gao and Goetz (1990) also demonstrated that it is possible to distinguish atmospheric water from the water present in vegetation using high quality imaging spectrometer data.

3.7

Man-Made Materials

The following sections describe some frequently encountered materials that are broadly described as man-made. The materials that are chemically manufactured and therefore “non-organic” often have spectral features which are unlike anything encountered in nature. Other materials in this broad category are essentially natural materials which are reprocessed or reconfigured from their natural state but retain the essential constituent components and, therefore, spectral features. We subdivide the man-made materials into fabrics, building materials, and plastics or other materials.

3.7.1

Fabrics

There is a wide diversity of fabric materials which are manufactured either from organic materials or from an involved chemical process. Polyester has a sharp absorption feature at $\sim 1.656 \mu\text{m}$ with other bands at $2.132 \mu\text{m}$, $2.254 \mu\text{m}$, and $2.328 \mu\text{m}$ as identified in Figure 3.24 (Haran, 2008). Similarly, nylon has a range of distinctive features which can also vary with the particular manufacturing process and concentrations of polymers. The structures in the infrared, from the shortwave and into the longwave, are distinct, making these man-made materials easy to distinguish from the naturally occurring materials discussed previously (Siesler, 1991). Cotton materials made from the spinning of cotton fibers into thread, and burlap, which is also manufactured from plant fibers, especially the jute plant, retain the distinctive spectral features that are found

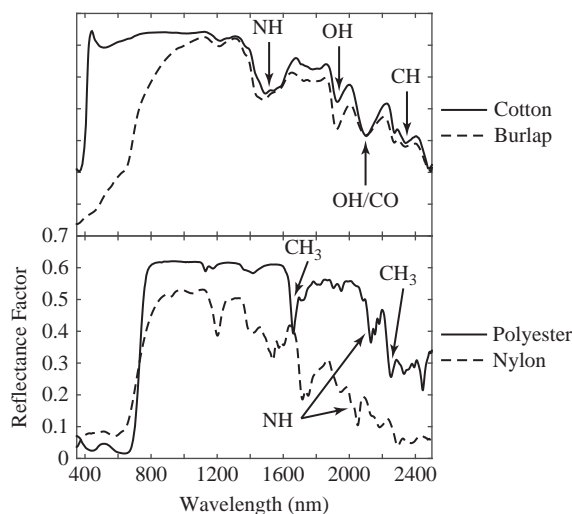


Figure 3.24 Spectra of fabric materials. Organic features identified in cotton and burlap. Polyester and nylon spectra are provided as example man-made fabric materials but exact features identified in spectra may be different depending on the manufacturing process (Clark et al., 2007). The reflectance factor scales are the same in the two graphs.

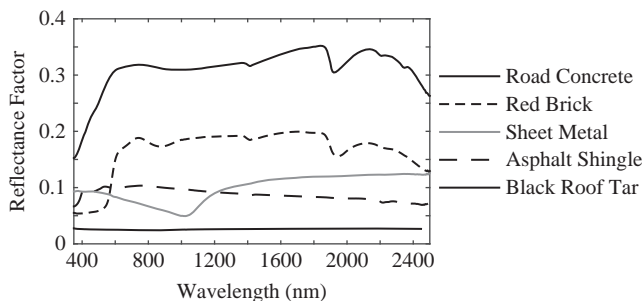


Figure 3.25 Spectra of various building materials found in an urban setting (Clark et al., 2007).

in senescent vegetation, including water absorption and OH and CH bond vibration features.

3.7.2 Building Materials

Remote sensing of urban environments is becoming an increasingly important topic as civil officials seek to characterize urban sprawl, assess rain run-off or evaluate “heat-island” effects. The man-made materials which largely constitute the urban landscape are characterized by spectra that range from highly structured examples to remarkably flat cases, lacking spectral features. Figure 3.25 provides five spectra of the urban setting. Asphalt is manufactured from the heaviest part of petroleum as part of the process of refinement of crude oil products and provides the basis for several ubiquitous building materials, including black roof tar as well as asphalt shingle. Another building material is galvanized sheet metal, which has a distinct but subtle spectral minimum reflectance at $\sim 1.025 \mu\text{m}$. Red paving brick and road concrete have a significantly higher reflectances as well as some spectral features that are identifiable in remotely sensed data. These material spectra are also provided in Figure 3.25.

3.7.3 Plastics and Other Materials

Plastic is the term used to describe the wide range of materials composed of polymers which are based on chains of carbon atoms, alone or with oxygen, sulfur, or nitrogen. Most plastics have additional organic or inorganic components. High-density polyethylene (HDPE) is used for many applications from plastic bottle caps to hard hats. The spectra labeled as white plastic HDPE in Figure 3.26 is of a white opaque plastic bag made from HDPE. The spectral organic features resulting from CH, CO and other bonds common in polymers can be identified in the spectra. Similarly, the spectra of polyvinyl chloride ($\text{C}_2\text{H}_3\text{Cl}_n$) or PVC which is used in plumbing pipes and joints as well as a variety of other modern products, has easily identifiable carbon and hydrocarbon spectral features.

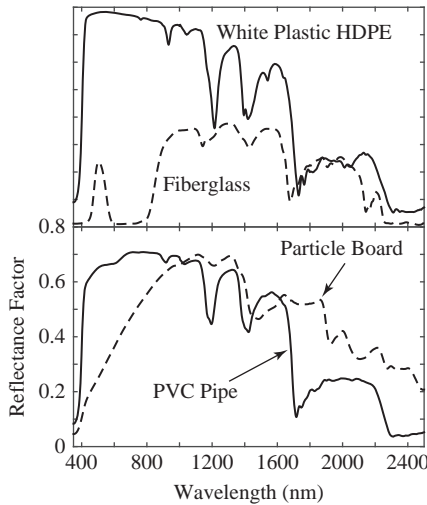


Figure 3.26 Spectra of two plastics, fiberglass, and particle board from Clark et al. (2007). The reflectance factor scales are the same in the two graphs.

Fiberglass is often used as a building material and is a fiber-reinforced polymer made of plastic and glass fibers. As with the other plastics, organic bonds dominate the spectral features in the shortwave bands. Finally, we have included particle board, which is wood chips or dust with a synthetic resin or other suitable binder. Formaldehyde (CH_2O)-based resins are often used, so CH and CO bonds are also clearly evident in the sample provided by Clark et al. (2007).

3.8

Long Wave Infrared Spectra

The spectral behavior of a material's reflectance $\rho(\lambda)$, or the more commonly referenced emissivity $\epsilon(\lambda) = (1 - \rho(\lambda))$ over the thermal LWIR window will play an important role in the reduction and analysis of at-aperture radiance data. In general, but especially prevalent in the thermal infrared, condensed phase materials have much wider spectral features than those of gases, due to the inverse relationship between the lifetimes of molecular vibrational states and the widths of the spectral features associated with transitions between such states. The molecules in a gas are relatively isolated, giving rise to long lifetimes and hence sharp features in the absorption spectrum. The highly coupled nature of condensed phase materials gives rise to many more available vibrational states, and hence shorter lifetimes and broader spectral features. The spectra of over 2400 natural and man-made materials are cataloged in the ASTER spectral library (Baldridge et al., 2009b). Several of these are shown over the LWIR window in Figure 3.27. These examples demonstrate the general rule that most natural surfaces tend to have high emissivities in this spectral window, which is particularly important for the atmospheric compensation of emissive imaging spectrometer data.

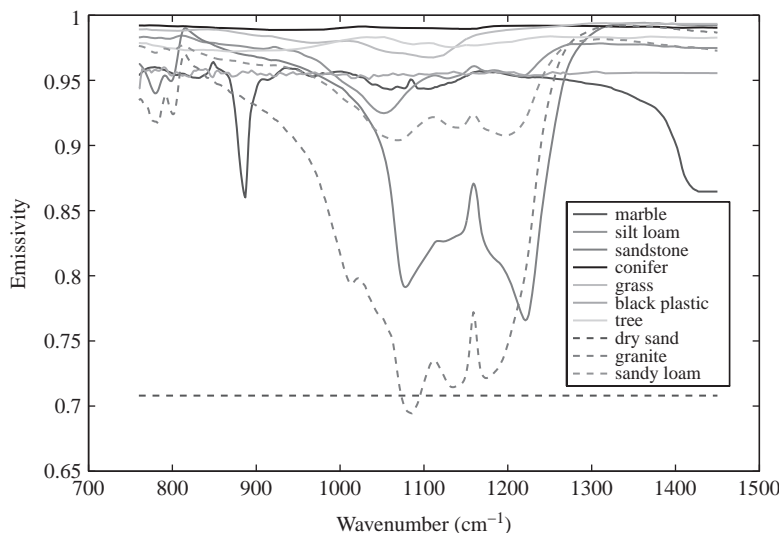


Figure 3.27 Sample emissivity spectra, over the LWIR atmospheric window, of a variety of materials from the ASTER library.

3.9

Summary and Further Reading

The geometrical description for reflectance has been developed, including both the bidirectional reflectance distribution function and the bidirectional reflectance factor. The BRF is often employed to describe the reflectance from surfaces in remote sensing applications. The field measurement of reflectance was also introduced. The remainder of the chapter was a brief overview of the reflectance properties of materials. Some effort was made to connect the features observed in reflectance spectra to the underlying quantum mechanical mechanisms of electronic and vibrational states. Often, one is primarily interested in the spectrum rather than the detailed solid-state physics that governs its features, and the United States Geological Survey and ASTER spectral libraries are examples of the extensive catalogs that are now available (Clark et al., 2007; Baldridge et al., 2009b).

The laboratory measurement of reflectance and emissivity is thoroughly presented in Germer et al. (2014), and Hapke's classic text provides a quantitative treatment of the theory (Hapke, 2012). A robust spectral remote sensing literature has resulted from the advent and ready availability of high quality imaging spectrometer data, such as AVIRIS data. Roger Clark's chapter in *Remote Sensing for the Earth Sciences* is an excellent introduction to the spectral properties of rocks and minerals and was used extensively in the writing of this chapter (Clark et al., 1999). The collection of articles in van der Meer and de Jong (2001) provides an introduction to the use of imaging spectrometers for a wide range of applications with the physical mechanisms for the generation of spectral signatures for a variety of materials introduced with references. Finally, the geologist will find Gupta (2003) a helpful reference.

Problems

1. Write an expression to find the normal to a target surface of unity reflectance with a given angle to an incident illumination such that the observer viewing the albedo from any θ and ϕ will receive a $BRF = R_{\text{observed}}$.
2. As a function of latitude and equitorial crossing, write an expression for the angular reflectance dependencies seen by a polar orbiting satellite at the winter and summer solstice as well as equinox for a nadir looking satellite.
3. Write an expression which accounts for diffuse radiation contribution to the error in a BRDF measurement made in the field under full sun. Express the error as a function of the Diffuse-to-Direct irradiance and identify all of the variables required for the general expression.
4. From the periodic table, identify three elements which are electronically active and describe their character and spectral features from the text. Relate or connect the features to their position in the periodic table.
5. Using Neodymium Oxide spectra provided in Figure 3.10, write a summary table for the energy conversion efficiency associated with producing a Nd:YAG laser at 1064 nm using each of the absorption features assuming that all absorption elements of higher energy than the laser are able to be converted into laser energy.
6. Calculate the combination of overtones required to arrive at the O_3^{-2} spectral features in calcite found in Figure 3.16.
7. Calculate the combination of overtones required to provide the H_2O absorption features in the gypsum spectra.
8. Calculate the overtones and combinations required to achieve the three smaller carbonate absorption features of calcite identified in Figure 3.14.
9. Identify at least six spectral features of the compound that are responsible for the white plastic High-Density Polyethylene (HDPE) in Figure 3.26.
10. Relate the physical characteristics of organic matter to the reflectance spectra by identifying and itemizing features in the spectrum.
11. Given the three material reflectance spectra below, what do you derive about the composition of the material?
12. For the vibrational modes of water, calculate and show all of the vibrational modes and their energies (and wavelengths) that are possible which are stronger than 0.01 percent of the base absorption features (assume that all primary absorption features have equal strength and that each combination of modes results in a $30\times$ decrease in absorption strength).
13. Describe or sketch a graph of the expected spectral radiance that reaches the bottom of a 30-foot pool of water. What happens to the radiance as fine dust particles (of high albedo) are gradually mixed into the pool water. What if the dust particles have a very low albedo?

14. As a function of wavelength, write an expression that relates the observed reflectance of a target in full sun to a target in the shadow of a single cloud of optical thickness $\tau(\lambda)$. What happens if the target is in the hard shadow of a building? Express the circumstances when a black tar roof appears to have the same reflectance as road concrete in shadow.
15. What minimum number of spectral bands and at what wavelength (approximately) are required to differentiate the following materials if only a digital number for each wavelength is provided? Assume all materials are collected under similar circumstances: bronzite and diopside; green aspen leaf, pink petunia and purple petunia; dry wood, yellow aspen leaf, calcite and dolomite. Now assume the lighting conditions for the materials are entirely unknown.

4 Imaging Spectrometers

This chapter will address the optical principles that underpin any imaging spectrometer and then delve into the details of the dominant optical designs. The complete imaging spectrometer typically includes a scan mechanism, such as a rotating mirror, a telescope fore optic to image the scene at the input of a spectrometer, the spectrometer, which can accomplish the separation of the radiance into the different wavelength bins either through dispersive or interferometric means, and the focal plane array where the signal is converted to digital numbers. The optical flow from the scene to the resulting digital signals is depicted in Figure 4.1. The details of the optical system are presented and the description focuses on the concepts required to enable the reader to understand, at an introductory level, how these complex systems work.

This chapter will also introduce the unifying concept of the measurement equation. All imaging spectrometers share spatial, spectral, and radiometric properties, which can be mathematically described in a general way. Important concepts that are common to all of the optical forms presented are captured succinctly in a simple and elegant way. It is the measurement equation that provides the explanatory framework upon which the optical details will be built. An understanding of Gaussian or geometrical optics is required, and an overview that includes the basics of image formation and the concepts of pupils and stops is presented as an appendix. The appendix also includes an introduction to optical aberrations. Some of the equations that are developed in the appendix are referenced in this chapter.

Optically, imaging spectrometers are properly thought of as integrated systems rather than being comprised of the individual subsystems of the fore optics, the spectrometer, and the detector or detector array. The optical design engineer considers the system in its entirety during the design phase to ensure that the spatial, spectral, radiometric, and signal-to-noise ratio goals are accomplished and that the imaging spectrometer is manufacturable. This is a rather obvious observation, but merits emphasis. An imaging spectrometer is a system and not the sum of its parts, even though they will be addressed here through a subsystem analysis. There are designs that do optically decouple the fore optics and the spectrometer, allowing each component to be considered separately, but for many designs, and almost all of the designs currently in broad usage, this will not be the case. The approach taken is to follow the light path through the system and address the fore optics or telescope first, followed by the spectrometer. Individual examples, particularly for the current widely implemented design forms, will be developed in detail, with the goal of equipping the reader with the tools to evaluate any system.

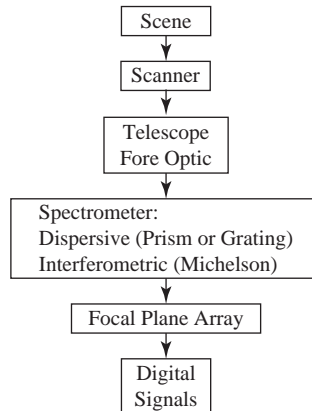


Figure 4.1 The generic optical flow for an imaging spectrometer with some sort of scan mechanism, a telescope fore optic, the spectrometer, and the focal plane array. The spectrometer can be either a dispersive or a interferometric design.

4.1 Telescopes

The telescope, or fore optic, of an imaging spectrometer provides a high quality image at a plane that is the input to the imaging spectrometer. This image plane becomes the object for the spectral sensor and the field is often defined by a spatial mask, such as a slit. The pointing for the system can be accomplished in several ways that will be addressed in Section 4.6. The telescopes are equivalent to the lens of a camera, forming a real image of an object. There is an amazing diversity of telescope designs that could be applied to imaging spectrometers, and we will only address the most basic forms. Additionally, only reflective telescopes which do not suffer from chromatic aberrations are described. There are refractive forms that are used over limited spectral ranges, and their analysis is similar to that used for mirror systems with the added complication of including chromatic effects. First the standard two-mirror Cassegrain telescope will be presented, to provide a basis for going forward, followed by the modification of the Cassegrain that produces the Ritchey–Chrétien form. At that point we will move to the three-mirror forms that are often used, particularly for airborne imaging spectrometers with relatively wide fields of view, and relate them to the simpler forms. Aberration control will be discussed in a qualitative way.

The Cassegrain telescope is one of the basic forms for compound telescopes composed of a positive, parabolic primary mirror and a negative, hyperbolic secondary with the radius of curvature of the primary mirror greater than that of the secondary as shown in Figure 4.2. This is an equivalent reflective form of the Galilean refractive telescope. The use of a parabolic primary is motivated by the perfect imaging of an on-axis point source at infinity for a paraboloid. The refraction and transfer equations are now applied to locate the image and the principal planes. Applying (A.32) to the primary mirror produces

$$n'_1 u'_1 = -h_1 c_1 (n'_1 - n_1)$$

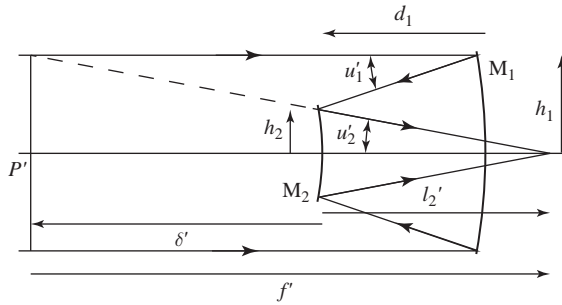


Figure 4.2 The Gaussian optics of a Cassegrain telescope. M_1 and M_2 are the primary and secondary mirrors respectively and the limiting aperture and entrance pupil are at the primary. Notice how the principal plane is quite a distance before the secondary mirror, illustrating how a long focal length can be achieved in a relatively compact telescope.

or

$$u'_1 = -2h_1 c_1 \quad (4.1)$$

since u_1 is zero for an object at infinity and $n'_1 = -1$ for light traveling from right to left. The transfer equation (A.33) yields

$$h_2 = h_1 + d_1 u'_1 = h_1(1 - 2d_1 c_1) \quad (4.2)$$

but note that d_1 is *negative* since the light is traveling from right to left between the primary and secondary mirrors. The refraction equation is applied to the secondary, yielding

$$u'_2 + u_2 = -h_2 c_2 (1 + 1) \Rightarrow u'_2 = 2h_1(c_1 - c_2 + 2d_1 c_1 c_2), \quad (4.3)$$

where $n_2 = -1$ and (4.1) and (4.2) have been substituted. The image location is therefore

$$l'_2 = -\frac{h_2}{u'_2} = -\frac{1 - 2d_1 c_1}{2(c_1 - c_2 + 2d_1 c_1 c_2)}. \quad (4.4)$$

The location of the image space principal plane is given by (A.34) or

$$\delta' = \frac{h_1 - h_2}{u'_2} = \frac{d_1 c_1}{c_1 - c_2 + 2d_1 c_1 c_2} \quad (4.5)$$

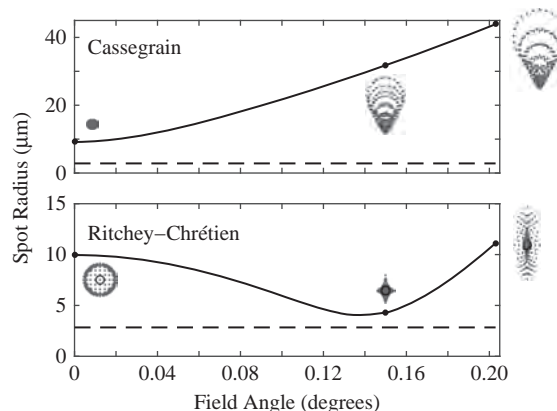
relative to the secondary mirror and the focal length is

$$F = -\frac{h_1}{u'_2} = -\frac{1}{2(c_1 - c_2 + 2d_1 c_1 c_2)}. \quad (4.6)$$

Suppose our application is to build a space-based imaging spectrometer that will go into a sun-synchronous orbit at an altitude of 705 km, an orbit that NASA has used frequently for science missions. A paraxial analysis will guide the preliminary design of the telescope based upon some requirements. The desired ground sample distance is 5 m which corresponds to an IFOV of 7.09 μ rad. An imaging spectrometer with unit magnification will be used and the available focal plane array has a 30 μ m pixel

Table 4.1 Derived paraxial quantities based on the telescope requirements.

quantity	value	quantity	value
u'_1	0.34	u'_2	-0.1182
c_1	-0.34 m^{-1}	R_1	-2.941 m
c_2	-0.693 m^{-1}	R_2	-1.443 m
l'_2	1.345 m	δ'	-2.876 m

**Figure 4.3**

The variation in the image of a point object as a function of field for both Cassegrain and Ritchey–Chrétien telescope designs. Note the change in scale of the ordinates in the two graphs. The spot diagrams correspond to 0° , 0.15° , and 0.203° field angles. The horizontal dashed lines show the diffraction limit and the small circles within the spot diagrams for the Ritchey–Chrétien indicate diffraction limited performance and are not visible at the Cassegrain scale. The root mean square (RMS) spot radius was calculated through exact ray tracing using ZEMAX®.

pitch. The magnification implies that the image of the pixel at the input of the imaging spectrometer is the same size and the telescope focal length is derived based on the pitch and the IFOV yielding 4.23 m. The telescope design is limited to a primary mirror diameter of 1 m due to volume constraints of the rocket fairing, which also limits the length of the sensor payload so the distance between the primary and secondary mirrors is also set to 1 m. The secondary has a diameter of 0.32 m for a central obscuration that is about 10 percent of the area of the primary. The derived paraxial parameters are in Table 4.1.

All surfaces are treated as spherical under the paraxial approximation, while the Cassegrain telescope is composed of aspheres and is analyzed using exact ray tracing. Figure 4.3 shows the results of such an analysis for both Cassegrain and Ritchey–Chrétien forms with 1000 spatial samples for a full field of view of 0.406° . Even though an optical designer would treat the imaging spectrometer as a whole, we will examine the performance of the telescope alone using spot diagrams that should be well contained within a pixel for optimal performance. The performance of the Cassegrain telescope is clearly not adequate since the spot diameter is much larger than the pixel pitch of a detector element. The design suffers primarily from coma. An improved design is achieved

by using the Ritchey–Chrétien form of the Cassegrain with hyperbolic primary and secondary mirrors. The spot diameter for this form is on the order of $20\text{ }\mu\text{m}$, well contained within a pixel. The primary aberrations in this are spherical aberration and astigmatism. ZEMAX® was used to optimize the conic constants that determine the exact form of the hyperboloids for the two designs with the paraxial quantities fixed.

The two-mirror telescope analysis illustrates the difficulty that an optical designer encounters as the field of view is increased. It is desirable to utilize large focal plane arrays for wide fields of view which translate into imagery from a large surface area. Two mirror forms fail as the field of view is extended beyond a rather narrow range and one solution is to add an additional mirror to maintain a sufficient level of aberration control. We will illustrate this process for the space-based system above using a particular three-mirror anastigmat (TMA) design by Dietrich Korsch (Korsch, 1977). An anastigmat is an optical design that is corrected for spherical aberration, coma, and astigmatism. The design presented is *not* fully optimized and would be improved by a true optical designer; however, it serves the purpose of demonstrating the desired level of aberration control that can be achieved.

Korsch's design combined a two-mirror configuration, similar to a Cassegrain telescope, that forms a real image just beyond the primary mirror with a tertiary mirror that reimages the first image to the final image point with approximately unit magnification. This configuration *relays* the intermediate image to the final image. The primary and tertiary mirrors are both ellipsoids and the secondary mirror is a hyperboloid. In one design from Korsch (1977), a small fold mirror was placed at the exit pupil to relay the image to a convenient location as illustrated in Figure 4.4. An advantage of the design is the accessibility of the exit pupil which simplifies the baffling so that stray light can be reduced. As a specific example a focal plane with 1600 spatial pixels corresponding to a full field of view of 0.650° and the $30\text{ }\mu\text{m}$ pitch is utilized. Figure 4.5 shows the aberration control for a Ritchey–Chrétien, optimized for the new focal plane array, and the Korsch TMA, with the Ritchey–Chrétien under performing over the field of view. In contrast, the Korsch TMA is diffraction-limited over the full field and, with the point spread function, well contained within a pixel. A comparison of the Seidel aberrations for the three forms is presented in Table 4.2, showing the aberration coefficients from the two mirror telescope analysis as well as a comparison for the wider field case between a Ritchey–Chrétien and the Korsch TMA.

All of the designs so far have had a central obscuration due to the secondary mirror. In most cases, particularly for airborne systems, imaging spectrometers utilize unobscured

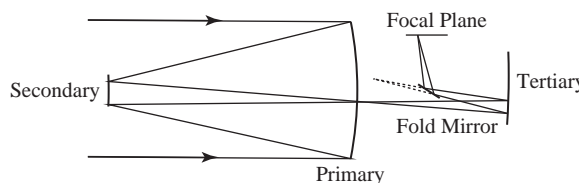


Figure 4.4 Illustration of an on-axis TMA adapted from Korsch (1977). The fold mirror is located at the exit pupil.

Table 4.2 Seidel coefficients in waves at 550 nm for the full field in the two cases calculated using ZEMAX®. RC is an abbreviation for Ritchey–Chrétien.

Aberration	0.406°		0.650°	
	Cassegrain	RC	RC	Korsch
Spherical	0.7815	1.6176	0.4598	−0.2796
Coma	−11.1815	0.3338	−0.6121	−0.0572
Astigmatism	1.6102	1.8659	4.7420	0.0002
Distortion	−0.0547	−0.0491	−0.2029	−1.8702
Field Curvature	1.0074	1.0074	2.5821	0.0000

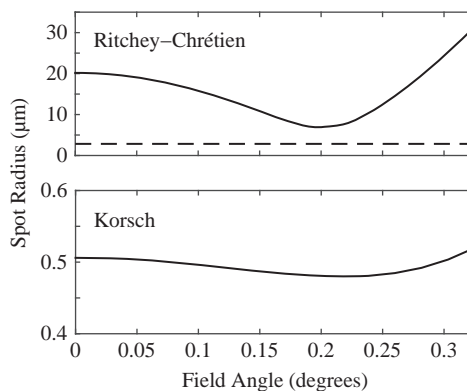


Figure 4.5 The variation in the image of a point object as a function of field for Ritchey–Chrétien and Korsch telescope designs. Note the change in scale of the ordinates in the two graphs and that the Ritchey–Chrétien modeled here has a wider field of view than the one modeled in Figure 4.3. The horizontal dashed line in the top graph shows the diffraction limit and both graphs are the root mean square (RMS) spot radius. Calculated through exact ray tracing using ZEMAX®.

forms, often off-axis TMAs. These designs are advantageous in that, since they don't have a central obscuration, more light is transmitted, allowing for a reduced aperture size with an equivalent signal-to-noise ratio. Additionally, well-designed unobscured forms are more efficient at the transmission of different spatial frequencies. We will not go into this latter point in detail, but briefly, the transmission and detection of the spatial frequencies through any optical system are determined using Fourier analysis, where the signal is decomposed into the various spatial frequency contributions and quantified by the modulation transfer function (MTF), defined as the ratio of the image modulation to the object modulation at all spatial frequencies. See Goodman (2005) for a full description. The MTF for an obscured telescope is decreased in the middle frequencies in comparison to an unobscured form with a resulting increase in the size of the point spread function.

An off-axis TMA can be configured in several ways depending on the location of the limiting aperture and whether or not it is relayed as in the Korsch TMA. One advantage

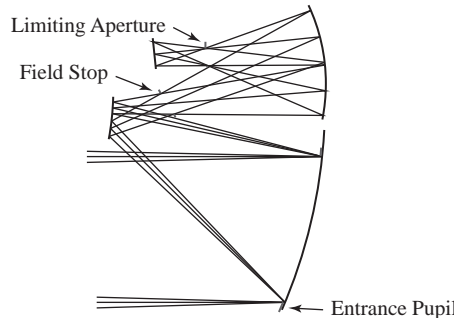


Figure 4.6 Schematic of a relayed Cook three-mirror anastigmat. Both the primary and the tertiary mirrors are ellipsoids and the secondary mirror is a hyperboloid similar to the Korsch TMA. Adapted from Cook (1981).

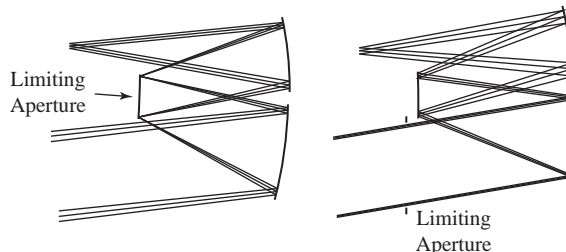


Figure 4.7 Schematic of two non-relayed three-mirror anastigmat designs. The left design is by Wetherell and Womble (1980) with the secondary mirror being the limiting aperture and is known as a three mirror compact. The right design is another one from Lacy Cook with the limiting aperture in front (Cook, 1988). Adapted from Cook (1992).

of these forms is their small size relative to the on-axis forms such as the Ritchey–Chrétien and Korsch telescope examples. This size reduction comes at the price of high complexity, with the three mirrors being aspheres with alignment challenges due to the required tilting and decentering with respect to the optical axis. Another key advantage is that these TMAs can be designed with low F-numbers while maintaining the required high degree of aberration control. Figure 4.6 illustrates a relayed off-axis TMA designed by Lacy Cook, where the primary and secondary mirrors form a Cassegrain-type telescope with an intermediate image at a field stop that is relayed by the tertiary mirror to the final image (Cook, 1981). Both the intermediate and the final images are accessible, which facilitates baffling, as is the limiting aperture so that it can be used as a cold stop to limit the irradiance in the final image to be from the object space alone.

Non-relayed TMAs have several advantages over the relayed forms. They are smaller for both the optical elements and the space in-between elements for an equivalent F-number since no intermediate image is required. Additionally, the total optical power is reduced, making aberration control simpler and enabling a larger field of view. Figure 4.7 shows two designs that differ primarily by the placement of the limiting aperture. In the left design the secondary mirror is also the limiting aperture and the

design is telecentric in the image space and has a virtual entrance pupil located behind the optical system. The right design has a limiting aperture in front of the primary, which also forms a real entrance pupil while the exit pupil is virtual but close to the telescope. The real entrance pupil is advantageous for systems with window constraints. However, the virtual entrance pupil design has superior aberration control for equivalent systems. These off-axis telescopes are challenging to both design and manufacture but are highly performing. A review article by Lacy Cook is recommended for a fuller appreciation of the diversity of designs and their relative performance (Cook, 1992).

The field of view requirements of the current imaging spectrometers are well served by the telescope designs presented here as well as other designs. For example, there are various Cook designs with fields of view up to 36° and even larger that have sufficient performance to be used with imaging spectrometers (see Cook and Silny, 2010 and the references contained therein). The optical designer creates an integrated spectral sensor where the pupils from the telescope and the spectrometer are well matched with the limiting aperture associated with the spectrometer. The aberration control challenge rests more with the spectrometer than the fore optic with telescope designs being close to diffraction limited in many cases. The size of the limiting aperture is also a critical design component that determines the amount of light that is transmitted through the system. This will be addressed in detail for the full imaging spectrometer in Section 4.2.1 and for performance modeling in Chapter 5.

4.2

Imaging Spectrometer Common Concepts

All optical measurements can be modeled through the application of the *measurement equation*. This model is an idealization, as are all models, of the optical system being analyzed, but it is extraordinarily useful for both general understanding and detailed quantitative performance analysis. It has been used in one form or another for measurement analysis in instrumental spectroscopy and was fully developed during the last century with seminal contributions from Pierre Jacquinot and his collaborators. In the context of radiometry, the utility of the measurement equation has been demonstrated by Henry Kostkowski and Fred Nicodemus at NIST (Kostkowski and Nicodemus, 1978).

The measurement equation is the system model that describes the conversion process of at-aperture radiance to the measured signal. The signal recorded at the detector is determined by the optical and electronic properties of the imaging spectrometer. For example, how much radiance is accepted by the instrument? How does the imaging spectrometer separate the light into the different bands? How efficient are the individual optical elements in transmitting the flux through to the focal plane array? How efficient is an individual detector element and its associated electronic readout circuitry in converting the incident flux into an electronic signal? These questions and others are modeled using the measurement equation.

Detectors, whether they measure photons or a thermal change, convert the flux falling upon them into an electronic signal. The flux responsivity R_Φ is defined as

$$R_\Phi(x, y, \theta, \phi, \lambda) \equiv \frac{dS(x, y, \theta, \phi, \lambda)}{d\Phi(x, y, \theta, \phi, \lambda)}, \quad (4.7)$$

where S is the measured signal and all of the quantities are a function of the position, direction, and spectral content of the rays that compose the at-aperture radiance. It should be clear from the context whether we are discussing either signal or the optical path length even though S is used to signify both. Writing the responsivity as $R_\Phi(x, y, \theta, \phi, \lambda)$ emphasizes that it varies as a function of position and direction for the rays that fill the system as well as having the designed spectral discrimination. The measurement is modeled by converting (4.7) to

$$dS(x, y, \theta, \phi, \lambda) = R_\Phi(x, y, \theta, \phi, \lambda) L_\lambda(x, y, \theta, \phi, \lambda) \cos \theta dA d\omega d\lambda, \quad (4.8)$$

where L_λ is the at-aperture spectral radiance and (2.57) has been applied.

The flux responsivity is the factor that relates the measured signal to the input radiant energy for an imaging spectrometer. Contained within it is, at a minimum, the optical efficiency of the various elements of an imaging spectrometer, the function that describes the spectral discrimination, and the efficiency of the detector for the conversion of flux to an electronic signal. The geometrical term $\cos \theta dA d\omega$, which describes the amount of flux that is transmitted through a lossless and non-diffraction-limited sensor from a source, is also a critical component of the measurement equation. Each of these terms is applicable to any imaging spectrometer regardless of its design, and will be defined and described in some detail.

The responsivity is a system quantity that will be decomposed into the contributions that are both optical and electronic in origin. These are largely separable, although not completely. For example, the response of a detector element may differ for non-uniform irradiance as a function of location and incident direction on the pixel. Another example is that the detector response may display non-linearities as the irradiance changes. The first example is not easily measured while the second is initially addressed in the sensor design and secondarily during calibration.

4.2.1

Étendue and Radiance

The amount of flux that any optical instrument can accept is proportional to the geometrical factor known as the étendue, or optical throughput, given by

$$U \equiv \int_A \int_\omega \cos \theta dA d\omega, \quad (4.9)$$

where the appropriate area A and solid angle ω remain to be defined. The concept of étendue will be developed for a generic pair of apertures and then for an optical system. In the discussion that follows it is assumed that all of the apertures are large compared to the wavelength so diffraction effects are negligible or, for the infinitesimal case, diffraction is ignored.

Figure 4.8 illustrates two arbitrary apertures of areas dA_1 and dA_2 in air ($n = 1$) with light flowing from the first to the second aperture. In the radiometry literature the rays

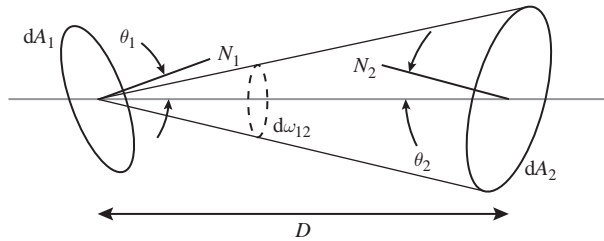


Figure 4.8 The ensemble of rays that join the points on the two differential apertures dA_1 and dA_2 define the elementary beam of radiation. N_1 and N_2 are the normal vectors for the two apertures. Figure adapted from Nicodemus and Kostkowski (1976).

that connect the two apertures comprise the elementary beam of radiation (Nicodemus and Kostkowski, 1976). At the first aperture the flux is given by

$$d\Phi_1 = L_1 \cos \theta_1 dA_1 d\omega_{12} = L_1 \cos \theta_1 dA_1 \frac{\cos \theta_2 dA_2}{D^2}, \quad (4.10)$$

where θ_1 and θ_2 are the angles between the normal and the line of length D connecting the centers of the two apertures, and $d\omega_{12}$ is the solid angle subtended by the second aperture from dA_1 . Recall that the differential solid angle $d\omega$ is the projected area $\cos \theta dA$ divided by the distance squared between the two apertures. Similarly, the flux at the second aperture is given by

$$d\Phi_2 = L_2 \cos \theta_2 dA_2 d\omega_{21} = L_2 \cos \theta_2 dA_2 \frac{\cos \theta_1 dA_1}{D^2}, \quad (4.11)$$

where $d\omega_{21}$ is the solid angle subtended by the first aperture from dA_2 .

These two equations, (4.10) and (4.11), have profound consequences. First, if the medium between the two apertures is lossless, uniform, and isotropic then the flux through the first aperture is the same as the flux through the second yielding

$$L_1 = L_2 \quad (4.12)$$

and consequently the radiance is geometrically invariant. Next, suppose the two apertures have some finite size so that the flux is obtained through

$$\Phi = \int_A \int_{\omega} L(x, y, \theta, \phi) \cos \theta d\omega dA, \quad (4.13)$$

where the radiance is specified at the coordinate (x, y) in either aperture for the directions (θ, ϕ) to the other one. Further, assume that the radiance is uniform and isotropic so that it can be removed from the integral in (4.13) yielding

$$\Phi = L \int_A \int_{\omega} \cos \theta d\omega dA = L \int_U dU = LU, \quad (4.14)$$

where the differential and total étendue have been identified. Additionally, for the elementary beam both $d\Phi$ and L are constant and therefore the differential étendue $\cos \theta d\omega dA$ must also be a constant.

The differential étendue is strictly a function of the ray geometry of the elementary beam and it isn't altered by attenuation. This implies that when the differential étendue for many elementary beams is summed through (4.9) it must also be invariant as long as no rays are added or subtracted, and therefore the total étendue is also invariant for a beam through an optical system. Also, if a finite-sized aperture is filled by uniform and isotropic radiance so that the beam is identical for every point (x, y) and fills every element of solid angle $d\omega$ in the same way, then (4.9) is separable, yielding

$$U = \left(\int_A dA \right) \times \left(\int_{\omega} \cos \theta d\omega \right) = A\Omega, \quad (4.15)$$

where Ω is the projected solid angle introduced in Chapter 2. This leads to the étendue sometimes being called the A-omega or area-solid angle product. Often, for quick calculations (4.15) is written as

$$U \approx \frac{A_1 A_2}{D^2} \quad (4.16)$$

where A_1 and A_2 are the areas of the two apertures centered on the optical axis with their normal vectors parallel and D being the axial distance between them. Equation (4.16) is reasonably accurate when the lateral dimensions of the two areas, such as the diameters for circular apertures, are about a tenth of the distance D .

Étendue is also a conserved quantity in any optical system that cannot be increased or decreased by the addition of lenses, unless an obstruction is added so that some rays are subtracted. This will be demonstrated in a couple of different ways. First, Figure 4.9 illustrates a thin lens that images an object ΔA onto an image $\Delta A'$. Consider only an area Δa at the lens that is close enough to the optical axis so that the paraxial approximation is reasonably accurate. For a small area ΔA the solid angle subtended by the object is $\Delta A/l^2$ and for the image it is $\Delta\omega' = \Delta A/l'^2$. The linear magnification is given by (A.50) and the magnification of the area is $(l'/l)^2$ from (A.42). The object side étendue is calculated using (4.15), yielding

$$U = \Delta a \frac{\Delta A}{l^2}$$

and similarly for the image side leading to

$$U' = \Delta a \frac{\Delta A'}{l'^2} = \Delta a \frac{m^2 \Delta A}{l'^2} = U,$$

demonstrating étendue conservation at least paraxially.

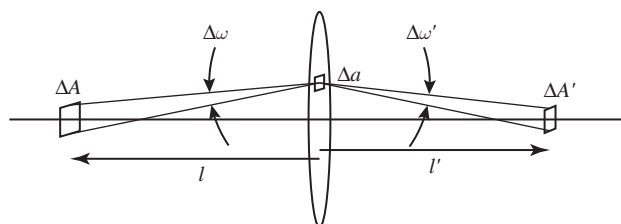


Figure 4.9

Paraxial conservation of étendue.

The second approach is to utilize the optical system illustrated in Figure A.11. Recall from the discussion in Section A.4 that the entrance and exit pupils are conjugates with all the rays from the object to the image passing through both. The flux through the system has already been characterized by (A.44) and (A.45) for circular entrance and exit pupils, and, assuming a lossless, uniform, and isotropic system where $L = L'$ from (4.12), the object- and image-space fluxes are equal, resulting in

$$\pi dA \sin^2 \theta_m = \pi dA' \sin^2 \theta'_m \quad (4.17)$$

which is just the equality between the object and image space étendues, and the derivation of (A.44) is the same as that used for (4.14). Again, the conservation of étendue, being strictly geometric, does not change for transmission losses. The areas used for the calculation are a limiting aperture, such as the entrance or exit pupil, and an area at an appropriately chosen field point, which can be at the object, the final image, or at an intermediate image. For a simple calculation the path between the two apertures should not be interrupted by any other optical element. For example, the exit pupil and a detector element form one such pair. Another example is the object area that is imaged onto a detector element and the entrance pupil. The field area is defined by the size of a detector element or its image.

Imaging spectrometers used from airborne and space-based platforms image an object from infinity onto a focal plane array detector element. There is typically an intermediate image location as well. For example, in a dispersive system there will be a slit located at the image plane of the telescope. For a spectrometer of unit magnification the slit width is equivalent to the width of a detector element. Figure 4.10 illustrates the telescope, in this case replaced by the principal planes, to demonstrate that the solid angle subtended by the portion of the slit that corresponds to the dimensions of the detector element is the same at each point of the entrance pupil projected on the object principal plane. The width of a detector element is on the order of tens of microns, and much less than the focal length, so the solid angle ω is simply A_d/f'^2 , where A_d is the area of the detector element at the slit, and the étendue is $A_e A_d/f'^2$. Note that the solid angle is constant across the object principal plane.

The telescope étendue associated with one detector element can equivalently be calculated from the solid angle subtended by the entrance pupil as viewed from the slit or

$$U = A_d \int_{\omega} \cos \theta d\omega = A_d \pi \sin^2 \theta_m \quad (4.18)$$

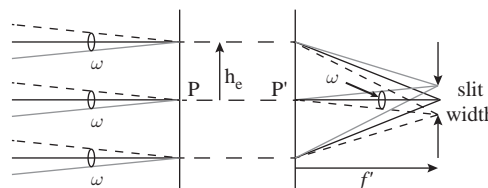


Figure 4.10 The solid angle corresponding to a detector element for a telescope focused at infinity under the paraxial approximation. The slit width is exaggerated.

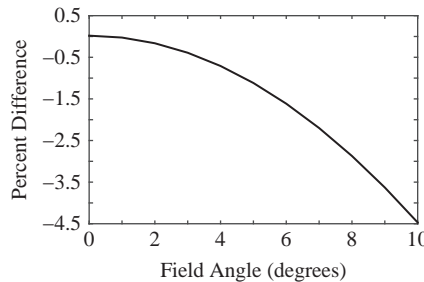


Figure 4.11 The percentage difference for on-axis versus off-axis étendue for an F/2.5 system with an exit pupil diameter of 2.5 cm located 4.7 cm from the detector element with a $30 \mu\text{m}$ pitch.

from (4.15), where θ_m is the angle from the optical axis to the marginal ray. The small size of the detector element is infinitesimal compared to the dimensions used to calculate the solid angle ($\sim A_e/f^2$) and therefore (4.18) is accurate for the on-axis case. This is alternatively expressed in terms of the F-number as

$$U = A_d \frac{\pi}{4N^2}, \quad (4.19)$$

where (A.53) and (A.54) have been used. Although this example was developed for clarity in terms of the telescope étendue, any optical system, such as a complete imaging spectrometer, is described by principal planes and pupils, so (4.18) and (4.19) apply there as well as for a system focused at infinity with a circular limiting aperture.

The telescope example above described the on-axis étendue. How accurate is this for an off-axis image location with an object at infinity? The right side of Figure A.14 shows the geometry for the exit pupil and an off-axis area dA' where the image forms. In this case dA' corresponds to a detector element of area A_d at the focal plane. These two apertures, the exit pupil and the pixel area, are used to define the étendue of the system. The étendue is numerically calculated for different field angles by integrating the differential étendue given by

$$dU_j = \frac{dA_j \cos \theta_j A_d \cos \theta_j}{d^2} \quad (4.20)$$

over the pupil where dA_j is an area element of the exit pupil, θ_j is the angle between the normal vectors to both the pupil area element and the pixel area A_d and the line connecting the two, and d is the distance between the two areas. The numerically calculated U for the different field angles is compared to the on-axis étendue calculated using (4.19). Figure 4.11 demonstrates the reduction in U as the field angle increases.

4.2.2 The Measurement Equation

Figure 4.12 is an overview of the process of conversion of at-aperture radiance to the measured signal, which is uncalibrated. The calibration process, where raw data are converted to physical units, will be addressed in detail in Chapter 5, but the measured signal is *always* degraded from the detailed at-aperture radiance due to the limitations

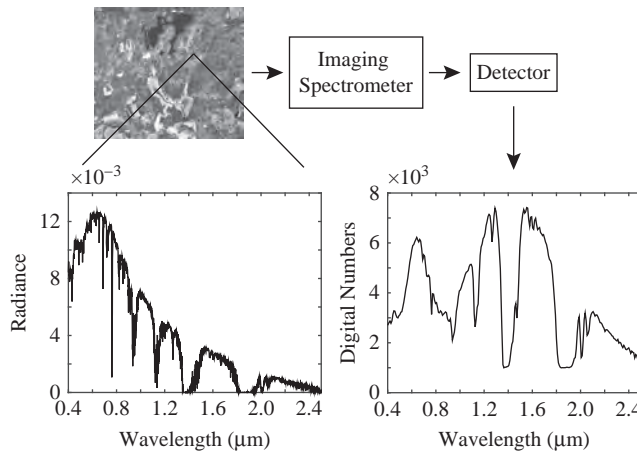


Figure 4.12 The conversion of radiance, in units of $\text{W}/\text{cm}^2\text{sr}/\mu\text{m}$, to digital numbers for a single location in a scene. The measured signal is quite different from the radiance due to the wavelength dependent effects of spectral sampling, optical transmission, and detector response and offset.

imposed by the physical processes of optical transmission, segregation of light into the different wavelength bands, and detection efficiency as a function of spectral unit. This is fundamentally a question of resolution, since any spectroscopic measurement bins the spectral information into channels of some width. The resulting signal typically has remarkably different characteristics from the actual at-aperture radiance.

The form of the measurement equation that will be used to describe the conversion of radiance to signal for an imaging spectrometer is developed from (4.8) by integration over the spectral range of interest to yield

$$S(A, \omega, \delta\lambda, \lambda_c) = \int_{\delta\lambda} \int_A \int_{\omega} R_{\Phi} L_{\lambda} \cos \theta \, d\omega \, dA \, d\lambda, \quad (4.21)$$

where ω is the solid angle, A is the entrance pupil area, $\delta\lambda$ is the wavelength band that is transmitted by the instrument, and λ_c is the center wavelength of the spectral response function that describes the bandpass of the instrument. It is understood that both R_{Φ} and L_{λ} vary with position, direction, and wavelength. The spectral unit that will be used for illustrative purposes will be the wavelength, but it could be another unit whose selection depends upon the type of imaging spectrometer under scrutiny. Comparing (4.21) to (4.13) shows that the signal modeled using the measurement equation is the flux received by the instrument weighted by the responsivity.

The measurement equation is simplified through several assumptions. The first is that the spectral radiance is uniform and isotropic so that it and the étendue of the imaging spectrometer are separable as in (4.14). The responsivity will also be assumed to be independent of the geometry and only dependent upon the spectral interval. This isn't as poor an assumption as one might think, since the transmission for any ray will be similar to any other for uniform and isotropic refractive materials and for mirrors. It was shown above that a highly performing design, where the aberrations have been minimized, is

one where all of the rays have traveled the same optical path. From (A.11), the optical path for a given ray is the sum over the product of the index of refraction and the distance within each material encountered by the beam. There is some variation in nd between particular rays for each material; however, for most systems, the difference in the distance traveled through any refractive material and the absorption within the material are both small so the geometric dependence of the transmission can be ignored. Also, many systems are composed primarily of mirrors where the reflective losses are very similar for the range of reflectance angles within the optical beam for any surface. Vignetting, the physical blockage of some rays due to an intrusion into the optical path, will also be minimized and would be treated as a modification to the étendue. Additionally, the geometric dependence of the response by a particular detector element is assumed to be negligible.

All imaging spectrometer designs separate the radiance into spectral bands and each band is represented by a transmission function. In a non-imaging dispersive monochromator used for spectroscopic analysis the wavelength is set to some value and the spectrometer transmits a distribution of wavelengths about the wavelength setting to a detector. The function that describes that distribution is represented by $T(\lambda - \lambda_c)$ where λ_c is the monochromator setting, typically corresponding to the center wavelength. The transmission function is *peak* normalized rather than area normalized as in a statistical distribution function. T mathematically describes the spectral discriminatory action of the spectrometer and is modeled in the instrument design but is ultimately known through measurements during the sensor characterization. An imaging spectrometer differs from a monochromator in that the entire spectrum for a particular spatial sample is recorded at once. This could be in a spectrograph for a dispersive system or by an interferogram for an interferometer.

Incorporating the approximations outlined above, the measurement equation for a single spectral band is now written as

$$S(\lambda_c) = \int_0^{\infty} U[L_{\lambda}(\lambda)\tau(\lambda)\eta(\lambda)]T(\lambda - \lambda_c) d\lambda, \quad (4.22)$$

where $\tau(\lambda)$ is the system transmission expressed as a fraction and $\eta(\lambda)$ is the response function of the detector, both as a function of wavelength. The detector response can be modeled in a variety of ways including, for example, as the quantum efficiency of the detector material, in which case it is the ratio of photoelectrons generated to the incident photons with the radiance proportional to photons per second rather than watts. It can also be a conversion function from flux to voltage with the amount of charge due to the irradiance stored in a capacitor in the readout circuitry. Aside from the étendue, which has negligible spectral dependence, the spectral radiance is weighted by the system transmission and the detector response function, both typically slowly varying with wavelength, and then integrated over the transmission function. This yields a single value for the signal corresponding to λ_c . The étendue is a constant for a given band, but, depending upon the type of imaging spectrometer, it can vary a small amount from band to band as the geometry changes. Equation (4.22) is also multiplied by the integration time t_{int} for one measurement

cycle since the value is proportional to the accumulated charge during one period to yield

$$S(\lambda_c) = t_{\text{int}} \int_0^{\infty} U[L_{\lambda}(\lambda)\tau(\lambda)\eta(\lambda)]T(\lambda - \lambda_c) d\lambda. \quad (4.23)$$

Equation (4.23) is mathematically similar to a convolution given by (2.127) with the transmission function $T(\lambda - \lambda_c)$ playing the role of $g(x - y)$, except that the order of the two variables has been reversed. To utilize the powerful convolution formalism a new function P , which is the reverse of the transmission function, is defined such that

$$P(\lambda_c - \lambda) = T(\lambda - \lambda_c) \quad (4.24)$$

with P known as the *instrumental profile*. In the imaging spectrometer literature, P is typically called the spectral response function or SRF. Including this change the final form of the measurement equation is

$$S(\lambda_c) = t_{\text{int}} \int_{-\infty}^{\infty} U[L_{\lambda}(\lambda)\tau(\lambda)\eta(\lambda)]P(\lambda_c - \lambda) d\lambda. \quad (4.25)$$

At first glance (4.24) appears to be merely a mathematical construct but it has a concrete physical meaning. In traditional spectroscopy, where the line spectrum due to emission or absorption is measured, the instrumental profile at a particular wavelength is directly determined by scanning the monochromator over a monochromatic source such as a very narrow atomic emission line as illustrated in Figure 4.13. An asymmetric instrumental profile is used to emphasize the process with the measured peak at the wavelength of the monochromatic line, 426 nm in this case. Mathematically a convolution involves scanning one function across another but notice that the scanned function,

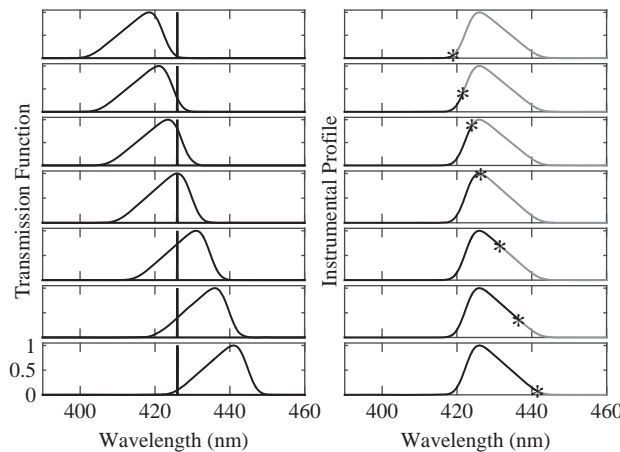


Figure 4.13 Illustration of the measurement of the instrumental profile using a monochromator where the transmission function is wavelength scanned across a monochromatic source at 426 nm represented by a delta function. The asterisks mark the measured points as the monochromator is scanned.

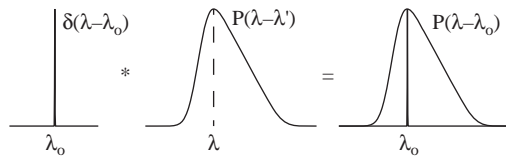


Figure 4.14 Mathematical representation of the process illustrated in Figure 4.13.

$T(\lambda - \lambda_c)$ in this case, is the *reverse* of the convolved function $P(\lambda_c - \lambda)$. In other words, $P(\lambda_c - \lambda)$ is mirrored, producing $T(\lambda - \lambda_c)$, before scanning it across the line function.

The convolution of a delta function representing the narrow emission feature from an atomic line source and the instrumental profile is given by

$$\begin{aligned} S(\lambda) &= \int_{-\infty}^{\infty} L_{\lambda}(\lambda') P(\lambda - \lambda') d\lambda' \\ &= \int_{-\infty}^{\infty} \delta(\lambda' - \lambda_o) P(\lambda - \lambda') d\lambda' \\ &= P(\lambda - \lambda_o), \end{aligned} \quad (4.26)$$

where (4.25) has been applied with τ , η , U , and t_{int} set equal to one. In the convolution notation (4.26) is

$$P(\lambda - \lambda_o) = \delta(\lambda - \lambda_o) * P(\lambda), \quad (4.27)$$

which is schematically illustrated in Figure 4.14. The important point is that the convolution of a delta function and any other function is simply the reproduction of the other function, in this case shifted by the amount λ_o .

In the case of an imaging spectrometer that measures a full spectrum at once, a tunable, quasi-monochromatic source is scanned to directly measure the transmission function. The source in this case is spectrally much narrower than the instrumental profile of the imaging spectrometer being characterized but is usually not monochromatic in the same sense as an atomic line source, although a tunable laser is a viable monochromatic option. In practice, the distinction between T and P is not an issue since, by design, the instrumental profile is a symmetric function in most cases.

4.2.3

The Effect of the Instrumental Profile

The impact of the instrumental profile is to limit our ability to recover the true spectrum of the at-aperture radiance in detail. Considering only the spectral sampling, the uncalibrated spectrum in Figure 4.12 demonstrates how the spectral signature is blurred due to the finite extent of the spectral response function. A perfect instrument, from the point of view of resolution, would be one for which the instrumental profile is a delta function, which is obviously impractical given that it would require an infinite number of infinitesimal detector elements to record a spectrum with essentially no signal in each! The width of P is characterized by a figure of merit known as the *resolving power* defined as

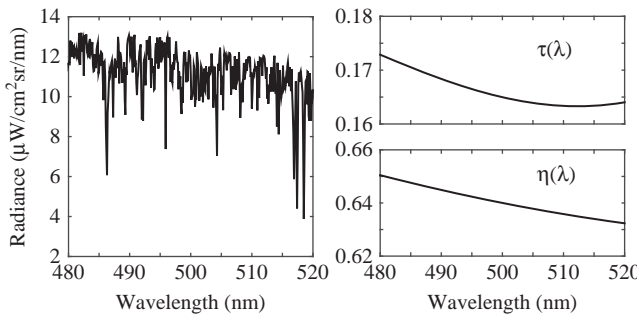


Figure 4.15 A high-resolution at-aperture radiance spectrum and both optical and quantum efficiencies over the 480 nm to 520 nm range.

$$R \equiv \frac{\lambda}{\delta\lambda} = \frac{\tilde{\nu}}{\delta\tilde{\nu}}, \quad (4.28)$$

where either $\delta\lambda$ or $\delta\tilde{\nu}$ is known as the *limit of resolution* for the band expressed in terms of the wavelength or the wave number. The limit of resolution is defined as the full width at half maximum of the instrumental profile. The resolution is a more realistic figure of merit for a traditional monochromator where resolving powers approaching 1,000,000 have been achieved using, for example, a Fabry–Perot interferometer to resolve the hyperfine structure of an atom. Imaging spectrometers are low-resolution instruments with R values on the order of 40 to 500, and the limit of resolution is used in practice to describe the resolving power, since most imaging spectrometers, although not all, are designed to have a constant $\delta\lambda$ or $\delta\tilde{\nu}$.

The measurement equation will be illustrated for a single channel with an instrumental profile represented by a peak normalized Gaussian function with a center wavelength at 500 nm and a limit of resolution of 10 nm. The imaging spectrometer images a solar illuminated area on the surface that corresponds to the projected pixel area with the light passing through the atmosphere twice and attenuated by both absorption and scattering as shown on the left side of Figure 4.15. The system has optical and quantum efficiencies given by $\tau(\lambda)$ and $\eta(\lambda)$ respectively, both of which are slowly varying with wavelength as shown on the right of Figure 4.15. The radiance weighted by $\tau(\lambda)$ and $\eta(\lambda)$ is illustrated in Figure 4.16 which also shows the impact of the instrumental profile. Finally the étendue is calculated to be $7.85 \times 10^{-7} \text{ cm}^2\text{sr}$ based upon an F/3 system with a 30 micron pixel pitch. The measured signal, expressed as the number of photoelectrons generated in the detector material, is 2.49×10^5 electrons for an integration time of 0.01 seconds.

4.3

Dispersive Imaging Spectrometer Fundamentals

Currently the dominant design forms for imaging spectrometers rely upon the angular separation of light into the different wavelengths, and much of the following discussion will focus on their details. The term “dispersion” refers to the variation in the refractive

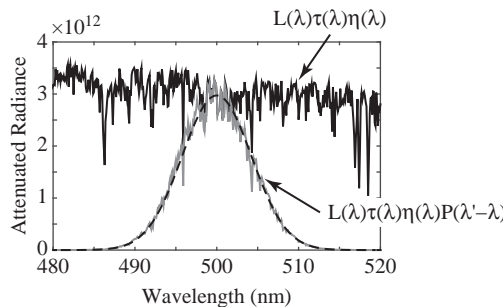


Figure 4.16 The at-aperture radiance, in units of photons/s/cm²sr/nm, is reduced by both τ and η and then multiplied by a spectral response function centered at 500 nm. The signal, in electrons due to the conversion by η , is the area under the curve and given by (4.25). The dashed line represents the scaled instrumental profile.

index of an optical material as a function of wavelength, which leads to angular spreading of light when, for example, it is incident on an optical material at some angle to the surface normal with the transmitted portion obeying Snell's law. In this section, dispersive designs have a broader context with forms that rely upon dispersion and use prisms for diffractive elements to separate the light into the wavelength bands. The second method exploits the wave nature of light through the effects of diffraction and interference where the wavefront is divided spatially through the action of a diffraction grating introducing the required path difference. Both methods of separation require a slit as a spatial mask at a field point in order to limit the range of angles that pass through the dispersing element, and, in the grating case, to provide the required coherence. The concepts that are common to all dispersive designs will be described followed by an analysis of the different optical forms currently utilized.

4.3.1 Development of the Instrumental Profile for a Slit Spectrometer

Both prism and grating systems angularly separate the different wavelengths and a common mathematical description can be applied to both without going into the details of the disperser itself. Figure 4.17 illustrates a generic imaging spectrometer with the dispersing element unspecified. An area of the surface is imaged by the telescope onto the slit of width w . Light from the slit is collimated by the first lens so that the wavefront that interacts with the dispersing element is planar. Following angular dispersion in the dimension that is perpendicular to the long side of the slit, the light is refocused onto the focal plane array with each square detector element having a width given by the pixel pitch p . The angle labeled θ_1 is fixed while θ_2 changes as a result of the action of the disperser as it provides the required separation of the light into the different bands. In this simple example the imaging spectrometer is an afoocal system, as described in Section A.6, with the focal lengths corresponding to the first and second collimating optics equal and the system having unit magnification from (A.70).

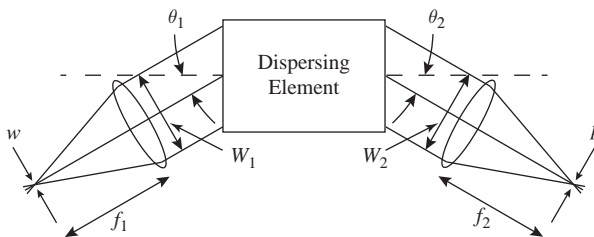


Figure 4.17 A generic imaging spectrometer is depicted with the dispersing element unspecified. The dashed lines represent the as yet undefined normals to the dispersing element with θ_1 and θ_2 being the angles between them and the collimated beams of widths W_1 and W_2 . The slit on the left side, whose long axis is out of the illustration plane, has a width w and a single detector element is on the right side with a pitch p .

The action of the dispersing element is to redirect light at a particular wavelength into a predictable angle. The resolution is related to the width of the slit, the spread of the light due to aberrations and diffraction, and the pixel pitch. A band centered on λ_c with a limit of resolution of $\delta\lambda$ will correspond to the angle θ_2 with an angular spread of $\delta\theta_2$ where θ_2 is the angle between the dispersing element normal and the wavefront direction corresponding to λ_c following dispersion. The angular dispersion D_θ is defined as

$$D_\theta \equiv \left. \frac{\partial\theta_2}{\partial\lambda} \right|_{\theta_1}, \quad (4.29)$$

with θ_1 fixed. D_θ will often have some dependence upon the center wavelength of the particular spectral channel. Examining the effect of (4.29), if the imaging spectrometer images a Lambertian calibration source the entrance slit will be uniformly illuminated. The first collimating lens produces plane waves at the slightly different angles that correspond to the width of the slit. For now we are not concerned with the slit length since the dispersion is perpendicular to the long slit dimension. If the dispersing element were replaced with a flat mirror the slit would be imaged as w' at the focal plane of the second collimating lens. The result of the dispersing element is to smear the slit image out into the different wavelengths. The spectral sampling is then dependent on the pixel pitch of a detector element. If we ignore any other processes the image of the slit width and the pixel pitch are what determine the spectral resolution.

The optical elements between the slit and the pixel impact the instrumental profile through broadening of the slit image. For now the imaging spectrometer is assumed to be diffraction limited with aberrations minimized. For a traditional monochromator with large F-numbers, diffraction limited performance is a good assumption. Imaging spectrometers have lower F-numbers to increase the étendue for better signal-to-noise performance and aberrations are not negligible and will be addressed below. The reader interested in aberration control for a non-imaging spectrometer is directed to James (2007).

First, what is meant by a diffraction limited system in this context? From the discussion in the appendix, an ideal image is formed when a spherical wave converges to a

Gaussian image point from the exit pupil of the optical system. If the aberrations are well controlled then this idealization is realized to a good approximation. It was shown in Chapter 2 that diffraction from any aperture can be calculated through the application of Huygens' construction. In this case, the aperture under consideration is the exit pupil of the system, with the limiting aperture being the outer dimensions of the dispersing element. The generic spectrometer design will be further constrained by specifying that the dispersing element is mounted at or a little less than one focal length away from both collimating lenses with the consequence that the exit pupil is virtual and very far away from the focal plane. If the limiting aperture is exactly one focal length away the system is known as *telecentric* with the exit pupil at infinity, an important design configuration that will be addressed in some detail below. With this condition the diffraction pattern at a point on the focal plane is described by the Fraunhofer case.

We'll assume that the dispersing element has a rectangular geometry of width W and height H , as illustrated in Figure 2.49 from Problem 4 in Chapter 2, where the reader showed that the diffraction pattern at a point on the focal plane is given by

$$E(\theta, \phi) = E(0, 0) \left(\frac{\sin \alpha'}{\alpha'} \right)^2 \left(\frac{\sin \beta'}{\beta'} \right)^2 \quad (4.30)$$

with

$$\alpha' = \frac{1}{2} kH \sin \phi$$

and

$$\beta' = \frac{1}{2} kW \sin \theta,$$

where k is the wave vector given by $2\pi/\lambda$. The primes are included to distinguish between the angular width of the long axis of the slit, given by α , and the angular width of a pixel, given by β , as illustrated in Figure 4.18. The irradiance given by (4.30) will be modified for the current geometry. Considering only the dimension perpendicular to the long slit axis, β' is rewritten as

$$\beta' = \frac{\pi W_2}{\lambda} \sin \theta \approx \frac{\pi W_2}{\lambda} \frac{x}{f_2} = \frac{\pi x}{e}, \quad (4.31)$$

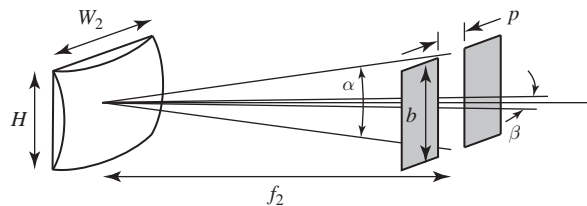


Figure 4.18 After dispersion, the light at a particular dispersion angle is focused onto a column of pixels of width p and height b equal to the number of pixels parallel to the long axis of the entrance slit times the pixel pitch. The angular width of the long axis of the slit is α and the angular width of a pixel on the optical axis is β . The pixel pitch is exaggerated.

where the small angle approximation has been used so that $\sin \theta$ is approximately $\tan \theta$ with x measured from the optical axis, and $e \equiv \lambda f_2 / W_2$. The width W has been replaced by W_2 since it is the projected width of the diffraction element that forms one side of the exit pupil. The one-dimensional diffraction function becomes

$$D(x) = \left(\frac{\sin \frac{\pi x}{e}}{\frac{\pi x}{e}} \right)^2 = \text{sinc}^2 \left(\frac{\pi x}{e} \right), \quad (4.32)$$

where the on-axis irradiance has been set to one since we are concerned with the functional form of the wavelength spread. As noted in Chapter 2, it can be shown that (4.32) is peak normalized by applying L'Hospital's rule, and the first minimum is at $x = e$. For convenience the width of (4.32) will be defined as e rather than the full width at half maximum, which is $0.88e$, and the angular width ϵ of the diffraction function, again applying the small angle approximation, is

$$\epsilon = \tan \theta_2 \approx \theta_2 = \frac{e}{f_2} = \frac{\lambda}{W_2}. \quad (4.33)$$

The analysis above addresses the spread of a single point due to diffraction from the square dispersing element imaged onto the focal plane. What is the impact of the finite slit width? For a diffraction-free system of unit magnification, the image of the slit w' is identical to w . The effect of diffraction is illustrated by segmenting the slit into infinitesimal widths dx each of which will be spread at the focal plane due to (4.32), as shown in Figure 4.19. Mathematically the image of the entrance slit is represented by a rectangle function defined by

$$\text{rect} \left(\frac{x - x_s}{w'} \right) = \begin{cases} 0, & \left| \frac{x - x_s}{w'} \right| > \frac{1}{2} \\ 1, & \left| \frac{x - x_s}{w'} \right| \leq \frac{1}{2} \end{cases}, \quad (4.34)$$

where x_s is the image center and w' is the width. The irradiance is proportional to the sum of all the contributions from $D(x)$ for every location x' within the slit image at the focal plane or

$$E(x - x_s) = \int_{-\infty}^{\infty} \text{rect} \left(\frac{x' - x_s}{w'} \right) \text{sinc}^2 \left[\frac{\pi}{e} (x - x') \right] dx'$$

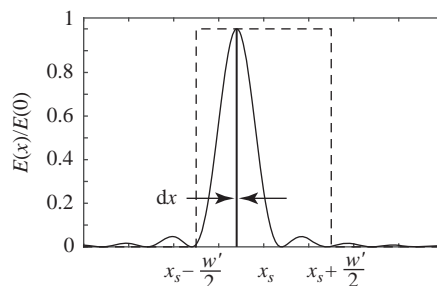


Figure 4.19 Diffraction due to the limiting aperture for uniform monochromatic illumination for a segment dx of the slit width w' centered at x_s represented by a rectangle function (dashed line). The effect of diffraction is given by (4.32) and illustrated with the solid lined curve.

$$= \int_{x_s - \frac{w'}{2}}^{x_s + \frac{w'}{2}} \text{sinc}^2 \left[\frac{\pi}{e} (x - x') \right] dx' \quad (4.35)$$

to within a constant, which is the convolution between a rectangle function and the diffraction function that is usually written as

$$E(x - x_s) = \text{rect} \left(\frac{x - x_s}{w'} \right) * D(x). \quad (4.36)$$

Figures 4.20 and 4.21 illustrate the convolution process with E expressed as a function of the focal plane location x . The simplest interpretation of a convolution is that it is the area under the curve for a product of the two functions, rect and D in this case, evaluated at every point x . The integral is a function of the independent variable x and by varying x' , $D(x)$ is shifted across the rectangle function.

The quantity of interest is the instrumental profile, so we would like to express the slit image width in terms of wavelength. This is accomplished through the application of (4.29). Figure 4.21 illustrates the one-dimensional irradiance from the slit convolved with the diffraction function at the focal plane for a monochromatic source. The width of this function is defined to be the full-width-at-half-maximum δx and the angular extent is $\delta\theta_2$. The width in terms of wavelength is therefore

$$\delta x = f_2 \delta\theta_2 = f_2 D_\theta \delta\lambda \Rightarrow \delta\lambda = \frac{\delta x}{f_2 D_\theta} \quad (4.37)$$

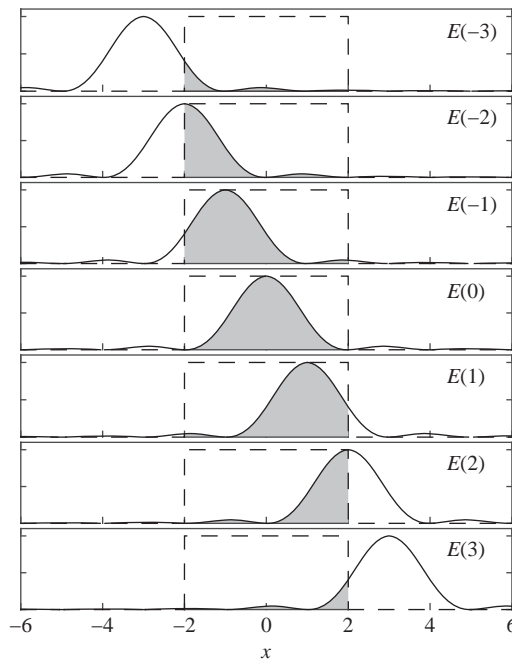


Figure 4.20 The convolution of the rectangle and diffraction functions for a few x locations at the focal plane. The integral is represented by the grayed area and x_s is zero.

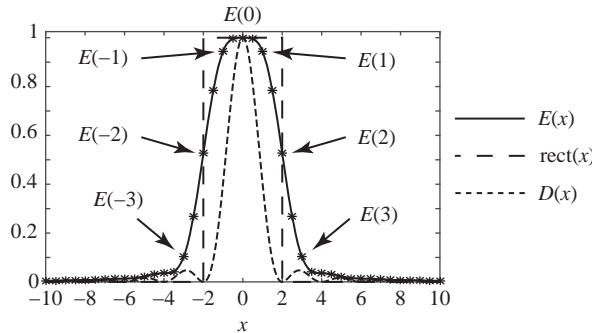


Figure 4.21 Full convolution of $\text{rect}(x)$ and $D(x)$ with $E(x)$ peak normalized. The asterisks represent the convolution results corresponding to particular values of x with those from Figure 4.20 marked.

for the on-axis case illustrated. The off-axis case will be only slightly different since the dimensions of the focal plane array are small compared to the focal length. For example, consider an imaging spectrometer designed to measure the spectrum from 400 nm to 2500 nm. A typical focal plane array will have pixels that are on the order of tens of microns and, to be quantitative, we will assume a pixel pitch of $30 \mu\text{m}$. An instrument will be designed to have about 200 to 400 channels with each one corresponding to a pixel. The width of the focal plane array is therefore between 0.6 cm and 1.2 cm and is centered on the optical axis. The focal length of the second collimating optic is taken to be on the order of 10 cm. Using these estimates, the distance to the image at the edge of the field compared to the on-axis case will be between 0.045 and 0.2 percent longer, yielding an insignificant change in (4.37).

The geometric width w' of the slit image is expressed as a rectangle function in terms of the wavelength or

$$\text{rect}\left(\frac{\lambda - \lambda_s}{\Delta\lambda_s}\right) = \begin{cases} 0, & \left|\frac{\lambda - \lambda_s}{\Delta\lambda_s}\right| > \frac{1}{2} \\ 1, & \left|\frac{\lambda - \lambda_s}{\Delta\lambda_s}\right| \leq \frac{1}{2} \end{cases}, \quad (4.38)$$

where $\Delta\lambda_s$ is the corresponding width and λ_s is the center wavelength of the slit image. Equation (4.36) is now rewritten as

$$E(\lambda - \lambda_s) = \text{rect}\left(\frac{\lambda - \lambda_s}{\Delta\lambda_s}\right) * D(\lambda). \quad (4.39)$$

The irradiance is sampled at the focal plane array by detector elements of pixel pitch p . In our case, the pixel pitch is equal to the slit image width and the spectrometer has unit magnification. Additionally, it will be assumed that the response of the detector element is uniform so that the pixel function is also represented by (4.34) with w' replaced by p . Figure 4.22 illustrates the case where the monochromatic image of the irradiance is sampled by a pixel centered at x_p . Applying (4.29) in the same way as was done for the slit yields

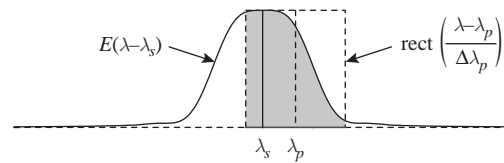


Figure 4.22 The monochromatic irradiance given by (4.39) sampled at the focal plane by a pixel. Both functions have been expressed in terms of wavelength through (4.37). The gray area is proportional to the measured signal.

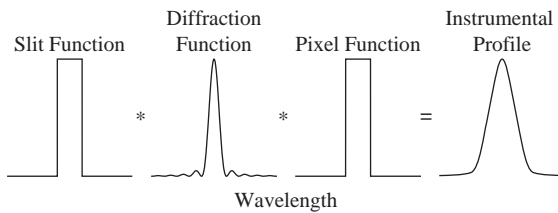


Figure 4.23 The instrumental profile for an imaging spectrometer with a very high degree of aberration control.

$$\text{rect}\left(\frac{\lambda - \lambda_p}{\Delta\lambda_p}\right) = \begin{cases} 0, & \left|\frac{\lambda - \lambda_p}{\Delta\lambda_p}\right| > \frac{1}{2} \\ 1, & \left|\frac{\lambda - \lambda_p}{\Delta\lambda_p}\right| \leq \frac{1}{2} \end{cases} \quad (4.40)$$

for the pixel rectangle function, where λ_p is the detector element center that would correspond to a monochromatic source at that wavelength and $\Delta\lambda_p$ is the corresponding pixel width. The flux that is sampled depends upon the area of the detector element and the signal is proportional to the irradiance $E(\lambda)$ within the pitch or

$$S(\lambda_p) \propto \int_{\lambda_p - \frac{\Delta\lambda_p}{2}}^{\lambda_p + \frac{\Delta\lambda_p}{2}} E(\lambda) d\lambda; \quad (4.41)$$

however, since we are interested in the instrumental profile, which is a relative function, the proportionality that was not included in (4.41) is unimportant. Notice the similarity between (4.35) and (4.41). This is another case of a convolution, here between $E(\lambda)$ and (4.40), that will be written as

$$P(\lambda_c - \lambda) = \text{rect}\left(\frac{\lambda - \lambda_s}{\Delta\lambda_s}\right) * D(\lambda) * \text{rect}\left(\frac{\lambda - \lambda_p}{\Delta\lambda_p}\right), \quad (4.42)$$

with the result illustrated in Figure 4.23.

In the discussion above, nothing has been said about diffraction from the slit itself. Assuming a high level of aberration control, the rays falling on the slit will be spherical about an image point and diffraction will be governed by the Fresnel case. The slit is typically many times the wavelength of the constituent light. For example, for a spectrometer designed to operate in the reflective spectral range with a $30 \mu\text{m}$ slit width the ratio of the width to the wavelength will vary from 12 at $2.5 \mu\text{m}$ to 75 at $0.4 \mu\text{m}$. In

this case, diffraction from the slit does not play a significant role in the analysis. In the longwave infrared, systems have been designed with slit widths that range from about 40 to 75 μm . Here the ratio is smaller and, for example, at a wavelength of 14 μm diffraction from the 40 μm slit plays a role. In this case the image of the slit is appropriately modified from a rectangle function to account for diffraction. The case of diffraction near a focus is discussed in Born and Wolf (1999).

4.3.2 Resolving Power

The instrumental profile that has been established though (4.42) is now explored at the limits with a case that is dominated by diffraction and one that is determined by the slit width and pixel pitch with negligible diffraction. In both cases it is assumed that aberrations are tightly controlled and are neglected. The diffraction limited case is illustrated by the upper series of graphs in Figure 4.24. In a traditional monochromator this case sets the limit for the highest possible resolving power and is known as the theoretical resolution and designated R_o . No monochromator is operated at this limit since the slits would be almost closed and the étendue of the system would approach zero. The *theoretical resolving power* is given by

$$R_o = \lim_{w,p \rightarrow 0} \frac{\lambda}{\delta\lambda} = \lim_{w,p \rightarrow 0} \frac{\lambda D_\theta}{\Delta\theta_2} = W_2 D_\theta \quad (4.43)$$

where (4.29) and (4.33) have been used with the width of the diffraction function given by ϵ rather than 0.88 ϵ .

The theoretical resolution sets the scale that is used in reference to the actual resolving power. In an imaging spectrometer the slit and pixel pitch are relatively wide so that enough light is detected for adequate signal-to-noise performance and due to limitations set by the available focal plane arrays. If both the slit width and the pitch are quite large in comparison to the diffraction function, then the situation illustrated by the lower series in Figure 4.24 results. A ratio, the reduced slit width, given by

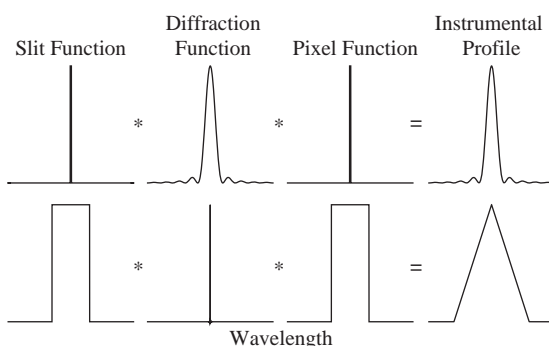


Figure 4.24 The limiting cases for the instrumental profile. The upper series corresponds to a diffraction limited case with the slit and the pixel pitch narrow in comparison to the diffraction function, and the lower series corresponds to the case where the slit width and pixel pitch dominate.

$$u_s \equiv \frac{w}{\epsilon}, \quad (4.44)$$

where the s subscript is used to distinguish it from the paraxial angle u , is defined to identify the resolution performance. A similar ratio is applied to the pixel with u_s and w replaced with u_p and p respectively. If u_s and u_p are much less than one, the resolution is given by R_o , while if both are much greater than one, diffraction effects can be ignored.

The resolving power for the $u_s, u_p \gg 1$ case is now determined with (4.42) being reduced to

$$P(\lambda_c - \lambda) = \text{rect}\left(\frac{\lambda - \lambda_s}{\Delta\lambda_s}\right) * \text{rect}\left(\frac{\lambda - \lambda_p}{\Delta\lambda_p}\right), \quad (4.45)$$

where $D(\lambda)$ has been removed. The lower series in Figure 4.24 demonstrates the outcome when the image of the slit width and the pixel pitch are equal yielding a triangle function. When the slit width and the pitch are unequal (4.45) yields a trapezoid function. The reader can show that the full-width-at-half-maximum is given by

$$\delta\lambda = \frac{1}{2}(u_s + u_p + |u_s - u_p|) \quad (4.46)$$

with the wider of the two determining the limit of resolution. On the other hand, the system étendue is determined by the narrower of the two. In most cases the magnification of the imaging spectrometer is one, or very close to it, and the slit width and pixel pitch are matched. The resolution in this case is strictly determined by geometric factors since diffraction is negligible. Defining the angular width of the slit image or pixel as $\beta = w'/f_2 = p/f_2$, the limit of resolution is written as $\delta\lambda = \beta/D_\theta$ from (4.29) and the resolution is

$$R = \frac{\lambda}{\delta\lambda} = \frac{\lambda D_\theta}{\beta} = R_o \frac{\epsilon}{\beta} = \frac{R_o}{u_s}, \quad (4.47)$$

where (4.33), (4.43), and (4.44) have been used. R is the *practical resolving power*.

Almost all imaging spectrometers are intermediate between the two cases described, with aberrations adequately controlled but not reduced to the point that diffraction dominates. In that more realistic case, (4.42) is rewritten with the diffraction function replaced by the one-dimensional form of the point spread function. The point spread function is the response from an optical system to an object point located at (x, y) and imaged at (x', y') , written as

$$p(x', y'; x, y) = H\delta(x' - x, y' - y), \quad (4.48)$$

where $\delta(x' - x, y' - y)$ is a two-dimensional delta function and H is the mathematical operator that transfers the impulse through the system (Goodman, 2005). This transfer depends upon the effects of the aberrations and of diffraction. The one-dimensional form, known as the line spread function, will be written as $h(\lambda)$ and replaces D in (4.42) to yield

$$P(\lambda_c - \lambda) = \text{rect}\left(\frac{\lambda - \lambda_s}{\Delta\lambda_s}\right) * h(\lambda) * \text{rect}\left(\frac{\lambda - \lambda_p}{\Delta\lambda_p}\right). \quad (4.49)$$

There is an example in the literature of an imaging spectrometer that was designed and demonstrated where the aberrations were so well controlled that the resulting point

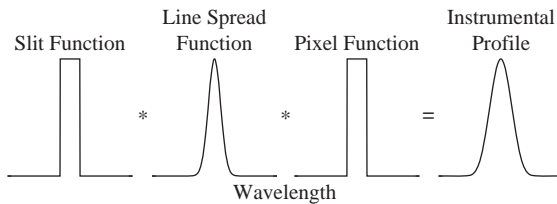


Figure 4.25 The convolution of the slit, line spread, and pixel functions as given by (4.49) for a point spread function with 80 percent of the energy contained within the pixel.

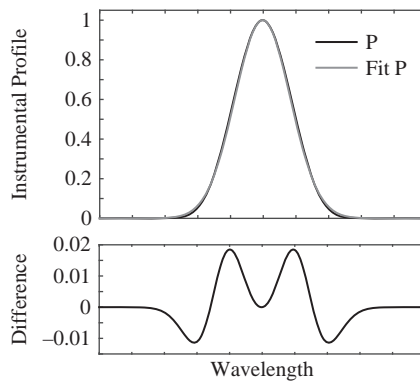


Figure 4.26 A Gaussian model is fit to the instrumental profile illustrated in Figure 4.25 using an iterative least-mean-square algorithm. The bottom graph is the difference between P generated through an application of (4.49) and the fit.

spread function was a small fraction of the pixel pitch (Mouroulis and McKerns, 2000). In this case, the instrumental profile was very nearly a triangle function.

Most dispersive imaging spectrometers have an instrumental profile that has a significant contribution from the line spread function and it is not uncommon to use a peak normalized Gaussian function to model it. This is effective since (4.49) is dominated by the two rectangle functions and the line spread function is controlled to be contained within the pixel width resulting in the rounding of the triangle function that would be produced by the convolution of the two rectangles alone. A quantitative example assumes that the point spread function is a two-dimensional Gaussian with 80 percent of its energy within a detector element. The convolution process is illustrated in Figure 4.25 and the resulting instrumental profile is also well described by a Gaussian function as shown in Figure 4.26. The significance of the small differences between P and the fit would be evaluated within the context of the measurement uncertainty from the sensor characterization.

4.3.3 Spatial–Spectral Uniformity

A goal for the optical engineer designing a dispersive imaging spectrometer is to optimize the uniformity of the spectral and spatial response functions across the full field

with the shape of both, when compared to like kind, being as identical as possible for each spatial–spectral sample. An imaging spectrometer that has a high level of uniformity enables an accurate retrieval of the spectral radiance for each spatial sample with the mixing from adjacent samples due to the instrument being minimized. The spatial response function is optimized so that adjacent spatial samples are not mixed, particularly as a function of wavelength. This implies that the point spread function is largely limited to a single pixel and is uniform across the full field, yielding identical shapes for the instrumental profile as a function of spectral position and similarly for the spatial response function in the spatial direction.

The spatial response function $P_s(x - x_c)$ associated with a detector element whose center is at x_c is produced by the convolution of the line spread function in the spatial direction with the rectangle function that represents the pixel and is given by

$$P_s(x - x_c) = \text{rect}\left(\frac{x - x_c}{p}\right) * h(x) \quad (4.50)$$

since the length of the slit is much larger than the dimensions of either the line spread function $h(x)$ in the spatial direction and the pixel pitch p . The spatial response function is more sensitive to the shape of the line spread function since it is convolved with only one rectangle function.

The aberrations will be artificially decoupled into point and field aberrations. Figure 4.27 shows the impact of distortion (see Figure A.22) with the left image illustrating the curvature of a monochromatic image of the slit, known as *smile*, and the right image showing the variation in magnification of the slit as a function of wavelength, known as *keystone*. These two combine to form the image in the middle. Both have a measurement impact, with smile being the least deleterious of the two since it does not mix the spectra from adjacent channels and can be characterized during the laboratory calibration and addressed in the data processing. Keystone, on the other hand, mixes spectra as a function of wavelength, essentially increasing the size of the spatial sampling. Keystone is not easily addressed in processing, with the best solution being an optimized design (Mouroulis et al., 2000).

The point aberrations will impact the uniformity through the variation in the line spread function in (4.49) and (4.50). The imaging spectrometer may approach diffraction limited performance at the longest wavelengths and will be dominated by point aberrations on the blue side. These two effects are balanced to produce the desired uniformity in $h(\lambda)$ and $h(x)$. It is possible for the design to have excellent point aberration performance at the shorter wavelengths resulting in a small point spread function well contained within a detector element and have a larger one at the longer wavelengths due to diffraction. In this case the instrumental profile and the spatial response function will vary as a function of wavelength across the field resulting in a nonuniform design that is inferior within this context, a rather counter-intuitive result.

The effect of point aberrations that vary as a function of wavelength is not as severe as keystone as long as they are well contained within a pixel. The spectral and spatial response functions will vary as a function of pixel location on the focal plane array but mixing from adjacent spatial samples is minimized. The shape of P can vary somewhat;

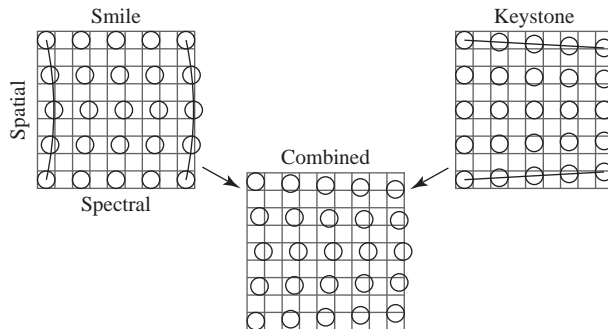


Figure 4.27 The rectilinear focal plane array is depicted with the point spread function at the center wavelengths for each spectral channel illustrated as a circle. The figure on the upper left is strictly smile and on the upper right strictly keystone. Both are combined in the center.

however, it will be dominated by the rectangle functions associated with the slit and the pixel pitch. The characterization of the individual spectral response functions will capture this variation, which could range from something approaching a triangle function for a narrow line spread function to an asymmetric function if $h(\lambda)$ is highly non-uniform. The variation in detector element response with position will also play a role.

Expansion of the point spread function to exceed the pixel pitch degrades the recovery of the spectral radiance, especially if it has a dependence upon the spectral channel. For example, if the point spread function is well contained at the shorter wavelengths but becomes progressively larger expanding outside of the detector element area at the longer wavelengths an error somewhat like keystone will be manifest with the degree of spatial mixing being wavelength dependent. Again this is best addressed through design rather than processing.

Highly uniform designs have been accomplished in hardware with the variation in the location of the point spread function within every detector element maintained at a tenth of the linear dimension of a pixel or less in both the spectral and spatial directions. The resulting variation in the instrumental profile and the spatial response function is less than 5 percent. See Mouroulis et al. (2000) for a description of an approach to the optimization problem, the first step to produce a highly performing imaging spectrometer.

4.3.4 Dispersive Optical Elements

As was introduced at the beginning of Section 4.3, angular separation is accomplished via a prism or a grating in dispersive spectrometers. The dispersing element in the generic imaging spectrometer illustrated in Figure 4.17 will now be specified and the physical processes that lead to the separation will be detailed in both cases. We will also show how the choice of disperser can impact the spatial–spectral uniformity. Following the description of the physics for both cases, particular designs will be addressed with their modifications to the generic form.

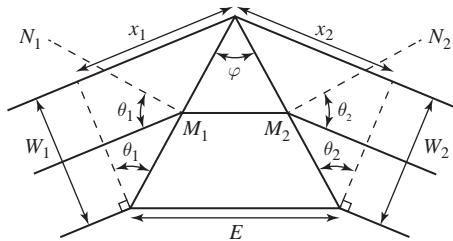


Figure 4.28 Isosceles prism in the minimum deviation configuration as the dispersing element in the imaging spectrometer. M_1 , M_2 , and E are the lengths of the various faces, N_1 and N_2 are the normals to the two faces, and ϕ is the apex angle.

Prism Dispersers

The generic dispersing element illustrated in Figure 4.17 is modified in Figure 4.28 with a prism disperser mounted in the minimum deviation condition with the entrance and exit angles equal. The two normal vectors are now defined as being perpendicular to the input and output faces of the prism. The width W_2 is therefore the projection of the width M_2 of the prism face in the direction of light propagation. Snell's law provides the angular deviation of the wavefront at the two faces through

$$\sin \theta_1 = n(\lambda) \sin \theta_{12} \quad \text{and} \quad n(\lambda) \sin \theta_{21} = \sin \theta_2, \quad (4.51)$$

where n and 1 are the indexes of refraction of the prism and air respectively, θ_{12} and θ_{21} are the internal angles at the two prism faces, and θ_1 and θ_2 are the external prism angles corresponding to the dispersing element normals. The wavelength dependence of the index of refraction of the prism material provides the angular separation of the light into the different colors.

The wavefront incident on the input face of the prism is planar and the emerging wavefronts will also be planar, but the associated perpendicular rays will be separated into different angles depending upon the wavelength. For this to be true for each monochromatic wavefront the optical paths through the different portions of the prism must be equal. Consider the prism in the minimum deviation condition where the light travels symmetrically through it and θ_1 is equal to θ_2 . The base length of the prism is given by E and the optical path for a ray of a particular wavelength traveling infinitesimally close to the prism base is $n(\lambda)E$. At the top of the prism the path length through the prism material is infinitesimally small and can be neglected and the equivalent optical path to nE is $M_1 \sin \theta_1 + M_2 \sin \theta_2$ where M_1 and M_2 are the lengths of the two prism faces as illustrated in Figure 4.28. For a prism with faces of equal length this reduces to

$$n(\lambda)E = M(\sin \theta_1 + \sin \theta_2). \quad (4.52)$$

Differentiating both sides of (4.52) and holding θ_1 fixed yields

$$\frac{dn}{d\lambda} E = (M \cos \theta) \frac{d\theta}{d\lambda} = W_2 \frac{d\theta}{d\lambda}, \quad (4.53)$$

where W_2 is the projected width of the diffracting element from (4.30) and $\theta = \theta_2$. The angular dispersion given by (4.29) is

$$D_\theta = \frac{E}{W_2} \frac{dn}{d\lambda} \quad (4.54)$$

and therefore the theoretical resolving power is

$$R_o = E \frac{dn}{d\lambda} \quad (4.55)$$

from (4.43).

It can be shown that, at minimum deviation, θ is related to the apex angle ϕ through

$$\sin \theta = n \sin \frac{\phi}{2} \quad (4.56)$$

and from geometry

$$E = 2M \sin \frac{\phi}{2} \quad (4.57)$$

The limit of resolution is therefore

$$\delta\lambda = \frac{n\beta}{2 \tan \theta \frac{dn}{d\lambda}} \quad (4.58)$$

from (4.47), with the angular width of the pixel given by $\beta = p/f_2$. The wavelength dependence of the index of refraction of any optical material is not a linear function and the functional form of (4.58) is typically a higher-order polynomial. This leads to nonlinear dispersion with the instrumental profile varying extensively with wavelength. Figure 4.29 illustrates two such cases with one for a VNIR/SWIR prism material, Infrasil-SF1 used in the Hyperspectral Digital Imagery Collection Experiment (HYDICE) (Rickard et al., 1993), and the second for a LWIR prism material, sodium chloride used in the SEBASS sensor among others (Warren et al., 1997). The limit of

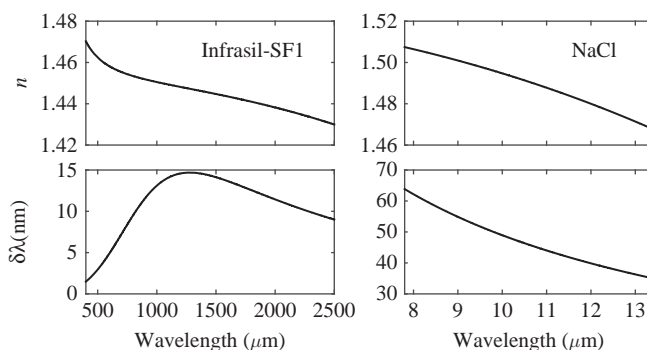


Figure 4.29 The two graphs on the left are the variation of the index of refraction for Infrasil-SF1 and the limit of resolution calculated using (4.58) for the HYDICE imaging spectrometer both as a function of wavelength and similarly on the right for sodium chloride and the SEBASS sensor. The Infrasil-SF1 data are from the data sheet provided by Heraeus Quarzglas GmbH & Co. KG and the NaCl data are from Li (1976).

resolution calculation in the figure used a prism apex angle of 60° and β was taken to be 0.24 mrad for the HYDICE case and 0.485 mrad for SEBASS, which were estimated based on the performance reported in the literature. The calculation is only approximate since neither sensor operated in the minimum deviation condition and the shape of the prism is not correct. The HYDICE sensor also binned adjacent instrumental profiles at the shortest wavelengths.

Grating Dispersers

The generic dispersing element in Figure 4.17 is next replaced with a diffraction grating. For clarity we will first describe a transmission grating even though imaging spectrometer designs universally employ reflection gratings. The action of a grating is more complicated, and the description incorporates the wave phenomena of diffraction and interference. Recall from Chapter 2 that for constructive interference at a particular wavelength to occur, a path difference δ is introduced between coherent sources with δ equal to an integer number of wavelengths. The left side of Figure 4.30 illustrates a transmission grating composed of a series of parallel slits of width a that are separated by a distance d . Collimated light from a slit is again incident from the left and each narrow slit diffracts the plane wave into the pattern given by (2.30). For particular incident and exit angles the path difference is $\delta = d \sin \theta_1 + d \sin \theta_2$ and constructive interference occurs when

$$m\lambda = d(\sin \theta_1 + \sin \theta_2), \quad m = 0, \pm 1, \pm 2, \dots \quad (4.59)$$

with m known as the *order* or order number of the diffracted wavefront. Note that for convenience (4.59) utilizes the absolute value of θ_1 and θ_2 rather than employing the sign convention from Section A.3. The gratings that are employed in an imaging spectrometer are reflection gratings and are visualized by replacing the slits by mirrors and folding the transmission grating picture about the grating plane, as shown on the right in Figure 4.30. Real reflection gratings have shaped facets, but the theory will first be developed with simple flat mirrors. One of the consequences of (4.59) is that multiple

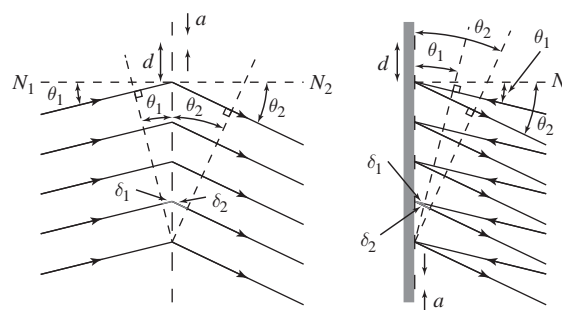


Figure 4.30 The left illustration is of a transmission grating and the right is of a reflection grating, both with the distance between slits or facets given by d and the slit or facet width given by a . The reflection grating is obtained by folding the transmission grating at the grating surface and replacing the slits with mirrored strips on a perfectly absorbing substrate.

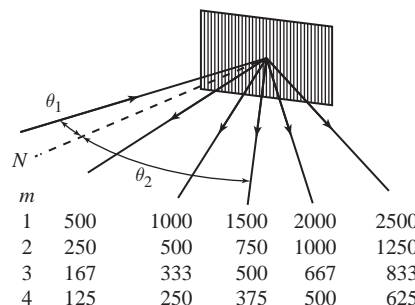


Figure 4.31 Wavelength coincidence due to $m\lambda$ for the first four orders and for particular values of θ_1 and θ_2 , with the later illustrated for the case corresponding to 1500 nm in first order. The wavelengths are in nanometers.

wavelengths will share the same geometry, as illustrated in Figure 4.31. This necessitates the use of some sort of order-sorting filtering to prevent spectral mixing.

The angular dispersion for a grating is obtained from (4.29) yielding

$$D_\theta = \frac{m}{d \cos \theta_2} \quad (4.60)$$

with the theoretical resolving power again calculated from (4.43) to be

$$R_o = W_2 D_\theta = (W \cos \theta_2) D_\theta = \frac{mW}{d} = mN, \quad (4.61)$$

where $W \cos \theta_2$ is again the projected width of the diffraction element with $N = W/d$ being the total number of slits or *rulings* contained by the grating. The practical resolving power (4.47) is used to calculate the limit of resolution giving

$$R = \frac{\lambda D_\theta}{\beta} \Rightarrow \delta\lambda = \frac{(d \cos \theta_2)\beta}{m}. \quad (4.62)$$

Note that the limit of resolution is proportional to $\cos \theta_2$ and is therefore a nonlinear function that has a slight dependence on wavelength. This is another factor that is dealt with in the design if strict spatial-spectral uniformity is to be achieved.

The distribution of monochromatic irradiance at the focal plane is derived by employing the same approach that was used in Section 2.2. For the grating illuminated by plane waves diffraction occurs at each slit and, since the entrance slit of the imaging spectrometer is narrow and forms a coherent source, light from each grating slit will interfere. Both the slit and the focal plane array are optically distant from the grating so that the Fraunhofer case applies. Returning to Figure 4.30 of a transmission grating with a large number of N slits, for simplicity we will further assume that the illumination is normal to the grating. The electric field at the focal plane array is composed of contributions from each slit and, since the distance is great, the directions of the individual amplitudes \mathbf{E}_i are parallel and the problem becomes one of scalar rather than vector addition.

The equation for diffraction for a single slit was derived in Section 2.2.2 and is given by (2.30). It remains for this to be generalized for the N slits that make up a grating. The function that was integrated in (2.29) is

$$f(x, R) = \exp\{i[k(R - x \sin \theta) - \omega t]\} \quad (4.63)$$

with the integration over the width of the slit. The approximation made in Section 2.2.2 was that the screen is so distant from the slit that r from any point within a slit can be replaced by $R - x \sin \theta$. This will be extended for the grating by assuming that the slits are very close together and the focal plane is optically distant so that it also applies for the entire grating. The electric field due to diffraction at a point at the focal plane will be the sum of the electric fields from each slit analogous to (2.29) or

$$\begin{aligned} \mathbf{E} = & \frac{\mathbf{E}_o}{R} \int_{-\frac{a}{2}}^{\frac{a}{2}} f(x, R) dx + \frac{\mathbf{E}_o}{R} \int_{d-\frac{a}{2}}^{d+\frac{a}{2}} f(x, R) dx \\ & + \frac{\mathbf{E}_o}{R} \int_{2d-\frac{a}{2}}^{2d+\frac{a}{2}} f(x, R) dx + \cdots + \frac{\mathbf{E}_o}{R} \int_{(N-1)-\frac{a}{2}}^{(N-1)+\frac{a}{2}} f(x, R) dx. \end{aligned} \quad (4.64)$$

Evaluating one of the integrals in (4.64) for an arbitrary slit yields

$$\begin{aligned} \mathbf{E}_j = & \frac{\mathbf{E}_o}{R} \int_{jd-\frac{a}{2}}^{jd+\frac{a}{2}} f(x, R) dx \\ = & \frac{\mathbf{E}_o}{R} e^{i(kR - \omega t)} \int_{jd-\frac{a}{2}}^{jd+\frac{a}{2}} \exp[-ikx \sin \theta] dx \\ = & \frac{\mathbf{E}_o a}{R} \left(\frac{\sin \alpha}{\alpha} \right) \exp\{i(kR - 2\beta j - \omega t)\}, \end{aligned} \quad (4.65)$$

where

$$\alpha \equiv \frac{1}{2} ka \sin \theta \quad (4.66)$$

and

$$\beta \equiv \frac{1}{2} kd \sin \theta \quad (4.67)$$

for the j th slit. Equation (4.64) is now rewritten as

$$\mathbf{E} = \sum_{j=0}^{N-1} \mathbf{E}_j = \frac{\mathbf{E}_o a}{R} \left(\frac{\sin \alpha}{\alpha} \right) e^{i(kR - \omega t)} \sum_{j=0}^{N-1} (e^{-i2\beta})^j \quad (4.68)$$

and the sum on the right is a geometrical progression that can be simplified, allowing (4.68) to be rewritten as

$$\mathbf{E} = \frac{\mathbf{E}_o a}{R} \left(\frac{\sin \alpha}{\alpha} \right) e^{i(kR - \omega t)} \frac{1 - e^{-i2N\beta}}{1 - e^{-i2\beta}} \quad (4.69)$$

for the total electric field at a particular point on the focal plane. From (2.11) the irradiance is therefore

$$\begin{aligned} E = & E_o \left(\frac{\sin \alpha}{\alpha} \right)^2 \frac{1 - \cos(2N\beta)}{1 - \cos(2\beta)} \\ = & E_o \left(\frac{\sin \alpha}{\alpha} \right)^2 \left(\frac{\sin N\beta}{\sin \beta} \right)^2, \end{aligned} \quad (4.70)$$

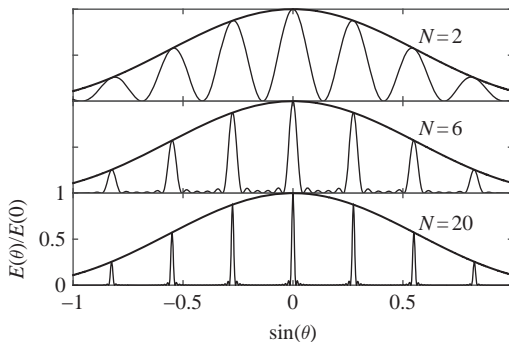


Figure 4.32 Diffraction and interference for collimated monochromatic 550 nm light normally incident on an array of slits. The slit array is based on a grating with 500 lines/mm yielding a slit spacing d of 2 μm and the slit width a is $d/5$. Each panel shows (4.72) with the diffraction envelope separately graphed with number of slits labeled.

where $E_o \propto |E_o|^2$ and the trigonometric identity $1 - \cos A = 2 \sin^2(A/2)$ has been applied.

Our primary interest here is in the functional form of the irradiance at the focal plane and therefore (4.70) will be peak normalized to one. The term in the leftmost parenthesis is already normalized so only the rightmost term needs to be addressed. From L'Hospital's rule,

$$\lim_{\beta \rightarrow m\pi} \frac{\sin N\beta}{\sin \beta} = \lim_{\beta \rightarrow m\pi} \frac{N \cos N\beta}{\cos \beta} = \pm N, \quad (4.71)$$

where m is again the order number. The normalized form of (4.70) is therefore

$$E = E_o \left(\frac{\sin \alpha}{\alpha} \right)^2 \left(\frac{\sin N\beta}{N \sin \beta} \right)^2 \quad (4.72)$$

with the first term identical to the irradiance for the diffraction pattern for a single slit of width a and the second term the interference term. Figure 4.32 shows three examples for different numbers of slits. The diffraction term forms the envelope with the interference pattern underneath and governs the overall efficiency of the grating, which in this case is highest for the zeroth order ($\sin \theta = 0$). Note that the interference pattern displays secondary maxima that essentially vanish as the number of rulings becomes high. The interested reader can consult Jenkins and White (1976) for a description of the details. The derivation of (4.72) was for normal illumination of the grating; however, in an imaging spectrometer, θ_1 is not zero. In this case, for the slit transmission grating, the peak of the diffraction envelope is centered on the zeroth order at the angle $\theta_2 = \theta_1$ and θ in α and β is replaced by θ_2 .

The separation of light into the different orders in the transmission grating, illustrated in Figure 4.33, is inefficient, with light thrown away in the orders that are not used. Much of the irradiance remains in the zeroth order, with the overall efficiency falling due to the diffraction envelope. This can be largely mitigated in either a transmission or reflection grating through the shaping of the individual facets. For a reflection grating

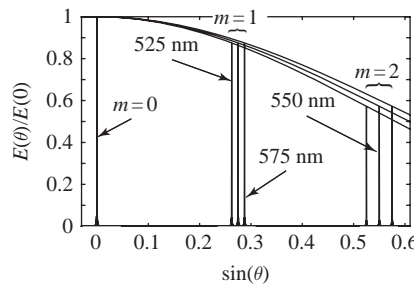


Figure 4.33 The irradiance from (4.72) for three wavelengths and the first three orders with the light in the zeroth order being undifferentiated. Each wavelength is diffracted at a slightly different angle and has its own associated efficiency from the diffraction envelope. The grating properties are the same as in Figure 4.32 except that N is 500.

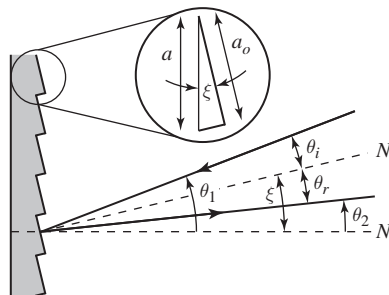


Figure 4.34 The details of a blazed reflection grating. Optimal efficiency is achieved when the input and output wavefronts correspond to the condition for specular reflection. N is the normal to the surface of the unblazed optical flat and N' is the normal to the facet surface. The distance between facets d is the same as the facet width a . The distance along the facet face is a_o , which is related to a through $a = a_o \cos \xi$.

this is accomplished by tilting a facet surface so that specular reflection coincides with the design order, typically $m = \pm 1$. The shaping is known as *blazing* and a grating with shaped facets is a blazed grating.

Figure 4.34 shows a cross section of a blazed grating. The angle ξ is the *blaze angle* between the grating normal N , defined as the normal to the unblazed optical flat, and the facet normal N' . Specular reflection occurs when the incident angle θ_i equals the reflected angle θ_r . From (4.59) only one wavelength corresponding to the particular angles θ_1 and θ_2 will meet the specular reflection requirement. Geometrically, the reflection condition is

$$\theta_2 = 2\xi - \theta_1 \quad (4.73)$$

and the wavelengths for the various orders that satisfy (4.73) are known as the blaze wavelengths.

Now that the concept of a blazed grating has been introduced we will return to the grating equation (4.59) and re-examine the sign convention as was applied to ray tracing

in Section A.3. There are a couple of different sign conventions used in the literature, with the choice being clear from the context. There are three cases that cover the range of possible configurations as illustrated in Figure 4.35 where the exitant angle θ_2 changes. The path difference was written as $\delta = d(\sin|\theta_1| + \sin|\theta_2|)$ for the case illustrated in Figure 4.30, which is only the first of three possible cases. The task is to define the form of the grating equation that is applicable to all three.

In all three cases, the incident angle θ_1 doesn't change. The first sign convention we'll address is the more common one where the two angles θ_1 and θ_2 have the same sign if they are on the same side of the grating normal and opposite signs otherwise. In case 1 the exitant ray is on the same side of N as the incident ray and therefore the path difference is $\delta = d(\sin \theta_1 + \sin \theta_2)$ and the order number m is positive. In the last two cases the exitant ray is on the opposite side of N . In case 2, the absolute value of θ_2 is less than the angle corresponding to specular reflection; however, the path difference is still written as $\delta = d(\sin \theta_1 + \sin \theta_2)$, where δ_2 is subtracted from δ_1 due to the sign of θ_2 . The path difference is a positive number and again m is positive. The final case has $|\theta_2| > \theta_r$ and the path difference expression doesn't change from case 2 except it is *negative*, since $|\theta_2| > |\theta_1|$, requiring that m also be negative, and the orders are referred to as negative orders.

The second sign convention is the one used in ray tracing, where the angles in the first and third quadrants are positive and are negative in the other two. For a reflection grating the grating equation is written as

$$m\lambda = d(n \sin \theta_1 - n' \sin \theta_2), \quad (4.74)$$

where n and n' are the indexes of refraction before and after reflection consistent with the sign convention for powered mirrors introduced in Section A.3. The condition for

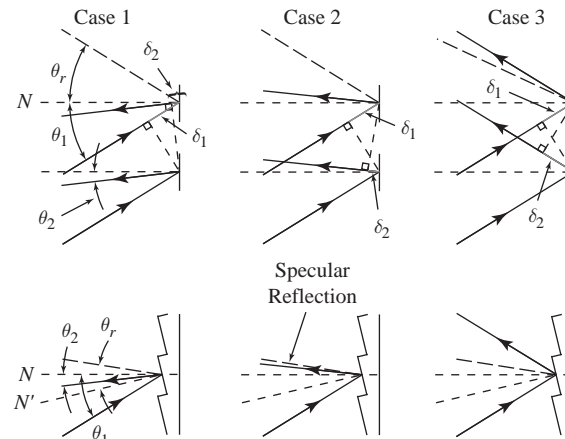


Figure 4.35 The three cases for reflection from a grating with the grating facets a distance d apart. The top row is an unblazed grating and the bottom is the corresponding blazed grating. In each example the incident ray is at θ_1 and specular reflection is identified by the heavy dashed line at the angle θ_r . The path difference associated with the incident and exitant rays is δ_1 and δ_2 respectively.

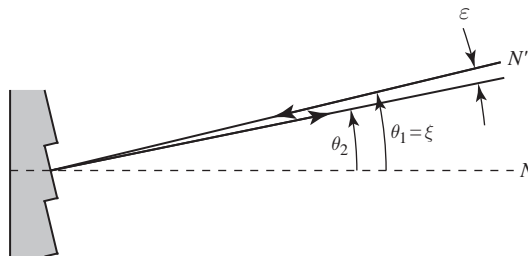


Figure 4.36 The Littrow configuration with the incoming ray along the facet normal and the outgoing ray only slightly displaced by the angle ϵ from the facet normal.

negative orders is the same as in the first sign convention. The reader is encouraged to explore other geometries to confirm that the two definitions are consistent.

The efficiency of a blazed grating can be rigorously modeled though the full vector application of Maxwell's equations that satisfy the boundary conditions at the grooved surface (Moharam and Gaylord, 1982, 1986). As an alternative, an elementary scalar theory where the facet width is much greater than the wavelength will be presented to provide insight into grating performance. The model is limited and does not address the effects of polarization that is parallel and perpendicular to the grooves, which have different efficiencies; however, it does do a reasonable job as long as the wavelength is shorter than the groove spacing. The model will be developed with the grating mounted in the *Littrow* configuration, where $\theta_1 = \theta_2$ as illustrated in Figure 4.36. This configuration, or close to it, is utilized in some imaging spectrometers and the functional form of the grating efficiency is broadly correct to a reasonable approximation. In the Littrow configuration, ξ equals θ_1 and θ_2 from (4.73) and the blaze wavelengths λ_{Bm} are

$$\lambda_{Bm} = \frac{2d \sin \xi}{m}, \quad (4.75)$$

where (4.59) has been applied. The exit angle θ_2 will depart from ξ for different wavelengths by the amount $\xi - \epsilon$ with (4.59) becoming

$$\begin{aligned} m &= \frac{d}{\lambda} [\sin \xi + \sin(\xi - \epsilon)] \\ &= \tilde{v} d (\sin \xi + \sin \xi \cos \epsilon - \cos \xi \sin \epsilon), \end{aligned} \quad (4.76)$$

where the wave number \tilde{v} has replaced the wavelength to simplify the algebra. The diffraction envelope in (4.72), which governs the grating efficiency, will be re-examined so that it can be appropriately modified. The original derivation was for plane waves normally incident on a transmission grating composed of N slits of width a and center-to-center distance d . For the Littrow configuration, a monochromatic plane wave is normally incident on the facet face of width $a_o = a \cos \xi$ and the refracted wavefront exits at an angle ϵ to the face normal. The appropriate modification to (4.66) is

$$\alpha = \frac{\pi}{\lambda} a \cos \xi \sin \epsilon = \pi \tilde{v} d \cos \xi \sin \epsilon, \quad (4.77)$$

where a is replaced by d since the two are equal.

The diffraction envelope in (4.72) is rewritten as

$$E_g \equiv \frac{E}{E_o} = \frac{\sin^2(\pi \tilde{v} d \cos \xi \sin \epsilon)}{(\pi \tilde{v} d \cos \xi \sin \epsilon)}, \quad (4.78)$$

with E_g signifying the grating efficiency, which is simplified using (4.76) through

$$\begin{aligned} \tilde{v} d \cos \xi \sin \epsilon &= \tilde{v} d \sin \xi (1 + \cos \epsilon) - m \\ &\approx 2\tilde{v} d \sin \xi - m, \end{aligned} \quad (4.79)$$

where the small angle approximation has been applied with $\cos \epsilon$ set equal to one. The Littrow condition is used to rewrite the order index as

$$m = 2\tilde{v}_{Bm} d \sin \xi \quad (4.80)$$

with the first-order blaze wave number given by

$$\tilde{v}_{B1} = \frac{1}{2d \sin \xi} \quad (4.81)$$

so that (4.79) becomes

$$\tilde{v} d \cos \xi \sin \epsilon = \frac{\tilde{v} - \tilde{v}_{Bm}}{\tilde{v}_{B1}}. \quad (4.82)$$

Substituting (4.82) into (4.78) yields

$$E_g = \frac{\sin^2\left(\frac{\pi(\tilde{v} - \tilde{v}_{Bm})}{\tilde{v}_{B1}}\right)}{\left[\frac{\pi(\tilde{v} - \tilde{v}_{Bm})}{\tilde{v}_{B1}}\right]^2} \quad (4.83)$$

for the final form of the grating efficiency. As written (4.83) is peak normalized and a constant multiplier is typically applied to account for the reflectivity of the substrate with a peak efficiency that is less than one. Two sets of data were fit to (4.83) with an offset, an amplitude multiplier, and the blaze wavelength included as fit parameters and the results presented in Figure 4.37. The amplitude multiplier captures the reflectivity of the

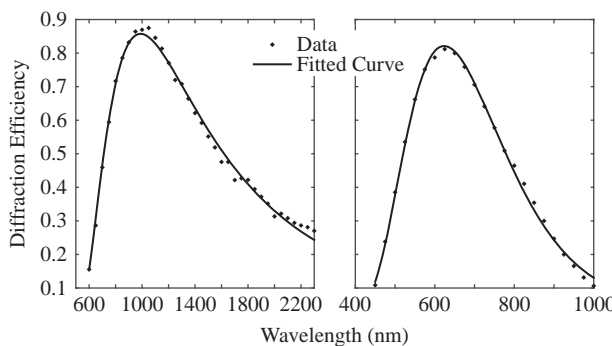


Figure 4.37 Measured and fit grating efficiencies. The left curve corresponds to the first-order diffracted wavefront efficiency from a blazed grating with a fit value of 988.5 nm for the blaze wavelength. The right curve is for the second-order diffraction efficiency with the blaze wavelength equal to 624 nm from the fit. Data from Mouroulis et al. (1998).

grating surface and the offset, which was small in the fit, accounts for any background contribution to the measurement. A more rigorous derivation of the grating efficiency based on the scalar theory can be found in Strong (1958).

The last topics of this section prior to moving on to specific imaging spectrometer designs is that all gratings introduce effects solely due to their dispersive properties. One such effect is magnification in the direction of dispersion, as is shown by differentiating (4.59), while keeping d , λ , and m fixed, which produces

$$0 = \cos \theta_1 \delta \theta_1 + \cos \theta_2 \delta \theta_2, \quad (4.84)$$

so that the magnification, signified as m' here rather than m as in (A.13) to distinguish it from the order number, is given by

$$m' = \frac{w'}{p} = \left| \frac{\delta \theta_2}{\delta \theta_1} \right| = \frac{\cos \theta_1}{\cos \theta_2}, \quad (4.85)$$

where w' is the width of the slit image, p is the pixel pitch, and the focal lengths of the two collimating optics are equal. It is clear that only the Littrow configuration satisfies this condition, and the slit width is adjusted to a compromise value. The effect is small in any case.

The second effect is of more consequence since it impacts the optical design in order to achieve the desired spatial-spectral uniformity. Consider rays from a point at the top of the slit that are collimated by the first lens in Figure 4.17. The resulting plane waves will intercept the grating at an angle η resulting in the path difference $\delta = d \cos \eta \sin \theta_1$, as illustrated in Figure 4.38. The wavefront exits the grating with a similar path difference, $\delta = d \cos \eta \sin \theta_2$. The grating equation is modified to

$$m\lambda = d \cos \eta (\sin \theta_1 + \sin \theta_2) \quad (4.86)$$

with the effect most easily understood through a comparison of the difference between the on-axis and off-axis cases. For monochromatic illumination of the slit (4.86) is rearranged as

$$\sin \theta_2 = \frac{m\lambda}{d} \sec \eta - \sin \theta_1 \quad (4.87)$$

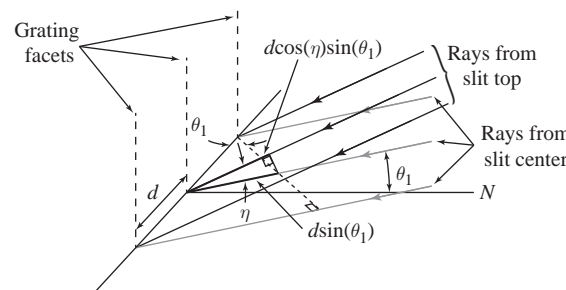


Figure 4.38 Collimated rays incident on the grating from the top, in black, and center, in gray, of the slit, illustrating the path difference geometry. The reflected rays have a similar geometry. Compare to Figure 4.30 where only the rays from the slit center are shown.

for the general case, which becomes

$$\sin \theta_{2_o} = \frac{m\lambda}{d} - \sin \theta_1 \quad (4.88)$$

for a ray from the center of the slit. For small values of η , (4.87) becomes

$$\sin \theta_2 = \frac{m\lambda}{d} \left(1 + \frac{\eta^2}{2}\right) - \sin \theta_1 = \sin \theta_{2_o} + \frac{m\lambda}{d} \frac{\eta^2}{2}$$

or

$$\sin \theta_2 - \sin \theta_{2_o} = \frac{m\lambda}{d} \frac{\eta^2}{2}, \quad (4.89)$$

which is further simplified by applying the trigonometric identity $\sin A - \sin B = 2 \sin \frac{1}{2}(A - B) \cos \frac{1}{2}(A + B)$ yielding

$$\Delta \theta_2 = \sec \theta_{2_o} \frac{m\lambda}{d} \frac{\eta^2}{2}, \quad (4.90)$$

where the small angle approximation has been applied to $\sin \frac{1}{2}(\theta_2 - \theta_{2_o})$ and θ_2 is approximately equal to θ_{2_o} in $\cos \frac{1}{2}(\theta_2 + \theta_{2_o})$. The monochromatic image of the slit is therefore a parabola at the focal plane. In a traditional monochromator this reduction in resolution is corrected through the use of curved entrance and exit slits. For an imaging spectrometer with a rectilinear array of detector elements this term contributes to smile and must be addressed in the design.

4.4

Dispersive Imaging Spectrometer Designs

Dispersive imaging spectrometer designs are the current workhorses in hyperspectral remote sensing. We will address a couple of different optical forms in some detail, even though there is quite a selection of potential designs. These designs are adaptations of micro-lithographic projection systems that were developed for the transfer of an optical mask to a photoresist used in, for example, the generation of integrated circuits. The first design is the Offner–Chrissp imaging spectrometer that was developed by Michael Chrissp, who adapted an optical form invented by Abe Offner. The Offner–Chrissp form is widely used for imaging spectrometers operating in the VNIR/SWIR. The second form is the Dyson imaging spectrometer with a particular design developed by David Warren, again by adapting a lithographic projector, in this case developed by J. Dyson. The design of the Dyson imaging spectrometer has had contributions from several optical engineers, and we have chosen Warren’s adaptation as an example (Mertz, 1977; Mouroulis et al., 2000). Some of the details of the aberrations that are controlled in either design will be developed, although in practice an optical engineer approaches the problem using powerful optical design software rather than the analytical analysis presented here.

4.4.1

The Offner–Chrissp Imaging Spectrometer

The Offner form was specifically invented as a mask projection system for micro-lithography applied to integrated circuits. The design requirements were to image a mask onto a photoresist on the surface of a silicon wafer with a resolution on the order of $2.5 \mu\text{m}$, requiring a high degree of aberration control, which Offner accomplished using a concentric optical form. The Offner form is made of two concentric mirrors as illustrated at the top left of Figure 4.39. The primary mirror has a radius of curvature R_1 and the secondary mirror has a radius $R_2 = R_1/2$. The object is placed on an axis that contains the center of curvature and is perpendicular to the optical axis. Paraxially the image of an object above the optical axis will form at the equivalent distance below it and the magnification is -1 . Another important feature of the Offner form is that it is telecentric with the limiting aperture being the secondary mirror, which is mounted at $R_1/2$ or one focal length from the primary. In the case of a mask projection system this has the advantage of relaxing the alignment of both the mask and the silicon wafer along the optical axis as shown at the bottom of Figure 4.39. When the limiting aperture is at the lens a small error in the alignment of the mask and the resist leads to degradation of the image in both position and focus.

If the secondary mirror's radius is exactly half the radius of the primary mirror then all of the Seidel aberrations are zero (Offner, 1975). This level of control was not good enough for the application of micro-lithography to integrated circuitry, since fifth-order

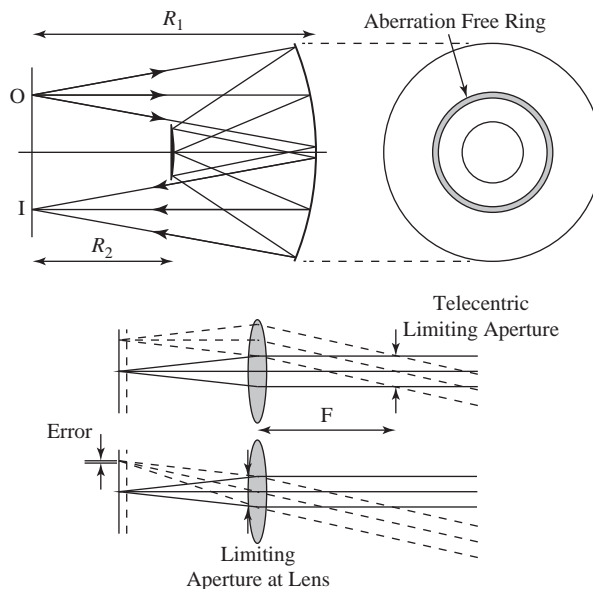


Figure 4.39 The Offner form is presented at the upper left with the object at O and the image at I. The geometry on the upper right illustrates the narrow region of excellent aberration control. The bottom two schematics show the effect of a telecentric limiting aperture with the image at the correct focal distance, the vertical solid line, and, for a misalignment, the dashed vertical line.

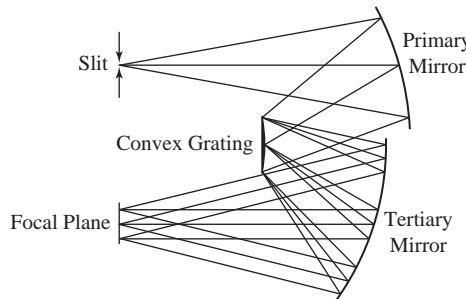


Figure 4.40 The Offner–Chrisp imaging spectrometer. In the most general design the concave mirror of the Offner form is broken into two concave mirrors and the convex secondary mirror is replaced by a convex grating.

astigmatism was sufficient to blur the image beyond the $2.5 \mu\text{m}$ requirement. As a result, Offner increased the radius of the secondary mirror so that it was slightly larger than the perfect factor of two relationship with the primary while maintaining the concentric design. The fifth-order astigmatism was balanced by Seidel (third-order) astigmatism, yielding the required performance, albeit over a rather narrow annulus. In Offner’s original design the annulus had a width of about a millimeter.

The Offner–Chrisp imaging spectrometer, illustrated in Figure 4.40, appears deceptively simple (Chrisp, 1999). At first glance the adaptation is primarily that the secondary mirror is simply replaced by a convex diffraction grating and the Offner–Chrisp form is merely a rather straightforward modification of Offner’s original design. This overlooks the fact that the grating breaks the symmetry of the Offner form and introduces a host of aberrations that must be controlled if the Offner–Chrisp is to be highly performing as an imaging spectrometer. The foundation of Chrisp’s solution to this problem rests upon the extensive body of technical development going back to the work of H. A. Rowland, who developed *concave* grating spectrometers for use in ultraviolet spectroscopy, where reflective losses are quite high (Rowland, 1882). The effective use of concave gratings required extensive research, particularly in their mounting, which was not perfected until the early 1960s (Welford, 1965). Chrisp was able to adequately control the aberrations by applying the mounting concepts for concave gratings to a convex grating and by breaking the single convex mirror of the Offner form into two mirrors. There is a brief reference without development to a design of this form in Mertz (1977).

The approach we will take to understanding the performance of the Offner–Chrisp imaging spectrometer will be first to isolate the action of the grating and develop the aberration function that it introduces on its own. This will be accomplished through the application of Fermat’s principle following the outline presented in Welford (1965) for a concave grating, which is required since the development of aberrations in Section A.7 was for a system that was cylindrically symmetric about the optical axis while a grating has only a plane of symmetry. There is a one-to-one correspondence between the action of a concave grating when compared to that of the convex one used in the Offner–Chrisp with the difference being the virtual object and image for the grating in the convex case,

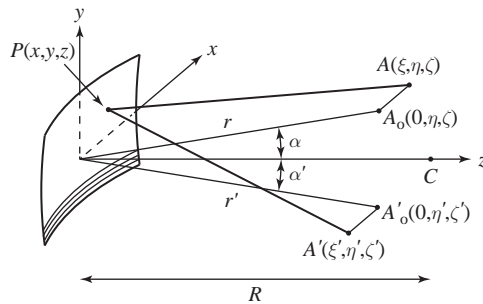


Figure 4.41 The coordinate system for the development of the optical path S for the convex grating with a radius of curvature R and the center of curvature at C . The grating grooves are parallel to the x -axis and the rays illustrated are virtual. Adapted from Welford (1965).

rather than the real object and image in the concave development. We will concentrate on developing the aberrations associated with the Rowland circle since that is the critical mounting arrangement in Chrissp's design.

Figure 4.41 illustrates the geometry that will be used to develop the optical path S from point A to A' . Fermat's principle is given by (A.5) which becomes

$$\frac{\partial S}{\partial x} = 0 \quad \text{and} \quad \frac{\partial S}{\partial y} = 0 \quad (4.91)$$

since the optical path between the two points only depends upon the position (x, y) on the grating. The grating grooves are parallel to the x -axis, so an additional path difference is introduced in the y direction due to the action of the grating with the total path length becoming

$$S = \overline{AP} + \overline{PA'} + m\lambda \frac{y}{d}, \quad (4.92)$$

where the last term is the path difference due to the separation of any two grooves.

The square of the distance from point A to point P on the grating surface is

$$\overline{AP}^2 = (x - \xi)^2 + (y - \eta)^2 + (z - \zeta)^2 \quad (4.93)$$

and similarly the square of the distance from P to A' is

$$\overline{PA'}^2 = (x - \xi')^2 + (y - \eta')^2 + (z - \zeta')^2, \quad (4.94)$$

as illustrated in Figure 4.41. \overline{AP}^2 is rewritten as

$$\overline{AP}^2 = r^2 + \xi^2 + 2Rz - 2y\eta - 2z\zeta - 2x\xi, \quad (4.95)$$

where $\zeta = r \cos \alpha$ and $\eta = r \sin \alpha$ have been applied. In order to eliminate z from (4.95) the equation for a spherical grating of radius R is written with z as a function of x and y through

$$x^2 + y^2 + (z - R)^2 = R^2$$

or

$$z = R - R \sqrt{1 - \frac{(x^2 + y^2)}{R^2}}, \quad (4.96)$$

which is expanded to yield

$$z = \frac{x^2 + y^2}{2R} + \frac{(x^2 + y^2)^2}{8R^3} + \frac{(x^2 + y^2)^3}{16R^5} + \dots \quad (4.97)$$

with the higher-order terms becoming progressively smaller since the radius of curvature of the grating is much greater than either spatial dimension. Substituting (4.97) into (4.95) and also applying $\xi = r \cos \alpha$ and $\eta = r \sin \alpha$ yields

$$\begin{aligned} \overline{AP}^2 &= (r - y \sin \alpha)^2 + y^2 (\cos^2 \alpha - \frac{r}{R} \cos \alpha) + x^2 (1 - \frac{r}{R} \cos \alpha) - 2x\xi + \xi^2 \\ &+ \frac{(x^2 + y^2)^2}{4R^2} (1 - \frac{r}{R} \cos \alpha) + \frac{(x^2 + y^2)^3}{8R^4} (1 - \frac{r}{R} \cos \alpha) + \dots \end{aligned} \quad (4.98)$$

from which \overline{AP} is derived as

$$\begin{aligned} \overline{AP} &= r - y \sin \alpha + \frac{y^2}{2} \left(\frac{\cos^2 \alpha}{r} - \frac{\cos \alpha}{R} \right) + \frac{x^2}{2} \left(\frac{1}{r} - \frac{\cos \alpha}{R} \right) \\ &- \frac{x\xi}{r} + \frac{\xi^2}{2r} + \dots + \frac{(x^2 + y^2)^2}{8R^2} \left(\frac{1}{r} - \frac{\cos \alpha}{R} \right) + \dots \\ &+ \frac{y^3 \sin \alpha}{2r} \left(\frac{\cos^2 \alpha}{r} - \frac{\cos \alpha}{R} \right) + \frac{x^2 y \sin \alpha}{2r} \left(\frac{1}{r} - \frac{\cos \alpha}{R} \right) \\ &+ \frac{y \sin \alpha}{2r^2} (-2x\xi + \xi^2) + \frac{(x^2 + y^2)^2}{8R^2} \frac{y \sin \alpha}{r} \left(\frac{1}{r} - \frac{\cos \alpha}{R} \right) + \dots \\ &+ \frac{y^4 \sin^2 \alpha}{2r^2} \left(\frac{\cos^2 \alpha}{r} - \frac{\cos \alpha}{R} \right) + \frac{x^2 y^2 \sin^2 \alpha}{2r^2} \left(\frac{1}{r} - \frac{\cos \alpha}{R} \right)^2 \\ &+ \frac{y^2 \sin^2 \alpha}{2r^3} (-2x\xi + \xi^2) - \frac{y^4}{8r} \left(\frac{\cos^2 \alpha}{r} - \frac{\cos \alpha}{R} \right)^2 \\ &+ \frac{3y^5 \sin \alpha}{r^2} \left(\frac{\cos^2 \alpha}{r} - \frac{\cos \alpha}{R} \right)^2 + \dots \end{aligned} \quad (4.99)$$

through binomial expansion of several terms with the similar expression for $\overline{PA'}$ obtained by replacing r by r' , ξ by ξ' , and α by α' .

By combining (4.92) with (4.99) and the expression for $\overline{PA'}$, the first few terms of the optical path are

$$\begin{aligned} S &= r + r' - \left(\sin \alpha + \sin \alpha' - \frac{m\lambda}{d} \right) y \\ &+ \frac{1}{2} \left[\left(\frac{1}{r} - \frac{\cos \alpha}{R} \right) + \left(\frac{1}{r'} - \frac{\cos \alpha'}{R} \right) \right] x^2 \\ &+ \frac{1}{2} \left[\left(\frac{\cos^2 \alpha}{r} - \frac{\cos \alpha}{R} \right) + \left(\frac{\cos^2 \alpha'}{r'} - \frac{\cos \alpha'}{R} \right) \right] y^2 \\ &+ \left(\frac{\xi^2}{r^2} \sin \alpha + \frac{\xi'^2}{r'^2} \sin \alpha' \right) y \end{aligned}$$

$$-\left(\frac{\xi}{r} + \frac{\xi'}{r'}\right)x + \text{higher-order terms.} \quad (4.100)$$

Note that the aberration function W developed in Section A.7.1 utilized the difference between the optical path of a ray from a particular point in the exit pupil to the ray from the center with the full function being the ensemble of such differences. In this case, the center of the pupil is located at the center of the grating and (4.100) reduces to $r + r' + \xi^2/2r + \xi'^2/2r'$ enabling an equivalent aberration description based on Fermat's principle. Applying (4.91) to (4.100) and examining the various terms individually yields

$$\frac{\partial S}{\partial x} = \frac{\xi}{r} + \frac{\xi'}{r'} = 0 \Rightarrow \xi' = -\frac{r'}{r}\xi \quad (4.101)$$

and

$$\frac{\partial S}{\partial y} = -(\sin \alpha + \sin \alpha' - \frac{m\lambda}{d}) = 0 \Rightarrow d(\sin \alpha + \sin \alpha') = m\lambda \quad (4.102)$$

for two of the terms that are independent of the x - and y -coordinates on the grating with (4.101) equivalent to the law of reflection and (4.102) is the grating equation. The second to the last term in (4.100) is now reduced to

$$\frac{1}{2}\left(\frac{\xi^2}{r^2} \sin \alpha + \frac{\xi'^2}{r'^2} \sin \alpha'\right)y = \frac{1}{2} \frac{\xi'^2}{r'^2} \frac{m\lambda}{d} y, \quad (4.103)$$

where (4.101) and the grating equation have been used. This term is the spectral line curvature due to the dispersion of the grating similar to that derived at the end of Section 4.3.4 for a flat grating.

Next, the third term in (4.100) is evaluated using Fermat's principle to obtain

$$\left[\left(\frac{\cos^2 \alpha}{r} - \frac{\cos \alpha}{R}\right) + \left(\frac{\cos^2 \alpha'}{r'} - \frac{\cos \alpha'}{R}\right)\right]y = 0$$

or

$$\cos \alpha \left(\frac{\cos \alpha}{r} - \frac{1}{R}\right) + \cos \alpha' \left(\frac{\cos \alpha'}{r'} - \frac{1}{R}\right) = 0 \quad (4.104)$$

with a solution being

$$r = R \cos \alpha \quad \text{and} \quad r' = R \cos \alpha', \quad (4.105)$$

which represents a circle of diameter R with r and r' being object and image locations respectively on the circle. The circle, known as the Rowland circle, is tangent to the grating at the center and its diameter is equal to the radius of curvature of the grating. For object and image locations on the Rowland circle, all of the terms in the optical path S that are proportional to

$$\frac{\cos^2 \alpha}{r} - \frac{\cos \alpha}{R}$$

in object and image space will vanish. These terms are all multiplied by powers of y starting at y^2 .

The second term in (4.100) describes the astigmatism introduced by a concave or convex grating. Again applying Fermat's principle yields

$$\left[\left(\frac{1}{r} - \frac{\cos \alpha}{R} \right) + \left(\frac{1}{r'} - \frac{\cos \alpha'}{R} \right) \right] x = 0 \quad (4.106)$$

or

$$\frac{1}{r} + \frac{1}{r'} = \frac{\cos \alpha + \cos \alpha'}{R} \quad (4.107)$$

with a solution of

$$r_a = \frac{R}{\cos \alpha} \quad \text{and} \quad r'_a = \frac{R}{\cos \alpha'}, \quad (4.108)$$

which is not on the Rowland circle. Equations (4.108) describe a straight line that is tangent to the Rowland circle at the point where it intersects the optical axis. For a point object on the Rowland circle the image is described by combining (4.101), (4.105), and (4.106) to obtain

$$\left(\frac{\sin^2 \alpha}{\cos \alpha} + \frac{\sin^2 \alpha'}{\cos \alpha'} \right) x - \frac{\xi}{\cos \alpha} - \frac{\xi'}{\cos \alpha'} = 0, \quad (4.109)$$

which reduces to

$$\xi' = x \left(\frac{\sin^2 \alpha}{\cos \alpha} + \frac{\sin^2 \alpha'}{\cos \alpha'} \right) \cos \alpha' \quad (4.110)$$

for a point object at $\xi = 0$. For a square grating with rulings of length L_g this yields an astigmatic focal line of length l_a given by

$$l_a = L_g \left(\frac{\sin^2 \alpha}{\cos \alpha} + \frac{\sin^2 \alpha'}{\cos \alpha'} \right) \cos \alpha' \quad (4.111)$$

at the Rowland circle. The outcome is that the point object is in focus on the Rowland circle in the y -direction while a line is formed in the x -direction with the size of the line depending upon the sizes of α and α' .

The higher-order terms, by which we mean terms of third degree in the grating coordinates x and y , in (4.100), are identified with spherical aberration, coma, and higher-order astigmatism. For example, the y^3 term is a variety of coma which identically vanishes on the Rowland circle; however, astigmatism plays such a large role in a spherical grating that the similar x^2y term, which is multiplied by

$$\left(\frac{1}{r} - \frac{\cos \alpha}{R} \right) + \left(\frac{1}{r'} - \frac{\cos \alpha'}{R} \right),$$

is best thought of as related to it, and other terms are similarly dominated by astigmatism (Welford, 1965).

The analysis of the aberrations introduced by a spherical grating provide an appreciation for the problem of constructing an imaging spectrometer based on the Offner form, with astigmatism the dominant aberration introduced for a Rowland circle mount. The primary and tertiary mirrors are used to correct these aberrations at the scale of the focal plane pixel pitches, which are currently on the order of $30 \mu\text{m}$ and constitute a more

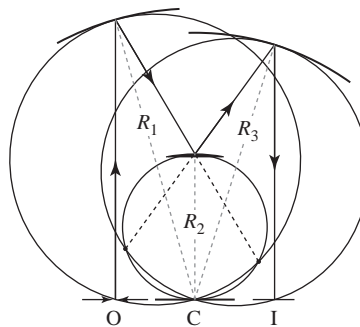


Figure 4.42 The Rowland circle geometry for the Offner–Chrissp imaging spectrometer. The principal ray travels from the object at O, to the center of the limiting aperture at the grating, and on to the image at I. Each Rowland circle has a diameter equal to the radius of curvature for the appropriate spherical element and along the axis from the center of the optic to the center of curvature C.

relaxed design challenge in this respect as compared to the micro-lithography problem that Offner addressed. Chrissp, however, was faced with the challenge of correcting the aberrations over a focal plane whose size is on the order of a square centimeter.

Figure 4.42 illustrates the imaging properties of the Offner–Chrissp with three Rowland circles, one for each mirror, in addition to the grating since a spherical mirror is equivalent to a spherical grating with $m = 0$. The Rowland circles intersect at the center of curvature of the three spherical optical elements and also at the intersection of the projection of the principal ray to the location of the virtual grating object and image. Prieto-Blanco et al. (2006) show analytically through geometrical arguments that astigmatism can be eliminated with Chrissp’s original design as an example of a particular solution. A rigorous solution using the full optical path from the slit to the focal plane array and employing Fermat’s principle to develop the aberration function, as was done above for the grating alone, has also been performed by González-Nuñez et al. (2012). This analysis demonstrates that the first nonzero terms in the expansion are of fourth order. They also show that astigmatism as a function of wavelength can be controlled over a broad range for a reflective system.

4.4.2

The Dyson Imaging Spectrometer

As with the Offner form, the Dyson form was invented for micro-lithographic purposes, with the problem that J. Dyson addressed being the photographic generation of diffraction gratings (Dyson, 1959). Dyson’s design is also concentric, as illustrated in Figure 4.43, and composed of a thick, plano-convex lens with index of refraction n and a spherical mirror, with the centers of curvature of both spherical surfaces on the optical axis at C. The spherical mirror is placed at the focal distance of the thick lens and an object is placed at the plano surface. The spherical mirror is the limiting aperture of the system and, since it is one focal length from the thick lens, the Dyson form is telecentric with the entrance and exit pupils at infinity. A paraxial analysis applying (A.32) and

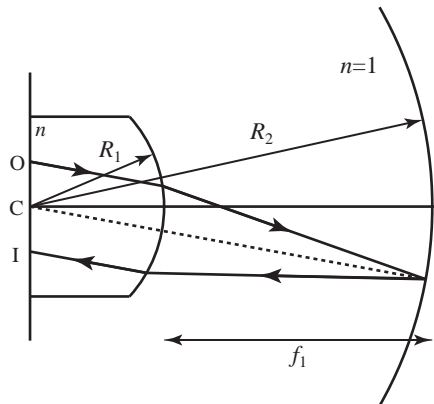


Figure 4.43 Schematic of the Dyson form composed of a plano-convex thick lens and a spherical mirror. The radii of curvature of each powered surface for both optics is centered on C . The concave mirror is positioned at the focal length of the thick lens.

(A.33) to the principal ray, the ray that passes through the pupil centers and determines the field, establishes the relationship between the two radii.

Referring to Figure 4.43, the principal ray travels horizontally from the object at the front surface of the thick lens to the convex back surface where it is bent toward the center of the spherical mirror. The paraxial angle at the plano surface is

$$\bar{u}'_1 = -\eta c_1(1 - n) = \frac{\eta}{r}(n - 1) = \bar{u}_2,$$

where (A.32) has been applied and η is the object height. The bar over the paraxial angle is to remind us that the ray tracing is for the principal ray. The transfer equation (A.33) gives

$$0 = \eta[n - \frac{R_2}{R_1}(n - 1)]$$

since the spherical mirror is the limiting aperture, yielding

$$\frac{R_2}{R_1} = \frac{n}{n - 1} \quad (4.112)$$

for the relationship between the two radii. Since the principal ray is reflected by the spherical mirror at the optical axis $\bar{u}'_2 = -\bar{u}_2$ and the transfer equation gives

$$\bar{h}_3 = d_2 \bar{u}'_2 = \eta(n - 1) \left(1 - \frac{R_2}{R_1} \right) = -\eta$$

for the height of the ray at the convex surface of the lens. Application of (A.32) yields $\bar{u}'_3 = 0$ as expected with the image height given by $\eta' = \bar{h}_3$ for a magnification of -1 . The reader can confirm that the image is located at the plano surface by tracing a second ray. It is relatively easy to show using aberration theory that all of the Seidel aberrations are zero.

The Dyson form is converted to an imaging spectrometer by replacing the concave mirror with a concave grating, which breaks the symmetry of the form and introduces a

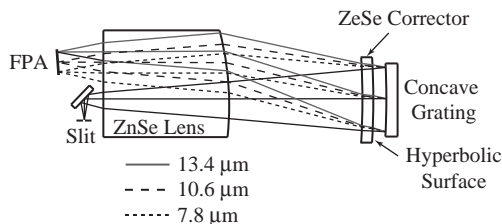


Figure 4.44 Warren's design of a LWIR Dyson Imaging Spectrometer. Adapted from Warren et al. (2008).

host of aberrations, with astigmatism being the most serious. As with the Offner–Chrissp, the aberrations through the third order vanish, which can be shown through an analysis similar to that given in González-Nuñez et al. (2012) where the optical path is evaluated through the application of Fermat's principle. A complication that is addressed in Warren's design is the positioning of the slit and focal plane array (Warren, 2009; Warren et al., 2008). In the original Dyson imaging spectrometer form, both are located at the plano face of the thick lens, which is challenging to achieve in practice due to the mounting requirements of the FPA in particular. Warren solved this problem by introducing a radially aspheric corrector lens with a hyperbolic surface mounted proximate to the concave grating as shown in Figure 4.44. The introduction of the corrector lens requires that the convex surface of the thick lens be modified from the Dyson configuration. It is shown in Warren et al. (2008) that excellent performance is achieved for an F/2.5 imaging spectrometer using zinc selenide for both refractive optics and a focal plane array with a pixel pitch of 75 μm .

4.4.3 Grating Enhancements

It was shown in Section 4.3.4 that gratings are quite efficient near the blaze wavelength but become rather inefficient at both shorter and longer wavelengths. Improved performance is achieved through the use of micro-lithography techniques where the facets on the grating are shaped in detail. Researchers at the NASA Jet Propulsion Laboratory (JPL) have pioneered the production of blazed gratings on curved substrates for use in both Offner–Chrissp and Dyson imaging spectrometers. Their approach utilizes e-beam lithography to shape the individual facets on scales of the order of tens of nanometers. The basic process is to expose a resist material that has been deposited on the curved substrate to a focused electron beam which alters its physical structure through the breakage of chemical bonds. The altered structure is subsequently removed through chemical etching and the blaze profile is measured using atomic force microscopy. One of the challenges that was overcome was the smooth stitching of the irradiated areas over the entire grating optic to ensure that no other periodic structures were introduced and to minimize scattered light. The final step is to apply a reflective coating such as aluminum. The application of the lithographic techniques has evolved with the generation of gratings progressing from single blaze to area blaze to dual-facet gratings (Mouroulis et al., 1998). Diamond machining techniques are also under development as a cost-effective

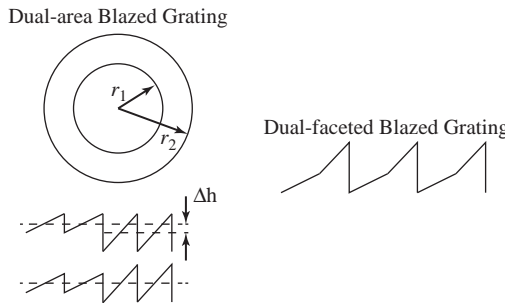


Figure 4.45 The left figure is a dual-area blazed grating with two zones. Matching the average height of the blaze profiles is shown at the bottom. The facet profile for a dual-facet blazed grating is shown on the right. Adapted from Mouroulis et al. (1998).

and more broadly available alternative to the JPL process (Davies et al., 2012; Cobb et al., 2006).

Area blaze gratings utilize a different blaze angle for different areas of the grating as shown on the left side of Figure 4.45. For example, a convex grating could have a centered circle of radius r_1 inside an annulus of width $r_2 - r_1$. A simple method to model such a grating is to use a weighted sum of contributions from the two areas given by

$$E_g = E_o \left(\frac{A_1}{A} E_{g1} + \frac{A_2}{A} E_{g2} \right), \quad (4.113)$$

where A_1 and A_2 are the areas of the central circle and the annulus respectively, A is the total area, E_{g1} and E_{g2} are the grating efficiencies for the two areas given by (4.83), and E_o is the peak efficiency. This equation works well within the limitations of the scalar theory. The stitching between the two areas has precise requirements for phase matching. If the average blaze height is not matched then the peaks of the main lobes of the diffraction envelopes, for example, those illustrated in Figure 4.37, will be mismatched with a decrease in overall efficiency.

Any phase difference due to a mismatch in the average blaze height has detrimental effects for both the Offner–Chrissp and the Dyson imaging spectrometers since the grating is the limiting aperture in both cases. The changing efficiency across the grating is a modification of the aperture function which can lead to broadening of the point spread function due to a reduction in aberration control. A solution is to shape the profile of each facet so that it has two angles as illustrated on the right in Figure 4.45 where no phase distortion is possible. The scalar model is not a good representation of the grating efficiency in this case although it can be used effectively to generate an approximate efficiency for system engineering purposes. More than two areas can be used in (4.113) in order to create the desired efficiency curve that can be used as a model to guide the grating design using numerical techniques. The NASA Moon Mineralogy Mapper that was flown on Chandrayaan-1, which employed the Offner–Chrissp form, utilized a grating of this type (Mouroulis et al., 2007).

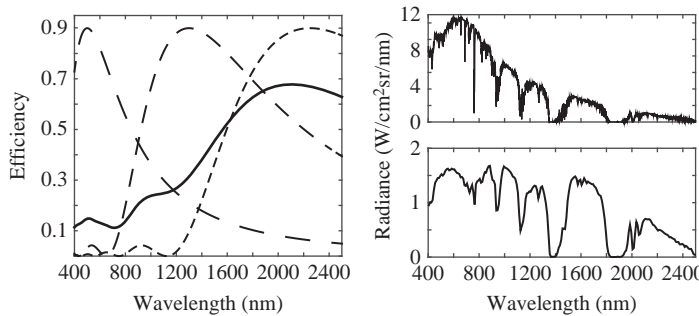


Figure 4.46 The left graph is a model based on (4.113) using three areas and blaze wavelengths with the dashed lines corresponding to the particular efficiencies for a given area and the solid curve corresponding to the total efficiency. The two graphs on the right show the result of applying the grating model to the at-aperture radiance (upper graph) for a uniform imaging spectrometer with 10 nm spectral spacing and a 12 nm width for the instrumental profile.

The ability to modify the efficiency of a grating is used to tailor the signal-to-noise performance of the imaging spectrometer. Figure 4.46 is an example of a model where an imaging spectrometer with a uniform instrumental profile utilizes a grating designed to balance the overall performance for the full spectral range. The left side of the figure shows the composite efficiency modeled using (4.113) modified for three zones with blaze wavelengths at 500 nm, 1300 nm, and 2250 nm with corresponding area fractions of 0.15, 0.25, and 0.6. The overall efficiency was taken to be 0.90. The right side shows how the at-aperture radiance is scaled by the grating efficiency and band-averaged using a uniform instrumental profile with 10 nm spacing and 12 nm widths. The signal produced by the imaging spectrometer is modeled with (4.25) and would include the transmission of all of the optical elements in addition to the grating efficiency incorporated into τ . This approach is used in the initial system engineering to estimate the grating efficiency as an input for the design of the final grating.

4.4.4 Additional Dispersive Designs

The Offner–Chrisp and Dyson imaging spectrometer forms have been treated in some detail as particular examples; however, other optical forms have been demonstrated and are highly performing. There are a great many particular designs, and it is beyond our scope to go into each in detail, so we will settle for a brief description of a few examples. The designs selected span a broad design range, with both prisms and gratings for dispersing elements with reflective and refractive optical elements. Aberrations are well controlled in each and will not be addressed in detail.

Researchers at the Aerospace Corporation have a long history of developing imaging spectrometers for use in the longwave infrared. A highly successful design, which was used in the SEBASS sensor and others, employs shaped prisms for aberration control and is well described in Warren et al. (1997). The design does not suffer from spherical aberration, coma, or astigmatism. The aplanatic condition for a sphere is presented in

Born and Wolf (1999) and Warren et al. (1997) apply the principle to the curved surfaces of a prism in a double pass arrangement. They demonstrate image formation on a focal plane array of 128×128 pixels with a $75 \mu\text{m}$ pitch that is nearly aplanatic, with aberration control below the diffraction limit for a 7.8 to $13.4 \mu\text{m}$ spectral range. SEBASS has both mid-wave and longwave infrared channels, employing lithium fluoride and sodium chloride prisms respectively, and has generated large volumes of high quality spectral imagery. The design was also cryogenically cooled for stabilization and to control the emission of light from the refractive optical elements.

Another example is a second imaging spectrometer design by Michael Chrisp for operation in the LWIR, illustrated in Figure 4.47 (Chrisp, 2008). Light from the entrance slit is approximately collimated by a catadioptric lens, a lens that is composed of both refractive and reflective elements, passes to a flat immersion grating where it is dispersed, and is focused by a doublet onto the focal plane array. An immersion grating is one that is constructed on the back side of an optical flat with index n with diffraction at the grating occurring within the material. The grating equation becomes

$$m\lambda_o = nd(\sin \theta_{1n} + \sin \theta_{2n}) \quad (4.114)$$

for constructive interference *inside* the material with λ_o signifying the vacuum wavelength and θ_{1n} and θ_{2n} being the incident and exitant angles. This increases the resolution compared to an equivalent grating in vacuum by a factor of n . The immersed grating forms the limiting aperture and the cold stop for the imaging spectrometer and the system is also approximately telecentric. Recall that the limiting aperture determines the amount of light that is passed through an optical system with the principal ray defining the size of the field. By making this aperture cold, Planck radiance from it is minimized and the flux at the focal plane array is limited to that from the object space. The design has the required degree of aberration control with smile and keystone controlled to less than a tenth of a pixel with a $40 \mu\text{m}$ pitch for F/3.5 designs in the examples included in Chrisp (2008). This design is very compact, with linear dimensions on the order of 10 cm or less, making it relatively easy to cool and stabilize to the operational temperatures required for the LWIR.

The reflective triplet, shown in Figure 4.48, is another example of an imaging spectrometer, in this case developed by Lacy Cook, and is a three-mirror design similar to

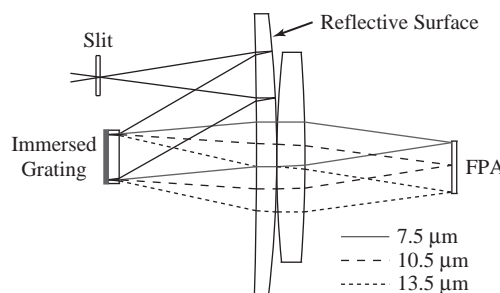


Figure 4.47 One example of a Chrisp LWIR imaging spectrometer. Adapted from Chrisp (2008).

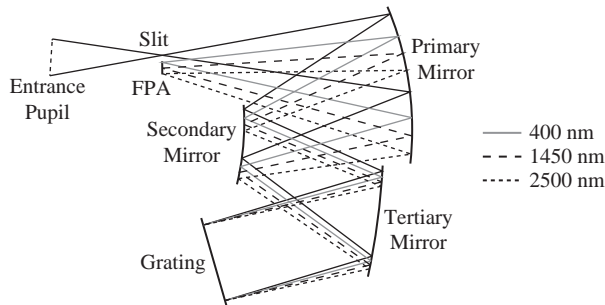


Figure 4.48 The Cook reflective triplet imaging spectrometer for operation in the VNIR/SWIR. The real pupil is shown and the dispersing element is also a pupil. Adapted from Cook and Silny (2010).

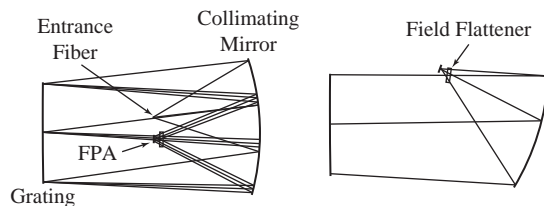


Figure 4.49 One of the four F/1 AVIRIS spectrometers. Note that the grating is an asphere. Adapted from Macenka and Chrisp (1987).

the Cook three-mirror anastigmat telescope (Cook, 1993, 2005, 2006). It is composed of a positively powered primary mirror, a negatively powered secondary mirror, a positively powered tertiary mirror, and a dispersing optic, which can be either a grating or a prism. The beam that is dispersed is collimated as in a traditional spectrometer. The instrument works in a double pass configuration with the dispersed image focused at a focal plane that is proximate to the entrance slit in a near Littrow configuration. The imaging spectrometer has a real pupil in the space preceding the slit and can be matched to a variety of telescopes making it highly versatile. It also supports a wider field of view than either the Offner–Chrisp or the Dyson forms. Additionally, the real pupil may serve as a cold stop for LWIR applications. In the reflective triplet the dispersing element is also a pupil and it must be cold as well for LWIR operation. The reflective triplet can support simultaneous spectral imaging of two spectral ranges such as the VNIR/SWIR and the LWIR (Cook, 2008).

The final dispersive imaging spectrometer presented is the Airborne Visible/Infrared Imaging Spectrometer, known universally as AVIRIS. The AVIRIS program at JPL is the most successful remote sensing program using an imaging spectrometer to date, with thousands of high-quality VNIR/SWIR spectral images acquired. AVIRIS is the successor instrument to the Airborne Imaging Spectrometer, also developed at JPL, which was the first to utilize area arrays for imaging spectroscopy (Vane et al., 1984). An overview of AVIRIS is in Green et al. (1998), with the full sensor details of the original design in Macenka and Chrisp (1987).

Table 4.3 AVIRIS specifications derived from Macenka and Chriss (1987) and Green et al. (1998). The angular width of the detector is estimated from the focal length of the collimating mirror and the detector pitches which are 200 μm for spectrometers A through C and 214 μm for D.

spectrometer	range (nm)	F (mm)	β (mrad)	θ_2 (degrees)	d (μm)	$\delta\lambda$ (nm)
A	400–700	189.75	1.05	3.35	8.5	9.7
B	700–1300	187.2	1.07	1.84	7.80	9.7
C	1300–1900	185.26	1.08	0.16	8.05	9.0
D	1900–2500	179.88	1.19	3.98	7.775	11.6

AVIRIS is composed of four separate classical spectrometers that are connected to an imaging fore optic through optical fibers. This is a rare example of an imaging spectrometer with the fore optics and the spectrometer decoupled. The image is subsequently accumulated through raster scanning the single image point across the surface, which is practical since AVIRIS has high étendue. The spectrometers are composed of a spherical primary mirror, an aspheric grating, and a field flattener. The limiting aperture is the grating located at the center of curvature of the collimating mirror. Each grating is diamond machined to have a single blaze angle with blocking filters used to remove any out of band radiance. Four line arrays of detector elements are used to record a spectrograph for a total of 224 samples. AVIRIS has inherent spatial–spectral uniformity, since it acquires a single spatial sample at a time, and excellent signal-to-noise performance.

4.5

Interference Imaging Spectrometer Fundamentals

Interference spectrometers utilize amplitude division of the wavefront, rather than its spatial division as with a grating, to extract the desired spectral information with the two primary designs being Fabry–Pérot and Michelson interferometers. In traditional spectroscopy these instruments are often used to measure atomic and molecular spectra with high resolving power. Additionally, they have high étendue and optical efficiency when used with a diffuse source with signal-to-noise advantages. We will limit our discussion to the application of Michelson interferometers to imaging spectroscopy. Fabry–Pérot etalon-based imaging spectrometers have been developed and applied to the problem of detecting chemical plumes in the LWIR (Marinelli et al., 1999); however, currently these systems are not widely utilized. In contrast, Michelson interferometers are commercially available and have been used extensively.

Figure 4.50 is a schematic of the most basic design of a Michelson interferometer, invented by Albert A. Michelson and subsequently used to determine that light does not require a medium of propagation (Michelson and Morley, 1887). Michelson and others soon began applying his invention to spectroscopy, although it wasn't until the 1950s that the technique became broadly applied (Connes, 1984). The effective use of these devices requires computers for the data acquisition and processing, which retarded their development as spectrometers. In the ideal interferometer, a point in the object plane

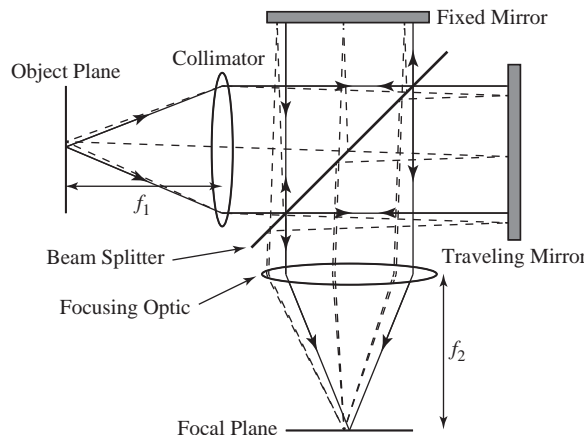


Figure 4.50 Schematic of an ideal Michelson interferometer showing ray paths for both the on- and off-axis cases.

emits spherical waves that are collimated by the first optic creating plane waves. A plane wave propagates to a beam splitter where half of the wave is reflected to a fixed flat mirror and half is transmitted to a moving flat mirror. The plane waves are reflected and recombine into one at the beam splitter, with the combined wave propagating to the focusing optic, and focused at the image plane. Interference occurs due to the unequal optical paths between the beam splitter and the mirrors. The output of the interferometer is an *interferogram*, a superposition of the additive frequency components. If a truly monochromatic source is viewed, the interferogram is just a sinusoid. The typical case has an interferogram that is made up of the superposition of sinusoids from a continuum of different frequencies over a spectral range. The spectral content of this encoded signal is recovered by taking a Fourier transform.

The theory of operation of a Michelson interferometer is developed starting with a monochromatic source. Recall from Chapter 2 that plane waves propagating in a non-absorbing medium are described by

$$\mathbf{E}(\mathbf{r}, t) = \mathbf{E}_o \exp[i(\mathbf{k} \cdot \mathbf{r} - \omega t)],$$

which reduces to

$$\mathbf{E}(x, t) = \mathbf{E}_o \exp[i(kx - \omega t)] \quad (4.115)$$

for the incident one-dimensional wave propagation prior to beam splitting into the two arms of the interferometer. The two electromagnetic waves after splitting are rewritten as

$$\mathbf{E}_1 = \mathbf{E}_{o1} \exp[-i(\omega t - \phi_1)] \quad (4.116)$$

and

$$\mathbf{E}_2 = \mathbf{E}_{o2} \exp[-i(\omega t - \phi_2)], \quad (4.117)$$

where ks_1 and ks_2 are identified as the phases ϕ_1 and ϕ_2 of the two waves for their different paths of propagation. The beam splitter has amplitude reflectance and transmittance of r_b and t_b and the two mirrors have amplitude reflectances of r_1 and r_2 that will be taken to be equal. The amplitude reflectance is related to the specular reflectance $\rho(\theta_i, \phi; -\theta_i, \phi + \pi)$, since θ_i equals $-\theta_r$, through $\rho = r^2$. Similarly the amplitude transmission t_b through the beam splitter is related to the transmission by $\tau_b = t_b^2$ with the angular dependence suppressed. The beam in the first arm, after all reflections and beam splitter transmission, is therefore given by

$$E_1 = E_o r_b t_b r_1 \exp[-i(\omega t - \phi_1)] \quad (4.118)$$

and the second beam is

$$E_2 = E_o r_b t_b r_2 \exp[-i(\omega t - \phi_2)] \quad (4.119)$$

with the resulting amplitude after recombination given by

$$E = E_1 + E_2 = E_o r_b t_b r_1 e^{-i\omega t} (e^{-i\phi_1} + e^{-i\phi_2}). \quad (4.120)$$

The irradiance at the focal plane after focusing is obtained from the Poynting vector yielding

$$\begin{aligned} E &= E_o \rho_b \tau_b \rho_1 (e^{-i\phi_1} + e^{-i\phi_2})(e^{i\phi_1} + e^{i\phi_2}) \\ &= 2E_o \rho_b \tau_b \rho_1 [1 + \cos(\phi_1 - \phi_2)], \end{aligned} \quad (4.121)$$

where $\cos \theta = (e^{-i\theta} + e^{i\theta})/2$ has been used and E_o is the irradiance from the equivalent area at the object plane.

It remains to determine the phase difference in (4.121) that is due to the different path lengths in the two arms. Figure 4.51 illustrates the Michelson interferometer unfolded along the beam-splitter with an off-axis ray traced through the system. The distance between the moving mirror and the projection of the fixed mirror onto the moving mirror axis is d and the back projections of the split off-axis ray intersects the optical axis at points that are a distance $2d$ apart. From the diagram, the path difference for an interferometer in air is given by

$$\delta = 2d \cos \theta = 2(l_2 - l_1) \cos \theta, \quad (4.122)$$

where l_1 and l_2 are the distances from the center of the beam splitter. If the interferometer was in a different medium than air or vacuum then the two distances would be multiplied by the appropriate refractive index. The phase difference is therefore

$$\phi_1 - \phi_2 = \frac{2\pi}{\lambda} \delta = 4\pi(l_2 - l_1) \tilde{v} \cos \theta, \quad (4.123)$$

where $\Delta\phi/2\pi = \delta/\lambda$ has been used and the wavelength has been converted to wave number. This leads to the irradiance expressed as

$$E = 2E_o \rho_b \tau_b \rho_1 \{1 + \cos[4\pi(l_2 - l_1) \tilde{v} \cos \theta]\}, \quad (4.124)$$

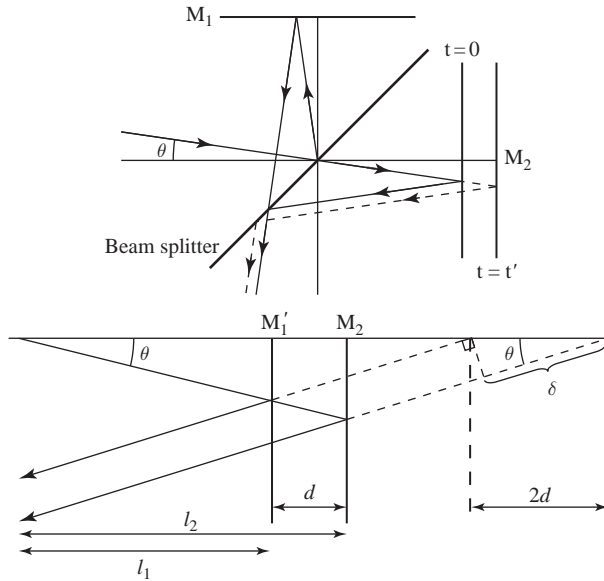


Figure 4.51 The Michelson interferometer unfolded about the beam splitter to project the ray paths in the two arms onto a single axis with an off-axis ray originating at the beam splitter center illustrated in the bottom schematic. The image of the fixed mirror M_1 is denoted by M'_1 and the moving mirror is M_2 . The path difference is $\delta = 2d \cos \theta$ with l_1 and l_2 being the respective mirror distances from the center of the beam splitter along the optical axis at $t = t'$. At $t = 0$ the mirrors are equidistant from the beam splitter.

which, if the beam splitter and the mirrors are ideal with $\rho_b = \tau_b = 0.5$ and $\rho_1 = 1$, reduces to

$$E = \frac{1}{2} E_o \{1 + \cos[4\pi(l_2 - l_1)\tilde{v} \cos \theta]\}. \quad (4.125)$$

For a uniform source, the interferometer produces an image at the focal plane of concentric rings or fringes. No interferometer has ideal optical components and (4.125) is multiplied by the optical efficiency factor τ . In this presentation the interferometer will be assumed to be ideal.

The on-axis interferometer path difference is defined as

$$x \equiv 2(l_2 - l_1) \quad (4.126)$$

with the maximum on-axis path difference given by $x = L_m$. The irradiance given by (4.124) is alternatively written as

$$E = 4E_o \rho_b \tau_b \rho_1 \cos^2[2\pi(l_2 - l_1)\tilde{v} \cos \theta], \quad (4.127)$$

where the trigonometric identity $1 + \cos A = 2 \cos^2(A/2)$ has been applied. The cosine in (4.127) has maximum values when

$$m = 2(l_2 - l_1)\tilde{v} \cos \theta \quad \text{where} \quad m = 0, 1, 2, \dots, m_o \leq L_m \tilde{v}, \quad (4.128)$$

since $\cos \theta \leq 1$ with m going to 0 as θ approaches 90° . It is unlikely that a peak will fall perfectly on the optical axis at the maximum path difference which implies that $L_m \tilde{v} - m_o = \varepsilon$ with ε being a small shift bounded by $0 \leq \varepsilon < 1$ and

$$\cos \theta = \frac{m}{L_m \tilde{v}} \Rightarrow 1 - \frac{\theta^2}{2} \approx \frac{m}{L_m \tilde{v}} = \frac{m}{m_o + \varepsilon}$$

for small angles. If the peaks are counted going from the optical axis ($\theta = 0$) outward using the index j where $m_o - m = j$, then

$$\frac{\theta^2}{2} = \frac{j + \varepsilon}{L_m \tilde{v}} \Rightarrow \theta_j = \sqrt{\frac{2(j + \varepsilon)}{L_m \tilde{v}}}, \quad (4.129)$$

where $j = 0, 1, 2, \dots$ and θ_j is the position of the fringe peaks as illustrated in the top graph of Figure 4.52.

In the typical case the source is polychromatic and (4.125) is modified. First, the spectral irradiance is $E(\tilde{v})$ and the irradiance within a spectral element of width $d\tilde{v}$ at wave number \tilde{v} at the image plane is $dI(x) = E(\tilde{v}) d\tilde{v}$ where x is again the on-axis path difference. The change in notation emphasizes that the interferogram $I(x)$ at a particular mirror position is composed of a range of spectral irradiances $E(\tilde{v})$. The full

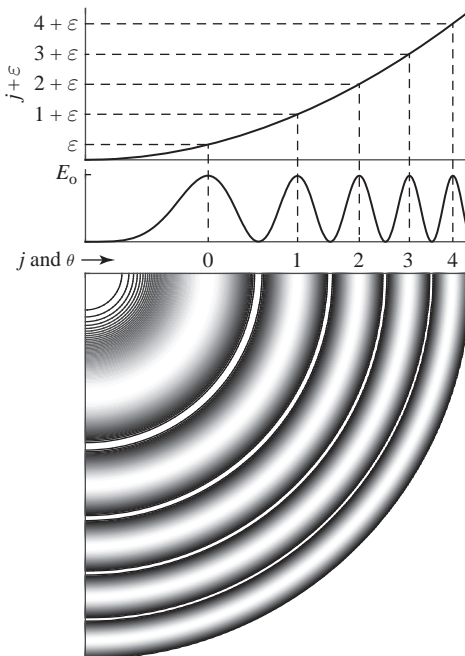


Figure 4.52 Illustration of the bullseye pattern produced by a Michelson interferometer for a large, spatially uniform, monochromatic source. The upper graph shows that the peak separation decreases as $\theta \sim (j + \varepsilon)^{1/2}$. The middle graph is the variation in the irradiance as a function of θ with the peaks indices j marked. The bottom is a corresponding contour graph of one quarter of the full ring pattern.

interferogram is a modification of (4.125) to reflect the spectral contributions across the bandpass or

$$I(x) = \frac{1}{2} \int_0^\infty E(\tilde{v}) d\tilde{v} + \frac{1}{2} \int_0^\infty E(\tilde{v}) \cos(2\pi \tilde{v}x) d\tilde{v}, \quad (4.130)$$

which is often written with the $1/2$ absorbed into the irradiance. The first term is a constant and (4.130) is simplified by subtracting the mean value of the interferogram yielding

$$I(x) - \overline{I(x)} = \int_0^\infty E(\tilde{v}) \cos(2\pi \tilde{v}x) d\tilde{v} \quad (4.131)$$

with the spectral irradiance obtained by taking the *cosine* transform or

$$E(\tilde{v}) = \int_{-\infty}^\infty I(x) \cos(2\pi \tilde{v}x) dx = 2 \int_0^\infty I(x) \cos(2\pi \tilde{v}x) dx. \quad (4.132)$$

The integral on the right side of (4.132) is from 0 to infinity, but mathematically two spectra are generated corresponding to $E(\tilde{v})$ and $E(-\tilde{v})$ since the cosine is an even function. Negative wave numbers are fictitious, even though the interferogram that would be generated by $E(-\tilde{v})$ is identical to the one actually generated. However, the symmetry of performing the integration over the full frequency domain ($-\infty$ to $+\infty$) justifies the utilization of the negative spectrum. To accomplish this the irradiance $E(\tilde{v})$ is symmetrized, making it an even function, through

$$E_e(\tilde{v}) = \frac{1}{2}[E(\tilde{v}) + E(-\tilde{v})] \quad (4.133)$$

with the interferogram and the recovered irradiance given by

$$I(x) = \int_{-\infty}^\infty E_e(\tilde{v}) \cos(2\pi \tilde{v}x) d\tilde{v} \quad (4.134)$$

and

$$E_e(\tilde{v}) = \int_{-\infty}^\infty I(x) \cos(2\pi \tilde{v}x) dx. \quad (4.135)$$

In reality, the spectral irradiance is recovered by taking the Fourier transform of the interferogram. Thus far, an ideal interferometer with no wave number dependence to the optical path has been described. Real interferometers are not so well behaved, with the sinusoids that are superposed to form the interferogram having phase differences that are not solely due to the mirror travel. The interferometer has a beam splitter made of a refractive material with not perfectly parallel surfaces, and it also has an optical coating that reflects half of the light with both of these, introducing phase shifts that depend upon the particular wave number. This means that at the zero path difference point, the ZPD, there will be a phase change in contrast to the ideal case. Figure 4.53 illustrates the effect for an interferogram made up of two sinusoids. In the ideal case there is a peak due to constructive interference at the ZPD, while in the more realistic case the two waves are not perfectly aligned when l_1 and l_2 are equal, and the interference is generally neither truly constructive nor destructive.

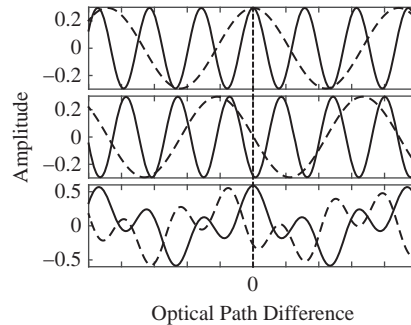


Figure 4.53 The ideal case and a more realistic case with travel independent phase shifts. The top graph illustrates the perfect case where the phase shift between two cosine waves is solely due to the path difference introduced by the mirror travel and both are aligned at the zero path difference point. The middle graph shows the case where phase shifts due to other factors are introduced. The bottom curve shows the corresponding interferograms with the solid curve representing the ideal case and the dashed curve the more realistic case.

It is clear from Figure 4.53 that the symmetry about the ZPD is broken in a real interferogram and therefore the cosine transform does not apply. This is addressed through the Fourier transform formalism. The full development of Fourier analysis is lengthy, to say the least, and will only be introduced here. The volumes by Gaskill (1978) and Bracewell (2000) are particularly recommended for a full discussion. Inherent in the description so far has been the assumption that the system is linear and the principle of superposition applies, with the signal resulting from a measurement being the sum of the individual component waves. In a real system this is only approximately true. For example, the detector may have a nonlinear response in general or at some signal levels, such as near saturation or at very low irradiances. These departures from linearity will not be addressed.

Figure 4.53 illustrates that real interferograms are no longer even functions, where $I(x) = I(-x)$, but are a combination of even and odd functions due to the additional phase shifts. The general form for the interferogram that includes both sine (odd) and cosine (even) functions is written as

$$I(x) = \int_{-\infty}^{\infty} E(\tilde{\nu}) e^{i2\pi\tilde{\nu}x} d\tilde{\nu}, \quad (4.136)$$

which reduces to

$$I(x) = \int_{-\infty}^{\infty} E(\tilde{\nu}) \cos(2\pi\tilde{\nu}x) d\tilde{\nu} + i \int_{-\infty}^{\infty} E(\tilde{\nu}) \sin(2\pi\tilde{\nu}x) d\tilde{\nu} \quad (4.137)$$

from Euler's formula. For a perfect interferometer, where the phase shift is only due to the mirror travel, the second term in (4.137) vanishes, implying that $E(\tilde{\nu})$ is both real and even in the ideal case. The consequence of the phase shift that is not due to the mirror travel is that $E(\tilde{\nu})$ is a *complex* function written as

$$E(\tilde{\nu}) = E_r(\tilde{\nu}) + iE_i(\tilde{\nu}), \quad (4.138)$$

where E_r and E_i are the real and complex parts while $I(x)$ must be a real function since it is a measured quantity. Equation (4.138) is rewritten in the polar form for the complex plane as

$$E(\tilde{v}) = |E(\tilde{v})|e^{i\phi(\tilde{v})} \quad (4.139)$$

where $|E(\tilde{v})|$ is the amplitude spectrum given by

$$|E(\tilde{v})| = \sqrt{E(\tilde{v})^*E(\tilde{v})} = \sqrt{[E_r(\tilde{v})]^2 + [E_i(\tilde{v})]^2} \quad (4.140)$$

and the phase is

$$\phi(\tilde{v}) = \tan^{-1} \left[\frac{E_i(\tilde{v})}{E_r(\tilde{v})} \right]. \quad (4.141)$$

The spectral irradiance is recovered through

$$E(\tilde{v}) = \int_{-\infty}^{\infty} I(x)e^{-i2\pi\tilde{v}x} dx \quad (4.142)$$

from the full Fourier development (Gaskill, 1978).

4.5.1

The Instrumental Profile for a Michelson Interferometer

It was shown in Section 4.2.2 that all spectrometers, imaging or otherwise, perform spectral discrimination described by the instrumental profile. In the case of a dispersive imaging spectrometer the instrumental profile was developed based upon the action of the dispersing element, the slit, and the size of the detector element and it is measured by scanning a monochromatic source. How is P developed for a Michelson interferometer, since the recorded signal is encoded with the contributions from the different wave numbers that make up the at-aperture radiance, and what property of the interferometer sets the limit of the resolution?

Figure 4.13 illustrated the measurement of the instrumental profile by scanning a monochromatic source. The equivalent for a Michelson interferometer is to measure a monochromatic source and take the Fourier transform of the signal to numerically recover the instrumental profile. For the ideal interferometer the interferogram is strictly a cosine wave that would extend from $-\infty$ to $+\infty$ if there was an limitless mirror travel. The Fourier transform of this fictitious interferogram is a delta function. In a real instrument with a finite travel the cosine wave is truncated, which leads to the finite width of the instrumental profile.

The rectangle function is used to mathematically model the effect of the finite travel on the interferogram through

$$\text{rect}\left(\frac{x}{2L_m}\right) = \begin{cases} 1, & |x| \leq L_m \\ 0, & |x| > L_m \end{cases}, \quad (4.143)$$

where L_m is the path difference for the maximum mirror travel from the zero path difference point with the measured interferogram given by

$$I_m(x) = I(x)\text{rect}\left(\frac{x}{2L_m}\right), \quad (4.144)$$

where $I(x)$ is the interferogram that would be measured with an infinite travel. The instrumental profile is recovered from the interferogram of a monochromatic source at wave number $\tilde{\nu}_o$ through the application of (4.135) or (4.142) to yield

$$\begin{aligned}
 E(\tilde{\nu} - \tilde{\nu}_o) &= \int_{-\infty}^{\infty} I_m(x) \cos(2\pi \tilde{\nu} x) dx \\
 &= \int_{-\infty}^{\infty} \cos(2\pi \tilde{\nu}_o x) \text{rect}\left(\frac{x}{2L_m}\right) \cos(2\pi \tilde{\nu} x) dx \\
 &= \int_{-L_m}^{L_m} \cos(2\pi \tilde{\nu}_o x) \cos(2\pi \tilde{\nu} x) dx \\
 &= L_m \{\text{sinc}[2\pi(\tilde{\nu}_o + \tilde{\nu})L_m] + \text{sinc}[2\pi(\tilde{\nu}_o - \tilde{\nu})L_m]\}, \quad (4.145)
 \end{aligned}$$

where $2 \cos A \cos B = \cos(A + B) + \cos(A - B)$ was used. The recovered irradiance has the symmetric peaks about $\tilde{\nu} = \tilde{\nu}_o$ and $\tilde{\nu} = -\tilde{\nu}_o$ as expected, with the negative wave numbers being fictitious and discarded. The instrumental profile is identified as

$$P(\tilde{\nu}_o - \tilde{\nu}) = \frac{\sin[2\pi(\tilde{\nu}_o - \tilde{\nu})L_m]}{[2\pi(\tilde{\nu}_o - \tilde{\nu})L_m]} = \text{sinc}[2\pi(\tilde{\nu}_o - \tilde{\nu})L_m], \quad (4.146)$$

which can be shown to be peak normalized at $\tilde{\nu} = \tilde{\nu}_o$ by applying L'Hospital's rule. This is another example of a symmetric spectral response function which is typically written as $P(\tilde{\nu} - \tilde{\nu}_o)$. Also notice that the center wave number is immediately recovered and it could have had any value within the broad bandpass of the interferometer.

The instrumental profile is illustrated in Figure 4.54, which shows both the FWHM and the distance from the center to the first zero crossing. The theoretical resolving power is universally written as

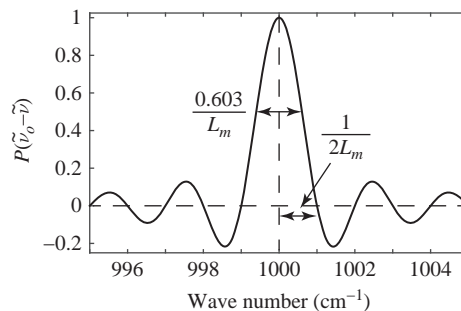


Figure 4.54 The instrumental profile for an ideal Michelson interferometer with L_m equal to 0.5 cm measuring a monochromatic source at 1000 cm^{-1} . The FWHM value is $0.603/L_m$ and the distance from the center to the first zero is $1/2L_m$.

$$R_o = \frac{\tilde{v}}{\delta\tilde{v}} = 2L_m\tilde{v}, \quad (4.147)$$

with the limit of resolution $\delta\tilde{v}$ taken to be $1/2L_m$ rather than $0.603/L_m$ from the FWHM since this is the spectral distance between *statistically* independent samples. Note that the limit of resolution is determined by the maximum path difference, a critical design parameter. The Michelson instrumental profile, which has negative values due to the discontinuity from the truncation of the interferogram using the rect function, is quite different from the similar function for a grating illustrated in Figure 4.26. It can be made to be similar through *apodization*, from the French word for removing the feet, by applying a function that smoothly goes to zero at the maximum path difference. In practice, when the data taken with a Michelson interferometer are analyzed, particularly for spectroscopic studies using high spectral resolution, the spectrum is fit using (4.146).

The finite path difference is not the only factor contributing to the shape of the instrumental profile. Figure 4.52 shows the ring pattern from an extended source due to the off-axis rays. A measurement is made using a detector element of a finite size that accepts waves whose rays span a range of angles. Considering only a detector element on-axis, the path difference is proportional to θ from (4.122) and the range of angles accepted is determined by the pixel half-width. Returning to the monochromatic case the interferogram is written as

$$I(x) = \cos(2\pi\tilde{v}x \cos \theta) \quad (4.148)$$

for unit irradiance. The solid angle subtended by a detector element at the focal plane of the focusing optic is $\omega = p^2/F^2 \approx \pi\alpha^2$ for small angles where p is the pixel pitch and α is the angular half width of the detector element approximated as circular for convenience. The interferogram is written as

$$\begin{aligned} dI(x) &= \cos(2\pi\tilde{v}x \cos \alpha) d\omega \\ &\approx \cos \left[2\pi\tilde{v}x \left(1 - \frac{\alpha^2}{2} \right) \right] d\omega \\ &= \cos \left[2\pi\tilde{v}x \left(1 - \frac{\omega}{2\pi} \right) \right] d\omega. \end{aligned} \quad (4.149)$$

The total irradiance at a particular mirror position is obtained by integrating over the area of the detector element or

$$\begin{aligned} I(x) &= \int_0^{\omega_m} \cos \left[2\pi\tilde{v}x \left(1 - \frac{\omega}{2\pi} \right) \right] d\omega \\ &= \frac{1}{\tilde{v}x} \left\{ \sin 2\pi\tilde{v}x + \sin \left[-2\pi\tilde{v}x \left(1 - \frac{\omega_m}{2\pi} \right) \right] \right\}, \end{aligned} \quad (4.150)$$

which reduces to

$$I(x) = \omega_m \left[\text{sinc} \left(\frac{\tilde{v}x\omega_m}{2} \right) \right] \cos \left[2\pi\tilde{v}x \left(1 - \frac{\omega_m}{4\pi} \right) \right], \quad (4.151)$$

where $\sin A + \sin B = 2 \sin[(A + B)/2] \cos[(A - B)/2]$ has been applied.

From (4.151) there are two effects of the finite detector size. The first is that the wave number is shifted from \tilde{v} to $\tilde{v}(1 - \omega_m/4\pi)$ or, alternatively, the path difference is changed by $x(1 - \omega_m/4\pi)$, with both representing scale changes. The second effect is the sinc multiplier that is wave number-dependent and suppresses the signal in the interferogram when the path difference becomes sufficiently large that the sinc function goes from positive to negative. This effect is known as self-apodization. Interferometers are typically designed with the $x\omega_m$ product optimized to avoid this signal reduction. For a set minimum resolving power given by (4.147) the optimum $x\omega_m$ requirement is

$$\frac{\tilde{v}L_m\omega_m}{2} < \pi \Rightarrow \omega_m < \frac{4\pi}{R_o} \quad (4.152)$$

with x set to the maximum value.

The optimum solid angle is determined by the number of fringes accepted at the detector. Figure 4.52 illustrates the bullseye pattern for a monochromatic source that is at the image plane of the interferometer. The image forms one focal length F away from the final focusing optic and the radius of a ring is $r_j = F \sin \theta_j \approx F\theta_j$ where θ_j is given by (4.129). The solid angle accepted at the detector for small angles is

$$\omega_m = \frac{2\pi}{L_m \tilde{v}_o} (j + \epsilon) = \frac{4\pi}{R_o} j, \quad (4.153)$$

where we set ϵ equal to zero and j becomes a proportionality constant. Both ω_m and R_o depend on \tilde{v} and therefore the solid angle is optimized in practice by maximizing the fringe amplitude at the highest wave number at the longest path difference. From the sinc envelope in (4.151), the fringe amplitude is greatest when $\sin[(\tilde{v}L_m\omega_m)/2]$ is one or

$$\frac{\tilde{v}L_m\omega_m}{2} = \frac{\pi}{2} \Rightarrow \omega_m = \frac{2\pi}{R_o} \quad (4.154)$$

which, by comparison to (4.153), means that half of a fringe is accepted at the detector element ($j = 1/2$). Figure 4.55 shows the fringe amplitude for a number of different j -values.

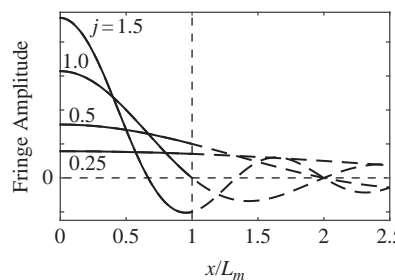


Figure 4.55 Fringe amplitude for several j -values. The fringe amplitude is given by ω_m times the sinc function in (4.151). The values of j vary from 0.25 to 1.5. Based on Brault (1985).

4.5.2

The Instrumental Profile of a Michelson Interferometer

The instrumental profile, given by (4.146), is modified to account for the finite size of the detector element. The full form of the interferogram is now

$$I(x) = \omega_m \left[\text{sinc}\left(\frac{\tilde{v}x\omega_m}{2}\right) \right] \text{rect}\left(\frac{x}{2L_m}\right) \cos\left[2\pi\tilde{v}x\left(1 - \frac{\omega_m}{4\pi}\right)\right], \quad (4.155)$$

where (4.144) and (4.151) have been combined. The instrumental envelope is just the first two terms in (4.155) or

$$I_e(x) = \omega_m \left[\text{sinc}\left(\frac{\tilde{v}x\omega_m}{2}\right) \right] \text{rect}\left(\frac{x}{2L_m}\right), \quad (4.156)$$

which determines the full form of the instrumental profile.

An important theorem for Fourier transforms, presented here without proof but see Gaskill (1978), is the convolution theorem, which states that the Fourier transform of a convolution is given by the product of the individual transforms. Applying the theorem to (4.156) yields

$$P(\tilde{v}_o - \tilde{v}) = \omega_m \frac{2\pi}{\tilde{v}_o\omega_m} \text{rect}\left[\frac{2\pi(\tilde{v}_o - \tilde{v})}{\tilde{v}_o\omega_m}\right] * 2L_m \text{sinc}[2\pi L_m(\tilde{v}_o - \tilde{v})] \quad (4.157)$$

for a monochromatic source at $\tilde{v} = \tilde{v}_o$. The first term is the Fourier transformation of the sinc function in (4.151), which is a rectangle function as was shown in the derivation of (4.145). In this case the rect function has a width of $\tilde{v}_o\omega_m/2\pi$.

Does the rectangle function due to the finite size of the aperture make physical sense? We'll evaluate that spectral function of the aperture, again assumed to be circular, by examining an annulus at the focal plane as illustrated in Figure 4.56. The detector element has an angular half-width α and the differential solid angle of the annulus is $d\omega = dA/F^2 = 2\pi\theta d\theta$, where θ is r/F for small angles. Differentiating (4.128) yields

$$\frac{d\tilde{v}}{\tilde{v}} = \frac{\sin\theta d\theta}{\cos\theta} \approx \theta d\theta, \quad (4.158)$$

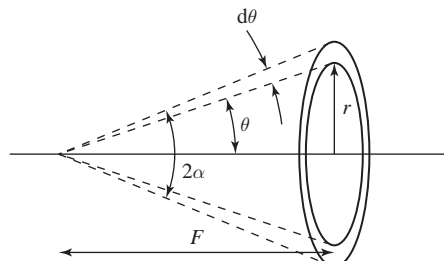


Figure 4.56 The solid angle subtended by an on-axis detector element at the focal plane. The angular width of the detector is 2α .

which is very nearly constant since \tilde{v} changes very little across the aperture, implying that equal $d\tilde{v}$'s contribute equally to the aperture function. The spectral width of the aperture is therefore

$$\delta\tilde{v} = \int_0^\alpha \tilde{v}\theta d\theta = \tilde{v} \frac{\alpha^2}{2} \quad (4.159)$$

for the wave number interval of the detector element. The resolution of the aperture is therefore

$$R_\alpha \equiv \frac{\tilde{v}}{\delta\tilde{v}} = \frac{2}{\alpha^2} \quad (4.160)$$

and R_α is the maximum possible resolution of the instrument with an aperture of angular radius α . The effect of the finite detector element is to smear the sinc function due to the finite travel with a rectangle function.

4.5.3 Transforming the Interferogram

The full power of a Michelson interferometer could not be exploited until digital computers became available and the fast Fourier transform (FFT) was developed. Digital sampling is accomplished by recording the amplitude of the interferogram at set intervals typically determined using a monochromatic reference beam, such as the output of a helium–neon laser, that triggers the data acquisition at the zero crossings of the resulting mean-subtracted sinusoid. The mathematical details of these methods will not be addressed here, but see Gaskill (1978), Goodman (2005), and Bracewell (2000). Only a few of the important points will be presented to introduce the principle.

Mathematically, this sampling is accomplished by using a series of delta functions, called the comb function which, for unit spacing, is defined as

$$\text{comb}(x) \equiv \sum_{n=-\infty}^{\infty} \delta(x - n), \quad (4.161)$$

where n is always an integer (Goodman, 2005). The comb function is also called the shah function, which is written as $\text{III}(x)$. For our specific case where the interferogram is sampled every δx in path difference, this converts to

$$\text{comb}\left(\frac{x}{\delta x}\right) = |\delta x| \sum_{n=-\infty}^{\infty} \delta(x - n\delta x), \quad (4.162)$$

which is an array of delta functions spaced at δx intervals. The continuous interferogram $I(x)$ is multiplied by the comb to accomplish the sampling. Additionally, the Fourier transform of (4.161) is also a comb function except in wave numbers rather than distance.

Applying the convolution theorem to the sampled interferogram yields

$$\mathcal{F}\left[I(x)\text{comb}\left(\frac{x}{\delta x}\right)\right] = E(\tilde{v}) * \text{comb}(\tilde{v}\delta x), \quad (4.163)$$

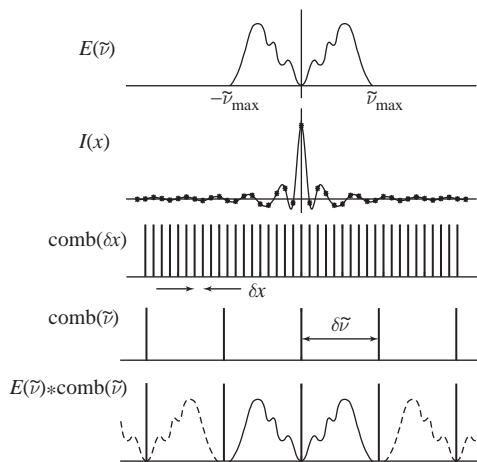


Figure 4.57 Illustration of the sampling and replication of a spectrum from taking the Fourier transform. The top graph is the transformed spectrum including the negative spectrum. The second graph is the continuous interferogram with the asterisks denoting the sampling locations. The third graph is the comb function corresponding to the sampling of the interferogram at path differences δx . The fourth graph shows the transformed comb function with the spacing $\delta \tilde{v} = 1/\delta x$. The bottom graph shows the replication of the spectrum. If δx had been too broad the transformed spectra would overlap.

where \mathcal{F} denotes taking the Fourier transform and the transform of the interferogram is the spectral irradiance $E(\tilde{v})$. The argument of the comb function is due to the scaling property of Fourier transforms and the spacing is $\delta \tilde{v} = 1/\delta x$. The result of (4.163) is that the spectrum is replicated with this $\delta \tilde{v}$ spacing requiring that the measured spectrum be no longer than $2\tilde{v}_{\max} \leq \delta \tilde{v}$ or $\delta x \leq 1/2\tilde{v}_{\max}$ in order that there be no overlap between replications. Figure 4.57 illustrates this point.

4.6

Data Acquisition with Imaging Spectrometers

The acquisition of spectral imagery depends upon the particular type of imaging spectrometer and there are three broad categories: whisk broom, push broom, and staring. Whisk broom acquisition is typically used for airborne dispersive systems utilizing a rotating mirror that scans the projected slit across the surface with the long axis parallel to the flight direction. Push broom dispersive systems, which are often used on space-based imagers, don't have the scan mirror and rely on either the satellite motion to perform the scanning or the data are acquired through a pitch back maneuver, where the imaging spectrometer is pointed forward initially and the satellite rotates as it flies over the surface being imaged, in order to meet the signal-to-noise requirements or frame rate limitations. In this case the long axis of the slit is perpendicular to the direction of travel. The final case is for a staring system such as an imaging spectrometer that employs a Michelson interferometer where the data are acquired over a relatively long period of

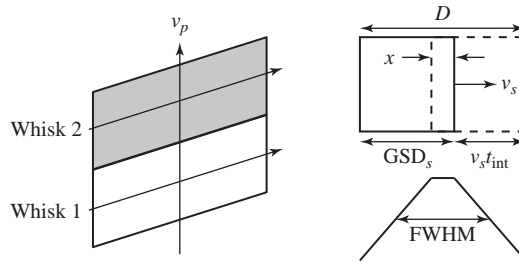


Figure 4.58 Illustration of the whisk broom pattern and the spatial sampling during a single readout of the focal plane array. The left illustration shows two successive whisks for a plane flying with a speed v_p . The right depicts the spatial sampling at the surface with the GSD_s sliding a distance $v_s t_{\text{int}}$ to the right during the integration time t_{int} . The resulting convolution is at the bottom right.

time in order to construct the interferogram. Staring imaging spectrometers are most often utilized with fixed deployments, although there are examples where these systems have been flown on airplanes. Another example from the meteorology community is the satellite-based Cross-track Infrared Sounder (CrIS), developed by the National Oceanic and Atmospheric Administration (NOAA) and flown at a nominal 833 km altitude in a polar orbit. CrIS is a Michelson interferometer system with a 3×3 array of detectors each having 14 km GSD. The interferograms are acquired by staring and the array is whisked along the surface for a 2,200 km swath width.

We will provide an analysis of a whisk broom dispersive imaging spectrometer to illustrate the spatial sampling concepts. Figure 4.58 shows an ideal whisk pattern where there is no impact from platform motion. Data are acquired with the slit projected at the left side of the whisk at $t = 0$ and finishing the whisk at $t = t_f$. The scan mirror is continuously scanned through the process so that the slit moves across the surface a short distance D within a single data frame acquisition. Using only geometric arguments and ignoring ground resolution distance effects, the instantaneous projection of a single spatial sample onto the surface is slightly rectangular in the off-nadir case and the ground coverage area is described by the convolution of this surface GSD, denoted as GSD_s , and the surface travel distance as illustrated on the right side of Figure 4.58. GSD_s is equivalent to the full width at half maximum (FWHM) of the convolution for a constant speed v_s as long as there is some overlap at the beginning and end of the acquisition. If the ground travel distance is more than twice the GSD_s then it is not equal to the convolution FWHM and the GSD is not a good metric for the spatial sampling.

The kinematics associated with the data acquisition for a whisk broom sensor flown at an altitude A are illustrated in Figure 4.59. The range R at an instant is $A / \cos \theta$, where θ is the off-nadir angle. The GSD_i is the product of the range and the IFOV and projecting GSD_i onto the surface yields

$$GSD_s = \frac{A \times \text{IFOV}}{\cos^2 \theta}. \quad (4.164)$$

Defining f_s as the fraction of overlap of GSD_s between the beginning and end of the acquisition allows the surface speed to be expressed as

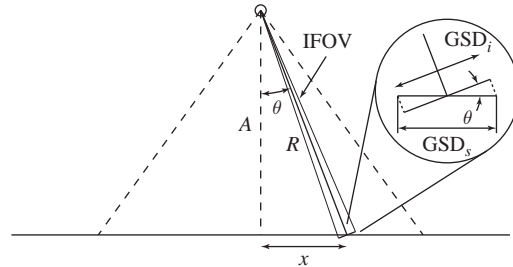


Figure 4.59 The imaging spectrometer IFOV is swept along the surface. The plane is flying at an altitude A and at a particular instant the range is R and the surface is sampled a distance x from the nadir point. The GSD_i is the product of the range and the IFOV and GSD_s is $GSD_i \cos \theta$.

$$v_s = \frac{(1-f_s)GSD_s}{t_{int}} = \frac{(1-f_s)A \times IFOV}{t_{int} \cos^2 \theta}, \quad (4.165)$$

which is alternatively developed by taking the time derivative of $x = A \tan \theta$ or

$$v_g = A \sec^2 \theta \frac{d\theta}{dt}. \quad (4.166)$$

Combining (4.165) and (4.166) yields

$$\omega_w = \frac{d\theta}{dt} = \frac{(1-f_s)IFOV}{t_{int}}, \quad (4.167)$$

where ω_w is the constant angular velocity of the rotating mirror performing the whisk.

The final consideration is to ensure that there are no gaps between successive whisks. The width W_s of a whisk is the length of the slit projected onto the surface. The whisk length, determined by the maximum angle θ assuming a symmetric travel about the nadir direction, is limited by the time it takes for the scan mirror to return to its initial position to start the next whisk. W_s is the sum of the distance the plane flies during the scan and the similar distance traveled during the mirror return, or $W_s = d_s + d_r = v_p(t_s + t_r)$. The scanning system is designed so that the return time is as short as possible in order to maximize the area coverage rate. In practice there will be some additional time added to ensure there is a small degree of overlap rather than the perfect scanning illustrated on the left in Figure 4.58.

4.7

Summary and Further Reading

This chapter was focused on the design of imaging spectrometers with a modest introduction to telescope design, followed by a more detailed description of the spectrometers themselves. The spectrometer analysis emphasizes the concepts that are universal to spectroscopic instruments utilizing the measurement equation as the fundamental model, followed by a detailed description of dispersive systems and a more modest description of interferometers. Two forms in particular, the Offner–Chrisp and the

Dyson, are treated in detail due to their current broad usage. Finally, there is a brief discussion of data acquisition.

Descriptions of spectroscopic techniques can be found in most optics textbooks, such as Jenkins and White (1976) and Born and Wolf (1999). A relatively brief but excellent treatment from the French school is Girard and Jacquinot (1967). Anne Thorne's book is an introductory text with broad coverage (Thorne, 1988). Gaskill's text, *Linear Systems, Fourier Transforms, and Optics*, is particularly recommended for his treatment of convolutions and Fourier analysis (Gaskill, 1978). Two other classic texts that cover much of the same material are Goodman (2005) and Bracewell (2000). Finally, J. W. Brault's review article on Fourier transform spectrometers is a concise but thorough introduction and see Griffiths and de Haseth for a complementary treatment (Brault, 1985; Griffiths and de Haseth, 1986).

Problems

1. Derive the paraxial quantities in Table 4.1. What is the size and location of the exit pupil?
2. An imaging spectrometer is F/5.6 and has a focal plane array with 40 m pixels. If a GSD of 1.25 m is desired from a 450 km orbit, how large must the aperture be? What is the IFOV? Is this realistic for a space sensor?
3. From Chapter 2, the minimum resolvable half-angle for a diffraction-limited telescope with an entrance pupil of diameter D is $\alpha = 1.22\lambda/D$. At what wavelength is the imaging spectrometer in the previous problem diffraction-limited?
4. Suppose an imaging spectrometer with a focal plane array had a magnification of 2 and was designed to operate far from the diffraction limited case. How wide should the slit be in order to produce an instrumental profile that is a triangle function? If oversampling by a factor of 2 is desired, how large should the slit be?
5. Show that the theoretical resolution for a grating spectrometer can be written as

$$R_o = \frac{\text{maximum path difference}}{\lambda}. \quad (4.168)$$

6. Plot the limit of resolution as a function of wavelength using (4.62).
7. How is the wavelength dependence of dispersion for a prism different from that of a grating?
8. Reproduce the left side of Figure 4.29 using the Sellmeier equation:

$$n^2 - 1 = \frac{B_1\lambda^2}{\lambda^2 - C_1} + \frac{B_2\lambda^2}{\lambda^2 - C_2} + \frac{B_3\lambda^2}{\lambda^2 - C_3}$$

where $B_1 = 4.76523070 \times 10^{-1}$, $B_2 = 6.27786368 \times 10^{-1}$, $B_3 = 8.72274404 \times 10^{-1}$, $C_1 = 2.84888095 \times 10^{-3}$, $C_2 = 1.18369052 \times 10^{-2}$, and $C_3 = 9.56856012 \times 10^1$ with the wavelength in microns. MatLab or something equivalent such as a spreadsheet program is required.

9. How much does light traveling through a NaCl prism deviate from the minimum deviation condition over the range illustrated in Figure 4.29? Assume a base distance of 4 cm.
10. An imaging spectrometer, with a grating dispersing element with 250 facets/mm, is equipped with an FPA with 40 m pixels, has a focal length of 5 cm, and is operated in second order. If the wavelength of interest is reflected from the grating at an angle of 7° what is the limit of resolution? Estimate the minimum size of the FPA if a spectral range of 0.4 to 2.5 m is desired. Is this realistic?
11. Show that the irradiance due to interference reduces to the two-slit case derived in Chapter 2.
12. Derive (4.65). Show that the distance from the j th slit to the focal plane is $R_j = R - jd \sin \theta$.
13. The irradiance at the focal plane for a spectrometer with a square grating is described by (4.72). The number of facets N is very large (on the order of 1000/mm). Show that (4.72) reduces to diffraction from a square aperture by replacing θ with $\theta + \delta\theta$ in (4.66) and (4.67) and applying the small angle approximation. You will need $\sin(A + B) = \sin A \cos B + \cos A \sin B$.
14. Derive (4.73).
15. A reflection grating has a blaze angle of 30° with 1250 grooves/mm and has a ruled width of 11.5 cm. What are the blaze wavelengths in the first three orders for a Littrow mounting? What is the theoretical resolution of this grating when used in the second order near the blaze wavelength? If the grating is used with 1 m focal length collimating and focusing lenses and slits that are 0.4 mm wide, what is the actual resolution of the spectrometer in the second order?
16. Show that (4.83) can be written as

$$E_g = \frac{\sin^2[\pi(\frac{\lambda_{B1}}{\lambda} - m)]}{[\pi(\frac{\lambda_{B1}}{\lambda} - m)]^2} = \frac{\sin^2[m\pi(\frac{\lambda_{Bm}}{\lambda} - 1)]}{[m\pi(\frac{\lambda_{Bm}}{\lambda} - 1)]^2}.$$

17. Show that in the Littrow configuration (4.90) reduces to $\Delta\theta_2 = \eta^2 \tan \theta_1$.
18. Perform the paraxial analysis of the Offner form using (A.23) and (A.29).
19. Develop the final expression for \bar{AP} given by (4.99). You will need to take the square root of (4.98) and then apply the binomial expansion of $(a + b)^n$, where $n = 1/2$, $a = (r - y \sin \alpha)^2$ and b is the rest of (4.98). Also,

$$(1 - \frac{y}{r} \sin \alpha)^{-1} \quad \text{and} \quad (1 - \frac{y}{r} \sin \alpha)^{-3}$$

require binomial expansion.

20. Prove that (4.105) represents a circle of diameter R .
21. Calculate the limit of resolution for AVIRIS. How does it compare to the last column in Table 4.3? Why is there a discrepancy?

22. Prove that GSD_s is equal to the FWHM of the convolution illustrated in Figure 4.58.
23. An imaging spectrometer is operated as a push broom sensor and flown on an airplane at 3000 m above the ground. The sensor is operated at a frame rate of 100 Hz and the instantaneous field of view (IFOV) is 0.67 mrad. The projection of a pixel is scanned across the ground at 225 m/s. Is the instantaneous GSD_s a good metric to describe the spatial sampling?

5 Imaging Spectrometer Characterization and Data Calibration

The utility of the data from an imaging spectrometer critically depends upon the quantitative relationship between the scene in nature and the scene as captured by the sensor. As was shown in Chapter 4, the raw data will only somewhat resemble the at-aperture spectral radiance from the surface due to the optical characteristics of the fore optic and the spectrometer. Additionally, the data acquisition by the focal plane array will further modify the irradiance that composes the image due to the spectral dependence of the detector material's quantum efficiency. It will also add noise terms that, if large enough, will further complicate the relationship between the scene and its raw image. The calibration of the data from an imaging spectrometer is the crucial data processing step that transforms the raw imagery into radiance that can be physically modeled. The science of radiometry provides the theoretical framework and the measurement processes that enable a sensor to be characterized and the data to be converted to physical units that are tied to reference standards. This chapter describes the process of sensor characterization that leads to calibration products that are applied to the raw data and some of the techniques that are used to evaluate the accuracy and precision of the calibrated data will be introduced. An overview of the important measurement and data reduction processes for vicarious calibration, which is critical for space-based systems, will also be presented.

5.1 Introduction

The characterization of an imaging spectrometer is challenging due to the spatial extent of the collected scene and the large spectral range that is relatively finely sampled, at least for an imager. For example, an Offner-Chrisp imaging spectrometer often has between 200 and 400 spectral and about 1000 spatial samples or about 400,000 individual measurements in a single readout of the focal plane array. To collect a scene the FPA is read out thousands of times. All of the data must be calibrated in order to be used to greatest effect, with the overarching goal being that the result should not depend upon the time or location of the collected scene, there should be no field of view dependence, and it should be immune, within reasonable limits, to the illumination and atmospheric conditions.

The terminology that is employed here for clarity is that sensors are characterized and data are calibrated, although calibration is broadly used to mean both activities in the metrology and remote sensing communities. The process of characterization involves

the three primary sampling attributes of the sensor: spectral, radiometric, and spatial. The characterization of the spectral performance allows a quantitative assignment to the spectral sampling as described by the instrumental profile. The radiometric characterization enables an absolute scale to be applied to the data amplitude. The spatial characterization provides information about the location of each spatial sample and is a requirement for a full assessment of the sensor performance. There are other important supporting measurements that contribute to the full understanding of the sensor.

Imaging spectrometer data calibration requires that the instrumental profile be known for each spatial–spectral sample and that a known radiance has been measured. The combination of these two is used to generate the calibration coefficients. Additional radiometric measurements establish the extent to which a sensor’s response is linear and therefore the precise form of the coefficients. Their application transforms the amplitude scale of the raw data into physical units with a known spectral sampling. Each step of this process relies upon sources whose properties are traceable to an absolute standard from a national metrology laboratory such as the National Institute of Standards and Technology (NIST). Traceability means that the data from a measurement or the reported calibration data from a standard are related to a standard maintained at a national metrology laboratory through an unbroken series of comparisons each with established uncertainties. We will examine how the particular characterizations are performed and how the calibration products are generated and applied. Once the characterization is complete so that the data can be calibrated then the sensor becomes an imaging spectroradiometer. The description is based on the extensive characterization and calibration literature and upon our own experience characterizing imaging spectrometers.

5.2

Application of the Measurement Equation

The measurement equation was introduced in Chapter 4 to describe the output of an imaging spectrometer due to the at-aperture radiance. It describes the performance of the entire imager as a function of the subsystems and can be quite complex as sensor details are added. It is worth repeating it here for convenience:

$$S(\lambda_c) = t_{\text{int}} \int_0^{\infty} U[L(\lambda)\tau(\lambda)\eta(\lambda)]P(\lambda_c - \lambda) d\lambda, \quad (5.1)$$

where again S is the measured signal for the channel centered on wavelength λ_c , U is the étendue, L is the spectral radiance, τ is the system optical transmission, η is the spectral quantum efficiency, and $P(\lambda_c - \lambda)$ is the instrumental profile for a spectral channel with its maximum at λ_c . Remember that η can be replaced with a more general term. For example, the detector response function, expressed as

$$R_{\Phi}(\lambda) = \frac{S_d(\lambda)}{\Phi(\lambda)}, \quad (5.2)$$

where S_d is the measured signal in digital numbers from a pixel in the focal plane array due to the flux Φ that the element receives, could be used to comprehensively describe the output of the detector rather than just the quantum efficiency of the detector material.

The measurement equation is the guide for what must be measured in order to characterize a system, and it is also a critical component of the error analysis that is performed to quantify the data calibration quality. Let's illustrate this using a very simple but also realistic filter radiometer example that has the characteristics of a single channel from an imaging spectrometer without the spatial sampling. The radiometer is designed to measure the radiance from a source at a particular wavelength and therefore it has a pair of precision apertures to establish the étendue, has a bandpass filter to perform the spectral discrimination, and has a detector with its associated electronics. The detector assembly in a well-designed radiometer will only be exposed to the source under test due to the arrangement of the limiting aperture and the field stop. Figure 5.1 illustrates the radiometer which also includes an inclined reflector that has a diffuse coating with low reflectivity so that light reflected from the instrument back to the source is minimized.

Every aspect of the radiometer is assessed from the viewpoint of characterization to establish the uncertainty of the data calibration. Working from left to right in Figure 5.1, the bandpass filter is measured with a scannable spectral source so that the shape of the instrumental profile is determined as well as the amount of light that leaks through from outside the band. The latter is known as the *contrast* C in traditional spectroscopy given by

$$C \equiv \frac{\tau_{\max}}{\tau_{\min}} \quad (5.3)$$

as illustrated in Figure 5.2. The measurement actually yields the transmission of the filter, which is typically an asymmetric function and not easily modeled. In our formalism

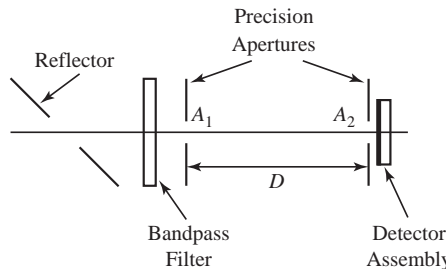


Figure 5.1 Schematic of the basic elements of a filter radiometer including a reflective shield. The precision apertures have circular holes of areas A_1 and A_2 which are a distance D apart.

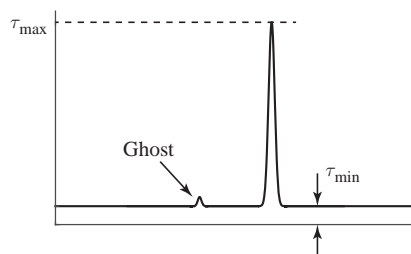


Figure 5.2 The contrast of a spectral filter with a transmission offset τ_{\min} and a maximum transmission τ_{\max} . An artifact known as a ghost is also shown.

it is equivalent to $\gamma P(\lambda_c - \lambda)$, where γ is the transmittance at the peak wavelength, which may not correspond to the center wavelength. An important point is that the monochromatic source must be sufficiently well understood to support the filter measurement. The precision apertures that define the étendue follow the filter and are known from precise metrology provided by the manufacturer or measured at an appropriate facility. Similarly, the distance between the two is well known. The detector is also characterized in order to apply (5.1). The measurements that quantify the properties of each item have an associated error analysis and the signal is modeled.

The system-level characterization of the radiometer is accomplished using well-understood sources, with, in the ideal case, several independent measurements being performed. This could include an irradiance measurement where the front aperture is removed and a source, whose irradiance is known from measurements at a metrology laboratory, directly illuminates the second aperture at the position of known irradiance. The radiance calibration is a derived product, in this case based on knowledge of the étendue of the original arrangement. Another option is to use a laboratory radiance source, again traceable to a standard ideally characterized by a national metrology laboratory, to directly measure the at-aperture radiance for the generation of the calibration coefficients. A final example is to apply a solar radiance based calibration, which will be described in detail below, with the sun as the source illuminating a reflectance standard viewed by the radiometer and supported by a separate suite of instruments that characterize the properties of the atmosphere. Each measurement is supported by a detailed error analysis and compared for consistency.

The details of each of these measurements, with the addition of the spatial characterization, applied to an imaging spectrometer will be treated in turn, with a description of the reduction of the measurement results and the generation of calibration products. The measurement equation is the unifying model that underpins the process. The goal of the measurement series is primarily to produce calibration coefficients to transform raw data to at-aperture spectral radiance, with a measure of uncertainty, to be applied to subsequent spectral imagery, but additionally it is to quantitatively understand the performance of the imaging spectrometer in terms of its signal-to-noise and optical characteristics.

5.3

Spectral Characterization

The first characterization measurement we will treat is the determination of the shape and centers of the spectral response functions for the individual channels. This is critical for the obvious purpose of establishing the spectral scale of the at-aperture radiance, but it is also required for the calculation of the calibration coefficients. Figure 5.3 is an example of the apparatus commonly used to perform the spectral characterization for a dispersive imaging spectrometer. Its basic components are a light source, a monochromator as the method used to separate the light into the different wavelengths, a collimator that produces a beam that fully illuminates the entrance pupil of the imaging spectrometer, and a monitor to measure any variation in radiance from the spectral calibration source. The description here focuses on the VNIR/SWIR spectral range but the concepts can be universally applied.

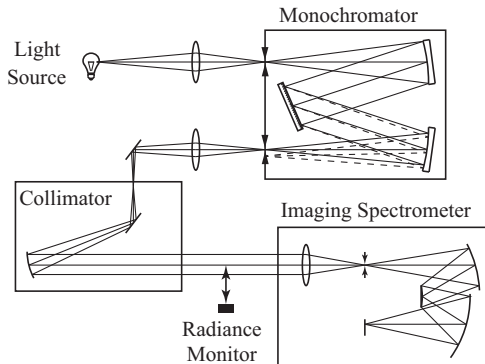


Figure 5.3 Spectral characterization apparatus composed of a light source, a monochromator, a collimator, and a radiance monitor. The monochromatic source illuminates a narrow range of wavelengths at the focal plane array.

The measurement consists of scanning the monochromator to different wavelengths with an imaging spectrometer measurement performed at each monochromator setting. An individual instrumental profile is sufficiently sampled so that its shape is accurately recovered through least squares fitting. Most imaging spectrometers have simple instrumental profiles by design; however, a detailed measurement is required to establish the form. In our work we typically sample the spectral response function about a dozen times so that any asymmetries are well characterized, with the limit of resolution of the instrumental profile of the monochromator set to about 1 nm. The amplitude of the output radiance of the monochromator will vary due to the spectral variation of both the light source and its optical transmission as illustrated in Figure 5.4.

The measurement of the instrumental profile of the imaging spectrometer is shown in Figure 5.5 for a Gaussian model with a 500 nm center wavelength and 10 nm limit of resolution. The imaging spectrometer signal is proportional to the convolution of its spectral response function and the monochromator output function. The measurement result is a series of values in digital numbers with each point corresponding to the center wavelength settings of the monochromator. The data are analyzed by first performing a dark subtraction to remove the detector offset. The monochromator source variation is removed by dividing the measurement at each wavelength by the signal from the radiance monitor shown in Figure 5.3, which has been corrected for the relative spectral response of the detector used to make that measurement. The data are then fit and the resulting curve is peak normalized and evaluated based on its difference from the data. The failure to correct for the spectral variation of the monochromator source leads to errors in the assignment of the center wavelength for the imaging spectrometer spectral response function as illustrated in Figure 5.6. The fit and the original data divided by the source radiance are indistinguishable.

An additional systematic error that is unavoidable comes from the finite width of the monochromator instrumental profile. Recall that the perfect reproduction of a particular imaging spectrometer spectral response function can only be achieved using a delta function source. Real measurements are limited by signal-to-noise considerations and

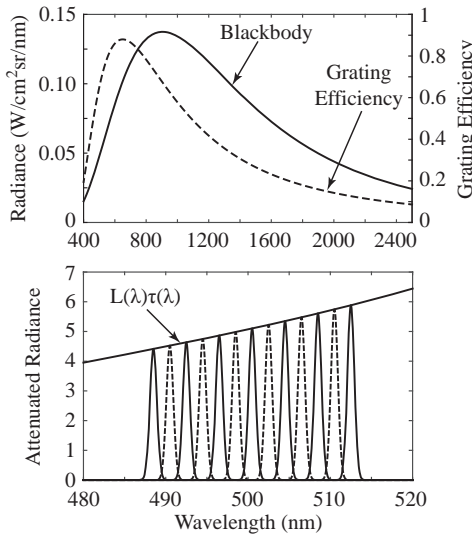


Figure 5.4 Radiance variation from a spectral calibration source. The upper graph shows the radiance from a 3200 K blackbody as an approximate model for a 1000 W tungsten–halogen light source and the grating efficiency of a monochromator with a blaze wavelength of 650 nm. The bottom graph shows the output of the monochromator with the upper curve being the attenuated radiance from 480 nm to 520 nm due to the optical transmission of the silver mirrors used in the monochromator and collimator as well as the grating efficiency. The instrumental profile is modeled by a Gaussian function with a 1 nm limit of resolution and the monochromator is scanned in 2 nm steps.

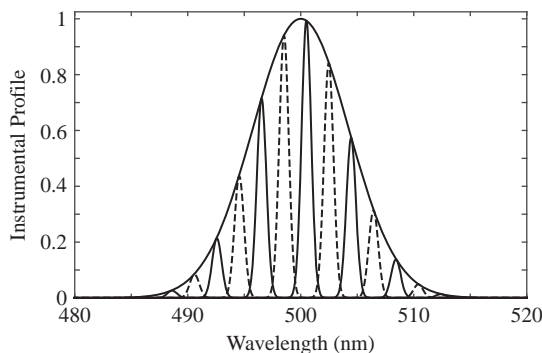


Figure 5.5 The measurement of the imaging spectrometer instrumental profile center at 500 nm with a 10 nm limit of resolution based on the output of the monochromator illustrated in Figure 5.4.

in practice the limit of resolution of the monochromator is set based on a signal-to-noise threshold. The rule of thumb that we use is that the peak signal due to the spectral source input should have a signal-to-noise ratio of 200 or better. The spectral characterization data are first dark-subtracted and then the amplitude of the measured instrumental profile is inspected. If the signal is inadequate then adjustments are made to the measurement methodology. Ideally this involves an improvement in the at-aperture radiance through

Table 5.1 Variation in the measured limit of resolution $\delta\lambda_{IS}$ for the imaging spectrometer for several different $\delta\lambda_m$ values for the monochromator. The true limit of resolution of the imaging spectrometer is 8 nm.

$\delta\lambda_m$ (nm)	$\delta\lambda_{IS}$ (nm)	Percent Difference
1	8.06	0.8
2	8.26	3.3
3	8.54	6.8
4	8.94	11.8
5	9.42	17.8

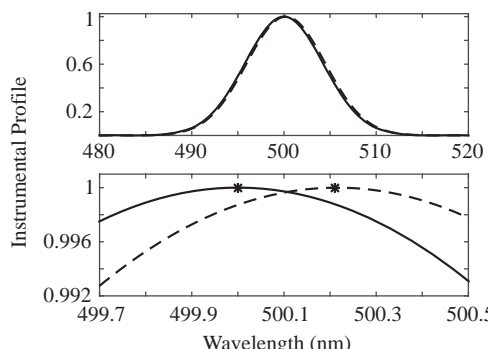


Figure 5.6 Spectral calibration error due to failure to compensate for the variation in the monochromatic source. The dashed curve in both graphs is the peak normalized result of a least squares fit to the data presented in Figure 5.5 without the correction of the source variation. The error is 0.21 nm with the peaks identified by the asterisks.

a change in the source illuminating the first slit, a change in the grating being used to improve the optical efficiency due to a better match between the channel being measured and the blaze wavelength, or a combination. As a last resort, after everything else is optimized, the limit of resolution of the monochromator is increased. Table 5.1 shows the impact of the convolution for a few widths.

In practice, we have been able to achieve adequate signal-to-noise in almost all cases; however, if the signal strength is inadequate then the slit width of the monochromator is increased. The values of the spectral calibration are then adjusted based on modeling the convolutions. This requires that the monochromator instrumental profile be well known by measuring it at several wavelengths to determine its variability. Some monochromators are not well behaved in this respect and have changing or asymmetric profiles complicating the modeling. Fortunately, a well-manufactured imaging spectrometer with high spatial-spectral uniformity is relatively simple to model. In practice, if most of the spectral channels have been measured with adequate signal-to-noise then the rest are modeled based on an overall assessment of the uniformity. Inadequately measured channels are modeled utilizing the surrounding channels or through interpolation if they are at the shortest or longest wavelengths.

An important detail of the apparatus illustrated in Figure 5.3 is the alignment of the slit of the imaging spectrometer with the image of the slit of the monochromator. The collimator projects the monochromator slit image to infinity and the telescope focuses that image onto the slit. In the perfect case the image of the monochromator slit and the imaging spectrometer slit are perfectly aligned, their sizes are the same, and the input matches the F-number of the imaging spectrometer. This is usually not the case and often the two slits are aligned perpendicularly. In this arrangement, the monochromator slit image is moved along the imaging spectrometer slit if every instrumental profile is to be measured. The image of the slit is typically a small number of spatial pixels wide and the monochromator is scanned through the spectral range and the process is repeated at a new slit image position in a rather time-consuming process. The measurement can be accelerated by only measuring a few field points and modeling the remaining channels.

The monochromator must also be spectrally characterized, usually by utilizing spectral line sources, often called pen-ray lamps. These are low-pressure, cold cathode discharge lamps with either a single gas, such as xenon, or a mixture such as mercury and argon. Since the sources are low-pressure lamps the atomic line widths are quite narrow, typically less than 0.001 nm. They are also well known from both theory and measurements, with an extensive database maintained by NIST (Kramida et al., 2014). An example of the lamp spectrum measurement methodology is given by Sansonetti et al. (1996). The pen-ray lamp is focused onto the entrance slit by a fore optic that matches the F-number of the monochromator and the grating is rotated with a detector recording the signal at the output slit. The initial alignment is accomplished with the grating at zero order and the white light signal is optimized. The spectral features from atomic line sources are concentrated at wavelengths below about 900 nm so, in order to spectrally calibrate the full range of grating angles, the order-sorting filters that are used in normal operation are removed and the higher orders at multiples of the line wavelength are also measured. The grating is rotated in small steps and the instrumental profile is recorded with enough points for fitting. If the monochromator is reasonably well calibrated to start with, this can be performed at discrete locations to minimize the effort. Since the wavelength is nonlinear with the angle of rotation of the grating a sine drive mechanism is employed by the manufacturer in order to linearize it. Traditionally, these systems utilized levers, but some current designs employ direct digital scanning systems. The absolute spectral calibration is accomplished through linear fitting of the center wavelengths to the linearized grating position.

The F-number of the monochromator is an important design parameter for the spectral calibration source. It should be as low as possible since the grating efficiency diminishes at wavelengths that differ from the blaze wavelength. Recall from Chapter 4 that the étendue can be written as $A\Omega$, where in this case A is the area of the slit and Ω is the solid angle subtended by the first collimating optic in the monochromator, which is written as $\pi/4N^2$. The optimal system will have as large an étendue as possible for the required resolution, with the limit of resolution proportional to the angular width of the slit β from (4.62). Fast monochromators that meet these requirements tend to have F-numbers of about 4 with focal lengths of 0.25 m to 0.35 m. The precision of a monochromator

can be quite high on the order of ± 0.005 nm with the absolute uncertainty being on the order of 0.1 nm.

A method to establish the accuracy of both the monochromator and imaging spectrometer is to use a spectral transmission filter. These filters have distinct and fairly broad spectral features that are well known. For example, NIST has developed a series of standard reference materials that are certified and therefore measurements performed with them have NIST traceable results if used properly. In the VNIR/SWIR the filters are manufactured from glass doped with a mixture of holmium oxide, samarium oxide, ytterbium oxide, and neodymium oxide which provides a fairly rich series of absorption features. The equivalent in the $3.2 \mu\text{m}$ to $18.5 \mu\text{m}$ is to use a polystyrene film. The requirements for NIST traceability are outlined in the accompanying certificate and include temperature, humidity, and spectral sampling specifications.

For use with an imaging spectrometer the filter sampling specifications are not met; however, the use of the filter is still recommended as a check on the absolute spectral scale. As an example, for a VNIR/SWIR imager the light source, such as an integrating sphere with a filter holder between the source bulb and the sphere port, is viewed with and without the filter in place and the ratio of the two dark-subtracted signals is taken. The data are analyzed by band-averaging the filter data using

$$\tau_{ba}(\lambda) = \frac{\int \tau_{\text{NIST}}(\lambda) P(\lambda_c - \lambda) d\lambda}{\int P(\lambda_c - \lambda) d\lambda}, \quad (5.4)$$

where $\tau_{\text{NIST}}(\lambda)$ are the transmission data from NIST and the imaging spectrometer instrumental profile $P(\lambda_c - \lambda)$ is from the monochromator measurement. The measured imaging spectrometer transmission data are compared to the band-averaged NIST transmission data with the center wavelengths varied slightly for each spectral channel until the difference is minimized. We typically perform a global shift since a high-quality monochromator is precise in terms of repeatability and sampling distance. Figure 5.7 shows an example of the NIST transmission curve and the equivalent band-averaged transmission.

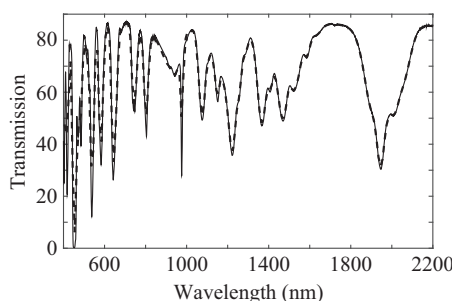


Figure 5.7

The transmission of an SRM 2065 filter. The solid curve is from data provided by NIST and the dashed curve is the band-averaged transmission for an imaging spectrometer with spectral channels every 10 nm over the range from 405 nm to 1195 nm with a constant limit of resolution of 12 nm. As of this writing the SRM 2065 filter has been replaced by the SRM 2035A.

There are alternative approaches to the one described. For example, the collimator can be replaced with a Lambertian reflector. In this arrangement the light from the monochromator illuminates an area of the reflector that is larger than the projected pupil of the imaging spectrometer. The diffuse source simultaneously illuminates each of the spatial samples and the monochromator is scanned with all of the spectral response functions measured. This works well if a very bright source is available, since $L = E/\pi$ for an ideal Lambertian reflector, and if the entrance pupil is not particularly large, such as is often the case for airborne imagers. For a space-based system either approach could be applied to the spectrometer alone, prior to the integration of the telescope, with the correct coupling optics. Another option is to use a tunable laser system in place of the monochromator depending upon the spectral range. Currently there are dye and solid state lasers, using optical parametric oscillators, that produce a broad range of wavelengths. As laser technology advances it is expected that this method will become a practical alternative to the monochromator apparatus.

5.3.1 Michelson Interferometer Spectral Calibration

It was shown in Chapter 4 that the instrumental profile of a Michelson interferometer is determined by the maximum path difference and the size of the detector element in the on-axis case. For an imaging spectrometer this is further complicated by the finite-sized elements that are off-axis. Recall that the instrumental profile is self-apodized as the size of a detector element increases with the interferometer typically designed to have half of an interference fringe accepted by a detector element at the longest path length for the highest wavenumber. This is due to the phase shift across the detector element resulting in a degree of destructive interference. For a square, off-axis detector (4.150) is modified so that the solid angle integration is performed relative to the half-angle appropriately centered on the pixel (Yap et al., 1982).

The spectral calibration calculated from the theoretical development is confirmed through laboratory and on-board spectral calibration sources. The spectral calibration of a Michelson interferometer depends upon knowledge of the maximum path difference. This is provided by counting the fringes due to interference from the coherent light of a metrology laser with a precise wavelength that travels through a channel of the interferometer with a dedicated detector. The spectral calibration also requires knowledge of the geometry of the detector elements that compose the focal plane array relative to the optical axis.

There are several approaches to performing the spectral calibration in the laboratory and the example described here is from the Cross-track Infrared Sounder (CrIS) calibration. The CrIS program has stringent spectral and radiometric requirements for atmospheric sounding that is reflected in the complexity of the spectral calibration. The on-board calibration system utilizes a low-pressure neon lamp and performs an on-axis measurement of the narrow emission line at 703.45 nm. This measurement is used to confirm the wavelength of the metrology laser or adjust its wavelength as required. The laboratory calibration utilized a gas absorption cell filled with either carbon dioxide,

methane, or hydrogen bromide and measured the transmission spectrum using black-body temperatures of 310 and 340 K with the background radiance removed using a measurement with the cell empty. These measurements were used to establish the neon and metrology laser calibrations using the on-axis detector element and, once established, the spectral calibration for the off-axis detectors was performed. This last set of measurements determined the spectral shift due to the detector geometry. A similar approach is applied on orbit utilizing atmospheric features in the at-aperture radiance in lieu of the absorption cell. Strow et al. (2013) provides a thorough description of the full process.

5.4

Radiometric Characterization

The radiometric characterization of an imaging spectrometer is in principle rather straightforward. For a sensor with linear response, one simply measures a known radiance source with the imaging spectrometer, dark subtracts the data, calculates the expected radiance by band-averaging the known radiance using the measured spectral response functions, and takes the ratio to generate the calibration coefficients for each spatial-spectral sample. All subsequent dark-subtracted data are transformed to physical units by multiplying by the calibration coefficient assigned to a particular spatial-spectral pixel identified by (i, j) indices. The calibration coefficient for the (i, j) -pixel, whose instrumental profile is centered on λ_c , is written as

$$K(i, j) = \frac{L_{\text{ba}}(i, j; \lambda_c)}{S_{i,j}(L) - S_{i,j}(0)}, \quad (5.5)$$

where the band-averaged radiance is given by

$$L_{\text{ba}}(i, j; \lambda_c) = \frac{\int L(\lambda) P_{i,j}(\lambda_c - \lambda) d\lambda}{\int P_{i,j}(\lambda_c - \lambda) d\lambda}, \quad (5.6)$$

where $L(\lambda)$ is the at-aperture radiance and $P_{i,j}(\lambda_c - \lambda)$ is the instrumental profile for the (i, j) -detector element centered at λ_c . The signals that correspond to the radiance and dark measurements are both in digital numbers.

The measurement is complicated by the size of the entrance pupil and the field of view of the imaging spectrometer in relation to the available radiance sources. Again using the VNIR/SWIR spectral range as a specific example, the simplest radiance standard combines an irradiance source illuminating a reflectance standard, both of which have calibration data that is traceable to an absolute standard. An imager with a small field of view can directly view the radiance standard and the analysis consists of modeling the irradiance and reflectance standards in the measurement geometry in order to generate at-aperture radiance and then to construct calibration coefficients using (5.5). In almost all cases the entrance pupil and the field of view are too large for this simple approach and another radiance source, typically an integrating sphere, must be employed. The challenge is to calibrate the integrating sphere source.

It is possible to have an integrating sphere directly characterized at a standards laboratory. This is usually expensive and the lifetime of the calibration data that results

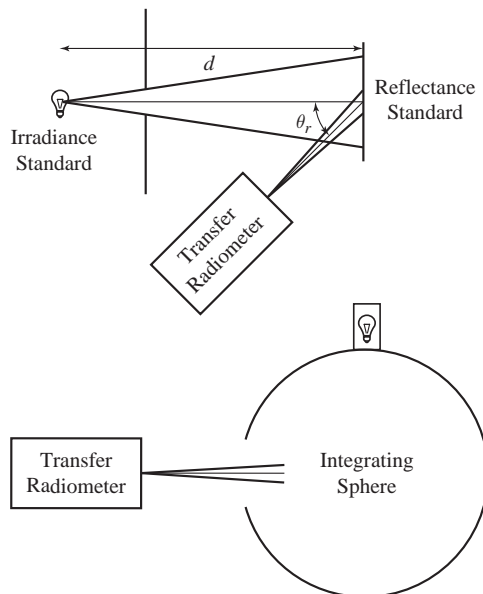


Figure 5.8 Schematic of a radiometric characterization apparatus. The irradiance standard is a distance d away from the reflectance standard that is normally illuminated and viewed by the transfer radiometer at the angle θ_r . The transfer radiometer views the integrating sphere in succession. The irradiance standard is also partitioned off, typically in a large enclosure that has highly absorbing surfaces, in order to reduce multiple scattering.

is limited. It also removes the integrating sphere from the calibration laboratory for relatively long periods. One could purchase multiple integrating spheres and use them successively, rotating them through the standards laboratory for repeated characterization. This is certainly a reasonable approach if there are no funding constraints. The alternative to this approach is to build or purchase a *transfer spectroradiometer*, or just a transfer radiometer for short, that views the illuminated reflectance standard followed by the integrating sphere as illustrated in Figure 5.8. In our experience this approach has a tremendous advantage over the former, as a high-quality transfer radiometer will be employed repeatedly in the laboratory for a variety of different uses. Additionally, the expense of replacing an irradiance standard is usually a small cost in the maintenance budget of a calibration facility.

5.4.1 Irradiance Source

The irradiance standard in Figure 5.8 has calibration data associated with it that is traceable to a national metrology laboratory. This can be accomplished either by purchasing the standard directly from the national laboratory or through a secondary standards supplier, who has performed a transfer from a standard that was calibrated by the national metrology laboratory. The supplier will specify the operating conditions and a calibrated power supply is used as the power source. A tremendous amount of research

Table 5.2 Relative uncertainty ($k = 2$) of the NIST irradiance scale (Yoon and Gibson, 2011). See Section 5.7 for an explanation of the uncertainty analysis.

Wavelength (nm)	Relative Uncertainty (%)
250	1.74
350	1.27
450	0.91
555	0.77
654.6	0.69
900	0.57
1600	0.47
2000	0.50
2300	0.49
2400	1.11

and development has been invested in the characterization of irradiance sources. Our experience is with NIST-traceable sources and the description here reflects that bias.

The NIST spectral irradiance characterization utilizes filter transfer radiometers calibrated for absolute spectral flux responsivity traceable to an absolute cryogenic radiometer. The cryogenic radiometer is a liquid helium-cooled electrical substitution device where the optical power of light absorbed by an almost perfectly absorbing cavity is compared to the equivalent amount of power required to heat the cavity to the same temperature. These types of radiometers were pioneered at the National Physical Laboratory (NPL) in the United Kingdom and the NIST high-accuracy cryogenic radiometer (HACR) was based on the NPL work (Quinn and Martin, 1985; Gentile et al., 1996). HACR has been replaced by the primary optical watt radiometer (POWR) which is used to establish the responsivity scale to various detectors and ultimately to the filter radiometer used for the characterization of a high-temperature blackbody (~ 3000 K) (Houston and Rice, 2006). The blackbody temperature is determined through the use of the measurement equation appropriate to the filter radiometer and blackbody. The blackbody is subsequently viewed by a spectroradiometer fitted with an integrating sphere with a precisely known aperture to establish the irradiance. The irradiance source under test, a 1000 W quartz tungsten–halogen lamp known as a FEL lamp, is then viewed and the irradiance is transferred. The process is well described in Yoon et al. (2002) and the uncertainty of the NIST scale is presented in Table 5.2.

NIST reports spectral irradiance values for a circular area with a radius of 6.65 mm at 35 wavelengths ranging from 250 nm to 2400 nm measured at a standard distance of 50 cm requiring that the irradiance at the intermediate wavelengths be determined through interpolation. The NIST-recommended interpolation is based on a fourth-order polynomial modification of the Wein approximation to Planck's law. The equation is

$$E_\lambda = \frac{A_0 + A_1\lambda + A_2\lambda^2 + A_3\lambda^3 + A_4\lambda^4}{\lambda^5} \exp\left(A_5 + \frac{A_6}{\lambda}\right), \quad (5.7)$$

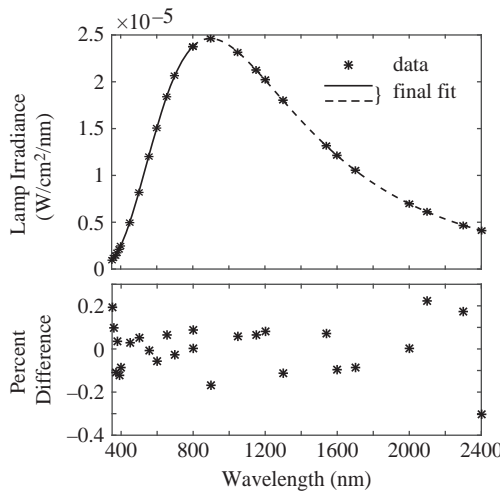


Figure 5.9 The upper graph is the least squares fit to FEL lamp data over the 350 to 800 nm (solid line) and 800 to 2400 nm (dashed line) ranges and the lower graph is the corresponding percent difference between the least squares fit and the data. Data from Yoon and Gibson (2011).

where A_o through A_6 are fit parameters and the polynomial term is used to estimate the spectral dependence of the emissivity. In practice we follow the fitting procedure outlined in Walker et al. (1987) where the first step is to replace the polynomial in (5.7) with 1 and linearize the remaining equation to

$$\ln(E_\lambda \lambda^5) = A_5 + \frac{A_6}{\lambda}, \quad (5.8)$$

where $\exp(A_5)$ represents a constant emissivity and A_6 is proportional to the temperature. A least squares fit is performed with a weighting of one to determine A_5 and A_6 , which are then fixed. A final fit is performed using (5.7) to determine the remaining fit constants with a $1/E_\lambda^2$ weighting, which accounts for any spectral variation in the emissivity. The process has an additional uncertainty of less than 0.5 percent and is separately performed over three spectral ranges: 250 nm to 350 nm, 350 nm to 800 nm, and 800 nm to 2400 nm (Yoon and Gibson, 2011). Figure 5.9 shows an example of the fit and the percentage difference between the fit and the measured values. In our work we extend the range to 2500 nm if required by the particular imaging spectrometer being characterized.

5.4.2 Reflectance Standard

The irradiance from the standard lamp is converted to radiance through reflection from a near-Lambertian reflectance standard with care taken to ensure that only the light from the lamp falls onto the reflector. As discussed in Chapter 3, most reflectance standards depart somewhat from the ideal diffuse case. For the best accuracy the standard is characterized in the laboratory geometry, such as $0^\circ/45^\circ$ where the notation refers to the

incident and exitant polar angles θ_i and θ_r . The $0^\circ/45^\circ$ geometry is particularly recommended since the performance of standards in this arrangement has been extensively investigated. The most accurate characterization is accomplished at a metrology laboratory as the expense of building the characterization system is prohibitive for such a rare measurement.

As an example of how the measurement is performed, the NIST Spectral Tri-function Automated Reference Reflectometer (STARR) is used to measure the reflectance at a particular geometry based upon the BRDF given by (3.6) which is converted to

$$d\rho(\theta_i, \phi_i; \theta_r, \phi_r) = f_r(\theta_i, \phi_i; \theta_r, \phi_r) \cos \theta_r d\omega_r \quad (5.9)$$

for the measurement case with a small solid angle and the BRDF is related to the reflected radiance and the incident irradiance through (3.6). Figure 5.10 illustrates the STARR geometry with the incident flux from a collimated, nearly monochromatic beam measured by a simple radiometer consisting of a precision aperture and a detector assembly, followed by a similar measurement of the reflected flux at θ_r . In this case the measurement equation is simply

$$S(\theta_i = 0, \theta_r; \lambda, \sigma) = R_d(\lambda, \sigma) d\Phi(0, \theta_r; \lambda, \sigma) \quad (5.10)$$

for the signal S due to the flux $d\Phi$ at wavelength λ in polarization state σ normally incident at the sample location with the detector response R_d , which is separately characterized. The azimuthal angle has been suppressed in the notation. The polarization state of the collimated beam is important since all monochromators polarize light due to the reflectance properties of the optics, particularly the grating. Two measurements are required with the light linearly polarized parallel and perpendicular to the plane of reflection in Figure 5.10.

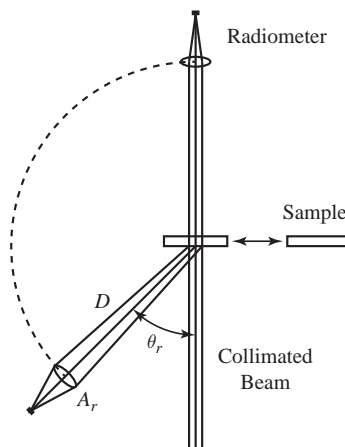


Figure 5.10 Schematic of the STARR facility. The incident irradiance is measured with the radiometer in the top position, normal to the collimated beam, with the sample moved to the right position. The reflected radiance is measured with the radiometer rotated to the angle θ_r with the sample moved to the left. Adapted from Cooksey et al. (2015).

The incident irradiance is related to the flux and the signal through

$$d\Phi_i = E_i(\lambda, \sigma) dA_i \Rightarrow E_i(\lambda, \sigma) = \frac{S_i(\lambda, \sigma)}{R_{d,i}(\lambda, \sigma) dA_i}, \quad (5.11)$$

where S_i is the incident signal, dA_i is the area of illumination, and the notation in (5.10) has been modified to represent the incident case. Similarly the reflected flux is related to the exitant radiance through

$$d\Phi_r(0, \theta_r; \lambda, \sigma) = L_r(0, \theta_r; \lambda, \sigma) \omega_r \cos \theta_r dA_i, \quad (5.12)$$

where ω_r is the solid angle from the center of the illuminated area at the sample to the aperture stop of the radiometer. Combining (5.10) and (5.12) gives

$$L_r(0, \theta_r; \lambda, \sigma) = \frac{S_r(0, \theta_r; \lambda, \sigma)}{R_{d,r}(\lambda, \sigma) \omega_r \cos \theta_r dA_i}, \quad (5.13)$$

which yields

$$f_r(0, \theta_r; \lambda, \sigma) = \frac{S_r(0, \theta_r; \lambda, \sigma)}{S_i(\lambda, \sigma)} \frac{R_{d,i}(\lambda, \sigma)}{R_{d,r}(\lambda, \sigma)} \frac{1}{\omega_r \cos \theta_r} \quad (5.14)$$

from (3.6). The solid angle ω_r is written as A_r/D^2 since the diameter of the aperture is small compared to the distance D so that the final form of the BRDF is

$$f_r(0, \theta_r; \lambda, \sigma) = \frac{S_r(0, \theta_r; \lambda, \sigma)}{S_i(\lambda, \sigma)} \frac{R_{d,i}(\lambda, \sigma)}{R_{d,r}(\lambda, \sigma)} \frac{D^2}{A_r \cos \theta_r} \quad (5.15)$$

and therefore the reflectance factor is

$$R(0, \theta_r; \lambda, \sigma) = \frac{\pi D^2}{A_r \cos \theta_r} \frac{S_r(0, \theta_r; \lambda, \sigma)}{S_i(\lambda, \sigma)} \frac{R_{d,i}(\lambda, \sigma)}{R_{d,r}(\lambda, \sigma)} \quad (5.16)$$

from (3.24). The final reflectance factor is the average of the two polarization measurements. The detector response ratio, $R_{d,i}(\lambda, \sigma)/R_{d,r}(\lambda, \sigma)$, is retained due to the different signal levels in the two cases which requires a change in gain in the NIST measurements. An example of the NIST measurement of a sintered polytetrafluoroethylene (PTFE) reflectance standard including the expanded uncertainties ($k = 2$) is shown in Figure 5.11.

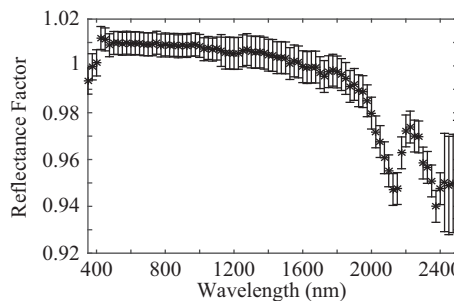


Figure 5.11 Calibration data from the NIST measurement of sintered PTFE. Data provided by Catherine Cooksey and previously published in Cooksey et al. (2015).

The characterization described produces accurate calibration data, with the STARR reflectance factor uncertainties for the VNIR/SWIR on the order of 0.01, but the measurement is highly specialized and not readily available outside of a national metrology laboratory. This level of accuracy is often required for science applications such as climate change studies; however, if the user's requirements are not so stringent, an alternative is to scale the calibration data from a directional-hemispherical measurement from a vendor, which is traceable to a national metrology laboratory measurement. Recent work at NIST has measured the ratio of the reflectance factors for the 0°/45° and 6°/hemispherical geometries for three materials and established a wavelength dependent linear fit (Cooksey et al., 2015). Sintered PTFE is the typical material used for reflectance standards although pressed PTFE, which has been studied extensively and is an intrinsic standard when it is properly prepared as described in Barnes et al. (1998), is an inexpensive option.

5.4.3 Transfer Radiometers

The known irradiance and reflectance factor produces the required radiance by combining (5.9), (3.6), and (3.24) giving

$$L_r(0, 45^\circ) = \frac{R(0, 45^\circ)}{\pi} E_i(0), \quad (5.17)$$

which can be measured by a transfer radiometer to generate calibration coefficients. The integrating sphere is measured next and the radiance from it is established through (5.5). The transfer radiometer is the critical piece of laboratory hardware that is used to establish the at-aperture radiance that is subsequently used to generate the calibration coefficients for the imaging spectrometer. These devices can be multispectral filter radiometers or grating-based spectroradiometers and, in practice, it is good to have both varieties. Filter radiometers have been developed to a high level of precision and accuracy, are relatively simple, at least in principle, as illustrated in Figure 5.1, and are more immune to systematic errors such as those produced by light scattering. Several properties are desirable in the design of a transfer radiometer. The instruments must be linear over a broad dynamic range, be temporally stable both during a measurement series and broadly to aging, and be relatively immune to the changes in the laboratory temperature. We will address two specific filter designs, trap and single-detector, that have these properties, and then proceed to grating designs.

In the most basic transfer radiometer design illustrated in Figure 5.1, the étendue is established by a pair of circular apertures. In most cases U can be written as

$$U = \pi r_1^2 \omega_{12}, \quad (5.18)$$

where r_1 is the radius of the first aperture and ω_{12} is the solid angle subtended by the second aperture from the center of the first, which is given by (2.49) for the half angle α . From Figure 5.12, α is given by

$$\alpha = \tan^{-1} \left(\frac{r_2}{D} \right) \quad (5.19)$$

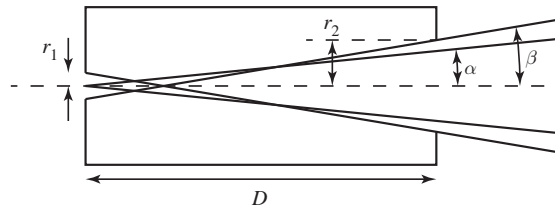


Figure 5.12 Aperture arrangement used to establish the angular distribution for the measurement of radiance. Typically the detector assembly is positioned at the smaller aperture.

and the full measurement half angle is

$$\beta = \tan^{-1} \left(\frac{r_1 + r_2}{D} \right). \quad (5.20)$$

Taking a representative example of two apertures with 5 mm diameters spaced 100 mm apart yields 0.3 percent difference for the étendue compared to the exact calculation. Note that the limiting diameter of the detector assembly must be large enough to exceed the full measurement half-angle so that the entire beam is measured. The basic design can be modified using powered optical elements, in which case the étendue is calculated from the exit pupil and the field stop. For example, if a singlet is placed at the first aperture then the second aperture becomes the field stop with the detector assembly mounted immediately behind it. Care must be taken to make sure that a transfer radiometer of this design is utilized in the proper imaging geometry.

Filter radiometers typically utilize a temperature stabilized filter wheel with a series of narrow bandpass dielectric filters. These filters are based on the model of the Fabry–Pérot interferometer and are made from interference films made of alternating layers of material with different refractive indexes deposited onto an optical substrate. The attenuation achieved for the out-of-band wavelengths can be very high and is often expressed in terms of the optical density OD defined as

$$OD(\lambda) \equiv \log \left[\frac{\Phi_o(\lambda)}{\Phi_t(\lambda)} \right] = -\log(\tau_\lambda) \Rightarrow \tau_\lambda = 10^{-OD(\lambda)}, \quad (5.21)$$

where Φ_o and Φ_t are the incident and transmitted spectral flux respectively and τ_λ is the filter spectral transmission. Out-of-band optical densities of better than 6 with in-band transmission near unity are achievable. The Fabry–Pérot filter has a limited out-of-band blocking range so a combination of the absorbing properties of the substrate and additional broadband coatings are applied to achieve high attenuation away from the bandpass. These filters should be used at near normal incidence to minimize angular and polarization effects. Figure 5.13 shows an example of a bandpass filter with the terminology that is typically applied by the vendor. Note, however, that the measurement wavelength that describes a filter is usually defined in the science community through

$$\lambda_m \equiv \frac{\int \lambda P(\lambda) d\lambda}{\int P(\lambda) d\lambda}, \quad (5.22)$$

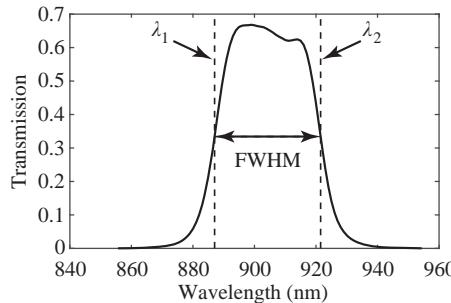


Figure 5.13 The Terra MODIS 17 filter is used to illustrate a bandpass filter with the wavelength positions of the half maximum points marked by λ_1 (887.04 nm) and λ_2 (921.50 nm). The center wavelength is calculated from $(\lambda_1 + \lambda_2)/2$ which is 904.3 nm and the FWHM is 34.46 nm.

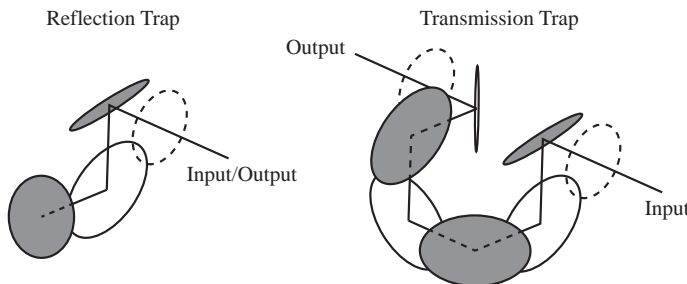


Figure 5.14 Illustration of both the reflection and the transmission, or tunnel, trap arrangements. The dashed ovals are the input and output apertures and the solid ovals are the silicon photodiodes. Adapted from Eppeldauer and Lynch (2000).

where P is the filter bandpass. The interested reader is directed to Macleod (2010) for a thorough treatment of filter design and manufacturing.

The trap filter radiometer is used in the VNIR where large, highly uniform silicon photodiodes are readily available. The terminology refers to the detector design where the photodiodes are coaxially mounted so that light that is not absorbed by one is reflected to the next one and so on. After a relatively small number of reflections there is essentially no unabsorbed light remaining. The highest accuracy design is known as a transmission or tunnel trap detector, shown on the right in Figure 5.14, where several silicon photodiodes are positioned in series along the optical path with the nonabsorbed light emerging after the final diode along the optical axis. The second type is a reflection trap where a photodiode is mounted normal to the optical axis and retroreflects the beam back along the input direction as illustrated on the left. Transmission trap detectors have no interaction due to back reflections with any optical components mounted at their inputs that could introduce uncertainty.

The detector response for a single silicon photodiode to monochromatic light at wavelength λ can be written from (5.2) as

$$R_\Phi(\lambda) = \frac{S(\lambda)}{\Phi(\lambda)} = \frac{n_e q_e}{n_{ph}(\lambda) h \nu} [1 - \rho(\lambda)] = \eta_i(\lambda) \frac{q_e \lambda}{h c} [1 - \rho(\lambda)], \quad (5.23)$$

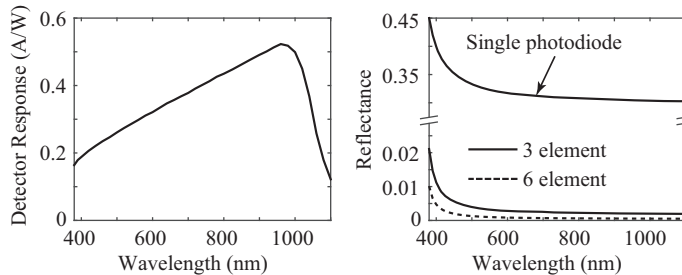


Figure 5.15 The detector response over the 380 nm to 1100 nm spectral range for a Hamamatsu S1337 photodiode is shown on the left. Data provided by Syleen Neely and Kento Sobukawa on behalf of the Hamamatsu Corporation. The right graph shows the reflectance of silicon for a single detector and for three-element reflection and six-element transmission trap assemblies. Note the abscissa scale change.

where S is the signal in amperes, Φ is the flux in watts incident on the photodiode, n_e is the number of photoelectrons collected per second, q_e is the change of the electron, n_{ph} is the number of incident photons per second, ρ is the reflectance of the photodiode, and η_i is the internal quantum efficiency of silicon. The external quantum efficiency, which is often provided by the manufacturer, is given by $\eta_e(\lambda) = [1 - \rho(\lambda)]\eta_i(\lambda)$. For a trap detector, where the photocurrents from each of the photodiodes are added to produce the final signal, the total reflectance of the detector assembly is ρ^m , where m is the number of reflections from the photodiodes, with the total being very close to zero. Figure 5.15 shows the detector response for a Hamamatsu S1337 photodiode on the left, and the reflectance of a single photodiode, a three-element reflective trap assembly, and a six-element transmission trap assembly on the right. The calculation of the total trap reflectance follows the methodology in Haapalinna et al. (1998) with additional data from Green and Keevers (1995). The photodiode model includes a thin, non-absorbing fused silica cover of 30 nm thickness. Eppeldauer and Lynch (2000) discuss the electronic design required for optimum performance.

In the SWIR and LWIR trap detectors are currently not viable due to detector limitations, although see Carter et al. (2009) for an MWIR/LWIR trap radiometer. In this case a single photodiode design is employed. The simplest approach expands upon Figure 5.1 with several of the components placed inside a dewar for cooling and a chopper added for phase-sensitive detection using a lock-in amplifier. Briefly, this method multiplies sinusoidal input and reference signals and then averages the resulting waveform over several periods. The out-of-phase portion of the combined waveform will average to zero and the in-phase part averages to half of the product of the amplitudes. The reference signal is input from a photodiode mounted on the chopper. The technique has high rejection for noise terms such as thermal emission from the component parts that are after the chopper. The two apertures in Figure 5.1, additional baffles to reduce scattered light, a cold filter for out-of-band blocking with low self-emission, and a photodiode detector are contained within a dewar for cooling and temperature control.

The temperature required depends upon the wavelength range and the detector material. For example, extended indium gallium arsenide (InGaAs) or indium antimonide

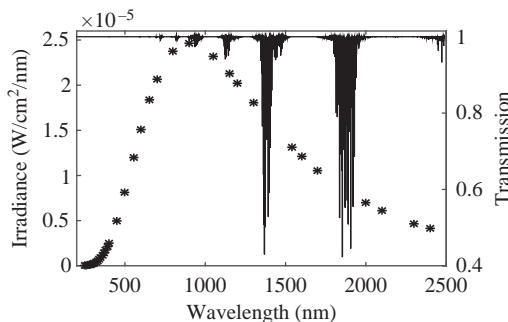


Figure 5.16 The effect of water absorption on the spectral irradiance from a FEL lamp. The water transmission was calculated using the HITRAN database over a 1 m path and for 20 percent humidity at a pressure of 1 atm and a temperature of 296 K (Rothman et al., 2013).

(InSb) could be used in the SWIR while mercury cadmium telluride (HgCdTe or MCT) or arsenic-doped silicon blacked-impurity-band devices (Si BIB) are employed in the LWIR. The cooling of the detector reduces the noise terms, such as the dark current due to thermal excitation of electrons in the material, while the cooling of the other components reduces the background irradiance falling on the detector. If this background signal is too large, the dynamic range will be unacceptably reduced and saturation can occur. Reducing the background is critical for LWIR applications. Cooling using liquid nitrogen has often been used, although it is insufficient for Si BIB detectors that operate below 10 K. An example of simple single-detector, SWIR transfer radiometer is described in Spyak et al. (2000) and a similar one for the LWIR using a MCT detector is presented in Gong et al. (2004).

It is important to note that the method assumes that there are no absorption features present, which can be a problem if the humidity is sufficiently high in the laboratory. The calculation of calibration coefficients will be degraded due to water absorption, particularly in the bands at 1.4 and 1.85 microns as shown in Figure 5.16. In most cases the imaging spectrometer views scenes where there is significant water present so the degradation in the resulting calibration coefficients due to the laboratory conditions is not a large problem with the impact in the 820 nm, 940 nm, and 1100 nm water bands being small, particularly after band averaging, and the other two bands will be optically thick. If it is anticipated that the imaging spectrometer will be used in cases with negligible water, such as for planetary missions or high altitude measurements, then the calibration must be performed in either vacuum or under a dry gas purge or the transmission in the laboratory is modeled.

The radiance from a few spectral locations has been accurately established by a filter transfer radiometer in conjunction with irradiance and reflectance standards. The next step is to measure the same radiance source with a spectroradiometer for the transfer to the integrating sphere. In the VNIR/SWIR the spectroradiometer is a grating-based instrument that can be a monochromator that measures a spectral sample successively or a spectrometer using, for example, a line array to record an entire spectrum at once. These instruments can also be a combination of the two with multiple internal modules.

The native resolution often depends upon the spectral region and can vary significantly within a given range for commercially available instruments. This is due to the availability of detectors and their different sampling elements. For example, a silicon-based line array could have 1000 detectors with the sampling from 380 nm to 1100 nm being about every 0.7 nm with the width of the instrumental profile on the order of 0.9 nm. The same transfer radiometer may also have an extended InGaAs line array with 512 detector elements and a sampling between 1100 nm and 2500 nm of about 2.7 nm with a FWHM for P of 3.3 nm. Commercial vendors typically have software that performs interpolation to put the measured radiance on the same sampling grid. In our work we bypass the vendor's software and acquire the data in the native format.

The calibration of the spectroradiometer follows the same approach as for a filter transfer radiometer, with the spectral response function for each spectral channel and the radiance standard measured and the calibration coefficients generated using (5.5). Systematic errors such as scattered light contamination should be evaluated and addressed if necessary. The radiance measurement of the integrating sphere source by both the filter and grating-based transfer radiometers is then compared for consistency. Finally, a full error analysis is performed for all of the transfer radiometers, as presented in Section 5.7, to establish the accuracy and precision. An example of a grating-based transfer radiometer and its characterization is presented in Brown et al. (1998).

The transfer radiometer's response to radiance will be linear over some broad range by design as nonlinearities complicate the characterization process and are best avoided. A photodiode is typically linear over a range of flux or irradiance values and it is critical that the electronic circuitry be well designed to optimize its performance. The upper limit is determined by the transition from linear behavior to saturation, where the signal becomes constant for increasing irradiance levels. The lower limit is determined by the noise floor where the flux on the detector produces a signal that equals the RMS noise. In practice the measured signal is usually considerably higher than the noise floor for an accurate measurement. Taking the VNIR/SWIR as an example, the transfer radiometer is characterized at the range of radiance values that are required to ensure that the transfer from the radiance standard to the integrating sphere is within the linear response. Photodiode linearity performance for a variety of detector materials has been extensively studied by researchers at national metrology laboratories and a well-designed transfer radiometer will have a broad linear operational range (Thompson and Chen, 1994; Yoon et al., 2003; Theocarous et al., 2004).

5.4.4 Integrating Spheres

We will digress briefly here to describe the properties of an integrating sphere, invented in England by W. E. Sumpner, which is a Lambertian source and ubiquitous in calibration facilities (Sumpner, 1892). We will develop the theory for the ideal case where the sphere ports are infinitesimally small. Figure 5.17 shows a sphere with a radius R and the geometry between two areas of equal size. The flux from dA_1 to dA_2 given by

$$d^2\Phi_{12} = \frac{L(\theta, \phi) dA_1 \cos \theta_1 dA_2 \cos \theta_2}{r^2}, \quad (5.24)$$

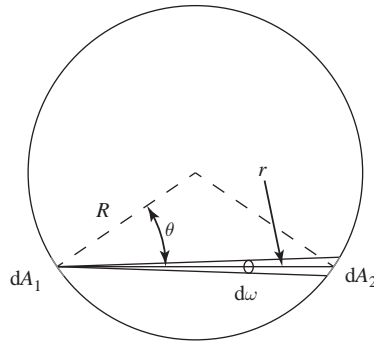


Figure 5.17 Idealized integrating sphere geometry for the transfer of flux from dA_1 to dA_2 a distance r apart. The infinitesimally small sphere ports are not illustrated.

with the radiometric quantities all functions of wavelength throughout this section. It is easy to show that θ_1 is equal to θ_2 , which will be relabeled as just θ , and that $r = 2R \cos \theta$. The interior surface of the sphere is assumed to be a Lambertian reflector and (3.25) is modified to include the spectral reflectance giving

$$L = \frac{E\rho}{\pi}. \quad (5.25)$$

The irradiance at dA_2 due to the flux from dA_1 for a given wavelength is

$$dE_2 = \frac{d\Phi_{12}}{dA} = \frac{L dA}{4R^2} = \frac{E\rho dA}{4\pi R^2}, \quad (5.26)$$

with the irradiance being independent of θ .

The integrating sphere functions as a Lambertian source due to the process of repeated reflections from the diffuse sphere walls, which completely remove any directional dependence to the output radiance regardless of the nonuniformity of the original input flux. Imagine that the source of the flux that illuminates the sphere has just been turned on and produces an irradiance E_o on the surface of a portion of the sphere. This initial irradiance will depend upon the details of the source and will vary significantly across the illuminated portion of the inner surface. The irradiance for an arbitrary point on the sphere after one reflection due to the entire interior surface is obtained by integrating (5.26) which yields

$$E_1 = \int_{\text{sphere}} \frac{E_o \rho}{4\pi R^2} dA = \frac{\rho}{4\pi R^2} \int_{\text{sphere}} E_o dA = \frac{\rho \Phi_o}{4\pi R^2}, \quad (5.27)$$

where E_1 is the irradiance after one reflection and Φ_o is the entire initial flux from the source prior to a reflection. For the second reflection E_o is replaced by E_1 in (5.27), giving

$$E_2 = \int_{\text{sphere}} \frac{E_1 \rho}{4\pi R^2} dA = \frac{\rho E_1}{4\pi R^2} \int_{\text{sphere}} dA = \rho E_1$$

or

$$E_2 = \frac{\rho^2 \Phi_o}{4\pi R^2}, \quad (5.28)$$

since the dependence upon the sphere area has been removed by the diffuse reflectance property. The process is repeated for successive reflections with the only change being the power of ρ . The final irradiance at the arbitrary point is obtained from an infinite series of reflections whose sum is

$$E_t = E_o + E_1 + E_2 + \dots = E_o + \frac{\Phi_o}{4\pi R^2} \sum_{n=1}^{\infty} \rho^n = E_o + \frac{\Phi_o}{A_s} \left(\frac{\rho}{1-\rho} \right) \quad (5.29)$$

since

$$\frac{1}{1-x} = 1 + x + x^2 + \dots$$

for $x^2 < 1$. For points that are not directly illuminated by the source E_o is zero and the final form of the equation is

$$E = \frac{\Phi_o}{A_s} \left(\frac{\rho}{1-\rho} \right) \quad (5.30)$$

or

$$L = \frac{\Phi_o}{\pi A_s} \left(\frac{\rho}{1-\rho} \right) \quad (5.31)$$

for the radiance where A_s is the surface area of the sphere. For a well-designed sphere none of the input flux will directly reach the exit port and (5.31) holds.

Real integrating spheres have finite-sized ports and the reflectance is modified to account for them. An integrating sphere with wall reflectance ρ_w and surface area A_s also has n areas a_i , each with reflectance ρ_i . If a particular a_i is an open port the reflectance will be zero but it could have a different material at the port to measure, for example, the directional-hemispherical reflectance. The ratio of a_i to A_s is denoted as f_i and the average reflectance of the sphere is

$$\bar{\rho}_w = \sum_{i=1}^n \rho_i f_i + \rho_w \left(1 - \sum_{i=1}^n f_i \right), \quad (5.32)$$

which replaces ρ in the denominator of (5.30) and (5.31). The ρ in the numerator corresponds to the reflectance of the initial area of illumination which is redesignated as ρ_o and could be the sphere wall or a sample. The final form of the integrating sphere radiance is therefore

$$L = \frac{\Phi_o}{\pi A_s} \left[\frac{\rho_o}{1 - \sum_{i=1}^n \rho_i f_i - \rho_w (1 - \sum_{i=1}^n f_i)} \right]. \quad (5.33)$$

For the directional-hemispherical measurement using an integrating sphere, (5.33) reduces to

$$L = \frac{\Phi_o}{\pi A_s} \left[\frac{\rho_s}{1 - \rho_s f_s - \rho_w (1 - f_s)} \right], \quad (5.34)$$

where ρ_s is the directional-hemispherical reflectance of the sample at the illumination angle. A similar derivation to that presented here except taking the port areas into account from the beginning is given in Carr (1997).

5.4.5 LWIR Radiometric Characterization

The characterization of a LWIR imaging spectrometer has particular challenges and the radiometric calibration of the data is typically accomplished using real-time techniques employing well-understood blackbody sources. The primary challenge is due to blackbody emission from both the instrument itself and the test equipment, which is designed to minimize the effect through the use of mirrors that employ coatings with low spectral emissivity or through cooling to a low temperature. The imaging spectrometer will typically suffer from instability due to temperature and electronic fluctuations which are mitigated through temperature stabilized in a dewar, particularly if refractive optical elements are used, and by frequent measurements of radiance standards. There are a variety of blackbodies employed depending upon the particulars of the sensor, ranging from flat panel to cavity types. For a linear sensor, the traceability to a standard is through the temperature, established by a direct measurement using a thermometer or the phase transition of a pure element depending upon the requirements, and through the emissivity known as a function of the viewing geometry as determined from traceable measurements.

A specific example is a large aperture space-based dispersive LWIR imaging spectrometer as illustrated in Figure 5.18. Due to the large aperture, radiance from the calibration blackbodies, including any relay optics, is input into the system via a flip mirror positioned after the telescope with the light focused onto the slit. For normal operation the flip mirror is positioned to relay light from the scene into the spectrometer. Care is taken in the design to ensure that the scene and blackbody radiances fill the spectrometer in the same way. The spectrometer is inside a dewar to maintain a low temperature so that the background light contribution to the signal is small. It also has a cold stop that limits the field of view to the scene and the low emissivity optics (Warren et al., 2008). The design includes low- and high-temperature blackbodies, 240 K and 300 K respectively, that represent the radiance range expected from a scene. The reflectance properties of the flip mirror are assumed to be uniform regardless of the direction.

The measurement equation (5.1) for the signal is rewritten as

$$S(\lambda_c) \approx U\tau\eta t_{\text{int}} \int_{-\infty}^{\infty} L_{\lambda}(\lambda)P(\lambda_c - \lambda) d\lambda \equiv R(\lambda_c)L(\lambda_c), \quad (5.35)$$

where it has been assumed that τ and η are approximately constant for a given instrumental profile. $R(\lambda_c)$ is the system responsivity for a particular channel and $L(\lambda_c)$ is the in-band radiance. The radiance has contributions from the scene and due to self-emission from the optics with the total designated as

$$L(\lambda_c) = L_s(\lambda_c) + L_t(\lambda_c) + L_{is}(\lambda_c), \quad (5.36)$$

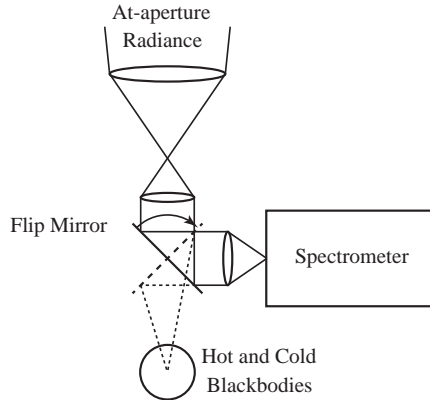


Figure 5.18 Schematic of the internal calibration scheme for an LWIR dispersive imaging spectrometer.

where $L_s(\lambda_c)$ is the scene radiance and the self-emission is $L_t(\lambda_c) + L_{is}(\lambda_c)$ for the telescope and imaging spectrometer, which includes the flip mirror, respectively. The self-emission from the telescope is written as

$$L_t(\lambda_c) = \epsilon_t(\lambda)B_t(\lambda_c, T) = [1 - \tau_t(\lambda)]B_t(\lambda_c, T_t), \quad (5.37)$$

where ϵ_t and τ_t are the telescope assembly emissivity and transmissivity respectively and $B_t(\lambda_c, T_t)$ is the radiance from a blackbody at the telescope temperature. It is assumed that the entire telescope assembly is at the same temperature and the transmissivity is a net quantity that has been measured. The measurement equation is modified becoming

$$S(\lambda_c) = \{\tau_t(\lambda_c)L_s(\lambda_c) + [1 - \tau_t(\lambda_c)]B_t(\lambda_c, T_t)\}R_{is}(\lambda_c) + S_{is}(\lambda_c), \quad (5.38)$$

where $R_{is}(\lambda_c)$ is the responsivity of the imaging spectrometer and $S_{is}(\lambda_c)$ is its signal offset due to self-emission, which should be small. It also includes the dark signal from the detector element.

The hot and cold blackbodies are measured in turn and the equivalent equation to (5.38) is

$$S_i(\lambda_c) = L_i(\lambda_c)R_{is}(\lambda_c) + S_{is}(\lambda_c) = B_i(\lambda_c)R_{is}(\lambda_c) + S_{is}(\lambda_c), \quad (5.39)$$

where i is either H for hot or C for cold. Subtracting the two measurements and rearranging yields

$$R_{is}(\lambda_c) = \frac{S_H(\lambda_c) - S_C(\lambda_c)}{B_H(\lambda_c, T_H) - B_C(\lambda_c, T_C)} \quad (5.40)$$

for the responsivity. Similarly (5.39) is used to solve for the offset, which is

$$S_{is}(\lambda_c) = \frac{S_C(\lambda_c)B_H(\lambda_c, T_H) - S_H(\lambda_c)B_C(\lambda_c, T_H)}{B_H(\lambda_c, T_H) - B_C(\lambda_c, T_C)}, \quad (5.41)$$

where S_i can be replaced by either S_C or S_H . Finally, returning to (5.38), the at-aperture radiance is

$$L_s(\lambda_c) = \frac{1}{\tau_t(\lambda_c)} \left\{ \frac{S(\lambda_c) - S_{is}(\lambda_c)}{R_{is}(\lambda_c)} - [1 - \tau_t(\lambda_c)]B_t(\lambda_c, T_t) \right\} \quad (5.42)$$

with the only unknown being the telescope transmissivity, which is determined through a view of deep space where there is negligible blackbody emission. The measurement equation for that view is

$$\begin{aligned} S_{ds}(\lambda_c) &= \{\tau_t(\lambda_c)L_{ds}(\lambda_c) + [1 - \tau_t(\lambda_c)]B_t(\lambda_c, T_t)\}R_{is}(\lambda_c) + S_{is}(\lambda_c) \\ &= [1 - \tau_t(\lambda_c)]B_t(\lambda_c, T_t)R_{is}(\lambda_c) + S_{is}(\lambda_c) \end{aligned} \quad (5.43)$$

to good approximation, which can be solved for τ_t and substituted into (5.42). The frequency of a deep space view depends upon the stability of the telescope transmissivity which will degrade over time in the harsh space environment.

Note that it has been assumed that the emissivity of the blackbody sources is unity. The actual sources will have an emissivity that is very close to 1, that will have been precisely measured, and $\epsilon_i(\lambda_c)$ will be included in (5.39). A similar approach is used for a small aperture imaging spectrometer that is deployed on an airplane except that the blackbody sources can be viewed from the front of the telescope so the entire optical train is included in their measurement. Additionally, the radiometric characterization of a Fourier transform imaging spectrometer is fundamentally the same with the added complication of performing the required transformations (Rivercomb et al., 1988). See Dykema and Anderson (2006) for a discussion of the methodology and associated challenges for highly accurate calibration products in the thermal infrared in support of science missions.

5.4.6 Additional Radiometric Measurements

For most aperture sizes it is possible to acquire an integrating sphere with an appropriately sized output port or a blackbody that is large enough to fill the entrance pupil. The radiance from the integrating sphere is known through the application of well-characterized transfer radiometers or from measurements performed at a metrology laboratory and, similarly, the radiance from the blackbody is known from the temperature and emissivity. For the VNIR/SWIR, the transfer radiometer in Figure 5.8 is replaced by the imaging spectrometer, the known at-aperture radiance is measured, and (5.5) and (5.6) are applied to produce calibration coefficients if the sensor response is linear. For sensors that operate in either the reflective or emissive spectral ranges, the linearity is determined through appropriate measurements and under-performing detector elements are also identified in what is known as a bad pixel map. Any systematic errors, such as scattered light contamination, must also be addressed as part of the full radiometric characterization.

Linearity Measurements

The linearity measurement can be performed in several ways, with all of the methods involving varying the at-aperture radiance, preferably over the full dynamic range of the sensor. This may involve using some short- or long-pass filtering since the sensor optical efficiency and the spectral radiance both vary over the spectral range of the imaging spectrometer. The data for each spatial-spectral sample are acquired at the various

radiance levels and a fit is performed and evaluated based upon the measurement uncertainties. The LWIR measurement utilizes blackbodies at different temperatures with the accuracy depending upon the thermometry. As a specific example, VNIR/SWIR approaches that require absolute measurements will be described followed by a relative measurement of the linearity.

Most integrating spheres are equipped with a variable aperture or a filter holder between the sphere and one of the source lamps. If it has a filter holder then neutral density (ND) filters can be inserted. An ideal neutral density filter is one that attenuates transmitted flux at a constant level for all wavelengths of interest. These filters are labeled by their optical density from (5.21) with their spectral attenuation, which is not perfectly constant, known from characterization measurements. For a sphere that has been characterized at a metrology laboratory, the output radiance is known as a function of aperture size or inserted ND filter with an uncertainty estimate provided by the vendor. A similar approach is to use linear transfer radiometers to establish the radiance levels from the integrating sphere with the variable output.

A potential relative approach is a modification of the technique developed to test the linearity of silicon detectors (Schaefer et al., 1983). The method involved irradiating a photodiode with two monochromatic beams one of which was modulated using a chopper wheel to produce an AC signal component while the second was held at a single level for a DC component. The measurement consisted of changing the DC component while keeping the amplitude of the AC component fixed. If the photodiode is linear then the AC component measured with a lock-in amplifier will be constant. This method can be adapted to an imaging spectrometer by using one sphere port as an input for a constant flux Φ_c and varying the flux input from another sphere source at a separate port, labeled as Φ_v . One measurement is taken corresponding to $\Phi_c + \Phi_v$ and a second one with just Φ_v varied over a range of values. The difference between the signal pairs should remain constant as Φ_v is changed.

Bad Pixel Determination

All detector arrays have some pixels that are under-performing to varying degrees. These detector elements could always register a single value, have very high dark current, be very noisy, be nonlinear, or be inconsistent from readout to readout. The bad pixel map is determined through comparison to the mean performance for the entire array. For example, an unilluminated array is read out a large number of times and the mean and standard deviation of the signal from each pixel by itself is calculated, as well as the mean and standard deviation for the entire focal plane. The per-pixel average is then compared to the global average and any outliers are identified based upon four or five standard deviations from the mean. Also, those pixels with very large standard deviations compared to the global standard deviation are similarly identified as noisy. The map has a numeric value assigned to each pixel with a normally performing “good” pixel labeled with a 0 and a poorly performing “bad” pixel labeled with a different number that can depend upon the failure mode. The process is repeated for an illuminated array and nonlinear pixels are identified from the analysis of the linearity data. Finally,

the focal plane array is monitored over time to determine if any pixel behaves erratically, with such pixels being known as blinkers.

Scattered Light Correction

The deleterious effects of stray light contamination in monochromators have long been recognized and a tremendous amount of work has been expended to minimize it by spectroscopists, particularly for absorption spectroscopy where absorption features are quantified against broadband sources. For a dispersive system, spectral scattering that contaminates a spectral channel occurs at the grating or prism, at the optics that follow the disperser, or from light dispersed by the disperser that interacts with the imaging spectrometer housing. A well-designed grating instrument will be minimally impacted by the latter two effects with the dominant source of scattering being the grating. There are also potential sources of broadband contamination, again by scattering from an optic or from the housing, that add to the background light in a system but which are minimized in a high-performing design with appropriate baffling and high-quality optical surface finishing. We will limit our discussion to spectrally scattered light in grating systems since they are currently the most commonly used dispersing element.

Scattered light can have a significant impact even though it is a small effect. The scattered-light properties of several different flat, single-blaze diffraction gratings illuminated by a monochromatic source are presented in Woods et al. (1994) with the relative signal proportional to the ratio of the dark-subtracted signal at an angle θ from the diffraction angle divided by the dark-subtracted signal at the center of the diffraction pattern. The scatter function typically falls from a peak value between 10^{-5} and 10^{-3} through several orders of magnitude over a 25 nm to 75 nm displacement depending upon the grating. This is clearly a small effect, but it must be remembered that an imaging spectrometer views an extended source with all wavelengths scattering to some degree. For a spectroradiometer that uses a spectrograph with a single line array, the total signal measured for a particular channel will be the signal portion in the channel, the in-band (IB) signal, and the fraction due to scattered light from the other channels, which is written as

$$S_{\text{meas},i} = S_1 F_{\text{SC}_1 \rightarrow i} + S_2 F_{\text{SC}_2 \rightarrow i} + \cdots + S_{\text{IB}} + \cdots + S_{n-1} F_{\text{SC}_{n-1} \rightarrow i} + S_n F_{\text{SC}_n \rightarrow i}, \quad (5.44)$$

where $F_{\text{SC}_k \rightarrow i}$ is the fraction of light that should have been in the k th channel but is scattered into the i th one instead and S_{IB} is the in-band signal. The challenge is to quantify the different F values. A broadband term can be included in (5.44) but we are assuming it is small. The degree to which scattered light contaminates the signal for a particular instrumental profile will still be small but can be significant for materials with low reflectance such as water. If uncorrected this leads to errors in the radiance, particularly at the shortest wavelengths where the scatter is most significant (Feinholz et al., 2009). It will also degrade the estimate of the amount of molecular absorbers, such as water, from scene data since the depth of the absorption feature is reduced compared to the wings, affecting the evaluation of the equivalent width.

A simple grating spectrograph with a single line array will be used to illustrate the scattered light measurement and data reduction. The experimental apparatus consists

of a tunable, monochromatic source, such as a laser, illuminating an integrating sphere that uniformly illuminates the entrance pupil of the spectroradiometer. It is critical that the source be truly monochromatic since the portion of the signal due to scattered light is small and must be only due to the instrument under test. The source is tuned to a center wavelength of an instrumental profile, the resulting signal is evaluated for saturation, and the measurement is then completed. It is not necessary to measure all of the spectral response functions of the spectroradiometer since the scattered light function typically changes smoothly as a function of wavelength. Most measurements are performed using continuous wave (CW) sources, although NIST has demonstrated accurate measurements using a kilohertz-pulsed tunable laser system that employs optical parametric oscillators (Zong et al., 2012). The signals described in this section are always dark-subtracted.

The data reduction and stray light correction method presented here is a matrix inversion approach that has been validated and compared to traditional iterative techniques (Brown et al., 2003; Zong et al., 2006; Feinholz et al., 2009). The upper two graphs in Figure 5.19 illustrate noise-free as well as more typical peak-normalized signals based upon the measurement from a single instrumental profile; this is known as the spectral line-spread function or LSF. The LSF is denoted as $f_{LSF,i,j}$ for every detector element i where j is the particular detector element corresponding to the center of the illuminated instrumental profile. The index i corresponds to all of the elements in the line array while the index j is fixed by the laser wavelength for each measurement. The line-spread function is peak normalized, which is required since the scattered light quantification is based upon the fraction of out-of-band signal present relative to the in-band signal. The in-band signal closely corresponds to that expected in the scatter-free case since the direct signal overwhelmingly dominates. Table 5.3 is the modeled in-band signal for a monochromatic source at 601 nm, slightly mistuned from the center of the spectral response function at 600 nm. The laser power is optimized to be near the upper limit of the dynamic range of the 14 bit system modeled. The two adjacent instrumental profiles also have significant signal due to the spectral extent of their wings.

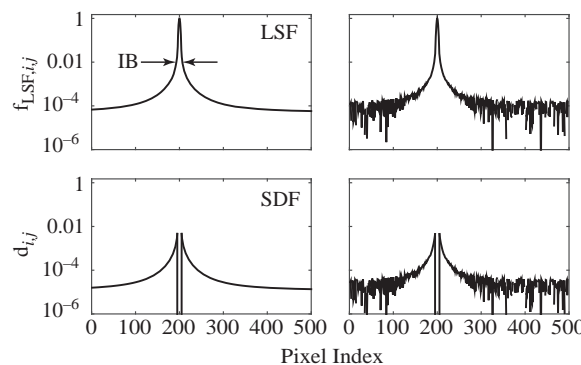


Figure 5.19 Simulated measurement of the spectral line-spread function (LSF) with and without noise (top two semilog graphs) and the reduction of the SDF to the spectral stray light signal distribution function (SDF).

Table 5.3 Model of the in-band signal from a monochromatic source centered at 601 nm. The second column is the modeled dark-subtracted signal and the third column is the signal normalized to the center channel value. The instrumental profiles, centered at λ_c , are modeled as Gaussian functions with a uniform limit of resolution of 12 nm. The model assumes that the 14-bit resolution is at 95 percent of the full range with a background signal of 2500 DN.

λ_c (nm)	Signal (DN)	Normalized Signal
570	0	0
580	3	2.09×10^{-4}
590	1296	0.10
600	13100	1
610	2800	0.21
620	13	9.77×10^{-4}
630	0	0

The next step in the data reduction is to remove the in-band signal from the LSF, replacing it with zeros, integrate the in-band portion to a single value, and divide it into the remaining function. This is known as the spectral stray light signal distribution function (SDF), denoted as $d_{i,j}$ and given by

$$d_{i,j} = \begin{cases} \frac{f_{\text{LSF},i,j}}{\sum_{i \in \text{IB}} f_{\text{LSF},i,j}}, & i \notin \text{IB} \text{ (pixel } i \text{ outside IB),} \\ = 0, & i \in \text{IB} \text{ (pixel } i \text{ inside IB),} \end{cases} \quad (5.45)$$

where i identifies a detector element whose values range from 1 to n in the line array and j is the index of the laser illuminated pixel. The SDF, illustrated on the bottom of Figure 5.19 for a single laser wavelength, is the fractional amount of scattered flux incident on each of the i th pixels compared to the in-band flux. Each instrumental profile has a calculated fraction derived from the monochromatic laser measurements that quantifies the amount of signal at a particular spectral channel from scattered light corresponding to the laser illuminated channel. It is a constant as long as the sensor configuration and cleanliness remains unchanged. Assuming the measurement is performed for every channel, the SDF can be written as a matrix yielding

$$\mathbf{D} = \begin{bmatrix} d_{1,1} & d_{1,2} & \dots & d_{1,j} & \dots & d_{1,n-1} & d_{1,n} \\ d_{2,1} & d_{2,2} & \dots & d_{2,j} & \dots & d_{2,n-1} & d_{2,n} \\ \vdots & \vdots & \dots & \vdots & \dots & \vdots & \vdots \\ d_{i,1} & d_{i,2} & \dots & d_{i,j} & \dots & d_{i,n-1} & d_{i,n} \\ \vdots & \vdots & \dots & \vdots & \dots & \vdots & \vdots \\ d_{n-1,1} & d_{n-1,2} & \dots & d_{n-1,j} & \dots & d_{n-1,n-1} & d_{n-1,n} \\ d_{n,1} & d_{n,2} & \dots & d_{n,j} & \dots & d_{n,n-1} & d_{n,n} \end{bmatrix}, \quad (5.46)$$

where each column corresponds to an individual laser measurement.

The calculation of the SDF allows (5.44) to be rewritten as

$$S_{\text{meas},i} = S_{\text{IB},i} + S_{\text{SC},i}^{\text{total}} = S_{\text{IB},i} + \sum_{j=1}^n d_{i,j} S_{\text{IB},j} \quad (5.47)$$

for the signal in the i th channel and in the absence of any additional broadband scattering. In matrix form (5.47) is written as

$$\mathbf{S}_{\text{meas}} = \mathbf{S}_{\text{IB}} + \mathbf{S}_{\text{SC}} = \mathbf{S}_{\text{IB}} + \mathbf{D}\mathbf{S}_{\text{IB}}, \quad (5.48)$$

where \mathbf{S}_{IB} and \mathbf{S}_{SC} are column vectors of the in-band and scattered light signals respectively. A column vector with n elements can be represented by the product of the $n \times n$ identity matrix \mathbf{I} and itself enabling (5.48) to be rewritten as

$$\mathbf{S}_{\text{meas}} = (\mathbf{I} + \mathbf{D})\mathbf{S}_{\text{IB}} = \mathbf{A}\mathbf{S}_{\text{IB}}, \quad (5.49)$$

where \mathbf{A} is an $n \times n$ coefficient matrix. The in-band signal is retrieved by performing a matrix inversion to yield

$$\mathbf{S}_{\text{IB}} = \mathbf{A}^{-1}\mathbf{S}_{\text{meas}} = \mathbf{C}\mathbf{S}_{\text{meas}}, \quad (5.50)$$

where \mathbf{C} is the spectral stray light correction matrix. Note that \mathbf{A} is almost equal to the identity matrix since the scattered light contribution to the off-diagonal elements is very small. This implies that small errors in \mathbf{D} will only result in small errors in the recovered in-band signal. The matrix correction method has been compared to more traditional iterative techniques by researchers at NIST with Zong et al. (2006) reporting comparison results.

The scattered light correction for an imaging spectrometer with a two-dimensional array is more complicated in the details but is conceptually the same with a scattered light contribution from the spatial dimension in addition to the spectral dimension. The measurement process is now performed over the spatial and spectral dimensions of the array, and again it is not required to measure every spatial–spectral sample as the unmeasured elements are predicted through interpolation or extrapolation. Even with this sparse sampling the experimental process is tedious and time-consuming. The apparatus requires the coupling of the laser source to a collimator that illuminates each spatial sample at the slit successively. The full two-dimensional scattered light correction method is developed in Feinholz et al. (2012). Consider an array with n spatial and m spectral samples; the measurement of the i th spectral sample for all of the spatial positions is given by $\mathbf{S}_{\text{meas}}^i = \mathbf{S}_{\text{IB}}^i + \mathbf{S}_{\text{SC}}^i$ written as

$$\mathbf{S}_{\text{X}}^i = \begin{bmatrix} S_{\text{X}}^{i,1} \\ S_{\text{X}}^{i,2} \\ \vdots \\ S_{\text{X}}^{i,n} \end{bmatrix}, \quad (5.51)$$

where X corresponds to meas , IB , or SC . Each of the spectral channels is measured and the final form of the signal is

$$\mathbf{S}_X = \begin{bmatrix} S_X^1 \\ S_X^2 \\ \vdots \\ S_X^m \end{bmatrix}, \quad (5.52)$$

where each $n \times 1$ element corresponds to (5.51) for the full m spectral samples to produce an $(m \times n) \times 1$ single-column vector. The development from here follows the spectroradiometer case above with the note that the \mathbf{D} and \mathbf{C} matrices become rank-two tensors.

An example of the scattered light correction as applied to an operational imaging spectrometer is presented in Lenhard et al. (2015). A full characterization was performed on a HySpex VNIR-1600 sensor with a spectral range of 416 to 992 nm. The scattered light measurement utilized a pulsed laser and, for the spatial-spectral samples measured, the laser was amplitude tuned to below and above saturation. The resulting data were then combined with the unsaturated data used to quantify the in-band signal and the saturated data characterized the wings. The two datasets are then stitched together through the application of a normalization factor. The correction factor for the unmeasured samples was calculated through interpolation. Figure 5.20 shows the impact of the

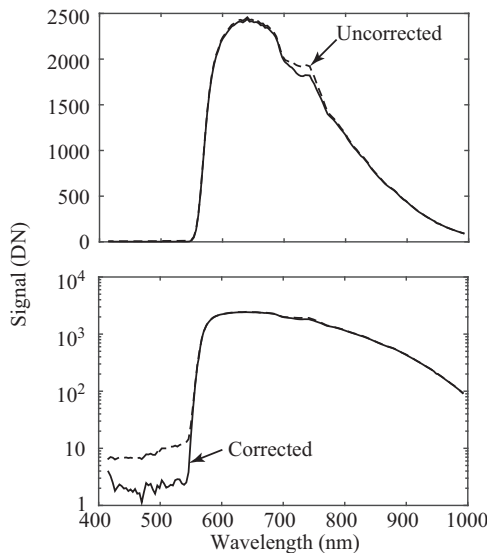


Figure 5.20 Laboratory measurement of scattered light in a HySpex VNIR-1600 imaging spectrometer. A longpass filter is used to block wavelengths shorter than 570 nm. The y-axis on the upper and lower graphs are linear and logarithmic respectively with the uncorrected signal represented by the dashed line and the corrected by the solid line. Data provided by Andreas Baumgartner from the German Aerospace Center (DLR) and previously presented in Lenhard et al. (2015).

correction utilizing a longpass filter. The imaging spectrometer was then applied to the problem of remote sensing of water depth with an estimated improvement of 19 percent.

On-board Calibration Sources

On-board blackbodies are a requirement for emissive imaging spectrometers but are not always included for systems working in the solar reflective spectral range. However, these sources are integral parts of most space-based spectral imagers and are used to provide a known and repeatable radiance to the sensor and are traceable to a national standard through the preflight calibration process. For the reflective spectral range there are a variety of internal calibration sources that are used to provide both spectral and radiometric information. A particularly good example is the suite of instruments used to monitor the MODerate resolution Imaging Spectroradiometer (MODIS) which includes a solar diffuser and a blackbody for the radiometric calibration of the reflective and emissive bands as well as a spectral calibration capability that utilizes both a monochromator and a didymium filter (Xiong and Barnes, 2006). The latter is also used to monitor the spatial performance. These internal sources will degrade in the harsh space environment over the life of the mission and the calibration maintenance is augmented through the use of vicarious techniques as discussed in Section 5.9.

5.5

Spatial Characterization

The spatial characterization of an imaging spectrometer is not required for the data calibration but is helpful for the evaluation of the sensor for spatial-spectral uniformity and also for problems such as electronic cross talk where signal from one detector element is erroneously recorded in another. Figure 5.21 is one approach to performing the spatial characterization with a collimated broadband source illuminating the entrance pupil of the imaging spectrometer. The sensor is slowly rotated about the center of the entrance pupil so that the focused point moves along the slit. The measurement consists of a series of FPA readouts at known angular positions on a fine scale so that each spatial response function is quantified in a similar manner to the instrumental profile measurement described in Section 5.3. An individual readout of the FPA will record a spectrum

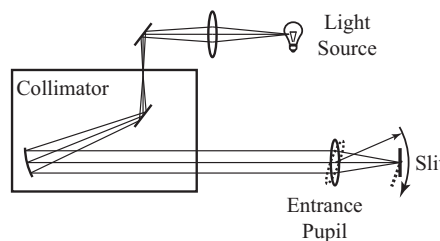


Figure 5.21 Spatial characterization apparatus composed of a light source, a collimator, and a precision rotation stage. The imaging spectrometer is rotated about the center of the entrance pupil and the point resulting from the telescope focus is slowly scanned along the slit.

at a small number, two to three for example, of spatial locations depending upon the details of the collimator and telescope.

The data for a particular spatial response function measurement are peak normalized and typically fit using a Gaussian model for the amplitude, center location, width, and an offset. The actual function is most likely not a Gaussian as was developed in Chapter 4, so the fit is not precise in the center region. This approach is adequate since the desired outcome is the location of the center and the widths, typically in micro-radians. If a superior fit is desired then the shape can be modeled in detail using, for example, the convolution of Gaussian and rectangle functions. The fits are subsequently evaluated for the spatial sampling interval and FWHM as a function of location on the focal plane array. The imaging spectrometer is then quantitatively evaluated for focus, keystone aberration, and tilt. For example, the FWHM should vary only slightly across the array if the sensor is in good focus and keystone is evaluated by determining if the slit image changes as a function of spectral channel. The full spatial-spectral performance is determined by combining this dataset with the spectral characterization.

Spatial characterization in the field is for the purpose of establishing the pointing characteristics and is best termed as geometrical characterization. This involves a camera or boresight model that may include the system aberrations. The camera model mathematically describes the viewing geometry in an appropriate coordinate system. These models calculate the intersection of the earth's surface and the projection of the GSD based upon the output of an inertial navigation system (INS) that provides the position, orientation, and velocity of the sensor on the airborne or space-based platform. The pointing characteristics of the imaging spectrometer are captured in the camera model. The camera model includes the translation of the sensor from the INS unit and the angular dependence of the optical axis at any given instance, such as during the rotation of a scan mirror. Small errors in the knowledge of the boresight will lead to large geolocation errors and typically a characterization flight is performed over a location with well-known ground control points, usually determined using a differential global position system (GPS) measurement, in order to refine the parameters in the camera model. The full system incorporates a digital elevation model to depict the surface terrain. An introduction to this process for MODIS is described in Qu et al. (2006).

5.6

Advanced Calibration Techniques

The description of the spectral, radiometric, and spatial characterizations describes a series of measurements that can be performed in a well-equipped calibration facility. They have the advantage of being reasonably simple to execute with equipment that can, for the most part, be purchased from vendors, with the possible exception of the filter transfer radiometers. A significant effort goes into putting the laboratory into operation but the amount of development required is not overwhelming. There are limitations to the uncertainties that are achievable with the approach, which are on the order of 2 to 5 percent for most spectral channels, depending upon the particulars of the equipment and facility. If this uncertainty is too large, as it is for some science applications such as

climate change studies, then an entirely different methodology that is much more tightly coupled to the fundamental standards at a national metrology laboratory is required.

Researchers at NIST have developed a highly accurate characterization system for spectral irradiance and radiance responsivity calibrations using uniform sources (SIRCUS) employing tunable lasers and building on the long history of using laser sources for radiometry (Brown et al., 2006). Only the radiance mode operation will be addressed here in the context of characterizing an imaging spectrometer or transfer radiometer. Currently the spectral range of SIRCUS is from about 200 nm to 5300 nm. High-powered, stabilized, tunable lasers produce monochromatic light, with the wavelength known with an uncertainty of 0.01 nm or less, that is input into an integrating sphere resulting in a nearly Lambertian radiance source. The source is characterized by standard detectors, Si trap or InGaAs detectors depending upon the wavelength, that have previously been characterized against POWR. This represents the largest portion of the overall uncertainty budget. The substitution method is employed where the standard detector measures the output of the integrating sphere followed by the equivalent measurement for the sensor being characterized. The radiance over the exit port of the integrating sphere is mapped to ensure that it is uniform over the entrance pupil.

SIRCUS produces at-aperture radiance with a combined standard uncertainty, estimated by combining the standard deviation of each measured parameter, of 0.1 percent or better. The uncertainties associated with the imaging spectrometer are quantified to establish the overall uncertainty in the data calibration. This includes the sensor linearity, temporal and thermal stability, light contamination from beyond the field of view, scattered light contamination, and so on. In order for a sensor to be calibrated at this level it must be highly stable without long-term changes in the signal, must be thermally stable, and have a high degree of off-axis rejection to reduce out of field contamination. It will also include a thorough stray light reduction system with the residual stray light quantified during testing. SIRCUS can be used for the scattered light quantification with the correct transfer optics.

5.7

Error Analysis

The methods that are utilized to produce data calibrated to physical units have been presented in some detail but without addressing the process by which the calibration products are accessed. A measurement is incomplete without a quantitative estimate of the uncertainty. There are a number of books that fully develop the statistical analysis of experimental data and we will settle for a brief introduction without deriving the equations used. The Joint Committee for Guides in Metrology has produced the “Evaluation of measurement data—Guide to the expression of uncertainty in measurement” from which researchers at NIST have distilled their own guidelines (BIPM et al., 2008; Taylor and Kuyatt, 1994). This presentation is based on the NIST guidelines and it is assumed that the reader has a working knowledge of basic statistics.

The uncertainty or error is the parameter that quantifies the difference between the measured values and the true values for a particular quantity called the *measurand*.

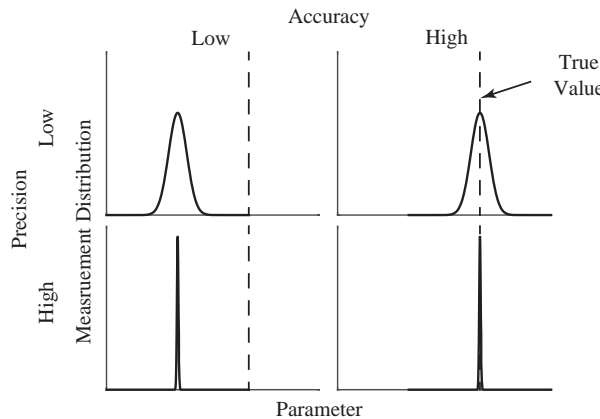


Figure 5.22 Illustration of distribution of measurements for a particular parameter with the true value shown by the vertical dashed line. The two left graphs show an inaccurate measurement due to a systematic error with high and low precision. The two right graphs illustrate an accurate measurement with low and high precision.

Quantifying the uncertainty is a critical step in establishing the traceability to a national standard and in identifying the dominant sources of error. The errors are categorized in terms of *accuracy* and *precision*. Accuracy refers to absolute measurements where the value obtained is compared to the true value, implying traceability to a standard. Precision is a measure of the reproducibility of measurements performed using the same device. The difference between accuracy and precision is illustrated in Figure 5.22. Errors are either *random* or *systematic*, with random errors referring to the spread in values that is obtained when a measurement is repeated many times, while systematic errors are due to factors that are common to all wavelengths and are correlated. In the case of random errors an accurate measurement can be obtained through averaging, even if this error is large, as long as no systematic errors are present. No amount of averaging will improve the measurement result for a systematic error; it can only be made more precise, while remaining inaccurate. The scattered light correction described in Section 5.4.6 is an example of a systematic error. Errors are grouped into two broad categories referred to as Type A and Type B, assigned according to the method used to estimate them. Type A errors are those which are evaluated by statistical methods and Type B are evaluated through other means (Taylor and Kuyatt, 1994).

The standard uncertainty in a measurand with a number of input parameters is determined through their functional relationship. Each of the Type A quantities will have an estimated *standard uncertainty* associated with them given by $u(x_i)$ where x_i corresponds to each of the input parameters. The standard uncertainty is determined from the appropriate probability distribution associated with each x_i . For example, averages of many measurements of a random variable are normally distributed and the standard uncertainty $u(x_i)$ is the standard deviation $\sigma(x_{i,n})$ divided by the \sqrt{n} , where n is the number of measurements performed, and the *relative uncertainty* is the standard uncertainty divided by the mean. The basic equations that govern the statistical analysis are listed

Table 5.4 Type A uncertainty parameters for n measurements of the x_i input parameter.

Quantity	Symbol	Equation
Mean	x_i	$\frac{1}{n} \sum_{j=1}^n x_{i,j}$
Variance	$\sigma^2(x_{i,n})$	$\frac{1}{n-1} \sum_{j=1}^n (x_{i,j} - x_i)^2$
Standard deviation	$\sigma(x_{i,n})$	$\sqrt{\sigma^2(x_{i,n})}$
Covariance	$u(x_i, x_j)$	$\frac{1}{n} \sum_{k=1}^n (x_{i,k} - x_i)(x_{j,k} - x_j)$
Standard uncertainty	$u(x_i)$	$\frac{\sigma(x_{i,n})}{\sqrt{n}}$
Relative uncertainty	—	$\frac{u(x_i)}{x_i}$

in Table 5.4. The evaluation of the uncertainty for a Type B error is more difficult and is based on the vendor's specification, the evaluation of an established authority such as reporting from a national metrology laboratory, scientific judgment, and experience. Taylor and Kuyatt (1994) provide guidelines for estimating Type B uncertainties using statistical modeling.

Suppose the different parameters in (5.5) and (5.6) have all been measured or otherwise determined in order to generate calibration coefficients, how is the overall uncertainty determined? In many cases a quantity will not be directly measured; how is the uncertainty assigned in that case? An obvious example of the latter case is that the signal in the denominator of (5.5) is the result of dark-subtraction. The measurand y is a function of the input parameters written as

$$y = f(x_1, x_2, \dots, x_i, \dots, x_m) \quad (5.53)$$

and the *combined standard uncertainty*, $u_c(y)$, is developed using a first-order Taylor series approximation. The result is known as the law of propagation of uncertainty whereby the standard uncertainties of the input parameters are propagated through

$$u_c^2(y) = \sum_{i=1}^m \left(\frac{\partial f}{\partial x_i} \right)^2 u^2(x_i) + 2 \sum_{i=1}^{m-1} \sum_{j=i+1}^m \frac{\partial f}{\partial x_i} \frac{\partial f}{\partial x_j} u(x_i, x_j), \quad (5.54)$$

where $u(x_i, x_j)$ is the covariance of x_i and x_j . The relative standard uncertainty is $u_c(y)/y$, where y is the average value of the measurand. If an input parameter is an independent variable then the second part of (5.54) vanishes since $u(x_i, x_j)$ is zero. On the other hand, if the input parameters are completely correlated then (5.54) reduces to

$$u_c^2(y) = \left[\sum_{i=1}^m \frac{\partial f}{\partial x_i} u(x_i) \right]^2, \quad (5.55)$$

since $u(x_i, x_j)$ equals $u(x_i)u(x_j)$. There are components of uncertainty that contribute to the overall error in y that are not readily apparent in a measurement equation. For example (5.5) implies sensor linearity but linearity is not an explicit term. Errors of this type,

Table 5.5 Coverage factors and confidence levels for a Gaussian distribution.

Coverage factor k	Confidence level (%)
1.000	68.27
1.645	90.00
1.960	95.00
2.000	95.45
2.576	99.00
3.000	99.73

if they are uncorrelated, are accounted for through addition in quadrature. In this case (5.54) is written as

$$u_c^2(y) = \sum_{i=1}^m \left(\frac{\partial f}{\partial x_i} \right)^2 u^2(x_i) = \sum_{i=1}^m u_i^2(y), \quad (5.56)$$

where $u(x_i)$ is the standard uncertainty of the input parameter upon which the measurand y depends and $u_i(y)$ is one of the standard uncertainties that compose the combined standard uncertainty. An additional factor is applied to the combined uncertainty in order to define an interval about the measurement result y that defines the confidence level for the measurand. This is known as the *expanded uncertainty* and is given by

$$U = k u_c(y) \quad (5.57)$$

with the interval given by $y \pm U$. A coverage factor of $k = 2$ is conventionally quoted which implies that the measurand will fall outside of the combined uncertainty only once in twenty times. The various coverage factors for a Gaussian distribution are tabulated in Table 5.5.

The procedure for evaluating the uncertainty is to first express the functional relationship between the measurand y and the input parameters x_i as in (5.53). The values for each x_i are determined through either a statistical analysis of a series of measurements or through other means, as was done for the irradiance standard. The standard uncertainty $u(x_i)$ is calculated next using the appropriate Type A or Type B techniques and the combined standard uncertainty is generated using (5.54). Finally the expanded uncertainty U is calculated for the desired coverage factor, usually 2. Each of these steps is described in the calibration report for review by the interested data user.

We'll go through a practical example in order to make the error analysis a little less abstract. An Offner-Chrisp imaging spectrometer operating in the solar reflective spectral range has been thoroughly characterized and calibration coefficients have been generated. Each coefficient depends upon the at-aperture radiance, the particular instrumental profile, and the radiance and dark signals. Table 5.6 lists the different input parameters, whether a parameter is due to a random or systematic error, and identifies the uncertainty as either Type A or B. The distinction between repeatability and reproducibility is that the former refers to measurements performed under the same conditions while the latter is for measurements performed under different conditions.

Table 5.6 Uncertainty sources and classifications. This is a representative list and is not exhaustive.

Input Parameter	Random (R) or Systematic (S)	Type
$L(\lambda)$	S	B
$P(i,j)$	S	B
$S_{i,j}(L)$	R	A
$S_{i,j}(0)$	R	A
Linearity (LNR)	S	A
Repeatability (RPT)	R	A
Reproducibility (RPD)	S	B
Temperature Stability (TS)	S	A

Typically most characterization measurements will be performed under normal laboratory conditions which depend upon the type of imaging spectrometer (VNIR/SWIR or LWIR) and the calibration requirements that establish the rigor. For example, if an instrument is to be used for material identification it may be satisfactory to perform the measurements in a room temperature laboratory while for detailed science missions a rigorously controlled environment is required. Following the standard characterization process the sensor could be subjected to a series of measurements in different temperature, vibration, or vacuum conditions in order to establish the reproducibility in an environment that is more typical of the expected operational conditions. This is often referred to as “test as you fly”.

Applying (5.56) to (5.5), including the uncertainties listed in Table 5.6 with the assumption that the individual $u_i(y)$ components are uncorrelated yields

$$u_c^2(y) = [u_s(K)]^2 + [u_\lambda(K)]^2 + [u(LNR)]^2 + [u(RPT)]^2 + [u(RPD)]^2 + [u(TS)]^2, \quad (5.58)$$

where $u_s(K)$ is the uncertainty directly due to the generation of the calibration coefficient K and $u_\lambda(K)$ is the uncertainty in K due to the wavelength calibration. The uncertainty due to the linearity is evaluated based upon the range of radiance levels that were measured, the known linearity of the transfer radiometers, and the statistics of the linear fit. The repeatability uncertainty is estimated using the statistics from signal measurements both during a single measurement series, such as during a day, and within several measurements where the sensor has been power cycled. The uncertainties associated with reproducibility and temperature stability are typically estimated through thermal-vacuum testing where the operational environment is varied.

The uncertainty term $u_s(K)$ is evaluated through

$$u_s^2(K) = \left[\frac{\partial K}{\partial S_{i,j}(L)} u(S_{i,j}(L)) \right]^2 + \left[\frac{\partial K}{\partial S_{i,j}(0)} u(S_{i,j}(0)) \right]^2 + \left[\frac{\partial K}{\partial L_{ba}(i,j; \lambda_c)} u(L_{ba}(i,j; \lambda_c)) \right]^2. \quad (5.59)$$

The partial derivatives in the first two terms of (5.59) are $K/[S_{ij}(L) - S_{ij}(0)]$, ignoring an unimportant sign change, and $u(S_{ij}(L))$ and $u(S_{ij}(0))$ are estimated by calculating the statistics from many measurements. The final term is more challenging since the band-averaged radiance depends upon both the at-aperture radiance and the instrumental profile, which are correlated. The partial derivative is easily evaluated yielding K/L_{ba} . In order to simplify the calculation of $u(L_{ba})$ the approximation will be made that there is no random component to the uncertainty in L_{ba} enabling the application of (5.55) which is applied to (5.6) yielding

$$u^2(L_{ba}) = \left[\frac{\partial L_{ba}}{\partial L} u(L) + \frac{\partial L_{ba}}{\partial P} u(P) \right]^2, \quad (5.60)$$

where $L_{ba}(i, j; \lambda_c)$ and $P_{ij}(\lambda_c - \lambda)$ have been shortened to L_{ba} and P . The partial derivatives are determined by approximating the integrals in (5.6) as sums through

$$L_{ba}(i, j; \lambda_c) = \frac{\sum_k L(\lambda_k) P_{ij}(\lambda_c - \lambda_k) \Delta \lambda}{\sum_k P_{ij}(\lambda_c - \lambda_k) \Delta \lambda}, \quad (5.61)$$

where $\Delta \lambda$ is a constant equal to the difference between successive samples of wavelength $\lambda_{k+1} - \lambda_k$ and the sum is over the effective range of the instrumental profile. The partial derivatives at a particular λ_k are

$$\frac{\partial L_{ba}}{\partial L(\lambda_k)} = \frac{P(\lambda_c - \lambda_k)}{\sum_k P(\lambda_c - \lambda_k)} \quad (5.62)$$

and

$$\frac{\partial L_{ba}}{\partial P(\lambda_c - \lambda_k)} = \frac{L(\lambda_k) - L_{ba}}{\sum_k P(\lambda_c - \lambda_k)}, \quad (5.63)$$

which are summed over the wavelength range and inserted into (5.60) to yield

$$u^2(L_{ba}) = \left[u(L) + \frac{\sum_k L(\lambda_k) - L_{ba}}{\sum_k P(\lambda_c - \lambda_k)} u(P) \right]^2. \quad (5.64)$$

The estimate of $u(L)$ is accomplished using the uncertainty values for the irradiance and reflectance standards, the errors introduced by the irradiance interpolation, the characterization of the transfer radiometers which have undergone a full error analysis, and from measurements of the radiance standard and integrating sphere. The assumption that the random uncertainty in $L_{ba}(i, j; \lambda_c)$ can be neglected is justified as long as the random errors from transfer radiometer measurements of the radiance standard and integrating sphere are small in comparison to the other uncertainties. The uncertainty for the instrumental profile is evaluated based upon repeated measurements.

The wavelength uncertainty of the instrumental profile affects the radiance measurement accuracy depending upon the slope of the spectral radiance curve. The relative uncertainty in K is

$$\frac{u_\lambda(K)}{K} = \frac{u(\lambda)}{L(\lambda)} \frac{\partial L(\lambda)}{\partial \lambda}, \quad (5.65)$$

where $u(\lambda)$ is the standard uncertainty in the wavelength from the monochromator, $L(\lambda)$ is the integrating sphere spectral radiance, and the derivative of the radiance is

obtained through the known spectral radiance curve. Note that this uncertainty can vary significantly channel to channel depending upon the slope of the spectral radiance.

The uncertainty analysis can be much more complex than this presentation and often is for sensors that have additional correction factors. For example, the sensor could have a range of other effects that are captured in the calibration equation such as a nonlinear response, temperature variation, a field-dependent correction due to off-axis extended source effects, a scan mirror correction factor, or a gain correction. These effects are captured in a much more elaborate calibration equation with the associated error analysis performed for each. The additional corrections will be minimized in a high-performing imaging spectrometer; however, there are many examples from the science community that demonstrate how these effects are treated in sensor calibration and in the error analysis. An example of a similar analysis for a trap transfer radiometer is found in Biggar (1998).

5.8 Radiometric Performance Modeling

The measurement equation has been utilized throughout this chapter in support of the characterization of instruments and calibration of data. It is also used in imaging spectrometer design in order to predict if performance requirements can be met. Performance modeling can be quite complex including many quantities that impact the utility of a data product such as detailed FPA/detector modeling, optical point spread or modulation transfer function modeling, pointing and jitter, atmospheric turbulence effects, out-of-band or out-of-field contamination, spatial resolution, and higher-order parameters such as the size, weight, and power of the system. We will limit our discussion to radiometric performance modeling with signal-to-noise metrics which, at a fundamental level, is the critical first step in the system engineering of a spectral sensor. The components of the model are the modeled signal as a function of spectral channel, using the measurement equation, and the various noise terms. The signal and noise will be modeled as the number of electrons measured from a detector element following the methodology in Lomheim and Hernández-Baquero (2002). Models for both VNIR/SWIR and LWIR imaging spectrometers will be developed to illustrate the principles.

5.8.1 Introduction to Photodetectors

The signal and noise of the system depend in part upon the properties of the focal plane array detector material and circuitry. The solid state physics that governs the processes of photon absorption and charge conduction in a photodetector is beyond our scope, and we will settle for a brief and qualitative description keeping in mind the quantum mechanical basics from Chapter 2. Photodetectors are composed of semiconductors with a crystal lattice structure where a photon is absorbed in the material, promoting an electron, and leaving behind a hole, from an energy band analogous to the ground state, known as the valence band, into an excited state, the conduction band, with the energy between the bands known as the band gap E_g . A semiconductor is a material where

the band gap is small enough that electrons can be relatively easily promoted from the valence band to the conduction band ($0 < E_g < 3.5$ eV). In contrast, an insulator has a much larger band gap that effectively prohibits the promotion. As the name suggests, once an electron is promoted into the conduction band it is relatively free to move about and a current that is proportional to the photon flux is collected when a voltage is applied between the two contacts of a photodetector. All photodetectors have a long wavelength cutoff that corresponds to $\lambda_g = hc/E_g$ to good approximation where h is Planck's constant and c is the speed of light.

There are two types of photodetectors that are currently used in focal plane arrays for imaging spectrometers: photoconductive and photovoltaic. In photoconductive detectors, the incident photon flux produces free electrons that are measured as a current with the conductance or resistance of the material changing as a function of the irradiance. Photovoltaic devices, also known as photodiodes, contain a junction between a region where the conductivity is due to electrons and one where it is due to holes. This is known as a p–n junction, corresponding to positive (holes) and negative (electrons) charge carriers. An n-type material has a surplus of electrons and vice versa for a p-type with the contact region depleted of charge carriers due to thermal excitation, diffusion, and electron–hole recombination. This establishes a local potential difference known as the contact potential that reaches a steady state. When light is incident upon a photodiode with an applied voltage, an electron–hole pair is produced generating a photocurrent. A well-designed photodiode allows for rapid diffusion of the charge carriers. In many semiconductor materials the band gap is narrowed through the addition of an impurity that readily donates either electrons or holes. Some detector materials, such as silicon and HgCdTe, can be either photoconductive or photovoltaic.

The quantum efficiency η of a detector material has been discussed in the context of the measurement equation without a precise definition. It is the number of electrons that are measured for each photon which depends upon the absorption, reflection, scattering, and recombination properties, typically expressed as a fraction or a percent. The flux that is absorbed is given by

$$\Phi_a(\lambda) = \Phi_i(\lambda)[1 - \rho(\lambda)][1 - e^{-\alpha(\lambda)x}], \quad (5.66)$$

where Φ_a and Φ_i are the absorbed and incident spectral flux respectively, ρ is the reflectance, α is the absorption coefficient in units of inverse length, and x is the distance of light travel in the material. The absorbed flux divided by the photon energy, $\Phi_a/h\nu$, is the number of photons absorbed in the material and, if each generates a charge carrier that is measured, the quantum efficiency is

$$\eta(\lambda) = [1 - \rho(\lambda)][1 - e^{-\alpha(\lambda)x}], \quad (5.67)$$

which is between 0 and 1. The reciprocal of α is known as the penetration depth where $1/e$ of the flux that wasn't reflected remains unabsorbed. Typically the absorption coefficient declines gradually as the photon energy decreases until the band gap energy is approached, at which point it declines precipitously. For higher-energy photons the quantum efficiency decreases because most are absorbed near the surface and the electrons recombine quickly to produce the short wavelength limit. The quantum

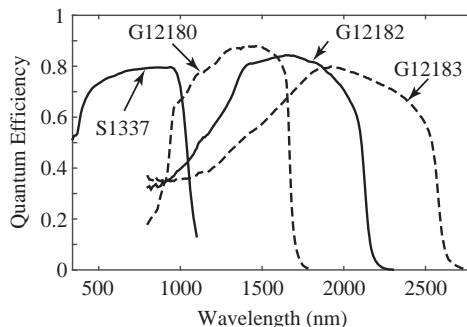


Figure 5.23 The quantum efficiency of a silicon (S1337) and three InGaAs photodiodes (G12180, G12182, and G12183) over the 340 nm to 2800 nm spectral range. Data provided by Syleen Neely and Kento Sobukawa on behalf of the Hamamatsu Corporation.

efficiency is often obtained from the manufacturer where it has been measured for the particular device or as an average over measurements from many devices. If the focal plane array is available for testing, the quantum efficiency can be measured by utilizing a monochromatic source of known spectral irradiance for illumination and lock-in detection if required. Figure 5.23 shows representative quantum efficiency examples for silicon and InGaAs photodiodes.

5.8.2 Signal Modeling

Offner–Chrisp and Dyson imaging spectrometers, each with a three-mirror anastigmat telescope and a scan mirror, will be used to illustrate the modeling for the VNIR/SWIR and LWIR respectively. The Offner–Chrisp is at room temperature and the spectrometer portion of the Dyson is in a liquid nitrogen-cooled dewar at 80 K. There are three sources of signal that will be modeled separately and summed to produce the total signal. The first is the signal that results from radiance that is at the aperture and external to the sensor. This can be further separated into the portions from the surface and from the atmosphere itself. Another component is due to the self-emission of radiance from the optical elements that make up the imaging spectrometer. This contribution is quite small for a VNIR/SWIR imaging spectrometer but is significant for a LWIR system. The final signal component is due to the dark current from the detector itself. The total signal is also compared to the detector well depth to check for saturation.

The signal corresponding to the at-aperture radiance $L_a(\lambda)$ measured by an imaging spectrometer is modeled using a simplified form of (5.1) converted to the number of electrons measured or

$$S_a(\lambda_c) \approx U\tau(\lambda_c)\eta(\lambda_c)t_{\text{int}} \int_0^{\infty} \frac{L_a(\lambda)}{h\nu} P(\lambda_c - \lambda) d\lambda, \quad (5.68)$$

where the spectral radiance is in standard units (W/cm²sr/nm for example) and it has been assumed that the étendue, optical transmission, and quantum efficiency are nearly constant for a particular spectral channel and can be taken outside of the integral as was

Table 5.7 Modeling parameters for the Offner–Chrisp and Dyson imaging spectrometers. Both assume a Gaussian instrumental profile.

Parameter	Offner–Chrisp	Dyson
Spectral Range (μm)	0.4–2.5	7.5–14
Limit of Resolution (nm)	12	30.5
Number of Channels	210	256
F-number	2.5	2.5
Number of Mirrors	6	5
Mirror Material	Aluminum	Gold
Pixel Pitch (μm)	30	30
Frame Rate (Hz)	100	100
Well Depth (electrons)	1,000,000	4,500,000
Quantum Efficiency	0.6	0.6
Refractive Material	Fused Silica	Zinc Selenide

done for (5.35). The étendue is written as $p^2\pi/4N^2$ from (4.19), where p is the pitch of a detector element and N is the system F-number. The final form of the measurement equation is therefore

$$S_a(\lambda_c) = \frac{\pi p^2 \tau(\lambda_c) \eta(\lambda_c) t_{\text{int}}}{4N^2 hc} \int_0^\infty L_a(\lambda) \lambda P(\lambda_c - \lambda) d\lambda, \quad (5.69)$$

where v has been replaced by c/λ . The models for the two designs are broadly similar, with the exception of the self-emission from the optical elements of the Dyson, and will be developed in parallel. The modeling parameters for the two types are tabulated in Table 5.7.

The optical efficiency will have multiple components and is calculated based upon the number of mirrors, the mirror reflectance, the transmission of the refractive elements, and the grating efficiency. The mirrors are assumed to have either an aluminum (Offner–Chrisp) or a gold (Dyson) reflective coating with the reflectance illustrated in Figure 5.24 for the two cases. The transmission due to the mirrors is calculated by raising the coating reflectivity to the power of the number of mirrors. The grating of the Offner–Chrisp is also aluminum coated and the concave grating in the Dyson, illustrated in Figure 4.43, is gold coated. The grating efficiency for the two cases is also illustrated in Figure 5.24 based on (4.83) and (4.113). Both designs have scan mirrors and windows, and the Dyson has two zinc selenide (ZnSe) refractive elements. The Offner–Chrisp has the added transmission of the order-sorting filter at the focal plane array, which is not needed for the Dyson wavelength range, and the Dyson employs a cold filter.

Developing the transmission of the refractive elements requires knowledge of the spectral absorption coefficient of the material and the reflectance properties for the broadband anti-reflection (AR) coating that is applied. As a specific example the shaped ZnSe lenses and window in the Dyson design will be modeled with the two lenses

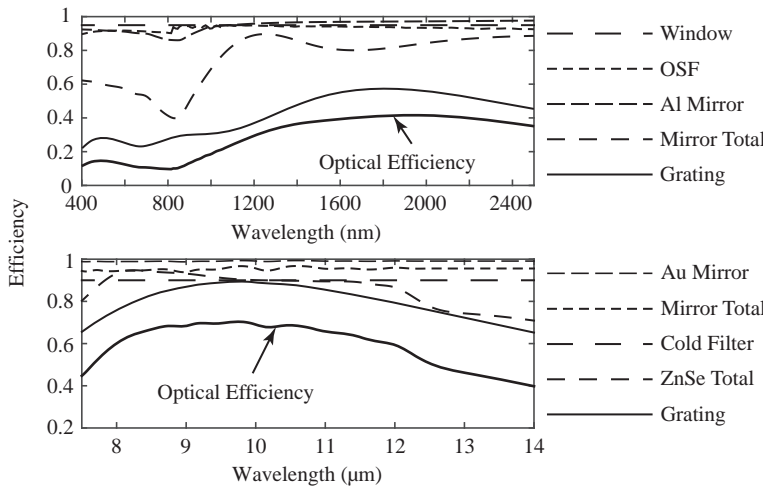


Figure 5.24 The total optical efficiency (lowest solid curve) and the composite terms for both the Offner–Chrisp and Dyson imaging spectrometer examples. The upper graph is for the Offner–Chrisp and includes the reflectance of a single aluminum mirror and the total mirror reflectance for the six. The Dyson model includes the composite transmission of the ZnSe lenses and window, the reflectance of a single gold mirror, and the total mirror reflectance of the five mirrors.

approximated as 6 cm and 0.5 cm windows with AR coatings. The transmission τ for near normal incidence is modeled following Klein et al. (1994) and is given by

$$\tau = \frac{(1 - \rho)^2 \exp(-\alpha_\lambda t)}{1 - \rho^2 \exp(-2\alpha_\lambda t)}, \quad (5.70)$$

where ρ is the spectral reflectance, α_λ is the spectral absorption coefficient, and t is the material thickness. This equation is sometimes approximated by setting the denominator equal to 1. The absorption coefficient has a dependence upon temperature and the two lenses inside the dewar are at 80 K while the window is at 293 K in the model. Figure 5.25 includes the spectral dependence of the bulk absorption coefficient as well as a graph of the reflectance of the AR coating and the transmission for the two refractive elements and the window. Note that the dependence upon the temperature of the material is slight. The same approach is applied to the fused silica window used in the Offner–Chrisp.

The measurement also includes signal that does not come from the at-aperture radiance but is from the FPA dark current and self-emission of the optics. Both are important components to the model, not only due to the noise associated with each, but also because they compete with the at-aperture radiance signal in filling the storage capacity of each detector element. The dark current is measured for a darkened focal plane array. In the design process it can be estimated based on models or from representative data provided by the manufacturer. For example, if a HgCdTe focal plane is expected to operate at temperatures above 77 K an empirical model has been developed by Tennant

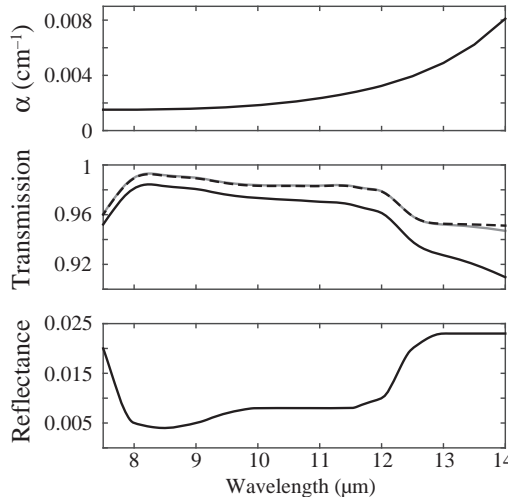


Figure 5.25 The upper graph shows the absorption coefficient for zinc selenide. The middle graph is the transmission for the thick lens (solid curve), the thin lens (dashed curve), and the window (gray curve). The difference between the thin lens and the window is due to the absorption coefficient temperature dependence. The lower graph is the reflectance of the anti-reflection coated surface. Calculation follows Klein et al. (1994).

et al. (2008) that predicts the current density based on the temperature and the cutoff wavelength.

The self-emission signal is modeled through a modification of (5.69) and is critical to predicting the performance of a LWIR spectral sensor. The Dyson imaging spectrometer is equipped with a cold filter at the focal plane array and a cold stop that limit both the spectral range and the field of view respectively of the flux illuminating the detector. The windowed dewar maintains the temperature of the spectrometer at 80 K while the telescope and scan mirror are at an ambient temperature T_e of 293 K. The reflectance, and therefore the emissivity, of the mirrors is also known. The scan mirror emits radiance within the field of view through $\epsilon(\lambda)B_\lambda(T_e)$, where $B_\lambda(T_e)$ is the blackbody radiance, that is reflected by the primary mirror of the TMA, which also emits radiance. The combined radiance from the primary is

$$L_2(\lambda) = \rho\epsilon B_\lambda(T_e) + \epsilon B_\lambda(T_e) = (1 - \rho^2)B_\lambda(T_e) \quad (5.71)$$

since $\epsilon = 1 - \rho$ and the wavelength dependence is understood. The similar process occurs for the secondary and tertiary mirrors with the total radiance from optical self-emission external to the dewar given by

$$L_m(\lambda) = (1 - \rho^4)B_\lambda(T_e) \quad (5.72)$$

for the self-emission radiance from the four mirrors. The self-emission of the window is also included using $\epsilon_w B_\lambda(T_e)$ with its emissivity ϵ_w calculated from $\epsilon_w = 1 - \tau$ using (5.70) and conservatively assuming it is at ambient temperature. Each element inside the dewar also emits a small amount of radiance, due to their 80 K temperature, that is

transmitted by the successive elements. The total self-emission radiance from within the field of view is the sum of all these terms which replaces $L_a(\lambda)$ in (5.69) to produce the self-emission signal S_e . The self-emission from inside the dewar that is not within the field of view is from emission outside the solid angle defined by $\pi/4N^2$ which does not undergo dispersion. The radiance L_d from this term is similarly $\epsilon_d B_\lambda(T_d)$ with the T_d equal to 80 K. The emissivity inside the dewar is poorly known and set equal to 1. The dewar signal is

$$S_d(\lambda_c) = \left(1 - \frac{1}{4N^2}\right) \frac{\pi p^2 t_{\text{int}}}{hc} \int_0^\infty B_\lambda(T_d) \lambda \eta(\lambda) \tau(\lambda) d\lambda, \quad (5.73)$$

where the solid angle in (5.69) has been replaced and the quantum efficiency and transmission have been taken into the integral. Here τ is the transmission of the cold filter at the FPA.

The spectral radiance used in (5.69) is selected based upon the particular application of the imaging spectrometer. For terrestrial remote sensing in the VNIR/SWIR a spectrally flat surface reflectance under solar illumination from a standardized illumination geometry through one of the standard atmospheres is selected. Figure 5.26 shows two examples of reference radiances, one for AVIRIS and a second lower radiance case. The AVIRIS reference radiance is calculated using a 0.5 reflectance target with solar zenith angle of 23.5° for a mid-latitude summer standard atmosphere (Green et al., 1998). We have scaled the water in the model by 50 percent and assumed a visibility of 23 km with a rural aerosol model. The second reference radiance differs by using a lower reflectance of 0.25 and a larger solar zenith angle of 45°. If the sensor is to be used primarily for a particular purpose, such as for ocean color measurements, a much different radiance model is used. For the LWIR the radiance used here is for a surface with a uniform 0.1 reflectance at 288 K and 320 K with the same mid-latitude summer standard atmosphere.

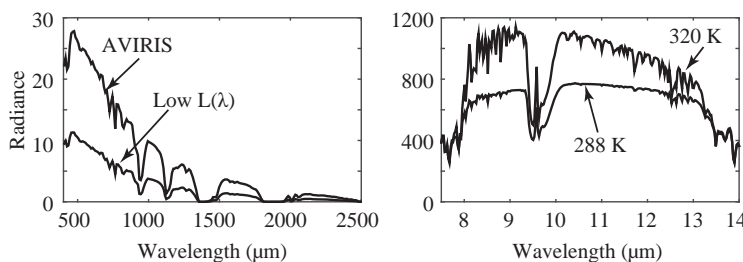


Figure 5.26 Examples of reference radiances for the VNIR/SWIR and LWIR. The left graph shows AVIRIS and lower radiance cases, in units of $\mu\text{W}/\text{cm}^2\text{sr}/\text{nm}$, for a sensor at 20,000 feet above ground level. The right graph shows the similar case for 288 K and 320 K reference radiances, in units of $\mu\text{W}/\text{cm}^2\text{sr}/\mu\text{m}$, at an altitude of 100 km, essentially from the top of the atmosphere. Calculated using MODTRAN®.

5.8.3 Noise Sources

So far we have applied the measurement equation to describe the signal and have discussed the noise inherent in a measurement only from the point of view of the error analysis in terms of random errors. Noise is the random fluctuation of the signal from the detector with contributions from several sources that contaminate a measurement, including the noise inherent in the random nature of the arrival of photons at the detector element, thermal noise within the photodetector, one-over-frequency (1/f) noise, electronic noise in the readout circuitry, and the quantization noise. This list is not exhaustive but includes the primary sources. We will assume each term follows Poisson statistics and is independent, so that they can be added quadratically.

The best possible spectral sensor is a photon-noise-limited system with the signal-to-noise ratio solely due to the creation of charge pairs in the material from the photon flux. This flux is due to the at-aperture radiance and also the radiation from the sensor itself. For Poisson statistics the expected noise N_s is the square root of the mean n of the measured independent events, in our case the generation of the electron–hole pairs, over a certain time interval and is given by

$$N_s = \sqrt{n} \quad (5.74)$$

and the signal-to-noise ratio (SNR) is

$$\text{SNR} = \frac{S}{N_s} = \frac{n}{\sqrt{n}} = \sqrt{n}. \quad (5.75)$$

If we separate the noise from charge carriers due to the at-aperture radiance from those due to the self-emission of the optics this is written as

$$N_s = (N_L^2 + N_{se}^2)^{1/2} = (n_L + n_{se})^{1/2}, \quad (5.76)$$

where the two terms are independent. All noise sources will be combined in this way. An additional term that adds an offset to the measured signal is the dark current that is proportional to the temperature of the photodetector and is due to the random generation of electron–hole pairs due to thermal excitation. In addition to the offset it also adds noise through random fluctuations of the photocurrent which follows a Poisson distribution. The amount of dark current is reduced by cooling the focal plane array.

The other contributors to the noise will be briefly summarized. There is another term that is also due to the temperature and is referred to variously as thermal, Johnson, or Nyquist noise. It is due to the random thermal motions of the electrons in the resistive components of the detector and associated circuitry and is present even in the absence of current. The 1/f-noise is a poorly understood term that has been empirically determined to be proportional to the inverse of the frequency. There is always some noise introduced during the readout of the focal plane array with the degree depending upon the design. The final noise term that we will address is the quantization noise associated with the conversion of the analog signals to a digital number (DN). This error is given by

$$N_Q = \frac{w}{2^m \sqrt{12}}, \quad (5.77)$$

Table 5.8 Constant noise terms used in the performance modeling of the Offner–Chrissp and Dyson imaging spectrometers. The well depth for the Offner–Chrissp and Dyson is 1,000,000 and 4,500,000 electrons respectively and each has 14 bits of analog to digital conversion.

Noise Term	Offner–Chrissp	Dyson
N_d	10	1600
N_r	250	125
N_Q	18	79
N_d	220	960

where w is the well depth in electrons and m is the number of bits supported by the analog to digital converter with the signal separated into 2^m quantization levels. It is possible to predict each of these terms through a photodetector or focal plane array model or, if an array is available, to measure some of these terms in the laboratory. Also, they are typically provided by the focal plane array manufacturer. See Johnson, 1999 for an example of a signal-to-noise model for a complementary metal–oxide–semiconductor (CMOS) infrared focal plane array.

5.8.4 Figures of Merit

There are several figures of merit that can be used to succinctly describe the radiometric performance of an imaging spectrometer, all of which are based upon determining the minimum level of a measured quantity that is equivalent to the noise floor. In addition to the signal-to-noise ratio, we will discuss two other figures of merit: the noise-equivalent spectral radiance (NESR) and the noise equivalent temperature difference (NE Δ T), which is used in the LWIR. Table 5.8 is a list of the noise terms, neglecting the 1/f noise, and some representative values that are constant and from which is calculated the stationary system noise referred to as “everything but photon noise”, given by

$$N_{\text{ebpn}} = \sqrt{N_d^2 + N_r^2 + N_Q^2 + N_d^2}, \quad (5.78)$$

where N_d is the noise due to the dark current, N_r is the read and electronic noise, N_Q is the quantization noise, and $N_d = \sqrt{S_d}$ from (5.73) is the noise due to the photon flux from within the dewar. This last term is assumed to be constant for every pixel in the focal plane array since the dewar temperature doesn't vary. The dark noise is based on a dark current of 10,000 e/s and 1.12×10^8 e/s of the Offner–Chrissp and Dyson respectively.

The signal-to-noise ratio for a particular instrumental profile is defined as the signal due to the at-aperture radiance divided by the total noise or

$$\text{SNR}(\lambda_c) = \frac{S_a(\lambda_c)}{N_t} = \frac{S_a(\lambda_c)}{\sqrt{S_a(\lambda_c) + S_e(\lambda_c) + N_{\text{ebpn}}^2}}, \quad (5.79)$$

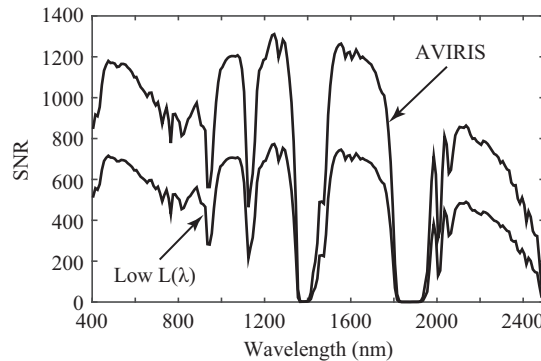


Figure 5.27 Offner–Chrisp SNR results for the AVIRIS and low reference radiances.

where N_t is the total noise for the detector element corresponding to λ_c , and S_e is the signal due to self-emission external to the dewar, which can be set to zero for the Offner–Chrisp, resulting in the SNR shown in Figure 5.27. The SNR is easily converted to the NESR through

$$\text{NESR}(\lambda_c) = \frac{L_a(\lambda_c)}{\text{SNR}(\lambda_c)}, \quad (5.80)$$

where in this case $L_a(\lambda_c)$ has been band-averaged using (5.6), which can be rewritten as

$$\begin{aligned} \text{NESR}(\lambda_c) &= \frac{L_a(\lambda_c)N_t}{\frac{\pi p^2 \tau(\lambda_c)\eta(\lambda_c)t_{\text{int}}}{4N^2hc} \int_0^\infty L_a(\lambda)\lambda P(\lambda_c - \lambda) d\lambda} \\ &= \left(\frac{N_t}{p^2 \eta(\lambda_c)t_{\text{int}}} \right) \frac{4N^2hcL_a(\lambda_c)}{\pi \tau(\lambda_c) \int_0^\infty L_a(\lambda)\lambda P(\lambda_c - \lambda) d\lambda} \\ &\approx \text{NEI}(\lambda_c) \frac{4N^2hc}{\pi \tau(\lambda_c)\lambda_c \Delta\lambda}, \end{aligned} \quad (5.81)$$

where it has been assumed that the radiance does not vary over the limit of resolution and the noise equivalent irradiance, $\text{NEI}(\lambda_c)$, has been defined in terms of photons. Note that η and τ are considered to be average values at λ_c . This is the NESR at the sensor which can be converted to the NESR at the surface by dividing by the upward atmospheric transmission, which is shown in Figure 5.28 for the Dyson.

The $\text{NE}\Delta T$ is a measure of the temperature change of a radiator that produces a radiance change that is equivalent to the noise in the imaging spectrometer. A sensor with a low $\text{NE}\Delta T$ can distinguish between objects that have a small temperature difference in a scene. The first step in determining the $\text{NE}\Delta T$ is to take the derivative of (5.68) with respect to temperature to obtain

$$\begin{aligned} \frac{dS_a(\lambda_c)}{dT} &= \frac{\pi p^2 \tau(\lambda_c)\eta(\lambda_c)t_{\text{int}}}{4N^2hc} \int_0^\infty \frac{dL_a(\lambda)}{dT} \lambda P(\lambda_c - \lambda) d\lambda \\ &\approx \frac{\pi p^2 \tau(\lambda_c)\eta(\lambda_c)t_{\text{int}}}{4N^2hc} \frac{dL_a(\lambda_c)}{dT} \lambda_c \Delta\lambda, \end{aligned} \quad (5.82)$$

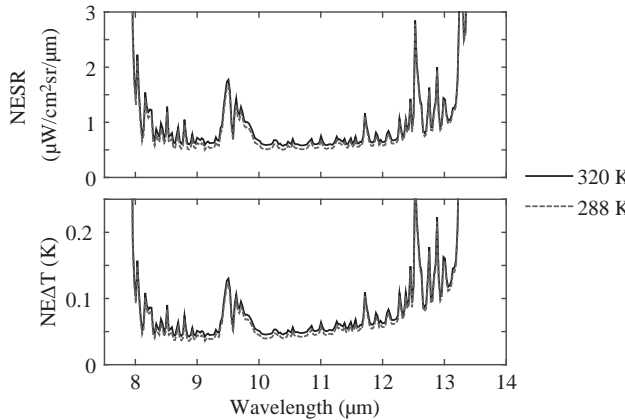


Figure 5.28 The Dyson NESR and NE Δ T modeling results for the hot and cold reference radiances.

again making the approximation that the quantities don't vary much across the instrumental profile. The at-aperture radiance is replaced by the surface-to-sensor atmospheric transmission multiplied by the surface-leaving radiance since that is the quantity of interest and the differentials are approximated as small, rather than infinitesimal, changes yielding

$$\frac{\Delta S_a(\lambda_c)}{\Delta T} = \frac{\pi p^2 \tau(\lambda_c) \eta(\lambda_c) t_{\text{int}}}{4N^2 hc} \tau_{\text{atm}}(\lambda_c) \frac{dL_a(\lambda_c)}{dT} \lambda_c \Delta \lambda, \quad (5.83)$$

where $\tau_{\text{atm}}(\lambda_c)$ is the average atmospheric transmission for the λ_c spectral channel. ΔS_a is replaced by the total system noise N_t and the equivalent temperature change is

$$\text{NE}\Delta T = \frac{4N^2 hc}{\pi \lambda_c \Delta \lambda \tau(\lambda_c) \tau_{\text{atm}}(\lambda_c) \frac{dL_a(\lambda_c)}{dT}} \text{NEI}(\lambda_c), \quad (5.84)$$

where again the noise equivalent irradiance has been used. The derivative of the radiance is calculated by replacing $L_a(\lambda_c)$ with (2.64) multiplied by the surface emissivity and taking the derivative to obtain

$$\frac{dL_a(\lambda_c)}{dT} = \frac{2\epsilon(\lambda_c)h^2c^3 \exp\left(\frac{hc}{\lambda_c kT}\right)}{\lambda_c^6 kT^2 \left[\exp\left(\frac{hc}{\lambda_c kT}\right) - 1 \right]^2}. \quad (5.85)$$

The NE Δ T for the Dyson is shown in Figure 5.28.

In practice, radiometric modeling is a powerful tool to estimate the expected performance of an proposed imaging spectrometer and to track and verify the actual performance as the sensor is manufactured and tested. The model is refined as more information becomes available and the measured and predicted performance will converge. It can also be used as a component of a more inclusive model to predict the outcome of measurements and analysis of data from the field. There are also other metrics that can be developed, such as the noise equivalent reflectance for a VNIR/SWIR spectral sensor. The theoretical best performance achievable can be predicted by setting N_{ebpn} equal to zero. This is known alternatively as BLIP, from “background-limited

infrared photodetection”, or as-shot noise-limited. For a similar analysis applied to imaging Fourier transform spectrometers see Keller and Lomheim (2005).

5.9

Vicarious Calibration

The characterization of a sensor in the operational environment can be accomplished using vicarious techniques where a well-understood site is viewed with concurrent atmospheric and surface measurements, with the sun as the source in the solar reflective spectral region, or the surface itself in the emissive. The measurement products are then used as inputs to a radiative transfer code to predict the at-aperture radiance. The calibration procedure entails measurement campaigns typically with experienced researchers in the field during the data acquisition. This process has been termed vicarious calibration with the first reference in the refereed literature in 1982 by Koepke (1982). Vicarious calibration techniques have been vigorously developed since the early 1980s when extensive work was performed utilizing both surface measurements and radiometer overflights to adjust the calibration of the Coastal-Zone Color Scanner (Gordon et al., 1983; Hovis et al., 1985) and for the radiometers on Meteosat (Koepke, 1982). At this same time researchers at what was then the Optical Sciences Center at the University of Arizona began their pioneering vicarious calibration work which still continues (Slater et al., 1987). The primary focus has been the validation and maintenance of space-based spectral sensors such as the Landsat series with researchers from a broad spectrum of organizations utilizing vicarious calibration approaches. As the accuracy and precision of the measurements have improved vicarious calibration has become a valuable method for the intercomparison of multiple spectral sensors. Vicarious techniques have also been used in support of airborne missions such as in the JPL AVIRIS program (Green et al., 1998). We will focus on vicarious calibration for the solar reflective range and briefly on the approach used for space-based emissive sensors.

There are several approaches to performing vicarious calibration measurements and we will follow the classification presented in Slater et al. (1996). The first approach is the *reflectance-based method*, which relies upon extensive measurements of both the surface reflectance for the calibration site and the atmosphere to provide the inputs to a radiative transfer code that is used to predict the at-aperture radiance. This method is the most well developed, reaching the point that automated systems have been successfully deployed to very well-understood field sites (Czapla-Myers et al., 2008, 2010; Anderson et al., 2013). A modified version of this method with more extensive atmospheric aerosol characterization is known as the irradiance-based method or the improved reflectance-based method. For our purposes we will treat it as a variant of the reflectance-based method. The final method is the *radiance-based method* which originally relied upon concurrent measurements using an airborne spectroradiometer flown at an altitude that is above most of the aerosols and the water. In this case, the radiative transfer modeling is for the atmospheric path from the aircraft altitude to the satellite. Variants of the radiance-based approach now use on-orbit sensors.

5.9.1 Site Requirements

The first requirement for a high-quality at-aperture radiance prediction is the characteristics of the site surface. The ideal site is a Lambertian reflector with a high, >0.3 , and spectrally flat reflectance so that the direct component of solar illumination is dominant. A Lambertian site is critical since the solar illumination and the viewing geometries will vary. Additionally the site must be spatially uniform over a large area enabling a test site to be embedded within it that is distant from any areas that are spectrally distinct. This limits the impact of multiple scattering effects where the reflectance signature from a distant point can contaminate the test site reflectance through the adjacency effect, which is described in detail in Chapter 6. The ideal site is also at an elevation of at least 1 km and higher if possible. Referring to Figure 2.45, the aerosol concentration declines rapidly as a function of altitude particularly for the remote continental model which is applicable to many sites. The site should also be seasonally invariant and free of vegetation. Additional considerations are the probability of clear viewing and the accessibility (Thome, 2001). Sites in the United States that at least partially meet these requirements and have the added advantage of having a long measurement history include the White Sands Missile Range in New Mexico, Railroad Valley Playa and Lunar Lake in Nevada, and Ivanpah Playa in California, with examples of the reflectance values given in Figure 5.29. The data are degraded at the water bands, which is particularly evident in the standard deviations for each site. Additionally, a worldwide catalog is maintained by the United States Geological Survey and is accessed through their website (Stensaas and Christopherson, 2013).

5.9.2 Reflectance-Based Method

Figure 5.30 is a flow diagram of the reflectance-based method. The reflectance of the test site, whose geometry is based on the requirements of the particular sensor being characterized and is typically marked in some way so that it is apparent in the spectral imagery, is measured concurrent with the imaging spectrometer overflight. For example, the calibration site geometry for a space-based dispersive imaging spectrometer that performs push-broom data acquisition with a nadir view could utilize a 0.5 km by 0.1 km rectangle that is oriented with the long-axis perpendicular to the ground-projected satellite path. The site size is limited to ensure adequate characterization proximate to the imaging spectrometer data acquisition. At the same time a suite of instruments performs measurements to characterize the atmosphere. The field data are reduced to appropriate inputs to the radiative transfer code and the at-aperture radiance is predicted. Calibration coefficients are then computed using the predicted radiance and the image-based digital numbers using (5.5), or something more elaborate if required.

Atmospheric Measurements

Vicarious calibration measurements are typically limited to clear days when the atmosphere is stable to facilitate accurate measurement and modeling. A suite of instruments is used to measure the local conditions such as surface pressure, temperature, humidity, and cloud cover. Also, data from a radiosonde taken proximate to the vicarious

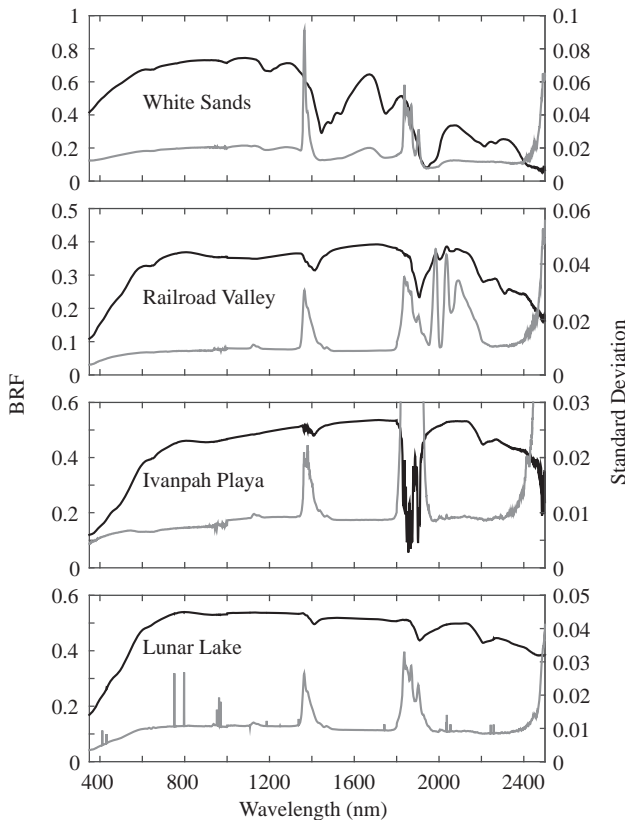


Figure 5.29 Vicarious calibration site reflectances (solid black upper lines) and the standard deviation (gray lower lines) from 480 spectral measurements for White Sands, Railroad Valley, Ivanpah Playa, and Lunar Lake. Note the scale change on each graph. Data courtesy of Kurtis Thome of the NASA Goddard Space Flight Center.

calibration collection is used if available. The primary instrument used to characterize the atmosphere is an automated solar radiometer or ASR that measures atmospheric extinction following Beer's law. There are various designs for these instruments with most utilizing narrow-bandpass filter radiometers with a well-defined field of view and silicon detectors. For example, the AERONET global network utilizes a CIMEL Electronique 318A spectral radiometer and a similar ASR was developed at the University of Arizona (Holben et al., 1998; Ehsani et al., 1998). We will describe the design, operation and characterization of the latter. The basic design is similar to the filter radiometer depicted in Figure 5.1 with a pair of apertures a distance D apart defining the étendue. In the ASR the interference filter follows the second aperture and is immediately in front of the detector assembly. There is a total of 10 radiometers packaged into one ASR with the center wavelengths at 380, 400, 441, 520, 611, 670, 780, 870, 940, and 1030 nm. The filter bandpasses are selected to avoid most atmospheric absorption features, with the exception of ozone, nitrogen dioxide, and the 940 nm water band. The measured solar irradiance is utilized to calculate the optical extinction from Beer's law. The two

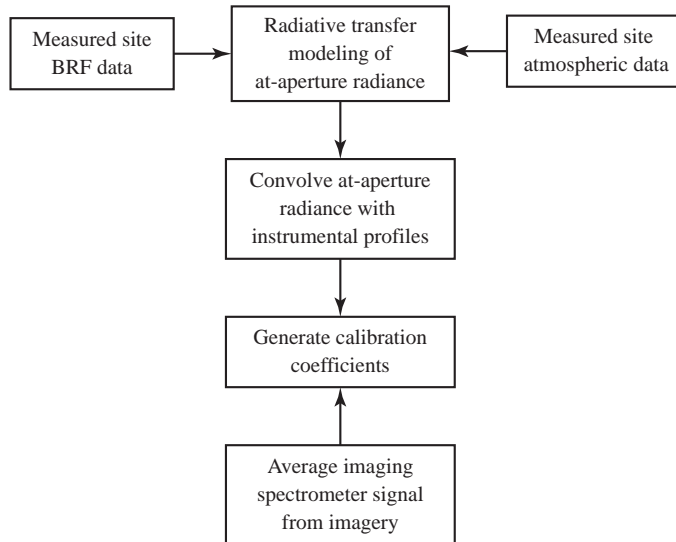


Figure 5.30 Flow diagram for the data acquisition and processing for the reflectance-based method. From Slater et al. (1996).

apertures and the known distance define the field of view. There are limitations to the technique such as the excessive multiple scattering on an overcast day when Beer's law does not apply.

The calculation of the optical extinction requires knowledge of the variation in molecular density as a function of altitude that is developed from (2.186) and (2.187) to yield

$$\rho(z) = \rho(z_o) \frac{T(z_o)}{T(z)} \exp \left[- \int_{z_o}^z \frac{dz'}{H(z')} \right] \quad (5.86)$$

for the vertical distribution. The approximation is made that the temperature and scale height are constant as a function of altitude so that (5.86) becomes

$$\rho(z) = \rho(z_o) e^{-(z-z_o)/H} = \rho_o e^{-z/H}, \quad (5.87)$$

where z_o has been set equal to 0 and ρ_o is the molecular density at the surface. The column mass along a vertical path is the integral of (5.87) between the surface and z or

$$m_v(z) = \int_0^z \rho(z') dz' = \rho_o \int_0^z e^{-z'/H} dz = \rho_o H (1 - e^{-z/H}) \quad (5.88)$$

or, for the full atmosphere,

$$m_v = \rho_o H, \quad (5.89)$$

where z has been set to infinity. Equation (5.88) is modified for a slant path between the surface and r to

$$m_s(r) = \rho_o \int_0^r e^{-z(r')/H} dr' = \rho_o \int_0^r e^{-z'/H} \frac{dz'}{\cos \theta}, \quad (5.90)$$

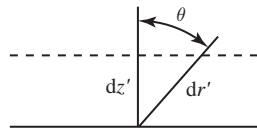


Figure 5.31 Slant path geometry for calculating the column mass along an arbitrary path through the atmosphere.

where θ is the angle from the vertical and $\cos \theta = dz'/dr'$ from Figure 5.31 has been used. It has been assumed that the atmosphere has only vertical variation. Performing the integration for a slant path from the surface through the full atmosphere yields

$$m_s = \rho_o H \sec \theta \quad (5.91)$$

for the column mass along a slant path. The relative optical air mass, or just the air mass, is the ratio of (5.91) and (5.89) or

$$m(\theta) = \frac{m_s}{m_v} = \sec \theta. \quad (5.92)$$

The same argument can be applied to (A.11) and (2.170) with Beer's law rewritten as

$$E(\lambda) = E_o(\lambda) e^{-\tau(\lambda) \sec \theta} = E_o(\lambda) e^{-m(\theta) \tau(\lambda)}, \quad (5.93)$$

where (2.168) has been written in terms of spectral irradiance rather than spectral radiance and λ has been added to the optical depth to emphasize its spectral dependence. In this case $\tau(\lambda)$ is the total optical depth of the atmosphere, $E_o(\lambda)$ is the solar spectral irradiance at the top of the atmosphere, corrected for the earth–sun distance using (2.63), $E(\lambda)$ is at the surface after atmospheric attenuation, and θ is the solar zenith angle. The air mass from (5.92) is only correct for solar zenith angles less than about 70° . For larger angles the curvature of the atmosphere and refraction must be taken into account. The correct formula to be used in (5.93) is

$$m(\theta) = [\cos \theta + 0.50572(96.07995^\circ - \theta)^{-1.6364}]^{-1}, \quad (5.94)$$

where θ is in degrees (Kasten and Young, 1989).

The measurement equation for the automated solar radiometer is a modification of (5.1) with the quantum efficiency replaced by the detector response function (5.2) and the detector signal is a voltage rather than a digital number. The output voltage is given by

$$\begin{aligned} S(\lambda_c) &= U \int_0^\infty L(\lambda) R_\Phi(\lambda) \tau P(\lambda_c - \lambda) d\lambda \\ &= A_d \tau \int_0^\infty E(\lambda) R_\Phi(\lambda) P(\lambda_c - \lambda) d\lambda, \end{aligned} \quad (5.95)$$

where τP is the transmission function of the filter and the radiance multiplied by the solid angle has been replaced with the irradiance. Substituting the irradiance from (5.93) yields

$$\begin{aligned}
S(\lambda_c) &= A_d \gamma \int_0^\infty E_o(\lambda) e^{-m(\theta)\tau(\lambda)} R_\Phi(\lambda) P(\lambda_c - \lambda) d\lambda \\
&\approx [A_d \gamma R_\Phi(\lambda_c) E_o(\lambda_c) \Delta\lambda] e^{-m(\theta)\tau(\lambda_c)} \\
&= S_o(\lambda_c) e^{-m(\theta)\tau(\lambda_c)},
\end{aligned} \tag{5.96}$$

where it has been assumed that the filter transmission function is narrow and the irradiance doesn't vary significantly across it. $S_o(\lambda_c)$ is the top of the atmosphere signal for the ASR.

The first-order analysis of the data is through a Langley plot with the natural logarithm of both sides taken to linearize (5.96) yielding

$$\ln S(\lambda_c) = \ln S_o(\lambda_c) - m(\theta)\tau(\lambda_c), \tag{5.97}$$

where the data have been collected as a function of the air mass. The transformed data are plotted using (5.97) to become the Langley plot with $S_o(\lambda_c)$ obtained from the y -intercept and the slope yielding the optical depth, which is constant for a stable measurement period. The field data are taken with the ASR starting shortly after sunrise and continuing until after the overpass of the imaging spectrometer. The method is applied to each of the ten ASR bands.

The optical depth includes contributions from molecular and aerosol scattering as well as absorption, primarily from ozone and water but also from trace species such as nitrogen dioxide and is rewritten as

$$\tau(\lambda) = \tau_{\text{molecular}} + \tau_{\text{aerosol}} + \tau_{\text{H}_2\text{O}} + \tau_{\text{O}_3} + \tau_{\text{trace}}, \tag{5.98}$$

where the last term refers to molecular absorption from trace gas species. The scattering components will be addressed first followed by an outline of the process for calculating the absorption optical depth based on the presentation in Chapter 2. The details can be found in the references.

The molecular optical depth can be determined for a particular wavelength, surface pressure, and temperature using a Rayleigh approximation

$$\tau_{\text{molecular}} = \frac{8\pi^3(n^2 - 1)^2 N_c}{3\lambda^4 n_s} \frac{6 + 3\gamma}{6 - 7\gamma} \frac{p}{p_o} \frac{T_o}{T}, \tag{5.99}$$

where n is the refractive index of air, γ is the depolarization factor, N_c is the columnar number density in cm^{-2} , n_s is the molecular number density at standard conditions (101,325 Pa and 273.15 K), p and p_o are the atmospheric pressure at the local altitude and at standard conditions respectively, and similarly for the temperatures T and T_o (Teillet, 1990). The aerosol optical depth is developed using a Junge distribution given by (2.197) which has been found to apply in the locations where vicarious calibration measurements are performed. This is accomplished using two spectral bands that are unaffected by molecular absorption, for example, the bands at 441 nm and 870 nm, and by subtracting the optical depth from molecular scattering. The estimate can be further refined using an iterative approach (Biggar et al., 1990).

The absorption optical depth in (5.98) due to ozone is from the Chappuis band at about 611 nm with no other absorber there. Again τ_{O_3} is calculated by subtracting the

now known molecular and aerosol optical depths. The Chappuis band is optically thin and the extinction can be calculated as described in Section 2.8.3. Typically the ozone concentration is converted from Dobson units to total columnar ozone in atm-cm and multiplying by the absorption coefficient. The absorption due to trace gases is similarly calculated. The water vapor calculation is more difficult since it is optically thick. The standard Langley method is modified with the slant path optical depth from (5.93) written as

$$m(\theta)\tau_{\text{H}_2\text{O}}(\lambda) = a + b[m(\theta)u]^{1/2}, \quad (5.100)$$

where a is a correction factor used to model the transition from linear to square law behavior with increasing water, b is the slope of the line relating the slant-path optical depth to the square root of the slant path precipitable water, and u is the vertical precipitable or columnar water vapor. The method uses three channels with the 940 nm channel used for the water measurement and the 870 nm and 1030 nm channels used for the background determination without water. The constants are estimated using a linear regression of $\ln \tau_{\text{H}_2\text{O}}(\lambda)$ versus \sqrt{mu} for a known columnar water vapor allowing for the determination of the y -intercept for the zero air mass case. The final determination of the water vapor is from

$$u = \frac{1}{mb^2} [\ln S(\lambda) + m\tau_{\text{H}_2\text{O}} - a - \ln S_o(\lambda)]^2, \quad (5.101)$$

where $S(\lambda)$ and $S_o(\lambda)$ refer to the water signal at the sensor and at the top of the atmosphere respectively (Thome et al., 1992).

Surface Reflectance Measurements

Surface reflectance measurements utilize a portable field spectrometer that can rapidly acquire data by either a person traveling on foot or in a vehicle. The operator measures the surface repeatedly with the spectrometer equipped with a relatively small field of view fore optic over the full test area. This is kept to a reasonably short time period in order to match the solar and viewing geometries that occurred during data acquisition by the spectral imager. The spectrometer does not need to be a calibrated spectroradiometer since an absolute reflectance standard with a well-understood bidirectional reflectance factor is used in the field.

Each measurement is performed with the field spectrometer taking a nadir view of the surface. The standard is also viewed relatively frequently throughout the measurement period so that the illumination geometry is well matched to a particular series of surface measurements. The measurements are converted from the raw signal to the surface BRF through

$$R_s(2\pi, \omega_r) = \left(\frac{S_s}{S_p}\right) R_p(2\pi, \omega_r), \quad (5.102)$$

where $R_i(2\pi, \omega_r)$ and S_i are the hemispherical-conical reflectance factors and the measured signals for the surface or panel. The reflectance standard has been previously characterized in a metrology laboratory and its calibration data are updated at least

yearly due to aging and contamination from use in the field environment. This is a critical component of the vicarious calibration process as the primary source of error in the reflectance-based method is the retrieval of the surface reflectance.

Radiative Transfer Modeling

The modeling of the transfer of radiation through the atmosphere is addressed in some detail in Chapter 6 with a limited discussion of the available codes. In brief, the calculation assumes a horizontally homogeneous atmospheric model and includes the processes absorption, single and multiple scattering, and atmospheric refraction. We will settle for a brief description of the input parameters and defer the discussion of the details. The output product of the calculation is the at-aperture radiance from which the calibration coefficients are calculated.

The inputs to the radiative transfer code are the top of the atmosphere solar irradiance, the solar illumination and sensor viewing geometries, the optical depths for the various molecular species such as ozone and water, the aerosol optical depth, the columnar water vapor and ozone, the Junge parameter that is used to model the size distribution, the real and imaginary parts of the aerosol index of refraction that are used for the Mie scattering calculation, and the surface reflectance. The surface reflectance is characterized by the bidirectional reflectance factor for the radiative transfer code which is approximated from the hemispherical-conical reflectance factor that is measured. This is a good approximation due to the near-Lambertian and high surface reflectance coupled with the low aerosol loading that is characteristic of the sites. The resulting at-aperture radiance is convolved with the instrumental profiles of the channels to produce calibration coefficients that are evaluated in comparison to the current coefficients.

Error Analysis

The evaluation of the errors summarized here is based on Slater et al. (1996) and updated by Thome et al. (2005), which should be consulted for a more complete discussion. The error sources for the reflectance-based method are presented in Table 5.9. The values are based on calibrations performed on cloud-free days with high visibility for the Landsat bands at about 487, 565, 660, 825, 1650, 2220 nm. Table 5.9 lists both the source of the error and its effect as it is propagated to the at-aperture radiance at the top of the atmosphere. It is clear that the calibration products have been significantly improved during the intervening decade with the total error reduced from 4.9 to 2.5 percent.

Currently the largest error is the determination of the surface reflectance in contrast to the state of the art in 1996 when the atmospheric characterization was the dominant source. The accuracy of the surface reflectance is limited by knowledge of the BRF of the standard, the contribution of the diffuse illumination that is uncorrected, the measurement errors introduced by the field spectrometer, and registering the site within the imaging spectrometer data. Note that improvements at NIST on the characterization of reflectance standards should reduce this error. Additionally, the surface is measured with a nadir view for the field spectrometer while the imaging spectrometer will most likely have a different viewing geometry with BRDF effects contributing some error from non-Lambertian surface properties.

The uncertainty in the optical depth measurement is due to errors in the estimate of the aerosol size distribution and amounts. The errors in the calibration of the automated solar radiometer and the assumed spectral dependence, which is based on the model that is adopted for the size distribution, are the primary contributors. The calibration of the ASR is carried out on clear days with a stable atmosphere and usually from a high altitude such as a mountain top. In this way the intercepts are known so that the spectral optical depths can be determined when the sky conditions are not ideal with, for example, intermittent clouds. If the intercept is known then an instantaneous measurement of the optical depth is possible. The aerosol size distribution and absorption are inferred from the ASR analysis. A sensitivity analysis of the assumption of a Junge distribution combined with field measurements indicates that the impact to the at-aperture radiance is 0.3 percent. Aerosol absorption, which is determined by the complex index of refraction, is difficult to quantify and is therefore 100 percent in Table 5.9. The errors due to molecular absorption have also been reduced from a more accurate and comprehensive

Table 5.9 Reflectance-based errors for the Landsat bands adapted from Thome et al. (2005). The molecular absorption estimates were not included since they require knowledge of the particular sensor and the non-Lambertian characteristic is included in the reflectance retrieval for the 2005 estimate. The total error is the RSS of the individual errors. The values in parentheses were in error in Slater et al. (1996).

Source	1996 error		2005 error	
	Source	TOA	Source	TOA
Ground reflectance measurement			2.1	2.2
Reference panel calibration	2.0		2.0	
Diffuse-field correction	0.5		0.5	
Measurement errors	0.5		1.0	
Optical depth measurement	5.4	1.1	0.5	<0.1
Extinction optical depth	5.0		0.5	
Mie/Rayleigh partition	2.0		—	
Absorption			1.3	—
Column ozone	20.0		2.0	
Column water vapor	N/A		5.0	
Aerosol complex index	(2.0)	2.0	100	0.5
Aerosol size distribution			3.0	0.3
Size limits	(0.2)		—	
Junge parameter	(0.5)		0.3	
Non-Lambertian characteristics	(1.2)	1.2	10	—
Other				
Vertical distribution	1.0	1.0	—	
Polarization	0.1	0.1	0.1	
Radiative transfer code inaccuracy	1.0	1.0	1.0	
Solar zenith angle uncertainty	0.2	0.2	0.2	
Total RSS error			4.9	2.5

understanding of the molecular distributions in the atmosphere, of the absorption cross sections, and improved radiative transfer modeling. For example, there are external measurements of ozone that are readily available and more accurate than the retrievals from the ASR (Thome et al., 2005). The assessment of the columnar water vapor remains problematic with an uncertainty on the order of 5 percent.

Irradiance-Based Method

The irradiance-based method further characterizes the aerosol loading by adding additional measurements of the diffuse to global ratio of the irradiance. This is accomplished by using a spectroradiometer with a nadir view of a reflectance standard. The panel is viewed first with both the direct solar and diffuse components followed by a view with the direct component bocked. A correction factor is applied to account for the portion of the diffuse illumination that is blocked by the spectroradiometer support structure. The measurements enable the quantification of multiple scattering effects that create the diffuse radiation field, which are treated in some detail in Chapter 6. The result further constrains the at-aperture radiance calculation and the total error is estimated to be 2.8 percent (Slater et al., 1996).

5.9.3 Radiance-Based Method

The radiance-based method flow diagram is illustrated for an aircraft-based case on the right side of Figure 5.32, where a well-calibrated and stable radiometer is flown above most of the atmospheric aerosols and water. The best approach is to fly a calibrated imaging spectrometer rather than a simple radiometer. This enables the use of fiducials,

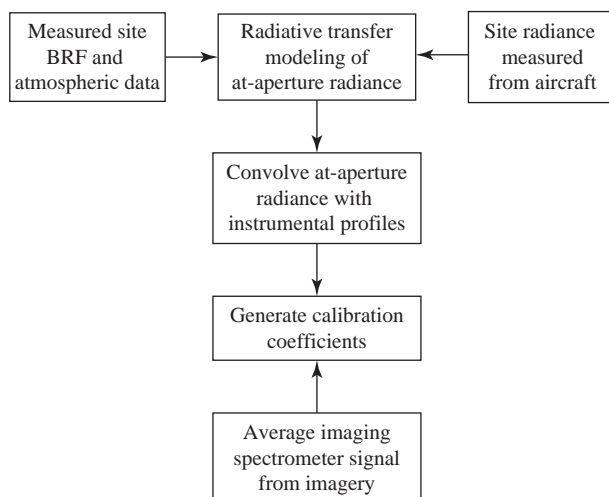


Figure 5.32 Flow diagram for the data acquisition and processing for the radiance-based method. The radiative transfer modeling is to calculate the contribution to the at-aperture radiance from above the airplane. Adapted from Slater et al. (1996).

such as colored tarps, for demarcation that are apparent in both the target sensor and the reference imaging spectrometer data. The main uncertainty in this method is the radiometric calibration of the reference imaging spectrometer since the characterization of the atmosphere is only critical in the modeling of the portion that is above the aircraft. If a high-altitude airplane is used, such as a NASA ER-2 that flies as high as 20 km, the impact of the radiation transfer modeling becomes negligible. Slater et al. (1996) estimate that the error in the method was 2.8 percent in 1996 and was expected to decline to 2.0 percent. An example where this approach was used for an imaging spectrometer was the calibration of the NASA EO-1 Hyperion sensor (Green et al., 2003). A satellite-based example of the radiance-based method, also applied to Hyperion, can be found in Thome et al. (2003).

5.9.4 Vicarious Spectral Calibration

A benefit of the accurate at-aperture radiance produced during vicarious calibration experiments is that it offers the opportunity to evaluate the spectral calibration of the target sensor. The spectral calibration can vary for a variety of reasons in the operational environment. For example, if an airborne system is not in a stable thermal environment there will be small alignment changes due to thermal expansion. A thermal gradient across the imaging spectrometer can be particularly troublesome and many systems are stabilized in dewars to prevent this problem. Another example is the small changes in a space-based system due to launch trauma or thermal issues. Vicarious calibration measurements enable a quantitative evaluation of the instrumental profile.

Figure 5.33 shows the nominal band-averaged at-aperture radiance and the corresponding signal from a vicarious calibration measurement with the oxygen and carbon dioxide features labeled. For a particular channel, where the optical transmission and the detector response don't vary significantly, the dark-subtracted signal is proportional to the convolution of the instrumental profile and the at-aperture radiance from (5.1). Using the example of a space-based system, the known at-aperture radiance from the vicarious calibration measurements is band-averaged to the preflight instrumental profiles and then divided by the dark-subtracted signal. The processes are repeated for a different set of spectral response functions. The effect is illustrated in Figure 5.34 showing the results for shifts in ± 0.25 nm increments near the absorption features corresponding to the 760 nm oxygen and the carbon dioxide features at about 2000 nm. The smoothest ratio corresponds to the correct spectral assignment. A least-square fitting process can be applied to determine the optimum shift that produces the smoothest curve with a similar approach applied to the limit of resolution as was demonstrated for Hyperion (Green et al., 2003). The technique is limited by the signal-to-noise ratio although vicarious calibration measurements are typically performed over high reflectance areas so the SNR is optimal. The process is also limited to those spectral locations where there is a fairly sharp absorption feature but the shift at least can be broadly applied to a well-behaved imaging spectrometer. A similar approach that also relies on atmospheric absorption features has been applied to operational data where the smoothness criterion is applied to the retrieved reflectance data (Guanter et al., 2006).

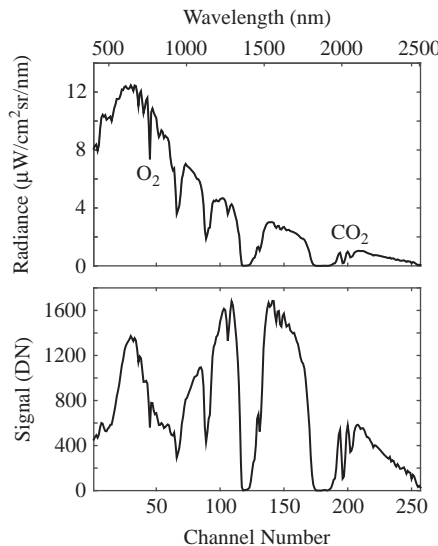


Figure 5.33 Illustration of the at-aperture radiance calculated from a radiative transfer code and the dark-subtracted signal measured by an imaging spectrometer from a vicarious calibration campaign. The oxygen and carbon dioxide absorption features are labeled.

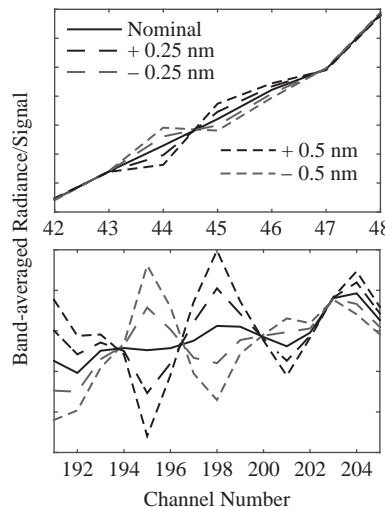


Figure 5.34 Ratio of band-averaged radiance and imaging spectrometer signal in arbitrary units at the oxygen and carbon dioxide bands for several instrumental profile shifts about the nominal values.

5.9.5 Emissive Vicarious Calibration

The vicarious calibration for space-based longwave infrared spectral imagers is challenging since the target area must have both a uniform emissivity and temperature. Additionally some temperature variation during the year is required to confirm the

radiometric performance over a reasonable range of at-aperture radiance levels. These techniques augment the onboard blackbody characterization that is routine for any LWIR imaging spectrometer. The primary targets are large water bodies such as Lake Tahoe and the Salton Sea in California, the Great Lakes, and oceans. The target area is instrumented so that the water temperature, water-leaving radiance, and atmospheric conditions are quantified. The at-aperture radiance is modeled using a radiative transfer code to compute the atmospheric upwelling and downwelling radiance, and the surface emission. These techniques are described in Barsi et al. (2014) for the calibration of the Landsat-5 and Landsat-7 thermal band with an uncertainty on the order of 0.5 K.

5.10 Summary and Further Reading

The goal of this chapter was to provide a detailed description of the laboratory characterization of an imaging spectrometer and an overview of the techniques used for vicarious calibration. The entire process rests on the exhaustive work performed at national metrology laboratories such as the National Institute of Standards and Technology in the United States. Again, as in Chapter 4, the unifying concept of the measurement equation was applied to establish the explanatory framework as well as the quantitative basis of sensor characterization. The important process of error analysis so that the data calibrated to physical units can be evaluated was also introduced. Well-calibrated data are critical to the process of atmospheric compensation introduced in Chapter 6 where a physical model is applied. A modeling methodology was described that is used as a systems engineering tool and also to evaluate the sensor performance once it is built.

In addition to the particular articles cited here a spectrum of high-quality books are available. The NIST Special Publication 250 series is a tremendous resource that describes in detail the measurement services NIST provides. They are also a superb reference for laboratory development and practice. All are available from the NIST website. The NBS Technical Note Series 910 edited by Fred E. Nicodemus is also outstanding but sadly out of print (Nicodemus and Kostkowski, 1976). A superb compendium of articles written by researchers at the various national metrology laboratories is Parr et al. (2005). There are a variety of radiometry textbooks available and two are Grum and Becherer (1979) and Boyd (1983). The statistical techniques applied to experimentation at an introductory level is provided by Bevington and Robinson (2003) and Taylor (1996) and at a more advanced level in Box et al. (2005) and Dietrich (1991). The science and engineering of photodetectors is presented in Kasap (2013) and Saleh and Teich (2007). An area of interest for a space-based imaging spectrometer is the cross calibration to other spectral sensors and an overview is in Thome (2004).

Problems

1. The monochromator used for a spectral calibration source has a grating with 300 grooves/mm, equivalent focal lengths of 350 mm, the exit angle θ_2 equal to 14.5° , and is operated in first order. Show that the limit of resolution is given by

$$\delta\lambda = \frac{aw \cos \theta_2}{kf}, \quad (5.103)$$

where a is the groove spacing, w is slit width, f is the focal length, and k is the order number. What is the slit width if a limit of resolution of 1 nm is desired?

2. An integrating sphere has one input port of area A_i and one exit port of area A_e . If the initial flux illuminates the sphere wall what does (5.33) reduce to?
3. An integrating sphere is a near-Lambertian source. Plot the distribution of radiance as a function of the angle from the normal to the port area.
4. Radiance L_a is incident on the area dA with a solid angle $d\omega$ at an angle θ_a at the interface between air and glass (index of refraction n_g) where the rays are refracted. Show that

$$\frac{L_a}{1} = \frac{L_g}{n_g}, \quad (5.104)$$

where L_g is the radiance in the glass. L/n is known as the basic radiance.

5. Derive the calibration equations for an airborne LWIR sensor where the blackbodies are external to the telescope, similar to the equations in Section 5.4.5.
6. The radiance from a calibration source is well described by Planck's law. Calculate the relative uncertainty in the calibration coefficients as a function of wavelength if the standard uncertainty from the monochromator is 0.1 nm.
7. A silicon photodiode has a bandgap energy of 1.12 eV. What is the cutoff wavelength?
8. A mercury–cadmium–telluride detector can be tuned by varying the amount of mercury and cadmium with the relationship given by $\text{Hg}_{1-x}\text{Cd}_x\text{Te}$ where x is the fraction of cadmium. What is the bandgap energy for each of the cutoff wavelengths in Table 5.10?
9. The absorption coefficient for a silicon photodiode operated at 300 K at 700 nm is 1900/cm. At what depth has 90 percent of the incident flux been absorbed?
10. Derive (5.84) and (5.85).

Table 5.10 Mercury–cadmium fractions and cutoff wavelengths for MCT photodiodes

x	Cutoff wavelength (μm)
0.194	16.99
0.205	13.63
0.225	10.08
0.31	4.56
0.44	2.62
0.62	1.66

11. Show that the noise-equivalent reflectance is given by

$$\text{NE}\Delta\rho = \frac{4N^2hc}{\pi\lambda_c\Delta\lambda\tau(\lambda_c)\tau_{\text{atm}}(\lambda_c)\frac{E_t(\lambda_c)}{\pi}}\text{NEI}(\lambda_c),$$

where $\tau_{\text{atm}}(\lambda_c)$ is the atmospheric transmission from the top of the atmosphere to the surface and up to the imaging spectrometer. $E_t(\lambda_c)$ is the top-of-the-atmosphere solar irradiance.

12. Plot the airmass using (5.92) and (5.94). When does the error exceed 1 percent?
13. Each filter radiometer of an automated solar radiometer has two 0.5 cm apertures that are 100 mm apart. What is the field of view? Is this reasonable?

6 Radiative Transfer and Atmospheric Compensation

The next processing step for calibrated imaging spectrometer data is the conversion from the at-aperture radiance to a surface reflectance signature, for the VNIR/SWIR spectral range, or to a surface emissivity signature and temperature, for the LWIR spectral range. This requires that the transmission and emission of the atmosphere be quantified from the aggregated information that is present in the at-aperture radiance. In the solar reflective range this includes estimates of the amount of water in the scene, which is highly variable, and of the aerosol loading in order to calculate both the diffuse radiance and the contribution from light that is scattered and reflected from the directly viewed pixel and the surrounding area. Similarly, for a sensor operating in the emissive regime, the water and the atmospheric thermal emission is quantified in order to retrieve the ground-leaving radiance that is used to estimate the temperature and emissivity of the surface.

In this chapter, the physics of radiative transfer will be developed first, in order to establish a basis for the discussion of the particular techniques that are applied in the reflective and emissive regimes. The modeling tools that are used to quantitatively describe the processes of absorption, transmission, and emission in a forward sense, i.e. in the direction of light propagation, are introduced prior to delving into the problem of retrieving the surface properties of interest. The reflectance retrieval is treated in detail and includes the derivation of the inverse radiative transfer model, the estimation of the quantities that are required to apply the inverse model, and the algorithms that are utilized, using both physics-based modeling and empirical techniques. The final sections address the problem of atmospheric compensation in the longwave infrared.

6.1 Radiative Transfer

The propagation of radiation through the atmosphere is described by the theory of radiative transfer. A complete description of radiative transfer is beyond our scope; however, the critical concepts required to understand the processes of atmospheric compensation are introduced within the limitations of a book devoted to remote sensing using an imaging spectrometer. Radiative transfer as a discipline was established by Arthur Schuster's paper in 1905, where he recognized the importance of multiple scattering (Schuster, 1905). Numerous scientists have contributed to the theoretical development and Subrahmanyan Chandrasekhar in particular made seminal contributions to the field

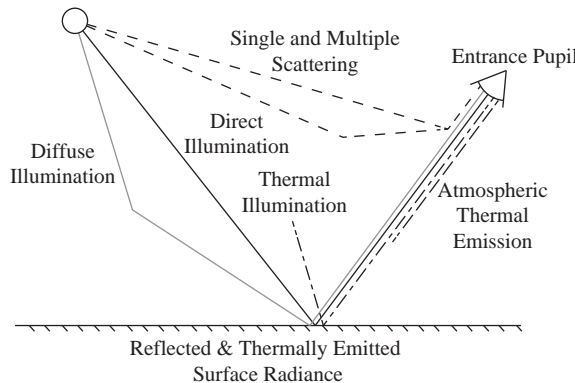


Figure 6.1 Contributions to the at-aperture radiance from the various physical processes including direct solar, diffuse atmospheric, and atmospheric thermal illumination of the imaged area that is reflected to the sensor, thermal emission of the surface point (part of the solid black line from the surface to the sensor), scattered radiance that does not interact with the surface, and atmospheric thermal emission. The bends in the gray and dashed lines represent scattering points.

and published his landmark book *Radiative Transfer* in 1950 (Chandrasekhar, 1960). The introduction to radiative transfer theory developed here is based upon that presented by several authors (Goody and Yung, 1989; Liou, 2002; Thomas and Stammes, 1999).

The fundamental phenomena of absorption, emission, and scattering that govern the transfer of radiation through the atmosphere were introduced in Chapter 2. The topic for this section is the equation that is solved in a radiative transfer calculation to predict the radiance that arrives at the entrance pupil of an imaging spectrometer. The full description also includes the reflection or emission properties of the surface, as was described in Chapter 3. Figure 6.1 illustrates the various contributions to the at-aperture radiance and each contributor will be described by a different term in the radiative transfer equation.

We are typically interested in calculating the radiative transfer for a ray path along the unit vector $\hat{\omega}$ and over a distance r through the atmosphere. A ray that originates from the sun and arrives at the top of the atmosphere travels toward the earth's surface with the atmosphere becoming increasingly dense. Refraction, the retardation of the speed of light in a medium, occurs, increases with density, and is a function of temperature and wavelength. This refraction also leads to bending of the rays as given by Snell's law. The path description here neglects this complication, although the problem is computationally solved using an atmospheric refraction model that describes the ray path incorporating the index of refraction of the atmosphere as a function of pressure, temperature, and wavelength.

6.1.1

The Source Function and the Radiative Transfer Equation

Mathematically, radiative transfer problems are solved through the application of an integro-differential equation that describes the variation in radiance at a given point along a particular direction that depends upon both the local processes of extinction

(absorption and scattering) and self-emittance of the medium, and the additional contributions from scattering from a local region. Consider a differential volume element within the medium that is emitting radiation in a certain direction. The volume has a cross-sectional area dA and a thickness dr . The added radiance can be through any emission process, such as thermal emission, or from scattering of light as it passes through the volume. The emission coefficient is defined as the spectral flux emitted from the infinitesimal volume and into the solid angle $d\omega$ in the direction of viewing, described by the unit vector $\hat{\omega}$, or

$$j_\lambda(\mathbf{r}, \hat{\omega}) \equiv \frac{d^4\Phi(\mathbf{r}, \hat{\omega})}{dA d\omega dr d\lambda} = \frac{dL_\lambda(\mathbf{r}, \hat{\omega})}{dr} \quad (6.1)$$

for the volume located at \mathbf{r} . L_λ is the spectral radiance in the direction of $\hat{\omega}$ as defined by (2.57) and the emission coefficient is in units of spectral radiance per unit length.

The emission coefficient becomes the counterpart to Beer's law, which describes the loss of radiance along a ray, and the two are combined to describe the radiative transfer through the volume $dA dr$, as illustrated in Figure 6.2. Therefore, the change in radiance is

$$dL_\lambda(\mathbf{r}, \hat{\omega}) = -k_e(\lambda)L_\lambda(\mathbf{r}, \hat{\omega}) dr + j_\lambda(\mathbf{r}, \hat{\omega}) dr, \quad (6.2)$$

where (2.167) and (6.1) have been applied. Equation (6.2) is rewritten by dividing by the differential optical path, $d\tau_r = k_e(\lambda) dr$, to give

$$\frac{dL_\lambda(\mathbf{r}, \hat{\omega})}{d\tau_r} = -L_\lambda(\mathbf{r}, \hat{\omega}) + \frac{j_\lambda(\mathbf{r}, \hat{\omega})}{k_e(\lambda)}, \quad (6.3)$$

with the *source function* defined as

$$S_\lambda(\mathbf{r}, \hat{\omega}) \equiv \frac{j_\lambda(\mathbf{r}, \hat{\omega})}{k_e(\lambda)} \quad (6.4)$$

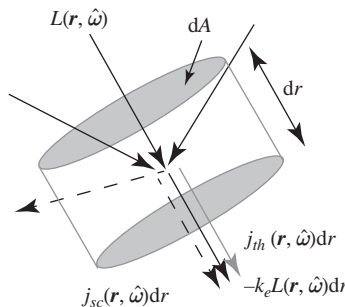


Figure 6.2 Change in radiance $L(\mathbf{r}, \hat{\omega})$ within a differential volume element illustrating the losses due to extinction, represented by $-k_e L(\mathbf{r}, \hat{\omega}) dr$, and the gains due to thermal and scattering emission, represented by $j_{th}(\mathbf{r}, \hat{\omega}) dr$ and $j_{sc}(\mathbf{r}, \hat{\omega}) dr$. The solid lines represent radiance that is undergoing extinction, the dashed arrowed lines represent scattering, and the gray arrowed line represents thermal emission.

in the expected units of spectral radiance. Applying the definition of the source function to (6.3) yields

$$\frac{dL_\lambda(\mathbf{r}, \hat{\omega})}{d\tau_r} = -L_\lambda(\mathbf{r}, \hat{\omega}) + S_\lambda(\mathbf{r}, \hat{\omega}), \quad (6.5)$$

which is the most general form of the radiative transfer equation. It remains to explicitly define the source function in order to solve (6.5).

The source function is due to thermal emission and scattering. Thermal emission will be addressed first. In Section 2.4.2 the emission of blackbody radiation from a surface was described using Planck's and Kirchhoff's laws. These concepts will now be generalized to describe thermal emission from the volume dV . We will assume that the atmosphere contained in dV is in local thermodynamic equilibrium and can be described by the local temperature T (see Section 2.6.4). From (2.70), α is defined as the ratio of the absorbed to the incident radiance and is therefore a dimensionless quantity that is also equal to the emissivity as a consequence of Kirchhoff's law. For the present purposes, α is replaced by the absorption coefficient $k_a(\lambda)$, the absorption per unit length along a beam, and the thermal emission coefficient is written as

$$j_\lambda^{th} = k_a(\lambda)B_\lambda(T) \quad (6.6)$$

for the emitted radiance along the path of interest. Note that this is the spectral flux emitted from the volume $dA dr$ into the solid angle $d\omega$. The thermal source function is therefore

$$S_\lambda^{th} = \frac{k_a(\lambda)}{k_e(\lambda)}B_\lambda(T), \quad (6.7)$$

where the directional coordinates are not needed since blackbody radiation is isotropic and T is the temperature at \mathbf{r} . Comparing (6.7) to (2.69), the volume emissivity is expressed as

$$\epsilon_v(\lambda, \hat{\omega}, T) = \frac{S_\lambda^{th}(\hat{\omega}, T)}{B_\lambda(T)}, \quad (6.8)$$

where the directional dependence has been made explicit. This is alternatively expressed as

$$\epsilon_v(\lambda, \hat{\omega}, T) = \frac{k_a(\lambda, \hat{\omega}, T)}{k_e(\lambda, \hat{\omega})}, \quad (6.9)$$

which, under the simplifying assumption of isotropic emitters, reduces to

$$\epsilon_v(\lambda, T) = \frac{k_a(\lambda, T)}{k_e(\lambda)}, \quad (6.10)$$

where the volume emissivity is proportional to the absorption coefficient. Note the difference between (2.71), which expressed the relationship between emission and absorption for a surface, and (6.10), the equivalent expression for emission from a volume.

The source function for scattering is more complex since the full directionality, as captured by the scattering phase function, must be included. As illustrated in Figure 6.2,

rays from all directions that enter into the differential volume dV can be scattered into the solid angle $d\omega$ in the direction of interest. Recall that, if a ray has been scattered, $p(\hat{\omega}_o, \hat{\omega})d\omega/4\pi$ is the probability of scattering of that ray from the $\hat{\omega}_o$ direction into the solid angle $d\omega$ centered on $\hat{\omega}$. Also, (2.133) is modified to reflect the infinitesimal gain in radiance over the distance dr giving

$$k_s = \frac{1}{L} \frac{dL}{dr} \quad (6.11)$$

for the probability of scattering per unit length. Therefore, the scattered radiance into $d\omega$ from the volume dV at \mathbf{r} is the sum of all the scattered light contributions from all incoming directions multiplied by the probability of scattering occurring over the distance dr or

$$dL_\lambda(\mathbf{r}, \hat{\omega}) = k_s(\lambda, \mathbf{r}) dr \int_{4\pi} \frac{p(\mathbf{r}, \hat{\omega}_o, \hat{\omega})}{4\pi} L_\lambda(\mathbf{r}, \hat{\omega}_o) d\omega_o. \quad (6.12)$$

The scattering emission coefficient is defined using (6.1) to give

$$j_\lambda^{sc}(\mathbf{r}, \hat{\omega}) = k_s(\mathbf{r}, \lambda) \int_{4\pi} \frac{p(\mathbf{r}, \hat{\omega}_o, \hat{\omega})}{4\pi} L_\lambda(\mathbf{r}, \hat{\omega}_o) d\omega_o \quad (6.13)$$

and the scattering source function is therefore

$$S_\lambda^{sc}(\mathbf{r}, \hat{\omega}) = \frac{j_\lambda^{sc}(\mathbf{r}, \hat{\omega})}{k_e(\mathbf{r}, \lambda)} = \frac{k_s(\mathbf{r}, \lambda)}{k_e(\mathbf{r}, \lambda)} \int_{4\pi} \frac{p(\mathbf{r}, \hat{\omega}_o, \hat{\omega})}{4\pi} L_\lambda(\mathbf{r}, \hat{\omega}_o) d\omega_o, \quad (6.14)$$

from (6.4). The ratio $k_s(\mathbf{r}, \lambda)/k_e(\mathbf{r}, \lambda)$ is known as the single-scattering albedo $\tilde{\omega}(\mathbf{r}, \lambda)$ and, when this definition is applied to (6.7), it yields

$$S_\lambda^h = [1 - \tilde{\omega}(\mathbf{r}, \lambda)] B_\lambda(\mathbf{r}, T) \quad (6.15)$$

for the thermal source function.

Finally, the radiative transfer equation is rewritten by combining (6.5), (6.14), and (6.15) to produce

$$\begin{aligned} \frac{dL_\lambda(\mathbf{r}, \hat{\omega})}{d\tau_r} &= -L_\lambda(\mathbf{r}, \hat{\omega}) + [1 - \tilde{\omega}(\mathbf{r}, \lambda)] B_\lambda(\mathbf{r}, T) \\ &+ \tilde{\omega}(\mathbf{r}, \lambda) \int_{4\pi} \frac{p(\mathbf{r}, \hat{\omega}_o, \hat{\omega})}{4\pi} L_\lambda(\mathbf{r}, \hat{\omega}_o) d\omega_o, \end{aligned} \quad (6.16)$$

which includes thermal emission and multiple scattering. The radiative transfer equation is the fundamental description of all of the physical processes of absorption, emission, and scattering that light can undergo in an atmosphere. As we will show, when combined with the concepts of reflectance and emittance, it also governs the coupling between the surface and the atmosphere. The solution to (6.16) is accomplished by dividing the radiation field into portions from the different physical processes that contribute to the scattering source function. It is necessary to solve (6.16) for the inversion from radiance to reflectance or radiance to temperature and emissivity, which is accomplished numerically.

6.1.2

Simplification of the Radiative Transfer Equation using a Slab Geometry

The solution to (6.16) is extremely challenging, involving the identification and characterization of the absorbing, emitting, and scattering species along the path, the local temperatures, and the scattering phase functions for a given input radiance. In this section the radiative transfer equation will be simplified from the arbitrary path through the atmosphere, which depends upon all three spatial coordinates, as described by the optical path τ_r , to a vertical parameterization that only depends upon the optical depth τ , which is a vertical coordinate. This parameterization leads to a tremendous simplification of (6.16), resulting in a more tractable one-dimensional problem that is readily applicable to imaging spectroscopy.

The conversion of (6.16) to a one-dimensional equation rests on the property that the quiescent atmosphere is highly stratified with the density, pressure, temperature, and species constituents varying to a much greater degree in the vertical direction when compared to the horizontal variation, enabling the atmosphere to be divided into plane parallel “slabs”. Obviously weather can and does introduce conditions where this simplification no longer applies, since some types of clouds, and the boundaries between different air masses, display both vertical and horizontal changes. The distribution of aerosols will also introduce horizontal inhomogeneities. In our case, the utility of remote sensing using an imaging spectrometer is maximized when the atmospheric conditions, to a good approximation, conform to the slab geometry.

Optical Depth as the Vertical Coordinate

The concept of optical depth, which was introduced in Section 2.8.1, has great utility under the slab approximation where the extinction coefficient is simplified from $k_e(r, \lambda)$ to $k_e(z, \lambda)$, enabling the optical path to be easily related to the optical depth. Figure 6.3 shows rays propagating upward and downward at a polar angle θ and over the infinitesimal distance dr along the ray path. The infinitesimal gain in altitude dz is related to dr through

$$\cos \theta = \frac{dz}{dr} \quad (6.17)$$

with $\cos \theta$ between 0 and 1 for upward propagation and between 0 and -1 for downward. It is convenient to define the variable μ as

$$\mu = |\cos \theta|, \quad (6.18)$$

ensuring that $0 \leq \mu \leq 1$, independent of the direction of propagation.

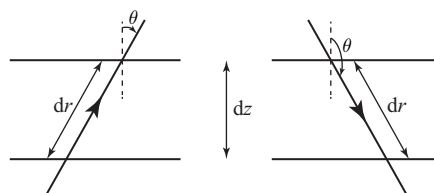


Figure 6.3

Geometry for the definition of $\mu = |\cos \theta|$.

The optical depth τ , defined in (2.170) with $z_2 > z_1$, must be modified in order for it to be used as a vertical coordinate, rather than a relative value between two altitudes. This requires that an absolute reference point be defined. By convention, the top of the atmosphere is selected, with z_2 becoming infinity. As a practical matter, the top of the atmosphere is reached when the density becomes so low that no significant scattering or absorption occurs at about 100 km.

With this definition, (2.170) becomes

$$\tau(z, \lambda) = \int_z^{z_{\text{top}}} k_e(z', \lambda) dz' = \int_z^{\infty} k_e(z', \lambda) dz', \quad (6.19)$$

with z' being the variable of integration. The optical depth is now related to the optical path using (6.17) and (6.18). Consider an upward-propagating ray along a slant path from an initial altitude z_1 to a final altitude z_2 . The optical depth between the two altitudes is

$$\begin{aligned} \tau(z_2, \lambda) - \tau(z_1, \lambda) &= \int_{z_2}^{z_{\text{top}}} k_e(z, \lambda) dz - \int_{z_1}^{z_{\text{top}}} k_e(z, \lambda) dz \\ &= - \int_{z_1}^{z_2} k_e(z, \lambda) dz \\ &= -\mu \int_{r_1}^{r_2} k_e(r, \lambda) dr \\ &= -\mu \tau_r(r_1, r_2, \lambda) \end{aligned} \quad (6.20)$$

since $k_e(z, \lambda)$ is equal to $k_e(r, \lambda)$ in the slab approximation. This is the expected result since the optical depth between z_1 and z_{top} is greater than that from z_2 to z_{top} . The derivation for a downward-propagating ray along a slant path yields a similar result to (6.20), except without the minus sign. For ray propagation over an infinitesimal distance, (6.20) is expressed as

$$d\tau_r = \begin{cases} -\frac{d\tau}{\mu} & \text{upward propagation} \\ \frac{d\tau}{\mu} & \text{downward propagation} \end{cases}, \quad (6.21)$$

relating the optical path to the optical depth for the two cases. The above derivation is consistent with the definition of the optical depth between two altitudes, given by (2.170), which is equivalent to

$$\tau(z_1, z_2, \lambda) = \tau(z_1, \lambda) - \tau(z_2, \lambda) \quad (6.22)$$

with $z_2 > z_1$.

The Radiative Transfer Equation for the Slab Geometry

The optical depth can now be used as the vertical coordinate in the radiative transfer equation. The choice of definition for μ makes it convenient to separate (6.16) into two different equations, one each for upward and downward propagation. There are alternatives to this definition, but it emphasizes the differences between the two cases.

Applying (6.21) to the source function, $S_\lambda(\mathbf{r}, \hat{\omega}) = S_\lambda^{th}(T) + S_\lambda^{sc}(\mathbf{r}, \hat{\omega})$, yields

$$S_\lambda(\tau, \hat{\omega}) = [1 - \tilde{\omega}(\tau, \lambda)]B_\lambda(\tau) + \tilde{\omega}(\tau, \lambda) \int_{4\pi} \frac{p(\tau, \hat{\omega}_o, \hat{\omega})}{4\pi} L_\lambda(\tau, \hat{\omega}_o) d\omega_o, \quad (6.23)$$

where τ is the independent variable and the other variables, for example, the location and the temperature, can be expressed as functions of the optical depth. For the slab approximation, the source function is rewritten in terms of μ in order to identify the upward and downward portions. First, the upward and downward radiances, signified by the arrows, are defined as

$$L_\lambda^{\uparrow}(\tau, \hat{\omega}) \equiv L_\lambda^{\uparrow}(\tau, \theta \leq \pi/2, \phi) \quad (6.24)$$

$$L_\lambda^{\downarrow}(\tau, \hat{\omega}) \equiv L_\lambda^{\downarrow}(\tau, \theta > \pi/2, \phi) \quad (6.25)$$

for use in the separation of (6.23) into components. The scattering source function will contribute radiance into both directions due to the totality of radiance incident into the volume element. For example, upwardly propagating radiance from dV will be due to both $L_\lambda^{\uparrow}(\tau, \theta, \phi)$ and $L_\lambda^{\downarrow}(\tau, \theta, \phi)$ inputs into the volume since the radiance is redirected due to scattering as weighted by the phase function.

Equation (6.23) is decomposed into two parts with the source functions given by

$$S_\lambda^{\uparrow}(\tau, \hat{\omega}) = [1 - \tilde{\omega}(\tau, \lambda)]B_\lambda(\tau) + \tilde{\omega}(\tau, \lambda) \int_{\uparrow} \frac{p(\tau, \hat{\omega}_o^{\uparrow}, \hat{\omega}^{\uparrow})}{4\pi} L_\lambda^{\uparrow}(\tau, \hat{\omega}_o) d\omega_o + \tilde{\omega}(\tau, \lambda) \int_{\downarrow} \frac{p(\tau, \hat{\omega}_o^{\downarrow}, \hat{\omega}^{\downarrow})}{4\pi} L_\lambda^{\downarrow}(\tau, \hat{\omega}_o) d\omega_o \quad (6.26)$$

and

$$S_\lambda^{\downarrow}(\tau, \hat{\omega}) = [1 - \tilde{\omega}(\tau, \lambda)]B_\lambda(\tau) + \tilde{\omega}(\tau, \lambda) \int_{\uparrow} \frac{p(\tau, \hat{\omega}_o^{\uparrow}, \hat{\omega}^{\downarrow})}{4\pi} L_\lambda^{\uparrow}(\tau, \hat{\omega}_o) d\omega_o + \tilde{\omega}(\tau, \lambda) \int_{\downarrow} \frac{p(\tau, \hat{\omega}_o^{\downarrow}, \hat{\omega}^{\downarrow})}{4\pi} L_\lambda^{\downarrow}(\tau, \hat{\omega}_o) d\omega_o \quad (6.27)$$

with the notation in the scattering phase function indicating whether the incoming ray is into the upper hemisphere or downward one, and similarly for the outgoing ray. For example, $p(\tau, \hat{\omega}_o^{\uparrow}, \hat{\omega}^{\downarrow})$ indicates that the direction of an incoming ray, given by $\hat{\omega}_o^{\uparrow}$, is upward and the scattered ray direction, $\hat{\omega}^{\downarrow}$, is downward. With this source division, and applying (6.21), (6.16) is rewritten as

$$-\mu \frac{dL_\lambda^{\uparrow}(\tau, \hat{\omega})}{d\tau} = -L_\lambda^{\uparrow}(\tau, \hat{\omega}) + S_\lambda^{\uparrow}(\tau, \hat{\omega}) \quad (6.28)$$

$$\mu \frac{dL_\lambda^{\downarrow}(\tau, \hat{\omega})}{d\tau} = -L_\lambda^{\downarrow}(\tau, \hat{\omega}) + S_\lambda^{\downarrow}(\tau, \hat{\omega}) \quad (6.29)$$

for the two radiances using the optical depth as the independent variable. These two equations are the one-dimensional form, in terms of optical depth, of the radiative transfer equation where the optical path has been replaced under the slab approximation. The slant path of the radiation, as captured by μ and $\hat{\omega}$, remains but the properties of the atmosphere are reduced to a one-dimensional parameterization.

Equations (6.28) and (6.29) are also separated into the direct, or unscattered, solar component and the diffuse illumination from the atmosphere itself due to thermal emission and scattering in order to simplify their solutions as will be shown in Sections 6.2.4 and 6.2.5. Formally, the radiance from the volume element is written as

$$L^{\uparrow}(\tau, \hat{\omega}) = L_b^{\uparrow}(\tau, \hat{\omega}) + L_d^{\uparrow}(\tau, \hat{\omega}) \quad (6.30)$$

$$L^{\downarrow}(\tau, \hat{\omega}) = L_s^{\downarrow}(\tau, \hat{\omega}) + L_d^{\downarrow}(\tau, \hat{\omega}), \quad (6.31)$$

where $L_s^{\downarrow}(\tau, \hat{\omega})$ is the direct solar illumination from above, $L_b^{\uparrow}(\tau, \hat{\omega})$ is the direct solar illumination from below due to reflection from the surface or boundary, and $L_d^{\uparrow}(\tau, \hat{\omega})$ and $L_d^{\downarrow}(\tau, \hat{\omega})$ are the diffuse radiance terms for the upper and lower hemispheres respectively. The wavelength dependence has been suppressed here, and will continue to be throughout the discussion that follows to avoid an even more cumbersome notation, but it is understood that the spectral radiance is the quantity of interest.

6.2

General Solution to the Radiative Transfer Equation

The solutions to (6.28) and (6.29) are obtained by separating the radiation field into the various contributors. The full solution is only obtained through computational methods; however, the problem is formulated through the identification of the various physical processes as separate terms. Through this approach, the inherent complexity illustrated by the different contributions to the at-aperture radiance in Figure 6.1 is distilled to a relatively small number of physical phenomena that, while not easily calculated, are relatively simple to understand. Additionally, the different terms that are developed, such as the direct illumination and the scattering components, often correspond to the outputs of a radiative transfer code. In this section the various terms will be developed that govern each of the processes in Figure 6.1.

6.2.1

Direct Solar Illumination

The first term that contributes to the radiation field is direct illumination of the surface. The direct solar component is composed of collimated light, due to the large earth–sun distance, that reaches the earth with the resulting solar spectral radiance at the top of the atmosphere, written as

$$\begin{aligned} L_s^{\downarrow}(\tau = 0, \hat{\omega}_s) &= E_s \delta(\hat{\omega} - \hat{\omega}_s) \\ &= E_s \delta(\cos \theta - \cos \theta_s) \delta(\phi - \phi_s) \\ &= E_s \delta(\mu - \mu_s) \delta(\phi - \phi_s), \end{aligned} \quad (6.32)$$

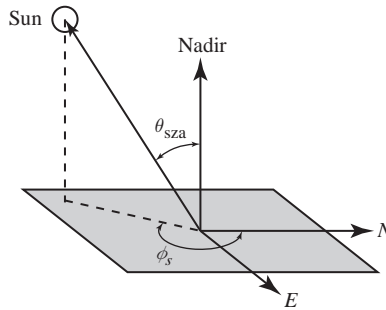


Figure 6.4 Solar geometry

where $\delta(\hat{\omega} - \hat{\omega}_s)$ is the Dirac delta function, E_s is the top of the atmosphere solar spectral irradiance and $\hat{\omega}_s$ is the direction of the collimated solar illumination, which is described using μ_s and ϕ_s coordinates. The solar zenith angle θ_{sza} , illustrated in Figure 6.4, is defined as the polar angle between the local normal vector, defined along the direction from the center of the earth to the point of interest, which may be a location on the surface or some point in the atmosphere, and the unit vector from the point of interest to the sun. The relevant angle used in μ to describe the atmospheric transmission is also illustrated and is equivalent to $\mu_s = \cos \theta_{sza}$. Figure 6.4 also shows the definition of the azimuthal angle ϕ_s .

The Dirac delta function, introduced in (6.32), is the mathematical method used to describe the physical situation of collimated light from the sun. It is written in its most basic form as $\delta(x)$, and is a function that is zero everywhere except in an infinitesimally narrow range about $x = 0$. Historically, the development of the delta function goes back to the work of Poisson, Fourier, Cauchy, Heaviside, and others, but the modern treatment was developed by Dirac (1958) and most rigorously by Schwartz (Lützen, 1982). Dirac introduced the delta function as

$$\int_{-\infty}^{\infty} \delta(x) dx = 1$$

$$\delta(x) = 0 \text{ for } x \neq 0 \quad (6.33)$$

with the property

$$\int_{-\infty}^{\infty} f(x) \delta(x) dx = f(0), \quad (6.34)$$

where $f(x)$ is a continuous function. Changing the origin of the delta function yields

$$\int_{-\infty}^{\infty} f(x) \delta(x - x_o) dx = f(x_o), \quad (6.35)$$

where x_o is any real number.

The delta function is adapted to the angular case, as already applied in (6.32), through

$$\delta(\hat{\omega} - \hat{\omega}_s) = \delta(\cos \theta - \cos \theta_s) \delta(\phi - \phi_s) \quad (6.36)$$

with the normalization given by

$$\int_0^{2\pi} \int_0^\pi \delta(\hat{\omega} - \hat{\omega}_s) \sin \theta \, d\theta \, d\phi = 1. \quad (6.37)$$

The integration is over the full hemisphere and, in this case, μ is defined as $\cos \theta$ rather than $|\cos \theta|$ since θ_{sza} is always between 0 and $\pi/2$. Note that (6.36) is different from what is obtained by starting in a three-dimensional Cartesian coordinate system and performing the transformation to a new coordinate system through the application of the Jacobian. The delta function is a dimensionless quantity, but the angular delta function will be regarded as having units of inverse steradians.

The attenuation of the top of the atmosphere solar radiance as it travels downward is given by (2.168). In the slab approximation, with the altitude described by the optical depth, the transmission is modified to be

$$T(\tau, \lambda) = e^{-\tau/\mu_s}, \quad (6.38)$$

where $\tau(z, \lambda) = \mu \tau_r(r_1, r_2, \lambda)$ has been used. The direct solar radiance at an optical depth τ is written as

$$L_s^\downarrow(\tau, \hat{\omega}_s) = E_s e^{-\tau/\mu_s} \delta(\hat{\omega} - \hat{\omega}_s) = E_s e^{-\tau/\mu_s} \delta(\mu - \mu_s) \delta(\phi - \phi_s) \quad (6.39)$$

and, if the optical depth is at the surface, τ is replaced with τ^* to signify transmission through the entire atmosphere.

6.2.2

Reflection and Emission from the Earth's Surface

Incident light interacts with the surface of the earth through reflection and absorption, and the earth emits radiance as well. In Chapter 2 it was shown that these processes are all interrelated through (2.71) and (2.72) with a point on the surface having a reflectance ρ and an emissivity ϵ . Also the reflectance can be characterized by the bidirectional reflectance distribution function $f_r(\theta_i, \phi_i; \theta_r, \phi_r)$ in units of sr^{-1} as introduced in Chapter 3. The BRDF will be used in the discussion that follows. The incident light at the boundary, as depicted in Figure 6.5, is due to direct solar radiance, thermal emission from the atmosphere, and the diffusely scattered radiance. The reflected light will subsequently travel through, and interact with, the atmosphere with some fraction reaching the volume element of interest.

The first term that will be considered is direct solar illumination of the boundary point associated with the direct line of site along $\hat{\omega}$ between the surface and the volume element. The solar radiance that reaches the surface, having travelled through the full atmosphere, is characterized by $L_s^\downarrow(\tau^*, \hat{\omega}_s)$. Applying the definition of the BRDF yields

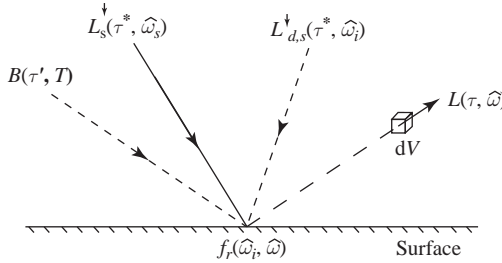


Figure 6.5 Reflectance of the various radiance terms that contribute to the radiance at dV . The finely spaced dashed lines correspond to diffuse radiance illuminating the surface.

$$\begin{aligned}
 L_{s,r}^\uparrow(\tau^*, \hat{\omega}) &= \int f_r(\hat{\omega}_i^\downarrow, \hat{\omega}^\uparrow) L_s^\downarrow(\tau^*, \hat{\omega}_s) \cos \theta_i d\omega_i \\
 &= E_s e^{-\tau^*/\mu_s} \int_0^{2\pi} \int_0^1 f_r(-\mu_i, \phi_i; \mu, \phi) \delta(\mu_i - \mu_s) \delta(\phi_i - \phi_s) \mu_i d\mu_i d\phi_i \\
 &= E_s e^{-\tau^*/\mu_s} f_r(-\mu_s, \phi_s; \mu, \phi) \mu_s,
 \end{aligned} \tag{6.40}$$

where $\hat{\omega}^\uparrow$ (or $\hat{\omega}$) is in the direction of interest, i.e. within the sensor field of view, and $\hat{\omega}_i^\downarrow$ is the downward illumination direction. The minus sign multiplying μ_s is due to definition of μ as applied to the BRDF. It is understood that the BRDF here, and in the discussion that follows, is at the appropriate surface coordinate.

Unlike the direct solar radiance, both the atmospheric thermal emission and the scattered radiance into the downward hemisphere have a broad angular distribution so that a given point on the surface is illuminated from a variety of directions. These two sources will be combined into the diffuse radiation field, $L_d^\downarrow(\tau^*, \hat{\omega}_i)$, illuminating the surface. It was assumed in (6.10) that thermal emission is isotropic and, additionally, it is attenuated with the degree depending upon the emission point in the atmosphere. The thermal emission reflected from the surface is therefore given by

$$\begin{aligned}
 L_{t,r}^\uparrow(\tau^*, \hat{\omega}) &= \int_0^{\tau^*} \int_{\omega_i} [1 - \tilde{\omega}(\tau')] B(\tau', T) e^{-(\tau^* - \tau')/\mu_i} \times \\
 &\quad f_r(\hat{\omega}_i^\downarrow, \hat{\omega}^\uparrow) \cos \theta_i d\omega_i \frac{d\tau'}{\mu_i},
 \end{aligned} \tag{6.41}$$

with the attenuation occurring from the emission point, τ' , to the surface. The diffusely scattered downward radiance at the boundary, $L_{d,s}^\downarrow(\tau^*, \hat{\omega}_i)$, is developed from the scattering portion of (6.27) yielding

$$\begin{aligned}
 L_{d,s}^\downarrow(\tau^*, \hat{\omega}_i) &= \int_0^{\tau^*} \tilde{\omega}(\tau') \left[\int_{\uparrow} \frac{p(\tau', \hat{\omega}_o^\uparrow, \hat{\omega}_i^\downarrow)}{4\pi} L^\uparrow(\tau', \hat{\omega}_o) d\omega_o \right. \\
 &\quad \left. + \int_{\downarrow} \frac{p(\tau', \hat{\omega}_o^\downarrow, \hat{\omega}_i^\downarrow)}{4\pi} L^\downarrow(\tau', \hat{\omega}_o) d\omega_o \right] e^{-(\tau^* - \tau')/\mu_i} \frac{d\tau'}{\mu_i},
 \end{aligned} \tag{6.42}$$

with the attenuation occurring from the scattering location to the surface. Note that the radiance at the scattering points can be due to either direct or diffuse illumination, the latter due to scattering from other points in the atmosphere. Theoretically, it could also be due to thermal illumination although in all the cases considered here this contribution is vanishingly small and will be neglected. The directional dependence of the upward-reflected diffuse radiance is defined by the reflective surface properties through

$$L_{d,s,r}^{\uparrow}(\tau^*, \hat{\omega}) = \int f_r(\hat{\omega}_i^{\downarrow}, \hat{\omega}^{\uparrow}) L_{d,s}^{\downarrow}(\tau^*, \hat{\omega}_i) \cos \theta_i d\omega_i, \quad (6.43)$$

where the integration is over all the possible incident angles. The scattered component of the diffuse radiation field at the surface, $L_{d,s}^{\downarrow}(\tau^*, \hat{\omega}_i)$, has contributions from the entire hemisphere centered on the point of reflection, and its calculation requires knowledge of the aerosol and molecular distributions as a function of altitude and the associated phase functions.

The surface will also emit radiance due to its temperature given by

$$L_e^{\uparrow}(\tau^*, \hat{\omega}) = \epsilon(\hat{\omega}^{\uparrow}) B(T_b), \quad (6.44)$$

where T_b is the boundary temperature. As was shown in Chapter 2, the surface emissivity has a directional dependence that is related to the reflectance through (2.71) and (2.72).

Additional radiance in the $\hat{\omega}$ direction will be contributed by light reflected from various points on the surface and then scattered into the line of site as shown in Figure 6.6. This requires that the specification of the BRDF for each location on the surface. The scattered radiance therefore depends upon the surface location where the reflectance occurs, the attenuation between the reflectance point and the scattering point, and the scattering phase function at the scattering point. The boundary radiance is modified to reflect the variety of possible angles of reflection as captured by the local BRDF, and then (6.14) is applied. The resulting source function is

$$S_b^{\uparrow}(\tau', \hat{\omega}) = \tilde{\omega}(\tau') \int_{\uparrow} \frac{p(\tau', \hat{\omega}_o^{\uparrow}, \hat{\omega}^{\uparrow})}{4\pi} [L_{s,r}^{\uparrow}(\tau^*, \hat{\omega}_o) + L_{d,r}^{\uparrow}(\tau^*, \hat{\omega}_o) + L_e^{\uparrow}(\tau^*, \hat{\omega}_o)] e^{-(\tau^* - \tau')/\mu_o} d\omega_o, \quad (6.45)$$

where $\hat{\omega}_o$ is the ensemble of possible reflectance angles into the upper hemisphere, τ' is the optical depth at which the scattering into $\hat{\omega}$ occurs, and the exponential term is the

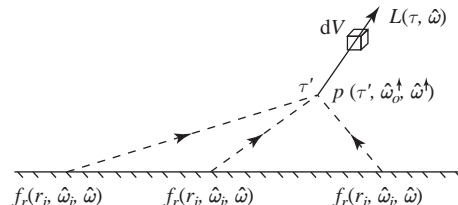


Figure 6.6 Rays that are reflected from various points r_i on the surface and scattered at an optical depth τ' into dV along $\hat{\omega}$.

attenuation between the point on the surface where reflection occurs and the scattering location. Also $L_{d,r}^{\uparrow}(\tau^*, \hat{\omega}_o)$ is given by $L_{t,r}^{\uparrow}(\tau^*, \hat{\omega}_o) + L_{d,s,r}^{\uparrow}(\tau^*, \hat{\omega}_o)$.

The range of possible values for $\hat{\omega}_o$ depends upon the details of the local BRDF. For example, scattering into the $\hat{\omega}$ direction occurring at a certain height above the surface, specified by the corresponding optical depth τ' , will be due to radiance from the boundary points where there is appreciable reflectance. This limits the range of locations across the surface, and therefore the possible values of $\hat{\omega}_o$ that will contribute radiance at that scattering point. The challenge is to solve the radiative transfer equation to yield values for the different radiance contributions (solar, thermal, diffuse, and emitted) at all of the scattering points that contribute. To do this very precisely requires detailed knowledge of the variation in the BRDF across the surface.

The scattering case just described can be generalized to the situation where light is repeatedly reflected and scattered back and forth between the atmosphere and the surface until it is scattered into the volume of interest in the $\hat{\omega}$ direction. This would also include a single reflection followed by multiple scattering, or multiple reflections with multiple scattering occurring between reflections. In theory, one could iteratively apply the local BRDFs and the scattering phase functions to describe these effects. How this is practically accomplished will be presented in Section 6.4, where atmospheric compensation is addressed.

6.2.3

The Atmospheric Path Upward Source Terms

The path between the boundary and dV will also contribute radiance, through scattering and thermal emission, that is attenuated as it travels upward. Each point along the line connecting the surface to the volume element will be illuminated by direct solar and diffuse radiance that has not interacted with the surface, with some fraction being scattered into the direction $\hat{\omega}$. The atmosphere will also emit radiance due to its temperature given by $[1 - \tilde{\omega}(\tau')]B(\tau')$ for the particular optical depth τ' . All of these are source terms for the radiative transfer equation.

The two scattered light source terms that have not been reflected by the surface are

$$\begin{aligned} S_s^{\uparrow}(\tau', \hat{\omega}) &= \tilde{\omega}(\tau') \int_{\uparrow} \frac{p(\tau', \hat{\omega}_o^{\downarrow}, \hat{\omega}^{\uparrow})}{4\pi} L_s^{\downarrow}(\tau', \hat{\omega}_o) d\omega_o \\ &= \frac{\tilde{\omega}(\tau')}{4\pi} E_s e^{-\tau'/\mu_s} \int_{\uparrow} p(\tau', \hat{\omega}_o^{\downarrow}, \hat{\omega}^{\uparrow}) \delta(\hat{\omega}_o - \hat{\omega}_s) d\omega_o \\ &= \frac{\tilde{\omega}(\tau')}{4\pi} E_s e^{-\tau'/\mu_s} p(\tau', \hat{\omega}_s^{\downarrow}, \hat{\omega}^{\uparrow}) \end{aligned} \quad (6.46)$$

for the direct solar, where (6.39) has been used, and

$$\begin{aligned} S_d^{\uparrow}(\tau', \hat{\omega}) &= \tilde{\omega}(\tau') \int_{\uparrow} \frac{p(\tau', \hat{\omega}_o^{\downarrow}, \hat{\omega}^{\uparrow})}{4\pi} L_d^{\uparrow}(\tau', \hat{\omega}_o) d\omega_o \\ &+ \tilde{\omega}(\tau') \int_{\downarrow} \frac{p(\tau', \hat{\omega}_o^{\downarrow}, \hat{\omega}^{\uparrow})}{4\pi} L_d^{\downarrow}(\tau', \hat{\omega}_o) d\omega_o \end{aligned} \quad (6.47)$$

for the diffuse term where τ' is between τ^* and τ at the point of interest. Equations (6.46) and (6.47) have a simple interpretation. The first represents single scattering of the direct solar illumination while the second equation describes multiple scattering due to the diffuse radiation field. The first term is the source of the second.

6.2.4 The Total Upward Radiance

The stage has been set to solve the one-dimensional radiative transfer equation, (6.28), for the total upward radiance $L_\lambda^\uparrow(\tau, \hat{\omega})$ from the volume of interest. The various source terms for upward radiance from dV have been derived and are collected here yielding

$$S^\uparrow = (1 - \tilde{\omega})B + S_s^\uparrow + S_d^\uparrow + S_b^\uparrow, \quad (6.48)$$

where the first term is the thermal emission of the atmosphere, the second term is the scattered direct solar radiance, the third term is the scattered diffuse radiance, and the final term is the scattered radiance that has interacted with the boundary. The radiance will be separated into two components: the portion that is reflected or emitted from the surface directly to the volume element without scattering, and the diffuse radiance $L_d^\uparrow(\tau, \hat{\omega})$. The direct boundary component is

$$L_b^\uparrow(\tau, \hat{\omega}) = [L_{s,r}^\uparrow(\tau^*, \hat{\omega}) + L_{d,r}^\uparrow(\tau^*, \hat{\omega}_o) + L_e^\uparrow(\tau^*, \hat{\omega})]e^{-(\tau^* - \tau)/\mu}, \quad (6.49)$$

where the attenuation from the surface to the volume element has been applied.

Equation (6.28) is now rewritten as

$$-\mu \frac{dL_b^\uparrow}{d\tau} - \mu \frac{dL_d^\uparrow}{d\tau} = -L_b^\uparrow - L_d^\uparrow + (1 - \tilde{\omega})B + S_s^\uparrow + S_d^\uparrow + S_b^\uparrow, \quad (6.50)$$

which are all functions of τ and $\hat{\omega}$. After rewriting (6.49) as

$$L_b^\uparrow(\tau, \hat{\omega}) = L_b^\uparrow(\tau^*, \hat{\omega})e^{-(\tau^* - \tau)/\mu}$$

for simplicity, it is left to the reader to show that

$$-\mu \frac{dL_b^\uparrow}{d\tau} = -L_b^\uparrow. \quad (6.51)$$

Then (6.50) reduces to

$$\begin{aligned} -\mu \frac{dL_d^\uparrow}{d\tau} &= -L_d^\uparrow + (1 - \tilde{\omega})B + S_s^\uparrow + S_d^\uparrow + S_b^\uparrow \\ &= -L_d^\uparrow + S^\uparrow, \end{aligned} \quad (6.52)$$

where the source terms have been grouped together. This differential equation is solved through the application of the integration factor $e^{-\tau/\mu}$ yielding

$$-\mu \frac{dL_d^\uparrow}{d\tau} e^{-\tau/\mu} + L_d^\uparrow e^{-\tau/\mu} = -\mu \frac{d}{d\tau} (L_d^\uparrow e^{-\tau/\mu}) = S^\uparrow e^{-\tau/\mu}$$

or

$$\frac{d}{d\tau} (L_d^\uparrow e^{-\tau/\mu}) = -\frac{S^\uparrow}{\mu} e^{-\tau/\mu}, \quad (6.53)$$

which is integrated over the optical depth from the surface to the point of interest. Performing the integration

$$\int_{\tau^*}^{\tau} \frac{d}{d\tau'} (L_d^{\uparrow} e^{-\tau'/\mu}) d\tau' = - \int_{\tau^*}^{\tau} \frac{S^{\uparrow}}{\mu} e^{-\tau'/\mu} d\tau'$$

yields

$$L_d^{\uparrow}(\tau, \hat{\omega}) = L_d^{\uparrow}(\tau^*, \hat{\omega}) e^{-(\tau^* - \tau)/\mu} + \int_{\tau}^{\tau^*} \frac{S^{\uparrow}(\tau', \hat{\omega})}{\mu} e^{-(\tau' - \tau)/\mu} d\tau', \quad (6.54)$$

where the first term is the contribution from the diffuse light at the surface followed by atmospheric attenuation between τ^* and τ . The final form of the total upward radiance at dV is

$$\begin{aligned} L^{\uparrow}(\tau, \hat{\omega}) = & [L_{r,s}^{\uparrow}(\tau^*, \hat{\omega}) + L_{r,d}^{\uparrow}(\tau^*, \hat{\omega}) + \epsilon(\hat{\omega}^{\uparrow}) B(T_b)] e^{-(\tau^* - \tau)/\mu} \\ & + L_d^{\uparrow}(\tau^*, \hat{\omega}) e^{-(\tau^* - \tau)/\mu} + \int_{\tau}^{\tau^*} \frac{S^{\uparrow}(\tau', \hat{\omega})}{\mu} e^{-(\tau' - \tau)/\mu} d\tau' \end{aligned} \quad (6.55)$$

with the term in brackets describing the reflected radiance due to direct solar illumination, diffuse atmospheric illumination, and the surface thermal emission. The final term is the contribution from the source function described by (6.48), which is composed of scattering along the full path from the surface to the volume element, as well as scattering within the volume element itself.

Equation (6.55) merits some additional discussion. Knowledge of the source function and the atmospheric temperature as a function of optical depth is required to describe the diffuse radiation field at any point in the atmosphere. For example, the VNIR/SWIR diffuse radiation field, where atmospheric thermal emission can be neglected, is entirely determined by the scattering terms in the source function. Conversely, in the LWIR, thermal emission is the term of importance in (6.48) and the remaining components, all due to scattering, can often be neglected. Knowledge of the source function is also required to calculate $L_{r,d}^{\uparrow}(\tau^*, \hat{\omega})$, the reflected component from the diffuse radiation field at the surface. A tremendous amount of effort and ingenuity has been devoted to solving this problem in radiative transfer codes.

6.2.5

The Total Downward Radiance

The description of the downward radiation field at dV is produced through a similar analysis only the results presented here. The full development is left as an exercise for the reader. The source function for the downward radiance, analogous to (6.48), is

$$S^{\downarrow} = (1 - \tilde{\omega}) B + S_s^{\downarrow} + S_d^{\downarrow} + S_b^{\downarrow} \quad (6.56)$$

with the dependence on τ and $\hat{\omega}$ suppressed. Here $\hat{\omega}$ is an arbitrarily chosen downward direction of interest. An equation similar to (6.50) is derived yielding

$$\mu \frac{dL_s^\downarrow}{d\tau} + \mu \frac{dL_d^\downarrow}{d\tau} = -L_s^\downarrow - L_d^\downarrow + (1 - \tilde{\omega})B + S_s^\downarrow + S_d^\downarrow + S_b^\downarrow, \quad (6.57)$$

where L_s^\downarrow is the direct solar radiance given by (6.39) and each term has been appropriately modified for the downward case. For example, S_s^\downarrow is developed similarly to (6.46) to yield

$$S_s^\downarrow(\tau', \hat{\omega}) = \frac{\tilde{\omega}(\tau')}{4\pi} E_s e^{-\tau'/\mu_s} p(\tau', \hat{\omega}_s^\downarrow, \hat{\omega}^\downarrow) \quad (6.58)$$

for the scattered direct solar illumination at τ' .

Again, it can be shown that

$$\mu \frac{dL_s^\downarrow}{d\tau} = -L_s^\downarrow \quad (6.59)$$

so that (6.57) reduces to

$$\mu \frac{dL_d^\downarrow}{d\tau} = -L_d^\downarrow + S^\downarrow, \quad (6.60)$$

where the source terms have been combined. Equation (6.60) is solved using an integrating factor, in this case $e^{\tau/\mu}$, to yield

$$L_d^\downarrow(\tau, \hat{\omega}) = L_d^\downarrow(0, \hat{\omega}) e^{-\tau/\mu} + \int_0^\tau \frac{S^\downarrow(\tau', \hat{\omega})}{\mu} e^{-(\tau-\tau')/\mu} d\tau' \quad (6.61)$$

with the integration performed from the top of the atmosphere down to the τ . $L_d^\downarrow(0, \hat{\omega})$ is zero by definition, since there is no thermal emission or scattering at the top of the atmosphere. Finally, the total downward radiance at dV is

$$L^\downarrow(\tau, \hat{\omega}) = L_s^\downarrow(\tau, \hat{\omega}) + \int_0^\tau \frac{S^\downarrow(\tau', \hat{\omega})}{\mu} e^{-(\tau-\tau')/\mu} d\tau' \quad (6.62)$$

with the first term describing the direct illumination at τ and the second representing the contributions from thermal emission and scattering.

6.2.6 Summary

The basics of the theory of radiative transfer have been introduced, starting with the most general form of the radiative transfer equation (6.16), followed by the simplification to the slab geometry for a stratified atmosphere yielding the integro-differential equations (6.28) and (6.29). The radiative transfer processes outlined in Figure 6.1 are now connected to the theoretical terms in Figure 6.7. The formal solution to the one-dimensional problem was presented, which can be solved if the extinction coefficients, scattering phase functions, and temperature are known as a function of altitude. Additionally, the most accurate solution would include the details of the surface reflectance. Fortunately,

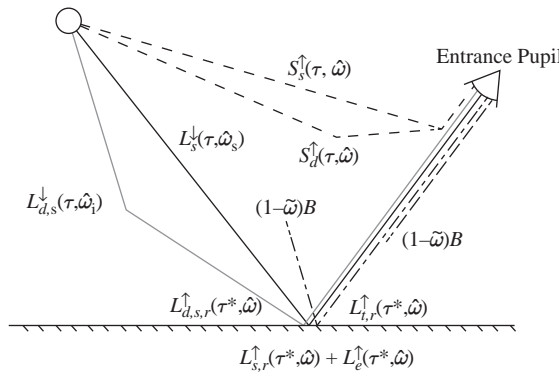


Figure 6.7 Identification of the atmospheric processes illustrated in Figure 6.1. The reflected direct component, indicated by the middle solid black line from the surface to the entrance pupil, is composed of both reflected direct solar radiance and the thermal emission of the surface itself. Each radiance term is also attenuated by Beer's law.

the spectroscopic information is available and continues to be improved, Rayleigh scattering has been extensively studied and is also well understood, and there are aerosol models that are based upon atmospheric measurements that likewise continue to be improved.

The actual solution of (6.28) and (6.29) relies upon numerical techniques that closely approach an exact solution. The discrete-ordinate method is an example of one of these methods where the angular dependence is separated into a large number of sub-angles or streams. The integrals involved in the source functions are approximated by finite sums whereby the radiative transfer equation is converted into a set of ordinary coupled differential equations and solved using numerical quadrature (Thomas and Stamnes, 1999). The presentation that follows culminates in the solution to the inverse problem where the spectral reflectance or temperature and spectral emissivity are retrieved, all of which rely upon an accurate solution to (6.28) and (6.29).

6.3

Modeling Tools of Radiative Transfer

The theoretical description for radiative transfer has been outlined, showing how the physical mechanisms of absorption, emission, and scattering impact the propagation of radiation through the atmosphere. Computationally there are two approaches that are most commonly used to solving the radiative transfer equation for the propagation of light: line-by-line models and band models. Both are *forward* models, where the aperture radiance is predicted based upon a set of known input parameters that include, for example, the known illumination and viewing geometries, a model atmosphere as discussed in Chapter 2, the amount of variable species such as water present, the aerosol types and distribution, the surface reflectance and emissivity, and so on. This is in contrast to *inverse* models that utilize data to derive the parameters that are the inputs to a forward radiative transfer model. These latter models are applied to perform atmospheric

compensation in order to estimate the parameters of interest, such as surface reflectance or emissivity and temperature.

Line-by-line models, particularly at wavelengths where scattering is negligible, perform monochromatic calculations of atmospheric transmission and emission as well as surface reflection and emission. These models are exact to within the knowledge of the spectroscopic properties of the molecular species present, but since the absorption coefficient often changes rapidly over a spectral range, many thousands of calculations may be required to model the transmission. More recently, techniques have been developed that also incorporate scattering. Line-by-line models have the advantage of being highly accurate, but tend to be computationally intensive.

Band models, on the other hand, are approximate solutions to the radiative transfer equations and rely upon an average transmittance for a spectral band. For monochromatic radiation propagating through different atmospheric slabs, the transmission is the product of the transmission through the individual slabs through Beer's law. For a band model the transmission is an average for a spectral band, since the distribution of extinction coefficients changes within the band as a function of molecular species and altitude, and therefore Beer's law does not hold. One approach to the solution to this problem is to reformulate the transmission calculation as a weighted sum of monochromatic calculations through the use of the correlated- k distribution method that is described in Section 6.3.2. The computation is much reduced in comparison to the line-by-line codes by sorting the k distribution into ascending order since the transmission within the band is independent of the spectral order.

These two types of forward models are important for the analysis of imaging spectrometer data in order to transform the data from at-aperture radiance to, in the VNIR/SWIR spectral range, surface reflectance spectrum, or to, in the LWIR spectral range, surface emissivity spectrum and temperature. The retrieved spectral signatures are subsequently utilized to fully characterize a scene and to detect and identify a material of interest. The application of an inverse model for spectral signature retrieval, as described in Sections 6.4 and 6.7, incorporates a forward model. The forward models employed are typically band models due to their computational efficiency although, if one were interested in retrieving, for example, information about the temperature profile of the atmosphere utilizing the edge of a strong absorption feature from a well-mixed species such as carbon dioxide, a line-by-line approach would potentially produce more accurate results. A few examples of the two forward models will be introduced in preparation for the description of the inverse models that play a critical role in the reduction of imaging spectrometer data to useful products.

6.3.1 Introduction to Line-by-Line Radiative Transfer Tools

The equations derived in Section 6.2 are used to calculate monochromatic radiance given a spectral absorption database that contains the spectroscopic information for each molecule encountered in the model atmosphere. As a concrete example consider a non-scattering atmosphere where the only processes are absorption and emission. in this case, using the upward radiance at an optical depth τ as an example, (6.55) reduces to

$$L^{\uparrow}(\tau, \hat{\omega}) = L_b(\tau^*, \hat{\omega})e^{-(\tau^*-\tau)/\mu} + \int_{\tau}^{\tau^*} \frac{B(\tau', T)}{\mu} e^{-(\tau'-\tau)/\mu} d\tau', \quad (6.63)$$

where the boundary radiance $L_b(\tau^*, \hat{\omega}) = L_{r,s}^{\uparrow}(\tau^*, \hat{\omega}) + \epsilon(\hat{\omega}^{\uparrow})B(T_b)$ with contributions from the reflected direct solar radiance and the surface emission. In this case the single-scattering albedo is zero.

The solution to (6.63) requires that the optical depth be known for each altitude from the surface to the sensor at a given wavelength. In this case, τ is given by

$$\tau(z_1, z_2; \lambda) = \int_{z_1}^{z_2} k_a(z, \lambda) dz \quad (6.64)$$

and the absorption coefficient at λ is

$$k_a(z, \lambda) = \sum_i^N S_i(\lambda_o, n_i) f_i(\lambda - \lambda_o, z) \quad (6.65)$$

where N is the number of different absorbers, $n_i(z)$ is the number density that must be known at every location along the optical path, and f_i is the line shape that also evolves as a function of altitude. By implication, the appropriate Einstein coefficients and degeneracies for each absorber with features centered at a particular λ_o , whose line shapes contribute to the absorption at λ , must also be known. An additional term that isn't included in (6.65) is the contribution to the absorption due to the water vapor continuum.

A line-by-line calculation is highly accurate but computationally intensive. If time is not a limitation and the best possible accuracy is desired, then they are the method of choice and are often used in atmospheric science but are of limited utility in remote sensing, where large volumes of imagery are collected under diverse conditions. They do play a very important role in the validation of the radiative transfer models that are used in imaging spectroscopy, in addition to comparisons to calibrated laboratory or atmospheric measurements under realistic conditions. Because the line-by-line approach does not take simplifying steps for a given model atmosphere to compute the extinction within the limit of the spectral resolution of the individual calculation, which can be vanishingly small, line-by-line radiative transfer models are able to capture both accuracy and precision at the cost of computational time. The accuracy is fundamentally limited by the database of the atmospheric molecules available to the line-by-line radiative transfer code. The global high-resolution molecular spectroscopy community exemplifies the open sharing of data to create widely available databases of molecular species spectral absorption features. An example is the HITRAN database that is highly validated, widely used, and freely available (Rothman, 2014). Each of the naturally occurring molecules in the earth's atmosphere have all of their spectroscopic properties as validated with measurements and detailed physical models captured in the extensive database.

The use of a database of molecular features to numerically solve the radiative transfer equation requires algorithms that efficiently use the spectral line information. An example of these algorithms is referred to as a line-by-line code where the contribution of each database “line” is systematically evaluated for the desired sample of wavelengths at the different optical depths as a function of temperature, absorber concentration, and pressure and therefore line broadening. For example, at high altitudes, where the pressure is low, the absorption features are much narrower when compared to the absorption feature from the same line at low altitude. The atmosphere is split into many slabs and the spectral sampling interval is determined by the highest layer since the absorption features are narrowest there.

Fast approaches have been developed to accomplish this computationally intensive task (Clough et al., 1981). The algorithm Line-By-Line Radiative Transfer Model (LBLRTM) is widely used for detailed studies on atmospheric radiative transfer due to its accuracy and computational efficiency (Alvarado et al., 2013). The detail and accuracy of the LBLRTM model has been validated by comparing model results to many different and varied calibrated atmospheric measurements, including the measurements from the US Department of Energy funded Atmospheric Radiation Measurement campaigns that have provided decades of high quality data (Clough et al., 2005). With extensive validation, the line-by-line calculations for a given atmospheric condition and point-to-point path is accepted as the standard for truth of a model atmosphere for the full radiative transfer expression of equations (6.28) and (6.29).

The inclusion of multiple scattering in line-by-line codes has proven to be challenging for computational reasons. Line-by-line codes calculate absorption and emission rigorously for an inhomogeneous atmosphere and at any spectral resolution, however small. The difficulty arises from the approach adopted in the design of the codes where the radiative transfer is calculated by integrating along the line of sight to obtain the radiance. This assumes that the source function is known, but it is clear from the development of the radiative transfer equation that the source function that includes scattering depends broadly upon the radiation field. Approaches have been developed to address this problem with relative computational efficiency (Moncet and Clough, 1997).

6.3.2 Band Models

As we have seen, the quantum mechanical description of atoms and molecules often yields many thousands of spectroscopic features over a spectral range, resulting in complex absorption and emission. Combining these processes with scattering can result in a very heavy computational burden when many broad-band calculations are needed. This gives rise to the need to create a band model to alleviate the detailed line-by-line calculations while maintaining acceptable accuracy. The solution to the radiative transfer equation over a band of width $\Delta\tilde{\nu}$, for example, is quite challenging given that the absorption can rapidly vary from being optically thin to thick, so the effective transmission is not achievable through a simple average of the extinction coefficients at the different wavelengths within the band used in Beer’s law. Band models address the

complex transmission process involving numerous lines within a band with a minimum number of parameters.

The band models that are used for imaging spectroscopy are known as narrow-band models where the Planck function and the unresolved component of the band itself are approximately constant. A band model calculation involves the average transmission within an interval given by

$$\langle T_b \rangle = \frac{1}{\Delta \tilde{\nu}} \int_{\tilde{\nu}_1}^{\tilde{\nu}_2} T(\tilde{\nu}) d\tilde{\nu}, \quad (6.66)$$

where the width of the interval is $\Delta \tilde{\nu} = \tilde{\nu}_2 - \tilde{\nu}_1$ and $T(\tilde{\nu})$ is the monochromatic transmission at wavenumber $\tilde{\nu}$. Note that we are switching notation here to avoid confusion since the symbol for the optical depth in the atmospheric physics community is τ , which is what we have been using for transmission. An important physical property that enables band models to be formulated is that the transmission of a mixture of gases is the product of the transmissions of the individual gas components (see Goody and Yung, 1989, for a discussion of the multiplicative property).

Band models have been approached by modeling the lines within a band as being equally spaced or as being randomly spaced. We will illustrate the concept using the random band model and limit the discussion to absorption. The underpinning of the random band model is that, for a random distribution of lines with an average of N lines per spectral interval, the probability p of a single, randomly placed line in the full band $\Delta \tilde{\nu}$ being present in an infinitesimal range $d\tilde{\nu}$ is $p = d\tilde{\nu}/N\delta$, where δ is the average distance between lines given by $\delta = \Delta \tilde{\nu}/N$. The statistical distribution that applies in this case is a Poisson distribution. The motivation for a random selection of lines is that atmospheric absorbers such as water have a complex absorption spectrum that can be approximated as a random distribution of lines. Goody and Yung (1989) provide a lengthy description of band models for the interested reader, and what follows is a brief outline based on their treatment and that in Thomas and Stamnes (1999).

The transmission within a band $\Delta \tilde{\nu}$ is assumed to be due to N uncorrelated lines so that the transmission from each one can be computed separately and the multiplicative property applied. The total average transmission is therefore just the multiple of the transmissions from each individual line or

$$\langle T_b \rangle = \langle T_1 \rangle \langle T_2 \rangle \cdots \langle T_N \rangle = \left[\frac{1}{\Delta \tilde{\nu}} \int_{\Delta \tilde{\nu}}^{\infty} p(S) e^{-k_a(\tilde{\nu})u} dS d\tilde{\nu} \right]^N, \quad (6.67)$$

where $p(S)$ is the continuous distribution function of the line strengths within the band. In this case the absorption coefficient is defined as

$$k_a(\tilde{\nu}) \equiv -\frac{1}{\rho L_{\tilde{\nu}}} \frac{dL_{\tilde{\nu}}}{dr}, \quad (6.68)$$

where k_a is the mass absorption coefficient, typically in units of square meters per kilogram, and ρ is the density. The mass path is defined as

$$M = \int \rho(r) dr \Rightarrow u = \int \rho(z) dz, \quad (6.69)$$

which is expressed as u in the slab approximation. From the line shape discussion in Chapter 2, the absorption coefficient is related to the line strength through $k_a = Sf(\tilde{v} - \tilde{v}_o)$ and S is appropriately modified to be consistent with (6.68). Goody and Yung (1989) discuss the different analytical distribution functions that are used to describe the fraction of lines with line strengths between S and $S + dS$ within a spectral range; for our purposes it is sufficient to note that the distribution of line strengths within a band can be modeled.

The individual line transmittances in (6.67) are related to the absorptances through $\alpha_i(\tilde{v}) = 1 - T_i(\tilde{v})$ the i th species. Over the band the individual line strengths often vary substantially. Consider a large number of lines with absorption coefficients α_i with their distribution within the band described by $p(S)$. The average absorptance is

$$\langle \alpha_b \rangle = \frac{1}{\Delta \tilde{v}} \int_0^{\infty} \int_{\Delta \tilde{v}} p(S) [1 - e^{-k_a(\tilde{v})u}] dS d\tilde{v}, \quad (6.70)$$

where the N lines within the band have an average separation δ . Applying (6.70) to (6.67) yields

$$\langle T_b \rangle = \left[1 - \frac{\langle \alpha_b \rangle}{N} \right]^N = e^{-\langle \alpha_b(u) \rangle} \quad (6.71)$$

in the limit of the number of lines going to infinity and where the normalization $\int_0^{\infty} p(S) dS = 1$ has been applied. The bottom line is that the transmission of a large number of uncorrelated randomly placed lines is equal to the negative exponential of the average absorptance (Thomas and Stamnes, 1999).

There are multiple band models which have been developed to reduce the computational complexity while maintaining an acceptable level of accuracy and precision. The effects of atmospheric pressure broadening are described by scaling the absorber amount with pressure and applying the appropriate lineshape. This single-parameter scaling was widely used in early atmospheric work and continues to be used when simple parameterizations for radiative transfer modeling are needed. Although this approach is often adequate for modeling the troposphere over limited absorber and pressure ranges, it can lead to large errors when applied to the lower pressure regions of the stratosphere and upper troposphere. Two-parameter scaling methods such as the Curtis–Godson approximation (Curtis, 1952; Godson, 1953) have been frequently used in radiative transfer calculations and have produced accurate results in most situations. However, the inverse pressure-concentration distribution of atmospheric ozone is difficult to model using two-parameter scaling methods.

Correlated- k

The correlated- k distribution has emerged as a commonly used band model that is able to closely match the detailed line-by-line calculations with acceptable accuracy under many normal situations encountered in hyperspectral applications. The method involves

grouping the strength of absorption coefficients within a given frequency interval to produce a distribution of absorption that requires far fewer points, or subintervals, to represent the spectral absorption than is required for line-by-line calculations. Once the coefficients have been regrouped the integration over the spectrum is over a smooth function as opposed to the native line spectrum. We follow the development and examples from Lacis and Oinas (1991), an early and seminal work for the description of the correlated- k band model based on Goody and Yung (1989).

Consider the spectral interval of 1510 to 1520 cm^{-1} at two different atmospheric pressures and temperatures of 10 mbar at 240 K and 1 bar at 296 K, respectively, representative of two different layers within the earth's atmosphere. The monochromatic dependence in (6.20), expressed here in wave number rather than wavelength, is reconsidered since band models employ bins of finite widths. As a result the absorption optical depth is rewritten as

$$\tau(z_1, z_2, \tilde{\nu}_1, \tilde{\nu}_2) = \int_{\tilde{\nu}_1}^{\tilde{\nu}_2} \int_{z_1}^{z_2} k_a(z, \tilde{\nu}) \, dz \, d\tilde{\nu}, \quad (6.72)$$

with the integration over the bin width. The absorption coefficient spectra for the two atmospheric pressures and temperatures are given in Figure 6.8. The figures in this section are based on those presented in Lacis and Oinas (1991) but have been updated using the current HITRAN database (Rothman et al., 2013).

As can be seen from Figure 6.8, k_a is a highly repetitive function of wave number so computational efficiency is gained by replacing the integration over wave number with a reordered grouping of spectral sub-intervals with similar absorption coefficient

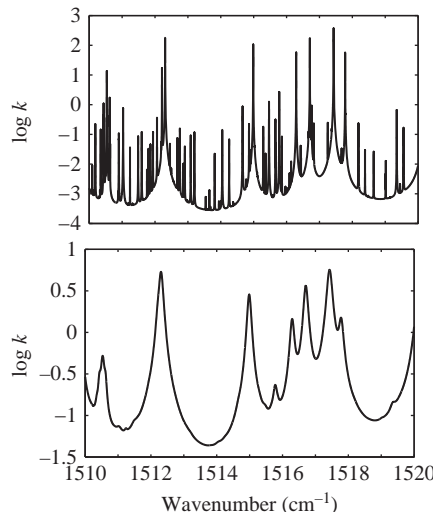


Figure 6.8 High-resolution absorption coefficient spectra for a high-altitude pressure of 10 mbar and temperature of 240 K (upper graph) and for a sea-level pressure of 1 bar and temperature of 296 K (lower graph).

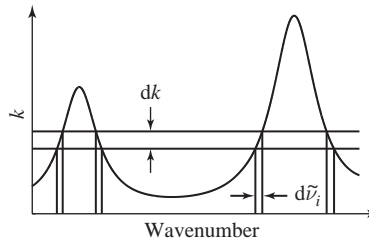


Figure 6.9 Illustration of the k -binning procedure. The slope for each section within dk is summed according to (6.73).

strengths k_i . We divide the absorption coefficient range into a suitable number of sub-intervals or bins of width Δk_i . A large number of sub-intervals may be required to resolve the absorption coefficient spectrum. The frequency distribution $f(k)$ is obtained directly from the absorption coefficient spectrum by binning and summing wavelength sub-intervals $\Delta \tilde{\nu}_i$, which have absorption coefficient strengths within a specified range between k_i and $k_i + \Delta k_i$ so that

$$f(k_i) = \frac{1}{\tilde{\nu}_2 - \tilde{\nu}_1} \sum_j^M \left| \frac{\Delta \tilde{\nu}_j}{\Delta k_i} \right| W(k_i, k_i + \Delta k_i) \quad (6.73)$$

where $W(k_i, k_i + \Delta k_i)$ is a “window” function that is zero everywhere except in the interval between k_i and $k_i + \Delta k_i$, where it is equal to unity. The procedure is to divide the absorption coefficient spectrum into monotonically increasing or decreasing sections and then to sum the slopes over an appropriately narrow k_a interval as illustrated in Figure 6.9. The absolute value is included so that any change in slope in the sum is ignored.

Figure 6.10 is the resulting frequency distribution $f(k)$ for the spectral absorption coefficients of Figure 6.8. The spikes arise from local maxima and minima in the k_a spectrum, where small changes in Δk_i are associated with large changes of wave number subintervals $\Delta \tilde{\nu}_k$ causing apparent discontinuities. The characteristic $k^{-3/2}$ slope of Figure 6.10 arises from the low-pressure Lorentz wing absorption where the absorption lines become increasingly narrow and constitute a tiny fraction of the total spectral interval, which is otherwise filled by the absorption of the wings.

Due to the presence of spikes in Figure 6.10, it is more convenient to express the absorption coefficient strength distribution in terms of a cumulative frequency distribution

$$g(k_n) = \sum_{i=1}^n f(k_i) \Delta k_i, \quad (6.74)$$

where $g(k_n)$ for the frequency distributions of Figure 6.10 are provided in the upper graph in Figure 6.11. Because the wave number distribution is normalized over the given interval $\Delta \tilde{\nu}$, the cumulative frequency distribution increments, $\Delta g_i = f(k_i) \Delta k_i$, define the fraction of the interval for which the absorption coefficient k_a is between k_i and $k_i + \Delta k_i$. The distribution $g(k_n)$ ranks k from weakest ($g(k_n) = 0$) to strongest ($g(k_n) = 1$).

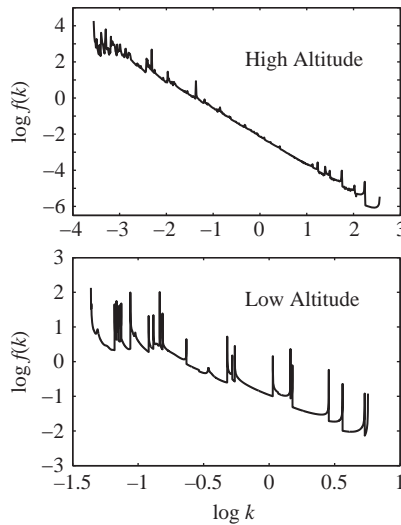


Figure 6.10 Absorption coefficient frequency distribution corresponding to absorption spectra of Figure 6.8.

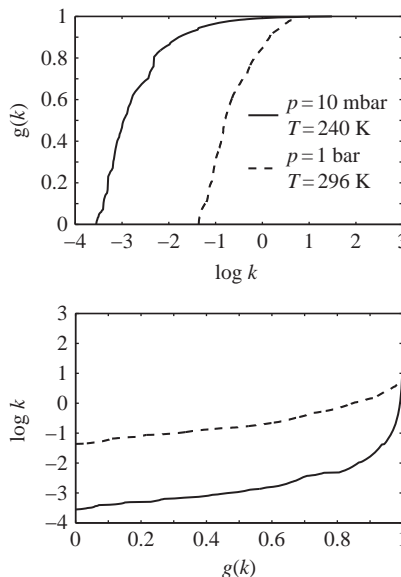


Figure 6.11 The upper graph is the cumulative frequency distribution of the absorption coefficient spectra of both graphs in Figure 6.8 and the lower graph is the corresponding k distribution.

1) for a given layer and band. The cumulative frequency distribution does not have the discontinuities and is thus more amenable to numerical computation. The inverse of the cumulative frequency distribution is obtained from (6.74) by

$$k_n(g) = g^{-1}(k_n). \quad (6.75)$$

The inverse of the cumulative frequency distribution, $k(g)$ is defined as the k distribution. By comparing the k distribution in the lower curve of Figure 6.11 to the two atmospheric condition absorption spectra of Figure 6.8, the reader can see that the abscissas of the graph have been normalized for the k distribution but the aggregate absorption over the entirety of the band has been reordered but otherwise preserved and re-rendered in a smooth and therefore more manageable function. The k distribution can now be closely approximated by an appropriate polynomial such as rendered by Malkmus (1967). It is not within the scope of this book to detail the myriad ways a k distribution can be approximated with increasing accuracy but the interested reader is encouraged to review the references cited thus far and Berk et al. (1998).

Just as the spectral distribution changes slowly with pressure and temperature so that the absorption spectra through neighboring atmospheric layers is highly correlated, so too is the k distribution strongly correlated in adjoining atmospheric layers. This correlation persists through most of the well-mixed atmosphere and is the origin of the correlated- k distribution. Importantly, within the dominant absorption region of the lower atmosphere, which is characterized by pressure broadening, the monotonically ordered absorption sub-intervals do not change order from one layer to the next. Said differently, the specific rank-ordered location of any given spectral sub-interval is constant between atmospheric layers providing the layers are dominated by pressure spectral broadening rather than Doppler broadening.

The physical understanding that has been developed for this section describing the correlated- k band model is the approach used broadly in radiative transfer codes such as MODTRAN®. There are various implementations of the correlated- k method, but the basic approach described here is well established. For example, the presentation here utilizes a Lorentzian line shape to model the k distribution, which has been modified using a Padé approximation to model the absorption line tails (Berk et al., 2008). Band models are validated against both accurate atmospheric measurements and in comparison to line-by-line models and have been demonstrated to be highly accurate and are relatively computationally efficient.

Optimal Spectral Sampling (OSS)

Another similar approach to band modeling that is able to achieve a high degree of accuracy is known as Optimal Spectral Sampling (OSS) (Moncet et al., 2008). OSS has been designed specifically for the modeling of radiances measured by sounding radiometers in the infrared and has been extended to the microwave, visible, and ultraviolet spectrum. It is particularly well suited for remote sensing applications and for the assimilation of satellite observations in numerical weather prediction models. The OSS approach is an extension of the exponential sum fitting of transmittances technique in that channel-average radiative transfer is obtained from a weighted sum of monochromatic calculations as accomplished in line-by-line approaches.

The fact that OSS is fundamentally a monochromatic method provides the ability to accurately treat surface reflectance and spectral variations of the Planck function and surface emissivity within the channel passband, given that the proper training is

applied. In addition, the method is readily coupled to multiple scattering calculations, an important factor for treating sensor data with radiances from clouds.

Where a correlated- k distribution relies on the detailed band calculations of sufficiently fine sub-intervals being rank-ordered, OSS is accomplished by selecting representative spectra from within the band to be modeled which span the absorption range and training the selected spectral weighting function to mimic that of the full line-by-line calculations over the range of anticipated atmosphere. Because the training process is computationally complex, this band model works very well for rapid calculations for fixed bands. The National Oceanographic and Atmospheric Administration employs OSS band model calculations extensively for well-established and fixed-spectral operational channels because of the speed and accuracy that can be attained once training is complete. OSS is less well suited for applications when the spectral channels are not firmly determined as when spectral calibration calculations are being made.

Other Band Models

There are other spectral atmospheric band models beyond those presented. Second Simulation of a Satellite Signal in the Solar Spectrum (6S) has been developed and is an accurate radiative transfer model for most applications (Vermote et al., 1997). Additional models include such methods as: invariant imbedding; stream approximations and moments of intensity; Monte Carlo techniques; and Gauss-Seidel iteration schemes (see Herman et al., 1994, and internal references).

6.4

Reflective Atmospheric Compensation

In this section we use the radiative transfer formalism developed in Section 6.1 to perform the inversion from at-aperture radiance to reflectance for every spatial sample within a scene. This is the process known alternatively as *atmospheric compensation* or *atmospheric correction*. The radiance data are used to determine the atmospheric parameters, such as the amount of absorbing molecular species that vary in the atmosphere (water and ozone, for example), and the aerosol loading or visibility. A radiative transfer code, such as MODTRAN® or another numerical solution to the radiative transfer equation, is then applied to model the atmosphere, with the resulting model used to perform the radiance to reflectance conversion.

Shortwave atmospheric compensation has been developed for use in the reflective portion of the spectrum from about 375 nm to 2500 nm. In this spectral range, thermal emission from the atmosphere and the surface can be neglected without deleterious effects. One of the underlying assumptions is that the reflective properties of the surface are approximately Lambertian over a limited range of viewing and illumination angles. This is a better assumption than one might think, since rough surfaces tend to approximate Lambertian behavior. A good rule of thumb is that many natural surfaces are Lambertian for viewing angles up to 40° from the surface normal. If a desert or snow is being viewed, the angle can be extended by an additional 10° to 20° (Slater, 1980).

When the scene has extensive topographic variation, such as a mountainous region, the formalism developed here, which assumes an approximately flat surface, will fail and the standard atmospheric compensation product should be used with caution (Smith et al., 1980).

The theory that is applied in the inverse modeling has a long history going back at least to the work of Subrahmanyam Chandrasekhar (Chandrasekhar, 1960). The forms of the inversion equation developed here are presented in a variety of sources in the literature. A good place to start for the reader to gain a comprehensive understanding is Tanre et al. (1979), Kaufman and Sendra (1988), Miesch et al. (2005) and the references therein.

6.4.1 Apparent Reflectance

A useful concept is the apparent reflectance ρ_a , which is also known as the top-of-the-atmosphere reflectance. Consider the radiance recorded from a particular spatial pixel that is illuminated by direct solar radiance given by (6.32) as if there were no intervening atmosphere. Recall from Chapter 3 that, for a Lambertian reflector, the isotropic radiance reflected from a surface point is related to the irradiance through

$$L = \frac{E\rho}{\pi}, \quad (6.76)$$

where E is the irradiance illuminating the surface and ρ is the reflectance. The irradiance at the point due to solar illumination is calculated using (2.54) and (6.32) or

$$\begin{aligned} E(\tau = 0, \hat{\omega}) &= \int L_s(\tau = 0, \hat{\omega}_s) \cos \theta \, d\omega \\ &= E_s \int_0^{2\pi} \int_{-1}^1 \delta(\mu - \mu_s) \delta(\phi - \phi_s) \mu \, d\mu \, d\phi \\ &= \mu_s E_s, \end{aligned} \quad (6.77)$$

where E_s is the solar irradiance at a unit area whose normal vector is parallel to the path from the center of the sun to the surface location. A more intuitive way of deriving the same result is to consider the flux at dA as illustrated in Figure 6.12. The flux at dA_s , the differential area element perpendicular to the line connecting the point and the

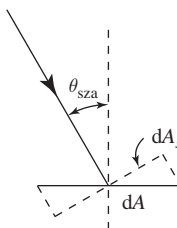


Figure 6.12 Projected area

sun, is the same as the flux at dA . The two differential elements are related through $dA_s = dA \cos \theta_{sza}$ and the flux is

$$d\Phi = E_s dA_s = E_s dA \cos \theta_{sza} = \mu_s E_s dA, \quad (6.78)$$

which reduces to (6.77) since $E = d\Phi/dA$. The apparent reflectance is therefore

$$\rho_a = \frac{\pi L}{\mu_s E_s}, \quad (6.79)$$

where L is the radiance recorded by the imaging spectrometer and E_s , which is tabulated at the average earth–sun distance of 1 AU, has been adjusted for the earth–sun distance for the particular date of the measurement through (2.63).

6.4.2 At-Aperture Radiance

The radiance that appears to originate at a particular spatial sample collected by the imaging spectrometer, designated as the viewed pixel within a particular IFOV, has contributions from a variety of sources. Foremost is the radiance due to reflected direct solar illumination, L_s , represented by the solid black ray in Figure 6.13, which corresponds to the first boundary term on the right side of (6.49). There is also additional radiance due to scattered light from the atmosphere that is composed of a variety of components. The most obvious is radiance given by the source terms (6.46) and (6.47) that is scattered, either singly or multiply, into the IFOV of the viewed pixel but has never interacted with the surface. This term is designated as the diffuse radiance L_d .

The scattered light that interacts with the surface is rather complex in its origins as was shown in Section 6.2.2. The simplest case is scattered light that has interacted with the viewed pixel and is reflected into the IFOV, which is described by the second boundary term on the right side of (6.49). This is designated as L_{av} , with the “a” for atmospheric scattering and the “v” for the viewed pixel. Scattered light can also interact with the

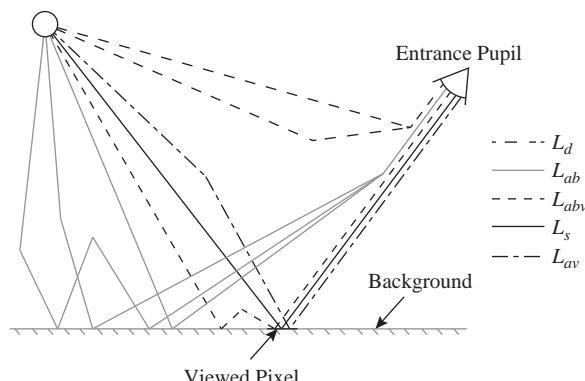


Figure 6.13 The various contributions to the at-aperture radiance. The different line patterns, which are offset for clarity, are representative of the variety of paths that rays travel before reaching the entrance pupil of the imaging spectrometer. Each term in (6.80) is identified to the right.

surrounding area and then be scattered into the IFOV without having interacted with the viewed pixel at all with the source function for the single scattering case given by (6.45). This scattered radiance, several examples of which are illustrated by the gray rays in Figure 6.13, is labeled L_{ab} , with the “b” referring to the background. There is also some scattered light that has interacted with both the viewed pixel and the surrounding background that is also collected in the IFOV, labeled L_{abv} . These last terms, L_{ab} and L_{abv} , constitute the adjacency effect where the radiance due to the spectral reflectance signature of the background is mixed with the radiance due to the viewed pixel reflectance signature.

The total at-aperture radiance that appears to originate at the viewed pixel is therefore

$$L_v = L_d + L_s + L_{av} + L_{ab} + L_{abv}, \quad (6.80)$$

with each term derived from (6.55) and modeled to extract the spectral reflectance signature of interest. Figure 6.14 provides some insight into the spectral behavior and the magnitudes of the different terms that compose (6.80) as a function of the solar zenith

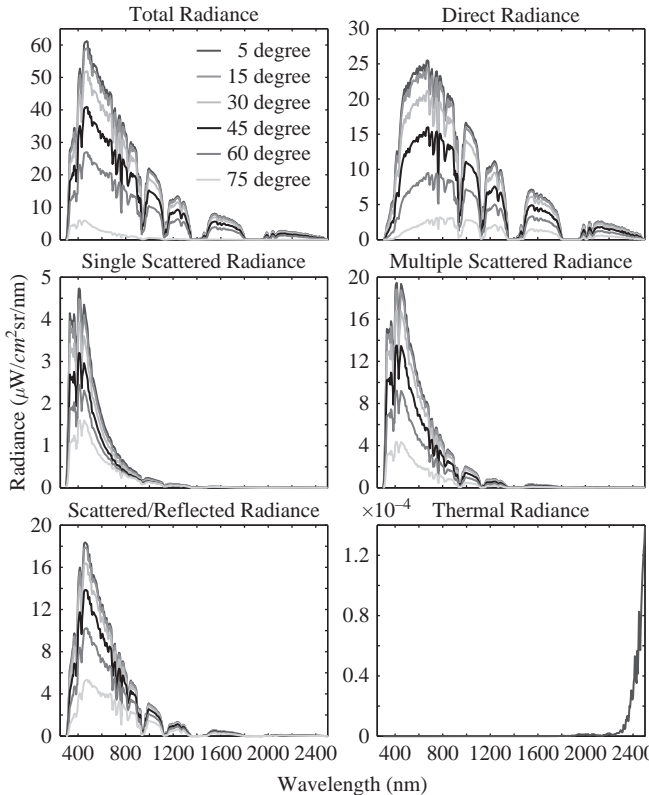


Figure 6.14 Contributions to the at-aperture radiance from the various sources in (6.80). The model radiances were generated using MODTRAN® with the visibility parameter, described in Section 6.5.3, set to 23 km. Radiance ($\mu\text{W}/\text{cm}^2\text{sr}/\text{nm}$)

angle for a space-based imaging spectrometer viewing a uniform Lambertian surface of unit reflectance from directly overhead. The total and the direct solar radiances, the upper two graphs corresponding to L_v and L_s in (6.80), vary by a factor of 10 for the range of different illumination angles. The middle two graphs illustrate the impact of scattered light that does not interact with the surface with the component from singly scattered light on the left and multiply scattered light on the right, which sum to L_d in (6.80). Notice the scale differences and the strongly peaked wavelength dependence with scattering becoming insignificant at wavelengths longer than about 1200 nm. The bottom-left graph shows that the radiance from scattered light that interacts with the surface is an important term for consideration, again at wavelengths shorter than 1200 nm. The final graph on the lower right demonstrates that thermal emission from the atmosphere is insignificant. Note that the surface does not contribute any radiance from thermal emission due to its unit reflectance.

6.4.3 Surface Irradiance

The irradiance that falls on the surface must be established in order to apply the Lambertian approximation to determine each of the terms in (6.80). First, the direct solar irradiance is calculated from (6.39) similar to the derivation of (6.77), and is designated E_s^* since the collimated radiance has passed through the entire atmosphere to an optical depth τ^* . This yields

$$E_s^* = \mu_s E_s e^{-\tau^*/\mu_s} = \mu_s E_s T_s, \quad (6.81)$$

where T_s is the direct transmission to the surface from (6.38). The top-of-the-atmosphere solar irradiance is known from measurements and solar models (see Labs and Neckel, 1968, and Thuillier et al., 2003, for subsequent updates) and the attenuation is calculated within the radiative transfer code using the appropriate extinction coefficient.

The diffuse irradiance E_{av} of the viewed pixel is related to E_s through the introduction of the diffuse solar transmission. First, E_{av} is derived from the downward diffuse radiance through

$$E_{av} = \int L_d^\downarrow(\tau^*, \hat{\omega}) \cos \theta_i d\omega_i, \quad (6.82)$$

where $L_d^\downarrow(\tau^*, \hat{\omega})$ is from (6.42) and the integration is over the entire hemisphere centered on the viewed pixel. The diffuse solar transmission, T_{ds} , is defined as the ratio of the diffuse irradiance at the surface, from light that has been scattered at least one time, to the direct irradiance at the top of the atmosphere, or

$$T_{ds} \equiv \frac{E_{av}}{\mu_s E_s}, \quad (6.83)$$

and is another quantity modeled using the radiative transfer code. It is convenient to group E_s^* and E_{av} into one term, since there is no adjacency effect involved, which will be labeled E_{sav} . Alternatively, if the irradiance refers to a background point it is labeled E_{sab} , and E_{av} is re-designated E_{ab} to distinguish between the two cases. The diffuse transmission is similarly adjusted. There is physically no difference between E_{sav} and E other than the final illumination point on the surface.

In order to treat the remaining irradiance term, associated with L_{abv} and designated as E_{abv} , the fraction of light scattered back down to the surface must be addressed. This is accomplished by introducing the spherical albedo S from the surface, which is the fraction of the radiance from a source, the diffusely reflected light from the surface in this case, that is scattered back toward the source. The concept of albedo was introduced by Johann Lambert in 1760 (Johnston, 2001) to describe diffuse reflectance from a surface, and the spherical albedo is also used to describe the total reflectance for an entire planet (Thomas and Stamnes, 1999). The spherical albedo can be calculated by assuming a uniform and isotropic upward radiation field of unit radiance at the bottom of the atmosphere and determining the resulting radiance that is returned to a point on the surface due to the scatterers present in the atmosphere. Mathematically, S is given by

$$S = \frac{\int L^\downarrow(\tau, \hat{\omega}) \cos \theta d\omega}{\int L^\uparrow(\tau, \hat{\omega}) \cos \theta d\omega} = \frac{1}{\pi} \int_0^{2\pi} \int_0^1 L^\downarrow(\tau, \mu) \mu d\mu d\phi \quad (6.84)$$

under the slab approximation that assumes the atmosphere, and therefore the scattering, is azimuthally symmetric. The calculation of (6.84) requires knowledge of the scattering phase functions, the absorption and extinction coefficients, and the optical depth between the surface and the scattering locations. Its derivation is similar to that of (6.42). An example of the spherical albedo with the visibility parameter set to 23 km is given in Figure 6.15. Again, note the short wavelength dependence.

Figure 6.16 illustrates the processes of multiple scattering and multiple reflections that generate E_{abv} . Initially a background point on the surface is illuminated by E_{sab} and the irradiance is diffusely reflected. A portion of this reflected light is reflected back down

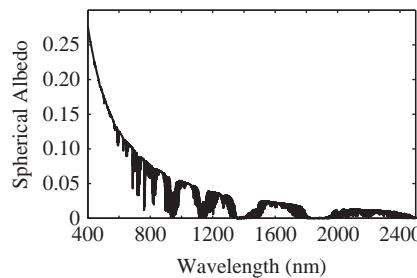


Figure 6.15 Spherical albedo calculated using MODTRAN®.

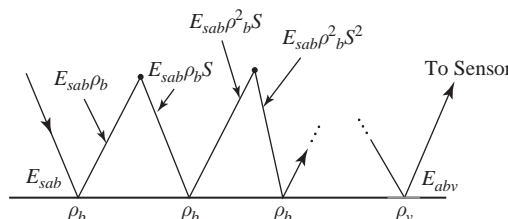


Figure 6.16 Target irradiance due to multiple scattering and reflections.

to the surface due to the spherical albedo, some of which illuminates the viewed pixel, and some portion of the remaining light being again reflected by the background and the atmosphere. The process is subsequently repeated, and the detected light is either directly reflected into the IFOV from the viewed pixel, or reflected from a background point and scattered into the IFOV by the atmosphere.

Mathematically, the irradiance contributed to the viewed pixel due to the various possible reflections from the surface and the atmosphere is the sum of the different reflection processes, or

$$\begin{aligned} E_{abv} &= E_{sab}\rho_b S + E_{sab}\rho_b^2 S^2 + E_{sab}\rho_b^3 S^3 + \dots \\ &= E_{sab}\rho_b S(1 + \rho_b S + \rho_b^2 S^2 + \dots), \end{aligned}$$

where ρ_b is the background reflectance. This reduces to

$$E_{abv} = E_{sab} \frac{\rho_b S}{1 - \rho_b S} = E_{sab} \left(\frac{1}{1 - \rho_b S} - 1 \right), \quad (6.85)$$

when the binomial expansion for $(1 - x)^{-1}$ is applicable since $\rho_b^2 S^2$ is always less than one. The total irradiance at the viewed pixel, E_v , is therefore

$$E_v = E_{sav} + E_{abv} = \frac{E_{sav}}{1 - \rho_b S}, \quad (6.86)$$

where the equality between E_{sav} and E_{sab} has been applied. An analogous derivation yields

$$E_b = \frac{E_{sab}}{1 - \rho_b S} \quad (6.87)$$

for the total irradiance at a background point. Again, (6.86) and (6.87) are physically identical and only distinguish between the two different final illumination points on the surface.

6.4.4 The Inversion Equations

The Lambertian approximation, (6.76), is now applied to develop the terms in (6.80). The surface-leaving radiance can be calculated since the irradiance is known, and the different radiance terms are subsequently attenuated as the light propagates upward through the atmosphere to the entrance pupil. The direct transmittance from a point on the surface to the entrance pupil is simply $T_u = e^{-(\tau^* - \tau)/\mu}$ where τ is the optical depth at the sensor. The diffuse upward transmittance between the surface and the sensor, analogous to (6.83), remains to be defined.

The calculation of the diffuse upward transmission appears at first glance to be very challenging, as the radiance from many points on the surface interacts with the atmosphere and we are only interested in the small portion that is collected within the IFOV. The calculation is made tractable through the application of the principle of reciprocity. This principle states that, due to time reversal in the physical laws for electromagnetic wave propagation, the directions of illumination and viewing are interchangeable. Therefore, reflectance and transmission are symmetric with respect to the interchange

of direction. Note, however, that this assumption does not hold in rare situations, as discussed in Chapter 3. As a consequence, if the diffuse transmission at the bottom of the atmosphere for collimated light at the top is calculated, then the reverse process, the transmission of diffuse radiance at the bottom of the atmosphere into a collimated beam at the top, is also known. The detailed proof of this is provided in Thomas and Stamnes (1999). The calculation of the diffuse upward transmission, T_{du} , is similar to the calculation for (6.83) except μ describes the viewing geometry.

Equation (6.80) is now rewritten as

$$L_v = L_d + \frac{\rho_v E_s^*}{\pi} T_u + \frac{\rho_v E_{av}}{\pi} T_u \\ + \frac{\rho_b E_{sab}}{\pi(1 - \rho_b S)} T_{du} + \frac{\rho_v E_{sav}}{\pi} \left(\frac{1}{1 - \rho_b S} - 1 \right) T_u$$

or

$$L_v = L_d + \frac{\rho_v E_{sav}}{\pi(1 - \rho_b S)} T_u + \frac{\rho_b E_{sab}}{\pi(1 - \rho_b S)} T_{du}, \quad (6.88)$$

where (6.79) and $E_{sav} = E_s^* + E_{av}$ have been used. This equation is sometimes written as

$$L_v = L_d + \frac{A \rho_v}{1 - \rho_b S} + \frac{B \rho_b}{1 - \rho_b S}, \quad (6.89)$$

where $A = E_{sav} T_u / \pi$ and $B = E_{sab} T_{du} / \pi$ (see, for example, Adler-Golden et al. (1998)). Note that A and B are radiances. A is related to the transmitted radiance from the viewed pixel and includes L_s and L_{av} , while B is due to the radiance that has not interacted with the viewed pixel, only with the surrounding surface, and is subsequently scattered into the IFOV.

Equation (6.88) can also be expressed in terms of the apparent reflectance. The irradiance at the viewed pixel is rewritten as

$$E_{sav} = E_s^* + E_{av} = \mu_s E_s (T_s + T_{ds}) \quad (6.90)$$

using (6.81) and (6.83). When this relation, and (6.79), is applied to (6.88), the apparent reflectance measured at the aperture corresponding to L_v is

$$\rho = \rho_d + \left[\frac{(T_s + T_{ds}) T_u}{1 - \rho_b S} \right] \rho_v + \left[\frac{(T_s + T_{ds}) T_{du}}{1 - \rho_b S} \right] \rho_b, \quad (6.91)$$

where L_d has been replaced with $\mu_s E_s \rho_d / \pi$, through the application of the diffuse apparent reflectance of the atmosphere. Equation (6.91) is the fundamental equation that is solved for the retrieval of surface reflectance. Its application requires that all of the atmospheric parameters be known or modeled. The apparent reflectance ρ is known from the measurement and the information in the measured at-aperture radiance is utilized to obtain the transmissions and the spherical albedo. The different elements of (6.91) are illustrated in Figure 6.17 with the irradiance of the background having both direct and diffuse illumination components, as signified by the sum of the corresponding transmissions.

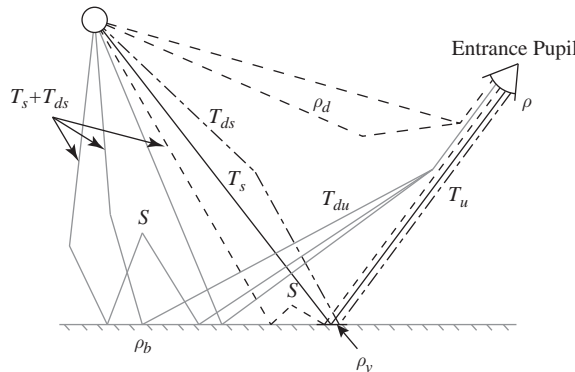


Figure 6.17 The elements of (6.91) with examples of the different transmittances, reflectances, and spherical albedo identified. The apparent reflectance is obtained directly from the measured data, the surface reflectances, ρ_v and ρ_b , are retrieved as part of the inversion process, and the diffuse reflectance, the various transmittances, and the spherical albedo are modeled based upon information derived from the spectral imagery.

6.5 Estimating Model Parameters from Scene Data

A great strength of the data acquired using an imaging spectrometer is the wealth of information about the atmosphere itself. This detailed information enables the retrieval of the amount of a particular atmospheric species, such as water or ozone, as well as an estimate of the aerosol loading or scene visibility. An accurate estimation of these quantities is critical for the retrieval of the surface reflectance signature, in the case of the solar reflective spectral range, or the temperature and emissivity for the emissive range. In this section we will demonstrate the retrieval of water through a simple method and describe more accurate but computationally intensive methods, and address scattering through the concept of visibility and introduce the atmospheric point spread function. The discussion that follows neglects the topic of cloud detection and masking; but an introduction to this topic is given by Gao et al. (1993).

The quality of the imaging spectrometer and accuracy of the calibration are critical to the retrieval process that utilizes physical modeling. For example, as shown in Chapter 5, a spectrometer that suffers from reduced contrast due to scattered light contamination will have corrupted calibration coefficients if the scatter is not addressed. The resulting inaccurate radiance will degrade the retrieval of a spectral signature and, depending upon the spectral contrast between the signature of interest and the background material signatures, can seriously degrade the quality of the exploitation products. This is particularly problematic if the contrast reduction occurs spectrally where the signature of interest has the greatest spectral uniqueness. A poor spectral or radiometric calibration of the data can have similar consequences. As always, the signal-to-noise ratio is also critical for an accurate retrieval of information.

6.5.1 Columnar Water Estimation

There are various techniques that have been applied to the estimation of the quantity of an atmospheric species. These range from rather simple, but often effective, procedures that utilize ratios between the shoulders and the minimum of a particular absorption feature to detailed retrievals that employ least squares fitting to an atmospheric model. As an example, the continuum interpolated band ratio (CIBR) technique will be presented in some detail for estimating the amount of water within a scene, followed by a discussion of the more computationally intensive and accurate methods.

A differential absorption technique for the estimation of the amount of atmospheric water was first applied by Fowle (1912) and is routinely used in sun photometry (see Thome et al., 1992, Ingold et al., 2000, and the references therein). As developed in Chapter 5, these applications use automated solar radiometers that view the sun directly with narrow fields of view and narrow-band optical filters spectrally centered on a water band and just outside of it. The similar measurement using an imaging spectrometer viewing the surface has the added complication of the spectral reflectance signature modifying the measured at-aperture radiance. The CIBR approach is an adaptation for imaging spectroscopy of the differential absorption technique (Carrère and Conel, 1993).

We will digress briefly at this point to consider the units used to quantify the amount of an atmospheric species within a vertical column from the earth's surface to the top of the atmosphere. Taking water as the particular example, within an atmospheric slab dz of unit area there are $n_w(z) dz$ water molecules, where $n_w(z)$ is the water number density at a given altitude. The mass of water in the column is therefore

$$M_w = \int_0^{\infty} n_w(z) \left(\frac{M}{N_A} \right) dz \quad (6.92)$$

in units of mass per unit area where M is the molar mass of water (18.01528 g/mol) and N_A is Avogadro's number (6.02214×10^{23} molecules/mol). This is also expressed as the depth the water would occupy if it were condensed into a liquid at the base of the column given by M_w/ρ_w where ρ_w is the density of water (1 g/cm³ at 4°C). Yet a third way of expressing this same quantity, used by atmospheric scientists, is the thickness of the resulting column if all of the water in the atmospheric column of air from the surface to the top of the atmosphere were brought to standard temperature and pressure. This layer would have a depth expressed in, for example, atm-cm, since if the pressure were halved, the thickness would be doubled due to the dependency between the two quantities. For water, this layer is fictitious since the water vapor would condense into liquid in many cases.

The CIBR algorithm relies upon radiance measurements within an absorption feature referenced to the radiance values from spectral channels outside the feature, where the absorption due to the gas of interest and other atmospheric species is negligible. A linear interpolation is used to model the radiance at the center of the absorption feature in the

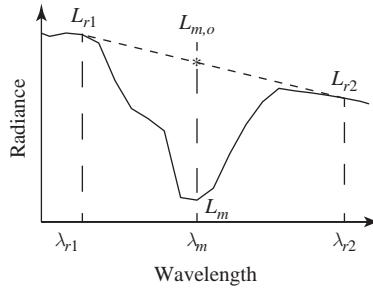


Figure 6.18 The CIBR ratio of the absorbed radiance to the estimated radiance in the absence of absorption. The absorbed radiance is obtained from the data at the minimum of the absorption feature and $L_{m,o}$ estimated based on the radiance values at the shoulders of the absorption feature, L_{r1} and L_{r2} .

absence of the absorber to the depth of the feature with the absorber present. For example, Figure 6.18 illustrates the radiance from an absorption feature with a minimum at λ_m and two reference channels at λ_{r1} and λ_{r2} . The zero absorption estimate is provided by the linear interpolation

$$\frac{L_{m,o} - L_{r1}}{\lambda_m - \lambda_{r1}} = \frac{L_{r2} - L_{r1}}{\lambda_{r2} - \lambda_{r1}}, \quad (6.93)$$

which is solved for $L_{m,o}$, the predicted radiance in the absence of absorption, to yield

$$L_{m,o} = \left(\frac{\lambda_{r2} - \lambda_m}{\lambda_{r2} - \lambda_{r1}} \right) L_{r1} + \left(\frac{\lambda_m - \lambda_{r1}}{\lambda_{r2} - \lambda_{r1}} \right) L_{r2} = \omega_1 L_{r1} + \omega_2 L_{r2}, \quad (6.94)$$

where ω_1 and ω_2 are the interpolation coefficients. The CIBR ratio is defined as

$$R_{\text{CIBR}} \equiv \frac{L_m}{L_{m,o}} = \frac{L_m}{\omega_1 L_{r1} + \omega_2 L_{r2}} \quad (6.95)$$

and L_{r1} and L_{r2} are referred to as the continuum radiances.

Figure 6.19 is an example of the atmospheric transmission for a columnar water amount of 1.5 g/cm² that is evaluated for the selection of the reference channels. All of the MODTRAN® simulations use a nadir viewing geometry and a 45° solar zenith angle, and correspond to the mid-latitude summer model. The visibility is 5 km for all of the calculations with the exception of the transmission depicted in Figure 6.19, where it is 23 km. The carbon dioxide is set to 391 parts per million by volume, taken from 2011 measurements on Mauna Loa, Hawaii (see Thoning et al., 1989, and the references therein for a review of the measurement methodology). The azimuthal angle of the sensor ground track is taken to be 30° west of north, which is used in the aerosol modeling. Water has absorption bands at about 820, 940, and 1140 nm, which are reduced to broad features when measured by an imaging spectrometer with 10 nm sample spacing and a Gaussian instrumental profile with a width of 12 nm, which will be the imaging spectrometer spectral sampling used in the examples that follow. There is little or no water absorption at 779 nm just to the right of the 760 nm oxygen feature, at 869 nm between the 820 and 940 nm water absorption features, and at 1040 nm between the 940 and

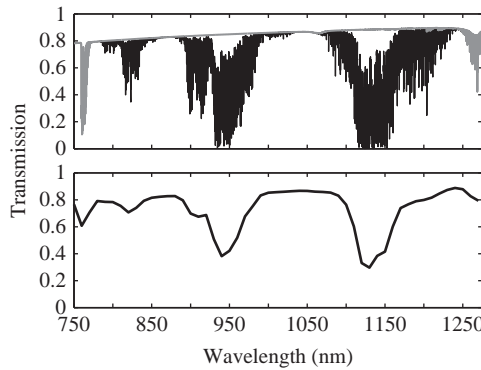


Figure 6.19 Atmospheric water transmission. The upper graph is a high-resolution MODTRAN® model with the black curve representing the water transmission and the gray curve the transmission from all the atmospheric components except water with a visibility of 23 km. The lower curve is the band-averaged full transmission corresponding to 10 nm-spaced instrumental profiles starting at 750 nm.

1140 nm features. The long wavelength side of the 1140 nm band is problematic with absorption due to both oxygen and carbon dioxide interfering with the estimate of the continuum radiance there. The slight absorption at 1066 nm, which is difficult to see in Figure 6.19, is also due to oxygen and is to be avoided.

Equation (6.95) is understood from a radiative transfer point of view by considering (6.88) rewritten as

$$L_v = L_d + \frac{\mu_s E_s}{\pi} \left[\frac{(T_s + T_{ds})T_u}{1 - \rho_b S} \right] \rho_v + \frac{\mu_s E_s}{\pi} \left[\frac{(T_s + T_{ds})T_{du}}{1 - \rho_b S} \right] \rho_b, \quad (6.96)$$

where (6.90) has been applied. Additionally, the problem will be simplified by considering a uniform field where ρ_v equals ρ_b , with (6.96) reducing to

$$L_v = L_d + \frac{\mu_s E_s}{\pi} \left[\frac{(T_s + T_{ds})(T_u + T_{du})}{1 - \rho_v S} \right] \rho_v = L_d + \frac{\mu_s E_s}{\pi} \frac{T_{tot}}{1 - \rho_v S} \rho_v, \quad (6.97)$$

where the $(T_s + T_{ds})(T_u + T_{du})$ has been identified as the total transmittance T_{tot} . The total transmittance is now separated into contributions from the water content and everything else and the CIBR ratio is written as

$$R_{\text{CIBR}} = \frac{L_d + \frac{\mu_s E_s}{\pi} \frac{T_{tot,o} T_w}{1 - \rho_v S} \rho_v}{L_{d,o} + \frac{\mu_s E_s}{\pi} \frac{T_{tot,o}}{1 - \rho_v S_o} \rho_v}, \quad (6.98)$$

where S_o is the spherical albedo for a dry atmosphere, and $T_{tot,o}$ is the atmospheric transmittance in the absence of water and T_w is the transmittance of the water alone, both at the band minimum.

Equation (6.98) is now evaluated at the reflectance limits with ρ_v set to 0 and 1 while maintaining the overall visibility. In the first case R_{CIBR} becomes the ratio between the diffuse radiance from the atmosphere with water to that without. The left graph in Figure 6.20 shows an example of this case and the CIBR ratio calculated is 0.3559 using (6.95) and 0.3798 using (6.98) for a 6.3 percent difference. When ρ_v is unity (6.98)

is dominated by the direct reflected radiance since the diffuse atmospheric radiance is much smaller as shown in Figure 6.20. In this case, the CIRB ratio is 0.2546 and 0.2571 using (6.95) and (6.98) respectively, for a 0.97 percent difference. These results suggest that the CIBR algorithm works best for a high reflectance case where the water transmission of the full atmosphere is sampled, which is not the case when radiance due to diffuse atmospheric scattering dominates.

In the recovery of atmospheric water vapor content, the CIBR ratio for a particular water absorption feature is calculated for each spatial pixel in the imaging spectrometer data and is compared to the equivalent calculation generated using a radiative transfer code to model the at-aperture radiance. The model-generated data, appropriately band-averaged for the spectral response functions of the imaging spectrometer, are calculated for a range of values of the atmospheric water content. Intermediate unmodeled columnar water amounts are obtained through an interpolation such as a cubic spline. The graphs in Figure 6.21 show the results of model calculations of the CIBR ratio using

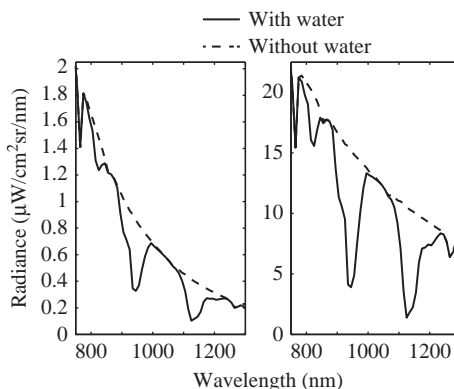


Figure 6.20 Diffuse atmospheric radiance (left panel) and total radiance for a unit Lambertian reflectance, with and without water vapor in both cases. The visibility is set to 5 km and the columnar water amount is 1.5 g/cm^2 for the water vapor case. Note the change in the radiance scale.

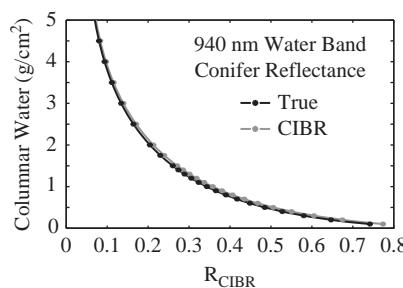


Figure 6.21 Model calculation of the CIBR ratio for the 940 nm water band. The True curve is calculated using (6.98) and the CIBR curve uses (6.95). The solid lines are generated using a cubic spline interpolation.

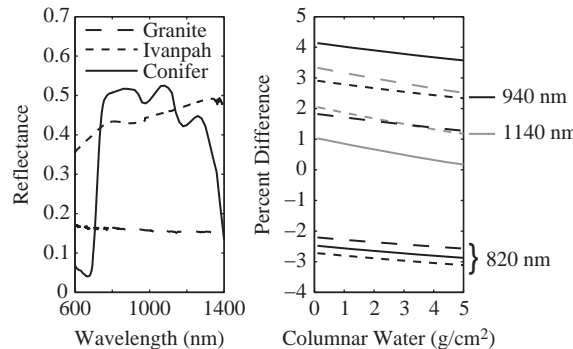


Figure 6.22 The CIBR algorithm applied to uniform surfaces characterized by a reflectance from granite, vegetation, and dry soil (Ivanpah Playa). The spectral reflectances are illustrated on the left and the percent difference between the CIBR method and (6.98) as a function of columnar water content on the right, with the latter treated as the true ratio. The discontinuity at 975 nm in the Ivanpah Playa signature is due to the field spectrometer measurement. The line structure represent the signature and the gray and black lines distinguish the 940 nm and 1140 nm water absorption features on the right. The Ivanpah Playa signature was provided by Kurtis Thome of the NASA Goddard Space Flight Center and the granite and conifer signatures are from the ASTER database (Baldridge et al., 2009b).

(6.95) and (6.98) for a variety of columnar water amounts, displayed as asterisks, and for the reflection of a uniform field composed of conifer trees.

The accuracy of the CIBR algorithm is evaluated using three Lambertian surface reflectances that range from about 0.15 to 0.5 with almost no spectral variation to significant variation. The three reflectances, illustrated on the left side of Figure 6.22, are for granite, the dry soil of Ivanpah Playa, and conifer trees. Granite has a low and almost flat reflectance while Ivanpah Playa has a relatively high and upward sloped reflectance. Vegetation, as illustrated by the conifer signature, is spectrally structured in comparison to the other signatures with a steep change in reflectance at about 700 nm due to the edge of the chlorophyll absorption feature and broad liquid water absorption features at 1000 and 1200 nm. The right side of Figure 6.22 illustrates the percent difference again using (6.95) and (6.98) with the latter used as the true ratio. It is clear that the CIBR ratio is a good approximation if the surface reflectance is known. Similar results are obtained when the spectral sampling is reduced to 5 nm with the instrumental profile width of 6 nm.

In practice, when the surface reflectance is unknown, the CIBR ratio is calculated by assuming a spectrally uniform Lambertian reflectance, such as 25 percent, and a visibility or surface meteorological range, 23 km for example, for the radiative transfer model. The radiative transfer code is executed using a series of columnar water vapor amounts with the intermediate values obtained through interpolation or through a calibration model (Carrère and Conel, 1993). A comparison between this reference model and the models generated using the example signatures above is illustrated in Figure 6.23. The spectral reflectance signature variation leads to an overestimate of the columnar water amount for both vegetation and dry soil and an underestimate in the granite signature

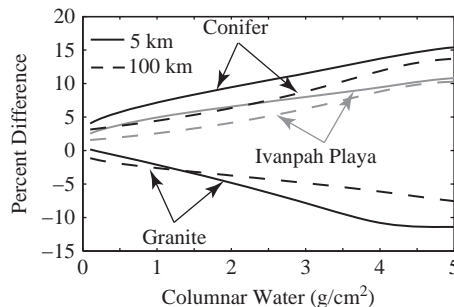


Figure 6.23 Comparison of CIBR ratios using a spectrally flat 25 percent reference signature and a 25 km visibility and conifer, dry soil, and granite signatures at 5 km and 100 km visibilities

case for both 5 km and 100 km visibilities. An iterative approach, where the water is estimated and the reflectance signature retrieved followed by signature smoothing and reinsertion into a new radiative transfer model, will improve the retrieved water amount at a computational cost.

This model based analysis is somewhat misleading since real imaging spectrometer data contain noise and potential calibration errors, and scenes are typically spatially complex, with both direct and adjacent contributions from a variety of different reflectance signatures. Nonetheless, it does indicate that the CIBR technique has utility as an efficient method to estimate the water content for each spatial sample within a scene. A simple sorting routine that removes all of the dark pixels below a threshold, such as those due to reflection from water, where the at-aperture radiance is dominated by the diffuse component would be beneficial, particularly for a scene with a heavy aerosol load. The CIBR technique has been evaluated using scene data from AVIRIS (Carrère and Conel, 1993) where the columnar water was underestimated by 13 percent. This discrepancy was attributed to small radiance differences between the AVIRIS data and the radiative transfer model due to both calibration errors and the inability to precisely model the atmosphere. Carrère and Conel (1993) also provide a thorough comparison between the CIBR technique and another approach known as the Narrow/Wide ratio method.

6.5.2

Additional Columnar Water Estimation Methods

A modified form of the CIBR has been developed to account for the diffuse radiance term. This extended method is called the Atmospheric Precorrected Differential Absorption (APDA) technique, with an evaluation based on both modeling and analysis of AVIRIS data (Schläpfer et al., 1998). The analysis presented, which utilized simulated data where the reflectance was varied with the columnar water amount fixed and the visibility set to 23 km, demonstrated that discrepancies between the CIBR and APDA techniques were prevalent at low reflectance values where the diffuse term has a greater contribution. When applied to AVIRIS data taken over a mountainous area, the water retrieval was consistent with radiosonde measurements. The APDA algorithm is

also computationally efficient if a lookup table has been precomputed using a radiative transfer code.

The errors associated with the CIBR or APDA techniques may be too large, depending upon the accuracy required, for a given application. A more accurate but computationally intensive approach has been developed by Gao and Goetz (1990) that curve-fits the measured spectra to an atmospheric model using nonlinear least squares fitting. They were able to retrieve the columnar water amounts for both soil and vegetation surface reflectances. Additionally, the liquid water content of the vegetation was also determined by assuming that the water contained within the leaves could be modeled by an equivalent amount of liquid water to first order.

Their fitting approach starts by calculating the apparent reflectance from the imaging spectrometer data using (6.79) and by estimating the atmospheric transmission in the spectral region containing the water band based upon assumed reflectance and atmospheric models. The apparent reflectance is again calculated by multiplying the transmission and reflectance model outputs, appropriately convolved with the spectral response function, which are subsequently compared to the apparent reflectance calculated from the data. At this point the process is iterated with different transmission and reflectance models, by implementing a regression analysis using nonlinear least squares fitting, until the data and the model outputs converge. This approach is undoubtedly the most accurate, but is computationally intensive.

6.5.3 Visibility Estimation

A critical step in the atmospheric compensation process is to quantify the effect of scattering from molecules and aerosols in order to model the diffuse radiance L_d , the transmittances, and the spherical albedo that are required to retrieve the viewed pixel apparent reflectance by inverting (6.91). The formalism developed in Section 6.1.1 requires that both the optical depth and the scattering phase function be known in order to solve the radiative transfer equation. In the case of Rayleigh scattering, the optical depth is known (Teillet, 1990) and the phase function was derived in Chapter 2. For aerosols, a radiative transfer code will have both internal models, which include representative vertical profiles of the aerosol number density and size distributions based on historic measurements, and the ability to input an external model from field measurements, such as those made using automated solar radiometers for vicarious calibration purposes. The aerosol phase function calculation is based on Mie scattering as presented in Chapter 2.

An effective approach to determine the visibility over land if vegetation is present is to locate the pixels in the scene data that have low radiance, particularly at about $2.2 \mu\text{m}$ where there is empirical evidence that relates the reflectance there to the reflectance in the visible wavelengths (Kaufman et al., 1997b). Typical aerosol types, with the exception of dust particles, are transparent at $2.2 \mu\text{m}$ making this practical for the detection of “dark” materials. The scene data are converted to apparent reflectance and sorted to identify the pixels with reflectances that are less than or equal to 0.10 at $2.2 \mu\text{m}$. It was shown by Kaufman et al. (1997b) that the reflectance at $0.49 \mu\text{m}$, $\rho_{0.49}$, is equal to

$\rho_{2.2}/4$ with an uncertainty $\Delta\rho/\rho$ of 0.33, and the $0.66\text{ }\mu\text{m}$ reflectance, $\rho_{0.66}$, is equal to $\rho_{2.2}/2$ with an uncertainty of 0.17. These relationships allow the surface reflectance at the two visible wavelengths to be predicted with an error of about 0.006 for vegetated pixels. This approach, with some modifications to increase the reflectance retrieval range, has been implemented to retrieve aerosol properties using data from the Moderate Resolution Imaging Spectroradiometer (MODIS) (Kaufman et al., 1997a; Remer et al., 2005).

The technique does not detect water bodies, which are challenging to atmospherically correct since the at-aperture radiance is composed of the diffuse, surface-reflected, and surface-leaving radiance terms. The last term is particularly difficult to quantify since it depends upon the suspended particle size and depth distributions, the vegetation content, and the water depth. For example, the water-leaving radiance from a shallow flooded field is quite different from that leaving a lake or pond that is comparatively deep. This is also true for atmospheric compensation for the littoral zone in comparison to the deep ocean. Atmospheric compensation over water bodies is beyond our scope but there is a robust ocean color literature available (e.g. Gao et al. (2000) and more recently retrievals from the space-borne instrument described by Lucke et al. (2011)).

Dark pixel detection is the first step in quantifying the aerosol optical depth since ρ_d , S , and the transmission terms in (6.91) are all functions of τ . Additionally, we know from Section 6.1.2 that the radiative transfer equation depends upon the single scattering albedo $\tilde{\omega}$ and the phase function $p(\tau, \hat{\omega}_o, \hat{\omega})$. The calculation proceeds via a radiative transfer code in order to generate a lookup table, since it is currently computationally prohibitive to execute a radiative transfer model for every pixel in a scene. In the context of visibility modeling to generate the table, the model inputs are representative aerosol models based upon direct measurements or upon the climatology for the regions imaged, a range of viewing and illumination geometries, the appropriate standard atmosphere for the time of year and the region, and a range of values for the variable atmospheric species such as water and ozone. The lookup table is comprised of a range of transmittances, spherical albedos, and diffuse radiances (or reflectances) for the different geometries and species concentrations.

A measured aerosol model for the scene or region is in most cases unknown and a standard model, such as those described by Shettle and Fenn (1979), is used. These models are incorporated into the radiative transfer code. For example, in MODTRAN® the atmosphere is divided into four altitude regions: 0 to 2 km, 2 to 10 km, 10 to 30 km, and 30 to 100 km. Each is characterized by a different aerosol model that describes the density and size variations as well as the composition. Only the boundary layer model will be addressed in any detail since that is most easily accessed through the visibility parameter. The various models are described in Kneizys et al. (1996) and the references therein.

The lowest or boundary layer is described by the meteorological range or the horizontal visibility, which is the greatest distance for which an object is identifiable with the unaided eye (Middleton, 1958). This is simply the inverse function of Beer's law (2.166) and, since visual acuity is involved, it is appropriate to use the extinction coefficient at 550 nm near the peak visual response of the eye. The transmission is assumed

to be constant and set to 0.02 by convention. Neglecting ozone, the atmosphere is non-absorbing at the surface at 550 nm and the extinction coefficient reduces to just the scattering coefficients for molecular and aerosol scattering. Inverting (2.166) yields

$$V = -\frac{\ln T}{k_e} = \frac{\ln(50)}{k_{ae} + k_r}, \quad (6.99)$$

where V is the visibility in units of length, k_{ae} is the aerosol scattering coefficient, and k_r is the Rayleigh scattering coefficient given by 0.01149 km^{-1} at a pressure of 1013.25 mbars and a temperature of 288.15 K (Bucholtz, 1995).

MODTRAN® has several aerosol models that include a rural model that represents regions without urban or industrial pollutants, an urban model that adds combustion and industrial aerosols to the rural model, and a maritime model composed of a salt component added to the rural model. Both fog and volcanic models are also available. MODTRAN® is highly flexible when applied by a skilled user ranging from a simple adjustment of the visibility parameter, with the selected aerosol model appropriately scaled, to the input of a fully defined external model. 6S is an alternative that is also a powerful radiative transfer code with the full aerosol modeling capability but see Vermote et al. (1997) for its limitations with respect to absorption modeling.

6.5.4 The Atmospheric Point Spread Function

The derivation of (6.88) neglected one important aspect of radiative transfer: the atmospheric point spread function that governs the spatial range over which the background reflectance is important. Atmospheric scattering couples the signature of the area surrounding a viewed pixel to the viewed pixel in two ways. The first is through the coupling of the background reflectance to the directly viewed surface location through the irradiance given by (6.86), and the second is through single and multiple scattering of background radiance into the IFOV without interacting with the directly viewed surface location as captured by the final term in (6.88). As written, both of these terms contain the same background reflectance ρ_b and are only accurate if the viewed pixel reflectance ρ_v is in a uniform background. We will illustrate the more realistic situation through the single scattering approximation followed by a discussion of the techniques that are employed in atmospheric correction codes to approximate the atmospheric point spread function. The wavelength dependence will continue to be suppressed as a notational convenience.

Figure 6.24 illustrates the geometrical sampling of a nadir viewing imaging spectrometer with radiance originating outside of the IFOV being scattered into it through a single scattering event, the case developed here for its simplicity. Returning to (6.45) and neglecting the radiance due to thermal emission from the atmosphere and the surface yields the source function

$$S_b^\uparrow(\tau', \hat{\omega}) = \tilde{\omega}(\tau') \int_{\uparrow} \frac{p(\tau', \hat{\omega}_o^\uparrow, \hat{\omega}^\uparrow)}{4\pi} [L_{s,r}^\uparrow(\tau^*, \hat{\omega}_o) + L_{d,r}^\uparrow(\tau^*, \hat{\omega}_o)] e^{-(\tau^* - \tau')/\mu_o} d\omega_o \quad (6.100)$$

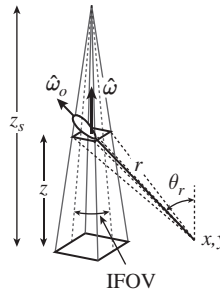


Figure 6.24 Illustration of single scattering of reflected radiance from outside of the viewed pixel directly sampled by the IFOV of a nadir viewing imaging spectrometer. A notional scattering phase function is illustrated at the altitude z and the sensor is located at z_s . The solid angle $\Delta\omega_o(x, y, z)$ is captured by the dotted lines from the (x, y) point to the area encompassed by the IFOV at altitude z .

describing the light scattered in the volume dV at the altitude τ' into the direction $\hat{\omega}$ from the surface reflected radiances, $L_{s,r}$ and $L_{d,r}$, that enter the volume in the $\hat{\omega}_o$ direction. Rather than the total contribution due to single scattering, given by (6.100), we require the contributions from the various reflection points on the surface and the scattering points at different altitudes. This is quantified by converting (6.100) into a sum over the differential solid angles $\Delta\omega_o$ associated with each reflection location (x, y) on the surface.

The reflected radiances, given by (6.40) and (6.43), both depend upon the BRDF at the point of reflection, written generically here as $f_r(x, y, \hat{\omega}_i^\downarrow, \hat{\omega}_o^\uparrow)$ and explicitly specifying the surface location. The reflected radiance from (x, y) is rewritten as $L_r^\uparrow(x, y, \tau^*, \hat{\omega}_o)$ to include both terms and the source term at τ' becomes

$$\Delta S_b^\uparrow(x, y, \tau', \hat{\omega}) = \tilde{\omega}(\tau') \frac{p(\tau', \hat{\omega}_o^\uparrow, \hat{\omega}^\uparrow)}{4\pi} L_r^\uparrow(x, y, \tau^*, \hat{\omega}_o) e^{-(\tau^* - \tau')/\mu_o} \Delta\omega_o \quad (6.101)$$

due to reflection from a given surface location. Note that $\Delta\omega_o$ is a function of surface coordinates and altitude as well as the local area encompassed by the IFOV, as illustrated in Figure 6.24. The solid angle is approximated as

$$\Delta\omega_o(x, y, z) = \frac{(z_s - z)^2 IFOV^2 \cos \theta_r}{r^2}, \quad (6.102)$$

where z_s is the sensor altitude, r is the distance from the point of reflection to the scattering point, and θ_r is the angle between the normal and r .

The total contribution to the at-aperture radiance involves the sum over the atmospheric layers from the surface to the sensor, as was shown in the solution of the radiative transfer equation for the total upward radiance (6.55). In particular, the final term in (6.55) is the contribution to the upward radiance from the source function summed over the atmosphere between the sensor and the surface. Dividing the atmosphere into slabs of thickness $\Delta\tau$ allows the radiance from the (x, y) point due to the adjacency effect to be written as

$$\begin{aligned}
L_{adj}^{\uparrow}(x, y, \hat{\omega}) &= \sum_{\tau}^{\tau^*} \frac{\Delta S_b^{\uparrow}(x, y, \tau', \hat{\omega})}{\mu} e^{-(\tau' - \tau)/\mu} \Delta \tau' \\
&= \sum_{\tau}^{\tau^*} \Delta S_b^{\uparrow}(x, y, \tau', \hat{\omega}) e^{-(\tau' - \tau)} \Delta \tau' \tag{6.103}
\end{aligned}$$

since μ equals one for the nadir viewing case and the sensor is located at τ . The final form of the radiance from the single scattering adjacency approximation is

$$\begin{aligned}
L_{adj}^{\uparrow}(x, y, \hat{\omega}) &= \sum_{\tau}^{\tau^*} \tilde{\omega}(\tau') \frac{p(\tau', \hat{\omega}_o^{\uparrow}, \hat{\omega}^{\uparrow})}{4\pi} L_r^{\uparrow}(x, y, \tau^*, \hat{\omega}_o) \times \\
&\quad T(\tau^*, \tau') T(\tau', \tau) \Delta \omega_o \Delta \tau', \tag{6.104}
\end{aligned}$$

where the two exponential terms have been replaced with $T(\tau^*, \tau')$ for the transmission between the point of reflection to the scatter point and $T(\tau', \tau)$ for the transmission from the scatter point to the sensor.

The next step is to develop a description of the atmospheric point spread function. In the context of atmospheric transmission, the point spread function is the probability that the energy reaching the entrance pupil from the directly imaged viewed pixel (x_v, y_v) originates at a surface pixel at (x, y) outside of the IFOV. Applying the Lambertian approximation to (6.104) and assuming the surface is approximately uniform allows the radiance to be rewritten as $E_r(x, y)\rho(x, y)/\pi$ and to be removed from the summation. The fraction of radiance contributed by the background reflectance at (x, y) is calculated from

$$\begin{aligned}
F(x - x_v, y - y_v) = & \\
\frac{\sum_{\tau}^{\tau^*} \tilde{\omega}(\tau') p(\tau', \hat{\omega}_o^{\uparrow}, \hat{\omega}^{\uparrow}) T(\tau^*, \tau') T(\tau', \tau) \Delta \omega_o(x - x_v, y - y_v, z) \Delta \tau'}{\sum_{x', y'}^{\tau^*} \sum_{\tau}^{\tau^*} \tilde{\omega}(\tau') p(\tau', \hat{\omega}_o^{\uparrow}, \hat{\omega}^{\uparrow}) T(\tau^*, \tau') T(\tau', \tau) \Delta \omega_o(x' - x_v, y' - y_v, z) \Delta \tau'} \tag{6.105}
\end{aligned}$$

where the altitude z is a function of the optical depth. The dependence of the solid angle upon the ground location and altitude has been made explicit. The range over which the summation in the denominator is taken depends upon the phase functions. As the surface point becomes more removed from the location of the direct line of sight increasing the angle between $\hat{\omega}_o^{\uparrow}$ and $\hat{\omega}^{\uparrow}$, its contribution to F is minimized and the summation is truncated. Recall from Chapter 2 that the phase functions for both Rayleigh and Mie scattering are smallest as the scattering angle approaches 90° . The transmission also decreases with range.

The above derivation of the single scattering point spread function is only an approximate solution. First, the denominator in the final two terms of (6.96) was derived based on an infinite series of reflections between the surface and the atmosphere. The background reflectance ρ_b has spatially broad contributions from the surface that depend upon both single and multiple scattering and is thus an average of the actual scene reflectance. This can be modeled as

$$\rho_b(x, y) = \iint_{\substack{x, y \in R(x', y') \\ x', y' \in R(x', y')}} \rho_{hh}(x', y') G(x' - x, y' - y) dx' dy', \quad (6.106)$$

where $G(x' - x, y' - y)$ is the probability that the flux reaching (x, y) originates at (x', y') , $R(x', y')$ is the range over which the surface-atmosphere coupling is effective, and $\rho_{hh}(x', y')$ is the bi-hemispherical reflectance. The bi-hemispherical reflectance is derived from (3.11), with the integration over the full hemisphere for both the incident and reflected radiance to yield

$$\rho_{hh}(x, y) = \frac{1}{\pi} \int_{2\pi} \int_{2\pi} f_r(x, y; \theta_i, \phi_i; \theta_r, \phi_r) \cos \theta_i d\omega_i \cos \theta_r d\omega_r, \quad (6.107)$$

which reduces to a constant at each wavelength for a Lambertian surface. Modeling the background reflectance this way is appropriate since the radiation field due to multiple scattering is approximately isotropic and the contribution to the at-aperture radiance due to $\rho_b S$ is relatively small. The transfer function, $G(x' - x, y' - y)$, is a different function from $F(x - x_v, y - y_v)$, although the two are the result of the same scattering processes.

The second limitation is that the final term in (6.96), which is the radiance L_{ab} due to atmospheric scattering and the background reflectance, should be convolved with F to produce the area averaged background radiance. This average, denoted as $\langle L_{ab} \rangle$, is

$$\langle L_{ab}(x_v, y_v) \rangle = \iint_{\substack{x, y \in R(x', y') \\ x', y' \in R(x', y')}} L_{ab}(x', y') F(x' - x_v, y' - y_v) dx' dy' \quad (6.108)$$

for the contribution to the (x_v, y_v) pixel directly viewed by the sensor. Again, the more realistic atmospheric point spread function will include the effects of multiple scattering. If the Lambertian approximation is applied, an average reflectance that accounts for the influence of the atmosphere is used instead of (6.108) by replacing ρ_b with

$$\langle \rho_b(x_v, y_v) \rangle = \iint_{\substack{x, y \in R(x', y') \\ x', y' \in R(x', y')}} \rho_b(x', y') F(x' - x_v, y' - y_v) dx' dy' \quad (6.109)$$

in the numerator of the last term in (6.96). The final form of the inversion equation including the effects of the atmospheric point spread function is therefore

$$\rho = \rho_d + \left[\frac{(T_s + T_{ds})T_u}{1 - \rho_b(x, y)S} \right] \rho_v + \left[\frac{(T_s + T_{ds})T_{du}}{1 - \rho_b(x, y)S} \right] \langle \rho_b(x_v, y_v) \rangle, \quad (6.110)$$

where $\rho_b(x, y)$ and $\langle \rho_b(x_v, y_v) \rangle$ are given by (6.106) and (6.109) respectively.

The calculation of F and G is challenging and is typically only accomplished by invoking several approximations. While not exact, (6.105) is used to identify the information that is needed to model the two atmospheric functions. Foremost, the phase function $p(\Theta)$ depends on the type and distribution of particles at a particular optical depth, which are seldom known since they require direct measurements when the scene is collected. The approach is to use a representative model based upon climatological data where the phase function has contributions from both Rayleigh and aerosol scattering. The aerosol phase functions depend upon the wavelength, the aerosol radius, the

index of refraction, and must be averaged in order to realistically represent the ensemble of particles in a particular volume. This is accomplished through the integration over the ensemble of aerosol particles

$$p(\Theta) = \frac{\int_0^\infty \sigma_s(r, n) n_p(r) p(r, n, \Theta) dr}{\int_0^\infty \sigma_s(r, n) n_p(r) dr}, \quad (6.111)$$

where $n_p(r) dr$ is the fraction of particles whose radii fall between r and $r + dr$ normalized by

$$\int_0^\infty n_p(r) dr = 1$$

and $\sigma_s(r, n)$ is the scattering cross section, introduced in Chapter 2, as a function of the radius and index of refraction. There is an extensive literature on aerosol distributions and their properties and a thorough review is provided by d'Almeida et al. (1991).

The phase functions are calculated from the Mie theory or approximated by a two-term Henyey–Greenstein phase function given by

$$p(\Theta) = \frac{(1 - g_1^2)a}{(1 + g_1 - 2g_1 \cos \Theta)^{\frac{3}{2}}} + \frac{(1 - g_2^2)(1 - a)}{(1 + g_2 - 2g_2 \cos \Theta)^{\frac{3}{2}}}, \quad (6.112)$$

where g_1 and g_2 are asymmetry parameters that can assume values between -1 and 1 and a is a weighting factor between 0 and 1 . The Henyey–Greenstein phase function models the behavior of both the forward- and backward-scattering peaks with the function peaking in the forward direction for positive values of g (Henyey and Greenstein, 1941). Figure 6.25 contrasts the ensemble averaged aerosol phase function for unpolarized light based on the continental model, one of the standard aerosol models, to that calculated using the Henyey–Greenstein phase function. The continental model is composed of water-soluble, dust-like, and soot aerosol components modeled as a sum of log-normal size distributions (Kaufman et al., 1997a).

The two point spread functions, F and G , have been directly calculated by employing Monte Carlo techniques to trace the paths of a large number of individual photons

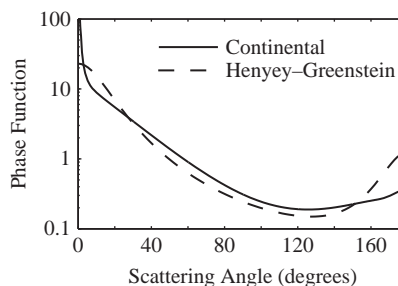


Figure 6.25 Comparison between the continental aerosol and the two-term Henyey–Greenstein phase functions. The parameters for the Henyey–Greenstein calculation were $a = 0.9618$, $g_1 = 0.731$, and $g_2 = -0.7598$ (Reinersman and Carder, 1995).

through the atmosphere. These photons follow the various paths illustrated in Figure 6.13 to be absorbed or scattered, and reflected by the surface if appropriate. The Monte Carlo method statistically reproduces the physical effects by modeling the fates of a large ensemble of photons. Recall that the probability of interaction while going over a distance dr is proportional to the absorption and scattering coefficients, k_a and k_s . If a photon is scattered, the phase function at the scattering location is proportional to the probability of a photon on a particular trajectory to be scattered into another direction within a solid angle $d\omega$. Similarly, the probability of a photon being reflected at the surface into a particular direction can be modeled through the BRDF. F and G , both probability functions, are calculated by recording the outcomes for a large number of photons that follow the appropriate paths (Tanre et al., 1981; Reinersman and Carder, 1995; Miesch et al., 1999, 2005).

6.6

Reflective Compensation Implementation

In this section the approaches to performing reflective compensation are described. These range from empirical techniques that rely to varying degrees on knowledge of the reflectance of scene materials to the application of the radiative transfer theory developed in Section 6.4. The simplifications and approximations that are employed to make the radiative transfer solution more computationally efficient are identified first. In the case of model-based approaches, the approximations are primarily in the calculation of the adjacency effect and in assuming that the surface is Lambertian. Empirical methods that do not use a model, which have been broadly applied, are also developed and linked to the radiative transfer formalism with their advantages and disadvantages described. The section finishes with a brief discussion of the pitfalls that are encountered in the atmospheric compensation process.

6.6.1

Simplifications for Model-Based Approaches

The inversion of (6.110) requires the use of a radiative transfer model for the transmittances and the spherical albedo and an additional method to model the atmospheric point spread functions. In the ideal, but unrealistic, case a direct measurement that quantifies the concentration of variable species, such as water, as well as the aerosol type, size, and vertical distribution would be used to generate a model of the at-aperture radiance as is done for vicarious calibration measurements. A Monte Carlo simulation would then be employed to model the atmospheric point spread functions. In lieu of this, the Monte Carlo technique applied to a standard aerosol model is the most accurate approach but is computationally intensive even with reasonable simplifications, such as computation for a limited number of angles and wavelengths followed by interpolation (Miesch et al., 2005).

The quantification of water and the visibility can be implemented as described above. Some iteration on the solution is best since the amount of water influences the transmission and visibility retrievals as water forms droplets that scatter and also condenses

onto other aerosol particles changes their absorption and scattering properties. The first iterations ignore the adjacency and uses (6.89) rewritten as

$$L_v = L_d + \frac{(A + B)\rho_b}{1 - \rho_b S}, \quad (6.113)$$

which can be inverted to solve for ρ_b . The water and visibility retrievals first utilize radiative transfer code-generated lookup tables based upon a first guess at the scene reflectance and interpolation of the model. The initial reflectance value can be as simple as a spectrally flat reflector, or series of flat reflectances, or it could be based on knowledge of what the scene contains. An initial reflectance is retrieved that is used in subsequent iterations to refine the water and visibility estimates. The water estimate is typically accomplished on a pixel-by-pixel basis, while the visibility retrieval is based on the dark pixel approach if there is vegetation present or upon a priori knowledge of the reflectance of some of the pixels in the scene. The final water retrieval should follow the visibility estimate in order to optimize the accuracy.

The adjacency effect is addressed through some approximations. First, the surface is assumed to be Lambertian and the unknown BRDF is ignored. An estimate of the BRDF could be retrieved through iteration on the final solution if desired. The second approximation is to use (6.109) for the background reflectance in (6.88) and assume that G and F are equivalent. This assumption has been shown to introduce only a small error for most situations (Tanre et al., 1979). The third approximation is the single scattering assumption introduced to derive (6.105). Tanre et al. (1981) calculate that this assumption also introduces a small error as the atmospheric conditions are varied by increasing the aerosol loading and that error is primarily due to the transmission terms.

Using these approximations the atmospheric point spread function can be calculated directly from (6.105) with an assumed aerosol model. The optical depth and scattering coefficients as a function of altitude are required to perform the modeling. Again, a lookup table would be employed to select the appropriate F based on the visibility model and viewing geometry. Another way is to utilize Monte Carlo calculations to populate a database with varying sensor altitudes and aerosol modes as was implemented in the 6S code (Vermote et al., 1997). They also fit the Rayleigh and aerosol point spread functions to parameterize the viewing angle impact to F . The relative contributions to F by Rayleigh and aerosol scattering are weighted through

$$F(x - x_t, y - y_t) = \frac{T_{du}^R(\mu)F_R(x - x_t, y - y_t) + T_{du}^A(\mu)F_A(x - x_t, y - y_t)}{T_{du}(\mu)}, \quad (6.114)$$

where $T_{du}^R(\mu)$ and $T_{du}^A(\mu)$ are the diffuse transmissions from Rayleigh and aerosol scattering for the sensor viewing geometry respectively, $T_{du}(\mu)$ is the total diffuse transmission, and F_R and F_A are the separately modeled components of the point spread function from the two scattering sources (Vermote et al., 1997). Additionally, the lookup table describes the cases of different surface and sensor altitudes.

6.6.2 Model-Based Atmospheric Compensation

Having derived equation (6.110) and shown how the visibility, water vapor retrieval, and adjacency effect can be determined, we are now in a position to summarize the steps for compensation of the atmosphere using a physics-based model. Many steps may require a lookup table in order to converge on the solution. Figure 6.26 provides a generalized flow diagram for retrieving surface reflectance from calibrated radiance, assuming the input radiance data has adequate spectral coverage and resolution for the algorithms. The initial water vapor retrieval is based on (6.95).

The cloudy pixels are found using a combination of brightness, band ratio, and water vapor tests, as described by Ackerman et al. (1998). Selection of a nominal aerosol model as described in Section 6.5.3 is needed to inform the future steps, including the calculation of visibility, scattering phase function, and adjacency effects. Normally, standard atmospheric aerosol types, such as rural or maritime, can be inexact with minor impacts to the final retrieval. If, however, the aerosol distribution is markedly different from the standard aerosol types, significant differences and errors can arise. Examples of aerosol conditions which may cause phase function and distribution discrepancies include significant stratospheric aerosols resulting from a volcanic eruption, forest fires, large dust-storm-generated aerosols, or heavy industry dominated aerosols.

The solution method to calculate the average surface reflectance involves computing a spatially averaged radiance image from which the spatially averaged reflectance is estimated. As noted in Section 6.5.4, a Lambertian assumption is often adequate and has significant computational benefits. Because a large collection area may have quite different average reflectances, as is the case in littoral zones when dark ocean is juxtaposed with white sandy beaches, it is prudent to include the adjacency effect as large errors may result if only an average scene albedo is used. A full calculation of the adjacency effect is the most accurate for the determination of the scattered source function, but can also be computationally demanding as outlined in Section 6.5.4. The calculation of the reflectance for individual pixels is typically accomplished by using lookup tables to linearly extrapolate to a computational solution. With all of the steps involved in retrieving the surface reflectance using radiative transfer codes, the motivation for alternative empirical techniques which avoid the layered calculations is self-evident.

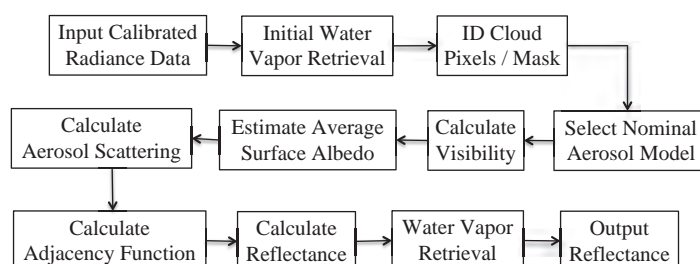


Figure 6.26 Flow diagram for atmospheric compensation.

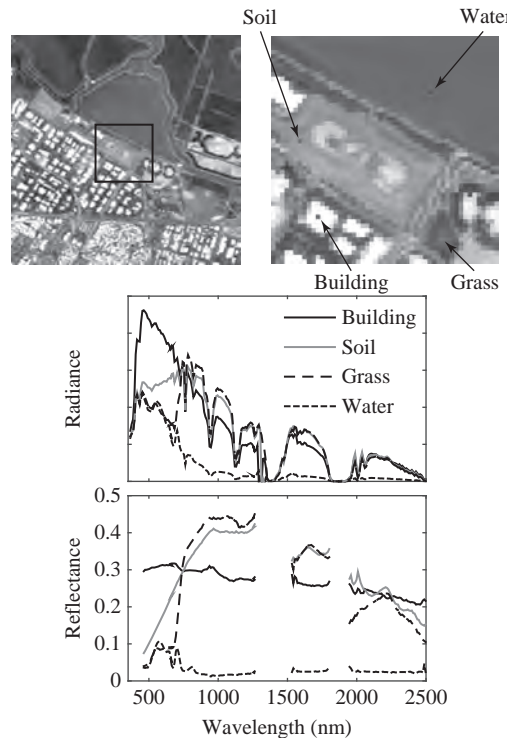


Figure 6.27 Atmospheric compensation example using FLAASH on AVIRIS data. The different radiance and reflectance values are from locations identified in the image in the upper right. The radiance is in arbitrary units.

Example Model-Based Atmospheric Compensation Codes

There are several atmospheric compensation codes for use over land available with different degrees of capability. Gao et al. (2009) provide a review of many of the algorithms that were available in the 2007 time frame. Their treatment uses the atmospheric removal algorithm (ATREM) as a specific example of the technology but they briefly review several of the other codes available at that time, such as Fast Line-of-sight Atmospheric Analysis of Spectral Hypercubes (FLAASH) atmospheric correction algorithm/code and the ATCOR® code, both of which perform the adjacency correction. FLAASH and ATCOR® utilize MODTRAN® as the forward radiative transfer model. Figure 6.27 is an atmospheric compensation example using FLAASH. Although beyond our scope, there is a robust ocean color literature that describes the techniques for atmospheric compensation over water bodies. A good starting point for the interested reader is to review the SeaWiFS and MODIS ocean color publications.

6.6.3 Empirical Atmospheric Compensation

The primary empirical approach to atmospheric compensation is known as the Empirical Line Method (ELM), which assumes that the spectral reflectance of a clearly identifiable

surface or surfaces in the data, given by $\rho_v(\lambda)$, is known. With the generous assumption of a scatter-free atmosphere, the observed dark-subtracted response, $R_{DN}(\lambda)$, from the focal plane array measured in digital numbers, is directly proportional to the reflected radiance. The simplest empirical atmospheric correction factor, given a scatter-free atmosphere, corresponding to the known object reflectance is given by

$$R_{DN}(\lambda) = C_{ELM}(\lambda)\rho_v(\lambda), \quad (6.115)$$

where $C_{ELM}(\lambda)$ is the conversion coefficient. It should be clear that this approach does not require a radiometric calibration in order to solve for $C_{ELM}(\lambda)$. Since there is no diffuse scattering there will be no additive signal that doesn't originate from the surface, so, if a viewed pixel is black or non-reflecting at a given spectral channel, the received radiance is zero. However, both molecular and aerosol scattering will always contribute to the measured signal, and (6.115) must contain an additive component. The slope, $C_{ELM}(\lambda)$, is insufficient to correct for the atmospheric affects and an offset is added to yield

$$R_{DN}(\lambda) = C_{ELM}(\lambda)\rho_v(\lambda) + R_d(\lambda), \quad (6.116)$$

where $R_d(\lambda)$ are the digital numbers due to diffuse atmospheric scattering.

The empirical line technique requires either field or laboratory measurements of a reflectance signature, $\rho_v(\lambda)$, that must be clearly identifiable and large enough to completely fill at least one pixel in the scene. The measurements of various objects or regions in the imaged area are then correlated with the at-sensor measurements for the image pixel(s) for which the reflectance is assumed or known. The assumptions inherent in the ELM approach are understood by rearranging (6.89) to match the terms in (6.116) so that

$$L_v = \left(\frac{A}{1 - \rho_b S} \right) \rho_v + \left(\frac{B \rho_b}{1 - \rho_b S} + L_d \right), \quad (6.117)$$

where radiance due to the diffuse and adjacency terms are grouped. The second term is sometimes referred to as $L_{black}(\lambda)$ because it is the radiance observed from a viewed black pixel and it is assumed that each pixel in the image has the same additive radiance.

The practitioner determines an estimate of $L_{black}(\lambda)$ which, because no calibration or atmospheric model is assumed, must come from the data itself. The multispectral remote sensing community has for many years used a large body of water to estimate the dark radiance providing there is no sun glint from the observed viewing angle. This approach can also work reasonably well for an imaging spectrometer but a better estimate can be obtained by using the spectral reflectance of water from a spectral library, which has a low albedo across the solar reflected spectrum. The availability and quality of a dark or black pixel in the scene directly contributes to the derived empirical reflectance as an error analysis of equation (6.116) would provide.

The basic ELM atmospheric compensation can now be derived by subtracting the signal due to the dark radiance from the entire scene followed by an application of the scaling coefficient, $C_{ELM}(\lambda)$. If there is a pixel darker than the dark pixel which defines $L_{black}(\lambda)$ in any spectral band then the resultant reflectance will be negative, which is physically impossible. This is one of the intrinsic problems with ELM compensation

technique. One proposed approach to solve this problem is to select the single darkest spectral pixel in the scene as the black reference. This approach has the unintended consequence of selecting those pixels for which the product of the detector responsivity and the radiance is the lowest or finding dead pixels in the focal plane array which were previously unidentified.

Other ELM approaches have been developed that rely on the presence of characteristic signatures. For example, a chlorophyll-dominated signature can be used as the reference in a highly vegetated environment, or an asphalt signature in an urban environment. In both cases, the library signature can be used to match a statistical mean or feature as the basis for the ELM atmospheric compensation. The best approach, although limited in its application, is to utilize ground truth measurements from the scene from areas of low and high spectral reflectance with the gain and offset in (6.116) determined through linear regression.

Considerations of the Empirical Line Method

The advantages of the Empirical Line Method are manifold. First, ELM is simple to apply provided there is a known spectral reflectance in the scene. Second, it is not required to know the details of the diffuse and adjacent radiances for any atmospheric conditions as no measurements or assumptions are required. Third, it works for any sun and sensor geometry, or sensor altitude and is therefore applicable to airborne or satellite sensors, and, finally, it does not require a calibrated sensor. This enables an uncalibrated sensor to be used by first taking imagery of a known material and then performing measurements over an area of interest. The resulting spectral imagery can be exploited as long as the atmospheric conditions and the illumination geometry remain relatively unchanged.

One of the disadvantages to the ELM technique is that, for best results, the object of known reflectance signature should be measured at the time of the image acquisition to minimize errors in the reflectance reference spectrum. For example, if the scene is highly structured and there is a large aerosol load then the reflectance from the reference material will be mixed with that from the surrounding area. Additional disadvantages are that the atmosphere must be uniform and stable for the entire data collection, the “known object” spectral reflectance or field measurement errors are directly transferred into the retrieved final reflectance spectra, variations in the responsivity of the sensor or any field dependent aberrations will not be accounted for in the compensation output, and finally any additive radiance from the atmosphere will only be compensated in a linear scaling of the product and not part of an additive radiance source as is the case for aerosols over a dark region.

Obtaining a pure pixel utilizing some sensors can be very challenging due to the size of the ground sample and ground resolution distances. As these grow, single-material pixels become less common, making the ELM atmospheric compensation more difficult to apply. It is for this reason that researchers have looked for ways to use dominant features such as vegetation, bodies of water, or parking lots in urban settings as the known reflectance object since they are usually multi-pixel and relatively uniform. In the absence of clearly unique uniform objects, this approach can often achieve a “quick

and dirty” compensation for the atmospheric effects on scene reflectance but reflectance errors of greater than 10 percent should be expected.

If more than one distinct object of known reflectance can be used, and especially if the known objects approximately span the range of reflectances found in the scene (i.e. dark and bright reflectance surfaces for the range of spectra collected), the empirical line can be derived as a best fit line to the available spectral reflectances. The fit can include a radiance offset so that the dark objects, which are not observed as zero-radiance from the sensor due to atmospheric scattering, can be retrieved as “true black.” As noted previously, this additional degree of freedom in the solution also allows for the possibility of a negative reflectance which, although mathematically possible, is nonphysical and therefore must be addressed.

The measured spectra can be in any units, such as digital numbers or calibrated radiance, and $C_{\text{ELM}}(\lambda)$ is calculated for the individual spectral channels. If the ground or laboratory measurements are collected using a sensor with different spectral channels than the utilized imaging spectrometer, resampling of the known reflectance into the spectral channels of the imaging sensor will be required. Variations of the object reflectance based on illumination geometries and BRDF, as discussed in Chapter 3, or other variables will directly degrade the resultant atmospheric compensation. Additionally, the technique is also predicated on a normalized and linear response of the detectors so a relative calibration must be accomplished or assumed in order to apply this compensation technique.

The ELM technique has been implemented where scene materials are identified and the reference spectral reflectance signature is selected from a library. An approach that uses this concept is known as QUick Atmospheric Correction (QUAC). QUAC is based on an empirical observation that many scenes contain diverse materials that span a large range of reflectance values whose average can be used as an approximate reflectance signature for the entire scene. The average spectral reflectance used is derived from a library and a gain term is estimated from the library average and a subset of end-members extracted from the scene with highly structured reflectances, such as those from vegetation, removed (Bernstein et al., 2012). This approach has the advantage of being computationally efficient when compared to a model-based approaches, but with reduced accuracy.

6.6.4

Solar Reflectance Compensation Considerations

Shortwave atmospheric compensation has been developed for use in the reflective portion of the spectrum from below 400 nm to 2500 nm. In this spectral range, thermal emission from the atmosphere and the surface can be neglected without deleterious effects as demonstrated in Chapter 2. Figure 6.13 illustrates the different contributions that comprise the at-aperture radiance. One of the underlying assumptions is that the reflective properties of the surface are largely Lambertian. As stated previously, this is a better assumption than one might think since rough surfaces tend to approximate Lambertian behavior. For example, a surface painted with a flat paint will largely conform to this approximation, at least for nadir angles that are not too large.

It is important to recognize that for the solar reflectance solution, two generally unrelated paths through the atmosphere must be calculated: the solar illumination of the viewed area; and the viewed pixel to the viewing sensor. Because the geometry of these two paths can also be similar, a very common mistake is to simply make one calculation for transmittance from the top-of-the-atmosphere to the surface for the solar attenuation and reuse the transmittance calculation for the surface to the viewing sensor. Rarely, and more by chance than design, does this shortcut lead to satisfying results. If the atmospheric models such as MODTRAN® are employed, separate and accurate calculations of each path should be calculated.

Using the sun as the source of radiation requires a good model of the solar spectral irradiance at the top of the atmosphere (Labs and Neckel, 1968; Thuillier et al., 2003). The solar output does vary by approximately 0.1 percent based on the activity on the surface of the sun over the ~11-year solar cycle. This small amount of variation is normally not important but it is larger in the 200 to 300 nm spectral range where the variation is approximately 1.5 percent from solar maxima to minima. The various solar source models used in radiative transfer codes are based upon the limited set of measurements that are available and are broadly similar.

An essential input to any radiative transfer problem is obtaining an accurate illumination and viewing geometry. Although this might seem easy and straightforward, in the case of an off-axis, wide field of view (FOV) sensor, the viewing geometry used for the radiative transfer calculations becomes an important source of errors as simplifying approximations are often made to minimize the number of atmospheric transmittance calculations. Consider an airborne whisk-broom sensor with a modest 3° FOV viewing 75° off nadir at its maximum extreme. The atmospheric path length will vary as $\sec(\theta)$ where θ is the off-nadir viewing angle. At a viewing angle of 80° degrees off nadir, a 1° difference in viewing accumulates a 10 percent difference in atmospheric thickness.

6.7

Atmospheric Compensation in the Thermal Infrared

The final section of this chapter is devoted to atmospheric compensation in the long-wave infrared. First, a review of the radiative transfer theory as applied to the LWIR in the 8–14 μm atmospheric transmission window, where atmospheric scattering and reflected solar radiation are neglected, will be presented. The techniques will be utilized first to recover the ground-leaving radiance and then a brief discussion of the process of separating the temperature and emissivity based upon ground-leaving radiance will be introduced. This section is less comprehensive than the development for the reflective region primarily because atmospheric compensation in the LWIR is not as mature. No development of techniques for the midwave infrared will be presented since there is very limited data available and, as a result, no atmospheric compensation techniques have been developed. Such techniques would be hybrids since both thermal emission and reflected solar radiation would have to be addressed.

6.7.1 LWIR Radiative Transfer Theory

Revisiting the expression of the upwelling at-aperture radiance from equation (6.55), where we now seek to simplify the expression for the thermal infrared region of the spectrum, in the LWIR, the various upward source terms from (6.48) can now be reduced to

$$S^{\uparrow} = (1 - \tilde{\omega})B + S_b^{\uparrow}, \quad (6.118)$$

where we retain the thermal emission term $(1 - \tilde{\omega})B$ as the dominant term from the atmosphere. Recall that the single scattering albedo $\tilde{\omega}$ is the ratio of the scattering coefficient to the extinction coefficient and will be vanishingly small in the LWIR and is neglected. The boundary source term, S_b^{\uparrow} , can be simplified from (6.45) by eliminating both the direct and diffuse solar contributions since they are vanishingly small for wavelengths longer than $5 \mu\text{m}$. The radiance source S_b^{\uparrow} from the boundary or surface, in the atmospheric layer identified by τ' in the direction of $\hat{\omega}$, can now be rewritten as

$$S_b^{\uparrow}(\tau', \hat{\omega}) = \tilde{\omega}(\tau') \int_{\uparrow} \frac{p(\tau', \hat{\omega}_o^{\uparrow}, \hat{\omega}^{\uparrow})}{4\pi} \left[L_{t,r}^{\uparrow}(\tau^*, \hat{\omega}_o) + L_e^{\uparrow}(\tau^*, \hat{\omega}_o) \right] e^{-(\tau^* - \tau')/\mu_o} d\omega_o, \quad (6.119)$$

where $L_{d,r}^{\uparrow}$ has been reduced to $L_{t,r}^{\uparrow}$. This simplification is merited because, for almost all situations, scattering in the LWIR is a small contribution since the wavelength is much longer than the diameter of the typical aerosol scatterer and is therefore approximated by Rayleigh scattering with the scattering cross section being proportional to λ^{-4} and, in addition, the number density is typically low. Therefore, scattering is neglected since the scattering coefficient is equal to the number density times the scattering cross section. Figure 6.28 illustrates the contribution to the at-aperture radiance in the thermal infrared with the direct solar and scattering components shown in Figure 6.7 removed.

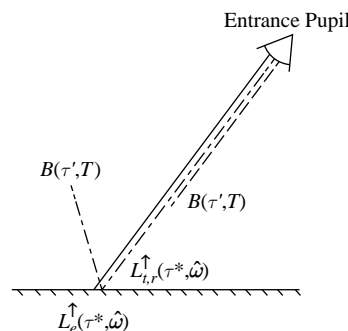


Figure 6.28 Modification of Figure 6.7 showing only those radiative transfer processes that contribute to the at-aperture radiance in the LWIR spectral region. The atmospheric thermal emission is a function of the optical depth at a particular altitude as well as the local temperature.

As a result, the differential equation for the diffuse radiance to be solved from the more general case expressed in (6.52) becomes

$$-\mu \frac{dL_d^\uparrow}{d\tau} = -L_d^\uparrow + B \quad (6.120)$$

since $\tilde{\omega}$ is zero when there is no scattering. The upwelling radiance term from (6.55) is

$$\begin{aligned} L^\uparrow(\tau, \hat{\omega}) = & [L_{t,r}^\uparrow(\tau^*, \hat{\omega}) + \epsilon(\hat{\omega}^\uparrow)B(T_b)]e^{-(\tau^*-\tau)/\mu} \\ & + \frac{1}{\mu} \int_{\tau}^{\tau^*} B(\tau')e^{-(\tau'-\tau)/\mu} d\tau', \end{aligned} \quad (6.121)$$

where $L_{t,r}^\uparrow(\tau^*, \hat{\omega})$ is given by a modified form of (6.41) that will be derived from first principles. The radiance at a point on the surface due solely to thermal illumination is calculated from

$$\mu \frac{dL^\downarrow(\tau, \hat{\omega})}{d\tau} = -L^\downarrow(\tau, \hat{\omega}) + B(\tau, T), \quad (6.122)$$

which yields

$$L^\downarrow(\tau^*, \hat{\omega}_i) = L^\downarrow(0, \hat{\omega}_i)e^{-\tau^*/\mu} + \int_0^{\tau^*} \frac{B(\tau', T)}{\mu} e^{-(\tau^*-\tau')/\mu} d\tau' \quad (6.123)$$

for the radiance from a particular surface illumination direction $\hat{\omega}_i$. Note that the temperature T is a function of the optical depth and B is isotropic. The reflected radiance at the surface is given by

$$L_{t,r}^\uparrow(\tau^*, \hat{\omega}) = \int_{2\pi} f_r(\hat{\omega}_i^\downarrow, \hat{\omega}^\uparrow) \left[\int_0^{\tau^*} \frac{B(\tau', T)}{\mu} e^{-(\tau^*-\tau')/\mu} d\tau' \right] \cos \theta_i d\omega_i, \quad (6.124)$$

where the top of the atmosphere radiance $L^\downarrow(0, \hat{\omega}_i)$ has been set equal to zero in (6.123).

The incident radiance has an angular dependence through μ even though B is isotropic and, therefore, (6.124) can only be simplified if the surface is Lambertian so that f_r is a constant. Applying the Lambertian approximation yields

$$\begin{aligned} L_{t,r}^\uparrow(\tau^*, \hat{\omega}) &= f_{r,d} \int_{2\pi} \int_0^{\tau^*} \frac{B(\tau', T)}{\mu} e^{-(\tau^*-\tau')/\mu} d\tau' \cos \theta_i d\omega_i \\ &= f_{r,d} E(\tau^*), \end{aligned} \quad (6.125)$$

where $f_{r,d}$ is the Lambertian reflectance and $E(\tau^*)$ is the irradiance from illumination over the full hemisphere at the surface. Equation (6.125) is further simplified by applying (3.18) and Kirchhoff's law to produce

$$L_{t,r}^\uparrow(\tau^*) = \frac{\rho}{\pi} E(\tau^*) = \rho L^\downarrow(\tau^*) = (1 - \epsilon) L^\downarrow(\tau^*), \quad (6.126)$$

where $L_{t,r}$ no longer depends upon $\hat{\omega}$. In general, this term should be included unless ε is approaching unity, which is often the case for thermal IR surfaces such as water, or the thermal emission of the atmosphere is very small, which is also a good assumption under many cold sky conditions. Equation (6.121) captures the required elements to understand inversion approaches for the thermal infrared portion of the spectrum.

Chapter 3 provided a discussion of material spectral properties in the thermal infrared spectral range. Although various measurements have been made to characterize the directional impact of different surface types for thermal infrared wavelengths (Jakosky et al., 1990), most uniform surfaces do not exhibit a strong thermal emission directional dependence. Some large directional variations in thermal emission have been found for natural surfaces resulting from the presence of surface roughness at large scales producing spatial variations in temperature driven by solar illumination geometries or shadowing and at small scales producing emissivity variations. Because directional thermal emission effects are difficult to model, computationally intensive, and are often inconsequential to the resulting radiative transfer, a uniform or Lambertian thermal emission is almost always assumed. Any differences in apparent temperature from a surface are not allocated to the directionally varying emissivity of the surface but to the temperature of the surface. This approach works well for most remote sensing problems unless independent calibrated measurements of the same surface are made and must be reconciled from other effects.

6.7.2 Thermal Infrared Atmospheric Correction

Atmospheric compensation in the thermal infrared is challenging given that two surface properties, the spectral emissivity and the surface temperature, are the objects of the retrieval. Again, both model-based and empirical methods will be addressed, although the detail presented is considerably less than that for the reflective case. The techniques that were used to estimate the amount of a molecular absorber could be applied in the LWIR, for example, to determine the ozone present by applying the CIBR approach to the $9.6\text{ }\mu\text{m}$ band. For the model-based approach the In-Scene Atmospheric Correction algorithm will be presented as it is well established and validated. Extensions of this approach for the separation of the surface temperature and spectral emissivity are discussed and referenced. The emissive empirical line method will round out the brief discussion of thermal infrared atmospheric compensation.

Model-Based Thermal Atmospheric Compensation

The In-Scene Atmospheric Correction (ISAC) algorithm was the first algorithm to be widely used for thermal spectral imaging spectrometers and is well described in Young et al. (2002). The ISAC algorithm requires only the calibrated, at-aperture spectral radiance for a particular surface location to estimate the upwelling radiance and transmissivity of the atmosphere through (6.121), rewritten as

$$\begin{aligned} L^{\uparrow}(\lambda, \tau) = & \epsilon_v(\lambda)B(\lambda, T_v)e^{-(\tau^* - \tau)/\mu} + L_d^{\uparrow}(\lambda, \tau) \\ & + [1 - \epsilon_v(\lambda)]L_{t,r}^{\downarrow}(\tau^*)e^{-(\tau^* - \tau)/\mu}, \end{aligned} \quad (6.127)$$

where $L_d^\uparrow(\lambda, \tau)$ is the diffuse upward emission from the atmosphere replacing the final term in (6.121), ϵ_v and T_v are the emissivity and the surface temperature of the viewed pixel, and τ is the optical depth at the location of the imaging spectrometer. Note that the Lambertian approximation has been applied removing the dependence on $\hat{\omega}$ and the spectral dependence has been made explicit. Other simplifying assumptions include that the solar contribution and the scattering function of thermal infrared radiation are both zero.

The ISAC model depends on the natural occurrence of blackbody, or near blackbody, surfaces within the scene, such as areas covered by green vegetation or water, and exploits the natural temperature variations over these surfaces. For such surfaces, where $\epsilon_v \approx 1$, (6.127) reduces to

$$\begin{aligned} L^\uparrow(\lambda, \tau) &= B(\lambda, T_v) e^{-(\tau^* - \tau)/\mu} + L_d^\uparrow(\lambda, \tau) \\ &= B(\lambda, T_v) T_a(\lambda, \tau) + L_d^\uparrow(\lambda, \tau) \end{aligned} \quad (6.128)$$

for each wavelength channel. L^\uparrow is represented as a linear function of the independent variable $B(\lambda, T_v)$ with $T_a(\lambda, \tau) = e^{-(\tau^* - \tau)/\mu}$ and $L_d^\uparrow(\lambda, \tau)$ acting as the line slope and zero-intercept parameters, respectively. We have introduced the transmission T_a , where the a reminds us that it is atmosphere transmittance and not temperature. A plot of $L^\uparrow(\lambda, \tau)$ versus $B(\lambda, T_v)$, as illustrated in Figure 6.29, for all the pixels in a scene for which $\epsilon_v \approx 1$ is analyzed with linear regression techniques.

Unfortunately, the materials in a scene for which the assumption of unity emissivity is valid are rarely identified for the practitioner but must be found in the data. Therefore, the first step is to select a wavelength, λ_o , such that the transmission through the atmosphere is very high ($\tau \approx 1$) and at this spectral window the path radiance $L_d^\uparrow(\lambda_o, \tau)$ is likely to also be negligible so (6.128) simplifies to $L^\uparrow(\lambda_o, \tau) = B(\lambda_o, T_t)$. In reality, true blackbody characteristics are rare so a small finite reflectance is often assumed for the surface materials which will cause the emissivity to be just under unity (e.g. $\epsilon_v \approx 0.99$).

With these spectral windows through the atmosphere now identified, the ISAC method next utilizes the apparent surface temperature identified through the windows to bound (6.128) at other wavelengths to obtain the diffuse radiance $L_d(\lambda, \tau)$ and transmittance T_a . Drawing from the image date and plotting $L^\uparrow(\lambda, \tau)$ versus $B(\lambda, T_v)$ in a

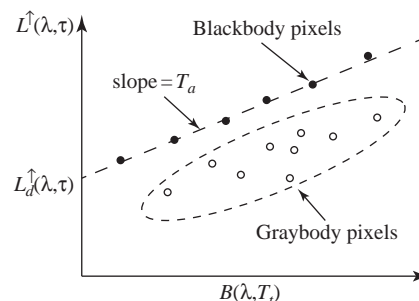


Figure 6.29 Illustration of the ISAC method showing the linear regression line.

separate scatter plot at each wavelength, the maximum radiance L^{\uparrow} upper boundary should be well approximated by a straight line which is the blackbody radiation ($\epsilon_v \approx 1$). The points below the upper boundary are graybodies ($\epsilon_v < 1$) for the given wavelength λ which appear to have a lower temperature as the clear sky is generally colder than the surface, so the reflected radiance is lower than the emitted. The line defining the upper bound has a slope and intercept which can be extracted for each scatter plot to provide the $T_a(\lambda, \tau)$ and $L_d(\lambda, \tau)$ respectively. A sensor may not be well calibrated, in which case the derived quantities are proportional to $T_a(\lambda, \tau)$ and $L_d(\lambda, \tau)$ and can be calculated using the λ_o as a point of reference.

The transmission and upwelling terms are then used to estimate the ground-leaving radiance from the at-aperture radiance for each pixel in the original spectral data. Outputs of the ISAC process include the generation of atmospheric profile plots of transmission, $T_a(\lambda, \tau)$ and upwelling radiance, $L_d(\lambda, \tau)$ and the spectral emissivity, $\epsilon_v(\lambda)$, by noting that the atmosphere does not typically vary dramatically from pixel to pixel so the terms $T_a(\lambda, \tau)$ and $L_d(\lambda, \tau)$ can be applied for all of the pixels in the image. Young et al. (2002) also describe the techniques used for the linear regression and the water estimation in detail. Variations in the methods to implement this basic ISAC model have been explored. For example, in ENVI®, a version of ISAC called “Thermal Atm Correction” has been implemented.

Temperature Emissivity Separation

In any kind of thermal radiometric measurements, the temperature and surface emissivity are linked because the dominant term from the surface is the product $\epsilon(\lambda, \hat{\omega}^{\uparrow})B(T)$, where we have reintroduced the inherent wavelength dependency λ to highlight its importance. However, the useful measurement parameter for the scientist and consumer of remote sensing data is either the emissivity $\epsilon(\lambda, \hat{\omega}^{\uparrow})$ or the temperature T or both. The challenge with the extraction of these two terms is that the problem is underdetermined since there are N spectral measurements while there are $N+1$ variables (temperature and emissivity at each measurement wavelength) required to solve (6.121). This challenge has been approached in various ways for thermal sensors (Gillespie et al., 1998).

While the ISAC approach can be used effectively in many situations to accurately retrieve both the temperature and emissivity of any object in a scene, there are often data sets where thermal atmospheric compensation cannot be accomplished with the ISAC model alone because the required assumptions are violated. It is a common observation that most solid materials exhibit smoothly varying spectral emissivity as compared to spectral atmospheric absorption features. This observation was first utilized by Borel (2008) to provide an additional criterion to assist in the separation of temperature and surface emissivity while discerning the spectral features of the atmosphere from the surface in complex thermal infrared spectral data.

Following an ISAC determination as described above, the temperature and emissivity of each pixel can be further refined so that the high frequency features from the atmosphere are minimized. For each pixel, an optimum temperature T_{opt} is modeled such that the emissivity spectrum $\epsilon_{\text{opt}}(\lambda)$ becomes smooth. A metric criterion can be designed to

iteratively minimize for smoothness of the emissivity as the surface temperature is varied along with the model atmosphere.

Other variations have been explored in recent years to robustly separate the temperature from the spectral emissivity but a truly robust method has been elusive and provides an opportunity for further research. A combination of empirical and analytic techniques may be required to achieve a temperature emissivity separation algorithm which can be applied to any thermal spectral imager.

6.7.3 Empirical Thermal Atmospheric Compensation

An empirical approach to thermal atmospheric compensation is the Emissive Empirical Line Method (EELM), the infrared extension of the Empirical Line Method atmospheric compensation technique. EELM is a simple linear regression for each spectral band to equate at-sensor radiance to ground-leaving radiance $L_t^\uparrow(\tau^*, \hat{\Omega})$, which is the sum of the emitted radiance and the reflected atmospheric thermal radiance assuming the Lambertian approximation from (6.126), expressed as

$$L_t^\uparrow(\tau^*) = \epsilon_v B(T_t) + (1 - \epsilon_v) L_t^\downarrow(\tau^*), \quad (6.129)$$

where the $\hat{\omega}$ dependence has been removed and the measurement is within a non-emitting atmospheric window. The surface-leaving radiance can be calculated based on known (or inferred) in-scene materials or objects where both the emissivity and temperature are known or inferred. The second term is often omitted, especially for known high-emissivity materials ($\epsilon_v \approx 1$), as discussed previously, thus, simplifying (6.129) further to

$$L_t^\uparrow(\tau^*) = \epsilon_v B(T_v). \quad (6.130)$$

where we have preserved the ϵ_v term to preserve accuracy of the dominant radiance contributor term. Equation (6.121) is now solved using a model atmosphere to converge on a least square fit to equate the measured radiance with the modeled upwelling radiance, $L_t^\uparrow(\tau^*)$.

In practice, EELM generally requires at least three sets of values of at-sensor radiance from the data collection, their corresponding emissivity spectra from ground truth or a library, and a temperature measurement. Ideally, the known or inferred objects used for the EELM have a wide range of temperatures which span the observed temperature range in the entire scene. The atmospheric transmission and diffuse radiance for a given wavelength is taken as the best fit for the model atmosphere.

A choice of $\lambda_o = 9.24 \mu\text{m}$ provides a very clear atmosphere in which the assumption of very high transmission with negligible radiation is appropriate, provided there are no clouds or large aerosols in the intervening atmosphere. In this case, (6.121) can be simplified as the atmospheric emission term is negligible so that

$$L^\uparrow(\tau) = L_t^\uparrow(\tau^*) = \epsilon_v B(T_t) \quad (6.131)$$

since the transmission is one. This single channel observation of a known ground material and temperature can provide a simple check of the radiometric calibration of the thermal infrared spectral sensor.

EELM has been implemented with a custom ENVI® plug-in routine. The code matches emissivity and imaging spectrometer data cube spectra, which is normally accomplished by creating regions of interest on calibration materials in the imagery and pairing the regions of interest with library or in-situ measured emissivity spectra and material temperature. Outputs include the generation of atmospheric profile plots as well as the generation of a $L_t^\uparrow(\tau^*)$ data cube that may be used as an input to a temperature emissivity separation algorithm.

6.8

Summary and Further Reading

We have discussed in some detail the critical step of converting at-aperture radiance to either a reflectance or emissivity measurement which requires the intervening atmosphere to be effectively removed from the data. The emphasis has been upon the physical principles that govern radiative transfer through the atmosphere and their application to the inversion problem. An introduction to the approaches utilized in radiative transfer models has also been presented including both line-by-line calculations and band models. Atmospheric compensation in the reflective spectral range has been treated in particular detail and the techniques used in the LWIR have been introduced. Both inverse problems remain an area of active research, particularly in terms of the efficient and accurate application of the principles of radiative transfer to spectral imagery. It is computationally difficult to achieve a near-real-time reflectance or emissivity product, as is desirable given that imaging spectrometers accumulate a tremendous volume of data in a short period. Often, rapid but inaccurate approaches are applied and the resulting exploitation products are degraded.

The theory of radiative transfer is well developed in several texts. The theoretical presentation here is primarily based upon Thomas and Stamnes (1999) and Goody and Yung (1989). Liou (2002) is another valuable reference and a more advanced treatment is Chandrasekhar (1960). There is no text that we are aware of that is devoted to the theory and implementation of atmospheric compensation. The references in this chapter from the refereed journal literature are by no means comprehensive, but are a good place for the interested student to start in order to master this complicated topic.

Problems

1. Derive equation (6.62).
2. Estimate the spectral radiance emitted by healthy vegetation in the VNIR/SWIR spectral range. How does this compare to the emission from Ivanpah Playa? Perform the estimate in 50 nm intervals from 400 nm to 2500 nm.

3. The aerosol extinction coefficient at 550 nm varies from 0.5×10^{-4} to 2.5×10^{-4} m^{-1} . What visibility range does this correspond to?
4. Use the Henyey–Greenstein phase function depicted in Figure 6.25 to estimate the range for the adjacency effect using (6.101) at 870 nm for a scattering altitude of 1 km. Assume that the surface has a flat, Lambertian reflectance of 0.25, the IFOV of the nadir viewing imaging spectrometer at 6 km is $166.7 \mu\text{rad}$, the total atmospheric transmission is 0.8, the solar zenith angle is 23 degrees, and the single scattering albedo is 1. You will need to look up the top-of-the-atmosphere solar irradiance.
5. The absorption coefficient for a Lorentzian line relative to the center wave number is given by

$$k(\tilde{\nu}) = \frac{S\alpha_C}{\pi(\tilde{\nu}^2 + \alpha_C^2)}.$$

Solve for $\tilde{\nu}(k)$ and then show that $f(k)$ is given by

$$f(k) = \frac{1}{\Delta\tilde{\nu}/2} \frac{d\tilde{\nu}}{dk} = \frac{1}{\Delta\tilde{\nu}\pi k} \frac{S\alpha_C}{[(S\alpha_C k/\pi) - \alpha_C^2 k^2]^{1/2}}$$

for the interval from $-\Delta\tilde{\nu}/2$ to $\Delta\tilde{\nu}/2$. What is the dependence on k in the far wings when it is small?

6. From the previous problem show that $g(k)$ is given by

$$g(k) = \frac{2}{\Delta\tilde{\nu}} \sqrt{(S\alpha_C/\pi k) - \alpha_C^2} - 1$$

and the inverse is given by

$$k(g) = g^{-1}(k) = \frac{S\alpha_C/\pi}{[(\Delta\tilde{\nu}/2)(1+g)^2] + \alpha_C^2}.$$

7 Statistical Models for Spectral Data

In this chapter we provide a concise introduction to the statistical characterization of random variables and vectors with emphasis on concepts and properties that will be repeatedly used in the subsequent chapters for the characterization of spectral data. Special attention is given to the multivariate normal distribution because it is mathematically tractable and provides the basis for the development of most practical statistical techniques. In practice, it is impossible to find a normal or non-normal distribution that captures all aspects of hyperspectral imaging data. Therefore, we focus on distributions that capture those distributional aspects which are useful to specific applications. Our guide in this exploration is the following quote (Box and Draper, 1987): “Remember that all models are wrong; the practical question is how wrong do they have to be to not be useful.”

7.1 Univariate Distributions – Variance

Suppose that we wish to study the pixel-to-pixel variation of reflectance in a monochromatic (single band) image. Prior to obtaining the measurements, the value of each pixel reflectance is an uncertain quantity: even with more sophisticated models we cannot predict its value exactly. We say that the reflectance x_i of the i th pixel is a random variable, in the sense that until measured it could take a range of different values, with some values more likely than others.

To better understand the pixel-to-pixel (spatial) spectral variability we construct a *histogram* of the data. To this end, we first divide the horizontal axis into intervals of appropriate size Δx and we determine the number n_i of observations in the i th interval. Then we draw over each interval a rectangle with area proportional to the relative frequency $f_i = n_i/N$, where N is the total number of the observations. If we make the height of each rectangle equal to $n_i/(N\Delta x)$, the area under the histogram is equal to unity. A histogram constructed with this scaling is illustrated in Figure 7.1. In this case, the area between any two values a_1 and a_2 provides the percentage of observations within this interval.

If we knew all observations that might conceptually occur, which are typically infinite, we could obtain a theoretical histogram by making Δx arbitrarily small. The result is a smooth continuous curve $f(x)$ called the *probability distribution* or *probability density function*. The name arises because the integral

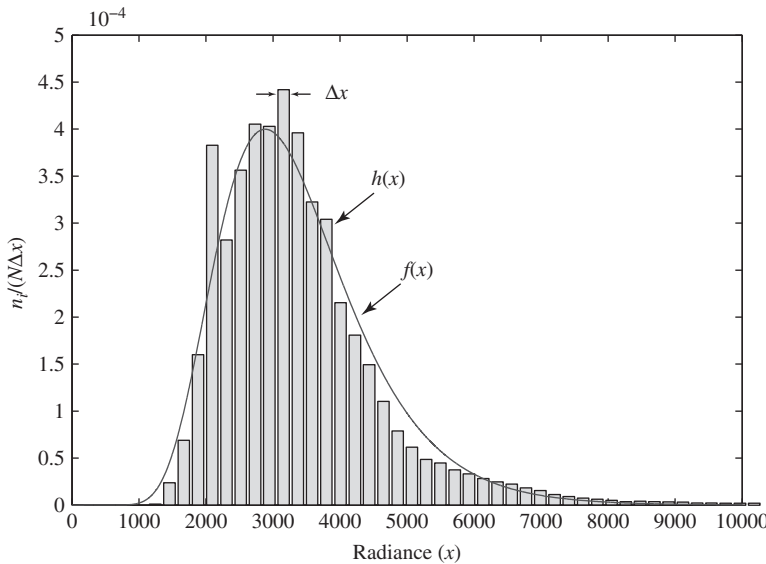


Figure 7.1 Illustration of the concepts of histogram and probability density function.

$$\Pr(a_1 < x \leq a_2) = \int_{a_1}^{a_2} f(x) dx \quad (7.1)$$

gives the probability that a value x lies between a_1 and a_2 . Thus, if $f(a_1) > f(a_2)$, then values close to a_1 are *more likely* to occur than values close to a_2 . We emphasize that it is the *area* under $f(x)$ and *not* any specific value $f(a)$ that represents probability. Clearly, the area under $f(x)$ should be equal to one.

The *cumulative distribution function* (CDF) of a random variable is defined by

$$F(a) \triangleq \Pr(x \leq a) = \int_{-\infty}^a f(x) dx, \quad (7.2)$$

which is the area under the curve $f(x)$ from $-\infty$ to a . The probability that an observation x will *exceed* a value a is given by the *probability of exceedance*

$$\Pr(x > a) = \int_a^{\infty} f(x) dx = 1 - F(a), \quad (7.3)$$

which is equal to the area under the tail of the curve $f(x)$ from $x = a$ to $x = \infty$.

The *mean value* or *expected value* of a random variable is defined by

$$m_x \triangleq \int_{-\infty}^{\infty} x f(x) dx. \quad (7.4)$$

The mean value m_x provides a good estimate of the center or location of a symmetric unimodal distribution. The mean value is usually denoted by $m_x = E(x)$, where

$$E(\cdot) \triangleq \int_{-\infty}^{\infty} (\cdot) f(x) dx \quad (7.5)$$

is the well-known *mathematical expectation* operator. The deviation $x - m_x$ provides a measure of how far any particular observation x is from the mean value m_x . The mean value of the square of these deviations is called the *variance* of x :

$$\sigma_x^2 = \text{var}(x) = E[(x - m_x)^2] = \int_1^1 (x - m_x)^2 f(x) dx. \quad (7.6)$$

The variance provides a measure of the spread of the distribution about its mean and determines an interval around the mean where the values of the random variable are most likely to occur. A small variance indicates that x is more likely to assume values close to its mean. In contrast, a large variance indicates that the values of x are spread over a wider interval about the mean. Thus, we often use the variance as a measure of uncertainty or a measure of variability of a random variable. The *standard deviation* σ_x provides a measure of spread, which has the same units as the original observations.

μ

A probability distribution, which plays a major role in probability and statistics, is the *normal* or *Gaussian distribution* defined by

$$f(x) = \frac{1}{\sqrt{2\pi}\sigma} e^{-\frac{(x-\mu)^2}{2\sigma^2}}, \quad -\infty < x < \infty, \quad (7.7)$$

where $m = E(x)$ and $\sigma^2 = \text{var}(x)$. Note that when there is no ambiguity we drop the subscript from m_x and σ_x^2 . We use the shorthand notation $x \sim N(m, \sigma^2)$ to indicate a normal random variable with mean m and variance σ^2 . The normal or Gaussian density is a bell-shaped curve that is symmetric about its mean $E(x) = m$. The peak of the distribution has value $f(m) = 1/\sqrt{2\pi}\sigma$ and 95 percent of the area under the bell curve is in the range $|x - m| \leq 2\sigma$. The width of the distribution is determined by its variance $\text{var}(x) = \sigma^2$ (see Figure 7.2). Data generated from normal distributions tend to cluster about the mean, with a spread related to the standard deviation.

The *standardized* normal random variable z is defined by

$$z = \frac{x - \mu}{\sigma} \sim N(0, 1). \quad (7.8)$$

The cumulative distribution function $\Phi(z)$ of the standard normal distribution is

$$\Phi(a) = \frac{1}{\sqrt{2\pi}} \int_{-\infty}^a e^{-\frac{z^2}{2}} dz, \quad -\infty < a < \infty, \quad (7.9)$$

which can be evaluated by numerical techniques. Simple inspection of (7.7) shows that the likelihood of a value x depends on the quantity

$$\Delta^2 = \frac{(x - \mu)^2}{\sigma^2}, \quad (7.10)$$

which is the squared distance of x from the mean m in units of standard deviations. We stress that what matters in statistical investigations is not the usual distance $(x - m)^2$ but the “statistical” distance Δ^2 .

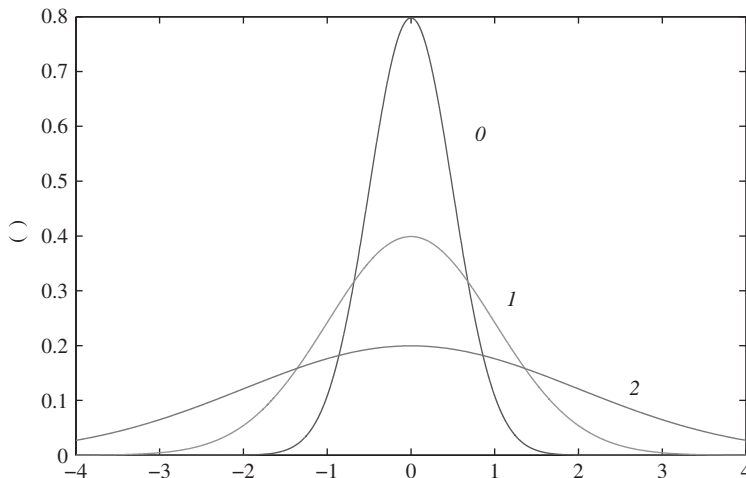


Figure 7.2 The probability density function of a normal distribution for various values of the standard deviation. The spread of the distribution increases with increasing σ ; the height is reduced because the area is always equal to unity.

7.2

Bivariate Distributions – Covariance

Consider now two random variables x_1 and x_2 that measure the reflectance of each pixel at two different spectral bands centered at wavelengths λ_1 and λ_2 . We can certainly use the distributions $f_1(x_1)$ and $f_2(x_2)$ to characterize the reflectance at each individual band. However, the variables x_1 and x_2 are often related. The best way to bring out the relationship between the two variables is by a scatter plot: that is, a graph where each observation (x_{1i}, x_{2i}) is represented by a dot. Figure 7.3 shows the scatter plot for the pixels from a grass area. The swarm of points in a scatter plot reveals the relationship between the two variables. There are several ways to characterize the information provided by a scatter diagram. One way is to construct a two-dimensional histogram of the data. First, the (x_1, x_2) plane is divided into a rectangular grid, where each cell has area $\Delta x_1 \times \Delta x_2$. Then, on top of each cell we raise a rectangular column with height equal to $n_{ij}/(N\Delta x_1 \Delta x_2)$, where n_{ij} is the number of points in the ij th cell. If we knew all observations that might conceptually occur, we could obtain a smooth probability distribution $f(x_1, x_2)$ by making Δx_1 and Δx_2 arbitrarily small. The volume enclosed between the $f(x_1, x_2)$ surface and the (x_1, x_2) plane is equal to one. The volume under the probability density function $f(x_1, x_2)$ above a two-dimensional area A gives the probability for an observation (x_1, x_2) to be in A . The function $f(x_1, x_2)$, known as the *joint probability density function*, provides a complete statistical characterization of the random variables x_1 and x_2 .

If we consider a narrow vertical strip raised over the range $a < x_1 < a + \Delta a$, we can determine the histogram of x_2 for all pixels within the strip. As Δa becomes arbitrarily small, we obtain the conditional distribution of x_2 given that $x_1 = a$. We write

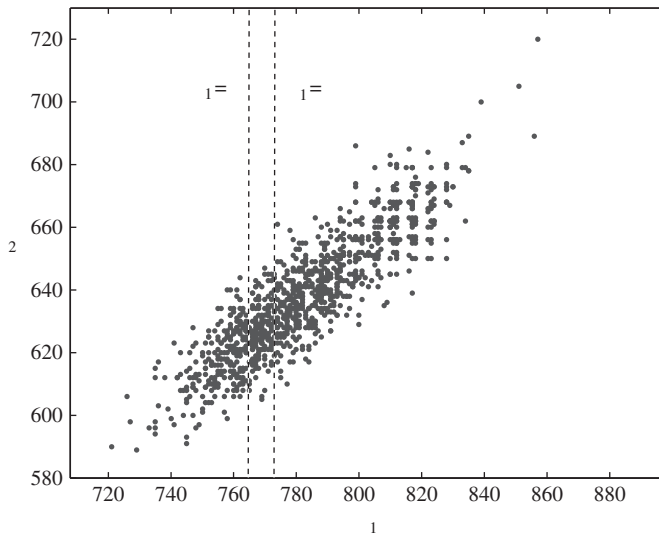


Figure 7.3 Scatter plot for the reflectances x_1 and x_2 of a grass area at two wavelength bands centered at $\lambda_1 = 827$ nm and $\lambda_2 = 837$ nm, respectively.

$f(x_2|x_1 = a)$, where the symbol $|$ stands for the word “given.” In general, the conditional distribution changes with $x_1 = a$. If $f(x_2|x_1) = f(x_2)$, we say that x_1 and x_2 are *statistically independent*. From these interpretations, we can easily see that

$$f(x_1, x_2) = f(x_2|x_1)f(x_1) = f(x_1|x_2)f(x_2). \quad (7.11)$$

If x_1 and x_2 are statistically independent, we have

$$f(x_1, x_2) = f(x_1)f(x_2); \quad (7.12)$$

that is, the joint probability density may be obtained by multiplying the individual densities. This product formula does *not* apply to random variables that are statistically dependent.

Suppose that we wish to summarize numerically the information provided by the scatter plot in Figure 7.3. We can use the mean and standard deviation of x_1 and x_2 to describe the center of the cloud and its horizontal and vertical spread. However, these quantities do *not* describe the relationship between the two variables. The most widely used measure of the relationship between two random variables is the covariance. The covariance between the random variables x_1 and x_2 , denoted by $\text{cov}(x_1, x_2)$ or $\sigma_{x_1 x_2}$, is defined by

$$\text{cov}(x_1, x_2) = E[(x_1 - m_1)(x_2 - m_2)] \quad (7.13)$$

$$= E(x_1 x_2) - m_1 m_2, \quad (7.14)$$

which is the mean of the product of $x_1 - m_1$ with $x_2 - m_2$. If x_1 and x_2 are independent, their covariance is zero; however, the converse is not true.

To gain insight into the meaning of covariance, we consider the scatter plots shown in Figure 7.4 and we draw a vertical line at \hat{m}_1 and a horizontal line at \hat{m}_2 , where \hat{m}_1 and

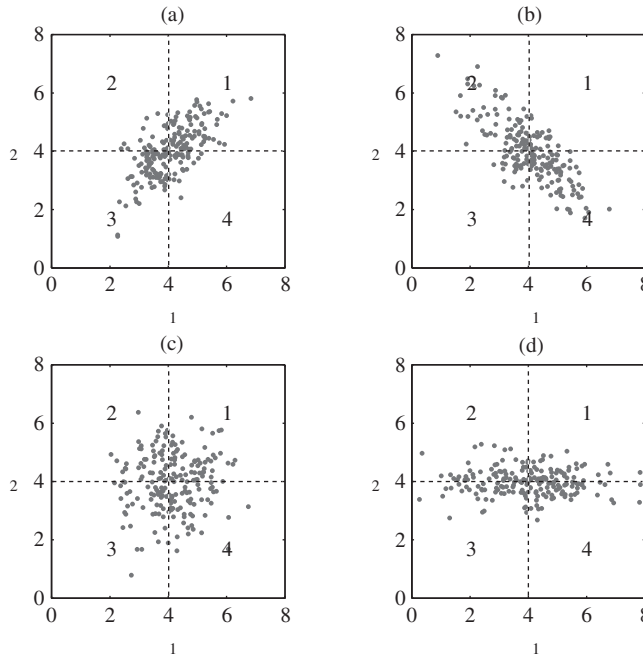


Figure 7.4 Plots illustrating the meaning of covariance between two random variables: (a) positive correlation, (b) negative correlation, (c) uncorrelated variables with equal variances, and (d) uncorrelated variables with unequal variances. The vertical and horizontal lines denote the average values of x_1 and x_2 .

\hat{m}_2 are the estimated mean values of the two sets of data. The two lines divide the plot into four quadrants. It is clear that the products $(x_{1i} - \hat{m}_1)(x_{2i} - \hat{m}_2)$ are positive in the first and third quadrants, and negative in the second and fourth quadrants. If there are more points in the first and third quadrant, the relationship between x_1 and x_2 is positive (as x_1 increases x_2 increases), and the sum $\sum_i (x_{1i} - \hat{m}_1)(x_{2i} - \hat{m}_2)$ is likely to be positive (see Figure 7.4(a)). Conversely, if the relationship between x_1 and x_2 is negative (as x_1 increases x_2 decreases), then there are more points in the second and fourth quadrants, and the sum $\sum_i (x_{1i} - \hat{m}_1)(x_{2i} - \hat{m}_2)$ is likely to be negative (see Figure 7.4(b)). A value of the sum close to zero, which results from a “circular” swarm of points, does not provide any indication about how the changes in x_1 and x_2 are related (see Figure 7.4(c)). Two random variables with zero covariance are said to be *uncorrelated*, otherwise they are said to be *correlated*. Figure 7.4(d) shows the scatter plot for two uncorrelated random variables with unequal variances.

In summary, we can use the covariance to measure the “direction” of the relationship between the two variables. When a scatter diagram is tightly clustered around a line, there is a strong linear association between the variables. Covariance is a measure of the *linear relationship* between two random variables. If the relationship between the random variables is nonlinear, the covariance may *not* reflect the strength of this relationship.

As can be seen from the following property, the covariance of two random variables depends upon the units of measurement:

$$\text{cov}(ax_1 + c, bx_2 + d) = ab \text{cov}(x_1, x_2). \quad (7.15)$$

To avoid this drawback we evaluate the covariance of the standardized variables $z_i = (x_i - m_i)/\sigma_i$, that is,

$$\rho_{12} = \text{cov}(z_1, z_2) = \frac{\text{cov}(x_1, x_2)}{\text{var}(x_1) \text{var}(x_2)}. \quad (7.16)$$

The quantity ρ_{12} is known as the *correlation coefficient* between the two random variables. Since the variance cannot be negative, we have

$$\text{var}(z_1 \pm z_2) = \text{var}(z_1) + \text{var}(z_2) \pm 2\text{cov}(z_1, z_2) = 2(1 \pm \rho_{12}) \geq 0. \quad (7.17)$$

Thus, the correlation coefficient satisfies the condition

$$-1 \leq \rho_{12} = \frac{\sigma_{12}}{\sigma_1 \sigma_2} \leq 1. \quad (7.18)$$

We can easily see that if the random variables are linearly related, that is, $x_2 = ax_1 + b$, we have $\rho_{12} = 1$ if $a > 0$ (positive slope) and $\rho_{12} = -1$ if $a < 0$ (negative slope). A strong correlation, that is, a value of ρ_{12} close to ± 1 , implies that we can accurately predict one variable from the other using a linear relationship.

If we have N observations $\{(x_{1i}, x_{2i}), i = 1, \dots, N\}$ of the random variables x_1 and x_2 , we can estimate the correlation coefficient (7.16) with the *sample correlation coefficient* defined by

$$\hat{\rho}_{12} = \frac{\hat{\sigma}_{12}}{\hat{\sigma}_1 \hat{\sigma}_2} = \frac{(1/n) \sum_{i=1}^N (x_{1i} - \hat{m}_1)(x_{2i} - \hat{m}_2)}{(1/N) \sum_{i=1}^N (x_{1i} - \hat{m}_1)^2 (1/N) \sum_{i=1}^N (x_{2i} - \hat{m}_2)^2}, \quad (7.19)$$

where $\hat{m}_k = (1/N) \sum_{i=1}^N x_{ki}$ is the sample mean, $\hat{\sigma}_1$ and $\hat{\sigma}_2$ the sample variances, and $\hat{\sigma}_{12}$ the sample covariance. Note that $-1 \leq \hat{\rho}_{12} \leq 1$.

If we do not remove the mean from (7.19) we obtain the formula

$$\text{SAM} = \frac{\sum_{i=1}^N x_{1i} x_{2i}}{\sqrt{\sum_{i=1}^N x_{1i}^2} \sqrt{\sum_{i=1}^N x_{2i}^2}}, \quad (7.20)$$

which is known in hyperspectral imaging as the *spectral angle mapper (SAM)*. If we define a vector \mathbf{x}_1 with components x_{11}, \dots, x_{1N} and a vector \mathbf{x}_2 with components x_{21}, \dots, x_{2N} , the SAM is equal to the cosine of the angle formed by the two vectors; therefore, $-1 \leq \text{SAM} \leq 1$. The SAM is widely used to measure the similarity of shapes of two spectral signatures. An in-depth geometrical interpretation of (7.19) and (7.20) is provided in Section 9.5.3.

7.3 Random Vectors – Covariance Matrix

We often need to determine the mean and variance of the linear combination

$$y = a_1x_1 + a_2x_2, \quad (7.21)$$

where a_1, a_2 are constants and x_1, x_2 are random variables. The mean is given by

$$m_y \quad E(y) = a_1E(x_1) + a_2E(x_2) = a_1m_1 + a_2m_2. \quad (7.22)$$

To compute the variance, we first subtract (7.22) from (7.21) to determine $y - m_y$, and then we square both sides. This yields

$$(y - m_y)^2 = a_1^2(x_1 - m_1)^2 + a_2^2(x_2 - m_2)^2 + 2a_1a_2(x_1 - m_1)(x_2 - m_2).$$

Taking the expectation of both sides, we obtain the following relation

$$\text{var}(y) = a_1^2\text{var}(x_1) + a_2^2\text{var}(x_2) + 2a_1a_2\text{cov}(x_1, x_2). \quad (7.23)$$

We note that the mean of y can be expressed in terms of the means of x_1 and x_2 . However, we cannot determine the variance of y if only the variances of x_1 and x_2 are known; we need the covariance between x_1 and x_2 . If the random variables are uncorrelated, that is, $\text{cov}(x_1, x_2) = 0$, we have

$$\text{var}(y) = a_1^2\text{var}(x_1) + a_2^2\text{var}(x_2), \quad (7.24)$$

which is significantly simpler than (7.23). We will see many times in the sequel that the assumption of uncorrelated random variables simplifies the solution of many problems.

7.3.1 Mean Vector and Covariance Matrix

When we deal with many random variables x_1, x_2, \dots, x_p it is convenient to organize them as a p -dimensional random vector

$$\begin{matrix} x_1 \\ x_2 \\ \vdots \\ x_p \end{matrix} = \begin{matrix} \begin{matrix} x_1 \\ x_2 \\ \vdots \\ x_p \end{matrix}^T \end{matrix}^T, \quad (7.25)$$

where the superscript T denotes transposition: that is, changing a column vector to a row vector, and vice versa. The statistical properties of the random vector $\begin{matrix} x_1 \\ x_2 \\ \vdots \\ x_p \end{matrix}$ are completely specified by the joint probability density function $f(\cdot) = f(x_1, x_2, \dots, x_p)$. However, in most practical applications, only the mean values m_k and the covariances σ_{ij} are readily available.

The mean values $m_k = E(x_k)$ are organized as a p -dimensional mean vector

$$= \begin{matrix} m_1 & m_2 & \dots & m_p \end{matrix}^T. \quad (7.26)$$

The covariances $c_{ij} = \text{cov}(x_i, x_j)$, for all $i, j = 1, 2, \dots, p$ can be organized as a $p \times p$ matrix, called the *covariance matrix*, as follows

$$\begin{matrix} c_{11} & c_{12} & \dots & c_{1p} \\ c_{21} & c_{22} & \dots & c_{2p} \\ \vdots & \vdots & \ddots & \vdots \\ c_{p1} & c_{p2} & \dots & c_{pp} \end{matrix} \quad (7.27)$$

Since $\text{cov}(x_i, x_j) = \text{cov}(x_j, x_i)$, the covariance matrix is symmetric. The covariance matrix of the standardized variables $z_k = (x_k - m_k)/\sigma_k$, which has elements ρ_{ij} , is known as the *correlation coefficient matrix* \mathbf{R} , that is,

$$(\mathbf{R})_{ij} = \rho_{ij}. \quad (7.28)$$

The matrix \mathbf{R} with elements $E(x_i x_j)$ is called the *correlation matrix*, that is,

$$(\mathbf{R})_{ij} = E(x_i x_j). \quad (7.29)$$

We note that in the statistical literature the term correlation matrix is used for the matrix \mathbf{R} . The covariance and correlation matrices summarize the entire correlation structure of a hyperspectral image since each element measures the correlation between any two spectral bands.

The correlation between two random vectors \mathbf{x} and \mathbf{y} is determined by generalizing the covariance matrix. For convenience we shall use the concise notation

$$\text{cov}(\mathbf{x}, \mathbf{y}) = \mathbf{x} \mathbf{y}^T \quad (7.30)$$

to denote a covariance matrix with elements

$$(\mathbf{x} \mathbf{y}^T)_{ij} = \text{cov}(x_i, y_j). \quad (7.31)$$

The covariance matrix $\mathbf{x} \mathbf{y}^T$ is not symmetric; however, it is easy to show that

$$\mathbf{y} \mathbf{x}^T = \mathbf{x} \mathbf{y}^T, \quad (7.32)$$

For $\mathbf{x} = \mathbf{x}$ we use the simplified notation $\text{cov}(\mathbf{x}, \mathbf{x}) = \text{cov}(\mathbf{x})$ and $\mathbf{x} \mathbf{x}^T = \mathbf{x} \mathbf{x}$.

A linear combination of p random variables can be expressed more concisely using vector notation as follows

$$\mathbf{y} = \sum_{i=1}^p a_i x_i = \mathbf{a}^T \mathbf{x}, \quad (7.33)$$

where $\mathbf{a}^T \mathbf{x}$ denotes the dot or inner product of the vectors \mathbf{a} and \mathbf{x} . As we recall the Euclidean length or norm of a vector \mathbf{x} is the scalar quantity

$$\|\mathbf{x}\| = (\mathbf{x}^T \mathbf{x})^{1/2} = (x_1^2 + \dots + x_p^2)^{1/2}. \quad (7.34)$$

If the vector \mathbf{x} has unit length, that is $\|\mathbf{x}\| = 1$, then $\mathbf{y} = \mathbf{a}^T \mathbf{x}$ is a scalar that represents the projection of \mathbf{y} onto a line in the direction of \mathbf{x} .

The mean value $E(y)$ in (7.33) can be written as

$$E(y) = \sum_{i=1}^p a_i E(x_i) = \mathbf{a}^T \mathbf{x} . \quad (7.35)$$

Simple matrix operations show that the variance (7.23) of y in (7.21) can be expressed as

$$\text{var}(y) = \begin{pmatrix} a_1 & a_2 & c_{11} & c_{12} & a_1 \\ & & c_{21} & c_{22} & a_2 \end{pmatrix} = a_1^2 c_{11} + a_2^2 c_{22} + 2a_1 a_2 c_{12}. \quad (7.36)$$

In general, the variance of (7.33) can be expressed in compact matrix form as

$$\text{var}(y) = \text{var}(\mathbf{x}^T) = \mathbf{a}^T \mathbf{a} . \quad (7.37)$$

If the random variables x_i are uncorrelated, the covariance matrix becomes diagonal and (7.37) takes a form similar to the one in (7.24).

The scalar quantity defined by (7.37) is called a *quadratic form* in the variables a_1, a_2, \dots, a_p because all terms are of a second degree; that is, they involve only squares a_i^2 or products $a_i a_j$. A quadratic form is called *positive definite* if $\mathbf{a}^T \mathbf{a} > 0$, *nonnegative definite* if $\mathbf{a}^T \mathbf{a} \geq 0$, and *negative definite* if $\mathbf{a}^T \mathbf{a} < 0$, for every $\mathbf{a} \neq 0$. Similarly, we have the definitions

$$\mathbf{a}^T \mathbf{a} > 0 \Rightarrow \text{is positive definite} \quad (7.38a)$$

$$\mathbf{a}^T \mathbf{a} \geq 0 \Rightarrow \text{is nonnegative definite} \quad (7.38b)$$

$$\mathbf{a}^T \mathbf{a} < 0 \Rightarrow \text{is negative definite} \quad (7.38c)$$

Since $\text{var}(y) \geq 0$, we conclude from (7.38b) that the covariance matrix \mathbf{a} is guaranteed to be nonnegative definite; however, in most cases it is positive definite.

Finally, we note that a set of q linear transformations of the form

$$y_i = \mathbf{a}_i^T \mathbf{x} + b_i, \quad 1 \leq i \leq q \quad (7.39)$$

can be combined into a single $q \times p$ linear transformation as follows

$$\begin{matrix} y_1 \\ \vdots \\ y_q \end{matrix} = \begin{matrix} \mathbf{a}_1^T \\ \vdots \\ \mathbf{a}_q^T \end{matrix} \mathbf{x} + \begin{matrix} b_1 \\ \vdots \\ b_q \end{matrix} \quad \text{or} \quad \mathbf{y} = \mathbf{A}^T \mathbf{x} + \mathbf{b} . \quad (7.40)$$

The mean vector and covariance matrix of the transformed vector \mathbf{y} are given by

$$E(\mathbf{y}) = \mathbf{A}^T \mathbf{x} + \mathbf{b} \quad (7.41)$$

$$\text{cov}(\mathbf{y}) = \mathbf{A}^T \mathbf{A}, \quad (7.42)$$

which are straightforward generalizations of (7.35) and (7.37). We can also show the more general property (Rencher, 1998)

$$\text{cov}(\mathbf{y}, \mathbf{y}) = \text{cov}(\mathbf{x}, \mathbf{x})^T = \mathbf{A}^T \mathbf{A}, \quad (7.43)$$

which is very useful when we deal with linear transformations of random vectors.

7.3.2 Spectral Decomposition of a Symmetric Matrix

A linear transformation \mathbf{A} changes the direction determined by a vector \mathbf{v} to another direction determined by the vector $\mathbf{A}\mathbf{v}$. A natural question now is: are there any directions which, under the transformation matrix \mathbf{A} , remain unchanged? It turns out that for a $p \times p$ symmetric matrix \mathbf{A} there exist p such invariant directions, known as *canonical* directions. If \mathbf{v} is a vector along one of these directions, we have that

$$\mathbf{A}\mathbf{v} \text{ must satisfy } \mathbf{A}\mathbf{v} = \lambda \mathbf{v} \text{ for some scalar } \lambda. \quad (7.44)$$

The number λ , known as an *eigenvalue*, determines whether \mathbf{v} , known as an *eigenvector*, is stretched, shrunk, or left unchanged. Although \mathbf{A} can be any square matrix, we restrict attention to symmetric matrices, because our subsequent applications involve such matrices. For $p > 4$ there are no closed-form formulas and the eigenvalues must be found using numerical techniques. The algorithms for eigenvalues depend on the structure and size of \mathbf{A} .

The main use of eigenvalues and eigenvectors is in the *spectral decomposition* or *eigenvalue decomposition* of a symmetric matrix. This result states that every symmetric matrix \mathbf{A} with distinct eigenvalues can be written as (Strang, 2005; Golub and Van Loan, 2012)

$$\begin{aligned} \mathbf{A} &= \mathbf{V}\mathbf{\Lambda}\mathbf{V}^T = \begin{vmatrix} \lambda_1 & & & \\ & \ddots & & \\ & & \lambda_p & \\ & & & \ddots \end{vmatrix} \leq \begin{vmatrix} \lambda_1 & & & \\ & \ddots & & \\ & & \lambda_p & \\ & & & \ddots \end{vmatrix} \\ &= \lambda_1 \mathbf{v}_1 \mathbf{v}_1^T + \cdots + \lambda_p \mathbf{v}_p \mathbf{v}_p^T = \sum_{i=1}^p \lambda_i \mathbf{v}_i \mathbf{v}_i^T, \end{aligned} \quad (7.45) \quad (7.46)$$

where λ_i are the eigenvalues and \mathbf{v}_i the eigenvectors of \mathbf{A} ; that is, $\mathbf{A}\mathbf{v}_i = \lambda_i \mathbf{v}_i$.

All eigenvalues of a symmetric matrix are real and eigenvectors corresponding to distinct eigenvalues are orthogonal. We always normalize the eigenvectors to have unit length; therefore, the eigenvector matrix \mathbf{V} is orthogonal.

The eigenvalue decomposition provides a convenient way to check whether a symmetric matrix is positive definite. Indeed, using (7.46) we have

$$\mathbf{v}_j^T \mathbf{A} \mathbf{v}_j = \lambda_j, \quad j = 1, \dots, p. \quad (7.47)$$

Therefore, from (7.38a) and (7.47) we conclude that a positive definite matrix has positive eigenvalues. The square root of a positive definite matrix \mathbf{A} is given by

$$\mathbf{A}^{1/2} = \mathbf{V} \mathbf{\Lambda}^{1/2} \mathbf{V}^T = \sum_{i=1}^p \sqrt{\lambda_i} \mathbf{v}_i \mathbf{v}_i^T, \quad (7.48)$$

because $\mathbf{A}^{1/2} \mathbf{A}^{1/2} = \mathbf{A}$.

7.3.3 Whitening and Coloring Transformations

If the matrix \mathbf{A} in the linear transformation (7.40) is $p \times p$ and invertible, the random vectors \mathbf{x} and \mathbf{y} are equivalent; that is, they carry the same information. The solution to

many problems can be simplified if we choose \mathbf{c} such that

$$\text{cov}(\mathbf{c}) = \mathbf{c}^T \mathbf{c} = \mathbf{I}. \quad (7.49)$$

If \mathbf{c} is positive definite, we can compute its Cholesky decomposition (Strang, 2005)

$$\mathbf{c} = \mathbf{R}^T \mathbf{R} \quad (7.50)$$

where \mathbf{R} is an upper triangular matrix with positive diagonal elements. Substitution of (7.50) into (7.49) yields that $\mathbf{c} = \mathbf{R}^{-1}$. Therefore, we obtain the transformation

$$\mathbf{z} = (\mathbf{R}^{-1})^T \mathbf{x} = \mathbf{R}^{-T} \mathbf{x}. \quad (7.51)$$

The transformation (7.51) is known as *whitening* or *spherizing* transformation because it creates a set of uncorrelated random variables with equal (unit) variances. The term “spherizing” comes from the application of (7.51) to random vectors with normal distributions (see Section 7.4.2).

Conversely, given a random vector \mathbf{x} with $E(\mathbf{x}) = \mathbf{0}$ and $\text{cov}(\mathbf{x}) = \mathbf{I}$ we can easily show that the random vector

$$\mathbf{z} = \mathbf{R}^T \mathbf{x} + \mathbf{c} \quad (7.52)$$

has mean \mathbf{c} and covariance $\mathbf{R}^T \mathbf{R}$. This process, which “introduces” correlation in the components of \mathbf{z} , is sometimes referred to as a *coloring* transformation.

Another approach to whitening is obtained using the inverse square root of the covariance matrix. Indeed, using (7.48) for \mathbf{c} , we define the transformation

$$\mathbf{z} = \mathbf{x}^{1/2}. \quad (7.53)$$

We can easily show that $\text{cov}(\mathbf{z}) = \mathbf{x}^{1/2} \text{cov}(\mathbf{x}) \mathbf{x}^{1/2} = \mathbf{I}$. The transformation

$$\mathbf{z} = \mathbf{x}^{1/2} + \mathbf{c} \quad (7.54)$$

generates a random vector with mean vector \mathbf{c} and covariance matrix \mathbf{I} .

7.4

Multivariate Distributions

We next discuss some multivariate distributions that have been found useful in modeling hyperspectral imaging data and in developing statistical algorithms for their analysis.

7.4.1

Multivariate Normal Distribution

The multivariate normal distribution provides the grounds for the development of the majority of statistical estimation and decision-making techniques. While real data may deviate from normality, often their distributions can be approximated by a multivariate normal distribution, and statistical techniques developed for normal distributions are robust to deviations from normality.

The generalization of the bell-shaped univariate normal density function

$$f(x) = \frac{1}{\sqrt{2\pi}\sigma} \exp \left(-\frac{1}{2} \frac{(x-m)^2}{\sigma^2} \right), \quad -\infty < x < \infty \quad (7.55)$$

to $p \geq 2$ dimensions is the multivariate normal probability density

$$f(\mathbf{x}) = \frac{1}{(2\pi)^{p/2} |\Sigma|^{1/2}} \exp \left(-\frac{1}{2} (\mathbf{x} - \mathbf{m})^T \Sigma^{-1} (\mathbf{x} - \mathbf{m}) \right). \quad (7.56)$$

In this representation we see immediately that the variable x has been replaced by a vector \mathbf{x} , the mean \mathbf{m} is now a vector of means, and σ^2 has been generalized to a $p \times p$ symmetric nonnegative definite covariance matrix Σ . The role of variance σ^2 has been assumed by the determinant $|\Sigma|$ of Σ , which is often referred to as *generalized variance*. If x_i and x_j are statistically independent, then $\sigma_{ij} = 0$ and $f(\mathbf{x})$ reduces to the product of the univariate normal densities for the components of \mathbf{x} .

The squared term $(\mathbf{x} - \mathbf{m})^T \Sigma^{-1} (\mathbf{x} - \mathbf{m})$ in the exponent of the univariate density has been replaced by a quadratic form of the standardized variables

$$\Delta^2(\mathbf{x}) = (\mathbf{x} - \mathbf{m})^T \Sigma^{-1} (\mathbf{x} - \mathbf{m}) \quad (7.57)$$

known as the squared *Mahalanobis distance* between the vectors \mathbf{x} and \mathbf{m} . The characteristics of the Mahalanobis distance are discussed in Section 7.4.3. When \mathbf{x} has the density (7.56), we say that \mathbf{x} is distributed as $N_p(\mathbf{m}, \Sigma)$ or simply $\mathbf{x} \sim N_p(\mathbf{m}, \Sigma)$. The formula for $f(\mathbf{x})$ in (7.56) is often denoted by $N_p(\mathbf{x} | \mathbf{m}, \Sigma)$.

From (7.56) it should be clear that the multivariate normal density is constant on surfaces where the Mahalanobis distance (7.57) is constant. A contour of constant density is defined by all \mathbf{x} such that

$$(\mathbf{x} - \mathbf{m})^T \Sigma^{-1} (\mathbf{x} - \mathbf{m}) = c^2. \quad (7.58)$$

To better understand the meaning of (7.58) we consider a random vector with uncorrelated components. When all components have the same variance we have

$$\sigma^2 = \sigma^2 \Rightarrow \sum_{k=1}^p (x_k - m_k)^2 = \sigma^2 c^2, \quad (7.59)$$

which shows that the contours become a hypersphere with center at \mathbf{m} and radius σc . In this case, the Mahalanobis distance is equivalent to the Euclidean distance. However, when the variances are different we have

$$\begin{matrix} \sigma_1^2 & 0 & \cdots & 0 \\ 0 & \sigma_2^2 & \cdots & 0 \\ \vdots & \vdots & \ddots & \vdots \\ 0 & 0 & \cdots & \sigma_p^2 \end{matrix} \Rightarrow \sum_{k=1}^p \frac{(x_k - m_k)^2}{\sigma_k^2} = c^2. \quad (7.60)$$

The last equation defines a hyperellipsoid with center at \mathbf{m} and principal axes coinciding with the coordinate axes. Setting $x_i = 0$ for $i \neq k$ yields $x_k = \pm c \sqrt{\sigma_k}$, which is the length of the k th principal axis. The major (minor) axis corresponds to the component with the largest (smallest) variance. We note that the Euclidean distance $(x_k - m_k)^2$ along the k th axis is normalized by the variance σ_k^2 of x_k . In the presence of correlation, the principal axes are rotated in a way determined by the covariance matrix.

μ

We shall illustrate the key properties and characteristics of the multivariate normal distribution for $p = 2$. The covariance matrix for $p = 2$ can be written as

$$= \begin{matrix} c_{11} & c_{12} \\ c_{21} & c_{22} \end{matrix} = \begin{matrix} \sigma_1^2 & \rho\sigma_1\sigma_2 \\ \rho\sigma_1\sigma_2 & \sigma_2^2 \end{matrix} \quad (7.61)$$

because $c_{12} = c_{21} = \rho\sigma_1\sigma_2$. Since the determinant is given by

$$| \cdot | = \sigma_1^2\sigma_2^2(1 - \rho^2), \quad (7.62)$$

we can easily show that the inverse covariance matrix can be expressed as

$$1 = \frac{1}{\sigma_1^2\sigma_2^2(1 - \rho^2)} \begin{matrix} \sigma_2^2 & -\rho\sigma_1\sigma_2 \\ -\rho\sigma_1\sigma_2 & \sigma_1^2 \end{matrix}. \quad (7.63)$$

Thus, the Mahalanobis distance can be expressed as

$$\Delta^2 = \frac{1}{1 - \rho^2} \left(\frac{x_1 - m_1}{\sigma_1} \right)^2 - 2\rho \left(\frac{x_1 - m_1}{\sigma_1} \right) \left(\frac{x_2 - m_2}{\sigma_2} \right) + \left(\frac{x_2 - m_2}{\sigma_2} \right)^2. \quad (7.64)$$

Figure 7.5 illustrates the familiar bell-shaped surface and elliptical contours of the bivariate normal distribution. Figure 7.6 shows contours of equal density for various values of ρ , σ_1 , and σ_2 . We note that the effect of correlation is to squeeze the circle into an ellipse and then rotate its principal axes. The degree of correlation is shown by the “concentration of probability” along a line between the two axes. The concentration along the line increases as ρ approaches to 1. We stress that only in the case of elliptical contours whose major and minor axes do *not* coincide with the coordinate axes the two

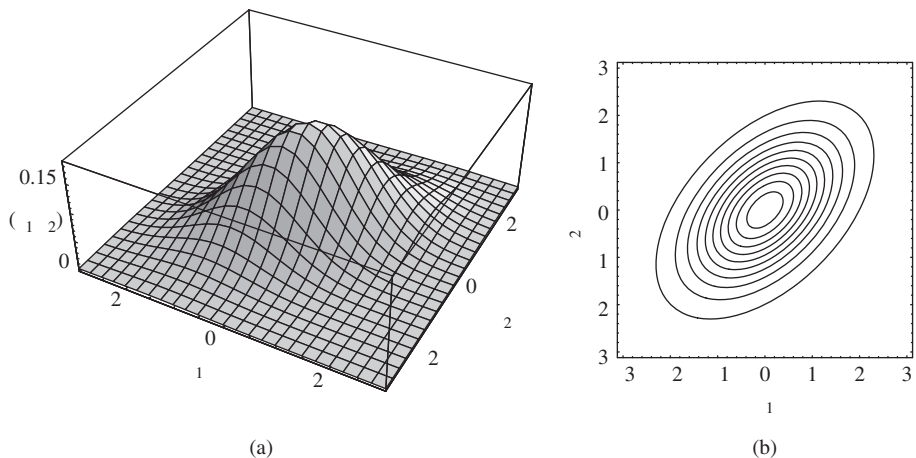


Figure 7.5

(a) Plot of the probability density function of a bivariate normal distributions for $\rho = 0.5$. Intersections with vertical planes parallel to the (f, x_1) and (f, x_2) planes resemble the familiar bell curve. (b) Contours of equal probability density, $f(x_1, x_2) = \text{constant}$, for the normal distribution shown in (a).

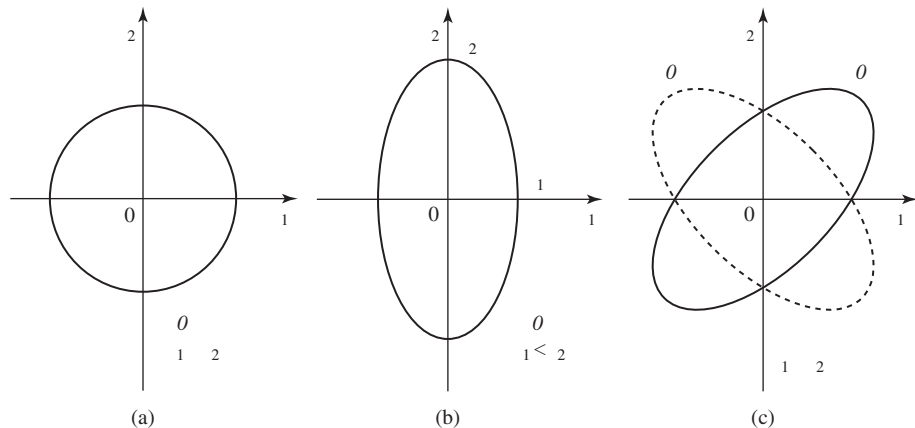


Figure 7.6 Contours of equal probability density for a bivariate normal distribution with uncorrelated and correlated components.

variables tend to co-vary: large (small) values of x_1 are associated with large (small) values of x_2 .

Relation (7.64) provides some insight into the nature of Mahalanobis distance. The first and third terms imply that if one component has a much larger variance than another, it will contribute less to the squared distance. The middle term shows that two highly correlated components will contribute less than two components that are nearly uncorrelated. Essentially, the use of Σ^{-1} in (7.57) standardizes all components and eliminates the effect of correlation.

7.4.2 Properties of Multivariate Normal Distribution

Linear combinations of jointly normally distributed random variables, independent or not, are normally distributed. Indeed, any normal random vector $\mathbf{x} \sim N_p(\mu, \Sigma)$ has the following properties (Rencher, 1998):

1. linear combinations of the components of \mathbf{x} are normally distributed;
2. all subsets of the components of \mathbf{x} have a multivariate normal distribution;
3. zero covariance implies that the corresponding components are independently distributed (the reverse is not generally true);
4. the conditional distributions of a set of components given the remaining ones are multivariate normal.

If \mathbf{x} is a $p \times 1$ vector and \mathbf{A} is a constant $q \times p$ matrix of rank q , where $q \leq p$, we have the following fundamental relations

$$\mathbf{x} \sim N_p(\mu, \Sigma) \Rightarrow \mathbf{A}^T \mathbf{x} \sim N_1(\mathbf{A}^T \mu, \mathbf{A}^T \Sigma \mathbf{A}) \quad (7.65)$$

$$\mathbf{x} \sim N_p(\mu, \Sigma) \Rightarrow \mathbf{A}^T \mathbf{x} \sim N_q(\mathbf{A}^T \mu, \mathbf{A}^T \Sigma \mathbf{A}). \quad (7.66)$$

In geometrical language we say that any projection of a normal random vector onto a lower-dimensional subspace is a normal random vector. The proofs of these and additional properties can be found in Anderson (2003). These properties are responsible for the popularity of normal distributions. For example, from (7.52) and (7.66) we conclude that

$$\sim N_p(\mathbf{0}, \mathbf{I}) \Rightarrow \mathbf{z} = \mathbf{R}^T \mathbf{z} \sim N_p(\mathbf{0}, \mathbf{I}). \quad (7.67)$$

Thus, given a vector of p independent normal random variables $z_i \sim N(0, 1)$, which can be easily generated by most software packages, we can generate a normally distributed random vector with any desired mean and covariance. The converse is also true, that is, the whitening operation

$$\mathbf{z} = \mathbf{R}^T (\mathbf{z} - \mathbf{m}) \sim N_p(\mathbf{0}, \mathbf{I}) \quad (7.68)$$

converts \mathbf{z} to a set of uncorrelated random variables with zero mean and unit variance.

To illustrate the whitening process we assume that $\sigma_1 = \sigma_2 = 1$ and $c_{12} = \rho$. The Cholesky decomposition can be obtained from the relationship

$$\begin{pmatrix} 1 & \rho \\ \rho & 1 \end{pmatrix} = \mathbf{R}^T \mathbf{R} = \begin{pmatrix} a & 0 \\ b & c \end{pmatrix} \begin{pmatrix} a & b \\ 0 & c \end{pmatrix} = \begin{pmatrix} a^2 & ab \\ ab & b^2 + c^2 \end{pmatrix} \quad (7.69)$$

by solving for a , b , and c . The result is given by

$$\mathbf{R}^T = \begin{pmatrix} 1 & 0 \\ \rho & \sqrt{1-\rho^2} \end{pmatrix}. \quad (7.70)$$

Figure 7.7 shows 100 observations and an equal probability contour for a normal random vector with $(m_1 = 1, m_2 = 3)$ and $\rho = 0.75$ and the results of the whitening transformation $\mathbf{z} = \mathbf{R}^T \mathbf{z}$. The results demonstrate, as expected, that the whitening transformation yields a normal distribution with spherical contours.

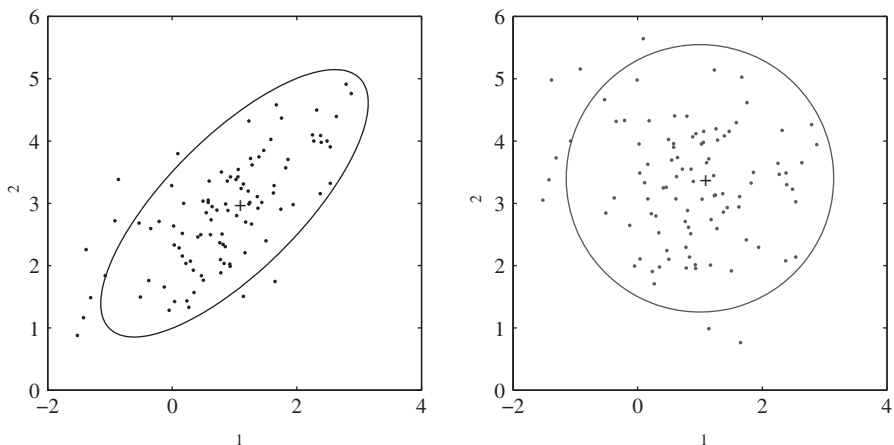


Figure 7.7 Illustration of the whitening transformation $\mathbf{z} = \mathbf{R}^T \mathbf{z}$ for a normal distribution with $p = 2$. The spherical distribution is centered at $\mathbf{z} = \mathbf{R}^T \mathbf{z}$.

7.4.3 Mahalanobis Distances and Angles

In this section we look more closely at two quantities that are central to detection and classification algorithms: the Mahalanobis distance and the Mahalanobis angle. We start with the definition of the chi-square distribution, which describes the distribution of the Mahalanobis distance of Gaussian random vectors.

If z_1, z_2, \dots, z_v are independent standard normal random variables, that is, $z_i \sim N(0, 1)$, the random variable x defined by

$$x = z_1^2 + z_2^2 + \dots + z_v^2 \quad (7.71)$$

is said to have a *chi-squared distribution* with v degrees of freedom and is denoted by $x \sim \chi_v^2$. The probability density is given by

$$f(x) = \frac{1}{2^{v/2} \Gamma(v/2)} x^{v/2-1} e^{-x/2}, \quad x > 0, \quad (7.72)$$

where $\Gamma(\)$ is the Gamma function. The mean and the variance are $E(x) = v$ and $\text{var}(x) = 2v$, respectively.

If $z_i \sim N(m_i, 1)$ we say that x follows a *noncentral chi-squared distribution*

$$x = \sum_{i=1}^p z_i^2 \sim \chi_p^2(\delta), \quad \delta = \sum_{i=1}^p m_i^2, \quad (7.73)$$

where δ is known as the noncentrality parameter. When $\delta = 0$ we have a *central chi-squared distribution*. More information about the chi-squared distribution can be found in (Ross, 2009; Forbes et al., 2011).

From (7.68) and (7.71) we conclude that the Mahalanobis distance follows a central chi-square distribution with p degrees of freedom, that is,

$$\Delta^2 = (\mathbf{z} - \mathbf{z})^T (\mathbf{z} - \mathbf{z}) = \mathbf{z}^T \mathbf{z} = z_1^2 + \dots + z_p^2 \sim \chi_p^2. \quad (7.74)$$

The chi-squared distribution helps to determine the probability content of constant density ellipsoids; that is, the probability α that the tip of $\mathbf{z} \sim N_p(\mathbf{z}, \mathbf{I})$ is inside the ellipsoid

$$\text{all } \mathbf{z} \text{ such that } \Delta^2(\mathbf{z}) = (\mathbf{z} - \mathbf{z})^T (\mathbf{z} - \mathbf{z}) \leq c^2. \quad (7.75)$$

This probability is evaluated using the cumulative chi-square distribution as follows

$$\Pr(\Delta^2 \leq c^2) = \Pr(z_1^2 + \dots + z_p^2 \leq c^2) = \int_0^{c^2} \chi_p^2(v) dv = \alpha. \quad (7.76)$$

The surface defined by $\Delta(\mathbf{z}) = c > 0$ is called the $\alpha \times 100$ percent density contour of the normal distribution. The normal distribution becomes very sparse for large p . Indeed, using (7.76) we can show that $\Pr(\Delta^2 \leq 3.84) = 0.95$ for $p = 1$, but for $p = 10$ the probability is reduced to nearly 0.05.

The volume of the hyperellipsoid defined by (7.75) is given by

$$V = V_p | \mathbf{z} |^{1/2} c^p \quad (7.77)$$

where $V_p = (2\pi)^{p/2} \Gamma(p/2)/p$ is the volume of a p -dimensional unit hypersphere. Thus, for a given dimensionality, the scatter of normally distributed data varies directly with $| |^{1/2}$.

Consider a set of random vectors \mathbf{v}_i from the same distribution $N_p(\mathbf{m}, \mathbf{S})$. The Mahalanobis distance between the random vectors \mathbf{v}_i and \mathbf{v}_j is given by

$$\Delta_{ij}^2 = (\mathbf{v}_i - \mathbf{v}_j)^T \mathbf{S}^{-1} (\mathbf{v}_i - \mathbf{v}_j). \quad (7.78)$$

From Figure 7.8 we see that this is equal to the Mahalanobis distance between the zero-mean vectors $\mathbf{v}_i - \mathbf{m}$ and $\mathbf{v}_j - \mathbf{m}$. If we use the whitening transformation (7.51), that is, $\mathbf{v}_k = \mathbf{U}^T (\mathbf{v}_k - \mathbf{m})$, we can easily show that

$$(\mathbf{v}_i - \mathbf{v}_j)^T \mathbf{S}^{-1} (\mathbf{v}_i - \mathbf{v}_j) = \| \mathbf{v}_i - \mathbf{v}_j \|^2. \quad (7.79)$$

Therefore, the Mahalanobis distance in the original variable space is equal to the Euclidean distance in the whitened space. The Mahalanobis distance is invariant under all nonsingular transformations. Indeed, it can be easily shown that if \mathbf{U} is a $p \times p$ invertible matrix and $\mathbf{v}_i = \mathbf{U}^T \mathbf{v}_i$, then $\Delta_{ij}^2 = \Delta_{ij}^2$.

The angle between the vectors \mathbf{v}_i and \mathbf{v}_j is given by

$$\cos \theta_{ij} = \frac{\mathbf{v}_i^T \mathbf{v}_j}{\| \mathbf{v}_i \| \| \mathbf{v}_j \|}. \quad (7.80)$$

Using the whitening transformation (7.68) yields the *Mahalanobis angle*

$$\cos \theta_{ij} = \frac{(\mathbf{v}_i - \mathbf{m})^T \mathbf{S}^{-1} (\mathbf{v}_j - \mathbf{m})}{[(\mathbf{v}_i - \mathbf{m})^T \mathbf{S}^{-1} (\mathbf{v}_i - \mathbf{m})]^{1/2} [(\mathbf{v}_j - \mathbf{m})^T \mathbf{S}^{-1} (\mathbf{v}_j - \mathbf{m})]^{1/2}}. \quad (7.81)$$

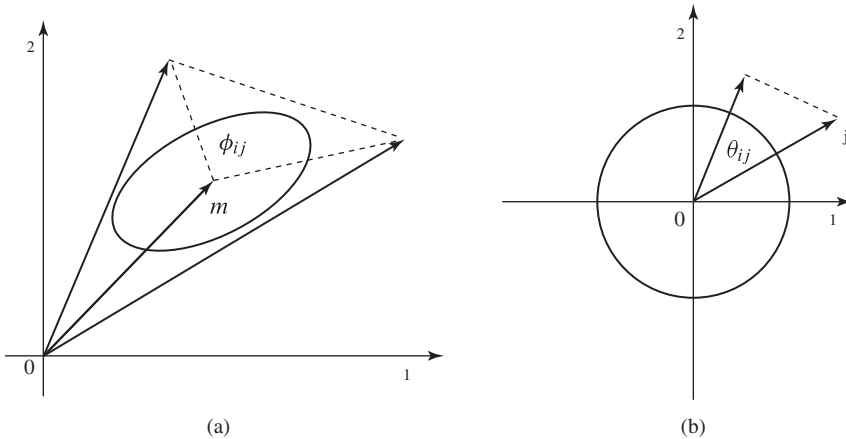


Figure 7.8 Geometrical interpretation of Mahalanobis distance and angle. The Mahalanobis distance and angle between the vectors $\mathbf{v}_i - \mathbf{m}$ and $\mathbf{v}_j - \mathbf{m}$ in the original variable space (a) is equal to the Euclidean distance and angle of the vectors \mathbf{v}_i and \mathbf{v}_j in the whitened space (b).

Thus, it is natural to define the Mahalanobis angle between vectors $\mathbf{z}_i - \mathbf{z}_j$ and $\mathbf{z}_j - \mathbf{z}_i$; this is different from the angle between the vectors \mathbf{z}_i and \mathbf{z}_j . We note that *only in the zero-centered whitened space equal angles correspond to equal probabilities*.

7.4.4 Multivariate t -Distribution

Now let y and w be independent random variables such that $y \sim N(\delta, 1)$ and $w \sim \chi^2_v(0)$. We say that the random variable t has a *noncentral t-distribution* with v degrees of freedom and noncentrality parameter δ , denoted $t_v(\delta)$, if

$$t = \frac{y}{w/v} \sim t_v(\delta). \quad (7.82)$$

If $\delta = 0$, we say that t has a *central t-distribution*. More information about the t -distribution can be found in (Ross, 2009; Forbes et al., 2011).

To generalize to p dimensions, we start with a random vector $\mathbf{z} \sim N_p(\mathbf{0}, \mathbf{I})$, we subsequently randomly modulate the components y_1, y_2, \dots, y_p with a statistically independent random variable $s \sim \chi^2_v$, and then we add a constant vector δ . The result is

$$= \frac{s}{s/v} + \delta. \quad (7.83)$$

The random vector \mathbf{z} has a multivariate t -distribution, denoted by $\mathbf{z} \sim t_p(\delta, \mathbf{0}, v)$, with probability density function (Kotz and Nadarajah, 2004)

$$f(\mathbf{z}) = \frac{\Gamma(\frac{p+v}{2})}{(\pi v)^{\frac{p}{2}} \Gamma(\frac{v}{2})} \frac{1}{|1 + \frac{1}{v}(\mathbf{z} - \delta)^T \mathbf{z}^{-1}(\mathbf{z} - \delta)|^{\frac{p}{2}}}, \quad (7.84)$$

where $\Gamma(\cdot)$ is the Gamma function. We note that (7.83) provides a method to generate samples from a multivariate t -distribution. It can be shown that

$$E(\mathbf{z}) = \delta, \quad v > 1 \quad (7.85)$$

$$\text{cov}(\mathbf{z}) = \frac{v}{v-2} \mathbf{I}, \quad v > 2. \quad (7.86)$$

From the definition (7.71) of the chi-square distribution, we have

$$\frac{s}{v} = \frac{z_1^2 + \dots + z_p^2}{v}, \quad (7.87)$$

which shows that $\sqrt{s/v}$ is an estimate of the standard deviation of a standardized normal random variable. For small v this estimate has large variability which increases the variability of x . For large v , we have the approximation $s/v = (z_1^2 + \dots + z_p^2)/v \simeq E(z_i^2) = 1$, because $z_i \sim N(0, 1)$. Thus, for large v ($v > 30$) the t -distribution resembles a normal distribution. For small v ($v < 30$) the t -density has thicker tails, that is, it has larger variability, than the normal density. For $v = 1$, the t -distribution is identical to the Cauchy distribution, which has the heaviest tails because it has infinite variance. This behavior is illustrated in Figure 7.9 for the univariate Student's distribution $x \sim t_1(0, 1, v)$.

To find the distribution of the Mahalanobis distance we need the F -distribution. Let x_1 and x_2 be independent random variables with $x_1 \sim \chi^2_v(\delta)$ and $x_2 \sim \chi^2_v(0)$. We

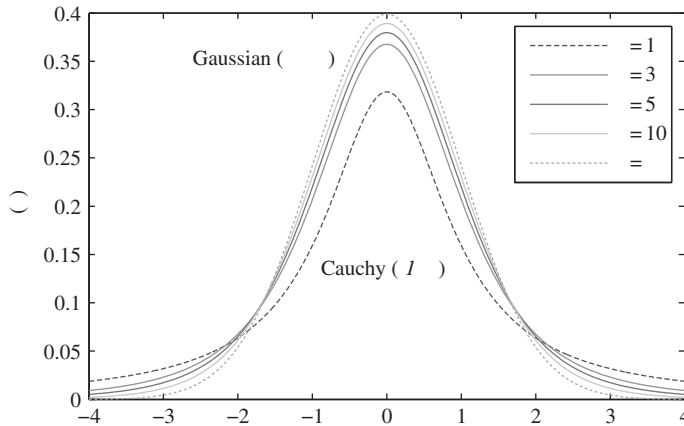


Figure 7.9 The univariate marginals of the t -distribution have increasingly heavy tails and become successively less peaked about 0 as ν decreases towards unity.

say that a random variable F has a *noncentral F-distribution* with ν_1 and ν_2 degrees of freedom and noncentrality parameter δ , denoted $F \sim F_{\nu_1, \nu_2}(\delta)$, if

$$F = \frac{x_1/\nu_1}{x_2/\nu_2} \sim F_{\nu_1, \nu_2}(\delta). \quad (7.88)$$

If $\delta = 0$, we say that F has a *central F-distribution*. More details about the F -distribution can be found in (Ross, 2009; Forbes et al., 2011).

The Mahalanobis distance from \mathbf{x} to the center \mathbf{c} , with respect to \mathbf{S} , follows a central F -distribution with p and ν degrees of freedom:

$$\frac{1}{p} \Delta^2(\mathbf{x}) = \frac{1}{p} (\mathbf{x} - \mathbf{c})^T \mathbf{S}^{-1} (\mathbf{x} - \mathbf{c}) \sim F_{p, \nu}. \quad (7.89)$$

Because $f(\mathbf{x})$ in (7.84) depends on \mathbf{x} only through $\Delta^2(\mathbf{x})$, the probability density is the same for all \mathbf{x} that have the same Mahalanobis distance from \mathbf{c} , and thus the distribution is ellipsoidally symmetric about \mathbf{c} . The distribution of the Mahalanobis distance with respect to $\text{cov}(\mathbf{x})$ can be obtained from (7.86) and (7.89):

$$\Delta^0(\mathbf{x}) = \frac{1}{p} \frac{\nu}{\nu - 2} (\mathbf{x} - \mathbf{c})^T \mathbf{S}^{-1} (\mathbf{x} - \mathbf{c}) \sim F_{p, \nu}. \quad (7.90)$$

Figure 7.10 shows 100 samples and the 90 percent contours for random vectors generated by $\mathbf{x} \sim N_2(\mathbf{c}, \mathbf{S})$ and $\mathbf{t} \sim t_2(\mathbf{c}, \mathbf{S}, 6)$, where \mathbf{c} is given by (7.69) with $\rho = 0.5$. We note that the area under the 90 percent contour of the t -distribution is larger; this happens because for $\nu = 6$ the t -distribution has heavier tails than a normal distribution with the same mean and covariance.

One of the advantages of the multivariate t -distribution is the presence of the second degree of freedom ν which adjusts the shape of the distributional tail. When $\nu = 1$ the multivariate t -distribution is equal to the multivariate Cauchy distribution and has very

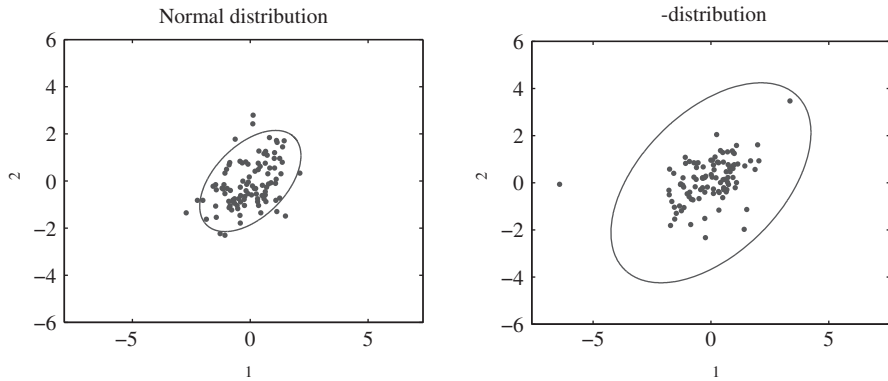


Figure 7.10 The 90 percent contours of a bivariate normal distribution and a t -distribution, with $v = 6$ degrees of freedom, that have the same mean and covariance.

heavy tails. The Cauchy distribution is a member of the family of stable distributions, which have no second-order moments. As $v \rightarrow \infty$ the distribution tends towards the multivariate normal distribution with covariance matrix Σ and has lighter tails.

7.4.5 Elliptically Contoured Distributions

The multivariate normal distribution and the multivariate t -distribution belong to the class of *elliptically contoured distributions (ECDs)*. These distributions have elliptical contours of equal probability density and a “bell-shaped surface” with lighter or heavier tails than the normal distribution.

A random vector \mathbf{x} has an elliptical distribution with location vector μ and scale positive definite matrix Σ_0 , if its density takes the form

$$f(\mathbf{x}) = c_p |\Sigma_0|^{-1/2} g(\mathbf{x} - \mu)^T \Sigma_0^{-1} (\mathbf{x} - \mu), \quad (7.91)$$

where the function g is typically known as the density generator. For a vector \mathbf{x} distributed according to (7.91), we use the notation $\text{ECD}_p(\mathbf{x}; \mu, \Sigma_0; g)$ or simply $\text{ECD}_p(\mathbf{x}; \mu, \Sigma_0)$. For the multivariate normal distribution $N_p(\mu, \Sigma)$, we have $g(u) = \exp(-u^2/2)$, $c_p = (2\pi)^{-p/2}$, and $\Sigma_0 = \Sigma$. This class of symmetric distributions includes the normal, Student’s t , Cauchy, and logistic distributions, among others.

If $\mathbf{x} \sim \text{ECD}_p(\mu, \Sigma)$ we say that the random vector \mathbf{x} has a *spherically invariant* or simply a spherical distribution. Clearly, spherical distributions are invariant to rotation transformations. If $\Sigma_0 = \mathbf{R}^T \mathbf{R}$ is the Cholesky decomposition of matrix Σ , the whitening transform (7.68) yields an equivalent spherical distribution:

$$\mathbf{x} \sim \text{ECD}_p(\mu, \Sigma) \Leftrightarrow \mathbf{z} = \mathbf{R}^T (\mathbf{x} - \mu) \sim \text{ECD}_p(\mathbf{0}, \mathbf{I}). \quad (7.92)$$

Thus, the distribution of a random vector \mathbf{x} can be characterized by considering the centered and whitened transformed random vector \mathbf{z} .

An interesting property of a spherically distributed vector \mathbf{x} is that a transformation to polar coordinates yields angles and a radius which are all independently distributed,

with the angles having the same distribution for all random vectors \mathbf{z} . If the random vector \mathbf{z} has density $c_p g(\mathbf{z}^T)$ and

$$\begin{aligned} z_1 &= r \sin \theta_1 \sin \theta_2 \dots \sin \theta_{p-2} \sin \theta_{p-1} \\ z_2 &= r \sin \theta_1 \sin \theta_2 \dots \sin \theta_{p-2} \cos \theta_{p-1} \\ z_3 &= r \sin \theta_1 \sin \theta_2 \dots \cos \theta_{p-2} \\ &\vdots \\ z_{p-1} &= r \sin \theta_1 \cos \theta_2 \\ z_p &= r \cos \theta_1, \end{aligned} \quad (7.93)$$

where $r > 0$, $0 < \theta_i \leq \pi$, $i = 1, \dots, p-2$, and $0 < \theta_{p-1} \leq 2\pi$, then $r, \theta_1, \dots, \theta_{p-1}$ are independent, the distributions of all $\theta_1, \dots, \theta_{p-1}$ are the same for all \mathbf{z} , with θ_k having density proportional to $\sin^{p-1-k} \theta_k$ (so that θ_{p-1} is uniformly distributed from 0 to 2π), and $y = r^2 = \mathbf{z}^T \mathbf{z}$ has density function

$$f_{r^2}(y) = \frac{c_p \pi^{p/2}}{\Gamma(p/2)} y^{m/2-1} g(y), \quad y > 0. \quad (7.94)$$

A proof and more details are provided by Muirhead (1982). This property is illustrated in Figure 7.11 for a spherically invariant t -distribution. Clearly, the polar coordinates

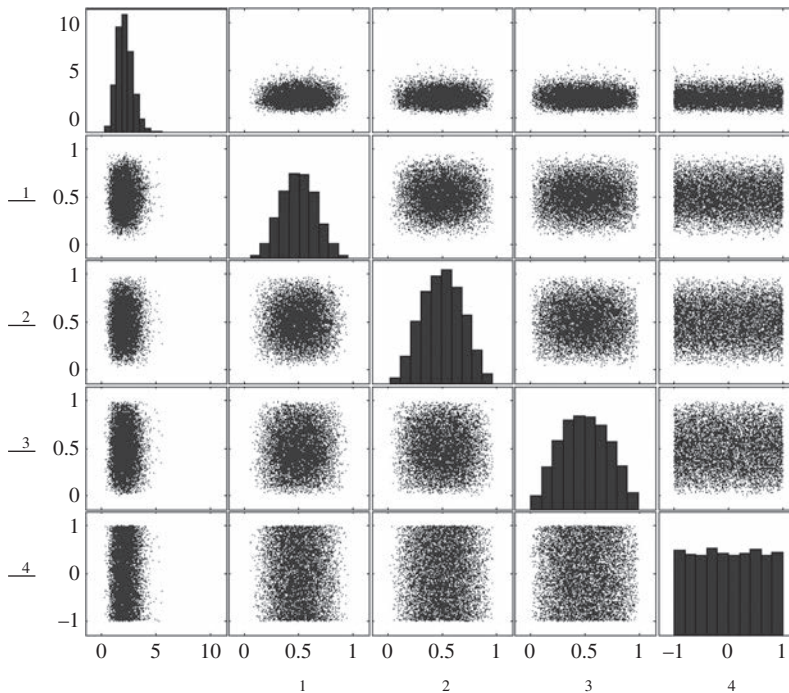


Figure 7.11 Estimated probability density functions and pairs of scatter plots for the random variables representing the spherically invariant random vector $\mathbf{z} \sim t_5(\mathbf{0}, \mathbf{I}, 100)$ in polar coordinates.

are pairwise uncorrelated and their empirical distributions resemble the underlying theoretical distributions. The representation of a spherically symmetric distribution in polar coordinates provides the basis for developing visual and formal tests to check whether hyperspectral data follow a p -dimensional elliptical distribution (Niu et al., 2010).

Using the polar representation (7.93), we conclude that any vector \mathbf{x} with a spherically invariant distribution can be expressed as (Muirhead, 1982)

$$\mathbf{x} = r \mathbf{\hat{x}}, \quad (7.95)$$

where $\mathbf{\hat{x}}$ is a function of the angular variables $\theta_1, \dots, \theta_{p-1}$. The variables r and $\mathbf{\hat{x}}$ are statistically independent and $\mathbf{\hat{x}}$ is uniformly distributed on the unit sphere in \mathcal{R}^p . Indeed, if $\Pr(\mathbf{\hat{x}} = \mathbf{0}) = 0$, then we have $r = \|\mathbf{x}\|$ and $\mathbf{x} = r\mathbf{\hat{x}}$.

We emphasize that the distributions of the angles remain *unchanged* regardless of the spherical distribution considered; only the distribution of r changes from one spherical distribution to another. Therefore, the probability distribution of

$$y = r^2 = \mathbf{x}^T \mathbf{x} = (\mathbf{x} - \mathbf{\hat{x}})^T \mathbf{\Omega}_0^{-1} (\mathbf{x} - \mathbf{\hat{x}}) \quad (7.96)$$

is sufficient to identify the probability density function of the spherical distribution. This result holds regardless of whether we are dealing with a spherical or elliptical distribution. For example, the distribution of y is χ_p^2 if \mathbf{x} is a multivariate normal distribution (see (7.74)) and $F_{p,v}$ if \mathbf{x} is a multivariate t -distribution (see (7.90)). These results, which are illustrated in Figure 7.12, suggest useful visual aids to discriminate between p -dimensional normal and t -distributions.

Elliptically contoured distributions have contours of equal density with elliptical shape, like the multivariate normal density. However, they provide greater flexibility

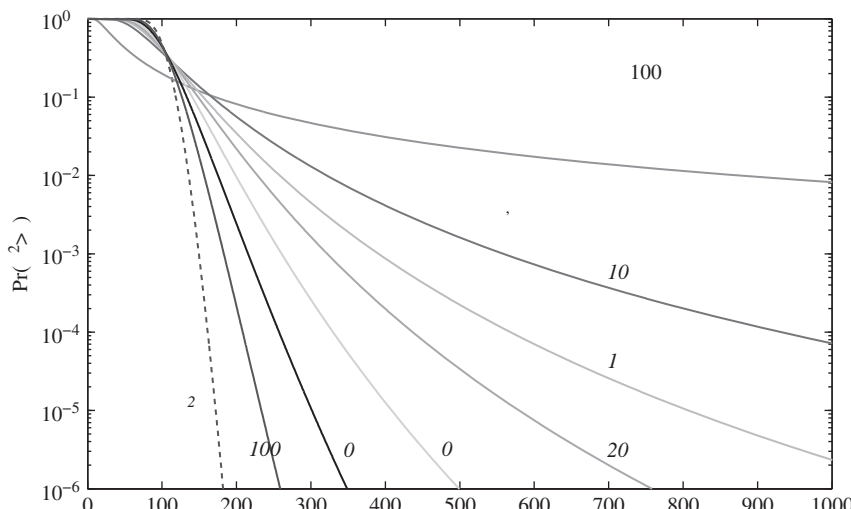


Figure 7.12 Distribution of Mahalanobis distance (Δ^2) for a multivariate normal distribution and various t -distributions with different degrees of freedom and $p = 100$. We note that $F_{p,v}$ approaches χ_p^2 as the tail index v approaches infinity.

because they allow for heavier or lighter tails than the normal. We emphasize that the simplicity of elliptical distributions implies that they cannot capture all departures from normality that can occur in real data. Elliptical distributions are useful in studying the robustness of methods developed for normal distributions to departures from the assumed normality. It has been shown that many properties of this class are very similar to analogous properties of the multivariate normal distribution. For further details about elliptical distributions we refer to Muirhead (1982), Fang et al. (1990), and Anderson (2003).

7.5

Maximum Likelihood Parameter Estimation

In practical applications we know or assume a functional form for a distribution function and we wish to estimate its parameters from a set of observations. Many good statistical procedures use estimated parameter values that “best” explain the observed data. One meaning of “best” is to select the parameter values that maximize the joint density evaluated at the observations. This technique is known as *maximum likelihood estimation*, and the maximizing parameter values are called *maximum likelihood estimates*. We next illustrate the method of maximum likelihood estimation for the case of univariate and multivariate normal distributions.

7.5.1

Univariate Normal Distribution

Consider a set x_1, x_2, \dots, x_N of mutually independent normal random variables with mean m and variance σ^2 . Since x_1, x_2, \dots, x_N are mutually independent, the joint density is given by the product of their individual densities

$$f(x_1, \dots, x_N) = \frac{1}{(2\pi)^{N/2}(\sigma^2)^{N/2}} \exp \left(-\frac{1}{2\sigma^2} \sum_{i=1}^N (x_i - m)^2 \right). \quad (7.97)$$

The density function (7.97) gives the frequency of occurrence of different data values for the specified values of the parameters m and σ . When the numerical values of the observations become available, they may be substituted for the x_i in (7.97). The resulting expression, now considered as a function of m and σ^2 for the fixed set of observations x_1, x_2, \dots, x_N , is called the *likelihood function*. The likelihood function, denoted by $L(m, \sigma^2)$, shows how likely the observed data are as a function of the possible parameter values. *Maximizing the likelihood gives the parameter values which specify the member of the density family which “most likely” has generated the observed data.*

The maximum likelihood (ML) estimates of the parameters are obtained by maximizing the likelihood function $L(m, \sigma^2)$ with respect to m and σ^2 . Because the exponential function is monotonic, it is more convenient to work with the natural logarithm of the likelihood

$$\ln L(m, \sigma^2) = -\frac{N}{2} \ln(2\pi) - \frac{N}{2} \ln \sigma^2 - \frac{1}{2\sigma^2} \sum_{i=1}^N (x_i - m)^2. \quad (7.98)$$

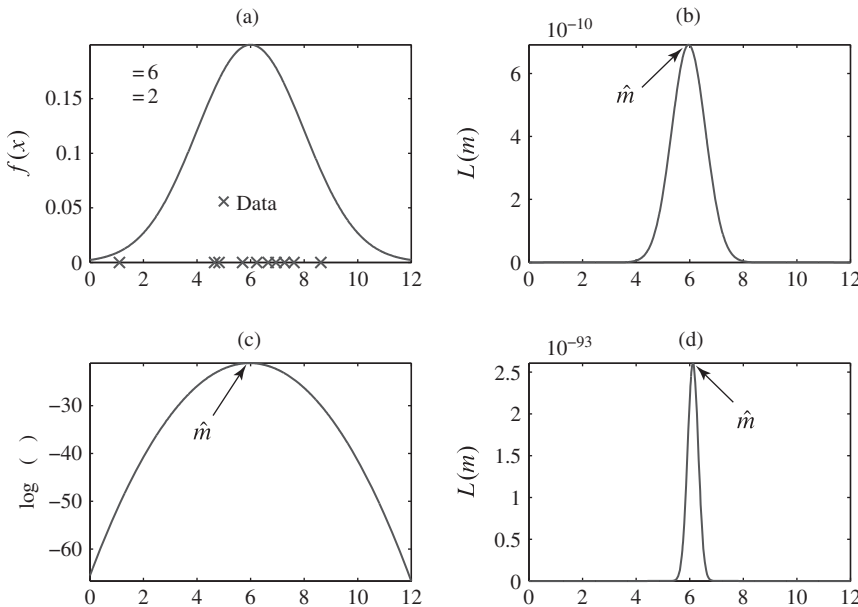


Figure 7.13 (a) The density of the normal random variable $x \sim N(6, 4)$ and ten observations (\times) drawn from this distribution. (b) Plot of likelihood function $L(m)$ as a function of the unknown parameter m for $N = 10$ observations; the variance is assumed known ($\sigma^2 = 4$). (c) The logarithm of the likelihood function for $N = 10$ observations. (d) The likelihood function for $N = 100$ observations.

Figure 7.13 shows the likelihood as a function of the unknown parameter m , if we assume that the variance σ^2 is known. The quality of the estimator is determined by the center and shape of the likelihood function. A flat shape implies an imprecise estimator; in contrast if the likelihood function is concentrated about the ML estimate, the parameter is precisely estimated. We note that as the number of observations increases, the likelihood function becomes more concentrated about the true parameter leading to a better estimate. Finally, we note that taking the logarithm helps numerically because the product of a large number of small probabilities can easily underflow the numerical precision of the computer. This can be seen by comparing the range of $L(m, \sigma^2)$ and $\ln L(m, \sigma^2)$ in Figure 7.13.

In general, the partial derivatives of the log likelihood function with respect to the unknown parameters m and σ^2 are

$$\begin{aligned}\frac{\partial \ln L(m, \sigma^2)}{\partial m} &= \frac{1}{\sigma^2} \sum_{i=1}^N (x_i - m) \\ \frac{\partial \ln L(m, \sigma^2)}{\partial \sigma^2} &= -\frac{N}{2\sigma^2} + \frac{1}{2\sigma^4} \sum_{i=1}^N (x_i - m)^2.\end{aligned}$$

If we equate these to zero and cancel any extraneous factors, we obtain a system of two simultaneous equations

$$\begin{array}{ll} \sum_{i=1}^N x_i - Nm = 0, & \sum_{i=1}^N (x_i - m)^2 - N\sigma^2 = 0. \end{array}$$

We solve the first for the estimate of m , and then we substitute in the second to obtain the estimate of σ^2 . This decoupling of equations for m and σ^2 is a nice feature of the normal distribution; typically maximum likelihood estimation requires the solution of nonlinear systems of equations. The resulting maximum likelihood estimates are

$$\hat{m} = \frac{1}{N} \sum_{i=1}^N x_i \quad (7.99)$$

$$\hat{\sigma}^2 = \frac{1}{N} \sum_{i=1}^N (x_i - \hat{m})^2. \quad (7.100)$$

These estimates are intuitively plausible, because they are obtained as the average of the observations and the average of squared deviations from the estimated mean. In addition, the maximum of the likelihood is easily shown to be

$$L(\hat{m}, \hat{\sigma}^2) = \frac{e^{-N/2}}{(2\pi\hat{\sigma}^2)^{N/2}}. \quad (7.101)$$

There are several criteria for judging the quality of an estimator. If we assume that the observations in (7.99) are random variables and take expectations, we have

$$E(\hat{m}) = \frac{1}{N} \sum_{i=1}^N E(x_i) = \frac{1}{N} \sum_{i=1}^N m = m. \quad (7.102)$$

We say that \hat{m} is an *unbiased* estimator of m because it gives the correct value on the average. The expectation of $\hat{\sigma}^2$ involves more lengthy computations. The result is

$$E(\hat{\sigma}^2) = 1 - \frac{1}{N} \sigma^2, \quad (7.103)$$

which shows that $\hat{\sigma}^2$ is not an unbiased estimate of the variance. However, if we replace the divisor N in (7.100) by $(N - 1)$ we obtain an unbiased estimator. We will use the maximum likelihood estimator because for large values of N the difference between the two estimators is negligible.

To find the variance of the estimator \hat{m} we set $a_i = 1/N$ and $\sigma^2 = \sigma^2$ in (7.37). The resulting variance is

$$\text{var}(\hat{m}) = \frac{\sigma^2}{N}, \quad (7.104)$$

which shows that the estimate is concentrated closer to the true value as N increases. A good estimator should have zero bias and the smallest possible variance. If the observations x_i are correlated, the variance $\text{var}(\hat{m})$ can be significantly higher than the one given by (7.104).

7.5.2 Multivariate Normal Distributions

The maximum likelihood estimation approach for normal random variables ($p = 1$) can be extended to normal random vectors ($p \geq 2$). Although the mathematical derivations for random vectors are much more complicated, the results resemble the ones obtained for random variables.

Suppose that $\mathbf{x}_1, \mathbf{x}_2, \dots, \mathbf{x}_N$ are $p \times 1$ observation vectors from a multivariate normal distribution with mean vector μ and covariance matrix Σ . If these data are realizations from N mutually independent normal random vectors with distribution $N_p(\mu, \Sigma)$, the likelihood function is

$$\begin{aligned} L(\mu, \Sigma) &= \prod_{i=1}^N \frac{1}{(2\pi)^{p/2} |\Sigma|^{1/2}} \exp \left(-\frac{1}{2} (\mathbf{x}_i - \mu)^T \Sigma^{-1} (\mathbf{x}_i - \mu) \right) \\ &= \frac{1}{(2\pi)^{pN/2} |\Sigma|^{N/2}} \exp \left(-\frac{1}{2} \sum_{i=1}^N (\mathbf{x}_i - \mu)^T \Sigma^{-1} (\mathbf{x}_i - \mu) \right). \end{aligned} \quad (7.105)$$

Maximization of (7.105) with respect to μ and Σ gives the maximum likelihood estimates (Johnson and Wichern, 2007)

$$\hat{\mu} = \frac{1}{N} \sum_{i=1}^N \mathbf{x}_i \quad (7.106)$$

and

$$\hat{\Sigma} = \frac{1}{N} \sum_{i=1}^N (\mathbf{x}_i - \hat{\mu})(\mathbf{x}_i - \hat{\mu})^T. \quad (7.107)$$

Substitution of (7.106) and (7.107) into (7.105) gives the maximum of the likelihood function

$$L(\hat{\mu}, \hat{\Sigma}) = \frac{e^{-pN/2}}{(2\pi)^{pN/2} |\hat{\Sigma}|^{N/2}}. \quad (7.108)$$

The expectations of sample mean and covariance are

$$E(\hat{\mu}) = \mu, \quad E(\hat{\Sigma}) = \frac{N-1}{N} \Sigma. \quad (7.109)$$

Thus, the sample mean estimator is always unbiased and the sample covariance estimator is unbiased for $N \gg 1$. The variance and covariances of \hat{c}_{ij} are hard to compute exactly. A simple approximation can be obtained when Σ is diagonal. For example, we can easily show that $\text{var}(\hat{c}_{ij}) \approx c_{ii}c_{jj}/N$, which confirms that the approximations are good for large N (Fukunaga, 1990).

The statistical and numerical properties of the estimated covariance matrix, which are extremely important for all applications to be discussed in this book, are formulated in terms of the unbiased sample covariance matrix

$$= \frac{N}{N-1} \hat{\Sigma} = \frac{1}{N-1} \sum_{i=1}^N (\mathbf{x}_i - \hat{\mu})(\mathbf{x}_i - \hat{\mu})^T. \quad (7.110)$$

If $N \leq p$, that is, the number of observations is less or equal to the number of variables, then $\mathbf{1}^\top \mathbf{1} = 0$ for any set of observations. However, if $\text{var}(\mathbf{x}_i) > 0$ for every $i \neq j$ and all $i = 1, \dots, N$, provided $N > p$, the matrix $\mathbf{1}^\top \mathbf{1}$ has full rank with probability 1 and $\mathbf{1}^\top \mathbf{1} > 0$ (Johnson and Wichern, 2007). However, even when N is larger than p , the unbiased sample covariance \mathbf{S} has a significant amount of sampling error, and its inverse is a poor estimator for \mathbf{S}^{-1} . For example, under normality assumption, the expected value of the inverse $E(\mathbf{S}^{-1}) = \frac{N-p-2}{N-p-2} \mathbf{S}^{-1}$. While \mathbf{S} is an unbiased estimator of \mathbf{S}^{-1} , \mathbf{S}^{-1} is a highly biased estimator of \mathbf{S}^{-1} if p is close to N . In particular, for $N = 2p + 4$, we have $E(\mathbf{S}^{-1}) = 2 \mathbf{S}^{-1}$. More information about the statistical properties of the sample covariance matrix estimator and other improved estimators can be found in (Anderson, 2003; Muirhead, 1982; Ledoit and Wolf, 2004; Pourahmadi, 2013).

7.5.3 Univariate and Multivariate t -Distributions

Suppose a random variable x has a t -distribution with center c , scale parameter s , and ν degrees of freedom. The corresponding standardized t random variable is

$$u = \frac{x - c}{s}. \quad (7.111)$$

The probability density function of u is

$$f(u) = \frac{\Gamma(\frac{\nu-1}{2})}{\Gamma(\frac{\nu}{2}) (\pi \nu)^{\frac{1}{2}}} \left(1 + \frac{u^2}{\nu}\right)^{-\frac{(\nu-1)}{2}}. \quad (7.112)$$

If we have a set of observations x_1, \dots, x_N with corresponding standardized variables u_1, \dots, u_N , the log likelihood function is

$$\ln L = N \ln \frac{\Gamma(\frac{\nu-1}{2})}{\Gamma(\frac{\nu}{2}) (\pi \nu)^{\frac{1}{2}}} - \frac{1}{2}(\nu+1) \sum_{i=1}^N \ln \left(1 + \frac{u_i^2}{\nu}\right), \quad (7.113)$$

which can be solved for c , s , and ν using nonlinear optimization techniques. Estimating the parameters of a multivariate t -distribution is more complicated and can be done using the method of expectation-maximization (McLachlan and Peel, 2000).

7.6

Statistical Analysis of Hyperspectral Imaging Data

As we have seen, the data acquired by a hyperspectral imaging sensor are organized as a “datacube” with two spatial dimensions and one spectral dimension. The value of each element provides either the at-sensor measured spectrum of a ground resolution cell with coordinates (x_i, y_j) at a wavelength band centered at λ_k . These data can be viewed as a collection of simultaneously taken images, one at each spectral band, or as a collection of spectra, one for each ground resolution cell. Thus, we should consider two image types. The first, in which each pixel has a single scalar value associated with it, is a *scalar* image. The second type is a *vector* image, in which each pixel is represented by a vector of values. Understanding the distributional characteristics of

hyperspectral images is the first step in data exploitation. In this section we discuss statistical techniques for the analysis of scalar and vector spectral images, and statistical models for hyperspectral images of natural backgrounds in the reflective and thermal regions of the infrared spectrum.

7.6.1

Statistical Analysis of Scalar (Monochromatic) Images

According to Chambers et al. (1983), “there is no statistical tool as powerful as a well-chosen graph”. Graphical analysis helps to uncover the structure of the data, evaluate the “goodness-of-fit” of statistical models, and understand the operation of data exploitation algorithms.

The starting point for scalar image analysis is the histogram. At a minimum, we can use the histogram to find the pixels with minimum and maximum values, which features in an image account for the main histogram peaks, and identify theoretical distributions to model the data.

Figure 7.14(a) shows a scalar hyperspectral image (spectral channel at 875 nm) and its histogram. The presence of a few pixels with radiance values beyond 6000 results in a low-contrast image. We can enhance the contrast by saturating or clipping all pixels above 6000; the resulting image and the corresponding histogram are shown in Figure 7.14(b). The image histogram is a useful tool for contrast enhancement; this subject is discussed in Gonzalez and Woods 2008. The shape of the histogram is strongly bimodal, which indicates two dominant surface materials in the scene. A primitive segmentation of these two classes can be achieved by selecting a threshold at the valley between the two histogram peaks. If pixels with radiance above (below) the threshold are assigned to white (black), the result is the binary image shown in Figure 7.14(c). The right tail of the histogram is typically used to determine outliers; that is, pixels with “unusual” measurements caused by instrumentation errors or materials with unusual properties. This idea is illustrated in Figure 7.14(d).

Many statistical analysis methods assume that the data follow a particular distribution, most commonly a normal distribution. The agreement between the distribution of the data and the theoretically expected distribution is evaluated visually using a probability plot. There are two basic types of plots for comparing two probability distributions, the *probability–probability (P–P) plot* and the *quantile–quantile (Q–Q) plot*. The basic ideas are illustrated in Figure 7.15. A plot of points whose coordinates are the cumulative probabilities $\{p_1(q), p_2(q)\}$ for different values of q is a P–P plot, while a plot of the points whose coordinates are the quantiles $\{q_1(p), q_2(p)\}$ for different values of p is a Q–Q plot. A linear relationship indicates that the assumed distribution provides a good fit for the distribution of the data. The widely used normal Q–Q plot is obtained by plotting the ordered data values $x_{(1)} \leq x_{(2)} \leq \dots \leq x_{(N)}$ against the quantiles of a standard normal distribution, where usually $p_i = (i - 0.5)/N$ and $q_i = \Phi^{-1}(p_i)$. Figure 7.16(a) shows the normal Q–Q plot for data generated by a *t*-distribution with $v = 4$ degrees of freedom. We note that although the center of the data follows a normal distribution, the tails are much heavier than those predicted by a normal distribution. Figure 7.16(b) shows the Q–Q plot for the scalar image in Figure 7.14(a). The shape of

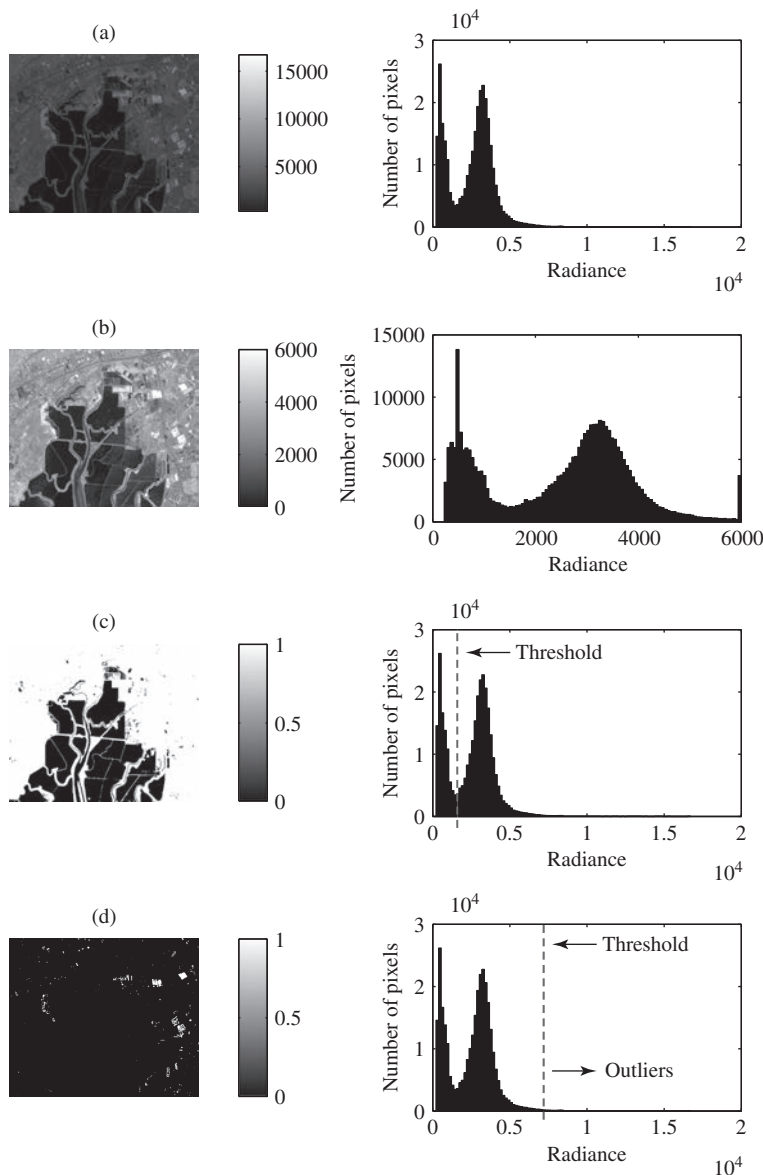


Figure 7.14 Illustration of scalar image histograms and their implications.

the Q–Q plot clearly reflects the cut-off in the left tail, the heaviness of the right tail, and the bimodality of the histogram shown in Figure 7.14(b).

If the data comes from a single land cover their histogram is typically unimodal (that is, it has a single peak). If there are multiple ground covers in the scene, the histogram is multimodal and it provides some information about the spatial distribution.

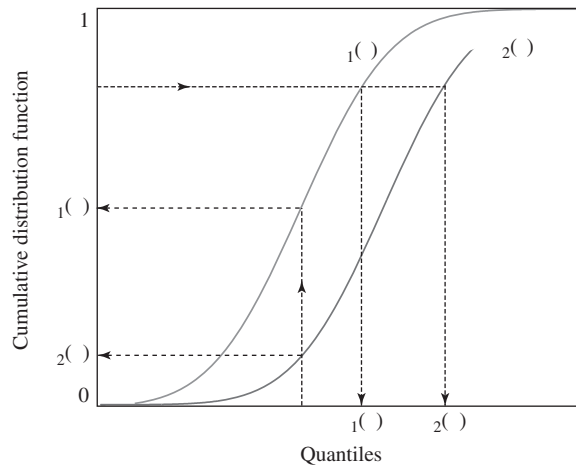


Figure 7.15 Diagram used to illustrate the generation of probability–probability plots and quantile–quantile plots.

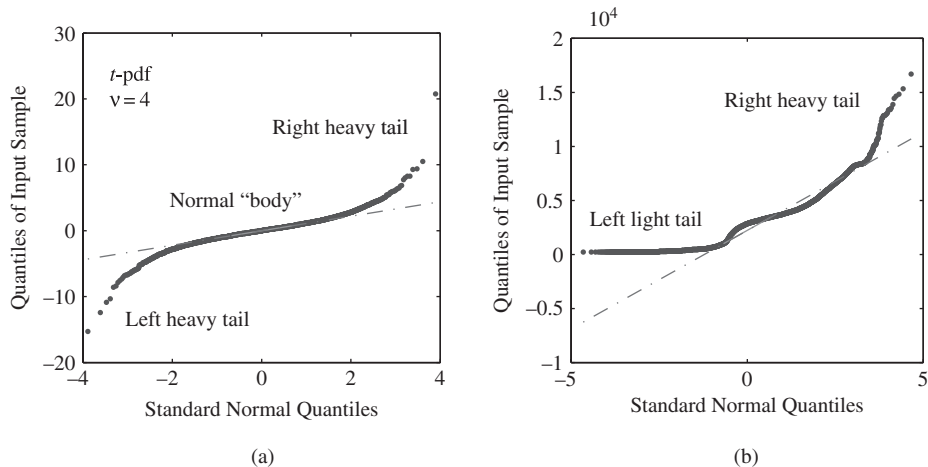


Figure 7.16 (a) Normal Q–Q plot of data derived from a heavy tail t distribution. (b) Normal Q–Q plot for the scalar radiance image shown in Figure 7.14(a).

7.6.2 Statistical Analysis of Vector (Polychromatic) Images

The starting point for vector image analysis is the scatter plot. Two-channel scatter plots are used to show where groups of pixels on an image are located in the data spectral space, and how the brightness in different channels co-varies. Figure 7.17 shows the images of two spectral channels from the Moffett radiance data cube, their scatter plot, and pseudocolor representation of their joint histogram. This two-dimensional histogram is obtained as explained in Section 7.2. Clearly, the histogram (or density scatter plot) reveals more vividly the clustering of pixels with similar spectra.

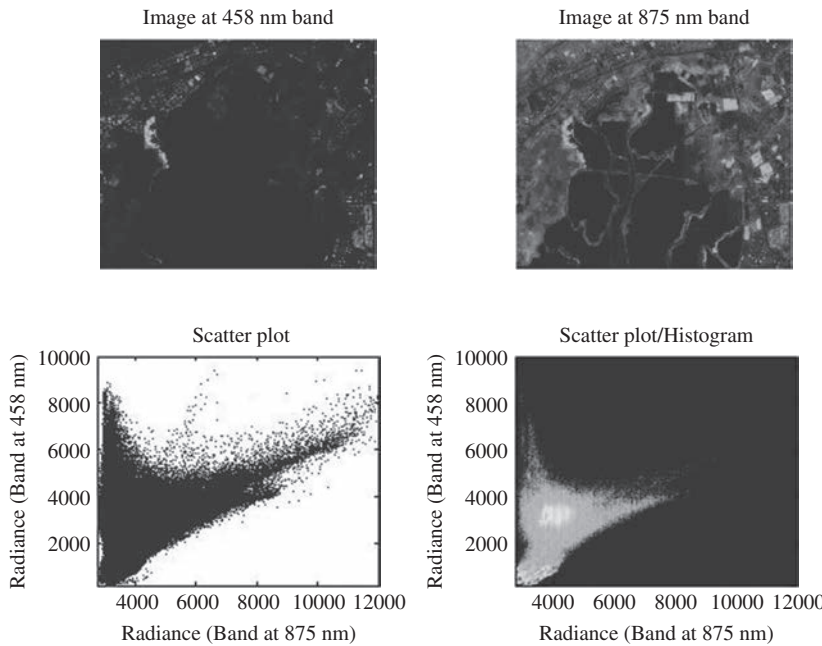


Figure 7.17 Scatter plot and two-dimensional histogram of two images corresponding to different spectral bands. Note that the scatter plot does not show any density or concentration information. (A black and white version of this figure will appear in some formats. For the color version, please refer to the plate section.)

The covariation between two channels or bands is characterized by their correlation. The correlation between spectral bands arises from a combination of factors (Schowengerdt, 2007):

1. *Material spectral correlation*: A potential cause for this component is the relatively low reflectance of vegetation across the visible spectrum; the result is a similar signature in all visible bands. The wavelength range of high correlation is determined by the spectral reflectance of the material.
2. *Topography correlation*: In the solar reflectance region this component is the result of topographic shading, which is a dominant image component in mountainous areas and at low sun angles. Note that shading is independent of surface material and its effects are different in the thermal region.
3. *Sensor band overlap correlation*: The cause of this correlation component is the common energy between two adjacent spectral bands introduced by overlapping spectral sensor responses. This effect, which is important for precise sensor calibration, can be minimized by good sensor design, but it cannot be totally eliminated.

A visual investigation of band-to-band (or spectral) correlation can be done using pairwise scatter plots; for a quantitative assessment we must use the correlation coefficient matrix because its entries are normalized between the values -1 and 1 .

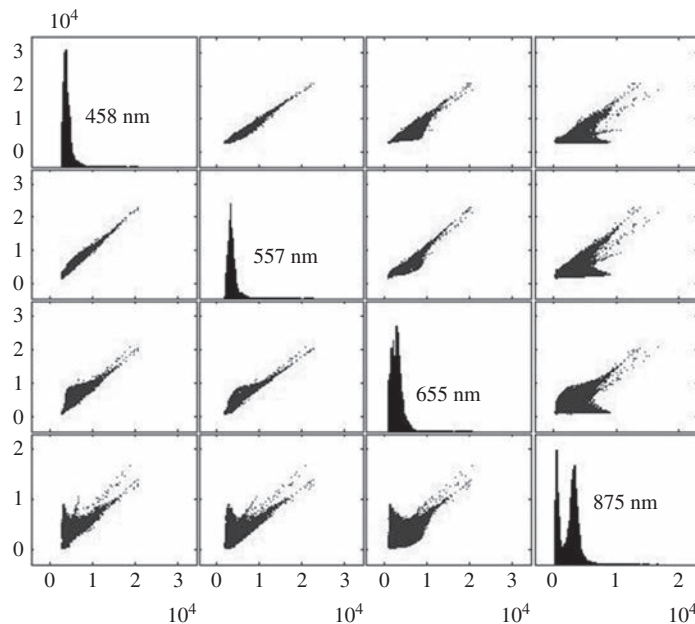


Figure 7.18 Bivariate or pairwise scatter plots and histograms of four spectral images arranged as elements of a scatter plot matrix.

Scatter plots of more than two channels are impossible to visualize. Therefore, we obtain scatter plots of each pair of channels. Although these two-dimensional projections do *not* always reveal the structure of the data, they still provide useful information. Arranging the pairwise scatter plots in the form of a square grid, known as the scatter plot matrix, can help in assessing a number of scatter plots at the same time (see Figure 7.18). The scatter plot matrix is a square symmetric grid of bivariate scatter plots; the diagonal plots show the histogram of each spectral channel.

Careful inspection of many scatter plots and two-dimensional histograms clearly demonstrates the hyperspectral data have multimodal distributions. This should be expected because most natural scenes consist of multiple ground cover classes, with each class characterized by a unimodal distribution. Thus, it is important to find suitable models for the distribution of homogeneous ground cover classes. Since multivariate normal distributions have been almost exclusively used in classification algorithms for multispectral imaging data (Landgrebe, 2003; Richards, 2013), we need to evaluate how accurately they characterize the distribution of hyperspectral data.

In contrast to scalar data, goodness-of-fit tests for multivariate data are impractical due to the inherent “sparseness” of the data in the observation space. In practice, we can assess multivariate normality using techniques from the following categories (Gnanadesikan, 1997; Johnson and Wichern, 2007):

1. Univariate techniques for evaluating marginal normality. We use such methods to check if the distributions of the elements of n appear to be normal.

2. Multivariate techniques for evaluating joint normality. For example, check if the scatter plots of pairs of observations show the elliptical appearance expected from normal distributions.
3. Techniques that use unidimensional views of multivariate data. Examples include linear projections and the Mahalanobis distance.

In practice, the most widely used approach is to investigate the distribution of the Mahalanobis distance. We will carry out these investigations using the results obtained in Section 7.4. Since the multivariate normal distribution is a member of the class of ECDs, the basic tool is the matrix plot shown in Figure 7.11. We first convert the data into polar coordinates, we next estimate their probability density functions, and then we create the scatter plot matrix. To investigate the distribution of the Mahalanobis distance, we use the probability of exceedance, defined by

$$(y) = \Pr(y_i > y). \quad (7.114)$$

Plotting this function in log-linear scale provides good insight into the behavior of the tails of the distribution. The theoretical distributions in (7.74) and (7.89) do not hold when the true covariance matrix is replaced by its maximum likelihood estimate; however, the approximation is quite accurate for practical applications when $N \gg p$ (Krzanowski, 2000).

Figure 7.19 shows an example of the probability of exceedance of the Mahalanobis distance for a homogeneous spectral class. Close inspection of the theoretical exceedance curves shows that the multivariate data distribution cannot be accurately modeled using a normal distribution because the Mahalanobis distance does not follow a chi-squared distribution. A detailed investigation of the distribution of Mahalanobis distance showed that homogeneous classes from natural hyperspectral backgrounds can

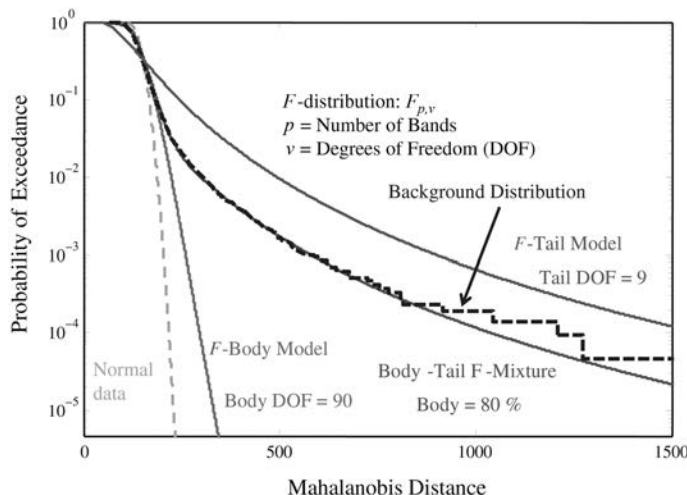


Figure 7.19 Illustration of modeling the distribution of Mahalanobis distance of hyperspectral imaging data using a mixture of two central F -distributions.

be characterized statistically using mixtures of multivariate t -distributions (Marden and Manolakis, 2003). It was shown that the following density mixture

$$\sim w t_p(v_1, \dots, \mathcal{R}) + (1 - w) t_p(v_2, \dots, \mathcal{R}), \quad 0 \leq w \leq 1 \quad (7.115)$$

provides a good model for hyperspectral backgrounds. The first component models the body of the distribution and the second component models the tails. The model of the tails provides useful information for target detection applications. Since (7.115) is a mixture of two t -ECDs, its Mahalanobis distance follows a mixture of two central F -distributions. Thus, the quadratic form corresponding to (7.115) has the normalized distribution (see equation (7.89)):

$$\Delta^0(\mathbf{x})^2 \sim w F_{p,v} + (1 - w) F_{p,v}. \quad (7.116)$$

To estimate the parameters of the model specified by (7.115), we fit equation (7.116) to the Mahalanobis distance of the data by minimizing the “exceedance” metric, discussed next, on a grid of parameter values (Marden and Manolakis, 2004). If $\Pr(x) = \Pr\{x_i > x\}$ is the probability of exceedance and $\mathcal{N}^{-1}(P_i)$ is the point x_i where $\Pr(x_i) \simeq P_i$, the exceedance metric is defined by

$$D = \sum_{i=1}^K \left| \left[\mathcal{N}^{-1}(P_i) - \mathcal{M}^{-1}(P_i) \right] \right|, \quad (7.117)$$

where P_i are K equally log spaced points on the probability axis of the exceedance curves. $\mathcal{N}(x)$ is the empirical value obtained from the data and $\mathcal{M}(x)$ is the theoretical value predicted by the model. To avoid undue influence of the results by extreme outliers of the data, the smallest probability point that the metric evaluates is often chosen as one or two orders of magnitude above the smallest probability step, which is equal to $1/N$. This approach has been used to model several land cover classes extracted from AVIRIS data cubes from Fort A. P. Hill, Virginia, covering regions of loblolly pine plantations, coniferous and deciduous forests, mixed forests and agricultural fields. The results show that mixed tree canopies exhibited the heaviest tail index (Manolakis et al., 2008).

7.7

Gaussian Mixture Models

While the Gaussian distribution has some attractive analytical properties, it suffers from significant limitations when it comes to modeling real hyperspectral data sets. Consider, for example, the scatter plot shown in Figure 7.20. We note that the data set forms at least three dominant clumps, and that a simple Gaussian distribution cannot capture this structure. The solution is to use a linear superposition of Gaussians or t -distributions, which, as shown by Manolakis et al. (2008), provide a better characterization of natural hyperspectral background data. Although Gaussian mixtures are sufficient for classification applications, mixtures of t -distributions are more accurate for detection performance prediction. We focus on Gaussian mixtures because they are easier to estimate and they have more applications.

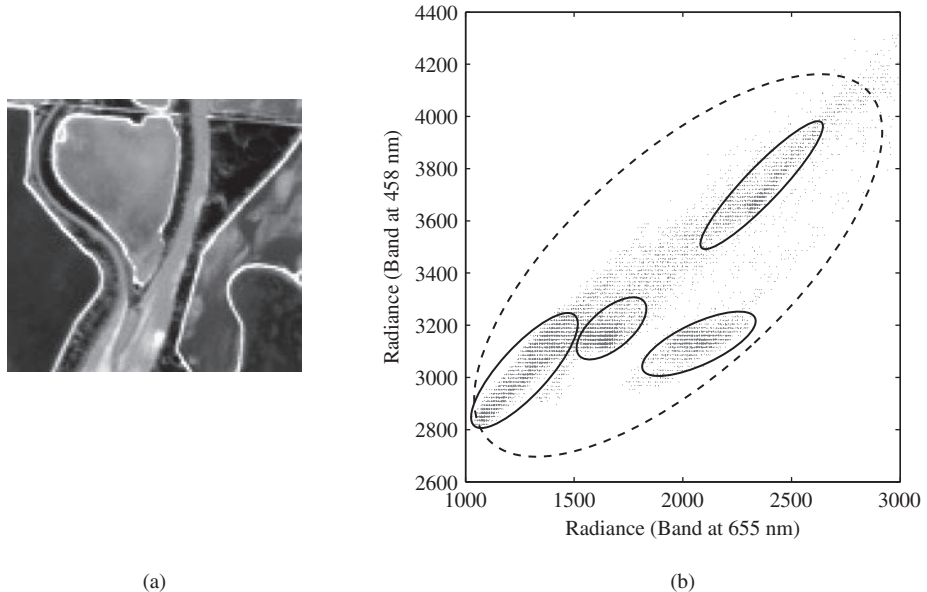


Figure 7.20 (a) A subimage from the Moffett data set; and (b) a scatter plot of the channels corresponding to the red and blue colors. The appearance of multiple clumps is explained by the presence of multiple ground covers in the scene.

7.7.1 Mixtures of Gaussian Distributions

In general, a mixture of K Gaussian distributions takes the form

$$f(\mathbf{r} | \boldsymbol{\theta}) = \sum_{k=1}^K p_k g_k(\mathbf{r} | \boldsymbol{\mu}_k, \boldsymbol{\Sigma}_k), \quad (7.118)$$

where $\boldsymbol{\theta}$ is a vector containing all parameters required to specify the Gaussian mixture model (GMM) in (7.118); that is,

$$\{p_1, \dots, p_K, \boldsymbol{\mu}_1, \dots, \boldsymbol{\mu}_K, \boldsymbol{\Sigma}_1, \dots, \boldsymbol{\Sigma}_K\}. \quad (7.119)$$

Each Gaussian density $g_k(\mathbf{r} | \boldsymbol{\mu}_k, \boldsymbol{\Sigma}_k)$, which is specified by (7.56), is known as a *component* of the mixture and has its own mean $\boldsymbol{\mu}_k$ and covariance $\boldsymbol{\Sigma}_k$. The parameters p_k are called *mixing coefficients*. If we integrate both sides of (7.118) we obtain that

$$\sum_{k=1}^K p_k = 1 \quad (7.120)$$

because $\int g_k(\mathbf{r} | \boldsymbol{\mu}_k, \boldsymbol{\Sigma}_k) d\mathbf{r} = 1$ for every component. Also, the requirements that $f(\mathbf{r} | \boldsymbol{\theta}) \geq 0$ and $g_k(\mathbf{r} | \boldsymbol{\mu}_k, \boldsymbol{\Sigma}_k) \geq 0$ imply that $p_k \geq 0$ for all k . Combining this with condition (7.120) we conclude that

$$0 \leq p_k \leq 1. \quad (7.121)$$

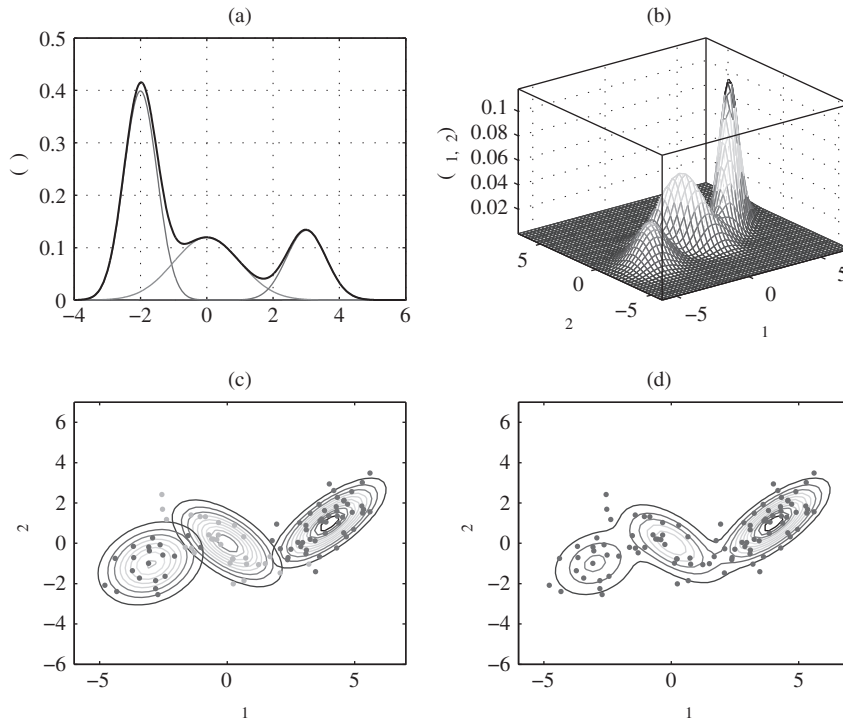


Figure 7.21 Illustration of a mixture of three Gaussian distributions. (a) Scaled Gaussian components and their sum in one dimension. (b) Example of Gaussian mixture probability density function in two dimensions. (c) Contours of the three components and sample data generated by each distribution. (d) Contours of the mixture distribution superimposed on the sample data shown in (c). (A black and white version of this figure will appear in some formats. For the color version, please refer to the plate section.)

Since the mixing coefficients satisfy the requirements to be probabilities, we can view p_k as the prior probability of picking the k th component and $g_k(\cdot | \mu_k, \Sigma_k)$ as the probability of \cdot conditioned on k .

The plots in Figure 7.21 show that a mixture of Gaussians can give rise to very complex densities. Therefore, by using a sufficient number of components, and by properly adjusting their means, covariances, and mixing coefficients, we can approximate any continuous distribution to arbitrary accuracy. We focus on mixtures with Gaussian components; however, mixtures with other component distributions are possible (McLachlan and Peel, 2000).

To generate data with the GMM (7.118) we first pick one of the components or classes with probability π_k , and then we draw an observation x_n from that component. These two steps are repeated for each data point in the set $\mathcal{X} = \{x_1, \dots, x_N\}$. We use the notation $x_m \in \mathcal{C}_k$ to denote that the data point x_n was generated by the k th component or it belongs to the k th class.

Suppose now that we wish to invert this process; that is, given a data set \mathcal{X} and the order K of the model, estimate the mixing coefficients, means, and covariances in

(7.118). Since the maximum likelihood method provides good estimators, it is natural to consider this method for estimating the parameters of the GMM. The log of the likelihood function for the data set \mathbf{x} is given by

$$\ln L(\boldsymbol{\theta}) = \sum_{n=1}^N \ln \sum_{k=1}^K p_k g_k(x_n | \boldsymbol{\theta}_k, \boldsymbol{\theta}_k) . \quad (7.122)$$

The presence of the summation over k inside the logarithm makes the dependence of the likelihood on the parameters highly nonlinear and prevents a closed-form analytical solution. Another significant problem with the maximization of (7.122) is the presence of singularities. To illustrate this issue consider a GMM with $\boldsymbol{\theta}_k = \sigma_k^2$, $k = 1, \dots, K$. Suppose that one of the data points is equal to the mean of the k th component: that is, $x_k = x_n$. This data point will contribute the term $\sqrt{2\pi}/\sigma_k$ in the likelihood function. We note that as $\sigma_k \rightarrow 0$, this term goes to infinity and the log likelihood function will also go to infinity. Although singular solutions are of no interest, in practice we obtain meaningful solutions by restricting attention to the largest of the finite local maxima of the likelihood function (Duda et al., 2001).

The maximum likelihood parameters can be determined using standard nonlinear optimization techniques (Nocedal and Wright, 2006) or the expectation–maximization approach (Bishop, 2006; McLachlan and Peel, 2000). We focus on expectation–maximization algorithms because they are broadly used in hyperspectral imaging applications.

7.7.2

The Expectation–Maximization (EM) Algorithm

If we knew which component generated each observation, we could easily compute the maximum likelihood estimates of the model parameters by fitting each component to the corresponding class (see Section 7.5). The resulting estimates are

$$\hat{p}_k = \frac{N_k}{N} \quad (7.123a)$$

$$\hat{\boldsymbol{\theta}}_k = \frac{1}{N_k} \sum_{n=1}^{N_k} \mathbf{x}_n \quad (7.123b)$$

$$\hat{\boldsymbol{\sigma}}_k^2 = \frac{1}{N_k} \sum_{n=1}^{N_k} (\mathbf{x}_n - \hat{\boldsymbol{\theta}}_k)(\mathbf{x}_n - \hat{\boldsymbol{\theta}}_k)^T, \quad (7.123c)$$

where N_k is the number of observations in \mathcal{C}_k . When class information is not available, which is typically the case, the estimation problem is more complicated. We next provide an informal derivation for a solution using the *Expectation–Maximization (EM) algorithm*. The equations that must be satisfied by the maximum likelihood estimators, are obtained by equating the first partial derivatives of (7.122) with respect to the unknown parameters to zero. To simplify the derivation we assume $p = 1$, that is,

$$g_k(x_n | m_k, \sigma_k^2) = \frac{1}{\sqrt{2\pi\sigma_k^2}} \exp \left(-\frac{1}{2} \frac{(x_n - m_k)^2}{\sigma_k^2} \right) , \quad (7.124)$$

where $c_k = \sigma_k^2$. The approach for $p > 1$ involves the same steps, but the algebraic manipulations are more complicated (Duda et al., 2001).

We start by differentiating (7.122) with respect to the mean value m_k . This yields

$$\frac{\partial \ln L(\cdot)}{\partial m_k} = \sum_{n=1}^N \frac{1}{f(x_n|\cdot)} \frac{\partial f(x_n|\cdot)}{\partial m_k} = \sum_{n=1}^N \frac{p_k}{f(x_n|\cdot)} \frac{\partial g_k(x_n|m_k, c_k)}{\partial m_k}. \quad (7.125)$$

Evaluating the partial derivative on the right-hand side of (7.125), we obtain

$$\begin{aligned} \frac{\partial g_k(x_n|m_k, c_k)}{\partial m_k} &= \frac{1}{\sqrt{2\pi}\sigma_k} \exp\left(-\frac{1}{2}\frac{(x_n - m_k)^2}{\sigma_k^2}\right) \frac{\partial}{\partial m_k} \left(-\frac{1}{2}\frac{(x_n - m_k)^2}{\sigma_k^2}\right) \\ &= g_k(x_n|m_k, c_k)\sigma_k^{-2}(x_n - m_k). \end{aligned} \quad (7.126)$$

Substituting (7.126) to (7.125) and equating to zero yields the equation

$$\frac{\partial \ln L(\cdot)}{\partial m_k} = \sum_{n=1}^N \frac{p_k g_k(x_n|m_k, c_k)}{f(x_n|\cdot)} c_k^{-1}(x_n - m_k) = 0. \quad (7.127)$$

Solving the last equation for m_k we obtain the expression

$$m_k = \frac{1}{\sum_{n=1}^N P(k|x_n)} \sum_{n=1}^N P(k|x_n) x_n, \quad (7.128)$$

where

$$P(k|x_n) = \frac{p_k g_k(x_n|m_k, c_k)}{\sum_{k=1}^K p_k g_k(x_n|m_k, c_k)}. \quad (7.129)$$

The quantity $P(k|x_n)$ is the posterior probability that observation x_n belongs to \mathcal{C}_k ; it is evaluated from (7.129), which is essentially Bayes' theorem. Another interpretation is that $P(k|x_n)$ is the responsibility that component k takes for “explaining” the observation x_n (Bishop, 2006).

Following a similar approach for the variance σ_k^2 , we have

$$\begin{aligned} \frac{\partial \ln L(\cdot)}{\partial \sigma_k} &= \sum_{n=1}^N \frac{p_k}{f(x_n|\cdot)} \frac{\partial g_k(x_n|m_k, c_k)}{\partial \sigma_k} \\ &= \sum_{n=1}^N \frac{p_k g_k(x_n|m_k, c_k)}{f(x_n|\cdot)} - \frac{1}{\sigma_k} + \frac{(x_n - m_k)^2}{\sigma_k^3} \\ &= \sigma_k^{-3} \sum_{n=1}^N P(k|x_n) c_k - (x_n - m_k)^2 = 0. \end{aligned} \quad (7.130)$$

Solving the last equation for $c_k = \sigma_k^2$ yields the formula

$$c_k = \frac{1}{\sum_{n=1}^N P(k|x_n)} \sum_{n=1}^N P(k|x_n)(x_n - m_k)^2. \quad (7.131)$$

To determine the mixing coefficients p_k we use the method of Lagrange multipliers to incorporate the constraint (7.120). The Lagrangian is

$$L_p(\boldsymbol{\theta}, \lambda) = \sum_{n=1}^N \ln \sum_{k=1}^K p_k g_k(x_n | m_k, c_k) + \lambda \sum_{k=1}^K p_k - 1. \quad (7.132)$$

Hence

$$\frac{\partial L_p(\boldsymbol{\theta}, \lambda)}{\partial p_k} = \sum_{n=1}^N \frac{g_k(x_n | m_k, c_k)}{f(x_n | \boldsymbol{\theta})} + \lambda = 0. \quad (7.133)$$

If we now multiply both sides by p_k and sum over k and make use of the constraint (7.120), we find $\lambda = -N$. Using this to eliminate λ and rearranging we obtain

$$p_k = \frac{1}{N} \sum_{n=1}^N P(k|x_n). \quad (7.134)$$

We can now write formulas (7.134), (7.128), and (7.131) into an intuitively attractive form for the general multivariate case ($p > 1$). The resulting estimators are

$$\hat{p}_k = \frac{1}{N} \sum_{n=1}^N \hat{P}(k|x_n) \quad (7.135a)$$

$$\hat{\boldsymbol{\theta}}_k = \frac{1}{\hat{p}_k N} \sum_{n=1}^N \hat{P}(k|x_n) \mathbf{x}_n \quad (7.135b)$$

$$\hat{\boldsymbol{\theta}}_k = \frac{1}{\hat{p}_k N} \sum_{n=1}^N \hat{P}(k|x_n) (\mathbf{x}_n - \hat{\boldsymbol{\theta}}_k) (\mathbf{x}_n - \hat{\boldsymbol{\theta}}_k)^T, \quad (7.135c)$$

where

$$\hat{P}(k|x_n) = \frac{p_k g_k(x_n | m_k, c_k)}{\sum_{k=1}^K p_k g_k(x_n | m_k, c_k)}. \quad (7.136)$$

Comparing (7.135) to (7.123) we can see that the maximum likelihood estimators for the parameters of the GMM are closely analogous to those for estimating the parameters of each individual component except that each observation is weighted by the posterior probability (7.129). In the extreme case, where $\hat{P}(k|x_n) = 1$ when $\mathbf{x}_n \in \mathcal{C}_k$ and zero otherwise, the two sets of estimators are identical. In general, $\hat{P}(k|x_n)$ is between zero and one, and all observations play some role in the estimates. From (7.123a) and (7.135a) we conclude that the quantity

$$N_k = \sum_{n=1}^N \hat{P}(k|x_n) \quad (7.137)$$

can be interpreted as the effective number of observations assigned to class \mathcal{C}_k .

We must emphasize that (7.123) and (7.135) do not, of course, give the estimators explicitly; instead, they must be solved using some type of iterative procedure. The most widely used approach, which is essentially an application of the EM algorithm (Dempster et al., 1977), consists of the following steps:

1. Initialize the means μ_k , covariances Σ_k , and mixing coefficients p_k , and evaluate the initial value of the log likelihood (7.122).
2. Expectation Step (E-step): evaluate the posterior probabilities $\hat{P}(k|n)$ using (7.136) and the current parameter estimates.
3. Maximization Step (M-step): revise the parameter estimates using (7.135) and the current posteriors.
4. Evaluate the log likelihood (7.122) and check for convergence. If the convergence criterion is not satisfied, return to step 2.

Initial estimates of p_k , μ_k , and Σ_k are obtained by one of a variety of methods and these are used to calculate initial values for the posterior probabilities. Usually, we obtain classes with a clustering algorithm and estimate parameters using (7.123). Alternatively, we can directly assign initial values to the posterior probabilities. The initialization, convergence properties, and various approaches for speeding-up the EM algorithm are discussed in (McLachlan and Peel, 2000).

7.7.3

The Classification EM Algorithm and k-Means Clustering

The expectation–maximization (EM) algorithm is a general algorithm to compute the ML estimates of the parameters of the GMM. Using the obtained ML estimates, we can partition the data \mathbf{x}_n into K classes $\{\mathcal{C}_1, \dots, \mathcal{C}_K\}$ by assigning each \mathbf{x}_n to the component with the greatest posterior probability $\hat{P}(k|n)$; this method is known as maximum a posteriori probability (MAP) rule of classification.

A classification version of the EM algorithm was obtained by Celeux and Govaert (1992) by incorporating a classification step between the E-step and the M-step. The classification step, which uses the MAP rule to partition the data, simplifies the updating of parameters because only observations from each class are used to compute the estimates; this is clear from (7.123).

A further simplification is obtained if we assume that $p_k = 1/K$ and $\Sigma_k = \sigma^2 I$ for all components. In this case, the posterior probability is given by

$$\hat{P}(k|n) = \frac{\exp(-\|\mathbf{x}_n - \mu_k\|^2/2\sigma^2)}{\sum_{i=1}^K \exp(-\|\mathbf{x}_n - \mu_i\|^2/2\sigma^2)}. \quad (7.138)$$

Since the mean μ_k closest to observation \mathbf{x}_n maximizes the posterior probability (7.138), according to the MAP rule, we assign \mathbf{x}_n to class \mathcal{C}_k . Then, we compute the unknown means using (7.123b). This simplified algorithm has an independent history and is known as *k-means clustering*. The *k*-means algorithm has the following steps:

1. *Initialization*: Assign at random K points from $\mathbf{x}_1, \dots, \mathbf{x}_n$ to μ_1, \dots, μ_K ;
2. *E-step*: Assign each data point \mathbf{x}_n to the class \mathcal{C}_k whose mean μ_k has the shortest Euclidean distance from \mathbf{x}_n ;
3. *M-step*: For all k re-estimate the mean $\hat{\mu}_k = (1/N_k) \sum_{n=1}^{N_k} \mathbf{x}_n$;
4. *Termination*: Stop when the means $\hat{\mu}_k$ do not change.

The k -means clustering algorithm minimizes the so-called variance criterion

$$J = \sum_{k=1}^K \|x_n - \mu_k\|^2, \quad (7.139)$$

where μ_k are the centers of the clusters; more details about the k -means algorithm and its applications can be found in (Duda et al., 2001; Bishop, 2006)

7.7.4 The Stochastic EM (SEM) Algorithm

Using the expectation–maximization (EM) algorithm to fit a GMM to hyperspectral imaging data for modeling or classification applications has the following limitations: (a) the number K of components is assumed to be known, (b) the solution depends strongly on the initialization, (c) the algorithm has slow convergence and may converge to local minima of the likelihood function. The last two pitfalls, which are due to the deterministic nature of the algorithm, can occur when the mixture components are not well separated.

To avoid these limitations, Masson and Pieczynski (1993) proposed the use of the *Stochastic Expectation Maximization (SEM) algorithm*, which was introduced by Celeux and Govaert (1992). The SEM algorithm incorporates a stochastic step (S-step) between the E-step and M-step of the EM algorithm. The S-step partitions the data into K classes $\{\mathcal{C}_1, \dots, \mathcal{C}_K\}$ by randomly assigning each x_n to a component according to a draw from a multinomial distribution specified by the posterior probabilities. This step provides the iterative process with an opportunity to escape from local minima; this is desirable if the algorithm has started from a pure initial location. On the other hand, this random step would be undesirable if the process were near a valid convergence point.

In practice, it turns out that the SEM algorithm has the following advantages compared to the EM algorithm: (a) only an upper bound on the number of classes K is required, (b) the solution is essentially independent of the initialization, and (c) the speed of convergence is significantly improved. The user of SEM algorithm must provide the maximum number of classes K and the minimum mixing coefficient δ required for a set of observations to form a valid class. The version of SEM algorithm summarized below is described by Masson and Pieczynski (1993).

1.

- (a) Choose the number of components (classes) K ;
- (b) Choose minimum allowable mixing coefficient δ ;
- (c) Initialize posterior probability for $k = 1, \dots, K$ and $n = 1, \dots, N$

$$\hat{P}^{\text{old}}(k|x_n) \sim \text{Uniform Distribution } [0, 1].$$

2.

- (a) For each observation x_n generate a random sample from a multinomial distribution with parameters $\{\hat{P}^{\text{old}}(1|x_n), \dots, \hat{P}^{\text{old}}(K|x_n)\}$;
- (b) Assign x_n to the class specified by the random sample.

3.

- (a) Compute the number of pixels N_k in each class;
- (b) Compute mixing coefficients $\hat{p}_k = N_k/N$;
- (c) If $\hat{p}_k < \delta$, then return to Step 1(c) with $K = K - 1$;
- (d) Update mean and covariance for each class

$$\hat{\mu}_k = \frac{1}{N_k} \sum_{n=1}^{N_k} \mathbf{x}_n, \quad \hat{\Sigma}_k = \frac{1}{N_k} \sum_{n=1}^{N_k} (\mathbf{x}_n - \hat{\mu}_k)(\mathbf{x}_n - \hat{\mu}_k)^T.$$

4.

Update the posterior probabilities for all k and n

$$\hat{P}(k|n) = \frac{p_k g_k(\mathbf{x}_n|k)}{\sum_{i=1}^K p_i g_i(\mathbf{x}_n|i)}.$$

5.

- (a) Evaluate the log likelihood

$$\ln L(\mathbf{x}^{\text{new}}) = \sum_{n=1}^N \ln \sum_{k=1}^K p_k g_k(\mathbf{x}_n|k).$$

- (b) Check if $\ln L(\mathbf{x}^{\text{new}}) - \ln L(\mathbf{x}^{\text{old}}) < \eta$, where η is a preset threshold. If the convergence criterion is not satisfied return to step 2.

One important practical detail is that the values of the normal density function are often so small as to underflow to zero; thus, it is preferable to work with logarithms of these densities, rather than the densities themselves (Press et al., 2007). Another practical issue is the large number of the parameters to be estimated, which is equal to $Kp(p+1)/2 + Kp + K$, compared to the number N of data points. One way to simplification is to make Σ_k diagonal matrices. Another way is to use the decomposition (Fraley and Raftery, 2007)

$$\Sigma_k = V_k \Lambda_k V_k^T, \quad (7.140)$$

where $V_k = |\Sigma_k|^{1/p}$ defines the component volume, Λ_k the matrix of eigenvectors of Σ_k defines the component orientation, and Λ_k the diagonal matrix of normalized eigenvalues defines the component shape, leading to very different and easily interpreted models by allowing some of these quantities to vary between components. This parametrization is used by Biernacki et al. (2006) in their implementation of EM, classification EM, and SEM algorithms. For hyperspectral data we typically reduce the dimensionality of the data using principal component analysis (see Chapter 8) and then we apply the SEM algorithm; this is possible because the GMM is invariant under linear transformations. The SEM algorithm provides a mechanism for elimination of classes based on a class size criterion. The use of the algorithm for hyperspectral clustering applications can be further improved by incorporating a class “split-and-merge” procedure (Simpson et al., 2000).

To illustrate the application of SEM algorithm we use the `moffett_ref` data set. In practice, before we apply the SEM algorithm we reduce the dimensionality of the hyperspectral data using the method of principal components (see Section 8.3). Figure 7.22

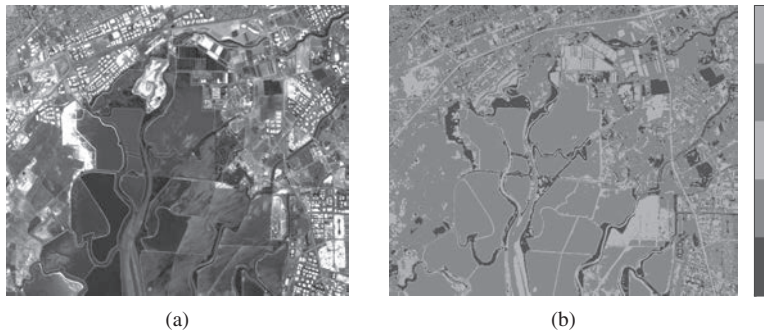


Figure 7.22 Illustration of hyperspectral image classification using the SEM algorithm and the dataset. (a) image and (b) class map for $K = 5$ classes. (A black and white version of this figure will appear in some formats. For the color version, please refer to the plate section.)

shows a color image of the scene and a class map obtained by the SEM algorithm for $K = 5$ classes (see Problem 20 for details). Note that class maps change each time we run the algorithm, even if we use the same number of classes; the changes are more pronounced when we change the number of classes. Therefore, we must emphasize that the major challenge with classification algorithms is the interpretation of the results.

7.8

Summary and Further Reading

This chapter provides a concise introduction to probability models and statistical techniques that are useful for the analysis of spectral imaging data. This is a huge area and our objective was to present basic concepts and analysis techniques that are used in practical applications. Most of the techniques belong to the area of multivariate statistical analysis, which is the subject of many excellent textbooks. Johnson and Wichern (2007) and Rencher (1995) provide balanced introductions between theory and application, whereas Anderson (2003) and Muirhead (1982) provide excellent theoretical treatments. The representation of spectra as vectors in a high-dimensional space requires a good understanding of linear algebra, which can be found in various textbooks, including Strang (2005), Schott (2005), and Vasilevsky (1983). The most useful statistical representation of hyperspectral imaging data is by a mixture of multivariate normal or t -distributions. Both distributions are members of the family of elliptically contoured distributions (Fang et al., 1990); the main difference is that the normal distributions have “fixed” tails, whereas the tails of the t -distribution are controlled by the number of degrees of freedom. The components of the mixture are usually determined by expectation–maximization type algorithms (McLachlan and Peel, 2000). Useful advice on the application of multivariate statistical techniques in practical applications is given by Gnanadesikan (1997).

Problems

1. Answering the questions of this problem requires the `moffett_ref` data set. (a) Compute the mean and variance of each band and plot them as a function of

- wavelength. (b) Compute the mean and variance of all bands for each pixel, and plot the results as a gray-scale “mean-image” and a gray-scale “variance-image”. (c) Plot the histograms of the mean and variance images. (d) Comment upon the results of the previous questions.
2. Answering the questions of this problem requires the `moffett_ref` data set. (a) Plot the scatterplot (x_i, y_i) for the 15th and 17th bands and look at the shape of the data cloud. Does the joint pdf look Gaussian? Explain your conclusions. (b) Repeat (a) for the 30th and 168th bands. (c) Compute the correlation coefficient of the two bands in (a). Does the result agree with the shape of the scatterplot? (d) Repeat (c) for the bands in (b).
 3. Repeat Problem 2 with the `moffett_rad` data set and compare the findings in the two problems.
 4. Answering the questions of this problem requires the `moffett_ref` data set. (a) Compute the correlation coefficient and SAM for the pixels (232, 175) and (246, 176). Plot the pixel spectra and check whether the computed values are justified by the spectral shapes. (b) Repeat (a) for pixels (175, 323) and (69, 254).
 5. Repeat Problem 4 with the `moffett_rad` data set and compare the findings in the two problems.
 6. Answering the questions of this problem requires the `mississippi` data set. (a) Compute the covariance, correlation, and correlation coefficient matrices. (b) Plot all pairwise scatterplots and check if their shapes explain the values of the matrices in (a). Which matrix explain the shape of the scatterplots better? (c) Check whether the matrices in (a) are positive definite.
 7. Prove equations (7.41), (7.42), and (7.43). Verify your results for $p = 2$.
 8. Use the formulas for the Gaussian distribution to replicate Figures 7.5 and 7.6. Experiment with different values of ρ , σ_1 , and σ_2 to understand their effect on the contours of the Gaussian distribution.
 9. (a) Use (7.67) and a Gaussian random number generator to compute $N = 100$ samples from the distribution $\sim N(\mu, \Sigma)$ with mean $\mu = [2, 3]$, and covariance matrix given by (7.61) with $\sigma_1 = 2$, $\sigma_2 = 1$, and $\rho = 0.8$. (b) Look at a scatterplot of the data to check whether the results resemble a Gaussian distribution.
 10. Use (7.68) to whiten the data in Problem 9 and use a scatterplot to evaluate the success of this process.
 11. In this problem we explore the distribution of the Mahalanobis distance. (a) Generate $N = 10000$ samples from the Gaussian distribution $\sim N_p(\mu, \Sigma)$ with $p = 10$ and compute their Mahalanobis distance Δ_i^2 using the theoretical mean and covariance. (b) Plot the histogram and probability of exceedance of Δ_i^2 and compared with the theoretical results. (c) Investigate what happens if we compute the Mahalanobis distance using the estimated covariance. (d) Repeat (a)–(c) for $N = 100000$ and $p = 150$, which are typical values for practical hyperspectral imaging cubes.
 12. Repeat Problem 11 assuming that $\sim N_p(\mu, \Sigma)$, where $\mu = [1 \dots 1]^T$.

-
13. Reproduce the results shown in Figure 7.10 for $\nu = 3$.
 14. Reproduce the results shown in Figure 7.11.
 15. Reproduce the results shown in Figure 7.12.
 16. Reproduce the results shown in Figure 7.13. Try different values of N to see how estimation improves as we increase the number of data points.
 17. Complete the steps of the derivation from (7.98) to (7.99) and (7.100).
 18. Repeat the analysis in Figures 7.14 and 7.16 for each band of the `mississippi` data set; then, generate Figure 7.18 for all bands of the data set.
 19. Replicate Figure 7.19 for the `moffett_ref` and `moffett_rad` data sets and comment upon the obtain results.
 20. The objective of this problem is to use the SEM algorithm to (a) derive class maps for the `moffett_ref` and `moffett_rad` data sets, and (b) understand the challenges of mapping the spectral classes to physical classes. A detailed description of the problem can be found in the book website.

8 Linear Spectral Transformations

Hyperspectral imaging data are typically treated as vectors in a high-dimensional space. Dimensionality reduction refers to a variety of techniques that enable the representation of vector data using a lower number of components without significant loss of information. The information in a data set is conveyed by the geometrical arrangement of points in the p -dimensional scatter plot rather than by the system of coordinates used for their specification. Therefore, besides the natural coordinate system defined by the *original* variables (spectral channels), we may wish to analyze the data in other coordinate systems with more desirable properties. Typically, the new coordinates are *derived* variables without any physical meaning. In this chapter we introduce linear spectral transformations for dimensionality reduction and “feature enhancement” of hyperspectral imaging applications. The most widely used technique is principal component analysis, followed by discriminant analysis, and canonical correlation analysis. We conclude with the related subject of spectral band prediction and its applications.

8.1 Introduction

The dimension of hyperspectral imaging data space is equal to the number of the spectral channels used by the sensor, which is typically in the range of a few hundred channels. High dimensionality has two important implications in hyperspectral data processing and exploitation. First, the resulting huge volume of data requires tremendous storage and processing resources. Second, the high-dimensionality of the feature space leads to a large increase in the amount of data required for statistically oriented detection and classification algorithms.

Given a hyperspectral data cube, dimensionality reduction can be achieved in essentially two different approaches. The first, which is called *band selection* or *feature selection*, attempts to identify a subset of the *original* bands that contribute to performance. Given a set of p bands, what is the best subset of size m ? To solve this problem, we should evaluate the adopted optimality criterion for all possible combinations of m bands out of p and select the combination that minimizes or maximizes the criterion. The main problem is that the number of possible combinations, which is given by $p!/[p - m)!m!]$, the selected subset is extremely large, even for small values of m and p . There exist both optimum and suboptimum search methods, but they are, in general, computationally demanding or infeasible (Webb and Copsey, 2011). In

hyperspectral imaging band selection, which is mainly used for the design of simpler multispectral systems, the selected subset is primarily based on the needs of specific applications.

The second approach is to find a linear or nonlinear transformation of the original bands to a smaller set of *derived* variables. In this case all available bands are used and the data are transformed, using a linear or nonlinear mapping, to a reduced-dimension space. As a result of the transformation, the original observations are replaced by derived variables whose physical meaning or interpretations may be ambiguous. These band transformations, which are essentially mappings from the spectral space to a reduced-dimension space, are known as *feature extraction* techniques (Webb and Copsey, 2011).

Band selection attains dimensionality reduction in the original measurement space; band transformation leads to derived variables that may or may not have any physical meaning or interpretation. An appealing feature of the band selection approach is that it can avoid the cost of making measurements on unnecessary bands. In both approaches, the reduction is performed according to an optimality criterion that depends on the prospective application. Feature selection and feature extraction may be considered as mappings that apply a set of weights to the spectral bands to obtain the new variables. The fundamental difference is that the weights in feature selection take binary values, whereas in feature extraction they take continuous values. The relationship between these two approaches, in the context of linear regression, is discussed by Hastie et al. (2009).

The type of optimization criterion used for dimensionality reduction depends on the prospective application. Examples include receiver operating characteristic curves for detection, probability of error or confusion matrices for classification, or some distortion measure for data compression. However, direct utilization of these criteria in the optimization process, either in theory or in practice, is extremely difficult if not impossible. The approach used in practice is to select a criterion of performance that is both meaningful and mathematically tractable. Both attributes are satisfied by the widely used mean squared error criterion. However, use of other criteria, such as entropy and mutual information, is also possible. Such metrics have been used to derive the method of independent component analysis (Hyvärinen and Oja, 2000).

The design of dimensionality reduction techniques optimized for detection or classification applications is almost impossible. In practice, we select a dimensionality reduction technique with certain desirable properties, and then we evaluate its effect on detection or classification applications. However, certain efforts to approach the problem from a different perspective have been reported. For example, a band selection technique that seeks to maximize the angle between target and background spectra has been developed by Keshava (2003). In this case, dimensionality reduction is the byproduct of a process that seeks to increase the angular separation between the target and background spectra beyond that existing in the full band space. Another effort uses an information theory-based criterion and genetic optimization algorithms (Shen and Bassett III, 2002). In contrast, we seek dimensionality reduction techniques that lead to insignificant performance degradation or help to deal effectively with the curse of dimensionality effects (Duda et al., 2001).

Dimensionality reduction techniques are routinely used in hyperspectral data exploitation as a preprocessing stage for compression and classification applications. The objective of dimensionality reduction algorithms is to obtain a parsimonious representation of multivariate (vector) data by reducing or eliminating statistically redundant components. Since high-dimensional spaces have a huge volume, data tend to occupy a very small subspace; in essence, high-dimensional spaces are mostly empty. As a consequence, high-dimensional data can be projected to a lower dimensional subspace without losing significant information, at least, for classification applications. For target detection applications, dimensionality reduction must be avoided or has to be used with extreme care. Therefore, dimensionality reduction algorithms are used to reduce the computational complexity in some applications or to help understand the structure of the data with visualization in two- or three-dimensional projections.

We focus on three families of linear dimensionality reduction techniques that are widely used in practical hyperspectral imaging applications: principal component analysis, canonical correlation analysis, and discriminant analysis. The reason for their success is the conceptual simplicity, ease of implementation, and acceptable performance.

8.2

Implications of High-Dimensionality

Since hyperspectral imaging data are represented by points in a Euclidean space, we often use intuition from two or three dimensions to provide motivation or explain the operation of data analysis algorithms. However, as we show next, concepts gained from our intuition in two and three dimensions can be misleading when used in high-dimensional settings (Scott, 1992; Bishop, 2006).

The volume of a hypersphere of radius r in a p -dimensional space is given by

$$V_s(r) = \frac{r^p \pi^{p/2}}{\Gamma(p/2 + 1)}, \quad (8.1)$$

where $\Gamma(\cdot)$ is the gamma function. From Figure 8.1, which shows values of $V_s(r)$ for $r = 1$, we see that the volume increases until $p = 5$ and then quickly approaches zero. The volume of a hypercube in $[-r, r]^p$ is

$$V_c(r) = (2r)^p. \quad (8.2)$$

The fraction of the volume of the cube contained in the inscribed hypersphere is

$$f_{p1} = \frac{V_s(a)}{V_c(a)} = \frac{\pi^{p/2}}{2^p \Gamma(p/2 + 1)}. \quad (8.3)$$

The first few values of the ratio f_p are given in Figure 8.1, which shows how the ratio decreases as the dimensionality increases. Surprisingly, the ratio tends to zero when p increases. Thus, as p increases, the volume of the hypercube concentrates in its corners. Intuitively, this means that as the dimensionality increases, a cube becomes more and more spiky; that is, the spherical body gets smaller and smaller, the number of spikes increases, and the spikes occupy almost all the available volume.

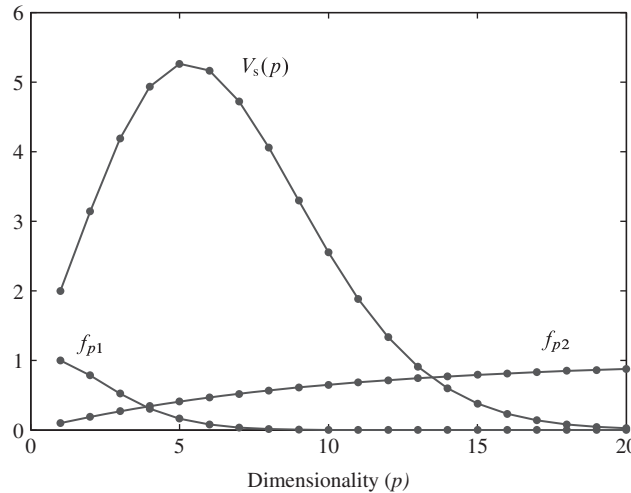


Figure 8.1 Dependence of some geometric quantities on dimensionality.

Consider next a thin spherical shell defined by a sphere of radius $(r - \epsilon)$ inscribed inside a sphere of radius r . The fraction of the volume inside the shell to the volume of the large sphere is

$$f_{p2} = \frac{V_s(r) - V_s(r - \epsilon)}{V_s(r)} = \frac{r^p - (r - \epsilon)^p}{r^p} = 1 - \left(1 - \frac{\epsilon}{r}\right)^p. \quad (8.4)$$

From Figure 8.1 we see, for the case of $\epsilon = r/10$, that as the dimension increases, the volume concentrates in the outside shell. Thus, all of the content of a hypersphere is concentrated close to its surface, which is only a $(p - 1)$ -dimensional manifold. A similar result holds for hyperellipsoids (Jimenez and Landgrebe, 1998).

These results have important implications in the statistical behavior of normally distributed multivariate data at high dimensionality. To this end, consider a spherically invariant normal random vector $\mathbf{x} \sim N_p(\mathbf{0}, \sigma^2 \mathbf{I})$. The likelihood of finding a point at distance $r = \|\mathbf{x}\|$ from the origin is given by the generalized Rayleigh distribution

$$f(r) = \frac{2r^{p-1}}{(2\sigma^2)^{p/2} \Gamma(p/2)} \exp\left(-\frac{r^2}{2\sigma^2}\right), \quad (8.5)$$

which is a unimodal density function with mode (maximum) at $r/\sigma = \sqrt{p-1}$. From Figure 8.2, which shows this distribution for various values of p , we conclude that for large p the probability mass of the Gaussian is concentrated in a thin shell. It is important to realize from Figure 8.2 that, if samples are drawn from a normal distribution in a high-dimensional space, most samples fall in a doughnut-type ring and no samples fall in the center region where the value of the density function is largest (Fukunaga, 1990). Similar results apply to normal distributions with a general full-rank covariance matrix, except that the contours are hyper ellipsoids.

Consider the hypercube $[-1, 1]^p$ and let any of the diagonal vectors from the center to a corner be denoted by \mathbf{v} . Then \mathbf{v} is one of the 2^p vectors of the form $[\pm 1, \pm 1, \dots, \pm 1]^T$.

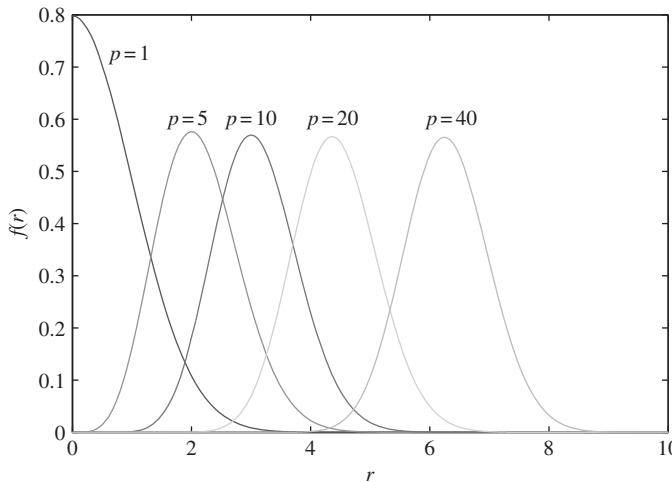


Figure 8.2 Probability density function of the distance of normally distributed zero-mean random vectors from the origin as a function of dimensionality.

The angle between a diagonal vector v and a Euclidean axis $e_i = [0, \dots, 0, 1, 0, \dots, 0]^T$ is given by

$$\cos \theta_d = \frac{v^T e_i}{\|v\| \|e_i\|} = \frac{\pm 1}{\sqrt{p}} \xrightarrow{p \rightarrow \infty} 0. \quad (8.6)$$

Thus, when the dimensionality grows, the cosine tends to zero, meaning that the diagonals are nearly orthogonal to all coordinate axes. Hence, the visualization of high-dimensional data using bivariate scatter plots can be misleading. Indeed, a cluster of points lying near a diagonal of the space will surprisingly be plotted near the origin, whereas a cluster lying near a coordinate axis is plotted as intuitively expected. Therefore, the choice of coordinate system in high-dimensional data analysis is a very important decision.

The important conclusion from the previous results, which is known as “empty space phenomenon”, is that high-dimensional spaces are “almost empty”. Furthermore, local neighborhoods of points are almost empty and most data are concentrated at the borders of the volume of interest. Another consequence of high-dimensionality is the “concentration of measure phenomenon”, which basically says that the mean of the norm of random vectors grows proportionally to \sqrt{p} and the variance remains essentially constant for sufficiently large p (Verleysen et al., 2003). In practice, the concentration phenomenon makes the nearest-neighbor search problem difficult to solve in high-dimensional spaces.

The term “curse of dimensionality” was originally coined by Bellman (Duda et al., 2001) to highlight the difficulty of numerical integration in high-dimensional spaces. This led to the more general use of the term to describe the difficulty of dealing with statistical problems in high dimensions because *we can never have enough data to cover every part of the observation space*. To see this, we divide the axis of each input variable

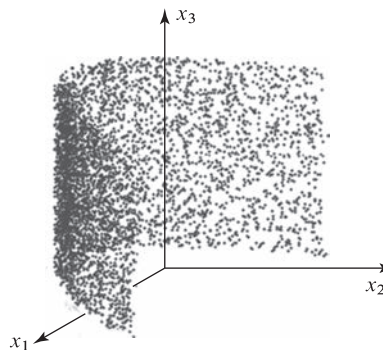


Figure 8.3 Horseshoe distribution in three dimensions.

into K uniform intervals (or “bins”). This partition divides the entire observation space into K^p hyperbins. If there has to be at least one data point in each hyperbin, then the number of points $N = K^p$ needed to cover the observation space increases exponentially with p . As we increase p the number, we cannot keep up with the number of observations required to obtain good statistical estimates. Therefore, after a certain point, increasing the number of features p does not necessarily result in better performance. More details about this topic and its implications in classification applications can be found in Bishop (2006) and Duda et al. (2001).

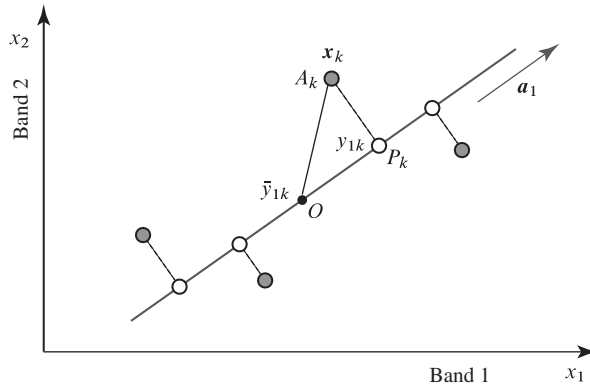
The fact that high-dimensional spaces are mostly empty implies that multivariate data in \mathbb{R}^p reside in a lower-dimensional structure because of the redundancy between variables. As a result, high-dimensional data can be projected to a lower-dimensional subspace without losing significant information in terms of separability among the different statistical classes. However, this may not be the case for information pertinent to target detection problems.

A key question to answer before we attempt to reduce the dimension of a data set is that of the “dimensionality” of the data. To touch the surface of this difficult question, let us have a look at Figure 8.3, which shows the well-known “horseshoe” distribution in a three-dimensional space. A simple inspection of this data set shows that we should project onto a two-dimensional space. Thus, the number of degrees of freedom of the variables in the set, which is known as *intrinsic dimension* of the data, is two. However, estimating the intrinsic dimensionality of real data is a hard task because real distributions have varying intrinsic dimensions. Linear and nonlinear projections for dimensionality reduction are discussed by Lee and Verleysen (2007).

8.3

Principal Components Analysis: Theory

Principal Component Analysis or *PCA* is a special linear transformation that is widely used for applications like dimensionality reduction, data compression, feature extraction, and data visualization. Principal components were first proposed by Pearson in 1901 and further developed by Hotelling in 1933; see Jolliffe (2002) for a comprehensive

**Figure 8.4**

Geometrical illustration of PCA as an orthogonal projection to a lower-dimensional subspace: points in a plane are projected onto a line.

survey. In the signal processing literature PCA is known as the Hotelling transform or the discrete Karhunen–Loëve transform (Manolakis and Ingle, 2011).

The basic idea of PCA is illustrated in Figure 8.4 with two-dimensional data. The problem we wish to solve can be stated as follows: What is the best line through the set of data points denoted by the black circles? To answer this question we must clarify what we mean by “best”. A line is a one-dimensional subspace specified by a unit vector \mathbf{a}_1 . The orthogonal projection of the observation \mathbf{x}_k onto the line is the point $y_{1k} = \mathbf{a}_1^T \mathbf{x}_k$ (open circle). PCA determines the best line by minimizing the sum of the squares of the perpendicular distances $\sum_k (A_k P_k)^2$ of the data points from the line. Note that $A_k P_k$ is the error we make when we approximate the data point A_k by its projection P_k . The mean value of the projections y_{1k} is $\bar{y}_1 = (1/N) \sum_k y_{1k} = (1/N) \sum_k \mathbf{a}_1^T \mathbf{x}_k = \mathbf{a}_1^T \hat{\mathbf{m}}$: that is, the projection of the data mean onto the line. Thus, the variance of the projections y_{1k} is proportional to $\sum_k (OP_k)^2$. From the orthogonal triangle $OP_k A_k$ and the Pythagorean theorem, we have

$$\sum_k (OA_k)^2 = \sum_k (OP_k)^2 + \sum_k (A_k P_k)^2. \quad (8.7)$$

Since the sum $\sum_k (OA_k)^2$ is fixed for a given swarm of points, minimization of mean square error $(1/N) \sum_k (A_k P_k)^2$ is equivalent to maximization of variance $(1/N) \sum_k (OP_k)^2$ under the constraint $\mathbf{a}_1^T \mathbf{a}_1 = 1$. Therefore, as we show next, there are two formulations of PCA that give rise to the same algorithm.

8.3.1 Maximum Variance Formulation

The method of principal components analysis consists of transforming a set of variables x_1, x_2, \dots, x_p to a new set y_1, y_2, \dots, y_p , known as *principal components*, using the linear transformation

$$y_k = a_{k1} x_1 + a_{k2} x_2 + \dots + a_{kp} x_p = \mathbf{a}_k^T \mathbf{x}, \quad k = 1, \dots, p, \quad (8.8)$$

or more compactly

$$\mathbf{y} = \mathbf{A}^T \mathbf{x}. \quad (8.9)$$

The principal components transformation is specified by the matrix \mathbf{A} that satisfies the following requirements:

- the derived random variables y_1, y_2, \dots, y_p are mutually uncorrelated;
- the variance $\text{var}(y_k)$ of each derived random variable is as large as possible;
- the derived variables are arranged in order of decreasing variance.

The main idea behind this procedure is that the first few principal components may account for most of the variability in the data. Thus, we could discard the remaining principal components without significant loss of information.

The first principal component (that is, the linear combination)

$$y_1 = \mathbf{a}_1^T \mathbf{x} \quad (8.10)$$

is found by choosing \mathbf{a}_1 such that y_1 has the largest possible variance. If \mathbf{x} has mean \mathbf{m} and covariance \mathbf{C} , the variance of y_1 is given by [see (7.37)]

$$\text{var}(y_1) = \text{var}(\mathbf{a}_1^T \mathbf{x}) = \mathbf{a}_1^T \mathbf{C} \mathbf{a}_1. \quad (8.11)$$

The value of $\text{var}(y_1)$ can be increased by multiplying \mathbf{a}_1 by some constant. To avoid this indeterminacy, we maximize (8.11) subject to the constraint $\mathbf{a}_1^T \mathbf{a}_1 = 1$. One way to solve this problem is by using the method of Lagrange multipliers (Nocedal and Wright, 2006). We start by forming the Lagrangian

$$g(\mathbf{a}_1) = \mathbf{a}_1^T \mathbf{C} \mathbf{a}_1 + \lambda_1 (1 - \mathbf{a}_1^T \mathbf{a}_1) \quad (8.12)$$

where λ_1 is a Lagrange multiplier. Differentiating (8.12) with respect to \mathbf{a}_1 , setting the result equal to zero and solving, gives the necessary condition

$$\frac{\partial g(\mathbf{a}_1)}{\partial \mathbf{a}_1} = 2\mathbf{C} \mathbf{a}_1 - 2\lambda_1 \mathbf{a}_1 = \mathbf{0} \quad \text{or} \quad \mathbf{C} \mathbf{a}_1 = \lambda_1 \mathbf{a}_1. \quad (8.13)$$

By definition, the solution to (8.13) is an eigenvector of the covariance matrix corresponding to the eigenvalue λ_1 . Note that the use of symbol λ for eigenvalues in matrix theory should not be confused with its use for wavelength in spectroscopy. Substitution of (8.13) into (8.11) yields

$$\text{var}(y_1) = \mathbf{a}_1^T \mathbf{C} \mathbf{a}_1 = \lambda_1 \mathbf{a}_1^T \mathbf{a}_1 = \lambda_1. \quad (8.14)$$

Since we wish to maximize this variance, we choose λ_1 to be the largest eigenvalue of \mathbf{C} and \mathbf{a}_1 the corresponding eigenvector. As we recall, the covariance matrix \mathbf{C} , which is nonnegative definite, has the eigenvalue decomposition

$$\mathbf{C} = \mathbf{Q} \mathbf{\Lambda} \mathbf{Q}^T = \sum_{k=1}^p \lambda_k \mathbf{q}_k \mathbf{q}_k^T, \quad (8.15)$$

where the eigenvalues have been ordered so that $\lambda_1 \geq \lambda_2 \geq \dots \geq \lambda_p \geq 0$. Therefore, we choose $\mathbf{a}_1 = \mathbf{q}_1$. If some of the eigenvalues are equal, there is no unique way to

choose their eigenvectors. However, the above argument can be extended if we ensure that the chosen eigenvectors are orthogonal.

The second principal component, $y_2 = \mathbf{a}_2^T \mathbf{x}$, is obtained by choosing \mathbf{a}_2 to maximize $\text{var}(y_2) = \mathbf{a}_2^T \mathbf{C} \mathbf{a}_2$ subject to the constraints $\mathbf{a}_2^T \mathbf{a}_2 = 1$ and $\text{cov}(y_2, y_1) = 0$. With the help of (8.13) the second constraint implies that

$$\text{cov}(y_2, y_1) = \mathbf{a}_2^T \mathbf{C} \mathbf{a}_1 = \lambda_1 \mathbf{a}_2^T \mathbf{a}_1 = 0, \quad (8.16)$$

which is equivalent to $\mathbf{a}_2^T \mathbf{a}_1 = 0$; that is, \mathbf{a}_2 is orthogonal to \mathbf{a}_1 .

Using the method of Lagrange multipliers again, we seek the minimization of the Lagrangian

$$g(\mathbf{a}_2) = \mathbf{a}_2^T \mathbf{C} \mathbf{a}_2 + \lambda_2 (1 - \mathbf{a}_2^T \mathbf{a}_2) + \nu (0 - \mathbf{a}_2^T \mathbf{a}_1). \quad (8.17)$$

Differentiating with respect to \mathbf{a}_2 and equating to zero gives

$$2\mathbf{C} \mathbf{a}_2 - 2\lambda_2 \mathbf{a}_2 - \nu \mathbf{a}_1 = \mathbf{0}. \quad (8.18)$$

Since $\mathbf{a}_1^T \mathbf{a}_2 = 0$, multiplying (8.18) by \mathbf{a}_1^T gives

$$2\mathbf{a}_1^T \mathbf{C} \mathbf{a}_2 - \nu = 0. \quad (8.19)$$

Also, by (8.13), $\mathbf{a}_1^T \mathbf{C} \mathbf{a}_2 = \mathbf{a}_2^T \mathbf{C} \mathbf{a}_1 = 0$, therefore $\nu = 0$. Equation (8.18) becomes

$$\mathbf{C} \mathbf{a}_2 = \lambda_2 \mathbf{a}_2. \quad (8.20)$$

Thus, \mathbf{a}_2 is also an eigenvector of \mathbf{C} , orthogonal to \mathbf{a}_1 . Since we seek to maximize the variance $\text{var}(y_2) = \mathbf{a}_2^T \mathbf{C} \mathbf{a}_2 = \lambda_2$, we must choose \mathbf{a}_2 to be the eigenvector corresponding to the second largest eigenvalue of \mathbf{C} . Hence

$$y_2 = \mathbf{a}_2^T \mathbf{x} \quad \text{and} \quad \text{var}(y_2) = \lambda_2. \quad (8.21)$$

The remaining principal components can be obtained in a similar way. Therefore, the k th principal component is the linear combination $y_k = \mathbf{a}_k^T \mathbf{x}$ that maximizes $\text{var}(y_k)$ subject to $\mathbf{a}_k^T \mathbf{a}_k = 1$ and $\text{cov}(y_i, y_k) = 0$ for $i < k$. Therefore, the PCA transformation is given by

$$\mathbf{y} = \mathbf{Q}^T \mathbf{x}. \quad (8.22)$$

Since \mathbf{Q} is orthogonal, that is, $\mathbf{Q}^{-1} = \mathbf{Q}^T$, the inverse PCA transform is given by

$$\mathbf{x} = \mathbf{Q} \mathbf{y} = \sum_{k=1}^p y_k \mathbf{q}_k, \quad (8.23)$$

which provides an expansion of \mathbf{x} into orthogonal components using as a basis the eigenvectors of its covariance matrix. The covariance matrix and the variance of the principal components are given by

$$\text{cov}(\mathbf{y}) = \mathbf{Q}^T \mathbf{C} \mathbf{Q} = \mathbf{\Lambda}, \quad \text{var}(y_k) = \mathbf{q}_k^T \mathbf{C} \mathbf{q}_k = \lambda_k. \quad (8.24)$$

Using the property $\text{tr}(\mathbf{C}) = \text{tr}(\mathbf{Q} \mathbf{\Lambda} \mathbf{Q}^T) = \text{tr}(\mathbf{\Lambda} \mathbf{Q}^T \mathbf{Q}) = \text{tr}(\mathbf{\Lambda})$, we obtain

$$\sum_{k=1}^p \text{var}(x_k) = \sum_{k=1}^p \lambda_k = \sum_{k=1}^p \text{var}(y_k). \quad (8.25)$$

From (8.25) it follows that the total variability is invariant under the PCA transformation. However, PCA provides a more “compact” redistribution of variance: that is, it packs as much variance as possible into the smallest number of variables. The determinant, $|\mathbf{C}| = \lambda_1 \lambda_2 \cdots \lambda_p$, provides another measure of total variability. However, it is not widely used because it is sensitive to small eigenvalues.

8.3.2 Minimum Mean Square Error Formulation

We now discuss an alternative formulation of PCA based on projection error minimization. To do this, we note that every vector in \mathbb{R}^p can be represented exactly by

$$\mathbf{x} = \sum_{k=1}^p y_k \mathbf{a}_k, \quad (8.26)$$

where $\{\mathbf{a}_1, \dots, \mathbf{a}_p\}$ is a complete set of orthonormal basis vectors that satisfy

$$\mathbf{a}_i^T \mathbf{a}_j = \begin{cases} 1, & i = j \\ 0, & i \neq j \end{cases}. \quad (8.27)$$

Using (8.26) and the orthogonality property (8.27), the inner product $\mathbf{a}_i^T \mathbf{x}$ leads to

$$y_i = \mathbf{a}_i^T \mathbf{x}, \quad i = 1, \dots, p. \quad (8.28)$$

Suppose now that we wish to approximate \mathbf{x} by using only the first m ($m \leq p$) components in (8.26). This operation corresponds to a projection onto a lower-dimensional subspace. Without loss of generality, we can do this by retaining the first m coefficients in (8.26) and replacing the $(p - m)$ unused ones with preselected constants b_k . This results to the following approximation

$$\hat{\mathbf{x}}_m = \sum_{k=1}^m y_k \mathbf{a}_k + \sum_{k=m+1}^p b_k \mathbf{a}_k. \quad (8.29)$$

The error introduced by this approximation is given by

$$\mathbf{e}_m = \mathbf{x} - \hat{\mathbf{x}}_m = \sum_{k=m+1}^p (y_k - b_k) \mathbf{a}_k. \quad (8.30)$$

Using the orthogonality property, we can easily show that the mean square approximation error is given by

$$J_m = E(\mathbf{e}_m^T \mathbf{e}_m) = \sum_{k=m+1}^p E[(y_k - b_k)^2]. \quad (8.31)$$

The coefficients b_k that minimize J_m are obtained from the equations

$$\frac{\partial J_m}{\partial b_k} = -2[E(y_k) - b_k] = 0, \quad k = m + 1, \dots, p, \quad (8.32)$$

which yield

$$b_k = E(y_k) = E(\mathbf{a}_k^T \mathbf{x}) = \mathbf{a}_k^T \mathbf{m}. \quad (8.33)$$

Substitution of (8.33) into (8.31) shows that the resulting MSE is given by

$$J_m = E(\mathbf{e}_m^T \mathbf{e}_m) = \sum_{k=m+1}^p \text{var}(y_k) = \sum_{k=m+1}^p \mathbf{a}_k^T \mathbf{C} \mathbf{a}_k, \quad 1 \leq m \leq p. \quad (8.34)$$

Since $\mathbf{a}_k^T \mathbf{C} \mathbf{a}_k \geq 0$, we can minimize J_m by minimizing each term in the summation subject to the orthonormality constraint (8.27). Following the approach in (8.12)–(8.14) we conclude that the minimum of $\mathbf{a}_k^T \mathbf{C} \mathbf{a}_k$ subject to $\mathbf{a}_k^T \mathbf{a}_k = 1$, which is determined by $\mathbf{C} \mathbf{a}_k = \lambda_k \mathbf{a}_k$, is equal to λ_k . Therefore, the minimum mean square error is obtained by dropping the coefficients corresponding to the $(p - m)$ smaller eigenvalues.

This property justifies the use of the PCA for dimensionality reduction and data compression applications. The beauty of this result is that we can improve the quality of reconstruction by adding “corrections” to the already existing approximation. If some eigenvalues are small, we can neglect them and represent the points fairly well with fewer than p dimensions. For example, if $p = 3$ and λ_3 is small, then the swarm of points is an “elliptical pancake”, and a two-dimensional representation will adequately portray the configuration of points.

8.3.3 Properties of PCA

We next discuss some properties of PCA which should be taken into consideration before we apply the transform or when we interpret the obtained results. This will help to avoid unwarranted expectations or misinterpretation of the outcomes.

To understand how PCA works we consider a two-dimensional normal distribution with mean vector \mathbf{m} and covariance matrix \mathbf{C} (see Figure 8.5). The major (minor) axis of the ellipsoid is along the direction of the first (second) eigenvector; the ratio of the

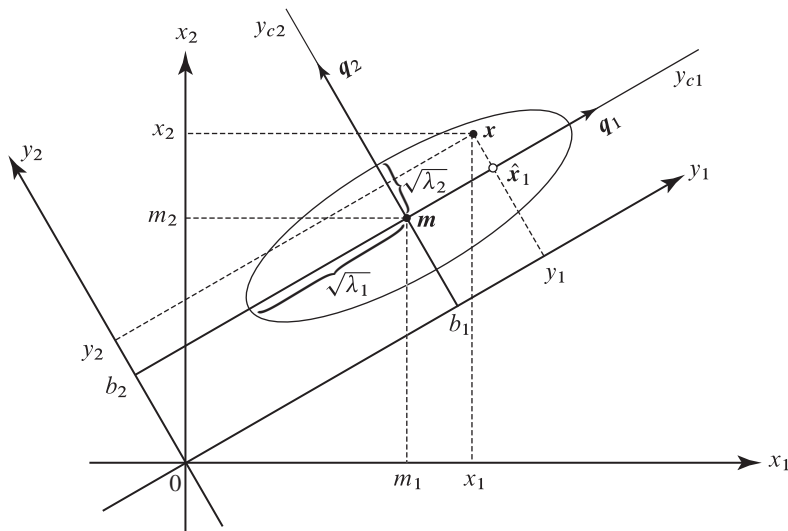


Figure 8.5 Illustration of PCA in two dimensions.

eigenvalues determines the elongation of the ellipsoid. The principal components are evaluated by

$$\mathbf{y} = \mathbf{Q}^T \mathbf{x}. \quad (8.35)$$

Since $y_1 = \mathbf{q}_1^T \mathbf{x}$ and $y_2 = \mathbf{q}_2^T \mathbf{x}$, the principal components provide the rectangular coordinates of point \mathbf{x} with respect to a rotated set of rectangular axes centered at zero and aligned with the two eigenvectors. The coordinates of the mean vector in the rotated system are given by $b_1 = \mathbf{q}_1^T \mathbf{m}$ and $b_2 = \mathbf{q}_2^T \mathbf{m}$. The best approximation using the first m principal components is given by

$$\hat{\mathbf{x}}_m = \sum_{k=1}^m y_k \mathbf{q}_k + \sum_{k=m+1}^p b_k \mathbf{q}_k. \quad (8.36)$$

If $\lambda_2 = E[(y_2 - b_2)^2] = \text{var}(y_2)$ is small, y_2 stays close to b_2 . Thus, we can approximate \mathbf{x} by $\hat{\mathbf{x}}_1 = y_1 \mathbf{q}_1 + b_2 \mathbf{q}_2$, which is the orthogonal projection of \mathbf{x} onto the first eigenvector (see Figure 8.5). In practice, it is more convenient to remove the mean from the data, perform PCA, and reinsert the mean as follows:

$$\mathbf{y} = \mathbf{Q}^T(\mathbf{x} - \mathbf{m}) \quad \text{and} \quad \hat{\mathbf{x}}_m = \sum_{k=1}^m y_k \mathbf{q}_k + \mathbf{m}. \quad (8.37)$$

We note that if $\mathbf{Cq}_k = \lambda_k \mathbf{q}_k$, we also have $\mathbf{C}(-\mathbf{q}_k) = \lambda_k(-\mathbf{q}_k)$. Thus, either $\mathbf{q}_k^T \mathbf{x}$ or $-\mathbf{q}_k^T \mathbf{x}$ can serve as the k th principal component; this is because the signs of the eigenvectors are arbitrary. The choice as to which sign is used has to be made by the user.

The choice of how many components m to retain is very much application-specific; however, some theoretical criteria and advice are provided in Rencher (1998), Jackson (1991), and Jolliffe (2002). A good starting point is to plot the eigenvalues in decreasing order and check if there is a point where the values fall sharply before leveling off at small values (the “scree” test). Another way is to plot the percentage of the total variance accounted by the first m principal components; that is, the ratio

$$c_m = \frac{\sum_{k=1}^m \lambda_k}{\sum_{k=1}^p \lambda_k} \quad (8.38)$$

for $m = 1, 2, \dots, p$. Typically, only the first few principal components are considered useful for capturing the major variability in the data. However, the last few components may contain information critical to detection applications.

We recall that PCA transforms \mathbf{x} to a random vector \mathbf{y} with uncorrelated components ordered in terms of decreasing variance. If we normalize each y_k by its standard deviation – that is, $z_k = y_k / \sqrt{\lambda_k}$ – we obtain a random vector \mathbf{z} with $\text{cov}(\mathbf{z}) = \mathbf{I}$. This process is called whitening or spherizing [see discussion following equation (7.51)]. In matrix form we have

$$\mathbf{z} = \Lambda^{-1/2} \mathbf{Q}^T \mathbf{x}, \quad (8.39)$$

where $\Lambda^{-1/2}$ is the diagonal matrix with elements $\{1/\sqrt{\lambda_1}, \dots, 1/\sqrt{\lambda_p}\}$. The difference between PCA and whitening is illustrated in Figure 8.6.

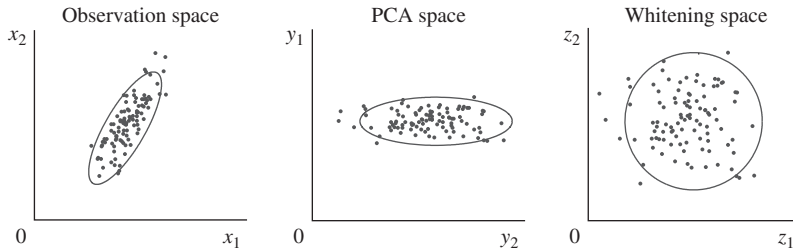


Figure 8.6 Illustration of PCA and whitening using a normal distribution.

The PCA transformation is not invariant under linear transformations (except shifting or translation) of the variables because such transformations change the eigenstructure of the covariance matrix. Indeed, if $\mathbf{v} = \mathbf{Ax} + \mathbf{b}$, then $\text{cov}(\mathbf{v}) = \mathbf{A}\text{cov}(\mathbf{x})\mathbf{A}^T$. Thus, the principal components of the covariance matrix are not the same as those of the correlation matrix or the correlation coefficient matrix. To see that scaling has an effect on the eigenvalues, we look at (8.25). If a variance $\text{var}(x_k)$ is increased by a scale change, then one or more of the eigenvalues will increase. In hyperspectral remote sensing applications, principal components are usually calculated from the covariance matrix because each band has the same physical units and all bands have comparable width.

The PCs are correlated with the original variables (Rencher, 1998); that is,

$$\text{cov}(\mathbf{x}, y_k) = \text{cov}(\mathbf{x}, \mathbf{q}_k^T \mathbf{x}) = \mathbf{C} \mathbf{q}_k = \lambda_k \mathbf{q}_k. \quad (8.40)$$

The correlation coefficients, which are known as PC loadings, are given by

$$\rho_{ij} = \frac{\text{cov}(x_i, y_j)}{\sqrt{\text{var}(x_i)} \sqrt{\text{var}(y_j)}} = \frac{q_{ij} \lambda_j}{\sqrt{\sigma_{ii} \lambda_j}} = \frac{q_{ij} \sqrt{\lambda_j}}{\sqrt{\sigma_{ii}}}. \quad (8.41)$$

Inspection of the correlation coefficient matrix, say $\mathbf{P}_{\text{PC}} = [\rho_{ij}]$, will show which variables (bands) are the most influential in each of the principal components.

There are two situations in which a principal component essentially duplicates one of the original variables. (a) If one variable has a much greater variance than the other variables, then this variable will dominate the first principal component. (b) If one variable, say x_p , is uncorrelated with the other variables, then its variance $\text{var}(x_p)$ is one of the eigenvalues of \mathbf{C} , and the corresponding eigenvector has components $\{0, \dots, 0, 1\}$. Hence, x_p itself is the principal component. If the original variables are highly correlated, a few principal components will reproduce most of the variation in the data as measured by $\text{tr}(\mathbf{C})$. If the variables are only slightly correlated, the resulting principal components will largely reflect the original variables; therefore, there is little to be gained with PCA.

Typically, only the first few principal components are considered useful for summarizing data. However, the last few principal components, which have the smallest variances, also carry information that may be useful for specific applications. If the variance of a component is close to zero, the component defines a linear relationship among the variables (see Section 9.10).

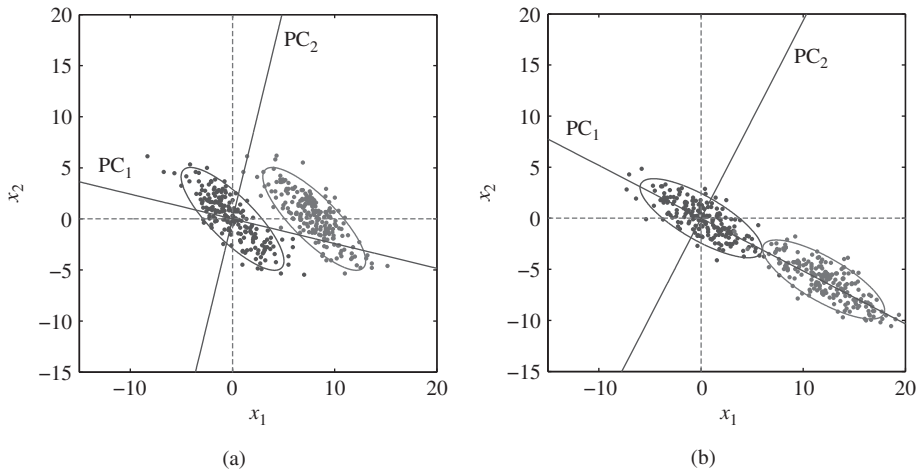


Figure 8.7 Two cases where using the first principal component (PC₁) for classification will (a) fail or (b) be successful.

Despite its widespread use, PCA is crippled by its reliance on second-order statistics. Though uncorrelated, the principal components can be highly statistically dependent. In this case, PCA cannot obtain the most compact representation of the nonlinear dependencies in the data compared to alternative nonlinear techniques. PCA provides an optimum representation for Gaussian and other elliptically contoured distributions because it rotates the coordinate axes to align them with the principal axes of the hyperellipsoid. Independent component analysis (ICA), in contrast to PCA which only decorrelates the data, attempts to make the derived variables as independent as possible by reducing higher-order statistical dependencies (Hyvärinen and Oja, 2000). The directions of the axes in ICA are determined by both the second- and higher-order statistics and they are not necessarily orthogonal. However, ICA is not widely used because the assumptions required for its success are not typically satisfied in practical hyperspectral imaging applications.

Finally, we emphasize that PCA takes *no* account of classes within the data; that is, it is an unsupervised technique. Although it is possible for separate classes to emerge as a result of projecting the data to a smaller number of dimensions, this is not always the case. Indeed, many times the projection onto a lower-dimensional space may obscure the existence of separate classes (see Figure 8.7). We stress that PCA is optimized for effective data representation; *not* for data classification.

8.3.4 Computation of PCA

In practical applications, the mean vector \mathbf{m} and the covariance matrix \mathbf{C} are unknown and have to be estimated from the available data $\mathbf{x}_1, \dots, \mathbf{x}_N$. Typically, the first step is to compute the maximum likelihood estimates

$$\hat{\mathbf{m}} = \frac{1}{N} \sum_{k=1}^N \mathbf{x}_k \quad (8.42)$$

$$\hat{C} = \frac{1}{N} \sum_{k=1}^N (x_k - \hat{m})(x_k - \hat{m})^T = \frac{1}{N} \begin{pmatrix} T \\ c \\ c \end{pmatrix} \begin{pmatrix} T \\ c \\ c \end{pmatrix}^T, \quad (8.43)$$

where $\begin{pmatrix} T \\ c \\ c \end{pmatrix}$ is an $p \times N$ matrix, whose columns are the mean-centered vectors $x_k - \hat{m}$. The original uncentered data matrix, with columns x_k , is denoted by $\begin{pmatrix} T \\ c \\ c \end{pmatrix}^T$.

The next step is to find the eigenvectors \hat{q}_k and eigenvalues $\hat{\lambda}_k$ of \hat{C} , which are determined by

$$\frac{1}{N} \begin{pmatrix} T \\ c \\ c \end{pmatrix} \hat{q}_k = \hat{\lambda}_k \hat{q}_k. \quad (8.44)$$

This is done using standard numerical procedures provided by most software packages. The desired principal components are evaluated by

$$\hat{y}_k = \hat{Q}^T x_k. \quad (8.45)$$

The principal components of each pixel are formed by a linear combination of all spectral bands of the pixel. The spectral bands are weighted by the components of the k th eigenvector; the variance of the resulting principal component is given by λ_k , the corresponding eigenvalue.

To determine the quality of the estimated principal components, we need to know the distribution of the random vector x . Approximate results based on normal or elliptically contoured distributions are available (Anderson, 2003); however, these results are seldom used in practice.

High-dimensional data

If $N < p$ (more bands than pixels), the $p \times p$ matrix \hat{C} is singular. The N data points define a linear subspace whose dimensionality is at most $N - 1$. Thus, at least $p - N + 1$ eigenvalues of \hat{C} are zero, corresponding to eigenvectors along directions with zero variance. In such cases, it is more efficient to perform the PCA using only the first $N - 1$ eigenvectors of \hat{C} , which can be determined using the following procedure.

We start by pre-multiplying both sides of (8.44) by $\begin{pmatrix} T \\ c \\ c \end{pmatrix}$ to obtain

$$\frac{1}{N} \begin{pmatrix} T \\ c \\ c \end{pmatrix} \begin{pmatrix} T \\ c \\ c \end{pmatrix} \hat{q}_k = \hat{\lambda}_k \begin{pmatrix} T \\ c \\ c \end{pmatrix} \hat{q}_k \quad \text{or} \quad \frac{1}{N} \begin{pmatrix} T \\ c \\ c \end{pmatrix} \tilde{q}_k = \hat{\lambda}_k \tilde{q}_k, \quad (8.46)$$

where

$$\tilde{q}_k, \quad \begin{pmatrix} T \\ c \\ c \end{pmatrix} \hat{q}_k \quad (8.47)$$

are the eigenvectors and λ_k the eigenvalues of the $N \times N$ matrix $(1/N) \begin{pmatrix} T \\ c \\ c \end{pmatrix} \begin{pmatrix} T \\ c \\ c \end{pmatrix}^T$. The eigenvalues $\hat{\lambda}_k$ are the same for both matrices; however, we cannot obtain \hat{q}_k from \tilde{q}_k because $N < p$ (fewer equations than unknowns). To overcome this problem, we multiply both sides of (8.46) by $\begin{pmatrix} T \\ c \\ c \end{pmatrix}^T$ to obtain

$$\frac{1}{N} \begin{pmatrix} T \\ c \\ c \end{pmatrix} \begin{pmatrix} T \\ c \\ c \end{pmatrix} \begin{pmatrix} T \\ c \\ c \end{pmatrix}^T \tilde{q}_k = \hat{\lambda}_k \begin{pmatrix} T \\ c \\ c \end{pmatrix} \begin{pmatrix} T \\ c \\ c \end{pmatrix}^T \tilde{q}_k, \quad (8.48)$$

which shows that $(\frac{T}{c}\tilde{q}_k)$ is an eigenvector of \hat{C} with eigenvalue $\hat{\lambda}_k$. Thus, $\hat{q}_k = \kappa \frac{T}{c}\tilde{q}_k$; the constant κ is chosen so that $\|\hat{q}_k\| = 1$. The desired result is

$$\hat{q}_k = \frac{1}{N\hat{\lambda}_k} \frac{T}{c}\tilde{q}_k, \quad (8.49)$$

where $\hat{\lambda}_k$ and \tilde{q}_k are the eigenvalues and eigenvectors of $(1/N)\frac{T}{c}\frac{T}{c}$. More details can be found in Fukunaga (1990) and Bishop (2006).

8.4

Principal Components Analysis: Application

The main purpose of PCA is to find a lower-dimensional space, $\{q_1, \dots, q_m\}$, where most of the observations can be assumed to lie within a specified accuracy. The first step is to create the centered data matrix

$$\frac{T}{c} = x_1 - \hat{m}, \dots, x_N - \hat{m} . \quad (8.50)$$

The matrix $(1/N)\frac{T}{c}\frac{T}{c}$ is equal to the estimated covariance matrix \hat{C} in (8.43). Since $\frac{T}{c}\frac{T}{c}$ is a nonnegative definite symmetric matrix, all its eigenvalues will be real and greater than or equal to zero, and the eigenvectors will be mutually orthogonal. The resulting orthogonal transformation preserves the trace of $\frac{T}{c}\frac{T}{c}$: that is, the sum of the elements on the main diagonal when we keep all principal components ($m = p$). Therefore, the variability in the data set, defined as the trace of the matrix $\frac{T}{c}\frac{T}{c}$, is preserved. The size of the variability in the data depends upon which matrix is factored: if we use $\frac{T}{c}\frac{T}{c}$, the variation is about the mean; if we use $\frac{T}{c}$, where $\frac{T}{c}$ is the original data matrix, the variation is about the origin.

Note that, in PCA, the data are usually mean-centered or viewed from the centroid of the cloud. The eigenvalues and eigenvectors used in the analysis are therefore quite different from those that would be obtained by using the original uncentered data. The eigenvectors of $\frac{T}{c}\frac{T}{c}$ identify the greatest spread in the data, in decreasing order, viewed from the centroid; in contrast, the eigenvectors of $\frac{T}{c}$ identify the greatest spread in the data, in decreasing order, viewed from the origin. The method of PCA is especially useful when the band-to-band correlations in the data are high; that is, the band-to-band numerical variations for each pixel are small, even though illumination may change significantly from pixel to pixel. We emphasize that PCA is an unsupervised technique because it does *not* take into account any class information about the data, even if it is available.

The eigenvectors of $\frac{T}{c}\frac{T}{c}$ form a new orthonormal basis for the data; the principal components are the coordinates of the data points in the new axes. By construction, principal components are uncorrelated with each other and their variance is equal to the corresponding eigenvalue. The eigenvectors indicate weights for different input bands (direction of projection); the eigenvalues indicate importance of direction (spread of data in that direction). Often the first few eigenvalues will explain most of the variation in the data set. The final step in PCA is the interpretation of the retained components.

Table 8.1 Correlation coefficient matrix and variance of Landsat data.

Band	1	2	3	4	5	7	Variance
1	1.0000	0.8720	0.9070	0.2363	0.0812	0.1661	18.3444
2	0.8720	1.0000	0.9171	0.1616	-0.0849	-0.0120	9.7994
3	0.9070	0.9171	1.0000	0.1881	0.0176	0.1015	19.8041
4	0.2363	0.1616	0.1881	1.0000	0.8043	0.7369	78.5729
5	0.0812	-0.0849	0.0176	0.8043	1.0000	0.9727	483.5313
7	0.1661	-0.0120	0.1015	0.7369	0.9727	1.0000	115.8600

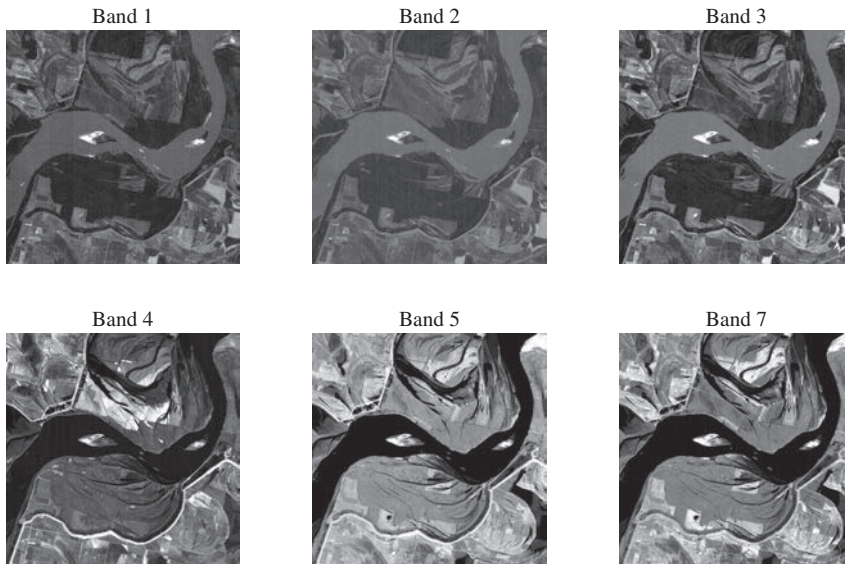


Figure 8.8 Images of TM bands, from the Mississippi area, used in PCA. The images have been linearly stretched to maximize contrast for display purposes.

According to Adams and Gillespie (2006), PCA is a valuable tool for reconnaissance and organization of the data; however, its proper use requires experience with photo interpretation and field work. The major uses of PCA are to reduce the dimensionality of hyperspectral imaging data for visualization, modeling, and classification applications.

To illustrate the method of PCA, it is preferable to use a multispectral data set from the Landsat ETM+ sensor. Since it is important that the input variables have the same physical meaning and are measured in the same units, we use only the reflective bands (numbered 1 – 5 and 7); the thermal IR band (number 6) is excluded from the analysis. The six bands of a Landsat TM image of the Mississippi area used in PCA are shown in Figure 8.8. To evaluate the correlation among different bands we consider Table 8.1, which shows the correlation coefficient matrix for the six reflective bands and their variance. We note that there are two groups of strongly correlated bands: (a) bands 1, 2, and 3 and (b) bands 4, 5, and 7. However, the correlation between the two groups of bands is weak. These correlations can be seen by inspection of the images in Figure 8.8.

Table 8.2 Eigenvectors and eigenvalues for of andsat data.

	PC 1	PC 2	PC 3	PC 4	PC 5	PC 6
Band 1	-0.0198	-0.5610	0.2382	-0.0645	0.7893	-0.0324
Band 2	0.0056	-0.4197	0.0973	-0.0556	-0.2971	0.8503
Band 3	-0.0094	-0.5936	0.2447	-0.1857	-0.5325	-0.5192
Band 4	-0.2897	-0.3675	-0.8473	0.2426	0.0044	-0.0651
Band 5	-0.8631	0.1467	0.0932	-0.4720	0.0176	0.0427
Band 7	-0.4131	-0.0138	0.3838	0.8226	-0.0696	-0.0186
Eigenvalue	646.6032	49.4526	24.3028	2.8022	1.8247	0.9239
% Variance	89.0749	6.8125	3.3479	0.3860	0.2514	0.1273
Cum % var	89.0749	95.8874	99.2353	99.6214	99.8727	100.0000

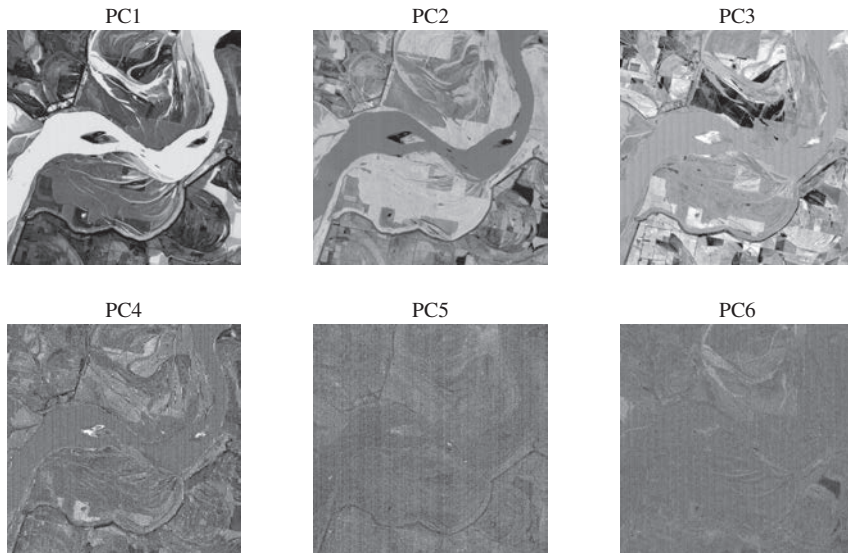


Figure 8.9 Images for the six PCs of the six TM bands of the Mississippi area shown in Figure 8.8. The images have been linearly stretched for display purposes.

The eigenvalues and eigenvectors for PCA, which are derived from the covariance matrix of the data, are shown in Table 8.2. The images produced by PCA are shown in Figure 8.9. We note that about 90 percent of the variability in the data lies in the direction defined by the first PC. Column PC 1 in Table 8.2 shows the relationship between PC 1 and the six TM bands. We note that the major contributor to PC 1 is band 5, followed by bands 7 and 4. The negative signs in the components of the eigenvector explain why the PC 1 image looks like the negative of the band 5 image. The heavy contribution of bands 4, 5, and 7 to the first PC can also be explained by looking at the first column in Table 8.3, which shows the principal component loadings (8.41) for the TM data.

Table 8.3 Principal component loadings for the andsat data.

	PC 1	PC 2	PC 3	PC 4	PC 5	PC 6
Band 1	-0.1178	-0.9210	0.2741	-0.0252	0.2489	-0.0073
Band 2	0.0454	-0.9428	0.1533	-0.0297	-0.1282	0.2611
Band 3	-0.0540	-0.9381	0.2711	-0.0699	-0.1616	-0.1121
Band 4	-0.8311	-0.2915	-0.4712	0.0458	0.0007	-0.0071
Band 5	-0.9980	0.0469	0.0209	-0.0359	0.0011	0.0019
Band 7	-0.9760	-0.0090	0.1758	0.1279	-0.0087	-0.0017

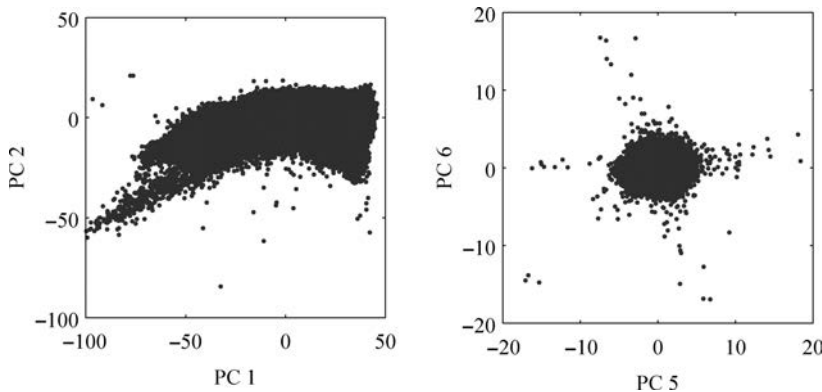


Figure 8.10 Scatter plots of (a) PC 1 versus PC 2 and (b) PC 5 versus PC 6 of the data set. Note that PC 5 and PC 6 are jointly spherically distributed.

Principal components 4 – 6 contain less than 1 percent of the variability in the data. If the noise present in the image data set is evenly distributed among the PCs, then the higher-numbered PCs typically have lower SNR than the lower-numbered ones. However, this does not necessarily mean that these “noisy-looking” PCs do not contain useful information. Figure 8.10 shows scatter plots of the first two and the last two PCs. By construction, all PCs are uncorrelated; however, the scatter plots of the least significant PCs usually have spherical shapes because they are dominated by noise. We emphasize that the use of the higher-numbered PCs depends on the objectives of the analysis. If the goal is data compression or classification, PCs corresponding to very small eigenvalues can be omitted. However, for target detection applications all PCs must be retained.

8.5

Diagonalizing Two Different Covariance Matrices

In Section 8.3.1 we derived the first PC by maximizing the quadratic form $a^T C a$ subject to the constraint $a^T a = 1$. The solution requires the diagonalization of a covariance matrix using eigenvalue decomposition. In this section we replace $a^T a = 1$ with the

more general constraint $a^T B a = 1$, where B is a positive definite matrix. The solution of this problem requires the simultaneous diagonalization of two different covariance matrices.

8.5.1 Extrema of Rayleigh Quotient

We start with an alternative derivation of PCA (Johnson and Wichern, 2007) using the eigenvalue decomposition of covariance matrix to find the extrema of the *Rayleigh quotient* defined by (Strang, 2005):

$$\lambda, \frac{a^T C a}{a^T a}. \quad (8.51)$$

If we set $d = a/\|a\|$ we can write (8.51) as $\lambda = d^T C d$, where $d^T d = 1$. Thus, maximizing (8.51) is equivalent to maximizing $a^T C a$ subject to $a^T a = 1$.

Using the eigenvalue decomposition (8.15), the orthogonality condition $Q Q^T = I$, and the definition $b = Q^T a$, we can express the ratio (8.51) as

$$\lambda = \frac{a^T C a}{a^T a} = \frac{a^T Q Q^T a}{a^T Q Q^T a} = \frac{b^T b}{b^T b} = \frac{\sum_{k=1}^p \lambda_k b_k^2}{\sum_{k=1}^p b_k^2} \leq \lambda_1 \frac{\sum_{k=1}^p b_k^2}{\sum_{k=1}^p b_k^2} = \lambda_1. \quad (8.52)$$

The choice $a = q_1$ gives $b = Q^T q_1 = [1 \ 0 \dots \ 0]^T$, which implies $q = \lambda_1$. Thus,

$$\max_{a \neq 0} \frac{a^T C a}{a^T a} = \lambda_1 \quad (\text{attained when } a = q_1). \quad (8.53)$$

Using a similar argument we can show that

$$\min_{a \neq 0} \frac{a^T C a}{a^T a} = \lambda_p \quad (\text{attained when } a = q_p). \quad (8.54)$$

Now, $a = Qb = b_1 q_1 + b_2 q_2 + \dots + b_p q_p$, so $a \perp q_1, \dots, q_m$ implies

$$0 = q_k^T a = b_1 q_k^T q_1 + \dots + b_p q_k^T q_p = b_k, \quad k \leq m. \quad (8.55)$$

Therefore, for a perpendicular to the first m eigenvectors q_k , the left-hand side of the inequality in (8.52) becomes

$$\frac{a^T C a}{a^T a} = \frac{\sum_{k=m+1}^p \lambda_k b_k^2}{\sum_{k=m+1}^p b_k^2} / \frac{\sum_{k=m+1}^p b_k^2}{\sum_{k=m+1}^p b_k^2}. \quad (8.56)$$

Taking $b_{m+1} = 1, b_{m+2} = \dots = b_p = 0$ gives for $m = 1, 2, \dots, p-1$

$$\max_{a \neq q_1, \dots, q_m} \frac{a^T C a}{a^T a} = \lambda_{m+1} \quad (\text{attained when } a = q_{m+1}). \quad (8.57)$$

Equation (8.53) says that the largest eigenvalue, λ_1 , is the maximum value of the quadratic form $a^T C a$ for all points a whose distance from the origin is unity; that is,

for all points on the unit hypersphere. Similarly, λ_p is the smallest value of the quadratic form for all points on the unit hypersphere.

8.5.2 Extrema of Generalized Rayleigh Quotient

Suppose now that we wish to find the extrema of the *generalized Rayleigh quotient*

$$\lambda, \frac{a^T C a}{a^T B a}, \quad (8.58)$$

where B is a positive definite matrix. Let \mathbf{w} be any matrix of order p satisfying

$$B = \mathbf{w}^T. \quad (8.59)$$

We typically use \mathbf{w} as the Cholesky factor of B (Golub and Van Loan, 1996). Since B is positive definite and hence nonsingular, R is also nonsingular. If we define

$$\mathbf{w}, \mathbf{a} \quad (8.60)$$

we can express the generalized Rayleigh quotient as

$$\lambda = \frac{a^T C a}{a^T B a} = \frac{\mathbf{w}^T C^{-1} \mathbf{w}}{\mathbf{w}^T \mathbf{w}} = \frac{\mathbf{w}^T D \mathbf{w}}{\mathbf{w}^T \mathbf{w}}, \quad (8.61)$$

where

$$D, \mathbf{w}^T C^{-1}. \quad (8.62)$$

Therefore, according to (8.53), (8.54), and (8.56), the extrema of $(a^T C a)/(a^T B a)$ can be determined from the eigenvalue decomposition of the symmetric matrix D , which is given by

$$D = \bar{Q}^{-1} \bar{Q}^T. \quad (8.63)$$

For example, the maximum of (8.61) is equal to the largest eigenvalue $\bar{\lambda}_1$ of D and it is attained when $\mathbf{w} = \bar{q}_1$ or equivalently when

$$\mathbf{a} = \bar{q}_1. \quad (8.64)$$

To specify the solution $\mathbf{a} = \bar{q}_1$ in terms of C and B , we note from (8.63) that $D\bar{Q} = \bar{Q}^{-1}$ or $D\bar{q}_1 = \bar{\lambda}_1\bar{q}_1$. Using (8.59) and (8.62), we obtain the equation

$$C\mathbf{a} = \lambda B\mathbf{a} \quad \text{or} \quad B^{-1}C\mathbf{a} = \lambda\mathbf{a}, \quad (8.65)$$

which is known as the *symmetric-definite generalized eigenvalue problem* (Golub and Van Loan, 1996). The matrix $B^{-1}C$ is nonsymmetric even if it is the product of two symmetric matrices; therefore, the generalized eigenvectors $\mathbf{a}_1, \dots, \mathbf{a}_p$ are not orthogonal.

We can solve (8.65) using the following algorithm: (a) compute the Cholesky factorization (8.59); (b) compute the symmetric matrix D using (8.62); and (c) compute the symmetric eigenvalue decomposition (8.63) using the symmetric QR algorithm. Using (8.59), (8.62), and the matrix

$$\mathbf{A} = \bar{Q}^{-1} \quad (8.66)$$

we can show that

$$A^T C A = \bar{Q}^T C^{-1} \bar{Q} = \bar{Q}^T D \bar{Q} = I \quad (8.67)$$

$$A^T B A = \bar{Q}^T B^{-1} \bar{Q} = I. \quad (8.68)$$

Therefore, the matrix $A = \bar{Q}^{-1}$ can be used to simultaneously diagonalize two different covariance matrices.

8.5.3 Canonical Space Transformation

An interesting interpretation of this optimization problem can be obtained by considering the sequence of linear transformations

$$z = B^{-1/2} x \quad (8.69)$$

$$y = \bar{Q}^T z. \quad (8.70)$$

The effect of the first transformation on the covariance matrices is

$$\text{cov}(z) = B^{-1/2} \text{cov}(x) B^{-1/2} = \begin{cases} I, & \text{if } \text{cov}(x) = B \\ B^{-1/2} C B^{-1/2}, & \text{if } \text{cov}(x) = C. \end{cases} \quad (8.71)$$

The effect of the second transformation on the covariance matrices is

$$\text{cov}(y) = \bar{Q}^T \text{cov}(z) \bar{Q} = \begin{cases} I, & \text{if } \text{cov}(z) = I \\ \bar{Q}^T B^{-1/2} C B^{-1/2} \bar{Q}, & \text{if } \text{cov}(z) = B^{-1/2} C B^{-1/2}, \end{cases} \quad (8.72)$$

We note that the transformation $z = B^{-1/2} x$ whitens (spherizes) the distribution with covariance matrix B and changes the covariance C of the other distribution to D . The PCA transformation $y = \bar{Q}^T z$ with respect to D is a solid rotation that preserves the spherical distribution and aligns the eigenvectors of D with the new axes. This process is illustrated in Figure 8.11.

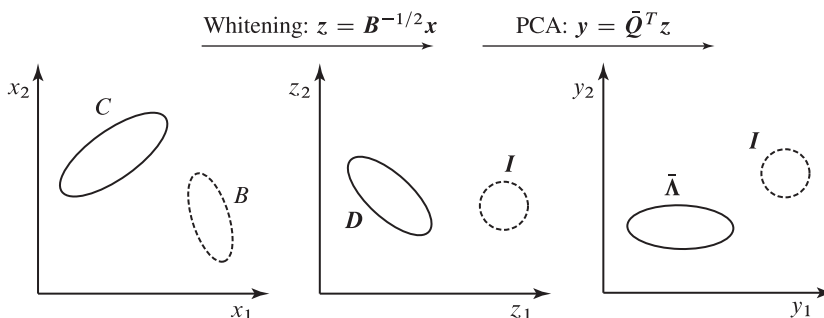


Figure 8.11 Illustration of simultaneous diagonalization of two covariance matrices by a whitening transform followed by a principal component transform.

8.6

Maximum Noise Fraction (MNF) Transform

In practical applications, remote sensing data are corrupted by noise. If we assume that the noise is additive, we have

$$x = x_0 + n, \quad (8.73)$$

where x_0 is the ideal noiseless signal and n is the unwanted noise. If x_0 and n are uncorrelated, the covariance matrix of the measured signal is given by

$$C = C_s + C_n, \quad (8.74)$$

where C_s and C_n are the covariance matrices of x_0 and n , respectively. Consider the set of linear filters

$$y_k = a_k^T x, \quad k = 1, \dots, p. \quad (8.75)$$

The signal-to-noise ratio at the output of the k th filter is

$$\text{SNR}_k = \frac{\text{var}(a_k^T x_0)}{\text{var}(a_k^T n)} = \frac{a_k^T C_s a_k}{a_k^T C_n a_k} = \frac{a_k^T C a_k}{a_k^T C_n a_k} - 1. \quad (8.76)$$

The objective is to create a set of uncorrelated outputs y_1, \dots, y_p by maximizing the SNR (*not* the variance) at each filter output. To satisfy the first condition, we require that

$$\text{cov}(y_i, y_j) = \text{cov}(a_i^T x, a_j^T x) = a_i^T C a_j = 0, \quad i \neq j. \quad (8.77)$$

Maximizing the SNR_k is equivalent to maximizing the *inverse* of the “noise fraction” $a_k^T C_n a_k / a_k^T C a_k$. Therefore, we have to solve the optimization problem

$$\max_{a_k} \frac{a_k^T C a_k}{a_k^T C_n a_k}. \quad (8.78)$$

The solution is given by (8.63) if we set $B = C_n$. Therefore, we have

$$D = C_n^{-1/2} C C_n^{-1/2} = \bar{Q}^{-1} \bar{Q}^T. \quad (8.79)$$

The maximum of (8.78) is equal to $\bar{\lambda}_k$ and it is attained when $a_k = C_n^{-1/2} \bar{q}_k$. Also, from (8.76) and (8.78) we obtain

$$\bar{\lambda}_k = \text{SNR}_k + 1. \quad (8.80)$$

The *Maximum Noise Fraction (MNF) transform*, introduced by Green et al. (1988) and further discussed by Lee et al. (1990), is given by

$$y = A^T x = C_n^{-1/2} \bar{Q}^T x = \bar{Q}^T C_n^{-1/2} x. \quad (8.81)$$

The first step spherizes the noise component n of the data, whereas the second step provides the principal components of the transformed data. If $C_n = \sigma_n^2 I$, the MNF transform and the PCA are identical, because $C = \sigma_n^{-2} C$.

The MNF transform requires knowledge of the noise covariance matrix of the data. However, the estimation of C_n is not an easy task, which limits the use of MNF transform

in practical applications. If the data have a homogeneous area, we can estimate C_n by averaging the covariance matrices from two different data cubes; one cube is obtained by shifting horizontally by one pixel, and the other by shifting vertically by one pixel. More details can be found in Green et al. (1988). Although this approach is widely used in practice, the validity of the obtained noise covariance estimate is questionable, to say the least.

8.7

Canonical Correlation Analysis (CCA)

Canonical Correlation Analysis (Hotelling, 1936) deals with two sets of random variables arranged in a $p \times 1$ vector x and a $q \times 1$ vector y . The goal is to find linear combinations $u = a^T x$ and $v = b^T y$ such that u and v have the largest possible correlation. Such linear combinations, known as *canonical variables*, can give insight into the relationships between the two sets of variables. In hyperspectral imaging we can use CCA to investigate the relationship between two sets of bands from the same cube or the relationship between two cubes of the same scene collected at different times; the later case is useful in change detection applications.

Suppose that x and y have means m_x and m_y , and that

$$\text{cov}(x) = C_x, \quad \text{cov}(y) = C_y, \quad \text{cov}(x, y) = C_{xy} = C_{yx}^T. \quad (8.82)$$

These quantities can be obtained by proper partitioning of the covariance matrix

$$\text{cov} \begin{pmatrix} x \\ y \end{pmatrix} = C = \begin{pmatrix} C_x & C_{xy} \\ C_{yx} & C_y \end{pmatrix}. \quad (8.83)$$

Consider now the canonical variables

$$u = a^T x, \quad v = b^T y. \quad (8.84)$$

Using results for the transformation of random vectors (see Section 7.3) we obtain

$$\text{var}(u) = a^T C_x a, \quad \text{var}(v) = b^T C_y b, \quad \text{cov}(u, v) = a^T C_{xy} b. \quad (8.85)$$

The correlation coefficient between u and v , which depends on a and b , is given by

$$\rho_{uv} = \frac{\text{cov}(u, v)}{\sqrt{\text{var}(u)} \sqrt{\text{var}(v)}} = \frac{a^T C_{xy} b}{\sqrt{a^T C_x a} \sqrt{b^T C_y b}}. \quad (8.86)$$

Since ρ_{uv} does not depend on the scaling of a and b , we can maximize (8.86) by solving the equivalent problem

$$\max_{a, b} a^T C_{xy} b \quad \text{subject to} \quad a^T C_x a = b^T C_y b = 1. \quad (8.87)$$

The solution to this problem can be simplified by defining the vectors

$$, \quad C_x^{1/2} a, \quad , \quad C_y^{1/2} b. \quad (8.88)$$

Using (8.88) we can express (8.87) as

$$\max_{\mathbf{M}} \mathbf{M}^T \mathbf{M} \quad \text{subject to} \quad \mathbf{M}^T \mathbf{M} = \mathbf{I} = 1, \quad (8.89)$$

where \mathbf{M} , the *coherence matrix* of x and y , is given by

$$\mathbf{M} = \tilde{C}_{xy} / C_x^{1/2} C_{xy} C_y^{1/2} \quad (8.90)$$

with C_x and C_y assumed positive definite. For convenience, we use the symbol \mathbf{M} instead of the more descriptive symbol \tilde{C}_{xy} . Consider now the Lagrangian function

$$\psi = \mathbf{M}^T \mathbf{M} - \frac{1}{2} \lambda (\mathbf{M}^T \mathbf{M} - 1) - \frac{1}{2} \mu (\mathbf{M}^T \mathbf{M} - 1), \quad (8.91)$$

where λ and μ are Lagrange multipliers. The vectors of derivatives set equal to zero are

$$\frac{\partial \psi}{\partial \mathbf{M}} = \mathbf{M} - \mu \mathbf{I} = \mathbf{0} \quad (8.92a)$$

$$\frac{\partial \psi}{\partial \lambda} = \mathbf{M}^T - \lambda \mathbf{I} = \mathbf{0}. \quad (8.92b)$$

Multiplication of (8.92a) on the left by \mathbf{M}^T and (8.92b) on the left by \mathbf{M} gives

$$\lambda = \mu = \mathbf{M}^T \mathbf{M} \quad (8.93)$$

Multiplication of (8.92a) on the left by \mathbf{M}^T and (8.92b) on the left by \mathbf{M} gives

$$\mathbf{M} \mathbf{M}^T = \lambda^2 \quad (8.94a)$$

$$\mathbf{M}^T \mathbf{M} = \lambda^2 \quad (8.94b)$$

From (8.86) and (8.93) we see that $\lambda = \mathbf{M}^T \mathbf{M} = a^T C_{xy} b$ is the correlation coefficient between u and v when $\text{var}(u) = \text{var}(v) = 1$. Since we want the maximum correlation, we choose the eigenvectors and corresponding to the largest eigenvalue of $\mathbf{M} \mathbf{M}^T$ and $\mathbf{M}^T \mathbf{M}$.

A simpler way to determine the eigenvectors and is using the singular value decomposition (SVD) of matrix \mathbf{M} . The SVD of \mathbf{M} is given by Strang (2005)

$$\mathbf{M} = \mathbf{P} \mathbf{D} \mathbf{Q}^T, \quad (8.95)$$

where \mathbf{P} is a $p \times p$ orthogonal matrix, \mathbf{Q} is a $q \times q$ orthogonal matrix, and \mathbf{D} is a $p \times q$ diagonal matrix with diagonal elements

$$\rho_1 \geq \rho_2 \geq \dots \geq \rho_r > 0. \quad (8.96)$$

The integer r , where $r \leq \min\{p, q\}$, is the rank of the matrix \mathbf{M} . Starting with the SVD (8.95), it is straightforward to show that

$$\mathbf{M} \mathbf{M}^T = \mathbf{P} \mathbf{D}^2 \mathbf{P}^T \quad \text{or} \quad \mathbf{M} \mathbf{M}^T \mathbf{p}_k = \rho_k^2 \mathbf{p}_k \quad (8.97a)$$

$$\mathbf{M}^T \mathbf{M} = \mathbf{Q} \mathbf{D}^2 \mathbf{Q}^T \quad \text{or} \quad \mathbf{M}^T \mathbf{M} \mathbf{q}_k = \rho_k^2 \mathbf{q}_k, \quad (8.97b)$$

where \mathbf{p}_k and \mathbf{q}_k are the columns of \mathbf{P} and \mathbf{Q} . Comparing (8.97a) to (8.94a) and (8.97b) to (8.94b) shows that $\mathbf{p}_1 = \mathbf{a}_1$, $\mathbf{q}_1 = \mathbf{b}_1$, and $\rho_1 = \lambda_1^2$. Therefore, the first canonical variables are

$$u_1 = \mathbf{a}_1^T \mathbf{x}, \quad v_1 = \mathbf{b}_1^T \mathbf{y}, \quad (8.98)$$

where a_1 and b_1 are the first *canonical correlation vectors*

$$a_1 = C_x^{-1/2}p_1, \quad b_1 = C_y^{-1/2}q_1. \quad (8.99)$$

The correlation coefficient between the canonical variables u_1 and v_1 is called the first *canonical correlation* between x and y . We can easily see that

$$\rho_{u_1 v_1} = \rho_1 = \sqrt{\lambda_1}. \quad (8.100)$$

To find the second canonical variables u_2 and v_2 , we must solve the problem

$$\begin{aligned} \max_{a_2, b_2} \quad & a_2^T C_{xy} b_2 \\ \text{subject to} \quad & a_2^T C_x a_2 = b_2^T C_y b_2 = 1 \\ & a_2^T C_x a_1 = b_2^T C_y b_1 = 0. \end{aligned} \quad (8.101)$$

Note that $\text{cov}(u_2, u_1) = a_2^T C_x a_1$ and $\text{cov}(v_2, v_1) = b_2^T C_y b_1$. Thus, the constraints require that the second canonical variables u_2 and v_2 are uncorrelated with both u_1 and v_1 and have unit variance. It can be shown, using Lagrange multipliers, that the correlation between u_2 and v_2 is $\rho_2 = \sqrt{\lambda_2}$, the second largest singular value of M , and the vectors a_2 and b_2 are obtained from the corresponding singular vectors. This process is continued for all nonzero singular values of M .

If we put the r canonical variables and vectors in matrix form, we have

$$u, \quad u_1 \quad u_2 \quad \dots \quad u_r^T, \quad v, \quad v_1 \quad v_2 \quad \dots \quad v_r^T \quad (8.102)$$

$$A, \quad a_1 \quad a_2 \quad \dots \quad a_r, \quad B, \quad b_1 \quad b_2 \quad \dots \quad b_r, \quad (8.103)$$

where r is the rank of M . Then, the CCA transformation can be expressed as

$$u = A^T x, \quad A, \quad C_x^{-1/2} P \quad (8.104)$$

$$v = B^T y, \quad B, \quad C_y^{-1/2} Q. \quad (8.105)$$

Using the relationships (8.104), (8.105) and (8.95), we obtain

$$\text{cov}(u) = P^T C_x^{-1/2} C_x C_x^{-1/2} P = P^T P = I \quad (8.106)$$

$$\text{cov}(v) = Q^T C_y^{-1/2} C_y C_y^{-1/2} Q = Q^T Q = I \quad (8.107)$$

$$\text{cov}(u, v) = P^T C_x^{-1/2} C_{xy} C_y^{-1/2} Q = P^T M Q = D. \quad (8.108)$$

Therefore, the covariance matrix of the canonical variables is

$$\text{cov} \quad \begin{matrix} u \\ v \end{matrix} \quad = \quad \begin{matrix} I & D \\ D^T & I \end{matrix}. \quad (8.109)$$

Thus, the entire relationship between the p variables x and the q variables y is expressed *only* in terms of the r parameters ρ_1, \dots, ρ_r ; hence the names, canonical correlations and canonical variables.

Unlike PCA, canonical correlations are invariant under simultaneous nonsingular linear transformations of the variables. Therefore, the canonical correlations of x and y are identical to those of $Fx + f$ and $g^T + g$, where F and g are invertible matrices.

A consequence of this result is that, unlike PCA, a CCA using the covariance matrix will give the same canonical correlations as a CCA using the corresponding correlation coefficient matrix. More information about CCA can be found in Johnson and Wichern (2007), Rencher (1998), and Anderson (2003). Different algorithms for the practical implementation of CCA are discussed by Golub and Van Loan (1996).

To illustrate CCA we shall use the Landsat data cube discussed in Section 8.4. The components of x are bands 1, 2, and 3 and the components of y are bands 4, 5, and 6. Because CCA is invariant under invertible linear transformations, it is preferable to use the correlation coefficient matrix (see Table 8.1) to obtain C_x , C_y , and C_{xy} according to the matrix partitioning shown in (8.83). The next step is to compute the matrix

$$M = C_x^{-1/2} C_{xy} C_y^{-1/2} = \begin{matrix} 2 & 0.1901 & -0.1018 & 0.3554 & 3 \\ 4 & 0.2626 & -0.4460 & -0.0768 \\ & 0.0886 & -0.1668 & 0.2479 \end{matrix} . \quad (8.110)$$

The SVD $M = PDQ^T$ provides all we need for CCA. The orthogonal matrices P and Q are used in (8.104) and (8.105) to transform the spectral bands to canonical components. Note that the canonical components are artificial variables without physical meaning. However, their visual inspection may provide an experienced analyst with useful information. The canonical correlations, which are the singular values of M , are given by

$$\rho_1 = 0.6087, \quad \rho_2 = 0.4101, \quad \rho_3 = 0.0707. \quad (8.111)$$

We note that only the first canonical correlation is above 0.5. We cannot draw more conclusions because there is not strong correlation between the two sets of bands; this lack of correlation is also evident from the correlation coefficient matrix in Table 8.1. The application of CCA in change detection is discussed by Nielsen et al. (1998), Zhang et al. (2007), and in Section 11.5.

8.8

Linear Discriminant Analysis

PCA and CCA make *no* a priori assumptions about the existence of classes in the data; even if class information is available, it is not used. Linear discriminant analysis, on the other hand, assumes that the N observation vectors x_1, \dots, x_N are divided a priori into K classes with N_k observations in the k th class, where $N = N_1 + \dots + N_K$ (Rencher, 1998). In the presence of class structure, the best type of linear transformation will be dictated by the objective of the analysis. In general, we use PCA to highlight *similarities* in the data and linear discriminant analysis to highlight *differences* between the classes.

8.8.1

Fisher's Linear Discriminant

The projection of an observation x onto the line specified by a vector a is

$$y = a^T x. \quad (8.112)$$

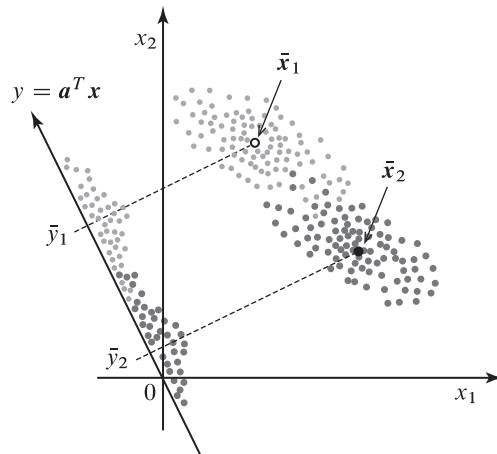


Figure 8.12 Projection of two-dimensional data onto a one-dimensional subspace of the observation space.

In general, the projection onto one dimension leads to a considerable loss of information, and classes that are well separated in the original p -dimensional space may become strongly overlapping in one dimension. However, by properly choosing the vector a we may find a direction that maximizes class separation.

To clarify the basic ideas we begin with the two-class problem illustrated in Figure 8.12. The two classes will be well separated if the projected points from each class are scattered in a small region about their mean and the two means are as far apart as possible. The means of the class projections are

$$\bar{y}_k = \frac{1}{N_k} \sum_{y=k} y = \frac{1}{N_k} \sum_{x=k} a^T x = a^T \bar{x}_k \quad (8.113)$$

where \bar{x}_k , the average of the class, is defined by

$$\bar{x}_k = \frac{1}{N_k} \sum_{x=k} x. \quad (8.114)$$

The variance of each class is given by s_k^2/N_k , where s_k^2 is the *scatter* defined by

$$\begin{aligned} s_k^2 &= \sum_{y=k} (y - \bar{y}_k)^2 \\ &= \sum_{x=k} [a^T(x - \bar{x}_k)]^2 \\ &= \sum_{x=k} a^T(x - \bar{x}_k)(x - \bar{x}_k)^T a \\ &= a^T S_k a \end{aligned} \quad (8.115)$$

and S_k is the within-class scatter matrix

$$S_k, \quad \sum_{x \in k} (x - \bar{x}_k)(x - \bar{x}_k)^T. \quad (8.116)$$

The measure of class separation used by Fisher is given by

$$J(a) = \frac{(\bar{y}_1 - \bar{y}_2)^2}{s_1^2 + s_2^2} = \frac{|a^T(\bar{x}_1 - \bar{x}_2)|^2}{a^T(S_1 + S_2)a} = \frac{|a^T(\bar{x}_1 - \bar{x}_2)|^2}{a^T S_W a}, \quad (8.117)$$

where S_W is the total *within-class* scatter matrix

$$S_W, \quad S_1 + S_2. \quad (8.118)$$

Using the Cholesky decomposition $S_W = \mathbf{L}^T \mathbf{L}$ and setting $w = a/\|\mathbf{L}^T a\|$, we have

$$J(a) = \frac{|a^T(\bar{x}_1 - \bar{x}_2)|^2}{a^T S_W a} = \frac{(w^T d)^2}{w^T w} \leq d^T d, \quad (8.119)$$

where $d = \mathbf{L}^T(\bar{x}_1 - \bar{x}_2)$. The last inequality follows from the Cauchy–Schwarz inequality $(w^T d)^2 \leq (w^T d)(d^T d)$; the equality holds when $w = \kappa d$, where κ is a constant. Therefore, the direction for best class separation is attained when

$$a_F = \kappa S_W^{-1}(\bar{x}_1 - \bar{x}_2). \quad (8.120)$$

Because it is the direction which is important, the choice of κ is not critical. The maximum value of the separation criterion (8.119) is given by

$$S(a_F) = d^T d = (\bar{x}_1 - \bar{x}_2)^T S_W^{-1}(\bar{x}_1 - \bar{x}_2). \quad (8.121)$$

A different derivation can be obtained by writing (8.119) as

$$J(a) = \frac{a^T S_B a}{a^T S_W a} \quad (8.122)$$

where S_B is a rank one matrix defined by

$$S_B, \quad (\bar{x}_1 - \bar{x}_2)(\bar{x}_1 - \bar{x}_2)^T. \quad (8.123)$$

The vector a that maximizes (8.122) is given by (see Section 8.5.2)

$$S_W^{-1} S_B a = \lambda a. \quad (8.124)$$

In this particular case, we do not need to solve the eigenvalue problem because $S_B a = (\bar{x}_1 - \bar{x}_2)(\bar{x}_1 - \bar{x}_2)^T a \propto (\bar{x}_1 - \bar{x}_2)$; that is, $S_B a$ is always in the direction of $(\bar{x}_1 - \bar{x}_2)$. Therefore, the solution of (8.124) is identical to (8.120).

The vector specified by (8.120), which was introduced by Fisher (1936), provides the direction yielding the maximum ratio of between-class scatter to within-class scatter. The projection values

$$y = \kappa a_F^T x = \kappa (\bar{x}_1 - \bar{x}_2)^T S_W^{-1} x \quad (8.125)$$

can be used for classification and detection purposes by choosing a proper threshold. In Section 10.5 we illustrate that there is a close relation between Fisher's linear discriminant and the matched filter detector. Figure 8.12 illustrates the effect of using two

different directions: the line connecting the two means and Fisher's optimum direction. The two directions are identical for isotropic ($S_W = s_W^2 I$) distributions. Finally, we emphasize that if the class distributions are multimodal and highly overlapping, even the best direction is highly unlikely to provide adequate separation between the classes.

8.8.2 Multiple Linear Discriminant Analysis

In the case of $K > 2$ classes, the projection from the original space to a d -dimensional space is attained by d discriminant functions

$$y_k = a_k^T x, \quad k = 1, \dots, d. \quad (8.126)$$

These projections can be written more concisely in matrix form as

$$y = A^T x. \quad (8.127)$$

The grand centroid \bar{x} is the sample mean of the entire data set, that is,

$$\bar{x} = \frac{1}{N} \sum_x x. \quad (8.128)$$

To measure the total dispersion from the grand centroid we use the *total scatter matrix* defined by

$$S_T, \quad (x - \bar{x})(x - \bar{x})^T. \quad (8.129)$$

The total within-class dispersion matrix S_W is equal to

$$S_W = \sum_{k=1}^K S_k. \quad (8.130)$$

To establish a relation between S_T and S_W we start with the identity

$$x - \bar{x} = (x - \bar{x}_k) + (\bar{x}_k - \bar{x}). \quad (8.131)$$

Substituting (8.131) into (8.129) and using (8.116), we obtain the fundamental relation

$$S_T = S_W + S_B, \quad (8.132)$$

where S_B is the “between-class” scatter matrix

$$S_B, \quad \sum_{k=1}^K N_k (\bar{x}_k - \bar{x})(\bar{x}_k - \bar{x})^T, \quad (8.133)$$

which measures the dispersion of class centroids from the grand centroid.

The $p \times p$ scatter matrices S_T , S_W , and S_B after projection are given by the $d \times d$ matrices $A^T S_T A$, $A^T S_W A$, and $A^T S_B A$, respectively. We want a scalar criterion of performance which is large when $A^T S_B A$ is large and $A^T S_W A$ is small. We note that for a scatter (or covariance) matrix, a measure of spread is the determinant. Therefore, we often determine A by maximizing the function

$$J(A) = \frac{|A^T S_B A|}{|A^T S_W A|}. \quad (8.134)$$

The solution is given by the generalized eigenvalue problem (Duda et al., 2001)

$$S_B a_k = \lambda_k S_W a_k. \quad (8.135)$$

The possible rank of the discriminant subspace to be fitted in the observation space depends on the relative sizes of K and p . If $K - 1 < p$, the maximum possible rank of the discriminant space is $K - 1$ because the K centroids have to coexist in a $K - 1$ subspace regardless of the value of p . For example, the centroids of three classes have to coexist in a plane. On the other hand, if $K - 1 \geq p$, then it is possible to fit as many as p discriminant functions. Linear discriminant analysis for $K > 2$ is rarely used for dimensionality reduction of hyperspectral imaging data.

8.8.3 Global and Pooled Covariance Matrices

Suppose that the data from the k th class are samples from a distribution with prior probability π_k , mean m_k , and covariance C_k . If we define the quantities

$$\hat{\pi}_k = \frac{N_k}{N}, \quad \hat{C}_k = \frac{1}{N_k} S_k, \quad \hat{C}_T = \frac{1}{N} S_T \quad (8.136)$$

and we use (8.130) and (8.133), the fundamental relation (8.132) can be written as

$$\hat{C}_T = \sum_{k=1}^K \hat{\pi}_k \hat{C}_k + \sum_{k=1}^K \hat{\pi}_k (\bar{x}_k - \hat{m})(\bar{x}_k - \hat{m})^T. \quad (8.137)$$

In terms of the theoretical parameters of the distributions, the *global* or *total* covariance matrix – that is, the scatter measured from the grand mean – is given by

$$C_T = \sum_{k=1}^K \pi_k C_k + \sum_{k=1}^K \pi_k (m_k - m)(m_k - m)^T. \quad (8.138)$$

The weighted average of the class mean vectors and covariance matrices are

$$m = \sum_{k=1}^K \pi_k m_k, \quad C_W = \sum_{k=1}^K \pi_k C_k. \quad (8.139)$$

The matrix C_W is known as the *pooled* covariance matrix. If we define the between-classes covariance matrix

$$C_B = \sum_{k=1}^K \pi_k (m_k - m)(m_k - m)^T \quad (8.140)$$

equation (8.138) can be written as

$$C_T = C_W + C_B. \quad (8.141)$$

We use equation (8.138) when we need to determine the covariance matrix of a data cube using the means and covariances of the constituent classes.

8.9 Linear Spectral-Band Estimation

In this section, we use the theory of linear prediction and the concept of partial correlation coefficients to provide a simple theoretical framework for understanding where spectral inter-band information is concentrated in hyperspectral data and how this information can be effectively and efficiently exploited. Given that the inverse covariance matrix appears in many detection and classification algorithms, we investigate how spectral information affects its structure and how it may help to design effective and efficient data analysis algorithms. We also derive a spectral-innovations representation of hyperspectral data and we compare it with the widely used principal components transformation as a data whitening tool. However, we must emphasize that the linear transformations introduced in this section are not useful for dimensionality reduction.

8.9.1 Spectral Wiener Filters

To illustrate the key ideas we consider estimating the reflectance x_i in the i th band using a linear combination of the remaining bands $x_1, \dots, x_{i-1}, x_{i+1}, \dots, x_p$. The estimation error is given by

$$e_i = x_i - \hat{x}_i = \sum_{k=1}^p a_{ik} x_k = a_i^T x, \text{ where } a_i = 1. \quad (8.142)$$

The variance of the prediction error is given by

$$\text{var}(e_i) = a_i^T C a_i, \quad (8.143)$$

where $C = \text{cov}(x)$. In the sequel we use c_{ij} for the elements of C , c^{ij} for the elements of C^{-1} , and $D(c_{ii})$ for a diagonal matrix with elements c_{11}, \dots, c_{pp} on its diagonal. Minimization of (8.143) subject to the constraint $a_i = 1$ yields the optimum spectral Wiener filter or spectral linear smoother. The p Wiener filter vectors a_1, \dots, a_p can be arranged in matrix form as $A = [a_1 \dots a_p]$. It can be shown (Manolakis et al., 2000) that the spectral Wiener filter A is

$$e = A^T(x - m), \quad (8.144)$$

where the matrix A is given by

$$A = (\text{diag}(C^{-1}))^{-1} C^{-1} = D(1/c^{ii}) C^{-1}. \quad (8.145)$$

The minimum error variance for the i th band is given by

$$\sigma_i^2 = 1/c^{ii}, \quad i = 1, \dots, p. \quad (8.146)$$

Figure 8.13 shows the coefficients of the Wiener filter for the AVIRIS Moffett data set. We note that A is a sparse matrix; that is, most of its off-diagonal coefficients are essentially zero.

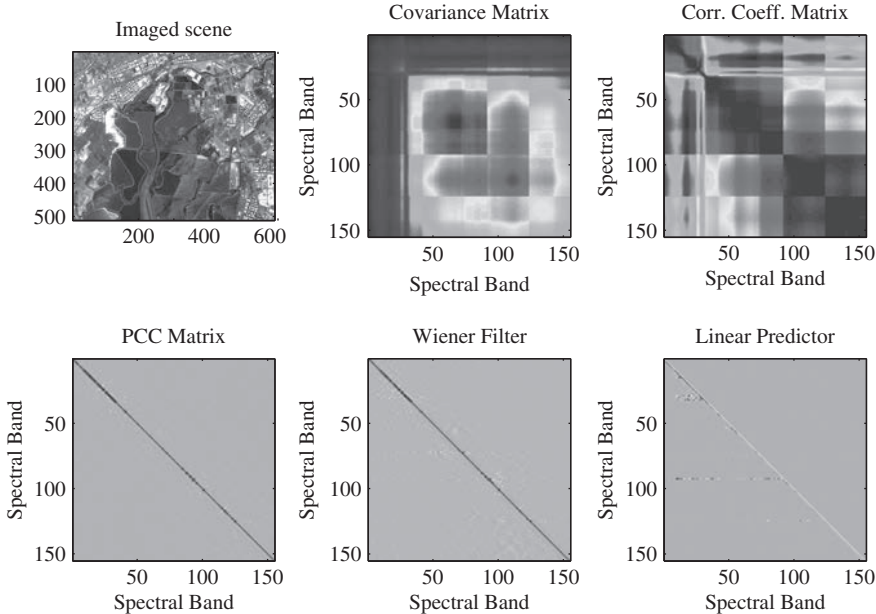


Figure 8.13 Illustration of spectral correlation properties, spectral Wiener filter, and visual to IR spectral linear predictor for the Moffett data set. (A black and white version of this figure will appear in some formats. For the color version, please refer to the plate section.)

8.9.2 Partial Correlation Coefficients

The “linear dependency” between two spectral bands x_i and x_j is measured by the correlation coefficient

$$\rho_{ij} = \mathbf{p} \frac{\text{cov}(x_i, x_j)}{\text{var}(x_i)\text{var}(x_j)}, \quad -1 \leq \rho_{ij} \leq 1. \quad (8.147)$$

The correlation coefficient matrix P is given by

$$P = D(1/\sqrt{c_{ii}})CD(1/\sqrt{c_{ii}}). \quad (8.148)$$

The correlation coefficient matrix for the Moffett data cube, shown in Figure 8.13, suggests a strong correlation between spectral channels that are up to $40 - 50$ bands away.

To further investigate the strength of these correlations, we compute the correlation coefficient between the estimation errors e_i and e_j of the spectral Wiener filter

$$\tilde{\rho}_{ij} = \mathbf{p} \frac{\text{cov}(e_i, e_j)}{\text{var}(e_i)\text{var}(e_j)}, \quad -1 \leq \tilde{\rho}_{ij} \leq 1. \quad (8.149)$$

This result, which is known as a *Partial Correlation Coefficient (PCC)* (Anderson, 2003), measures the “linear dependency” between two spectral bands after the effect of all other bands has been removed. The PCC matrix can be evaluated by normalizing the inverse covariance matrix as follows (Kshirsagar, 1972):

$$\tilde{P} = D(1/\sqrt{c^{ii}})C^{-1}D(1/\sqrt{c^{ii}}). \quad (8.150)$$

The partial correlation coefficient matrix for the Moffett data set, shown in Figure 8.13, reveals that only neighboring bands have significant linear dependence.

The partial correlation coefficient matrix can be used to analyze the operation of spectral Wiener filters, optimum linear spectral predictors, and spectral matched filters because all these optimum processors are specified in terms of C^{-1} .

8.9.3 Spectral Linear Prediction: Visible to IR and IR to Visible

Suppose that we wish to estimate the reflectance x_i using the reflectance from the first $(i-1)$ bands using the “visible to IR” linear predictor

$$e_i = x_i - \hat{x}_i = \sum_{k=1}^{i-1} b_k x_k = b_i^T x_i, \text{ with } b_i = 1, \quad (8.151)$$

where

$$b_i = [b_1 \ b_2 \ \dots \ b_{i-1}]^T \quad (8.152)$$

$$x_i = [x_1 \ x_2 \ \dots \ x_{i-1}]^T. \quad (8.153)$$

We note that the order of the linear predictors increases from 1 to $(p-1)$. The variance of the error is given by

$$\text{var}(e_i) = b_i^T C_i b_i, \quad (8.154)$$

where C_i is the $i \times i$ principal submatrix of C . The optimum linear predictor is obtained by minimizing (8.151) subject to the constraint $b_i = 1$. It turns out that the $(p-1)$ linear predictors are the rows of $B = L^{-1}$ (Manolakis et al., 2000). L is a unit lower triangular matrix obtained from the lower-upper Cholesky decomposition

$$C = LDL^T, \quad (8.155)$$

where D is a diagonal matrix

$$D = \text{diag}\{d_1, d_2, \dots, d_p\}. \quad (8.156)$$

The minimum prediction error variance is given by

$$\tilde{\sigma}_i^2 = d_i \geq 0, \quad i = 1, \dots, p. \quad (8.157)$$

Figure 8.13 shows the coefficients of the “Visible to IR” optimum linear predictor for the Moffett data set. We note that most off-diagonal coefficients of the lower-triangular matrix are zero. In general, the minimum mean square error resulting from the estimation of each spectral band using a Wiener filter is lower than that for a linear predictor because the Wiener filter uses all remaining spectral bands for the estimation.

In a similar way we can obtain an “IR to Visible” linear predictor by reversing the order of spectral bands. The optimum coefficient vectors \bar{b}_i are provided by the rows of matrix C^{-1} in upper-lower Cholesky decomposition

$$C = \bar{D}^{-T}. \quad (8.158)$$

The minimum prediction error variance is given by

$$\bar{\sigma}_i^2 = \bar{d}_i \geq 0, \quad i = 1, \dots, p. \quad (8.159)$$

The outputs of the “visible to IR” and “IR to Visible” linear predictors are evaluated by (8.144) with $A^T = L^{-1}$ or $A^T = -L^{-1}$, respectively.

In Section 7.3.3 we discussed a whitening transformation using the Cholesky decomposition. Since this triangular decomposition is unique, comparing (8.155) with (7.50), we conclude that the optimum linear predictor

$$z = D^{-1/2} L^{-1} x \quad (8.160)$$

is essentially a whitening transformation. An alternative whitening transformation using the eigenvalue decomposition $C = Q^{-1} Q^T$ is

$$y = D^{-1/2} Q^T x. \quad (8.161)$$

Equation (8.160) is a whitening transformation known as *innovations representation*. We note that each innovations component z_k brings in the “new information” present in the “current” band. The innovations representation adds one band at a time; the PCA transform uses *all* spectral bands to determine each principal component. Figure 8.14 shows a spectral band from the Moffett data set and the corresponding images produced by PCA, the innovations representation, and the Wiener filter.

The minimum variances of the optimum estimators can be used to study the spectral quality and the inherent variability of the data. For example, the variance of the error associated with the linear estimators (smoothing or prediction) could be used as a rough measure of noise and other modeling errors. Thus, we could use the quantity $E(x_i)/\text{var}(e_i)$, where $E(x_i)$ is the mean of the i th band and e_i is the corresponding estimation error, as a rough signal-to-noise ratio for the i th band. However, we emphasize that this quantity is *not* a measure of the sensor SNR. This and other issues related to band estimation are discussed in the Problems.

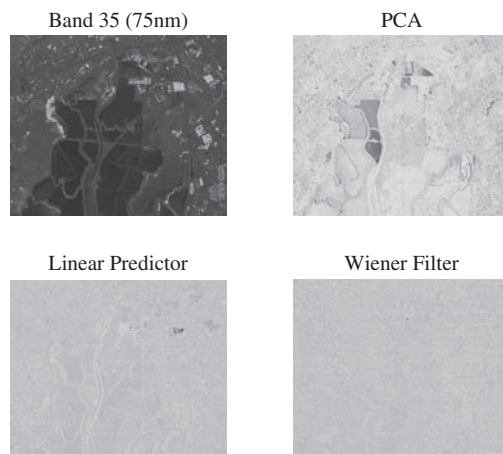


Figure 8.14 A spectral band from the Moffett data set and the corresponding images produced by PCA, the innovations representation, and the Wiener filter. (A black and white version of this figure will appear in some formats. For the color version, please refer to the plate section.)

8.10 Summary and Further Reading

In this chapter we introduced several linear transformations that are useful for the analysis of hyperspectral imaging data. Principal Component Analysis is essentially a linear transformation based on the eigenvectors of the spectral covariance matrix. PCA is a widely used technique because it is simple to implement and apply. However, PCA is often misused because users fail to appreciate the assumptions that must be satisfied for the method to be successful. Canonical Correlation Analysis is a method closely related to PCA. However, whereas PCA considers interrelationships within a set of bands, the focus of CCA is on the relationship between two groups of bands. Both PCA and CCA maximize the variance of projections under different sets of constraints. Finally, linear discriminant analysis uses class labels to find projections that maximize the separability between classes. In contrast, PCA and CCA do not use any class information even if it is available. Finally, we analyzed the structure of the spectral covariance matrix and its inverse using optimum linear estimation interpretations. In this context, we described the concept of the partial correlation coefficient and we established a relationship between the partial correlation matrix and the inverse covariance matrix.

The problems of dimensionality reduction and feature selection and extraction have been extensively investigated in the areas of pattern recognition and machine learning (Webb and Copsey, 2011; Alpaydin, 2010). The application of subspace projections, nonlinear manifolds, and sparsity based approaches to dimensionality reduction of hyperspectral imaging data are discussed in various publications, including Bioucas-Dias and Nascimento (2008); Bachmann et al. (2005); Charles et al. (2011); and Bioucas-Dias et al. (2012); however, the utility of these techniques to many practical applications is still an open question.

Problems

1. (a) Determine the principal components y_1 and y_2 for the covariance matrix

$$C = \begin{matrix} 1 & 4 \\ 4 & 100 \end{matrix}$$

and calculate the proportion of the total variance explained by the first principal component. (b) Convert the covariance matrix C to a correlation matrix R . (c) Determine the principal components y_1 and y_2 from R and compute the proportion of the total variance explained by y_1 . (d) Compare the components calculated in (c) with those obtained in (a). Are they the same? Should they be?

2. Consider a random vector x with components defined by

$$x_i = v + \epsilon_i, \quad v \sim N(a, \sigma^2), \quad \epsilon_i \sim N(0, \sigma_\epsilon^2), \quad i = 1, 2.$$

(a) Compute the mean m and covariance matrix C of x . (b) Determine analytically the eigenvalues and eigenvectors of C . (c) Determine the principal components y_1 and y_2 and their variances. (d) If $\sigma_\epsilon^2 \ll \sigma^2$ we can ignore the second principal

component. What is the reconstruction formula and the corresponding error? Explain the meaning of the results. Do we need the normality assumption?

3. In Problem 2, find the correlation between v and y_1 and the correlation between v and y_2 , as functions of σ_ϵ^2 and σ^2 . Comment upon the results.
4. Consider a random vector x with zero mean and covariance matrix

$$C = \text{cov}(x) = \begin{matrix} 1 & 1/2 \\ 1/2 & 1 \end{matrix}.$$

Denote the principal components of x by y_1 and y_2 . Let $z = [2x_1 \quad x_2]^T$, and denote the principal components of z by u_1 and u_2 . Write u_1 and u_2 as functions of x_1 and x_2 , and verify they are not identical to y_1 and y_2 . Is this expected? Why?

5. Generate 200 samples from a zero-mean normal random vector with covariance matrix specified by $\sigma_1 = 1, \sigma_2 = 1, \rho = 0.8$, and use them to reproduce the results in Figure 8.6.
 6. (a) Use the Landsat data set to reproduce the results shown in Figures 8.8 and 8.9, and Tables 8.1, 8.2, and 8.3. (b) Plot the pairwise scatterplot matrix, with histograms at the diagonal, for both the image bands and the PCA bands. (c) Verify that the eigenvalues of the covariance matrix provide the variance of each PC image. (d) Verify that the total image variance is equal to the total PC image variance.
 7. (a) Compute the principal components of the data set. (b) Use the eigenvalues plot to select a “reasonable” number m of significant components. (c) Reconstruct the data using m components and compute the reconstruction error. (d) Check whether the computed reconstruction error agrees with the theoretically predicted one. (e) Repeat (a)–(d) using the correlation coefficient matrix.
 8. Repeat Problem 7 using the data set.
 9. Generate samples from two-dimensional Gaussian distributions to verify the results shown in Figure 8.11.
 10. (a) Add increasing amounts of white Gaussian noise to to evaluate the performance of MNF. (b) Repeat with spatial correlated Gaussian noise.
 11. Use the following covariance matrices
- $$C_x = \begin{matrix} 1.0 & 0.4 \\ 0.4 & 1.0 \end{matrix}, \quad C_y = \begin{matrix} 1.0 & 0.2 \\ 0.2 & 1.0 \end{matrix}, \quad C_{xy} = \begin{matrix} 0.5 & 0.6 \\ 0.3 & 0.4 \end{matrix}$$
- to illustrate the CCA results developed in Section 8.7.
12. Illustrate the use of CCA using the data set to replicate the results discussed in Section 8.7.
 13. Illustrate Fisher’s linear discriminant analysis using two classes from the data set.
 14. Use the data set to reproduce the results shown in Figure 8.9.1.
 15. Use the data set to reproduce the results shown in Figure 8.14.

9 Spectral Mixture Analysis

Analysis of spectral mixtures is important in remote sensing imaging spectroscopy, because essentially the spectrum of any pixel of a natural scene is a mixture. The analysis of mixed spectra, known as *Spectral Mixture Analysis (SMA)*, is the subject of this chapter. SMA attempts to answer two questions: (a) What are the spectra of the individual materials? (b) What are the proportions of the individual materials? We focus on linear mixing because of its relative analytical and computational simplicity and because it works satisfactorily in many practical applications. We discuss the physical aspects of the linear mixing model, geometrical interpretations and algorithms, and statistical analysis using the theory of least squares estimation. The main applications of SMA are in the areas of hyperspectral image interpretation and subpixel target detection.

9.1 Spectral Mixing

When a ground resolution element contains several materials, all these materials contribute to the individual pixel spectrum measured by the sensor. The result is a composite or mixed spectrum, and the “pure” spectra that contribute to the mixture are called *end-member* spectra. Spectral mixtures can be macroscopic or intimate depending on what scale the mixing is taking place (see Figure 9.1).

In a *macroscopic* mixture the materials in the field of view are optically separated in patches so there is no multiple scattering between components (each reflected photon interacts with only one surface material). Such mixtures are linear: that is, the combined spectrum is simply the sum of the fractional area times the spectrum of each component. Linear mixing is possible as long as the radiation from component patches remains separate until it reaches the sensor.

In an *intimate* mixture, such as the microscopic mixture of mineral grains in a soil or rock, a single photon interacts with more than one material. In this case, mixing occurs when radiation from several surfaces combines before it reaches the sensor. These types of mixtures are nonlinear in nature and therefore more difficult to analyze and use.

To illustrate some of the issues involved in SMA, we discuss some examples of mixed spectra provided by Adams and Gillespie (2006). Figure 9.2(a) shows spectra for mixtures of a material having a featureless spectrum (quartz) with a material having a spectrum with diagnostic absorption bands (alunite). We note that only the presence of alunite is evident in the spectra of quartz–alunite mixtures. Mixing the spectra of quartz

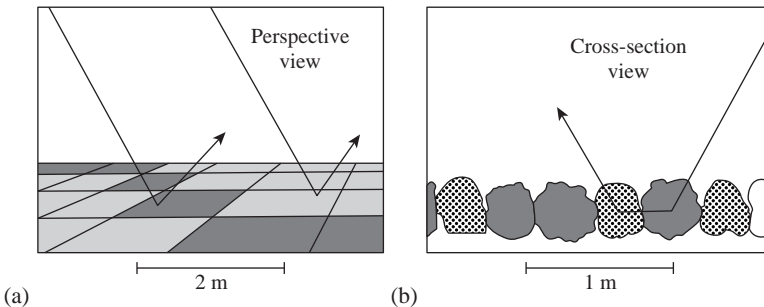


Figure 9.1 Illustration of spectral mixing at different scales. (a) The spectra of two different materials at the scale of meters mix linearly according to area. (b) The spectra of different mineral grains, at the scale of millimeters, mix non-linearly according to Beer's law. After Adams and Gillespie (2006).

and alunite in Figure 9.2(a) using a linear and a nonlinear mixing model yields the spectra shown in Figures 9.2(b) and 9.2(c), respectively. Comparing these results with the spectra of *physically* mixed samples in Figure 9.2(a) shows that linear mixing does not match well the spectra of physical mixtures in the absorption bands. The discrepancy between linear and nonlinear models becomes important when we want to estimate the proportions of the mixed materials from their spectra (Keshava and Mustard, 2002).

In contrast to the quartz–alunite mixed spectra, the mixed spectrum of olivine (forsterite) and pyroxene (enstatite) in Figure 9.2(d) shows absorption features from both minerals. Therefore, if we know the spectra of the pure minerals, we can interpret the mixed spectrum. The spectrum of the physically mixed powders differs from the arithmetic average of the forsterite and enstatite spectra due to nonlinear absorption and the differences in packing the particulate samples which results in intimate mixing.

Figure 9.2(e) shows a mixed spectrum of the shadow cast by a green leaf on bare soil. The spectrum of the soil that is illuminated by light transmitted through the leaf resembles the spectrum of the leaf; however, it is “darker” (lower reflectance) and it has a smaller dynamic range. This is another good example of intimate mixing because light is partially absorbed by one material before entering another material; this is a nonlinear process governed by Beer's law. We emphasize that mixing is essentially always nonlinear; however, many times there is a small degree of nonlinearity that can be approximated reasonably well by a linear model.

We focus on linear mixing because of its relative analytical and computational simplicity and because it works satisfactorily in many practical applications when we move from the laboratory scale to the scale of remote sensing. Indeed, in most cases the spectra of adjacent meter-scale patches mix linearly for most practical purposes, because the amount of intimate mixing at patch boundaries is negligible. Furthermore, in situations where radiation interacts with more than one component and mixing is nonlinear, we could convert reflectance values to single scattering albedo, where linear mixing mechanisms do apply (Mustard and Pieters, 1989). More details and references about nonlinear mixing are given by Mustard and Sunshine (1998), Keshava and Mustard (2002) and Adams and Gillespie (2006).

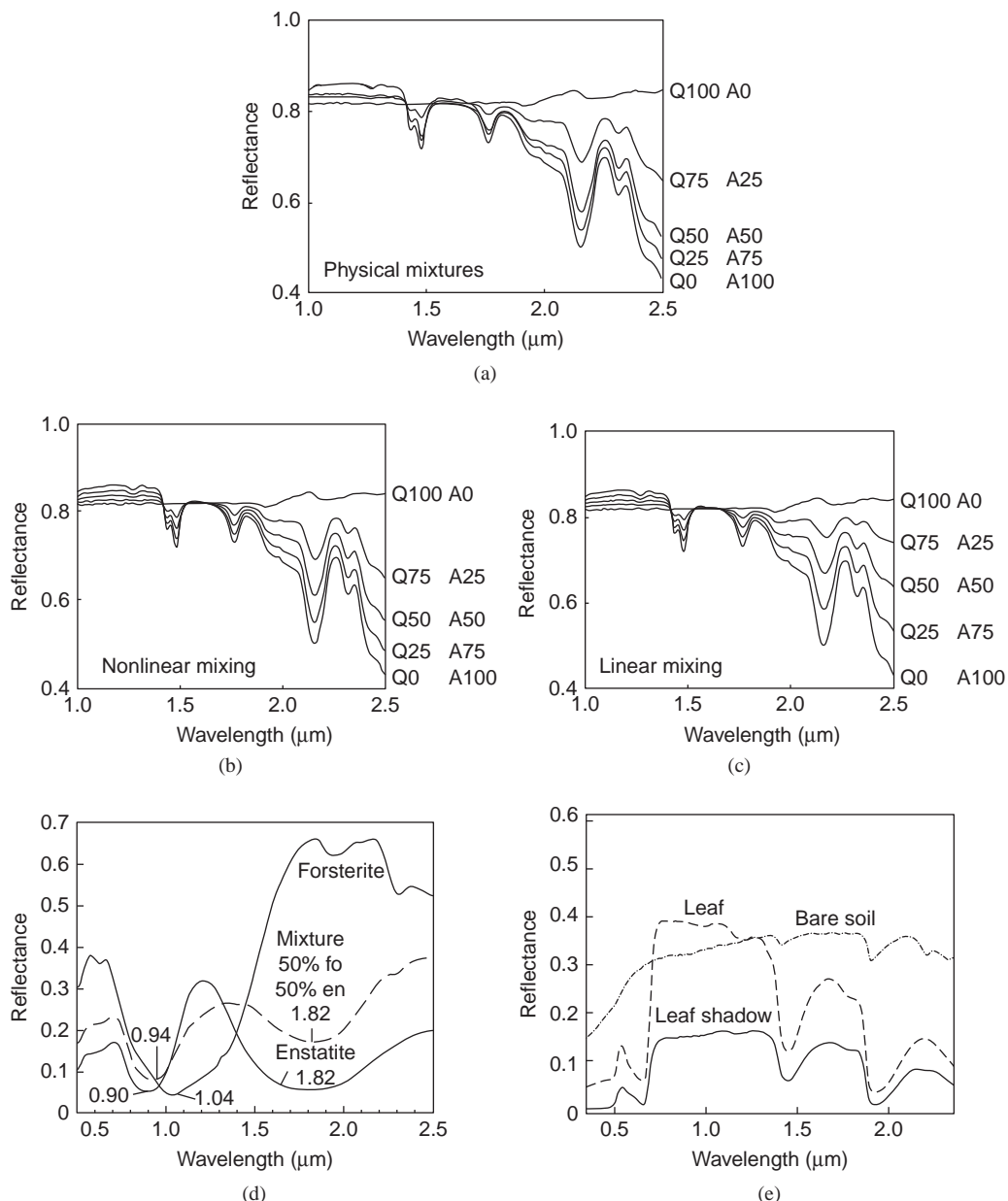


Figure 9.2 Examples of mixed spectra. (a) Mineral powders: quartz (Q) and alunite (A). Numbers on the right of the graph indicate mixing ratios. (b) Mixed spectra of quartz (Q) and alunite (A) using a nonlinear mixing model. (c) Spectra of same mixtures using a linear model. (d) Mineral powders: forsterite (fo) and enstatite (en). (e) Green leaf, soil, and leaf shadow on soil. After Adams and Gillespie (2006).

9.2

The Linear Mixing Model

A spectral mixture model is a physically based model in which a mixed spectrum is modeled as a combination of pure spectra, called *endmembers (EMs)*. When photons interact with a single component within the field of view, the mixture can be modeled as a linear sum of each component weighted by the proportion of the components within the field of view. The equation for a linear mixing model with m components is

$$\mathbf{x} = \sum_{k=1}^m a_k \mathbf{s}_k + \mathbf{e} = \mathbf{S}\mathbf{a} + \mathbf{e}, \quad (9.1)$$

where \mathbf{x} is the measured spectrum of the mixed pixel, \mathbf{s}_k is the spectrum of each EM, a_k is the fractional abundance or fill-fraction of each EM, and \mathbf{e} is the residual that accounts for the difference between the observed and modeled spectra. The residual includes measurement error, noise, and contributions from any EMs that have been left out. The columns of \mathbf{S} are the EM spectra and the components of \mathbf{a} are the corresponding fill-fractions. Since the fill-fractions, a_k , are defined as fractions of the pixel, they are constrained as follows:

$$a_1 + a_2 + \cdots + a_m \triangleq \mathbf{u}^T \mathbf{a} = 1 \quad (\text{sum-to-one constraint}) \quad (9.2)$$

$$a_1 \geq 0, \dots, a_m \geq 0 \quad (\text{nonnegativity constraint}), \quad (9.3)$$

where \mathbf{u} is a $p \times 1$ vector of ones. The enforcement of these constraints is necessary if we wish to assure physically meaningful values for the fill-fractions. We also note that the modeled spectrum and the EM spectra must have nonnegative components. The exact linear model $\mathbf{S}\mathbf{a} = \mathbf{x}$ and the constraint $\mathbf{u}^T \mathbf{a} = 1$ form a linear system of $(p + 1)$ equations with m unknowns. This system has a unique solution if $m = p + 1$; that is, if the number of EMs equals the number of spectral bands plus one. In practice, we always have $m < p + 1$, which leads to an overdetermined system of linear equations. We note that in practical applications we typically use three to seven EMs (Adams and Gillespie, 2006).

9.2.1

Linear Mixing and Geometry

The LMM has associated with it certain unique geometrical properties which provide insight into behavior and application. In order to illustrate the relationships between the EM vectors, the fill-fractions, and the observed spectrum vector, we consider some simple cases which may be represented pictorially. For $m = 2$ and $p = 2$, a perfect LMM is described by the equations

$$\mathbf{x} = a_1 \mathbf{s}_1 + a_2 \mathbf{s}_2 \quad (9.4a)$$

$$a_1 + a_2 = 1 \quad (9.4b)$$

$$a_1 \geq 0, a_2 \geq 0. \quad (9.4c)$$

To provide a geometrical interpretation of this model we refer to Figure 9.3(a). Without any constraints on a_1 and a_2 , the mixture $\mathbf{x} = a_1 \mathbf{s}_1 + a_2 \mathbf{s}_2$ can be anywhere on the

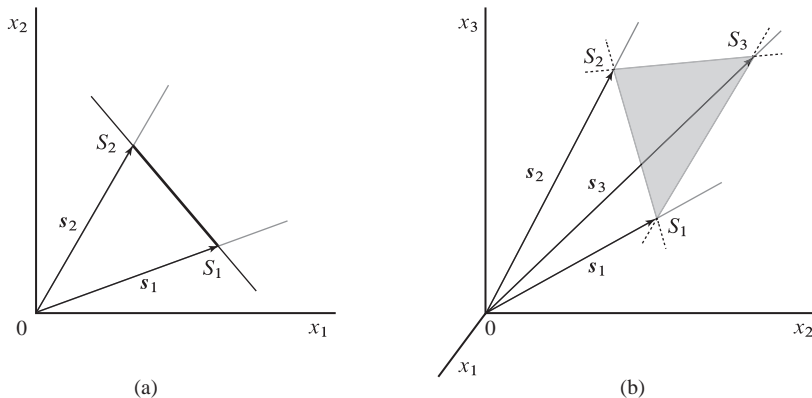


Figure 9.3 Geometrical interpretation of the linear mixing model. All feasible (fully-constrained) mixtures are located inside a simplex: (a) 1-D simplex (line segment S_1S_2) and (b) 2-D simplex (plane triangle $S_1S_2S_3$).

subspace (plane) defined by s_1 and s_2 . The constraint $a_1 + a_2 = 1$ confines the mixture \mathbf{x} on the line passing through the tips S_1 and S_2 of the EM vectors. In contrast, the constraints $a_1 \geq 0$ and $a_2 \geq 0$ confine the mixture \mathbf{x} on the shaded cone specified by the EMs. Thus, enforcing both constraints confines all *feasible* mixtures \mathbf{x} on the line segment S_1S_2 . Mixtures whose tips lie above or below the line will violate the constraint $a_1 + a_2 = 1$. On the other hand, mixtures whose tips lie on the line, but do not lie on the segment S_1S_2 will violate the constraint $a_1 \geq 0$, $a_2 \geq 0$.

Figure 9.3(b) shows that if $m = p = 3$, the tips of the EM vectors form a triangle $S_1S_2S_3$ which defines a plane. Mixture vectors whose tips lie above or below the plane will violate the sum-to-one constraint. On the other hand, mixtures whose tips lie in the plane, but do not lie inside the triangle will violate the nonnegativity constraint. For a perfect model, the observation vectors must lie inside the triangular region formed by the tips of the three EM vectors. The distribution of the points in this region depends upon the distribution of a_k s in the data set. Furthermore, the “thickness” of the region occupied by the data in the direction normal to the plane defined by the s_k vectors would be zero.

These ideas can be extended into higher dimensions using the concept of convex hull and simplex (Lay, 1982). A set of points S is *convex* if it contains the line segment between any two points in the set. The *convex hull* of a set of points is the smallest convex set that contains the points. The convex hull \mathcal{C} of a set of m points S_1, \dots, S_m , specified by the vectors s_1, \dots, s_m , is given by the expression

$$\mathcal{C} = \left\{ \mathbf{x} = \sum_{k=1}^m a_k s_k, \sum_{k=1}^m a_k = 1, a_1, \dots, a_m \geq 0 \right\}. \quad (9.5)$$

If the vectors $s_2 - s_1, \dots, s_m - s_1$ are linearly independent, then (9.5) determines an $(m - 1)$ -simplex \mathcal{S} that includes all points satisfying the perfect LMM. The points S_1, \dots, S_m , are known as vertices (singular: vertex) of the simplex. In geometry, a

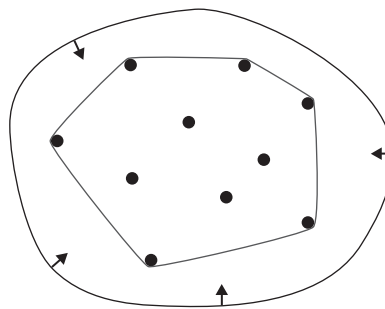


Figure 9.4 Obtaining the convex hull of a finite set of points in two dimensions using the elastic-band analogy.

simplex (plural: simplexes or simplices) is a generalization of the notion of a triangle or tetrahedron to arbitrary dimension. The simplex is a line segment for $m = 2$, a plane triangle for $m = 3$, and a tetrahedron for $m = 4$. Clearly, any point in the simplex \mathcal{S} can be expressed as a convex combination of its vertices. Therefore, convex geometry provides a natural framework for the analysis of linearly mixed spectra. The convex hull of any nonempty subset of the vertices S_1, \dots, S_m that define a simplex is called a *face* of the simplex; faces are simplexes themselves. The 0-faces are the vertices (singular: vertex), the 1-faces are called the edges, the $(m - 2)$ -faces are called the *facets*, and the sole $(m - 1)$ -face is the whole n -simplex itself. Spectra with tips on the faces are not complete mixtures because one or more EMs are missing from the combination.

To further clarify the difference between simplex and convex hull, we consider a finite set of points on the plane, as shown in Figure 9.4. To obtain the convex hull, we put a pin at each point, we stretch a rubber band to surround the entire set, and then we release it; when the rubber becomes taut, it encloses the convex hull of the set of points. The simplex in \mathbb{R}^2 is a triangle (3-simplex) because the number of vertices is equal to the dimensionality of the space plus one. Thus, any three points that do not lie on the same line define a simplex. The intersection of these triangles is the convex hull obtained by the rubber band. Determining the convex hull of a set of points is a problem in computational geometry and many algorithms have been proposed for its solution (Barber et al., 1996).

Finally, we note that the linear model $\mathbf{x} = a_1 \mathbf{s}_1 + \dots + a_m \mathbf{s}_m$, where $\mathbf{s}_1, \dots, \mathbf{s}_m$ are linearly independent, can generate three types of sets in \mathbb{R}^p . If the coefficients can take any value, the result is an m -dimensional subspace. If we require $a_1 + \dots + a_m = 1$, we obtain an affine set of points. If we require that $a_1 \geq 0, \dots, a_m \geq 0$, the result is a convex cone. Enforcing both constraints generates the convex hull (9.5). Since the elements of S are nonnegative, all these sets of points lie in the positive orthant of \mathbb{R}^p .

9.2.2

Linear Mixing and Principal Component Analysis

In reality, even if a perfect mixing process has been at work, the presence of sensor noise shifts mixed spectra points away from the mixing simplex. With real data,

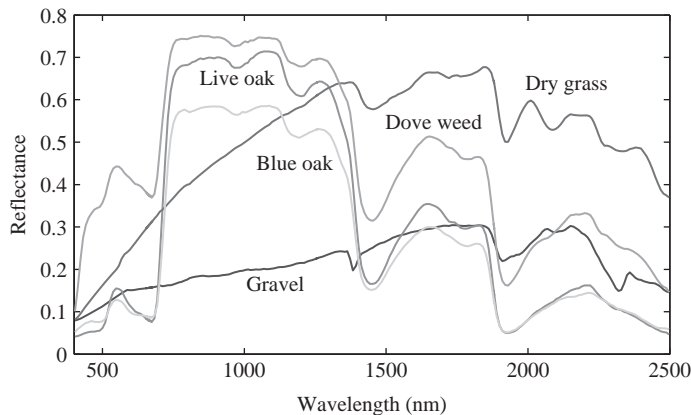


Figure 9.5 Examples of spectra used to illustrate the properties of LMM.

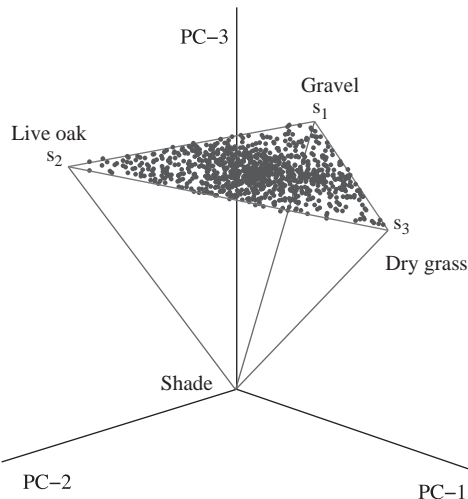


Figure 9.6 Data cloud for LMM with three EMs and low noise level.

the ideal conditions of the perfect LMM do not hold. To illustrate the basic ideas we use reflectance spectra from Figure 9.5 to generate synthetic data according to the LMM

$$\mathbf{x} = \mathbf{S}\mathbf{a} + \mathbf{e}, \quad \mathbf{e} \sim N(\mathbf{0}, \sigma^2 \mathbf{I}) \quad (9.6)$$

by enforcing the constraints $a_i \geq 0$ and $a_1 + \dots + a_m = 1$. For example, if the amount of additive noise is relatively small, the region occupied by the data in Figure 9.3(b) will slightly extend outside the simplex triangle as shown in Figure 9.6. However, with the assumption that the major variability of the data is due to variations in the a_k s, it is reasonable to expect the covariance matrix of the data to have two “significant” eigenvalues. The eigenvectors corresponding to these eigenvalues

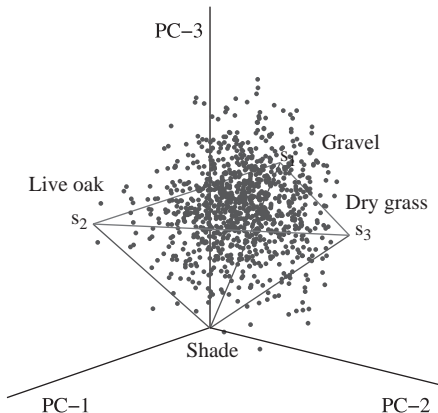


Figure 9.7 Data cloud for LMM with three EMs and high noise level.

define the plane in which the major variability in the data occurs. Note that we have used PCA to reduce the dimensionality of the data for display in a three-dimensional space.

If we assume that S is a fixed matrix and a is a random vector statistically independent of e , the covariance matrix of x in (9.1) is given by

$$\text{cov}(x) = S \text{cov}(a) S^T + \text{cov}(e). \quad (9.7)$$

If we neglect the residual term in (9.7), assume the EMs are linearly independent, and impose the sum-to-one constraint, then $\text{cov}(x)$ has rank $(m - 1)$. Thus, the tips of the EM vectors lie in a subspace defined by the mean vector of the data and the eigenvectors corresponding to the “significant” eigenvalues. For example in Figure 9.6 these eigenvectors lie on the plane defined by the triangle formed by the tips of the EMs. However, as illustrated in Figure 9.7, if the amount of noise is significant the data cloud does not resemble the geometrical structure implied by the LMM.

In theory, application of PCA to a spectral data set should result in the number of “significant” eigenvalues to be one less than the number of EMs. The spectra can be converted to the relevant dimensionality by a linear transformation with the significant eigenvectors computed from PCA. Maximum or minimum values of the elements of each eigenvector define those wavelengths most significant to each independent axis of variation. The shape of the eigenvector elements as a function of wavelength is determined by the set of EMs contributing to the spectra. Thus, while the eigenvectors may show similarities to the spectra of EMs, they do not directly correspond to these EMs. These issues are explored in Problem 2.

In conclusion, we stress that there is *not* a one-to-one correspondence between the dominant eigenvectors of the data covariance matrix and spectral EMs. However, what the two groups share in common is that both provide *equivalent bases* for the subspace accounting for the majority of spectral variability in the scene.

9.2.3 Fitting a Linear Mixing Model to Data

The main objective of SMA is to model an image as linear mixtures of EMs. Fitting a linear mixing model involves two steps: (a) EM determination and (b) fill-fraction estimation. Although there are algorithms where the two steps are interwoven, the objectives of most applications are better served by keeping the two steps distinct. In general, accurate fill-fraction estimation is more difficult than EM identification. In the next two sections we discuss the basic principles of EM determination and fill-fraction estimation. We then continue with an in-depth discussion of the computational and statistical aspects of linear model estimation and hypothesis testing. These results are useful in SMA, target detection, and target identification.

9.3 Endmember Determination Techniques

There are two ways to select EM spectra. The first is to determine EMs from the image itself (image EMs). The second is to select EMs from a collection of laboratory or field spectra (reference EMs). Clearly, the use of reference EMs requires the conversion of hyperspectral data from radiance to reflectance. EMs can be determined interactively by experienced spectroscopists or by automated processing algorithms. EM determination algorithms are either geometrical or statistical in nature.

To introduce the basic idea underlying the geometrical algorithms, we recall that the perfect LMM has exactly the same constraints as a simplex. The vertices of the simplex correspond to the EMs and any point within the simplex is a feasible mixed spectrum. This is illustrated in Figure 9.8(a) for a mixture with three EMs. Thus, in principle, we could determine the EMs of a data set produced by a perfect LMM by finding the vertices of the corresponding simplex. This idea, which was introduced by Craig (1994), has led to a family of geometrical approaches that seek to find EMs by defining the minimum volume simplex that includes all data points. If the data include at least one pure pixel per EM (that is, there is at least one spectrum on each vertex of the simplex), we can

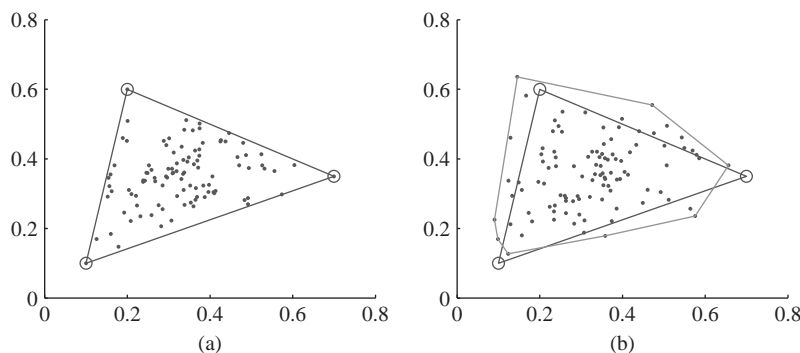


Figure 9.8 (a) Data generated by a perfect LMM with three EMs are enclosed by a 3-simplex. (b) The addition of sensor noise into the perfect LMM pushes some data points outside the 3-simplex.

determine the EMs by finding the vertices of the simplex. If there are not pure pixels representing the m EMs, we can still determine the simplex if each facet contains at least $(m - 1)$ spectral points. For example, we can determine the triangle in Figure 9.8(a) if there are two points on each of its sides. These algorithms, which essentially find the set of the “most pure” pixels in the data, are widely used in practice because they have a clear meaning and they are computationally efficient.

In practice, the LMM is not perfect due to sensor noise and other limitations; as a result, there are spectra outside the feasible region of the simplex. This is illustrated in Figure 9.8(b), which shows the simplex corresponding to the perfect LMM and the convex hull of the data (perfect LMM plus gaussian noise). A simple inspection of this plot reveals the big challenges facing automated EM determination algorithms. Clearly, finding the “true” 3-simplex from the convex hull of the data is a hard or impossible task. The situation is even worse in practice, where the data volumes of real hyperspectral data are much messier. Because the convex hull is determined by data points without regard for their meaning in the image, it often consists of noisy pixels, outliers, or defects that lie outside the main data population. However, even if we remove these pixels, some spectra on the convex hull correspond to unusual scene components that do not mix with other scene components (Adams and Gillespie, 2006). These situations create many problems for algorithms deriving EMs from the data volume alone.

Another problem is that EMs that are obvious on the ground may be much more difficult to determine from the image itself. For example, suppose that half of the pixels in an image contain trees that occupy less than half of any single pixel. Clearly, EMs determined from this image would not include a true “tree EM.” If the image data do not include pure EM pixels, the simplex enclosing the data is determined by minimizing its volume. This is a hard nonconvex optimization problem and the vertices of the obtained simplex may lead to EMs that do not actually exist as image spectra. Such spectra, which are known as “*virtual EMs*”, may be selected from a spectral library.

The most well known and used geometrical EM determination algorithms assume the presence of pure EM pixels in the data. Two algorithms of this type are the pixel purity index (PPI) algorithm (Boardman et al., 1993) and the N-FINDR algorithm (Winter, 1999). Information about other geometrical algorithms is provided by Keshava and Mustard (2002) and Bioucas-Dias et al. (2012).

The sequential maximum angle convex cone (SMACC) algorithm (Gruninger et al., 2004) is based on a convex cone for representing the spectral vectors. The algorithm starts with a single EM, obtained from the brightest pixel, and adds new EMs based on the angle they make with the existing cone. The data vector making the maximum angle with the existing cone is chosen as the next EM to enlarge the EM set. The algorithm terminates when all of the data vectors are within the convex cone, to some tolerance.

Statistical methods, which mostly use a Bayesian framework, are highly complicated and difficult to use and interpret. Since the fill-fractions are distributed over a simplex, they are typically modeled by a Dirichlet distribution, which is obtained by normalizing a set of beta-distributed random variables by their sum (Minka, 2000). Bayesian algorithms always provide feasible solutions and, as a result, they completely hide from the analyst the possibility that one or more specified EMs may be totally false.

A detailed overview of geometrical, statistical, and sparse regression-based SMA algorithms with emphasis on their mathematical aspects is given by Bioucas-Dias et al. (2012) and Ma et al. (2014). However, we must emphasize again that a major concern with the use of most EM finding algorithms is not so much understanding their operation, but the meaningful interpretation of their results.

9.4

Fill-Fraction Estimation Techniques

If we know the EMs s_k , unmixing can be viewed either as a linear estimation problem or as a linear model fitting problem. Given the observed spectrum \mathbf{x} and the EMs s_k , the problem is to determine the fill-fractions, a_k , subject to the model and constraints. The solution of this problem depends on what information is available and what assumptions we make about the model.

9.4.1

Deterministic Endmembers

The key assumption of this model is that the major spectral variability in the observed data is due to variations in the values of a_k from pixel to pixel. The model explicitly assumes that the spectral signatures of the EMs are *constant*, that is, deterministic quantities. When we have chosen the EMs “correctly” the value of the residuals should be small. Thus, we typically estimate the fill-fractions for each pixel by minimizing the weighted residual sum-of-squares

$$S(\mathbf{a}) = \left(\mathbf{x} - \sum_{k=1}^m a_k \mathbf{s}_k \right)^T \Psi \left(\mathbf{x} - \sum_{k=1}^m a_k \mathbf{s}_k \right), \quad (9.8)$$

subject to the nonnegativity and sum-to-one constraints. The positive definite weighting matrix Ψ is used to account for correlation in the residuals. Various techniques may be used to solve this constrained minimization problem (Gill et al., 1981). If the nonnegativity constraint (9.3) is removed, the solution is easily obtained using the method of least squares (Golub and Van Loan, 1996).

9.4.2

Stochastic Endmembers

In this case, we assume that the EMs exhibit spectral variability. It is known from experience that within a given class of materials and spectra there can be considerable natural variability (Somers et al., 2011). The key assumption for the widely discussed *stochastic mixing model (SMM)* is that the spectral signatures of EMs are realizations of mutually uncorrelated normal random vectors distributed as $\mathbf{s}_k \sim N_p(\mathbf{m}_k, \mathbf{C}_k)$ (Stocker and Schaum, 1997). The mean and covariance of the spectrum generated by the LMM (9.1) with $\mathbf{e} = \mathbf{0}$ (perfect model) are

$$\mathbf{m}_a = \sum_{k=1}^m a_k \mathbf{m}_k \quad \text{and} \quad \mathbf{C}_a = \sum_{k=1}^m a_k^2 \mathbf{C}_k. \quad (9.9)$$

The practical use of SMMs is limited because the estimation of their parameters leads to highly nonlinear optimization problems and the interpretation of their results is difficult. We also note that the SMM requires training data sets for each EM to estimate the required means and covariances. To bypass these obstacles, the first SMM, introduced by Horwitz et al. (1975) for multispectral data, postulates that

$$\mathbf{C}_a = \sum_{k=1}^m a_k \mathbf{C}_k. \quad (9.10)$$

The likelihood function based on (9.10) and the constraints (9.2) and 9.3), is still not convex and its maximization, to determine a_k , is a difficult problem. However, if we assume that $\mathbf{C}_k = \mathbf{C}$, for all k , we obtain that $\mathbf{C}_a = \mathbf{C}$. Since \mathbf{C}_a is no longer a function of a_k , maximizing the likelihood is equivalent to minimizing the quantity

$$S(\mathbf{a}) = \left(\mathbf{x} - \sum_{k=1}^m a_k \mathbf{m}_k \right)^T \mathbf{C}^{-1} \left(\mathbf{x} - \sum_{k=1}^m a_k \mathbf{m}_k \right) \quad (9.11)$$

subject to the nonnegativity and sum-to-one constraints.

A comparison of the expressions for $S(\mathbf{a})$ in (9.8) and (9.11) shows that if we set $s_k = \mathbf{m}_k$ and $\Psi = \mathbf{C}^{-1}$, the two models become mathematically identical. For this reason we focus on the LMM (9.1) and the criterion (9.8) with $\Psi = \sigma^2 \mathbf{I}$ (classical least squares) or $\Psi = \sigma^2 \mathbf{C}$ (generalized least squares). Since this is essentially a linear estimation problem, many well-established techniques are available for its solution (Draper and Smith, 1998).

9.4.3

Significance and Impact of Constraints in Practice

Given a set of EMs, estimation of pixel fill-fractions requires the solution of an overdetermined set of linear equations without or with constraints (Settle and Drake, 1993). In Section 9.5 we discuss the solution of the overdetermined system using the method of least squares without any constraints or by imposing the sum-to-one constraint. The inclusion of the nonnegativity constraints requires the use of more complicated nonlinear optimization techniques (Boyd and Vandenberghe, 2004). A major disadvantage caused by the enforcement of convexity constraints is that we always obtain “feasible” solutions whether or not the specified EMs are correct. Therefore, the possibility that the model may be wrong is completely hidden from the analyst.

9.5

The Method of Least Squares Estimation

Suppose we know the mixed spectrum \mathbf{x} and the EMs s_k in (9.1) and we wish to estimate the abundance coefficient vector \mathbf{a} . Although we do not observe the error vector, we can calculate the value implied by any hypothetical value of \mathbf{a} , as

$$\mathbf{e} = \mathbf{x} - \mathbf{S}\mathbf{a}. \quad (9.12)$$

The components of this vector provide a measure of the deviation between the actual spectrum and the spectrum predicted by the hypothetical value of \mathbf{a} . The sum of the squares of these deviations is

$$S(\mathbf{a}) = \sum_{k=1}^p e_k^2 = (\mathbf{x} - \mathbf{S}\mathbf{a})^T (\mathbf{x} - \mathbf{S}\mathbf{a}). \quad (9.13)$$

The method of least squares (LS) selects, as the best estimate of \mathbf{a} , the value that makes $S(\mathbf{a})$ as small as possible. We next present two different, but equivalent, ways to obtain the least squares estimate.

9.5.1 Geometric approach

If we consider the Euclidean space of p dimensions, denoted by \mathbb{R}^p , we may think of the spectrum vector \mathbf{x} as defining a point from the origin to the point with coordinates x_1, x_2, \dots, x_p . The matrix \mathbf{S} consists of m column vectors $\mathbf{s}_1, \mathbf{s}_2, \dots, \mathbf{s}_m$. Each of these $p \times 1$ vectors defines a vector from the origin to a point in \mathbb{R}^p . Any linear estimate of \mathbf{x} , based on $\mathbf{s}_1, \mathbf{s}_2, \dots, \mathbf{s}_m$, is expressed as a linear combination

$$\hat{\mathbf{x}} = \sum_{k=1}^q a_k \mathbf{s}_k = \mathbf{S}\mathbf{a}. \quad (9.14)$$

Therefore, the m vectors $\mathbf{s}_1, \mathbf{s}_2, \dots, \mathbf{s}_m$ form an m -dimensional subspace $\langle \mathbf{S} \rangle$ of \mathbb{R}^p , called the *estimation space*. These concepts are illustrated in Figure 9.9 for $p = 3$ and $m = 2$. Every estimate $\hat{\mathbf{x}}$ can be represented by a point in this subspace by (9.14). We note that, whereas the vectors \mathbf{s}_k determine the entire estimation subspace, the values of the parameters a_k determine the tip of a specific estimation vector $\hat{\mathbf{x}}$. Let the vectors \mathbf{x} and $\hat{\mathbf{x}}$ determine the points B and A in Figure 9.9. The distance from B to A is equal to the length of the error vector $\mathbf{e} = \mathbf{x} - \hat{\mathbf{x}}$. Thus, the sum of squared errors equals the squared Euclidean length of the error vector, that is,

$$S(\mathbf{a}) = \sum_{k=1}^p e_k^2 = \|\mathbf{e}\|^2 = \|\mathbf{x} - \hat{\mathbf{x}}\|^2. \quad (9.15)$$

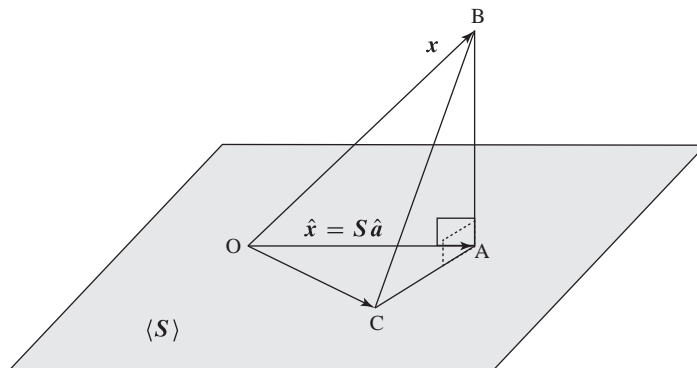


Figure 9.9 Illustration of least squares geometry.

Minimizing this squared distance requires finding the point A in the estimation space that is closest to B. This point is the foot of the line from B normal (or perpendicular) to the estimation space. This means that the error vector $\mathbf{e} = \mathbf{x} - \mathbf{S}\hat{\mathbf{a}}$ must be orthogonal to all vectors \mathbf{s} in $\langle \mathbf{S} \rangle$, denoted as $\mathbf{e} \perp \langle \mathbf{S} \rangle$. Since two vectors in \mathbb{R}^p are orthogonal if $\mathbf{a}^T \mathbf{b} = 0$, the condition $\mathbf{e} \perp \langle \mathbf{S} \rangle$ is equivalent to $\mathbf{s}_i^T (\mathbf{x} - \hat{\mathbf{x}}) = 0$ for $i = 1, 2, \dots, p$. Hence, the error vector corresponding to the LS estimate $\hat{\mathbf{x}}$ must be orthogonal to the columns of matrix \mathbf{S} ; that is,

$$\mathbf{S}^T (\mathbf{x} - \hat{\mathbf{x}}) = \mathbf{0}, \quad (9.16)$$

which is known as the *orthogonality principle*. Here $\hat{\mathbf{x}}$ is uniquely determined, being the *unique* orthogonal projection of \mathbf{x} onto $\langle \mathbf{S} \rangle$. Assuming that the columns of \mathbf{S} are linearly independent, there exists a unique parameter vector $\hat{\mathbf{a}}$ such that $\hat{\mathbf{x}} = \mathbf{S}\hat{\mathbf{a}}$. Therefore, substituting in (9.16) we have

$$\mathbf{S}^T \mathbf{S} \hat{\mathbf{a}} = \mathbf{S}^T \mathbf{x}, \quad (9.17)$$

which is a set of m linear equations known as *normal equations* because $\hat{\mathbf{e}}$ is *normal* to $\langle \mathbf{S} \rangle$. Furthermore, (9.17) has a unique solution, given formally by

$$\hat{\mathbf{a}} = (\mathbf{S}^T \mathbf{S})^{-1} \mathbf{S}^T \mathbf{x}. \quad (9.18)$$

Equation (9.18) simply means that we compute $\hat{\mathbf{a}}$ by solving the normal equations (9.17). The normal equations can be solved using any technique for the solution of linear systems of equations. It should be emphasized that we never compute the inverse matrix $(\mathbf{S}^T \mathbf{S})^{-1}$ to determine $\hat{\mathbf{a}}$.

The difference between the observed value x_k and the corresponding *fitted* or *estimated* value \hat{x}_k is the *residual* $\hat{e}_k \triangleq x_k - \hat{x}_k$. The p residuals can be compactly written in matrix notation as

$$\hat{\mathbf{e}} \triangleq \mathbf{x} - \hat{\mathbf{x}} = \mathbf{x} - \mathbf{S}\hat{\mathbf{a}}. \quad (9.19)$$

To determine the minimum residual sum of squares, $S(\hat{\mathbf{a}})$, we apply the Pythagorean theorem to the right-angled triangle OBA in Figure 9.9. This yields

$$S(\hat{\mathbf{a}}) = \|\hat{\mathbf{e}}\|^2 = \|\mathbf{x}\|^2 - \|\hat{\mathbf{x}}\|^2. \quad (9.20)$$

The observation vector $\mathbf{x} = \hat{\mathbf{x}} + \hat{\mathbf{e}}$ is thus divided into two components: (a) the estimate $\hat{\mathbf{x}}$, which lies entirely in the estimation space, and (b) the residual $\hat{\mathbf{e}}$, which lies in what is called the *residual space*. The residual space is defined as the $(p - m)$ -dimensional subspace of the observation space that is orthogonal to the estimation subspace.

For the solution of (9.17) to exist, the matrix $\mathbf{S}^T \mathbf{S}$ must be invertible. Conditions for invertibility are provided by the following result: *The matrix $\mathbf{S}^T \mathbf{S}$ is positive definite and hence invertible if and only if the columns of \mathbf{S} are linearly independent, that is, when \mathbf{S} has full rank q .* To prove this result we note that if the columns of \mathbf{S} are linearly independent, then for every $\mathbf{a} \neq \mathbf{0}$ we have $\mathbf{S}\mathbf{a} \neq \mathbf{0}$. This implies that $\mathbf{a}^T (\mathbf{S}^T \mathbf{S})\mathbf{a} = (\mathbf{S}\mathbf{a})^T (\mathbf{S}\mathbf{a}) = \|\mathbf{S}\mathbf{a}\|^2 > 0$; that is, $\mathbf{S}^T \mathbf{S}$ is positive definite and hence non-singular. Conversely, if the columns of \mathbf{S} are linearly dependent, then there is a vector $\mathbf{a}_0 \neq \mathbf{0}$ such that $\mathbf{S}\mathbf{a}_0 = \mathbf{0}$. Hence, $(\mathbf{S}^T \mathbf{S})\mathbf{a}_0 = \mathbf{0}$, which implies that $\mathbf{S}^T \mathbf{S}$ is singular.

If the columns of S are not linearly independent, S does not have full rank. In this case, it is sometimes incorrectly believed that the LS problem has no solution. However, from Figure 9.9, we can see that there is always a LS solution, because we can always drop a perpendicular onto the estimation space at A. Since the point A is unique, the LS estimate \hat{x} and the LS residual $\hat{e} = x - \hat{x}$ are, as always, unique. What is not unique is the description of \hat{x} in terms of s_1, s_2, \dots, s_m , that is, the parameter vector \hat{a} . Consider for example a matrix S consisting of three coplanar vectors. We can easily see that there is an infinite number of ways to express \hat{x} as a linear combination of these linearly depended vectors. The normal equations always exist and can be solved, but the solution for the parameter estimates is not unique and may be difficult to find (see Section 9.6).

9.5.2 Orthogonal Projection Matrices

The least squares estimate \hat{x} is determined geometrically by the foot of the perpendicular from x to the estimation space specified by the columns of S . When the columns of S are linearly independent, that is, S is full rank, \hat{x} is given by

$$\hat{x} = S\hat{a} = S(S^T S)^{-1} S^T x. \quad (9.21)$$

We note that the matrix

$$P_S \triangleq S(S^T S)^{-1} S^T \quad (9.22)$$

computes the orthogonal projection of x onto the column space of S and is known as an *orthogonal projection matrix*. The matrix P_S is not invertible because there are many vectors x which have the same projection onto the estimation space. It can be easily shown that matrix P_S has the following properties

$$P_S^2 = P_S \quad (\text{Idempotent}) \quad (9.23)$$

$$P_S^T = P_S \quad (\text{Symmetric}). \quad (9.24)$$

In general, any square idempotent and symmetric matrix is an orthogonal projection matrix; however, if P_S is idempotent but not symmetric, it is an *oblique* projection matrix (Vasilevsky, 1983). Using the projection matrix (9.22), the LS estimate and its residual can be written as

$$\hat{x} = P_S x \quad (9.25)$$

$$\hat{e} = x - \hat{x} = P_S^\perp x, \quad (9.26)$$

where P_S^\perp is an orthogonal projection matrix defined by

$$P_S^\perp \triangleq I - P_S. \quad (9.27)$$

The sum of LS residual errors can be written as

$$S(\hat{a}) = \|\hat{e}\|^2 = \|P_S^\perp x\|^2 = x^T P_S^\perp x, \quad (9.28)$$

because P_S^\perp is idempotent. The space in which $\hat{e} = x - \hat{x}$ lies is called the *error space*, and it has $(p - m)$ dimensions. The estimation space (m dimensions) and the error space

($p-m$ dimensions) together constitute the data space \mathbb{R}^p . Hence, least squares estimation splits up the data space into two orthogonal subspaces; every vector in the estimation space is orthogonal to every vector in the error space.

9.5.3 Least Squares Goodness of Fit Metrics

A key issue in LS estimation is to quantify how well the adopted model fits the data. The quality of fit is typically assessed using two related quantities: the residual sum of squares and the multiple correlation coefficient.

The residual sum of squares (RSS), which is defined by

$$\text{RSS} = \sum_{i=1}^p (x_i - \hat{x}_i)^2 = \|\mathbf{x} - \hat{\mathbf{x}}\|^2, \quad (9.29)$$

measures the lack of fit or how well the model $\hat{\mathbf{x}} = \mathbf{S}\hat{\mathbf{a}}$ predicts the data \mathbf{x} . The best model yields $\text{RSS} = 0$ and the worst model yields $\text{RSS} = \|\mathbf{x}\|^2$. From the geometrical construction in Figure 9.10 we have $\text{RSS} = (\mathbf{BA})^2$. From the orthogonal triangle OAB and the Pythagorean theorem, we obtain

$$\text{TSS} = \text{MSS} + \text{RSS}, \quad (9.30)$$

where TSS is the total sum of squares

$$\text{TSS} = \sum_{i=1}^p x_i^2 = \|\mathbf{x}\|^2, \quad (9.31)$$

and MSS is the total sum of squares of the model predictions

$$\text{MSS} = \sum_{i=1}^p \hat{x}_i^2 = \|\hat{\mathbf{x}}\|^2. \quad (9.32)$$

The RSS provides an absolute measure of lack of fit of the model to the data. Since RSS is measured in the units of x_i , it is not clear what value of RSS provides a good fit. To avoid this problem we consider the ratio

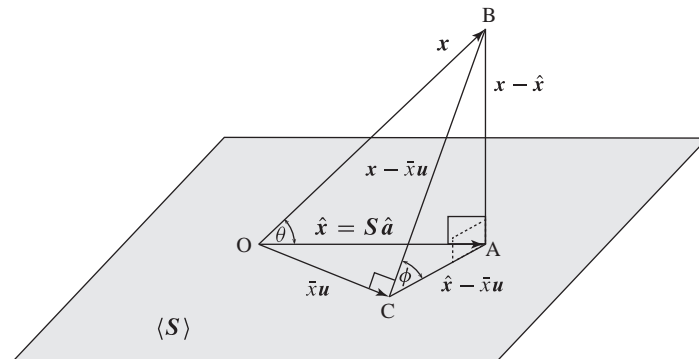


Figure 9.10 Geometrical illustration of LS goodness of fit metrics.

$$R^2 \triangleq \frac{\|\hat{\mathbf{x}}\|^2}{\|\mathbf{x}\|^2} = \frac{\text{MSS}}{\text{TSS}} = 1 - \frac{\text{RSS}}{\text{TSS}}, \quad (9.33)$$

which is bounded by $0 \leq R^2 \leq 1$. From the right triangle OAB we have

$$R = \cos \theta = \frac{\mathbf{x}^T \hat{\mathbf{x}}}{\|\mathbf{x}\| \|\hat{\mathbf{x}}\|} = \frac{\sum_{i=1}^p x_i \hat{x}_i}{\sqrt{\sum_{i=1}^p x_i^2} \sqrt{\sum_{i=1}^p \hat{x}_i^2}}, \quad (9.34)$$

which shows that R measures the correlation between the actual and predicted data.

However, from a statistical perspective, what is significant is the variability of the data about their mean value

$$\bar{x} \triangleq \frac{1}{p} \sum_{i=1}^p x_i = \frac{1}{p} \mathbf{u}^T \mathbf{x}, \quad (9.35)$$

where \mathbf{u} is a $p \times 1$ vector with unit components. This variability, which is proportional to the variance of the data, is measured by the centered TSS, defined by

$$\text{TSS}_c \triangleq \sum_{i=1}^p (x_i - \bar{x})^2 = \|\mathbf{x} - \bar{x}\mathbf{u}\|^2. \quad (9.36)$$

We can easily show that the vectors $(\mathbf{x} - \bar{x}\mathbf{u})$ and \mathbf{u} are orthogonal. Therefore, the algebraic orthogonal projection of \mathbf{x} onto \mathbf{u} is its average value \bar{x} . Since the triangle OCA is orthogonal, the projection of $\hat{\mathbf{x}}$ onto \mathbf{u} is its average value, which implies that $\bar{\hat{x}} = \bar{x}$. Therefore, we define the centered MSS by

$$\text{MSS}_c \triangleq \sum_{i=1}^p (\hat{x}_i - \bar{\hat{x}})^2 = \sum_{i=1}^p (\hat{x}_i - \bar{x})^2 = \|\hat{\mathbf{x}} - \bar{x}\mathbf{u}\|^2. \quad (9.37)$$

From Figure 9.10 we note that the RSS does *not* change. These results lead to the definition of the well-known *multiple correlation coefficient*

$$R_c^2 \triangleq \frac{\text{MSS}_c}{\text{RSS}} = \frac{\left[\sum_{i=1}^p (x_i - \bar{x})(\hat{x}_i - \bar{x}) \right]^2}{\sum_{i=1}^p (x_i - \bar{x})^2 \sum_{i=1}^p (\hat{x}_i - \bar{x})^2} = \cos^2 \phi. \quad (9.38)$$

We note that for centered, that is, zero-mean data, we have that $R = R_c$. Unless otherwise stated we assume centered data for the rest of this chapter.

In general, given two $p \times 1$ vectors \mathbf{x} and \mathbf{y} , the cosine of the angle formed by the two vectors

$$\cos \theta = \frac{\mathbf{x}^T \mathbf{y}}{\|\mathbf{x}\| \|\mathbf{y}\|}, \quad (9.39)$$

measures the similarity of their shapes. In contrast, the angle between the zero-centered vectors $\mathbf{x}_0 = \mathbf{x} - \bar{x}\mathbf{u}$ and $\mathbf{y}_0 = \mathbf{y} - \bar{y}\mathbf{u}$, defined by

$$\cos \theta_0 = \frac{\mathbf{x}_0^T \mathbf{y}_0}{\|\mathbf{x}_0\| \|\mathbf{y}_0\|} = \frac{(\mathbf{x} - \bar{x}\mathbf{u})^T (\mathbf{y} - \bar{y}\mathbf{u})}{\|\mathbf{x} - \bar{x}\mathbf{u}\| \|\mathbf{y} - \bar{y}\mathbf{u}\|}, \quad (9.40)$$

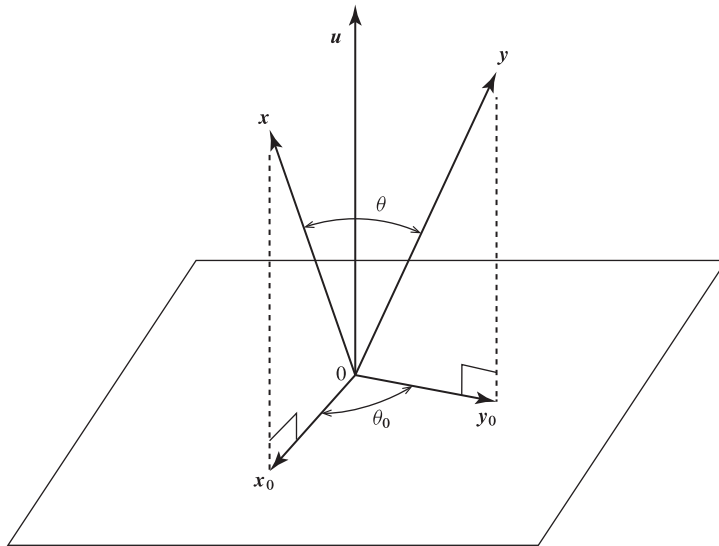


Figure 9.11 Geometrical interpretation of angles between two vector spectra and their mean-removed versions, which are orthogonal projections onto the hyperplane perpendicular to the diagonal vector u .

measures the similarity of the shapes of their projections onto the hyperplane perpendicular to the diagonal vector u . The geometrical interpretation of the two spectral angles is shown in Figure 9.11.

9.5.4 Algebraic approach

To determine the LS estimate, using standard optimization techniques, we first expand (9.13) as follows:

$$\begin{aligned} S(\mathbf{a}) &= (\mathbf{x} - S\mathbf{a})^T(\mathbf{x} - S\mathbf{a}) \\ &= \mathbf{x}^T\mathbf{x} - \mathbf{a}^T S^T \mathbf{x} - \mathbf{x}^T S \mathbf{a} + \mathbf{a}^T S^T S \mathbf{a} \\ &= \mathbf{x}^T\mathbf{x} - 2\mathbf{a}^T S^T \mathbf{x} + \mathbf{a}^T S^T S \mathbf{a}. \end{aligned} \quad (9.41)$$

The last equation follows because the scalar expression $\mathbf{a}^T S^T \mathbf{x}$ equals its transpose $\mathbf{x}^T S \mathbf{a}$.

To determine the conditions on the estimate $\hat{\mathbf{a}}$ that minimizes $S(\mathbf{a})$, we differentiate $S(\mathbf{a})$ with respect to \mathbf{a} and equate the result to zero. The result is

$$\frac{\partial S(\mathbf{a})}{\partial \mathbf{a}} = -2S^T \mathbf{x} + 2S^T S \hat{\mathbf{a}} = \mathbf{0}, \quad (9.42)$$

which leads to the normal equations (9.17). However, this is only a necessary condition for the minimization of (9.41). Therefore, we need to check whether the parameters $\hat{\mathbf{a}}$ specified by the normal equations achieve the minimum, not the maximum. If we substitute (9.18) into (9.41), we obtain

$$S(\hat{\mathbf{a}}) = \mathbf{x}^T\mathbf{x} - \mathbf{x}^T S (S^T S)^{-1} S^T \mathbf{x}. \quad (9.43)$$

To show that this is a minimum and not a maximum, we evaluate (9.41) at $\hat{\mathbf{a}} + \boldsymbol{\delta}$. Indeed, using (9.41), (9.18), and (9.43), we obtain

$$S(\hat{\mathbf{a}} + \boldsymbol{\delta}) = S(\hat{\mathbf{a}}) + \boldsymbol{\delta}^T (\mathbf{S}^T \mathbf{S}) \boldsymbol{\delta}. \quad (9.44)$$

If the matrix $\mathbf{S}^T \mathbf{S}$ is positive definite, $\boldsymbol{\delta}^T (\mathbf{S}^T \mathbf{S}) \boldsymbol{\delta} > 0$ for all $\boldsymbol{\delta} \neq \mathbf{0}$. Therefore, the solution $\hat{\mathbf{a}}$ of the normal equations yields the LS estimate if and only if $\mathbf{S}^T \mathbf{S}$ is positive definite. A geometric interpretation of this result is given in Figure 9.9, where we note that choosing any point C different than A increases the error.

9.5.5 Data matrices with orthogonal columns

If the columns of matrix \mathbf{S} are orthogonal, that is, $s_i^T s_j = 0$ for all $i \neq j$, the matrix $\mathbf{S}^T \mathbf{S}$ becomes diagonal and the solution of the least squares problem is highly simplified. Indeed, we can easily show that

$$\hat{a}_k = s_k^T \mathbf{x} / s_k^T s_k, \quad k = 1, 2, \dots, q \quad (9.45)$$

$$S(\hat{\mathbf{a}}) = \mathbf{x}^T \mathbf{x} - \sum_{k=1}^m \frac{(s_k^T \mathbf{x})^2}{s_k^T s_k}. \quad (9.46)$$

Therefore, when the columns of \mathbf{S} are orthogonal, (1) the components of $\hat{\mathbf{a}}$ can be obtained independently of each other, (2) the solution of the m th-order least squares problem is reduced to the solution of m first-order least squares problems, and (3) the inclusion of s_k in the model reduces $S(\hat{\mathbf{a}})$ by $(s_k^T \mathbf{x})^2 / s_k^T s_k$ whether or not the other parameters are in the model.

Similarly, if \mathbf{S} has orthogonal columns, the matrix $\mathbf{S}^T \mathbf{S}$ is diagonal, and the projection matrix is simplified to a sum of one-dimensional projection matrices

$$\mathbf{P}_S = \mathbf{S}(\mathbf{S}^T \mathbf{S})^{-1} \mathbf{S}^T = \sum_{k=1}^m s_k (s_k^T s_k)^{-1} s_k^T. \quad (9.47)$$

Thus, the least squares estimate can be expressed as

$$\hat{\mathbf{x}} = \mathbf{P}_S \mathbf{x} = \sum_{k=1}^m \frac{s_k^T \mathbf{x}}{s_k^T s_k} s_k. \quad (9.48)$$

The quantity $(s_k^T \mathbf{x} / s_k^T s_k) s_k$ is the one-dimensional projection of \mathbf{x} onto the s_k axis. Therefore, the projections of \mathbf{x} onto the axes are uncoupled and their sum provides the least squares estimate $\hat{\mathbf{x}}$. The orthogonality of s_k s allows the use of the Pythagorean theorem to obtain the expression for $S(\hat{\mathbf{a}})$ in (9.46).

If the columns of \mathbf{S} are not orthogonal, we can solve the LS problem by orthogonalizing them. Indeed, more stable algorithms than direct solution of (9.17) are based on decomposing \mathbf{S} into the product of an orthogonal matrix and an easily inverted matrix. In general, consider a linear transformation (or equivalently a change of basis) defined by an invertible matrix \mathbf{T} . The matrix \mathbf{S} in the new coordinates is $\mathbf{Z} = \mathbf{S}\mathbf{T}$, which leads to a new coefficient vector $\hat{\mathbf{a}}_z = (\mathbf{Z}^T \mathbf{Z})^{-1} \mathbf{Z}^T \mathbf{x}$ for the least squares estimator. It can be easily shown that the least squares estimate is $\hat{\mathbf{x}}_z = \mathbf{Z}\hat{\mathbf{a}}_z = \hat{\mathbf{x}}$. Therefore, an invertible

transformation of the data matrix changes the coordinates of $\hat{\mathbf{a}}$ but not the least squares estimate $\hat{\mathbf{x}}$. The matrix \mathbf{T} is chosen to simplify the solution of the LS problem.

9.5.6

Linearly Constrained Least Squares Estimation

If we enforce the sum-to-one constraint, we still have to solve a linear optimization problem. To address future needs, with a slight increase in complexity, we consider a more general set of linear constraints defined by

$$\mathbf{G}\mathbf{a} = \mathbf{g}, \quad (9.49)$$

where \mathbf{G} is a known $r \times m$ matrix with full rank and \mathbf{g} is a known $r \times 1$ vector. For the sum-to-one constraint we set $\mathbf{G} = \mathbf{u}^T$ and $\mathbf{g} = 1$. Using the method of Lagrange multipliers (Seber, 1977) we can show that the least squares estimate of \mathbf{a} subject to the linear constraints (9.49) is given by

$$\hat{\mathbf{a}}_c = \hat{\mathbf{a}} - (\mathbf{S}^T \mathbf{S})^{-1} \mathbf{G}^T [\mathbf{G}(\mathbf{S}^T \mathbf{S})^{-1} \mathbf{G}^T]^{-1} (\mathbf{G}\hat{\mathbf{a}} - \mathbf{g}), \quad (9.50)$$

where $\hat{\mathbf{a}}$ is the unconstrained least squares estimate (9.18). To obtain a geometrical interpretation of $\hat{\mathbf{a}}_c$ we note that $\langle \mathbf{S}_G \rangle = \{\mathbf{S}\mathbf{a} : \mathbf{a} \in \mathbb{R}^m, \mathbf{G}\mathbf{a} = \mathbf{g}\}$ is a linear subspace of $\langle \mathbf{S} \rangle$. Since $\langle \mathbf{S}_G \rangle$ is formed from $\langle \mathbf{S} \rangle$ by imposing r constraints $\mathbf{G}\mathbf{a} = \mathbf{g}$, $\langle \mathbf{S}_G \rangle$ is of $(m - r)$ dimensions. For example, if $p = 3$ and $m = 2$, and we impose the constraint $s_1 = s_2$, the constrained subspace $\langle \mathbf{S}_G \rangle$ is the line $s_1 = s_2$. The estimator $\hat{\mathbf{a}}_c$ is the vector such that $\hat{\mathbf{x}}_c = \mathbf{S}\hat{\mathbf{a}}_c$ is the orthogonal projection of \mathbf{x} on the space $\langle \mathbf{S}_G \rangle$. This geometric interpretation is illustrated in Figure 9.12.

Let $\hat{\mathbf{x}} = \mathbf{S}\hat{\mathbf{a}}$ be the projection of \mathbf{x} on $\langle \mathbf{S} \rangle$ and $\hat{\mathbf{x}}_c = \mathbf{S}\hat{\mathbf{a}}_c$ be the projection of \mathbf{x} on $\langle \mathbf{S}_G \rangle$. Note that $\hat{\mathbf{x}} - \hat{\mathbf{x}}_c = \mathbf{S}(\hat{\mathbf{a}} - \hat{\mathbf{a}}_c)$ lies in $\langle \mathbf{S} \rangle$ and that $\mathbf{x} - \hat{\mathbf{x}}$ is orthogonal to $\langle \mathbf{S}_G \rangle$. Therefore, $\mathbf{x} - \mathbf{S}\hat{\mathbf{a}}$ is orthogonal to $\mathbf{S}(\hat{\mathbf{a}} - \hat{\mathbf{a}}_c)$, which implies

$$\|\mathbf{x} - \mathbf{S}\hat{\mathbf{a}}_c\|^2 = \|\mathbf{x} - \mathbf{S}\hat{\mathbf{a}}\|^2 + \|\mathbf{S}(\hat{\mathbf{a}} - \hat{\mathbf{a}}_c)\|^2, \quad (9.51)$$

according to the Pythagorean theorem. Equivalently, we have

$$\mathbf{S}(\hat{\mathbf{a}}_c) = \mathbf{S}(\hat{\mathbf{a}}) + \|\mathbf{S}(\hat{\mathbf{a}} - \hat{\mathbf{a}}_c)\|^2 \geq \mathbf{S}(\hat{\mathbf{a}}). \quad (9.52)$$

Thus, the residual sum of squares is increased by enforcing the constraints. This is intuitively obvious since $\hat{\mathbf{a}}$ minimizes $\mathbf{S}(\mathbf{a})$ and hence $\hat{\mathbf{a}}_c$ cannot do any better.

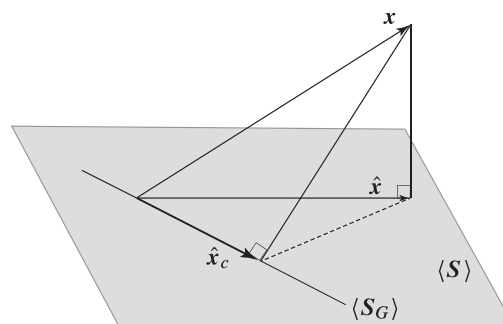


Figure 9.12 Geometrical illustration of constrained least squares estimation.

Now if the coefficients \mathbf{a} of the LMM (9.1) satisfy the constraints $\mathbf{G}\mathbf{a} = \mathbf{g}$, then $\hat{\mathbf{x}}$ should be close to $\hat{\mathbf{x}}_c$ (for an exact model $\hat{\mathbf{x}} = \hat{\mathbf{x}}_c$) and, from (9.51), the distance $\|\mathbf{x} - \hat{\mathbf{S}}\hat{\mathbf{a}}_c\|$ should be close to the distance $\|\mathbf{x} - \hat{\mathbf{S}}\hat{\mathbf{a}}\|$. On the other hand, if \mathbf{a} does not satisfy $\mathbf{G}\mathbf{a} = \mathbf{g}$ then the distance $\|\mathbf{x} - \hat{\mathbf{S}}\hat{\mathbf{a}}_c\|$ tends to be substantially larger than the distance $\|\mathbf{x} - \hat{\mathbf{S}}\hat{\mathbf{a}}\|$ (see Figure 9.12). This intuition is behind the statistical tests used to evaluate the adequacy of linear mixing models.

9.6 Least Squares Computations

The LS problem can be solved using the normal equations, the QR decomposition, or the singular value decomposition (SVD) methods. In terms of speed, solving the normal equations via Cholesky decomposition is faster than QR, which is faster than SVD. If \mathbf{S} is quite well-conditioned, then Cholesky decomposition is as accurate as the other methods. When \mathbf{S} is not well-conditioned but far from rank deficient we should use the QR decomposition. SVD is the slowest and most reliable method for solving *any* least squares problem.

9.6.1 Using the Normal Equations

We saw in Section 9.5.1 that when \mathbf{S} has full rank, $\boldsymbol{\Gamma} \triangleq \mathbf{S}^T \mathbf{S}$ is a square, symmetric, and positive definite matrix. Then, we can solve the normal equations using the Cholesky decomposition (Watkins, 2002),

$$\boldsymbol{\Gamma} = \mathbf{R}^T \mathbf{R}, \quad (9.53)$$

where \mathbf{R} is an upper triangular matrix with positive diagonal elements. The normal equations can then be written as $\mathbf{R}^T(\mathbf{R}\hat{\mathbf{a}}) = \mathbf{S}^T \mathbf{x}$, which is equivalent to the triangular systems

$$\mathbf{R}^T \mathbf{k} = \boldsymbol{\gamma} \quad (9.54)$$

$$\mathbf{R}\hat{\mathbf{a}} = \mathbf{k}, \quad (9.55)$$

where $\boldsymbol{\gamma} = \mathbf{S}^T \mathbf{x}$. We solve the first system for \mathbf{k} and then the second system for $\hat{\mathbf{a}}$. The least squares estimate $\hat{\mathbf{x}}$ and the minimum SSE can be computed by

$$\hat{\mathbf{x}} = \mathbf{S}\hat{\mathbf{a}} = \mathbf{S}\mathbf{R}^{-1}\mathbf{k} \quad (9.56)$$

$$S(\hat{\mathbf{a}}) = \|\mathbf{x}\|^2 - \|\hat{\mathbf{x}}\|^2 = \|\mathbf{x}\|^2 - \|\mathbf{k}\|^2. \quad (9.57)$$

The elements γ_{ij} of $\boldsymbol{\Gamma}$ can be formed by computing the inner products $\gamma_{ij} = \mathbf{s}_i^T \mathbf{s}_j$; however, because of symmetry, we need only form the upper (or lower) part of $\boldsymbol{\Gamma}$.

9.6.2 Using the QR Decomposition

Every $p \times m$ ($p \geq m$) matrix \mathbf{S} has a full QR decomposition given by (Watkins, 2002)

$$\mathbf{S} = \mathbf{Q} \begin{bmatrix} \mathbf{R} \\ \mathbf{0} \end{bmatrix} = [\mathbf{Q}_0 \quad \mathbf{Q}_\perp] \begin{bmatrix} \mathbf{R} \\ \mathbf{0} \end{bmatrix} = \mathbf{Q}_0 \mathbf{R}, \quad (9.58)$$

where \mathbf{Q} is an $p \times p$ orthogonal matrix ($\mathbf{Q}^T \mathbf{Q} = \mathbf{Q} \mathbf{Q}^T = \mathbf{I}$) and \mathbf{R} is a $m \times m$ matrix with zeros below the main diagonal. The matrix \mathbf{Q}_0 contains the first m columns of \mathbf{Q} and \mathbf{Q}_\perp contains the last $(p - m)$ columns of \mathbf{Q} . The columns of \mathbf{Q}_0 provide an orthonormal basis for \mathbf{S} and the columns of \mathbf{Q}_\perp provide an orthonormal basis for the orthogonal complement of \mathbf{S} ; hence, $\mathbf{S}^T \mathbf{Q}_\perp = \mathbf{0}$. The QR decomposition is usually computed using the Householder or Givens transformations (Watkins, 2002).

Since orthogonal transformations preserve the length of a vector, we have

$$S(\mathbf{a}) = \|\mathbf{x} - \mathbf{S}\mathbf{a}\|^2 = \|\mathbf{Q}^T(\mathbf{x} - \mathbf{S}\mathbf{a})\|^2 = \left\| \mathbf{z} - \begin{bmatrix} \mathbf{R}\mathbf{a} \\ \mathbf{0} \end{bmatrix} \right\|^2, \quad (9.59)$$

where \mathbf{z} is a rotated observation vector defined by the orthogonal transformation

$$\mathbf{z} \triangleq \mathbf{Q}^T \mathbf{x} = \begin{bmatrix} \mathbf{Q}_0^T \mathbf{x} \\ \mathbf{Q}_\perp^T \mathbf{x} \end{bmatrix} \triangleq \begin{bmatrix} \mathbf{z}_0 \\ \mathbf{z}_\perp \end{bmatrix}. \quad (9.60)$$

Essentially, the rotation $\mathbf{z} = \mathbf{Q}^T \mathbf{x}$ aligns the first m orthogonal axes with the estimation subspace and the last $(p - m)$ axes with the error subspace. Using the partitioning (9.60), the sum of squared errors (9.59) can be written as

$$S(\mathbf{a}) = \|\mathbf{z}_0 - \mathbf{R}\mathbf{a}\|^2 + \|\mathbf{z}_\perp\|^2. \quad (9.61)$$

Because $\|\mathbf{z}_\perp\|$ is independent of \mathbf{a} , it follows that $\|\mathbf{x} - \mathbf{S}\mathbf{a}\|^2$ is minimal if and only if $\|\mathbf{z}_0 - \mathbf{R}\mathbf{a}\| = 0$. Thus, we have

$$\mathbf{R}\hat{\mathbf{a}} = \mathbf{z}_0 \quad (9.62)$$

$$S(\hat{\mathbf{a}}) = \|\mathbf{z}_\perp\|^2. \quad (9.63)$$

We usually solve the upper triangular system (9.62) for $\hat{\mathbf{a}}$ by back substitution. The QR decomposition (9.58) can be used for reliable computation of the projection matrices using the easily derived formulas

$$\mathbf{P}_S = \mathbf{S}(\mathbf{S}^T \mathbf{S})^{-1} \mathbf{S}^T = \mathbf{Q}_0 \mathbf{Q}_0^T \quad (9.64)$$

$$\mathbf{P}_S^\perp = \mathbf{I} - \mathbf{P}_S = \mathbf{I} - \mathbf{Q}_0 \mathbf{Q}_0^T = \mathbf{Q}_\perp \mathbf{Q}_\perp^T. \quad (9.65)$$

The last relation has been obtained using $\mathbf{Q}\mathbf{Q}^T = \mathbf{Q}_0\mathbf{Q}_0^T + \mathbf{Q}_\perp\mathbf{Q}_\perp^T = \mathbf{I}$. We note that although the basis is not unique, the projection matrix is unique. Furthermore, although the projection matrix is useful for the brevity of notation, projections are more economically computed using orthogonal basis vectors; use (9.48) after replacing s_k by \mathbf{q}_k .

The LS estimates of \mathbf{x} and \mathbf{e} can be evaluated by the formulas

$$\hat{\mathbf{x}} = \mathbf{P}_S \mathbf{x} = \mathbf{Q}_0 \mathbf{z}_0, \quad \|\hat{\mathbf{x}}\|^2 = \|\mathbf{P}_S \mathbf{x}\|^2 = \|\mathbf{z}_0\|^2 \quad (9.66)$$

$$\hat{\mathbf{e}} = \mathbf{P}_S^\perp \mathbf{x} = \mathbf{Q}_\perp \mathbf{z}_\perp, \quad \|\hat{\mathbf{e}}\|^2 = \|\mathbf{P}_S^\perp \mathbf{x}\|^2 = \|\mathbf{z}_\perp\|^2. \quad (9.67)$$

If we use the economy QR decomposition, only the first part \mathbf{Q}_0 of \mathbf{Q} is available. In this case, instead of (9.63), we evaluate the minimum sum of squared errors using $S(\hat{\mathbf{a}}) = \|\mathbf{x}\|^2 - \|\mathbf{z}_0\|^2$.

9.6.3 Using the Singular Value Decomposition (SVD)

The SVD of a $p \times m$ data matrix S with $p > m$ and rank $r \leq m$ is given by

$$S = UDV^T = \sum_{i=1}^r \sigma_i u_i v_i^T, \quad (9.68)$$

where U is an $p \times p$ orthogonal matrix, V is an $m \times m$ orthogonal matrix, and $D = \text{diag}\{\sigma_1, \dots, \sigma_r, 0, \dots, 0\}$ is an $p \times m$ diagonal matrix. The singular values σ_i satisfy the condition $\sigma_1 \geq \dots \geq \sigma_r > 0$. The number r of nonzero singular values is equal to the rank of the matrix. A matrix S with linearly independent columns has full rank $r = m$. If $r < m$, some columns are linearly dependent and the matrix is known as rank deficient (Watkins, 2002).

The SVD provides the most reliable tool for solving both full rank and rank deficient least squares problems. Since an orthogonal transformation preserves the length of a vector and $U^T S = DV^T$, we have

$$S(a) = \|x - Sa\|^2 = \|U^T(x - Sa)\|^2 = \|U^T x - DV^T a\|^2. \quad (9.69)$$

If we define the vectors $y \triangleq U^T x$ and $b \triangleq V^T a$, we can rewrite (9.69) as

$$S(b) = \|y - Db\|^2 = \sum_{k=1}^r |y_k - \sigma_k b_k|^2 + \sum_{k=r+1}^p |y_k|^2. \quad (9.70)$$

Since the last term does not depend on b_k , it follows that $S(b)$ is minimized if and only if $y_k - \sigma_k b_k = 0$. Hence, we have

$$\hat{b}_k = \frac{y_k}{\sigma_k}, \quad k = 1, \dots, r \quad (9.71)$$

and

$$S(\hat{b}) = \sum_{k=r+1}^p |y_k|^2. \quad (9.72)$$

As long as none of the singular values are zero, that is X has full rank $r = m$, we can uniquely select all \hat{b}_k s by (9.71). In this case, the least squares problem has a unique solution. However, if $r < m$ the coefficients $\hat{b}_{r+1}, \dots, \hat{b}_m$ do not appear in the summation. Then, $\hat{b}_{r+1}, \dots, \hat{b}_m$ can be chosen arbitrarily and all choices give exactly the same sum of square errors (9.72). In this case, the least squares problem does *not* have a unique solution. In practice, the usual convention is to set $\hat{b}_k = 0$ whenever $\sigma_k = 0$. The corresponding least squares estimate \hat{a} can be expressed as

$$\hat{a} = V\hat{b} = \sum_{k=1}^r \frac{u_k^T x}{\sigma_k} v_i \quad (9.73)$$

using the first r columns of U and V . Since $\hat{a} = V\hat{b}$ and V is orthogonal, $\|\hat{a}\|^2 = \|\hat{b}\|^2$. Thus, $\|\hat{a}\|^2$ is minimum when and only when $\|\hat{b}\|^2$ is minimum. The norm $\|\hat{b}\|^2$ is clearly minimized when and only when $\hat{b}_{r+1} = \dots = \hat{b}_m = 0$. Therefore, the least

squares problem has exactly one minimum norm solution. Since (9.73) requires only the first m columns of \mathbf{U} , we only need the reduced SVD.

The projection matrix onto the estimation space can also be evaluated as follows:

$$\mathbf{P}_S = \mathbf{S}(\mathbf{S}^T \mathbf{S})^{-1} \mathbf{S}^T = \mathbf{U}_r \mathbf{U}_r^T = \sum_{k=1}^r \mathbf{u}_k \mathbf{u}_k^T. \quad (9.74)$$

Therefore, the sum of square errors can be evaluated as

$$\hat{\mathbf{x}} = \mathbf{U}_r \mathbf{U}_r^T \mathbf{x} = \sum_{k=1}^r (\mathbf{u}_k^T \mathbf{x}) \mathbf{u}_k, \quad S(\hat{\mathbf{a}}) = \|\mathbf{x}\|^2 - \|\hat{\mathbf{x}}\|^2. \quad (9.75)$$

If \mathbf{S} has full rank $r = m$, then \mathbf{U}_m spans $\langle \mathbf{S} \rangle$ and the last $(p - m)$ columns of \mathbf{U} yield the orthogonal complement \mathbf{U}_\perp of $\langle \mathbf{S} \rangle$. Then, we have

$$\mathbf{P}_S = \mathbf{S}(\mathbf{S}^T \mathbf{S})^{-1} \mathbf{S}^T = \mathbf{U}_m \mathbf{U}_m^T = \sum_{k=1}^m \mathbf{u}_k \mathbf{u}_k^T \quad (9.76)$$

$$\mathbf{P}_S^\perp = \mathbf{I} - \mathbf{P}_S = \mathbf{I} - \mathbf{U}_m \mathbf{U}_m^T = \sum_{k=m+1}^p (\mathbf{u}_k^T \mathbf{x}) \mathbf{u}_k. \quad (9.77)$$

Note the similarity of (9.64) with (9.76); \mathbf{Q}_0 and \mathbf{U}_m are, in general, two different orthogonal bases for the column space of \mathbf{S} . One leads to a triangular system (9.62); the other to a diagonal system (9.71). Finally, we note that when the solution of the least squares problem is not unique, we can obtain a unique solution by imposing a minimum norm constraint. Basically, we reformulate the problem as follows: of all \mathbf{a} that minimize $\|\mathbf{x} - \mathbf{S}\mathbf{a}\|^2$, find the one for which $\|\mathbf{a}\|$ is as small as possible (*minimum norm solution*).

9.7

Statistical Properties of Least Squares Estimators

Least squares estimators are obtained by postulating a model $\mathbf{x} = \mathbf{S}\mathbf{a} + \mathbf{e}$ and fitting the model to the data. However, a good fit (small residual sum of squares) does not provide any information about the quality of the estimated parameters. Suppose now that we make certain assumptions about the model. It turns out that if the assumptions hold, the estimator $\hat{\mathbf{a}}$ has some good properties; if the assumptions do not hold, the model may fit the data well (small sum of squared errors), but the estimator may have some poor properties.

To investigate the statistical properties of LS estimators we assume that the observations or equivalently the errors follow a spherical normal distribution. That is, we consider the following linear model

$$\mathbf{x} = \mathbf{S}\mathbf{a} + \mathbf{e}, \quad \mathbf{x} \sim N(\mathbf{S}\mathbf{a}, \sigma^2 \mathbf{I}) \quad \text{or} \quad \mathbf{e} \sim N(\mathbf{0}, \sigma^2 \mathbf{I}). \quad (9.78)$$

To simplify the analysis, we first transform the linear model (9.78) into what is called the *canonical form* $\mathbf{z} = \mathbf{Q}^T \mathbf{S}\mathbf{a} + \mathbf{\epsilon}$, where $\mathbf{z} = \mathbf{Q}^T \mathbf{x}$ as in (9.60) and $\mathbf{\epsilon} \triangleq \mathbf{Q}^T \mathbf{e}$. Partitioning

z and ϵ as in (9.60), we obtain the following partitioned canonical form of the linear model

$$\begin{bmatrix} z_0 \\ z_{\perp} \end{bmatrix} = \begin{bmatrix} \mathbf{R}\mathbf{a} \\ \mathbf{0} \end{bmatrix} + \begin{bmatrix} \epsilon_0 \\ \epsilon_{\perp} \end{bmatrix}. \quad (9.79)$$

Since $E(\epsilon) = \mathbf{Q}^T E(\mathbf{e}) = \mathbf{0}$, $\text{cov}(\epsilon) = \mathbf{Q}^T \text{cov}(\mathbf{e}) \mathbf{Q} = \sigma^2 \mathbf{I}$, and a spherical normal distribution is invariant under orthogonal transformations, we conclude that

$$\epsilon \sim N(\mathbf{0}, \sigma^2 \mathbf{I}). \quad (9.80)$$

In contrast, the covariance matrix of the residuals (9.26) is given by

$$\text{cov}(\hat{\epsilon}) = \text{cov}(\mathbf{P}_S^{\perp} \mathbf{x}) = \mathbf{P}_S^{\perp} \text{cov}(\mathbf{x}) \mathbf{P}_S^{\perp} = \sigma^2 \mathbf{P}_S^{\perp}. \quad (9.81)$$

We see that the residuals may be correlated with each other and that different residuals may have different variances even when $\text{cov}(\mathbf{e}) = \sigma^2 \mathbf{I}$. Information concerning whether or not the model fits well the data, is contained in the vector of the residuals. For a good model fit both ϵ and $\hat{\epsilon}$ should mimic the distribution of e .

The expectation vector $\zeta = E(z)$ can be partitioned as follows

$$\zeta_0 = E(z_0) = \mathbf{Q}_0^T \mathbf{S}\mathbf{a} = \mathbf{R}\mathbf{a}, \quad \zeta_{\perp} = E(z_{\perp}) = \mathbf{Q}_{\perp}^T \mathbf{S}\mathbf{a} = \mathbf{0}. \quad (9.82)$$

Therefore, the rotated vector z is also normally distributed as

$$z_0 \sim N_m(\mathbf{R}\mathbf{a}, \sigma^2 \mathbf{I}), \quad z_{\perp} \sim N_{p-m}(\mathbf{0}, \sigma^2 \mathbf{I}). \quad (9.83)$$

The LS estimator for \mathbf{a} and the corresponding SSE are given by (9.62) and (9.63):

$$\hat{\mathbf{a}} = \mathbf{R}^{-1} z_0, \quad S(\hat{\mathbf{a}}) = \|z_{\perp}\|^2. \quad (9.84)$$

The mean vector and covariance matrix of the LS estimator $\hat{\mathbf{a}}$ are given by

$$E(\hat{\mathbf{a}}) = \mathbf{R}^{-1} E(z_0) = \mathbf{R}^{-1} \mathbf{R}\mathbf{a} = \mathbf{a} \quad (9.85)$$

$$\text{cov}(\hat{\mathbf{a}}) = \mathbf{R}^{-1} \text{cov}(z) (\mathbf{R}^{-1})^T = \sigma^2 (\mathbf{R}^T \mathbf{R})^{-1} = \sigma^2 (\mathbf{S}^T \mathbf{S})^{-1}, \quad (9.86)$$

where the last expression in (9.86) follows from $\mathbf{S} = \mathbf{Q}_0 \mathbf{R}$. We emphasize that (9.85) and (9.86) hold for any distribution because we have *not* used the assumption of normality. Thus, $\hat{\mathbf{a}}$ is an unbiased estimator of \mathbf{a} even if the errors are correlated and have non-constant variance.

The reason we choose $\hat{\mathbf{a}}$ as our estimate of \mathbf{a} is its optimality according to the Gauss–Markov theorem (Hocking, 1996). This theorem states that, for the class of linear unbiased estimators, \hat{a}_k is the estimator of a_k with the smallest variance. The term linear means that the estimators are linear functions of the observations \mathbf{x} .

If the observations are normally distributed according to (9.78), the LS estimate is also normally distributed as

$$\hat{\mathbf{a}} \sim N(\mathbf{a}, \sigma^2 (\mathbf{S}^T \mathbf{S})^{-1}). \quad (9.87)$$

To evaluate the accuracy of $\hat{\mathbf{a}}$ we must use confidence “volumes”. Using (9.85) and (9.86) we obtain that $\mathbf{b} \triangleq (\mathbf{S}^T \mathbf{S})^{1/2}(\hat{\mathbf{a}} - \mathbf{a})/\sigma \sim N_m(\mathbf{0}, \mathbf{I})$. Therefore, from the definition of chi-square distribution we have

$$(\hat{\mathbf{a}} - \mathbf{a})^T \mathbf{S}^T \mathbf{S}(\hat{\mathbf{a}} - \mathbf{a})/\sigma^2 \sim \chi_m^2, \quad (9.88)$$

which can be used to obtain approximate confidence ellipsoids for $\hat{\mathbf{a}}$. The confidence ellipsoid is centered at the maximum likelihood estimate $\hat{\mathbf{a}}$ and its orientation and size are determined by the eigenvalues and eigenvectors of $\mathbf{S}^T \mathbf{S}$. If an eigenvalue is nearly zero, the confidence ellipsoid will be very long in the direction of the corresponding eigenvector. When only two parameters are involved construction of the confidence ellipse is not difficult. However, in practice, confidence ellipsoids are seldom used, even for two parameters (Draper and Smith, 1998).

In order to use formula (9.86) to access the quality of $\hat{\mathbf{a}}$, the variance σ^2 must be known or estimated. To obtain an estimator for σ^2 , we note that (9.63) yields

$$E[S(\hat{\mathbf{a}})] = E(\|z_{\perp}\|^2) = \sum_{k=m+1}^p E(z_k^2) = (p-m) \sigma^2. \quad (9.89)$$

Therefore, an unbiased estimator of σ^2 is given by the following formula

$$\hat{\sigma}_u^2 = \frac{S(\hat{\mathbf{a}})}{p-m} = \frac{\|z_{\perp}\|^2}{p-m}. \quad (9.90)$$

It can be also shown that both $\hat{\mathbf{a}}$ and $\hat{\mathbf{a}}_c$ are unbiased estimates of \mathbf{a} in the constrained model (Hocking, 1996). Furthermore, the variance of the estimate of any component of \mathbf{a} is decreased by enforcing the constraints.

9.8

Generalized Least Squares Estimation

From the discussion in Section 7.6.2 it is clear that the assumption $\text{cov}(\mathbf{x}) = \sigma^2 \mathbf{I}$ does not hold for hyperspectral imaging data. To introduce correlations among the observations of the linear model, we assume that $\text{cov}(\mathbf{x}) = \sigma^2 \mathbf{C}$, where \mathbf{C} is a known positive definite matrix. In general, when the vector \mathbf{x} does *not* have a covariance matrix equal to $\sigma^2 \mathbf{I}$, the LS estimator is *not* the best, linear, unbiased estimator. However, a straightforward transformation adjusts the covariance matrix so that LS estimation can be used. We shall show that if

$$E(\mathbf{x}) = \mathbf{S}\mathbf{a}, \quad \text{cov}(\mathbf{x}) = \sigma^2 \mathbf{C}, \quad (9.91)$$

we can obtain the best linear unbiased estimator of \mathbf{a} , if we transform the original data so that the covariance matrix of the transformed errors has the form $\sigma^2 \mathbf{I}$. Such a whitening transformation is always possible because \mathbf{C} is positive definite. Let $\mathbf{C}^{1/2}$ be the square root matrix of \mathbf{C} , that is, $\mathbf{C} = \mathbf{C}^{1/2} \mathbf{C}^{1/2}$, and consider the transformed model

$$\tilde{\mathbf{x}} = \tilde{\mathbf{S}}\mathbf{a} + \tilde{\mathbf{e}}, \quad (9.92)$$

where

$$\tilde{\mathbf{x}} \triangleq \mathbf{C}^{-1/2}\mathbf{x}, \quad \tilde{\mathbf{S}} \triangleq \mathbf{C}^{-1/2}\mathbf{S}, \quad \text{and} \quad \tilde{\mathbf{e}} \triangleq \mathbf{C}^{-1/2}\mathbf{e}. \quad (9.93)$$

Since $\tilde{\mathbf{e}} = \sigma^2 \mathbf{I}$, the transformed model (9.92) obeys the classical assumptions. Thus, the best linear unbiased estimate of \mathbf{a} is given by

$$\hat{\mathbf{a}}_g = (\tilde{\mathbf{S}}^T \tilde{\mathbf{S}})^{-1} \tilde{\mathbf{S}}^T \tilde{\mathbf{x}} \quad (9.94)$$

$$= (\mathbf{S}^T \mathbf{C}^{-1} \mathbf{S})^{-1} \mathbf{S}^T \mathbf{C}^{-1} \mathbf{x}. \quad (9.95)$$

The estimator $\hat{\mathbf{a}}_g$ is unbiased with covariance matrix

$$\text{cov}(\hat{\mathbf{a}}_g) = \sigma^2 (\tilde{\mathbf{S}}^T \tilde{\mathbf{S}})^{-1} = \sigma^2 (\mathbf{S}^T \mathbf{C}^{-1} \mathbf{S})^{-1}. \quad (9.96)$$

The sum of squared errors for the model (9.92) can be written as

$$S_g(\mathbf{a}) = (\tilde{\mathbf{x}} - \tilde{\mathbf{S}}\mathbf{a})^T (\tilde{\mathbf{x}} - \tilde{\mathbf{S}}\mathbf{a}) \quad (9.97)$$

$$= (\mathbf{x} - \mathbf{S}\mathbf{a})^T \mathbf{C}^{-1} (\mathbf{x} - \mathbf{S}\mathbf{a}). \quad (9.98)$$

The minimum sum of squared errors is given by

$$S_g(\hat{\mathbf{a}}_g) = \tilde{\mathbf{x}}^T \tilde{\mathbf{x}} - \tilde{\mathbf{x}}^T \tilde{\mathbf{S}} (\tilde{\mathbf{S}}^T \tilde{\mathbf{S}})^{-1} \tilde{\mathbf{S}}^T \tilde{\mathbf{x}} \quad (9.99)$$

$$= \mathbf{x}^T \mathbf{C}^{-1} \mathbf{x} - \mathbf{x}^T \mathbf{C}^{-1} \mathbf{S} (\mathbf{S}^T \mathbf{C}^{-1} \mathbf{S})^{-1} \mathbf{S}^T \mathbf{C}^{-1} \mathbf{x}. \quad (9.100)$$

An unbiased estimator of variance is given by

$$\hat{\sigma}_{\text{gu}}^2 = \frac{S(\hat{\mathbf{a}}_g)}{p - m}. \quad (9.101)$$

Clearly, for $\mathbf{C} = \mathbf{I}$ we obtain the classical least squares estimation results. For $\mathbf{C} = \text{diag}\{\sigma_1^2, \dots, \sigma_p^2\}$, we have $\mathbf{C}^{-1/2} = \text{diag}\{\sigma_1^{-1}, \dots, \sigma_p^{-1}\}$, which leads to the weighted least squares estimation case.

The estimator defined by (9.95) is called the *generalized least squares* (GLS) estimator and is an obvious generalization of the ordinary LS estimator. If we incorrectly use the LS estimator $\hat{\mathbf{a}} = (\mathbf{S}^T \mathbf{S})^{-1} \mathbf{S}^T \mathbf{x}$ instead of the correct GLS estimator (9.105) when $\text{cov}(\mathbf{x}) \neq \sigma^2 \mathbf{I}$, the mean and covariance for $\hat{\mathbf{a}}$ are

$$E(\hat{\mathbf{a}}) = \mathbf{a} \quad (9.102)$$

$$\text{cov}(\hat{\mathbf{a}}) = \sigma^2 (\mathbf{S}^T \mathbf{S})^{-1} \mathbf{S}^T \mathbf{C} \mathbf{S} (\mathbf{S}^T \mathbf{S})^{-1}. \quad (9.103)$$

Thus, the estimator $\hat{\mathbf{a}}$ is unbiased, but the covariance matrix differs from (9.86). Typically, when we mis-specify the covariance the variances of the \hat{a}_k s in (9.103) will be larger than the variances of $\hat{a}_{g,k}$ in (9.96).

Note that (9.95) cannot be used to estimate the coefficients if \mathbf{C} is unknown. The matrix \mathbf{C} has $p(p + 1)/2 + p$ distinct elements; if \mathbf{C} is unknown, it cannot be estimated from a sample of p observations. However, in some applications, we can compute an estimate $\hat{\mathbf{C}}$ of \mathbf{C} from multiple observations of \mathbf{x} . Then $\hat{\mathbf{C}}$ may be used in place of \mathbf{C} in (9.95).

9.9

Maximum Likelihood Estimation

If the distribution of \mathbf{x} is known, we can estimate the parameters of the linear model using the method of maximum likelihood (see Section 7.5). In general ML estimators have better statistical properties than LS estimators because they require a full distributional assumption. Here, we assume a normal distribution given by

$$\mathbf{x} \sim N(\mathbf{S}\mathbf{a}, \sigma^2 \mathbf{C}), \quad (9.104)$$

where \mathbf{C} is a known positive definite matrix. The likelihood function, or more simply, the likelihood $\mathcal{L}(\mathbf{a}, \sigma^2 | \mathbf{x})$, for \mathbf{a} and σ^2 is identical in form to the joint pdf $f(\mathbf{x} | \mathbf{a}, \sigma^2)$ except that $\mathcal{L}(\mathbf{a}, \sigma^2 | \mathbf{x})$ is regarded as a function of the parameters conditional on the observed data, rather than as a function of the data conditional on the values of the parameters. Hence, the likelihood function for (9.104) is

$$\begin{aligned} \mathcal{L}(\mathbf{a}, \sigma^2 | \mathbf{x}) &= \frac{1}{(2\pi\sigma^2)^{p/2} |\mathbf{C}|^{1/2}} \exp \left[-\frac{1}{2\sigma^2} (\mathbf{x} - \mathbf{S}\mathbf{a})^T \mathbf{C}^{-1} (\mathbf{x} - \mathbf{S}\mathbf{a}) \right] \\ &= \frac{1}{(2\pi\sigma^2)^{p/2} |\mathbf{C}|^{1/2}} \exp \left[-\frac{S_g(\mathbf{a})}{2\sigma^2} \right]. \end{aligned} \quad (9.105)$$

For each value of σ^2 , known or unknown, the likelihood is maximized with respect to \mathbf{a} when $S_g(\mathbf{a})$ in (9.105) is a minimum. Expanding the quadratic form we have

$$S_g(\mathbf{a}) = \mathbf{x}^T \mathbf{C}^{-1} \mathbf{x} - 2\mathbf{a}^T \mathbf{S}^T \mathbf{C}^{-1} \mathbf{x} + \mathbf{a}^T \mathbf{S}^T \mathbf{C}^{-1} \mathbf{S}\mathbf{a}. \quad (9.106)$$

Differentiation of (9.106) with respect to \mathbf{a} yields

$$\frac{\partial S_g(\mathbf{a})}{\partial \mathbf{a}} = -2\mathbf{S}^T \mathbf{C}^{-1} \mathbf{x} + 2\mathbf{S}^T \mathbf{C}^{-1} \mathbf{S}\mathbf{a}. \quad (9.107)$$

Equating (9.107) to zero and solving for \mathbf{a} yields the maximum likelihood estimator

$$\hat{\mathbf{a}}_{\text{ML}} = (\mathbf{S}^T \mathbf{C}^{-1} \mathbf{S})^{-1} \mathbf{S}^T \mathbf{C}^{-1} \mathbf{x}, \quad (9.108)$$

which is identical to the GLS estimator (9.95). To maximize with respect to σ^2 , we first determine the derivative of the log-likelihood function

$$\ln \mathcal{L}(\hat{\mathbf{a}}, \sigma^2 | \mathbf{x}) = |\mathbf{C}|^{-1/2} \left[-\frac{p}{2} \ln 2\pi - \frac{p}{2} \ln \sigma^2 - \frac{1}{2\sigma^2} S_g(\hat{\mathbf{a}}) \right]. \quad (9.109)$$

Taking the partial derivatives of (9.109) with respect to σ^2 and setting the result equal to zero gives

$$-(p/2) \frac{1}{\sigma^2} + \frac{1}{2(\sigma^2)^2} S_g(\hat{\mathbf{a}}_{\text{ML}}) = 0, \quad (9.110)$$

whose solution provides the ML estimator of σ^2 . Thus, we have

$$\hat{\sigma}_{\text{ML}}^2 = \frac{S_g(\hat{\mathbf{a}}_{\text{ML}})}{p} = \frac{1}{p} [\mathbf{x}^T \mathbf{C}^{-1} \mathbf{x} - \mathbf{x}^T \mathbf{C}^{-1} \mathbf{S} (\mathbf{S}^T \mathbf{C}^{-1} \mathbf{S})^{-1} \mathbf{S}^T \mathbf{C}^{-1} \mathbf{x}]. \quad (9.111)$$

The maximum likelihood estimator of σ^2 in (9.111) is biased since the denominator is p rather than $(p - m)$. The maximum likelihood value is

$$\mathcal{L}(\hat{\mathbf{a}}_{\text{ML}}, \hat{\sigma}_{\text{ML}}^2 | \mathbf{x}) = \left[\frac{2\pi}{S_g(\hat{\mathbf{a}}_{\text{ML}})/p} \right]^{p/2} \exp(-p/2). \quad (9.112)$$

We note that the assumption of a spherical ($\mathbf{C} = \mathbf{I}$) normal distribution for the observed data establishes the equivalence between ML and LS estimates and makes the use of Euclidean geometry statistically meaningful.

In summary, the method of least squares is appropriate when the errors can be assumed to be statistically independent, to have constant variance σ^2 , and to be normally distributed.

9.10 Regularized Least Squares Problems

As we showed in Section 9.5.1, if at least one column of \mathbf{S} is linearly dependent on (that is, is a linear combination of) the other columns, the matrix $\mathbf{S}^T \mathbf{S}$ is singular, and the normal equations do not have a unique solution. In the statistical literature this condition is known as *collinearity* or *multicollinearity* (Draper and Smith, 1998). In practice, the linear dependence of the columns of \mathbf{S} is *approximate*: that is, there is a set of constants a_k , such that $a_1 s_1 + \cdots + a_m s_m = \mathbf{S}\mathbf{a}$ is very close to, but not exactly, zero. In such cases, the data matrix is said to be *ill-conditioned*. Ill-conditioning leads to unreliable estimates of a_k s, which then have large variances and covariances. However, it should be always kept in mind that whether the data are ill-conditioned or well-conditioned is a function of both the data and the adopted model. The problem can be often corrected by reducing the order of the model: that is, dropping some of the variables. However, when this is not possible, we have to resort to other techniques. The process of making an ill-conditioned problem well-conditioned by imposing extra conditions on the solution is called *regularization*. We look at both the numerical aspects of the problem and its statistical implications.

9.10.1 Ridge Regression or Diagonal Loading

Given a full-rank linear model $\mathbf{x} = \mathbf{S}\mathbf{a} + \mathbf{e}$, we can express the least squares estimator of \mathbf{a} and its variance in terms of the eigenvalue decomposition

$$\mathbf{S}^T \mathbf{S} = \mathbf{Q} \boldsymbol{\Lambda} \mathbf{Q}^T = \sum_{k=1}^m \lambda_k \mathbf{q}_k \mathbf{q}_k^T, \quad (9.113)$$

where the eigenvalues λ_k and the corresponding eigenvectors \mathbf{q}_k have been arranged so as $\lambda_1 \geq \lambda_2 \geq \cdots \geq \lambda_m > 0$; the results are

$$\hat{\mathbf{a}} = (\mathbf{S}^T \mathbf{S})^{-1} \mathbf{S}^T \mathbf{x} = \sum_{k=1}^m \frac{\mathbf{q}_k^T (\mathbf{S}^T \mathbf{x})}{\lambda_k} \mathbf{q}_k \quad (9.114)$$

and

$$\sum_{k=1}^m \text{var}(\hat{a}_k) = \sigma^2 \text{tr}(\mathbf{S}^T \mathbf{S})^{-1} = \sum_{k=1}^m \frac{\sigma^2}{\lambda_k}, \quad (9.115)$$

respectively. Equation (9.115) implies that, if one or more of the λ_k s is small, the total variance of the \hat{a}_k s will be very large. Small eigenvalues, besides inflating the total variance, they induce near-dependence or ill-conditioning in the columns of \mathbf{S} . To demonstrate this, we premultiply the eigenvalue equation $\mathbf{S}^T \mathbf{S} \mathbf{q}_k = \lambda_k \mathbf{q}_k$ from the left by \mathbf{q}_k^T . The result is $\mathbf{q}_k^T \mathbf{S}^T \mathbf{S} \mathbf{q}_k = \lambda_k \mathbf{q}_k^T \mathbf{q}_k = \lambda_k$ from which it follows that $\mathbf{S} \mathbf{q}_k \simeq \mathbf{0}$, that is, the columns of \mathbf{S} are approximately linearly dependent, when $\lambda_k \simeq 0$.

The main cause of variance inflation in least squares estimates, obtained from ill-conditioned data, is the requirement for unbiasedness. Since the mean squared error of any estimator equals its variance plus the square of its bias, it is meaningful to focus on the potential reduction of its variance by allowing a little bias. This is the essence of what regularization techniques in least squares estimation try to accomplish. Inspection of (9.115) shows that we can reduce the total variance of the \hat{a}_k s by either deleting some of the components corresponding to the smaller eigenvalues or by adding a small positive constant $\delta^2 > 0$ to all eigenvalues. Each approach leads to a different biased regularized least squares estimator. Note that the reduction of variance is done at the expense of introducing some bias into the estimates.

Deciding which components to delete in practical applications is a difficult problem because a component may have a small λ_k but may correlate better with the observed vector \mathbf{x} than a component with a larger λ_k . Therefore, deleting a principal component may improve the precision of the estimated coefficients, but may or may not improve the estimate (prediction) of the observed vector \mathbf{x} . Therefore, it is preferable to add a small positive constant δ^2 to the eigenvalues λ_k in (9.114); the result is $\mathbf{Q}(\mathbf{\Lambda} + \delta^2 \mathbf{I})\mathbf{Q}^T = \mathbf{S}^T \mathbf{S} + \delta^2 \mathbf{I}$. This process, which is known as *diagonal loading*, results to the following biased estimator:

$$(\mathbf{S}^T \mathbf{S} + \delta^2 \mathbf{I})\hat{\mathbf{a}}(\delta) = \mathbf{S}^T \mathbf{x}. \quad (9.116)$$

We note that $\hat{\mathbf{a}}(0) = \hat{\mathbf{a}}$, the standard least squares estimator. In the statistical literature, $\hat{\mathbf{a}}(\delta)$, known as *ridge regression* estimator, was introduced and analyzed by Hoerl and Kennard (1970). A Bayesian derivation and interpretation is provided by Draper and Smith (1998).

The estimator (9.114) can be expressed in terms of the eigenvalue decomposition (9.113) or the SVD $\mathbf{S} = \mathbf{U} \mathbf{D} \mathbf{V}^T$. Indeed, using $\mathbf{S}^T \mathbf{S} = \mathbf{V} \mathbf{D}^2 \mathbf{V}^T = \mathbf{Q} \mathbf{\Lambda} \mathbf{Q}^T$ and (9.73), we obtain

$$\hat{\mathbf{a}}(\delta) = \sum_{k=1}^m f_k \frac{\mathbf{q}_k^T (\mathbf{S}^T \mathbf{x})}{\lambda_k} \mathbf{q}_k = \sum_{k=1}^m f_k \frac{\mathbf{u}_k^T \mathbf{x}}{\sigma_k^2} \mathbf{v}_k, \quad (9.117)$$

where $\lambda_k = \sigma_k^2$ and f_k is the so called “filter factor”, which is given by

$$f_k = \frac{\sigma_k^2}{\sigma_k^2 + \delta^2} \simeq \begin{cases} 1 & \text{if } \delta \ll \sigma_k \\ 0 & \text{if } \delta \gg \sigma_k \end{cases}. \quad (9.118)$$

The parameter δ provides a balance between the goodness of fit $\|\mathbf{x} - \mathbf{S}\hat{\mathbf{a}}(\delta)\|^2$ and the size of the solution $\|\hat{\mathbf{a}}(\delta)\|^2$. The plot of $\log \|\mathbf{x} - \mathbf{S}\hat{\mathbf{a}}(\delta)\|$ versus $\log \|\hat{\mathbf{a}}(\delta)\|$ as a function of δ (known as L-curve) can be used to choose δ (Hansen, 1998).

To obtain additional insight into how diagonal loading regularization works, we notice that $\hat{\mathbf{a}}(\delta)$ can be obtained as the solution to two apparently different but basically equivalent optimization problems. The motivation is provided by the following observation: since $E(\hat{a}_k^2) = a_k^2 + \sigma^2/\lambda_k$, the expected squared length of \hat{a}_k becomes too large if $\lambda_k \ll 1$. Therefore, we could possibly reduce the variance by shrinking the size of the coefficient vector. The first approach uses the criterion

$$\min_{\mathbf{a}} \{\|\mathbf{x} - \mathbf{S}\mathbf{a}\|^2 + \delta^2 \|\mathbf{a}\|^2\}, \quad (9.119)$$

which penalizes the cost function with a quadratic penalty, $\delta^2 \mathbf{a}^T \mathbf{a}$, proportional to the length of the parameter vector. This is the approach to regularization introduced by Tikhonov (Hansen, 1998). The second approach minimizes the sum of squares by imposing an explicit size constraint on the parameters

$$\min_{\mathbf{a}} (\mathbf{x} - \mathbf{S}\mathbf{a})^T (\mathbf{x} - \mathbf{S}\mathbf{a}) \text{ subject to } \|\mathbf{a}\|^2 \leq \eta^2. \quad (9.120)$$

Both problems lead to the same solution (9.116), which simply adds a positive constant to the diagonal of $\mathbf{S}^T \mathbf{S}$ before inversion (Draper and Smith, 1998). As a result, we can obtain a solution even if $\mathbf{S}^T \mathbf{S}$ is singular. There is a one-to-one correspondence between the positive parameters δ^2 in (9.119) and η^2 in (9.120).

Formulation (9.120) shows that diagonal loading regularization can be viewed as a least squares problem subjected to a spherical restriction on the parameters. This provides a nice geometrical interpretation which is illustrated in Figure 9.13 for a hypothetical problem involving only two parameters a_1 and a_2 . The usual (unconstrained) least squares solution is the point $\hat{\mathbf{a}}$ at the center of the ellipses, where $S(\mathbf{a})$ achieves its minimum. Each ellipse is the locus of points in the (a_1, a_2) plane where $S(a_1, a_2)$ is constant at some value. The circle with radius η about the origin defines the region of all allowed parameter vectors. The restricted solution is determined by the point where

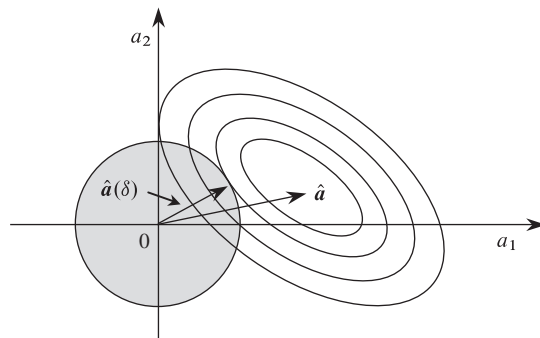


Figure 9.13 Geometrical illustration of regularized least squares estimation. The concentric ellipses are the contours of the least squares error function whereas the solid disk is the constrained region.

the innermost elliptical contour just touches the spherical restriction. Thus, this is the shortest vector that gives the same residual sum of squares, $S(\hat{\mathbf{a}}(\delta))$, as any vector on the same contour.

9.10.2 Solving the Ridge Regression Problem

To solve (9.120) we use the method provided by Golub and Van Loan (2012). To this end suppose that

$$\mathbf{S} = \mathbf{U}\Sigma\mathbf{V}^T = \sum_{i=1}^r \sigma_i \mathbf{u}_i \mathbf{v}_i^T \quad (9.121)$$

is the SVD of \mathbf{S} which we assume to have rank r . If the unconstrained minimum norm solution (see Section 9.6.3)

$$\hat{\mathbf{a}}_R = \sum_{i=1}^r \frac{\mathbf{u}_i^T \mathbf{x}}{\sigma_i} \mathbf{v}_i \quad (9.122)$$

satisfies $\|\hat{\mathbf{a}}_R\|^2 \leq \eta^2$, then it obviously solves (9.179). Otherwise,

$$\|\hat{\mathbf{a}}_R\|^2 = \sum_{i=1}^r \left(\frac{\mathbf{u}_i^T \mathbf{x}}{\sigma_i} \right)^2 \geq \eta^2, \quad (9.123)$$

which implies that the solution of (9.179) is on the boundary of the constraint sphere. Thus, we can approach this constrained optimization problem using the method of Lagrange multipliers. We consider the Lagrangian function

$$g(\mathbf{a}, \lambda) = \frac{1}{2} \|\mathbf{x} - \mathbf{S}\mathbf{a}\|^2 + \frac{\lambda}{2} (\|\mathbf{a}\|^2 - \eta^2) \quad (9.124)$$

and set its gradient equal to zero. This yields the diagonally loaded normal equations

$$(\mathbf{S}^T \mathbf{S} + \lambda \mathbf{I}) \mathbf{a}(\lambda) = \mathbf{S}^T \mathbf{x}. \quad (9.125)$$

The goal is to choose λ so that $\|\mathbf{a}(\lambda)\|^2 = \eta^2$. Using the SVD (9.121), this leads to the problem of finding a zero of the function

$$f(\lambda) = \|\mathbf{a}(\lambda)\|^2 - \eta^2 = \sum_{k=1}^r \left(\frac{\sigma_k \mathbf{u}_k^T \mathbf{x}}{\sigma_k^2 + \lambda} \right)^2 - \eta^2. \quad (9.126)$$

This is an example of a secular equation problem. From (9.123) we obtain $f(0) > 0$. Since $f'(\lambda) < 0$ for $\lambda > 0$, it follows that f has a unique positive root λ_+ . It can be shown that

$$\rho(\lambda) = \|\mathbf{S}\mathbf{a}(\lambda) - \mathbf{x}\|^2 = \|\mathbf{S}\hat{\mathbf{a}}_R - \mathbf{x}\|^2 + \sum_{i=1}^r \left(\frac{\sigma_i \mathbf{u}_i^T \mathbf{x}}{\sigma_i^2 + \lambda} \right)^2, \quad (9.127)$$

which implies that $\mathbf{a}(\lambda_+)$ solves (9.179). Thus, if (9.123) holds, the solution is

$$\hat{\mathbf{a}}_R = \sum_{i=1}^r \left(\frac{\sigma_i \mathbf{u}_i^T \mathbf{x}}{\sigma_i^2 + \lambda_+} \right) \mathbf{v}_i. \quad (9.128)$$

The SVD is the dominant computation in this algorithm; see Golub and Van Loan (2012) for more details. Some additional properties of the diagonal loading regularized estimator are discussed by Montgomery et al. (2012).

9.11 Consequences of Model Misspecification

To consider the consequences of misspecifying the parameters of the linear model, we partition the coefficient vector and spectral matrix as follows:

$$\mathbf{x} = \mathbf{S}\mathbf{a} + \boldsymbol{\epsilon} = [\mathbf{S}_1 \quad \mathbf{S}_2] \begin{bmatrix} \mathbf{a}_1 \\ \mathbf{a}_2 \end{bmatrix} + \boldsymbol{\epsilon} \quad (9.129)$$

$$= \mathbf{S}_1\mathbf{a}_1 + \mathbf{S}_2\mathbf{a}_2 + \boldsymbol{\epsilon}, \quad (9.130)$$

where \mathbf{a}_1 and \mathbf{a}_2 are vectors of length m_1 and $m_2 = m - m_1$ with conformable partitioning of \mathbf{S} . This formulation can be used to introduce two cases of model misspecification or mismatch: (a) if we leave out $\mathbf{S}_2\mathbf{a}_2$ when it should be included (that is, when $\mathbf{a}_2 \neq \mathbf{0}$), we are *underfitting* the model. (b) If we include $\mathbf{S}_2\mathbf{a}_2$ when it should be excluded (that is, when $\mathbf{a}_2 = \mathbf{0}$), we are *overfitting* the model. We note that the consequences of misspecifying the model variance have been discussed in Section 9.8.

To investigate the consequences of using a mismatched (that is, incorrectly specified) model on the estimated coefficients, we shall use the canonical form (9.79), which we partition as

$$\begin{bmatrix} \mathbf{z}_1 \\ \mathbf{z}_2 \\ \mathbf{z}_\perp \end{bmatrix} = \begin{bmatrix} \mathbf{R}_{11} & \mathbf{R}_{12} \\ \mathbf{0} & \mathbf{R}_{22} \\ \mathbf{0} & \mathbf{0} \end{bmatrix} \begin{bmatrix} \mathbf{a}_1 \\ \mathbf{a}_2 \end{bmatrix} + \begin{bmatrix} \boldsymbol{\epsilon}_1 \\ \boldsymbol{\epsilon}_2 \\ \boldsymbol{\epsilon}_\perp \end{bmatrix}, \quad (9.131)$$

in a manner conformable to (9.129). Since $\mathbf{Q} = [\mathbf{Q}_1 \quad \mathbf{Q}_2 \quad \mathbf{Q}_\perp]$, we obtain

$$\mathbf{S}_1 = \mathbf{Q}_1 \mathbf{R}_{11}, \quad \mathbf{S}_2 = \mathbf{Q}_1 \mathbf{R}_{12} + \mathbf{Q}_2 \mathbf{R}_{22}, \quad \mathbf{Q}_1^T \mathbf{Q}_2 = \mathbf{0}. \quad (9.132)$$

We first consider estimation of \mathbf{a}_1 when underfitting. To this end, we consider the *reduced model* using only \mathbf{S}_1 ; that is, we assume that $\mathbf{a}_2 = \mathbf{0}$. The model is

$$\mathbf{z}_1 = \mathbf{R}_1 \mathbf{a}_1^R + \boldsymbol{\epsilon}_1. \quad (9.133)$$

We use the notation \mathbf{a}_1^R to emphasize that, in general, these parameters and their estimates will be different from \mathbf{a}_1 and its estimate in the full model (9.129). The estimated coefficients and sum of squared residuals for the reduced model are given by

$$\hat{\mathbf{a}}_1^R = \mathbf{R}_1^{-1} \mathbf{z}_1 \quad (9.134)$$

$$\text{RSS}_R = \|\mathbf{P}_{\mathbf{S}_1}^{\perp} \mathbf{x}\|^2 = \|\mathbf{z}_2\|^2 + \|\mathbf{z}_\perp\|^2. \quad (9.135)$$

The estimated coefficients and the sum of squared residuals for the *full model*, described by (9.129), are

$$\begin{bmatrix} \hat{\mathbf{a}}_1 \\ \hat{\mathbf{a}}_2 \end{bmatrix} = \begin{bmatrix} \mathbf{R}_{11} & \mathbf{R}_{12} \\ \mathbf{0} & \mathbf{R}_{22} \end{bmatrix}^{-1} \begin{bmatrix} \mathbf{z}_1 \\ \mathbf{z}_2 \end{bmatrix} = \begin{bmatrix} \mathbf{R}_{11}^{-1} & -\mathbf{R}_{11}^{-1} \mathbf{R}_{12} \mathbf{R}_{22}^{-1} \\ \mathbf{0} & \mathbf{R}_{22}^{-1} \end{bmatrix} \begin{bmatrix} \mathbf{z}_1 \\ \mathbf{z}_2 \end{bmatrix}, \quad (9.136)$$

$$\text{RSS}_F = \|\mathbf{z}_\perp\|^2. \quad (9.137)$$

Using (9.132) we obtain $(S_1^T S_1)^{-1} S_1^T S_2 = \mathbf{R}_{11}^{-1} \mathbf{R}_{12}$. Thus, from (9.134) and (9.136) we obtain

$$\hat{\mathbf{a}}_1^R = \hat{\mathbf{a}}_1 + (S_1^T S_1)^{-1} S_1^T S_2 \hat{\mathbf{a}}_2. \quad (9.138)$$

Since the estimator (9.136) for the full model is unbiased, the expectation of the reduced model (9.138) is

$$E(\hat{\mathbf{a}}_1^R) = \mathbf{a}_1 + (S_1^T S_1)^{-1} S_1^T S_2 \mathbf{a}_2. \quad (9.139)$$

Careful inspection of (9.139) shows that $\hat{\mathbf{a}}_1^R$ is a biased estimate of \mathbf{a}_1 unless the coefficients of the deleted variables are zero, that is, $\mathbf{a}_2 = \mathbf{0}$, or the deleted variables are orthogonal to the retained variables, that is, $S_1^T S_2 = \mathbf{0}$. Thus, deleting variables from the correct model potentially introduces bias into the estimates of the coefficients of the retained variables.

The covariance of estimated coefficients for the reduced model (9.134) is

$$\text{cov}(\hat{\mathbf{a}}_1^R) = \sigma^2 (S_1^T S_1)^{-1} = \sigma^2 (\mathbf{R}_{11}^T \mathbf{R}_{11})^{-1}. \quad (9.140)$$

Using (9.136) and (9.140) we can show that the covariance

$$\text{cov}(\hat{\mathbf{a}}_1) = \text{cov}(\hat{\mathbf{a}}_1^R) + \Phi^T \Phi, \quad \Phi^T \triangleq \mathbf{R}_{11}^{-1} \mathbf{R}_{12} \mathbf{R}_{22}^{-1}. \quad (9.141)$$

Since the matrix $\Phi^T \Phi$ is positive definite, we have $\text{var}(\hat{a}_k) > \text{var}(\hat{a}_k^R)$; that is, the variance $\text{var}(\hat{a}_k)$ in the full model is greater than $\text{var}(\hat{a}_k^R)$ in the reduced model. Thus, overfitting increases the variance of the estimated coefficients. On the other hand, underfitting reduces the variance of \hat{a}_k s but introduces bias. Therefore, the variance of the estimated parameters increases with the order of the model. If the reduced model is correct, but we use the full model, the parameter estimates are unbiased for both models but with increased variances in the full model. In conclusion, there is danger in retaining negligible variables, that is, variables with zero coefficients or coefficients less than their corresponding standard errors from the full model. This danger is an increase in the variances of the estimates of the parameters of the model.

To determine the effect of underfitting on the estimated variance, we recall that the variance estimator for the reduced model is

$$(\hat{\sigma}_1^R)^2 = \frac{\text{RSS}_R}{p - m_1}. \quad (9.142)$$

Since $\xi_2 = E(z_2) = \mathbf{R}_{22} \mathbf{a}_2$, taking the expectation of $\|z_2\|^2$ we obtain

$$E(\|z_2\|^2) = \sum_{k=m_1+1}^m E(z_k^2) = m_2 \sigma^2 + \|\xi_2\|^2 = m_2 \sigma^2 + \|\mathbf{R}_{22} \mathbf{a}_2\|^2, \quad (9.143)$$

because $\text{cov}(z) = \sigma^2 \mathbf{I}$. Substitution of (9.143) and (9.89) into (9.135) yields

$$E(\text{RSS}_R) = \sigma^2 (p - m_1) + \sigma^2 \mathbf{a}_2^T S_2^T S_2 \mathbf{a}_2. \quad (9.144)$$

Since the quadratic form in (9.144) is positive definite, the estimator (9.142) overestimates the variance of the model if $\mathbf{a}_2 \neq \mathbf{0}$ (underfitting).

In summary, *underfitting leads to biased model parameters whereas overfitting increases the variances of the estimated coefficients*. Thus, in practical applications, it is important to seek a balance between a biased model and a model with large variances by selecting an optimum subset of variables.

9.12 Hypotheses Tests for Model Parameters

Once we have estimated the parameters in the linear model $\mathbf{x} = \mathbf{S}\mathbf{a} + \mathbf{e}$, defined by (9.129), we face two immediate and important questions:

- What is the overall adequacy of the full model?
- Which of the spectra s_1, s_2, \dots, s_m are the most important?

To deal with such issues, we need to develop a method of testing hypotheses concerning the entire set or arbitrary subsets of the set of parameters a_1, a_2, \dots, a_m . We shall rely on the geometrical interpretation in Figure 9.14 to provide insight and the canonical form (9.131) to simplify the derivation of statistical distributions; a formal procedure using statistical decision theory is provided in Chapter 10. The tests developed in this section are useful for spectral target identification applications.

To answer the first question, that is, to test for adequacy of the full linear model $\mathbf{x} = \mathbf{S}\mathbf{a} + \mathbf{e}$, we must consider the hypotheses

$$H_0 : \mathbf{a} = \mathbf{0} \quad \text{versus} \quad H_1 : \mathbf{a} \neq \mathbf{0}. \quad (9.145)$$

The part of \mathbf{x} explained by the model is $\hat{\mathbf{x}} = \mathbf{P}_S \mathbf{x}$. If the model is adequate, then $\|\mathbf{P}_S \mathbf{x}\|$ should be large relative to $\|\mathbf{P}_S^\perp \mathbf{x}\|$; that is, most of the variability in the modeled data should be attributed to the linear model rather than to random sources. Thus, to develop a test statistic for (9.145) it is natural to compare these two components in some way. From (9.66) and (9.67) we recall that

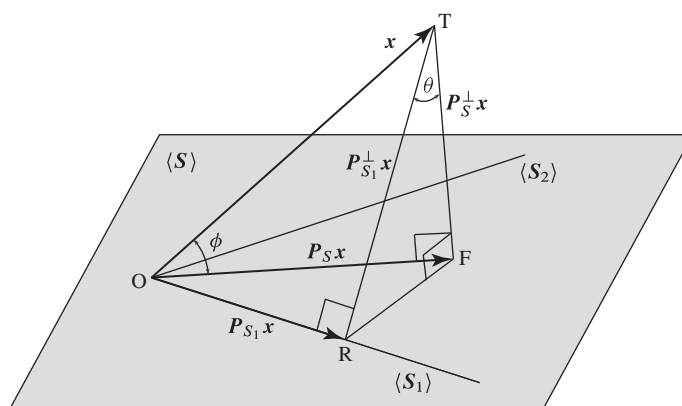


Figure 9.14 Geometrical construction for the interpretation of model adequacy and model comparison tests for linear models with spherical error distributions.

$$\text{MSS}_F = \|\mathbf{P}_S \mathbf{x}\|^2 = \|z_0\|^2 \quad (9.146)$$

$$\text{RSS}_F = \|\mathbf{P}_S^\perp \mathbf{x}\|^2 = \|z_\perp\|^2. \quad (9.147)$$

For reasons to be seen shortly we use as a test the ratio

$$F \triangleq \frac{\text{MSS}_F/m}{\text{RSS}_F/(p-m)}, \quad (9.148)$$

where we have normalized the squared length of each vector by its dimensionality.

To answer the second question, without loss of generality, we assume that the variables in the subset of interest have been arranged last in \mathbf{a} and in the columns of \mathbf{S} according to the partitioned model (9.130). The goal is to develop a test for choosing between the hypotheses

$$H_0 : \mathbf{a}_2 = \mathbf{0} \text{ (Reduced Model)} \quad (9.149a)$$

$$H_1 : \mathbf{a}_2 \neq \mathbf{0} \text{ (Full Model).} \quad (9.149b)$$

The residual sum of squares resulting from fitting the reduced model is

$$\text{RSS}_R = \|\mathbf{P}_{S_1}^\perp \mathbf{x}\|^2 = \|z_2\|^2 + \|z_\perp\|^2. \quad (9.150)$$

Therefore, the extra sum of squares, resulting from potential underfitting, is

$$\text{RSS}_{\text{extra}} \triangleq \text{RSS}_R - \text{RSS}_F = \|z_2\|^2. \quad (9.151)$$

We note that if H_0 is true ($\mathbf{a}_2 = \mathbf{0}$) most of the variability in \mathbf{x} should be explained by the reduced model and hence RSS_R and RSS_F should be close in value, forcing $\|z_2\|^2$ to be small. On the other hand, if H_1 is true, we expect the extra sum of squares $\|z_2\|^2$ to assume relatively large values. Thus, it is natural to form a test comparing $\text{RSS}_{\text{extra}}$ to RSS_F in some way. Again for reasons to be seen shortly, we use as a test the ratio

$$F_R \triangleq \frac{(\text{RSS}_R - \text{RSS}_F)/(m_2)}{\text{RSS}_R/(p-m)}. \quad (9.152)$$

The dimensions used for normalization can be easily obtained from the geometrical construction in Figure 9.14.

In the remaining of this section we shall derive the distribution of the random variables F and F_R used to implement the tests (9.148) and (9.152). These distributions are required to determine the significance of each hypothesis.

To understand the range of values taken by the F and F_R tests, we recall that

$$E(\|z_0\|^2)/m = \sigma^2 + \|\mathbf{R}\mathbf{a}\|^2 \quad (9.153)$$

$$E(\|z_2\|^2)/m_2 = \sigma^2 + \|\mathbf{R}_{22}\mathbf{a}_2\|^2/m_2 \quad (9.154)$$

$$E(\|z_\perp\|^2)/(p-m) = \sigma^2. \quad (9.155)$$

We note that the first and third quantities are equal when $\mathbf{a} = \mathbf{0}$. Thus, we intuitively expect that the ratio

$$F = \frac{\|z_0\|^2/m}{\|z_\perp\|^2/(p-m)} = \frac{\|\mathbf{P}_S \mathbf{x}\|^2/m}{\|\mathbf{P}_S^\perp \mathbf{x}\|^2/(p-m)} \quad (9.156)$$

should have a value close to one when $\mathbf{a} = \mathbf{0}$ and larger than one when $\mathbf{a} \neq \mathbf{0}$. Thus, if the observed value of the ratio (9.156) is larger than one, then it is likely that at least one $a_k \neq 0$.

To decide which hypothesis to choose, we need to compare F to a threshold η . The selection of the threshold requires the distribution of the random variable F . Using the definition of chi-squared distribution, we can show that

$$z_0 \sim N_m(\mathbf{R}\mathbf{a}, \sigma^2 \mathbf{I}) \Rightarrow \frac{\|z_0\|^2}{\sigma^2} \sim \chi_m^2(\delta_F), \quad \delta_F \triangleq \frac{1}{\sigma^2} \|\mathbf{R}\mathbf{a}\|^2, \quad (9.157)$$

$$z_2 \sim N_{m_2}(\mathbf{R}_{22}\mathbf{a}_2, \sigma^2 \mathbf{I}) \Rightarrow \frac{\|z_2\|^2}{\sigma^2} \sim \chi_{m_2}^2(\delta_R), \quad \delta_R \triangleq \frac{1}{\sigma^2} \|\mathbf{R}_{22}\mathbf{a}_2\|^2, \quad (9.158)$$

$$z_{\perp} \sim N_{p-m}(\mathbf{0}, \sigma^2 \mathbf{I}) \Rightarrow \frac{\|z_{\perp}\|^2}{\sigma^2} \sim \chi_{p-m}^2(0). \quad (9.159)$$

Since the random vectors z_0 and z_{\perp} are statistically independent, using the definition of the F-distribution from (7.88), we conclude that

$$F \sim F_{m,p-m}(\delta_F), \quad (9.160)$$

where $\delta_F = 0$ under H_0 and $\delta_F > 0$ under H_1 . The non-centrality parameter (9.157) also indicates that the observed value of F should be larger than one if $\mathbf{a} \neq \mathbf{0}$. Clearly (9.156) is a test statistic because it has a fully known distribution under the H_0 hypothesis. Therefore, to test the hypothesis $H_0 : \mathbf{a} = \mathbf{0}$, compute the test statistics F and reject H_0 if $F > \eta$; the threshold η is determined by the $(1 - \alpha)$ percentile of the central F distribution (9.160). Typically, we use $\alpha = 0.05$ which corresponds to a 95 percent percentile. This procedure is called the *F-test* because (9.160) follows an F distribution.

Inspection of (9.154) and (9.155) shows that their left-hand sides are equal when $\mathbf{a}_2 = \mathbf{0}$. Therefore, it is reasonable to use a test statistic based on the ratio

$$F_R = \frac{\|z_2\|^2/m_2}{\|z_{\perp}\|^2/(p-m)} = \frac{(\|\mathbf{P}_{S_1}^{\perp} \mathbf{x}\|^2 - \|\mathbf{P}_S^{\perp} \mathbf{x}\|^2)/m_2}{\|\mathbf{P}_S^{\perp} \mathbf{x}\|^2/(p-m)}. \quad (9.161)$$

It is easy to see that if H_0 is true, the ratio F_R should assume a value near one. However, if H_0 is not true, the numerator (9.154) should be larger than σ^2 , producing a ratio F_R that exceeds one. Thus, the hypothesis $H_0 : \mathbf{a}_2 = \mathbf{0}$ should be rejected for large values of the test statistic.

Since the vectors z_2 and z_{\perp} are statistically independent, we can easily see that

$$F_R \sim F_{m_2,p-m}(\delta_R). \quad (9.162)$$

The non-centrality parameter $\delta_R = 0$ under H_0 and $\delta_R > 0$ under H_1 . The F-ratio test defined by (9.161) is known as the *partial F-test*.

To provide a geometrical interpretation of the F-tests we refer to Figure 9.14. The full F-test is related to the cotangent of the angle ϕ formed by the observation \mathbf{x} and its orthogonal projection onto the full model subspace, that is,

$$\frac{p-m}{m} F = \frac{\|\mathbf{P}_S \mathbf{x}\|^2}{\|\mathbf{P}_S^{\perp} \mathbf{x}\|^2} = \left(\frac{\text{OF}}{\text{TF}} \right)^2 = \cot^2 \phi. \quad (9.163)$$

The partial F-test is related to the tangent of the angle θ formed by the orthogonal projections of \mathbf{x} onto the reduced and full model subspaces, that is,

$$\frac{p-m}{m_2} F = \frac{\|\mathbf{P}_{S_1}^\perp \mathbf{x}\|^2 - \|\mathbf{P}_S^\perp \mathbf{x}\|^2}{\|\mathbf{P}_S^\perp \mathbf{x}\|^2} = \left(\frac{RF}{TF} \right)^2 = \tan^2 \theta. \quad (9.164)$$

Equivalent tests can be developed using the cosine of angles ϕ or θ . The corresponding random variables follow beta distributions (Hocking, 1996). We limit our attention to the most widely used F-test form.

To test for a single coefficient a_k , we set $m_2 = 1$ and rearrange the variables to make a_k the last component of \mathbf{a} . Then, we have $\mathbf{a}_2 = a_k$ and $r_{22}\hat{a}_k = z_2$. Thus,

$$F_R = \frac{z_2^2}{\|\mathbf{z}_\perp\|^2/(p-m)} = \frac{\hat{a}_k^2}{\hat{\sigma}_u^2/r_{22}^2} \sim F_{1,p-q}(\delta). \quad (9.165)$$

Since $\text{cov}(\hat{\mathbf{a}}) = \sigma^2(\mathbf{S}^T \mathbf{S})^{-1}$, we have $\text{var}(\hat{a}_k) = \sigma^2 \gamma_{kk}$, where γ_{kk} is the k th diagonal element of $(\mathbf{S}^T \mathbf{S})^{-1}$. From the partitioning (9.136) we conclude that $\gamma_{kk} = 1/r_{22}^2$. Therefore, $\hat{\sigma}_u^2/r_{22}^2$ provides an estimate of $\text{var}(\hat{a}_k)$. Since $F_{1,v} = t_{1,v}^2$, we can also test H_0 using the following *t-test*

$$t_R = \frac{z_2}{\|\mathbf{z}_\perp\|/\sqrt{p-m}} = \frac{\hat{a}_k}{\sqrt{\text{var}(\hat{a}_k)}} \sim t_{1,p-m}(\delta_R). \quad (9.166)$$

The advantage of the t-test is that it is two-sided: that is, the algebraic sign of the t-statistic is indicative of the sign of a_k ; the F-test is always positive and gives an indication only of whether or not a_k differs from 0. The t-tests (9.166) must be interpreted with caution because they indicate the need to include a_k in the model that already contains all the other parameters.

9.13

Model Selection Criteria

In model selection there are two problems: (a) assigning a “score” to each model which measures, according to some criterion, how good the model is, and (b) searching through all the models to find the model with the best score.

We start with a discussion of criteria for model selection. We recall that choosing a linear model that includes only a subset of the available variables involves compromise between two conflicting objectives. First, we wish to include as many variables as possible to avoid introducing bias into the estimates of the coefficients of retained variables and the output. Second, we want as few variables as possible because the variance of the estimated coefficients and the complexity of the model increase as their number increases. Thus, the more parameters there are in the model, the better the fit. We could obtain a perfect fit if we had a separate parameter for each data point, but this model would not have any explanatory value. There is always going to be a trade-off between the goodness of fit and the number of parameters required by parsimony. Therefore, most model selection criteria include two components:

$$\text{Lack of fit} + \text{Complexity penalty.} \quad (9.167)$$

The first term in (9.167) measures the fit of the model and the second measures the complexity of the model. These criteria can be used to select among a set of models with different numbers of variables. We next discuss three model selection criteria that are used in many practical applications.

The first criterion, introduced by Mallows (Montgomery et al., 2012), uses an estimate of the mean square prediction error. Suppose that we try to predict the mean value $E(\mathbf{x}) = \mathbf{Sa}$ using the reduced model $\hat{\mathbf{x}} = \mathbf{S}_1 \hat{\mathbf{a}}_1$ (see Section 9.11). The expected mean square error is given by (see Problem 6)

$$\begin{aligned}\Gamma &= E[(\hat{\mathbf{x}} - E(\mathbf{x}))^2] \\ &= E[(\mathbf{S}_1 \hat{\mathbf{a}}_1 - \mathbf{Sa})^T (\mathbf{S}_1 \hat{\mathbf{a}}_1 - \mathbf{Sa})] \\ &= E(\mathbf{x}^T \mathbf{P}_{S_1} \mathbf{x}) - 2\mathbf{a}^T \mathbf{S}^T \mathbf{P}_{S_1} \mathbf{Sa} + \mathbf{a}^T \mathbf{S}^T \mathbf{S} \mathbf{a}.\end{aligned}\quad (9.168)$$

Using the next identity for the expectation of quadratic forms (Seber and Lee, 2003)

$$E(\mathbf{x}^T \mathbf{A} \mathbf{x}) = \text{tr}[\text{Acov}(\mathbf{x})] + E(\mathbf{x})^T \mathbf{A} E(\mathbf{x}), \quad (9.169)$$

we obtain the following relationship

$$E(\mathbf{x}^T \mathbf{P}_{S_1} \mathbf{x}) = \sigma^2 m_1 + \mathbf{a}^T \mathbf{S}^T \mathbf{P}_{S_1} \mathbf{S} \mathbf{a}. \quad (9.170)$$

Substitution of (9.170) to (9.169) yields

$$\Gamma = \sigma^2 m_1 + \mathbf{a}^T \mathbf{S}^T \mathbf{P}_{S_1}^\perp \mathbf{S} \mathbf{a}, \quad (9.171)$$

where m_1 is the order of the reduced model. Using (9.170) we can express the RSS of the reduced model as

$$E[\text{RSS}(m_1)] = E(\mathbf{x}^T \mathbf{P}_{S_1}^\perp \mathbf{x}) = \sigma^2 (p - m_1) + \mathbf{a}^T \mathbf{S}^T \mathbf{P}_{S_1}^\perp \mathbf{S} \mathbf{a}. \quad (9.172)$$

Substitution of (9.172) into (9.171) yields the desired formula

$$\Gamma = E[\text{RSS}(m_1)] + (2m_1 - p)\sigma^2. \quad (9.173)$$

To compute (9.173) we need an unbiased estimate of σ^2 . We typically use the estimate $\hat{\sigma}^2$ from the full model. Then, starting with (9.173), we obtain

$$\frac{\hat{\Gamma}}{\hat{\sigma}^2} = \frac{\text{RSS}(m_1)}{\hat{\sigma}^2} + (2m_1 - p). \quad (9.174)$$

If the reduced model is correct, using (9.90) we obtain $\hat{\sigma}^2 = \text{RSS}(m_1)/(p - m_1)$. In this case we have $\hat{\Gamma}/\hat{\sigma}^2 \approx m_1$, which is the correct model order. Formula (9.174) is the original expression for the *Mallow criterion*. To simplify notation and for consistency with the other criteria we discuss, we denote the order of the fitted model by m and the order of the full model by m_0 . This yields the following form of Mallow's criterion:

$$C_m = \frac{\text{RSS}(m)}{\hat{\sigma}^2} + (2m - p), \quad (9.175)$$

where $\hat{\sigma}^2$ is obtained from the full model. Comparison of (9.175) with (9.167) shows the trade-off between model fit and model complexity. The other two criteria are modifications of (9.175); however, their theoretical justification and derivations are quite different.

The *Akaike Information Criterion (AIC)* is based on the idea of a discrepancy between the true distribution of the data and the distribution specified by the candidate model (Hastie et al., 2009). Among the several forms of the criterion, we have chosen the following:

$$\text{AIC} = \frac{\text{RSS}(m)}{\hat{\sigma}^2} + 2m. \quad (9.176)$$

We note that in this case, the AIC is very similar to C_m .

The last type of criterion, known as the *Bayesian Information Criterion (BIC)*, is given by (Hastie et al., 2009)

$$\text{BIC} = p \ln(\text{RSS}(m)/p) + m \ln p. \quad (9.177)$$

The BIC is similar to AIC but the penalty is more severe; thus, the BIC tends to choose simpler models. This criterion is based on a Bayesian framework and it is used to determine the posterior model probability in Bayesian model averaging applications (see Section 9.14.2).

We can use any of the discussed criteria to score all possible models and choose the model with the biggest score. However, if the maximum value of m is large, searching through all 2^m models is infeasible. One common method is to use stepwise regression (Draper and Smith, 1998). Stepwise regression can be run backward, forward, or in both directions. In forward stepwise regression, we start with no endmembers in the model. We then add the one endmember that leads to the best score. We continue adding endmembers one at a time this way. Backwards stepwise regression is the same except that we start with the biggest model and drop one variable at a time. Both are greedy searches and neither is guaranteed to find the model with the best score.

9.14

Variable Selection in Linear Signal Models

Consider the linear signal model (see Section 9.12)

$$\mathbf{x} = \mathbf{S}\mathbf{a} + \mathbf{e}, \quad \mathbf{e} \sim N(\mathbf{0}, \sigma^2 \mathbf{I}), \quad (9.178)$$

where \mathbf{x} is a $p \times 1$ vector, \mathbf{S} is a $p \times m$ matrix, \mathbf{a} is a $m \times 1$ vector, and \mathbf{e} is a $p \times 1$ normal vector with uncorrelated components having zero mean and equal variance.

As we saw in Section 9.10, under fitting leads to bias while over fitting inflates variance. Linear signal modeling or linear regression usually has two goals, predicting future observations and studying the relationship between the response \mathbf{x} and the predictors s_1, \dots, s_m . The latter goal, which is related to model interpretation, is usually accomplished through variable selection (see Section 9.12). In this section we introduce two additional variable selection techniques that are useful in hyperspectral imaging applications.

9.14.1

Least Absolute Shrinkage and Selection Operator (LASSO)

We saw in Section 9.10 that $E(\|\hat{\mathbf{a}}\|^2) \geq \|\mathbf{a}\|^2$ despite that the LS estimator $\hat{\mathbf{a}} = (\mathbf{S}^T \mathbf{S})^{-1} \mathbf{S}^T \mathbf{x}$ is unbiased for \mathbf{a} . To control the length of $\hat{\mathbf{a}}$ we consider the ridge regression estimator obtained by solving the following constrained LS problem

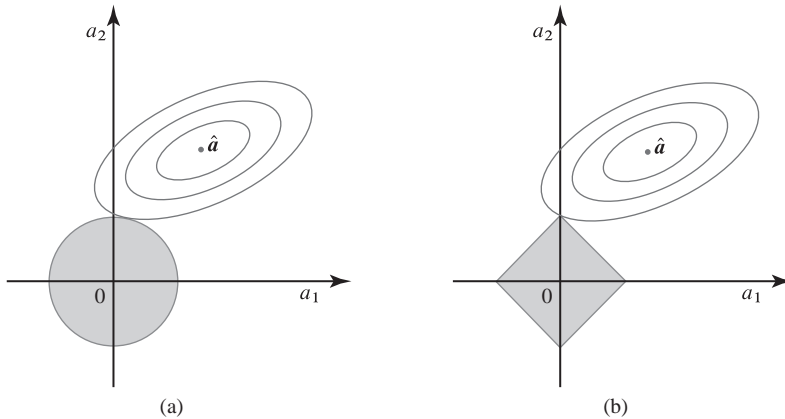


Figure 9.15 Illustration of shrinkage estimators in the two-dimensional case: (a) ridge estimator and (b) LASSO estimator.

$$\min_{\mathbf{a}} \|\mathbf{x} - \mathbf{S}\mathbf{a}\|^2 \quad \text{subject to} \quad \|\mathbf{a}\|^2 \leq \eta^2, \quad (9.179)$$

where η is a constant specified by the user. To gain insight into this problem, we first observe that

$$\|\mathbf{x} - \mathbf{S}\mathbf{a}\|^2 = \|\mathbf{x} - \mathbf{S}\hat{\mathbf{a}} + \mathbf{S}\hat{\mathbf{a}} - \mathbf{S}\mathbf{a}\|^2 \quad (9.180)$$

$$= \|\mathbf{x} - \mathbf{S}\hat{\mathbf{a}}\|^2 + (\mathbf{a} - \hat{\mathbf{a}})^T \mathbf{S}^T \mathbf{S} (\mathbf{a} - \hat{\mathbf{a}}), \quad (9.181)$$

where the first term does not involve \mathbf{a} . Thus, we can rewrite the optimization problem (9.179) as

$$\min_{\mathbf{a}} (\mathbf{a} - \hat{\mathbf{a}})^T \mathbf{S}^T \mathbf{S} (\mathbf{a} - \hat{\mathbf{a}}) \quad \text{subject to} \quad \|\mathbf{a}\|^2 \leq \eta^2. \quad (9.182)$$

The objective function is a hyperellipsoid centered at the LS estimate $\hat{\mathbf{a}}$, while the constraint is a disc centered at the origin. A graphical illustration for the two-dimensional case is given in Figure 9.15(a). The solution is where the elliptical contours touch the boundary of the constraint disk. The solution of (9.179) is the ridge regression estimator discussed in Section 9.10. One drawback of the ridge approach is that, unlike variable selection, it retains all variables in the model, thus sacrificing the possibility of a simple model with fewer variables.

An alternative to ridge regression that also can lead simpler models is the LASSO, a relatively recent approach introduced by Tibshirani (1996). The LASSO solves the following constrained LS problem:

$$\min_{\mathbf{a}} \|\mathbf{x} - \mathbf{S}\mathbf{a}\|^2 \quad \text{subject to} \quad \|\mathbf{a}\|_1 \triangleq \sum_{i=1}^m |a_i| \leq \eta^2. \quad (9.183)$$

Comparing (9.183) to (9.179), we see that the LASSO and ridge regression have similar formulations. The only difference is that the Euclidean norm or ℓ_2 constraint $\|\mathbf{a}\|^2 \triangleq \sum_{i=1}^m |a_i|^2$ has been replaced by the ℓ_1 norm $\|\mathbf{a}\|_1 \triangleq \sum_{i=1}^m |a_i|$. Solving (9.183) is equivalent to minimizing the Lagrangian function

$$\min_{\mathbf{a}} \|\mathbf{x} - \mathbf{S}\mathbf{a}\|^2 + \lambda \|\mathbf{a}\|_1 \quad (9.184)$$

for a value of λ determined by the value of η . In other words, for every value of η , there is some value of λ such that (9.183) and (9.184) have the same solution. In the two-dimensional case, the constraint $|a_1| + |a_2| \leq \eta^2$ requires that the LASSO estimated coefficients must lie inside the diamond area shown in Figure 9.15(b). Therefore, the LASSO shrinks the estimated coefficients like ridge regression. In contrast, the LASSO constraint has corners at each of the axes, and this results in a fundamental difference between the two estimators. The solution of each problem is determined by the first point at which an elliptical contour contacts the constrain region. Since spherical constraints do not have corners, the intersection will not generally occur on an axis, and the ridge regression coefficients will be exclusively nonzero. However, the LASSO constraint has corners at each axis, and often some elliptical contour will intersect one of the corners. In Figure 9.15(b), the intersection occurs at $a_1 = 0$, and so the resulting model will only include the coefficient a_2 . For $m = 3$ the constraint region becomes a polyhedron, and for $m > 3$ becomes a polytope. The increased number of corners implies that it is possible for more coefficients to be assigned the value zero. This property makes LASSO a variable selection algorithm and justifies the choice of its name. More details about LASSO and its application in variable selection are provided by James et al. (2013). An efficient implementation of LASSO using a coordinate descent algorithm is described by Friedman et al. (2010); software implementations in MATLAB and R are provided by Qian et al. (2013).

To understand the nature of LASSO we note that, like the ridge estimator, it produces a different set of coefficients for each value of λ . Selecting a good value for λ is critical and it is usually done using cross-validation (James et al., 2013). Figure 9.16 shows the ridge and LASSO coefficients, as a function of tuning parameter λ , for a linear model with $m = 10$ variables and only three nonzero coefficients (see Problem 8 for details). For $\lambda = 0$ both approaches yield the LS coefficients; however, as we increase λ the coefficients shrink, and for very large values of λ are essentially zero. Between these

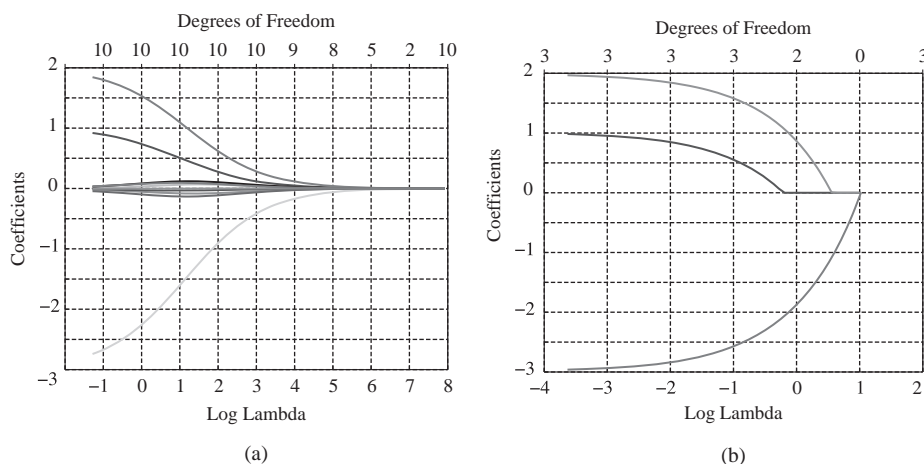


Figure 9.16 Plots of ridge regression coefficients (a) and LASSO coefficients (b) as a function of λ . Note the shrinkage of the coefficients with increasing λ .

two extremes the ridge regression and LASSO models have quite different behavior. Indeed, careful inspection of these plots shows the variable selection potential of the LASSO model. The ridge regression model always includes all variables; in contrast, the LASSO model selects different parameters depending on the value of λ . This example illustrates the basic concepts; a detailed account of the practical issues encountered in practical applications is provided in (Hastie et al., 2009; James et al., 2013).

A review of advancements in regression shrinkage and variable selection via the LASSO, including a detailed bibliography, is given by Tibshirani (2011).

9.14.2 Bayesian Model Averaging

We shall now discuss a Bayesian approach used to address model uncertainty, known as *Bayesian Model Averaging (BMA)*, and describe its use for variable selection in the linear model. BMA has a rich theoretical background and has been used in many applications (Hoeting et al., 1999; Raftery, 1995; Kass and Raftery, 1995). Although our treatment of BMA is at a simplified level, we provide sufficient information for its implementation and practical application.

Consider the linear model (9.178) which includes m variables. If we define a model for each possible subset of the m variables, there are $K = 2^m$ possible models $\mathcal{M} = \{M_1, \dots, M_K\}$, including the model with no variables at all. Models for different subsets may be represented by a vector of binary variables, $\gamma = [\gamma_1, \dots, \gamma_m]^T$, where γ_j is an indicator for the inclusion of s_j under model M_k . Under M_k there are $m_k = \sum_{j=1}^m \gamma_j$ nonzero parameters, \mathbf{a}_k , with a $p \times m_k$ spectral matrix S_k ; the model is specified by $\mathbf{x} = S_k \mathbf{a}_k + \mathbf{e}$.

To create a probabilistic setup for model uncertainty, suppose that a set of models $\mathcal{M} = \{M_1, \dots, M_K\}$ are under consideration for modeling a data set D obtained by the following three-stage data generation process:

1. Choose a model M_k with probability $P(M_1), \dots, P(M_K)$;
2. Generate a parameter vector \mathbf{a}_k from the conditional distribution $f(\mathbf{a}_k | M_k)$;
3. Generate the data D from the conditional distribution $f(D | \mathbf{a}_k, M_k)$.

The Bayesian approach proceeds by assigning a prior density $f(\mathbf{a}_k | M_k)$ to the parameters of each model, and a prior probability $P(M_k)$ to each model. There are two problems of interest: model selection and model averaging.

Model selection means to find the model $M_k \in \mathcal{M}$ that actually generated the data. We first note that the posterior probability for model M_k can be evaluated using Bayes' theorem (Papoulis and Pillai, 2002) by the formula

$$P(M_k | D) = \frac{f(D | M_k)P(M_k)}{\sum_{i=1}^K f(D | M_i)P(M_i)}, \quad (9.185)$$

where $f(D | M_k)$ is the integrated likelihood of model M_k given by

$$f(D | M_k) = \int f(D | \mathbf{a}_k, M_k) f(\mathbf{a}_k | M_k) d\mathbf{a}_k. \quad (9.186)$$

Bayesian model selection proceeds by choosing the most probable M_k : that is, the model for which $P(M_k|D)$ is largest. The major practical challenges with this approach are the specification of priors and the multidimensional integration required to evaluate (9.186). Conventional numerical integration techniques are not much help in this situation, but recently, specialized methods have been introduced to cope with this problem. In particular, the Laplace approximation, importance sampling, and Markov chain Monte Carlo techniques have all proved quite effective (Evans and Swartz, 2000).

We next turn our attention to model averaging. If Q is a quantity of interest, for example, a future observation or a model parameter, all information about Q given the data D is included in the posterior distribution

$$f(Q|D) = \sum_{k=1}^K P(M_k|D) f(Q|D, M_k). \quad (9.187)$$

Note that the posterior of Q is found by taking an average of the posterior distributions under each candidate model, weighted by the posterior model probabilities.

Under the mean squared error criterion, the best prediction of Q based on the data D is the overall posterior mean (Van Trees et al., 2013) given by

$$\begin{aligned} E(Q|D) &= \int Q \left[\sum_{k=1}^K P(M_k|D) f(Q|D, M_k) \right] dQ \\ &= \int \left[\sum_{k=1}^K Q f(Q|D, M_k) dQ \right] P(M_k|D) \\ &= \sum_{k=1}^K E(Q|D, M_k) P(M_k|D), \end{aligned} \quad (9.188)$$

where $\hat{Q}_k \triangleq E(Q|D, M_k)$ is the best prediction under M_k .

Since \hat{Q} is a Bayesian point estimator, a Bayesian analog of the standard error is provided by the following conditional variance (Raftery, 1995):

$$\text{var}(Q|D) = \sum_{k=1}^K [\text{var}(Q|D, M_k) + \hat{Q}_k^2] P(M_k|D) - [E(Q|D)]^2. \quad (9.189)$$

Implementation of BMA is difficult for two reasons. First, the integrals in (9.186) can be hard to compute. Second, the number of terms in (9.187) can be enormous. Kass and Raftery (1995) provide a discussion of various approaches to evaluate (9.186), including the Laplace method of approximation. However, a powerful result relating the posterior $P(M_k|D)$ to the Bayesian Information Criterion leads to practically feasible approaches for model selection and averaging.

In large-sample settings, it turns out that the quantity $-2 \log P(M_k|D)$ can be approximated by the Bayesian Information Criterion (see Section 9.13):

$$\text{BIC}_k = -2 \log L(\hat{\alpha}_k|D) + m_k \log p, \quad (9.190)$$

where $\hat{\mathbf{a}}_k$ is the maximum likelihood estimate of \mathbf{a}_k , m_k is the number of parameters, and p is the number of observations (Neath and Cavanaugh, 2012). The preceding implies that in large-sample settings, the following proportionality holds approximately

$$P(M_k|D) \propto \exp\{(-1/2)[-2 \log L(\hat{\mathbf{a}}_k|D) + m_k \log p]\} \quad (9.191)$$

$$= \exp\{(-1/2) \text{BIC}_k\}. \quad (9.192)$$

Thus, in large-sample settings, we can approximate the posterior $P(M_k|D)$ by

$$P(M_k|D) = \frac{\exp(-\text{BIC}_k/2)}{\sum_{i=1}^K \exp(-\text{BIC}_i/2)}. \quad (9.193)$$

The main advantage of using the BIC to approximate the posterior probability is its computational simplicity. The process of model averaging is seen to improve estimation and prediction (Hoeting et al., 1999).

Consider now the linear regression model M_k defined by

$$\mathbf{x} = S_k \mathbf{a}_k + \mathbf{e}, \quad \mathbf{e} \sim N(\mathbf{0}, \sigma^2 \mathbf{I}), \quad (9.194)$$

where m_k is the number of parameters and p the number of observations. The BIC for the linear regression model (9.194) is easily evaluated by

$$\text{BIC}_k = p \log(\text{RSS}_k/n) + m_k \log p, \quad (9.195)$$

where

$$\text{RSS}_k = (\mathbf{x} - S_k \hat{\mathbf{a}}_k)^T (\mathbf{x} - S_k \hat{\mathbf{a}}_k) \quad (9.196)$$

is the sum of squared residuals and $\hat{\mathbf{a}}_k$ the maximum likelihood estimate of \mathbf{a}_k .

In Section 9.13 we discussed the use of BIC for subset variable selection in linear models. We now discuss the use of BMA to determine the presence of variables in a linear regression model. To this end, consider the event

$$A = \{\text{the } j\text{th variable } s_j \text{ is present in the model}\}. \quad (9.197)$$

The probability of the event A is given by

$$P(A) = \sum_{k=1}^K I(A \in M_k) P(M_k|D), \quad (9.198)$$

where $I(\cdot)$ is one if its argument is true. We can use the quantities $f(Q|D)$, $E(Q|D)$, and $\text{var}(Q|D)$ to make inference about A , including testing, point estimation, and approximate interval estimation (Viallefont et al., 2001).

9.15 Linear Spectral Mixture Analysis in Practice

The LMM is a physics-based model that transforms radiance or reflectance values to physical variables, which are linked to the subpixel abundances of EMs within each pixel. Thus, we can view SMA as a physics-based transformation from spectral-space to fraction-space. In this respect, all the strengths of SMA depend on the accuracy of

EM selection; therefore, we must always keep in mind that if the EMs are incorrect in a physical sense, then the fractional abundances are also incorrect (and potentially meaningless) and SMA becomes little more than another statistical transform or basis representation of the data (Tompkins et al., 1997).

If we use the same set of EMs for all pixels of a hyperspectral imaging cube, we have the following set of LMM equations

$$\mathbf{x}_k = \sum_{i=1}^m a_{ik} \mathbf{s}_i + \mathbf{e}_k = \mathbf{S} \mathbf{a}_k + \mathbf{e}_k, \quad k = 1, 2, \dots, N, \quad (9.199)$$

where N is the number of pixels. These equations can be compactly written as

$$\begin{aligned} [\mathbf{x}_1 \dots \mathbf{x}_N] &= \mathbf{S} [\mathbf{a}_1 \dots \mathbf{a}_N] + [\mathbf{e}_1 \dots \mathbf{e}_N], \\ \mathbf{X}^T &= \mathbf{S} \mathbf{A} + \mathbf{E}^T, \end{aligned} \quad (9.200)$$

where the rows of \mathbf{X} contain the spectra of the data cube. From a computational perspective, the basic task in SMA is to determine the matrices \mathbf{S} and \mathbf{A} from the data matrix \mathbf{X} . We display the results using EM spectral plots and *fraction images*: that is, images that show the fraction of each EM for each pixel of the data cube. The inputs and outputs of the SMA process are illustrated in Figure 9.17. We emphasize that proper use of SMA requires knowledge of the physical aspects of the application, understanding how the results will be used, and experience. Dealing with real data will quickly reveal that the mathematical aspects of LMM algorithms are easier to grasp and handle compared to the interpretation of the results.

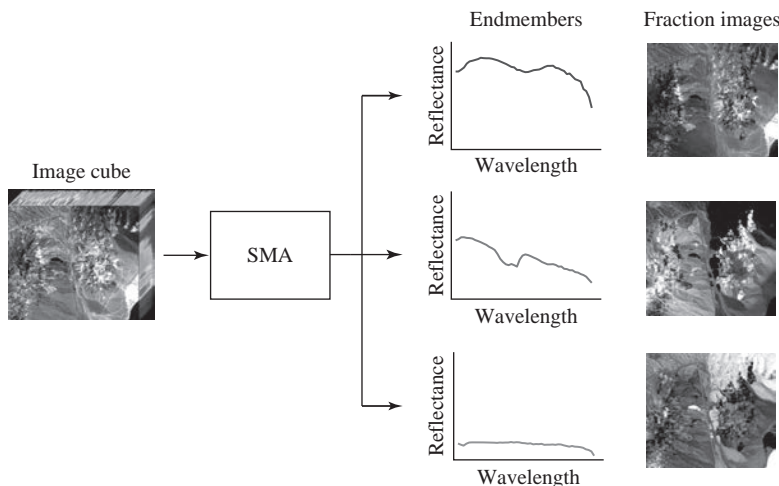


Figure 9.17 Illustration of SMA as a transformation from *spectral-space* to *fraction-space*. The input is a data cube and the output a set of EMs with the corresponding fraction images.

9.15.1 Finding Endmembers

The first step in SMA is to find “good” EMs, which are typically determined from the image data. Most EM-finding algorithms use brute force exhaustive search methods to check whether each new pixel can be described as a mixture of spectra from previously tested pixels; if not, the new pixel represents a new EM. Experienced spectroscopists can identify EMs using reference spectral libraries; however, this approach requires atmospherically compensated data.

For the purpose of SMA, we define “spectral EMs” simply as spectra that are constituent parts of a spectral mixture (Adams and Gillespie, 2006). Therefore, to be a useful EM a spectrum must mix with one or more other spectra, must have physical meaning, and must help us to interpret a spectral image. For example, the spectrum of a body of water is distinct and “pure” (not a mixture), but it may not be a useful EM for the rest of the image, because pixels with water occur only locally. EM spectra must be spectrally distinct from one another because collinear, that is, linearly dependent EMs lead to numerically unstable unmixing methods. However, mimicking among spectra and their mixtures is common in practice. The best way to separate materials from one another and to avoid mimicking is using more spectral bands.

We note that EM spectra are essentially proxies of materials on the ground, and may or may not correspond to “pure” materials. Thus, a significant breakthrough in SMA was the introduction of the *shade* EM, which does *not* correspond to any material, by Adams et al. (1986). In SMA we use the term “shade” to refer to a dark spectral EM that represents shadows and the effect of shading. The shade EM has zero or low values in all channels (bands). A shade EM is necessary to account for spectral variations in illumination caused by topography and surface texture.

The most critical question in SMA is how many EMs to use in the model. Since too many EMs result in large fill-fraction estimation error, we must not use more EMs than necessary. In practice, three to seven EMs are usually adequate to model any given area of an image at a given spatial resolution (Adams et al., 1993). However, this may not be true for complex scenes such as urban areas. Scenes with “large” spectral complexity require too many EMs to construct good mixing models. In such cases it is better to segment the image and use *only* the EMs present in each segment. This approach, which allows EMs to change from segment to segment, helps to develop more complex models to handle the increased variability of natural scenes (Roberts et al., 1998). In the extreme case, we can allow EMs to change from pixel to pixel; however, this makes image interpretation very difficult or impossible.

9.15.2 Unmixing Spectral Images

Once the EMs have been identified we can use them to estimate the fractional abundances or fill-fractions for each pixel. As we recall from Section 9.2, mixed pixels satisfying the constraints $a_k \geq 0$ and $\sum_k a_k = 1$, for all k , have spectra lying inside the simplex defined by the EM spectra. Algorithms enforcing these constraints produce always feasible fill-fraction values even if the model is incorrect; in this respect, they do

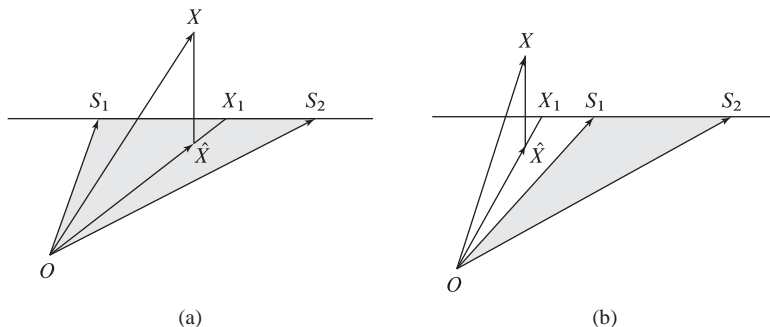


Figure 9.18 The orthogonal projection \hat{X} of mixed spectrum X determines the coefficients of the LMM $\hat{x} = a_1s_1 + a_2s_2$. The line $O\hat{X}$ meets the line S_1S_2 (simplex) at X_1 and defines a model $x_1 = \alpha_1s_1 + \alpha_2s_2$ with $\alpha_1 + \alpha_2 = 1$. The quality of model fit is measured by the angle $XO\hat{X}$. (a) Since S_1 and S_2 are extreme points, $\alpha_1, \alpha_2 > 0$. (b) Since S_1 is not extreme, $\alpha_1 > 0$ but $\alpha_2 < 0$.

not help the analyst to validate or improve the model. If $a_k < 0$ or $a_k > 1$ we have fill-fraction overflow and the resulting mixed spectra lie outside the mixture simplex. This is illustrated in Figure 9.18 for a LMM with two EMs s_1 and s_2 that define the simplex S_1S_2 . Note how the simple normalization $\alpha_k = a_k/(a_1 + a_2)$, $k = 1, 2$, enforces the sum-to-one constraint. We emphasize that there is no analytical way to tell whether the fractions that fall between 0 and 1 are correct.

As we saw in Section 9.7, LS estimators without constraints or with the sum-to-one constraint are unbiased (Settle and Drake, 1993). However, this property is lost when we enforce the nonnegativity constraints. The accuracy of estimated FFs will be highest when the exact number of correct EMs that are required to account for spectral variability are utilized by the model.

- Too few EMs will partition the unmodeled EMs into the modeled ones creating a fraction error and increase the RMS.
- Too many EMs will make the model sensitive to noise, atmospheric distortion, and spectral variability, resulting in fraction errors.

In statistical terms, we wish to keep the number of EMs to a minimum, because the variance of estimated coefficients increases with the number of EMs, even if the number of bands is large. Furthermore, EM variability can be an important consideration when the objective is to estimate fill-fractions, and when we want to assess the detection threshold of a spectrum. Clearly, the required accuracy of fill-fraction estimates depends on the application.

9.15.3 Model Adequacy Checking and Validation

In general, after fitting a model to available data we must deal with two important tasks: *model adequacy checking* and *model validation* (Montgomery et al., 2012). Model adequacy checking includes residual analysis, testing for lack of fit, and other procedures that investigate the fit of the model to the available data. Model validation, which

requires subject-matter expertise, is directed toward determining if the model will function successfully in the intended application. We must emphasize that a model that fits the data well will not necessarily be successful in the final application.

There are several formal statistical procedures that use analysis of residuals or hypotheses tests to check for model adequacy (Montgomery et al., 2012). These tests are used in target detection and gas identification applications (see Chapter 11). However, when we use SMA for image interpretation applications, the main concern is to determine how well the LMM accounts for the actual spectral variability in the acquired scene. We next discuss three ways to address this matter (Adams et al., 1993; Adams and Gillespie, 2006).

First, we compute the spectral residuals separately for each pixel in the scene

$$\hat{e}_k = \mathbf{x}_k - \mathbf{S}\hat{\mathbf{a}}_k, \quad k = 1, 2, \dots, N. \quad (9.201)$$

Since we fit a linear model to each pixel spectrum, the quality of model fitting is measured by the spectral root mean square error

$$\epsilon_k = \left(\frac{1}{p} \sum_{i=1}^p \hat{e}_{ki}^2 \right)^{1/2} = \frac{1}{\sqrt{p}} \|\hat{\mathbf{e}}_k\|, \quad (9.202)$$

which is a measure of the spectral residue that cannot be explained by the mixing model. If we have chosen the appropriate set of EMs the value of the residual will be small. High residual values call attention to pixels that need to be modeled by different sets of EM spectra. Spatial patterns and variability in the root mean square error can be examined by displaying ϵ_k pixel by pixel to form an “error-fit” image. For a “good” model the error-fit image should have “small” values and no visible structure.

Second, we compute, display, and analyze fraction images using topographical and other information. Fraction images allow the analyst to examine variability in the model in a spatial context, apply image interpretation skills, and test the validity of the model using other types of related information.

For a third test we compute and display “fraction overflow” images. As we know, fill-fractions for each pixel in the scene must range from zero to unity. However, if the model is inadequate to describe the variability in the image, the estimated fill-fractions may fall outside this range, even if they sum to unity. Note that this valuable test is not applicable if we enforce the nonnegativity constraint.

There are several reasons for a model failing to fit the data or not accounting for the spectral variation in the data (model inadequacy): (a) some important part of the image, for example another EM, has been missed; (b) one or more of the EMs employed are inappropriate; (c) part of the spectral variation in the image is caused by atmospheric, instrumental, or other effects. We can improve the model by changing the image EMs or selecting one or more additional EMs. Inadequacies due to (c) can be addressed by converting the image cube to reflectance and use “reference EMs” obtained from spectral libraries or laboratory measurements. We emphasize that selecting an LMM that includes only a subset of the available EMs involves compromise between two conflicting objectives. First, we wish to include as many EMs as possible to avoid introducing

bias into the estimates of the coefficients of retained EMs and the output. Second, we want as few EMs as possible because the variance of the estimated coefficients and the complexity of the model increase as their number increases. Some unmixing projects using real and synthetic data are provided in the book website to illustrate the challenges of using unmixing in practical applications.

9.16

Summary and Further Reading

Spectral mixture analysis is essentially an image interpretation technique that produces fraction images corresponding to the abundance of physically meaningful scene materials. SMA works with spectra that mix together to estimate fill-fractions for each pixel in a scene. Therefore, materials that are rare or do not mix are not useful EMs.

Simple scenes with a small number of distinct materials are the exception rather than the rule. Most practical applications deal with complex scenes that contain many spectrally distinct materials and the typical mistake is trying to use too many EMs. The result is a large number of fraction images that are often inaccurate and extremely difficult to interpret. The right number and identity of EMs is usually obtained by trial and error rather than by automated blind unmixing algorithms.

The application of SMA to hyperspectral image interpretation requires deep understanding of phenomenology, appreciation of the potential and limitations of the linear mixing model, and considerable experience with the pertinent application. For every serious user of SMA the material in Adams et al. (1993) and Adams and Gillespie (2006) is required reading.

Problems

1. The file `jasper_lib_info.txt` contains information about the reflectance spectra stored in file `jasper_lib_spectra.txt`. (a) Load the data and reproduce the plot shown in Figure 9.5. (b) Compute the angle between the different pairs of spectra. (c) Compute the angle between the different pairs of zero centered spectra. (d) Compare the results in (b) and (c).
2. In this problem we use the `jasper_lib` spectra to understand the data generated by a fully constrained LMM with uncorrelated additive Gaussian noise. (a) Generate $N = 1000$ mixed pixels with $\sigma^2 = 0.0001$ and $\sigma^2 = 0.01$ and use them to reproduce the results shown in Figures 9.6 and 9.7. Generate the mixing coefficients using a uniform distribution and then enforce the sum-to-one constraint. (b) Compute and plot eigenvectors using the covariance and correlation matrices and compare them with the EMs used in the model. (c) Compare the ranks of the two matrices to the number of EMs.
3. In the presence of noise, estimating material abundance can be problematic. The estimates produced may not satisfy the sum-to-one or nonnegativity constraints. Using

estimation techniques that enforce constraints is tempting, but may introduce bias. In this problem we explore results from several different estimation techniques. For parts (a)–(c), generate synthetic data using a mixture of the first two signatures with $\sigma^2 = 0.01$ and with $\sigma^2 = 0.0001$. Plot the estimates of a and the residual errors. How do the estimates differ with each technique? How does the distribution of the estimated coefficients change?

- (a) Estimate with least squares.
 - (b) Estimate with sum-to-one constraint.
 - (c) Estimate with fully-constrained model.
4. Again, generate mixed spectra but with colored noise. Estimate a using LS and with GLS. What effect does the coloring have on the LS estimates of a ? How do the GLS estimates compare to the LS estimates of the previous question?
 5. Underfitting and overfitting occur when the wrong number of signatures is included in a LMM. For these problems, generate a synthetic spectrum using a mixture with $\mathbf{a}^T = [0.5 \ 0 \ 0 \ 0.5 \ 0]$. Use LS estimation to fit the following four models: (1) the null model, (2) s_1 , (3) s_1s_4 , and (4) $s_1s_3s_4$.
 - (a) Plot the PDF of a chi-squared distribution and the RSS values for each model.
 - (b) Compute and indicate on the plot the value for a significance level of 0.05 to reject the null model. Should we reject the null model?
 - (c) Use the F-test to compare models 2 and 3. Plot the PDF of the F-statistic under the null distribution.
 - (d) Repeat part (c) for models 3 and 4.
 - (e) Use an F-test and a t-test to compare the null model and model 1. What are the differences between the two approaches?
 6. Use the LS solution $\hat{\mathbf{a}}_1 = (\mathbf{S}_1^T \mathbf{S}_1)^{-1} \mathbf{S}_1^T \mathbf{x}$ and the corresponding projection matrix \mathbf{P}_{s_1} to prove equation (9.168).
 7. Illustrate the effects of ridge regression by choosing two of the spectra to be almost collinear. Generate $N = 1000$ mixed spectra of the Live Oak and the Blue Oak signatures with additive noise ($\sigma^2 = 0.01$). Compute estimates of a with the ridge parameter δ^2 set to 0, 0.1 and 100. Plot \hat{a}_2 versus \hat{a}_1 . How do the estimates change with the ridge parameter? Plot \hat{a}_1 versus a_1 . What effect does increasing the ridge parameter have? How does the ridge parameter affect the mean and variance of the RSS values?
 8. Reproduce the paths in Figure 9.16 using a mixture of three spectra. What is the significance of the number of nonzero entries in the LASSO solution? What effect does shrinking the coefficients have on the solution?

10 Signal Detection Theory

Statistical signal detection theory provides a natural framework for the solution of target detection and landscape classification problems. This approach is based on the assumption that the decision problem is posed in probabilistic terms, and that all relevant probability models are known. In this chapter we develop the fundamental theory and algorithms; in Chapter 11 we show how they can be applied to practical hyperspectral target detection and background classification problems. It turns out that most useful algorithms can be explained by simple geometrical arguments, which formalize some intuitive common-sense procedures.

10.1 A Simple Decision-Making Problem

We shall introduce the key terminology and concepts of statistical decision-making theory by means of a simple game of chance involving casting two ordinary dice and one odd die. Each ordinary die has 1 to 6 spots on its sides and the odd die has three sides with three spots on each side and three sides with no spots.

Player A rolls the dice and announces the total number, say x_k , of spots showing on all three dice resulting from the roll to player B, who should guess whether the odd die shows a “3” or a “0.” How should player B play the game? In the context of statistical decision theory, the state of the odd die is specified by the following two *hypotheses*

$$H_0 : \text{ odd die shows a “0”} \quad (10.1a)$$

$$H_1 : \text{ odd die shows a “3”} \quad (10.1b)$$

Player B should choose between the two hypotheses based on the *observed value* x_k provided by player A. To understand the nature of the problem we look at the values assumed by x_k under each hypothesis (see Table 10.1). The symbol $x_k|H_i$ denotes the values taken by x_k when the hypothesis H_i is true. The set of values $\mathcal{R} = \{2, 3, \dots, 15\}$, taken by x_k , is known as the *observation space*. We note that for $x_k = 2, 3, 4$ we can say with certainty that H_0 is true; similarly, for $x_k = 13, 14, 15$ we can accept with certainty that H_1 is true. However, if $x_k = 5, 6, \dots, 12$ it is impossible to choose with certainty between H_0 and H_1 because either hypothesis could have produced these values. The objective of player B is to develop a decision rule that ensures the greatest long-run success in many rolls of the dice. Every *decision rule* partitions the observation space \mathcal{R} into two regions \mathcal{R}_0 and \mathcal{R}_1 such that

Table 10.1 Observations and probabilities under the two states of the odd die.

Quantity	Value													
	2	3	4	5	6	7	8	9	10	11	12	0	0	0
$x_k H_0$	2	3	4	5	6	7	8	9	10	11	12	0	0	0
$x_k H_1$	0	0	0	5	6	7	8	9	10	11	12	13	14	15
x_k	2	3	4	5	6	7	8	9	10	11	12	13	14	15
$P(x_k H_0)$	$\frac{1}{36}$	$\frac{2}{36}$	$\frac{3}{36}$	$\frac{4}{36}$	$\frac{5}{36}$	$\frac{6}{36}$	$\frac{5}{36}$	$\frac{4}{36}$	$\frac{3}{36}$	$\frac{2}{36}$	$\frac{1}{36}$	0	0	0
$P(x_k H_1)$	0	0	0	$\frac{1}{36}$	$\frac{2}{36}$	$\frac{3}{36}$	$\frac{4}{36}$	$\frac{5}{36}$	$\frac{6}{36}$	$\frac{5}{36}$	$\frac{4}{36}$	$\frac{3}{36}$	$\frac{2}{36}$	$\frac{1}{36}$
$\Lambda(x_k)$	0	0	0	$\frac{1}{4}$	$\frac{2}{5}$	$\frac{3}{6}$	$\frac{4}{5}$	$\frac{5}{4}$	$\frac{6}{3}$	$\frac{5}{2}$	$\frac{4}{1}$	∞	∞	∞

$$\text{if } x_k \in \mathcal{R}_0 \Rightarrow \text{choose } H_0 \quad (10.2a)$$

$$\text{if } x_k \in \mathcal{R}_1 \Rightarrow \text{choose } H_1, \quad (10.2b)$$

where the notation $x_k \in \mathcal{R}_i$ denotes that x_k belongs in the set \mathcal{R}_i . We shall use the symbol D_i to indicate that the decision rule chooses the i th hypothesis. The notation $(D_i|H_j)$ will be used to indicate that the decision rule selects the i th hypothesis, given that the j th hypothesis is true. If $i = j$ the decision is correct; if $i \neq j$ the decision is wrong.

To seek an optimal decision rule, we need an appropriate criterion to measure its performance. Once a performance criterion has been chosen, we can use it to develop and evaluate different decision rules. For each performance criterion or metric there is an optimal decision rule that best fulfills the criterion. We emphasize that the term “*optimal decision rule*” means that no other rule can do better on the average. When we consider a small number of decisions, random fluctuations may cause a non-optimal decision rule to do better than the optimum decision rule. However, in the long run the optimum decision rule will have the best performance.

Suppose that the objective of player B is to make as many correct decisions as possible. In the language of probability theory, this means to find a decision rule that minimizes the *probability of error*:

$$P(\text{error}) = P(D_1|H_0)P(H_0) + P(D_0|H_1)P(H_1). \quad (10.3)$$

The quantity $P(H_j)$ is the a priori probability that hypothesis H_j is true, before the observation becomes available. The quantity $P(D_i|H_j)$ is known as the *conditional probability* of deciding D_i given that H_j is true. The two conditional probabilities of error can be expressed as

$$P(D_1|H_0) = P(x_k \in \mathcal{R}_1|H_0) = \sum_{x_k \in \mathcal{R}_1} P(x_k|H_0) \quad (10.4a)$$

$$P(D_0|H_1) = P(x_k \in \mathcal{R}_0|H_1) = \sum_{x_k \in \mathcal{R}_0} P(x_k|H_1), \quad (10.4b)$$

where $P(x_k|H_i)$ is the conditional probability of x_k given that H_i is true. Table 10.1 shows the probabilities $P(x_k|H_i)$ for the different values of x_k under each hypothesis. Substitution of (10.4a) and (10.4b) into (10.3) yields

$$P(\text{error}) = \sum_{x_k \in \mathcal{R}_1} P(x_k | H_0)P(H_0) + \sum_{x_k \in \mathcal{R}_0} P(x_k | H_1)P(H_1). \quad (10.5)$$

To minimize this expression with respect to the regions \mathcal{R}_0 and \mathcal{R}_1 , we compare $P(x_k | H_0)P(H_0)$ and $P(x_k | H_1)P(H_1)$ for each x_k . If $P(x_k | H_0)P(H_0) < P(x_k | H_1)P(H_1)$ we should include x_k into region \mathcal{R}_1 ; otherwise, into region \mathcal{R}_0 . Values of x_k where the two expressions are equal may be assigned arbitrarily. This leads to the following decision rule

$$\text{if } P(x_k | H_0)P(H_0) < P(x_k | H_1)P(H_1) \Rightarrow \text{Choose } H_1 \quad (10.6a)$$

$$\text{if } P(x_k | H_0)P(H_0) > P(x_k | H_1)P(H_1) \Rightarrow \text{Choose } H_0, \quad (10.6b)$$

which is more conveniently written in the following equivalent form

$$\Lambda(x_k) \triangleq \frac{P(x_k | H_1)}{P(x_k | H_0)} \stackrel{H_1}{\gtrless} \eta \triangleq \frac{P(H_0)}{P(H_1)}. \quad (10.7)$$

The quantity $\Lambda(x_k)$ is called *likelihood ratio* (LR) because the value of $P(x_k | H_i)$ provides the likelihood that observation x_k was generated under hypothesis H_i . The decision rule (10.7) makes a decision by comparing the LR $\Lambda(x_k)$ of the observation x_k to a *threshold* η determined by the a priori probabilities. Thus, minimizing the probability of error leads to a *likelihood ratio test* (LRT).

The values of the LR for the dice game are given in Table 10.1. Since the odd die has three sides with three spots and three sides with no spots, we have $P(H_0) = P(H_1) = 1/2$; hence, the threshold is set to $\eta = 1$. It can be easily seen that any other choice for the threshold increases the probability of error. Suppose now that we alter the game by using an odd die which has two sides with three spots and four sides with no spots. In this case $P(H_0) = 2/3$ and $P(H_1) = 1/3$, which yields $\eta = 2$. We note that as $P(H_1)$ increases, a smaller and smaller LR is required for H_1 to be chosen.

The important point here is that the conditional probabilities determine the likelihood ratio and the a priori probabilities the threshold; both are required by the LRT (10.7). If the a priori probabilities $P(H_0)$ and $P(H_1)$ are *not* available, it is impossible to derive an optimal decision rule that minimizes the probability of error (10.5); in such cases, we must use alternative criteria based on the conditional probabilities $P(D_i | H_i)$.

10.2

Elements of Statistical Hypotheses Testing

The material in this section will lay the groundwork for many of the detection and classification algorithms used in hyperspectral imaging.

Suppose that we must choose between two hypotheses H_0 and H_1 based on p observations x_1, x_2, \dots, x_p , which are concisely represented by a vector \mathbf{x} . These observations may represent successive measurements of the same physical parameter, the simultaneous measurement of p different parameters, or any combination of these possibilities. In the statistical literature H_0 is known as the null hypothesis and H_1 as the alternative hypothesis. We adopt the radar literature terminology where H_0 is called the “target

Table 10.2 Possible outcomes for a detection algorithm; the radar-inspired terminology is enclosed in parentheses.

State of Nature		
Decision	H_0 true (target absent)	H_1 true (target present)
Choose H_0	Correct (Rejection)	Type II error (Miss)
Choose H_1	Type I error (False Alarm)	Correct (Detection)

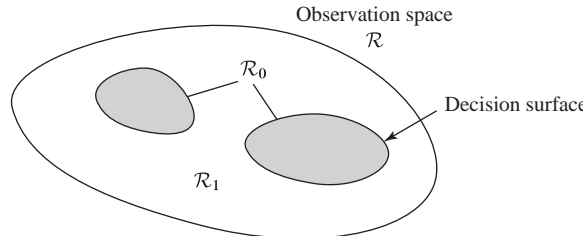


Figure 10.1 Illustration of decisions and decision surfaces in two dimensions.

“absent” hypothesis and H_1 is known as the “target present” hypothesis. In summary, we have

$$H_0 : \text{ Null hypothesis (target absent)}$$

$$H_1 : \text{ Alternative hypothesis (target present).}$$

A test of H_0 against H_1 has four possible outcomes, two of which are correct and two of which are incorrect; these outcomes are shown schematically in Table 10.2.

The design of a decision rule starts with the adoption of a probability density model that describes the distribution of the observation vector \mathbf{x} under each of the two hypotheses:

$$H_0 : \mathbf{x} \sim f(\mathbf{x}|H_0) \triangleq f_0(\mathbf{x}) \quad (\text{Target absent}) \quad (10.8a)$$

$$H_1 : \mathbf{x} \sim f(\mathbf{x}|H_1) \triangleq f_1(\mathbf{x}) \quad (\text{Target present}). \quad (10.8b)$$

We assume that both hypotheses are *simple*; that is, the density functions $f_0(\mathbf{x})$ and $f_1(\mathbf{x})$ contain *no* unknown parameters. *Composite* hypotheses, which involve unknown parameters, are discussed in Section 10.2.4. Besides these conditional probabilities, the rate of occurrence of each hypothesis is an important factor. The fractions of H_0 and H_1 in many repetitions of the experiment are specified by the a priori probabilities $P(H_0)$ and $P(H_1)$, respectively.

Each observation vector \mathbf{x} corresponds to a point in a p -dimensional space. The set of all possible values of \mathbf{x} is known as the *observation space* \mathcal{R} (see Figure 10.1). A decision rule or test is specified by partitioning the observation space \mathcal{R} into two disjoint regions. One region \mathcal{R}_0 contains the values of \mathbf{x} for which we accept H_0 , and the other region \mathcal{R}_1 contains the values of \mathbf{x} for which we accept H_1 . Note that one of these regions may consist of multiple disjoint regions. The boundaries between the

two decision regions are hypersurfaces called *decision boundaries* or *decision surfaces*. Clearly, there are two ways in which an error can occur: an observation \mathbf{x} from $f(\mathbf{x}|H_0)$ falls in region \mathcal{R}_1 or an observation \mathbf{x} from $f(\mathbf{x}|H_1)$ falls in region \mathcal{R}_0 .

The next step in designing a decision rule is to choose a criterion that specifies what constitutes an optimal choice between the two hypotheses. In decision-making, we need a different criterion of performance than in estimation. Here the answer is right or wrong. We can assign a cost to our decisions, but we cannot easily quantify how wrong we are. An appropriate cost function should be related to how often we are right or wrong. We next consider two criteria that surprisingly lead to the same decision rule.

10.2.1 Bayes Criterion

The Bayes criterion is a natural choice in applications that satisfy the following assumptions: (a) the a priori probabilities $P(H_0)$ and $P(H_1)$ of the two hypotheses are known, and (b) the two types of errors are treated equivalently. The Bayes criterion seeks to minimize the average probability of error, which can be expressed as

$$\begin{aligned} P(\text{error}) &= P(\mathbf{x} \in \mathcal{R}_1, H_0 \text{ true}) + P(\mathbf{x} \in \mathcal{R}_0, H_1 \text{ true}) \\ &= P(\mathbf{x} \in \mathcal{R}_1|H_0)P(H_0) + P(\mathbf{x} \in \mathcal{R}_0|H_1)P(H_1) \\ &= \int_{\mathcal{R}_1} f(\mathbf{x}|H_0)P(H_0)d\mathbf{x} + \int_{\mathcal{R}_0} f(\mathbf{x}|H_1)P(H_1)d\mathbf{x}. \end{aligned} \quad (10.9)$$

To minimize this expression with respect to the regions \mathcal{R}_0 and \mathcal{R}_1 , we check which integral will give the smallest value when a specific observation \mathbf{x} is included in its region of integration. Thus, if $f(\mathbf{x}|H_0)P(H_0) < f(\mathbf{x}|H_1)P(H_1)$, we should include \mathbf{x} into region \mathcal{R}_1 ; otherwise, into region \mathcal{R}_0 . Values of \mathbf{x} where the two expressions are equal may be assigned arbitrarily. This leads to the following decision rule

$$\Lambda(\mathbf{x}) \triangleq \frac{f(\mathbf{x}|H_1)}{f(\mathbf{x}|H_0)} \stackrel{H_1}{\gtrless} \stackrel{H_0}{\lessgtr} \eta_B \triangleq \frac{P(H_0)}{P(H_1)}. \quad (10.10)$$

The comparison relation means choosing hypothesis H_1 if $\Lambda(\mathbf{x}) > \eta_B$ and hypothesis H_0 if $\Lambda(\mathbf{x}) < \eta_B$. The value of $f(\mathbf{x}|H_i)$ provides the likelihood that the observation vector \mathbf{x} was generated under hypothesis H_i , $i = 0, 1$ (see Section 7.5). This leads to the name *likelihood ratio (LR)* for the quantity $\Lambda(\mathbf{x})$ and *likelihood ratio test (LRT)* for the decision rule (10.10). The LRT makes a decision by comparing the LR $\Lambda(\mathbf{x})$ of the observation vector \mathbf{x} to a *threshold* η_B determined by the a priori probabilities. The LR $\Lambda(\mathbf{x})$ is a random variable because it is a function of the random vector \mathbf{x} .

The Bayes decision rule minimizes the probability of error by choosing the regions so that the integrands in (10.9) are minimum; no other partitioning, that is, no other decision rule can yield a smaller probability of error. This is illustrated in Figure 10.2 in the case of one-dimensional observation space. The errors corresponding to the two terms of (10.9) are shown by the shaded areas under the tails of the corresponding distributions. Because the decision boundary has been chosen arbitrarily, the probability of error is not as small as it might be. Moving the decision boundary to the point where $f(\mathbf{x}|H_0)P(H_0) = f(\mathbf{x}|H_1)P(H_1)$, the probability of error is minimized because the dark

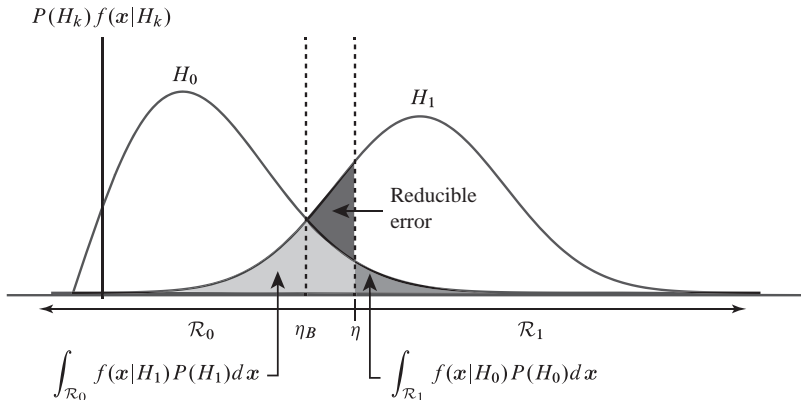


Figure 10.2 Illustration of the Bayes decision rule (Duda et al., 2001).

triangular area is eliminated. We can easily see that by moving this decision boundary can only lead to an increase in the probability of error.

We emphasize that, in practice, the Bayes criterion is meaningful if $P(H_0)$ and $P(H_1)$ are of the same order of magnitude. Indeed, if one of them is very small, we can easily minimize the probability of error by choosing always the other hypothesis regardless of the conditional probabilities, which is meaningless.

10.2.2 Neyman–Pearson Criterion

Many applications, like radar surveillance, satisfy the following conditions: (a) the a priori probabilities are either unavailable or meaningless to define, (b) the hypothesis H_1 is true extremely rarely, and (c) some costly action (e.g., firing an expensive missile) is taken when H_1 is chosen. Since $P(H_1)$ is negligible, the dominant factor in the probability of error (10.9) is determined by the conditional *probability of false alarm*, defined by

$$P_{\text{FA}} = \int_{\mathcal{R}_1} f(x|H_0)dx. \quad (10.11)$$

Under such circumstances it is appropriate for the user to determine the value of P_{FA} that he can afford, and seek a decision rule that attains this value and at the same time maximizes the conditional *probability of detection*, defined by

$$P_{\text{D}} = \int_{\mathcal{R}_1} f(x|H_1)dx. \quad (10.12)$$

A strategy that maximizes the probability of detecting a target at a given false alarm rate is known as the Neyman–Pearson criterion. Ideally, we would like to make P_{FA} as small as possible and P_{D} as large as possible. However, these are conflicting requirements. Indeed, since probability density functions are nonnegative, increasing \mathcal{R}_1 to increase P_{D} leads to an increase in P_{FA} . The Neyman–Pearson criterion requires the solution of the following optimization problem:

$$\max_{\mathcal{R}_1} P_D \text{ subject to } P_{FA} \leq \alpha. \quad (10.13)$$

The solution of this optimization problem can be obtained by using the method of Lagrange multipliers. A simpler derivation is obtained by noting that (10.12) can be written as

$$P_D = \int_{\mathcal{R}_1} \Lambda(\mathbf{x}) f(\mathbf{x}|H_0) d\mathbf{x}. \quad (10.14)$$

The quantities $\Lambda(\mathbf{x})$ and $f(\mathbf{x}|H_0)$ are positive. To make P_D as large as possible, for a fixed value of P_{FA} , we assign points \mathbf{x} with large values of $\Lambda(\mathbf{x})$ to the region \mathcal{R}_1 and points with small values of $\Lambda(\mathbf{x})$ to \mathcal{R}_0 . Suppose that these regions are separated by a surface D defined by the equation $\Lambda(\mathbf{x}) = \eta$, where the threshold η is chosen so that the integral (10.11) equals to the preassigned value α . If we change the decision surface D by moving points from \mathcal{R}_1 to \mathcal{R}_0 or vice versa, even if we satisfy the condition $P_{FA} \leq \alpha$, we can only decrease the P_D (10.12) because larger values of $\Lambda(\mathbf{x})$ in the integrand of (10.14) are replaced with smaller values. This shows that the original choice of the decision surface D is optimal. The optimal decision rule, according to the Neyman–Pearson criterion, is given by

$$\Lambda(\mathbf{x}) = \frac{f(\mathbf{x}|H_1)}{f(\mathbf{x}|H_0)} \stackrel{H_1}{\gtrless} \stackrel{H_0}{\lessdot} \eta. \quad (10.15)$$

If we denote by $f(\Lambda|H_0)$ the probability density function of the continuous random variable $\Lambda(\mathbf{x})$ under H_0 , we can obtain the Neyman–Pearson threshold η by solving the following equation

$$P_{FA} = \int_{\eta}^{\infty} f(\Lambda|H_0) d\Lambda = \alpha. \quad (10.16)$$

10.2.3

Performance Evaluation of LR Tests: ROC Curves

Simple inspection of (10.10) and (10.15) leads to a fundamental result: *the Bayes criterion and the Neyman–Pearson criterion make use of the same likelihood ratio; only the threshold to which the ratio is compared depends on the criterion.* This property, which demonstrates the optimality of likelihood ratio tests, holds for the minimax and other criteria (Van Trees, 1968). Thus, an optimum detector consists of two parts: a likelihood ratio processor and a threshold selection algorithm; both are required to ensure optimum performance. This decomposition is illustrated in Figure 10.3.

Besides the likelihood ratio $\Lambda(\mathbf{x})$, we can make identical decisions using any monotonic function $\ell(\mathbf{x}) = G[\Lambda(\mathbf{x})]$ of $\Lambda(\mathbf{x})$. The most commonly used function is the logarithm of the likelihood ratio

$$\ell(\mathbf{x}) \triangleq \ln \Lambda(\mathbf{x}) = \ln \frac{f(\mathbf{x}|H_1)}{f(\mathbf{x}|H_0)} \quad (10.17)$$

because it leads to particularly simple forms when the conditional distributions are jointly Gaussian. Often, further manipulation of (10.17) leads to simpler monotonic functions of the likelihood ratio.

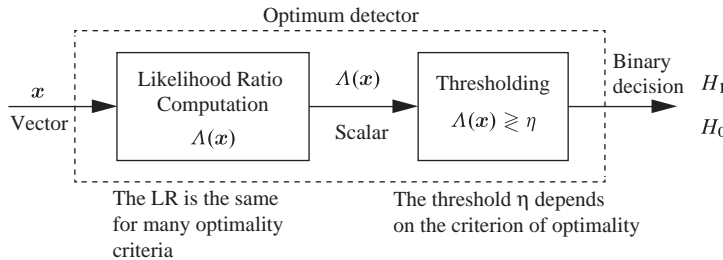


Figure 10.3 An optimum detector computes the likelihood ratio for each observation vector and then makes a decision by comparing this value to a fixed threshold.

The quantities $\Lambda(\mathbf{x})$ and $\ell(\mathbf{x})$ are random variables whose probability density depends on which hypothesis is true. If these densities are known, we can use them to find expressions for P_D and P_{FA} . In the case of likelihood ratio, we have

$$P_D(\eta) = \int_{\eta}^{\infty} f(\Lambda|H_1)d\lambda \quad (10.18a)$$

$$P_{FA}(\eta) = \int_{\eta}^{\infty} f(\Lambda|H_0)d\lambda. \quad (10.18b)$$

Both quantities are clearly functions of the threshold η . For a Bayes test we use the optimum threshold $\eta = \eta_B = P(H_0)/P(H_1)$ to determine the corresponding minimum probability of error using the formula

$$P(\text{error}) = P(H_0)P_{FA}(\eta_B) + P(H_1)P_D(\eta_B). \quad (10.19)$$

For a Neyman–Pearson test there is a trade-off between probability of detection and probability of false alarm. To study this trade-off we use a parametric plot of P_D versus P_{FA} as the threshold η varies. The resulting curve is known as *receiver operating characteristic (ROC)*.

10.2.4 Composite Hypothesis Testing

In Sections 10.2.1 and 10.2.2 we developed optimum decision rules for simple hypotheses: that is, hypotheses where the conditional probability densities $f(\mathbf{x}|H_0)$ and $f(\mathbf{x}|H_1)$ are completely known. When a distribution $f(\mathbf{x}|H_k)$ contains some unknown parameters, the hypothesis H_k is called *composite*. For example, $f(\mathbf{x}|H_k)$ may be Gaussian, but the mean or variance may be unspecified. Most of the difficulties of decision theory arise when one or both hypotheses are composite (Lehmann, 1959).

We shall use the notation $f(\mathbf{x}|H_k, \boldsymbol{\theta}_k)$ or $f_k(\mathbf{x}|\boldsymbol{\theta}_k)$ to describe the dependence of the conditional densities on a set of q parameters represented by the components of a vector $\boldsymbol{\theta}_k$. There are three cases of composite hypothesis problems:

1. The decision rule is independent of the unknown parameters $\boldsymbol{\theta}_k$;
2. The parameter vector $\boldsymbol{\theta}_k$ is a random vector with a known probability density function $f(\boldsymbol{\theta}_k)$ on the parameter space Θ_k ;
3. The parameter vector $\boldsymbol{\theta}_k$ is an unknown deterministic constant.

In the first case, which is very rare, the presence of unknown parameters does not affect the detection problem in the sense that there exists a detector which is best for all values of these parameters. Such tests are called *uniformly most powerful* (UMP) tests; unfortunately, UMP tests seldom exist.

In the second case, the *Bayesian likelihood ratio* is evaluated by

$$\Lambda_B(\mathbf{x}) = \frac{\int_{\Theta_1} f_1(\mathbf{x}|\boldsymbol{\theta}_1) f(\boldsymbol{\theta}_1) d\boldsymbol{\theta}_1}{\int_{\Theta_0} f_0(\mathbf{x}|\boldsymbol{\theta}_0) f(\boldsymbol{\theta}_0) d\boldsymbol{\theta}_0}. \quad (10.20)$$

Knowing the probability density of $\boldsymbol{\theta}$ enables the reduction of the problem to a simple hypothesis-testing problem by integrating over $\boldsymbol{\theta}$. However, this likelihood ratio test has two major faults. First, the integrals in (10.20) are typically complicated and hard to evaluate. Second, in most practical applications we do not know the probability density function of the unknown parameters.

We shall focus on the third case which leads to simpler and practically useful solutions of the composite hypothesis problem. When a UMP test does not exist, we have to use a suboptimal test. In these cases, it is very useful to compare the performance of the suboptimal test with that of the optimal Neyman–Pearson test, which assumes perfect knowledge of the unknown parameters. The Neyman–Pearson test provides an upper bound on performance, which can be used to assess the performance of suboptimal detectors. The perfect measurement bound suggests that a logical approach is to replace the unknown parameters with their estimates under each hypothesis. Because the likelihood function tends to be highest near the true value, we typically use the maximum likelihood estimates of the unknown parameters. The result, which is known as the *generalized LRT* (GLRT), is given by

$$\Lambda_G(\mathbf{x}) = \frac{\max_{\boldsymbol{\theta}_1} f_1(\mathbf{x}|\boldsymbol{\theta}_1)}{\max_{\boldsymbol{\theta}_0} f_0(\mathbf{x}|\boldsymbol{\theta}_0)} = \frac{f_1(\mathbf{x}|\hat{\boldsymbol{\theta}}_1)}{f_0(\mathbf{x}|\hat{\boldsymbol{\theta}}_0)} \quad (10.21)$$

where $\hat{\boldsymbol{\theta}}_0$ and $\hat{\boldsymbol{\theta}}_1$ are the maximum likelihood estimators of $\boldsymbol{\theta}_0$ and $\boldsymbol{\theta}_1$ under hypothesis H_0 and H_1 , respectively.

10.2.5 Multiple or M -ary Hypotheses Testing

In the case of multiple hypotheses, there are more ways to be wrong than to be right and it is simpler to compute the probability of being correct. Thus, we have

$$P_C = \sum_{k=0}^{M-1} P(\mathbf{x} \in \mathcal{R}_k, H_k \text{ true}) = \sum_{k=0}^{M-1} \int_{\mathcal{R}_k} f(\mathbf{x}|H_k) P(H_k) d\mathbf{x}, \quad (10.22)$$

which shows that the probability of being correct is maximized by associating each value of \mathbf{x} with the largest term in (10.22). This leads to the Bayes decision rule:

$$\text{Given } \mathbf{x}, \text{ choose } H_k \text{ for which the product } f(\mathbf{x}|H_k) P(H_k) \text{ is largest.} \quad (10.23)$$

To determine the largest of M quantities, we need $(M - 1)$ numeric comparisons; for $M = 2$ this reduces to the computation of the likelihood ratio and its comparison to a

threshold. Multiple hypotheses testing provides the natural framework for classification problems (Duda et al., 2001). The generalization of the Neyman–Pearson criterion to M hypotheses is possible; however, it is not widely used in practical classification problems (Levy, 2008).

10.3 The General Gaussian Detection Problem

The optimum detector for two *arbitrary* conditional probability densities $f(\mathbf{x}|H_0)$ and $f(\mathbf{x}|H_1)$ is specified by the following likelihood ratio test (LRT):

$$\Lambda(\mathbf{x}) = \frac{f(\mathbf{x}|H_1)}{f(\mathbf{x}|H_0)} \stackrel{H_1}{\gtrless} \stackrel{H_0}{\lessgtr} \eta. \quad (10.24)$$

The function $\Lambda(\mathbf{x})$ has the same form for a number of optimality criteria; only the value of threshold η is specified by the used criterion. In general, the LR could be a complicated function of the observations that may be difficult to compute and analyze, especially if the number p of observations is large. In addition, setting thresholds for the Neyman–Pearson criterion or evaluation of performance requires the computation of complicated multivariate integrals. However, there are some special distributions which lead to simple and intuitively appealing optimum detectors. These detectors have easily implemented structures and their performance can be thoroughly analyzed. The multivariate Gaussian distribution leads to simple optimum detectors that can be used even when the distributions of the actual observations are not Gaussian. However, we must emphasize that, when the assumed and actual distributions differ, the optimum detectors provide suboptimum performance.

We recall that a p -dimensional Gaussian vector \mathbf{x} with mean vector \mathbf{m}_k and covariance matrix \mathbf{C}_k has a probability density function defined by

$$f(\mathbf{x}|H_k) = \frac{1}{(\sqrt{2\pi})^p |\mathbf{C}_k|^{1/2}} \exp\left[-\frac{1}{2}(\mathbf{x} - \mathbf{m}_k)^T \mathbf{C}_k^{-1} (\mathbf{x} - \mathbf{m}_k)\right]. \quad (10.25)$$

We note that the background clutter distribution corresponds to $k = 0$ and the target distribution to $k = 1$. Therefore, the LRT is given by

$$\Lambda(\mathbf{x}) = \frac{|\mathbf{C}_0|^{1/2} \exp\left[-\frac{1}{2}(\mathbf{x} - \mathbf{m}_1)^T \mathbf{C}_1^{-1} (\mathbf{x} - \mathbf{m}_1)\right]}{|\mathbf{C}_1|^{1/2} \exp\left[-\frac{1}{2}(\mathbf{x} - \mathbf{m}_0)^T \mathbf{C}_0^{-1} (\mathbf{x} - \mathbf{m}_0)\right]} \stackrel{H_1}{\gtrless} \stackrel{H_0}{\lessgtr} \eta_0. \quad (10.26)$$

Taking logarithms, the LRT for the general Gaussian problem can be stated as

$$y = \ln \Lambda(\mathbf{x}) = (\mathbf{x} - \mathbf{m}_0)^T \mathbf{C}_0^{-1} (\mathbf{x} - \mathbf{m}_0) - (\mathbf{x} - \mathbf{m}_1)^T \mathbf{C}_1^{-1} (\mathbf{x} - \mathbf{m}_1) \stackrel{H_1}{\gtrless} \stackrel{H_0}{\lessgtr} \eta_0 \quad (10.27)$$

where

$$\eta \triangleq 2 \ln \eta_0 + \ln \frac{|\mathbf{C}_1|}{|\mathbf{C}_0|}. \quad (10.28)$$

The detection statistic y in (10.27) is the difference between two quadratic forms: the Mahalanobis distances of the observation vector \mathbf{x} from the means of the two

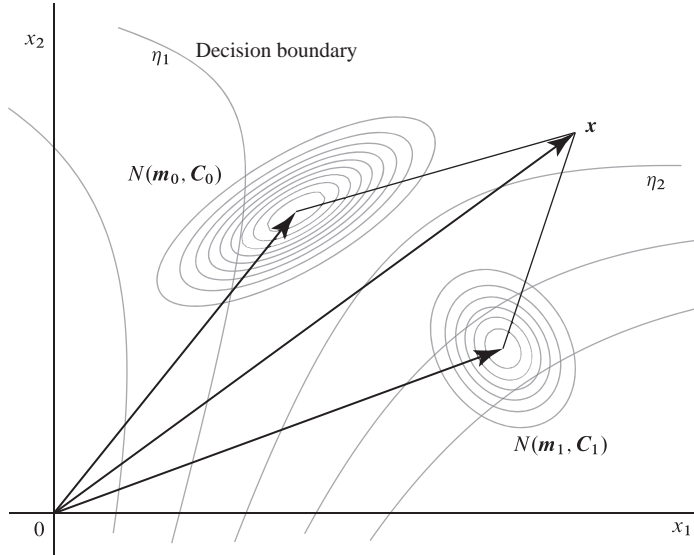


Figure 10.4 Geometrical illustration of the general Gaussian detection problem.

distributions. This result, which provides the ground for many of our later discussions, is illustrated in Figure 10.4.

The locus of all points \mathbf{x} such that $y = \ln \Lambda(\mathbf{x}) = \eta$ determines the decision surface for a threshold equal to the value of η . The decision surfaces for $\mathbf{C}_0 \neq \mathbf{C}_1$ belong to the family of hyperquadratics; their exact shape depends on the form, location, and orientation of the Gaussian hyperellipsoids. Figure 10.5a shows an example of quadratic decision lines in two dimensions.

The implementation of the LRT is still straightforward but the exact evaluation of performance is extremely complicated. We next discuss some special cases of the general problem, where we can easily derive the optimum detector structure and obtain simple expressions for the ROC curves.

10.3.1 Equal Covariance Matrices

Suppose that the two hypotheses have equal covariance matrices but different mean vectors, that is,

$$\mathbf{C}_0 = \mathbf{C}_1 \triangleq \mathbf{C} \quad (10.29a)$$

$$\mathbf{m}_1 \neq \mathbf{m}_0. \quad (10.29b)$$

Then, the LRT (10.27) becomes

$$(\mathbf{x} - \mathbf{m}_0)^T \mathbf{C}^{-1} (\mathbf{x} - \mathbf{m}_0) - (\mathbf{x} - \mathbf{m}_1)^T \mathbf{C}^{-1} (\mathbf{x} - \mathbf{m}_1) \stackrel{H_1}{\underset{H_0}{\gtrless}} 2 \ln \eta_0. \quad (10.30)$$

Using the symmetry of \mathbf{C}^{-1} , we can simplify (10.30) to the equivalent expression

$$(\mathbf{m}_1 - \mathbf{m}_0)^T \mathbf{C}^{-1} \mathbf{x} \stackrel{H_1}{\underset{H_0}{\gtrless}} \ln \eta_0 + \frac{1}{2} (\mathbf{m}_1^T \mathbf{C}^{-1} \mathbf{m}_1 - \mathbf{m}_0^T \mathbf{C}^{-1} \mathbf{m}_0) \triangleq \eta. \quad (10.31)$$

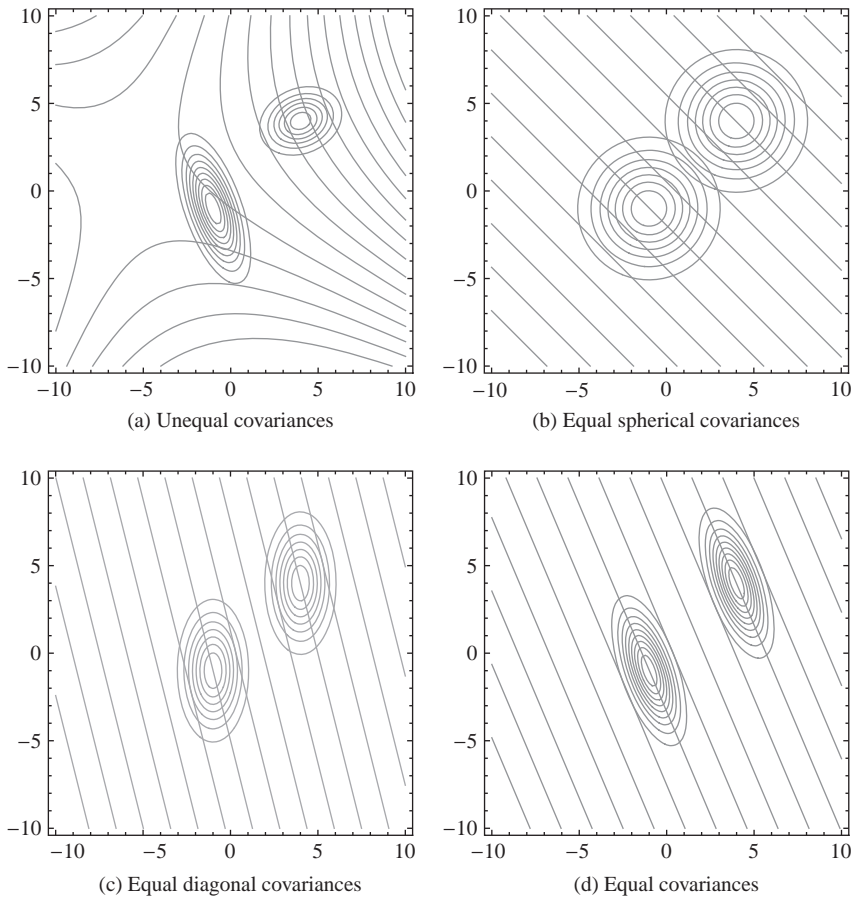


Figure 10.5 Examples of decision surfaces for the Gaussian detection problem.

Therefore, the LRT for Gaussian distributions with equal covariance matrices is

$$y = (\mathbf{m}_1 - \mathbf{m}_0)^T \mathbf{C}^{-1} \mathbf{x} \stackrel{H_1}{\underset{H_0}{\gtrless}} \eta. \quad (10.32)$$

To understand the meaning of (10.32) we define a $p \times 1$ coefficient vector \mathbf{h} by

$$\mathbf{h} \triangleq \mathbf{C}^{-1}(\mathbf{m}_1 - \mathbf{m}_0) = \mathbf{C}^{-1}\boldsymbol{\delta}, \quad (10.33)$$

where $\boldsymbol{\delta}$ is the vector from \mathbf{m}_0 to \mathbf{m}_1 , that is,

$$\boldsymbol{\delta} \triangleq \mathbf{m}_1 - \mathbf{m}_0. \quad (10.34)$$

Then, the detection statistics (10.32) can be expressed as follows

$$y = \mathbf{h}^T \mathbf{x} = \sum_{k=1}^p h_k x_k \stackrel{H_1}{\underset{H_0}{\gtrless}} \eta. \quad (10.35)$$

The detection test specified by (10.33) and (10.35), which is known as *matched filter detector*, plays a prominent role in hyperspectral target detection. We note that the dot product $y = \mathbf{h}^T \mathbf{x}$ carries all the information required by the LRT to make an optimum decision: all observations x_1, \dots, x_p with the same dot product, lead to identical decisions. We say that the scalar quantity $y = \mathbf{h}^T \mathbf{x}$ is a *sufficient statistic* for this particular detection problem.

Before we analyze the performance of this test, we consider two special cases that help to geometrically understand its operation in the observation space.

Equal Spherical Covariance Matrices

The simplest multivariate case occurs when the components x_i of the observation vector \mathbf{x} , under both hypotheses, are statistically independent with different means and common variance σ^2 ; that is,

$$\mathbf{C} \triangleq \mathbf{C}_0 = \mathbf{C}_1 = \sigma^2 \mathbf{I}. \quad (10.36)$$

In this case, the contours of equal probability are hyperspherical surfaces centered at the mean vectors \mathbf{m}_0 and \mathbf{m}_1 . The Mahalanobis distance is

$$\Delta^2 = \frac{\|\mathbf{m}_1 - \mathbf{m}_0\|^2}{\sigma^2} = \frac{\|\boldsymbol{\delta}\|^2}{\sigma^2}, \quad (10.37)$$

which shows that Δ increases as the Euclidean distance between the centers of the two distributions increases or the common standard deviation σ decreases.

To determine the type of decision surface we note that the matched filter vector

$$\mathbf{h} = \frac{1}{\sigma^2}(\mathbf{m}_1 - \mathbf{m}_0) = \frac{1}{\sigma^2} \boldsymbol{\delta} \quad (10.38)$$

is parallel to the line between the means. The decision surface separating \mathcal{R}_0 and \mathcal{R}_1 is a hyperplane defined by the linear equation $\mathbf{h}^T \mathbf{x} = \eta$. This equation defines a hyperplane orthogonal to the vector \mathbf{h} : that is, perpendicular to the line connecting the centers of the two distributions. If observation vectors \mathbf{x}_1 and \mathbf{x}_2 are both on the decision surface, we have $\mathbf{h}^T(\mathbf{x}_1 - \mathbf{x}_2) = 0$, which shows that \mathbf{h} is normal to any vector lying in the hyperplane. The point where this hyperplane “cuts” the vector $\boldsymbol{\delta} = \mathbf{m}_1 - \mathbf{m}_0$ is specified by the value of threshold η . Figure 10.5b shows a set of hyperplanes for various values of the threshold. We can make a decision by checking whether the tip of the observation vector \mathbf{x} lies on the left or on the right of the decision hyperplane. In summary, *the orientation of the decision hyperplane is determined by the requirement to be perpendicular to the vector \mathbf{h} and its location is specified by the value of the threshold η* .

The quantity $y = (1/\sigma^2)\boldsymbol{\delta}^T \mathbf{x}$ measures the correlation or similarity or “matching” between the vectors $\boldsymbol{\delta}$ and \mathbf{x} . The test decides in favor of H_1 when the “matching score” y exceeds the threshold. For this reason, the linear processor specified by (10.33) is known as a *matched filter* detector.

Equal Diagonal Covariance Matrices

If the observations x_i are statistically independent but have different variances, the covariance matrix is

$$\mathbf{C} \triangleq \mathbf{C}_0 = \mathbf{C}_1 = \text{diag}\{\sigma_1^2, \sigma_2^2, \dots, \sigma_p^2\}. \quad (10.39)$$

Then, the sufficient statistic and the Mahalanobis distance become

$$y = \boldsymbol{\delta}^T \mathbf{C}^{-1} \mathbf{x} = \sum_{k=1}^p \frac{\delta_k \cdot x_k}{\sigma_k^2} \quad (10.40)$$

$$\Delta^2 = \boldsymbol{\delta}^T \mathbf{C}^{-1} \boldsymbol{\delta} = \sum_{k=1}^p \frac{\delta_k^2}{\sigma_k^2}. \quad (10.41)$$

The various observations contribute to y and Δ^2 with weighting that is inversely proportional to their variance. That is, *components with large variance (or uncertainty) contribute less to the detection statistic and vice versa*. We note that the vector $\mathbf{h} = \mathbf{C}^{-1} \boldsymbol{\delta}$ is no longer parallel to $\boldsymbol{\delta}$ because each component $h_k = \delta_k / \sigma_k^2$ is scaled differently. Therefore, the decision surfaces are hyperplanes orthogonal to \mathbf{h} but not to $\boldsymbol{\delta}$.

An interesting interpretation of these results follows if we define a new coordinate system so that the variances of the new variables are all equal to one. This can be done using the following transformation

$$\tilde{x}_k = x_k / \sigma_k \sim N(m_k / \sigma_k, 1) \quad (10.42)$$

Therefore, the optimum decision rule can be viewed as a two-step process: first, the observations are normalized so that each one has unit variance, and then the decision rule for this simpler covariance structure is used.

Equal General Covariance Matrices

Geometrically, this situation arises when the observations fall in two hyperellipsoidal clusters of equal size and shape centered at different locations. The decision surfaces are hyperplanes perpendicular to the matched filter vector; however, because $\mathbf{h} = \mathbf{C}^{-1} \boldsymbol{\delta}$ is not in the direction of $\boldsymbol{\delta}$, these hyperplanes are not orthogonal to the line between the means (see Figure 10.5d). Geometrically, if $\|\mathbf{h}\| = 1$, y is the scalar projection of the observation vector \mathbf{x} onto a line in the direction of \mathbf{h} . The magnitude of \mathbf{h} is not significant, because it merely scales y ; however, as we will see in Section 10.5, the direction of \mathbf{h} is very important. Finally, we note that by using a whitening transformation the optimum matched detector $y = \boldsymbol{\delta}^T \mathbf{C}^{-1} \mathbf{x} = (\mathbf{C}^{-1/2} \boldsymbol{\delta})^T (\mathbf{C}^{-1/2} \mathbf{x}) \triangleq \tilde{\boldsymbol{\delta}}^T \tilde{\mathbf{x}}$ can be reduced to a two-step process: whitening, $\tilde{\mathbf{x}} = \mathbf{C}^{-1/2} \mathbf{x}$, followed by the simple correlation detector $y = \tilde{\boldsymbol{\delta}}^T \tilde{\mathbf{x}}$. This two-step process will be used repeatedly in the sequel to explain the operation and performance of matched filter detection algorithms.

Performance Evaluation of Matched Filter Detector

The performance of the test is completely determined by a ROC curve. Since the detection statistic y in (10.35) is a linear combination of correlated normal random variables, the mean and variance of y under the two hypotheses are (see Section 7.3)

$$E(y|H_0) = \mathbf{h}^T E(\mathbf{x}|H_0) = \mathbf{h}^T \mathbf{m}_0 \triangleq m_0 \quad (10.43a)$$

$$E(y|H_1) = \mathbf{h}^T E(\mathbf{x}|H_1) = \mathbf{h}^T \mathbf{m}_1 \triangleq m_1 \quad (10.43b)$$

and

$$\text{var}(y|H_0) = \text{var}(y|H_1) = \mathbf{h}^T \mathbf{C} \mathbf{h} \triangleq \sigma_y^2. \quad (10.44)$$

Thus, the probabilities of detection and false alarm are given by

$$P_{\text{FA}} = \int_{\eta}^{\infty} f(y|H_0) dy = Q\left(\frac{\eta - m_0}{\sigma_y}\right) \quad (10.45a)$$

$$P_{\text{D}} = \int_{\eta}^{\infty} f(y|H_1) dy = Q\left(\frac{\eta - m_1}{\sigma_y}\right), \quad (10.45b)$$

where $Q(\cdot)$ is a function defined by

$$Q(a) \triangleq \frac{1}{\sqrt{2\pi}} \int_a^{\infty} \exp(-z^2/2) dz. \quad (10.46)$$

Solving (10.45a) for η and substituting into (10.45b) yields

$$P_{\text{D}} = Q\left[Q^{-1}(P_{\text{FA}}) - \Delta_y\right], \quad (10.47)$$

where

$$\Delta_y \triangleq \frac{m_1 - m_0}{\sigma_y}. \quad (10.48)$$

Equation (10.47) describes the ROC curve with Δ_y as a parameter. We note that Δ_y is the distance between the means of the detection statistics in units of standard deviation. Using (10.48), (10.43a), (10.44), and (10.33) we can show that

$$\Delta_y^2 = (\mathbf{m}_1 - \mathbf{m}_0)^T \mathbf{C}^{-1} (\mathbf{m}_1 - \mathbf{m}_0) = \boldsymbol{\delta}^T \mathbf{C}^{-1} \boldsymbol{\delta} = \Delta^2. \quad (10.49)$$

Therefore, for the equal covariance case, detection performance is completely determined by the Mahalanobis distance between the two distributions.

We note that the ROC curves for the equal variance case are completely characterized by the parameter Δ and they have the shape shown in Figure 10.6. Each ROC curve in Figure 10.6 shows a trade-off between P_{D} and P_{FA} which is controlled by the threshold η . A conservative threshold will make P_{FA} low at the cost of also making P_{D} low, whereas an aggressive threshold will make P_{D} high at the cost of making P_{FA} high. We can always increase the probability of detection at the expense of a higher false alarm rate.

10.3.2 Unequal Covariance Matrices

There are two cases of special interest, where the two hypotheses have unequal covariance matrices.

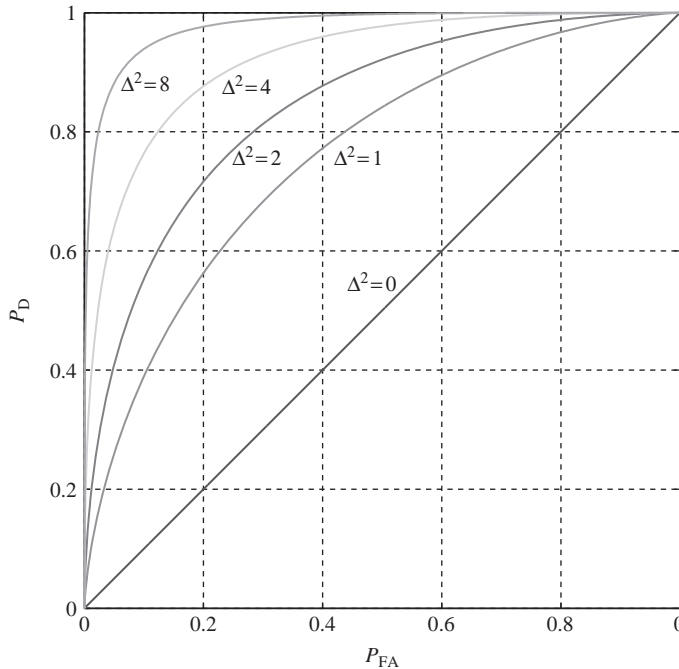


Figure 10.6 Receiver operating characteristic (ROC) curves corresponding to different values of the detectability index Δ for the equal covariance case.

Equal Mean Vectors

In the first case of special interest the mean-value vectors on the two hypotheses are equal but the covariance matrices are different; that is,

$$\mathbf{m}_1 = \mathbf{m}_0 \triangleq \mathbf{m} \quad (10.50a)$$

$$\mathbf{C}_0 \neq \mathbf{C}_1. \quad (10.50b)$$

Without loss of generality, we assume that $\mathbf{m} = \mathbf{0}$. Then, the detection statistic (10.27) is reduced to a single quadratic form given by

$$y = \mathbf{x}^T (\mathbf{C}_1^{-1} - \mathbf{C}_0^{-1}) \mathbf{x} \quad (10.51)$$

This is the dot product of the Gaussian vectors \mathbf{x} and $(\mathbf{C}_1^{-1} - \mathbf{C}_0^{-1})\mathbf{x}$; therefore, the distribution of the detection statistic y is *not* Gaussian. For details see Section 4.14 in Scharf (1991).

Proportional Covariance Matrices

In the second case of special interest, the mean-value vectors are unequal but the covariance matrices are proportional; that is,

$$\mathbf{m}_1 \neq \mathbf{m}_0 \quad (10.52a)$$

$$\mathbf{C}_1 \triangleq \gamma^2 \mathbf{C}_0, \quad (10.52b)$$

where $0 \leq \gamma^2 \leq 1$. In this case it is possible to derive analytical expressions for the distribution of detection statistic. The results are used to understand the performance degradation of the matched filter when $\mathbf{C}_1 \neq \mathbf{C}_0$.

Assume, without loss of generality, that $\mathbf{m}_0 = \mathbf{0}$ and $\mathbf{m}_1 = \boldsymbol{\delta}$. Then, the LRT (10.27) can be written as follows

$$y_1 = \mathbf{x}^T \mathbf{C}_0^{-1} \mathbf{x} - (\mathbf{x} - \boldsymbol{\delta})^T \gamma^{-2} \mathbf{C}_0^{-1} (\mathbf{x} - \boldsymbol{\delta}) \stackrel{H_1}{\underset{H_0}{\gtrless}} \eta_1. \quad (10.53)$$

Multiplying both sides with the positive constant γ^2 yields the equivalent test:

$$y_2 = \gamma^2 \mathbf{x}^T \mathbf{C}_0^{-1} \mathbf{x} - (\mathbf{x} - \boldsymbol{\delta})^T \gamma^{-2} \mathbf{C}_0^{-1} (\mathbf{x} - \boldsymbol{\delta}) \stackrel{H_1}{\underset{H_0}{\gtrless}} \eta_1 \gamma^2 \quad (10.54)$$

or, after simplification,

$$y_2 = (\gamma^2 - 1) \mathbf{x}^T \mathbf{C}_0^{-1} \mathbf{x} + \boldsymbol{\delta}^T \mathbf{C}_0^{-1} \mathbf{x} + \mathbf{x}^T \mathbf{C}_0^{-1} \boldsymbol{\delta} - \boldsymbol{\delta}^T \mathbf{C}_0^{-1} \boldsymbol{\delta} \stackrel{H_1}{\underset{H_0}{\gtrless}} \eta_1 \gamma^2. \quad (10.55)$$

Multiplying both sides by the negative constant $\beta \triangleq 1/(\gamma^2 - 1)$ reverses the inequality and provides the equivalent test

$$y_3 = \mathbf{x}^T \mathbf{C}_0^{-1} \mathbf{x} + \beta \boldsymbol{\delta}^T \mathbf{C}_0^{-1} \mathbf{x} + \beta \mathbf{x}^T \mathbf{C}_0^{-1} \boldsymbol{\delta} - \beta \boldsymbol{\delta}^T \mathbf{C}_0^{-1} \boldsymbol{\delta} \stackrel{H_1}{\underset{H_0}{\gtrless}} \eta_1 \gamma^2 \beta. \quad (10.56)$$

Replacing the constant term $-\beta \boldsymbol{\delta}^T \mathbf{C}_0^{-1} \boldsymbol{\delta}$ by $\beta^2 \boldsymbol{\delta}^T \mathbf{C}_0^{-1} \boldsymbol{\delta}$ changes the threshold but not the distribution of the test. This test can be written as

$$y = (\mathbf{x} + \beta \boldsymbol{\delta})^T \mathbf{C}_0^{-1} (\mathbf{x} + \beta \boldsymbol{\delta}) \stackrel{H_1}{\underset{H_0}{\gtrless}} \eta. \quad (10.57)$$

The distribution of y in this form is easily expressed in terms of a non-central chi-square distribution. Indeed, using the results in Section 7.4.1 we have

$$H_0 : \mathbf{x} \sim N(\mathbf{0}, \mathbf{C}_0) \Rightarrow y \sim \chi_p^2(\beta^2 \boldsymbol{\delta}^T \mathbf{C}_0^{-1} \boldsymbol{\delta}) \quad (10.58a)$$

$$H_1 : \mathbf{x} \sim N(\boldsymbol{\delta}, \gamma^2 \mathbf{C}_0) \Rightarrow y \sim \gamma^2 \chi_p^2(\gamma^2 \beta^2 \boldsymbol{\delta}^T \mathbf{C}_0^{-1} \boldsymbol{\delta}), \quad (10.58b)$$

which can be used to compute ROC curves (see Problem 3). We note that performance depends on $\Delta_0^2 \triangleq \boldsymbol{\delta}^T \mathbf{C}_0^{-1} \boldsymbol{\delta}$ and γ^2 ; for $\gamma = 1$, we have a matched filter detector and performance depends solely on Δ_0^2 , as expected.

10.3.3 Gaussian Detection Problem in Canonical Space

As we saw in Section 8.5, for any covariance matrices \mathbf{C}_0 and \mathbf{C}_1 , we can find a linear transformation which simultaneously reduces \mathbf{C}_1 to the identity matrix and diagonalizes \mathbf{C}_0 or vice versa. For example, consider the canonical representation transformation

$$\tilde{\mathbf{x}} = \mathbf{Q}^T \mathbf{C}_1^{-1/2} (\mathbf{x} - \mathbf{m}_0), \quad (10.59)$$

where \mathbf{Q} is an orthogonal matrix such that \mathbf{D} is a diagonal matrix specified by

$$\mathbf{C}_1^{-1/2} \mathbf{C}_0 \mathbf{C}_1^{-1/2} = \mathbf{Q} \mathbf{D} \mathbf{Q}^T. \quad (10.60)$$

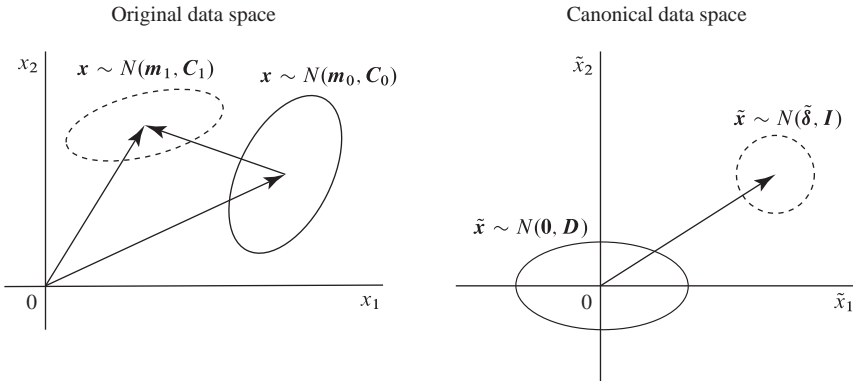


Figure 10.7 Every Gaussian detection problem with arbitrary covariance matrices is equivalent to a problem involving a general diagonal covariance matrix and an identity covariance matrix.

The density of \tilde{x} under hypothesis H_0 and hypothesis H_1 will then be

$$H_0 : \tilde{x} \sim N(\mathbf{0}, \mathbf{D}) \quad (10.61a)$$

$$H_1 : \tilde{x} \sim N(\tilde{\delta}, \mathbf{I}), \quad (10.61b)$$

where

$$\tilde{\delta} \triangleq \mathbf{Q}^T \mathbf{C}_1^{-1/2} (\mathbf{m}_1 - \mathbf{m}_0). \quad (10.62)$$

Since a linear transformation leaves the LRT invariant, there is no loss of generality in considering only the case specified by (10.61). Figure 10.7 illustrates the canonical transformation for $\mathbf{C}_1 \neq \mathbf{C}_0$.

The transformation is considerably simplified when $\mathbf{C}_1 = \gamma^2 \mathbf{C}_0$. In this case

$$\mathbf{D} = \gamma^{-2} \mathbf{I} \quad (10.63a)$$

$$\tilde{x} = \gamma^{-1} \mathbf{C}_0^{-1/2} (\mathbf{x} - \mathbf{m}_0) \quad (10.63b)$$

$$\tilde{\delta} = \gamma^{-1} \mathbf{C}_0^{-1/2} (\mathbf{m}_1 - \mathbf{m}_0), \quad (10.63c)$$

that is, the canonical transformation is reduced to whitening by $\mathbf{C}_0^{-1/2}$. The detector remains quadratic because the transformed spherical distributions are not equal and the decision surface remains nonlinear. For $\gamma = 1$, the covariances under the two hypotheses are equal, and the decision surface becomes a hyperplane; this case leads to the matched filter detector.

10.4 Gaussian Detectors in the Presence of Unknowns

In this section we develop detection algorithms for the Gaussian target and clutter problem illustrated in Figure 10.8 when some of the parameters are unknown, incompletely specified, or estimated from training data. If we know $\mathbf{m}_0, \mathbf{m}_1, \sigma^2$ and \mathbf{C} we can use the matched filter (10.32), which is the optimum Neuman–Pearson detector. In some cases,

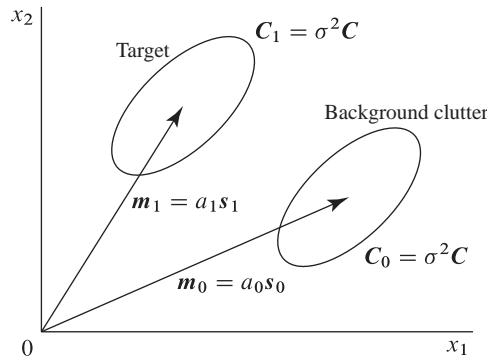


Figure 10.8 Detection problem for incompletely specified Gaussian distributions with different mean vectors and equal covariance matrices.

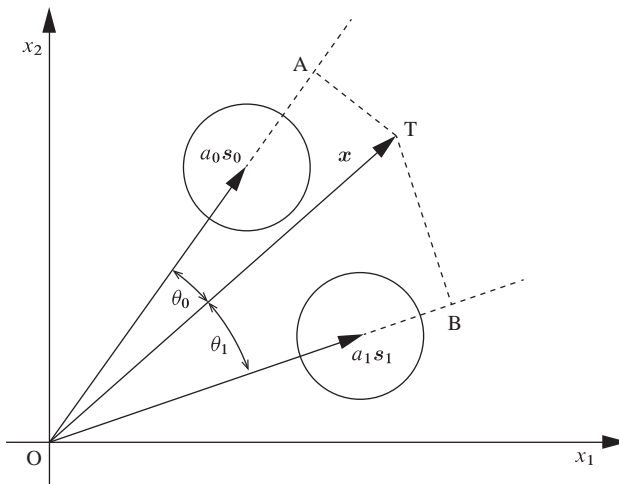


Figure 10.9 Geometrical setup for the interpretation of detection algorithms for spherical covariance matrices: $\mathbf{C} = \sigma^2 \mathbf{I}$.

we know only the direction of a mean vector; that is, we assume that $\mathbf{m}_i = a_i \mathbf{s}_i$, where a_i is unknown. In other cases, we assume that the covariance matrix of the test vector is a scaled version of the known covariance matrix \mathbf{C} ; that is, $\mathbf{C}_0 = \mathbf{C}_1 = \sigma^2 \mathbf{C}$, where σ^2 is an unknown scalar.

Assuming the same covariance under both hypotheses leads to algorithms with intuitive appeal and good performance. If $\mathbf{C} = \sigma^2 \mathbf{I}$, the contours of equal likelihood become hyperspheres, and we can use Euclidean geometry to explain the meaning of different algorithms. The base for such interpretations will be the configuration shown in Figure 10.9. The results, which are obtained using the GLRT approach, illustrate how changes in the available information lead to different algorithms. This analysis provides the ground for the development of practical hyperspectral target detection algorithms in Chapter 11.

10.4.1 Unknown Mean Vector

To illustrate the basic idea, suppose we have to choose between the hypotheses

$$H_0 : \mathbf{x} \sim N(\mathbf{m}_0, \sigma^2 \mathbf{C}) \quad \text{and} \quad H_1 : \mathbf{x} \sim N(\mathbf{m}_1, \sigma^2 \mathbf{C}), \quad (10.64)$$

where \mathbf{m}_1 is unknown. The maximum of the likelihood function (10.25) under H_1 is obtained at $\mathbf{m}_1 = \mathbf{x}$. The likelihood function under H_0 is completely specified. Therefore, the GLRT, which is obtained from (10.27) with $\mathbf{m}_1 = \mathbf{x}$, is given by

$$y = T_G(\mathbf{x}) = (\mathbf{x} - \mathbf{m}_0)^T \mathbf{C}^{-1} (\mathbf{x} - \mathbf{m}_0) \stackrel{H_1}{\underset{H_0}{\gtrless}} \eta, \quad (10.65)$$

where we have assumed $\sigma^2 = 1$ for simplicity. Note that the detection statistic is the Mahalanobis distance of the observation vector \mathbf{x} from the known mean \mathbf{m}_0 . This algorithm, which is known as the squared-law detector, provides the basis for most anomaly detection algorithms used in hyperspectral imaging.

10.4.2 Equal Covariances and a Mean with Known Direction

Suppose now that we wish to choose between the hypotheses

$$H_0 : \mathbf{x} \sim N(\mathbf{m}_0, \sigma^2 \mathbf{C}) \quad \text{and} \quad H_1 : \mathbf{x} \sim N(a_1 \mathbf{s}_1, \sigma^2 \mathbf{C}) \quad (10.66)$$

where a_1 is the only unknown parameter. Since $\mathbf{m}_1 = a_1 \mathbf{s}_1$, we know the direction of the mean vector but not its length.

Suppose for a moment that the parameter a_1 is known. The LRT statistic (10.27) for the hypotheses (10.66) is now given by

$$\sigma^2 y = (\mathbf{x} - \mathbf{m}_0)^T \mathbf{C}^{-1} (\mathbf{x} - \mathbf{m}_0) - (\mathbf{x} - a_1 \mathbf{s}_1)^T \mathbf{C}^{-1} (\mathbf{x} - a_1 \mathbf{s}_1). \quad (10.67)$$

After some simple algebraic manipulations this can be written as

$$\begin{aligned} \sigma^2 y = & -\mathbf{m}_0^T \mathbf{C}^{-1} \mathbf{x} - \mathbf{x}^T \mathbf{C}^{-1} \mathbf{m}_0 + \mathbf{m}_0^T \mathbf{C}^{-1} \mathbf{m}_0 \\ & + a_1 \mathbf{s}_1^T \mathbf{C}^{-1} \mathbf{x} + a_1 \mathbf{x}^T \mathbf{C}^{-1} \mathbf{s}_1 - a_1^2 \mathbf{s}_1^T \mathbf{C}^{-1} \mathbf{s}_1. \end{aligned} \quad (10.68)$$

Matched Filter

A case of special interest occurs when $\mathbf{m}_0 = \mathbf{0}$. Indeed, if we set $\mathbf{m}_0 = \mathbf{0}$ and we ignore the constant term, the detection statistic (10.68) is simplified to

$$y_1 = a_1 \mathbf{s}_1^T \mathbf{C}^{-1} \mathbf{x} / \sigma^2 \stackrel{H_1}{\underset{H_0}{\gtrless}} \eta_1. \quad (10.69)$$

We note that computation of (10.69) requires knowledge of a_1 . Suppose now that we have to choose between the hypotheses

$$H_0 : \mathbf{x} \sim N(\mathbf{0}, \sigma^2 \mathbf{C}) \quad \text{and} \quad \mathbf{x} \sim N(a_1 \mathbf{s}_1, \sigma^2 \mathbf{C}), \quad a_1 > 0. \quad (10.70)$$

Since $a_1 > 0$ under H_1 , we can divide both sides of (10.69) by a_1 without affecting the direction of the inequality. This yields the LRT

$$y = \mathbf{s}_1^T \mathbf{C}^{-1} \mathbf{x} / \sigma^2 \stackrel{H_1}{\underset{H_0}{\gtrless}} \eta. \quad (10.71)$$

Note that the test (10.71) is now completely independent of a_1 and it has the same form with the matched filter (10.32). Therefore, the optimum Neyman–Pearson detector for the hypotheses (10.70) is the matched filter (10.71). Such a detector, which is best for all values of the unknown parameters, is called *uniformly most powerful (UMP)* (Levy, 2008). For reasons to be seen later, we use the following normalized matched filter formula:

$$y_{\text{MF}} = \frac{\mathbf{s}_1^T \mathbf{C}^{-1} \mathbf{x}}{\sigma \sqrt{\mathbf{s}_1^T \mathbf{C}^{-1} \mathbf{s}_1}}. \quad (10.72)$$

In practical applications we incorporate the parameter σ into the threshold.

Energy Matched Filter

If the sign of a_1 is unknown, we cannot take the step from (10.69) to (10.71) because when $a_1 > 0$ the direction of the inequality is preserved, but when $a_1 < 0$, it is reversed. In this case, we can use the GLRT approach to derive a test for arbitrary \mathbf{m}_0 . Since H_0 does not depend on a_1 , the GLRT requires maximizing the likelihood function

$$f(\mathbf{x}|a_1) = \frac{1}{(2\pi)^{p/2} |\mathbf{C}|^{1/2}} \exp \left[-\frac{1}{2\sigma^2} (\mathbf{x} - a_1 \mathbf{s}_1)^T \mathbf{C}^{-1} (\mathbf{x} - a_1 \mathbf{s}_1) \right] \quad (10.73)$$

with respect to a_1 . Taking the derivative of (10.73) with respect to a_1 , equating to zero, and solving for a_1 yields

$$\hat{a}_1 = \frac{\mathbf{s}_1^T \mathbf{C}^{-1} \mathbf{x}}{\mathbf{s}_1^T \mathbf{C}^{-1} \mathbf{s}_1}. \quad (10.74)$$

Substituting (10.74) into (10.68), we obtain the following detection statistic:

$$\sigma^2 y = \frac{(\mathbf{s}_1^T \mathbf{C}^{-1} \mathbf{x})^2}{\mathbf{s}_1^T \mathbf{C}^{-1} \mathbf{s}_1} - 2\mathbf{m}_0^T \mathbf{C}^{-1} \mathbf{x} + \mathbf{m}_0^T \mathbf{C}^{-1} \mathbf{m}_0. \quad (10.75)$$

We note that for $\mathbf{m}_0 = \mathbf{0}$, we have the detection statistic

$$y_{\text{EMF}} = \frac{(\mathbf{s}_1^T \mathbf{C}^{-1} \mathbf{x})^2}{\sigma^2 \mathbf{s}_1^T \mathbf{C}^{-1} \mathbf{s}_1} = y_{\text{MF}}^2. \quad (10.76)$$

The statistic (10.76) is called *energy matched filter (EMF)* because it is proportional to the square of the optimum detector (10.71). No optimality criterion is associated with (10.76). The squaring operation in (10.76) is basically used to compensate for the unknown sign of a_1 .

10.4.3 Equal Covariances and Means of Known Direction

This case corresponds to the following hypotheses:

$$H_0 : \mathbf{x} \sim N(a_0 \mathbf{s}_0, \sigma^2 \mathbf{C}) \quad \text{and} \quad H_1 : \mathbf{x} \sim N(a_1 \mathbf{s}_1, \sigma^2 \mathbf{C}) \quad (10.77)$$

where a_0 and a_1 are unknown parameters. The likelihood ratio is

$$y = (\mathbf{x} - a_0 \mathbf{s}_0)^T \mathbf{C}^{-1} (\mathbf{x} - a_0 \mathbf{s}_0) - (\mathbf{x} - a_1 \mathbf{s}_1)^T \mathbf{C}^{-1} (\mathbf{x} - a_1 \mathbf{s}_1). \quad (10.78)$$

The maximum likelihood estimate of a_i , $i = 0, 1$, under each hypothesis is

$$\hat{a}_i = \frac{\mathbf{s}_i^T \mathbf{C}^{-1} \mathbf{x}}{\mathbf{s}_i^T \mathbf{C}^{-1} \mathbf{s}_i}. \quad (10.79)$$

Substitution of (10.79) into (10.78) yields the detection statistic

$$T_G(\mathbf{x}) = \frac{(\mathbf{s}_1^T \mathbf{C}^{-1} \mathbf{x})^2}{\mathbf{s}_1^T \mathbf{C}^{-1} \mathbf{s}_1} - \frac{(\mathbf{s}_0^T \mathbf{C}^{-1} \mathbf{x})^2}{\mathbf{s}_0^T \mathbf{C}^{-1} \mathbf{s}_0}. \quad (10.80)$$

If $\mathbf{s}_0 = \mathbf{0}$, then (10.80) is reduced to (10.76). Note that the detection statistic in (10.80) is the difference between the squared outputs of two matched filters: one for \mathbf{s}_1 and the other for \mathbf{s}_0 .

Subspace Means

If the mean vectors lie on known subspaces, that is, $\mathbf{m}_0 = \mathbf{S}_0 \mathbf{a}_0$ and $\mathbf{m}_1 = \mathbf{S}_1 \mathbf{a}_1$, where \mathbf{S}_0 ($p \times q_0$) and \mathbf{S}_1 ($p \times q_1$) are known matrices, we can show that (10.80) becomes

$$T_G(\mathbf{x}) = \mathbf{x}^T \mathbf{C}^{-1} \mathbf{S}_1 (\mathbf{S}_1^T \mathbf{C}^{-1} \mathbf{S}_1)^{-1} \mathbf{S}_1^T \mathbf{C}^{-1} \mathbf{x} - \mathbf{x}^T \mathbf{C}^{-1} \mathbf{S}_0 (\mathbf{S}_0^T \mathbf{C}^{-1} \mathbf{S}_0)^{-1} \mathbf{S}_0^T \mathbf{C}^{-1} \mathbf{x}. \quad (10.81)$$

When $\mathbf{S}_0 = \mathbf{0}$ we have the simplified expression

$$T_G(\mathbf{x}) = \mathbf{x}^T \mathbf{C}^{-1} \mathbf{S}_1 (\mathbf{S}_1^T \mathbf{C}^{-1} \mathbf{S}_1)^{-1} \mathbf{S}_1^T \mathbf{C}^{-1} \mathbf{x}. \quad (10.82)$$

If $q_1 = p$ and the matrix matrix \mathbf{S}_1 has full rank, the subspace $\langle \mathbf{S}_1 \rangle$ fills the entire observation space. Then, the inverse of \mathbf{S}_1 exists and (10.82) becomes

$$T_G(\mathbf{x}) = \mathbf{x}^T \mathbf{C}^{-1} \mathbf{x}, \quad (10.83)$$

which is identical to the anomaly detector (10.65) for zero-centered clutter.

10.4.4 Means of Known Direction and Covariance with Unknown Scaling

We next introduce more unknown parameters by considering the hypotheses

$$H_0 : \mathbf{x} \sim N(a_0 \mathbf{s}_0, \sigma^2 \mathbf{C}) \quad \text{and} \quad H_1 : \mathbf{x} \sim N(a_1 \mathbf{s}_1, \sigma^2 \mathbf{C}), \quad (10.84)$$

where a_0 , a_1 , and σ^2 are unknown. The conditional probability density function is

$$f(\mathbf{x} | a_i, \sigma^2) = \frac{1}{(2\pi\sigma^2)^{p/2} |\mathbf{C}|^{1/2}} \exp \left[-\frac{1}{2\sigma^2} (\mathbf{x} - a_i \mathbf{s}_i)^T \mathbf{C}^{-1} (\mathbf{x} - a_i \mathbf{s}_i) \right]. \quad (10.85)$$

To find the maximum of (10.85) with respect to a_i and σ^2 we follow the approach in Section 9.9. The maximum of (10.85), which occurs at

$$\hat{a}_i = \frac{\mathbf{s}_i^T \mathbf{C}^{-1} \mathbf{x}}{\mathbf{s}_i^T \mathbf{C}^{-1} \mathbf{s}_i} \quad \text{and} \quad \hat{\sigma}_i^2 = \frac{1}{p} (\mathbf{x} - \hat{a}_i \mathbf{s}_i)^T (\mathbf{x} - \hat{a}_i \mathbf{s}_i) = \frac{1}{p} S(\hat{a}_i), \quad (10.86)$$

is given by

$$\max_{a_i, \sigma^2} f(\mathbf{x} | \hat{a}_i, \hat{\sigma}_i^2) = \frac{\exp(-p/2)}{(2\pi \hat{\sigma}_i^2)^{p/2} |\mathbf{C}|^{1/2}}. \quad (10.87)$$

Therefore, the GLR is given by

$$\Lambda_G(\mathbf{x}) = \frac{\max_{a_1, \sigma^2} f(\mathbf{x} | a_1, \sigma^2)}{\max_{a_0, \sigma^2} f(\mathbf{x} | a_0, \sigma^2)} = \left(\frac{\hat{\sigma}_0^2}{\hat{\sigma}_1^2} \right)^{p/2} = \left[\frac{S(\hat{a}_0)}{S(\hat{a}_1)} \right]^{p/2}, \quad (10.88)$$

where $S(\hat{a}_i)$ is the least squares error

$$S(\hat{a}_i) = \mathbf{x}^T \mathbf{C}^{-1} \mathbf{x} - \frac{(\mathbf{s}_i^T \mathbf{C}^{-1} \mathbf{x})^2}{\mathbf{s}_i^T \mathbf{C}^{-1} \mathbf{s}_i}. \quad (10.89)$$

Combining (10.89) with (10.88) leads to the following equivalent detection statistic

$$T_G(\mathbf{x}) = \frac{S(\hat{a}_1)}{S(\hat{a}_0)} = \frac{1 - \cos^2 \theta_1}{1 - \cos^2 \theta_0}, \quad (10.90)$$

where

$$\cos \theta \triangleq \frac{\mathbf{s}_1^T \mathbf{C}^{-1} \mathbf{x}}{\sqrt{\mathbf{s}_1^T \mathbf{C}^{-1} \mathbf{s}_1} \sqrt{\mathbf{x}^T \mathbf{C}^{-1} \mathbf{x}}} \quad (10.91)$$

and θ is the Mahalanobis angle between the test vector \mathbf{x} and the vector \mathbf{s}_1 . If $\mathbf{C} = \sigma_0^2 \mathbf{I}$, the Mahalanobis angle is equal to the Euclidean angle.

Energy Normalized Matched Filter

If $\mathbf{s}_0 = \mathbf{0}$, we have the following simpler set of hypotheses:

$$H_0 : \mathbf{x} \sim N(\mathbf{0}, \sigma^2 \mathbf{C}) \quad \text{and} \quad \mathbf{x} \sim N(a_1 \mathbf{s}_1, \sigma^2 \mathbf{C}), \quad a_1 \neq 0. \quad (10.92)$$

In this case, the test (10.90) takes the following simplified form:

$$y_{\text{ENMF}} = \cos^2 \theta_1 = \frac{(\mathbf{s}_1^T \mathbf{C}^{-1} \mathbf{x})^2}{(\mathbf{s}_1^T \mathbf{C}^{-1} \mathbf{s}_1)(\mathbf{x}^T \mathbf{C}^{-1} \mathbf{x})}. \quad (10.93)$$

Normalized Matched Filter

If we know that $a_1 > 0$, that is, we consider the hypotheses

$$H_0 : \mathbf{x} \sim N(\mathbf{0}, \sigma^2 \mathbf{C}) \quad \text{and} \quad H_1 : \mathbf{x} \sim N(a_1 \mathbf{s}_1, \sigma^2 \mathbf{C}), \quad a_1 > 0, \quad (10.94)$$

we can avoid the squaring operation in (10.93). This results in the detector

$$y_{\text{NMF}} = \cos \theta_1 = \frac{\mathbf{s}_1^T \mathbf{C}^{-1} \mathbf{x}}{(\mathbf{s}_1^T \mathbf{C}^{-1} \mathbf{s}_1)^{1/2} (\mathbf{x}^T \mathbf{C}^{-1} \mathbf{x})^{1/2}}. \quad (10.95)$$

The NMF is UMP in the class of detectors that are invariant to rotation and scaling; this result is further discussed in Section 10.6.

Subspace Means

If the mean vectors lie on known subspaces, that is, $\mathbf{m}_0 = S_0\mathbf{a}_0$ and $\mathbf{m}_1 = S_1\mathbf{a}_1$ with S_0 and S_1 known, we can show that (10.90) becomes

$$T_G(\mathbf{x}) = \frac{\frac{1 - \frac{\mathbf{x}^T \mathbf{C}^{-1} S_1 (S_1^T \mathbf{C}^{-1} S_1)^{-1} S_1^T \mathbf{C}^{-1} \mathbf{x}}{\mathbf{x}^T \mathbf{C}^{-1} \mathbf{x}}}{1 - \frac{\mathbf{x}^T \mathbf{C}^{-1} S_0 (S_0^T \mathbf{C}^{-1} S_0)^{-1} S_0^T \mathbf{C}^{-1} \mathbf{x}}{\mathbf{x}^T \mathbf{C}^{-1} \mathbf{x}}}}, \quad (10.96)$$

which for $S_0 = \mathbf{0}$ is simplified to

$$T_G(\mathbf{x}) = \frac{\mathbf{x}^T \mathbf{C}^{-1} S_1 (S_1^T \mathbf{C}^{-1} S_1)^{-1} S_1^T \mathbf{C}^{-1} \mathbf{x}}{\mathbf{x}^T \mathbf{C}^{-1} \mathbf{x}}. \quad (10.97)$$

10.5

Matched Filter and Maximization of Deflection

In Section 10.3 we showed that the matched filter is the optimum detector for two Gaussian distributions with different mean vectors and the same covariance matrix. We next derive the matched filter by maximizing a criterion known as detectability, which uses means and variances without making any distributional assumptions. Then, we derive the NMF detector by a simple geometric argument; however, in contrast to the derivations in Section 10.4, this approach is not associated with any optimality criterion.

Maximization of Deflection

Consider a linear filter defined by

$$y = \mathbf{h}^T \mathbf{x}. \quad (10.98)$$

The dot product (10.98) projects the p -dimensional vector \mathbf{x} onto the vector \mathbf{h} . The distribution of y under each hypothesis is obtained by projecting the corresponding multidimensional distribution onto \mathbf{h} . The average filter responses under the H_0 and H_1 hypotheses are given by $E(y|H_0)$ and $E(y|H_1)$, respectively. The squared distance $E(y|H_1) - E(y|H_0)$ divided by the variance $\text{var}(y|H_0)$, that is, the quantity defined by

$$D \triangleq \frac{[E(y|H_1) - E(y|H_0)]^2}{\text{var}(y|H_0)} \quad (10.99)$$

provides a normalized measure of the separation between the average responses, under the two hypotheses, in units of standard deviations. Equivalently, as illustrated in Figure 10.10, D is a dimensionless measure of the separation between the densities functions $f(y|H_0)$ and $f(y|H_1)$.

Choosing \mathbf{h} to maximize D results in the greatest possible average normalized separation of the filter output between the two classes of signals it is desired to discriminate; thus, the obtained filter optimizes the detection performance. For this reason, the quantity D is known as *deflection* or *detection index* (Van Trees et al., 2013). In radar and communications applications, the detection index is known as Signal-to-Clutter Ratio (SCR), Signal-to-Noise plus Interference Ratio (SNIR), or Signal-to-Noise Ratio (SNR).

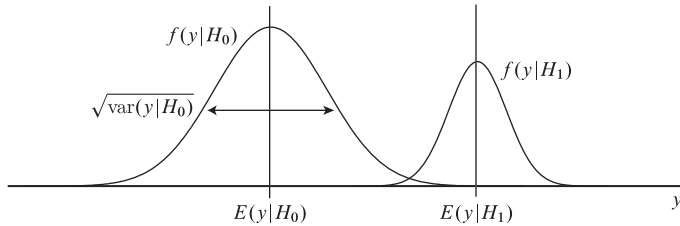


Figure 10.10 Quantities used for the computation of detectability.

The use of any specific term depends on where we wish to put the emphasis based on the phenomenology and the application.

Using (10.98), (10.43a), and (10.44) we can express (10.99) as follows:

$$D = \frac{[\mathbf{h}^T(\mathbf{m}_1 - \mathbf{m}_0)]^2}{\mathbf{h}^T \mathbf{C}_0 \mathbf{h}} = \frac{(\mathbf{h}^T \boldsymbol{\delta})^2}{\mathbf{h}^T \mathbf{C}_0 \mathbf{h}}, \quad (10.100)$$

where

$$\boldsymbol{\delta} = \mathbf{m}_1 - \mathbf{m}_0. \quad (10.101)$$

To find the maximum of (10.100) we express D in terms of the transformed vectors $\tilde{\mathbf{h}} \triangleq \mathbf{C}_0^{1/2} \mathbf{h}$ and $\tilde{\boldsymbol{\delta}} \triangleq \mathbf{C}_0^{-1/2} \boldsymbol{\delta}$, where $\mathbf{C}_0^{1/2}$ is the square root of \mathbf{C}_0 . The result is

$$D = \frac{(\tilde{\mathbf{h}}^T \tilde{\boldsymbol{\delta}})^2}{\tilde{\mathbf{h}}^T \tilde{\mathbf{h}}} \leq \tilde{\boldsymbol{\delta}}^T \tilde{\boldsymbol{\delta}}, \quad (10.102)$$

where the inequality follows from the Cauchy–Schwartz inequality (Strang, 2005). Thus, the maximum of (10.100) occurs when $\tilde{\mathbf{h}} = \kappa \tilde{\boldsymbol{\delta}}$ or equivalently

$$\mathbf{h} = \kappa \mathbf{C}_0^{-1} \boldsymbol{\delta} \triangleq \mathbf{h}_{\text{opt}} \quad (10.103)$$

for any $\kappa \neq 0$. Thus, the length of the maximizing vector \mathbf{h}_{opt} is *not* unique; however, its direction is unique. The maximum possible value of detectability (10.100) is given by

$$D_{\text{opt}} = \boldsymbol{\delta}^T \mathbf{C}_0^{-1} \boldsymbol{\delta}. \quad (10.104)$$

The choice of normalization constant κ , which clearly does not affect the value of D_{opt} , is arbitrary and is dictated by the use of the output. Figure 10.11 illustrates the optimum separation achieved by the matched filter (10.103) for two elliptically shaped distributions. Projection in any other direction gives a larger overlap between the projected distributions.

Since (10.100) does not change by scaling \mathbf{h} or $\boldsymbol{\delta}$, we can maximize the detectability index by solving the following constrained optimization problem

$$\min_{\mathbf{h}} \mathbf{h}^T \mathbf{C}_0 \mathbf{h} \quad \text{subject to} \quad \mathbf{h}^T \boldsymbol{\delta} = 1. \quad (10.105)$$

The filter coefficients obtained by solving (10.105) minimize the output power for a given value of the gain in a prescribed direction. Using the method of Lagrange multipliers we can easily show that the solution of (10.105) is given by (10.103)

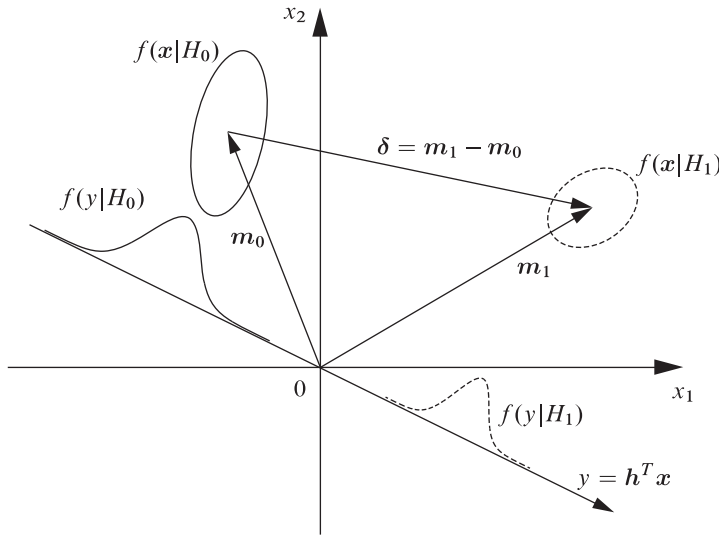


Figure 10.11 Projection of observation vectors onto the matched filter direction.

with $\kappa = 1/D_{\text{opt}}$. Using the constraint $\mathbf{h}^T \boldsymbol{\delta} = \alpha$ simply changes the value of the normalization constant κ .

Constrained Energy Minimization (CEM)

The energy at the output of linear filter (10.98) is given by

$$E = \frac{1}{n} \sum_{i=1}^n y_i^2 = \mathbf{h}^T \hat{\mathbf{R}} \mathbf{h}, \quad (10.106)$$

where $\hat{\mathbf{R}} = (1/n) \sum_{i=1}^n \mathbf{x}_i \mathbf{x}_i^T$ is an estimate of the correlation matrix. Minimization of the energy (10.106) subject to the directionality constraint $\mathbf{h}^T \mathbf{s} = 1$ yields

$$\mathbf{h}_{\text{CEM}} = \frac{\hat{\mathbf{R}}^{-1} \mathbf{s}}{\mathbf{s}^T \hat{\mathbf{R}}^{-1} \mathbf{s}}, \quad (10.107)$$

which is known as a constrained energy minimization (CEM) filter (Harsanyi, 1993). If we minimize $E(y^2)$ the result is a constrained power minimization filter, which is given by (10.107) with $\hat{\mathbf{R}}$ replaced by \mathbf{R} ; see Problem 4 for more details.

Normalization of Optimum Matched Filter

To simplify subsequent analysis, we subtract the constant $\kappa \boldsymbol{\delta}^T \mathbf{C}_0^{-1} \mathbf{m}_0$ from the output of matched filter. This changes the threshold but not the distribution of the filter output. The result is

$$y = \kappa \boldsymbol{\delta}^T \mathbf{C}_0^{-1} (\mathbf{x} - \mathbf{m}_0). \quad (10.108)$$

We next discuss two widely used choices for the normalization of matched filter output. The first, which requires the optimum matched filter to have unity output in the direction of $\boldsymbol{\delta} = \mathbf{m}_1 - \mathbf{m}_0$, yields

$$\mathbf{h}_{\text{opt}}^T \boldsymbol{\delta} = 1 \quad \Rightarrow \quad \kappa = (\boldsymbol{\delta}^T \mathbf{C}_0^{-1} \boldsymbol{\delta})^{-1}. \quad (10.109)$$

Substituting (10.109) into (10.108) yields

$$y = \frac{\boldsymbol{\delta}^T \mathbf{C}_0^{-1} (\mathbf{x} - \mathbf{m}_0)}{\boldsymbol{\delta}^T \mathbf{C}_0^{-1} \boldsymbol{\delta}}. \quad (10.110)$$

The mean and variance at the output of this filter are

$$E(y|H_0) = 0, \quad E(y|H_1) = 1, \quad \text{var}(y|H_0) = \boldsymbol{\delta}^T \mathbf{C}_0^{-1} \boldsymbol{\delta}. \quad (10.111)$$

This normalization justifies the term *minimum-variance distortionless response (MVDR)* matched filter because the filter passes signals in the direction of $\boldsymbol{\delta}$ undistorted while minimizing the response of signals in all other directions.

The second normalization approach keeps the variance $\text{var}(y|H_0)$ at the output of the optimum filter constant. In this case, we have

$$\mathbf{h}_{\text{opt}}^T \mathbf{C}_0 \mathbf{h}_{\text{opt}} = 1 \quad \Rightarrow \quad \kappa = (\boldsymbol{\delta}^T \mathbf{C}_0^{-1} \boldsymbol{\delta})^{-1/2}. \quad (10.112)$$

The output variance normalized matched filter is given by

$$y = \frac{\boldsymbol{\delta}^T \mathbf{C}_0^{-1} (\mathbf{x} - \mathbf{m}_0)}{\sqrt{\boldsymbol{\delta}^T \mathbf{C}_0^{-1} \boldsymbol{\delta}}}. \quad (10.113)$$

The mean and variance at the output of this filter are

$$E(y|H_0) = 0, \quad E(y|H_1) = (\boldsymbol{\delta}^T \mathbf{C}_0^{-1} \boldsymbol{\delta})^{-1/2}, \quad \text{var}(y|H_0) = 1. \quad (10.114)$$

Normalization (10.113) is useful for detection applications because keeping the variance of output clutter constant simplifies threshold selection.

Geometrical Interpretation

To understand the optimality properties of a matched filter we consider its operation in the whitened space defined by the transformation

$$\tilde{\mathbf{x}} = \mathbf{C}_0^{-1/2} (\mathbf{x} - \mathbf{m}_0). \quad (10.115)$$

The matched filter response in the whitened space is

$$y = \kappa \boldsymbol{\delta}^T \mathbf{C}_0^{-1} (\mathbf{x} - \mathbf{m}_0) = \kappa \tilde{\boldsymbol{\delta}}^T \tilde{\mathbf{x}}, \quad (10.116)$$

where

$$\tilde{\boldsymbol{\delta}} \triangleq \mathbf{C}_0^{-1/2} \boldsymbol{\delta} = \mathbf{C}_0^{-1/2} (\mathbf{m}_1 - \mathbf{m}_0). \quad (10.117)$$

If we use the variance normalization (10.112) we have $\kappa = (\boldsymbol{\delta}^T \mathbf{C}_0^{-1} \boldsymbol{\delta})^{-1/2} = \|\tilde{\boldsymbol{\delta}}\|$. In this case

$$y = \frac{\boldsymbol{\delta}^T \mathbf{C}_0^{-1} (\mathbf{x} - \mathbf{m}_0)}{\sqrt{\boldsymbol{\delta}^T \mathbf{C}_0^{-1} \boldsymbol{\delta}}} = \frac{\tilde{\boldsymbol{\delta}}^T \tilde{\mathbf{x}}}{\|\tilde{\boldsymbol{\delta}}\|}. \quad (10.118)$$

Thus, the output of the matched filter is equal to the scalar projection (see Leon 1998) of $\tilde{\mathbf{x}}$ onto $\tilde{\boldsymbol{\delta}}$; the vector projection is given by $\mathbf{x}_{\text{MF}} = y \tilde{\boldsymbol{\delta}} / \|\tilde{\boldsymbol{\delta}}\|$. We recall that $\tilde{\boldsymbol{\delta}}$ is the

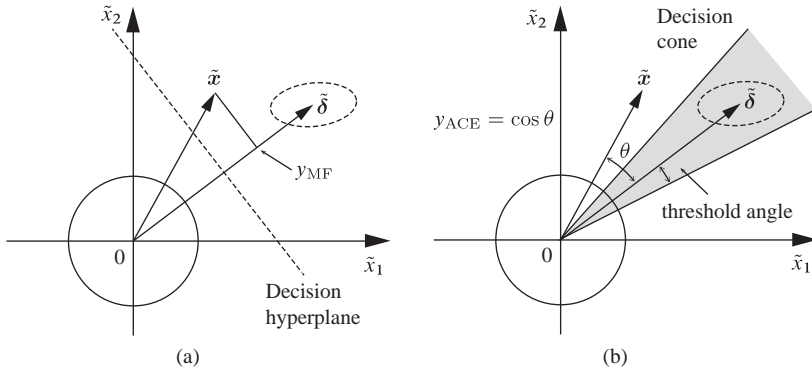


Figure 10.12 Geometrical interpretation of matched filter and ACE detectors.

vector from the tip of \mathbf{m}_0 to the tip of \mathbf{m}_1 . This is illustrated in Figure 10.12a assuming Gaussian distributions for the two hypotheses.

“Cosine” or “Normalized” Matched Filter

Careful inspection of Figure 10.12a reveals that observations from the $f(\mathbf{x}|H_1)$ distribution have larger projections onto $\tilde{\delta}$ and therefore larger matched filter responses than observations from $f(\mathbf{x}|H_0)$. The decision surface is a hyperplane perpendicular to $\tilde{\delta}$; its position is determined by the desired threshold. We also note that observation vectors from $f(\mathbf{x}|H_1)$ form small angles with vector $\tilde{\delta}$; therefore, we could use as a detection statistic the angle between these two vectors. We typically use the cosine of the angle because it measures the correlation or similarity between the two vectors.

The cosine of the angle formed by the vectors $\tilde{\mathbf{x}}$ and $\tilde{\delta}$ is given by

$$y_{\cos} \triangleq \cos \theta = \frac{\tilde{\delta}^T \tilde{\mathbf{x}}}{\|\tilde{\delta}\| \|\tilde{\mathbf{x}}\|}. \quad (10.119)$$

The detection statistics defined by (10.119) is *scale invariant*; that is, the value of the statistics does not change if we replace $\tilde{\delta}$ by $c_1 \tilde{\delta}$ and $\tilde{\mathbf{x}}$ by $c_2 \tilde{\mathbf{x}}$ ($c_1 > 0$ and $c_2 > 0$). This property justifies the term “normalized” matched filter. The decision surface for the NMF detector is the surface of a cone with vertex at the origin of $\tilde{\delta}$ and axis the line specified by $\tilde{\delta}$. The vertex angle is specified by the detection threshold (see Figure 10.12b). We emphasize that this derivation of the NMF detector, despite its simplicity and intuitive appeal, it is not associated with any optimality criterion.

In the signal observation space the NMF detector is given by

$$y_{\cos} = \frac{\delta^T \mathbf{C}_0^{-1} (\mathbf{x} - \mathbf{m}_0)}{\sqrt{\delta^T \mathbf{C}_0^{-1} \delta} \sqrt{(\mathbf{x} - \mathbf{m}_0)^T \mathbf{C}_0^{-1} (\mathbf{x} - \mathbf{m}_0)}}. \quad (10.120)$$

As we shall see in Section 10.6, the MF and NMF detectors have different performance because they have different decision surfaces.

Table 10.3 Generalized likelihood detectors for the signal model $\mathbf{x} \sim N(a\mathbf{s}, \sigma^2 \mathbf{C})$, where a is unknown, \mathbf{s} is known, and \mathbf{C} is known; the covariance scaling factor σ^2 can be either known or unknown.

Hypotheses	σ^2	Detector	Distribution
$H_0 : a = 0$	Known	$\frac{\mathbf{s}^T \mathbf{C}^{-1} \mathbf{x}}{\sqrt{\mathbf{s}^T \mathbf{C}^{-1} \mathbf{s}}}$	$N(\mu\sigma\sqrt{D}, \sigma^2)$
$H_1 : a > 0$			
$H_0 : a = 0$	Known	$\frac{(\mathbf{s}^T \mathbf{C}^{-1} \mathbf{x})^2}{\mathbf{s}^T \mathbf{C}^{-1} \mathbf{s}}$	$\sigma^2 \chi_1^2(\mu D)$
$H_1 : a \neq 0$			
$H_0 : a = 0$	Unknown	$\frac{\mathbf{s}^T \mathbf{C}^{-1} \mathbf{x}}{\sqrt{\mathbf{s}^T \mathbf{C}^{-1} \mathbf{s} \sqrt{\mathbf{x}^T \mathbf{C}^{-1} \mathbf{x}}}} = \cos \theta$	$\cot \theta \sim \frac{t_{p-1}(\mu\sqrt{D})}{\sqrt{(p-1)}}$
$H_1 : a > 0$			
$H_0 : a = 0$	Unknown	$\frac{(\mathbf{s}^T \mathbf{C}^{-1} \mathbf{x})^2}{(\mathbf{s}^T \mathbf{C}^{-1} \mathbf{s})(\mathbf{x}^T \mathbf{C}^{-1} \mathbf{x})} = \cos^2 \theta$	$\cot^2 \theta \sim \frac{F_{1,p-1}(\mu D)}{p-1}$
$H_1 : a \neq 0$			

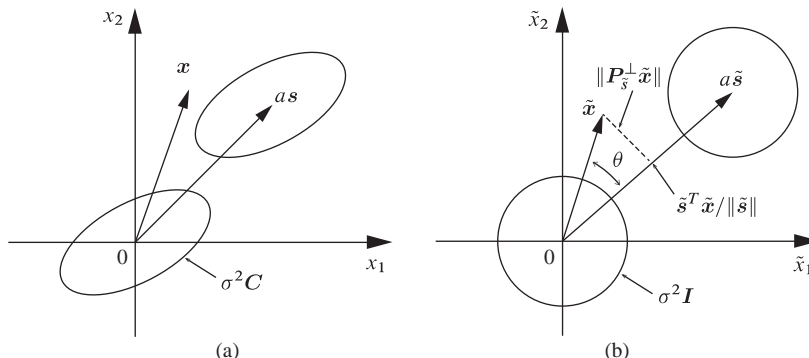


Figure 10.13 Geometrical illustration of the Gaussian detection problem defined by the hypotheses $H_0 : \mathbf{x} \sim N(\mathbf{0}, \sigma^2 \mathbf{C})$ and $H_1 : \mathbf{x} \sim N(a\mathbf{s}, \sigma^2 \mathbf{C})$: (a) original observation space and (b) whitened observation space.

10.6 Performance Analysis of Matched Filter Detectors

Up to this point we have focused on the derivation of detection algorithms for Gaussian distributions with completely or partially described mean vectors and covariance matrices. In this section we derive ROC curves for some detection algorithms which are useful in many problems of practical importance. Although the exact results hold under ideal conditions, the conclusions can be used to guide the selection and design of detection algorithms for practical applications.

Table 10.3 provides a summary of the distance-based and angle-based GLRT detectors for the Gaussian signal model $\mathbf{x} \sim N(a\mathbf{s}, \sigma^2 \mathbf{C})$. Note that for simplicity we have dropped the subscript from the target signature and the fill fraction parameter. The deflection is given by $D = a^2 \mathbf{s}^T (\sigma^2 \mathbf{C})^{-1} \mathbf{s}$. For spherical Gaussian distributions, where $\mathbf{C} = \mathbf{I}$, the formulas in Table 10.3 are simplified by dropping \mathbf{C} . Detector formulas in the whitened space are obtained by using the transformations $\tilde{\mathbf{x}} = \mathbf{C}^{-1/2} \mathbf{x}$, $\tilde{\mathbf{s}} = \mathbf{C}^{-1/2} \mathbf{s}$, and the identity $\mathbf{C}^{-1} = \mathbf{C}^{-1/2} \mathbf{C}^{-1/2}$.

10.6.1 Geometric Interpretations and Invariances

We next use some geometrical arguments to explain the distribution of the detection statistic and some invariances that provide insight into the performance of the corresponding detectors. To this end consider the decomposition of the whitened observation $\tilde{\mathbf{x}}$ to two orthogonal components: one in the signature subspace $\langle \tilde{\mathbf{s}} \rangle$ and the other in the orthogonal complement subspace $\langle \tilde{\mathbf{s}} \rangle^\perp$. From Figure 10.14 we deduce that

$$\tilde{\mathbf{x}} = \mathbf{P}_{\tilde{\mathbf{s}}}\tilde{\mathbf{x}} + \mathbf{P}_{\tilde{\mathbf{s}}}^\perp\tilde{\mathbf{x}}, \quad (10.121)$$

where

$$\mathbf{P}_{\tilde{\mathbf{s}}} = \tilde{\mathbf{s}}(\tilde{\mathbf{s}}^T\tilde{\mathbf{s}})^{-1}\tilde{\mathbf{s}}^T \quad \text{and} \quad \mathbf{P}_{\tilde{\mathbf{s}}}^\perp = \mathbf{I} - \mathbf{P}_{\tilde{\mathbf{s}}} \quad (10.122)$$

are the orthogonal projection matrices onto $\langle \tilde{\mathbf{s}} \rangle$ and $\langle \tilde{\mathbf{s}} \rangle^\perp$, respectively (see Section 9.5). Using the Pythagorean theorem we have

$$\|\tilde{\mathbf{x}}\|^2 = \|\mathbf{P}_{\tilde{\mathbf{s}}}\tilde{\mathbf{x}}\|^2 + \|\mathbf{P}_{\tilde{\mathbf{s}}}^\perp\tilde{\mathbf{x}}\|^2, \quad (10.123)$$

which shows the decomposition of observation vector energy in the two subspaces.

The *energy matched filter (EMF)* makes decisions by evaluating the component of the energy in the signature subspace

$$y_{\text{EMF}} = \|\mathbf{P}_{\tilde{\mathbf{s}}}\tilde{\mathbf{x}}\|^2 = \tilde{\mathbf{x}}^T \mathbf{P}_{\tilde{\mathbf{s}}}\tilde{\mathbf{x}}. \quad (10.124)$$

Using (10.122) we obtain

$$\mathbf{P}_{\tilde{\mathbf{s}}}\tilde{\mathbf{x}} = \frac{\tilde{\mathbf{s}}}{\|\tilde{\mathbf{s}}\|} \frac{\tilde{\mathbf{s}}^T\tilde{\mathbf{x}}}{\|\tilde{\mathbf{s}}\|}. \quad (10.125)$$

Since $\tilde{\mathbf{s}}/\|\tilde{\mathbf{s}}\|$ is a unit vector, the output of the matched filter detector

$$y_{\text{MF}} = \frac{\tilde{\mathbf{s}}^T\tilde{\mathbf{x}}}{\sqrt{\tilde{\mathbf{s}}^T\tilde{\mathbf{s}}}} = \frac{\mathbf{s}^T \mathbf{C}^{-1} \mathbf{x}}{\sqrt{\mathbf{s}^T \mathbf{C}^{-1} \mathbf{s}}} \quad (10.126)$$

is the scalar projection of $\tilde{\mathbf{x}}$ onto the whitened signature subspace.

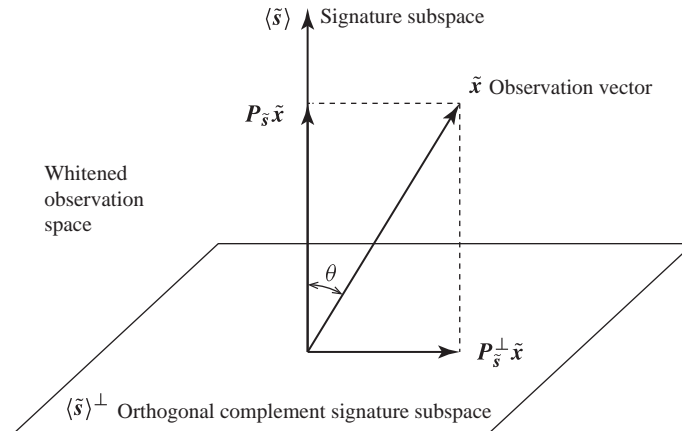


Figure 10.14 Orthogonal projections of the whitened observation vector onto the signature and its orthogonal complement subspaces.

Substitution of (10.125) into (10.124) yields

$$y_{\text{EMF}} = \frac{(\tilde{s}^T \tilde{x})^2}{\tilde{s}^T \tilde{s}} = y_{\text{MF}}^2. \quad (10.127)$$

The normalized matched filter uses the angle between the whitened signature and observation vectors. If we use the scalar projection (10.126) we obtain

$$y_{\text{NMF}} = \cos \theta = \frac{y_{\text{MF}}}{\|\tilde{x}\|} = \frac{\tilde{s}^T \tilde{x}}{\sqrt{\tilde{s}^T \tilde{s}} \sqrt{\tilde{x}^T \tilde{x}}} = \frac{s^T C^{-1} x}{\sqrt{s^T C^{-1} s} \sqrt{x^T C^{-1} x}}. \quad (10.128)$$

From the orthogonal triangle in Figure 10.14 we obtain the *energy NMF (ENMF)*:

$$y_{\text{ENMF}} = \cos^2 \theta = \frac{\|\mathbf{P}_s \tilde{x}\|^2}{\|\tilde{x}\|^2} = \frac{\tilde{x}^T \mathbf{P}_s \tilde{x}}{\tilde{x}^T \tilde{x}}. \quad (10.129)$$

We note that expressions (10.124) and (10.129) hold when the vector signature s is replaced by a “subspace” signature; that is, a $p \times q$ matrix S , where $q \leq p$ (Manolakis et al., 2003). Note that the denominator of (10.129) depends on the quantity

$$y_{\text{AD}} = x^T C^{-1} x = \tilde{x}^T \tilde{x}, \quad (10.130)$$

which is the Euclidean length of the whitened observation. This is essentially the anomaly detector (10.65) for zero mean clutter.

Instead of $\cos^2 \theta$ we can equivalently use the following detection statistic

$$\cot^2 \theta = \frac{\|\mathbf{P}_s \tilde{x}\|^2}{\|\mathbf{P}_{\tilde{s}}^{\perp} \tilde{x}\|^2} = \frac{\tilde{x}^T \mathbf{P}_{\tilde{s}}^{\perp} \tilde{x}}{\tilde{x}^T \mathbf{P}_{\tilde{s}}^{\perp} \tilde{x}} = \frac{y_{\text{MF}}^2}{y_{\text{AD}}^2 - y_{\text{MF}}^2}, \quad (10.131)$$

where we have used (10.122). A two-sided statistic is given by

$$\cot \theta = \frac{y_{\text{MF}}}{\sqrt{y_{\text{AD}}^2 - y_{\text{MF}}^2}}. \quad (10.132)$$

The numerator and denominator quantities in (10.131) and (10.132) find application in false alarm mitigation algorithms (DiPietro et al., 2012).

Figure 10.15 shows contours of equal probability under each hypothesis and the decision surfaces for the four matched filter detectors in the whitened space. Careful inspection of the decision surfaces shows that for every detector there are multiple observation vectors which yield the same detection statistic. Since these vectors can be obtained from a given observation vector using some geometrical transformations, we say that the detection statistic is invariant under these transformations. Detectors that are best among the subclass of detectors that are invariant under a set of transformations are called *uniformly most powerful invariant (UMPI)* (Levy, 2008).

Figure 10.16 illustrates the geometry and invariances of the four matched filter detectors. Careful inspection of the defining formulas and Figure 10.16 shows that:

- the MF is invariant to translation of the observations in the orthogonal subspace $\langle \tilde{s} \rangle^{\perp}$;
- the EMF is invariant to rotation of the observations in $\langle \tilde{s} \rangle$ and to translation in the orthogonal subspace $\langle \tilde{s} \rangle^{\perp}$;
- the NMF is invariant to rotations in $\langle \tilde{s} \rangle$ and to scaling of the observations;
- the ENMF is invariant to rotations in $\langle \tilde{s} \rangle$ and $\langle \tilde{s} \rangle^{\perp}$, and to scaling of the observations.

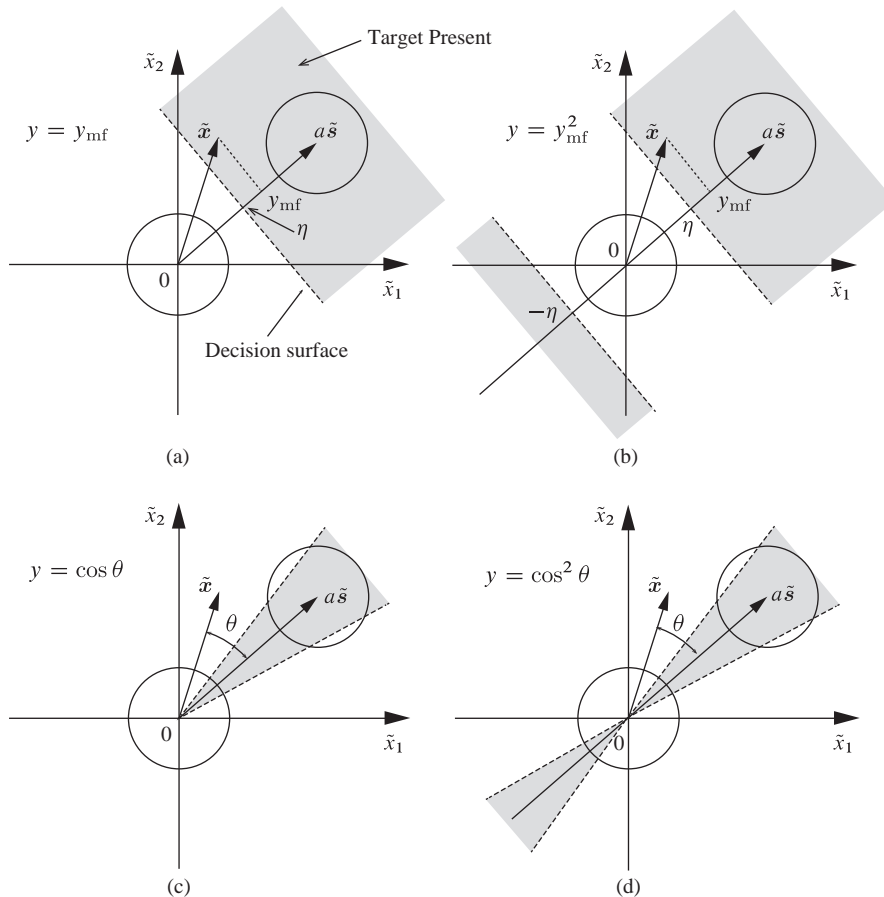


Figure 10.15 Decision surfaces for the four matched filter detectors in the whitened domain. The shaded areas show the “target present” part of the observation space and the dotted lines the decision boundaries.

These properties can be used to understand the operation of the four algorithms and their application to hyperspectral target detection applications.

10.6.2 Detection Performance

To evaluate ROC curves we need the distribution of the detection statistics under each hypothesis. The whitened observation vector is distributed as

$$\tilde{\mathbf{x}} \sim N(\mu a\tilde{\mathbf{s}}, \sigma^2 \mathbf{I}), \quad \mu \triangleq \begin{cases} 0, & \text{under } H_0, \\ 1, & \text{under } H_1. \end{cases} \quad (10.133)$$

To simplify the derivations, we rotate the whitened target signature vector into the direction of the first standard basis vector $\mathbf{e}_1 = [1 \ 0 \ \dots \ 0]^T$ using an orthogonal matrix \mathbf{Q} , where $\mathbf{Q}^T \mathbf{Q} = \mathbf{I}$. We can always obtain such a matrix using Householder’s transformation. If we pick \mathbf{Q} by

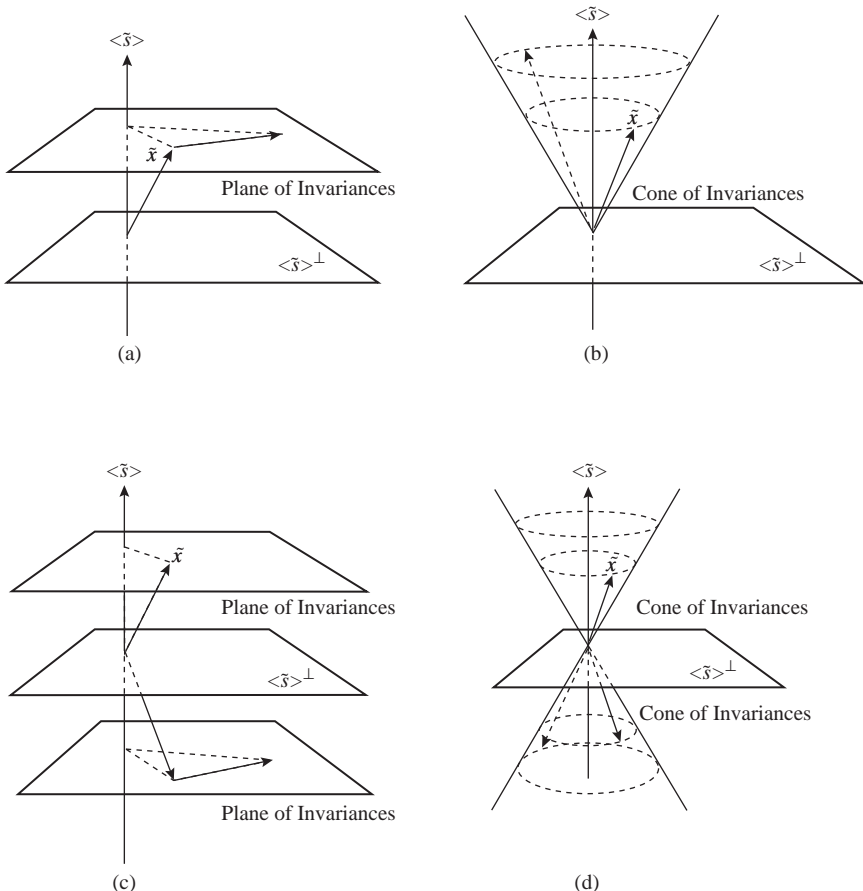


Figure 10.16 Invariance surfaces for matched-signature detectors in the whitened domain: (a) matched filter, (b) normalized matched filter, (c) energy-matched filter, and (d) energy-normalized matched filter (Kraut et al., 2001).

$$\mathbf{Q} = [\mathbf{q}_1 \quad \mathbf{Q}_2], \quad \mathbf{q}_1 = \frac{\tilde{s}}{\|\tilde{s}\|}, \quad \mathbf{Q}_2^T \tilde{s} = \mathbf{0} \quad (10.134)$$

we have

$$\mathbf{Q}^T \tilde{s} = \|\tilde{s}\| \mathbf{e}_1. \quad (10.135)$$

Applying the same rotation to the whitened observation vector we have

$$\mathbf{z} \triangleq \begin{bmatrix} z_1 \\ z_2 \end{bmatrix} = \mathbf{Q}^T \tilde{x} \sim N(\mu a \|\tilde{s}\| \mathbf{e}_1, \sigma^2 \mathbf{I}) \quad (10.136)$$

because $E(\mathbf{z}) = \mathbf{Q}^T E(\tilde{x}) = \mu a \|\tilde{s}\| \mathbf{e}_1$, $\text{cov}(\mathbf{z}) = \mathbf{Q}^T \text{cov}(\tilde{x}) \mathbf{Q} = \sigma^2 \mathbf{I}$, and spherical normal distributions are invariant under orthogonal transformations. We emphasize that since z_1 and z_2 are normally distributed and uncorrelated, they are also statistically independent.

The detection statistic for the MF detector can be written as

$$y_{\text{MF}} = \frac{\tilde{s}^T \tilde{x}}{\sqrt{\tilde{s}^T \tilde{s}}} = z_1 \sim N(\mu\sigma\sqrt{D}, \sigma^2), \quad (10.137)$$

where D is the detection index

$$D \triangleq (a/\sigma)^2 \|\tilde{s}\|^2. \quad (10.138)$$

Under H_0 , the detection statistic is distributed as $y_{\text{MF}} \sim N(0, \sigma^2)$; therefore, the probability of false alarm is $\alpha = Q(\eta/\sigma)$, which gives $\eta = \sigma Q^{-1}(\alpha)$. Since the detection statistic y_{MF} and threshold η are independent of the value $a > 0$ under H_1 , the test (10.72) is uniformly most powerful (UMP). Since σ is known, we can choose $\eta = \sigma Q^{-1}(\alpha)$ to ensure that the false alarm rate will be equal to a desired constant value α . Thus, the matched filter (10.72) has the *constant false alarm rate (CFAR)* property.

The detection statistic and the distribution of the EMF are given by

$$y_{\text{EMF}} = z_1^2 \sim \sigma^2 \chi_1^2(\mu D), \quad (10.139)$$

where $\chi_v^2(\delta)$ denotes a noncentral chi-square distribution with v degrees of freedom and non-centrality parameter δ . For known σ the EMF has the CFAR property.

The anomaly detector (10.130) and its distribution are

$$y_{\text{AD}} = \|\tilde{x}\|^2 = \|\mathbf{Q}^T \tilde{x}\|^2 = \|z\|^2 \sim \sigma^2 \chi_p^2(\mu D), \quad (10.140)$$

because the matrix \mathbf{Q} is orthogonal.

Since $\|\tilde{z}\|^2 = \|\mathbf{Q}^T \tilde{x}\|^2 = \|\tilde{x}\|^2$, the distribution of ENMF is given by

$$y_{\text{ENMF}} = \frac{(\tilde{s}^T \tilde{x})^2}{\|\tilde{s}\|^2 \|\tilde{x}\|^2} = \frac{z_1^2}{\|z\|^2} = \frac{z_1^2}{z_1^2 + \|z_2\|^2} \sim \beta_{\frac{1}{2}, \frac{1}{2}(p-1)}(\mu D), \quad (10.141)$$

where $0 \leq \beta_{m,n}(\delta) \leq 1$ is a beta distribution with non-centrality parameter δ . Since z_1 and z_2 are statistically independent, using the definition of the F-distribution, we have

$$F = \cot^2 \theta = \frac{z_1^2}{\|z_2\|^2} \sim \frac{1}{p-1} F_{1,p-1}(\mu D) \quad (10.142)$$

for the F -form of the EMNF detector.

To derive the distribution of the NMF, we first note that

$$y_{\text{NMF}} = \frac{\tilde{s}^T \tilde{x}}{\|\tilde{s}\| \|\tilde{x}\|} = \frac{z_1}{\|z\|} = \frac{t}{\sqrt{1+t^2}}, \quad t \triangleq \frac{z_1}{\|z_2\|}. \quad (10.143)$$

The random variable t is distributed as

$$t = \frac{z_1}{\|z_2\|} \sim \frac{1}{\sqrt{p-1}} t_{p-1}(\mu D), \quad (10.144)$$

where $t_v(\delta)$ is a t -distribution with v -degrees of freedom and non-centrality parameter δ .

Careful inspection of pertinent formulas reveals that the distributions of y_{NMF} and y_{ENMF} are completely characterized under H_0 . Therefore, in contrast to y_{MF} and y_{EMF} ,

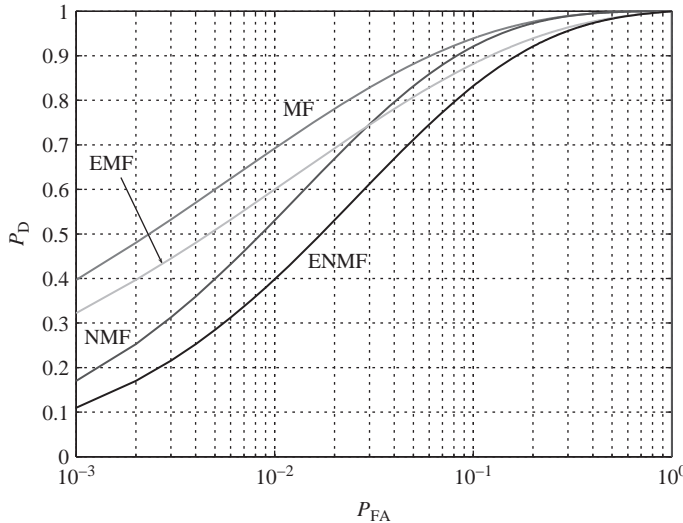


Figure 10.17 Comparative performance of matched filter type detectors for $p = 10$ dimensions and detection index $D = 8$. Note the crossover of ROC curves for the EMF and NMF detectors.

the normalized matched filter detectors have the CFAR property even when σ^2 is unknown.

Figure 10.17 shows ROC curves for the four matched filter detectors summarized in Table 10.3; these detectors have different performance because they have different a priori information about the parameters a and σ^2 . The MF detector (10.137), which is identical with the Neyman–Pearson detector (10.32), provides the optimum performance. The ENMF, which does not have access to the value of σ^2 or the sign of a , has the worst performance. For the y_{NMF} and y_{EMF} detectors there is no clear performance ordering because their ROC curves intersect; furthermore, their performance is bounded by the performance of y_{MF} and y_{ENMF} detectors.

Figure 10.18 shows a set of ROC curves for the NMF with fixed detection index D and the dimensionality p as a parameter. We note that as p increases the performance of NMF approaches the performance of the MF, which does not depend on p . This is intuitively expected because as p increases the t -distribution converges to a normal distribution. The NMF detector has worse performance than the matched filter because it assumes that the variance σ^2 is unknown.

10.6.3 Matched Subspace Detectors

Suppose that $\mathbf{x} \sim N(\mathbf{S}\mathbf{a}, \sigma^2 \mathbf{C})$; that is, the mean vector lies in a $p \times q$ subspace \mathbf{S} , where \mathbf{S} has full rank q and \mathbf{a} is a $q \times 1$ vector with $q \leq p$. The orthogonal projection operators in the whitened space are

$$\mathbf{P}_{\tilde{\mathbf{S}}} \triangleq \tilde{\mathbf{S}}(\tilde{\mathbf{S}}^T \tilde{\mathbf{S}})^{-1} \tilde{\mathbf{S}}^T, \quad \mathbf{P}_{\tilde{\mathbf{S}}}^\perp = \mathbf{I} - \mathbf{P}_{\tilde{\mathbf{S}}}, \quad (10.145)$$

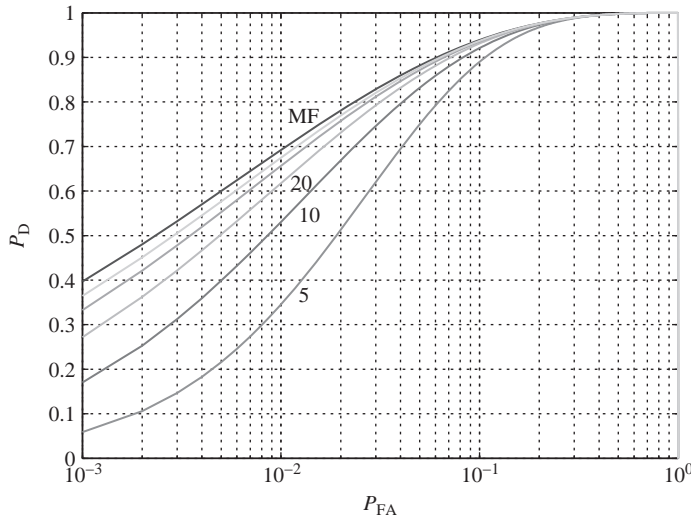


Figure 10.18 Performance of NMF detector as a function of data dimensionality ($D = 8$ and $p = 5, 10, 20, 40, 80$). The NMF attains asymptotically ($p \rightarrow \infty$) the performance of the optimum MF detector.

where $\tilde{\mathbf{x}} = \mathbf{C}^{-1/2}\mathbf{x}$ and $\tilde{\mathbf{S}} \triangleq \mathbf{C}^{-1/2}\mathbf{S}$. The subspace MF detector is

$$y_{\text{SubMF}} = \frac{\tilde{\mathbf{x}}^T \mathbf{P}_{\tilde{\mathbf{S}}} \tilde{\mathbf{x}}}{\sigma^2} \sim \chi_q^2(\mu D) \quad (10.146)$$

and the subspace NMF detector is

$$y_{\text{SubNMF}} = \frac{\tilde{\mathbf{x}}^T \mathbf{P}_{\tilde{\mathbf{S}}} \tilde{\mathbf{x}}}{\tilde{\mathbf{x}}^T \mathbf{P}_{\tilde{\mathbf{S}}}^\perp \tilde{\mathbf{x}}} \sim \frac{q}{p-q} F_{q,p-q}(\mu D), \quad (10.147)$$

where

$$D = (\mathbf{S}\mathbf{a})^T (\sigma^2 \mathbf{C}_b)^{-1} (\mathbf{S}\mathbf{a}). \quad (10.148)$$

Figure 10.19 illustrates the performance of subspace NMF as a function of target dimensionality. As expected, performance decreases with increasing q because the uncertainty about the target increases.

10.6.4 Performance in Elliptically Distributed Clutter

The four MF detection algorithms have been derived using the Gaussianity assumption. To study the robustness of these detectors to deviations from Gaussianity, we consider the following alternative characterization of normal distributions (Papoulis and Pillai, 2002):

$$\mathbf{x} \sim N(\mathbf{0}, \sigma^2 \mathbf{I}) \text{ if and only if } \begin{cases} \text{(a) } x_1, x_2, \dots, x_p \text{ are independent} \\ \text{(b) } f(\mathbf{x}) \text{ is spherically symmetric,} \end{cases} \quad (10.149)$$

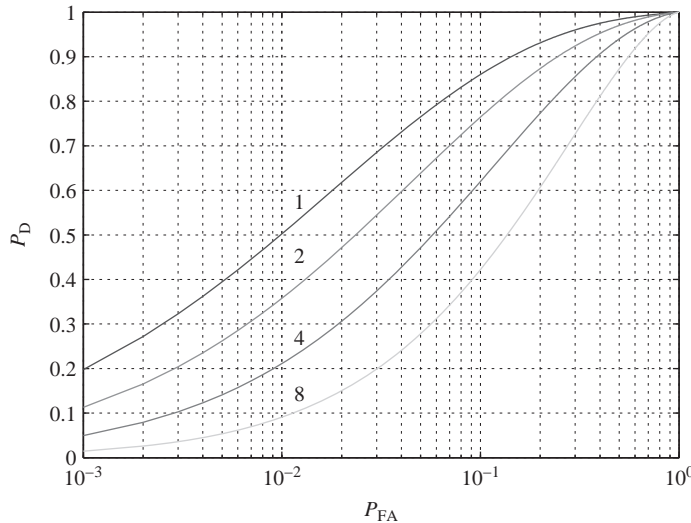


Figure 10.19 Performance of subspace NMF detector as a function of target subspace dimensionality ($D = 8$, $p = 20$, and $q = 1, 2, 4, 8$).

where, without loss of generality, we have assumed a spherical symmetry. Since (a) and (b) are mutually exclusive unless \mathbf{x} is normal, either (a) or (b) can be assumed for non-normal distributions. Note, however, that the adoption of sphericity (b) sacrifices the independence of samples. A critical question is: what happens to the optimality of Neyman–Pearson detectors derived under normality when we drop (a) or (b)? It has been shown that if we keep (a) the detectors lose their optimality because most optimal properties depend on spherical symmetry. In contrast, if we keep (b) the detectors preserve their structure and the P_{FA} remains unchanged (Richmond, 1996). However, maximizing the P_{D} is difficult because it depends, besides the spherical symmetry, on the distribution of the Mahalanobis distance.

The NMF is the uniformly most powerful invariant (UMPI) detector in spherically invariant clutter that follows a scale mixture of normal distributions. Furthermore, as we recall from Section 7.4.5, if $\mathbf{x} \sim E_p(\mathbf{m}, \mathbf{C}_b)$, then we have that $\tilde{\mathbf{x}} = \mathbf{C}_b^{-1/2}(\mathbf{x} - \mathbf{m}) \sim E_p(\mathbf{0}, \mathbf{I})$ and $\tilde{\mathbf{x}}$ can be expressed in polar form as $\tilde{\mathbf{x}} = \tilde{\mathbf{s}}\mathbf{u}$. Hence, under the H_0 hypothesis, the NMF statistic can be expressed as

$$y_{\text{NMF}} = \frac{\tilde{\mathbf{s}}^T \tilde{\mathbf{x}}}{\|\tilde{\mathbf{s}}\| \|\tilde{\mathbf{x}}\|} = \frac{\tilde{\mathbf{s}}^T \mathbf{u}}{\|\tilde{\mathbf{s}}\| \|\mathbf{u}\|}. \quad (10.150)$$

We note that the distribution of NMF under H_0 is the same for all ECDs and we can use the normal distribution to derive the required formulas. The practical value of (10.150) is that the false alarm rate for the NMF is robust to clutter with heavy tails.

10.6.5 Effects of Signature Mismatch

In many practical applications, the actual signature s_0 measured by the sensor may be different from the signature s used by the detector: that is, the signal model is

$$\mathbf{x} \sim N(\mu a s_0, \sigma^2 \mathbf{C}), \quad (10.151)$$

where $s_0 \neq s$. The equivalent model in the whitened space is given by

$$\tilde{\mathbf{x}} \sim N(\mu a \tilde{s}_0, \sigma^2 \mathbf{I}), \quad (10.152)$$

where $\tilde{s}_0 = \mathbf{C}^{-1/2} s_0$ is the actual whitened signature. This detection problem is illustrated geometrically in Figure 10.20. We will use the approach in Section 10.6.2 to evaluate performance when there is signature mismatch.

The mean and covariance of the rotated observation vector $\mathbf{z} = \mathbf{Q}^T \tilde{\mathbf{x}}$ are

$$E(\mathbf{z}) = \mathbf{Q}^T E(\tilde{\mathbf{x}}) = \mu a \mathbf{Q}^T s_0, \quad \text{cov}(\mathbf{z}) = \sigma^2 \mathbf{I}. \quad (10.153)$$

The components of $E(\mathbf{z})$ onto the subspaces $\langle \tilde{s} \rangle$ and $\langle \tilde{s} \rangle^\perp$ are given by

$$E(z_1) = \mu a \mathbf{q}_1^T s_0 = \mu a \|s_0\| \cos \theta_m \quad (10.154)$$

$$E(z_2) = \mu a \mathbf{q}_2^T s_0 = \mu a \|s_0\| \sin \theta_m, \quad (10.155)$$

where θ_m is the mismatch angle between the actual and assumed signatures

$$\cos \theta_m \triangleq \frac{\tilde{s}^T \tilde{s}_0}{\|\tilde{s}\| \|\tilde{s}_0\|}. \quad (10.156)$$

Therefore, we have the following distributions

$$z_1 / \sigma \sim N_1(\mu \delta_1, 1) \quad (10.157)$$

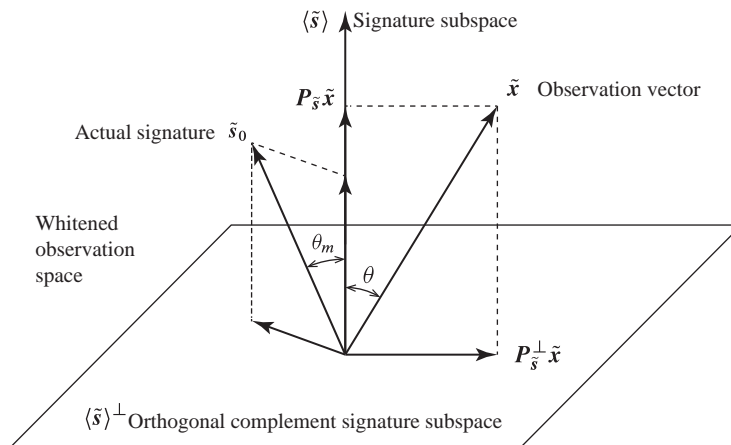


Figure 10.20 Geometrical illustration of mismatch between the reference signature s and the actual signature s_0 in the whitened observation space.

$$z_2/\sigma \sim N_{p-1}(\mu(a/\sigma)Q_2^T \tilde{s}_0, I), \quad (10.158)$$

where

$$\delta_1 \triangleq (a/\sigma) \|\tilde{s}_0\| \cos \theta_m. \quad (10.159)$$

From the definition of non-central chi square distribution (7.73), we have

$$\|z_2\|^2/\sigma^2 \sim \chi_{p-1}^2(\mu \delta_2^2), \quad (10.160)$$

where the non-centrality parameter is

$$\delta_2^2 = \|E(z_2)\|^2/\sigma^2 = (a/\sigma)^2 \|Q_2^T \tilde{s}_0\|^2 = (a/\sigma)^2 \|\tilde{s}_0\|^2 \sin \theta_m^2. \quad (10.161)$$

Using (10.138), (10.159) and (10.161) we obtain

$$D = (a/\sigma)^2 \|\tilde{s}_0\|^2 = \delta_1^2 + \delta_2^2, \quad (10.162)$$

which shows the decomposition of detectability index into two components: one parallel and one orthogonal to the signature subspace.

The performance of the MF is determined by

$$y_{\text{MF}} = z_1 \sim \sigma N_1(\mu \delta_1, 1). \quad (10.163)$$

The distributions of NMF is

$$t = \cot \theta = \frac{z_1}{\|z_2\|} \sim \frac{1}{\sqrt{p-1}} \frac{N_1(\mu \delta_1, 1)}{\sqrt{\chi_{p-1}^2(\mu \delta_2^2)/(p-1)}}. \quad (10.164)$$

Under the H_0 ($\mu = 0$) hypothesis, t follows a central t -distribution. However, under the H_1 ($\mu = 1$) hypothesis, t follows a doubly non-central t -distribution with non-centrality parameters δ_1 and δ_2^2 and $p-1$ degrees of freedom (Johnson et al., 1995). Using these results we can plot the P_D as a function of SCR for a fixed P_{FA} with $\cos^2 \theta$ as a parameter. A typical set of plots is shown in Figure 10.21 for the MF and NMF detectors. We note that the NMF is more sensitive to mismatch compared to the MF, especially for small values of the dimensionality p . This is intuitively expected because the NMF is essentially an angle-based detector.

The distributions for the corresponding energy NM and NMF detectors are found by squaring (10.163) and (10.164). The results are

$$y_{\text{ENMF}} = z_1^2 = \sigma^2 \chi_1^2(\mu \delta_1^2) \quad (10.165)$$

and

$$F = \cot^2 \theta = \frac{z_1^2}{\|z_2\|^2} \sim \frac{1}{\sqrt{p-1}} F_{1,p-1}(\mu \delta_1^2, \delta_2^2), \quad (10.166)$$

where F follows a doubly non-central F -distribution with non-centrality parameters δ_1^2 and δ_2^2 (Johnson et al., 1995). The distribution of ENMF can be expressed in terms of the doubly non-central beta distribution (Johnson et al., 1995).

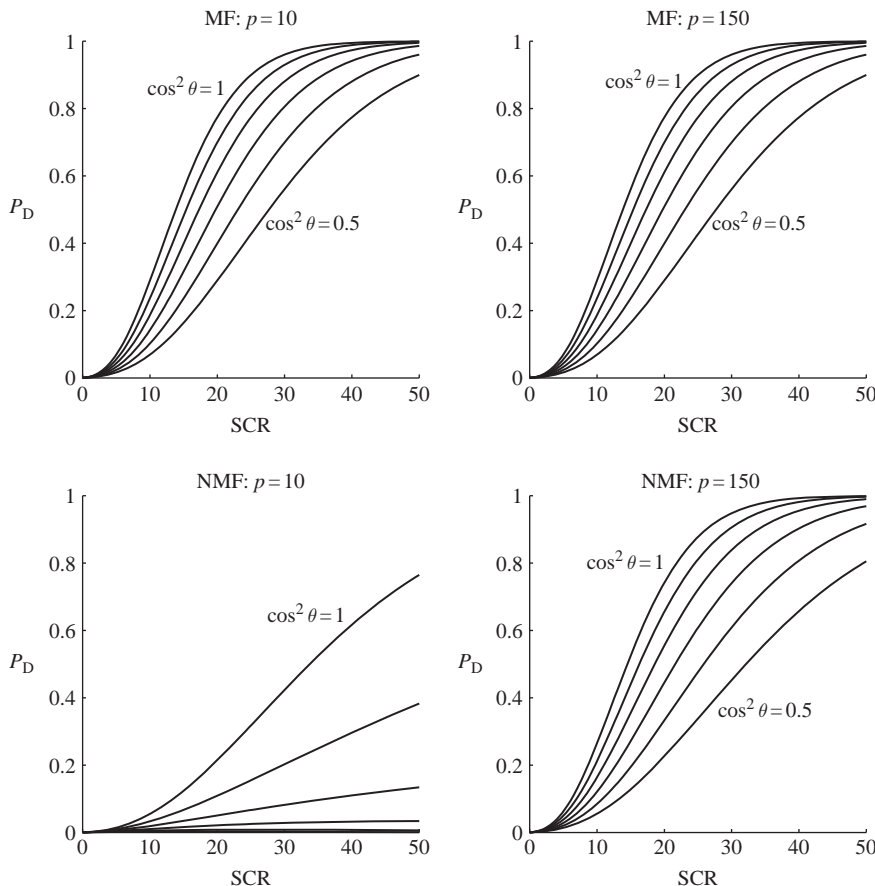


Figure 10.21 Illustration of the effects of signature mismatch on the performance of MF and NMF detectors. The plots show the P_D as a function of SCR for $P_{FA} = 10^{-4}$, $\cos^2 \theta = 0, 0.5, 0.6, 0.7, 0.8, 0.9, 1$, and $p = 10$ or 150 .

10.7 Detectors for Signals in Subspace Clutter and Isotropic Noise

There are applications where the target and clutter observations lie on known subspaces and the noise follows an isotropic normal distribution. In this case, the observed signal can be modeled as

$$\mathbf{x} = \mathbf{S}\mathbf{a} + \mathbf{B}\mathbf{c} + \mathbf{n}, \quad \mathbf{n} \sim N(\mathbf{0}, \sigma^2 \mathbf{I}), \quad (10.167)$$

where the target subspace matrix $\mathbf{S}(p \times q_t)$ and the clutter or background subspace matrix $\mathbf{B}(p \times q_b)$ are known and have linearly independent columns. If the target is present, we have $\mathbf{a} \neq \mathbf{0}$; otherwise, we have $\mathbf{a} = \mathbf{0}$. This problem is similar to the model comparison problem discussed in Section 9.12.

10.7.1 Derivation of Detection Tests

We will seek a test to choose among the following hypotheses

$$H_0 : \mathbf{a} = \mathbf{0} \quad \text{versus} \quad H_1 : \mathbf{a} \neq \mathbf{0}. \quad (10.168)$$

The conditional probability density function of $\mathbf{x} \sim N(\mathbf{Sa} + \mathbf{Bc}, \sigma^2 \mathbf{I})$ is

$$f(\mathbf{x}|\mathbf{a}, \mathbf{c}, \sigma^2) = \frac{1}{(2\pi\sigma^2)^{\frac{p}{2}}} \exp \left[-\frac{(\mathbf{x} - \mathbf{Sa} - \mathbf{Bc})^T(\mathbf{x} - \mathbf{Sa} - \mathbf{Bc})}{2\sigma^2} \right]. \quad (10.169)$$

Since the density (10.169) depends on unknown parameters, we shall use the GLRT defined by (10.21). To find the maximum of (10.169) with respect to the unknown parameters we follow the approach in Section 9.9. There are two cases of interest.

Noise variance known

When σ^2 is known, the GLRT is given by

$$\Lambda_G(\mathbf{x}) = \frac{\max_{\mathbf{a}, \mathbf{c}} f(\mathbf{x}|\mathbf{a}, \mathbf{c}, \sigma^2)}{\max_{\mathbf{c}} f(\mathbf{x}|\mathbf{0}, \mathbf{c}, \sigma^2)} = \exp \left(\frac{\mathbf{x} \mathbf{P}_B^\perp \mathbf{x} - \mathbf{x} \mathbf{P}_{SB}^\perp \mathbf{x}}{2\sigma^2} \right) \stackrel{H_1}{\underset{H_0}{\gtrless}} \eta_0, \quad (10.170)$$

where $\mathbf{x} \mathbf{P}_B^\perp \mathbf{x}$ and $\mathbf{x} \mathbf{P}_{SB}^\perp \mathbf{x}$ are the least squares errors under H_0 and H_1 . The orthogonal projection matrices are defined by

$$\mathbf{P}_A = \mathbf{A}(\mathbf{A}^T \mathbf{A})^{-1} \mathbf{A}^T \quad (10.171)$$

$$\mathbf{P}_A^\perp = \mathbf{I} - \mathbf{P}_A, \quad (10.172)$$

where $\mathbf{A} = \mathbf{B}$ or $\mathbf{A} \triangleq [\mathbf{S} \ \mathbf{B}]$. The GLRT in (10.170) can be written in the following more convenient form

$$T_1(\mathbf{x}) = \mathbf{x} \mathbf{P}_B^\perp \mathbf{x} - \mathbf{x} \mathbf{P}_{SB}^\perp \mathbf{x} \stackrel{H_1}{\underset{H_0}{\gtrless}} \eta_1 \sigma^2. \quad (10.173)$$

From the discussion in Section 9.12 we conclude that $T_1(\mathbf{x})$ is the extra sum of squares, resulting from potential underfitting when we require that $\mathbf{a} = \mathbf{0}$. From (9.151) and (9.158) we conclude that $T_1(\mathbf{x})$ follows a non-central chi-square distribution

$$T_1(\mathbf{x})/\sigma^2 \sim \chi_{q_t}^2(D) \quad (10.174)$$

with non-centrality parameter

$$D = \frac{1}{\sigma^2} \mathbf{a}^T \mathbf{R}_{22}^T \mathbf{R}_{22} \mathbf{a} = \frac{1}{\sigma^2} \mathbf{a}^T \mathbf{S}^T \mathbf{P}_b^\perp \mathbf{S} \mathbf{a}, \quad (10.175)$$

where $D = 0$ under H_0 and $D > 0$ under H_1 . Since σ^2 is unknown, we cannot set a CFAR threshold; however, we can use the test with an arbitrary threshold.

Noise variance unknown

When σ^2 is unknown, the GLRT is given by

$$\Lambda_G(\mathbf{x}) = \frac{\max_{\mathbf{a}, \mathbf{c}, \sigma^2} f(\mathbf{x}|\mathbf{a}, \mathbf{c}, \sigma^2)}{\max_{\mathbf{c}, \sigma^2} f(\mathbf{x}|\mathbf{0}, \mathbf{c}, \sigma^2)} = \left(\frac{\mathbf{x} \mathbf{P}_B^\perp \mathbf{x}}{\mathbf{x} \mathbf{P}_{SB}^\perp \mathbf{x}} \right)^{p/2} \stackrel{H_1}{\underset{H_0}{\gtrless}} \eta_0, \quad (10.176)$$

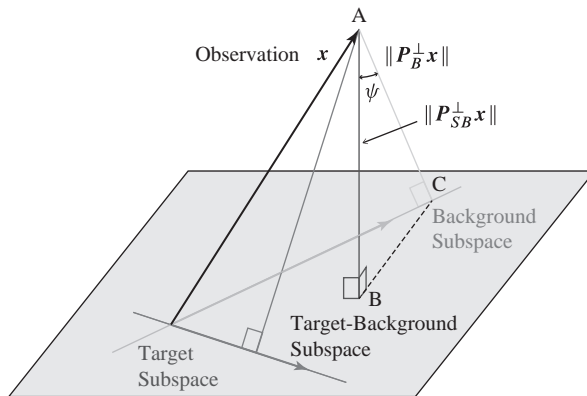


Figure 10.22 Geometrical interpretation of subspace detection algorithms.

where we have used (9.112) to determine the maximum of the likelihood function. In practice, we use the monotonically related test

$$T_2(\mathbf{x}) = \Lambda_G(\mathbf{x})^{2/p} - 1 = \frac{\mathbf{x} \mathbf{P}_B^\perp \mathbf{x} - \mathbf{x} \mathbf{P}_{SB}^\perp \mathbf{x}}{\mathbf{x} \mathbf{P}_{SB}^\perp \mathbf{x}}. \quad (10.177)$$

To determine the distribution of $T_2(\mathbf{x})$ we use (9.161) and (9.162). The result is

$$T_2(\mathbf{x}) \frac{p - (q_t + q_b)}{q_t} \sim F_{q_t, p - (q_t + q_b)}(D), \quad (10.178)$$

which is a non-central F-distribution with non-centrality parameter given by (10.175). A geometrical interpretation of $T_1(\mathbf{x})$ and $T_2(\mathbf{x})$ is provided in Figure 10.22. Although the two detectors use the difference and the ratio of the same two distances, they have different performance because they use different a priori information (known or unknown σ^2). This is demonstrated by the fact that the two tests have different distributions (see Problem 11). Note that any trigonometric number (\cos, \sin, \tan, \cot) of the angle ψ formed by the vectors $\mathbf{P}_B^\perp \mathbf{x}$ and $\mathbf{P}_{SB}^\perp \mathbf{x}$ can also be used as a detection statistic.

One-dimensional targets

If $q_t = 1$ we have $\mathbf{x} = a\mathbf{s} + \mathbf{B}\mathbf{c} + \mathbf{n}$, where a is a scalar. Under the H_1 hypothesis, the MLE of a is given by

$$\hat{a}_1 = \frac{\mathbf{s}^T \mathbf{P}_B^\perp \mathbf{x}}{\mathbf{s}^T \mathbf{P}_B^\perp \mathbf{s}}. \quad (10.179)$$

In this case we can develop additional tests (see Scharf and Friedlander, 1994) to choose between the following hypotheses

$$H_0 : a = 0 \quad \text{versus} \quad H_1 : a > 0. \quad (10.180)$$

When σ^2 is known, the test has the form

$$T'_1(\mathbf{x}) = \begin{cases} 0, & \hat{a}_1 \leq 0 \\ \mathbf{x} \mathbf{P}_B^\perp \mathbf{x} - \mathbf{x} \mathbf{P}_{SB}^\perp \mathbf{x}, & \hat{a}_1 > 0. \end{cases} \quad (10.181)$$

In case σ^2 is unknown, we use the following test

$$T'_2(\mathbf{x}) = \begin{cases} 0, & \hat{a}_1 \leq 0 \\ \mathbf{x}P_B^\perp \mathbf{x} / \mathbf{x}P_{SB}^\perp \mathbf{x}, & \hat{a}_1 > 0. \end{cases} \quad (10.182)$$

The distributions of (10.181) and (10.182) and their optimality properties are discussed in Scharf and Friedlander (1994).

10.7.2 Geometrical Interpretations and Invariances

The tests derived in the previous section involve the lengths of the projections $P_B^\perp x$ and $P_{SB}^\perp x$. These projections are related through the following formula:

$$\mathbf{P}_B^\perp = \mathbf{P}_{SB}^\perp + \mathbf{P}_{P_B^\perp S} \mathbf{P}_B^\perp, \quad (10.183)$$

which can be obtained from Figure 10.23 using simple geometrical arguments. Indeed, we first obtain the orthogonal projection $\mathbf{P}_B^\perp \mathbf{x}$ of the observation \mathbf{x} onto the background-free subspace. Then, we decompose $\mathbf{P}_B^\perp \mathbf{x}$ in two orthogonal components parallel to the sides of the orthogonal triangle OAD. This yields

$$P_B^\perp x = P_{SB}^\perp x + P_{P_B^\perp S} P_B^\perp x, \quad (10.184)$$

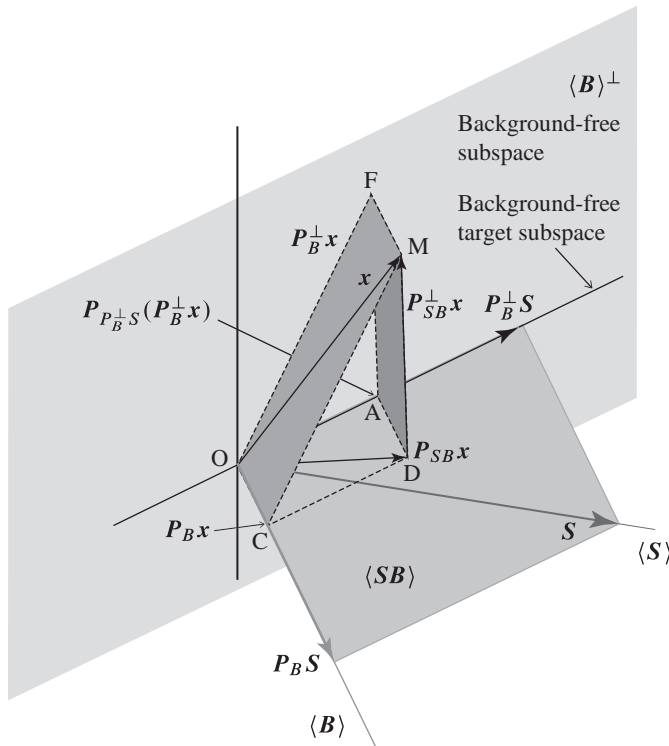


Figure 10.23 Illustration of various orthogonal projection operations in the signal and background subspaces.

which leads to (10.183). To simplify notation, we define the matrix

$$\mathbf{G} \triangleq \mathbf{P}_B^\perp \mathbf{S}. \quad (10.185)$$

Since \mathbf{P}_B^\perp is symmetric, $(\mathbf{P}_B^\perp)^T = \mathbf{P}_B^\perp$, and idempotent, $(\mathbf{P}_B^\perp)^2 = \mathbf{P}_B^\perp$, we have

$$\mathbf{P}_G = \mathbf{P}_B^\perp [\mathbf{P}_B^\perp \mathbf{S} (\mathbf{S}^T \mathbf{P}_B^\perp \mathbf{S})^{-1} \mathbf{S}^T \mathbf{P}_B^\perp] \mathbf{P}_B^\perp = \mathbf{P}_B^\perp \mathbf{P}_G \mathbf{P}_B^\perp. \quad (10.186)$$

Using (10.186) in conjunction with (10.183) we obtain the following identities:

$$\mathbf{P}_B^\perp - \mathbf{P}_{SB}^\perp = \mathbf{P}_G = \mathbf{P}_B^\perp \mathbf{P}_G \mathbf{P}_B^\perp \quad (10.187)$$

$$\mathbf{P}_{SB}^\perp = \mathbf{P}_B^\perp \mathbf{P}_G^\perp \mathbf{P}_B^\perp. \quad (10.188)$$

We note that $\langle \mathbf{P}_B^\perp \rangle$ is the *background-free subspace* and $\langle \mathbf{G} \rangle = \langle \mathbf{P}_B^\perp \mathbf{S} \rangle$ is the *background-free target subspace* of the observation space.

Using (10.173) and (10.187) we obtain

$$T_1(\mathbf{x}) = \mathbf{x} \mathbf{P}_B^\perp \mathbf{x} - \mathbf{x} \mathbf{P}_{SB}^\perp \mathbf{x} = \mathbf{x}^T \mathbf{P}_G \mathbf{x} = \|\mathbf{P}_G \mathbf{x}\|^2. \quad (10.189)$$

Similarly, from (10.177), (10.187) and (10.188) we have

$$T_2(\mathbf{x}) = \frac{\mathbf{x} \mathbf{P}_B^\perp \mathbf{x} - \mathbf{x} \mathbf{P}_{SB}^\perp \mathbf{x}}{\mathbf{x}^T \mathbf{P}_{SB}^\perp \mathbf{x}} = \frac{\mathbf{x}^T \mathbf{P}_B^\perp \mathbf{P}_G \mathbf{P}_B^\perp \mathbf{x}}{\mathbf{x}^T \mathbf{P}_B^\perp \mathbf{P}_G^\perp \mathbf{P}_B^\perp \mathbf{x}} = \frac{\|\mathbf{P}_G \mathbf{P}_B^\perp \mathbf{x}\|^2}{\|\mathbf{P}_G^\perp \mathbf{P}_B^\perp \mathbf{x}\|^2}. \quad (10.190)$$

10.7.3 Targets Described by a Single Vector

We shall focus on the important case of one-dimensional targets; the more general case is discussed by Scharf and Friedlander (1994). For $q_t = 1$, the projection matrix \mathbf{P}_G , becomes

$$\mathbf{P}_G = \mathbf{G}(\mathbf{G}^T \mathbf{G})^{-1} \mathbf{G}^T = \mathbf{P}_B^\perp \mathbf{s} (\mathbf{s}^T \mathbf{P}_B^\perp \mathbf{s})^{-1} \mathbf{s}^T \mathbf{P}_B^\perp. \quad (10.191)$$

Substitution of (10.191) to (10.189) and (10.190) yields

$$T_1(\mathbf{x}) = \frac{(\mathbf{s}^T \mathbf{P}_B^\perp \mathbf{x})^2}{\mathbf{s}^T \mathbf{P}_B^\perp \mathbf{s}} \quad (10.192)$$

and

$$T_2(\mathbf{x}) = \frac{T_1(\mathbf{x})}{\mathbf{x}^T \mathbf{P}_B^\perp \mathbf{x} - T_1(\mathbf{x})} = \frac{T_1(\mathbf{x}) / \mathbf{x}^T \mathbf{P}_B^\perp \mathbf{x}}{1 - T_1(\mathbf{x}) / \mathbf{x}^T \mathbf{P}_B^\perp \mathbf{x}} \quad (10.193)$$

respectively. The test (10.193) is equivalent to the test

$$T'_2(\mathbf{x}) = \frac{T_1(\mathbf{x})}{\mathbf{x}^T \mathbf{P}_B^\perp \mathbf{x}} = \frac{(\mathbf{s}^T \mathbf{P}_B^\perp \mathbf{x})^2}{(\mathbf{s}^T \mathbf{P}_B^\perp \mathbf{s})(\mathbf{x}^T \mathbf{P}_B^\perp \mathbf{x})}. \quad (10.194)$$

We note that if we replace \mathbf{P}_B^\perp by \mathbf{C}^{-1} in (10.192) and (10.194), we obtain the formulas for the energy matched filter detectors in Table 10.3. Since \mathbf{P}_B^\perp can be viewed as a low-rank approximation of \mathbf{C}^{-1} (see Section 10.8), we will use the term “low-rank”

to refer to the corresponding detectors. Thus, the low-rank versions of MF and NMF detectors are

$$y_{\text{LRMF}}(\mathbf{x}) = \frac{\mathbf{s}^T \mathbf{P}_B^\perp \mathbf{x}}{\sqrt{\mathbf{s}^T \mathbf{P}_B^\perp \mathbf{s}}} \quad (10.195)$$

and

$$y_{\text{LRNMF}}(\mathbf{x}) = \frac{\mathbf{s}^T \mathbf{P}_B^\perp \mathbf{x}}{\sqrt{\mathbf{s}^T \mathbf{P}_B^\perp \mathbf{s}} \sqrt{\mathbf{x}^T \mathbf{P}_B^\perp \mathbf{x}}} = \cos \theta \quad (10.196)$$

respectively. The corresponding energy versions are given by (10.192) and (10.194). We also easily conclude that a low-rank anomaly detector is given by

$$y_{\text{LRAD}} = \mathbf{x}^T \mathbf{P}_B^\perp \mathbf{x}. \quad (10.197)$$

A geometric interpretation of low-rank matched filters is provided in Figure 10.24. The response of the MF is the projection of the observation \mathbf{x} onto $\langle \mathbf{P}_B^\perp \mathbf{x} \rangle$ (background-free target subspace). The response of the NMF is given by the cosine of the angle formed by the projections of the target and observation vectors onto the background-free subspace: that is, $\cos \theta = \cos(\mathbf{P}_B^\perp \mathbf{s}, \mathbf{P}_B^\perp \mathbf{x})$; an equivalent test is provided by $\cos \phi = \cos(\mathbf{P}_B^\perp \mathbf{s}, \mathbf{x})$. The decision surfaces and invariances of low-rank detectors are analogous to the ones shown in Figure 10.16 if we replace $\langle \tilde{\mathbf{s}} \rangle$ by $\langle \mathbf{P}_B^\perp \mathbf{s} \rangle$. Therefore, the axis of symmetry is the component of the target outside the background subspace; the operator \mathbf{P}_B^\perp essentially removes (“nulls”) components parallel to the background subspace.

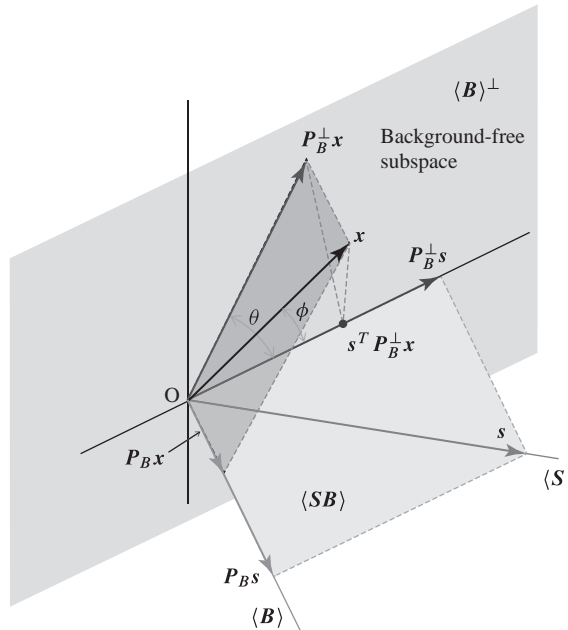


Figure 10.24 Geometrical interpretation of low-rank MF and NMF detectors.

10.8 Eigenvector Matched Filters

We recall that the output of the MF is a linear function of the input observation vector \mathbf{x} ; that is,

$$y_{\text{MF}} = \mathbf{h}_{\text{MF}}^T \mathbf{x} = (\kappa \mathbf{C}^{-1} \mathbf{s})^T \mathbf{x}, \quad (10.198)$$

where \mathbf{s} is the target vector, \mathbf{C} is the clutter-plus-noise covariance matrix, and κ is a normalization constant defined by

$$\kappa = \begin{cases} (\mathbf{s}^T \mathbf{C}^{-1} \mathbf{s})^{-1/2}, & \text{MF} \\ (\mathbf{s}^T \mathbf{C}^{-1} \mathbf{s})^{-1}, & \text{MVDR.} \end{cases} \quad (10.199)$$

We can gain significant insight into the operation and performance of the MF (10.198) by expressing its response in terms of the eigenvalues and eigenvectors of the covariance matrix

$$\mathbf{C} = \mathbf{Q} \mathbf{\Lambda} \mathbf{Q}^T = \sum_{k=1}^p \lambda_k \mathbf{q}_k \mathbf{q}_k^T, \quad (10.200)$$

where the eigenvalues have been ordered from largest to smallest, that is, $\lambda_1 \geq \lambda_2 \geq \dots \geq \lambda_p$. The response of the MF (10.198) can be written as

$$y_{\text{MF}} = \kappa \sum_{k=1}^p \frac{1}{\lambda_k} (\mathbf{q}_k^T \mathbf{s})(\mathbf{q}_k^T \mathbf{x}). \quad (10.201)$$

Careful inspection of (10.201) shows that (a) each of the constituent dot products in the summation is largest when the target and observation vectors have strong components parallel to \mathbf{q}_k , and (b) the product of these dot products is weighted by the inverse of the associated eigenvalue λ_k . Since the eigenvalues of the covariance matrix measure the clutter-plus-noise variance in the direction of the associated eigenvectors, the MF tries to select components in the observations which are both similar to the target and have small clutter-plus-noise variance.

As we saw in Section 10.6.2, the ideal performance of MF is completely specified by the detection index D given by (10.138). Using (10.200) we can express D in terms of eigenvalues and eigenvectors as

$$D = a^2 \mathbf{s}^T \mathbf{C}^{-1} \mathbf{s} = a^2 \sum_{k=1}^p D_k, \quad D_k \triangleq (\mathbf{q}_k^T \mathbf{s})^2 / \lambda_k. \quad (10.202)$$

This is a useful expression that shows, for a given signature, the contribution of each eigenvector to the detection index.

In many practical applications the eigenvectors of the covariance matrix can be subdivided into two groups. One group includes the eigenvectors associated with large eigenvalues and spans the signal and background subspace. The other group includes the eigenvectors associated with the small eigenvalues and spans essentially the noise subspace. Thus, we have

$$\begin{aligned} \mathbf{C} &= \sum_{k=1}^d \lambda_k \mathbf{q}_k \mathbf{q}_k^T + \sum_{k=d+1}^p \lambda_k \mathbf{q}_k \mathbf{q}_k^T \\ &= \mathbf{Q}_d \mathbf{\Lambda}_d \mathbf{Q}_d^T + \mathbf{Q}_d^\perp \mathbf{\Lambda}_d^\perp (\mathbf{Q}_d^\perp)^T. \end{aligned} \quad (10.203)$$

In practice, some of the smaller eigenvalues of \mathbf{C} may be zero or very small; that is, \mathbf{C} is ill-conditioned. Since the small eigenvalues and their eigenvectors are difficult to estimate and hard to compute accurately, we seek an approximation of \mathbf{C} that avoids these eigenvectors. We discuss two approaches to deal with this problem.

The first approach uses a *reduced-rank* approximation of the covariance matrix

$$\mathbf{C}_{\text{PC}} = \mathbf{Q}_d \mathbf{\Lambda}_d \mathbf{Q}_d^T. \quad (10.204)$$

We usually form \mathbf{Q}_d using the eigenvectors corresponding to the d largest eigenvalues; the result is known as *principal components inversion method* (Kirsteins and Tufts, 1994). An alternative approach is to select the eigenvectors associated with the largest d components of the detection index (10.202); the drawback is that the selection depends on the target signature. The MF coefficient vector for (10.204) is given by

$$\mathbf{h}_{\text{PC}} = \kappa \mathbf{Q}_d \mathbf{\Lambda}_d^{-1} \mathbf{Q}_d^T \mathbf{s}, \quad (10.205)$$

where κ is given by (10.199) with $\mathbf{C} = \mathbf{C}_{\text{PC}}$.

The second approach replaces the $(p - d)$ smallest eigenvalues by their average:

$$\alpha = \frac{1}{p - d} \sum_{k=d+1}^p \lambda_k = \frac{1}{p - d} \left[\text{tr}(\mathbf{C}) - \sum_{k=1}^d \lambda_k \right]. \quad (10.206)$$

The result is the following *full-rank* approximation of the covariance matrix:

$$\mathbf{C}_{\text{DMR}} = \mathbf{Q}_d \mathbf{\Lambda}_d \mathbf{Q}_d^T + \alpha \mathbf{Q}_d^\perp (\mathbf{Q}_d^\perp)^T. \quad (10.207)$$

We refer to the d eigenvectors with the largest eigenvalues as *dominant modes*. The approach defined by (10.207) is known as *Dominal Mode Rejection (DMR)* (Cox and Pitre, 1997); the reason for the name will become clear after the derivation. The inverse covariance matrix is

$$\mathbf{C}_{\text{DMR}}^{-1} = \mathbf{Q}_d \mathbf{\Lambda}_d^{-1} \mathbf{Q}_d^T + \alpha^{-1} \mathbf{Q}_d^\perp (\mathbf{Q}_d^\perp)^T. \quad (10.208)$$

Therefore, the MF coefficient vector is given by

$$\mathbf{h}_{\text{DMR}} = \kappa \mathbf{Q}_d \mathbf{\Lambda}_d^{-1} \mathbf{Q}_d^T \mathbf{s} + (\kappa/\alpha) \mathbf{Q}_d^\perp (\mathbf{Q}_d^\perp)^T \mathbf{s}, \quad (10.209)$$

where κ is given by (10.199) with $\mathbf{C} = \mathbf{C}_{\text{DMR}}$. We note that if \mathbf{s} lies completely in the subspace $\langle \mathbf{Q}_d \rangle$, the second term in (10.209) vanishes; in this case, the PC and the DMR matched filters are identical.

We next show that we do not need \mathbf{Q}_d^\perp for the computation of $\mathbf{C}_{\text{DMR}}^{-1}$. Indeed, using () and the identity $\mathbf{Q}\mathbf{Q}^T = \mathbf{Q}_d \mathbf{Q}_d^T + \mathbf{Q}_d^\perp (\mathbf{Q}_d^\perp)^T = \mathbf{I}$, we obtain

$$\mathbf{C}_{\text{DMR}}^{-1} = \frac{1}{\alpha} \mathbf{I} - \mathbf{Q}_d \left(\frac{1}{\alpha} \mathbf{I} - \mathbf{\Lambda}_d^{-1} \right) \mathbf{Q}_d^T. \quad (10.210)$$

We note that using \mathbf{C}_{DMR} instead of \mathbf{C} involves a reduction in the degrees of freedom. Only the largest eigenvalues, their eigenvectors and $\text{tr}(\mathbf{C})$ need to be estimated; this requires about $3d$ (instead of $3p$) training data vectors (Cox and Pitre, 1997; Kirsteins and Tufts, 1985) for the same performance.

We can now use (10.210) to express the output of the MF detector as follows

$$y_{\text{DMR}} = \frac{\kappa}{\alpha} \left[\mathbf{s}^T \mathbf{x} - \sum_{k=1}^d \frac{\lambda_k - \alpha}{\lambda_k} (\mathbf{q}_k^T \mathbf{s})(\mathbf{q}_k^T \mathbf{x}) \right]. \quad (10.211)$$

To understand the operation of MF detector, we examine the term $(\lambda_k - \alpha)/\lambda_k$. For noise components we have $\lambda_k = \alpha$ and $(\lambda_k - \alpha)/\lambda_k = 0$; therefore, the noise eigenvectors have no effect on the output of the MF detector. For strong background components we have $\lambda_k \gg \alpha$ and $(\lambda_k - \alpha)/\lambda_k \approx 1$; therefore, when both \mathbf{s} and \mathbf{x} are aligned with \mathbf{q}_k , the corresponding component is rejected from the output of the MF detector. This aspect of MF behavior leads to the name Dominant Mode Rejection (DMR) method.

If we assume that $\lambda_k \gg \alpha$, $k = 1, 2, \dots, d$, that is, we have d strong background components that dominate the sensor noise, relation (10.210) becomes

$$\mathbf{C}_{\text{DMR}}^{-1} \approx \frac{1}{\alpha} (\mathbf{I} - \mathbf{Q}_q \mathbf{Q}_q^T) \triangleq \frac{1}{\alpha} (\mathbf{I} - \mathbf{P}_B) = \frac{1}{\alpha} \mathbf{P}_B^\perp, \quad (10.212)$$

where $\mathbf{P}_B = \mathbf{Q}_q \mathbf{Q}_q^T$ is the orthogonal projection onto the subspace spanned by the dominant eigenvectors (signal and background subspace) and \mathbf{P}_B^\perp is the projector onto the noise subspace. Therefore, the reduced rank MF

$$y_{\text{MF}} \approx (\kappa/\alpha) \mathbf{s}^T \mathbf{P}_B^\perp \mathbf{x} \quad (10.213)$$

is identical with the subspace detector (10.195). Clearly, input vectors closely aligned with dominant eigenvectors (background or target) will suffer significant degradation going through this filter.

In conclusion, since the DMR-based implementation of MF detector ensures numerical stability, improved estimation of clutter-plus-noise covariance matrix, and optimum weighting for background and noise, there are no compelling reasons to use subspace detectors.

10.9 Robust Matched Filters

In virtually all practical applications the target signature \mathbf{s} and the covariance matrix \mathbf{C} used to determine the MF differ from their actual (true) values \mathbf{s}_0 and \mathbf{C}_0 in the assumed signal model

$$\mathbf{x} = a\mathbf{s}_0 + \mathbf{v}, \quad E(\mathbf{v}) = \mathbf{0}, \quad \text{cov}(\mathbf{v}) = \mathbf{C}_0. \quad (10.214)$$

This situation is known as *signal model mismatch*. As we will see next, this mismatch can have profound implications on performance, particularly when the target of interest is present in the covariance matrix. The discussion is based on Cox (1973), where the interested reader can find more details.

10.9.1

Performance Loss Due to Target Signature Mismatch

The MF uses a spectral signature s obtained from a spectral library or a previous observation of the target. However, in reality, in-scene targets exhibit a spectral signature $s_0 \neq s$. The causes for signature mismatch include material variability, atmospheric transmission, sensor response, calibration, and atmospheric compensation.

The best MF performance is obtained when $s = s_0$ and $C = C_0$. For a MF with MVDR normalization (see Section 10.5) we have

$$\mathbf{h}_0 = (C_0^{-1}s_0)/(s_0^T C_0^{-1}s_0) \quad (10.215)$$

and

$$\text{SCR}_0 = a^2 s_0^T C_0^{-1} s_0. \quad (10.216)$$

Suppose now that the MF is determined by a library signature $s \neq s_0$; that is,

$$\mathbf{h}_1 = (C_0^{-1}s)/(s^T C_0^{-1}s). \quad (10.217)$$

The SCR at the output of MF (10.217) for the in-scene target s_0 is given by

$$\begin{aligned} \text{SCR}_1 &= \frac{(\mathbf{h}_1^T a s_0)^2}{\mathbf{h}_1^T C_0 \mathbf{h}_1} = \frac{a^2 (s^T C_0^{-1} s_0)^2}{s^T C_0^{-1} s} \\ &= \text{SCR}_0 \cdot \cos^2(s, s_0; C_0^{-1}), \end{aligned} \quad (10.218)$$

where the term $\cos(\cdot)$ measures the generalized (Mahalanobis) angle between the vectors s and s_0 weighted by the inverse covariance matrix C_0^{-1}

$$\cos^2(s, s_0; C_0^{-1}) \triangleq \frac{(s^T C_0^{-1} s_0)^2}{(s^T C_0^{-1} s)(s_0^T C_0^{-1} s_0)}. \quad (10.219)$$

From (10.218) we note that the performance loss due to signature mismatch depends only on the angle of mismatch and not upon the strength of the target.

We recall that $0 \leq \cos^2(s, s_0; C_0^{-1}) \leq 1$. We note that $s = s_0$ yields $\text{SCR}_1 = \text{SCR}_0$ (that is, the best performance); in case $\cos^2(s, s_0; C_0^{-1}) = 0$, the in-scene target is completely rejected by the filter. The MF (10.217) attempts to minimize the response from vectors not satisfying the unity-gain directional constraint $\mathbf{h}_1^T s = 1$. Therefore, the SCR loss due to signature mismatch increases with the angular separation between s_0 and s in the whitened space. If we substitute in (10.219) the eigendecomposition

$$C_0^{-1} = \sum_{k=1}^p \frac{1}{\lambda_k} \mathbf{q}_k \mathbf{q}_k^T \quad (10.220)$$

we obtain the following expression

$$\cos^2 \theta_m = \frac{\left[\sum_{k=1}^p \frac{1}{\lambda_k} (s^T \mathbf{q}_k) (\mathbf{q}_k^T s_0) \right]^2}{\left[\sum_{k=1}^p \frac{1}{\lambda_k} (s^T \mathbf{q}_k) (\mathbf{q}_k^T s_0) \right] \left[\sum_{k=1}^p \frac{1}{\lambda_k} (s^T \mathbf{q}_k) (\mathbf{q}_k^T s_0) \right]}, \quad (10.221)$$

which shows that weighting by \mathbf{C}_0^{-1} in (10.219) emphasizes components corresponding to small eigenvalues of \mathbf{C}_0 and deemphasizes components corresponding to large eigenvalues of \mathbf{C}_0 .

10.9.2 Performance Loss Due to Target in the Covariance Matrix

Suppose now that the MF is obtained using a covariance matrix $\mathbf{C} \neq \mathbf{C}_0$; that is,

$$\mathbf{h}_2 = (\mathbf{C}^{-1}\mathbf{s}) / (\mathbf{s}^T \mathbf{C}^{-1}\mathbf{s}). \quad (10.222)$$

The SCR at the output of this MF is given by

$$\text{SCR}_2 = \frac{(\mathbf{a}\mathbf{h}_2^T\mathbf{s}_0)^2}{\mathbf{h}_2^T \mathbf{C}_0 \mathbf{h}_2} = a^2 \frac{(\mathbf{s}^T \mathbf{C}^{-1}\mathbf{s}_0)^2}{\mathbf{s}^T \mathbf{C}^{-1}\mathbf{C}_0 \mathbf{C}^{-1}\mathbf{s}}, \quad (10.223)$$

which describes the effects of both signature and covariance mismatches. Evaluation of (10.223) for arbitrary covariance mismatch is difficult. We focus on an important special case, which occurs when the target is included in the computation of the covariance matrix. In this case, we have the following rank-one covariance mismatch

$$\mathbf{C} = \mathbf{C}_0 + a^2 \mathbf{s}_0 \mathbf{s}_0^T, \quad (10.224)$$

which follows from (10.214). Using (10.224) and the matrix-inversion lemma

$$(\mathbf{A} + \mathbf{B}\mathbf{C}\mathbf{D})^{-1} = \mathbf{A}^{-1} - \mathbf{A}^{-1}\mathbf{B}(\mathbf{C}^{-1} + \mathbf{D}\mathbf{A}^{-1}\mathbf{B})^{-1}\mathbf{D}\mathbf{A}^{-1} \quad (10.225)$$

we obtain

$$\mathbf{C}^{-1} = \mathbf{C}_0^{-1} [\mathbf{I} - a^2 \mathbf{s}_0 \mathbf{s}_0^T \mathbf{C}_0^{-1} (1 + D)^{-1}], \quad (10.226)$$

where

$$D = a^2 \mathbf{s}_0^T \mathbf{C}_0^{-1} \mathbf{s}_0 = \text{SCR}_0. \quad (10.227)$$

To evaluate the numerator of (10.223) we use (10.226) and (10.227). The result is

$$\mathbf{s}^T \mathbf{C}^{-1} \mathbf{s}_0 = \frac{\mathbf{s}^T \mathbf{C}_0^{-1} \mathbf{s}_0}{1 + D}. \quad (10.228)$$

To evaluate the denominator of (10.223), we write

$$\begin{aligned} \mathbf{s}^T \mathbf{C}^{-1} \mathbf{C}_0 \mathbf{C}^{-1} \mathbf{s} &= \mathbf{s}^T [\mathbf{I} - a^2 \mathbf{s}_0 \mathbf{s}_0^T \mathbf{C}_0^{-1} (1 + D)^{-1}] \\ &\quad \cdot [\mathbf{I} - a^2 \mathbf{s}_0 \mathbf{s}_0^T \mathbf{C}_0^{-1} (1 + D)^{-1}] \mathbf{s}, \end{aligned} \quad (10.229)$$

which is reduced to

$$\mathbf{s}^T \mathbf{C}^{-1} \mathbf{C}_0 \mathbf{C}^{-1} \mathbf{s} = \mathbf{s}^T \mathbf{C}_0^{-1} \mathbf{s} - \frac{2a^2 (\mathbf{s}^T \mathbf{C}_0^{-1} \mathbf{s}_0)^2}{1 + D} + \frac{a^2 (\mathbf{s}^T \mathbf{C}_0^{-1} \mathbf{s}_0)^2 D}{(1 + D)^2}. \quad (10.230)$$

From (10.218) and (10.219) we obtain the identity

$$a^2 (\mathbf{s}^T \mathbf{C}_0^{-1} \mathbf{s}_0)^2 = D (\mathbf{s}^T \mathbf{C}_0^{-1} \mathbf{s}) \cos^2 \theta_m, \quad (10.231)$$

where we have used the notation $\cos^2 \theta_m \triangleq \cos^2(s, s_0; C_0^{-1})$ for simplicity. Substituting (10.231) into (10.230), after some algebraic manipulations, we obtain

$$s^T C^{-1} C_0 C^{-1} s = \frac{s^T C_0^{-1} s}{(1+D)^2} [1 + (2D + D^2) \sin^2 \theta_m], \quad (10.232)$$

where $\sin^2 \theta_m = 1 - \cos^2 \theta_m$. Using (10.223), (10.228), and (10.232) we obtain the wanted result

$$\text{SCR}_2 = \frac{\text{SCR}_0 \cos^2(s, s_0; C_0^{-1})}{1 + (2\text{SCR}_0 + \text{SCR}_0^2) \sin^2(s, s_0; C_0^{-1})}. \quad (10.233)$$

Unlike the mismatch loss from (10.217), the loss due to signature mismatch when the target is present in the covariance matrix depends on the strength of the target. In fact, (10.233) shows a strong dependence on the target strength through the terms SCR_0 and SCR_0^2 in the denominator; this dependence is weighted by the sine term that measures the amount of mismatch. This can be shown by plotting the ratio $\text{SCR}_1/\text{SCR}_2$ as a function of $\sin^2 \theta_m$ (see Problem 12). Note that in the absence of mismatch (that is, for $\theta_m = 0$), there is no performance loss even if there is target included in the covariance matrix.

10.9.3 Robust Matched Filters

We saw that as the SCR_0 increases, the performance of a MF with target in the covariance matrix degrades significantly with mismatch. Therefore, techniques that avoid or minimize such performance losses are highly desirable in practical applications. There are two types of practical methods:

1. Eliminate or reduce the target components before estimating the covariance matrix C . This is the best approach, when it is practically feasible.
2. Impose additional constraints on the MF to reduce or prevent target elimination. Most practical approaches lead to a technique called *diagonal loading* (Van Trees, 2002).

Matched filters that are designed to preserve good performance in the presence of mismatch are known as *Robust Matched Filters (RMFs)*.

Many practical RMFs use some form of diagonal loading, which results from the imposition of a quadratic constraint on the filter coefficients. To explain why this constraint improves robustness to mismatch, we recall that the MVDR filter $y = \mathbf{h}^T \mathbf{x}$ satisfies the following criterion (see Section 10.5):

$$\min_{\mathbf{h}} \sigma_y^2 = \mathbf{h}^T C_0 \mathbf{h} \quad \text{subject to} \quad \mathbf{h}^T s = 1. \quad (10.234)$$

The MVDR filter coefficients and the minimum value of variance are given by

$$\mathbf{h}_{\text{mv}} = \frac{C_0^{-1} s}{s^T C_0^{-1} s}, \quad \sigma_{\text{mv}}^2 = \frac{1}{s^T C_0^{-1} s}. \quad (10.235)$$

Equivalently, the MVDR filter maximizes the output $\text{SCR} = (a \mathbf{h}^T s)^2 / \mathbf{h}^T C_0 \mathbf{h}$; the maximum value is given by $\text{SCR}_0 = a^2 s^T C_0^{-1} s$.

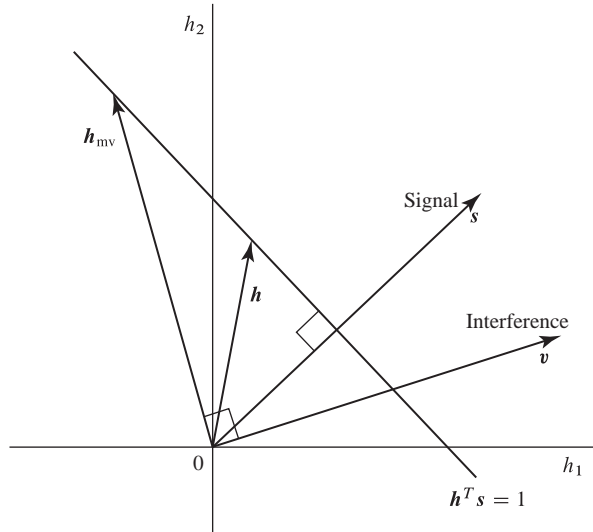


Figure 10.25 Geometrical illustration of the relationship between interference cancellation and the length of the MVDR filter coefficient vector.

The coefficient vector of the MVDR filter is unconstrained except at the steering direction specified by s . Consequently a signal tends to be regarded as an unwanted interference and is therefore suppressed in the filter output unless it is almost exactly aligned with the steering direction.

Figure 10.25 illustrates in a two-dimensional space the relationship between signal and coefficient vectors. The constraint $\mathbf{h}^T s = 1$ is a straight line (hyperplane) in the filter coefficient space. Any vector \mathbf{h} whose tip lies on this line satisfies the constraint. Now consider an interference signal v forming a small angle with s . By definition, the MVDR filter will try to form a null such that $\mathbf{h}_{mv}^T v = 0$; that is, by forcing \mathbf{h}_{mv} to become perpendicular to v . Consequently, as the interference becomes collinear with the signal, the length $\|\mathbf{h}_{mv}\|$ becomes infinite. Thus, to limit the signal suppression effect it is necessary to restrict the length of \mathbf{h} by imposing the quadratic constraint $\|\mathbf{h}\|^2 \leq \delta^2$. We can do this by solving the following optimization problem

$$\min_{\mathbf{h}} \sigma_y^2 = \mathbf{h}^T \mathbf{C}_0 \mathbf{h} \quad \text{subject to} \quad \mathbf{h}^T s = 1 \quad \text{and} \quad \|\mathbf{h}\|^2 = \delta^2, \quad (10.236)$$

where we have used an equality constraint for simplicity. To solve (10.236) we minimize the Lagrangian function

$$g = \mathbf{h}^T \mathbf{C}_0 \mathbf{h} + \xi(\mathbf{h}^T \mathbf{h} - \delta^2) + \lambda(\mathbf{h}^T s - 1). \quad (10.237)$$

Differentiating with respect to \mathbf{h} and setting the result to zero gives

$$2\mathbf{C}_0 \mathbf{h} + 2\xi \mathbf{h} + \lambda \mathbf{s} = \mathbf{0}. \quad (10.238)$$

Solving for \mathbf{h} and solving for λ by imposing the constraint $\mathbf{h}^T \mathbf{s} = 1$ yields

$$\mathbf{h}_{\text{dl}} = \frac{(\mathbf{C}_0 + \xi \mathbf{I})^{-1} \mathbf{s}}{\mathbf{s}^T (\mathbf{C}_0 + \xi \mathbf{I})^{-1} \mathbf{s}}, \quad (10.239)$$

where the value of ξ depends on the choice of δ^2 . The same solution can be obtained by solving the following problem

$$\min_{\mathbf{h}} \sigma_y^2 + \xi \|\mathbf{h}\|^2 = \mathbf{h}^T \mathbf{C}_0 \mathbf{h} + \xi \|\mathbf{h}\|^2 \quad \text{subject to} \quad \mathbf{h}^T \mathbf{s} = 1, \quad (10.240)$$

which involves a penalty term proportional to $\|\mathbf{h}\|^2$. The parameter $\xi > 0$ penalizes large values of $\|\mathbf{h}\|$ and has the general effect of “softening” the directivity constraint. We see that the effect of the quadratic constraint is to add a diagonal matrix $\xi \mathbf{I}$ to \mathbf{C}_0 (see Section 9.10). This is equivalent to designing an MVDR filter for higher white noise than is actually present in the data. A Bayesian interpretation of diagonal loading can be found in (Draper and Smith, 1998; Nasrabadi, 2008).

Several approaches have been proposed in the literature to design RMFs that satisfy specific optimality criteria. An interesting approach is to relax the strict directivity constraint $\mathbf{h}^T \mathbf{s} = 1$ by requiring the filter to keep its response above a certain value inside a sphere specified by the user. This leads to the following optimization problem (Lorenz and Boyd, 2005):

$$\min_{\mathbf{h}} \sigma_y^2 = \mathbf{h}^T \mathbf{C}_0 \mathbf{h} \quad \text{subject to} \quad \mathbf{h}^T \mathbf{s}_0 \geq 1 \text{ for all } \mathbf{s}_0 \in \|\mathbf{s} - \mathbf{s}_0\|^2 \leq \epsilon^2, \quad (10.241)$$

which provides a solution that is guaranteed to satisfy the minimum gain constraint for all points in the uncertainty hypersphere. The solution leads to the diagonal loading formula (10.239). A nonlinear relationship between the loading factor ξ and the uncertainty radius ϵ has been obtained by Li et al. (2003). However, in many practical applications it is adequate to determine the loading factor ξ by trial and error using the available data.

10.9.4

Dominant Mode Rejection and Diagonal Loading

Diagonal loading can be combined with dominant mode rejection to improve the robustness of the MF detector. The effect of adding ξ to the diagonal of \mathbf{C}_0 is to add ξ to α and each eigenvalue λ_k in (10.210). This results in

$$(\mathbf{C}_{\text{DMR}} + \xi \mathbf{I})^{-1} = \frac{1}{\alpha + \xi} \left[\mathbf{I} - \sum_{k=1}^d \left(\frac{\lambda_k - \alpha}{\lambda_k + \xi} \right) \mathbf{q}_k \mathbf{q}_k^T \right], \quad (10.242)$$

which is the formula we use in the practical implementation of MF detectors. From (10.242) we see that if ξ is larger than the small eigenvalues of \mathbf{C}_0 , diagonal loading of \mathbf{C}_0 produces a matrix with nearly the same eigenvalues as diagonally loading \mathbf{C}_{DMR} . More details about the nature and use of (10.242) can be found in (Cox and Pitre, 1997; Manolakis et al., 2009).

10.10 Adaptive Matched Filter Detectors

All the detectors we have discussed so far assume that the covariance matrix \mathbf{C} is known. In this section, we discuss how to derive detection algorithms when \mathbf{C} is unknown.

An obvious approach is to replace \mathbf{C} by its maximum likelihood estimate. This requires the availability of a set of independent and identically distributed training vectors $\mathcal{X} = \{\mathbf{x}_1, \mathbf{x}_2, \dots, \mathbf{x}_N\}$, each distributed as $N(\mathbf{0}, \mathbf{C})$, called *training data*. The maximum likelihood estimate of \mathbf{C} is given by (see Section 7.5)

$$\hat{\mathbf{C}} = \frac{1}{N} \sum_{i=1}^N (\mathbf{x}_i - \hat{\mathbf{m}})(\mathbf{x}_i - \hat{\mathbf{m}})^T, \quad \hat{\mathbf{m}} = \frac{1}{N} \sum_{i=1}^N \mathbf{x}_i. \quad (10.243)$$

We emphasize that the training data must *not* contain observations generated under the H_1 (signal present) hypothesis because they come from a distribution with different parameters (mean vector and/or covariance matrix).

When the covariance matrix is estimated from training data, the resulting detectors are called *adaptive*. In practice, all detectors are adaptive; however, optimum detectors are useful because they provide performance yardsticks. The “estimate-and-plug” approach results to various adaptive detectors. Reed et al. (1974) substituted the *sample covariance matrix* from (10.243) to the MVDR filter (10.235) to obtain the adaptive filter

$$\mathbf{h}_{\text{sni}} = \frac{\hat{\mathbf{C}}^{-1} \mathbf{s}}{\mathbf{s}^T \hat{\mathbf{C}}^{-1} \mathbf{s}}, \quad (10.244)$$

known as *sample matrix inversion* adaptive beamformer in the array processing literature. Since $\hat{\mathbf{C}} \neq \mathbf{C}_0$ there is a covariance mismatch that leads to a loss of performance. The SCR is found from (10.223) by assuming $\mathbf{s} = \mathbf{s}_0$ (no mismatch) and by replacing \mathbf{C} by $\hat{\mathbf{C}}$. The result is

$$\text{SCR}_{\text{sni}} = a^2 \frac{(\mathbf{s}^T \hat{\mathbf{C}}^{-1} \mathbf{s})^2}{\mathbf{s}^T \hat{\mathbf{C}}^{-1} \mathbf{C}_0 \hat{\mathbf{C}}^{-1} \mathbf{s}}. \quad (10.245)$$

The performance loss with respect to the optimum MVDR filter, $\text{SCR}_{\text{sni}}/\text{SCR}_0$, follows a beta distribution with mean (Reed et al., 1974)

$$E\left(\frac{\text{SCR}_{\text{sni}}}{\text{SCR}_0}\right) = \frac{N+2-p}{N+1}. \quad (10.246)$$

Using (10.246) we can deduce that $N = 2p$ results to a SCR loss of -3 dB and $N = 5p$ results approximately to a loss of -1 dB.

Robey et al. (1992) derived an adaptive detector, known as *adaptive matched filter* (AMF), by replacing \mathbf{C} by $\hat{\mathbf{C}}$ in (10.76). The result is

$$T_{\text{AMF}}(\mathbf{x}) = \frac{(\mathbf{s}^T \hat{\mathbf{C}}^{-1} \mathbf{x})^2}{\mathbf{s}^T \hat{\mathbf{C}}^{-1} \mathbf{s}}, \quad (10.247)$$

which is a slightly different scaled version of (10.244). The term “estimate-and-plug” is used here to emphasize the separation of the problem into two steps: (a) derivation of a

GLRT by assuming a known covariance matrix \mathbf{C} and (b) replacing \mathbf{C} by its maximum likelihood estimate.

A fundamentally different approach for the design of adaptive detectors was introduced by Kelly (1986). To avoid the two-step “estimate-and-plug” approach, Kelly formulated the decision problem using directly all available data; that is, the training data $\mathbf{x}_1, \mathbf{x}_2, \dots, \mathbf{x}_N$ and the test vector \mathbf{x} . More specifically, given the test vector $\mathbf{x} \sim N(a\mathbf{s}, \mathbf{C})$, we test the hypotheses $a = 0$ versus $a \neq 0$ by maximizing the likelihood ratio simultaneously with respect to a and \mathbf{C} . The result is Kelly’s GLRT detector:

$$T_{\text{Kelly}}(\mathbf{x}) = \frac{\max_{a,C} f_1(\mathbf{x}, \mathcal{X})}{\max_{\mathbf{C}} f_0(\mathbf{x}, \mathcal{X})} = \frac{(\mathbf{s}^T \hat{\mathbf{C}}^{-1} \mathbf{x})^2}{(\mathbf{s}^T \hat{\mathbf{C}}^{-1} \mathbf{s})(N + \mathbf{x}^T \hat{\mathbf{C}}^{-1} \mathbf{x})}. \quad (10.248)$$

We note that the one-step result (10.248) and the two-step estimate-and-plug result (10.247) differ by the normalization factor $(N + \mathbf{x}^T \hat{\mathbf{C}}^{-1} \mathbf{x})$. For large N , the normalization factor approaches a constant; for small values of N , this factor is strongly data dependent, and acts to mitigate the effects of limited training data.

We next consider the effect of an unknown scaling factor σ^2 in the covariance matrix. Here we assume that the test vector is distributed as $\mathbf{x} \sim N(a\mathbf{s}, \sigma^2 \mathbf{C})$ and the training data as $\mathbf{x}_k \sim N(\mathbf{0}, \sigma^2 \mathbf{C})$. Kraut and Scharf (1999) used this formulation to derive the well-known *adaptive cosine/coherence estimator (ACE)* detector:

$$T_{\text{ACE}}(\mathbf{x}) = \frac{\max_{a,\sigma^2,C} f_1(\mathbf{x}, \mathcal{X})}{\max_{\sigma^2,C} f_0(\mathbf{x}, \mathcal{X})} = \frac{(\mathbf{s}^T \hat{\mathbf{C}}^{-1} \mathbf{x})^2}{(\mathbf{s}^T \hat{\mathbf{C}}^{-1} \mathbf{s})(\mathbf{x}^T \hat{\mathbf{C}}^{-1} \mathbf{x})}. \quad (10.249)$$

In this case, the one-step GLRT approach and the “estimate-and-plug” approach result in the same detector. Once again, we notice how a different formulation of the detection problem produced a different detector. The ACE detector was first derived by Conte et al. (1995) as an asymptotically optimum test for compound Gaussian distributions and it was called adaptive NMF detector.

Since the sample covariance matrix depends on the training random vectors, it is itself a random quantity. This complicates the derivation of distributions for the detection statistic of adaptive detectors. However, when $N \gg p$ we can assume that $\hat{\mathbf{C}} \simeq \mathbf{C}$ and use the results for the known covariance case. This approximation is adequate for hyperspectral detection applications. Derivations of exact distributions for different adaptive matched filter detectors can be found in (Kelly, 1986; Richmond, 2000; Kraut et al., 2001).

10.11 Summary and Further Reading

This chapter provides an introduction to signal detection theory with the application to hyperspectral imaging data in mind. A key aspect of hyperspectral imaging data is that background clutter has *nonzero* mean values. Although this is not a fundamental difference with the zero mean assumption used in radar applications, it complicates the derivation of detection algorithms and has to be taken into account when we apply the

algorithms to practical problems. Detection theory is a huge area and, by necessity, we have focused on algorithms used in hyperspectral imaging. Our objective was to present the most widely used matched filter detection algorithms, detection performance metrics, performance evaluation under ideal conditions, and performance analysis when there is mismatch between the actual and assumed signal models. More details about detection theory and its applications can be found in Van Trees et al. (2013); Levy (2008); Kay (1998); Scharf (1991); Duda et al. (2001).

Problems

1. Consider two normal distributions with the following means and covariances:
$$\mathbf{m}_0 = \begin{bmatrix} -1.0 \\ 0.5 \end{bmatrix}, \mathbf{C}_0 = \begin{bmatrix} 1 & 0.6 \\ 0.6 & 1 \end{bmatrix}, \mathbf{m}_1 = \begin{bmatrix} 1.5 \\ -0.5 \end{bmatrix}, \mathbf{C}_1 = \begin{bmatrix} 1 & -0.8 \\ -0.8 & 1 \end{bmatrix}.$$

(a) Plot equal probability contours and equal LRT contours as in Figure 10.4. (b) Plot the optimum Bayesian decision surface if $P(H_0) = 0.75$ and $P(H_1) = 0.25$. (c) Repeat (a) for $\mathbf{C}_1 = \mathbf{C}_0$. What happens to the shape of the contours? (d) Repeat (a) for $\mathbf{C}_0 = \mathbf{C}_1 = \mathbf{I}$ and comment upon the results.
2. Consider the hypotheses $H_0 : \mathbf{x} \sim N(\mathbf{0}, \sigma_0^2 \mathbf{I})$ and $H_1 : \mathbf{x} \sim N(\mathbf{0}, \sigma_1^2 \mathbf{I})$. (a) Determine the LR and sufficient statistic for $\sigma_0^2 < \sigma_1^2$ and $\sigma_0^2 > \sigma_1^2$. (b) Determine the distribution of the sufficient statistic under each hypothesis. (c) Evaluate the performance of the detector using ROC curves.
3. (a) Use equation (10.58) to evaluate the performance of the LRT for proportional covariance matrices using ROC curves. (b) Compare the performance of this LRT to that of the MF detector for different values of γ^2 .
4. (a) Derive the equations for the CEM filter. (b) Determine the CEM filter and the MF for an input \mathbf{x} with a normal distribution defined by
$$\mathbf{m} = \begin{bmatrix} 2 \\ 3 \end{bmatrix} \quad \text{and} \quad \mathbf{C} = \begin{bmatrix} 1 & 0.8 \\ 0.8 & 1 \end{bmatrix}.$$

(c) Generate $N = 100$ samples of the input vector and compute $\mathbf{y} = \mathbf{C}^{-1/2} \mathbf{x}$ and $\mathbf{z} = \mathbf{R}^{-1/2} \mathbf{x}$. (d) Generate scatter plots of the vectors \mathbf{x} , \mathbf{y} , and \mathbf{z} . Does \mathbf{z} have a spherical distribution?

5. Reproduce the ROC curves in Figure 10.17. Repeat for different combinations of D and p and comment upon the results.
6. Reproduce the ROC curves in Figure 10.18. Repeat for different values of D and comment upon the results.
7. Reproduce the ROC curves in Figure 10.19. Repeat for different combinations of D and p and comment upon the results.
8. Reproduce the plots in Figure 10.21. Repeat for different values p and P_{FA} to study detection performance under signature mismatch.

9. Suppose we want to choose among the hypotheses: $H_0 : \mathbf{x} = \mathbf{v}$ and $H_1 : \mathbf{x} = \mathbf{s} + \mathbf{v}$, where $\mathbf{s} \sim N(\mathbf{0}, \mathbf{C}_t)$ and $\mathbf{x} \sim N(\mathbf{0}, \mathbf{C}_b)$. (a) Show that the LRT is given by

$$\log \Lambda(\mathbf{x}) = \sum_{i=1}^p \frac{\lambda_i}{1 + \lambda_i} (\mathbf{u}_i^T \mathbf{x})^2,$$

where λ_i ($\lambda_1 \geq \dots \geq \lambda_p$) and \mathbf{u}_i are, respectively, the eigenvalues and the corresponding eigenvectors of $\mathbf{C}_b^{-1} \mathbf{C}_t$. (b) Show that the linear filter \mathbf{h} that maximizes the SCR = $\mathbf{h}^T \mathbf{C}_b \mathbf{h} / \mathbf{h}^T \mathbf{C}_b \mathbf{h}$ is given by $\mathbf{h} = \mathbf{u}_1$ and $\text{SCR}_{\max} = \lambda_1$.

10. Consider the signal model $\mathbf{x} = \mathbf{S}\mathbf{a} + \mathbf{v}$, where $\mathbf{v} \sim N(\mathbf{0}, \mathbf{C}_b)$ and \mathbf{S} is a known $p \times q$ full-rank matrix. Show that: (a) If \mathbf{a} is a known vector, the LRT is the MF detector $y = \mathbf{x}^T \mathbf{C}_b^{-1} (\mathbf{S}\mathbf{a})$. (b) If \mathbf{a} is an unknown constant, the GLRT is given by

$$y = \mathbf{x}^T \mathbf{C}_b^{-1} \mathbf{S} (\mathbf{S}^T \mathbf{C}_b^{-1} \mathbf{S})^{-1} \mathbf{S}^T \mathbf{x}.$$

- (c) If $\mathbf{a} \sim N(\mathbf{0}, \mathbf{C}_a)$, the GLRT is given by

$$y = \sum_{i=1}^p \frac{\lambda_i}{1 + \lambda_i} (\mathbf{q}_i^T \mathbf{C}_b^{-1} \mathbf{q}_1).$$

(d) If $q = 1$ (one-dimensional targets), the tests in (b) and (c) yield the same detection statistics

$$y = \frac{(\mathbf{s}_1^T \mathbf{C}_b^{-1} \mathbf{x})^2}{\mathbf{s}_1^T \mathbf{C}_b^{-1} \mathbf{s}_1},$$

where \mathbf{s}_1 is the first column of \mathbf{S} .

11. Consider the detection statistics $T_1(\mathbf{x})$ and $T_2(\mathbf{x})$ for the subspace detectors discussed in Section 10.7.1. (a) Plot ROC curves for different values of D for $p = 20$ and $q_t = 5$. (b) Plot ROC curves for $D = 10$, $p = 20$, and $q_t = 1, 2, 5, 10, 20$. (c) Plot ROC curves for $D = 10$, $q_t = 5$, and $p = 10, 20, 50, 100$.
12. Use (10.233) to plot $\text{SCR}_1 / \text{SCR}_2$ as a function of $\sin^2 \theta_m$ for different values of SCR_0 and use the obtained curves to explain mismatch performance.

11 Hyperspectral Data Exploitation

The main objective of hyperspectral imaging remote sensing is the identification of materials or phenomena from their reflectance or emissivity spectra to serve the needs of different applications. In this chapter, building on the understanding of the phenomenology of spectral remote sensing and the introduced signal processing methods, we develop algorithms for some unique hyperspectral imaging applications: detection of hard targets, gas detection, change detection, and image classification. The emphasis is on algorithms developed based on phenomenologically sound signal models, realistic application-driven requirements, and rigorous signal processing procedures, rather than ad hoc algorithms or trendy theoretical algorithms based on unrealistic assumptions.

11.1 Target Detection in the Reflective Infrared

The objective of hyperspectral target detection is to find objects of interest (called “hard targets” or simply “targets”) within a hyperspectral image and to discriminate between various target types on the basis of their spectral characteristics. The advantages are automated signal processing and lower spatial resolution requirements for the sensor. In this section we discuss the defining features of the target detection problem, we explain how to choose target detection algorithms, we investigate the consequences of practical limitations, and we evaluate performance using field data. Predicting detection performance using theoretical models is discussed in Section 11.2.

11.1.1 Definition of the Target Detection Problem

Hyperspectral target detection algorithms search for targets by exploiting the spectral characteristics of the target’s surface material by looking at the spectrum of each pixel. Depending on the spatial resolution of the sensor, targets of interest may not be clearly resolved, and hence may appear in only a few pixels or even as part of a single pixel (subpixel target). Thus, the first key attribute of the hyperspectral target detection problem is that a “target present” versus “target absent” decision must be made individually for every pixel of a hyperspectral image. In most applications each target is characterized by its spectral signature and detection algorithms make decisions using the target signature and the data cube of the imaged scene.

Typical “search-and-detection” applications include the detection of man-made materials in natural backgrounds for the purpose of search and rescue, and the detection

of military vehicles for purposes of defense and intelligence. An essential characteristic of these operations is that the size of the objects to be detected is typically a minuscule fraction of the size of the search area; that is, the objects occur with a very low probability (“rare” targets). The term “rare” is used here to signify a relatively small number compared to the total number of pixels; for example, a few pixels in a million-pixel image. The “rare-target” attribute, which is the second key attribute of the hyperspectral target detection problem, has important implications on the approaches that can be used for the development and performance evaluation of hyperspectral target detection algorithms. As we have discussed in Section 10.2.2, the appropriate performance metric for such applications is the Neyman–Pearson criterion, which maximizes the probability of detection while keeping the false alarm rate below a fixed acceptable value. The obtained Neyman–Pearson detectors compute the likelihood ratio under the two hypotheses and make a decision by comparing the result to a threshold, which is selected to ensure an acceptable false alarm rate. Detection performance is measured by a ROC curve that shows P_D versus P_{FA} as a function of threshold.

The rare-target and subpixel attributes imply that, in practical applications, target training data sets are sparsely populated and possibly distorted by background interference. Therefore, the use of approaches from the areas of pattern recognition and machine learning to hyperspectral target detection may be challenging or even impossible. This will become clear in Section 11.4, where we discuss the application of classification techniques in hyperspectral data analysis.

11.1.2 Processing Domain: Radiance Versus Reflectance

In practical applications, targets of interest are typically specified by their reflectance spectra. However, the imaging spectrometer measures radiant energy, which is converted into physical units of radiance through the calibration process. Figure 11.1 shows the reflectance signature of a target measured on the ground by a spectrometer, the corresponding radiance spectrum measured by the sensor, and a reflectance signature of

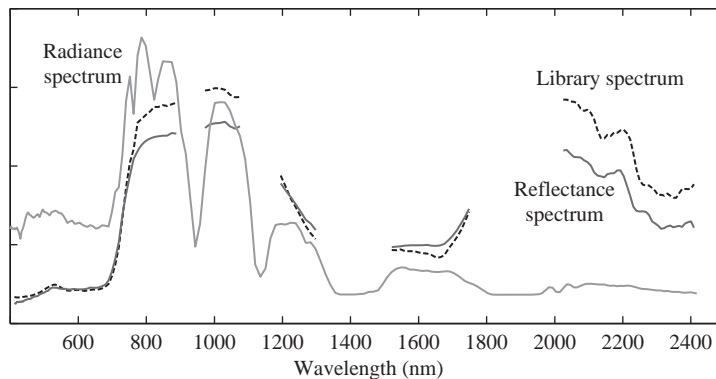


Figure 11.1 In-scene radiance and reflectance spectra of a green tarp imaged by the HYDICE imaging spectrometer. Radiance and reflectance are measured in different units. The library spectrum of the green tarp is in units of reflectance.

the target material from a spectral library. The large dissimilarity between the radiance and reflectance curves illustrates that meaningful processing requires that target signatures and scene data must be in the same domain. Thus, in practical applications we have two options:

1. Reflectance-Domain Processing: Convert the scene data cube from radiance to reflectance using one of the atmospheric compensation techniques discussed in Section 6.6.
2. Radiance-Domain Processing: Convert the target reflectance signature into radiance using a forward propagation model (see Section 6.4) or fly over a training set of targets to measure their radiance signatures before starting the mission.

In most target detection applications we work in the reflectance domain because we must use spectral libraries to specify the targets of interest and use target identification algorithms to reduce the false alarm rate.

11.1.3 Background Clutter Signal Modeling

The development of target detection algorithms and performance prediction models requires statistical models for the background clutter. A useful model for natural background clutter is the density mixture

$$f(\mathbf{x}) = \sum_{k=1}^{N_C} \pi_k f_k(\mathbf{x}), \quad \pi_k \geq 0, \quad \sum_{k=1}^{N_C} \pi_k = 1, \quad (11.1)$$

where π_k is the a priori probability, $f_k(\mathbf{x})$ is the density of the k th component (class), and N_C is the number of components. In classification applications each component $f_k(\mathbf{x})$ is modeled using a normal distribution (Landgrebe, 2003). In target detection applications, we model each $f_k(\mathbf{x})$ with a multivariate t -distribution to capture the heavy-tail behavior of natural hyperspectral backgrounds. The subject of background clutter modeling has been extensively discussed in Chapter 7. When we seek background models for the development of target detection algorithms, the major concern is accurate characterization of the background distribution; there is no need to associate the components of the distribution with natural classes. Figure 11.2 shows the two-dimensional histogram of a HYDICE data cube in the subspace of the first two principal components, which includes 95 percent of the total spectral variability of the scene. We note that the three major components of the distribution correspond to the grass, tree, and roads classes. Although density mixture models are useful for detection performance prediction (see Section 11.2), they are not needed for the implementation of practical detection algorithms. As we explain later in this section, the most useful practical detection algorithms use the covariance matrix of the background clutter.

11.1.4 Target Signal Modeling

The basic problem in radar and communications is to detect the presence of a signal of known fixed shape from observations corrupted by additive noise and clutter. Therefore, the observed signal is specified by the following *additive* signal model

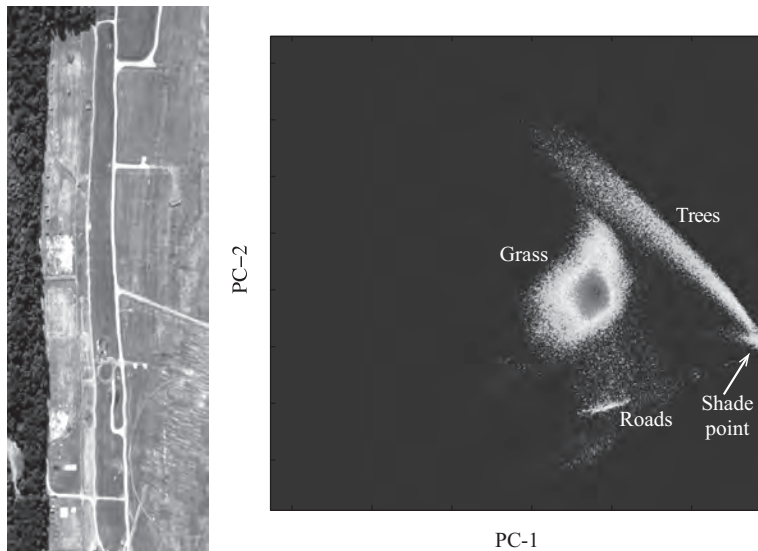


Figure 11.2 HYDICE scene and the distribution of clutter in the subspace of the first two principal components, which contains 95 percent of the total scene variance.

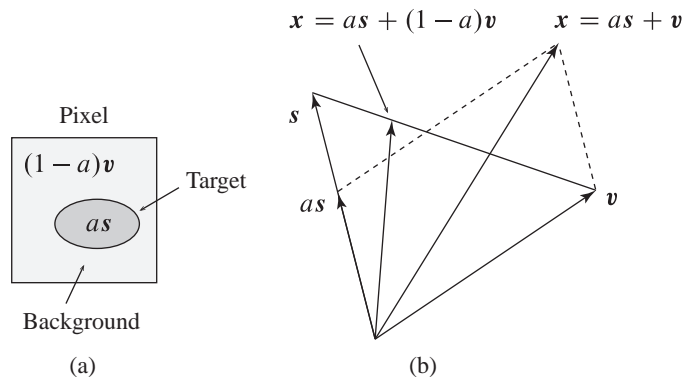


Figure 11.3 Illustration of observed subpixel target spectra using additive and replacement signal models.

$$x = as + v, \quad (11.2)$$

where s is the known signal, a is a scaling factor, and v represents the combined contribution of clutter and noise. According to this model, the signal merely shifts the noise and clutter distribution to a new mean without affecting its shape. Using binary hypothesis testing and the additive signal model has led to the development of a wide range of detection algorithms, including the celebrated matched filter detector (DiFranco and Rubin, 2004; Carlson and Crilly, 2009).

However, as we explain next, the signal model for hyperspectral subpixel targets is fundamentally different from the additive model (11.2). If the target occupies a fraction a of the pixel area (see Figure 11.3a), we have a mixed pixel whose spectrum

is determined by the linear mixing model (see Section 9.2). Therefore, the observed spectrum is given by

$$\mathbf{x} = a\mathbf{s} + (1 - a)\mathbf{v}, \quad 0 \leq a \leq 1, \quad (11.3)$$

where a is the target fill-fraction, \mathbf{s} is the spectrum of the target, and \mathbf{v} the spectrum of the background clutter surrounding the target. We stress that both the target and background spectra are affected by noise in the same manner. For notational convenience, sensor noise has been incorporated into the target and background spectra; that is, the vectors \mathbf{s} and \mathbf{v} in (11.3) include noise. The fundamental difference between (11.2) and (11.3) is that when a target is present in hyperspectral imaging data, it “replaces” (that is, removes) an equal part of the background. For this reason (11.3) is known as a *replacement* signal model. If $a = 1$ we have a resolved or full-pixel target, whereas if $0 < a < 1$ we have a subpixel target. Figure 11.3b illustrates the difference between additive and replacement target signal models.

The replacement signal model does *not* satisfy the superposition principle because of the constraint $0 \leq a \leq 1$. Furthermore, enforcing this constraint complicates the theoretical derivation and practical implementation of hyperspectral target detection algorithms. Since $0 < a \ll 1$ implies that $1 - a \approx 1$, the additive signal model is a good approximation to the replacement signal model for targets with small fill-fractions, only. For subpixel targets, that is, for $0 < a < 1$, the background acts as *interference* and distorts the shape of the observed target spectrum. This is illustrated in Figure 11.4 which shows the spectrum of a subpixel target created at the edge of a green tarp and grass. Although full pixel targets are not affected by background interference, the variability of target and background spectra still pose a major challenge to reliable target detection.

Since all materials exhibit spectral variability, we need to add a stochastic aspect to the replacement signal model (11.3). Since the tails of the target distribution have practically no effect on the probability of detection, we assume that

$$\mathbf{s} \sim N(\mathbf{m}_t, \mathbf{C}_t) \quad (11.4)$$

$$\mathbf{v} \sim N(\mathbf{m}_b, \mathbf{C}_b). \quad (11.5)$$

If we also assume that the fill-fraction a is constant, the observation \mathbf{x} in (11.3) follows a normal distribution

$$\mathbf{x} \sim N(\mathbf{m}(a), \mathbf{C}(a)), \quad 0 \leq a \leq 1, \quad (11.6)$$

with mean vector and covariance matrix given by

$$\mathbf{m}(a) = a\mathbf{m}_t + (1 - a)\mathbf{m}_b \quad (11.7)$$

$$\mathbf{C}(a) = a^2\mathbf{C}_t + (1 - a)^2\mathbf{C}_b. \quad (11.8)$$

This *stochastic mixing model*, which was introduced by Stocker and Schaum (1997), is illustrated in Figure 11.5 using synthetic data. We note that for $a = 0$ the observations follow the clutter distribution, whereas for $a = 1$ they follow the target distribution; for $0 < a < 1$ the observations follow a mixture of the two distributions. A major practical problem with this model is that we seldom have accurate estimates of the target covariance matrix.

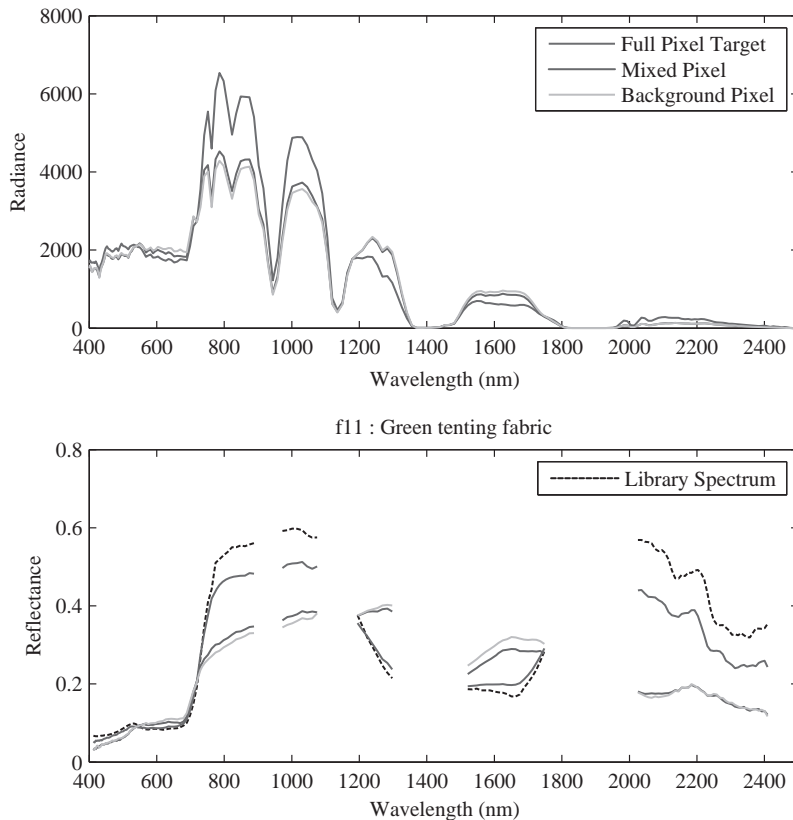


Figure 11.4 Illustration on how the local background distorts the spectrum of a subpixel target. Shows true spectra and model for full pixel target, B, and subpixel target.

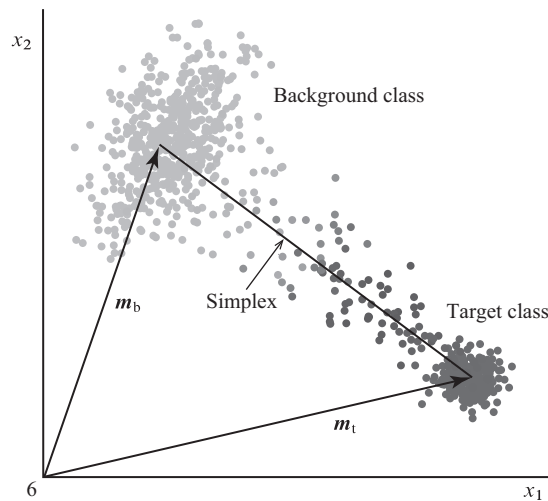


Figure 11.5 Illustration of stochastic mixing model for subpixel targets.

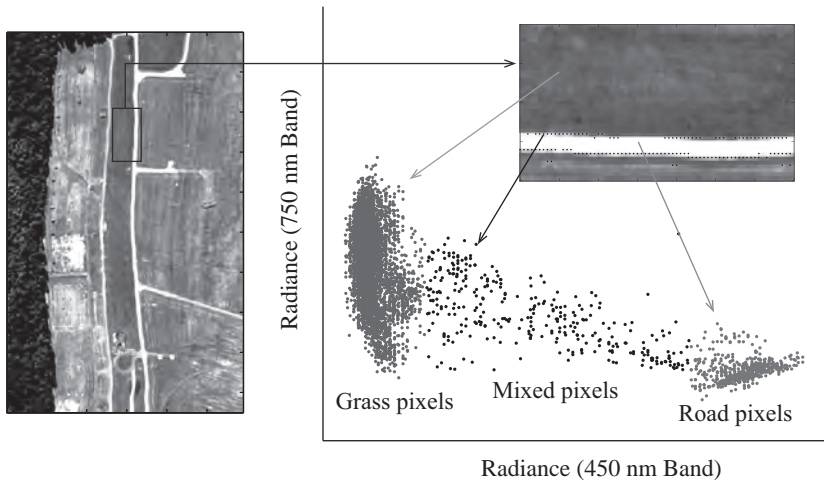


Figure 11.6 Illustration of the stochastic mixing model using grass and road spectra from a HYDICE hyperspectral imaging cube to create a scatter plot. (A black and white version of this figure will appear in some formats. For the color version, please refer to the plate section.)

Geometrically, observations from the additive model can be anywhere on the subspace defined by the target and background spectra, because the fill-factor a is unconstrained. In contrast, observations from the replacement model must lie on the line segment (simplex) connecting the target and background spectra.

To demonstrate that (11.6) is a reasonable model for subpixel targets, we consider a square area in Figure 11.6, which is dominated by grass and man-made road materials. The object of interest (target) is the road class and the grass class is the background clutter. The scatter plot of this image for the 450 nm and 750 nm bands clearly shows two distinct clouds corresponding to the grass and road classes, and a set of points between these two clusters that correspond to pixels along the borderline between the grass and the road. A plausible explanation is that the spectra of these pixels are obtained from the mixing of grass and road surface spectra. The crucial observation here is that *the mixed pixel points (subpixel targets) are clustered about the line connecting the centers of the target and background clouds*, which is in reasonable agreement with the model (11.3).

11.1.5 Detection Algorithms for Hyperspectral Targets

As we have seen in Chapter 10, the development of detection algorithms using the GLRT approach requires (a) the adoption of parametric probability models for the target and background clutter distributions, and (b) the maximization of the likelihood functions under each hypothesis. There are two practical problems with this approach: (a) the maximization process can be extremely complicated dependent on the type of utilized probability models; (b) detection performance depends on how well the assumed models describe the data and on how well we can estimate the unknown distribution parameters from the data.

However, regardless of the adopted signal models, the theoretical framework used to derive a detection algorithm, and its optimality properties, the ultimate criterion of success for any detector, is performance under the actual signal and clutter environments encountered during its operation. Indeed, it is not unusual that a detector which is optimal for the assumed signal models, may perform poorly in the actual environment. For this reason, in practice, we prefer detectors that are robust to mismatches between assumed and actual signal models.

In practice, the parameters of the target and clutter distributions are unknown; therefore, the development of detection algorithms must rely on the generalized likelihood ratio test (GLRT)

$$\Lambda_G(\mathbf{x}) = \frac{\max_{\boldsymbol{\theta}_1} f_1(\mathbf{x}|\boldsymbol{\theta}_1)}{\max_{\boldsymbol{\theta}_0} f_0(\mathbf{x}|\boldsymbol{\theta}_0)}, \quad (11.9)$$

where $f_1(\mathbf{x}|\boldsymbol{\theta}_1)$ is the normal distribution (11.6) with $\boldsymbol{\theta}_1 = \{a, \mathbf{m}_t, \mathbf{C}_t, \mathbf{m}_b, \mathbf{C}_b\}$ and $f_0(\mathbf{x}|\boldsymbol{\theta}_0)$ is a density mixture of normal distributions with parameters $\boldsymbol{\theta}_0 = \{\pi_k, \mathbf{m}_k, \mathbf{C}_k, k = 1, \dots, N_C\}$. The numerical computations for the evaluation of (11.9) are extremely difficult because they require non-linear optimization and computation of density of high-dimensional normal distributions. Furthermore, the quality of estimated covariance matrices is very poor for classes with small numbers of pixels. The situation becomes more challenging if we use multivariate t -densities. Simplified two-step approaches using clustering followed by detection, although intuitively appealing, have not resulted in any successful algorithms (Pieper et al., 2012). Therefore, we have chosen to introduce hyperspectral target detection algorithms using geometrical considerations in the spectral observation space.

From a geometrical viewpoint a detection algorithm partitions the observation space into two disjoint regions, say, \mathcal{R}_0 and \mathcal{R}_1 . Decisions are made using the rule

$$\mathbf{x} \in \mathcal{R}_0 \Rightarrow \text{Target absent} \quad (11.10a)$$

$$\mathbf{x} \in \mathcal{R}_1 \Rightarrow \text{Target present.} \quad (11.10b)$$

The decision rule is implemented using a scalar detection statistic $y = T(\mathbf{x})$ and a threshold η as follows

$$y = T(\mathbf{x}) < \eta \Rightarrow \text{Target absent} \quad (11.11a)$$

$$y = T(\mathbf{x}) > \eta \Rightarrow \text{Target present.} \quad (11.11b)$$

The equation $T(\mathbf{x}) = \eta$ determines the decision surface of the detector and the value of η determines the trade-off between P_D and P_{FA} . Therefore, we see that:

- a detection algorithm is completely specified by its decision surface, which surface is determined by its shape and positioning in the observation space;
- the performance of a detection algorithm is determined by its decision surface and the probability distributions of target and background clutter.

The first concern when we select a detection algorithm is how its decision surface partitions the observation space to obtain the best separation between the target and clutter distributions. To see how to select “good” detectors for hyperspectral imaging

targets, we recall the formulas for the AD, MF, and NMF algorithms in the spectral and whitened observation spaces (see Section 10.6.1):

$$y_{\text{AD}} = (\mathbf{x} - \mathbf{m}_b)^T \mathbf{C}_b^{-1} (\mathbf{x} - \mathbf{m}_b) = \tilde{\mathbf{x}}^T \tilde{\mathbf{x}} \quad (11.12)$$

$$y_{\text{MF}} = \frac{(\mathbf{s} - \mathbf{m}_b)^T \mathbf{C}_b^{-1} (\mathbf{x} - \mathbf{m}_b)}{\sqrt{(\mathbf{s} - \mathbf{m}_b)^T \mathbf{C}_b^{-1} (\mathbf{s} - \mathbf{m}_b)}} = \frac{\tilde{\mathbf{s}}^T \tilde{\mathbf{x}}}{\sqrt{\tilde{\mathbf{s}}^T \tilde{\mathbf{s}}}} \quad (11.13)$$

$$y_{\text{NMF}} = \frac{y_{\text{MF}}}{\sqrt{y_{\text{AD}}}} = \frac{\tilde{\mathbf{s}}^T \tilde{\mathbf{x}}}{\sqrt{\tilde{\mathbf{s}}^T \tilde{\mathbf{s}}} \sqrt{\tilde{\mathbf{x}}^T \tilde{\mathbf{x}}}} = \cos \theta, \quad (11.14)$$

where the whitened and clutter-centered vectors are given by

$$\tilde{\mathbf{x}} = \mathbf{C}_b^{-1/2} (\mathbf{x} - \mathbf{m}_b) \quad (11.15a)$$

$$\tilde{\mathbf{s}} = \mathbf{C}_b^{-1/2} (\mathbf{s} - \mathbf{m}_b). \quad (11.15b)$$

To implement the MF and NMF detectors we need the spectral signature of the target and the mean and covariance matrix of the background clutter; the anomaly detector does not require the signature of the target.

The operation and the decision surfaces of these detectors can be clearly explained in the clutter-centered whitened space, which is defined by (11.15). The whitening transformation produces a random vector having uncorrelated components with zero mean and unit variance. Furthermore, if the clutter distribution has elliptical contours, the whitened clutter distribution has spherical contours. Careful inspection of (11.12)–(11.14) and Figure 11.7(b) lead to the following conclusions:

- The decision surface of the AD algorithm is a hypersphere centered at $\tilde{\mathbf{x}} = \mathbf{0}$ with radius equal to the desired threshold η_{AD} .
- The decision surface of the MF is a hyperplane orthogonal to the vector $\tilde{\mathbf{s}} = \mathbf{C}_b^{-1/2} (\mathbf{s} - \mathbf{m}_b)$ at a point determined by the desired threshold η_{MF} .
- The decision surface of the NMF is a cone with vertex at zero, axis along the vector $\tilde{\mathbf{s}} = \mathbf{C}_b^{-1/2} (\mathbf{s} - \mathbf{m}_b)$, and angle determined by the desired threshold η_{NMF} .

To obtain the decision surfaces in the spectral space we use the “coloring” transformation

$$\mathbf{x} = \mathbf{C}_b^{1/2} \tilde{\mathbf{x}} + \mathbf{m}_b \quad (11.16)$$

which is the inverse of the whitening transformation (11.15). The decision surface of NMF is a cone with vertex at the mean of the clutter and axis pointing towards the target cloud; the direction of the axis is determined by the covariance matrix of the clutter. The decision surface of MF is a hyperplane forming an oblique angle with the line segment joining the centers of the clutter and target distributions; the angle is determined by the covariance matrix of the clutter. Finally, the decision surface of the AD becomes a hyper-ellipsoid centered at mean of the clutter distribution; its orientation and shape is determined by the clutter covariance matrix.

Careful inspection of the decision surfaces in Figure 11.7 and the scatter plot in Figure 11.8 unambiguously demonstrates that the MF and NMF detectors are irrefutable

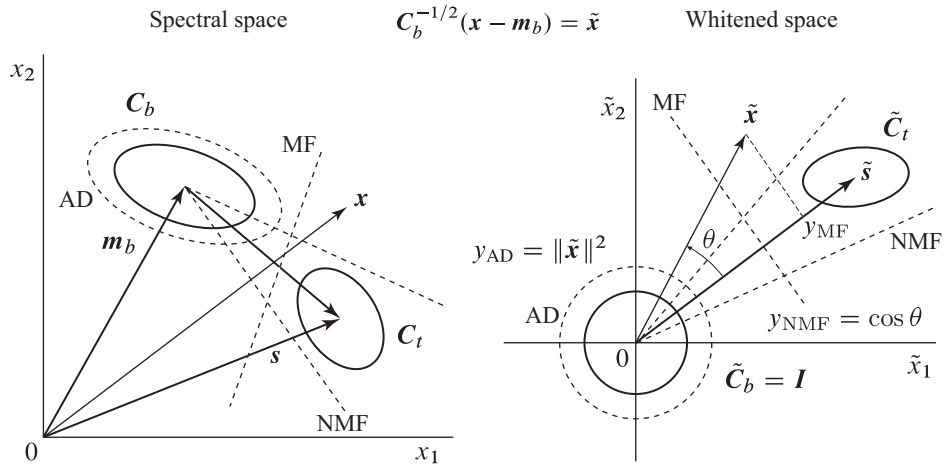


Figure 11.7 Illustration of the decision surfaces (shown as dashed lines) for the AD, MF, and NMF algorithms in the original observation space and in the whitened observation space.

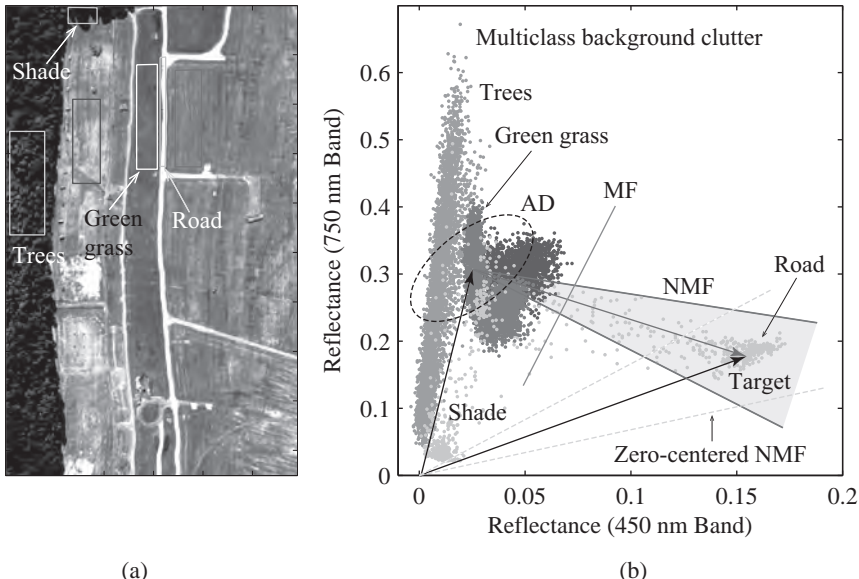


Figure 11.8 Scatter plot of different classes from a HYDICE data cube to illustrate the suitability of MF and NMF detectors for both subpixel and full pixel targets. The road pixels are considered as the “target class”. (A black and white version of this figure will appear in some formats. For the color version, please refer to the plate section.)

choices for hyperspectral target detection applications. This scatter plot also suggests that the NMF may have better performance than the MF for subpixel targets.

We next summarize some properties of MF and NMF detectors that help to understand their operation and performance.

1. The MF detectors find the best direction to project the data to maximize the separation between local background and full pixel target classes.
2. If the clutter and target classes follow a normal distribution with the same covariance matrix the MF maximizes the output SCR for full pixel targets. The maximum SCR is equal to the Mahalanobis distance

$$\text{SCR} = (\mathbf{s} - \mathbf{m}_b)^T \mathbf{C}_b^{-1} (\mathbf{s} - \mathbf{m}_b) \quad (11.17)$$

between the clutter and target distributions. Using the eigenvalue decomposition of \mathbf{C}_b , the SCR can be decomposed as follows

$$\text{SCR} = \sum_{k=1}^p \frac{[\mathbf{q}_k^T (\mathbf{s} - \mathbf{m}_b)]^2}{\lambda_k}, \quad (11.18)$$

where λ_k and \mathbf{q}_k are the eigenvalues and eigenvectors of \mathbf{C}_b . This expression shows which principal components are the most important for the detection of target \mathbf{s} in clutter with mean \mathbf{m}_b and covariance \mathbf{C}_b .

3. The conical decision surface of the NMF and its positioning with respect to the clutter and target distributions is better suited to the detection of subpixel targets compared to the hyperplane decision surface of the MF.
4. The NMF is invariant to the scale transformations $a\mathbf{x}$ and $a\mathbf{s}$ for all $a > 0$. As a result, the NMF has the same output distribution for clutter with any elliptically contoured distribution.
5. The normalization used in (11.13) ensures that the variance at the output of MF filter is constant; that is, $\text{var}(y_{\text{MF}}|H_0) = 1$ (see Section 10.5).
6. If we assume a linear signal model $\mathbf{x} = a\mathbf{s} + \mathbf{v}$, where $E(\mathbf{v}) = \mathbf{m}_b$ and $\text{cov}(\mathbf{v}) = \mathbf{C}_b$, the MF defined by

$$y_{\text{MF}}^{\text{MVDR}} = \frac{(\mathbf{s} - \mathbf{m}_b)^T \mathbf{C}_b^{-1} (\mathbf{x} - \mathbf{m}_b)}{(\mathbf{s} - \mathbf{m}_b)^T \mathbf{C}_b^{-1} (\mathbf{s} - \mathbf{m}_b)} = \frac{\tilde{\mathbf{s}}^T \tilde{\mathbf{x}}}{\tilde{\mathbf{s}}^T \tilde{\mathbf{s}}} \quad (11.19)$$

is the best linear unbiased estimator (BLUE) of the target fill-fraction a . This is identical to the MVDR filter defined in Section 10.5.

From the above discussion it is clear that the nonzero mean of the background clutter and the replacement target model favor a geometrical approach to the derivation and understanding of subpixel target detection algorithms. Furthermore, the lack of target training data makes difficult the use of pattern recognition algorithms.

11.1.6 Practical Target Detection Systems

We next discuss several issues regarding the practical application of MF and NMF detectors. Understanding these issues helps to properly use these detectors and to set realistic expectations for their performance. Figure 11.9 shows the key components of a hyperspectral target detection system. We next discuss the utility and functionality of each component and illustrate its operation with the HYDICE data cube. For the reasons explained in Section 11.1.2, we focus on reflectance-domain processing; however, the approach can easily be modified for processing in the radiance domain.

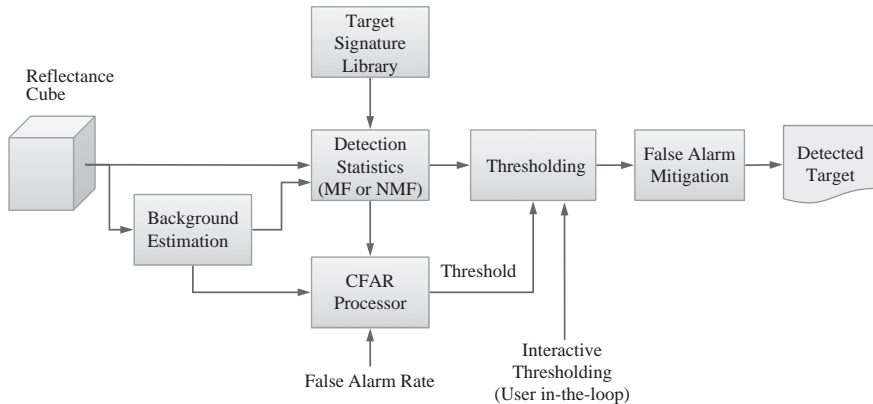


Figure 11.9 Block diagram of a practical hyperspectral target detection system.

Target Signature

We first select the signatures for the targets of interest from a reflectance target signature library. The selection is exclusively based on the requirements of the specific application. The input data cube has been converted to reflectance using the ELM approach, as described in Section 6.6.

The target signature s is obtained from a target training data set or from a spectral library. Collection of training data requires flying over a target of interest, collecting target signatures, and using the obtained spectral signatures for subsequent missions. The use of reflectance spectral libraries is mandatory for target identification applications. In this case, the hyperspectral data cube must be converted to reflectance using atmospheric compensation techniques. To illustrate the operation of MF and NMF detectors we will search for a green tarp target characterized by the library signature shown in Figure 11.10. We note that the mismatch between library and in-scene target spectra is unavoidable and imposes a limit in the performance of target detection and identification algorithms.

Background Estimation

To implement the AD, MF, and NMF algorithms we need the mean vector \mathbf{m}_b and the covariance matrix \mathbf{C}_b of the background clutter. However, in practice, these quantities are unknown and must be estimated using a training data set from the input cube. We typically use the entire input cube, or we partition it into smaller cubes and process each cube separately. Although it is possible to use adaptive local estimation techniques involving moving windows, this is not recommended due to increased computational cost and inferior performance. We focus on cube-based processing and we shall use the term “input cube” to refer to each individually processed cube. The size of the input cube is dictated by collection requirements or statistical considerations. The mean and the covariance are estimated using the maximum likelihood estimators (see Section 7.5.2)

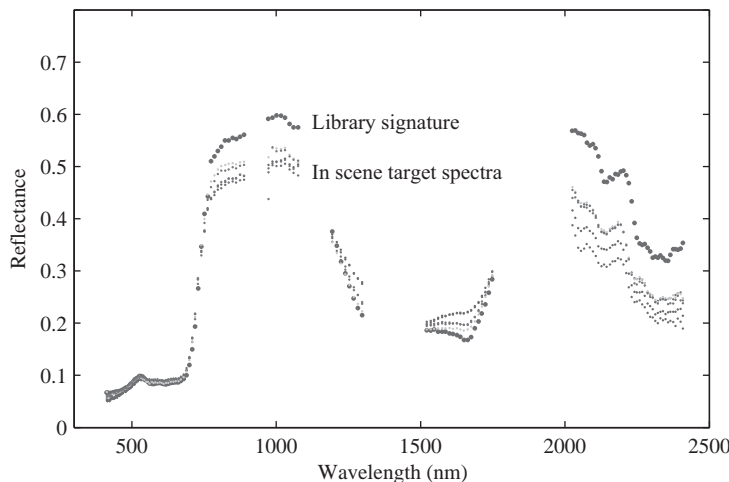


Figure 11.10 Library signature and in-scene reflectance spectra from the pixels of a green tarp target in the HYDICE data cube.

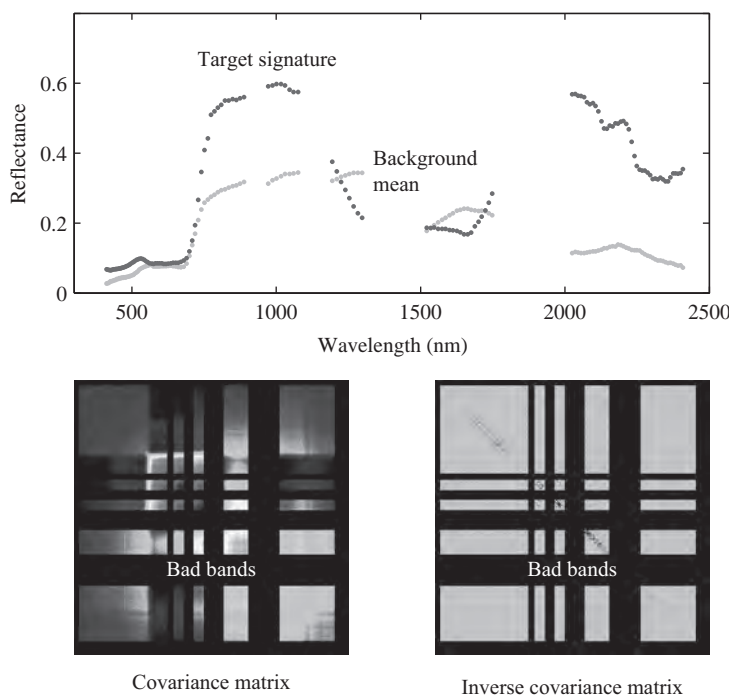


Figure 11.11 Target signature, mean of background clutter, image of covariance matrix, and image of inverse covariance matrix for the HYDICE data cube. Note that the nonzero elements of the inverse covariance matrix are close to its diagonal.

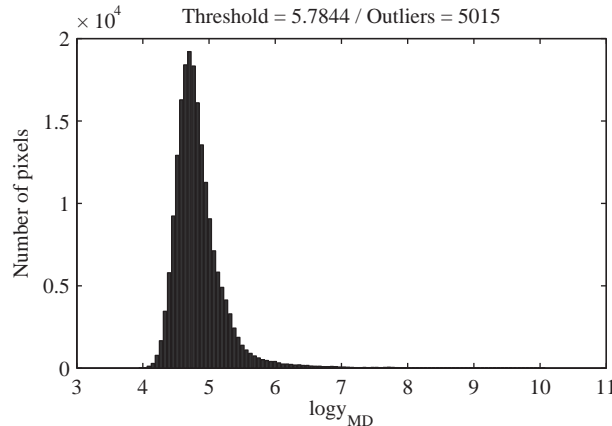


Figure 11.12 Distribution of anomaly detection statistic for the HYDICE data set. Setting the threshold at $\eta_{AD} = 5.7844$ leads to the removal of 5015 outliers.

$$\hat{\mathbf{m}}_b = \frac{1}{N} \sum_{k=1}^N \mathbf{x}_k, \quad \hat{\mathbf{C}}_b = \frac{1}{N} \sum_{k=1}^N (\mathbf{x}_k - \hat{\mathbf{m}}_b)(\mathbf{x}_k - \hat{\mathbf{m}}_b)^T. \quad (11.20)$$

The number of pixels N must be larger than $100p$, where p is the number of bands.

Clearly, if there are target pixels in the training data they will contaminate the estimated covariance matrix. To avoid this contamination, which has detrimental effects on detection performance (see Section 10.9.2), we need algorithms that remove target-like spectra and other sensor outliers from the background training data. There are two practical approaches to obtain “target-free” background clutter training data. The first approach is to use a detection algorithm to detect and remove target-like pixels. This approach, which is known as a “two-pass” detection process, requires a detector for each target of interest. The second approach uses anomaly detection algorithms to remove “spectrally suspicious” pixels. A simple yet effective approach uses the AD algorithm (11.12). As shown in Figure 11.12, the body of the distribution of $\log y_{AD}$ resembles a normal distribution. This facilitates the selection of the threshold in terms of the standard deviation; that is, we set $\eta_{AD} = k\sigma$, where k is chosen by trial and error.

MF and NMF Detectors

Matched filter detectors require the inversion of the estimated covariance matrix. To ensure invertibility of the covariance matrix, robustness to signature mismatch, and robustness to covariance contamination by target pixels, we use the dominant mode rejection with diagonal loading approach discussed in Section 10.9.4. The desired inverse matrix is given by

$$\bar{\mathbf{C}}_b^{-1} = (\mathbf{C}_{DMR} + \xi \mathbf{I})^{-1} = \frac{1}{\alpha + \xi} \left[\mathbf{I} - \sum_{k=1}^d \left(\frac{\lambda_k - \alpha}{\lambda_k + \xi} \right) \mathbf{q}_k \mathbf{q}_k^T \right], \quad (11.21)$$

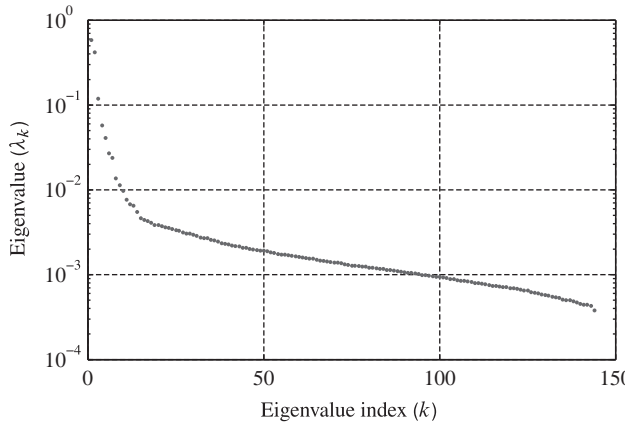


Figure 11.13 Eigenvalues plot for the covariance matrix of HYDICE dataset.

where λ_k and \mathbf{q}_k are the eigenvalues and eigenvectors of $\hat{\mathbf{C}}_b$, ξ is the diagonal loading factor, and $\alpha = (\lambda_{d+1} + \dots + \lambda_p)/(p - d)$. We typically choose d to exclude the last noisy eigenvalues of $\hat{\mathbf{C}}_b$ and ξ to be a small fraction of the variance $\text{tr}\hat{\mathbf{C}}_b/p$ of the input data by looking at an eigenvalue plot, like the one shown in Figure 11.13.

We next provide a detailed implementation of the AD, MF, and NMF algorithms, where we assume that the pixels of the input cube have been organized in a single indexed data set $\mathbf{x}_1, \dots, \mathbf{x}_N$. Steps 1 and 3 use the target-free background clutter training data set that includes N_b pixels. All other steps apply to the entire input data set. The computational steps required to compute the detection statistics are:

1. Compute the mean spectrum: $\hat{\mathbf{m}}_b = \frac{1}{N_b} \sum_{k=1}^{N_b} \mathbf{x}_k$;
2. Center the target spectrum $\bar{\mathbf{s}} = \mathbf{s} - \hat{\mathbf{m}}_b$ and the data $\bar{\mathbf{x}}_k = \mathbf{x}_k - \hat{\mathbf{m}}_b$, $k = 1, 2, \dots, N$;
3. Compute the covariance matrix: $\hat{\mathbf{C}}_b = \frac{1}{N_b} \sum_{k=1}^{N_b} \bar{\mathbf{x}}_k \bar{\mathbf{x}}_k^T$;
4. Compute the whitening matrix using (11.21): $\mathbf{A} = \bar{\mathbf{C}}_b^{-1/2}$;
5. Compute the MF vector $\mathbf{h} = \mathbf{A}\bar{\mathbf{s}}$ and the normalization constant $\kappa = \mathbf{h}^T \mathbf{h}$;
6. For every pixel $k = 1, 2, \dots, N$ compute:
 - (a) Whitening: $\mathbf{z}_k = \mathbf{A}\mathbf{x}_k$;
 - (b) Projection: $y_k = \mathbf{h}^T \mathbf{z}_k$;
 - (c) MF: $y_{\text{MF},k}^{\text{MVDR}} = y_k/\kappa$ (MVDR normalization);
 - (d) AD: $y_{\text{AD},k} = \mathbf{z}_k^T \mathbf{z}_k$;
 - (e) NMF: $y_{\text{NMF},k} = \frac{y_k}{\sqrt{\kappa} \sqrt{y_{\text{AD},k}}}$.

The most time-consuming operation is the computation of the covariance matrix, followed by whitening, mean subtraction, and computation of anomaly detector. The practical real-time implementation of MF and NMF algorithms is discussed by Brett et al. (2013). The whitening matrix can be also computed by $\mathbf{A} = (\mathbf{L}^{-1})^T$, where \mathbf{L}

is the Cholesky factor of the diagonally loaded matrix $(\hat{\mathbf{C}}_b + \xi\mathbf{I}) = \mathbf{L}\mathbf{L}^T$, which is guaranteed to be positive definite for $\xi > 0$ (Golub and Van Loan, 1996).

When the number of background training pixels is close to the number of bands, it is recommended to use the low-rank versions of MF and NMF detectors given by

$$y_{\text{LRMF}}^{\text{MVDR}}(\mathbf{x}) = \frac{\mathbf{s}^T \mathbf{P}_B^\perp \mathbf{x}}{\mathbf{s}^T \mathbf{P}_B^\perp \mathbf{s}} \quad (11.22)$$

and

$$y_{\text{LRNMF}}(\mathbf{x}) = \frac{\mathbf{s}^T \mathbf{P}_B^\perp \mathbf{x}}{\sqrt{\mathbf{s}^T \mathbf{P}_B^\perp \mathbf{s}} \sqrt{\mathbf{x}^T \mathbf{P}_B^\perp \mathbf{x}}} = \cos \theta \quad (11.23)$$

respectively. The corresponding energy versions are given by (10.192) and (10.194). The low-rank version of the anomaly detector is given by

$$y_{\text{LRAD}}(\mathbf{x}) = \mathbf{x}^T \mathbf{P}_B^\perp \mathbf{x}. \quad (11.24)$$

Threshold Selection

As we have seen in Section 10.2, a detection algorithm consists of two parts: a detection statistic and a threshold. The selection of the threshold is very important and its significance cannot be overestimated. In surveillance applications, it is almost always required that the system will maintain a constant false alarm rate (CFAR) as the background distribution changes. This objective is usually accomplished by adaptively estimating the background distribution and adjusting the threshold accordingly. The decision threshold η and the resulting probability of false alarm $P_{\text{FA}}(\eta)$ are related by

$$P_{\text{FA}}(\eta) = \int_{\eta}^{\infty} f(y|H_0) dy, \quad (11.25)$$

where y is the detection statistic. The distribution $f(y|H_0)$ is unknown and must be estimated from the background training data. To determine thresholds at very low false alarm rates, which is a requirement for practical systems, we must estimate the tails of $f(y|H_0)$. This is a difficult problem because it requires a very large number of pixels. In practice we express the false alarm rate (FAR) in units of false alarms per unit area, that is,

$$\text{FAR} = \frac{\text{Number of FAs in area } A}{\text{area } A} \approx \frac{P_{\text{FA}}}{\text{GSD} \times \text{GSD}} \frac{\text{FAs}}{\text{km}^2}. \quad (11.26)$$

To appreciate the difficulty of estimating probabilities, we recall that binary detection can be modeled by the binomial distribution (Echard, 1991)

$$\Pr(X = k) = \binom{N}{k} p^k (1-p)^{N-k}, \quad k = 0, 1, \dots, N, \quad (11.27)$$

where k is the number of successes, N is the number of trials, and p is the probability of success. The maximum likelihood estimator of p is given by

$$\hat{p} = \frac{k}{N}. \quad (11.28)$$

The mean and variance of the estimator (11.28) are

$$E(\hat{p}) = p, \quad \text{var}(\hat{p}) = \frac{p(1-p)}{N} \approx \frac{p}{N}, \quad \text{for } p \ll 1. \quad (11.29)$$

For a standard error $\sqrt{\text{var}(\hat{p})} \approx \sqrt{p}/\sqrt{N} \leq \alpha p$, the number of trials is given by

$$N \geq \frac{1}{\alpha^2 p}. \quad (11.30)$$

For example, to estimate a $P_{\text{FA}} = 10^{-5}$ with $\alpha = 0.1$ we need at least ten million pixels. A more rigorous analysis of the estimator (11.28) using confidence limits is provided by Echard (1991).

A practical approach to CFAR threshold selection is to model the tails of the clutter distribution $f(y|H_0)$ within the range of the available data, and then use the model to determine thresholds at lower false alarm rates. The basic idea is to obtain reliable estimates of the background statistics at low false alarm rates, and then extend these estimates beyond the range supported by the data to predict the thresholds at lower false alarm rates. These techniques are possible because the tail behavior can be determined by considering extreme observations without any assumptions about the center of the distribution. This is formally done in a practical way using the theory of extreme value distributions. More details about CFAR threshold selection using the Pareto distribution are provided by Manolakis et al. (2007); an alternative approach is discussed by Ensafi and Stocker (2008).

In practical systems all pixels that exceed the threshold are treated as potential targets and are subjected to further evaluation. The final decision is made by experienced analysts using interactive spectroscopic analysis and information from other sensors. The major concerns in these situations are that this process is time-consuming and the number of available analysts is limited. Therefore, automated techniques for False Alarm Mitigation (FAM) – see Section 11.3 – are very important.

Experimental Results

We can now turn attention to the operation of AD, MF, and NMF detection algorithms. Figure 11.14 shows a color picture of the imaged scene, the picture of the pixels selected for background training (black pixels), and image representations of detection statistics for the AD, MF, and NMF algorithms. The target of interest is a green tarp, which appears in three locations at the same row of the data cube. This is clearly evident in the second row of images of Figure 11.14.

The HYDICE scene contains many panel and vehicle targets, that are easy to detect spectrally. Most of these targets are picked up by the anomaly detector, resulting in a large number of false alarms. This must be expected because AD algorithms do *not* use any spectral information about the target. Therefore, AD algorithms have limited use as spectral target detectors; they are mostly used to remove artifacts (for example, bad pixels) and target-like pixels from background training data sets. Since the dynamic range of the AD statistic is very large, we usually plot the histogram of its logarithm (see Figure 11.12).

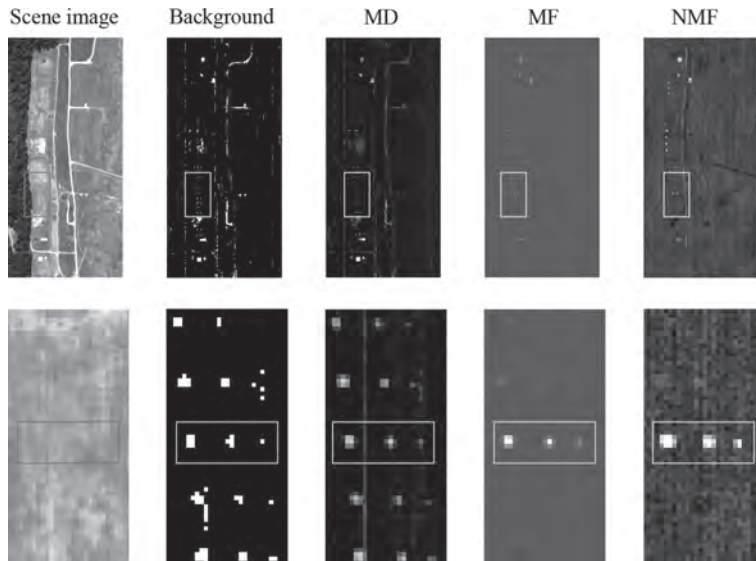


Figure 11.14 Pictorial illustration of imaged scene, background training data, and detection statistics for the AD, MF, and NMF algorithms. Images in the second row are enlargement of the images inside the yellow rectangles in the first row. The targets of interest (green tarp) are inside the yellow rectangles in the second row. (A black and white version of this figure will appear in some formats. For the color version, please refer to the plate section.)

Careful inspection of the images in Figure 11.14 shows that the MF and NMF algorithms detect the green tarp pixels with a few false alarms. However, based on visual observations only, it is difficult to assess the performance of a detection algorithm. To gain additional insight we look at the distribution of the detection statistics shown in Figure 11.15. We note that the MF has a very narrow histogram, which explains the low contrast of its detection statistic image. The NMF image has a larger contrast, which is explained by the larger width of its histogram. To see clearly pixels with responses away from the main body of the histogram, we plot histograms using the logarithm of the number of pixels in each bin (see second row of plots in Figure 11.15). Both histograms are skewed to the right due to the presence of target pixels in the scene that score higher than background pixels. The most amazing result is that the multimodal background clutter distribution (see Figure 11.2) “collapses” essentially into a unimodal distribution at the output of MF and NMF detectors. If we zoom at the center of the MF histogram, we can see that it resembles a gaussian with heavier tails, like the histogram of the NMF in Figure 11.15.

A useful way to understand the performance of a detector, when we have a limited number of target pixels, is illustrated in Figure 11.16. The top plot shows the probability of exceedance, that is, $\Pr(y_{\text{NMF}} > \eta)$, when the input is background clutter. The histogram underneath shows the response of pixels containing green tarp. Because we do not have perfect truth, we cannot exactly identify the subpixel targets. However, it is clear from the two plots that we can detect the full pixel targets without any false alarms.

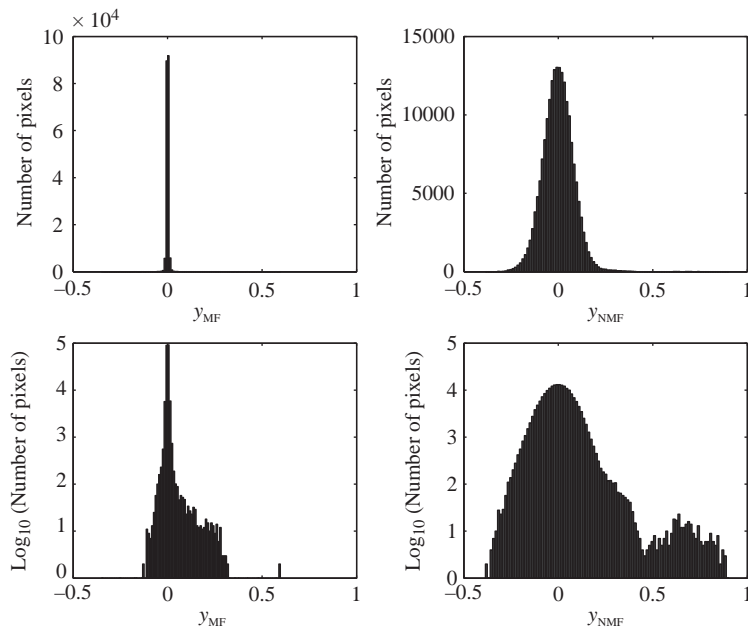


Figure 11.15 Histograms of detection statistic for the MF and NMF detectors.

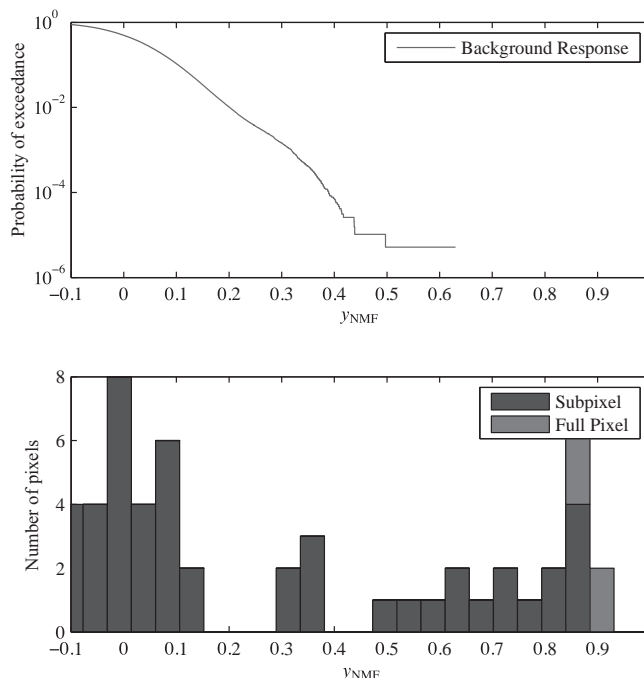


Figure 11.16 Performance evaluation of a NMF looking for a green tarp. (a) Probability of exceedance of NMF response to background clutter. (b) Histogram of NMF responses of pixels containing green tarp.

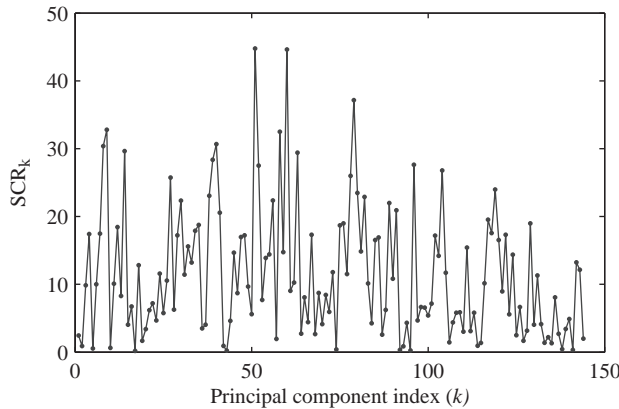


Figure 11.17 Contribution of each principal component to the SCR of the green tarp target of the HYDICE data cube.

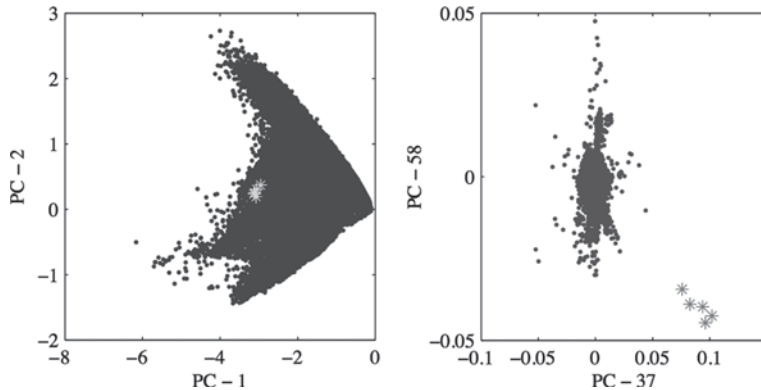


Figure 11.18 Principal component scatter plots showing the full pixels (red stars) of the green tarp target with respect to the pixels of the scene clutter.

Some additional insight can be obtained by investigating the operation of MF and NMF detectors in the principal component domain. As we have mentioned in Figure 11.2 the first two principal components contain 95 percent of the total clutter variability. However, what is important for target detection is the value of SCR and its distribution into the principal components as expressed by equation (11.18). The plot in Figure 11.17 shows that principal components 37 and 58 have the largest SCR contributions; in contrast principal components 1 and 2 have very small SCR contributions. The impact of these observations is demonstrated by the scatter plots in Figure 11.18, which show that the full pixel targets are separable from the clutter in the PC37 versus PC38 scatter plot but not in the PC1 versus PC2 scatter plot.

11.2 Target Detection Performance Assessment

A hyperspectral sensing system should perform satisfactorily under a wide range of conditions, as observed in actual trials. With respect to target detection, the fundamental

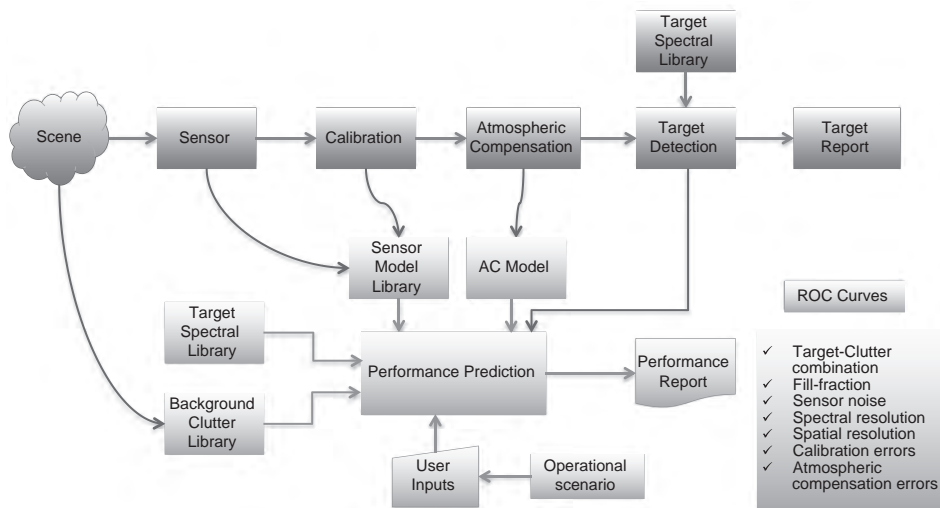


Figure 11.19 Basic parts of a target detection system and correspondence with the components of an “end-to-end” target detection performance prediction model.

questions posed by the hyperspectral user community are: (a) What is the expected detection performance for a target of interest mixed in a hyperspectral background? (b) How does performance change if the background, target, and target fill-fraction changes? And, (c) How difficult is it to distinguish different targets in the same background? To answer such questions, we need to derive ROC curves for the MF and NMF detectors using simple but realistic models for the target and clutter distributions.

A systematic approach to performance prediction requires the use of modeling and simulation tools to develop “end-to-end” performance prediction models (see Figure 11.19). These models can be used to: (a) provide utility in managing processing constraints, (b) provide connection between hyperspectral sensing system and actionable information for battlefield decisions, and (c) to facilitate trade-offs that impact detection performance. Such trade-offs include, among other things, background type, detection algorithm, target size and contrast. Note that any “end-to-end” performance prediction model should be based on a solid and simple theoretical framework that captures the effects of essential performance parameters. The development of “end-to-end” performance prediction models and their validation using data from actual trials are complex operations, and their discussion is beyond the scope of this book.

11.2.1

Signal-to-Clutter Ratio (SCR) as a Performance Metric

The matched filter maximizes the SCR for any input distributions. However, as we show next, the SCR is not always a good measure of detection performance. To illustrate this point we derive the ROC curves for the matched filter detector for full pixel targets with $C_b \neq C_t$.

The matched filter is specified by the background covariance matrix \mathbf{C}_b by

$$y = \mathbf{h}^T(\mathbf{x} - \mathbf{m}_b) \quad \text{and} \quad \mathbf{h} = \kappa \mathbf{C}_b^{-1}(\mathbf{m}_b - \mathbf{m}_t), \quad (11.31)$$

where κ is a normalization constant chosen according to (10.109) or (10.112).

The means and variances of matched filter output under the two hypotheses are

$$E(y|H_0) = \mathbf{h}^T(\mathbf{m}_b - \mathbf{m}_b) = 0 \quad (11.32a)$$

$$E(y|H_1) = \mathbf{h}^T(\mathbf{m}_t - \mathbf{m}_b) = \kappa \Delta^2 \quad (11.32b)$$

$$\text{var}(y|H_0) = \mathbf{h}^T \mathbf{C}_b \mathbf{h} = \kappa^2 \Delta^2 \quad (11.32c)$$

$$\text{var}(y|H_1) = \mathbf{h}^T \mathbf{C}_t \mathbf{h} = \kappa^2 \Delta_{bt}^2, \quad (11.32d)$$

where Δ and Δ_m are Mahalanobis distances defined by

$$\Delta^2 \triangleq \boldsymbol{\delta}^T \mathbf{C}_b^{-1} \boldsymbol{\delta} \quad (11.33)$$

$$\Delta_{bt}^2 \triangleq (\mathbf{m}_b - \mathbf{m}_t)^T (\mathbf{C}_b^{-1} \mathbf{C}_t \mathbf{C}_b^{-1}) (\mathbf{m}_b - \mathbf{m}_t). \quad (11.34)$$

Since y follows a Gaussian distribution with means and variances given by (11.32), the detection and false alarm probabilities are given by (see Section 10.3)

$$P_{\text{FA}} = \int_{\eta}^{\infty} f(y|H_0) dy = Q \left[\frac{\eta - E(y|H_0)}{\sqrt{\text{var}(y|H_0)}} \right] \quad (11.35a)$$

$$P_{\text{D}} = \int_{\eta}^{\infty} f(y|H_1) dy = Q \left[\frac{\eta - E(y|H_1)}{\sqrt{\text{var}(y|H_1)}} \right]. \quad (11.35b)$$

Eliminating the threshold η between the last two equations we obtain

$$P_{\text{D}} = Q \left[\frac{\Delta Q^{-1}(P_{\text{FA}}) - \Delta^2}{\Delta_{bt}} \right], \quad (11.36)$$

which expresses the performance of matched filter in terms of Δ and Δ_{bt} . Since κ does not appear in (11.36), detection performance is not affected by this scaling factor. If $\mathbf{C}_t = \gamma^2 \mathbf{C}_b$, $0 \leq \gamma^2 \leq 1$, expression (11.36) is simplified to

$$P_{\text{D}} = Q \left[\frac{Q^{-1}(P_{\text{FA}}) - \Delta}{\gamma} \right]. \quad (11.37)$$

The optimum performance, obtained when $\mathbf{C}_t = \mathbf{C}_b$ or $\gamma = 1$, is given by

$$P_{\text{D}} = Q \left[Q^{-1}(P_{\text{FA}}) - \Delta \right]. \quad (11.38)$$

We emphasize that only in this case the performance of the matched filter is completely specified by the Mahalanobis distance between the two normal distributions, which is equal to SCR.

11.2.2

Performance of MF and NMF in Multiclass Clutter

In Section 10.6 we analyzed the performance of MF detectors assuming that the conditions under which they are optimal are satisfied. We also evaluated performance loss

when there is mismatch between reference and in-scene target signatures. However, in most practical applications the background clutter follows the density mixture (11.1) and the target the stochastic mixture model (11.6). Therefore, we have

$$H_0 : \mathbf{x} \sim \sum_{k=1}^{N_C} \pi_k f_k(\mathbf{x}), \quad f_k(\mathbf{x}) = \begin{cases} N(\mathbf{m}_k, \mathbf{C}_k) \\ t(\mathbf{m}_k, \mathbf{C}_k, v_k) \end{cases} \quad (11.39a)$$

$$H_1 : \mathbf{x} \sim N(\mathbf{m}(a) = a\mathbf{m}_t + (1-a)\mathbf{m}_i, \mathbf{C}(a) = a^2\mathbf{C}_t + (1-a)^2\mathbf{C}_i), \quad (11.39b)$$

where we have assumed that the target is mixed with the i th background class. To simplify the analysis, we assume that the means, covariances, and tail-indexes of the component distributions are known. Figure 11.20 shows the class map, obtained using the SEM algorithm (see Section 7.7.4), for the HYDICE Forest Radiance scene.

The mean vector and covariance matrix required for the implementation of MF and NMF are evaluated from a set of clutter training data without taking into account any class assignment. These are the total mean and covariance matrices defined in Section 8.8 in terms of the class means and covariances by

$$\mathbf{m}_b = \sum_{k=1}^{N_C} \pi_k \mathbf{m}_k, \quad \mathbf{C}_b = \sum_{k=1}^{N_C} \pi_k \mathbf{C}_k + \sum_{k=1}^{N_C} \pi_k (\mathbf{m}_k - \mathbf{m})(\mathbf{m}_k - \mathbf{m})^T. \quad (11.40)$$

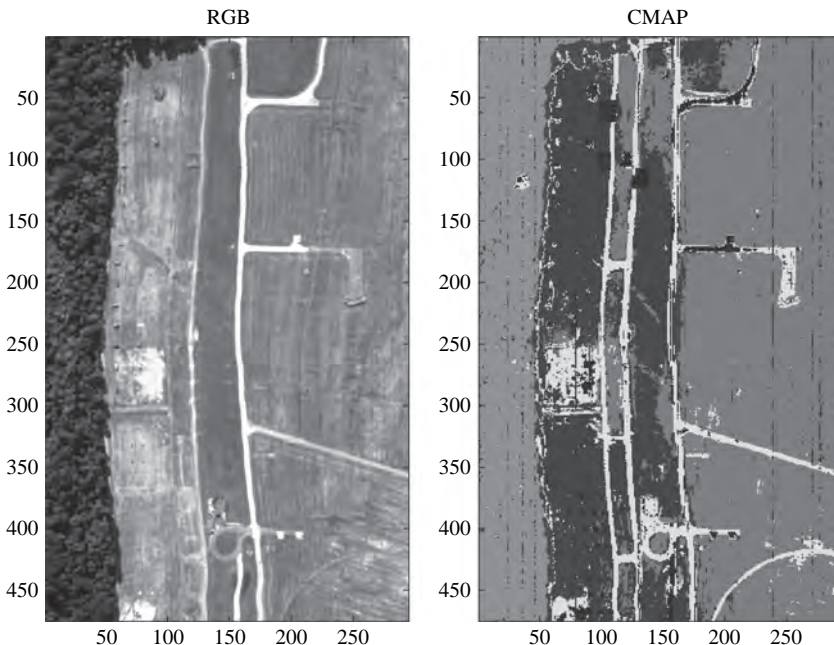


Figure 11.20 Color image of the HYDICE Forest Radiance scene and a class map obtained using the SEM clustering algorithm. (A black and white version of this figure will appear in some formats. For the color version, please refer to the plate section.)

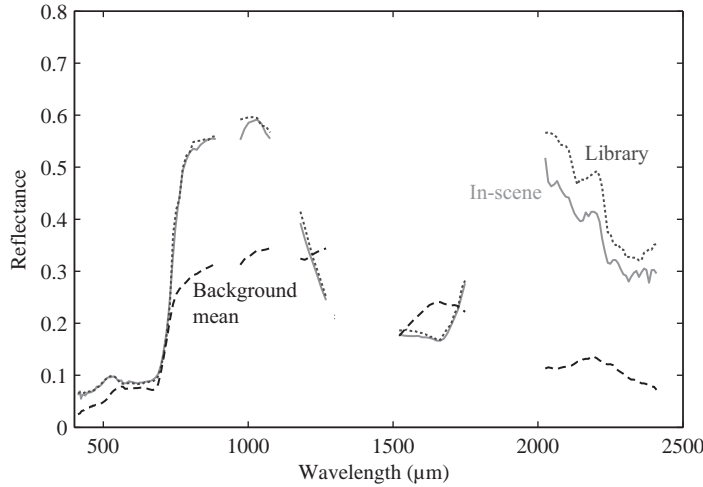


Figure 11.21 Library target signature, in-scene target signature, and background mean for the Hydice Forest Radiance data set.

To determine the performance of MF, we recall that the MF is defined by

$$y_{\text{MF}} = \mathbf{h}^T(\mathbf{x} - \mathbf{m}_b), \quad \mathbf{h} \triangleq \frac{\mathbf{C}_b^{-1/2}(\mathbf{s} - \mathbf{m}_b)}{\sqrt{(\mathbf{s} - \mathbf{m}_b)^T \mathbf{C}_b^{-1}(\mathbf{s} - \mathbf{m}_b)}}. \quad (11.41)$$

The reference signature \mathbf{s} used by the detector is obtained from a spectral library; the mean \mathbf{m}_t is often the in-scene reflectance signature for the target of interest (see Figure 11.21). The major challenge is the specification of the target covariance matrix, \mathbf{C}_t , due to the lack of target training data. In many cases, especially for small fill-fractions, we use the approximation $\mathbf{C}_t \approx \mathbf{C}_i$. Clearly, when $\mathbf{s} \neq \mathbf{m}_t$, the model takes into consideration target signature mismatch.

Since the MF is a linear operator, its response to a Gaussian distribution remains Gaussian. Therefore, under the H_1 hypothesis, the output is a Gaussian distribution with mean and variance given by

$$m_y(a) = \mathbf{h}^T \mathbf{C}_b^{-1/2} \mathbf{m}(a) \quad (11.42)$$

$$\sigma_y^2(a) = \mathbf{h}^T \mathbf{C}_b^{-1/2} \mathbf{C}(a) \mathbf{C}_b^{-1/2} \mathbf{h}. \quad (11.43)$$

The response of the MF to multivariate t -ECD is a univariate t distribution with the same tail index, and mean and covariance given by (Anderson, 2003)

$$m_k = \mathbf{h}^T \mathbf{C}_b^{-1/2} \mathbf{m}_k \quad (11.44)$$

$$\sigma_k^2 = \mathbf{h}^T \mathbf{C}_b^{-1/2} \mathbf{C}_k \mathbf{C}_b^{-1/2} \mathbf{h}. \quad (11.45)$$

In addition, each component of the mixture density is transformed by the MF independent of the other components. Therefore, for the target and clutter model (11.39), the detection statistic of the MF is distributed as

$$y_{\text{MF}} = \mathbf{h}^T(\mathbf{x} - \mathbf{m}_b) \sim \begin{cases} \sum_{k=1}^{N_C} \pi_k t_1(m_k, \sigma_k^2, v_k), & \text{under } H_0 \\ N_1(m_y(a), \sigma_y^2(a)), & \text{under } H_1. \end{cases} \quad (11.46)$$

These formulas are sufficient to determine ROC curves for any fill factor and any combination of target and background clutter classes (Manolakis, 2005).

Evaluating the output distribution of the NMF is more complicated because

$$y_{\text{NMF}} = \frac{y_{\text{MF}}}{\sqrt{(\mathbf{x} - \mathbf{m}_b)^T \mathbf{C}_b^{-1}(\mathbf{x} - \mathbf{m}_b)}} \quad (11.47)$$

is a nonlinear operator due to the presence of \mathbf{x} in the denominator. To circumvent this obstacle, we use the cotangent form of NMF in the whitened space defined by $\tilde{\mathbf{x}} = \mathbf{C}_b^{-1/2}(\mathbf{x} - \mathbf{m}_b)$ and $\tilde{\mathbf{s}} = \mathbf{C}_b^{-1/2}(\mathbf{s} - \mathbf{m}_b)$. This form is given by

$$y_t = \frac{\tilde{\mathbf{s}}^T \mathbf{P}_{\tilde{\mathbf{s}}} \tilde{\mathbf{x}}}{\sqrt{\tilde{\mathbf{s}}^T \tilde{\mathbf{s}}} \sqrt{\tilde{\mathbf{x}}^T \mathbf{P}_{\tilde{\mathbf{s}}}^\perp \tilde{\mathbf{x}}}} = \frac{y_{\text{MF}}}{\sqrt{q}}, \quad (11.48)$$

where $\mathbf{P}_{\tilde{\mathbf{s}}} = \tilde{\mathbf{s}}(\tilde{\mathbf{s}}^T \tilde{\mathbf{s}})^{-1} \tilde{\mathbf{s}}^T$ and $\mathbf{P}_{\tilde{\mathbf{s}}}^\perp = \mathbf{I} - \mathbf{P}_{\tilde{\mathbf{s}}}$ are projection matrices, and

$$q \triangleq \tilde{\mathbf{x}}^T \mathbf{P}_{\tilde{\mathbf{s}}}^\perp \tilde{\mathbf{x}} \quad (11.49)$$

is a low-rank quadratic form. The cumulative distribution function of y_t can be evaluated by conditioning on q using the formula (Papoulis and Pillai, 2002)

$$\begin{aligned} F_{y_t}(\eta) &= \Pr(y_t \leq \eta) = \Pr(y_{\text{MF}}/q \leq \eta) \\ &= \int_0^\infty \Pr(y_{\text{MF}} \leq \eta \sqrt{q} | q) f_q(q) dq \\ &= \int_0^\infty F_{\text{MF}}(\eta \sqrt{q} | q) f_q(q) dq, \end{aligned} \quad (11.50)$$

where $F_{\text{MF}}(\eta \sqrt{q} | q)$ is the conditional distribution of MF given q and $f_q(q)$ is the distribution of q . If $\tilde{\mathbf{x}} \sim N(\mathbf{a}, \mathbf{C})$, then q follows a non-central chi-square distribution if $\mathbf{a} = \tilde{\mathbf{s}}$ and $\mathbf{C} = \sigma^2 \mathbf{I}$. For arbitrary \mathbf{a} and \mathbf{C} , there are simple forms only for the characteristic function of q . A complete discussion of the computation of NMF ROC curves using (11.50) is provided by Truslow et al. (2013). Figure 11.22 shows the P_D of MF and NMF detectors, as a function of fill-fraction for a fixed P_{FA} , for the target signature shown in Figure 11.21 and the background classes shown in Figure 11.20. We note that the NMF performs better than the MF, but the performance of both detectors deteriorates for very small fill fractions. This trend, which is justified by the geometrical arguments in Figure 11.8, is supported by many performance comparisons based on field data tests.

The multiclass model has been used to develop a performance prediction tool useful in obtaining insight and evaluating sensors and detection algorithms under different deployment conditions. Another interesting and useful application of the model is shown in Figure 11.23, which shows a scatter plot of NMF versus MF responses for the Forest Radiance I data set. The ribbon shows a 95 percent confidence interval for the NMF and MF responses predicted by a five-class t -ECD model. We first note that the model does a reasonable job at predicting the range of detector responses and the majority of

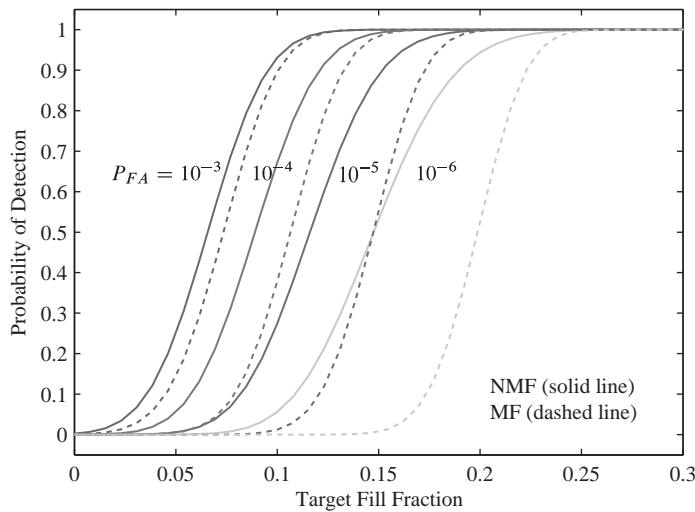


Figure 11.22 Performance comparison of MF and NMF detectors using the stochastic mixing target model and the multiclass background clutter model.

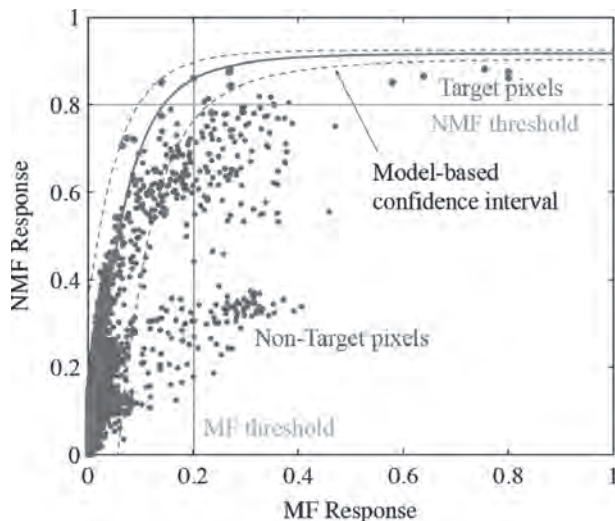


Figure 11.23 NMF versus MF values scatter plot and confidence “ribbon” for expected values constructed using the performance prediction model. For simplicity of interpretation the MF is normalized to provide an estimate of the fill-fraction.

background responses. Clearly, the NMF provides a better separation between target and clutter pixels compared to the MF. Most pixels that exceed the MF threshold belong to other targets and man-made objects present in the scene. We again stress that such results do not prove the validity of the model; a thorough validation of the predictive model is a laborious and expensive undertaking.

11.3 False Alarm Mitigation and Target Identification

In practice, all detection algorithms exhibit an unacceptable number of false alarms (Eismann et al., 2010). A promising approach to deal with this challenge is post-processing of the top hits with *false alarm mitigation (FAM)* algorithms. The NMF and MF detectors make decisions by exploiting the statistical distributions of targets and clutter in the clutter-whitened space. Practical experience has shown that both algorithms are relatively robust to model mismatches, including clutter multi-modality, covariance estimation, and target signature mismatch. Therefore, FAM algorithms must exploit information not available in the detection statistic. In this sense, the development of FAM algorithms is an art involving statistics, spectroscopy, and spatial image processing. False alarms can also be mitigated using information from co-registered high-resolution video data.

11.3.1 Matched Filter with FAM

A simple but useful FAM algorithm for the MF detector can be obtained by exploiting the geometry in Figure 11.24. We note that all observation vectors with tips touching the MF hyperplane decision surface have identical MF responses. However, according to the replacement target model (11.3), “true” subpixel targets have a normal distribution centered at the line connecting the centers of target and clutter distributions at a location specified by the target fill factor. To determine the center of the target distribution we use the estimate of fill factor provided by (11.19), which we repeat here for convenience

$$\hat{a} = y_{\text{MF}}^{\text{MVDR}}(\mathbf{x}) = \frac{(\mathbf{s} - \mathbf{m}_b)^T \mathbf{C}_b^{-1} (\mathbf{x} - \mathbf{m}_b)}{(\mathbf{s} - \mathbf{m}_b)^T \mathbf{C}_b^{-1} (\mathbf{s} - \mathbf{m}_b)}. \quad (11.51)$$

We note that $\hat{a} = 1$ when $\mathbf{x} = \mathbf{s}$. If we use the whitening transformation defined by (11.15), we obtain

$$\hat{a} = y_{\text{MF}}^{\text{MVDR}}(\mathbf{x}) = \frac{\tilde{\mathbf{s}}^T \tilde{\mathbf{x}}}{\|\tilde{\mathbf{s}}\|^2} = \frac{y_{\text{MF}}}{\|\tilde{\mathbf{s}}\|}. \quad (11.52)$$

Thus, the center of the target distribution is approximately located at the point $\mathbf{m}(\hat{a}) \approx \hat{a}\tilde{\mathbf{s}}/\|\tilde{\mathbf{s}}\|$. In addition, we have

$$\tilde{\mathbf{s}} = \mathbf{C}_b^{-1/2}(\mathbf{s} - \mathbf{m}_b), \quad \tilde{\mathbf{m}}_b = \mathbf{0}, \quad (11.53a)$$

$$\tilde{\mathbf{C}}_t = \mathbf{C}_b^{-1/2} \mathbf{C}_t \mathbf{C}_b^{-1/2}, \quad \tilde{\mathbf{C}}_b = \mathbf{I}, \quad (11.53b)$$

which leads to the geometrical representation shown in Figure 11.24.

Since the target covariance matrix is unavailable in most practical applications, we often use the approximation $\mathbf{C}(a) \approx \mathbf{C}_b$, which works reasonably well in practical applications (DiPietro et al., 2012). The Mahalanobis square distance, which for a normal distribution is inversely proportional to the likelihood that the test pixel is a subpixel target, is given by

$$\Delta^2(\mathbf{x}) = (\mathbf{x} - \hat{a}\tilde{\mathbf{s}})^T \mathbf{C}^{-1}(\hat{a})(\mathbf{x} - \hat{a}\tilde{\mathbf{s}}) \quad (11.54)$$

$$\approx (\mathbf{x} - \hat{a}\tilde{\mathbf{s}})^T \mathbf{C}_b^{-1}(\mathbf{x} - \hat{a}\tilde{\mathbf{s}}). \quad (11.55)$$

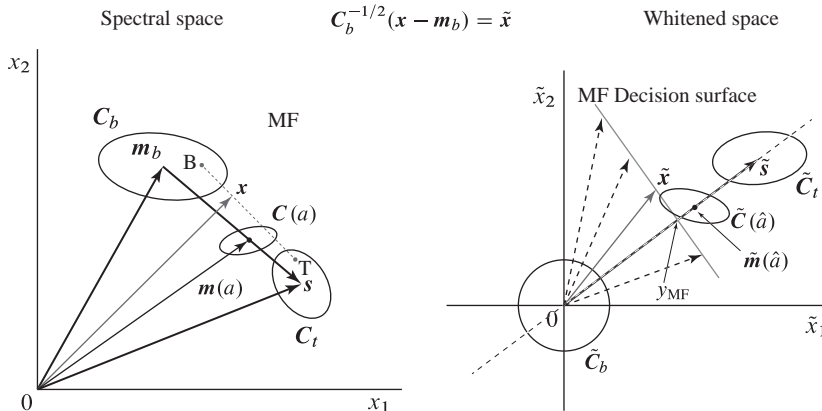


Figure 11.24 Geometrical interpretation of MF detector with FAM. The spectrum x is a mixture of two spectra generated from the background and target classes, with tips at points B and T, respectively.

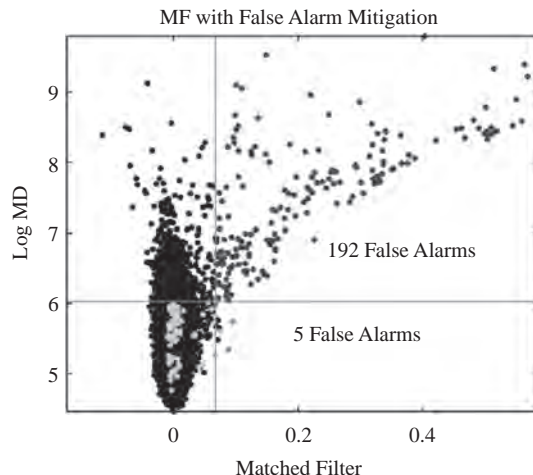


Figure 11.25 The MF with FAM uses a “subpixel likelihood metric” and double thresholding to reduce false alarms. The gray lines indicate the used thresholds.

Figure 11.25 shows a typical scatter plot of the Mahalanobis distance (11.55) versus the MF response (11.51) for a detection experiment involving a man-made target. We note that with the use of a second threshold, we can significantly reduce the number of false alarms. The use of a CFAR threshold is possible by modeling the distribution of (11.55). More details about the MF with FAM and comparison with other approaches can be found in DiPietro et al. (2012).

11.3.2 Normalized MF with FAM

Consider Figure 11.26, which illustrates the operation of NMF in the whitened domain. We note that all vectors passing through the dotted circle yield the same NMF value.

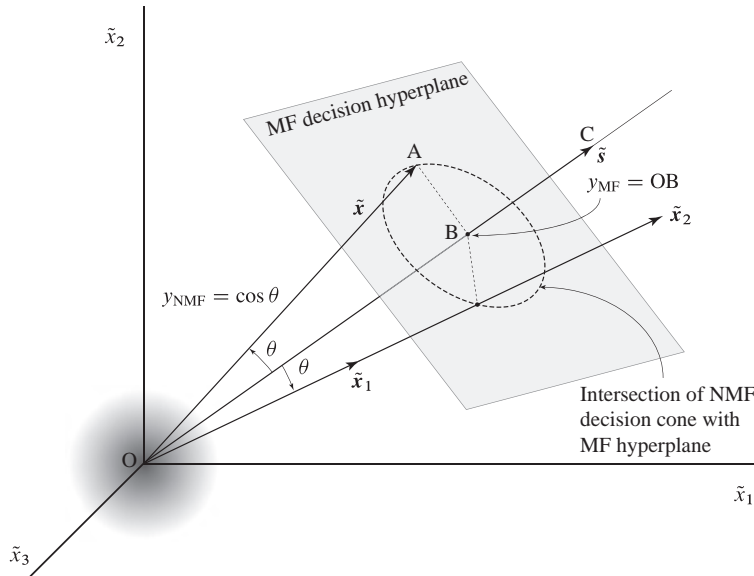


Figure 11.26 Geometrical interpretation of the NMF detector and false alarms caused by the inherent rotation invariance in the whitened space.

Thus, if \tilde{x} corresponds to a target, the vectors \tilde{x}_1 and \tilde{x}_2 lead to false alarms. The cause of such false alarms is the rotational invariance of the NMF detector. To understand how such false alarms affect the performance of NMF we recall that the MF response is length OB of the projection of \tilde{x} on \tilde{s} , whereas the value of the NMF is the cosine of the angle formed by \tilde{x} on \tilde{s} . That is,

$$y_{MF} = OB \quad \text{and} \quad y_{NMF} = \frac{y_{MF}}{\|\tilde{x}\|} = \frac{OB}{OA} = \cos \theta. \quad (11.56)$$

The estimated target fill-fraction, which is given by

$$\hat{a} = \frac{y_{MF}}{\|\tilde{s}\|} = \frac{OB}{OC}, \quad (11.57)$$

can be used to eliminate targets with unreasonably small fill-fractions. Consider next the quantity

$$y_{MFE} \triangleq \|\tilde{x} - y_{MF}(\tilde{s}/\|\tilde{s}\|)\| = \|\tilde{x} - \hat{a}\tilde{s}\| = AB, \quad (11.58)$$

which is the length of the perpendicular from the tip of \tilde{x} to \tilde{s} . We note that the angle θ can be specified using any two sides of the orthogonal triangle OBA.

To illustrate these ideas we consider the scatter plots in Figure 11.27, where we plot different quantities against the response of the MF. The scatter plot in Figure 11.27(a), which is similar to the one in Figure 11.25, shows the MF error y_{MFE} versus the MF response. Figure 11.27(b) shows the scatter plot of the NMF and MF responses. To understand the shape of the distribution, we recall that the response of the NMF is determined by the ratio between MF and MFE. We note that at high fill fractions, the response of NMF fluctuates about a constant threshold; however, the response quickly deviates from this line at lower fill fractions. The reason for this deviation can be observed by

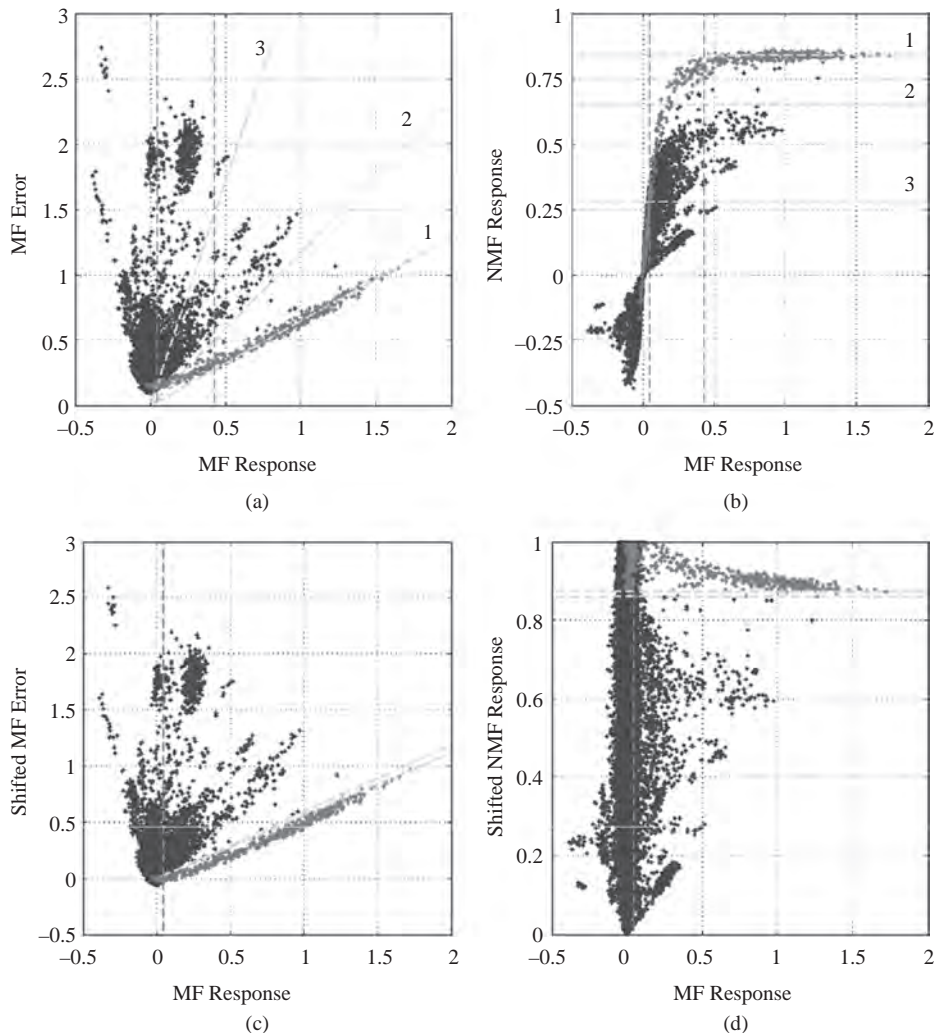


Figure 11.27 Scatter plots used to illustrate the performance of the NMF and “shifted” NMF detectors using the green tarp target in the Forest Radiance cube. Blue dots correspond to background pixels and red dots to target pixels. MF thresholds are shown by maroon dotted lines and NMF thresholds by green dotted lines.

plotting the constant NMF threshold on the MF versus MFE scatter plot. The NMF is evaluated using values of MF and MFE determined with respect to zero; however, the MFE of the background has a nonzero mean. This discrepancy causes the NMF response to drop off when the MF is comparable to the MFE of the background. To deal with this problem we shift the MFE to have zero mean clutter response and we use this response to produce the scatter plots shown in Figure 11.27(c) and Figure 11.27(d). The last figure indicates that the “shifted”-NMF provides a more convenient approach to target detection false alarm mitigation. More details about these issues are provided by Pieper et al. (2013).

11.3.3 Target Identification Algorithms

The task of a *target identification* algorithm is to determine whether a pixel picked out by the detector contains indeed the target of interest. This is a difficult undertaking because different scene components may result in similar or identical spectra (mimics). The problem is more prominent for subpixel targets because of spectral mixing. In this case, the first step is to estimate the target spectrum using unmixing techniques. Identification algorithms use the estimated spectrum and material spectral libraries to associate this spectrum with the reference spectrum of some material. Typical approaches exploit ideas from the areas of linear unmixing, F-test-based model selection, Bayesian model selection (Burr et al., 2008), band selection techniques (Keshava, 2004) and spectroscopy (Adams and Gillespie, 2006). Spectroscopic and library matching techniques for the analysis of hyperspectral data is covered in Clark et al. (2003). The development of target identification algorithms is an evolving area that requires the meaningful combination of pattern classification, linear mixture analysis, variable selection, spectroscopy, and practical experience.

11.4 Spectral Landscape Classification

This section provides an introduction to classification techniques used to extract land-cover information from hyperspectral imaging data. Essentially, classification is a mapping from the spectral signature of a pixel to a label that identifies it with what materials are present on the ground. We typically use the term *land-cover* or *theme* to refer to the type of material present on the landscape: for example, water, sand, crops, forest, wetland, and human-made materials such as asphalt.

If we assign a unique label, or theme, to every pixel of a data cube, the result is a map called a *thematic map*. The process of generating a thematic map it is called thematic mapping. However, since many pixels are mixed, using fraction images (see Section 9.15) would provide a more accurate interpretation of the data. Clearly, the need for spectral mixture analysis depends on the spatial resolution of the sensor and the composition of the imaged scene.

Thematic mapping with spectral data, which is widely used in remote sensing, requires considerable subject matter expertise and practical experience (Adams and Gillespie, 2006). Classification techniques for thematic mapping using multispectra and hyperspectral imaging data have been extensively studied in the literature (Landgrebe, 2003; Jensen, 2005; Schowengerdt, 2007; Richards, 2013). A detailed treatment of the subjects of pattern recognition and machine learning, which provide the theoretical framework for classification algorithms, can be found in (Duda et al., 2001; Bishop, 2006; Theodoridis and Koutroumbas, 2008; Webb and Copsey, 2011). Since an exhaustive treatment of these techniques is beyond the scope of this book, we explain the key ideas of unsupervised and supervised classification and we point out the differences between classification and target detection algorithms.

11.4.1 Supervised Classification

In hyperspectral remote sensing, image classification is a mapping from the measurement space of the sensor to a set of labels that represent the ground-cover types or themes of interest to the user. Figure 11.28 illustrates the key steps of the classification process.

The basic idea exploited by classification algorithms is that the spectra of pixels from the same ground-cover (theme) tend to gather in the same neighborhood of the spectral space; that is, they form a cluster that becomes the basis for the definition of a *spectral class*. Thus, spectra from different ground-covers tend to form spectral classes at different regions of the spectral space. Suppose next that we have sufficient information to label each class with a theme; for example, vegetation class, water class, and soil class. These classes are known as *information classes*, because they provide the information desired by the user. A list of established classification schemes for land information classes is provided by Jensen (2005). There are two major issues in classification applications: (a) do the spectral classes occupy unique regions in spectral space? And (b) is there a one-to-one mapping between spectral and information classes? The answer to these questions determines the degree of success of classification algorithms in practical applications (Landgrebe, 2002).

To introduce the methodology of supervised classification, suppose that (a) we know beforehand the information classes in the scene and (b) we have available a set of pixels for each class. Then, at least in principle, we could plot the spectra of these pixels in the spectral space, determine the location and shape of each class, use this information to draw boundaries that separate the different classes, and assign a class label to each region. This partitioning of the spectral space into an exhaustive set of non-overlapping regions, one for each class of interest, constitutes the design of a classifier. The classifier determines the label of each unknown or unseen pixel by determining the partition of the spectral space where the tip of the pixel spectrum falls. In reality, classification is complicated because the distributions of the classes of interest in the spectral space are not clearly separated.

The spectral variability of hyperspectral imaging data suggests that modeling each class with a probability distribution and using multiple or M -ary hypothesis testing

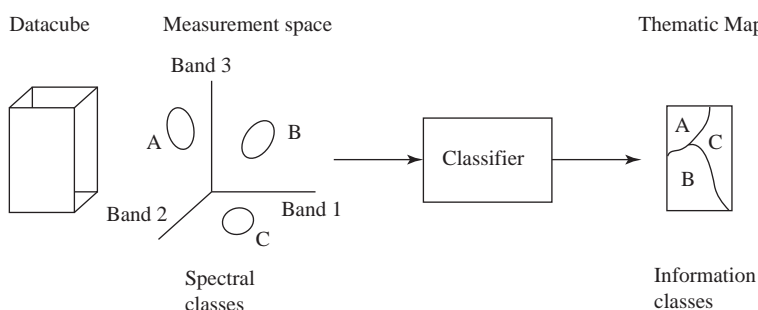


Figure 11.28 Key components of a classification system for thematic mapping.

provides a natural approach to image classification. To illustrate this approach, we shall use and extend the results of Sections 10.2.5 and 10.3 into multiple classes modeled by normal distributions. Suppose that we have M classes \mathcal{C}_i with a priori probabilities $P(\mathcal{C}_i)$ and conditional distributions $f(\mathbf{x}|\mathcal{C}_i)$ given by

$$\mathbf{x} \sim N_p(\mathbf{m}_i, \mathbf{C}_i), \quad i = 1, \dots, M. \quad (11.59)$$

We say that the H_i hypothesis is valid if an observation \mathbf{x} belongs to the \mathcal{C}_i class. Since there are more ways for the classifier to be wrong than to be right, it is simpler to compute the total probability of error or error rate using the probability of correct classification using

$$P_E = 1 - P_C = 1 - \sum_{i=1}^M P(\mathbf{x} \in \mathcal{R}_i, \mathbf{x} \in \mathcal{C}_i), \quad (11.60)$$

where \mathcal{R}_i is the decision region for the i th class. In addition to computing the total probability of error, we may also compute a *confusion* or *misclassification matrix*. The (i,j) th element of this matrix is the number of pixels of class \mathcal{C}_j that are classified as class \mathcal{C}_i by the rule. This is useful in identifying how the error rate is decomposed (Webb and Copsey, 2011). As we saw in Section 10.2.5, the minimum-error-rate classifier assigns a pixel \mathbf{x} to class \mathcal{C}_i if

$$g'_i(\mathbf{x}) = f(\mathbf{x}|\mathcal{C}_i)P(\mathcal{C}_i) > g'_j(\mathbf{x}) = f(\mathbf{x}|\mathcal{C}_j)P(\mathcal{C}_j) \quad \text{for all } j \neq i, \quad (11.61)$$

where $g'_i(\mathbf{x})$ is known as the *discrimination function*. For normal distributions it is more convenient to work with the logarithm of $g'_i(\mathbf{x})$, which is given by

$$g_i(\mathbf{x}) \triangleq \ln f(\mathbf{x}|\mathcal{C}_i) + \ln P(\mathcal{C}_i). \quad (11.62)$$

The discriminant functions for normally distributed classes are given by

$$g_i(\mathbf{x}) = -\frac{1}{2}(\mathbf{x} - \mathbf{m}_i)^T \mathbf{C}_i^{-1}(\mathbf{x} - \mathbf{m}_i) - \frac{p}{2} \ln 2\pi - \frac{1}{2} \ln |\mathbf{C}_i| + \ln P(\mathcal{C}_i). \quad (11.63)$$

If we have no useful information about the values of prior probabilities, we assume that they are all equal. Ignoring the class independent terms and the scaling factor $1/2$ from (11.63), we obtain

$$g_i(\mathbf{x}) = -(\mathbf{x} - \mathbf{m}_i)^T \mathbf{C}_i^{-1}(\mathbf{x} - \mathbf{m}_i) - \ln |\mathbf{C}_i|, \quad (11.64)$$

which is the discriminant function for the *Gaussian maximum likelihood classifier*. In general, the decision surfaces are hyperquadratics; however, they become hyperplanes when $\mathbf{C}_1 = \dots = \mathbf{C}_M$ (see Figure 10.5). In the special case $\mathbf{C}_i = \sigma^2 \mathbf{I}$, $i = 1, \dots, M$, we obtain the minimum distance classifier (Duda et al., 2001). For hyperspectral imaging data with a large number of bands, we usually reduce the dimensionality at the input of the classifier using PCA without significant loss in performance. The general problem of feature extraction for classification applications is discussed by Webb and Copsey (2011).

The essential attribute of supervised classification is the availability and use of labeled data, called *training data*, to determine the boundaries between information classes in

the spectral space. Many approaches are available for supervised classification, ranging from those using probability distributions and hypothesis testing to determine decision surfaces to those which partition geometrically the spectral space into class-specific regions. However, irrespective of the approach used, the design and application of a supervised classifier includes the following steps:

1. Select the ground-cover classes (themes) into which to segment the image. This process is driven by the requirements of a specific application. It is possible to either overlook a class or intentionally exclude a class from consideration.
2. Determine a *training* area for each ground-cover class. This is a challenging task that requires the use of ground truth data, site visits, photo-interpretation by an experienced analyst, or unsupervised classification products. The analyst must select training sites that are spectrally representative of the land-cover classes of interest throughout the region to be classified. This property is known as geographic signature extension (Jensen, 2005).
3. Determine a *test* area for each ground-cover class. A key property of every classifier is how it performs on previously unseen data, a property known as *generalization* (Duda et al., 2001). To assess generalization, we compare the performance of the classifier for training and test data.
4. Use the pixels from each training area (training data) to estimate the class distributions (for example, mean and covariance) or to directly determine the discriminant functions. This step is known as “training the classifier.” In general, for data with p bands, a minimum of $10p$ pixels per class is required for the estimation of the covariance matrix.
5. Apply the trained classifier to the test data and evaluate its performance.
6. Use the trained classifier to assign labels to unseen pixels. Fundamental assumption: the unseen data have the same statistical properties with the training data.

Since the density of the normal distribution is defined for every value of the observation vector, every pixel with spectrum at any point in spectral space will be classified into one of the available classes, irrespective of how small the actual probabilities of class membership are. This situation, which arises if spectral classes have been overlooked or there are not sufficient training data, may lead to poor classification results. To avoid this problem, we require that for a class to be classified its class membership must exceed a minimum threshold. Then, the decision rule becomes

$$\mathbf{x} \in \mathcal{C}_i \quad \text{if} \quad g_i(\mathbf{x}) > g_j(\mathbf{x}) \text{ for all } j \neq i \quad (11.65)$$

$$\text{and } g_i(\mathbf{x}) > \eta_i, \quad (11.66)$$

where η_i is the threshold for the i th class (Landgrebe, 2003; Richards, 2013). The inclusion of a “reject” option, which allows avoiding a decision in close cases or when the evidence is not strong, is useful when the cost of indecision is small (Duda et al., 2001).

Table 11.1 summarizes the key differences between detection and classification. The best way to clarify the steps of a classification application is using a maximum likelihood classifier to classify a data set from an early multispectra data collection experiment (Landgrebe, 2003). The attributes that make this data set valuable for illustrating the

Table 11.1 Comparison of detection and classification.

	Detection	Classification
Theory	Binary hypothesis testing	M -ary hypothesis testing
Performance	ROC curves	Confusion matrices
Application	Search for rare targets	Generate thematic map for ground-cover classes
Prerequisites	Target signature	Training data for each class

key aspects of classification are the following: it has more than a few spectral bands (12 bands), it contains a significant number of ground-cover classes, sufficient training and test data for each class, and good ground truth. Furthermore, this data set has been analyzed by the group that collected the data and put together the ground truth using a well-tested software package (Biehl and Landgrebe, 2002).

In conclusion, we must emphasize that we cannot say that one classifier is always better than another (Richards, 2005a). In other words, no classification method is inherently superior to any other. Duda et al. (2001) provide some useful advice: “We should have a healthy skepticism regarding studies that purport to demonstrate the overall superiority of a particular learning or recognition algorithm.” The performance of a classifier depends on the data to be classified. If the distributions of the spectral classes are widely separated, most well-designed classifiers will have approximately the same performance. If we take into consideration that the labeling of the training and test data is determined with finite accuracy, we can safely conclude that the search for the “best classifier” is quite elusive. A discussion of sampling and quantitative procedures used to assess the performance of a classifier and the accuracy of a thematic map is given by Congalton and Green (2008). An interesting comparison of classifier performance results (Wilkinson, 2005) shows that, in general, performance had not “practically” improved despite the discovery and use of new algorithms and methodologies. Therefore, the use of a well-understood and properly implemented classifier is usually sufficient for practical applications. As is clearly illustrated by Adams and Gillespie (2006), the meaningful application of classification algorithms to actual practical problems can be more challenging than the understanding of the underlying mathematical theory.

11.4.2 Unsupervised Classification

As the name implies, *unsupervised classification* or *clustering* is done without any supervision or guidance from the analyst. This means that unsupervised classification algorithms do not require training data for the ground-cover classes. The user specifies the number of classes and the algorithm automatically organizes pixels with similar spectra, according to some similarity metric, into groups that become the basis for different classes. For tutorial purposes it is common to introduce clustering by means of simple diagrams with distinct clusters. However, this approach is misleading because actual hyperspectral data consist of messy overlapping clusters in the spectral space.

The primary aim of clustering algorithms is to group together pixels with similar spectra, using some criterion of spectral similarity, without paying particular attention to their probability distribution. In contrast, the primary aim of mixture density models is to estimate the probability density function of the data. The derived model can be used to cluster the data or to provide a model of the scene for other applications. More about unsupervised classification and clustering can be found in (Duda et al., 2001; McLachlan and Peel, 2000).

One of the most common clustering methods is the k -means algorithm, introduced in Section 7.7.3 as a special case of the EM algorithm. The k -means algorithm uses a Euclidean distance metric; however, we can easily modify the algorithm to use a spectral angle similarity metric. The ISODATA algorithm (Richards, 2013) is a common modification of the k -means algorithm and includes merging of clusters if their separation is below a threshold, and splitting of a single cluster into two clusters if it becomes too large. In contrast to supervised classification, the labeling of the clusters is a separate stage that follows the clustering procedure. Several clusters may correspond to a single land-cover type. Methods relating the results of clustering to real-world categories (information classes) are described by Lark (1995a,b).

11.5 Change Detection

Change detection using hyperspectral imaging data is useful in many civilian and military applications. The solution of the general change detection problem is challenging because of the difficulty to provide a mathematical definition for what constitutes the “change of interest”. A review of techniques for general image change detection is given by Radke et al. (2005). General change detection techniques for spectral remote sensing are discussed by Lu et al. (2004) and Sui et al. (2008).

In this section we consider a special class of change detection applications concerned with “small” and “rare” changes (Eismann et al., 2008; Theiler, 2008). The key attributes of these *anomaly change detection* problems are:

1. **Available data** Two hyperspectral images of the same scene, taken at different times and under different conditions. The data may or may not be registered. Two data sets are called registered if there is a one-to-one correspondence between pixels of the same location. Techniques for image registration are discussed in (Zitova and Flusser, 2003).
2. **Objective** Detect small objects that have been inserted, deleted, or moved between the two observations. Typically, such objects are too subtle relative to the background clutter to detect in a single image. Environmental changes, like radiance changes due to illumination, are of no interest.

The basic assumptions underlying the operation of hyperspectral change detection algorithms are: (a) the background clutter and environmental conditions in the two images are correlated; therefore, we can predict one from the other; (b) “small” and “rare changes” in one image constitute “new” information which cannot be predicted

from the other image. Therefore, a reasonable approach to change detection involves two steps: (a) Create a *residual* image by simultaneously “amplifying the differences” and “attenuating the similarities” in the two images; (b) use a detection algorithm to find changes in the residual image. We next discuss two approaches that are widely used to create residual images: linear prediction and canonical correlation analysis. The same detection algorithms can be used for both approaches.

11.5.1 Linear Prediction

A reasonable approach to change detection, based on linear prediction, is illustrated in Figure 11.29. The basic idea is that if one of the images is created from the other image by replacing a few pixels by man-made objects, the prediction error must be large at the location of the changes. Since the spectral composition of the changed pixels is unknown, the detector in Figure 11.29 is usually an anomaly detector.

Suppose that \mathbf{x} is a $p \times 1$ pixel spectrum in the first image and \mathbf{y} is a $q \times 1$ spectrum from the corresponding pixel in the second image. The mean vectors and the covariance matrices of the images, which can be arranged as

$$\mathbf{m} = \begin{bmatrix} \mathbf{m}_x \\ \mathbf{m}_y \end{bmatrix}, \quad \mathbf{C} = \text{cov} \left(\begin{bmatrix} \mathbf{x} \\ \mathbf{y} \end{bmatrix} \right) = \begin{bmatrix} \mathbf{C}_x & \mathbf{C}_{xy} \\ \mathbf{C}_{yx} & \mathbf{C}_y \end{bmatrix}, \quad (11.67)$$

are assumed known. For convenience, without any loss in generality, we assume that $\mathbf{m}_x = \mathbf{0}$ and $\mathbf{m}_y = \mathbf{0}$.

The linear predictor of \mathbf{y} based on \mathbf{x} is defined by a $p \times q$ matrix \mathbf{A} as follows:

$$\hat{\mathbf{y}} = \mathbf{A}^T \mathbf{x}. \quad (11.68)$$

The error or residual between the actual and estimated spectrum is given by

$$\mathbf{e} = \mathbf{y} - \hat{\mathbf{y}} = \mathbf{y} - \mathbf{A}^T \mathbf{x} \quad \text{or} \quad e_i = y_i - a_i^T \mathbf{x}, \quad i = 1, \dots, p. \quad (11.69)$$

The optimum linear predictor is obtained by minimizing the mean squared error (MSE) criterion

$$J = E(\mathbf{e}^T \mathbf{e}) = E(\|\mathbf{e}\|^2) = \sum_{i=1}^p E(e_i^2) = \sum_{i=1}^p \text{var}(e_i) = \text{tr}(\mathbf{C}_e), \quad (11.70)$$

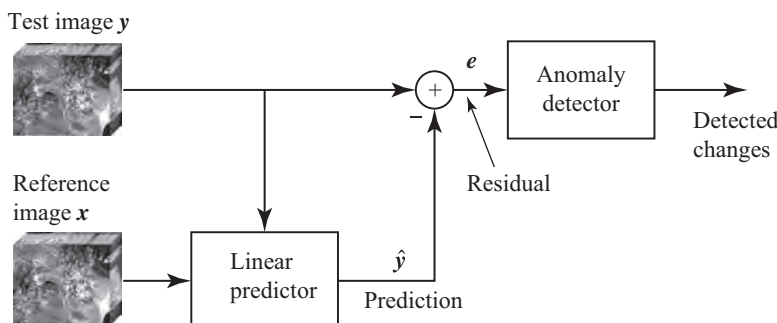


Figure 11.29 Change detection using linear prediction and anomaly detection.

where $\mathbf{C}_e = \text{cov}(\mathbf{e})$ is the covariance matrix of the error. This is a typical linear minimum MSE estimation problem (Levy, 2008; Kay, 1993), whose solution can be found by minimizing $\text{var}(e_i)$ for $i = 1, \dots, p$. From (11.69) and (11.70) we have

$$\text{var}(e_i) = \text{var}(y_i) - 2\mathbf{a}_i^T \mathbf{c}_{xy_i} + \mathbf{a}_i^T \mathbf{C}_x \mathbf{a}_i. \quad (11.71)$$

Completing the square by adding and subtracting the term $\mathbf{c}_{xy_i}^T \mathbf{C}_x^{-1} \mathbf{c}_{xy_i}$, yields

$$\text{var}(e_i) = \sigma_{y_i}^2 - \mathbf{c}_{xy_i}^T \mathbf{C}_x^{-1} \mathbf{c}_{xy_i} + (\mathbf{C}_x \mathbf{a}_i - \mathbf{c}_{xy_i})^T \mathbf{C}_x^{-1} (\mathbf{C}_x \mathbf{a}_i - \mathbf{c}_{xy_i}). \quad (11.72)$$

Since \mathbf{C}_x is positive definite, (11.72) attains its minimum if $\mathbf{C}_x \mathbf{a}_i = \mathbf{c}_{xy_i}$. Therefore, the optimum linear predictor and the attained minimum MSE are given by

$$\hat{\mathbf{y}} = \mathbf{A}^T \mathbf{x} = \mathbf{C}_x^{-1} \mathbf{C}_{yx} \mathbf{x} \quad (11.73)$$

$$J_{yx} = \text{tr}(\mathbf{C}_y - \mathbf{C}_{yx} \mathbf{C}_x^{-1} \mathbf{C}_{xy}). \quad (11.74)$$

The optimum predictor of \mathbf{x} from \mathbf{y} is obtained by simply interchanging the roles of \mathbf{x} and \mathbf{y} . This approach to change detection was first used by Schaum and Stocker (2003) under the name “chronochrome.”

11.5.2 Canonical Correlation Analysis

Consider now the generalized scheme shown in Figure 11.30, which uses a linear transformation for each image. The residual image is defined by

$$\mathbf{e} = \mathbf{v} - \mathbf{u} = \mathbf{B}^T \mathbf{y} - \mathbf{A}^T \mathbf{x}, \quad (11.75)$$

where \mathbf{A} is a $p \times r$ matrix, \mathbf{B} is a $q \times r$ matrix, and $r \leq \min(p, q)$. Minimization of MSE $J = E(\|\mathbf{e}\|^2)$ is meaningless without the use of constraints. Note that the constraint $\mathbf{B} = \mathbf{I}$ or $\mathbf{A} = \mathbf{I}$ results in an optimum linear predictor.

We shall present a specification of \mathbf{A} and \mathbf{B} using the method of canonical correlation analysis (CCA), which was introduced in Section 8.7. To this end, consider the random vectors defined by

$$\mathbf{u} = \mathbf{A}^T \mathbf{x}, \quad u_i = \mathbf{a}_i^T \mathbf{x}, \quad i = 1, \dots, r \quad (11.76)$$

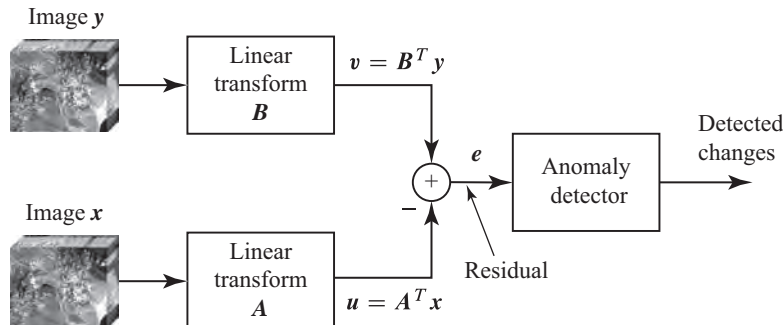


Figure 11.30 Generalized framework for change detection.

$$\mathbf{v} = \mathbf{B}^T \mathbf{y}, \quad v_i = \mathbf{b}_i^T \mathbf{y}, \quad i = 1, \dots, r. \quad (11.77)$$

The correlation coefficient between u_i and v_j is

$$\rho_{u_i v_j} = \frac{\text{cov}(u_i, v_j)}{\sqrt{\text{var}(u_i)} \sqrt{\text{var}(v_j)}} = \frac{\mathbf{a}_i^T \mathbf{C}_{xy} \mathbf{b}_j}{\sqrt{\mathbf{a}_i^T \mathbf{C}_x \mathbf{a}_i} \sqrt{\mathbf{b}_j^T \mathbf{C}_y \mathbf{b}_j}}. \quad (11.78)$$

The method of CCA seeks to maximize $\rho_i \triangleq \rho_{u_i v_i}$ among all linear combinations that are uncorrelated with the preceding variables $\{u_k, v_k, k = 1, \dots, i-1\}$. Note that maximization of (11.78) is equivalent to the following problem: find the maximum of $(\mathbf{a}_i^T \mathbf{C}_{xy} \mathbf{b}_i)^2$ subject to the constraints $\mathbf{a}_i^T \mathbf{C}_x \mathbf{a}_i = \mathbf{b}_i^T \mathbf{C}_y \mathbf{b}_i = 1$ and $\mathbf{a}_i^T \mathbf{C}_x \mathbf{a}_j = \mathbf{b}_i^T \mathbf{C}_y \mathbf{b}_j = 0$ for $j = 1, \dots, i-1$. The solution is determined by the left and right eigenvectors in the SVD of the coherence matrix

$$\tilde{\mathbf{C}}_{xy} \triangleq \mathbf{C}_x^{-1/2} \mathbf{C}_{xy} \mathbf{C}_y^{-1/2} = \mathbf{P} \mathbf{D} \mathbf{Q}^T, \quad (11.79)$$

where $\mathbf{P}^T \mathbf{P} = \mathbf{I}$, $\mathbf{Q}^T \mathbf{Q} = \mathbf{I}$, and $\mathbf{D} = \text{diag}(\rho_1, \dots, \rho_r, 0, \dots, 0)$ are the nonzero singular values of $\tilde{\mathbf{C}}_{xy}$. The optimum matrices are given by

$$\mathbf{A} = \mathbf{C}_x^{-1/2} \mathbf{P}, \quad \mathbf{B} = \mathbf{C}_y^{-1/2} \mathbf{Q}. \quad (11.80)$$

The variables $u_i, v_i, i = 1, \dots, r$ are known as canonical variables; the coefficients ρ_i arranged as $\rho_1^2 \geq \rho_2^2 \dots \rho_r^2 \geq 0$ are called canonical correlations.

The use of CCA matrices (11.80) in the system of Figure 11.30 yields

$$J_{\text{cca}} = E(\|\mathbf{e}\|^2) = 2r - 2(\rho_1 + \dots + \rho_r), \quad (11.81)$$

which follows from the minimization of $J = E(\|\mathbf{e}\|^2)$ subject to the constraints $\mathbf{A}^T \mathbf{C}_x \mathbf{A} = \mathbf{I}$ and $\mathbf{B}^T \mathbf{C}_y \mathbf{B} = \mathbf{I}$ (Brillinger, 2001).

However, if we only enforce the constraint $\mathbf{B}^T \mathbf{C}_y \mathbf{B} = \mathbf{I}$, we have (Rao, 1979)

$$\mathbf{A} = \mathbf{D}^T \mathbf{C}_x^{-1/2} \mathbf{P}, \quad \mathbf{B} = \mathbf{C}_y^{-1/2} \mathbf{Q}. \quad (11.82)$$

This ‘‘modified’’ CCA transformation results in a minimum MSE given by

$$J_{\text{mcca}} = r - (\rho_1^2 + \dots + \rho_r^2). \quad (11.83)$$

Note that relaxing the unit variance constraint $\mathbf{A}^T \mathbf{C}_x \mathbf{A} = \mathbf{I}$ results in a smaller MSE compared to the CCA.

Consider now the CCA problem with modified constraints. Suppose we wish to maximize $(\mathbf{a}_i^T \mathbf{C}_{xy} \mathbf{b}_i)^2$ subject to the constraints $\mathbf{a}_i^T \mathbf{a}_i = \mathbf{b}_i^T \mathbf{b}_i = 1$ and $\mathbf{a}_i^T \mathbf{a}_j = \mathbf{b}_i^T \mathbf{b}_j = 0$ for $j = 1, \dots, i-1$. The solution of this problem is determined by the left and right eigenvectors in the SVD of \mathbf{C}_{xy} . Therefore, given the SVD

$$\mathbf{C}_{xy} = \mathbf{P}_0 \mathbf{D}_0 \mathbf{Q}_0^T \quad (11.84)$$

we obtain the following transformation matrices:

$$\mathbf{A} = \mathbf{P}_0, \quad \mathbf{B} = \mathbf{Q}_0. \quad (11.85)$$

Table 11.2 Summary of change detection algorithms.

Method	\mathbf{A}	\mathbf{B}	Required quantities
Linear Prediction	\mathbf{I}	$\mathbf{C}_{yx}\mathbf{C}_y^{-1}$	$\mathbf{C}_x, \mathbf{C}_y, \mathbf{C}_{xy}$
Linear Prediction	$\mathbf{C}_{xy}\mathbf{C}_x^{-1}$	\mathbf{I}	$\mathbf{C}_x, \mathbf{C}_y, \mathbf{C}_{xy}$
CCA	$\mathbf{C}_x^{-1/2}\mathbf{P}$	$\mathbf{C}_y^{-1/2}\mathbf{Q}$	$\tilde{\mathbf{C}}_{xy} = \mathbf{P}\mathbf{D}\mathbf{Q}^T$
Modified CCA	$\mathbf{D}\mathbf{C}_x^{-1/2}\mathbf{P}$	$\mathbf{C}_y^{-1/2}\mathbf{Q}$	$\tilde{\mathbf{C}}_{xy} = \mathbf{P}\mathbf{D}\mathbf{Q}^T$
SVD	\mathbf{P}_0	\mathbf{Q}_0	$\mathbf{C}_{xy} = \mathbf{P}_0\mathbf{D}_0\mathbf{Q}_0^T$
Whitening	$\mathbf{C}_x^{-1/2}$	$\mathbf{C}_y^{-1/2}$	$\mathbf{C}_x, \mathbf{C}_y$

The resulting minimum MSE is given by

$$J_{\text{svd}} = \sum_{i=1}^r [\text{var}(u_i) + \text{var}(v_i) - 2d_i], \quad (11.86)$$

where $\mathbf{u} = \mathbf{P}_0^T \mathbf{x}$, $\mathbf{v} = \mathbf{Q}_0^T \mathbf{y}$, and d_i are the singular values of \mathbf{C}_{xy} . This approach is also known as *canonical covariance analysis* (Cherry, 1996).

11.5.3 Practical Considerations

The linear transformations used to derive the “change-enhanced” image are summarized in Table 11.2. We note that their implementation requires the matrix \mathbf{C}_{xy} , whose computation is meaningful only if the two data sets are registered with sufficient accuracy. If the images are not well registered, the estimate of \mathbf{C}_{xy} is practically unusable for change detection applications. When \mathbf{C}_{xy} is unavailable, we can use the whitening transformation

$$\mathbf{A} = \mathbf{C}_x^{-1/2}, \quad \mathbf{B} = \mathbf{C}_y^{-1/2}, \quad (11.87)$$

which follows from (11.80) after dropping the orthogonal matrices (rotation factors) \mathbf{P} and \mathbf{Q} . This heuristic approach to change detection was introduced by Schaum and Stocker (2003) under the name “covariance equalization”; we have adopted the term “whitening”, which provides a better description of the operation.

The “change-enhanced” images must subsequently be processed by an anomaly detection algorithm. The most widely used approach is to use the Mahalanobis distance

$$d_1 = \mathbf{e}^T \mathbf{C}_e^{-1} \mathbf{e}, \quad \mathbf{e} = \mathbf{v} - \mathbf{u} \quad (11.88)$$

where $\mathbf{C}_e = \text{cov}(\mathbf{e})$ is the covariance matrix of the error image.

Another approach is to apply anomaly detection on the concatenated or stacked image (Theiler et al., 2010):

$$\mathbf{w} \triangleq \begin{bmatrix} \mathbf{u} \\ \mathbf{v} \end{bmatrix}, \quad \mathbf{C}_w = \begin{bmatrix} \mathbf{C}_u & \mathbf{C}_{uv} \\ \mathbf{C}_{vu} & \mathbf{C}_v \end{bmatrix}, \quad (11.89)$$

where $\mathbf{C}_w \triangleq \text{cov}(\mathbf{w})$. An anomaly detector using the Mahalanobis distance of the stacked image is given by

$$d_2 = \mathbf{w}^T \mathbf{C}_w^{-1} \mathbf{w}. \quad (11.90)$$

The hyperbolic anomalous change detector, developed by (Theiler et al., 2010) using a likelihood ratio approach, is given by

$$d_3 = \mathbf{w}^T \mathbf{C}_w^{-1} \mathbf{w} - \mathbf{u}^T \mathbf{C}_u^{-1} \mathbf{u} - \mathbf{v}^T \mathbf{C}_v^{-1} \mathbf{v}. \quad (11.91)$$

This approach can be generalized to deal with elliptically contoured distributions.

Application of change detection algorithms involves many practical details and challenges which are beyond the scope of this book. A limited comparison of several algorithms discussed in this section, using real data, is provided by Pieper et al. (2015).

11.6

Unique Aspects of Spectral Exploitation in the Thermal Infrared

As we have already mentioned in Chapter 6, hyperspectral remote sensing in the thermal infrared (TIR) is not as mature as in the reflective infrared. The purpose of this section is to present some basic results and review some current work in this area. The following discussion builds upon the material presented in Section 6.7, which is essential for a deeper understanding of the challenges in the TIR.

The basic radiance signal model in the TIR, for the geometry shown in Figure 11.31, is described by the following formulas

$$L_g(\lambda) = \epsilon(\lambda)B(\lambda, T_g) + [1 - \epsilon(\lambda)]L_d(\lambda) \quad (11.92)$$

$$L_m(\lambda) = \tau_a(\lambda)L_g(\lambda) + L_u(\lambda), \quad (11.93)$$

where $L_g(\lambda)$ is the total ground-leaving radiance, $\epsilon(\lambda)$ is the surface emissivity, $B(\lambda, T_g)$ is the Plank function at the surface temperature, $L_d(\lambda)$ is the downwelling or down-emitted radiance, $L_m(\lambda)$ is the at-aperture radiance measured by the sensor, $\tau_a(\lambda)$ is the atmospheric transmission function, and $L_u(\lambda)$ is the upwelling or path radiance. The

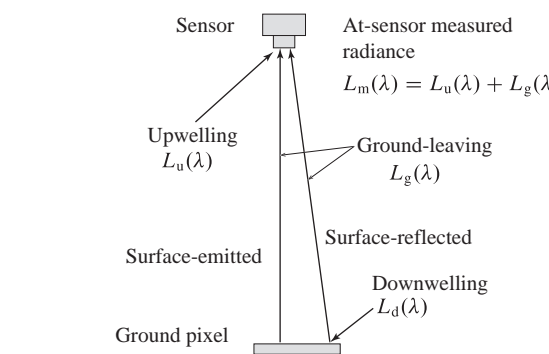


Figure 11.31 Components of the at-sensor radiance at the thermal infrared.

slight change in notation, compared to Chapter 6, has been made to comply with the notation used in the data exploitation literature.

Since the information-bearing signal about the imaged surface is the emissivity function, we need to retrieve $\epsilon(\lambda)$ from $L_m(\lambda)$. This is typically done in two steps:

1. *Atmospheric Compensation (AC)*. The objective of this process is to retrieve the ground-leaving radiance. Solving (11.93) for $L_g(\lambda)$ we obtain

$$L_g(\lambda) = \frac{L_m(\lambda) - L_u(\lambda)}{\tau_a(\lambda)}, \quad (11.94)$$

which shows that we need to estimate the atmospheric transmission function and the upwelling radiance of the atmosphere.

2. *Temperature–Emissivity Separation (TES)*. Solving (11.92) for $\epsilon(\lambda)$ yields

$$\epsilon(\lambda) = \frac{L_g(\lambda) - L_d(\lambda)}{B(\lambda, T_g) - L_d(\lambda)}, \quad (11.95)$$

which shows that TES requires estimates of the ground-leaving radiance, the surface temperature, and the downwelling radiance.

To proceed with AC we note that, for each spectral band, say $\lambda = \lambda_k$, equation (11.93) expresses an affine ($y = ax + b$) relationship between $L_m(\lambda)$ and $L_g(\lambda)$ with slope $\tau_a(\lambda)$ and intercept $L_u(\lambda)$. Therefore, if we knew $L_g(\lambda)$ for a set of pixels, we could determine the atmospheric parameters using the method of linear regression (Montgomery et al., 2012). To find such a set of pixels, we start by noticing that if $\epsilon(\lambda) \simeq 1$, then (11.92) becomes

$$L_g(\lambda) \simeq B(\lambda, T_g), \quad \text{if } \epsilon(\lambda) \simeq 1. \quad (11.96)$$

We note that the ground-leaving radiance for these pixels corresponds to a blackbody with temperature T_g . For such blackbody pixels we have the approximation

$$L_m(\lambda) \simeq \tau_a(\lambda)B(\lambda, T_g) + L_u(\lambda), \quad \text{if } \epsilon(\lambda) \simeq 1. \quad (11.97)$$

To proceed we need to determine the temperature T_g for each blackbody pixel. To this end, suppose that we find a “clear” spectral band $\lambda = \lambda_0$ such that $\tau_a(\lambda_0) \simeq 1$ and $L_u(\lambda_0) \simeq 0$. In this case (11.97) results in $L_m(\lambda_0) \simeq B(\lambda_0, T_g)$, which can be inverted to estimate the surface temperature as

$$\hat{T}_g = B^{-1}(\lambda_0, L_m(\lambda_0)). \quad (11.98)$$

To determine the “atmospherically clear” spectral band λ_0 we look at Figure 11.32, which provides graphs of $\tau_a(\lambda)$ and $L_u(\lambda)$ as a function of wavelength. Careful inspection of these graphs shows that we can choose λ_0 as the spectral band close to $\lambda \approx 10\mu\text{m}$; however, other approaches are possible.

As a result of these ideas an AC algorithm involves the following key steps:

1. Find the blackbody pixels in the data cube;
2. Estimate T_g for each pixel using (11.98);
3. Use linear regression to estimate the slope $\tau_a(\lambda_k)$ and the intercept $L_u(\lambda_k)$ for each spectral band λ_k , $k = 1, \dots, N_b$.

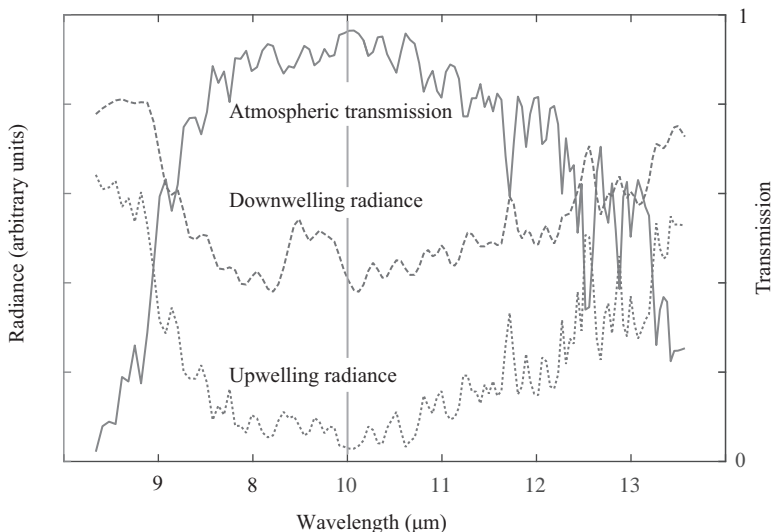


Figure 11.32 Atmospheric transmission, upwelling or path radiance, and downwelling radiance as a function of wavelength.

Clearly, the most challenging task is how to determine the blackbody pixels. The well-known ISAC algorithm, discussed in Section 6.7, determines the blackbody pixels by iteratively removing the pixels below the fitted regression line (see Figure 6.29). A detailed description of the ISAC approach is given by Young et al. (2002). In practice, because the analyst probably knows something about the scene or can make quality assumptions, the plight is not hopeless. As in the reflective domain, vegetation, water or a known material (e.g., asphalt or gypsum) can provide a foundation to initiate analysis. Vegetation and water are excellent blackbodies (very high emissivity) in the LWIR from which both temperature and atmospheric conditions can be reasonably extracted. If the sensor is well calibrated, as discussed in Chapter 5, the small spectral features of other unknown materials can then be identified.

If we wish to retrieve the emissivity using (11.95), we need to know the downwelling radiance. In the case of data with high emissivities, the downwelling radiance can be neglected from (11.95). Then, the emissivity can be retrieved by

$$\epsilon(\lambda_k) \simeq \frac{L_g(\lambda_k)}{B(\lambda_k, T_g)} = \frac{L_m(\lambda_k) - L_u(\lambda_k)}{B(\lambda_k, T_g) \tau_a(\lambda_k)}. \quad (11.99)$$

However, quite often the contribution of downwelling radiance is significant and the approximation (11.99) yields unacceptable results.

The problem with emissivity retrieval is that we cannot determine both the emissivity and the temperature by means of radiance measurements alone. We cannot use N_b spectral band radiance measurements to unambiguously determine N_b spectral emissivities and a temperature. To deal with this underdetermined problem, we must either find an extra equation or reduce the number of the unknowns.

The most widely used approaches for TES reduce the number of unknowns by exploiting the following common observation: the thermal infrared spectra of solids are much more smoother than the thermal infrared spectra of gases. The Automatic Retrieval of Temperature and Emissivity using Spectral Smoothness (ARTEMISS) algorithm (Borel, 2008) uses a spectral smoothness criterion to reduce the number of unknowns. In contrast, the method proposed by Wang et al. (2011) divides the LWIR range into M segments and uses a linear model $\epsilon(\lambda) = a\lambda + b$ to describe the emissivity at each segment. As a result we have $2M + 1$ unknowns and N equations. If $2M + 1 < N$, we have an overdetermined system of linear equations that can be solved using the method of least squares. TES is a challenging problem, and reliable algorithms for its solutions are still an active area of research.

The signal exploitation algorithms are the same in the reflective and emissive regions of the spectrum. However, the interactions of radiation with the environment are different so that the spectral variability of background clutter and the spectral separability between targets and clutter will be different for the two regimes of the spectrum. Target detection in the thermal infrared has not been studied and understood as well as similar techniques in the reflective region. Variations in the radiance in the thermal infrared are due largely to variations in temperature. Quantitative investigations of these attributes are not available in the literature; however, some qualitative discussions are available (Vaughan et al., 2003).

In Chapter 9 we discussed spectral mixture analysis in the reflective region of the spectrum. We mostly focused on linear mixtures and we provided algorithms for end-member identification and fill-fraction estimation. Spectral mixing in TIR hyperspectral images is more complicated because various scene components have different temperatures and the relationship between radiance and temperature is nonlinear. A useful simplification is to assume that the scene within the pixel is isothermal and that the mixing is linear (Gillespie, 1992). If we convert the data into emissivity, we avoid the problem of temperature variability, and we can use the techniques developed for unmixing the reflective domain. The key differences are that (a) the “shade” endmember must be replaced by the “virtual cold” endmember and (b) the fill-fraction estimation accuracy is worse in the TIR because of the temperature variability at the subpixel scale (Adams and Gillespie, 2006; Ramsey and Christensen, 1998).

It is important to pursue this challenging analysis with great caution, as many physical effects can be in play. An example of this is the small but important reflection of down welling radiation. Materials which have an appreciable reflectance (low emissivity) in the thermal infrared will exhibit significantly different upwelling radiance in the presence of clouds than under a clear sky because clouds provide substantial downwelling radiance in the infrared. This is especially true in the mid-wave IR where most materials have emissivity between 0.5 and 1.0. The LWIR materials can also be confused because, although the reflectivity is typically lower (emissivity is between 0.9 and 1.0), the downwelling radiance from clouds in the LWIR is significantly greater than in the MWIR. Many of the techniques of analysis from the reflective domains can be employed, but the physics of the scene collected can be less intuitive than analysis in the solar reflective domains.

11.7 Remote Sensing of Chemical Clouds: Physics

In this and the next section we discuss the use of hyperspectral imaging to detect and characterize chemical clouds. The three main tasks of gas-phase remote sensing are: detection of a plume, identification of its constituent gases, and quantification of the amounts present. The list of applications of standoff hyperspectral imaging for chemical gas sensing is long and growing. The major areas of application include environmental monitoring, emergency response, chemical warfare threat mitigation, and earth sciences. Figure 11.33 shows three typical geometries for standoff detection of chemical clouds. In early warning applications the imaging spectrometer collects data cubes at regular intervals of time, producing a “hyperspectral video” stream. In other applications, the sensor usually produces data cubes of the imaged scene on demand.

It turns out that the longwave infrared (LWIR) spectral region, which extends from 8 to $13\mu\text{m}$, is well suited for gas detection applications for two reasons:

- A wide range of chemical compounds have unique identifying spectral signatures in the LWIR region. This is illustrated in Figure 11.34, which shows the spectral signature of ammonia.
- The atmosphere is relatively transparent within the LWIR window. This is also illustrated in Figure 11.34, which shows the atmospheric transmittance as a function of wavelength.

In this section we provide an introduction to the radiance phenomenology that drives the models on which exploitation algorithms are based. In the next section we identify the fundamental aspects of the data-exploitation problem, develop algorithms that

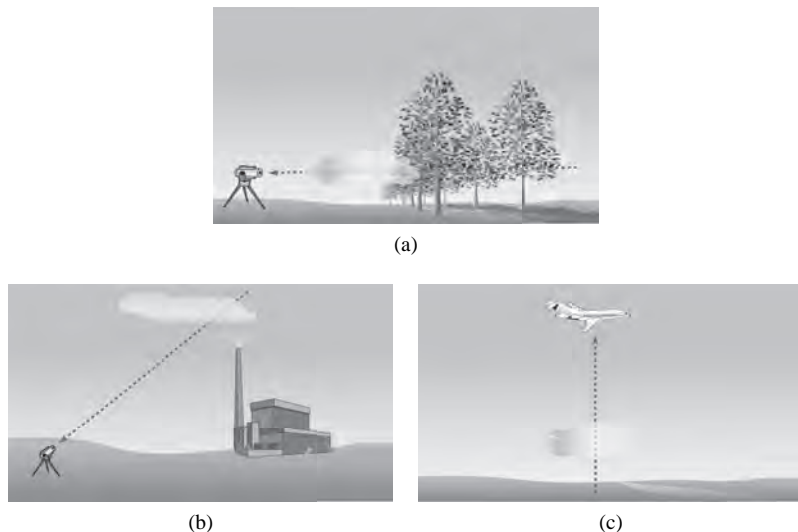


Figure 11.33 Three imaging geometries for standoff detection of chemical clouds: (a) Slant path, side looking; (b) slant path, up looking; (c) down looking.

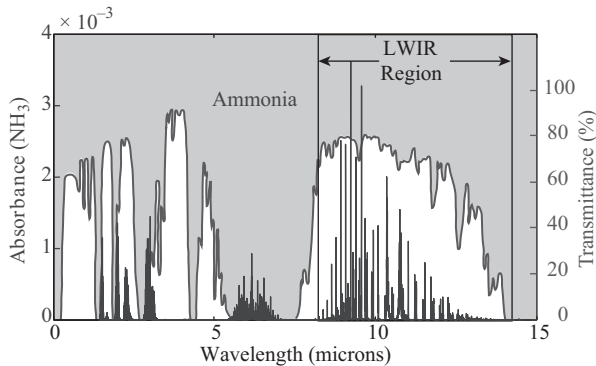


Figure 11.34 A wide range of chemical compounds, like ammonia, have unique identifying spectral signatures in the LWIR region ($8-13\mu\text{m}$). The atmospheric transmittance function shows the presence of an atmospheric window in the LWIR from 8 to $13\mu\text{m}$.

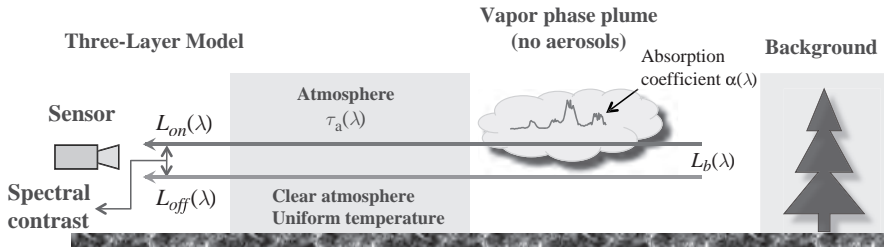


Figure 11.35 Pictorial representation of a three-layer side-looking radiative transfer radiance signal model for standoff chemical agent detection.

can successfully exploit data from many different sensors, and discuss some challenges related to their practical application. A detailed tutorial review of the area of chemical cloud sensing is provided by Manolakis et al. (2014b).

11.7.1 The Three-Layer Radiance Model

The radiance reaching the detector can often be well modeled using radiative transfer theory with three parallel atmospheric layers orthogonal to the line of sight of the sensor. The first layer extends from behind the plume to the background; the second layer is the plume itself; and the third layer is the atmosphere between the plume and the sensor. Each layer attenuates the radiation that passes through it as well as emitting radiation on the basis of its own content and temperature. This is illustrated in Figure 11.35 for a standoff sensor with horizontal line of sight.

Several simplifying assumptions are made to arrive at usable expressions for the at-sensor radiance in the presence and absence of the chemical plume.

- The atmosphere and plume are assumed free of aerosols and particulate matter, so that scattering may be neglected throughout;

- The plume and atmosphere are assumed homogeneous in both temperature and composition;
- The thickness of the plume layer, and the distance between the plume and background, are assumed small so that atmospheric transmittance can be neglected in those layers;
- Reflections off the background of both plume and downwelling atmospheric radiance are neglected.

With these assumptions, the at-sensor radiance in the absence of plume, as a function of wavelength, is given by radiative transfer theory (Goody and Yung, 1995) to be

$$L_{\text{off}}(\lambda) = L_a(\lambda) + \tau_a(\lambda)L_b(\lambda), \quad (11.100)$$

where $L_a(\lambda)$ represents atmospheric path radiance and the second term is the contribution of background radiance $L_b(\lambda)$ modulated by the atmospheric transmittance $\tau_1(\lambda)$. When the atmosphere is homogeneous, as the three-layer model assumes, the path radiance is given by

$$L_a(\lambda) = [1 - \tau_a(\lambda)]B(\lambda, T_a), \quad (11.101)$$

where T_a is the temperature of the atmosphere and $B(\lambda, T)$ is the Planck function evaluated at wavelength λ and temperature T , defined by

$$B(\lambda, T) = \frac{2hc^2}{\lambda^5} \frac{1}{e^{\frac{hc}{\lambda kT}} - 1}, \quad (11.102)$$

where h and k denote the Planck and Boltzmann constants, respectively, and c is the speed of light.

The presence of a plume has two effects: it absorbs part of the radiation emitted by the background, and it emits its own radiation. The resulting radiance is subsequently attenuated by transmission through the atmosphere, and is given by

$$L_{\text{on}}(\lambda) = L_a(\lambda) + \tau_a(\lambda)\tau_p(\lambda)L_b(\lambda) + \tau_a(\lambda)[1 - \tau_p(\lambda)]B(\lambda, T_p), \quad (11.103)$$

where $\tau_p(\lambda)$ is the plume transmittance and T_p its temperature. In (11.103), the three terms represent the at-sensor radiance due to the atmosphere, the background radiance as modulated by the plume and atmosphere, and the plume radiance as modulated by the atmosphere.

The spectral transmittance function, $\tau_p(\lambda)$, of a plume with N_G gas species can be modeled using Beer's law:

$$\tau_p(\lambda) = \exp \left[- \sum_{m=1}^{N_G} \gamma_m \alpha_m(\lambda) \right]. \quad (11.104)$$

The function $\alpha_m(\lambda)$, which is known as the *absorption coefficient spectrum*, is unique for each gaseous chemical and can be used as a spectral fingerprint. The quantity γ_m , which is called the *concentration pathlength*, is the product of two terms: the length ℓ along the sensor boresight that represents the depth of the cloud, and the average concentration C_m along that path. Figure 11.36 shows examples of spectra with and without plume

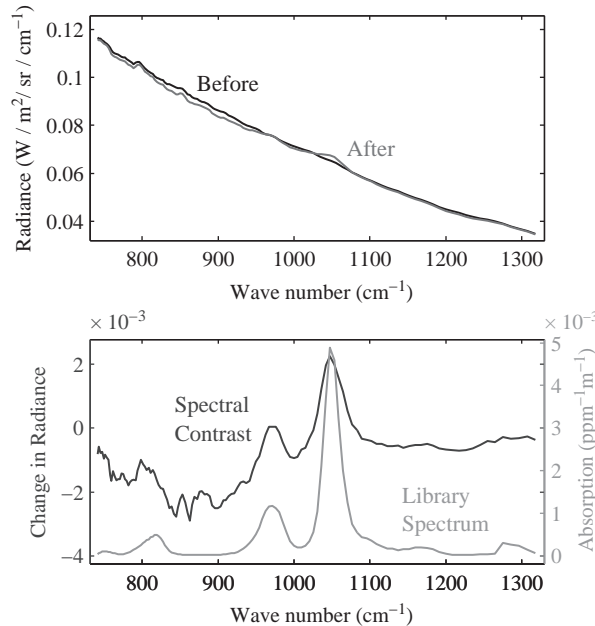


Figure 11.36 (a) Radiance spectra of the same pixel before and after the appearance of a TEP plume. (b) Plots of radiance spectral contrast $L_{\text{on}}(\lambda) - L_{\text{off}}(\lambda)$ and the absorption-coefficient library spectrum of TEP. (Notice the different units used for radiance and absorption.)

collected with a hyperspectral imaging spectrometer. The spectral contrast $L_{\text{on}}(\lambda) - L_{\text{off}}(\lambda)$ is shown on the same plot with the absorption coefficient spectrum $\alpha_m(\lambda)$ of TEP (TriEthylPhosphate), which is the released chemical agent. Notice how the presence of the chemical agent modifies the radiance spectrum of the background; this is precisely the information used by data exploitation algorithms to detect and identify chemical agents.

Another quantity used in the literature (Beil et al., 1998) is the *brightness temperature* T_B associated with a radiance $L(\lambda)$. This quantity, which is obtained by inverting the Planck function (11.102), is given by

$$T_B(\lambda, L(\lambda)) = \frac{hc}{\lambda k} \frac{1}{\ln \left(1 + \frac{2hc^2}{\lambda^5 L(\lambda)} \right)}. \quad (11.105)$$

The brightness temperature is, by definition, constant for a blackbody radiance distribution. Its utility for hyperspectral analysis in the LWIR window is that most background surfaces have emissivities very close to unity, meaning that their associated radiances are very close to those of blackbodies at the surface temperatures. Graphs of the brightness temperature as a function of wavelength will therefore not exhibit the slowly varying trends due to the structure of the Planck function, and subtle variations in radiance are much more visible than in graphs of the radiance itself. Figure 11.37 compares the same spectrum plotted as radiance or brightness temperature as a function of wave number

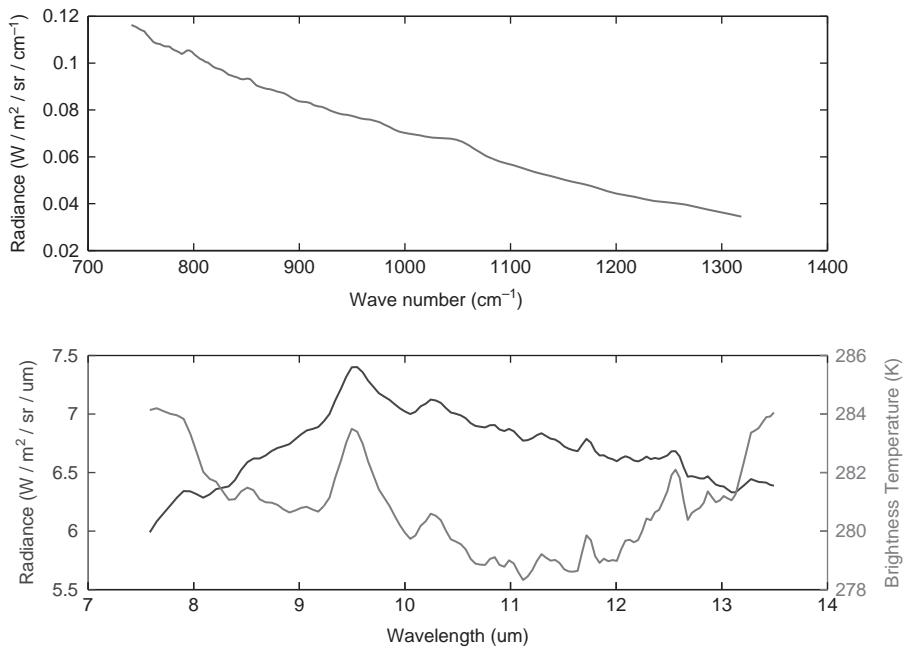


Figure 11.37 Illustration of how the same radiance spectrum changes shape dependent on the units used to express radiance and frequency; it should be stressed that all plots convey the same information.

or wavelength. To simplify the exposition, we will typically plot spectra as a function of wave number; however, plotting or processing spectra as a function of wavelength would lead to similar results.

11.7.2 Equivalent Radiance Signal Models

The form of the radiance expressions (11.100) and (11.103) elucidate the physical origins of the various contributions, but are not the most convenient for further analysis. We next present three alternate, mathematically equivalent, forms that are adapted for specific applications.

Atmospherically compensated form

If we collect all terms of (11.103) involving $\tau_a(\lambda)$ on the left-hand side we have

$$\frac{L_{on}(\lambda) - L_a(\lambda)}{\tau_a(\lambda)} = B(\lambda, T_p) - \tau_p(\lambda) (B(\lambda, T_p) - L_b(\lambda)). \quad (11.106)$$

We note that all dependence on the atmosphere is isolated on the left-hand side, while the right-hand side depends only on the plume and background properties. The atmospheric transmission parameters $\tau_a(\lambda)$ and $L_a(\lambda)$ are sometimes estimated separately, as discussed in Section 6.7, resulting in an estimate of the left-hand side of (11.106). The absence of atmospheric transmittance on the right-hand side of (11.106) can be exploited by some signal processing algorithms, as we will discuss later.

Plume embedding form

A second useful form is obtained by combining (11.100) with (11.103). The result is

$$L_{\text{on}}(\lambda) = L_{\text{off}}(\lambda) + [1 - \tau_p(\lambda)] \times \left\{ (B(\lambda, T_a) - L_{\text{off}}(\lambda) + \tau_a(\lambda)[B(\lambda, T_p) - B(\lambda, T_a)]) \right\}. \quad (11.107)$$

Here, the background radiance $L_b(\lambda)$ appears only implicitly through its contribution to $L_{\text{off}}(\lambda)$. The advantage of this form is for use in simulating the radiance of a plume given only measurements of the off-plume radiance. It is especially useful if the plume and atmospheric temperatures are equal, for then only the atmospheric temperature and plume transmittance are required to perform the embedding; the term containing $\tau_a(\lambda)$ vanishes.

Signal processing form

By expanding the off-plume radiance that multiplies the plume emissivity in (11.107), a third equivalent radiance expression is obtained, given by

$$L_{\text{on}}(\lambda) = \tau_a(\lambda)(1 - \tau_p(\lambda))(B(\lambda, T_p) - L_b(\lambda)) + L_{\text{off}}(\lambda). \quad (11.108)$$

This form, which is the starting point for most detection algorithms, expresses the effect of a plume as a contrast between the on- and off-plume radiance. Also, it highlights the *physical requirements for plume detection*: each of the terms in the product on the right-hand side of (11.108) must be nonzero. Due to their importance, we enumerate these plume visibility conditions as

1. $\tau_a(\lambda) > 0$; that is, the atmosphere must be not opaque,
2. $\tau_p(\lambda) < 1$; that is, the plume must be not transparent; and
3. $B(\lambda, T_p) - L_b(\lambda) \neq 0$; that is, there must be nonzero contrast between plume blackbody and background radiance.

In summary, *plume detection is possible only if there is contrast between the plume blackbody and background radiance for at least some spectral channels*.

Plume Radiance Phenomenology

A chemical plume that is present in a scene need not contribute to the at-sensor radiance, and when it does, it may be either in *emission* or *absorption*. A chemical is said to be visible in emission when its signature appears as peaks that lie above the radiance that would be present in the absence of the plume, while in the case of absorption the signature appears as valleys. We have already discussed necessary conditions for the plume to be visible at a given wavelength λ ; we now elaborate on the role of the *temperature–emissivity contrast* defined as

$$L_{\text{TEC}}(T_p, T_b, \lambda) = B(\lambda, T_p) - \epsilon_b(\lambda)B(\lambda, T_b). \quad (11.109)$$

The role that $L_{\text{TEC}}(T_p, T_b, \lambda)$ plays can be seen either from the optically thin plume approximation (11.112) or from the general, nonlinear Beer's law case (11.106). If the

plume and background have the same temperature, and the background is a true black-body ($\epsilon_b(\lambda) = 1$), then $L_{\text{TEC}}(T_p, T_b, \lambda) = 0$ and the plume is invisible at all wavelengths; it emits exactly as much thermal radiation as it absorbs from the background. In the realistic case of $\epsilon_b(\lambda) < 1$, still with $T_p = T_b$, we see that $L_{\text{TEC}}(T_p, T_b, \lambda)$ is strictly positive. In this case, the plume emits more thermal radiation than it absorbs from the background, and the characteristic plume features are visible in emission, as structure that lies above the background radiance. When $T_p > T_b$, the plume signal is again visible in emission, stronger than in the equal temperature case. When $T_p < T_b$ the contrast $L_{\text{TEC}}(T_p, T_b, \lambda)$ may be positive, negative, or zero, at different values of λ . When it is positive the plume is, again, visible in emission. When it is negative, the plume is visible in absorption, meaning that as the background radiance propagates through the plume more thermal radiation is absorbed than emitted, so the plume signature appears as troughs in the at-sensor radiance. At those wavelengths at which the contrast vanishes, the plume is completely invisible to the sensor. The behavior of background radiance, which plays an important role in plume detection, is discussed in Section 11.8.

11.7.3 Special Cases of Practical Interest

Expressions (11.108) and (11.104) represent the on-plume at-sensor radiance as a nonlinear function of the parameters that characterize the plume, atmosphere, and background. For some tasks these equations are of direct utility. However, there are many situations in which simplifying assumptions are both valid and advantageous in terms of algorithmic complexity and intuition. We next describe some of these special cases that are useful in different practical applications.

Linear signal exploitation model

We start with three approximations which, under a wide range of situations, lead to a powerful linear signal model.

Optically thin plume approximation

Many applications call for maximum sensitivity to very weak plumes. A plume is considered optically thin if

$$\sum_{m=1}^{N_G} \gamma_m \alpha_m(\lambda) \ll 1 \text{ for each } \lambda. \quad (11.110)$$

In such cases, Beer's law (11.104) may be linearized by using the first term of Taylor's expansion. The result is

$$1 - \tau_p(\lambda) \approx \sum_{m=1}^{N_G} \gamma_m \alpha_m(\lambda). \quad (11.111)$$

Then, the signal model (11.108) becomes

$$L_{\text{on}}(\lambda) = L_{\text{off}}(\lambda) + \sum_{m=1}^{N_G} \gamma_m \beta_m(\lambda), \quad (11.112)$$

where the quantity

$$\beta_m(\lambda) = \tau_a(\lambda)[B(\lambda, T_p) - L_b(\lambda)]\alpha_m(\lambda) \quad (11.113)$$

is known as the “in-scene target signature” for optically thin plumes. We note that the model (11.112) is linear in the gas concentration pathlengths γ_m .

Flat background emissivity approximation

The background radiance $L_b(\lambda)$ may be expressed as

$$L_b(\lambda) = \epsilon_b(\lambda)B(\lambda, T_b), \quad (11.114)$$

where $\epsilon_b(\lambda)$ is the background emissivity and T_b its temperature. Many background emissivity functions lack sharp spectral features, unlike most chemical plumes, leading to the “flat emissivity” approximation, $\epsilon_b(\lambda) \approx 1$. This approximation does not hold for plumes comprised of larger molecules having broad, featureless spectra (Foy, 2002). Under this approximation (11.113) becomes

$$\beta_m(\lambda) \approx \tau_a(\lambda)[B(\lambda, T_p) - B(\lambda, T_b)]\alpha_m(\lambda). \quad (11.115)$$

Linear Planck function approximation

When $|T_p - T_b|$ is small, typically less than 5°K, the Planck function may be linearized in the thermal contrast term. Furthermore, the wavelength dependence of this difference is weak over the LWIR window, leading to the approximation

$$B(\lambda, T_p) - B(\lambda, T_b) \approx C_B \Delta T, \quad (11.116)$$

where

$$C_B = \left. \frac{\partial B(\lambda, T)}{\partial T} \right|_{\substack{T=T_b \\ \lambda=\lambda_0}}, \quad (11.117)$$

and λ_0 is a reference wavelength chosen in the middle of the band. With these definitions, (11.113) becomes

$$\beta_m(\lambda) \approx C_B \Delta T \tau_a(\lambda) \alpha_m(\lambda). \quad (11.118)$$

Taking into consideration all three approximations, the at-sensor radiance signal model (11.108) becomes

$$L_{\text{on}}(\lambda) = \sum_{m=1}^{N_G} (C_B \Delta T \gamma_m) \tau_a(\lambda) \alpha_m(\lambda) + L_{\text{off}}(\lambda), \quad (11.119)$$

where C_B is a constant independent of wavelength and temperature. This “signal-plus-clutter” model provides the basis for most detection, identification, and quantification algorithms used in practical applications.

Plume-Atmosphere Thermal Equilibrium

We noted above that when the plume and atmosphere have the same temperature the plume embedding equation (11.107) takes a particularly simple form. An additional simplification that occurs in this situation is that the at-sensor radiance becomes insensitive to the position of the plume along the path, as is easily checked (Harig et al., 2002). In general, the radiance does depend on the position of the plume and, unless indicated otherwise, we always assume that the plume is close to the background, as shown in Figure 11.35.

Optically Opaque Plume Approximation

When $\tau_p(\lambda) \ll 1$, the plume is termed optically thick. In the limit $\tau_p(\lambda) \approx 0$, the plume is termed optically opaque. From equation (11.103), as $\tau_p(\lambda)$ approaches zero, no background radiance reaches the sensor. The background has effectively been replaced by the plume, which now acts like a pure blackbody radiator. Such an opaque condition requires use of a different signal model, usually called a replacement model.

Sensor Smoothing and Sampling

The expression (11.119) represents the radiance present at the sensor input. The measurements of radiance that are output by the sensor contain the effects of the detector *spectral response function* $R_F(\lambda)$, along with noise $n(\lambda)$ introduced by the sensor. If $\bar{L}(\lambda)$ denotes the measured radiance in a spectral channel centered at λ we have

$$\bar{L}_{\text{on}}(\lambda) = L_{\text{on}}(\lambda) * R_F(\lambda) + n(\lambda), \quad (11.120)$$

where the convolution operator $*$ is defined by

$$L_{\text{on}}(\lambda) * R_F(\lambda) \triangleq \int_{-\infty}^{\infty} L_{\text{on}}(\nu) R_F(\lambda - \nu) d\nu. \quad (11.121)$$

We stress that sensor measured radiances are always affected by sensor noise and other artifacts.

Suppose next that the sensor measures radiance at p spectral bands centered at wavelengths λ_k , $1 \leq k \leq p$. If we sample (11.120) at $\lambda = \lambda_k$, we obtain

$$x_k = \sum_{m=1}^{N_G} g_m s_{mk} + v_k, \quad k = 1, 2, \dots, p, \quad (11.122)$$

where

$$x_k \triangleq \bar{L}_{\text{on}}(\lambda_k) \quad (11.123a)$$

$$g_m \triangleq C_B \Delta T \gamma_m \quad (11.123b)$$

$$s_{mk} \triangleq \{[\tau_a(\lambda) \alpha_m(\lambda)] * R_F(\lambda)\}|_{\lambda=\lambda_k} \quad (11.123c)$$

$$v_k \triangleq \{L_{\text{off}}(\lambda) * R_F(\lambda)\}|_{\lambda=\lambda_k} + n(\lambda_k) \quad (11.123d)$$

are, respectively, the measured radiance, chemical contrast, at-sensor gas signature, and background clutter plus noise. This is the fundamental linear signal model for the systematic development of gas detection and identification algorithms.

Table 11.3 Radiance model factors that distinguish three common imaging geometries.

Factor	Geometry		
	Side looking	Slant-path, up-looking	Down-looking
Path uniformity	Uniform	Uniform	Inhomogeneous
Distance to background	Variable	n/a	Constant
Background surface	Condensed phase	Sky	Condensed phase
Reflected downwelling radiance	Yes	No	Yes

11.7.4 Down-Looking Versus Slant-Path Geometries

The three-layer radiance model of Section 11.7.1 is almost universally used in algorithms for remote sensing of chemical plumes. However, it is important to understand its limitations as a representation of the true at-sensor radiance in different scenarios. We distinguish three common imaging geometries in Figure 11.33. The primary differences between the three are summarized in Table 11.3.

The side-looking slant path of Figure 11.33(a) is commonly encountered in chemical warfare agent detection applications; for example, troop protection. Of the three geometries, it may be most closely approximated by the three-layer model as long as the background lies below the horizon and the air temperature and composition do not vary appreciably over the path length. This latter condition may hold for distances of several kilometers. If the background materials have smooth emissivity spectra, then the flat background approximation (11.115) holds, further simplifying the model. However, the path length itself will typically vary greatly between different parts of the image, which will affect the observed atmospheric transmittance in the corresponding pixels. This type of variation violates one of the underlying assumptions behind most atmospheric compensation algorithms (Section 6.7), making this operation much more challenging than in the down-looking geometry.

An imaging geometry that includes slant paths with viewing angles above the horizon is depicted in Figure 11.33(b). This geometry is often employed to study stack emissions, for example. When compared with the side-looking geometry, the primary complication is the presence of a sky, as opposed to solid material, background. In particular, the spectral smoothness assumption of $L_b(\lambda)$ no longer holds, invalidating the flat background approximation.

The third geometry, depicted in Figure 11.33(c), is that of a down-looking sensor, typically mounted on an airborne or space-borne platform. In contrast to the side-looking geometries, the path length from sensor to background is roughly constant over the image with this geometry, which satisfies a key assumption of atmospheric compensation algorithms. However, an airborne data collection will typically occur at altitudes for which the atmospheric path between the sensor and background is not homogeneous in composition or temperature. The simple relationship (11.101) between atmospheric path radiance, temperature, and transmittance therefore does not hold. The results of atmospheric compensation algorithms that postulate a three-layer model are

an approximation and not a faithful representation of reality, a point that is emphasized by Young et al. (2002). The results of these algorithms may be profitably used for many remote sensing tasks, but the more demanding application of temperature–emissivity separation requires a more involved approach.

11.8 Remote Sensing of Chemical Clouds: Algorithms

In this section we use the at-sensor radiance signal model to systematically develop detection, identification, and concentration path-length estimation algorithms using sound statistical signal processing methodology. We focus on basic principles that illuminate the fundamental aspects of the different problems, and we present algorithms with well-understood operation and performance. Practical details are discussed in the provided references and the problems.

11.8.1 Development of Gas Detection Algorithms

We start by writing the linear signal model (11.122) in a concise matrix form as

$$\mathbf{x}_0 = \sum_{m=1}^{N_G} g_m \mathbf{s}_m + \mathbf{v}_0 \triangleq \mathbf{Sg} + \mathbf{v}_0. \quad (11.124)$$

According to this model the radiance spectrum \mathbf{x}_0 of a plume pixel is a linear mixture of the at-sensor gas signatures superimposed upon the radiance spectrum of the background. In practice, it is usually assumed that chemical mixtures are made up of three or fewer gas species. The quantity g_m is the “strength” of each chemical in the plume. For optically thin plumes g_m is proportional to the concentration path length γ_m and the temperature contrast ΔT between the plume and the surrounding background. To proceed with the development of detection algorithms we need to determine (a) the at-sensor radiance gas signatures \mathbf{s}_m and (b) a probability distribution for the background clutter.

To obtain the signature \mathbf{s}_m using (11.123c) we need the absorption coefficient spectrum of each chemical, the atmospheric transmission function, and the spectral response function of the sensor. For ground-level remote sensing of chemical plumes, the absorbance spectra of chemicals of interest are needed at atmospheric pressure and temperatures close to typical surface values. The preferred approach for obtaining these spectra is to use experimentally measured spectra from a quality-assured reference database. Two such databases are publicly available, one maintained by the National Institute of Science and Technology (NIST) (Chu et al., 1999) and one by the Pacific Northwest National Laboratory (PNNL) (Sharpe et al., 2004). The atmospheric transmission function is obtained by MODTRAN using a “typical” atmosphere. The spectral response of the sensor is typically modeled using a Gaussian shape function. This process is illustrated in Figure 11.38.

To understand the distribution of background clutter we use the results shown in Figure 11.39. Figure 11.39(a) shows the average radiance at every pixel for a LWIR hyperspectral data cube collected with the Aerospace GBSS sensor (Hall et al., 2011).

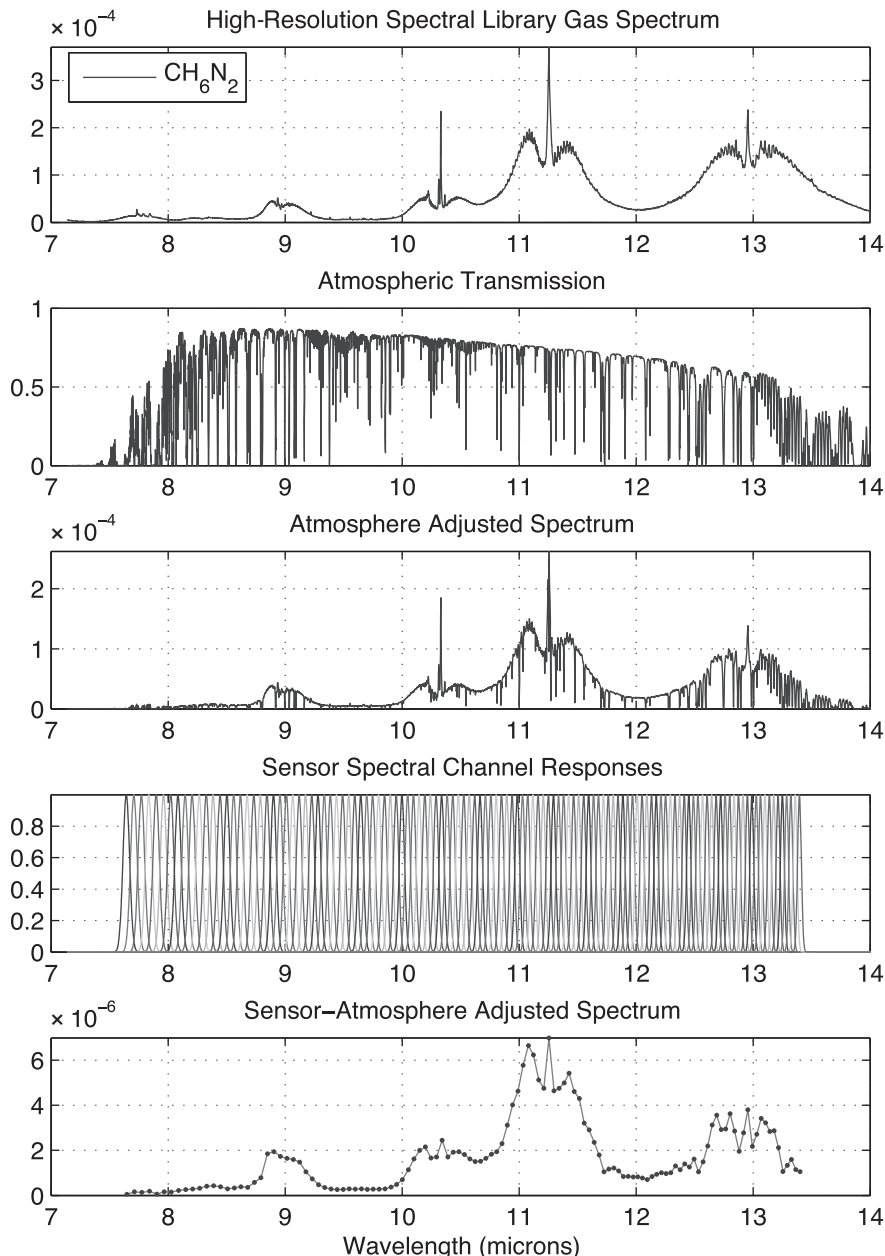


Figure 11.38 Illustration of the modulation, smoothing, and sampling processes used to derive the at-sensor radiance gas signature for methyl hydrazine (CH_6N_2).

Figure 11.39(b) shows a density scatter plot (two-dimensional histogram) in the first two principal components accounting for 99 percent of the overall data variance. The four significant clusters correspond to pixels associated with sky, clouds, mountain, and

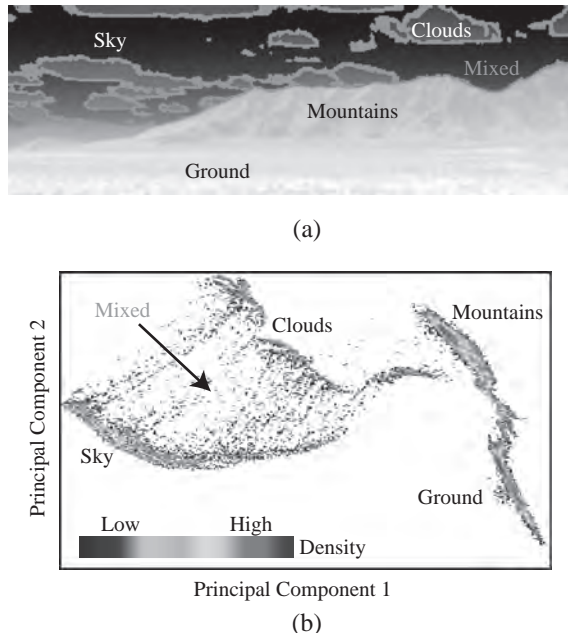


Figure 11.39 (a) Average spectral radiance for every pixel of a 128-spectral band LWIR data cube collected using the Aerospace GBSS sensor. (b) Density scatter plot (two-dimensional histogram) in the first two principal components of the LWIR cube shown in (a). (A black and white version of this figure will appear in some formats. For the color version, please refer to the plate section.)

ground surfaces, respectively. These clusters are comprised of physically similar pixels that exhibit a certain amount of random variation about a nominal mean value due to changes in physical composition, temperature, atmospheric transmission, and sensor noise. However, there is a set of pixels between the sky and cloud clusters that correspond to the borderline between sky and clouds. A plausible explanation is that the radiance spectra of these pixels are obtained from the mixing of sky and cloud spectra. These results suggest that density mixture models (see Chapter 7) are a natural candidate for modeling LWIR natural backgrounds.

As we saw in Chapter 7, normal distribution models provide mathematical tractability but often are inconsistent with SWIR hyperspectral imaging data. A similar conclusion holds for LWIR hyperspectral data. This is demonstrated in Figure 11.40, which shows probability of exceedance distributions of Mahalanobis square distance for the GBSS data in Figure 11.39 and the theoretical multivariate normal distribution. These results clearly indicate that LWIR backgrounds exhibit tails heavier than those predicted by a multivariate normal distribution. In contrast to SWIR data, the development of models for LWIR hyperspectral backgrounds is more challenging due to complications resulting from temperature–emissivity coupling.

Despite the fact that LWIR backgrounds do not follow a normal distribution, it turns out that detection algorithms derived under the assumption that the background clutter

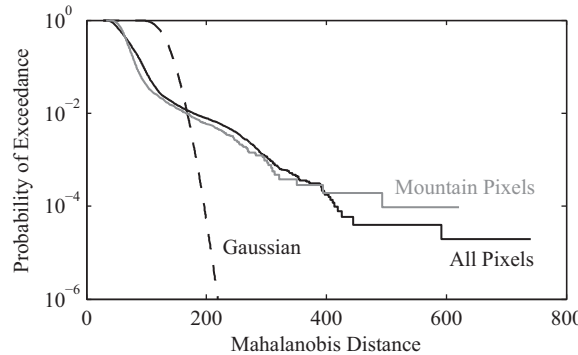


Figure 11.40 Empirical probability of exceedance for the scene in Figure 11.39. The dashed line represents a theoretical exceedance curve for a Gaussian distribution, which underestimates tail heaviness even for individual classes (for example, the mountain class).

is normally distributed are quite effective in practical applications. Therefore, we shall seek detection algorithms under the linear signal model

$$\mathbf{x}_0 = \sum_{k=1}^{N_G} g_k \mathbf{s}_k + \mathbf{v}_0 = \mathbf{Sg} + \mathbf{v}_0, \quad \mathbf{v}_0 \sim N(\mathbf{m}_b, \mathbf{C}_b), \quad (11.125)$$

where \mathbf{m}_b is the mean vector and \mathbf{C}_b is the covariance matrix of the background clutter. Careful inspection of Figure 11.36 shows the significance of using the spectral contrast, $L_{\text{on}}(\lambda) - L_{\text{off}}(\lambda)$, to reveal the presence of a gas at each pixel. Since $L_{\text{off}}(\lambda)$ is unavailable for plume pixels, we compute an approximate spectral contrast by subtracting \mathbf{m}_b from the radiance spectrum of each pixel. This yields

$$\mathbf{x} = \sum_{k=1}^{N_G} g_k \mathbf{s}_k + \mathbf{v} = \mathbf{Sg} + \mathbf{v}, \quad \mathbf{v} \sim N(\mathbf{0}, \mathbf{C}_b), \quad (11.126)$$

where $\mathbf{x} \triangleq \mathbf{x}_0 - \mathbf{m}_b$ and $\mathbf{v} \triangleq \mathbf{v}_0 - \mathbf{m}_b$. From model (11.126) we conclude that $\mathbf{x} \sim N(\mathbf{Sg}, \mathbf{C}_b)$. This signal model is identical with the model used to derive matched-filter detection algorithms in Section 10.6. To apply these algorithms to gas detection, we must take into consideration the following observations:

1. Optically thin plumes follow an *additive* signal model. When the plume becomes optically thick, the model becomes nonlinear, and ultimately the thick plume obscures the background (replacement model).
2. Because ΔT can be positive or negative, the sign of g_m is unknown.
3. The performance of subspace matched filter detection algorithms to simultaneously detect N_G gases, decreases significantly as N_G increases (see Figure 11.41). Therefore, in practice, it is better to use a bank of N_G single-gas detectors instead of a N_G -dimensional subspace detector.

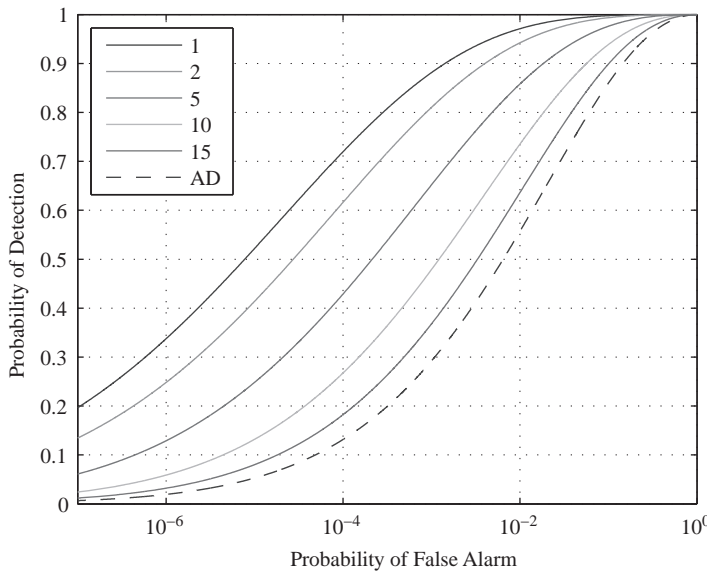


Figure 11.41 Performance of the MF with $N_G = 1, 2, 5, 10, 15$ chemicals. The sensor has $p = 20$ spectral channels and SCR = 20. As the number of chemicals in S increases, the MF's performance approaches the anomaly detector's performance. Equality occurs when the number of signatures in S reaches the number of spectral channels.

Therefore, for two-sided tests with two thresholds, we use the detectors

$$y_{\text{MF}} = \frac{s_k^T \mathbf{C}_b^{-1} \mathbf{x}}{s_k^T \mathbf{C}_b^{-1} s_k}, \quad \text{and} \quad y_{\text{NMF}} = \frac{s_k^T \mathbf{C}_b^{-1} \mathbf{x}}{\sqrt{s_k^T \mathbf{C}_b^{-1} s_k} \sqrt{\mathbf{x}^T \mathbf{C}_b^{-1} \mathbf{x}}}, \quad (11.127)$$

where the sign of the detection statistic reflects the direction of ΔT . The MF is normalized so that its output is an unbiased estimate of g_k . However, since the sign of g_k is unknown, the GLRT approach leads to the one-sided detection statistics

$$y_{\text{EMF}} = \frac{(s_k^T \mathbf{C}_b^{-1} \mathbf{x})^2}{s_k^T \mathbf{C}_b^{-1} s_k}, \quad \text{and} \quad y_{\text{ENMF}} = \frac{(s_k^T \mathbf{C}_b^{-1} \mathbf{x})^2}{(s_k^T \mathbf{C}_b^{-1} s_k) (\mathbf{x}^T \mathbf{C}_b^{-1} \mathbf{x})}, \quad (11.128)$$

which require the selection of a single threshold for each detector. We stress that, in contrast to the subpixel target detectors discussed in Section 11.1.6, we must *not* subtract the mean \mathbf{m}_b of the background clutter from the the signature s_k of each gas. The efficient implementation of matched filter detectors for real-time operation is discussed by Brett et al. (2013).

Conceptually, matched filter detection can be decomposed into two steps: whitening and matching (see Section 11.1.5). If we apply the whitening transformation

$$\tilde{\mathbf{x}} = \mathbf{C}_b^{-1/2} \mathbf{x} \quad \text{and} \quad \tilde{s} = \mathbf{C}_b^{-1/2} s, \quad (11.129)$$

to a background spectrum, a plume spectrum, and a gas signature, we obtain the results shown in Figure 11.42. Careful inspection of the whitened spectra vividly illustrates the

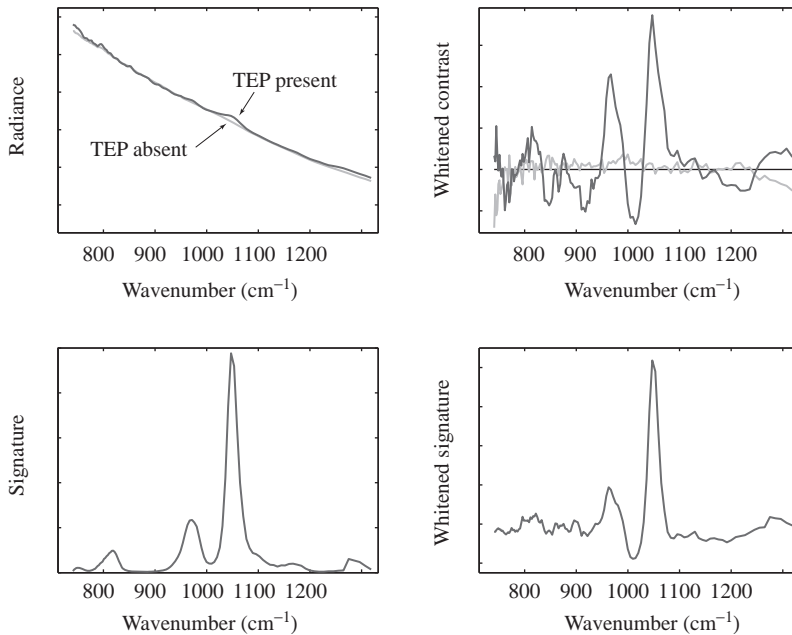


Figure 11.42 Illustration of the importance of whitening in matched filter detection. Note that a matched filter detector first “whitens” and then “matches”. The degree of matching is measured either by the length of the projection (MF) or the angle between the two vectors (NMF).

critical role of whitening in matched filter detection. Note how whitening “uncovers” similarities between in-scene and library gas signatures.

We have focused on detection algorithms based on the signal model (11.126), which characterizes the background clutter by its covariance matrix, because they are widely used in practice. However, we can develop algorithms that use background subspace models using the theory presented in Section 10.7; more details can be found in the problems.

11.8.2 Practical Aspects of Gas Detection Algorithms

Matched filter detectors require estimates of the at-sensor gas signatures s_k along with the background mean and covariance \mathbf{m}_b and C_b . The radiance signature requires knowledge of the atmospheric transmittance as well as the gas absorbance signature; the background mean and covariance must be estimated from background training data. Estimation error in any of these quantities will adversely affect the detector, in some cases, substantially.

The *sample size* of the covariance training set may be an issue with low spatial resolution, usually scanning, spectrometers, although it is not generally a problem with imaging spectrometers containing tens of thousands of pixels or more. However, the most serious issue involving the estimation of \mathbf{m}_b and C_b is the possibility that some of the pixels used as background training data contain the plume signal, which we refer

to as *contamination* of the background estimates. Contamination is primarily an issue through its effect on the covariance. It is well known that such contamination does not affect the matched filter detector statistic in the absence of signature mismatch. However, since some amount of mismatch between the estimated at-sensor gas signature and that present in the scene is inevitable, covariance contamination can be a serious problem.

A small part of signature mismatch is due to minor differences in sample composition and conditions (pressure and temperature) of the gas signature measured in the lab as compared to that in the field, and sensor calibration error. More significantly, the observed signature varies with concentration pathlength according to Beer's law (11.104), a minor effect for optically thin gases but a major effect for thick gases. Still more importantly, the atmospheric transmittance modulates the gas signature and must be estimated, either from ancillary measurements, substitution of a standard profile, or through an in-scene compensation algorithm. If the gas spectral features overlap those of the local atmosphere, substantial uncertainties in the at-sensor signatures will exist. Also, for slant-path imaging geometries $\tau_a(\lambda)$ will vary throughout the scene, further complicating matters.

In Figure 11.43, we illustrate the effects of covariance contamination with a data cube collected by the Aerospace GBSS sensor using the MF and NMF detectors. The detection results are substantially improved when the plume is removed from the training data used for covariance estimation.

Another explanation of the contamination problem may be obtained by decomposing the SCR as a sum of projections onto the background's principal components. When only a single gas s is present, the SCR can be written as

$$\text{SCR} = g^2 s^T C_b^{-1} s = g^2 \sum_{i=1}^p (1/\lambda_i) (q_i^T s)^2, \quad (11.130)$$

where λ_k and q_k are the eigenvectors and eigenvalues of C_b . Figure 11.44 shows this decomposition for a GBSS cube containing a plume. The vast majority of the variation in the image is contained in the first few eigenvectors (blue line, computed using *plume-free* training data), illustrating that principal-component-based dimensionality reduction using only a few components would preserve the background pixels of this cube almost perfectly. However, the SCR in these components (green line) is very small, showing that such a dimensionality reduction would retain almost no information about the plume. By contrast, very high SCR values are seen at many principal components corresponding to much higher index eigenvalues. These are the plume signal components that are visible to detection algorithms. The inset images show projections of the cube onto individual principal components. The first (largest) component shows the background clearly, but not the plume; the plume becomes visible in many of the higher-order components. The red line shows the SCR decomposition on the principal components of the plume-contaminated covariance matrix. Very little of the signal remains, which demonstrates

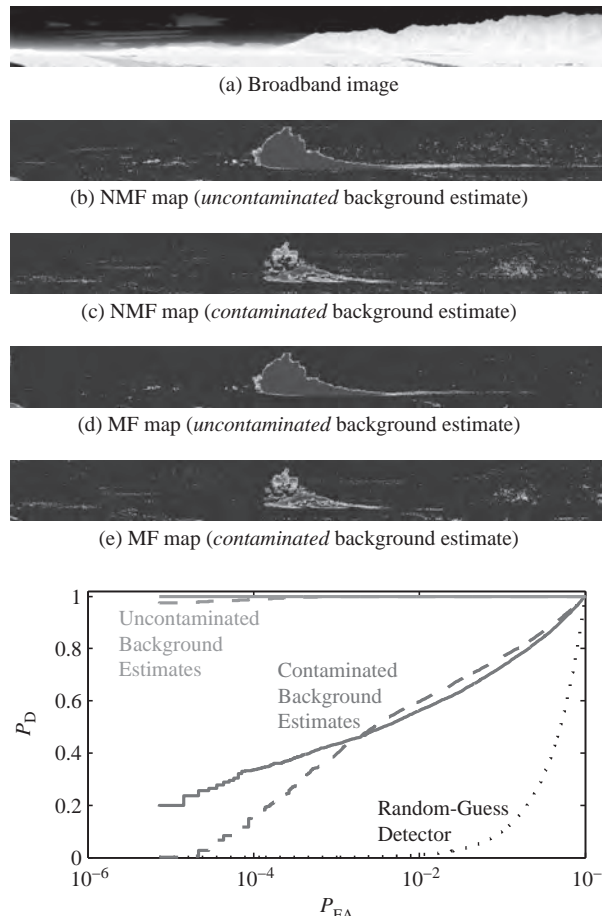


Figure 11.43 Detection images and receiver operator characteristics for a gas plume imaged by the GBSS sensor, illustrating the necessity of computing background statistics using plume-free training data. Each detection image is normalized by background response (0 to 30 dB color scale). The solid ROC curves correspond to the NMF and the dashed ROC curves to the MF. (A black and white version of this figure will appear in some formats. For the color version, please refer to the plate section.)

that the amount of signature mismatch present was sufficient to almost completely obliterate the signal. This result underlines the necessity of mitigating plume contamination of background training data during detection processing.

Finally, we note that chemical plumes may be widely distributed spatially over a scene, with variations in plume strength, temperature, and background characteristics over the spatial envelope of the plume. A spatially extended plume may be correlated with the background when the statistics of the latter are spatially non-stationary. This *plume-background correlation*, in conjunction with signature mismatch and covariance contamination, can cause additional performance loss (Theiler and Foy, 2006; Theiler et al., 2006).

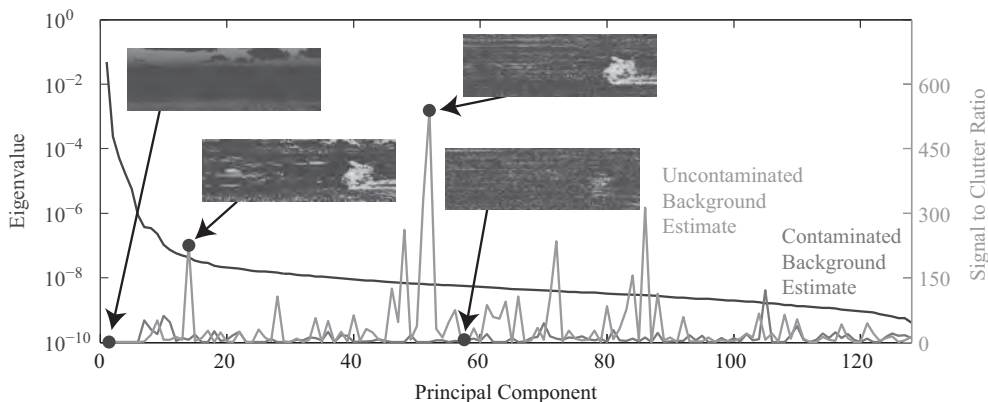


Figure 11.44 Signal-to-clutter illustration. As shown by the green and red curves, signal to clutter is significantly reduced when background estimates are contaminated with signal. We can also see that significant signal-to-clutter contributions come from seemingly insignificant principal components. Principal-component-based dimensionality reduction retains energy but reduces detectability.

The effects of signature mismatch and covariance contamination have been thoroughly investigated by Niu et al. (2013a), where it was shown that diagonal loading of the covariance matrix makes the MF and NMF detectors more robust to such model mismatches. The intuition behind this approach is that nearby signatures may be rendered effectively identical by sacrificing some of the discriminating ability of the detector. As it is the combination of mismatch and plume contamination that causes loss, small differences between the observed and assumed gas signatures are thus rendered benign.

The most effective strategy for dealing with the covariance contamination problem is to prevent the contamination of the background training data by the plume; we refer to such approaches as *plume-free background estimation*. This is a difficult task because excluding the plume pixels from the background training data requires the solution of the detection problem, which depends on the availability of background training data. A widely used approach is a two-pass detection process (see Figure 11.45). In the first pass, we estimate the covariance matrix from the entire data cube, compute the detection statistic, create a plume mask by selecting a “proper” threshold, and re-estimate the mean and covariance of the background. In the second pass, we repeat the detection process using the “plume-free” mean and covariance for the implementation of MF and NMF detectors. Plume-free background estimation, which is a critical component of practical gas detection systems, remains a challenging problem.

11.8.3 Performance Evaluation of Gas Detection Algorithms

Standoff chemical sensor systems are characterized by four key parameters: sensitivity, selectivity, probability of detection, and false alarm rate. A DARPA study (Carrano,

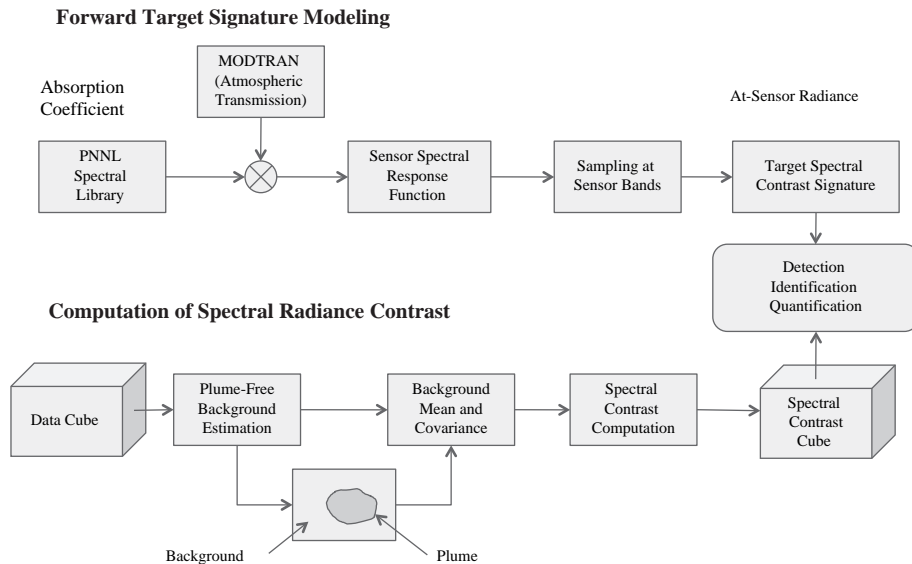


Figure 11.45 Signal processing components of a practical gas detection system. The forward modeling is done off-line; however, the processing of each data cube must be completed before the arrival of the next data cube.

2004) provides additional parameters and information. The performance of a sensor system depends upon the sensor, the environmental conditions, and the signal exploitation algorithms.

Sensitivity, which is also known as *detection limit*, is defined by the lowest concentration of a chemical agent that can be detected with high confidence and is typically specified in units of particles per million [ppm] or mass per unit air volume (particles/liter or mg/m³). Sensitivity may also be a measure of a system's ability to discriminate between small differences in the concentration of an agent. Hence, a sensitive detector gives a large change in signal intensity for a small change in concentration. Clearly, a meaningful quantitative definition of detection limit depends upon a quantitative definition of confidence.

Selectivity is the ability of a detection algorithm to respond only to the targeted chemicals in the field of view. A selective detector must be able to separate targeted compounds, over a broad range of concentrations, from any other substances which may be present. Note that selectivity is directly related to the signature mismatch properties of a detection algorithm.

The probability of detection and the probability of false alarm, evaluated on a pixel-by-pixel basis, are the fundamental indicators of detection performance. There is typically a trade-off between probability of detection and probability of false alarm (or false alarm rate). This trade-off is captured by the ROC curves, which show the probability of detection as a function of probability of false alarm. We stress that detection performance, quantified by a ROC curve, depends on the combined effect of concentration, path-length, agent spectral signature, noise, and background clutter. Thus, it is

meaningless to specify sensitivity without reference to a specific ROC curve because difference concentrations correspond to different ROC curves.

The evaluation of ROC curves for actual releases of chemical gases is very difficult because we cannot determine with certainty all pixels whose spectra have been affected by the plume. A simple way to understand and compare the performance of different algorithms is to use an approach known as “plume embedding”. The basic idea is to use equation (11.107) to “embed” one or more gases at a certain area of a hyperspectral data cube.

The matched filter detectors operate on a pixel-by-pixel basis, but often detection of the entire plume is desired. In this case, spatial processing can be performed to integrate the decisions of nearby pixels, for example, via binary integration (Richards, 2005b), and segment the scene into plume-present and plume-absent regions. When false alarms are spatially unstructured, this procedure boosts probability of detection and drives down probability of false alarm. Further ROC gains can be obtained by integrating across frames of a time series of hyperspectral images, resulting in an *event detector*, where the event is the release of a chemical agent. Obtaining ROC curves for an event-level detector is extremely time consuming and costly.

11.8.4 Cloud Characterization and False Alarm Mitigation

An alarm or hit from a detection algorithm does not necessarily mean that a chemical agent is present. If the hit is the correct response to the presence of a chemical agent, we have a detection (true positive). False alarms occur if a detector responds when a chemical agent is not present (false positive). When a detector fails to respond to a chemical agent that is present, we have a missed detection (false negative). For some applications, missed detections are more problematic than false alarms because the failure to produce an alarm may lead to dangerous situations.

To put these issues in a specific practical context, suppose that we wish to determine whether any of the gases from the search library s_1, \dots, s_L are present in a data cube. The first step is to process the cube with a detector bank, where each detector is “tuned” to one of the signatures in the search library. An example that illustrates the problem is given in Figure 11.46, which shows the detection statistics at the output of a filter bank for a TEP release observed by the Aerospace GBSS hyperspectral imaging sensor. Each detector uses an energy-normalized matched filter tuned to one of the library signatures. We note that the TEP-tuned filter shows the maximum response; however, the DEEP-tuned filter shows a significant response, and some response is visible with the TBP-tuned filter. Another view of these results is illustrated in Figure 11.47 by plotting the fraction of pixels that exceed a given threshold (probability of exceedance) for each detector, for sequences of cubes taken before and after the plume release. From the pre-release exceedance plots we observe that an optimal or ideal detection threshold is approximately 0.35; however, using this threshold, DEEP would incorrectly be declared as present in the scene. Furthermore, using a threshold below 0.3 would yield many false

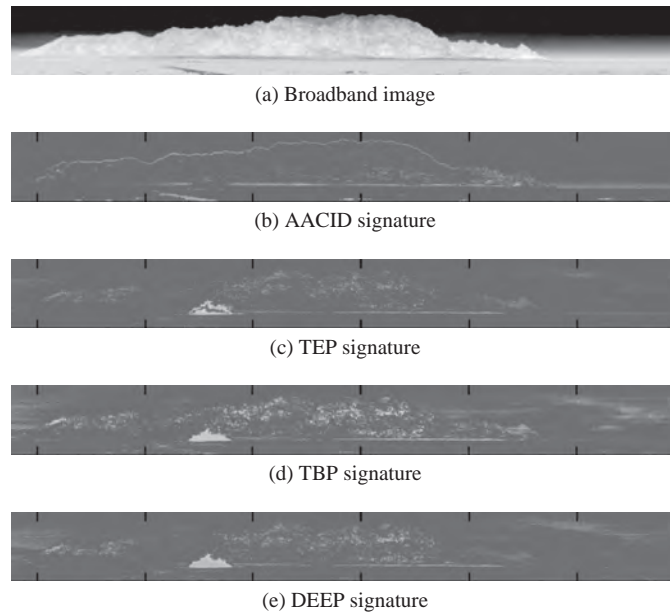


Figure 11.46 ENMF images for various chemical signatures (0 to 1 color scale). TEP was released and imaged using the Aerospace GBSS sensor; the other three chemicals are not present in the scene. (A black and white version of this figure will appear in some formats. For the color version, please refer to the plate section.)

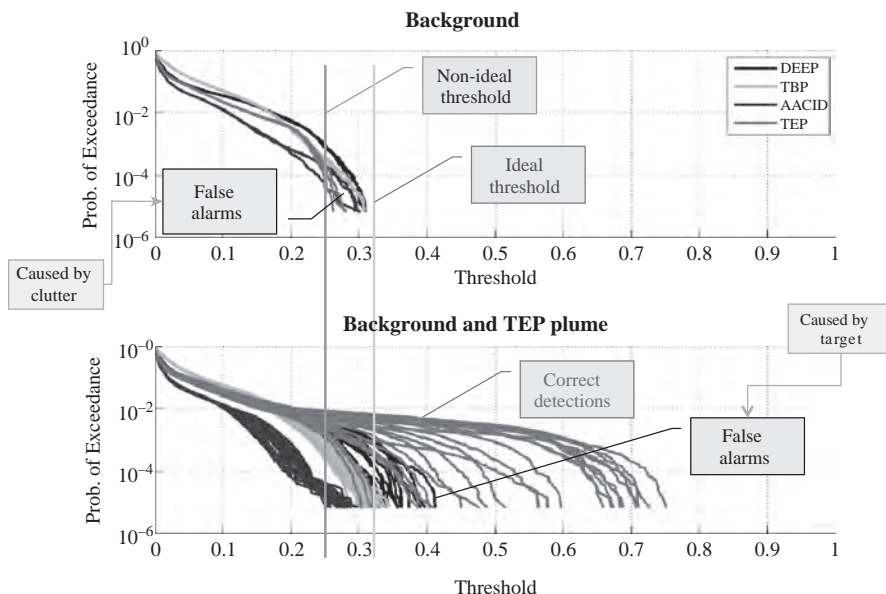


Figure 11.47 Probability of exceedance curves for a sequence of data cubes from the TEP release of Figure 11.46. The top plot is before TEP's release, the bottom plot after. The color of each curve corresponds to the signature used by the detection algorithm; different curves of the same color correspond to different cubes.

alarms caused by the background clutter. In this context, clutter refers to the pixel-to-pixel spectral variability caused by differences in material composition and temperature over the scene.

Ideally, the signal processing chain would not only detect the TEP release, but also reliably inform us if TEP is the only gas present; or, if not, what combination of gases is present. Detection algorithms do not address this latter task; that is, they do not give any information as to whether simultaneous TEP and DEEP detections means that both gases are present, or only one is present, nor, in the latter case, whether the stronger filter score corresponds to the gas that is present. It is also possible for false alarms to occur in pixels in which no gas from the detector bank is present at all, for a variety of reasons.

Therefore, to distinguish true chemical agent threats from false alarms, further processing of the spectroscopic measurements obtained by the sensor is required. Typically, we use the linear mixing model (11.126) to determine the composition of each pixel picked out by the detector (“hit”). We refer to this process as *chemical identification* or simply *identification*. Identification is a challenging process, which becomes more complicated in the following cases:

1. The hit is caused by a gas not included in the search library;
2. The hit is caused by a mixture of two or more gases that mimic the spectrum of another gas in the search library;
3. The signatures of two or more gases are so similar that they cannot be distinguished by practical detectors with limited selectivity;
4. The hit is caused by the emissivity structure of the background clutter, sky radiation reflected from the surface, or sensor artifacts;
5. The hit is caused by an optically thick plume, which lacks any spectral structure to enable its identification.

All the hits at the output of the detector bank, which include both true detections and false alarms, are further processed by the identification unit to determine the chemical composition of the corresponding pixel. In principle, we can determine the composition of a plume pixel by fitting the linear mixing model

$$x = \sum_{k=1}^m g_k s_k + v, \quad (11.131)$$

where $m = L$ is the size of the library, and checking which of the L values in $\{g_1, g_2, \dots, g_L\}$ are “significantly” different from zero. In linear regression theory this is known as a variable selection problem (Montgomery et al., 2012). Since L is usually quite large, we cannot usually fit the full model. Furthermore, it is quite improbable that a full model will ever describe a real plume. Since the number, 2^L , of all possible models can be very large, in practice, we typically assume that the true model has from zero to $m = 3$ chemicals from a library of L . Therefore, there are $M = \sum_{i=0}^m \binom{L}{i}$ models, including the null model (no chemicals present), and the problem of variable selection reduces to finding the “true model” or “correct” chemical subset (Burr et al., 2008).

The problem of model selection can be cast as a multiple hypothesis testing problem, where hypothesis H_0 corresponds to the null model and hypotheses H_1, \dots, H_{M-1} denote the remaining models. If we choose the H_i hypothesis, when the correct hypothesis (true model) is T_j we can provide a detailed description of performance by displaying all possible pairs (H_i, T_j) in the form of an $M \times M$ *confusion matrix*. The confusion matrix is a useful tool to break down the different types of errors in order to understand the performance of an identification algorithm. The diagonal elements of the confusion matrix correspond to correct identifications; the remaining off-diagonal elements correspond to false alarms, misses, partially correct and totally incorrect identifications. For gas detection systems, which use identification to improve detection performance, it would be useful to summarize the information in the confusion matrix using a scalar compact metric obtained by assigning costs to individual elements of the matrix. A scalar metric satisfying these requirements is the Dice metric discussed by Truslow et al. (2016).

The probability that gas A is present in the hit pixel is then given by

$$P(A) = \sum_{i=1}^M I(A \in M_i)P(M_i|D), \quad (11.132)$$

where $I(\cdot)$ equals 1 if its argument is true and $P(M_i|D)$ is the conditional probability of model M_i given the data D . The probabilities of each gas can be evaluated using the Bayesian Model Averaging approach presented in Section 9.14. This approach to chemical plume identification was introduced by (Burr et al., 2008). Chemical identification can be achieved either by choosing the gas with the highest probability or all gasses whose probability exceeds a certain threshold.

A typical chemical plume detection-identification system consists of a detector bank followed by an identification unit based on the linear mixing model. The identification unit analyses *only* the hits passed by the detection bank. A detailed investigation by Truslow et al. (2016), using the Dice metric, showed that this configuration outperforms either the detector bank or the BMA identifier used individually to process the entire data cube.

11.8.5 Concentration–Path-Length Estimation

To understand the key aspects of the concentration-pathlength (CL) estimation problem, we decompose (11.107) into two equations as follows:

$$L_{\text{plume}}(\lambda) = \tau_a(\lambda)B(\lambda, T_p) + [1 - \tau_a(\lambda)]B(\lambda, T_a) \quad (11.133)$$

$$L_{\text{on}}(\lambda) = \tau_p(\lambda)L_{\text{off}}(\lambda) + [1 - \tau_p(\lambda)]L_{\text{plume}}(\lambda). \quad (11.134)$$

Since we are dealing with positive quantities and $0 \leq \tau_p(\lambda) \leq 1$, then according to (11.134) the on-plume radiance $L_{\text{on}}(\lambda)$ lies between $L_{\text{off}}(\lambda)$ and $L_{\text{plume}}(\lambda)$. This is illustrated in Figure 11.48, which shows how the radiance of a background pixel changes after the insertion of a gas plume. Note how the dip introduced by the peak of the absorption coefficient spectrum of the gas (sulphur hexafluoride, SF_6) increases with increasing CL.

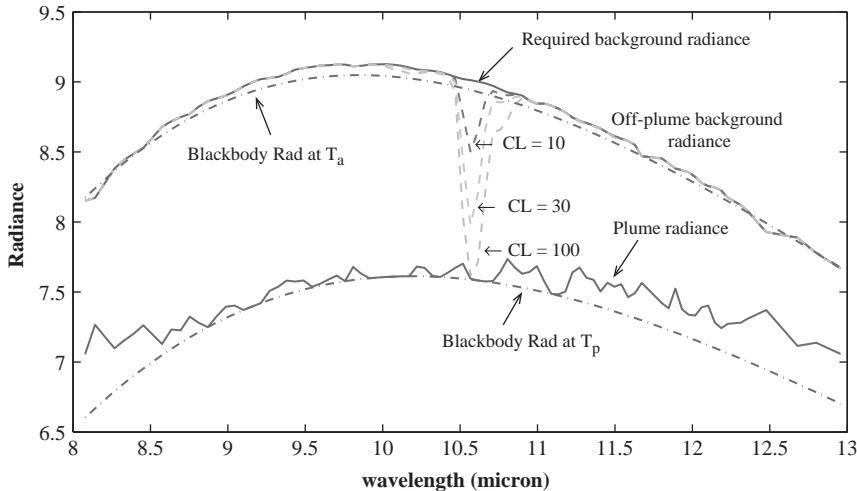


Figure 11.48 Plume-free background radiance and corresponding on-plume radiances for SF₆ at three different CL values for $T_p - T_a = 10$ K.

If, for simplicity, we assume a single gas, the CL parameter γ can be obtained from $\tau_p(\lambda)$ and the gas signature $\alpha(\lambda)$ using Beer's law as

$$\gamma = -\frac{\ln \tau_p(\lambda)}{\alpha(\lambda)}. \quad (11.135)$$

Note that since γ is a scalar, we need to apply (11.135) at a single spectral band. Solving (11.134) for $\tau_p(\lambda)$ and substituting to (11.135), we obtain

$$\gamma = \frac{1}{\alpha(\lambda)} \ln \left[\frac{L_{\text{off}}(\lambda) - L_{\text{plume}}(\lambda)}{L_{\text{on}}(\lambda) - L_{\text{plume}}(\lambda)} \right]. \quad (11.136)$$

In principle, since $L_{\text{on}}(\lambda)$ is measured, if we assume that $L_{\text{on}}(\lambda)$, $L_{\text{off}}(\lambda)$, and $L_{\text{plume}}(\lambda)$ are known, we can estimate γ . However, in practice, L_{plume} is not directly observed, and L_{on} and L_{off} are observed only in disjoint sets of pixels. Therefore, an approach based on estimation theory is necessary.

We begin with the signal processing form (11.108) of the radiance signal model

$$L_{\text{on}}(\lambda) = L_{\text{off}}(\lambda) + \tau_a(\lambda)[1 - e^{-\gamma\alpha(\lambda)}][B(\lambda, T_p) - L_b(\lambda)] + n(\lambda), \quad (11.137)$$

where we have included an additive noise term $n(\lambda)$ to account for sensor noise and other disturbances. The objective is to estimate γ from the radiances observed in pixels both on and away from the plume, L_{on} and L_{off} , the gas spectrum $\alpha(\lambda)$, the nuisance parameters $L_b(\lambda)$, $\tau_a(\lambda)$, and T_p , and the statistical characterization of the noise. This is a complex, non-linear optimization problem, whose solution depends on different assumptions and approximations:

- The background radiance is represented with a linear subspace model with a basis estimated from plume-free pixels by the method of principal components;

- The non-linear thermal contrast term $B(\lambda, T_p) - L_b(\lambda)$ can be replaced by a constant or the background term L_b may, again, be represented by a linear subspace model;
- The nonlinear Beer's law expression can remain as is, which leads to a non-linear optimization problem, or it can be approximated using the linear term of a series expansion;
- The atmospheric transmittance $\tau_a(\lambda)$ may be estimated from the observed off-plume radiances $L_{\text{off}}(\lambda)$ by an atmospheric compensation algorithm (see Section 6.7).

This formulation, under the assumption of Gaussian noise, allows the development of Cramer–Rao performance bounds for the CL estimation problem under different phenomenological conditions and applications (Golowich and Manolakis, 2013). Several algorithms for CL estimation have been developed by exploiting different assumptions and simplifications. However, there is still active research in this area to develop robust practical algorithms for CL estimation. A taxonomy and comparison of existing CL estimation algorithms can be found in (Niu et al., 2012, 2013b; Manolakis et al., 2014b).

11.9

Summary and Further Reading

The main objective of this chapter is the application of knowledge developed in the previous chapters to some common hyperspectral imaging applications. Although the selection of topics and the emphasis in coverage has been influenced by our experience, the selected uses are widely seen in civilian and military activities. A considerable amount of attention has been paid to hard target detection in the reflective part of the spectrum because it is one of the most mature and successful applications of hyperspectral imaging. We have discussed practical issues regarding the implementation of target detection algorithms and the important topics of performance evaluation and performance prediction for practical applications. Spectral landscape classification is an important area of remote sensing which has been extensively developed using multispectra data. A thorough treatment of this area would require another book; thus, we have chosen to emphasize practical requirements and differences from the target detection problem. The provided taxonomy of change detection algorithms is quite comprehensive; however, their practical application is challenging. Since the signal exploitation algorithms are the same in the reflective and emissive regions of the spectrum, we emphasized the unique aspects of processing in the thermal infrared. Finally, we provided a comprehensive treatment of chemical plume sensing using LWIR hyperspectral imaging data. Material for further reading about the practical aspects of different applications is more difficult to find because it's only available in the form of limited distribution internal organization reports.

Appendix Introduction to Gaussian Optics

To understand both the spectral discrimination and the image production from an imaging spectrometer requires both Gaussian, or geometrical, and physical optics that govern the processes of diffraction and interference. This appendix provides the barest introduction to Gaussian optics and a qualitative description of aberration theory. Physical optics is introduced in Chapter 4 when it is required, as in, for example, the action of a grating. The analysis presented is for centered or axially symmetric systems about an axis that passes through the centers of the sequential optical elements known as the optical axis. The concept of paraxial ray tracing, where the rays travel infinitesimally close to the optical axis, is also introduced, providing the location and size of the image. The brightness of an image is developed through the definition and placement of pupils and stops. Finally the quality of an image is determined through aberration theory.

A.1 The Optical Path

In Chapter 2 we introduced the concept of a wavefront as the surface of constant phase for an electromagnetic wave. This surface is perpendicular to the wave vector \mathbf{k} , which is in the direction of propagation of the wave. A ray of light is defined to be parallel to the wave vector and is in the direction of energy propagation as described by the Poynting vector. The ray, an infinitely narrow beam of light, is the construct used in geometrical optics but has no precise physical meaning. For example, if we attempt to create a narrow beam of light by illuminating a pinhole we are defeated by diffraction effects that spread the beam out, with the effect becoming larger as the pinhole diameter is reduced. Nevertheless the ray is an extremely useful and practical concept that is universally used in Gaussian optics and ray tracing. The wavefront, on the other hand, has a precise physical meaning and, for the isotropic materials used in imaging spectrometers, the direction of energy propagation is always along the wavefront normal.

In Gaussian optics, light is assumed to propagate rectilinearly along the rays with their directions changed only by the processes of reflection and refraction. The optical systems considered here are composed of a series of surfaces that can be either refracting or reflecting and have a common axis of rotational symmetry known as the optical axis. These surfaces redirect the rays from an object in order to form its image. The fundamental approximation assumed is that the angle between a ray and the optical axis is sufficiently small that the small angle approximation is valid and its sine or tangent can

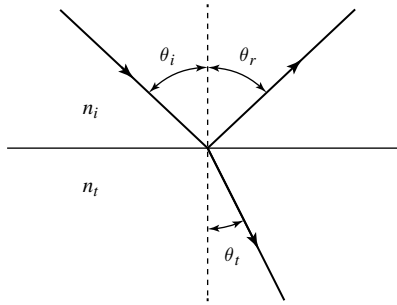


Figure A.1 Light reflection and refraction at the interface between two media of index n_i and n_t .

be replaced by the angle itself. The only information provided in this approximation, known as the paraxial approximation, is the image size and location; the image quality is assumed to be ideal.

The laws of reflection and refraction govern the propagation of light through an optical system and are illustrated in Figure A.1. The law of reflection is

$$\theta_i = -\theta_r, \quad (\text{A.1})$$

where θ_i and θ_r are the angles of incidence and reflection, respectively. By convention, the angles are measured from the surface normal at the point of ray intersection and are therefore of opposite sign. A counterclockwise angle is defined to be positive. The law of refraction for isotropic media, Snell's law, is given by

$$n_i \sin \theta_i = n_t \sin \theta_t, \quad (\text{A.2})$$

where n_i and n_t are the index of refraction of the media for the incident and transmitted light with the corresponding angles θ_i and θ_t . The sine function can be expanded using a power series to yield

$$\sin \theta = \theta - \frac{\theta^3}{3!} + \frac{\theta^5}{5!} - \frac{\theta^7}{7!} + \dots \quad (\text{A.3})$$

which, when inserted into (A.2) and applying the paraxial approximation, yields

$$n_i \theta_i = n_t \theta_t \quad (\text{A.4})$$

for the linearized form of Snell's law.

Both laws can be rather easily proven through the application of Fermat's principle, which states that the optical path S for a ray traveling between any two points is stationary or, equivalently,

$$\frac{\partial S}{\partial q_i} = 0, \quad (\text{A.5})$$

with q_i representing either the ray position or its directional cosine. For example, the law of reflection can be derived by applying (A.5) to the optical path given by

$$S = \sqrt{y_i^2 + x^2} + \sqrt{y_r^2 + (d - x)^2}, \quad (\text{A.6})$$

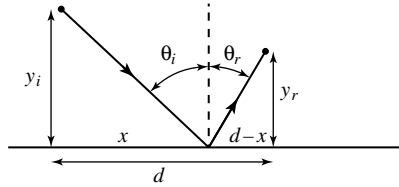


Figure A.2 Geometry for the development of the law of reflection from Fermat's principle.

as shown in Figure A.2. From (A.5), the partial derivative is taken with respect to x yielding

$$\frac{x}{\sqrt{y_i^2 + x^2}} = \frac{d - x}{\sqrt{y_r^2 + (d - x)^2}} \Rightarrow \sin \theta_i = \sin \theta_r, \quad (\text{A.7})$$

where the angles are both positive and therefore $\theta_i = \theta_r$. The sign convention that was applied in (A.1) is defined in Section A.3 below. The proof of Fermat's principle is developed in Born and Wolf (1999) through the application of the calculus of variations.

Let's look at the index of refraction in a little more detail. Recall that the real component of the index of refraction is the ratio of the speed of light in a vacuum to the speed of light in a medium. An optically dense medium has a high index of refraction and light travels through it relatively slowly. The materials used in optical systems have a small imaginary index to minimize absorption which is neglected for now, although we did address it in Chapter 3 for system modeling. When a wavefront crosses the boundary between a vacuum and an isotropic medium the frequency is unchanged while the wavelength and the speed of light vary. This implies that the speeds and wavelengths in the two media are related by

$$v = \frac{c}{\lambda_o} = \frac{v}{\lambda} = \frac{c}{n\lambda}, \quad (\text{A.8})$$

where λ_o is the vacuum wavelength, λ is the wavelength in the medium, and the definition of the refractive index has been applied. The two wavelengths are therefore related by

$$\lambda = \frac{\lambda_o}{n} \quad (\text{A.9})$$

with the wavelength shortened within the medium. The index of refraction for air is slightly different from the vacuum index of one but the two will be taken to be equal. Additionally, the index of refraction for an optical material is not a constant but varies as a function of wavelength. This variation is called dispersion and, for isotropic optical materials, typically decreases with increasing wavelength. This leads to the angular separation of different wavelengths that is observed using a prism.

The reduction in wavelength in an optically dense medium leads to the concept of the optical path length. Consider a material composed of a series of slabs of different optical densities. Light incident on the material travels through it with the distance in the i th slab given by d_i . The time it takes the light to pass through the material is therefore

$$t = \frac{d_1}{v_1} + \frac{d_2}{v_2} + \dots + \frac{d_n}{v_n} = \sum_{i=1}^n \frac{d_i}{v_i}, \quad (\text{A.10})$$

where v_i is the speed of light in a particular slab. Applying the definition of the index of refraction to (A.10) yields

$$t = \frac{1}{c} \sum_{i=1}^n n_i d_i, \quad (\text{A.11})$$

where the terms in the summation define the optical path S for isotropic media. It is the optical path that is used to calculate distances in Gaussian optics and the wavefronts are surfaces of constant optical path lengths.

A.2 Ideal Image Formation

Ideal image formation occurs when an object is perfectly reproduced in an image by the optical system. This image can be larger or smaller than the object due to optical magnification but it is a precise reproduction of the object in its details. This implies that all the rays that originate from a point on the object and are collected by the optical system will pass through the equivalent point on the image. The magnification is a simple scale factor, a constant ratio, between the length dimensions of the object and image. Implied is that an object plane is perfectly imaged onto an image plane.

Consider an arbitrary optical system composed of a number of optical elements, either refractive or reflective, centered on the optical axis and forming an image of an object. A ray r_1 is parallel to the optical axis and is incident from the left at a height h as depicted in Figure A.3. It emerges from the system on the right and intersects the optical axis at the point F' . Similarly, another ray r_2 parallel to the optical axis is incident from the right at the same height and emerges from the optical system on the left side and subsequently intersects the optical axis at the point F . The two rays, or their projections, intersect each other at P_h and P'_h . A perpendicular line is drawn from the optical axis at P to P_h and similarly from P' to P'_h . F and F' are the focal points and P and P' are the principal points. Since the height h of the rays was arbitrarily chosen and the optical system is cylindrically symmetric, the ensemble of all points P_h and P'_h will form two planes known as the principal planes. The unprimed quantities refer to the object space, the space prior to the intersection of the ray with the first optical surface, while the primed

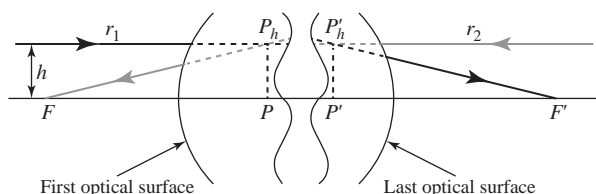


Figure A.3 Definition of the principal planes and focal points for ideal imaging. After Welford (1986).

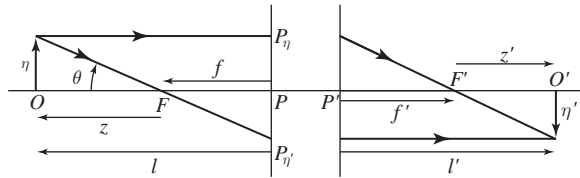


Figure A.4 Ideal imaging.

quantities refer to the image space, the space where the ray travels after intersecting the final optical surface. These object and image space quantities may be physically to the left or right of the optical system or of each other.

The principal planes play a central role in Gaussian optics. Consider a point source located at P_h . Rays that originate from the point source and pass through the ideal optical system will be imaged at P'_h . Similarly if a point source is located at P'_h it will be imaged at P_h . Pairs of object and image points, such as P_h and P'_h , are known as conjugate points and the two principal planes are conjugate planes. Additionally there is unit magnification between any two principal plane conjugate pairs. The distance between the object principal point and the object focal point is the object focal length f . The image focal length f' is similarly defined. By convention, if the focal length is to the right of the principal point it is positive and if it is to the left it is negative.

The two focal points and two principal points, known as cardinal points, are all that are required to develop the relationships between an object and its image for an ideal optical system. Figure A.4 illustrates an object of height η that is imaged into an image of height η' . Consider a ray originating from the top of the object and travelling parallel to the optical axis to intersect the object principal plane at P_η . It will emerge from the image principal plane at the same height, cross the optical axis at F' , and continue onward in image space. Similarly, a ray that travels from the top of the object through F will intersect the object principal plane at $P_{\eta'}$, emerge from the image principal plane again at the same height, and travel parallel to the optical axis. These two rays will intersect at the image conjugate point at a height η' below the optical axis. The full image is constructed from the ensemble of conjugate pairs.

The object distance l is defined as the distance from P to O at the base of the object. A similar distance z is defined from F to O . Both these distances are to the left and are therefore negative. Similar distances, l' and z' , are defined in the image space but are both to the right and positive. Note, these distances are always defined relative to a cardinal point with the sign convention positive to the right and negative to the left. Also, heights above the optical axis are positive while heights below are negative. Angles are measured from the optical axis to the ray with counterclockwise being positive.

Similar triangles will now be used to establish quantitative relationships. In object space,

$$\tan \theta = \frac{\eta}{z} = -\frac{\eta'}{f}, \quad (\text{A.12})$$

where the minus sign is required since θ , η' , and f are all negative. Rearranging (A.12) yields

$$m = \frac{\eta'}{\eta} = -\frac{f}{z} \quad (\text{A.13})$$

for the transverse or linear magnification m . A similar derivation produces the alternative form

$$m = \frac{\eta'}{\eta} = -\frac{z'}{f'} \quad (\text{A.14})$$

in image space. Equations (A.13) and (A.14) are combined to give

$$zz' = ff', \quad (\text{A.15})$$

which is known as Newton's equation.

It is more convenient to reference distances to the two principal planes. This is readily accomplished since the object and image distances are equal to the sum of the appropriate z and focal length. Combining these relationships with (A.13) and (A.14) produces, after some rearrangement,

$$l = f \left(\frac{m-1}{m} \right) \quad (\text{A.16})$$

and

$$l' = -f'(m-1) \quad (\text{A.17})$$

for the object and image distances respectively. Equations (A.16) and (A.17) are used to derive

$$\frac{f'}{l'} + \frac{f}{l} = 1 \quad (\text{A.18})$$

by eliminating m . The magnification can also be alternatively expressed as

$$m = -\frac{l'f}{lf}, \quad (\text{A.19})$$

again using (A.16) and (A.17).

The focal points are also conjugate points for an axial object or image at infinity. If the axial object is at infinity, then its image is at F' , and similarly, if the object is at F , its image is at infinity. One can also visualize this as having an object at infinity to the right with its image formed at F . For ideal image formation, an extended object at infinity will be imaged into a plane perpendicular to the optical axis at F' , and similarly for an extended object at F . This concept forms the basis for identifying the focal lengths.

The wavefront emanating from the object point is spherical. This incident wavefront is transformed by the optical system into the final wavefront that illuminates the corresponding image point. Ideal image formation implies that the transformed wavefront converging to an image point is also perfectly spherical. The departure from this strict sphericity is the result of geometrical and chromatic aberrations in the optical system. These aberrations, addressed in Section A.7, are characterized by the difference between the reference sphere for perfect imaging and the true wavefront.

A.2.1 Converging and Diverging Optical Systems

The image formation depicted in Figure A.4 has rays from each object point converging to an image point, therefore an image would be visible if a screen were placed at O' . This optical system, which could be composed of a single surface, a single lens, or a combination of lenses, is called *converging* and the image formed is called *real*. It can be condensed by removing the space between the principal planes, allowing the optical system to be simplified to a lens of zero thickness known as a thin lens. It must be remembered that the image has been shifted, to the left in this case, but in all other respects the two descriptions are equivalent. This simplification is the utility of the principal planes where the image location and magnification for any object can be easily determined.

Optical systems are not limited to this converging case with a real image. A similar case exists where the rays in image space diverge. Does an image exist in this case and, if so, how is it defined and what is it called? The parallel object ray in the converging case is bent to pass through the image focal point F' ; what is the equivalent in the diverging case? The upper diagram in Figure A.5 illustrates the action of a diverging optical system for parallel rays at height h as was done for the converging case in Figure A.3. The parallel ray travelling from the left is bent upward in image space and its projection backward intersects the optical axis at F' , the image space focal point. Similarly, a parallel ray travelling from the right to the left will be bent upward and its projection will intersect the optical axis at F , the object space focal point. The principal planes are illustrated in Figure A.5 and defined as above. Note that the locations of F and F' have

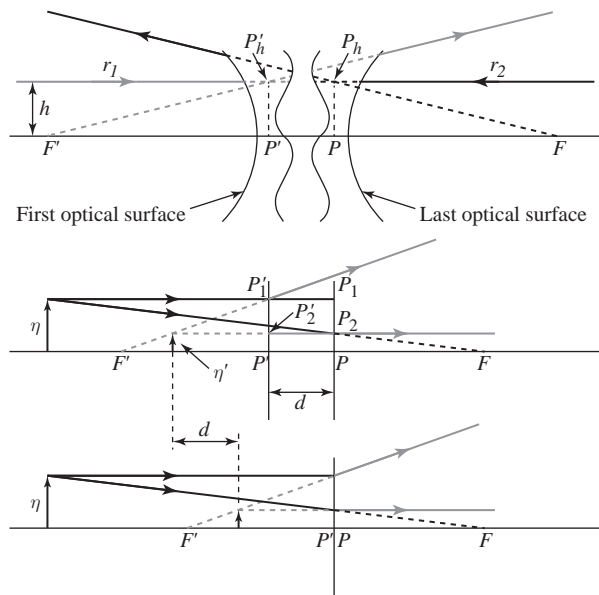


Figure A.5 Definition of the principal planes and focal points for ideal imaging for a diverging system and ray tracing example.

flipped, but they remain the focal points associated with the object and image space rays respectively.

The middle diagram shows imaging relative to the two principal planes with the object space rays and their projections in black while the image space rays and projections are gray. The parallel object ray from the top of η intersects the object space principal plane at P_1 and exits the image space principal plane at P'_1 , which is at the same height since the two points are conjugates of unit magnification. The ray emerging from P'_1 is along the line that links F' and P'_1 . Similarly, the parallel image ray that exits the image space principal plane at P'_2 is at the same height that the corresponding object space slant ray intersects the object space principal plane at P_2 along the line that links the top of η to P_2 and is then projected on to F . The image location is determined by projecting the rays backward until they intersect.

The lower diagram illustrates ideal imaging, with the space between the two principal planes removed and the location of η' shifted to the right by the separation distance d . The rays that form the image don't actually pass through it although it would be clearly visible if one were to look at it from the right. This is known as a virtual image. Another important difference between the converging and diverging optical systems is that the image is inverted for the first relative to the object and erect for the second.

A.3

The Paraxial Approximation

The first-order design of an optical system is governed by the paraxial approximation. It is instructive to consider a single refractive surface to illustrate the approach, which will subsequently be applied to a powered mirror. Figure A.6 illustrates such a refractive surface with indexes n and n' in object and image space. The sign convention that is often applied by optical engineers, already referred to above, is expanded and summarized as:

- Light initially travels from left to right. If light travels from right to left, due to a reflective optic, the index of refraction is taken to be negative, but note that flat, turning mirrors are ignored.
- The local coordinate system, point \mathcal{O} in Figure A.6, is located at the intersection between the optical axis and the surface and all distances are measured from \mathcal{O} . Distances to the left are negative and distances to the right are positive.
- Heights are measured from the optical axis and are positive if above it.
- Angles are:
 1. measured from the optical axis to the ray;
 2. measured from the surface normal to the ray at the point of intersection of the ray with the surface;
 3. always the smaller angle;
 4. defined to be positive for counterclockwise rotations.

The second part of the first bullet item enables powered mirrors to be treated as if they were refractive surfaces.

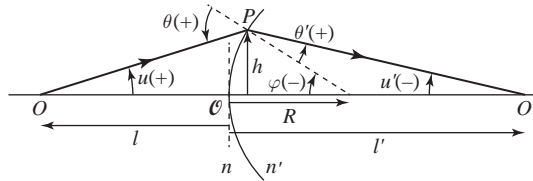


Figure A.6 The paraxial approximation applied to a single surface. The signs of the angles are in parentheses.

A ray originating from an object point on the optical axis can now be traced through our single surface optical system. The ray in object space intersects the surface at point P with the angle of incidence denoted by θ and the transmitted angle in image space is denoted by θ' . In the paraxial approximation, these two angles are related by the linearized form of Snell's law, $n\theta = n'\theta'$. In absolute numbers, θ is the sum of u and ϕ . However, after the sign convention is applied, θ is

$$\theta = u - \phi \quad (\text{A.20})$$

since u is positive and ϕ is negative. Similarly, in absolute numbers, θ' is the difference between ϕ and u' , but is given by

$$\theta' = u' - \phi \quad (\text{A.21})$$

when the sign convention is applied since θ' is positive and both u' and ϕ are negative angles. Equations (A.20) and (A.21) always give the correct sign for θ and θ' .

Snell's law is now applied at the point of intersection yielding

$$n(u - \phi) = n'(u' - \phi), \quad (\text{A.22})$$

which can be further reduced by noting that, under the paraxial approximation, $u = -h/l$, $u' = -h/l'$, and $\phi = -h/R$ with the minus signs due to the sign conventions. Substituting these relationships into (A.22) and canceling h produces

$$\frac{n'}{l'} - \frac{n}{l} = \frac{n' - n}{R} = c(n' - n) \equiv K, \quad (\text{A.23})$$

where the curvature c equals $1/R$. The term $c(n' - n)$ is called the power of the surface and is denoted by K . If c and $n' - n$ have the same sign then K is positive and the surface is converging. Similarly, if K is negative the surface is diverging. The image formed at O' does not depend upon h , but only upon l , l' , n , n' , and R , which implies perfect imaging.

We introduced the concept of the focal length in the context of perfect imaging for a ray travelling from infinity from either the left or right. Applying this concept to (A.23) with $l = \infty$ yields

$$\frac{n'}{l'} \rightarrow \frac{n'}{f'} = c(n' - n), \quad (\text{A.24})$$

which reduces to

$$f' = \frac{n'}{c(n' - n)} = \frac{n'}{K} \quad (\text{A.25})$$

for the image focal length. The object focal length is similarly derived to yield

$$f = -\frac{n}{c(n' - n)} = -\frac{n}{K}, \quad (\text{A.26})$$

where l' has been set to infinity in (A.23). The relationship between the power and the object and image focal lengths is therefore

$$K = \frac{n'}{f'} = -\frac{n}{f}, \quad (\text{A.27})$$

which, although derived for a single surface, is generally true. The equivalent focal length, abbreviated as *efl* or just F , is the reciprocal of K or

$$K = \frac{1}{F}, \quad (\text{A.28})$$

which is the image focal length for an optical system in air or vacuum. This has the advantage of fixing the sign so that a lens or surface is either positive (converging) or negative (diverging). The magnification of a single surface is therefore

$$m = \frac{n'l'}{n'l} = \frac{nu}{n'u'}, \quad (\text{A.29})$$

where (A.19), (A.27), and the relationships between the object and image distances and angles utilized in the derivation of (A.23) have been used. Pay particular attention to the geometry depicted in Figure A.6.

Recall from Section A.2 that the principal planes are determined by tracing a ray parallel to the optical axis and finding the focal point where the ray intersects the optical axis after passing through the optical system. If we start with an object space ray at height h , the image space principal plane is located by identifying where the image space ray crosses the height h on its way to the optical axis. For the single surface case and employing the paraxial approximation, this occurs at the intersection of the ray and the surface. The two principal planes are coincident.

A.3.1

A Single Mirror

We would like to apply the paraxial equations derived for a single refractive surface, or at least something very similar, to a reflective surface. The law of reflection, $\theta_i = -\theta_r$, can be rewritten by taking the sine of both sides or $\sin(\theta_i) = \sin(-\theta_r) = -\sin(\theta_r)$. This is analogous to Snell's law with $n = 1$ and $n' = -1$, enabling us to treat a mirror as a refractive optic. It is also the justification for the second half of our first sign convention bullet.

Applying this concept to (A.23) yields

$$\frac{1}{l'} + \frac{1}{l} = \frac{2}{R} = 2c \quad (\text{A.30})$$

with K obtained from $c(n' - n)$ producing $K = -2nc$, where n is the object space index of refraction. The focal length is therefore

$$f' = \frac{n'}{K} = \frac{1}{2c} = \frac{R}{2} \quad (\text{A.31})$$

which is independent of n since the focusing power of a mirror only depends upon its curvature, the index of the surrounding medium is irrelevant.

For the case where the light is initially propagating from the left to right, $n = 1$ and $n' = -1$ and the power is $K = -2c$. For a concave mirror, c is negative (R is measured from the mirror vertex and is to the left) making K positive and the mirror converging. Similarly, for a convex mirror, c is positive making K negative and the mirror diverging. The same result is obtained if the light travels from right to left prior to reflection with $n = -1$ and $n' = 1$. As expected, the power K is always determined by the mirror curvature and not by the direction of light propagation. A plane mirror has no power since $c = 0$.

A.3.2 Paraxial Ray Tracing

The formalism developed in Section A.3 will now be generalized to an optical system composed of many surfaces as illustrated in Figure A.7. The approach is to trace a ray from an object point, through each surface of the system and to repeatedly apply the linearized form of Snell's law and a transfer equation, until the conjugate image point is reached.

First (A.23) is rewritten by replacing K with $c(n' - n)$, l with $-h/u$, and l' with $-h/u'$ to give the refraction equation for a single surface as

$$n_j' u_j' - n_j u_j = -h_j c_j (n_j' - n_j) \quad (\text{A.32})$$

for a ray intersecting the j th surface with curvature c_j at height h_j . The transfer equation between any two surfaces is just the equation for a straight line with the slope given by u_j' or

$$h_{j+1} = h_j + d_j u_j', \quad (\text{A.33})$$

where d_j is the distance along the optical axis from the j th surface to the $j+1$ surface with h_j and h_{j+1} being the ray intersection heights. In the case where the $j+1$ surface is to the

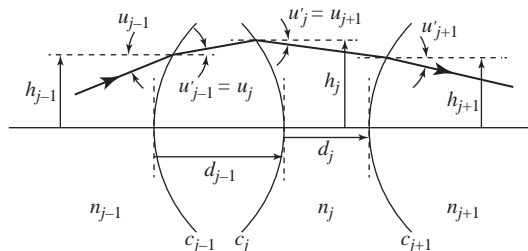


Figure A.7 Paraxial ray tracing through three surfaces within an optical system.

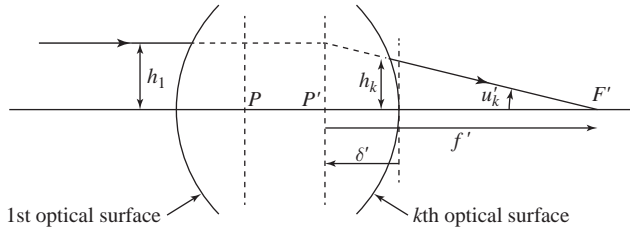


Figure A.8 Location of the image principal plane relative to the final optical surface.

left of the j th surface, d will be negative. Some bookkeeping is required since $\eta'_j = \eta_{j+1}$ and $u'_j = u_{j+1}$. The different values for u and u' are always measured relative to either the optical axis or a line parallel to it.

Determination of the principal planes in this case involves the selection of an appropriate reference point. The references chosen are the first and last optical surfaces. Again, a ray from an infinitely distant axial object is traced from both the object and image spaces. For the object space ray, δ' is the distance from the last or k th surface to the image side principal plane. As illustrated in Figure A.8, geometrically δ' is

$$\delta' = \frac{h_1 - h_k}{u'_k}, \quad (\text{A.34})$$

where h_1 is the ray height at the first surface, h_k is the height at the final surface, and u'_k is the final ray angle. A similar derivation for a parallel ray from an axial object point infinitely distant to the right yields

$$\delta = -\frac{h_1 - h_k}{u_1} \quad (\text{A.35})$$

for the location of the object side principal plane referenced to the first surface.

Now that the principal planes have been located, the system power is determined by tracing an axial object ray from infinity parallel to the optical axis through all the optical elements and determining where it, or its projection, intersects the optical axis. The ray intersects the first surface at h_1 and emerges from the last surface at an angle u'_k . Again referring to Figure A.8, the image focal length f' is given by $-h_1/u'_k$ and therefore the power is

$$K = -\frac{\eta'_k u'_k}{h_1}, \quad (\text{A.36})$$

where (A.27) has been used.

The system magnification is obtained by repeated applications of the individual magnifications of the intermediate optical surfaces, or

$$\begin{aligned} m &= m_1 m_2 \dots m_j \dots m_{k-1} m_k \\ &= \frac{\eta'_1}{\eta_1} \frac{\eta'_2}{\eta_2} \dots \frac{\eta'_j}{\eta_j} \dots \frac{\eta'_{k-1}}{\eta_{k-1}} \frac{\eta'_k}{\eta_k} \\ &= \frac{\eta'_k}{\eta_1}, \end{aligned} \quad (\text{A.37})$$

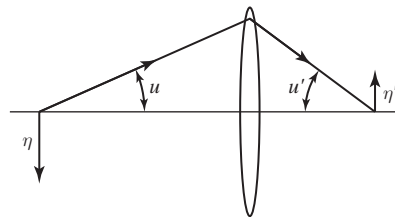


Figure A.9 The simplest form of the optical invariant H . Although shown for a simple lens it is equally applicable to any optical system with u and u' associated with the principal planes.

since $\eta'_1 = \eta_2$ and so on. This reduces to

$$m = \frac{n_1 u_1}{n'_k u'_k} \quad (\text{A.38})$$

when (A.29) is applied, since all the intermediate angles and refractive indices cancel.

An important concept in geometric optics is known as the optical or Lagrange invariant. The magnification is generally defined as the ratio of the image and object heights. Combining η'/η with (A.38) and identifying the indexes and angles with their equivalents in object and image space yields

$$\frac{\eta'}{\eta} = \frac{nu}{n'u'}, \quad (\text{A.39})$$

from which the optical invariant H is defined as

$$H \equiv nu\eta = n'u'\eta', \quad (\text{A.40})$$

as illustrated in Figure A.9. This brief introduction to the concept of an optical invariant does not provide the reader with an appreciation of its power. Optical invariants are such a critical concept in optics, employed to quantify the amount of light that is transmitted through an optical system in the absence of losses and in the development of the Seidel aberrations, that Welford (1986) devotes an entire chapter to them.

Paraxial ray tracing enables any optical system to be analysed to first order where the size and location of the image is determined. This is fundamentally a numerical process, rather than an algebraic one, with (A.32) and (A.33) applied recursively. Once the ray tracing is complete the system power and the location of the principal planes are calculated. The system can then be treated as an ideal imager and the formalism developed in Section A.2 is applied.

A.4

The Limiting Aperture

So far we have only been concerned with the location and the size of the image produced by an optical system, but we would also like to know the image irradiance as well. This requires the identification of the limiting aperture of the system. It is intuitive that

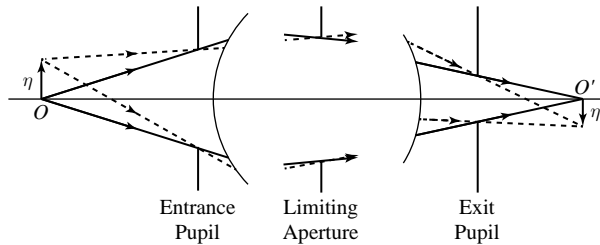


Figure A.10 Limiting aperture and pupils for an arbitrary system.

the amount of light that any optical system transmits is proportional to the area of the optical elements but we must determine which area, for a multi-element system, sets the transmission limit. That particular area is known as the limiting aperture or aperture stop and it can be the rim of an optical element or an appropriately placed aperture.

The single-lens reflex camera, as a familiar example, has a lens composed of several optical elements and an adjustable aperture typically somewhere in the middle that is the aperture stop. The limiting aperture is apparent when one looks into the camera lens from either the front or back sides. What is actually being seen are images of the limiting aperture, which are known as the entrance and exit pupils, respectively. For example, the entrance pupil is the image of the adjustable aperture made by the optical elements between the aperture and the front of the lens. The pupils are therefore conjugates of the aperture stop and of each other. Figure A.10 shows an arbitrary optical system with the entrance and exit pupils illustrated along with the associated light cones from an object and to an image. The critical concept is that all the rays that make it to the image must pass through the entrance and exit pupils.

There are two paraxial rays that have particular importance in the Gaussian description of any optical system. The first is the *marginal ray*, a ray from an axial object point that passes infinitesimally close to the edge of the limiting aperture and is subsequently imaged as the axial image point. Any rays with a larger angle to the optical axis will be obstructed, or vignetted, by the limiting aperture. The marginal ray will also just pass the edges of the entrance and exit pupils. Additionally, this ray determines the location of the image and the size of the pupils. The second paraxial ray is the *principal ray*, the ray that travels from the top of the object, through the centers of the pupils and limiting aperture, finally to the top of the image. This ray is often called the chief ray. The principal ray determines the locations of the pupils and the size of the image or field. Note that if the aperture stop is varied in size, the pupils will change but the object or image heights are unaffected.

A.4.1 Image Irradiance and the F-Number

The stage has been set to determine the image irradiance and to introduce the important concept of the F-number. This is a critical first step in the performance modeling of a real optical system. It has been shown that the light accepted by an optical system must pass through the pupils with the marginal ray at the limiting paraxial angle. Here we

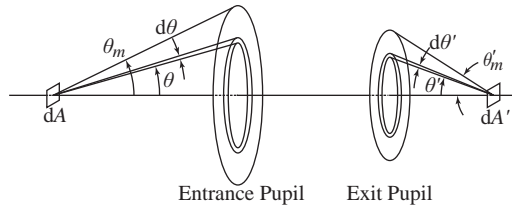


Figure A.11 The on-axis geometry for the flux accepted by the entrance pupil and transmitted from the exit pupil.

are required to make the transition from paraxial quantities to the finite angles encountered in real systems. The connection between real and paraxial rays, which requires justification through aberration theory, will not be presented here in any detail, merely motivated. The discussion that follows is based upon that given in Slater (1980).

Consider an axial, uniform and isotropic radiator of area dA producing a radiance L that is imaged into an area dA' as illustrated in Figure A.11. The size of the image is related to the object size through the linear magnification with

$$dA' = dx' dy' = m dx \times m dy = m^2 dA \quad (\text{A.41})$$

or

$$m^2 = \frac{dA'}{dA} \quad (\text{A.42})$$

for the magnification of the area.

The flux at the entrance pupil is related to that at the exit pupil. The entrance pupil subtends the marginal ray angle θ_m with the corresponding angle θ'_m subtending the exit pupil. The radiance from the source is given by (2.52) which, upon rearrangement, is

$$d^2\Phi = L dA \cos \theta d\omega \quad (\text{A.43})$$

for the flux accepted by an infinitesimal solid angle of the entrance pupil. Integrating over the entrance pupil yields

$$d\Phi = L dA \int_0^{2\pi} \int_0^{\theta_m} \cos \theta \sin \theta d\theta d\phi = \pi L dA \sin^2 \theta_m, \quad (\text{A.44})$$

where 2.48 has been applied and L is taken outside the integral since it is uniform and isotropic and therefore a constant. For a lossless system this same flux will be output at the exit pupil and form the image, albeit with a different geometry. A similar equation for the exit pupil flux is

$$d\Phi = \pi L' dA' \sin^2 \theta'_m \quad (\text{A.45})$$

where L' is the radiance incident upon dA' .

An underlying assumption is that the optical system has near-perfect performance so that the flux from dA is contained within dA' . This is assured by relating $\sin \theta_m$ to $\sin \theta'_m$ through the Abbe sine condition from aberration theory. The sine condition is

$$\frac{\sin \theta_m}{u} = \frac{\sin \theta'_m}{u'}, \quad (\text{A.46})$$

where u and u' are the paraxial marginal angles. In terms of the as yet undefined optical aberrations, this means that if (A.46) is satisfied and the system has no spherical aberration, then there is no coma or other aberrations linear in the field. We will defer the discussion of the aberration forms until Section A.7 and assume that (A.46) holds. In our case this is a rather good assumption, since excellent aberration control is required for optimal imaging spectrometer performance.

In order to derive the image irradiance, (A.46) will be rewritten in terms of the magnification by applying (A.38) yielding

$$m = \frac{u}{u'} = \frac{\sin \theta_m}{\sin \theta'_m} \quad (\text{A.47})$$

for an optical system in air. The image irradiance is obtained by combining (A.42), (A.44), (A.45), and (A.47) to produce

$$E' = \frac{d\Phi}{dA'} = \pi L \sin^2 \theta'_m = \pi L (\text{NA})^2, \quad (\text{A.48})$$

where $\sin \theta'_m$ has been identified as the numerical aperture (NA).

Notice that if the aberrations in the optical system are sufficiently well controlled that the Abbe sine condition holds, then the magnification is the same regardless of the sizes of θ_m and θ'_m . This is a critical point that merits some additional discussion. From (A.47), an alternative form for the magnification is

$$m = \frac{\sin \theta_m}{\sin \theta'_m} = \frac{h_p/l_m}{h'_p/l'_m} = \frac{l'_m}{l_m}, \quad (\text{A.49})$$

where the marginal ray distances, l_m and l'_m , are related to the principal plane heights, h_p and h'_p . Also, the fact that conjugate points on the principal planes, h_p and h'_p in this case, have unit magnification has been used. Note we have ignored our sign convention here (θ_m and θ'_m have opposite signs) since there is no set convention for the numerical aperture or the F-number defined below. Paraxially, the magnification is equivalently expressed as

$$m = \frac{l'}{l}, \quad (\text{A.50})$$

where (A.19) and (A.27) have been used for a system in air. This is equivalent to applying the small angle (paraxial) approximation to (A.49). Combining these last two equations yields

$$\frac{l_m}{l} = \frac{l'_m}{l'}, \quad (\text{A.51})$$

which relates the marginal to the axial distances. For an object at infinity, l_m/l converges to one and

$$l'_m = l' = f', \quad (\text{A.52})$$

where the image distance has been identified as the image focal length. The critical consequence of (A.52) is that the principal plane is not a plane, but a spherical surface of radius f' , as illustrated in Figure A.12. A similar argument holds for an image at

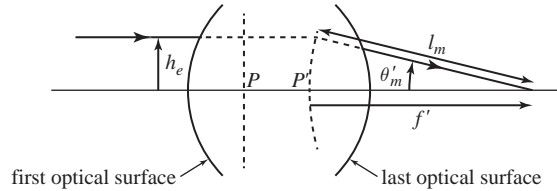


Figure A.12 The modification of the second principal plane for an object at infinity.

infinity. Even though the consequences of the sine condition have been developed for an on-axis object point, they also apply off-axis for fields that are not too large. An intuitive development of the Abbe sine condition that is well worth reading is found in Mansuripur (2009).

Referring to Figure A.12, the numerical aperture is alternatively expressed as

$$\text{NA} = \sin \theta'_m = \frac{h_e}{f'} = \frac{D_e}{2f'}, \quad (\text{A.53})$$

where h_e and D_e are the entrance pupil radius and diameter respectively. The F-number N is defined as

$$N \equiv \frac{F}{D_e} = \frac{1}{2(\text{NA})}, \quad (\text{A.54})$$

where it is assumed that the system is in air so that f' equals F and the F-number is associated with an object at infinity. The F-number is also frequently expressed as F/N ; for example, a system where N is 3 is written as $F/3$, which equals the diameter of the entrance pupil. The image irradiance is rewritten as

$$E' = \frac{\pi L}{4N^2}, \quad (\text{A.55})$$

emphasizing the importance of the F-number in determining it. Often an optical system with a small F-number is referred to as “fast”, since in photography for a smaller N the camera shutter speed is faster to achieve the correct exposure in comparison to a larger N . An important point is that N describes the light cone and not the optical system. Occasionally (A.55) is written as

$$E' = \frac{\pi L}{4N^2 + 1}, \quad (\text{A.56})$$

which is the form that is derived using the paraxial approximation with flat principal planes where $\sin \theta'_m = h_e / \sqrt{f'^2 + h_e^2}$. This form is incorrect for well-designed imagers or imaging spectrometers.

The F-number can be applied to the case of finite conjugates with a little modification. As illustrated in Figure A.13, the marginal angle is related to the finite conjugates through

$$\sin \theta'_m = \frac{D_p}{2l'_m} = \frac{D_p}{2l'} = \frac{D_p}{2(1-m)f'}, \quad (\text{A.57})$$

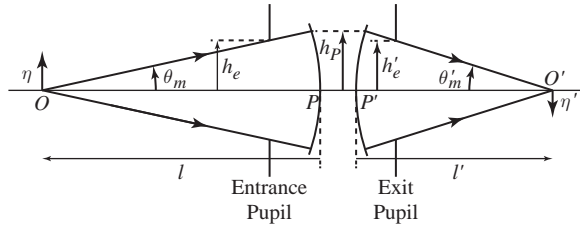


Figure A.13 Finite conjugate geometry.

where (A.17) has been used. For a typical system, h_p and h_e are about equal since the object distance is usually large compared to the focal length. This enables (A.57) to be rewritten as

$$\sin \theta'_m = \frac{D_p}{2(1-m)f'} \approx \frac{D_e}{2(1-m)f'} = \frac{1}{2N(1-m)} \quad (\text{A.58})$$

to good approximation for a system in air. Here $N(1-m)$ is regarded as an effective F-number and replaces N in (A.55). This is not used in remote sensing, since the object is effectively at infinity and therefore the linear magnification is no longer a useful concept.

A.4.2 Real and Paraxial Rays

Up to this point, with the exception of the discussion in Section A.4.1, we have treated all the quantities as paraxial. The angles are therefore infinitesimal, but in a real optical system this isn't true, and, in calculations, finite quantities are used. How is this reconciled? For a well-corrected optical system the paraxial angles are connected to the finite angles by a pair of simple formulas that are presented here without proof. The interested reader is encouraged to review the journal article by Hopkins (1991) for a full discussion, which goes into the limitations where the difference between the paraxial and real rays can be quite large.

The Abbe sine condition (A.46) also defines the relationship between the marginal ray, which is paraxial, and the real ray just passing the edge of the pupils and aperture stop for a well-corrected optical design. We define the relationship between u , the paraxial marginal angle, and θ_m , the actual marginal angle, to be

$$u = \sin \theta_m, \quad (\text{A.59})$$

and similarly for the image space marginal angle. In this context, u is thought of as a variable rather than a true angle.

The principal angle is related to the finite quantities through

$$\bar{u} = \tan \theta_p, \quad (\text{A.60})$$

where \bar{u} and θ_p are the paraxial and finite principal angles. A bar is customarily used to denote quantities associated with the principal ray, such as \bar{u} here. The finite principal angle represents the field of the optical system. For example, in a digital camera the image is in focus at the focal plane array (FPA) with the angle from the exit pupil to the

edge of the array defining the limits of the photograph, or field. The edges of the FPA, or a mask mounted immediately in front of it, form the field stop: the stop that limits the image size. Again, \bar{u} is interpreted as a variable and (A.60) is used to calculate the paraxial quantities. Equation (A.60) is only true if the magnification is constant across the field (there is no distortion).

A.4.3 Off-Axis Image Irradiance

The derivation of (A.55) was for an axial source of size dA_o ; however, real objects and images are extended. In Figure A.14 our uniform and isotropic radiator has been moved off-axis. Consider an infinitesimal area element of the entrance pupil illuminated by the source of area dA_o . The flux through the area dA_j in the entrance pupil is

$$d^2\Phi_j = L dA_o \cos \theta_j d\omega_j = L dA_o \cos \theta_j \frac{dA_j \cos \theta_j}{r_j^2} = L \frac{dA_o dA_j}{l_e^2} \cos^4 \theta_j, \quad (\text{A.61})$$

where θ_j is the angle between the normal to dA_j and the ray from dA_o to dA_j , r_j is the distance along the ray connecting the two areas, and l_e is the distance along the optical axis between the two infinitesimal areas, which is related to r_j since $\cos \theta_j = l_e/r_j$.

The flux through the entrance pupil is obtained by summing over its area or

$$d\Phi = L \frac{dA_o}{l_e^2} \int dA \cos^4 \theta \quad (\text{A.62})$$

which is approximated as

$$d\Phi = L \frac{dA_o}{l_e^2} A_e \cos^4 \theta_p, \quad (\text{A.63})$$

where θ_p is the principal ray angle and A_e is the area of the entrance pupil. For a lossless system, this flux will be incident on the area dA'_o which equals $m^2 dA_o$ from (A.42). The image irradiance at the edge of the field is therefore

$$E'(\theta_p) = \frac{d\Phi}{dA'_o} = \frac{LA_e}{m^2 l_e^2} \cos^4 \theta_p = E'_o \cos^4 \theta_p, \quad (\text{A.64})$$

demonstrating the $\cos^4 \theta$ roll-off as a function of field angle. It has been assumed that the magnification is constant across the field. Equation (A.63) is a good approximation for optical systems with relatively large F-numbers.

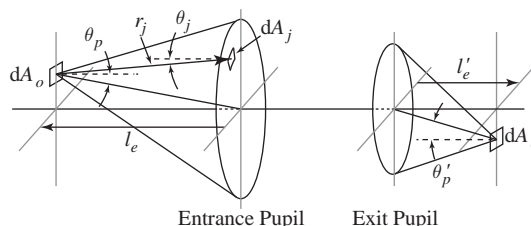


Figure A.14 Off-axis illumination geometry.

Table A.1 The surface curvatures and the distances with the associated indexes of refraction for a Cooke Triplet. The limiting aperture has a radius of 3.744 mm and the indexes are at $\lambda = 587.6 \text{ nm}$.

curvature	value(mm^{-1})	distance	value(mm)	index
c_{11}	0.0646	d_1	3	$n_1 = 1.5168$
c_{12}	-0.0058	d_2	5.6742	1
c_{21}	-0.0502	d_3	1	$n_2 = 1.62$
c_{22}	0.0724	d_4	1.5	1
c_{31}	0.0249	d_5	3.5167	1
c_{32}	-0.0661	d_6	3	$n_1 = 1.5168$

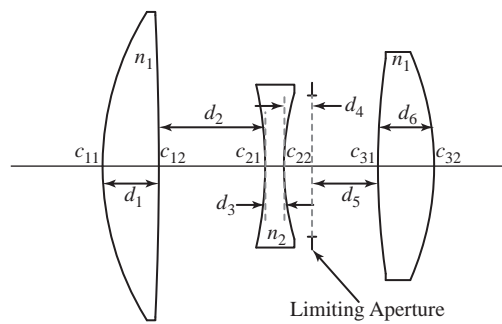


Figure A.15 The Cooke Triplet.

A.5 Example: The Cooke Triplet

The bare bones of the theory of Gaussian optics have been presented thus far and, at this point, it is appropriate to perform a sample calculation to tie it all together. The example we will use is an early but successful camera lens design known as the Cooke Triplet invented by H. D. Taylor in 1891 who worked at the telescope manufacturer T. Cooke and Sons of York in northern England (Kingslake, 1989).

The Cooke Triplet has two positive lenses on either side of a negative lens as in Figure A.15. The positive lenses are composed of a glass with a lower index of refraction, known as a crown glass, while the center, negative lens is made of a flint glass with a high index of refraction. An aperture stop is inserted after the negative lens. The numerical values of the various lens surface curvatures, the distances between adjacent surfaces, and also between the two adjacent surfaces and the stop are listed in Table A.1 and identified in Figure A.15. The aperture radius, h_a , is 3.744 mm.

The procedure to determine the location of the image principal plane is to perform paraxial ray tracing by repeated applications of (A.32) and (A.33) for an object at infinity, as illustrated in Table A.2 using the marginal ray. The first and third columns are the specific applications of the refraction and transfer equations respectively, with the exception of the last entry in the third column, which is the position of the principal

Table A.2 Paraxial ray tracing to determine the image principal plane. The entrance pupil radius, h_e , is 5 mm and $d_{45} \equiv d_4 + d_5$.

angle variable	value	height or distance	value(mm)
u_1	0	$h_1 = h_e$	5
$u'_1 = -\frac{1}{n_1} h_e c_{11}(n_1 - 1) = u_2$	-0.11	$h_2 = h_e + d_1 u'_1$	4.67
$u'_2 = n_1 u_2 - h_2 c_{12}(1 - n_1) = u_3$	-0.1807	$h_3 = h_2 + d_2 u'_2$	3.6446
$u'_3 = \frac{1}{n_2} [u_3 - h_3 c_{21}(n_2 - 1)] = u_4$	-0.0415	$h_4 = h_3 + d_3 u'_3$	3.6031
$u'_4 = n_2 u_4 - h_4 c_{22}(1 - n_2) = u_5$	0.0944	$h_5 = h_4 + d_{45} u'_4$	4.0768
$u'_5 = \frac{1}{n_1} [u_5 - h_5 c_{31}(n_1 - 1)] = u_6$	0.0277	$h_6 = h_5 + d_6 u'_5$	4.1599
$u'_6 = n_1 u_6 - h_6 c_{32}(1 - n_1)$	-0.1	$\delta' = (h_e - h_6)/u'_6$	-8.3992

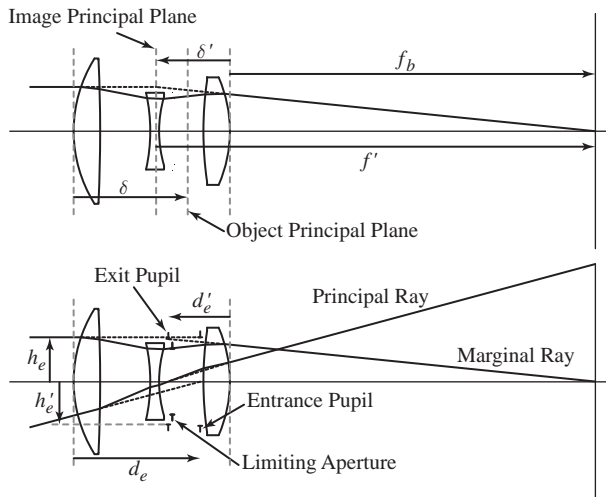


Figure A.16 Illustration of paraxial ray tracing to determine the image principal plane and the pupil locations and sizes.

plane relative to the last surface, δ' , determined from (A.34). The application of (A.34) requires the height of the entrance pupil, which is determined by finding the image of the limiting aperture in object space. In this case, paraxial ray tracing yields $h_e = 5$ mm for the radius of the entrance pupil. The focal length is calculated using the transfer equation to determine the back focal length, the distance from the last surface to the axial focal point given by $f_b = -h_6/u'_6$, added to the absolute value of δ' yielding $f' = F = 49.992$ mm. The F-number is calculated from (A.54) and is 4.9992, or about 5. Figure A.16 illustrates the ray tracing results.

The reader is encouraged to perform similar calculations to determine the positions and sizes of the entrance and exit pupils and also to find the object principal plane. The field of view, described by (A.60), is 15° . To determine the entrance pupil position and size it may be helpful to turn the system around and trace rays from the edge and the

Table A.3 Paraxial ray tracing to determine the entrance and exit pupils and the object principal plane. The front focal length is measured from the first surface. The other distances are identified in Figure A.16.

Pupils				Object Principal Plane	
location	value (mm)	radius	value (mm)	parameter	value (mm)
d_e	14.4066	h_e	5	δ	12.9856
d'_e	-7.0175	h'_e	4.862	f	-37.006

center of the aperture stop from left to right through the negative and the first positive lens. If you choose to do it this way, pay close attention to the signs. The object principal plane is similarly determined by turning the system around and repeating the procedure in Table A.2. The exit pupil is traced using the stop and just the last positive lens as drawn. Table A.3 summarizes the results of those calculations and again refer to Figure A.16.

A.6

Afocal Systems

We are primarily interested in systems that form an image at a particular location, but there are important cases where both the object and the image that apply to imaging spectrometers are at infinity. In these systems the principal planes are not useful concepts. Additionally, the system power, given by (A.36), is zero since u'_k is zero. Zero power systems are called afocal. The magnification is a better descriptor since an object height η is imaged to an image height η' .

A simple example, a Kepler telescope, will be used to illustrate an afocal system (King, 1955). This telescope has an objective lens and an eyepiece with corresponding effective focal lengths F_{obj} and F_{eye} . The distance between the two lenses is the sum of the two focal lengths, or $d = F_{\text{obj}} + F_{\text{eye}}$. The upper diagram in Figure A.17 shows the telescope as it is typically used while the lower diagram is more useful for the derivation of the system magnification.

We will digress briefly here to develop the formalism to describe a thin lens, a lens with zero thickness. The thin lens approximation is handy for quick but insightful calculations of system parameters. Again, we will apply the paraxial ray tracing formulae but the transfer equation reduces to $h_{j+1} = h_j$ since d_j is zero. For a thin lens in air with a refractive index n and incident ray height h , (A.32) reduces to

$$nu'_1 - u_1 = -hc_1(n - 1) \quad (\text{A.65})$$

for the first surface and

$$u'_2 - nu_2 = u'_2 - nu'_1 = -hc_2(1 - n) \quad (\text{A.66})$$

for the second, since $u'_1 = u_2$ and the ray height doesn't change. Combining (A.65) and (A.66) yields

$$u'_2 - u_1 = -h(n - 1)(c_1 - c_2) \Rightarrow u' - u = -hK, \quad (\text{A.67})$$

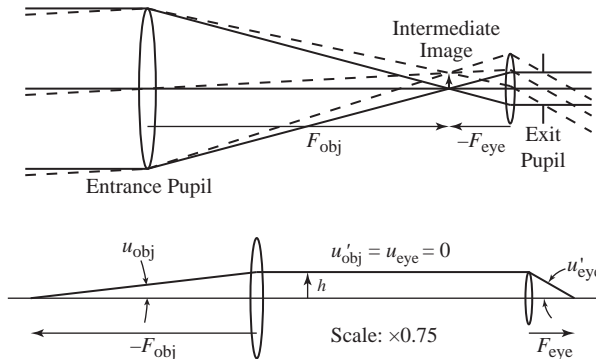


Figure A.17 The Kepler telescope. The upper diagram shows its normal usage with an object at infinity. The rim of the objective lens is both the limiting aperture and the entrance pupil. The exit pupil is shown on the right and, for a well-designed telescope, is the size of a dark adapted eye pupil (~ 5 mm). This form, with rather extensive adaptation for aberration control, is used for modern binoculars. Remember that the equivalent focal length F is related to the focal lengths through (A.27) and is always positive for a converging lens.

where u_1 and u'_2 have been identified as u and u' , the incident and exiting angle variables for the ray, and $(n - 1)(c_1 - c_2)$ is the thin lens power K . Note that for a thin lens the two principal planes are coincident and at the lens center.

Referring to the bottom diagram in Figure A.17, the Kepler telescope is now treated as a system of two thin lenses with $u'_\text{obj} = u'_\text{eye} = 0$ for the horizontal ray between them. The expressions for them are therefore

$$u'_\text{obj} - u_\text{obj} = -h_\text{obj}K_\text{obj} \Rightarrow u_\text{obj} = \frac{h_\text{obj}}{F_\text{obj}} \quad (\text{A.68})$$

$$u'_\text{eye} - u_\text{eye} = -h_\text{eye}K_\text{eye} \Rightarrow u'_\text{eye} = -\frac{h_\text{eye}}{F_\text{eye}}, \quad (\text{A.69})$$

where (A.28) has been applied. The transfer between the two thin lenses is trivial since the ray travels horizontally so (A.33) reduces to $h_\text{eye} = h_\text{obj}$. The linear magnification is written using (A.19) by replacing $n_1 u_1$ with $n_\text{obj} u_\text{obj}$ and $n'_k u'_k$ with $n'_\text{eye} u'_\text{eye}$, or

$$m = \frac{n_\text{obj} u_\text{obj}}{n'_\text{eye} u'_\text{eye}} = \frac{u_\text{obj}}{u'_\text{eye}} = -\frac{F_\text{eye}}{F_\text{obj}} \quad (\text{A.70})$$

for a telescope in air.

A better measure of the magnification is the angular magnification defined as the angular image size divided by the angular object size. Applying (A.60) yields

$$m_{\text{ang}} \equiv \frac{\bar{u}'}{\bar{u}} = \frac{\tan \theta_p'}{\tan \theta_p}, \quad (\text{A.71})$$

as illustrated in Figure A.18. It can be shown that

$$m_{\text{ang}} = \frac{1}{m} = -\frac{F_\text{obj}}{F_\text{eye}} = \frac{h_e}{h'_e}, \quad (\text{A.72})$$

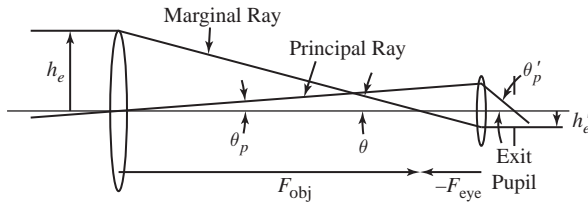


Figure A.18 Angular magnification geometry.

where $\tan \theta = -h_e/F_{\text{obj}} = h'_e/F_{\text{eye}}$ has been used. The ratio of h_e to h'_e is known as the beam compression ratio. Equation (A.72) applies to any afocal system.

A.7 Aberration Theory

Thus far the location, size, and irradiance of an image have been addressed but not the image quality. A true image is imperfect or aberrated with the image of a point on the object blurred or in the wrong location, or both, when compared to the Gaussian image point. There are two broad categories of aberrations: those that are caused by the changing index of refraction as a function of wavelength for a lens material and those that are caused by the departure of a monochromatic wavefront from strict sphericity at the Gaussian image point, due to either light refraction or reflection from a powered surface. The diversity of imaging spectrometer designs include optical forms that are composed only of mirrors and other forms that employ both mirrors and lenses. Each design must be evaluated for aberration control. We will focus on the theory of monochromatic aberrations in this section and address chromatic aberrations when they are encountered in a specific design.

It is beyond our scope to treat monochromatic aberrations in detail but, again, the interested reader is directed to Welford (1986), where aberration theory is fully developed. Another worthwhile resource is Hopkins (1950). The presentation here will be adequate to provide a conceptual understanding but will not be sufficient to perform any detailed calculations. The primary aberrations will be discussed as they are important in order to understand the challenges associated with the spatial-spectral uniformity requirements for an imaging spectrometer.

A.7.1 The Aberration Function

Recall that ideal image formation occurs when a spherical wavefront is centered on an image point. Wavefront aberrations are the result of the departure of the actual wavefront from this spherical ideal as illustrated in Figure A.19. The reference sphere, which is centered on the Gaussian image point and intersects the optical axis at the center of the exit pupil, represents the ideal case. The deviation of the real wavefront from the reference sphere is captured by the wavefront aberration function W , which describes the difference between the wavefront and the reference sphere as a function of pupil and

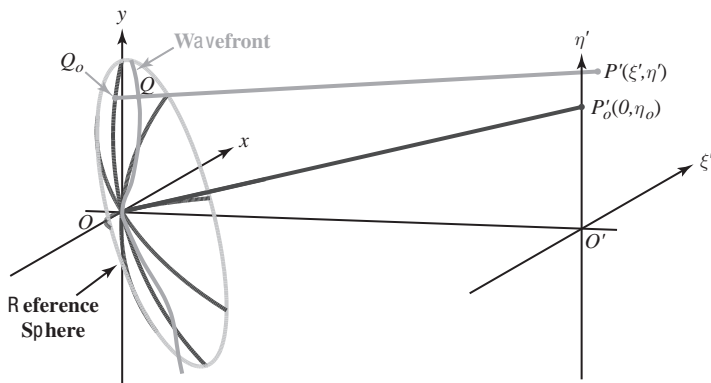


Figure A.19 Wavefront aberration and the transverse ray aberration. After Welford (1986).

field positions. An underlying assumption is that the difference between the wavefront and the reference sphere is small. The derivation here will be limited to optical systems that are rotationally symmetric about the optical axis and it is assumed that the functions that describe the optical interfaces will be continuous through their second derivatives.

The coordinate systems that will be used in the following discussion are defined for the exit pupil, the x - and y -axes in Figure A.19, and for the Gaussian image plane, the ξ' - and η' -axes. Figure A.19 shows a slice of the wavefront taken along the y -axis at the exit pupil with a local ray perpendicular to the wavefront at Q intersecting the Gaussian image plane at $P'(\xi', \eta')$. The Gaussian image point and center of the reference sphere is at $P'_o(0, \eta')$. The wavefront error W is the optical path along the ray between Q_o and Q , or nQ_oQ where n is the index of refraction of the medium. The difference between $P'(\xi', \eta')$ and $P'_o(0, \eta')$ is the transverse ray aberration. In the discussion that follows the primes will be left off with the understanding that we are referring to the image coordinates.

The wavefront is determined through finite ray tracing. The process is analogous to paraxial ray tracing with the application of a set of refraction and transfer equations to describe the ray in all three dimensions and with finite quantities. In this case, the refraction equations, one for each dimension, utilize the exact form of Snell's law that has been expressed in terms of directional cosines. The transfer equations are a generalization of (A.33), again using the directional cosines for the three-dimensional transfer from one surface to the next (Welford, 1986). The wavefront is subsequently determined by performing a two-dimensional polynomial interpolation to a finite number of points located at the same optical path length, and with every point corresponding to a different traced ray distributed within the limiting aperture. This interpolated wavefront coincides with the reference sphere at the center of the exit pupil.

The aberration description is restricted to cylindrically symmetric systems enabling us to simplify the problem through symmetry arguments. The aberration function will, in general, depend upon both the pupil and the field coordinates since optical systems typically display off-axis aberrations. These four coordinates, x and y in the exit pupil and ξ and η for the image point, are all that are required to specify W . The cylindrical

symmetry requires that the nature of the aberrations must remain unchanged for a rigid rotation of pupil and image axes about the optical axis. This implies that W can only be a function of rotationally invariant combinations of x , y , ξ and η .

It is easiest to determine the possible combinations by converting from Cartesian to polar coordinates. Following the normalization for the relative aperture and field in Hopkins (1950), for the pupil the relations are

$$x = r \sin \theta \quad y = r \cos \theta$$

with r normalized to the edge of the pupil using $r \equiv R/h_e$ where the radial distance is from the center of the pupil to the point in the pupil axes that corresponds to a particular ray piercing the reference sphere and is given by $R^2 = x^2 + y^2$. Similarly, for the image

$$\xi = \rho \sin \phi \quad \eta = \rho \cos \phi$$

with the normalization given by $\rho \equiv I/I_{max}$ where I is the radial distance of the image point, I_{max} is the maximum size of the field, and $\rho^2 = \xi^2 + \eta^2$. The aberration function is therefore expressed as

$$W(x, y, \xi, \eta) = W(r, \theta, \rho, \phi)$$

with W being a length and r and ρ being dimensionless quantities.

If the axes that describe the pupil and the image are rotated by the same fixed angle $-\alpha$, the aberration function becomes a function of the new coordinate system, but is equivalent to the original W . Note that this does not change the values of r and ρ . The new angles are $\theta_n = \theta + \alpha$ and $\phi_n = \phi + \alpha$. It can easily be shown that

$$\sin^2 \theta_n + \cos^2 \theta_n = \sin^2 \theta + \cos^2 \theta = 1,$$

which is equivalently expressed as $x_n^2 + y_n^2 = x^2 + y^2 = r^2$ and therefore r^2 is invariant. A similar argument applies to the image axes and ρ^2 is also invariant.

The difference between θ and ϕ in the new and old coordinate systems is also equivalent, therefore

$$\rho \cos(\theta_n - \phi_n) = \rho \cos(\theta - \phi),$$

implying that

$$\rho r(\cos \theta_n \cos \phi_n + \sin \theta_n \sin \phi_n) = \rho r(\cos \theta \cos \phi + \sin \theta \sin \phi) \quad (\text{A.73})$$

is also rotationally invariant. A similar argument follows from taking the sine of the differences yielding

$$\rho r(\sin \theta_n \cos \phi_n - \cos \theta_n \sin \phi_n) = \rho r(\sin \theta \cos \phi - \cos \theta \sin \phi). \quad (\text{A.74})$$

These last two equations are reconciled by adding two additional constraints. It is sufficient to choose the axes so that ξ , and therefore ϕ , are zero, since the system can always be rotated to make it so. Also, W must remain unchanged for points that are symmetric about the plane defined by the vertical, or y -coordinate, pupil axis and the η -axis. Therefore, only functions of $\cos \theta$ are allowed since $\sin \theta$ does not equal $\sin(-\theta)$.

Applying these two constraints to (A.73) and (A.74) eliminates the second equation with the acceptable function of the form $\rho r \cos \theta$.

Finally, it is assumed that W can be expanded as a power series in ρ^2 , r^2 , and $\rho r \cos \theta$ with terms of the form

$$(\rho^2)^i (r^2)^j (\rho r \cos \theta)^k \quad i, j, k = 0, 1, 2, \dots$$

or

$$\rho^{2i+k} r^{2j+k} \cos^k \theta \equiv \rho^l r^m \cos^n \theta \quad \text{where } \left\{ \begin{array}{l} l = 2i + k \\ m = 2j + k \\ n = k \end{array} \right\} = 0, 1, 2, \dots$$

and the series is given by

$$W(r, \theta, \rho) = \sum_{l,m,n} {}_l c_{mn} \rho^l r^m \cos^n \theta, \quad (\text{A.75})$$

with the coefficient for each term having length dimensions and labeled as ${}_l c_{mn}$ where the l -index corresponds to the field portion and the m - and n -indices to the pupil (Hopkins, 1950).

Equation (A.75) can be simplified since several coefficients will be zero. First, ${}_0 c_{00}$ will vanish since a constant difference between the wavefront and the reference sphere represents the difference between two concentric spheres. Also, coefficients associated with the principal ray ($r = 0$) are by definition zero since the wavefront and the reference sphere are coincident at the center of the exit pupil. This coincidence implies that there can be no terms that are independent of the exit pupil coordinates (the reference sphere and the wavefront must depart somewhere for there to be aberrations) and, therefore, all of the coefficients of the form ${}_l c_{00}$ will also vanish.

There are two terms that are not true aberrations but are shifts in the position of the focus. Intuitive arguments are presented to motivate this classification with the details in the references. The first is the transverse focal shift given by ${}_1 c_{11} \rho r \cos \theta$. Considering this term in isolation and at the full pupil and field, as θ is varied W goes from ${}_1 c_{11}$, to 0, to $-{}_1 c_{11}$, and back to 0. This is a lateral shift in the image point directly proportional to its distance from the axis, and requires an adjustment in the Gaussian image size but does not produce a degraded image. The second term is the longitudinal focal shift, ${}_0 c_{20} r^2$. Here the real wavefront has additional curvature and corresponds to a change in the focal position along the optical axis. This is eliminated by changing the radius of the reference sphere. Both of these effects are illustrated in Figure A.20.

Aberrations are classified in terms of orders given by

$$N = \frac{1}{2}(l + m) - 1,$$

with $N = 1$ corresponding to the primary or Seidel aberrations. Table A.4 shows the focal shifts and the Seidel aberration formulae. These formulae are of little practical use since the coefficients are not known as a function of optical design parameters, but they are of great conceptual utility. The primary aberrations are named after Seidel because

Table A.4 The focus shifts and the Seidel aberration terms. The focal shifts correspond to $N = 0$.

$lc_{mn} \rho^l r^m \cos^n \theta$	name
$1c_{11} \rho \cos \theta$	transverse focal shift
$0c_{20} r^2$	longitudinal focal shift
$0c_{40} r^4$	spherical aberration
$1c_{31} \rho r^3 \cos \theta$	coma
$2c_{22} \rho^2 r^2 \cos^2 \theta$	astigmatism
$3c_{11} \rho^3 r \cos \theta$	distortion
$2c_{20} \rho^2 r^2$	field curvature

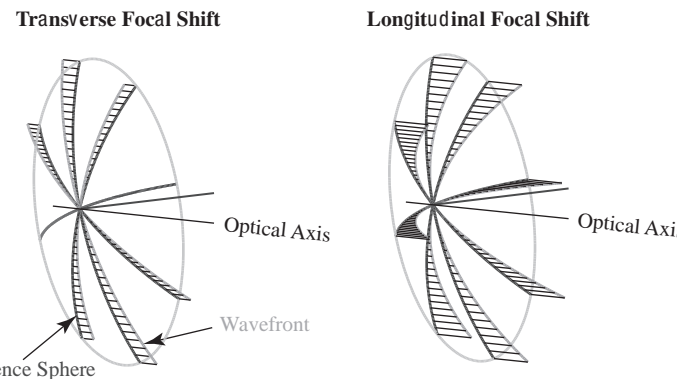


Figure A.20 Longitudinal and transverse focal shifts. In this figure and the next two, the darker gray surface represents the reference sphere with the circle illustrating the exit pupil diameter. The lighter gray surface is the wavefront. The dark gray projection line is to the Gaussian image point. The z -axis is positive along the optical axis with the x - and y -axes horizontal and vertical respectively (not illustrated).

he was the first to solve the problem of translating the heuristic forms presented here to forms that contain the construction parameters used to build an optical system. The practical forms are derived in Welford (1986).

The Seidel aberrations are valid for intermediate aperture and field angles where the higher-order terms in (A.75) can be neglected. Welford (1986) shows that the total wavefront aberration contributed by the Seidel aberrations are calculated by summing up the contributions from the individual optical surfaces. Thus the aberrations introduced by one surface can be cancelled by the aberrations introduced by another, enabling optical designs of high image quality. Additionally, a remarkable result of the full derivation is that the Seidel aberrations are calculated from the paraxial quantities.

A.7.2 Overview of the Seidel Aberrations

Optimized performance of an imaging spectrometer requires that the total aberration be highly controlled. The impact of aberrations is in both the spread in an image

point, known as the point spread function, and in its location. If an object point is perfectly imaged into an image point it is stigmatic. The Seidel aberrations are useful to illustrate both effects. It is noteworthy that spherical aberration is independent of the field point, and the field dependence of coma and astigmatism is only a scaling factor with the shape unchanged. These three—spherical aberration, coma and astigmatism—are all point aberrations and can be thought of as relative to the Gaussian image point. Distortion and field curvature, the field aberrations, do depend upon the field as the name implies, with the amount of aberration increasing as the field point location moves outward from the optical axis, but the shape of the wavefront is unaffected and stigmatic images of object points are produced, just in the wrong locations. Figure A.21 illustrates the point aberrations while Figure A.22 illustrates the field aberrations.

Spherical Aberration

This is the only on-axis aberration with no dependence on ρ and, both on- and off-axis, it is centered about the paraxial ray to the Gaussian image point. The top illustration in Figure A.21 shows the symmetric departure from the reference sphere for both the on- and off-axis cases. Note the rapid departure from the reference sphere as the edge of the exit pupil is approached due to the r^4 dependence. In the on-axis case illustrated on the right, the rays from different radii in the exit pupil will focus more prematurely for successively larger values of r for a positive ${}_0c_{40}$. The impact of spherical aberration can be somewhat mitigated by reducing the radius of the reference sphere to minimize the spot size.

Coma

The middle illustration in Figure A.21 shows both the wavefront aberration and the spot diagram for coma. Coma can be considered as an $r^3 \cos \theta$ term weighted by a ${}_1c_{31}\rho$ constant, evaluating the shape of the wavefront relative to a particular field point. Therefore, the wavefront has a cubic shape weighted by the cosine of the azimuthal angle in the exit pupil and is coincident with the reference sphere along the x -axis as shown on the left in Figure A.21.

One might erroneously conclude that the ray aberration corresponding to the wavefront along the x -axis would also be zero. Recall from vector calculus that the gradient of a function that describes a surface is perpendicular to the tangent plane at the point where the gradient is evaluated. The ray at a particular point is perpendicular to the wavefront and therefore the ray aberration, the departure of the location of the ray intersection in the image plane from the Gaussian image point, is proportional to the gradient of the wavefront (Welford, 1986). The wavefront has a finite gradient in the y direction across the x -axis, resulting in the ray aberration producing the illustrated spot pattern that is reminiscent of a comet. It isn't obvious from the figure, but considering rays originating from the numbered locations at the edge of the pupil, as depicted in the far right coma figure, the comatic circle is traced twice at the focal plane. Therefore, for example, the two rays from the locations labelled

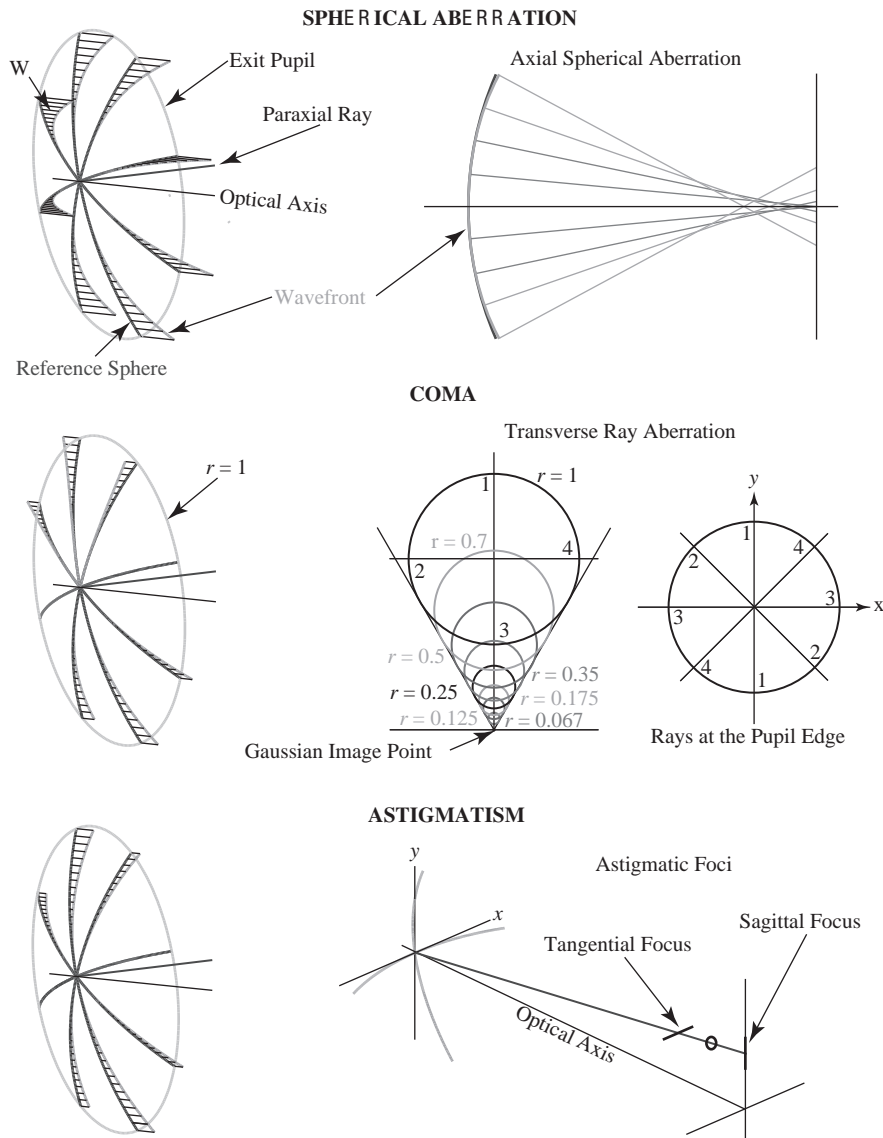


Figure A.21 Seidel point aberrations.

as “1” in the exit pupil intersect at the similarly labelled point in the comatic point image.

Astigmatism

The final Seidel point aberration is illustrated at the bottom of Figure A.21. Inspection of the figure shows that the departure of the wavefront from the reference sphere is cylindrical about the x -axis. This leads to a line focused at the Gaussian image point called the *sagittal focus*: the focus due to the bilateral symmetry about the y -axis. The

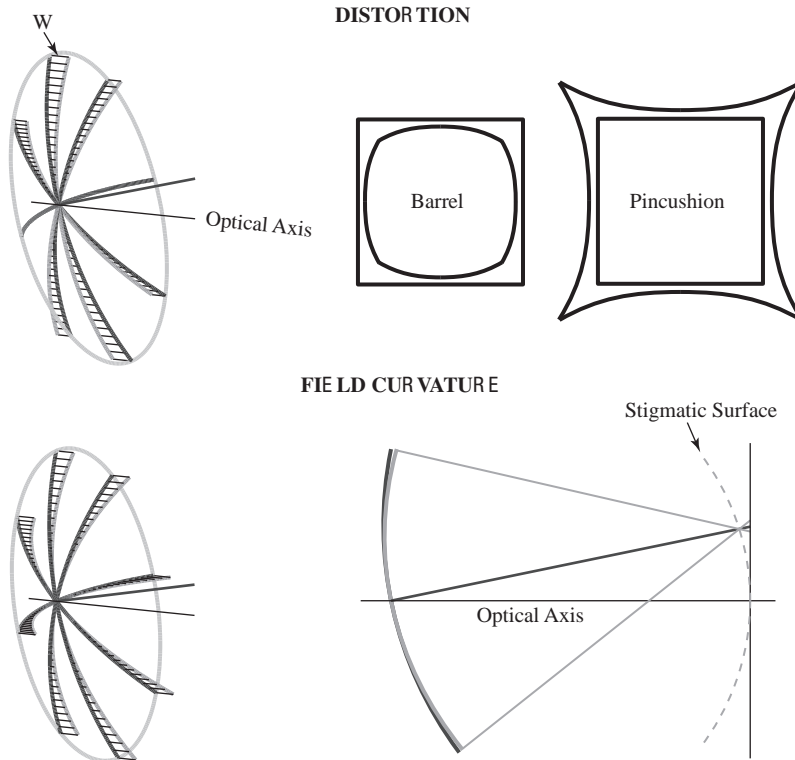


Figure A.22 Seidel field aberrations. The square in the distortion imagery corresponds to perfect imaging.

tangential focus, the line focused to the left of the sagittal focus, is due to the departure of the wavefront from the reference sphere in the y direction. A tangential ray is one that is confined to the plane containing the optical axis and the object point. The small circle between the two line foci is known as the circle of least confusion. The best focus is obtained by reducing the radius of the reference sphere to correspond to the circle of least confusion. The order of the sagittal and tangential foci depends upon the sign of $_{2}c_{22}$, with the tangential focus either in front of the Gaussian image plane for a positive $_{2}c_{22}$, as illustrated in Figure A.21, or beyond it for a negative $_{2}c_{22}$.

Distortion

The first Seidel field aberration is described by the distortion term $_{3}c_{11}\rho^3 r \cos \theta$, which is similar to $_{1}c_{11}\rho r \cos \theta$, the transverse focal shift term. Distortion is also a transverse focal shift but the shift is multiplied by ρ^2 , and therefore depends upon the distance of the object from the optical axis. The image is stigmatic, with the rays from a point on the object intersecting at a single point, but they are not in the correct locations. The two types of distortion, barrel and pincushion, depend upon the sign of $_{3}c_{11}$. The wavefront for barrel distortion, illustrated in the upper left of Figure A.20, corresponds to a positive $_{3}c_{11}$.

Field Curvature

The second field aberration is given by ${}_2c_{20}\rho^2r^2$, and comparison to the longitudinal focal shift, ${}_0c_{20}r^2$, shows that field curvature is also a longitudinal focal shift, but again multiplied by ρ^2 . This causes an object point to come into focus onto a curved image surface and leads to a progressively degraded image since it is invariably recorded on a flat detector positioned at the best focus.

A.7.3

Higher-Order Aberrations and the Abbe Sine Condition

The number of aberration terms increases rather rapidly as the order number increases. The classification of the higher-order terms in (A.75) is based upon an extension of the general types described in Table A.4. Spherical aberration types are independent of θ and of the field ($l = 0$). Comatic types are those that have odd powers of $\cos\theta$ and astigmatic types have even powers of $\cos\theta$. There is no equivalent terminology such as that applied to the Seidel aberrations for these higher-order terms.

Now that we have developed the basic aberration theory, let's return to the Abbe sine condition. There are two requirements for (A.46) to hold. The first is that all comatic terms of the form $\rho r^{\text{odd}} \cos\theta$, or

$$W_{\text{linear coma}} = \sum_{m \text{ odd}} {}_1c_{m1}\rho r^m \cos\theta, \quad (\text{A.76})$$

must add to zero. $W_{\text{linear coma}}$ has the same linear dependence in the field (ρ) and the same azimuthal variation in the exit pupil ($\cos\theta$) as Seidel coma. Additionally, there must be no spherical aberration. A system for which both spherical aberration and coma are corrected is referred to as *aplanatic*. An intuitive way of thinking about this result is that the principal planes are replaced by spheres that, near to the optical axis, coincide with the spherical wavefronts required for perfect imaging. The proof of (A.46) is presented in Welford (1986).

A.8

Summary and Further Reading

The basics of Gaussian optics have been presented in order to establish a foundation for the description of imaging spectrometers. Aberration theory is also introduced in a qualitative way in order to provide an appreciation of the difficulties associated with image formation in any optical system, particularly as the field of view is increased to well beyond the paraxial approximation. The pedagogical and technical literature on optics and optical design is vast and of high quality. The principles that underpin all optics and radiation are well described in Stone (1963) and the more ambitious reader is encouraged to consult the classic text by Born and Wolf (1999). The presentation of basic optics and optical phenomena in Jenkins and White (1976) is also recommended. Welford (1986) is a tremendous resource for both understanding Gaussian optics and for his presentation of aberration theory.

Problems

1. Develop the law of refraction from Fermat's principle.
2. Reproduce Figure A.5 for a converging optical system.
3. An afocal Galilean telescope is similar to the Kepler telescope illustrated in Figure A.17 except the eyepiece is a negative lens. Where is the image from the objective formed in this case? Perform the paraxial analysis of that design.

Bibliography

- S. A. Ackerman, K. I. Strabala, W. P. Menzel, R. A. Frey, C. C. Moeller, and L. E. Gumley. Discriminating clear sky from clouds with MODIS. *Journal of Geophysical Research*, 103(D24): 32141–32157, 1998.
- J. B. Adams and A. R. Gillespie. *Remote Sensing of Landscapes with Spectral Images: A Physical Modeling Approach*. Cambridge, UK: Cambridge University Press, 2006.
- J. B. Adams, M. O. Smith, and A. R. Gillespie. Imaging spectroscopy: Interpretation based on spectral mixture analysis. In C. M. Pieters and P. A. J. Englert, editors, *Remote Geochemical Analysis: Elemental and Mineralogical Composition*, Cambridge, UK: Cambridge University Press, 1993, pp. 145–166.
- J. B. Adams, M. O. Smith, and P. E. Johnson. Spectral mixture modeling: a new analysis of rock and soil types at the Viking Lander I site. *Journal of Geophysical Research*, 91: 8092–112, 1986.
- S. Adler-Golden, A. Berk, L. S. Bernstein, S. Richtsmeier, P. K. Acharya, M. W. Mather, G. P. Anderson, C. L. Allred, L. S. Jeong, and J. H. Chetwynd. FLAASH, a MODTRAN4 atmospheric correction package for hyperspectral data retrievals and simulations. In *Summaries of the Seventh Annual JPL Earth Science Workshop*, volume 1, January 1998. Pasadena, CA: Jet Propulsion Laboratory, California Institute of Technology, pp. 98–104.
- G. B. Airy. On the intensity of light in the neighbourhood of a caustic. *Transactions of the Cambridge Philosophical Society*, 6: 379–403, 1838.
- J. Aitchison and J. A. C. Brown. *The Lognormal Distribution Function*. Cambridge University Press, 1957.
- E. Alpaydin. *Introduction to Machine Learning*. Cambridge, MA: The MIT Press, 2010.
- M. J. Alvarado, V. H. Payne, E. J. Mlawer, G. Uymon, M. W. Shephard, K. E. Cady-Pereira, J. S. Delamere, and J. L. Moncet. Performance of the line-by-line radiative transfer model (lblrtm) for temperature, water vapor, and trace gas retrievals: recent updates evaluated with iasi case studies. *Atmos. Chem. Phys.*, 13: 6687–6711, 2013.
- N. Anderson, J. S. Czapla-Myers, N. Leisso, S. F. Biggar, C. Burkhardt, R. Kingston, and K. J. Thome. Design and calibration of field deployable ground-viewing radiometers. *Applied Optics*, 52(2): 231–240, 2013.
- T. W. Anderson. *An Introduction to Multivariate Statistical Analysis*, 3rd edition. New York, NY: John Wiley & Sons, 2003.
- C. M. Bachmann, T. L. Ainsworth, R. A. Fusina, M. J. Montes, J. H. Bowles, D. R. Korwan, and D. B. Gillis. Bathymetric retrieval from hyperspectral imagery using manifold coordinate representations. *IEEE Transactions on Geoscience and Remote Sensing*, 47(3): 884–897, 2009.
- C. M. Bachmann, T. L. Ainsworth, and R. A. Fusina. Exploiting manifold geometry in hyperspectral imagery. *IEEE Transactions on Geoscience and Remote Sensing*, 43(3): 441–454, 2005. ISSN 0196-2892. doi: 10.1109/TGRS.2004.842292.

- A. M. Baldrige, S. J. Hook, C. I. Grove, and G. Rivera. The ASTER spectral library: Version 2.0. *Remote Sensing of the Environment*, 113: 711–715, 2009a.
- A. M. Baldrige, S. J. Hook, C. I. Grove, and G. Rivera. The ASTER spectral library version 2.0. *Remote Sensing of Environment*, 113, 2009b.
- H. P. Baltes. On the validity of Kirchhoff's law of heat radiation for a body in a nonequilibrium environment. In E. Wolf, editor, *Progress in Optics XII*, North-Holland, 1976, pp. 3–25.
- C. B. Barber, D. P. Dobkin, and H. Huhdanpaa. The quickhull algorithm for convex hulls. *ACM Transactions on Mathematical Software*, 22 (4): 469–483, 1996.
- P. Y. Barnes, E. A. Early, and A. C. Parr. NIST measurement services: Spectral reflectance. Technical Report, NIST Special Publications 250–48, National Institute of Standards and Technology, 1998.
- J. A. Barsi, J. R. Schott, S. J. Hook, N. G. Raqueno, B. L. Markham, and R. G. Radocinski. Landsat-8 Thermal Infrared Sensor TIRS vicarious radiometric calibration. *Remote Sensing*, 6: 11607–11626, 2014.
- I. J. Barton and J. C. Scott. Remote measurement of surface pressure using absorption in the oxygen A-band. *Applied Optics*, 25(19): 3502–3507, 1986.
- A. Beil, R. Daum, G. Matz, and R. Harig. Remote sensing of atmospheric pollution by passive FTIR spectrometry. *Spectroscopic Atmospheric Environmental Monitoring Techniques*, 32: 32–45, 1998.
- R. Bell. *Introductory Fourier Transform Spectroscopy*. Elsevier, 2012.
- A. Berk, L. S. Bernstein, G. P. Anderson, P. K. Acharya, D. C. Robertson, J. H. Chetwynd, and S. M. Adler-Golden. MODTRAN cloud and multiple scattering upgrades with application to AVIRIS. *Remote Sensing of Environment*, 65(3): 367–375, 1998.
- A. Berk, P. K. Acharya, L. S. Bernstein, G. P. Anderson, P. Lewis, J. H. Chetwynd, and M. L. Hoke. Band model method for modeling atmospheric propagation at arbitrarily fine spectral resolution. Patent, 2008.
- L. S. Bernstein, X. Jin, B. Gregor, and S. M. Adler-Golden. Quick atmospheric correction code: algorithm description and recent upgrades. *Optical Engineering*, 51(11): 111719–1–111719–11, 2012.
- P. R. Bevington and D. K. Robinson. *Data Reduction and Error Analysis*, 3rd edition. McGraw-Hill Higher Education, 2003.
- L. Biehl and D. Landgrebe. Multispeca tool for multispectral–hyperspectral image data analysis. *Computers & Geosciences*, 28(10): 1153–1159, 2002.
- C. Biernacki, G. Celeux, G. Govaert, and F. Langrognet. Model-based cluster and discriminant analysis with the mixmod software. *Computational Statistics & Data Analysis*, 51 (2): 587–600, 2006.
- S. F. Biggar. Calibration of a visible and near-infrared portable transfer radiometer. *Metrologia*, 35: 701–706, 1998.
- S. F. Biggar, D. I. Gellman, and P. N. Slater. Improved evaluation of optical depth components from langley plot data. *Remote Sensing of Environment*, 32: 91–101, 1990.
- J. M. Bioucas-Dias and J. M. P. Nascimento. Hyperspectral subspace identification. *IEEE Transactions on Geoscience and Remote Sensing*, 46(8): 2435–2445, 2008. ISSN 0196-2892. doi: 10.1109/TGRS.2008.918089.
- J. M. Bioucas-Dias, A. Plaza, N. Dobigeon, M. Parente, Qian Du, P. Gader, and J. Chanussot. Hyperspectral unmixing overview: Geometrical, statistical, and sparse regression-based approaches. *IEEE Journal of Selected Topics in Applied Earth Observations and Remote Sensing*, 5(2): 354–379, April 2012. ISSN 1939-1404. doi: 10.1109/JSTARS.2012.2194696.

- BIPM et al. Evaluation of measurement data—guide to the expression of uncertainty in measurement. JCGM 100: 2008 GUM 1995 with minor corrections, 2008.
- C. M. Bishop. *Pattern Recognition and Machine Learning*. Springer, 2006.
- J. W. Boardman, F. A. Kruse, and R. O. Green. Mapping target signatures via partial unmixing of aviris data. In *Proc. JPL Airborne Geoscience Workshop*, 1993, pp. 23–26.
- N. Bohr. On the constitution of atoms and molecules. *Philosophical Magazine*, 26(6): 1–25, July 1913.
- C. F. Bohren and E. E. Clothiaux. *Fundamentals of Atmospheric Radiation*. Weinheim: WILEY-VCH Verlag GmbH & Co. KGaA, 2006.
- C. F. Bohren and D. R. Huffman. *Absorption and Scattering of Light by Small Particles*. John Wiley & Sons, 1983.
- C. Borel. Error analysis for a temperature and emissivity retrieval algorithm for hyperspectral imaging data. *International Journal of Remote Sensing*, 29 (17): 5029–5045, 2008.
- M. Born and E. Wolf. *Principles of Optics*, 7th edition. Cambridge University Press, 1999.
- G. Box and N. Draper. *Empirical Model-Building and Response Surfaces*. New York, NY: Wiley, 1987.
- G. E. P. Box, J. S. Hunter, and W. G. Hunter. *Statistics for Experimenters*, 2nd edition. Wiley-Interscience, 2005.
- R. W. Boyd. *Radiometry and the Detection of Optical Radiation*. John Wiley & Sons, 1983.
- S. Boyd and L. Vandenberghe. *Convex Optimization*. Cambridge University Press, 2004.
- R. N. Bracewell. *The Fourier Transform and Its Applications*, 3rd edition. McGraw-Hill Higher Education, 2000.
- J. W. Brault. Fourier transform spectroscopy. In *Proceedings of the Fifteenth Advanced Course of the Swiss Society of Astronomy and Astrophysics*, volume 1. Swiss Society of Astronomy and Astrophysics, 1985, pp. 1–61.
- C. L. Braun and S. N. Smirnov. Why is water blue? *Journal of Chemical Education*, 70(8): 612–614, 1993.
- C. J. C. Brett, R. S. DiPietro, D. G. Manolakis, and V. K. Ingle. Efficient implementations of hyperspectral chemical-detection algorithms. Proc. SPIE 8897, *Electro-Optical Remote Sensing, Photonic Technologies, and Applications VII; and Military Applications in Hyperspectral Imaging and High Spatial Resolution Sensing*, 88970T, 22 October 2013.
- D. R. Brillinger. *Time Series: Data Analysis and Theory*, volume 36. Siam, 2001.
- S. W. Brown, G. P. Eppeldauer, and K. R. Lykke. Facility for spectral irradiance and radiance responsivity calibrations using uniform sources. *Applied Optics*, 45(32): 8218–8237, 2006.
- S. W. Brown, B. C. Johnson, M. E. Feinholz, M. A. Yarbrough, S. J. Flora, K. R. Lykke, and D. K. Clark. Stray-light correction algorithm for spectrographs. *Metrologia*, 40: S81–S84, 2003.
- S. W. Brown, B. C. Johnson, and H. W. Yoon. Description of a portable spectroradiometer to validate EOS radiance scales in the shortwave infrared. *The Earth Observer*, 10(3): 43–48, 1998.
- A. Bucholtz. Rayleigh-scattering calculations for the terrestrial atmosphere. *Applied Optics*, 34(15): 2765–2773, 1995.
- T. Burr, H. Fry, B. McVey, E. Sander, J. Cavanaugh, and A. Neath. Performance of variable selection methods in regression using variations of the Bayesian information criterion. *Communications in Statistics—Simulation and Computation*, 37: 507–520, 2008.
- A. B. Carlson and P. Crilly. *Communication Systems*. New York, NY: McGraw-Hill Companies, Inc., 2009.
- K. F. Carr. Integrating sphere theory and applications part I: Integrating sphere theory and design. *Surface Coatings International*, 80(8): 380–385, 1997.

- J. Carrano. Chemical and biological sensor standards study. Technical report. Washington, DC: Defence Advanced Research Projects Agency, 2004.
- V. Carrère and J. E. Conel. Recovery of atmospheric water vapor total column abundance from imaging spectrometer data around 940 nm – sensitivity analysis and application to airborne visible/infrared imaging spectrometer (AVIRIS) data. *Remote Sensing of Environment*, 44: 179–204, 1993.
- A. C. Carter, S. I. Woods, S. M. Carr, T. M. Jung, and R. U. Datla. Absolute cryogenic radiometer and solid-state trap detectors for IR power scales down to 1 pW with 0.1% uncertainty. *Metrologia*, 46: S146–S150, 2009.
- G. Celeux and G. Govaert. A classification EM algorithm for clustering and two stochastic versions. *Computational Statistics & Data Analysis*, 14 (3): 315–332, 1992.
- T. Chakraborty and D. C. Ghosh. Computation of the internuclear distances of some heteronuclear diatomic molecules in terms of the revised electronegativity scale of Gordy. *The European Physical Journal D*, 59: 183–192, 2010.
- S. Chandrasekhar. *Radiative Transfer*. New York, NY: Dover Publications, 1960.
- A. S. Charles, B. A. Olshausen, and C. J. Rozell. Learning sparse codes for hyperspectral imagery. *IEEE Journal of Selected Topics in Signal Processing*, 5(5): 963–978, 2011. ISSN 1932-4553. doi: 10.1109/JSTSP.2011.2149497.
- S. Cherry. Singular value decomposition analysis and canonical correlation analysis. *Journal of Climate*, 9(9): 2003–2009, 1996.
- T. G. Chrien and L. G. Cook. Design concept for a Landsat-class imaging spectrometer with well-corrected spectral fidelity. In *Optical Science and Technology, SPIE's 48th Annual Meeting*. International Society for Optics and Photonics, 2003, pp. 90–97.
- M. P. Chrisp. Convex diffraction grating imaging spectrometer. Patent Number US 5880834, 1999.
- M. P. Chrisp. Imaging spectrometer wide field catadioptric design. Patent Number US 7414719 B2, 2008.
- P. M. Chu, F. R. Guenther, G. C. Rhoderick, and W. J. Lafferty. The NIST quantitative infrared database. *Journal of Research of the National Institute of Standards and Technology*, 104(1), 1999.
- J. Cipar, G. Anderson, and T. Cooley. Active volcano monitoring using a space-based short-wave infrared imager. In 3rd Workshop on *Hyperspectral Image and Signal Processing: Evolution in Remote Sensing (WHISPERS)*, IEEE, 2011, pp. 1–4.
- R. N. Clark, G. A. Swayze, A. Gallagher, T. V. V. King, and W. M. Calvin. The US Geological Survey, digital spectral library: Version 1: 0.2 to 3.0 μm . Technical report, US Geological Survey, 1993.
- R. N. Clark et al. Spectroscopy of rocks and minerals, and principles of spectroscopy. *Manual of Remote Sensing*, 3: 3–58, 1999.
- R. N. Clark, T. V. V. King, M. Klejwa, G. A. Swayze, and N. Vergo. High spectral resolution reflectance spectroscopy of minerals. *Journal of Geophysical Research*, 95: 12653–12680, 1990.
- R. N. Clark and T. L. Roush. Reflectance spectroscopy: Quantitative analysis techniques for remote sensing applications. *Journal of Geophysical Research*, 89(B7): 6329–6340, 1984.
- R. N. Clark, G. A. Swayze, K. E. Livo, R. F. Kokaly, S. J. Sutley, J. B. Dalton, R. R. McDougal, and C. A. Gent. Imaging spectroscopy: Earth and planetary remote sensing with the USGS tetracorder and expert systems. *Journal of Geophysical Research: Planets (1991–2012)*, 108(E12), 2003.
- R. N. Clark, G. A. Swayze, R. Wise, K. E. Livo, T. M. Hoefen, R. F. Kokaly, and S. J. Sutley. *USGS digital spectral library splib06a*. Reston, VA: US Geological Survey, 2007.

- S. A. Clough, M. W. Shephard, E. J. Mlawer, J. S. Delamere, M. J. Iacono, K. Cady-Pereira, S. Boukabara, and P. D. Brown. Atmospheric radiative transfer modeling: a summary of the aer codes. *Journal of Quantitative Spectroscopy and Radiative Transfer*, 91(2): 233–244, 2005.
- S. A. Clough, F. X. Kneizys, L. S. Rothman, and W.O. Gallery. Atmospheric spectral transmittance and radiance: Fascode1 b. In *1981 Technical Symposium East*. International Society for Optics and Photonics, 1981, pp. 152–167.
- J. M. Cobb, L. E. Comstock, P. G. Dewa, M. M. Dunn, and S. D. Flint. Advances in diamond turned surfaces enable unique cost effective optical system solutions. Volume 6269 of *Proceedings of SPIE*, 2006, pp. 62691L–1–62691L–9.
- R. G. Congalton and K. Green. *Assessing the Accuracy of Remotely Sensed Data: Principles and Practices*. CRC Press, 2008.
- P. Connes. Early history of Fourier transform spectroscopy. *Infrared Physics*, 24(2/3): 69–93, 1984.
- E. Conte, M. Lops, and G. Ricci. Asymptotically optimum radar detection in compound-Gaussian clutter. *IEEE Trans. on Aerospace and Electronic Systems*, 31 (2): 617–625, 1995.
- L. G. Cook. Three mirror anastigmatic optical system. Patent Number US 4265510, 1981.
- L. G. Cook. Reflective optical triplet having a real entrance pupil. Patent Number US 4733955, 1988.
- L. G. Cook. The last three-mirror anastigmat (tma)? Volume CR41 of *Proceedings of SPIE*, 1992, pp. 310–324.
- L. G. Cook. Compact all-reflective imaging spectrometer. Patent Number US 5260767, 1993.
- L. G. Cook. High-resolution all-reflective imaging spectrometer. Patent Number US 6886953 B3, 2005.
- L. G. Cook. High-resolution all-reflective imaging spectrometer. Patent Number US 7080912 B2, 2006.
- L. G. Cook. Two-channel imaging spectrometer utilizing shared objective, collimating, and imaging optics. Patent Number US 7382498 B1, 2008.
- L. G. Cook and J. F. Silny. Imaging spectrometer trade studies: A detailed comparison of the Offner-Chrisp and reflective triplet optical design forms. Volume 7813 of *Proceedings of SPIE*, 2010, pp. 78130F–1–78130F–14.
- C. C. Cooksey, D. W. Allen, B. K. Tsai, and H. W. Yoon. Establishment and application of the 0/45 reflectance factor scale over the shortwave infrared. *Applied Optics*, 54(10): 3064–3071, 2015.
- F. A. Cotton, G. Wilkinson, C. A. Murillo, M. Bochmann, and R. Grimes. *Advanced Inorganic Chemistry*, volume 5. New York, NY: Wiley, 1999.
- C. Cox and W. Munk. Measurement of the roughness of the sea surface from photographs of the sun's glitter. *JOSA*, 44(11): 838–850, 1954.
- H. Cox. Resolving power and sensitivity to mismatch of optimum array processors. *The Journal of the Acoustical Society of America*, 54 (3): 771–785, 1973.
- H. Cox and R. Pitre. Robust DMR and multi-rate adaptive beamforming. Volume 1, Nov 1997, pp. 920–924. doi: 10.1109/ACSSC.1997.680577.
- M. D. Craig. Minimum-volume transforms for remotely sensed data. *IEEE Transactions on Geoscience and Remote Sensing*, 32(3): 542–552, May 1994. ISSN 0196-2892. doi: 10.1109/36.297973.
- J. K. Crowley, D. E. Williams, J. M. Hammarstrom, N. Piatak, I-Ming Chou, and J. C. Mars. Spectral reflectance properties (0.4–2.5 μm) of secondary fe-oxide, fe-hydroxide, and fe-sulphate-hydrate minerals associated with sulphide-bearing mine wastes. *Geochemistry: Exploration, Environment, Analysis*, 3 (3): 219–228, 2003.

- A. R. Curtis. Contribution to a discussion of “a statistical model for water vapor absorption”. *Quart. J. Roy. Meteorol. Soc.*, 78: 638–640, 1952.
- J. S. Czapla-Myers, K. J. Thome, and S. F. Biggar. Design, calibration, and characterization of a field radiometer using light-emitting diodes as detectors. *Applied Optics*, 47(36): 6753–6762, 2008.
- J. S. Czapla-Myers, K. J. Thome, and N. P. Leisso. Radiometric calibration of earth-observing sensors using an automated test site at Railroad Valley, Nevada. *Canadian Journal of Remote Sensing*, 36(5): 474–487, 2010.
- G. A. d’Almeida, P. Koepke, and E. P. Shettle. *Atmospheric Aerosols Global Climatology and Radiative Characteristics*. Studies in Geophysical Optics and Remote Sensing. A. DEEPAK Publishing, 1991.
- O. Darrigol. *A History of Optics from Greek Antiquity to the Nineteenth Century*. Oxford University Press, 2012.
- M. A. Davies, B. S. Dutterer, T. J. Suleski, J. F. Silny, and E. D. Kim. Diamond machining of diffraction gratings for imaging spectrometers. *Precision Engineering*, 36: 334–338, 2012.
- A. Dempster, N. Laird, and D. Rubin. Maximum likelihood from incomplete data via the em algorithm. *Journal of the Royal Statistical Society. Series B (Methodological)*, 39(1): 1–38, 1977.
- C. F. Dietrich. *Uncertainty, Calibration and Probability*. Adam Hilger, 2nd edition, 1991.
- J. DiFranco and B. Rubin. *Radar Detection*. The Institution of Engineering and Technology, 2004.
- R. DiPietro, D. Manolakis, R. Lockwood, T. Cooley, and J. Jacobson. Hyperspectral matched filter with false-alarm mitigation. *Optical Engineering*, 51(1): 016202, January 2012.
- P. A. M. Dirac. *The Principles of Quantum Mechanics*, 4th edition. Oxford University Press, 1958.
- N. Draper and H. Smith. *Applied Regression Analysis*, 3rd edition. New York, NY: Wiley, 1998.
- R. Duda, P. Hart, and D. Stork. *Pattern Classification*, 2nd edition. New York, NY: John Wiley & Sons, Inc., New York, 2001.
- J. A. Dykema and J. G. Anderson. A methodology for obtaining on-orbit SI-traceable spectral radiance measurements in the thermal infrared. *Metrologia*, 43: 287–293, 2006.
- J. Dyson. Unit magnification optical system without Seidel aberrations. *Journal of the Optical Society of America*, 49 (7): 713–716, 1959.
- J. D. Echard. Estimation of radar detection and false alarm probabilities. *IEEE Trans. on AES*, 27(2): 255–260, March 1991.
- A. R. Ehsani, J. A. Reagan, and W. H. Erxleben. Design and performance analysis of an automate 10-channel solar radiometer instrument. *Journal of Atmospheric and Oceanic Technology*, 15: 697–707, 1998.
- A. Einstein. Zur quantentheorie der strahlung. *Physikalische Zeitschrift*, 18: 131–128, 1917.
- M. T. Eismann. *Hyperspectral Remote Sensing*. Bellingham, WA: SPIE, 2012.
- M. T. Eismann, J. Meola, A. D. Stocker, S. G. Beaven, and A. P. Schaum. Airborne hyperspectral detection of small changes. *Appl. Opt.*, 47(28): F27–F45, 2008.
- M. T. Eismann, J. Meola, and A. D. Stocker. Automated hyperspectral target detection and change detection from an airborne platform: Progress and challenges. In *Geoscience and Remote Sensing Symposium (IGARSS), 2010 IEEE International*, pp. 4354–4357, July 2010.
- C. Elachi and J. J. van Zyl. *Introduction To The Physics and Techniques of Remote Sensing*. Wiley, 2006.
- C. D. Elvidge. Visible and near infrared reflectance characteristics of dry plant materials. 11: 1,775–1,795, 1990.
- E. Ensafi and A. D. Stocker. An adaptive CFAR algorithm for real-time hyperspectral target detection. Proc. SPIE 6966, *Algorithms and Technologies for Multispectral, Hyperspectral, and Ultraspectral Imagery XIV*, 696605 (11 April 2008).

- G. P. Eppeldauer and D. C. Lynch. Opto-mechanical and electronic design of a tunnel-trap si radiometer. *Journal of Research of the National Institute of Standards and Technology*, 105(6): 813–828, 2000.
- M. Evans and T. Swartz. *Approximating Integrals via Monte Carlo and Deterministic Methods*. Oxford University Press, 2000.
- C. Fabry and A. Perot. Sur les franges des lames minces argentées et leur application à la mesure de petites épaisseurs d'air. *Ann. Chim. Phys.*, 12: 459–501, 1897.
- K. T. Fang, S. Kotz, and K. W. Ng. *Symmetric Multivariate and Related Distributions*. New York, NJ: Chapman and Hall, 1990.
- M. E. Feinholz, S. J. Flora, S. W. Brown, Y. Zong, K. R. Lykke, M. A. Yarbrough, B. C. Johnson, and D. K. Clark. Stray light correction algorithm for multichannel hyperspectral spectrographs. *Applied Optics*, 51(16): 3631–3641, 2012.
- M. E. Feinholz, S. J. Flora, M. A. Yarbrough, K. R. Lykke, S. W. Brown, B. C. Johnson, and D. K. Clark. Stray light correction of the marine optical system. *Journal of Atmospheric and Oceanic Technology*, 26: 57–73, 2009.
- G. W. Felde, G. P. Anderson, and T. W. Cooley. Atmospheric correction of spectral imagery from sensor systems with changing viewing geometry over a scene. In *Optical Remote Sensing of the Environment*, p. OMA3. Optical Society of America, 2010.
- R. A. Fisher. The use of multiple measurement in taxonomic problems. *Annals of Eugenics*, 7: 179–188, 1936.
- C. Forbes, M. Evans, N. Hastings, and B. Peacock. *Statistical Distributions*. Wiley, 2011.
- F. E. Fowle. The spectroscopic determination of aqueous vapor. *The Astrophysical Journal*, 35: 149–153, 1912.
- B. R. Foy. Comparisons between hyperspectral passive and multispectral active sensor measurements. In *Proceedings of SPIE*, Orlando, FL: SPIE 2002, pp. 98–109. doi: 10.1117/12.472253.
- C. Fraley and A. E. Raftery. Model-based methods of classification: using the mclust software in chemometrics. *Journal of Statistical Software*, 18(6): 1–13, 2007.
- J. Friedman, T. Hastie, and R. Tibshirani. Regularization paths for generalized linear models via coordinate descent. *Journal of Statistical Software*, 33(1): 1, 2010.
- K. Fukunaga. *Introduction to Statistical Pattern Recognition*, 2nd edition. Computer Science and Scientific Computing. New York, NY: Academic Press, 1990.
- S. J. Gaffey, L. A. McFadden, D. L. Nash, and C. M. Pieters. Ultraviolet, visible, and near-infrared reflectance spectroscopy: Laboratory spectra of geologic materials. *Remote Geochemical Analysis: Elemental and Mineralogical Composition*, pp. 43–77, 1993.
- Bo-Cai Gao and A. F. H. Goetz. Column atmospheric water vapor and vegetation liquid water retrievals from airborne imaging spectrometer data. *Journal of Geophysical Research*, 95(D4): 3549–3564, 1990.
- Bo-Cai Gao, A. F. H. Goetz, and W. J. Wiscombe. Cirrus cloud detection from airborne imaging spectrometer data using the $1.38 \mu\text{m}$ water vapor band. *Geophysical Research Letters*, 20(4): 301–304, 1993.
- Bo-Cai Gao, M. J. Montes, Z. Ahmad, and C. O. Davis. Atmospheric correction algorithm for hyperspectral remote sensing of ocean color from space. *Applied Optics*, 39(6): 887–896, 2000.
- Bo-Cai Gao, M. J. Montes, C. O. Davis, and A. F. H. Goetz. Atmospheric correction algorithms for hyperspectral remote sensing data of land and ocean. *Remote Sensing of Environment*, 113: S17–S24, 2009.
- J. D. Gaskill. *Linear Systems, Fourier Transforms, and Optics*. John Wiley & Sons, 1978.
- A. H. J. de Lassus Saint Genies. Apparatus for photography with or without color, December 13, 1938. US Patent 2,139,855.

- T. R. Gentile, J. M. Houston, J. E. Hardis, C. L. Cromer, and A. C. Parr. National Institute of Standards and Technology high-accuracy cryogenic radiometer. *Applied Optics*, 35(7): 1056–1068, 1996.
- T. A. Germer, J. C. Zwinkels, and B. K. Tsai, editors. *Spectrophotometry: Accurate Measurement of Optical Properties of Materials*, volume 46 of *Experimental Methods in the Physical Sciences*. Elsevier Academic Press, 2014.
- P. Gill, W. Murray, and M. Wright. *Practical Optimization*. London, UK: Academic Press, 1981.
- A. Gillespie, S. Rokugawa, T. Matsunaga, J. S. Cothern, S. Hook, and A. B. Kahle. A temperature and emissivity separation algorithm for advanced spaceborne thermal emission and reflection radiometer (ASTER) images. *IEEE Transactions on Geoscience and Remote Sensing*, 36(4): 1113–1126, 1998.
- A. R. Gillespie. Spectral mixture analysis of multispectral thermal infrared images. *Remote Sensing of Environment*, 42(2): 137–145, 1992.
- A. Girard and P. Jacquinot. Principles of instrumental methods in spectroscopy. In A. C. S. Van Heel, editor, *Advanced Optical Techniques*, Wiley Series in Pure and Applied Optics, chapter 3. North-Holland Publishing Company, 1967, pp. 73–121.
- R. Gnanadesikan. *Methods for Statistical Data Analysis of Multivariate Observations*, 2nd edition. New York, NJ: Wiley, 1997.
- W. L. Godson. The evaluation of infrared-radiative fluxes due to atmospheric water vapor. *Quart. J. Roy. Meteorol. Soc.*, 79: 367–379, 1953.
- A. F. H. Goetz. Three decades of hyperspectral remote sensing of the earth: A personal view. *Remote Sensing of Environment*, 113: S5–S16, 2009.
- S. E. Golowich and D. G. Manolakis. Cramer-rao bounds for long-wave infrared gaseous plume quantification. *Optical Engineering*, 53(2): 021109, 2013.
- G. H. Golub and C. F. Van Loan. *Matrix Computations*, 3rd edition. The Johns Hopkins University Press, Baltimore and London, 1996.
- G. H. Golub and C. F. Van Loan. *Matrix Computations*, 4th edition. The Johns Hopkins University Press, Baltimore and London, 2012.
- H. Gong, L. M. Hanssen, and G. P. Eppeldauer. Spatial and angular responsivity measurements of photoconductive HgCdTe LWIR radiometers. *Metrologia*, 41: 161–166, 2004.
- R. C. Gonzalez and R. E. Woods. *Digital Image Processing*. NB Upper Saddle River, NJ: Pearson Prentice Hall, 2008.
- H. González-Nuñez, X. Prieto-Blanco, and R. de la Fuente. Pupil aberrations in Offner spectrometers. *Journal of the Optical Society of America*, 29 (4): 442–449, 2012.
- J. W. Goodman. *Introduction to Fourier Optics*, 3rd edition. Roberts & Company Publishers, 2005.
- R. M. Goody and Y. L. Yung. *Atmospheric Radiation Theoretical Basis*, 2nd edition. Oxford University Press, 1989.
- R. M. Goody and Y. L. Yung. *Atmospheric Radiation: Theoretical Basis*. Oxford University Press, USA, 1995.
- H. R. Gordon, D. K. Clark, J. W. Brown, O. B. Brown, R. H. Evans, and W. W. Broenkow. Phytoplankton pigment concentrations in the middle Atlantic bight: comparison of ship determinations and CZCS estimates. *Applied Optics*, 22(1): 20–36, 1983.
- A. A. Green, M. Berman, P. Switzer, and M. D. Craig. A transformation for ordering multispectral data in terms of image quality with implications for noise removal. *IEEE Trans. on Geoscience and Remote Sensing*, 26 (1): 65–74, January 1988.
- M. A. Green and M. J. Keevers. Optical properties of intrinsic silicon at 300 k. *Progress in Photovoltaics: Research and Applications*, 3: 189–192, 1995.

- R. O. Green et al. Imaging spectroscopy and the airborne visible/infrared imaging spectrometer (AVIRIS). *Remote Sens. Environ.*, 65: 227–248, 1998.
- R. O. Green, B. E. Pavri, and T. G. Chrien. On-orbit radiometric and spectral calibration characteristics of EO-1 Hyperion derived with an underflight of AVIRIS and *In Situ* measurements at Salar de Arizaro, Argentina. *IEEE Transactions on Geoscience and Remote Sensing*, 41(6): 1194–1203, 2003.
- P. R. Griffiths and J. A. de Haseth. *Fourier Transform Infrared Spectroscopy*. John Wiley & Sons, 1986.
- F. Grum and R. J. Becherer. *Radiometry*, volume 1 of *Optical Radiation Measurements*. Academic Press, 1979.
- J. H. Gruninger, A. J. Ratkowski, and M. L. Hoke. The sequential maximum angle convex cone (smacc) endmember model. In *Defense and Security*. International Society for Optics and Photonics, 2004, pp. 1–14.
- L. Guanter, R. Richter, and J. Moreno. Spectral calibration of hyperspectral imagery using atmospheric absorption features. *Applied Optics*, 45(10): 2360–2370, 2006.
- R. P. Gupta. *Remote Sensing Geology*, 2nd edition. Springer, 2003.
- A. Haapalinna, P. Kärhä, and E. Ikonen. Spectral reflectance of silicon photodiodes. *Applied Optics*, 37(4): 729–732, 1998.
- J. A. Hackwell, D. W. Warren, R. P. Bongiovi, S. J. Hansel, T. L. Hayhurst, D. J. Mabry, M. G. Sivjee, and J. W. Skinner. Lwir/mwir imaging hyperspectral sensor for airborne and ground-based remote sensing. In *SPIE's 1996 International Symposium on Optical Science, Engineering, and Instrumentation*. International Society for Optics and Photonics, 1996, pp. 102–107.
- G. M. Hale and M. R. Querry. Optical constants of water in the 200-nm to 200- μ m wavelength region. *Applied Optics*, 12(3): 555–563, 1973.
- J. L. Hall, F. M. D'Amico, S. J. Kolodzey, Jun Qian, M. L. Polak, K. Westerberg, and C. S. Chang. Characterization of aerosol-containing chemical simulant clouds using a sensitive, thermal infrared imaging spectrometer. Volume 8018 *Chemical, Biological, Radiological, Nuclear, and Explosives (CBRNE) Sensing XII*, pages 801816–801816–10, 2011. doi: 10.1117/12.884238. URL <http://dx.doi.org/10.1117/12.884238>.
- P. C. Hansen. *Rank-Deficient and Discrete Ill-Posed Problems, Numerical Aspects of Linear Inversion*. SIAM Monographs on Mathematical Modeling and Computation. Philadelphia: SIAM, Society for Industrial and Applied Mathematics, 1998.
- B. Hapke. *Theory of Reflectance and Emittance Spectroscopy*. Cambridge University Press, 2012.
- T. Haran. Short-wave infrared diffuse reflectance of textile materials. 2008.
- R. Harig, G. Matz, and P. Rusch. Scanning infrared remote sensing system for identification, visualization, and quantification of airborne pollutants. In *Proc. SPIE*, volume 4574, pp. 83–94, 2002.
- J. C. Harsanyi. *Detection and Classification of Subpixel Spectral Signatures in Hyperspectral Image Sequences*. PhD thesis, University of Maryland, 1993.
- T. Hastie, R. Tibshirani, and J. Friedman. *The Elements of Statistical Learning*. New York: Springer, 2009.
- L. G. Henyey and J. L. Greenstein. Diffuse radiation in the galaxy. *Astrophysical Journal*, 93: 70–83, 1941.
- B. M. Herman, A. Ben-David, and K. J. Thome. Numerical technique for solving the radiative transfer equation for a spherical shell atmosphere. *Applied Optics*, 33(9): 1760–1770, 1994.
- G. Herzberg. *Atomic Spectra and Atomic Structure*. Dover Publications, 1944.

- G. Herzberg. *Molecular Spectra and Molecular Structure, Volume 1—Spectra of Diatomic Molecules*. Van Nostrand Reinhold Company, Inc., 1950.
- R. R. Hocking. *Methods and Applications of Linear Models*. New York, NJ: Wiley, 1996.
- A. Hoerl and R. Kennard. Ridge regression: Biased estimation for nonorthogonal problems. *Technometrics*, 12: 55–67, 1970.
- J. A. Hoeting, D. Madigan, A. E. Raftery, and C. T. Volinsky. Bayesian model averaging: a tutorial. *Statistical Science*, pp. 382–401, 1999.
- B. N. Holben, T. F. Eck, I. Slutsker, D. Tanré, J. P. Buis, A. Setzer, E. Vermote, J. A. Reagan, Y. J. Kaufman, T. Nakajima, F. Lavenu, I. Jankowiak, and A. Smirnov. AERONET—a federated instrument network and data archive for aerosol characterization. *Remote Sensing of Environment*, 66: 1–16, 1998.
- H. H. Hopkins. *Wave Theory of Aberrations*. Oxford University Press, 1950.
- H. H. Hopkins. The nature of the paraxial approximation I. Systems of uniform refractive index. *Journal of Modern Optics*, 38(3): 427–445, 1991.
- H. M. Horwitz, J. T. Lewis, and A. P. Pentland. Estimating proportions of objects from multispectral scanner data. Technical Report NASA-CR-141862, 1975.
- H. Hotelling. Relations between two sets of variates. *Biometrika*, 28: 321–377, 1936.
- J. M. Houston and J. P. Rice. NIST reference cryogenic radiometer designed for versatile performance. *Metrologia*, 43: S31–S35, 2006.
- W. A. Hovis, J. S. Knoll, and G. R. Smith. Aircraft measurements for calibration of an orbiting spacecraft sensor. *Applied Optics*, 24(3): 407–410, 1985.
- G. R. Hunt. Spectral signatures of particulate minerals in the visible and near infrared. *Geophysics*, 42(3): 501–513, 1977.
- G. R. Hunt and J. W. Salisbury. Visible and near infrared spectra of minerals and rocks. ii. Carbonates. *Modern Geology*, 2: 23–30, 1971.
- G. R. Hunt, J. W. Salisbury, and C. J. Lenhoff. Visible and near-infrared spectra of minerals and rocks. v. Halides, phosphates, arsenates, vanadates, and borates. *Modern Geology*, 3.3: 121–132, 1972.
- A. Hyvärinen and E. Oja. Independent component analysis: algorithms and applications. *Neural Networks*, 13(4): 411–430, 2000.
- T. Ingold, B. Schmid, C. Mätzler, P. Demoulin, and N. Kämpfer. Modeled and empirical approaches for retrieving columnar water vapor from solar transmittance measurements in the 0.72, 0.82, and 0.94 μm absorption bands. *Journal of Geophysical Research*, 105(D19): 24327–24343, 2000.
- Akira Iwasaki, Nagamitsu Ohgi, Jun Tanii, Takahiro Kawashima, and Hitomi Inada. Hyperspectral imager suite (hisui)—Japanese hyper-multi spectral radiometer. In *Geoscience and Remote Sensing Symposium (IGARSS), 2011 IEEE International*, pp. 1025–1028. IEEE, 2011.
- J. E. Jackson. *A User's Guide To Principal Components*. Wiley Series in Probability and Mathematical Statistics. New York, NY: John Wiley & Sons, 1991.
- R. D. Jackson, M. S. Moran, P. N. Slater, and S. F. Biggar. Field calibration of reference reflectance panels. *Remote Sensing of Environment*, 22: 145–158, 1987.
- R. Jaenicke. Tropospheric aerosols. In P. V. Hobbs, editor, *Aerosol-Cloud-Climate Interactions*, volume 54 of *International Geophysics Series*, Chapter 1. Academic Press, Inc., 1993, pp. 1–31.
- B. M. Jakosky, G. W. Finiol, and B. G. Henderson. Directional variations in thermal emission from geologic surfaces. *Geophysical Research Letters*, 17(7): 985–988, 1990.

- G. James, D. Witten, T. Hastie, and R. Tibshirani. *An Introduction to Statistical Learning*. Springer, 2013.
- J. James. *Spectrograph Design Fundamentals*. Cambridge University Press, 2007.
- F. A. Jenkins and H. E. White. *Fundamentals of Optics*. McGraw-Hill, Inc., 1976.
- J. R. Jensen. *Introductory Digital Image Processing: A Remote Sensing Perspective*, 3rd edition. Prentice-Hall Inc., 2005.
- L. O. Jimenez and D. A. Landgrebe. Supervised classification in high-dimensional space: geometrical, statistical, and asymptotical properties of multivariate data. *IEEE Transactions on Systems, Man, and Cybernetics, Part C: Applications and Reviews*, 28(1): 39–54, 1998.
- J. F. Johnson. Hybrid infrared focal plane signal and noise model. *IEEE Transactions on Electron Devices*, 46 (1): 96–108, 1999.
- N. L. Johnson, S. Kotz, and N. Balakrishnan. *Continuous Univariate Distributions*, volume 2. New York, NY: Wiley, 1995.
- R. A. Johnson and D. W. Wichern. *Applied Multivariate Statistical Analysis*, 6th edition. New Jersey: Prentice Hall, 2007.
- S. F. Johnston. *A History of Light and Colour Measurement: Science in the Shadows*, 1st edition. CRC Press, 2001.
- I. Jolliffe. *Principal Component Analysis*. Springer, 2002.
- C. Junge. The size distribution and aging of natural aerosols as determined from electrical and optical data on the atmosphere. *Journal of Meteorology*, 12: 13–25, 1955.
- S. O. Kasap. *Optoelectronics and Photonics: Principles and Practices*, 2nd edition. Pearson, 2013.
- R. E. Kass and A. E. Raftery. Bayes factors. *Journal of the American Statistical Association*, 90 (430): 773–795, 1995.
- F. Kasten and A. T. Young. Revised optical air mass tables and approximation formula. *Applied Optics*, 28(22): 4735–4738, 1989.
- Y. J. Kaufman, D. Tanré, L. A. Remer, E. F. Vermote, A. Chu, and B. N. Holben. Operational remote sensing of tropospheric aerosol over land from eos moderate resolution imaging spectroradiometer. *Journal of Geophysical Research*, 102(D14): 17051–17067, 1997a.
- Y. J. Kaufman and C. Sendra. Algorithm for automatic atmospheric corrections to visible and near-IR satellite imagery. *International Journal of Remote Sensing*, 9 (8): 1357–1381, 1988.
- Y. J. Kaufman, A. E. Wald, L. A. Remer, Bo-Cai Gao, Rong-Rong Li, and L. Flynn. The MODIS 2.1- μm channel – correlation with visible reflectance for use in remote sensing of aerosol. *IEEE Transactions on Geoscience and Remote Sensing*, 35(5): 1286–1298, 1997b.
- S. M. Kay. *Fundamentals of Statistical Signal Processing: Estimation Theory*, volume I. Prentice Hall, New Jersey, 1993.
- S. M. Kay. *Fundamentals of Statistical Signal Processing: Detection Theory*, volume II. Prentice Hall, New Jersey, 1998.
- R. A. Keller and T. S. Lomheim. Imaging fourier transform spectrometer (IFTS): Parameteric sensitivity analysis. Volume 5806 of *Proceedings of SPIE*, pp. 267–287. SPIE, 2005.
- E. J. Kelly. An adaptive detection algorithm. *IEEE Trans. on Aerospace and Electronic Systems*, 22 (1): 115–127, March 1986.
- N. Keshava. A survey of spectral unmixing algorithms. *Lincoln Laboratory Journal*, 14(1): 55–78, 2003.
- N. Keshava. Distance metrics and band selection in hyperspectral processing with applications to material identification and spectral libraries, *IEEE Transactions on Geoscience and Remote Sensing*, 42(7): 1552–1565, 2004.
- N. Keshava and J. F. Mustard. Spectral unmixing. *Signal Processing Magazine, IEEE*, 19(1): 44–57, January 2002. ISSN 1053-5888. doi: 10.1109/79.974727.

- H. C. King. *The History of the Telescope*. Charles Griffin and Company Ltd., 1955.
- Trude V.V. King and W. Ian Ridley. Relation of the spectroscopic reflectance of olivine to mineral chemistry and some remote sensing implications. *Journal of Geophysical Research: Solid Earth* (1978–2012), 92(B11): 11457–11469, 1987.
- R. Kingslake. *A History of the Photographic Lens*. Elsevier Science, 1989.
- I. P. Kirsteins and D. W. Tufts. On the probability density of signal-to-noise ratio in an improved adaptive detector. In *Acoustics, Speech, and Signal Processing, IEEE International Conference on ICASSP '85.*, volume 10, pages 572–575, 1985.
- I. P. Kirsteins and D. W. Tufts. Adaptive detection using low rank approximation to a data matrix. *IEEE Transactions on Aerospace and Electronic Systems*, 30(1): 55–67, 1994.
- C. A. Klein, R. P. Miller, and D. L. Stierwalt. Surface and bulk absorption characteristics of chemically vapor-deposited zinc selenide in the infrared. *Applied Optics*, 33(19): 4304–4313, 1994.
- G. R. D. S. Klingelhöfer, R. Van Morris, B. Bernhardt, C. Schröder, D. S. Rodionov, P. A. De Souza, A. Yen, R. Gellert, E. N. Evlanov, B. Zubkov, et al. Jarosite and hematite at meridiani planum from opportunity's Mössbauer spectrometer. *Science*, 306(5702): 1740–1745, 2004.
- F. X. Kneizys, L. W. Abreu, G. P. Anderson, J. H. Chetwynd, E. P. Shettle, A. Berk, L. S. Bernstein, D. C. Robertson, P. Acharya, L. S. Rothman, J. E. A. Selby, W. O. Gallery, and S. A. Clough. The MODTRAN 2/3 report and LOWTRAN 7 model. Technical report, Ontario Corporation, 1996.
- P. Koepke. Vicarious satellite calibration in the solar spectral range by means of calculated radiances and its application to Meteosat. *Applied Optics*, 21(15): 2845–2854, 1982.
- R. F. Kokaly. Investigating a physical basis for spectroscopic estimates of leaf nitrogen concentration. *Remote Sensing of Environment*, 75(2): 153–161, 2001.
- R. F. Kokaly, D. G. Despain, R. N. Clark, and K. Eric Livo. Mapping vegetation in Yellowstone national park using spectral feature analysis of aviris data. *Remote Sensing of Environment*, 84(3): 437–456, 2003.
- R. F. Kokaly, B. W. Rockwell, S. L. Haire, and T. VV. King. Characterization of post-fire surface cover, soils, and burn severity at the Cerro Grande fire, New Mexico, using hyperspectral and multispectral remote sensing. *Remote Sensing of Environment*, 106(3): 305–325, 2007.
- G. Kopp and J. L. Lean. A new, lower value of total solar irradiance: Evidence and climate significance. *Geophysical Research Letters*, 38, 2011.
- A. R. Korb, J. W. Salisbury, and D. M. D'Aria. Thermal-infrared remote sensing and Kirchhoff's law 2. Field measurements. *Journal of Geophysical Research*, 104(B7): 15,339–15,350, July 1999.
- D. Korsch. Anastigmatic three-mirror telescope. *Applied Optics*, 16(8): 2074–2077, 1977.
- H. J. Kostkowski and F. E. Nicodemus. Chapter 5: an introduction to the measurement equation. In F. E. Nicodemus, editor, *Self-Study Manual on Optical Radiation Measurements: Part I – Concepts, Chapters 4 and 5*, volume TN910-2 of *NBS Technical Note 910*. 1978.
- S. Kotz and S. Nadarajah. *Multivariate t-Distributions and Their Applications*. Cambridge, UK: Cambridge University Press, 2004.
- A. Kramida, Yu. Ralchenko, J. Reader, and NIST ASD Team. NIST Atomic Spectra Database, 2014. URL <http://physics.nist.gov/asd>.
- S. Kraut and L. Scharf. The CFAR adaptive subspace detector is a scale-invariant GLRT. *IEEE Trans. Signal Processing*, 47: 2538–2541, Sept. 1999.
- S. Kraut, L. L. Scharf, and L. T. McWhorter. Adaptive subspace detectors. *IEEE Transactions on Signal Processing*, 49 (1): 1–16, January 2001.
- W. Krzanowski. *Principles of Multivariate Analysis*, revised edition. Oxford Statistical Science Series. Oxford, UK: Oxford University Press, 2000.

- A. Kshirsagar. *Multivariate Analysis*. New York: Marcel Dekker, Inc., 1972.
- D. Labs and H. Neckel. The radiation of the solar photosphere from 2000 a to 100 um. *Jim, Z. Astrophysics*, 69: 1–73, 1968.
- A. A. Lacis and V. Oinas. A description of the correlated k distribution method for modeling nongray gaseous absorption, thermal emission, and multiple scattering in vertically inhomogeneous atmospheres. *Journal of Geophysical Research: Atmospheres* (1984–2012), 96(D5): 9027–9063, 1991.
- D. Landgrebe. Hyperspectral image data analysis. *IEEE Singel Processing Magazine*, 19(1): 17–28, January 2002.
- D. A. Landgrebe. *Signal Theory Methods in Multispectral Remote Sensing*. New York, NY: Wiley, 2003.
- R. M. Lark. A reappraisal of unsupervised classification, i: correspondence between spectral and conceptual classes. *International Journal of Remote Sensing*, 16 (8): 1425–1443, 1995a.
- R. M. Lark. A reappraisal of unsupervised classification, ii: optimal adjustment of the map legend and a neighbourhood approach for mapping legend units. *International Journal of Remote Sensing*, 16 (8): 1445–1460, 1995b.
- S. R. Lay. *Convex Sets and their Applications*. New York, NY: Wiley, 1982.
- O. Ledoit and M. Wolf. A well-conditioned estimator for large-dimensional covariance matrices. *Journal of Multivariate Analysis*, 88: 365–411, 2004.
- J. Lee and M. Verleysen. *Nonlinear Dimensionality Reduction*. Springer, 2007.
- J. B. Lee, A. S. Woodyatt, and M. Berman. Enhancement of high spectral resolution remote sensing data by a noise-adjusted principal components transform. *IEEE Trans. on Geoscience and Remote Sensing*, 28 (3): 295–304, May 1990.
- K. Lenhard, A. Baumgartner, P. Gege, S. Nevas, S. Nowy, and A. Sperling. Impact of improved calibration of a NEO HySpex VNIR-1600 sensor on remote sensing of water depth. *IEEE Transactions on Geoscience and Remote Sensing*, 53(11): 6085–6098, 2015.
- B. C. Levy. *Principles of Signal Detection and Parameter Estimation*. New York, NY: Springer, 2008.
- H. H. Li. Refractive index of alkali halides and its wavelength and temperature derivatives. *Journal of Physical and Chemical Reference Data*, 5 (2): 329–528, 1976.
- J. Li, P. Stoica, and Z. Wang. On robust Capon beamforming and diagonal loading. *IEEE Transactions on Signal Processing*, 51 (7): 1702–1715, July 2003.
- T. Lillesand, R. W. Kiefer, and J. Chipman. *Remote Sensing and Image Interpretation*. Wiley, 2007.
- K. N. Liou. *An Introduction to Atmospheric Radiation*, 2nd edition. Academic Press, 2002.
- T. S. Lomheim and E. D. Hernández-Baquero. Translation of spectral radiance levels, band choices, and signal-to-noise requirements to focal plane array specifications and design constraints. Volume 4486 of *Proceedings of SPIE* SPIE, 2002, pp. 263–307.
- R. Lorenz and S. Boyd. Robust minimum variance beamforming. *IEEE Trans. Signal Processing*, 53(5): 1684–1696, May 2005.
- P. Lorrain and D. Corson. *Electromagnetism: Principles and Applications*, 1st edition. W.H.Freeman and Co. Ltd, 1979.
- D. Lu, P. Mausel, E. Brondizio, and E. Moran. Change detection techniques. *International Journal of Remote Sensing*, 25 (12): 2365–2401, 2004.
- Guolan Lu and Baowei Fei. Medical hyperspectral imaging: a review. *Journal of Biomedical Optics*, 19(1): 010901–010901, 2014.

- P. G. Lucey, T. J. Williams, M. E. Winter, and E. M. Winter. Two years of operations of ah! an lww hyperspectral imager. In *AeroSense*. International Society for Optics and Photonics, 2000, pp. 31–40.
- R. L. Lucke, M. Corson, N. R. McGlothlin, S. D. Butcher, D. L. Wood, D. R. Korwan, R. R. Li, W. A. Snyder, C. O. Davis, and D. T. Chen. Hyperspectral imager for the coastal ocean: instrument description and first images. *Applied Optics*, 50(11): 1501–1516, 2011.
- J. Lützen. *The Prehistory of the Theory of Distributions*. Springer-Verlag New York Inc., 1982.
- W. K. Ma, J. M. Bioucas-Dias, P. Gader, T. H. Chan, N. Gillis, A. Plaza, A. Ambikapathi, and C. Y. Chi. A signal processing perspective on hyperspectral unmixing. *IEEE Signal Processing Magazine*, 31(1): 67–81, 2014.
- S. A. Macenko and M. P. Chrisp. Airborne visible/infrared spectrometer (AVIRIS) spectrometer design and performance. Volume 834 of *Proceedings of SPIE*, 1987, pp. 32–43.
- H. A. Macleod. *Thin-Film Optical Filters*, 4th edition. CRC Press, 2010.
- W. Malkmus. Random Lorentz band model with exponential-tailed S^{-1} line-intensity distribution function. *JOSA*, 57(3): 323–329, 1967.
- D. Manolakis. Realistic matched filter performance prediction for hyperspectral target detection. *Optical Engineering*, 44(11): 116401, November 2005.
- D. Manolakis, R. Lockwood, T. Cooley, and J. Jacobson. Hyperspectral detection algorithms: Use covariances or subspaces? In *Proc. of SPIE*, volume 7457, pages 74570Q–1, 2009.
- D. Manolakis, D. Marden, and G. Shaw. Target detection algorithms for hyperspectral imaging application. *Lincoln Laboratory Journal*, 14(1): 79–116, 2003.
- D. Manolakis, E. Truslow, M. Pieper, T. Cooley, and M. Brueggeman. Detection algorithms in hyperspectral imaging systems: An overview of practical algorithms. *Signal Processing Magazine, IEEE*, 31(1): 24–33, Jan 2014a.
- D. Manolakis, D. Zhang, M. Rossacci, R. Lockwood, T. Cooley, and J. Jacobson. Maintaining cfar operation in hyperspectral target detection using extreme value distributions. Volume 6565, page 65651W. SPIE, 2007.
- D. G. Manolakis and V. K. Ingle. *Applied Digital Signal Processing*. Cambridge, UK: Cambridge University Press, 2011.
- D. G. Manolakis, V. K. Ingle, and S. M. Kogon. *Statistical and Adaptive Signal Processing: Spectral Estimation, Signal Modeling, Adaptive Filtering and Array Processing*. Boston: McGraw-Hill Companies, Inc., 2000.
- D. G. Manolakis, S. E. Golowich, and R. S. DiPietro. Long-wave infrared hyperspectral remote sensing of chemical clouds: A focus on signal processing approaches. *Signal Processing Magazine, IEEE*, 31(4): 120–141, July 2014b.
- D. Manolakis, M. Rossacci, D. Zhang, J. Cipar, R. Lockwood, T. Cooley, and J. Jacobson. Statistical characterization of hyperspectral background clutter in the reflective spectral region. *Appl. Opt.*, 47(28): F96–F106, 2008.
- M. Mansuripur. *Classical Optics and its Applications*, 2nd edition. Cambridge UK: Cambridge University Press, 2009.
- D. Marden and D. Manolakis. Modeling hyperspectral imaging data using elliptically contoured distributions. In S. S. Shen and P. E. Lewis, editors, *Algorithms and Technologies for Multispectral, Hyperspectral, and Ultraspectral Imagery IX*, Orlando, FL: SPIE, 2003.
- D. B. Marden and D. G. Manolakis. Using elliptically contoured distributions to model hyperspectral imaging data and generate statistically similar synthetic data. Proc. SPIE 5425. *Algorithms and Technologies for Multispectral, Hyperspectral, and Ultraspectral Imagery X*, 12 August 2004, pp. 558–572.

- W. J. Marinelli, C. M. Gittins, A. H. Gelb, and B. D. Green. Tunable Fabry-Pérot etalon-based long-wavelength infrared imaging spectroradiometer. *Applied Optics*, 38(12): 2594–2604, 1999.
- P. Masson and W. Pieczynski. Sem algorithm and unsupervised statistical segmentation of satellite images. *IEEE Transactions on Geoscience and Remote Sensing*, 31(3): 618–633, May 1993.
- G. McLachlan and D. Peel. *Finite Mixture Models*. Wiley Series in Probability and Statistics. New York, NJ: John Wiley & Sons, Inc., 2000.
- M. Meroni, L. Busetto, R. Colombo, L. Guanter, J. Moreno, and W. Verhoef. Performance of spectral fitting methods for vegetation fluorescence quantification. *Remote Sensing of Environment*, 114(2): 363–374, 2010.
- L. Mertz. Concentric spectrographs. *Applied Optics*, 16(12): 3122–3124, 1977.
- A. A. Michelson and E. W. Morley. On the relative motion of the earth and the luminiferous ether. *The American Journal of Science*, 34(203): 333–345, 1887.
- E. M. Middleton, S. G. Ungar, D. J. Mandl, L. Ong, S. W. Frye, P. E. Campbell, D. R. Landis, J. P. Young, and N. H. Pollack. The earth observing one (eo-1) satellite mission: Over a decade in space. *Selected Topics in Applied Earth Observations and Remote Sensing, IEEE Journal of*, 6(2): 243–256, 2013.
- W. E. Knowles Middleton. *Vision Through the Atmosphere*. University of Toronto Press, 1958.
- C. Miesch, X. Briottet, Y. H. Kerr, and F. Cabot. Monte Carlo approach for solving the radiative transfer equation over mountainous and heterogeneous areas. *Applied Optics*, 38(36): 7419–7430, 1999.
- C. Miesch, L. Poutier, V. Achard, X. Briottet, X. Lenot, and Y. Boucher. Direct and inverse radiative transfer solutions for visible and near-infrared hyperspectral imagery. *IEEE Transactions on Geoscience and Remote Sensing*, 43(7): 1552–1562, 2005.
- T. P. Minka. Estimating a Dirichlet distribution, 2000 <http://research.microsoft.com/en-us/um/people/minka/papers/dirichlet/>.
- M. I. Mishchenko, J. W. Hovenier, and L. D. Travis, editors. *Light Scattering by Nonspherical Particles: Theory, Measurements, and Applications*. Academic Press, 1999.
- M. G. Moharam and T. K. Gaylord. Diffraction analysis of dielectric surface-relief gratings. *Journal of the Optical Society of America*, 72 (10): 1385–1392, 1982.
- M. G. Moharam and T. K. Gaylord. Rigorous coupled-wave analysis of metallic surface-relief gratings. *Journal of the Optical Society of America A*, 3 (11): 1780–1787, 1986.
- J. L. Moncet and S. A. Clough. Accelerated monochromatic radiative transfer for scattering atmospheres: Application of a new model to spectral radiance observations. *Journal of Geophysical Research*, 102(D18): 21853–21866, 1997.
- J.-L. Moncet, G. Uymin, A. E. Lipton, and H. E. Snell. Infrared radiance modeling by optimal spectral sampling. *Journal of the Atmospheric Sciences*, 65 (12): 3917–3934, 2008.
- D. Montgomery, E. Peck, and G. Vining. *Introduction to Linear Regression Analysis*, 5th edition. New Jersey: Wiley, 2012.
- P. Mouroulis, R. O. Green, and T. G. Chrien. Design of push-broom imaging spectrometers for optimum recovery of spectroscopic and spatial information. *Applied Optics*, 39(13): 2210–2220, 2000.
- P. Mouroulis and M. M. McKerns. Pushbroom imaging spectrometer with high spectroscopic data fidelity: experimental demonstration. *Optical Engineering*, 39(3): 808–816, 2000.
- P. Mouroulis, R. G. Sellar, D. W. Wilson, J. J. Shea, and R. O. Green. Optical design of a compact imaging spectrometer for planetary mineralogy. *Optical Engineering*, 46(6): 063001–1–063001–9, 2007.

- P. Mouroulis, D. W. Wilson, P. D. Maker, and R. E. Muller. Convex grating types for concentric imaging spectrometers. *Applied Optics*, 37(31): 7200–7208, 1998.
- R. Muirhead. *Aspects of Multivariate Statistical Theory*. John Wiley & Sons, Inc., 1982.
- J. Mustard and J. Sunshine. *Remote Sensing for the Earth Sciences: Manual of Remote Sensing*, 3rd edition, volume 3, chapter 5. New York, NY: John Wiley & Sons, 1998, pp. 251–306.
- J. F. Mustard and C. M. Pieters. Photometric phase functions of common geologic minerals and applications to quantitative analysis of mineral mixture reflectance spectra. *Journal of Geophysical Research: Solid Earth*, 94 (B10): 13619–13634, 1989. ISSN 2156-2202.
- N. M. Nasrabadi. Regularized spectral matched filter for target recognition in hyperspectral imagery. *Signal Processing Letters, IEEE*, 15: 317–320, 2008. ISSN 1070-9908. doi: 10.1109/LSP.2008.917805.
- A. A. Neath and J. E. Cavanaugh. The Bayesian information criterion: background, derivation, and applications. *Wiley Interdisciplinary Reviews: Computational Statistics*, 4(2): 199–203, 2012.
- F. E. Nicodemus, J. C. Richmond, J. J. Hsia, I. W. Ginsberg, and T. Limperis. Geometrical considerations and nomenclature for reflectance. Technical Report NBS MN-160, National Bureau of Standards, 1977.
- F. E. Nicodemus and H. J. Kostkowski. Chapter 2: Distribution of optical radiation with respect to position and direction. In F. E. Nicodemus, editor, *Self-Study Manual on Optical Radiation Measurements: Part I – Concepts, Chapters 1 to 3*, volume TN910-1 of *NBS Technical Note 910*. 1976.
- A. A. Nielsen, K. Conradsen, and J. J. Simpson. Multivariate alteration detection (mad) and maf postprocessing in multispectral, bitemporal image data: New approaches to change detection studies. *Remote Sensing of Environment*, 64(1): 1–19, 1998.
- S. Niu, S. E. Golowich, V. K. Ingle, and D. G. Manolakis. Implications and mitigation of model mismatch and covariance contamination for hyperspectral chemical agent detection. *Optical Engineering*, 52(2): 026202–026202, 2013a.
- S. Niu, S. E. Golowich, V. K. Ingle, and D. G. Manolakis. New approach to remote gas-phase chemical quantification: selected-band algorithm. *Optical Engineering*, 53(2): 021111, 2013b.
- S. Niu, S. E. Golowich, and D. G. Manolakis. Algorithms for remote quantification of chemical plumes: a comparative study. *Proceedings of the SPIE*, Volume 8390, pages 83902I–83902I–11, 2012. doi: 10.1117/12.919557. URL <http://dx.doi.org/10.1117/12.919557>.
- S. Niu, V. K. Ingle, D. G. Manolakis, and T. W. Cooley. Tests for the elliptical symmetry of hyperspectral imaging data. Proc. SPIE 7812, *Imaging Spectrometry XV*, 78120D, 13 August, 2010 NOAA, NASA, and USAF. *U. S. Standard Atmosphere*, 1976. US Government Printing Office, 1976.
- J. Nocedal and S. J. Wright. *Numerical Optimization*, 2nd edition. Springer, 2006.
- I. G. Nolt, J. V. Radostitz, G. DiLonardo, K. M. Evenson, D. A. Jennings, K. R. Leopold, M. D. Vanek, L. R. Zink, A. Hinz, and K. V. Chance. Accurate rotational constants of CO, HCl, and HF: Spectral standard for the 0.3- to 6-THz (10- to 200-cm⁻¹) region. *Journal of Molecular Spectroscopy*, 125: 274–287, 1987.
- A. Offner. New concepts in projection mask aligners. *Optical Engineering*, 14(1): 130–132, 1975.
- L. J. Otten III, R. G. Sellar, and B. Rafert. Mightysat ii. 1 fourier-transform hyperspectral imager payload performance. In *Satellite Remote Sensing II*. International Society for Optics and Photonics, 1995, pp. 566–575.
- G. Papageorgiou. Chlorophyll fluorescence: an intrinsic probe of photosynthesis. *Bioenergetics of photosynthesis*, pp. 319–371, 1975.
- A. Papoulis and S. U. Pillai. *Probability, Random Variables and Stochastic Processes with Errata Sheet*. New York, NY: McGraw-Hill Education, 2002.

- A. C. Parr, R. U. Datla, and J. L. Gardner, editors. *Optical Radiometry*, volume 41 of *Experimental Methods in the Physical Sciences*. Elsevier Academic Press, 2005.
- J. Pearlman, C. Segal, L. B. Liao, S. L. Carman, M. A. Folkman, W. Browne, L. Ong, and S. G. Ungar. Development and operations of the eo-1 hyperion imaging spectrometer. In *International Symposium on Optical Science and Technology*. International Society for Optics and Photonics, pp. 243–253, 2000.
- S. S. Penner. *Quantitative Molecular Spectroscopy and Gas Emissivities*. Addison-Wesley Publishing Company, Inc., 1959.
- D. L. Peterson and G. S. Hubbard. Scientific issues and potential remote sensing requirements for plant biochemical content. 1992.
- M. Pieper, D. Manolakis, E. Truslow, T. Cooley, and S. Lipson. Performance evaluation of cluster-based hyperspectral target detection algorithms. In *19th IEEE International Conference on Image Processing (ICIP)*, IEEE, 2012, pp. 2669–2672.
- M. L. Pieper, D. Manolakis, T. Cooley, M. Brueggeman, A. Weisner, and J. Jacobson. New insights and practical considerations in hyperspectral change detection. Technical report, 2015.
- M. L. Pieper, D. Manolakis, E. Truslow, T. Cooley, and M. Brueggeman. False alarm mitigation techniques for hyperspectral target detection. In *SPIE Defense and Security*, 2013.
- M. K. E. L. Planck. Ueber das gesetz der energieverteilung im normalspectrum. *Ann. d. Physik*, 4: 553–563, 1901.
- M. Pourahmadi. *High-Dimensional Covariance Estimation: With High-Dimensional Data*. John Wiley & Sons, 2013.
- W. Press, S. Teukolsky, W. Vetterling, and B. Flannery. *Numerical Recipes: The art of scientific computing*, 3rd edition. Cambridge, UK: Cambridge University Press, 2007.
- X. Prieto-Blanco, C. Montero-Orille, B. Couce, and R. de la Fuente. Analytical design of an offner imaging spectrometer. *Optics Express*, 14(20): 9156–9168, 2006.
- E. Purcell. *Electricity and Magnetism*, 1st edition. McGraw-Hill Book Co., 1965.
- J. Qian, T. Hastie, J. Friedman, R. Tibshirani, and N. Simon. glmnet for MATLAB. URL www.stanford.edu/~hastie/glmnet_matlab/. 2013.
- J. J. Qu, W. Gao, M. Kafatos, R. E. Murphy, and V. V. Salomonson, editors. *Earth Science Satellite Remote Sensing*. Springer, 2006.
- T. J. Quinn and J. E. Martin. A radiometric determination of the Stefan–Boltzmann constant and thermodynamic temperatures between –40 degrees C and +100 degrees C. *Philosophical Transactions of the Royal Society of London A*, 316(1536): 6–189, 1985.
- R. J. Radke, S. Andra, O. Al-Kofahi, and B. Roysam. Image change detection algorithms: a systematic survey. *IEEE Transactions on Image Processing*, 14 (3): 294–307, 2005.
- A. E. Raftery. Bayesian model selection in social research. *Sociological methodology*, 25: 111–164, 1995.
- M. S. Ramsey and P. R. Christensen. Mineral abundance determination: Quantitative deconvolution of thermal emission spectra. *Journal of Geophysical Research: Solid Earth*, 103 (B1): 577–596, 1998. ISSN 2156-2202. doi: 10.1029/97JB02784. URL <http://dx.doi.org/10.1029/97JB02784>.
- C. R. Rao. Separation theorems for singular values of matrices and their applications in multivariate analysis. *Journal of Multivariate Analysis*, 9(3): 362–377, 1979.
- I. S. Reed, J. D. Mallett, and L. E. Brennan. Rapid convergence rate in adaptive arrays. *IEEE Transactions on Aerospace and Electronic Systems*, AES-10(6): 853–863, 1974. ISSN 0018-9251. doi: 10.1109/TAES.1974.307893.
- F. Reif. *Fundamentals of Statistical and Thermal Physics*. McGraw-Hill Book Company, 1965.

- P. N. Reinersman and K. L. Carder. Monte Carlo simulation of the atmospheric point-spread function with an application to correction for the adjacency effect. *Applied Optics*, 34(21): 4453–4471, 1995.
- L. A. Remer, Y. J. Kaufman, D. Tanré, S. Mattoo, D. A. Chu, J. V. Martins, R.-R. Li, C. Ichoku, R. C. Levy, R. G. Kleidman, T. F. Eck, E. Vermote, and B. N. Holben. The MODIS aerosol algorithm, products, and validation. *Journal of the Atmospheric Sciences*, 62: 947–973, 2005.
- A. Rencher. *Multivariate Statistical Inference and Applications*. Wiley Series in Probability and Statistics. New York, NY: John Wiley & Sons, Inc., 1998.
- A. C. Rencher. *Methods of Multivariate Analysis*. New York, NY: Wiley, 1995.
- D. Riano, E. Chuvieco, S. Ustin, R. Zomer, P. Dennison, D. Roberts, and J. Salas. Assessment of vegetation regeneration after fire through multitemporal analysis of aviris images in the Santa Monica mountains. *Remote Sensing of Environment*, 79(1): 60–71, 2002.
- J. Richards. Is there a best classifier? In *Remote Sensing*, pp. 59820A–59820A. International Society for Optics and Photonics, 2005a.
- J. A. Richards. *Remote sensing digital image analysis: an introduction*. Springer, 2013.
- M. A. Richards. *Fundamentals of Radar Signal Processing*, 1st edition. McGraw-Hill, June 2005b.
- C. D. Richmond. Performance of the adaptive sidelobe blanker detection algorithm in homogeneous environments. *IEEE Transactions on Signal Processing*, 48 (5): 1235–1247, May 2000.
- C. D. Richmond. Adaptive array processing in non-Gaussian environments. In *Statistical Signal and Array Processing, 1996. Proceedings., 8th IEEE Signal Processing Workshop on (Cat. No. 96TB10004)*. IEEE, 1996, pp. 562–565.
- L. J. Rickard, R. Basedow, E. Zalewski, P. Silvergate, and M. Landers. HYDICE: An airborne system for hyperspectral imaging. Volume 1937 of *Proceedings of SPIE*, 1993, pp. 173–179.
- H. E. Rivercomb, H. Buijs, H. B. Howell, D. D. LaPorte, W. L. Smith, and L. A. Sromovsky. Radiometric calibration of IR Fourier transform spectrometers: solution to a problem with the High-Resolution Interferometer Sounder. *Applied Optics*, 27(15): 3210–3218, 1988.
- D. A. Roberts, M. Gardner, R. Church, S. Ustin, G. Scheer, and R. O. Green. Mapping chaparral in the Santa Monica mountains using multiple endmember spectral mixture models. *Remote Sensing of Environment*, 65(3): 267–279, 1998. ISSN 0034-4257.
- F. C. Robey, D. R. Fuhrmann, E. J. Kelly, and R. Nitzberg. A CFAR adaptive matched filter detector. *IEEE Trans. on Aerospace and Electronic Systems*, 28 (1): 208–218, January 1992.
- S. M. Ross. *Introduction to Probability and Statistics for Engineers and Scientists*. Academic Press, 2009.
- L. S. Rothman, et al. The HITRAN2012 molecular spectroscopic database. *Journal of Quantitative Spectroscopy & Radiative Transfer*, 130: 4–50, 2013.
- L. S. Rothman. The HITRAN database. Technical report, 2014. URL www.cfa.harvard.edu/hitran/.
- H. A. Rowland. Preliminary notice of the results accomplished in the manufacture and theory of gratings for optical purposes. *Philosophical Magazine and Journal of Science*, 13 (84): 469–474, 1882.
- F. F. Sabins. *Remote Sensing: Principles and Interpretation*. Waveland Press, Inc., 2007.
- B. E. Saleh and M. C. Teich. *Fundamentals of Photonics*, 2nd edition. Wiley Series in Pure and Applied Optics. Wiley-Interscience, 2007.
- J. W. Salisbury, A. Wald, and D. M. D'Aria. Thermal-infrared remote sensing and Kirchhoff's law 1. Laboratory measurements. *Journal of Geophysical Research*, 99(B6): 11,897–11,911, June 1994.

- S. R. Sandmeier. Acquisition of bidirectional reflectance factor data with field goniometers. *Remote Sensing of Environment*, 73: 257–269, 2000.
- C. J. Sansonetti, M. L. Salit, and J. Reader. Wavelengths of spectral lines in mercury pencil lamps. *Applied Optics*, 35(1): 74–77, 1996.
- A. R. Schaefer, E. F. Zalewski, and J. Geist. Silicon detector nonlinearity and related effects. *Applied Optics*, 22(8): 1232–1236, 1983.
- L. L. Scharf and B. Friedlander. Matched subspace detectors. *IEEE Trans. on Signal Processing*, 42(8): 2146–2157, August 1994.
- L. Scharf. *Statistical Signal Processing*. Reading, MA: Addison-Wesley, 1991.
- A. Schaum and A. Stocker. Linear chromodynamics models for hyperspectral target detection. In *Aerospace Conference, 2003. Proceedings. 2003 IEEE*, volume 4, pp. 4_1879–4_1885.
- D. Schläpfer, C. C. Borel, J. Keller, and K. I. Itten. Atmospheric precorrected differential absorption technique to retrieve columnar water vapor. *Remote Sensing of Environment*, 65: 353–366, 1998.
- J. Schott. *Remote Sensing: The Image Chain Approach*, 2nd edition. New York, NY: Oxford University Press, 2007.
- J. R. Schott. *Matrix Analysis for Statistics*, 2nd edition. New Jersey: Wiley, 2005.
- R. A. Schowengerdt. *Remote Sensing: Models and Methods for Image Processing*. San Diego, CA: Elsevier, 2007.
- E. Schrödinger. Quantisierung als eigenwertproblem. (erste mitteilung.). *Ann. d. Physik*, 79: 361–376, 1926.
- A. Schuster. Radiation through a foggy atmosphere. *The Astrophysical Journal*, 21(1): 1–22, 1905.
- D. W. Scott. *Multivariate density estimation: theory, practice, and visualization*. New York, NY: Wiley, 1992.
- G. A. F. Seber. *Linear Regression Analysis*. New York, NY: John Wiley & Sons, 1977.
- G. A. F. Seber and A. J. Lee. *Linear Regression Analysis*. Hoboken, NJ: John Wiley & Sons, Inc., 2003.
- J. Settle and N. Drake. Linear mixing and the estimation of ground cover proportions. *International Journal of Remote Sensing*, 14 (6): 1159–1177, 1993.
- S. W. Sharpe, T. J. Johnson, R. L. Sams, P. M. Chu, G. C. Rhoderick, and P. A. Johnson. Gas-phase databases for quantitative infrared spectroscopy. *Applied Spectroscopy*, 58(12): 1452–1461, 2004.
- S. S. Shen and E. M. Bassett III. Information-theory-based band selection and utility evaluation for reflective spectral systems. In *AeroSense 2002*. International Society for Optics and Photonics, 2002, pp. 18–29.
- E. P. Shettle and R. W. Fenn. Models for the aerosols of the lower atmosphere and the effects of humidity variations on their optical properties. Technical Report AFGL-TR-79-0214, Air Force Geophysics Laboratory, 1979.
- H. W. Siesler. Near-infrared spectroscopy of polymers. In *Makromolekulare Chemie. Macromolecular Symposia*, volume. Wiley Online Library, 1991, pp. 113–129.
- M. Šimečková, D. Jacquemart, L. S. Rothman, R. R. Gamache, and A. Goldman. Einstein A-coefficients and statistical weights for molecular absorption transitions in the HITRAN database. *Journal of Quantitative Spectroscopy & Radiative Transfer*, 98: 130–155, 2006.
- J. J. Simpson, T. J. McIntire, and M. Sienko. An improved hybrid clustering algorithm for natural scenes. *Geoscience and Remote Sensing, IEEE Transactions on*, 38(2): 1016–1032, 2000.
- P. N. Slater. *Remote Sensing Optics and Optical Systems*. Addison-Wesley Publishing Company, 1980.

- P. N. Slater, S. F. Biggar, K. J. Thome, D. I. Gellman, and P. R. Spyak. Vicarious radiometric calibrations of EOS sensors. *Journal of Atmospheric and Oceanic Technology*, 13: 349–359, 1996.
- P. N. Slater, S. F. Biggar, R. G. Holm, R. D. Jackson, Y. Mao, M. S. Moran, J. M. Palmer, and B. Yuan. Reflectance- and radiance-based methods for the in-flight absolute calibration of multispectral sensors. *Remote Sensing of Environment*, 22: 11–37, 1987.
- J. A. Smith, Tzeu Lie Lin, and K. J. Ranson. The Lambertian assumption and Landsat data. *Photogrammetric Engineering and Remote Sensing*, 46 (9): 1183–1189, 1980.
- W. C. Snyder, Zhengming Wan, and Xiaowen Li. Thermodynamic constraints on reflectance reciprocity and Kirchhoff's law. *Applied Optics*, 37(16): 3464–3470, 1998.
- B. Somers, G. P. Asner, L. Tits, and P. Coppin. Endmember variability in spectral mixture analysis: A review. *Remote Sensing of Environment*, 115(7): 1603–1616, 2011.
- P. R. Spyak, D. S. Smith, J. Thiry, and C. Burkhardt. Short-wave infrared transfer radiometer for the calibration of the Moderate-Resolution Imaging Spectrometer and the Advanced Spaceborne Thermal Emission and Reflection Radiometer. *Applied Optics*, 39(31): 5694–5706, 2000.
- G. L. Stensaas and J. Christopherson. USGS remote sensing technologies test site catalog, 2013. URL <http://calval.cr.usgs.gov/rst-resources/>.
- A. D. Stocker and A. Schaum. Application of stochastic mixing models to hyperspectral detection problems. *SPIE Proceedings*, 3071, April 1997.
- J. M. Stone. *Radiation and Optics: An Introduction to the Classical Theory*. McGraw-Hill Book Company, Inc., 1963.
- G. Strang. *Linear Algebra and Its Applications*, 4th edition. Cengage Learning, 2005.
- J. Strong. *Concepts of Classical Optics*. W. H. Freeman and Company, 1958.
- L. L. Strow, H. Motteler, D. Tobin, H. Revercomb, S. Hannon, H. Buijs, J. Predina, L. Suwinski, and R. Glumb. Spectral calibration and validation of the Cross-track Infrared Sounder on the Suomi NPP satellite. *Journal of Geophysics Research: Atmospheres*, 118: 12486–12496, 2013.
- J. Strutt. On the light from the sky, its polarization and colour. *Philosophical Magazine*, 41: 107–120, 274–279, 1871a.
- J. Strutt. On the scattering of light by small particles. *Philosophical Magazine*, 41: 447–454, 1871b.
- T. Stoffler, C. Kaufmann, S. Hofer, K. P. Förster, G. Schreier, A. Mueller, A. Eckardt, H. Bach, B. Penne, U. Benz, et al. The enmap hyperspectral imager—an advanced optical payload for future applications in earth observation programmes. *Acta Astronautica*, 61(1): 115–120, 2007.
- Haigang Sui, Qiming Zhou, Jianya Gong, and Guorui Ma. Processing of multi-temporal data and change detection. In *Advances in photogrammetry, remote sensing and spatial information sciences: 2008 ISPRS Congress Book*. CRC Press, 2008, pp. 227–247.
- W. E. Sumpner. The diffusion of light. *Proceedings of the Physical Society of London*, 12 (10): 10–29, 1892.
- D. Tanre, M. Herman, and P. Y. Deschamps. Influence of the background contribution upon space measurements of ground reflectance. *Applied Optics*, 20(2): 3676–3683, 1981.
- D. Tanre, M. Herman, P. Y. Deschamps, and A. de Leffe. Atmospheric modeling for space measurements of ground reflectances, including bidirectional properties. *Applied Optics*, 18(21): 3587–3594, 1979.
- B. N. Taylor and Chris E. Kuyatt. Guidelines for evaluating and expressing the uncertainty of NIST measurement results. Technical Report NIST Technical Note 1297, National Institute of Standards and Technology, 1994.

- J. R. Taylor. *An Introduction to Error Analysis: The Study of Uncertainties in Physical Measurements*, 2nd edition. University Science Books, 1996.
- P. M. Teillet. Rayleigh optical depth comparisons from various sources. *Applied Optics*, 29(13): 1897–1900, 1990.
- W. E. Tennant, D. Lee, M. Zandian, E. Piquette, and M. Carmody. MBE HgCdTe technology: A very general solution to IR detection, described by “rule 07”, a very convenient heuristic. *Journal of Electronic Materials*, 37(9): 1406–1410, 2008.
- J. Theiler, B. R. Foy, and A. M. Fraser. Nonlinear signal contamination effects for gaseous plume detection in hyperspectral imagery. In *Proc. SPIE*, volume 6233, 2006.
- J. Theiler and B. R. Foy. Effect of signal contamination in matched-filter detection of the signal on a cluttered background. *Geoscience and Remote Sensing Letters, IEEE*, 3 (1): 98–102, 2006.
- J. Theiler. Quantitative comparison of quadratic covariance-based anomalous change detectors. *Appl. Opt.*, 47(28): F12–F26, 2008.
- J. Theiler, C. Scovel, B. Wohlberg, and B. R. Foy. Elliptically contoured distributions for anomalous change detection in hyperspectral imagery. *Geoscience and Remote Sensing Letters, IEEE*, 7 (2): 271–275, 2010.
- E. Theocarous, J. Ishii, and N. P. Fox. Absolute linearity measurements on HgCdTe detectors in the infrared region. *Applied Optics*, 43(21): 4182–4188, 2004.
- S. Theodoridis and K. Koutroumbas. *Pattern Recognition*, 4th edition. New York, NY: Academic Press, 2008.
- G. E. Thomas and K. Stamnes. *Radiative Transfer in the Atmosphere and Ocean*. Cambridge University Press, 1999.
- K. Thome, C. Cattrall, J. D'Amico, and J. Geis. Ground-reference calibration results for Landat-7 ETM+. volume 5882 of *Proceedings of SPIE*, 2005, pp. 58820B–1–58820B–12.
- K. J. Thome. Absolute radiometric calibration of Landsat 7 ETM+ using the reflectance-based method. *Remote Sensing of Environment*, 78: 27–38, 2001.
- K. J. Thome. In-flight intersensor radiometric calibration using vicarious approaches. In S. A. Morain and A. M. Budge, editors, *Post-Launch Calibration of Satellite Sensors*, International Society for Photogrammetry and Remote Sensing (ISPRS) Book Series. A. A. Balkema Publishers, 2004, pp. 95–102.
- K. J. Thome, B. M. Herman, and J. A. Reagan. Determination of precipitable water from solar transmission. *Journal of Applied Meteorology*, 31, 1992.
- K. J. Thome, S. F. Biggar, and W. Wisniewski. Cross comparison of EO-1 sensors and other earth resources sensors to Landsat-7 ETM+ using Railroad Valley Playa. *IEEE Transactions on Geoscience and Remote Sensing*, 41(6): 1180–1188, 2003.
- A. Thompson and How-More Chen. Beamcon III, a linearity measurement instrument for optical detectors. *Journal of Research of the National Institute of Standards and Technology*, 99(6): 751–755, 1994.
- K. W. Thoning, P. P. Tans, and W. D. Komhyr. Atmospheric carbon dioxide at Mauna Loa Observatory 2. Analysis of the NOAA GMCC data, 1974–1985. *Journal of Geophysical Research*, 94(D6): 8549–8565, 1989.
- A. P. Thorne. *Spectrophysics*, 2nd edition. Chapman and Hall, 1988.
- G. Thuillier, M. Hersé, T. Foujols, W. Peetermans, D. Gillotay, P. C. Simon, H. Mandel, et al. The solar spectral irradiance from 200 to 2400 nm as measured by the solspec spectrometer from the atlas and eureka missions. *Solar Physics*, 214(1): 1–22, 2003.
- R. Tibshirani. Regression shrinkage and selection via the lasso. *Journal of the Royal Statistical Society. Series B (Methodological)*, 1996, pp. 267–288.

- R. Tibshirani. Regression shrinkage and selection via the lasso: a retrospective. *Journal of the Royal Statistical Society: Series B (Statistical Methodology)*, 73(3): 273–282, 2011.
- S. Tompkins, J. F. Mustard, C. M. Pieters, and D. W. Forsyth. Optimization of endmembers for spectral mixture analysis. *Remote Sensing of Environment*, 59(3): 472–489, 1997.
- M. Yu. Tretyakov, E. A. Serov, M. A. Koshelev, V. V. Parshin, and A. F. Krupnov. Water dimer rotationally resolved millimeter-wave spectrum observation at room temperature. *Physical Review Letters*, 110: 1–4, 2013.
- E. Truslow, D. Manolakis, M. Pieper, T. Cooley, M. Brueggeman, and S. Lipson. Performance prediction of Matched Filter and ACE hyperspectral target detectors. *IEEE Journal of Selected Topics in Applied Earth Observations and Remote Sensing*, 2013.
- E. Truslow, S. Golowich, D. Manolakis, and V. Ingle. Performance metrics for the evaluation of hyperspectral chemical identification systems. *Optical Engineering*, 2016.
- S. Ustin, editor. *Manual of Remote Sensing, Remote Sensing for Natural Resource Management and Environmental Monitoring (Volume 4)*, volume 4. Wiley, 2004.
- F. D. van der Meer and S. M. de Jong, editors. *Imaging Spectrometry*, volume 4 of *Remote Sensing and Digital Image Processing*. Kluwer Academic Publishers, 2001.
- B. L. van der Waerden, editor. *Sources of Quantum Mechanics*. Mineola, NY: North-Holland Publishing Company, 1967.
- H. L. Van Trees. *Optimum Array Processing*. New York, NY: Wiley, 2002.
- H. L. Van Trees, K. Bell, and Z. Tian. *Detection, Estimation, and Modulation Theory, Part I*, volume I. New Jersey: Wiley, 2013.
- G. Vane, A. F. H. Goetz, and J. B. Wellman. Airborne imaging spectrometer: A new tool for remote sensing. *IEEE Transactions on Geoscience and Remote Sensing*, GE-22(6): 546–549, 1984.
- A. Vasilevsky. *Applied Matrix Algebra in the Statistical Sciences*. Mineola, NY: Dover Publications, Inc., 1983.
- M. Vaughan. *The Fabry–Pérot Interferometer: History, Theory, Practice and Applications*. CRC Press, 1989.
- R. G. Vaughan, W. M. Calvin, and J. V. Taranik. Sebass hyperspectral thermal infrared data: surface emissivity measurement and mineral mapping. *Remote Sensing of Environment*, 85(1): 48–63, 2003.
- M. Verleysen, D. François, G. Simon, and V. Wertz. On the effects of dimensionality on data analysis with neural networks. In *Artificial Neural Nets Problem solving methods*. Springer, 2003, pp. 105–112.
- E. F. Vermote, D. Tanré, J. L. Deuzé, M. Herman, and J.-J. Morcrette. Second simulation of the satellite signal in the solar spectrum, 6S: An overview. *IEEE Transactions on Geoscience and Remote Sensing*, 35(3): 675–686, 1997.
- V. Viallefont, A. E. Raftery, and S. Richardson. Variable selection and Bayesian model averaging in case-control studies. *Statistics in Medicine*, 20(21): 3215–3230, 2001.
- A. J. Villemaire, S. Fortin, J. Giroux, T. Smithson, and R. J. Oermann. Imaging Fourier transform spectrometer. In *SPIE's 1995 Symposium on OE/Aerospace Sensing and Dual Use Photonics*. International Society for Optics and Photonics, 1995, pp. 387–397.
- J. H. Walker, R. D. Saunders, J. K. Jackson, and D. A. McSparron. NBS measurement services: Spectral irradiance calibrations. Technical Report NIST Special Publication 250-20, National Institute of Standards and Technology, 1987.
- Ning Wang, Hua Wu, F. Nerry, Chuanrong Li, and Zhao-Liang Li. Temperature and emissivity retrievals from hyperspectral thermal infrared data using linear spectral emissivity

- constraint. *Geoscience and Remote Sensing, IEEE Transactions on*, 49(4): 1291–1303, April 2011.
- D. W. Warren, D. J. Gutierrez, and E. R. Keim. Dyson spectrometers for high-performance infrared applications. *Optical Engineering*, 47(10): 103601–1–103601–9, October 2008.
- D. W. Warren, J. A. Hackwell, and D. J. Gutierrez. Compact prism spectrographs based on aplanatic principles. *Optical Engineering*, 36(4): 1174–1182, 1997.
- D. W. Warren. Compact, high-throughput spectrometer apparatus for hyperspectral remote sensing. Patent Number US 7609381, 2009.
- D. Watkins. *Fundamentals of Matrix Computations*, 2nd edition. New York, NY: Wiley, 2002.
- A. Webb and K. Copsey. *Statistical Pattern Recognition*, 3rd edition. Wiley, 2011.
- V. R. Weidner and J. J. Hsia. Reflectance properties of pressed polytetrafluoroethylene powder. *Journal of the Optical Society of America*, 71 (7): 856–861, 1981.
- W. T. Welford. Aberration theory of gratings and grating mountings. In E. Wolf, editor, *Progress in Optics*, volume 4, chapter IV. North-Holland Publishing Company, 1965, pp. 243–280.
- W. T. Welford. *Aberrations of Optical Systems*. Adam Hilger Ltd, 1986.
- M. Wendisch and J.-L. Brenguier. *Airborne Measurements for Environmental Research: Methods and Instruments*. John Wiley & Sons, 2013.
- W. B. Wetherell and D. A. Womble. All-reflective three element objective. Patent Number US 4240707, 1980.
- W. B. White. The carbonate minerals. *The Infrared Spectra of Minerals*, 4: 227–284, 1974.
- G. G. Wilkinson. Results and implications of a study of fifteen years of satellite image classification experiments. *IEEE Transactions on Geoscience and Remote Sensing*, 43(3): 433–440, 2005.
- M. E. Winter. N-FINDR: an algorithm for fast autonomous spectral end-member determination in hyperspectral data. Proc. SPIE 3753, *Imaging Spectrometry V*, pp. 266–275, 27 October, 1999. doi: 10.1117/12.366289. URL <http://dx.doi.org/10.1117/12.366289>.
- G. K. Woodgate. *Elementary Atomic Structure*, 2nd edition. Oxford University Press, 1983.
- T. N. Woods, R. T. Wrigley III, G. J. Rottman, and R. E. Haring. Scattered-light properties of diffraction gratings. *Applied Optics*, 33(19): 4273–4285, 1994.
- Xiaoxiong Xiong and W. Barnes. An overview of MODIS radiometric calibration and characterization. *Advances in Atmospheric Sciences*, 23(1): 69–79, 2006.
- B. K. Yap, W. A. M. Blumberg, and R. E. Murphy. Off-axis effects in a mosaic Michelson interferometer. *Applied Optics*, 21(22): 4176–4182, 1982.
- H. W. Yoon, J. J. Butler, T. C. Larason, and G. P. Eppeldauer. Linearity of InGaAs photodiodes. *Metrologia*, 40: S154–S158, 2003.
- H. W. Yoon and C. E. Gibson. NIST measurement services: Spectral irradiance calibrations. Technical Report NIST Special Publication 250-89, National Institute of Standards and Technology, 2011.
- H. W. Yoon, C. E. Gibson, and P. Y. Barnes. Realization of the National Institute of Standards and Technology detector-based spectral irradiance scale. *Applied Optics*, 41(28): 5879–5890, 2002.
- S. J. Young, B. R. Johnson, and J. A. Hackwell. An in-scene method for atmospheric compensation of thermal hyperspectral data. *Journal of Geophysical Research–Atmospheres*, 107 (D24): 4774, 2002.
- Lu Zhang, Mingsheng Liao, Limin Yang, and Hui Lin. Remote sensing change detection based on canonical correlation analysis and contextual Bayes decision. *Photogrammetric Engineering and Remote Sensing*, 73 (3): 311, 2007.

- B. Zitova and J. Flusser. Image registration methods: a survey. *Image and Vision Computing*, 21(11): 977–1000, 2003.
- Yuqin Zong, S. W. Brown, G. P. Eppledauer, K. R. Lykke, and Yoshi Ohno. A new method for spectral irradiance and radiance responsivity calibrations using kilohertz pulsed tunable optical parametric oscillators. *Metrologia*, 49: S124–S129, 2012.
- Yuqin Zong, S. W. Brown, B. C. Johnson, K. R. Lykke, and Yoshi Ohno. Simple spectral stray light correction method for array spectroradiometers. *Applied Optics*, 45(6): 1111–1119, 2006.

Index

- étendue, 162
 - conserved, 164
 - differential, 164
 - off-axis, 166
- wavelength, 36
- a priori probability, 495
- absorption
 - water, 101
- absorption coefficient, 40, 298
 - line strength, 77
 - quantum parameters, 98
 - shape factor, 77
- absorption coefficient spectrum, 597
- absorption features, 6
- absorptivity, 59
- active systems, 1
- adaptive cosine/coherence estimator (ACE), 548
- adaptive detectors, 547
- adaptive matched filter (AMF), 547
- adaptive matched filter detectors, 547
- additive signal model, 553, 608
- Akaike Information Criterion (AIC), 482
- along track dimension, 12
- angular dispersion, 173
- angular field of view, 12
- anomaly change detection, 586
- apparent reflectance, 323
- ARTEMIS algorithm, 594
- atmosphere, 102
 - absorption, 105
 - aerosol distribution functions, 108
 - aerosol models, 110
 - aerosol properties, 108
 - Junge distribution, 109
 - log-normal distribution, 109
 - model atmospheres, 112
 - ozone absorption, 106
 - pressure profile, 104
 - temperature profile, 103
 - US Standard Atmosphere, 102
 - volume mixing ratios, 105
- atmospheric absorption, 5
- atmospheric compensation, 17, 18, 322
 - ATCOR, 347
 - ATREM, 347
 - diffuse solar transmission, 326
 - ELM, 347
 - final radiance equation, 329
 - FLAASH, 347
 - flow diagram, 346
 - inversion equation, 342
 - meteorological range, 338
 - physics-based, 19
 - point spread function, 339
 - QUAC, 350
 - reciprocity, 328
 - scene-based, 18
 - spherical albedo, 327
 - surface apparent reflectance, 329
 - surface irradiance, 326
 - visibility estimation, 337
 - VNIR/SWIR radiance, 325
- atmospheric compensation (AC), 15, 592
- atmospheric propagation, 5
- atmospheric scattering, 5
- atmospheric windows, 5
- background clutter, 22
- background clutter modeling, 553
- background contamination, 611
- background estimation, 562
- bad pixel determination, 255
- band model
 - 6S, 322
 - correlated-k distribution, 321
 - k distribution, 321
 - MODTRAN®, 321
 - OSS, 321
- band selection, 406
- band-averaged radiance, 238
- Bayes criterion, 498
- Bayesian Information Criterion (BIC), 482
- Bayesian likelihood ratio, 502
- Bayesian Model Averaging (BMA), 485
- Beer's law, 40
 - generalized, 86

- optical depth, 96
optical path, 96
between-class scatter matrix, 435
bivariate normal distribution, 373
blackbody, 57
Planck's law, 58
Wien's law, 58
Boltzmann constant, 597
brightness temperature, 598
calibration coefficient, 238
canonical correlation, 431
Canonical correlation analysis, 429
canonical correlation vectors, 431
canonical correlations, 589
canonical covariance analysis, 590
canonical form, 466
Canonical space transformation, 427
canonical variables, 429
CCA, 429
central F -distribution, 379
central t -distribution, 378
central chi-squared distribution, 376
CFAR threshold selection, 567
change detection, 586
canonical correlation analysis, 588
linear prediction, 587
charge transfer absorption, 136
chemical identification, 617
chi-squared distribution, 376
classification, 26
classification algorithms, 24
classification EM algorithm, 400
clear spectral band, 592
clustering, 585
coherence, 43
coherence matrix, 430
collinearity, 471
coloring transformation, 371
complex numbers, 37
composite hypothesis, 497, 501
composite spectrum, 443
concentration of measure phenomenon, 410
concentration pathlength, 597
concentration-path length (CL) estimation, 618
conditional probability, 495
confusion matrix, 583
constant false alarm rate (CFAR), 566
constant false-alarm rate (CFAR) property, 527
Constrained Energy Minimization (CEM), 519
continuum interpolated band ratio
reflectance, 131
contrast, 230
convex hull, 447
convex set, 447
convolution, 80
delta function, 170
diffraction function and slit, 176
instrumental profile, 169
correlation coefficient, 366
correlation coefficient matrix, 368
correlation matrix, 368
covariance, 364
covariance equalization, 590
covariance matrix, 368
cross section, 85
absorption, 99
differential, 88
cross track dimension, 12
crystal field, 132
crystalline solids, 132
cumulative distribution function, 361
curse of dimensionality, 410
dark subtraction, 17
data acquisition
push broom, 222
staring, 222
whisk broom, 222
data calibration, 17
data cube, 3, 9
datacube, 387
decision boundaries, 498
decision rule, 494
decision surfaces, 498
deflection index, 517
derived variables, 406, 407
detection index, 517
detection limit, 614
deterministic endmembers, 453
diagonal loading, 472
diffraction, 41
Airy disk, 47
circular aperture, 46
Fraunhofer, 43
Fresnel, 43
slit, 44
diffraction grating, 186
blaze angle, 190
blaze wavelength, 192
blazed, 190
constructive interference condition, 186
dual facet, 205
efficiency, 192
efficiency function, 193
efficiency model, 205
immersion grating, 207
irradiance, 188
Littrow configuration, 192
magnification, 194
order, 186
order-sorting filter, 187

- parabolic image, 195
 reflection, 186
 rulings, 187
 sign convention, 190
 transmission, 186
 diffraction gratings
 micro-lithographic, 204
 diffuse illumination, 303
 diffuse reflectors, 6
 digital number (DN), 14
 dimensionality reduction, 26, 406
 Dirac delta function, 304
 direct solar radiance, 305
 directional absorptivity and BRDF, 127
 directional emissivity and BRDF, 127
 discrete Karhunen–Loève transform, 412
 discrimination function, 583
 Dominant Mode Rejection (DMR), 540
 dominant modes, 540
 down-looking geometry, 604
 dwell time, 15
 Dyson form, 202
- eigenvalue, 370
 eigenvalue decomposition, 370
 eigenvector, 370
 eigenvector matched filters, 539
 electromagnetic wave, 36
 elliptically contoured distributions (ECDs), 380
 elliptically distributed clutter, 529
 emission coefficient, 297
 emissivity, 59
 emissivity spectrum, 7
 empirical line method (ELM), 19
 empty space phenomenon, 410
 endmember determination, 451
 geometrical algorithms, 451
 statistical methods, 452
 endmember spectra, 443
 endmembers, 446
 energy matched filter, 514
 energy matched filter (EMF), 523
 energy NMF (ENMF), 524
 energy normalized matched filter, 516
 equivalent width, 96
 error analysis, 263
 accuracy and precision, 264
 combined standard uncertainty, 265
 covariance, 265
 coverage factor, 266
 error types, 264
 example, 266
 expanded uncertainty, 266
 law of propagation of uncertainty, 265
 measurand, 263
 random and systematic, 264
- relative uncertainty, 264
 standard uncertainty, 264
 estimation space, 455
 Euclidean length, 368
 event detector, 615
 Expectation–Maximization (EM) algorithm, 397
 expected value, 361
 extinction coefficient, 87
 total, 87
- F-test, 479
 face, 448
 false alarm mitigation (FAM) algorithms, 577
 feasible mixtures, 447
 feature extraction, 407
 feature selection, 406
 fill-fraction, 446
 filter radiometer, 230
 Fisher's linear discriminant, 432
 flat emissivity approximation, 602
 flux, 39, 50
 flux responsivity, 161
 Fourier Transform Imaging Spectrometer (FTIS), 11
 fraction images, 488
 fraction overflow images, 491
 fractional abundance, 446
 frequency, 36
- Gaussian detection problem, 503
 canonical space, 510
 equal covariance matrices, 504
 unequal covariance matrices, 508
 unknown parameters, 511
 Gaussian distribution, 362
 Gaussian maximum likelihood classifier, 583
 Gaussian mixture model (GMM), 395
 GBSS sensor, 611
 generalized eigenvalue problem, 426
 generalized least squares estimation, 468
 generalized likelihood ratio test (GLRT), 558
 generalized Rayleigh distribution, 409
 generalized Rayleigh quotient, 426
 generalized variance, 372
 global covariance matrix, 436
 grain size effects, 130
 ground resolution distance (GSD), 13
 ground resolution element, 11
 ground sample distance (GSD), 12
- Henyey–Greenstein phase function, 343
 histogram, 360
 HITRAN, 80, 99
 Hotelling transform, 412
 Huygens' construction, 42
 slit, 44
 hydroxyl, 138
 hyperbolic anomalous change detector, 591

- hyperspectral imaging sensors, 8
hypersphere, 408
hypothesis, 494
- ICA, 419
ill-conditioning, 471
image
 histogram, 388
 scalar, 387, 388
 vector, 387, 390
image endmembers, 451
image-derived spectra, 23
imaging spectrometer
 AVIRIS, 208
 Dyson, 203
 Fabry-Pérot, 209
 LWIR Chrissp, 207
 Michelson interferometer, 223
 Offner-Chrissp, 197
 Offner-Chrissp grating aberrations, 197
 reflective triplet, 207
 SEBASS, 206
imaging spectrometers, 8
 dispersive, 171
Independent component analysis, 419
index of refraction, 39
 water, 40
information classes, 582
infrared radiation, 3
innovations representation, 440
instantaneous field of view (IFOV), 12, 15
instrumental profile, 169
 dispersive spectrometer, 178
 geometric, 180
 measurement, 169
integrating sphere, 249
 radiance equation, 251
interference, 41, 555
 constructive, 43
 destructive, 44
 Young's experiment, 48
interference fringes, 41
intimate mixture, 443
intrinsic dimension, 411
iron, 134
irradiance, 39
 circular aperture, 47
 slit, 45
 two slits, 49
irradiance standard, 239
 interpolation, 240
 uncertainty, 240
isotropic noise, 533
- joint probability density function, 363
- k-means clustering, 400
- Kirchhoff's law, 60
 validity, 61
- Lambertian reflectors, 6
land-cover, 581
- LASSO, 482
least squares estimation, 454
 algebraic approach, 460
 generalized, 468
 geometric approach, 455
 goodness-of-fit metrics, 458
 minimum norm solution, 466
 normal equations, 463
 QR decomposition, 463
 residual, 456
 residual space, 456
least squares estimation:linear constraints, 462
least squares estimation:statistical properties, 466
least squares estimation:SVD, 465
ligand, 132
likelihood function, 383
likelihood ratio, 496
likelihood ratio (LR), 498
likelihood ratio test, 496
likelihood ratio test (LRT), 498
limit of resolution, 171
 prism, 185
line strength, 98
Linear discriminant analysis, 432
linear mixing model, 23
LWIR radiative transfer theory, 352
- macroscopic mixture, 443
Mahalanobis angle, 377
Mahalanobis distance, 372, 376
Mallow criterion, 481
matched filter, 513
matched filter detector, 506
 performance evaluation, 507
matched filter detectors
 performance analysis, 522
matched filter with FAM, 577
matched subspace detectors, 528
material spectral correlation, 391
mathematical expectation, 362
maximum likelihood estimates, 383
maximum likelihood estimation, 383, 470
Maximum Noise Fraction transform, 428
Maxwell-Boltzmann distribution, 64
mean value, 361
measurement equation, 161, 229
 final form, 169
 illustration, 167
 imaging spectrometer, 167
 simplifying assumptions, 167
 single spectral band, 168
Michelson interferometer, 11, 209

- apodization, 218
 bullseye pattern, 213
 cosine transform, 214
 fast Fourier transform, 221
 Fourier transform, 214
 fringes, 212
 instrumental profile, 217, 220
 interferogram, 210
 irradiance, 211
 path difference, 211
 path difference shift, 219
 phase difference, 211
 self-apodization, 219
 wave number shift, 219
 ZPD, 214
- minerals
 beryl, 136
 jarosite, 136
 olivine, 135
 pigeonite, 136
- minimum-variance distortionless response (MVDR)
 matched filter, 520
- mixed pixel, 22
- mixed spectrum, 443
- mixture types
 coatings, 129
 intimate, 129
 linear, 129
 molecular, 129
- MNF transform, 428
- model adequacy checking, 490
- model misspecification
 overfitting, 475
 underfitting, 475
- model validation, 490
- MODTRAN®, 108
- modulation transfer function, 159
- monochromator characterization, 235
- Multiclass Clutter, 572
- multicollinearity, 471
- multiple correlation coefficient, 459
- Multiple linear discriminant analysis, 435
- multivariate Cauchy distribution, 379
- multivariate normal distribution, 371
 likelihood function, 386
- N-FINDR algorithm, 452
- NDVI, 147
- near-infrared plateau, 145
- Neyman–Pearson criterion, 499, 500
- Neyman–Pearson threshold, 500
- NIST library, 605
- noncentral F -distribution, 379
- noncentral t -distribution, 378
- noncentral chi-squared distribution, 376
- noncentrality parameter, 376, 378, 379
- nonliteral exploitation, 20
 norm of vector, 368
 normal distribution, 362
 normal equations, 456
 normalized matched filter, 516, 521
 normalized matched filter with FAM, 578
- oblique projection matrix, 457
 observation space, 494
 Offner form, 196
 telecentric, 196
- optical density, 245
 optical depth, 300
 optical path difference (OPD), 11
 optical thickness, 95
 thick, 100
 thin, 97
- optically opaque plume approximation, 603
- original variables, 406
- orthogonal projection matrix, 457
 orthogonality principle, 456
- partial correlation coefficient, 438
 partial F-test, 479
- passive systems, 1
- path difference, 44
 between slits, 48
- PCA, 411
- performance modeling, 269
 dark current, 273
 dark current noise, 276
 everything but photon noise, 277
 figures of merit, 277
 measurement equation, 272
 NEΔT, 277, 278
 NEI, 278
 NESR, 277
 noise, 276
 photon limited, 276
 quantization noise, 276
 reference radiance, 275
 refractive element transmission, 272
 signal-to-noise ratio, 277
- phase, 38
 phase difference, 44
 photodetectors, 269
- physics-based models, 22
- picture element, 12
 pixel, 12
 pixel pitch, 172
 pixel purity index (PPI) algorithm, 452
 Planck constant, 597
 plane wave, 36
 plume–background correlation, 612
 plume-free background estimation, 613
 PNNL library, 605
 point spread function (PSF), 12

- polar coordinates, 380
pooled covariance matrix, 436
Poynting vector, 39
principal component analysis, 411
principle of superposition, 42
prism, 184
 minimum deviation, 184
probability density function, 360
probability distribution, 360
probability of detection, 499
probability of error, 495
probability of exceedance, 361
probability of false alarm, 499
probability–probability (P–P) plot, 388
projected area, 52
projected solid angle, 52
pushbroom scanning, 10
- quadratic form, 369
 negative definite, 369
 nonnegative definite, 369
 positive definite, 369
quantile–quantile (Q–Q) plot, 388
quantum efficiency, 168, 270
 equation, 270
quantum mechanics, 61
 absorption and emission, 63
 Einstein A coefficient, 65
 Einstein B coefficient, 65
 electronic transition, 63
 emission and absorption rates, 64
 energy levels, 63
 hydrogen, 63
 hydrogen atom energy states, 64
 molecular electronic structure, 75
 molecular emission and absorption, 68
 principal quantum number, 63
 rotation, 68
 rotational energy, 70
 rotational transition, 70
 rotational–vibrational energy, 74
 vibration, 71
 vibrational transition, 71
- radiance, 52
 definition, 52
 spectral conversion, 54
radiance-domain processing, 553
radiative transfer, 295
radiative transfer equation, 298, 299, 302
 downward, 311
 upward, 309
radiative transfer models
 band models, 313
 line-by-line, 313
radiometric characterization
 on-board sources, 261
 radiometric characterization, 238
 linearity, 254
 LWIR, 252
 radiometric sampling, 13
 radiometry, 50
 intensity, 53
 irradiance, 50
 radianc exitance, 50
 table of quantities, 54
 random vector, 367
 range, 12, 15
 rare earth elements, 133
 ray, 38
 Rayleigh quotient, 425
 receiver operating characteristic (ROC), 501
 red-edge, 144
 reduced model, 475
 reduced-rank approximation, 540
 reference endmembers, 451
 reference spectra, 18
reflectance
 biconical reflectance, 120
 BRDF, 118
 BRDF definition, 120
 BRDF/BRF relationship, 122
 BRF, 121
 BRF definition, 121
 definition, 119
 directional-hemispherical reflectance factor, 124
 field BRF measurement, 125
 field goniometer, 124
 geometry, 119
 Lambert's cosine law, 121
 Lambertian, 121
 Lambertian reflector, 123
 PTFE, 124
reflectance peaks, 7
reflectance spectrum, 6
reflectance standard, 241
 NIST STARR measurement, 242
 scintered PTFE, 243
reflectance-domain processing, 553
reflected diffuse boundary radiance, 307
reflected direct boundary radiance, 305
regularization, 471
regularized least squares, 471
remote sensing, 1
replacement signal model, 555
resolving power, 170
 diffraction grating, practical, 187
 diffraction grating, theoretical, 187
 Michelson interferometer, 217
 practical, 180
 prism, theoretical, 185
 theoretical, 179
ridge regression, 472

- robust matched filters, 541, 544
- sample correlation coefficient, 366
- sample covariance matrix, 547
- sample matrix inversion, 547
- sampling operations, 8
- scatter plot, 363
- scattered light source term, 308
- scattering, 84
- aerosol, 92
 - geometry, 88
 - Mie theory, 94
 - phase function, 88
 - Rayleigh, 89
 - Rayleigh phase function, 92
 - size parameter, 84
- scattering coefficient, 86
- scattering emission coefficient, 299
- scattering source function, 299
- scree test, 417
- selectivity, 614
- sensitivity, 614
- sensor, 2
- sensor band overlap correlation, 391
- sequential maximum angle convex cone (SMACC)
- algorithm, 452
- shade endmember, 489
- signal model mismatch, 541
- signal-to-clutter ratio (SCR), 561, 571
- signature mismatch, 531
- silicon photodiode response, 246
- simple hypothesis, 497
- simplex, 447
- single-scattering albedo, 299
- SIRCUS, 263
- slab geometry, 300
- slant-path geometry, 604
- slit, 44, 172
- reduced slit width, 179
- solar
- constant, 56
 - irradiance, 55
- solar illumination, 303
- solar spectral irradiance, 4
- solid angle, 50
- differential, 51
 - unit, 51
- source, 1
- source function, 297, 302
- downward, 310
- spatial characterization, 261
- spatial processing, 20
- spatial response function, 182
- spatial sampling, 11
- spatial-spectral uniformity, 181
- spectral angle maper (SAM), 366
- spectral angle metric, 366
- spectral bandwidth, 15
- spectral calibration
- Michelson interferometer, 237
- spectral characterization, 231
- instrumental profile, 232
 - source variation, 232
 - systemmatic error, 232
- spectral characterization source, 231
- spectral classes, 582
- spectral decomposition, 370
- spectral emissivity, 7
- spectral exploitation algorithms, 22
- spectral landscape classification, 581
- spectral line shapes, 76
- collisional broadening, 79
 - Doppler broadening, 77
 - Gaussian profile, 78
 - intermediate broadening, 80
 - Lorentzian profile, 79
 - Voigt profile, 81
- spectral linear prediction, 439
- spectral linear smoother, 437
- spectral mixture analysis, 443
- spectral processing, 20
- spectral radiant exitance, 4
- spectral remote sensing, 20
- spectral response function, 603
- spectral response function (SRF), 13
- spectral signature, 22
- spectral transmission filter, 236
- band-averaging, 236
- spectral variability, 21
- spectral Wiener filter, 437
- spectroradiometer, 248
- specular reflectors, 6
- speed of light, 36
- spherically invariant distributions, 380
- spherizing, 417
- spherizing transformation, 371
- standard deviation, 362
- standardized normal random variable, 362
- staring system, 10
- statistical independence, 363
- stochastic endmembers, 453
- Stochastic Expectation Maximization (SEM)
- algorithm, 401
- stochastic mixing model (SMM), 453
- stray light contamination, 256
- data reduction, 257
- sufficient statistic, 506
- supervised classification, 582
- t-distribution
- likelihood function, 387
- t-test, 480

- target, 551
 low probability, 552
 rare, 552
 resolved, 551
 subpixel, 551
target detection, 24, 26
 performance prediction models, 571
target detection performance assessment, 570
target identification algorithms, 581
target in covariance matrix, 543
target modeling, 553
target signature, 562
telecentric, 174
telescope
 Cassegrain, 155
 nonrelayed off-axis TMA, 160
 relayed off-axis TMA, 160
 Ritchey–Chrétien, 157
 three-mirror anastigmat (TMA), 158
temperature–emissivity separation (TES), 592
terrain composition, 15
test area, 584
thematic map, 581
theme, 581
thermal atmospheric compensation, 354
 emissive empirical line method (EELM), 357
 ISAC model, 354
 temperature–emissivity separation, 356
thermal emission coefficient, 298
thermal infrared, 4, 19
thermal source function, 298
three-layer radiance model, 596
threshold, 496, 498
topography correlation, 391
total covariance matrix, 436
total scatter matrix, 435
total upward source term, 309
traceability, 229
training spectra, 18
training area, 584
training data, 24, 583
transfer radiometer, 239, 244
 filter definition, 245
 filters, 245
 linear response, 249
 single detector type, 247
 trap type, 246
 water transmission effects, 248
transmission, 40
transmission function, 168
two-dimensional histogram, 363
unbiased estimator, 385
uncorrelated random variables, 365
uniformly most powerful (UMP) tests, 502
uniformly most powerful invariant (UMPI) tests, 524
unmixing, 26
unmixing spectral images, 489
unsupervised classification, 585
upward radiance, 310
variance, 362
vertex, 447
vibrational modes, 137
vicarious calibration, 280
 atmospheric measurements, 281
 automated solar radiometer, 282
 emissive spectral range, 291
 error analysis, 287
 irradiance-based method, 289
 radiance-based method, 280, 289
 reflectance-based method, 280, 281
 site requirements, 281
 spectral calibration, 290
 surface reflectance measurements, 286
virtual cold endmember, 594
virtual endmembers, 452
volume emissivity, 298
volume thermal emission, 298
water
 absorption coefficient, 141
 red algae, 143
 reflectance, 141
 sea water reflectance, 142
water estimation, 331
 APDA technique, 336
 CIBR, 331
 least squares fitting, 337
wave
 plane, 38
 spherical, 44
wave vector, 37
wavefront, 38
wavenumber, 54
whiskbroom scanning, 11
whitening, 417
whitening transformation, 371, 440
within-class scatter matrix, 434

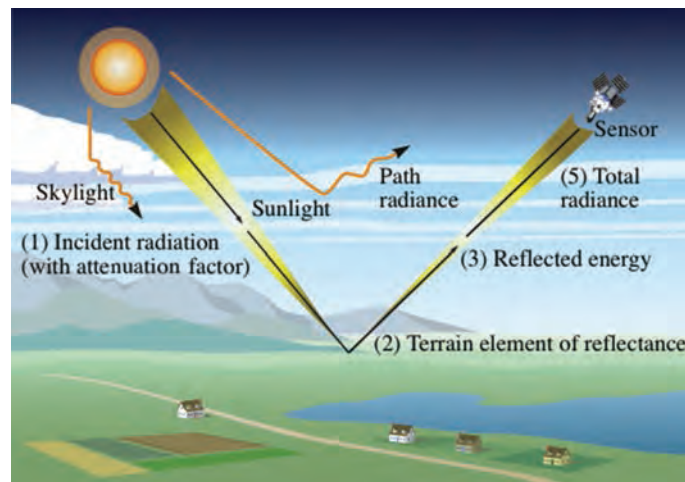


Figure 1.1 Pictorial illustration of how the atmosphere, the solar illumination, and the spectral response of the sensor affect the relationship between the observed radiance spectrum and the wanted reflectance spectrum of the ground resolution cell.

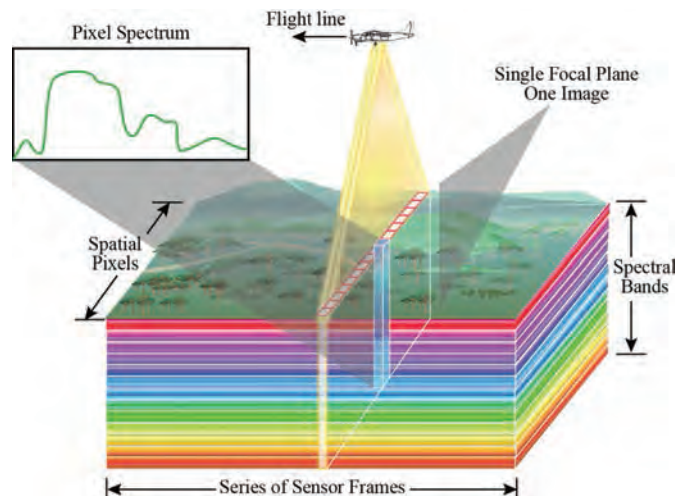


Figure 1.2 Principle of hyperspectral imaging sensing. The resulting “data cube” can be viewed as a set of co-registered images at multiple wavelength regions or as a set of spectra corresponding to each pixel of the image.

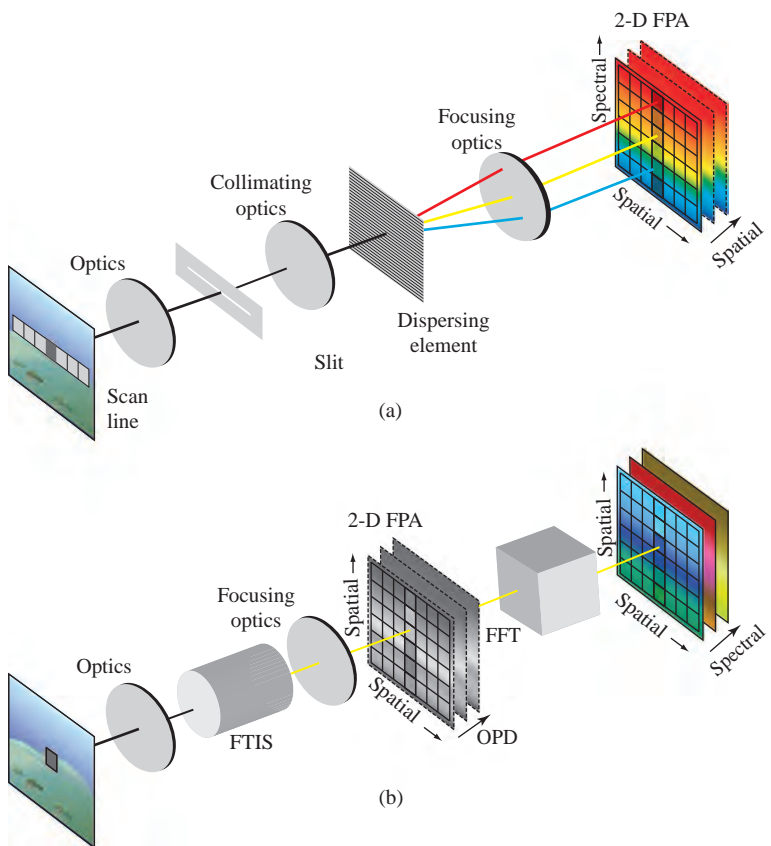


Figure 1.9 Illustration of two types of imaging spectrometers. Illustration (a) is a slit spectrometer with each data frame composed of spatial and spectral dimensions and the second spatial dimension generated through scanning the projection of the slit onto the scene. Illustration (b) is of a FTIS, with each data frame corresponding to both spatial dimensions at a particular OPD. The spectral information is recovered by taking the fast Fourier transform (FFT) of the interference data for each spatial location.

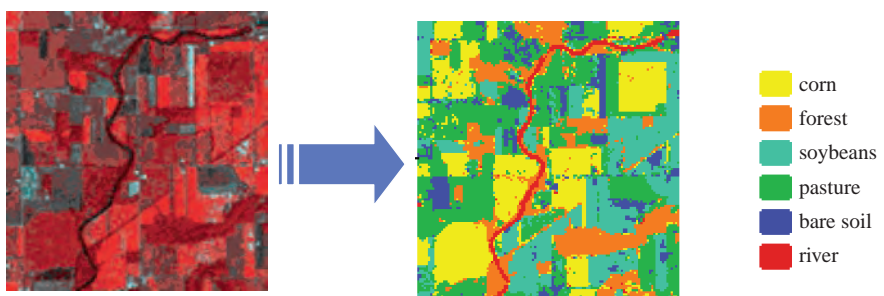


Figure 1.16 A classification map of an agricultural area created from Thematic Mapper multispectral data (Landgrebe, 2003).

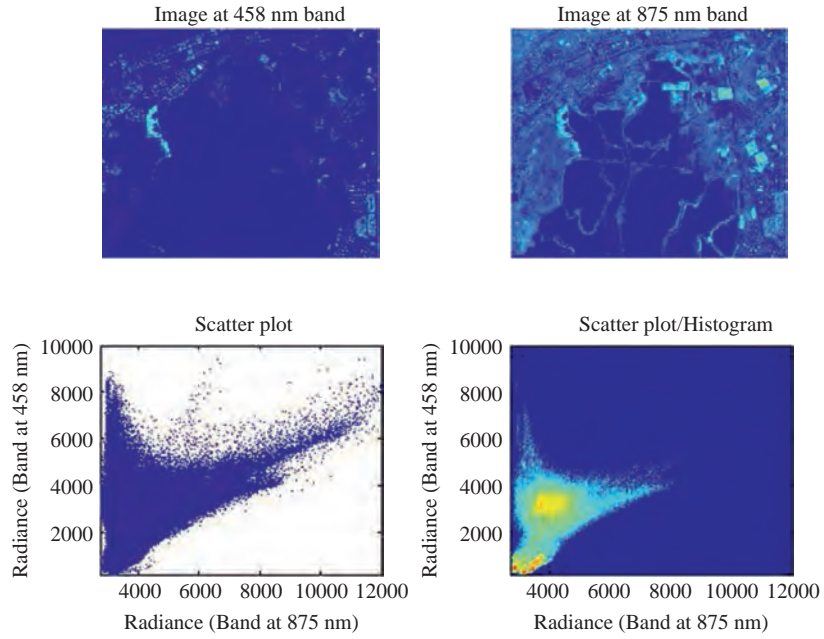


Figure 7.17 Scatter plot and two-dimensional histogram of two images corresponding to different spectral bands. Note that the scatter plot does not show any density or concentration information.

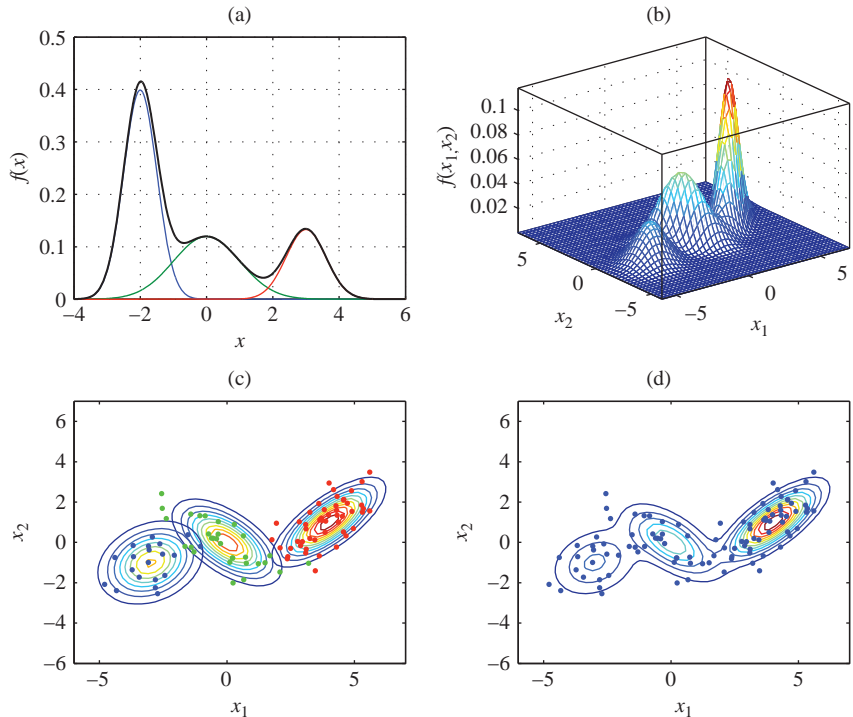


Figure 7.21 Illustration of a mixture of three Gaussian distributions. (a) Scaled Gaussian components and their sum in one dimension. (b) Example of Gaussian mixture probability density function in two dimensions. (c) Contours of the three components and sample data generated by each distribution. (d) Contours of the mixture distribution superimposed on the sample data shown in (c).

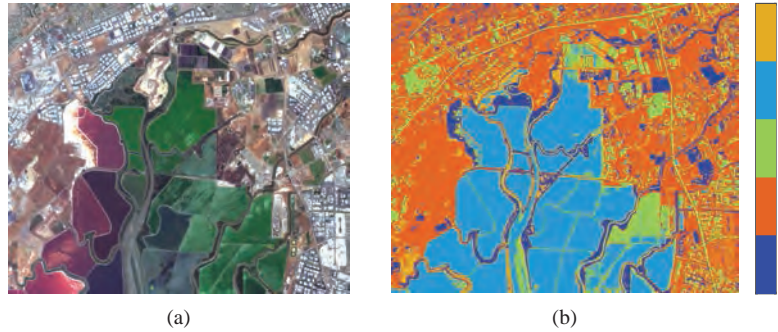


Figure 7.22 Illustration of hyperspectral image classification using the SEM algorithm and the *f1* dataset. (a) image and (b) class map for 5 classes.

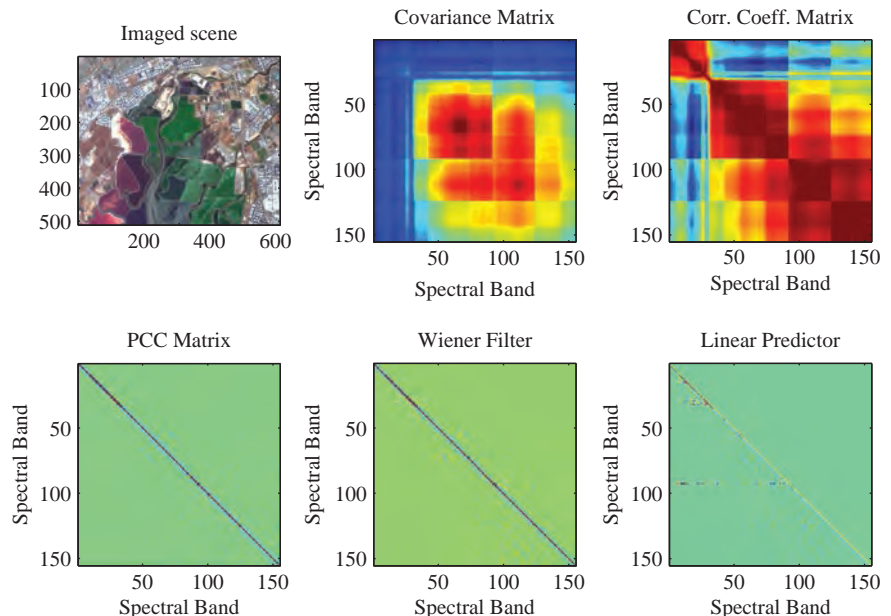


Figure 8.13 Illustration of spectral correlation properties, spectral Wiener filter, and visual to IR spectral linear predictor for the Moffett data set.

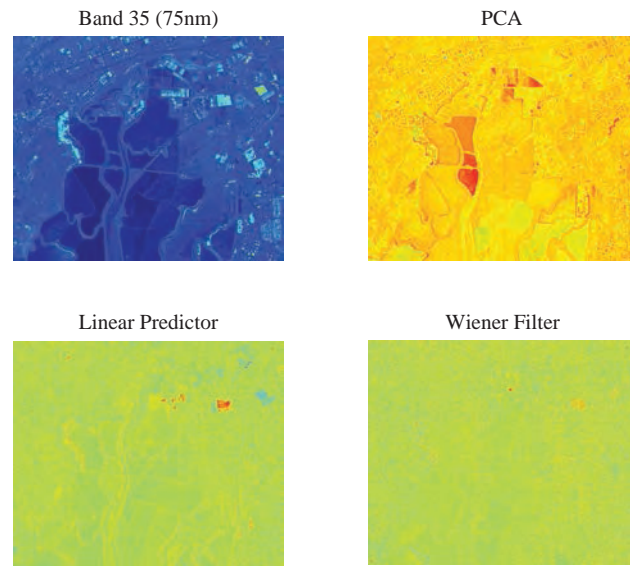


Figure 8.14 A spectral band from the Moffett data set and the corresponding images produced by PCA, the innovations representation, and the Wiener filter.

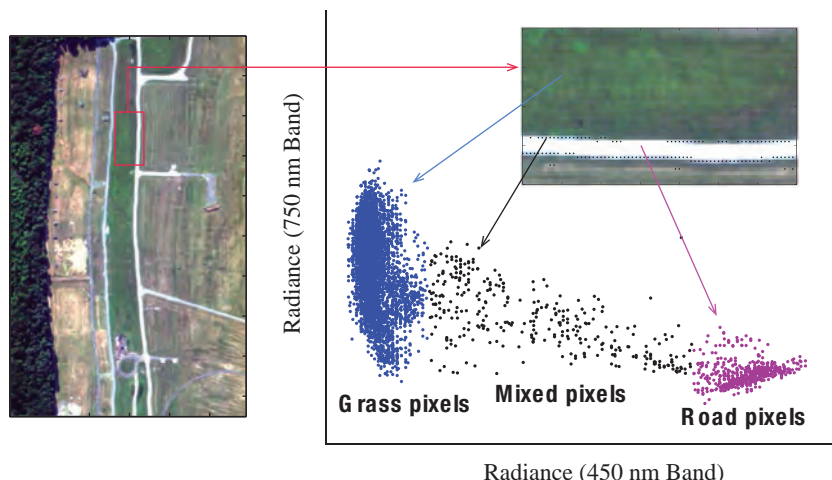
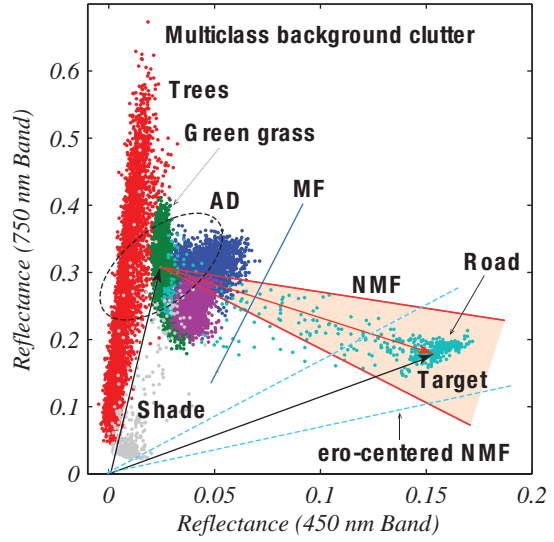


Figure 11.6 Illustration of the stochastic mixing model using grass and road spectra from a HYDICE hyperspectral imaging cube to create a scatter plot.



(a)



(b)

Figure 11.8 Scatter plot of different classes from a HYDICE data cube to illustrate the suitability of MF and NMF detectors for both subpixel and full pixel targets. The road pixels are considered as the “target class”.

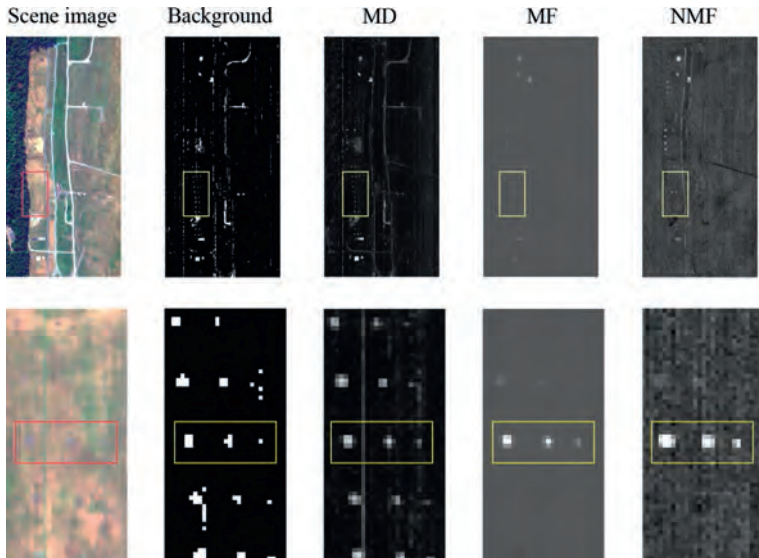


Figure 11.14 Pictorial illustration of imaged scene, background training data, and detection statistics for the AD, MF, and NMF algorithms. Images in the second row are enlargement of the images inside the yellow rectangles in the first row. The targets of interest (green tarp) are inside the yellow rectangles in the second row.

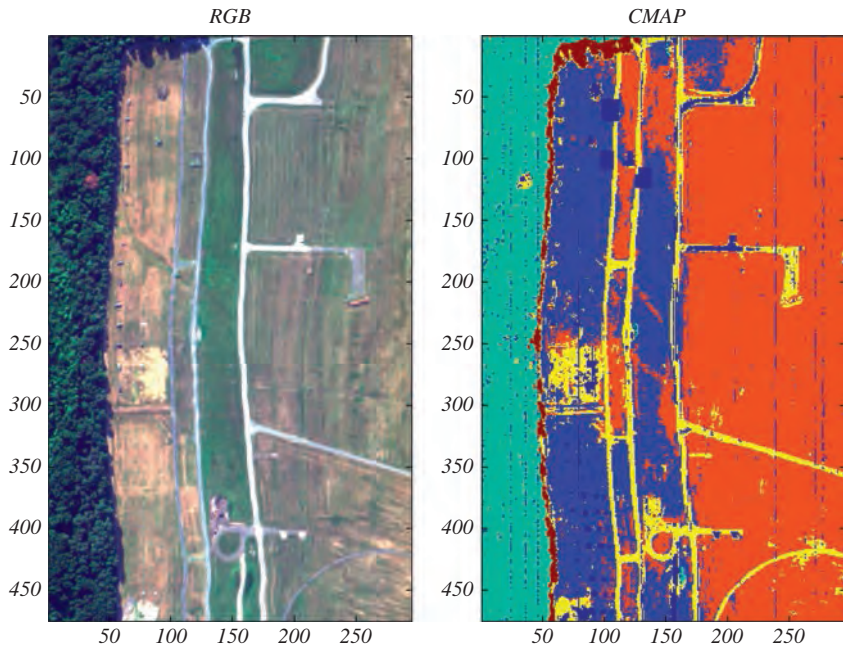


Figure 11.20 Color image of the HYDICE Forest Radiance scene and a class map obtained using the SEM clustering algorithm.

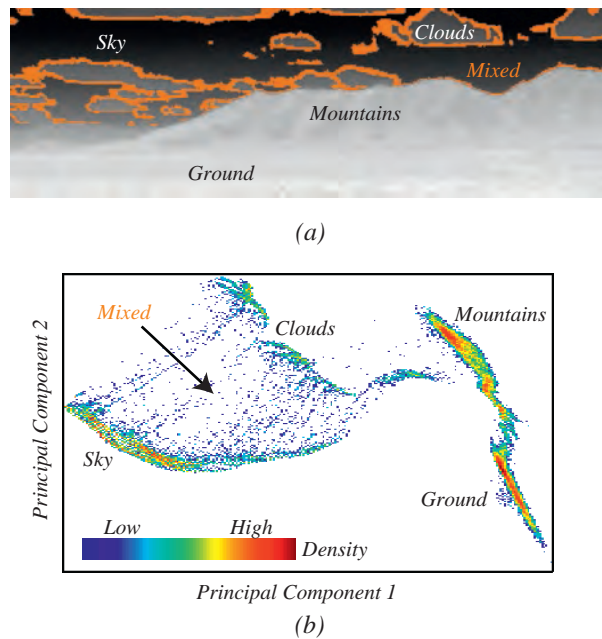


Figure 11.39 (a) Average spectral radiance for every pixel of a 128-spectral band LWIR data cube collected using the Aerospace GBSS sensor. (b) Density scatter plot (two-dimensional histogram) in the first two principal components of the LWIR cube shown in (a).

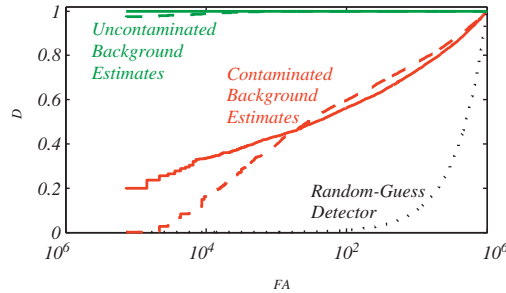
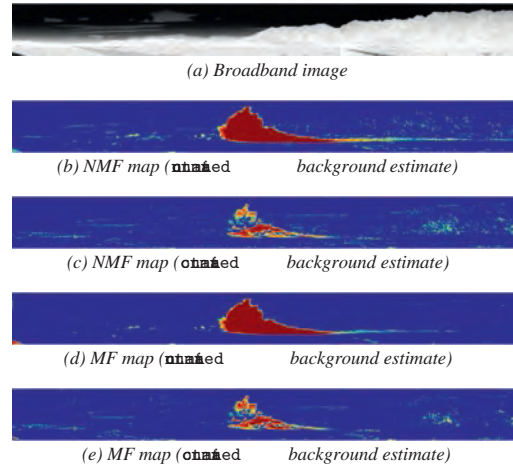


Figure 11.43 Detection images and receiver operator characteristics for a gas plume imaged by the GBSS sensor, illustrating the necessity of computing background statistics using plume-free training data. Each detection image is normalized by background response (0 to 30 dB color scale). The solid ROC curves correspond to the NMF and the dashed ROC curves to the MF.

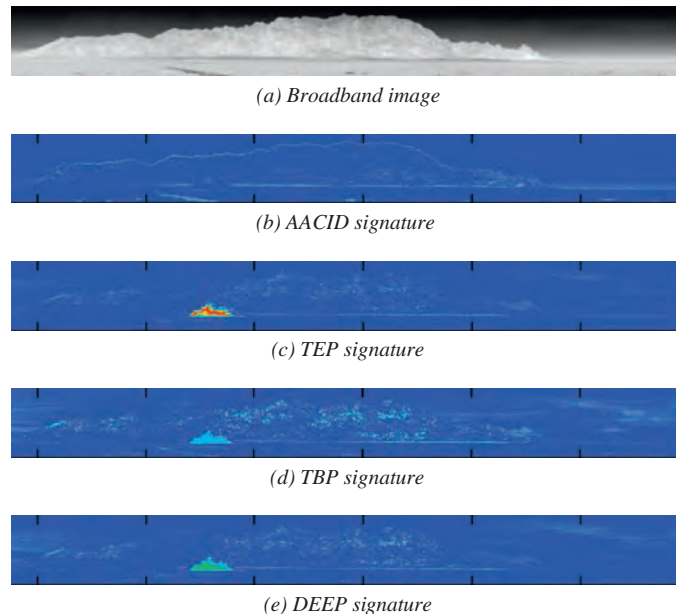


Figure 11.44 ENMF images for various chemical signatures (0 to 1 color scale). TEP was released and imaged using the Aerospace GBSS sensor; the other three chemicals are not present in the scene.